Proceedings of the

20th Particles and Nuclei International Conference PANIC2014

August 25–29, 2014

Hamburg, Germany

Editors: Alexander Schmidt, Christian Sander

Verlag Deutsches Elektronen-Synchrotron

Impressum

Proceedings of the 20th Particles and Nuclei International Conference (PANIC2014)

August 25–29, 2014, Hamburg, Germany

Conference homepage
`http://panic14.desy.de/`

Slides at
`https://indico.desy.de/event/panic14`

Online proceedings:
DOI: 10.3204/DESY-PROC-2014-04

Editors:
Christian Sander, Alexander Schmidt
March 2015
DESY-PROC-2014-04
ISBN 978-3-935702-91-1
ISSN 1435-8077

Published by
Verlag Deutsches Elektronen-Synchrotron
Notkestraße 85
22607 Hamburg
Germany

Printed by
Kopierzentrale Deutsches Elektronen-Synchrotron

Committees

Conference Chair: Matthias Kasemann

International Advisory Board

Torsten Akesson (Univ. Lund, Sweden), Ursula Bassler (CNRS-IN2P3, France), Reinhard Beck (Univ. Bonn, Germany), Sergio Bertolucci (CERN, Switzerland), Johannes Blümer (KIT, Germany), Martine Bosman (IFAE Barcelona, Spain), Philippe Chomaz (CEA, France), Luisa Cifarelli (Univ. di Bologna, Italy), Jean Cleymans (Univ. of Cape Town, South Africa), Umberto Dosselli (Frascati, Italy), George Dracoulis (ANU Canberra, Australia), Paula Eerola (Univ. of Helsinki, Finland), Masaki Fukushima (Univ. of Tokyo, Japan), Rolf-Dieter Heuer (CERN, Switzerland), Ralf Bernd Kaiser (IAEA, Austria), Matthias Kasemann (Chair, DESY, Germany), Young-Kee Kim (Univ. of Chicago, USA), Reiner Krücken (TRIUMF and UBC, Canada), Karlheinz Langanke (GSI, Germany), Nigel Lockyer (FNAL, USA), David MacFarlane (SLAC, USA), Victor Matveev (JINR Dubna, Russia), Giora Mikenberg (Weizmann, Israel), Richard Milner (MIT, U.S.A), Joachim Mnich (DESY, Germany), Hugh E. Montgomery (JLAB, USA), Tatsuya Nakada (EPFL, Switzerland), Stephan Paul (TU Munich, Germany), Mannque Rho (Hanyang Univ, South Korea), Johanna Stachel (Univ. Heidelberg, Germany), Horst Stöcker (GSI, Germany), Atsuto Suzuki (KEK, Japan), Nicholas Walker (DESY, Germany), Yifang Wang (IHEP, China), Nicolae-Victor Zamfir (ELI, Romania)

Programme Committee

Ralph Assmann (DESY, Germany), Rutger Boels (Univ. Hamburg, Germany), Will Brooks (Jeverson Lab, USA), Pierre Brun (Saclay, France), Jens Dilling (Triumf, Canada), Guido Drexlin (KIT, Germany), Laura Fabbietti (Tech. Univ. Munich, Germany), Sasha Glazov (DESY, Germany), Raphael Granier de Cassagnac (France), Michel Guidal (IPN Orsay, France), Johannes Haller (Univ. Hamburg, Germany), Stephanie Hansmann-Menzemer (Univ. Heidelberg, Germany), Dieter Horns (Univ. Hamburg, Germany), Josef Jochum (Univ. Tübingen, Germany), Andreas Jung (FNAL, USA), Ralf Kaiser (IAEA, Austria), David Kosower (Saclay, France), Kent Paschke (Virginia Univ., USA), Christian Sander (Chair, Univ. Hamburg, Germany), Alexander Schmidt (Chair, Univ. Hamburg, Germany), Thomas Schörner-Sadenius (DESY, Germany), Christoph Schwanda (OAW, Vienna, Austria), Frank Simon (Max-Planck-Inst. Munich, Germany), Andrew Sonnenschein (FNAL, USA), Hartmut Stadie (Univ. Hamburg, Germany), Raju Venugopalan (Brookhaven, USA), Janus Weil (FIAS, Univ. Frankfurt, Germany), Christian Weinheimer (Univ. Bonn, Germany), Drew Weissenberger (Jefferson Lab, USA), Dirk Zerwas (LAL Orsay, France)

Local Organizing Committee

Michaela Clayton - DESY; Manfred Fleischer - DESY; Michaela Grimm - DESY; Volker Gülzow - DESY; Magdalene Hack - University of Hamburg; Matthias Kasemann - DESY; Joachim Mnich - DESY; Kristina Price - DESY; Christian Sander - University of Hamburg; Peter Schleper - University of Hamburg; Alexander Schmidt - University of Hamburg; Thomas Schörner-Sadenius - DESY; Hartmut Stadie - University of Hamburg; Georg Steinbrück - University of Hamburg;

Preface

The PANIC Conference is a major international conference that brings together astroparticle physics, elementary particle physics and nuclear physics. The conference takes place every 3 years, and in 2014 the event was held in Hamburg (Germany). The previous conference was organised by the Massachusetts Institute of Technology (MIT) in Cambridge (Massachusetts, USA) in 2011.
This years conference was jointly organised by the Deutsches Elektronen Synchrotron (DESY) and the Institute for Experimental Physics of the University of Hamburg. One third of the 350 participants came from Germany, one third from Europe and one third from outside of Europe, it was a truly very international event. The conference took place from Monday, August 25, 2014 to Friday, August 29, 2014.
The programme included five days of plenary and parallel sessions and a poster session, all held in the main building of the University of Hamburg, right in the heart of the city of Hamburg. The social programme consisted of a reception at the Hamburg City Hall, a half-day excursion, a concert at DESY, a conference dinner, and a public evening lecture by Prof. Albrecht Wagner, former director of DESY.
During the conference, many results from the Large Hadron Collider (LHC) at CERN (Geneva, Switzerland) were presented together with final results from the experiments at the Tevatron collider at the Fermi National Accelerator Laboratory (Chicago) and at the HERA accelerator at DESY. A large number of physics studies were discussed also for an International Linear Collider (ILC) considered to be built in Japan. The conference programme included dedicated sessions on physics at the ILC and on the status of the project.
In neutrino and nuclear physics, there are a number of medium- and small-size experiments that provide highly accurate results. These experiments are often complementary to those at large accelerators at the energy frontier. The PANIC conference provided an excellent overview of these different fields.
The program was prepared in consultation with the international advisory committee (IAC). In the plenary sessions, 26 presentations of invited lectures and results from large experimental collaborations were given, while in the parallel sessions, a total of 220 talks were presented. The programme was completed by 28 posters, for which a poster contest was held. The three winning posters received a price and were presented in a dedicated plenary session.
DESY is one of the worlds leading accelerator centres. DESY researchers use the large-scale facilities at DESY and elsewhere to explore the microcosm in all its variety: high-energy particle collisions are used in elementary particle and astroparticle physics to investigate from the properties and interactions of elementary particles, and the brilliant light of state-of-the-art synchrotron sources and laser facilities is employed to study e.g.the behaviour of new types of nanomaterials or biomolecular processes that are essential to life. DESY scientists are involved in many international projects such as the LHC (experiments ATLAS and CMS), SuperKEKB (experiment Belle II), CTA and IceCube. DESY is also a central player in the preparatory work towards the next large-scale facility of particle physics, an e+e linear collider.
The particle physics and detector development group of Hamburg University studies the constituents of matter and their fundamental interactions using particle collisions at highest energies. The group is involved in detector construction, operation and data analysis of the Compact Muon Solenoid (CMS) experiment at the LHC. Research is done in several important aspects of particle physics using CMS data, from the study of the properties and production mechanisms of the top quark, the heaviest particle known today, to the search for new even heavier particles predicted by physics theories describing phenomena beyond the standard model of particle physics, such as supersymmetry.

Matthias Kasemann (conference chair), Hamburg, March 2015

Contents

Chapter 1

Plenary contributions

Neutrinos in Nuclear Physics

R. D. McKeown

Jefferson Lab, Newport News, VA, USA
Department of Physics, College of William and Mary, Williamsburg, VA, USA

DOI: http://dx.doi.org/10.3204/DESY-PROC-2014-04/305

Since the discovery of nuclear beta decay, nuclear physicists have studied the weak interaction and the nature of neutrinos. Many recent and current experiments have been focused on the elucidation of neutrino oscillations and neutrino mass. The quest for the absolute value of neutrino mass continues with higher precision studies of the tritium beta decay spectrum near the endpoint. Neutrino oscillations are studied through measurements of reactor neutrinos as a function of baseline and energy. And experiments searching for neutrinoless double beta decay seek to discover violation of lepton number and establish the Majorana nature of neutrino masses.

1 Introduction

The discovery of neutrino oscillations in the distribution of atmospheric neutrinos by the SuperKamiokande experiment in 1998 [1] was a major event in the history of neutrino physics. This result established that neutrino flavors oscillate and that at least one neutrino type has a non-zero rest mass. Subsequently, further experimental studies of neutrino oscillations and masses were pursued with increased vigor and broader scope. Soon thereafter, the Sudbury Neutrino Observatory (SNO) reported the observation of solar neutrinos via the neutral current [2]. The SNO result showed that the total neutrino flux (summed over all three flavors) is consistent with expectation in the standard solar model, and that the ν_e flux is reduced due to flavor transformations, explaining the long-standing solar neutrino puzzle. Shortly after that, the KamLAND experiment reported the observation a deficit of reactor antineutrinos [3] and subsequently a spectral distortion [4], establishing that electron antineutrinos oscillate with a large mixing angle in a manner completely consistent with expectation based on the SNO results.

In the decade since these major discoveries, there has been a great deal of effort to develop a program of experiments to further explore the properties of neutrinos. The important remaining questions include:

- What are the absolute values of neutrino masses (oscillation experiments only reveal squared mass differences Δm^2)?
- What is the correct ordering of the mass eigenstates ("normal" or "inverted" hierarchy)?
- Are the neutrino masses of a Majorana or Dirac type?
- What are the values of the mixing angles, and is there CP violation in the neutrino mixing matrix?

2 Absolute Neutrino Mass

From neutrino oscillation experiments, we now know the values of Δm^2 [5]:

$$\Delta m^2_{21} = 7.5 \times 10^{-5} \text{ eV}^2 \quad (1)$$

$$\Delta m^2_{31} = 2.4 \times 10^{-3} \text{ eV}^2. \quad (2)$$

Thus we can be sure that there is at least one neutrino mass eigenstate with a mass of at least $[\Delta m^2_{31}]^{1/2} \backsimeq 0.049$ eV. The endpoint energy in nuclear beta decay is modified by the effective neutrino mass

$$m_{\nu_e}^{(\text{eff})^2} = \sum_i |U_{ei}|^2 m^2_{\nu_i} \quad (3)$$

where the U_{ei} are neutrino mixing matrix elements the sum is over all the experimentally unresolved neutrino masses m_{ν_i}. During the last decade experiments studying tritium beta decay have constrained this effective neutrino mass to be [5]

$$m_{\nu_e}^{(\text{eff})} < 2 \text{ eV}. \quad (4)$$

So there is presently a gap between 0.05 eV and 2 eV where experiments are needed to establish the absolute mass scale of neutrinos.

The distribution of matter in the universe depends sensitively on the neutrino contribution to the total matter density. Neutrinos are very light compared to all other particles, so at the epoch of structure formation they have a non-negligible thermal velocity, which controls their free-streaming length. Since neutrinos do not clump on scales smaller than their free-streaming length this leads to smearing out of over-dense regions (structure) at small scales, leaving a characteristic imprint in the matter distribution. Current and upcoming surveys that probe the matter distribution can indirectly constrain or measure the sum of the neutrino masses. Current analyses constrain the sum of neutrino masses to be $\sum_i m_i < 0.23$eV(95%CL) [6]. In the next decade there are good prospects to reach, via multiple probes, a sensitivity at the level of $\sum_i m_i < 0.01$eV [7] . Nevertheless, it is essential to address the neutrino mass scale below 2 eV in terrestrial experiments.

The KATRIN experiment [8] is under construction at Forschungszentrum Karlsruhe and will provide measurements of the tritium endpoint spectrum with greater precision in the near future. This ambitious experiment utilizes a gaseous molecular tritium source. a pre-spectrometer to filter out lower energy electrons ($< E_0 - 0.3$ keV), a main spectrometer (resolution 0.93 eV), and a position sensitive detection system. The apparatus is 70 meters long and the main spectrometer has a diameter of 9.8 meters. The experiment will be sensitive to neutrino masses $m_{\nu_e}^{(\text{eff})} > 0.2$ eV with 90% CL (3 years running), extending the range of present knowledge by about an order of magnitude. Commissioning of the experiment is underway and KATRIN is expected to begin acquiring tritium decay data in 2016.

Improvements to the KATRIN experiment may be possible (for example using time of flight techniques) to further increase the sensitivity. However, the tritium source has reached the maximum density for transmission of the the 18 keV electrons of interest and a more sensitive spectrometer would need to be much larger than the main spectrometer of KATRIN. Therefore, it appears that another method may be necessary to make significant progress below 200 meV. A novel technique to detect the cyclotron radiation from a single electron in a uniform magnetic field using high-sensitivity microwave antennae has been proposed [9]. Preliminary R&D on this technique is in progress, and the first detection of cyclotron radiation from a single 30 keV electron has been reported at this conference and in [10].

3 Reactor Neutrinos

The neutrino mixing matrix contains 4 parameters: 3 mixing angles (θ_{12}, θ_{23}, and θ_{13}) and a CP violating phase δ_{CP}. The combination of solar neutrino experiments and KamLAND have provided a value of $\sin^2\theta_{12} \backsimeq 0.31$ [5]. In addition, accelerator based long baseline neutrino experiments determine $\sin^2\theta_{23} \backsimeq 0.39$ [5]. While there is room for improvement in these determinations, much attention has been focused in recent years on measuring the remaining angle θ_{13}. This problem has been effectively attacked by three reactor neutrino experiments: Double CHOOZ [11], RENO [12], and Daya Bay [13].

The formula for survival of electron neutrinos (or antineutrinos) in the 3 flavor case is given by

$$\begin{aligned} P(\nu_e \to \nu_e) &= 1 - \sin^2 2\theta_{13}(\cos^2\theta_{12}\sin^2\Delta_{31} + \sin^2\theta_{12}\sin^2\Delta_{32}) \\ &\quad - \cos^4\theta_{13}\sin^2 2\theta_{12}\sin^2\Delta_{12} \end{aligned} \tag{5}$$

where $\Delta_{ij} \equiv \Delta m^2_{ij} L/4E_\nu$. Note that the 2 terms oscillate with different "frequencies" depending on the values of the Δm^2_{ij}. Thus one can choose the baseline L to maximize (or minimize) the sensitivity to particular Δm^2_{ij}. For an average reactor antineutrino energy of 4 MeV and a value of $\Delta m^2_{32} = (2.43 \pm 0.13) \times 10^{-3}$ eV^2 one finds that the optimum distance for the first minimum is $L \simeq 2000$ m.

While all three reactor experiments have reported consistent values of θ_{13}, the results from the Daya Bay experiment in China are the most precise. The Daya Bay nuclear power plant consists of 6 reactor cores in two groups (Daya Bay and Ling Ao) with a total thermal power capacity of 17.6 GW. The experiment includes 8 antineutrino detectors, each with 20 Tons of Gd-loaded liquid scintillator. Two detectors are located near (364 m) the 2 Daya Bay reactors and two are located near ($\sim$ 500 m) the 4 Ling Ao reactors. Four detectors are located in the far experimental hall at 1912 m from the Daya Bay cores and 1540 m from the Ling Ao cores. The near detectors monitor the antineutrino fluxes from the two reactor groups so that the far detectors are sensitive to the degree of neutrino oscillations at the longer baseline. This method enables measurement of the oscillation effect with only slight sensitivity to the absolute flux of antineutrinos.

The Daya Bay experiment took data with only 6 detectors deployed from December 2011 to July 2012. In summer 2012, two additional detectors were installed, one at the Ling Ao location and one at the far location, which completed the final 8 detector configuration of the experiment described above. Data taking resumed after October 2012. New results, based on the complete data set of the 6-AD period with the addition of the 8-AD period from October 2012 to November 2013 (a total of 621 days) were recently reported [14]. The Daya Bay data display a substantial deficit in measured flux at the far site relative to the near sites, and also a distortion of the measured energy spectrum at the far site, consistent with the interpretation of neutrino oscillations as shown in Fig. 1.

The neutrino oscillation parameters are extracted from a fit to the rates and relative spectral shapes observed at the near and far sites, with the overall normalization of the flux as an independent parameter. The results yield the best fit values

$$\sin^2 2\theta_{13} = 0.084 \pm 0.005 \tag{6}$$

$$\Delta m^2_{ee} = 2.44^{+0.10}_{-0.11} \times 10^{-3}\ (\text{eV})^2 \tag{7}$$

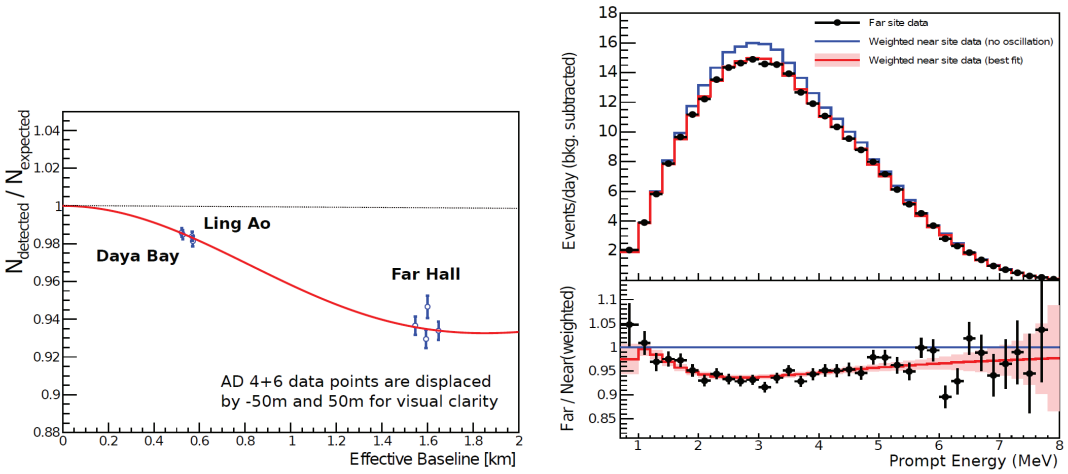

Figure 1: Daya Bay results reported in [14]. (left) Ratio of the detected to expected rates at the 8 antineutrino detectors (ADs) located in three experimental halls as a function of effective baseline. The expected signal accounts for the best-fit reactor antinuetrino flux normalization. The fitted oscillation survival probability is given by the red curve. (right) The top panel shows the measured background-subtracted spectrum at the far site compared to the expected spectrum based on the near site data both without oscillation and with the best-fit oscillation included. The bottom panel shows the ratio of the far site spectrum to the weighted near site spectrum. The red curve shows the expectation at the best-fit oscillation values from the rate and spectral analysis.

where Δm^2_{ee} is defined by $\sin^2(\Delta {m_{ee}}^2 L/4E_\nu) \equiv \cos^2\theta_{12}\sin^2\Delta_{31} + \sin^2\theta_{12}\sin^2\Delta_{32}$. This value of Δm^2_{ee} is consistent, with comparable uncertainty, to the value of $\Delta m^2_{\mu\mu}$ determined by muon neutrino disappearance experiments.

The Daya Bay collaboration has also recently reported a measurement of the absolute flux of antineutrinos [14], shown in Fig. 2. This first precision measurement at larger average baseline (573 m) is consistent with 21 previous short baseline experiments, indicating a flux deficit of $5.3 \pm 2.2\%$ relative to recent model predictions [15, 16].

New reactor neutrino projects [17], JUNO and RENO50, are being planned by international collaborations to constrain neutrino oscillation parameters more precisely and to determine the mass hierarchy. The RENO50 experiment would be sited 50 km away from the Hanbit(Yonggwang)nuclear plant in South Korea. The JUNO experiment would be sited in southern China, 53 km equidistant from two new nuclear power plants currently under construction: Yangjiang (17.4 GWth) and Taishan (18.4 GWth). For JUNO, spherical 20kT liquid scintillator detector would be deployed at a depth of 700 m, with almost complete photocathode coverage to achieve the energy resolution of 3% necessary to see the interference pattern in the energy spectrum for mass hierarchy determination. After 6 years of running, JUNO aims to achieve a $\Delta\chi^2 = 14$ determination of the mass hierarchy. In addition, the values of ${\Delta m_{12}}^2$, ${\Delta m_{23}}^2$ and $\sin^2\theta_{12}$ will be measured with substantially higher precision than at present.

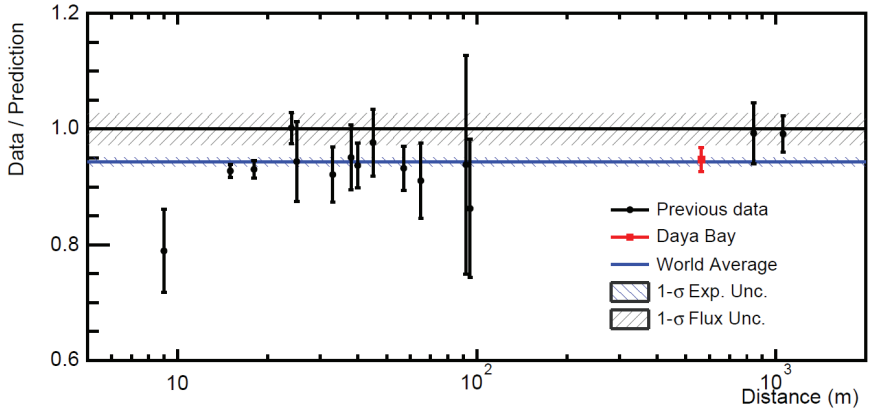

Figure 2: Measurements of antineutrino flux as reported in [14]. The reactor antineutrino interaction rate of the 21 previous short-baseline experiments as a function of the distance from the reactor, normalized to the Huber+Mueller model prediction [15, 16]. The Daya Bay result is placed at the effective baseline of 573 m. The rate is corrected for the survival probability at the distance of each experiment, assuming standard three-neutrino oscillation. The horizontal bar (blue) represents the global average of all experiments and its 1σ uncertainty. The 2.7% reactor flux uncertainty is shown as a band around unity.

4 Neutrinoless Double Beta Decay

Double beta decay is a rare transition between two nuclei with the same mass number A involving change of the nuclear charge Z by two units. The decay can proceed only if the initial nucleus is less bound than the final one, and both must be more bound than the intermediate nucleus. These conditions are fulfilled in nature for many even-even nuclei, and only for them. Typically, the decay can proceed from the ground state (spin and parity always 0^+) of the initial nucleus to the ground state (also 0^+) of the final nucleus, although the decay into excited states (0^+ or 2^+) is in some cases also energetically possible. Such nuclei can decay by the second order weak process, known as $2\nu\beta\beta$ in which two antineutrinos as well as two electrons are emitted. The summed energy of the two electrons is a continuous distribution ranging from $2m_e$ to the endpoint energy E_0 defined by the Q value of the decay. This process conserves lepton number, takes place for both Dirac and Majorana neutrinos, and is the rarest decay process in nature for which half-lives have been measured.

For neutrinoless double beta decay, $0\nu\beta\beta$, the distribution of summed β energies would exhibit a distinctive monoenergetic peak at the endpoint E_0. If it occurs, this process implies nonconservation of lepton number and would imply that neutrinos were Majorana type fermions. The half life for this process can be written

$$T_{1/2}^{0\nu\,-1} \;=\; G^{0\nu}(E_0, Z)\left|M^{0\nu}\right|^2 \langle m_{\beta\beta}\rangle^2 \tag{8}$$

where $G^{0\nu}$ is the exactly calculable phase space integral, $\langle m_{\beta\beta}\rangle$ is the effective neutrino mass and $M^{0\nu}$ is the nuclear matrix element (calculated using nuclear models). The effective neutrino

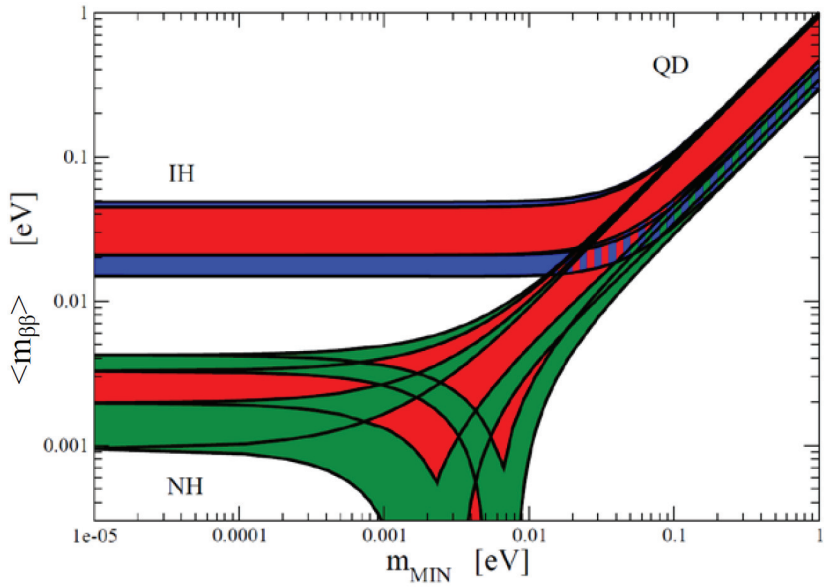

Figure 3: Allowed values of $\langle m_{\beta\beta} \rangle$ as a function of the lightest neutrino mass for the inverted (IH) and normal (NH) hierarchies (QD stands for "quasidegenerate"). The red, blue and green bands correspond to different allowed regions for the unknown CP violating phases in Eq. 9 and allowed 1σ variation in the other known neutrino parameters. (From the Particle Data Group [5].)

mass is

$$\langle m_{\beta\beta} \rangle = | \sum_i {U_{ei}}^2 m_{\nu_i} | \ , \tag{9}$$

where the sum is only over light neutrinos ($m_i < 10$ MeV), and contains the sensitivity to the neutrino masses and the elements of the neutrino mixing matrix U_{ei}. The U_{ei} depend upon the mixing angles discussed above, but also two additional phases that do not contribute to neutrino oscillation experiments. The range of allowed values of $\langle m_{\beta\beta} \rangle$ is indicated in Fig 3.

As can be seen in Fig. 3 the case of inverted mass hierarchy can lead to substantial values of $\langle m_{\beta\beta} \rangle$ even for very light values of the smallest neutrino mass. Thus there is considerable interest in performing experiments to address this region of parameter space. The current set of worldwide experimental efforts is summarized in Table 1. These efforts aim to achieve a sensitivity exceeding 10^{26} years in the next 5 years, and provide crucial information on background reduction in order to assess the feasibility of scaling the next generation experiment up to the Tonne scale. Complete coverage of the inverted mass hierarchy band in Fig. 3 will require multi-Tonne scale experiments.

Table 1: Current double beta decay projects, the fiducial isotopic mass, and the currently achieved half-life limit (90% CL).

Project	Isotope	Isotope fiducial mass (kg)	Currently achieved $T_{1/2}$ limit (10^{26} years)
CUORE	^{130}Te	206	> 0.028 [18]
Majorana	^{76}Ge	24.7	
GERDA	^{76}Ge	18-20	> 0.21 [19]
EXO200	^{136}Xe	79	> 0.11 [20]
NEXT-100	^{136}Xe	100	
SuperNEMO	^{82}Se, +	7	> 0.001 [21]
KamLAND-Zen	^{136}Xe	434	> 0.19 [22]
SNO+	^{130}Te	160	
LUCIFER	^{82}Se	8.9	

5 Summary

The study of neutrino properties with nuclear physics experiments is a very active field, with many experiments in progress and others in the planning stage. The absolute neutrino mass should be constrained by KATRIN to 0.2 eV before the end of the decade. Beyond KATRIN, R&D on the Project 8 method may offer a window to higher sensitivity measurements in the future. The present generation of reactor experiments will continue to reduce the uncertainties in θ_{13} and $\Delta {m_{ee}}^2$, and further study the flux and spectrum of reactor antineutrinos. A future experiment, JUNO, will be constructed in China with excellent potential to address the neutrino mass hierarchy. And an impressive suite of double beta decay experiments is underway that will extend the sensitivity towards the inverted mass hierarchy region in $\langle m_{\beta\beta} \rangle$.

These are indeed exciting times in the field of neutrino physics, with historic discoveries in the recent past, and the promise of much more to come in the future.

Acknowledgments

The recent Daya Bay results were first reported by Dr. Chao Zhang at the Neutrino 2014 conference, and I am very grateful to Dr. Zhang for supplying me with this material. The financial support of the U.S. National Science Foundation grant PHY-1205411 is gratefully acknowledged along with the support of the U.S. Department of Energy, Office of Science, Office of Nuclear Physics under contract DE-AC05-06OR23177.

References

[1] Y. Fukuda, *et al.*, Phys. Rev. Lett. **81**, 1562 (1998).

[2] Q. R. Ahmad *et al.*, Phys. Rev. Lett. **89**, 011301 (2002).

[3] K. Eguchi *et al.*, Phys. Rev. Lett. **90**, 021802 (2003).

[4] T. Araki *et al.*, Phys. Rev. Lett. **94**, 081801 (2005).

[5] J. Beringer *et al.* (Particle Data Group), Phys. Rev. **D86**, 010001 (2012).

[6] P. A. R. Ade, *et al.*, Astron. Astrophys. DOI: 10.1051/0004-6361/201321591 (2014) .

[7] K. N. Abazajian, et al., Astropart. Phys. 35, 177 (2011).

[8] G. Drexlin, *et al.*, Advances in High Energy Physics, 2013, Article ID 293986 (2013) .

[9] J. Formaggio and B. Monreal, Phys. Rev. D **80**, 051301(R), 2009.

[10] D. M. Asner, *et al.*, arxiv: 1408.5362 (2014).

[11] Y. Abe, *et al.*, Phys. Rev. D **86**, 052008 (2012).

[12] J. K. Ahn, *et al.*, Phys. Rev. Lett. 108, 191802 (2012).

[13] F. P. An, *et al.*, Phys. Rev. Lett. **108**, 171803 (2012); F. P. An, *et al.*, Phys. Rev. Lett. **112**, 061801 (2014); F. An, *et al.*, Nucl. Instr. Meth. A. **685**, 78 97 (2012); F. P. An, *et al.*, Chinese Phys. C. **37**, 011001 (2013). 569-647 (2003).

[14] Chao Zhang, https://indico.fnal.gov/getFile.py/access?contribId=256&sessionId=15&resId=0&materialId=slides&confId=8022 and to be published.

[15] P. Huber, Phys. Rev. C **84**, 024617 (2011).

[16] Th. A. Mueller, *et al.*, Phys. Rev. C **83**, 054615 (2011).

[17] L. Wen, https://indico.fnal.gov/materialDisplay.py?contribId=376&sessionId=15&materialId=slides&confId=8022 and to be published.

[18] E. Andreotti *et al.*, Astropart. Phys. **34**, 822 (2011).

[19] M. Agostini *et al.*, Phys. Rev. Lett. **111**, 122503 (2013) .

[20] J.B. Albert *et al.*, Nature **510**, 229-234 (2014).

[21] R. Arnold, *et al.*, Phys. Rev. D **89**, 111101 (2014).

[22] A. Gando *et al.*, (KamLAND-Zen Collaboration)] Phys. Rev. Lett. **110**, 062502 (2013).

Hadron structure from lattice QCD - outlook and future perspectives

Constantia Alexandrou

Department of Physics, University of Cyprus, PO Box 20537, 1678 Nicosia, Cyprus,
Computation-based Science and Technology Research Center, Cyprus Institute, 20 Kavafi Str., Nicosia 2121, Cyprus,
NIC, DESY, Platanenallee 6, D-15738 Zeuthen, Germany

DOI: http://dx.doi.org/10.3204/DESY-PROC-2014-04/307

We review results on hadron structure using lattice QCD simulations with pion masses close or at the physical value. We pay particular attention to recent successes on the computation of the mass of the low-lying baryons and on the challenges involved in evaluating energies of excited states and resonance parameters, as well as, in studies of nucleon structure.

1 Introduction

An impressive progress in algorithms and increased computational resources have allowed lattice QCD simulations with dynamical quarks with masses fixed at their physical values. Such simulations remove the need for a chiral extrapolation, thereby eliminating a significant source of a systematic uncertainty that has proved difficult to quantify in the past. However, new challenges are presented: An increase of statistical noise leads to large uncertainties on most of the observables of interest. New approaches to deal with this problem are being developed that include better algorithms to speed up the computation of the quark propagators, as well as, efficient (approximate) ways to increase the statistics. Another challenge is related to the fact that most of the particles become unstable if the lattice size is large enough and methods to study decays on a finite lattice in Euclidean time need further development.

In this talk we review recent results on hadron structure obtained using improved discretization schemes, notably Wilson-type fermion actions and domain wall fermions. In particular, the Wilson-type twisted mass fermion (TMF) action is particularly suitable for hadron structure studies, mainly due to the automatic $\mathcal{O}(a)$ improvement, where a is the lattice spacing. Several TMF ensembles have been produced including an ensemble simulated with two degenerate light quarks ($N_f = 2$) with mass being approximately the physical value, which, for technical reasons, also includes a clover term in the action but avoids smearing of the gauge links [1]. We will refer to this ensemble as the 'physical point ensemble' and present a number of new results. The other TMF ensembles are simulated with light quarks having masses larger than physical but where simulations are performed for three values of a allowing to study the dependence on the lattice spacing and to take the continuum limit. These ensembles include simulations with strange and charm quarks in the sea ($N_f = 2 + 1 + 1$) besides $N_f = 2$ TMF ensembles. In particular, we will use an $N_f = 2 + 1 + 1$ ensemble having a pion mass $m_\pi = 373$ MeV

to study lattice systematics by performing a high statistics analysis including all disconnected contributions to key nucleon observables.

2 Lattice formalism

An *ab Initio* non-perturbative solution of Quantum Chromodynamics (QCD) is based on defining the theory on a four-dimensional Euclidean lattice that ensures gauge invariance. While this approach allows a direct simulation of the original theory, it introduces systematic uncertainties. These so called lattice artifacts need to be carefully investigated before lattice QCD results can be compared to observables. In summary, in order to obtain final results in lattice QCD we need to take into account the following:

- Due to the finite lattice spacing, simulations for at least three values of a are needed in order to take the continuum limit $a \to 0$.
- Due to the finite lattice volume $L^3 \times T$, simulations at different volumes are needed in order to take the infinite volume limit $L \to \infty$. For zero-temperature calculations, as the ones reported here, the temporal extent T is typically twice the spatial extent L.
- Due to the tower of QCD eigenstates entering a typical correlation function one needs a careful identification of the hadron state of interest. How severe this so called contamination due to the excited states is differs depending on the observable e.g. for the nucleon axial charge g_A is found to be minimal, while for the σ-terms is large.
- In most hadron structure calculations contributions arising from the coupling of e.g. the electromagnetic current to sea quarks are neglected. These so called disconnected contributions are technically difficult to evaluate and have large gauge noise. They thus require new techniques and much larger statistics as compared to the connected contributions. Taking advantage of new approaches that are particularly suited for new computer architectures such as graphic cards (GPUs) the evaluation of these diagrams to sufficient accuracy has become feasible. This has been demonstrated for pion masses of about 300 MeV to 400 MeV [2, 3, 4, 5]. Their applicability for the physical point is being tested.
- Up to very recently, lattice QCD simulations were performed at larger than physical values of the light quark masses and thus the results required chiral extrapolation. Simulations with light quark masses fixed to their physical values are now feasible, which eliminates a systematic error inherent in all lattice QCD computations in the past. However, most lattice QCD results at the physical point are still preliminary since lattice artifacts have not been studied to the required accuracy. This issue is currently being addressed.

In order to evaluate hadron masses one needs the computation of two-point functions. For a hadron h we construct the two-point function of momentum $\mathbf{p}$ by acting on the vacuum with a creation operator $J_h^\dagger$ that has the quantum numbers of h

$$\langle J_h(t_s) J_h^\dagger(0)\rangle = \sum_{n,\mathbf{x}} e^{i\mathbf{p}.\mathbf{x}} \langle 0|J_h\, e^{-H_{QCD} t_s}|n><n|J_h^\dagger|0\rangle \quad (1)$$

$$= \sum_n |\langle 0|J_h|n\rangle|^2 e^{-E_n t_s} \overset{t_s\to\infty;\mathbf{p}=\mathbf{0}}{\longrightarrow} |\langle 0|J_h|h\rangle|^2\, e^{-m_h t_s}, \quad (2)$$

which yields its mass for $\mathbf{p} = \mathbf{0}$ in the large Euclidean time limit. Note that the noise to signal increases with t_s e.g. like $e^{(m_h - \frac{3}{2}m_\pi)t_s}$ for a baryon and thus in any lattice QCD computation there is a delicate balance between taking the large Euclidean time limit and controlling the gauge noise. So called smearing techniques are developed that allow the construction of interpolating fields that have larger overlap with the ground state and equivalently smaller overlap with excited states so that the latter are damped out faster.

3 Recent achievements

A number of collaborations are currently producing simulations with physical values of the quark mass with each collaboration typically using a different $\mathcal{O}(a)$-improved discretization scheme. Notably, the MILC [6], BMW (Budapest-Marseille-Wuppertal) [7] and ETM (European Twisted Mass) [1] collaborations have already generated simulations with light quark masses fixed to their physical value using staggered, clover and twisted mass fermions, respectively. Clover gauge configurations have also been produced by the QCDSF [8] and PACS-CS [9] collaborations at near physical pion mass value. Recently the RBC/UKQCD collaboration reported results using domain wall fermions (DWF) simulated with physical values of the light quark masses [10]. These recent developments are paving the way for lattice QCD to provide results, which can be directly compared to experimental measurements.

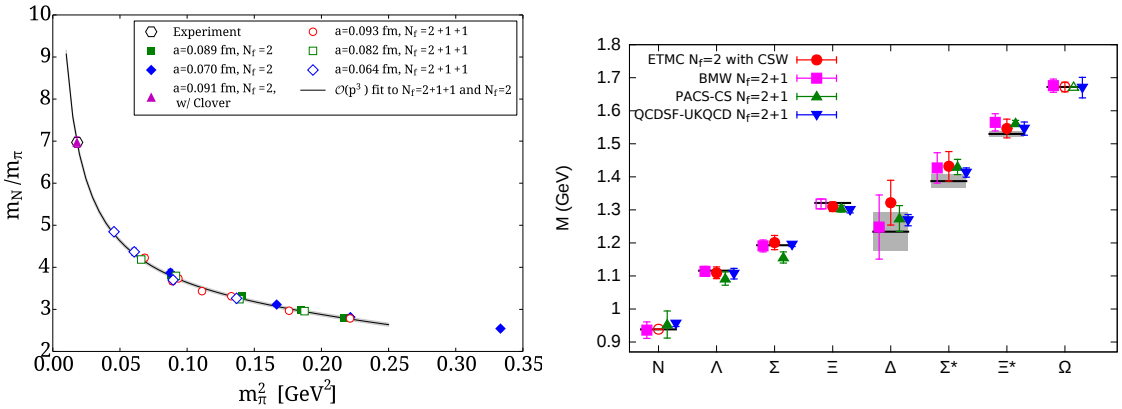

Figure 1: Left: Results on the ratio of the proton to the pion mass versus m_π^2 using TMF. The solid line is a leading oder chiral fit using $m_\pi < 300$ MeV excluding the value at the physical point. Right: Lattice QCD results on the octet and decuplet baryon masses compared to the experimental values shown by the horizontal bands. Results by the ETM collaboration are shown in red circles for the physical point ensemble [11]. Also shown are results using clover fermions from BMW [12] (magenta squares), from PACS-CS [13] (green triangles), and from QCDSF-UKQCD [14] (blue inverted triangles). Open symbols show the baryon mass used as input to the calculations.

In Fig. 1 we show the ratio of the nucleon mass to the pion mass m_N/m_π versus m_π^2 for a number of $N_f = 2$ and $N_F = 2 + 1 + 1$ TMF ensembles including the one with the physical point ensemble (with pion mass $m_\pi = 130$ MeV, $a = 0.094$ fm and $L = 4.5$ fm) for which the dimensionless ratio m_N/m_π agrees with its experimental value. In the same figure we also

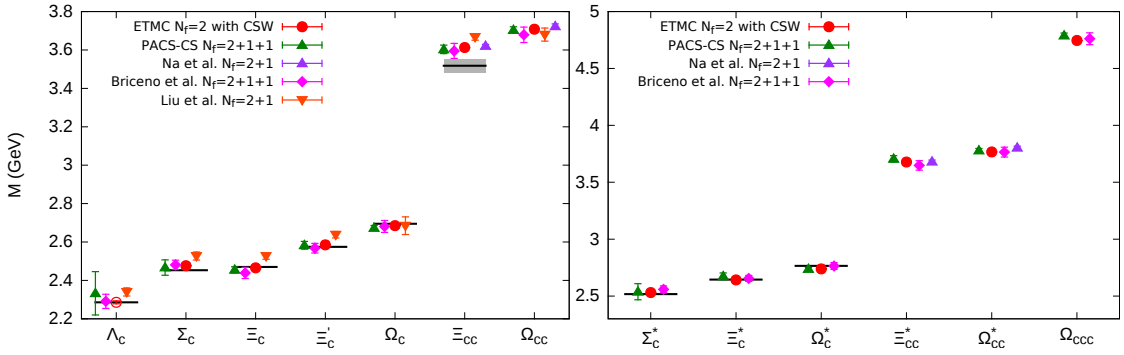

Figure 2: Results by ETMC are shown in red circles for the mass of the spin-1/2 (left) and spin-3/2 (right) charmed baryons for the physical point ensemble. Included are results from various hybrid actions with staggered sea quarks from Refs. [15] (purple triangles), [16] (magenta diamonds) and [17] (orange inverted triangles). Results from PACS-CS [18] are shown in green triangles.

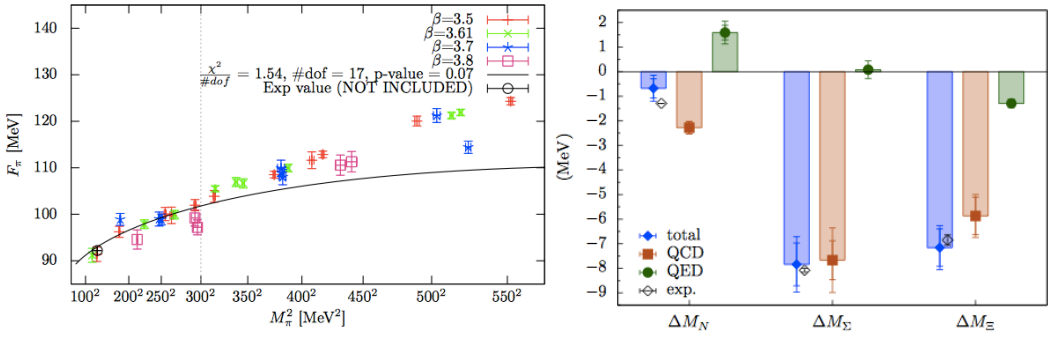

Figure 3: Left: Results on the pion decay constant f_π by BMW. The solid line is the result of fitting NLO SU(2) chiral perturbation theory for $m_\pi < 300$ MeV, taken from Ref. [7]. Right: Baryon spectrum with mass splitting by BMW taken from Ref. [21].

show results on the low-lying baryon spectrum from the ETM, BMW, PACS-CS and QCDSF-UKQCD collaborations. The set of TMF results shown in Fig. 1 is obtained using the physical point ensemble, thus requiring no chiral extrapolation, reducing drastically the systematic error that was found to be dominated by the chiral extrapolation in an earlier study using TMF [19]. These results are, however, obtained at one lattice spacing and volume. The analysis of Ref. [19] has shown that lattice artifacts both due to the finite volume and lattice spacing a are small and thus the values obtained for the physical point ensemble are expected to have small lattice artifacts. This is indeed corroborated by the fact that the 'raw' lattice data agree with the experimental values [11]. In Fig. 2 we show the corresponding results for the mass of the charmed baryons using the physical point ensemble in the case of TMF. As can be seen, the known values of the masses of the charmed baryons are reproduced and thus our computation

provides a prediction for the yet unmeasured masses. Our preliminary values for the Ξ^*_{cc} is 3.678(8) GeV, for the Ω^+_{cc} is 3.708(10) GeV, for Ω^{*+}_{cc} 3.767(11) GeV and for Ω^{++}_{ccc} 4.746(3) GeV.

The BMW collaboration has produced a number of ensembles using $N_f = 2 + 1$ clover improved Wilson fermions with HEX smearing. They represent the most comprehensive set of ensembles for light pion masses close to and at the physical point. Their results on the pion decay constant f_π are shown in Fig. 3. Fitting to NLO SU(2) chiral perturbation theory using pion masses up to 300 MeV they reproduce the physical value of f_π.

The BMW and QCDSF-UKQCD [20] collaborations investigated the mass splitting due to isospin breaking and electromagnetic effects. In Fig. 3 we show the results on the nucleon, Σ and Ξ baryons by the BMW collaboration [21] where isospin and electromagnetic effects were treated to lowest order. The agreement with the experimental values is a spectacular success of lattice QCD.

4 Challenges and future perspectives

The results shown in the previous section highlight the success of lattice QCD and the promise it holds to provide insight on many other observables. We will briefly discuss some of the challenges that need to be addressed in order for this to happen.

4.1 Excited states and resonances

In order to go beyond the low-lying spectrum one needs a formulation to extract excited states. The standard approach is to use a variational basis of interpolating fields to construct a correlation matrix of two-point functions:

$$G_{jk}(t_s) = \langle J_j(t_s) J^\dagger_k(0) \rangle \, , j, k = 1, \ldots N \tag{3}$$

and then solve the generalized eigenvalue problem (GEVP) defined by

$$G(t) v_k(t; t_0) = \lambda_k(t; t_0) G(t_0) v_k(t; t_0) \rightarrow \lambda_k(t; t_0) = e^{-E_k(t-t_0)} \quad , \tag{4}$$

which yields the N lowest eigenstates.

A lot of effort has been devoted to construct appropriate bases using lattice symmetries by e.g. the Hadron Spectrum Collaboration. In order to determine the energy of an excited state one: i) must extract all states lying below the state of interest, ii) include disconnected diagrams, iii) treat appropriately resonances and unstable particles that require including multi-hadron states. Given the increased complexity of the problem it comes with no surprise that the calculations performed so far have not reached the maturity of ground state mass computations. In Fig. 4 we show results obtained on the ρ-meson excited spectrum [22] at $m_\pi = 400$ MeV, as well as, on the width of the ρ-meson using using $N_f = 2 + 1$ clover fermions and 3 asymmetric lattices [23]. These results, although still at larger than physical pion masses, provide a promising framework for the study of unstable particles.

4.2 Nucleon Structure

In order to evaluate hadron matrix elements one needs the appropriate three-point functions. There are two contributions we typically need to evaluate: the so called connected and disconnected parts, the former having the current coupled to a valence quark, while the later to a sea

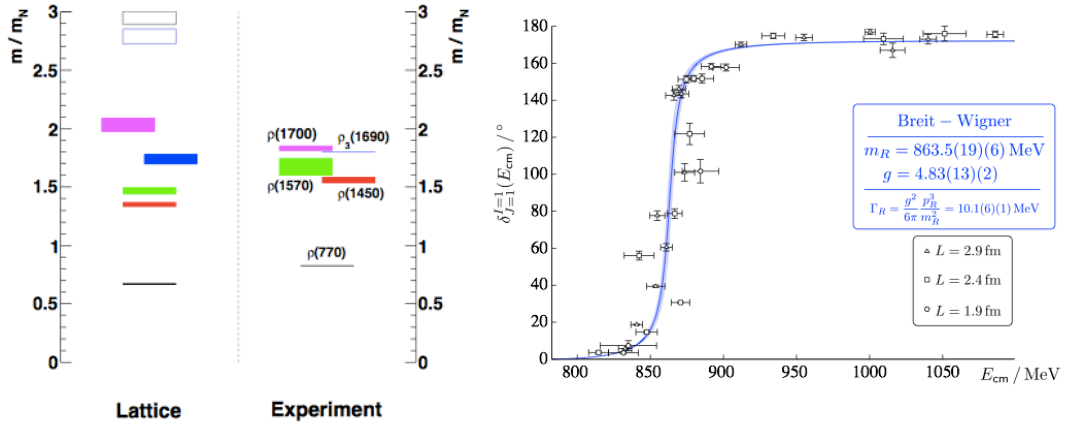

Figure 4: Left: Excited states of the ρ-meson at $m_\pi \sim 400$ MeV at one lattice spacing and one lattice volume, compared to experiment [22]. Right: The ρ-meson width, taken from Ref. [23].

quark. Methods to evaluate the connected contribution are well developed see e.g. [24]. The disconnected contributions are much more demanding for technical reasons but also because they are prone to large gauge noise. Thus in most hadron structure computations they were neglected.

4.2.1 Axial charges

Some important nucleon observables only need the connected part. These are isovector quantities for which the disconnected contributions vanish in the isospin limit. The nucleon axial charge g_A is extracted from the nucleon matrix element of the isovector axial-vector current and thus it is protected from disconnected contributions. It is also well-determined experimentally from β-decays and can be extracted directly at zero momentum transfer squared q^2 from $\langle N(\mathbf{p}')|j_A|N(\mathbf{p})\rangle|_{q^2=0}$. It thus comprises an ideal benchmark quantity for lattice QCD.

We show in Fig. 5 results on the nucleon axial charge using the TMF ensembles. They are the 'raw' lattice QCD data in the sense that they have not been volume corrected nor extrapolated to the continuum limit, but have been non-perturbatively renormalized. They are obtained by fitting to the plateau of an appropriately defined ratio of the three- to two-functions using a sink-source separation of about 1 fm. Within the current errors no dependence on the lattice spacing and volume is observed. While results at higher pion mass underestimate g_A, a fact observed by all lattice QCD collaborations, at the physical point we find a value that is in agreement with experiment. Despite the fact that the statistical error is still large, this is a very welcome result that would resolve a puzzle that persisted for some time showing the importance of computing observables at the physical point.

Having computed the axial charge it is straight forward to calculate the isovector scalar and tensor charges. The value of the latter is particularly relevant for searching for new type of interactions beyond the Standard Model. There is a planned SIDIS on ^{3}He/Proton experiment to take place at JLab after the upgrade at 11 GeV. In lattice QCD it is computed by replacing the axial-vector current by the tensor current $j_T^3 = \bar{\psi}(x)\sigma^{\mu\nu}\frac{\tau^3}{2}\psi(x)$. Studies have shown that

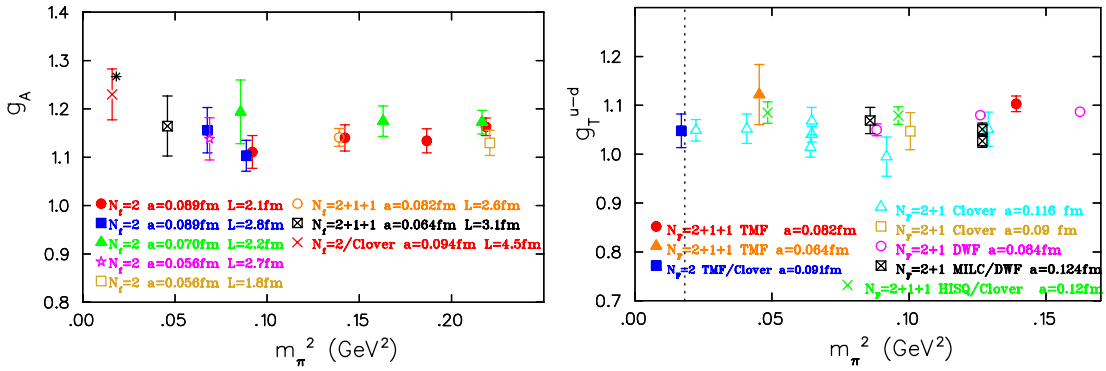

Figure 5: Left: Nucleon axial charge using TMF fermions. Right: Nucleon isovector tensor charge using TMF (ETMC) [25], DWF (RBC) [26], $N_f = 2$ (QCDSF-UKQCD) [27] and $N_f = 2 + 1$ (LHPC) [28] clover fermions, and clover on $N_f = 2 + 1 + 1$ staggered (PNDME) [29].

g_T^{u-d} has a similar behavior to g_A as far as the contribution from excited states is concerned. We show results in Fig. 5 obtained using TMF, clover, DWF and in a mixed action set-up of staggered sea and clover valence quarks. As can seen, all lattice QCD results are in agreement and a preliminary value of $g_T^{u-d} = 1.048(34)$ in $\overline{\text{MS}}$ at 2 GeV is obtained from the TMF ensemble directly at the physical point.

4.2.2 Disconnected quark loop contributions

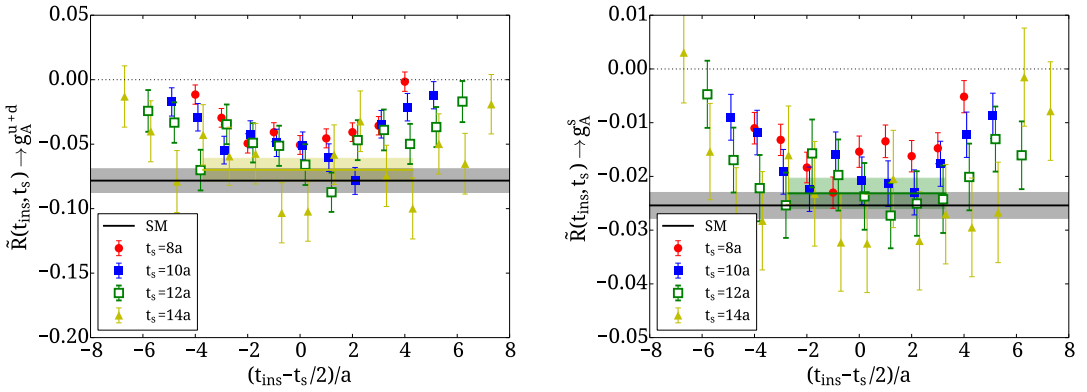

Figure 6: Disconnected contributions to the isoscalar (left) and strange (right) nucleon axial charge for the B55 ensemble.

Disconnected quark loop contributions arise from the coupling of the current to sea quarks. They are notoriously difficult to compute in lattice QCD. The technical reason is that one must compute a close quark loop given by $L(x) = Tr\left[\Gamma G(x;x)\right]$ for a general bilinear ultra-local operator of the form $\bar{\psi}(x)\Gamma\psi(x)$. This requires the computation of quark propagators from all $\mathbf{x}$ (all-to-all propagator) and thus it is L^3 more expensive as compared to the calculation

of hadron masses. The other reason is that these loops tend to have large gauge noise and therefore large statistics are necessary to obtain a meaningful result. Special techniques that utilize stochastic noise on all spatial lattice sites are utilized in order to allow for the computation of the all-to-all propagator reducing the number of inversions to N_r with $N_r \ll L^3$. The gauge noise is reduced by increasing statistics at low cost using low precision inversions and correcting for the bias (truncated solver method (TSM) or all-mode-averaging). Despite these new approaches the computation of these contributions would be too expensive using conventional computers. We take advantage of graphics cards (GPUs) for which we developed special multi-GPU codes. These computer architectures are ideal for approaches like TSM. We have illustrated the applicability of these methods by performing a high-statistics analysis using an $N_f = 2+1+1$ TMF ensemble with $L = 2.6$ fm, $a = 0.082$ fm at $m_\pi = 373$ MeV, referred to as the B55 ensemble. We analyzed 4700 gauge configurations yielding a total of $\sim 150,000$ statistics. The results on the disconnected contributions to the nucleon axial charge due to the light quarks g_A^{u+d} and due to the strange g_A^s are shown in Fig. 6. We obtain a non-zero negative value, which is $\mathcal{O}(10\%)$ for the u- and d-quarks and has to be taken into account when e.g. discussing the intrinsic spin $\frac{1}{2}\Delta\Sigma$ carried by quarks in the nucleon.

4.2.3 Electromagnetic form factors

The nucleon electromagnetic form factors are extracted from

$$\langle N(p',s')|j^\mu(0)|N(p,s)\rangle = \bar{u}_N(p',s')\left[\gamma^\mu F_1(q^2) + \frac{i\sigma^{\mu\nu}q_\nu}{2m}F_2(q^2)\right]u_N(p,s) \quad . \tag{5}$$

We would like to discuss here two studies at near physical pion mass: the one with the physical point ensemble of ETMC at $m_\pi = 130$ MeV [30] and the one by LHPC using $N_f = 2+1$ clover fermions configurations produced by the BMW collaboration with $a = 0.116$ MeV and $m_\pi = 149$ MeV [31].

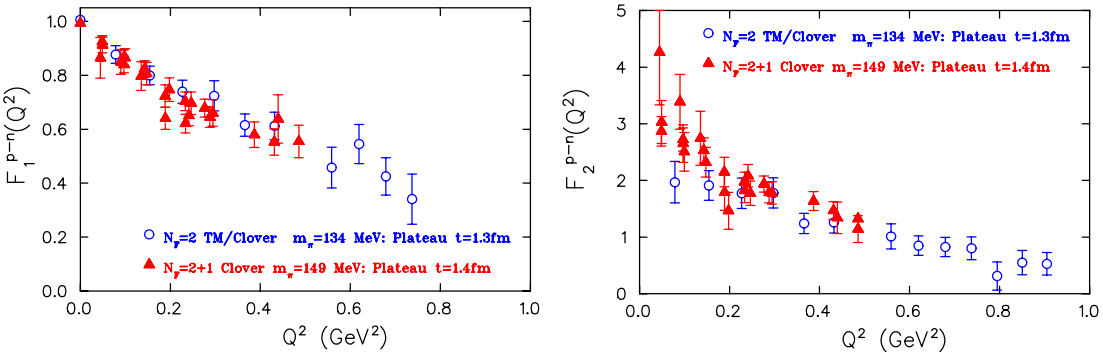

Figure 7: Results on the isovector Dirac (left) and Pauli (right) form factors versus $Q^2 = -q^2$. The statistics is about $\sim 10^3$ for ETMC and 7750 for LHPC.

Comparing the results on the Dirac and Pauli form factors between ETMC and LHPC in Fig. 7 we observe an overall agreement independently of the discretization scheme. The Dirac and Pauli radii can be extracted by fitting the Q^2-dependence of $F_1(Q^2)$ and $F_2(Q^2)$ to a dipole form, $\frac{A_i}{(1+Q^2/M_i^2)^2}$, with $i = 1, 2$, $A_1 = 1$ and taking the derivative: $\langle r_i^2\rangle = -\frac{6}{F_i}\frac{dF_i}{dQ^2}|_{Q^2=0} = \frac{12}{M_i^2}$.

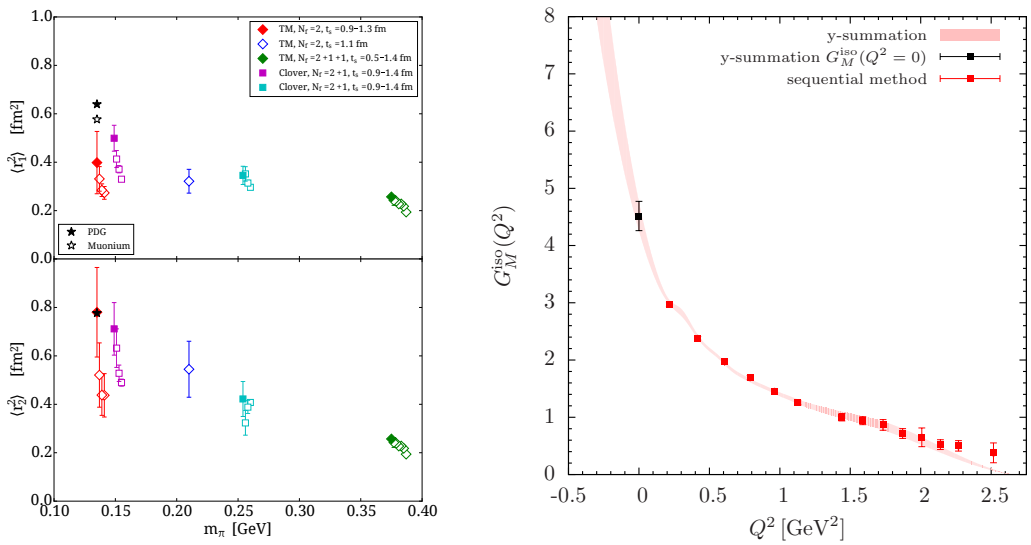

Figure 8: Left: Results on the isovector Dirac (top) and Pauli (bottom) radii versus m_π^2 from ETMC (diamonds) and LHPC (squares) [30]. Right: Magnetic form factor directly at $Q^2 = 0$, as determined by the red band [32]. The red points show the results with the conventional method.

The results are shown is Fig. 8 and clearly increase as the pion mass decreases, as well as the sink-source separation increases from ~ 1 fm to ~ 1.3 fm (see Ref. [30] for more details). However, fitting to a dipole to extract the radii introduces a model-dependence. We developed a novel method that extracts the value directly at $Q^2 = 0$. The first application of this method was to extract the anomalous magnetic moment determined by the magnetic form factor $G_M(0)$ or equivalently $F_2(0)$. In Fig. 8, our results on the isovector G_M for the B55 ensemble are shown with the red band. As can be seen, the method provides a good determination of $G_M(0)$ without requiring any assumption of its Q^2-dependence (see Ref. [32] for more details).

5 Conclusions

Simulations at the physical point are now feasible and this opens exciting possibilities for the study of hadron structure. In this work we presented an overview of lattice QCD results obtained directly at or close to the physical point from a number of lattice QCD collaborations, such as results on the hyperon and charmed baryon masses and isospin splitting, the pion decay constant, as well as, on the axial and tensor charges, and electromagnetic form factors of the nucleon. We find a value of g_A that is in agreement with experiment and provide a preliminary value for the tensor charge. The computation of disconnected contributions are briefly reviewed focusing on the disconnected quark contributions to the nucleon axial charge. First results at the physical point highlight the need for higher statistics in order that careful cross-checks can be carried out. Noise reduction techniques such as all-mode-averaging, improved methods for disconnected diagrams and smearing techniques are currently being pursued aiming at decreasing our errors on the quantities obtained at the physical point.

When this is achieved, lattice QCD can provide reliable predictions on quantities probing beyond the standard model physics such as g_T, as well as, on the nucleon σ-terms.

Acknowledgments

I would like to thank the members of the ETMC and in particular my close collaborators A. Abdel-Rehim, M. Constantinou, K. Jansen, K. Hadjiyiannakou, C. Kallidonis, G. Koutsou, K. Ottnad, M. Petschlies and A. Vaquero for their contributions to the TMF results shown in this talk. Partial support was provided by the EU ITN project PITN-GA-2009-238353 (ITN STRONGnet) and IA project IA-GA-2011-283286 HadronPhysics3 . This work used computational resources provided by PRACE, JSC, Germany and the Cy-Tera project (NEA ΥΠΟΔΟΜΗ/ΣΤΡΑΤΗ/0308/31).

References

[1] , A. Abdel-Rehim *et al.* (ETMC), PoS(LATTICE2013) 264 (2013); A. Abdel-Rehim *et al.*, (ETMC) PoS(LATTICE2014) 119 (2014).

[2] C. Alexandrou *et al.*, Comput. Phys. Commun. **185**, 1370 (2014) [arXiv:1309.2256].

[3] A. Abdel-Rehim *et al.*, Phys. Rev. D **89**, no. 3, 034501 (2014) [arXiv:1310.6339].

[4] C. Alexandrou *et al.*, PoS(LATTICE2014) 140 (2014).

[5] S. Meinel *et al.*, PoS(LATTICE2014) 139 (2014).

[6] A. Bazavov *et al.* [Fermilab Lattice and MILC Collaboration], arXiv:1407.3772 [hep-lat].

[7] S. Durr *et al.*, arXiv:1310.3626 [hep-lat].

[8] G. S. Bali *et al.*, Nucl. Phys. B **866**, 1 (2013).

[9] S. Aoki *et al.* [PACS-CS Collaboration], Phys. Rev. D **81**, 074503 (2010).

[10] S. Syritsyn *et al.*, (RBC/UKQCD) PoS(LATTICE2014) 134 (2014).

[11] C. Alexandrou *et al.*, PoS(LATTICE2014) 151 (2014).

[12] S. Durr *et al.* Science **322**, 1224 (2008).

[13] S. Aoki *et al.* [PACS-CS Collaboration], Phys. Rev. D **79**, 034503 (2009).

[14] W. Bietenholz *et al.*, Phys. Rev. D **84**, 054509 (2011).

[15] H. Na and S. A. Gottlieb, PoS LAT **2007**, 124 (2007); H. Na and S. Gottlieb, PoS LATTICE **2008**, 119 (2008).

[16] R. A. Briceno, H. W. Lin and D. R. Bolton, Phys. Rev. D **86**, 094504 (2012).

[17] L. Liu, H. W. Lin, K. Orginos and A. Walker-Loud, Phys. Rev. D **81**, 094505 (2010).

[18] Y. Namekawa *et al.* [PACS-CS Collaboration], Phys. Rev. D **87**, 094512 (2013).

[19] C. Alexandrou, V. Drach, K. Jansen, C. Kallidonis and G. Koutsou, arXiv:1406.4310 [hep-lat].

[20] R. Horsley *et al.* (QCDSF-UKQCD) Phys. Rev. D **86**, 114511 (2012); PoS Lattice **2013**, 499 (2013).

[21] Sz. Borsanyi *et al.*, Phys. Rev. Lett. 111 (2013) 252001.

[22] J. Bulava *et al.*, [arXiv:1310.7887[hep-lat]].

[23] J. J. Dudek, R. G. Edwards and C.E. Thomas, Phys. Rev. D 87 (2013) 034505.

[24] C. Alexandrou, Prog. Part. Nucl. Phys. **67**, 101 (2012) [arXiv:1111.5960 [hep-lat]].

[25] C. Alexandrou, M. Constantinou, K. Jansen, G. Koutsou and H. Panagopoulos, arXiv:1311.4670 [hep-lat].

[26] Y. Aoki *et al.*, Phys. Rev. D **82**, 014501 (2010).

[27] D. Pleiter *et al.* [QCDSF/UKQCD], PoS LATTICE **2010**, 153 (2010) [arXiv:1101.2326 [hep-lat]].

[28] J. R. Green *et al.*, Phys. Rev. D **86**, 114509 (2012).
[29] T. Bhattacharya *et al.*, Phys. Rev. D **89**, 094502 (2014).
[30] C. Alexandrou *et al.* (ETMC), PoS (LATTICE2014) 148 (2014).
[31] J. R. Green *et al.*, Phys. Rev. D **90**, 074507 (2014).
[32] C. Alexandrou *et al.* (ETMC), PoS (LATTICE2014) 144 (2014).

Recent Heavy Ion Results on the Hard Scattering and Jet Quenching from the ATLAS and CMS experiments at the LHC

Andrzej Olszewski[1] on behalf of the ATLAS and CMS Collaborations

[1]Institute of Nuclear Physics, PAS, Radzikowskiego 152, 31-342 Kraków, Poland

DOI: http://dx.doi.org/10.3204/DESY-PROC-2014-04/287

Recent results on studies of hard scattering processes and jet quenching in nuclear collisions from the ATLAS and CMS experiments at the Large Hadron Collider (LHC) are reviewed. They are based on high statistics samples of PbPb collisions at $\sqrt{s_{\rm NN}} = 2.76$ TeV collected at the LHC in 2011, and pp collisions at $\sqrt{s} = 2.76$ TeV and pPb collisions at $\sqrt{s_{\rm NN}} = 5.02$ TeV collected in 2013. New results for the jet nuclear modification factor, $R_{\rm AA}$, confirm a strong suppression of jet production. Modifications of jet fragmentation properties in PbPb collisions, are observed. In pPb collisions jets are not strongly modified, but some non-scaling behavior of jet rates in collisions with different centralities is observed by ATLAS. New measurements for the electroweak boson production in pPb collisions allow a more precise testing of parton distributions in lead nuclei with the conclusion that the EPS09 description of nuclear modifications of parton distribution functions is preferred.

1 Introduction

In collisions of heavy nuclei at very high energies, one expects creation of a hot and dense medium which may, under certain conditions, undergo transition to the so called Quark-Gluon Plasma (QGP) phase, where quarks and gluons are free to interact directly. In experiments at RHIC and LHC, it has been observed that properties of high transverse momentum particles and particle jets are modified in heavy nuclei collisions compared to collisions of protons and this was attributed to interactions of these particles with the medium created in the collision. It has been found that the best way to understand properties of the produced medium and whether it fits the properties of QGP is to study hard scattering processes. In such studies, we use nuclear modification factor $R_{\rm AB}$, defined as:

$$R_{\rm AB} = \frac{\frac{1}{\rm N}\frac{{\rm d}^2 N^{\rm jet}_{\rm cent}}{{\rm d}p_{\rm T}{\rm d}y}}{\langle T_{\rm AB}\rangle_{\rm cent}\frac{{\rm d}^2\sigma^{\rm jet}_{pp}}{{\rm d}p_{\rm T}{\rm d}y}}; \qquad N_{\rm coll} = T_{\rm AB}\times\sigma_{\rm NN},$$

to measure the deviation of yields produced in heavy ion collisions from the yield in pp scaled by the number of nucleon-nucleon collisions, $N_{\rm coll}$, proportional to the mean nuclear thickness, $T_{\rm AB}$, of the incoming nucleon fluxes. $R_{\rm AB} = 1$ means that production properties have not been modified with respect to pp collisions.

In the last few years experiments at LHC registered data from runs with collisions of lead nuclei at the center of mass energy of $\sqrt{s_{\rm NN}} = 2.76$ TeV, from proton-proton runs taken as a reference data at the same energy and from pPb runs at the energy of $\sqrt{s_{\rm NN}} = 5.02$ TeV resulting from a combination of asymmetric energies of lead nuclei at 1.58 TeV/N and protons at 4 TeV. Recent analyses from ATLAS [1] and CMS [2] are now using high statistics PbPb data from 2011, new pPb data from 2013, and high statistics pp data from 2013 with statistics 20 times higher than available before.

2 Jets in PbPb collisions

Jets provide a powerful tool to probe the hot and dense medium created in heavy ion collisions. Experiments at RHIC have shown first evidence of jet quenching by observation of suppression of high transverse momentum particles. At the LHC, a direct evidence of parton energy loss has been observed in significant modification of dijet and photon-jet $p_{\rm T}$-balance and suppression of inclusive jet spectra with increasing collision centrality.

Recently ATLAS has shown new results on the jet suppression in PbPb collisions [3]. The jet nuclear modification factor, $R_{\rm AA}$, has been measured as a function of jet transverse momentum, rapidity and centrality. A significant suppression of jets is observed at all centralities. The $R_{\rm AA}$ is as low as 0.5 in the most central (0-10%) collisions for jets with $p_{\rm T}$ up to 400 GeV. With increasing $p_{\rm T}$ a slow rise of $R_{\rm AA}$ is observed, with the slope varying with centrality and reaching zero in peripheral collisions. The jet $R_{\rm AA}$ measured as a function of rapidity shows no significant dependence within the measured rapidity range (Fig.1, top). $R_{\rm AA}$ measured as a function of centrality, expressed by number of participating nucleons, $\langle N_{\rm part}\rangle$, is decreasing monotonically from the value of 0.8 in most peripheral collisions to 0.4 in 1% of the most central ones (Fig.1, bottom), the behaviour observed before by CMS [4].

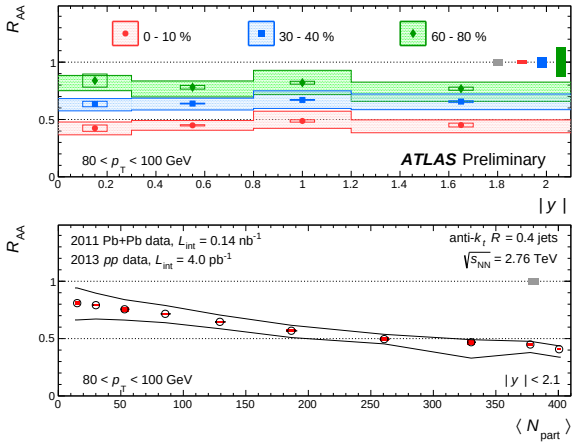

Figure 1: Top: $R_{\rm AA}$ for jets with $80 < p_{\rm T} < 100$ GeV shown as a function of $|y|$ for three centrality bins. Bottom: $R_{\rm AA}$ for jets with $80 < p_{\rm T} < 100$ GeV and $|y| < 2.1$ as a function of $\langle N_{\rm part}\rangle$ [3].

ATLAS presented also updated results on modifications of the jet fragmentation in PbPb collisions [5]. Modifications of distributions of longitudinal, $D(z)$, $z = p_{\rm T}^{\rm had}/p_{\rm T}^{\rm jet}\cos(\Delta R)$, and transverse, $D(p_{\rm T})$, momentum of jet particles relative to the jet axis have been studied by calculating ratios of distributions measured in central and peripheral collisions, $R_{D(z)} = D(z)_{\rm cent}/D(z)_{\rm periph}$. A significant modification of fragmentation is seen in more central collisions with enhancement of fragment yields at small values of momenta ($z < 0.04$, $p_{\rm T} < 4$ GeV) and at high ones ($z > 0.2$, $p_{\rm T} > 30$ GeV), and reduction at intermediate values (Fig.2). The enhancement at large z or $p_{\rm T}$ is seen more clearly for jets with small jet radii, $R = 0.2, 0.3$. Similar modifications in

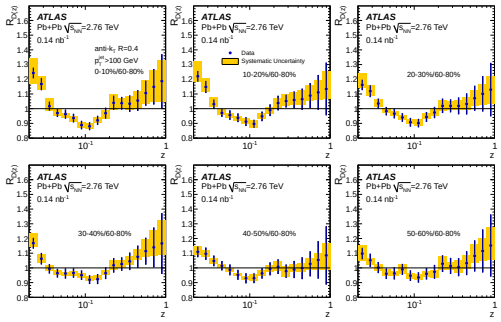

Figure 2: Ratios of $D(z)$ for six bins in collision centrality to those in peripheral (60-80%) collisions, for $R = 0.4$ jets [5].

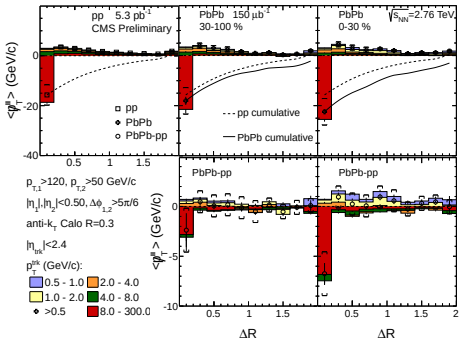

Figure 3: Top: Differential missing p_{T} distributions for pp and PbPb collisions, as a function of ΔR. Bottom: Difference between the PbPb and pp distributions [7].

jet fragmentation are seen also by the CMS experiment from the comparison of pp and PbPb collision data [6].

The CMS experiment studied also particle momentum balance in jets [7]. It has been found that jets in PbPb collisions comprise more particles than pp jets and the difference increases with the collision centrality leading to 15 extra particles in jets with large momentum asymmetry and high (0-10%) collision centrality. Furthermore, contributions from jet particles have been studied in bins of transverse momentum and it has been found that in PbPb jets there is an excess of particles with low $p_{\mathrm{T}} < 2$ GeV. The particle transverse momentum balance has been studied also as a function of ΔR, the distance from the jet axis. Results are shown in Fig.3. The momentum balance, shown by dashed and continuous lines for pp and PbPb collisions, respectively, is achieved only at large distances $\Delta R = 2$ and the excess of low p_{T} particles is seen up to large distances from the jet axis. A detailed measurement of the radial distribution of transverse momentum inside the core of the jet cone, called differential jet shape, has been shown by CMS in [8]. It has been found that jet shapes in peripheral (70-100%) PbPb collisions are similar to those in pp while in more central collisions (0-70%) a depletion is found in the range of $0.1 < R < 0.2$. In the most central PbPb collisions (10-30% and 0-10%), an excess of transverse momentum fraction emitted at large radii, $R > 0.2$, starts to show up, confirming moderate broadening of jets in the hot medium created in PbPb collisions.

3 Jets in pPb collisions

Studies of dijet properties in pPb collisions are of great importance to establish a QCD baseline for hadronic interactions with a cold nuclear matter. This is because these collisions are not expected to produce large volumes of hot partonic medium similar to PbPb collisions where both effects contribute.

Recently ATLAS performed measurements of jet production in pPb collisions [9]. In this analysis, inclusive jet modication factors, $R_{p\mathrm{Pb}}$, have been calculated as a function of p_{T} using as a reference 2013 pp data interpolated to pPb energy. Results are shown in Fig.4. The $R_{p\mathrm{Pb}}$ factors are all close to 1, so there is no jet suppression seen in inclusive pPb collisions.

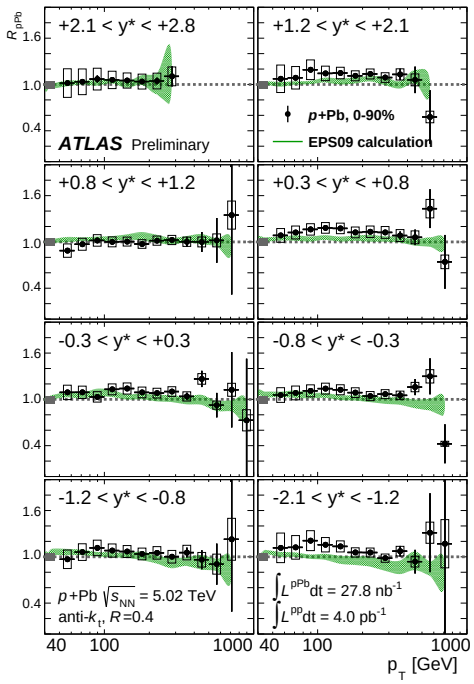

Figure 4: $R_{p\mathrm{Pb}}$ for $R = 0.4$ jets in 0-90% pPb collisions at different rapidity ranges. The green band represents a calculation using the EPS09 parton distribution function [9].

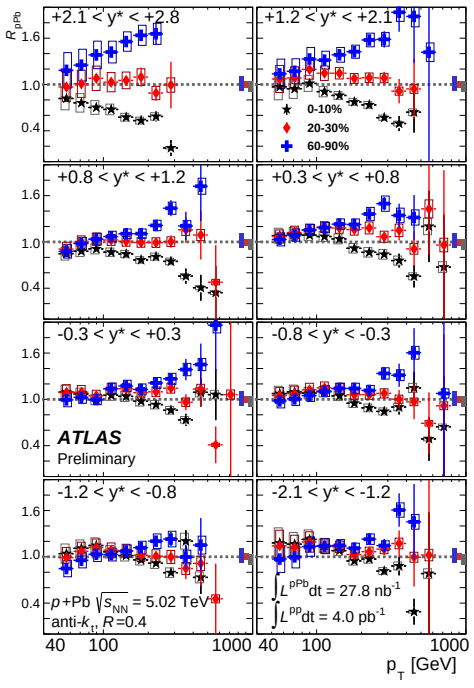

Figure 5: $\mathrm{R}_{p\mathrm{Pb}}$ for $R = 0.4$ jets in pPb collisions in central (black), mid-central (red) and peripheral (blue) events at different rapidity ranges [9].

Instead, a small 5-10% enhancement is visible over the scaled pp results. CMS has performed a similar measurement [10] and has come to similar conclusions except for observing some decrease in $R_{p\mathrm{Pb}}$ modification factors with jet p_{T} in the most backward range of the center-of-mass pseudorapidity, $-2.0 < \eta_{\mathrm{CM}} < -1.5$. ATLAS has measured also $R_{p\mathrm{Pb}}$ factors in 3 subsamples of events with different collision centrality (Fig.5). In such samples, jet rates have been found enhanced in peripheral collisions and suppressed in central collisions at forward rapidities, while not modified at low p_{T} and negative center-of-mass rapidity, y^* [9]. This pattern of the jet modification has been confirmed by R_{CP}, ratios of jet rates in central to peripheral pPb collisions. In addition, it has been found that R_{CP} ratios scale as a function of momentum p, in forward (proton going) direction $y^* > 0$, but not at $y^* < 0$ [9].

In order to study flavor dependence of the jet suppression CMS has measured also $R_{p\mathrm{Pb}}$ factors in production of b-quark jets [11] and B particles [12]. The b-jet measurements have been compared to PYTHIA Z2 tune pp calculations. The obtained $R_{p\mathrm{Pb}}$ ratios were found to be consistent with no suppression in the b-jet production. The same conclusion has been drawn also from the study of B meson production [12]. No flavor dependence of jet suppression has been found in PbPb collisions [13], despite the fact that jets are strongly quenched in these collisions.

A particularly useful tool for studying jet quenching are back to back jet pairs, called

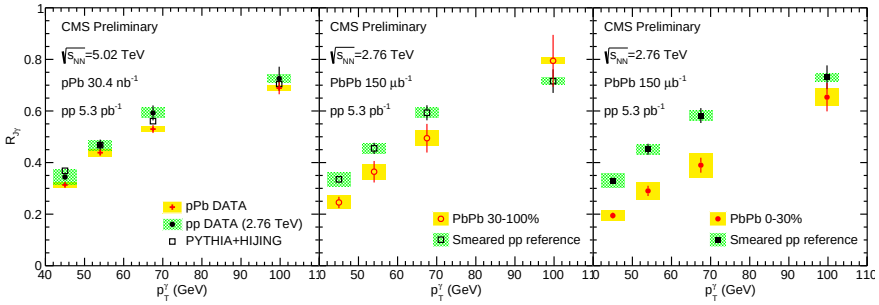

Figure 6: Fraction of photons associated to a jet (R_{J_γ}) as a function of the leading photon p_T in pPb (left), peripheral PbPb (middle), and central PbPb (right) [14].

dijets. CMS has measured a fraction of photons with a high p_T jet partner in pPb and in PbPb collisions and compared results to the measurements in pp collisions and to PYTHIA calculations [14]. It has been found (see Fig.6) that such dijets are not changed in pPb while they are suppressed in PbPb collisions. CMS has also measured directly distributions of the relative directions and momentum ratios of jets in pPb dijets and compared them with dijet properties in pp collisions. It has been found that in pPb collisions jets are not deflected and the jet momenta are essentially unmodified [15], while in PbPb collisions, the partner jets are pushed to lower p_T values [16].

Another dijet property studied by CMS in pPb collisions was an average dijet position in rapidity. This property is directly sensitive to momenta of interacting partons that could be modified in nuclear projectiles. CMS compared the pPb data with PYTHIA pp predictions and found that the best match is obtained if the EPS09 nuclear parton distribution function (PDF) is used in the model calculations [15].

4 Electroweak bosons in PbPb collisions

Electroweak (EW) bosons are colorless particles which are supposed not to interact with the hot and dense medium created in heavy ion collisions. Measured together with jets they may be used as a calibration tool in studies of jet quenching. In addition, the EW boson production mechanism (via $q\bar{q}$ annihilation) makes them sensitive to parton distribution functions, thus suitable for studying nuclear modifications to PDFs (nPDFs).

In PbPb collisions, ATLAS measured R_{AA} ratios for isolated, direct photon yields to the reference pp rates calculated by JETPHOX model [17]. They were shown as a function of photon transverse momentum and compared with JETPHOX calculations in pp and PbPb collisions. Also a ratio of yields in forward to central rapidity regions has been studied. The photon cross-sections have been found to agree with simple scaling of pp rates, but the measurements could not discriminate between different PDF versions due to large systematic uncertainties.

ATLAS has updated also their results on the production of W bosons in PbPb collisions [18]. Yields of $W^{\pm}$ bosons have been studied as a function of the number of participating nucleons (collision centrality) and compared to PYTHIA CT10 model calculations (Fig.7). Results have been found compatible with simple pp scaling and in agreement with model calculations.

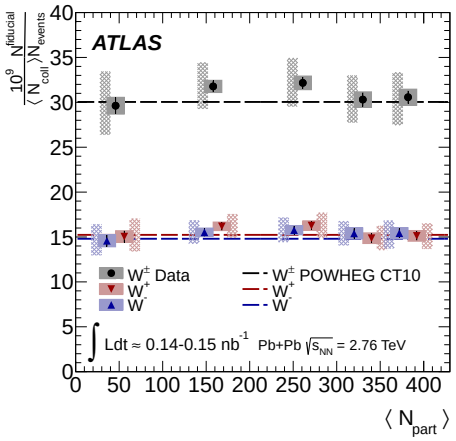

Figure 7: W boson production yield per binary collision as a function of the mean number of participants compared to the NLO QCD prediction [18].

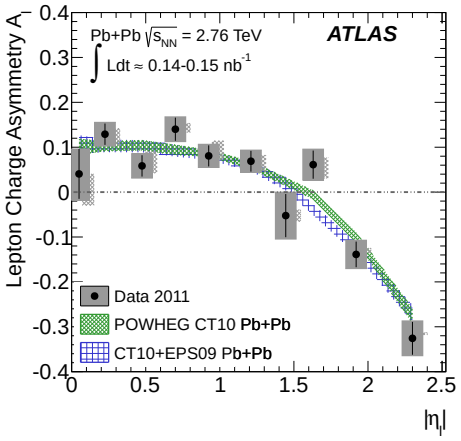

Figure 8: The lepton charge asymmetry $A_l = (N(l^+) - N(l^-))/(N(l^+) + N(l^-))$ from $W^{\pm}$ bosons as a function of the absolute pseudorapidity compared to predictions with CT10 and CT10+EPS09 NLO PDF sets [18].

The more sensitive to parton distributions, charge asymmetry in pseudorapidity, has also been studied (Fig.8) and found to be well described by model calculations, but results are not precise enough to see possible nuclear modifications to parton distributions.

5 Electroweak bosons in pPb collisions

Search for the effects of nuclear modifications to PDFs is even easier in pPb collisions, where final state effects are expected to be small or none. In such collisions, ATLAS measured recently the Z^0 boson production [19]. The cross-section measured as a function of boson rapidity exhibits a significant asymmetry in rapidity with excess over predictions from PYTHIA CT10 model in the backward (Pb-going) rapidity region. In the same measurement performed by CMS [20], Z^0 cross section has also asymmetric behavior, but a comparison is made with PYTHIA MSTW08 model and a good agreement with predictions is found (Fig.9). The forward to backward ratio of Z^0 production cross-sections measured by CMS favors parton distributions with nuclear modifications (Fig.10).

The production cross-sections for W boson in pPb collisions have been measured so far only by the CMS experiment [21]. They agree well with the scaled PYTHIA model predictions – only a small excess is seen in the production of W^- at negative η. This excess is investigated in the W^+/W^- charge asymmetry (Fig.11), which is a sensitive probe of the ratio of up to down quark PDFs. Explanation of the deviation between data and model predictions would require to assume a smaller nuclear modification to the down quark than to the up quark in the EPS09 nPDF. The forward/backward asymmetry in W boson production has been investigated by CMS to probe nuclear modifications in parton x distributions. There is a significant difference in this asymmetry as a function of $\eta_{\rm lab}$ between predictions from PYTHIA CT10 and EPS09

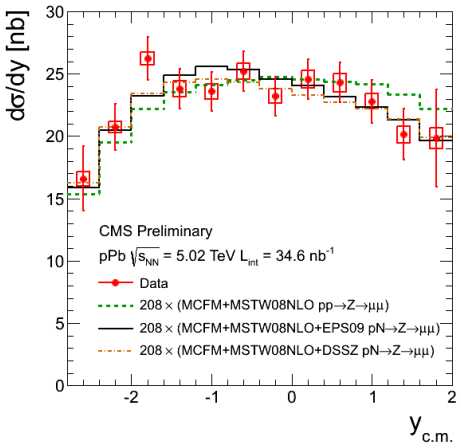

Figure 9: Differential cross-section of the Z^0 boson production in pPb collisions as a function of rapidity, compared to predictions from PYTHIA generator with different versions of PDFs [20].

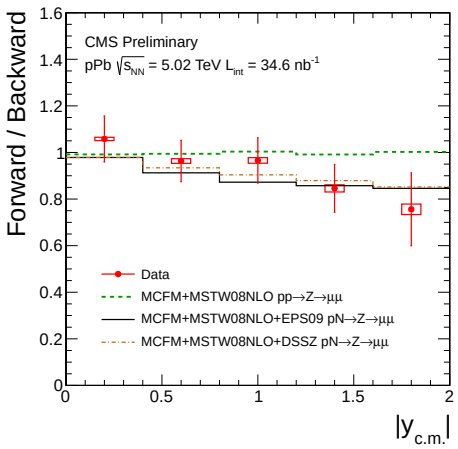

Figure 10: Forward-backward ratio of Z^0 boson cross-section in pPb collisions as a function of rapidity compared to predictions with nuclear modifications (EPS09 or DSSZ) and without them (green, dashed line) [20].

versions, but results of the measurement don't fully agree with either version (Fig.12), although a slightly better agreement is found with EPS09 nPDF calculations.

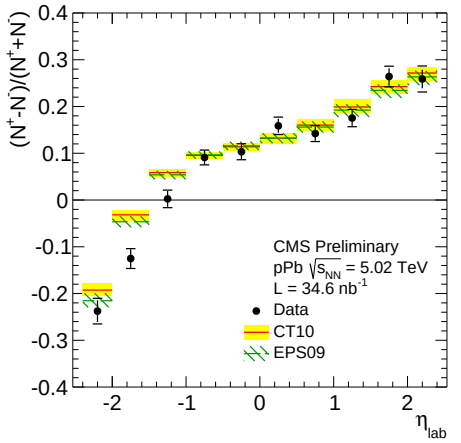

Figure 11: W boson charge asymmetry, $(\mathrm{N}^+ - \mathrm{N}^-)/(\mathrm{N}^+ + \mathrm{N}^-)$, as a function of the lepton pseudorapidity in the laboratory frame [21].

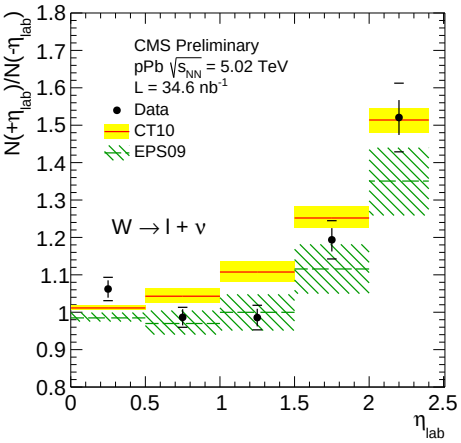

Figure 12: W boson forward/backward asymmetries $\mathrm{N}(+\eta_{\mathrm{lab}})/N(-\eta_{\mathrm{lab}})$ for positively charged leptons [21].

6 Summary

Recent results on hard scattering processes in nuclear collisions, obtained by ATLAS and CMS, are presented. They confirm that in PbPb collisions, jets are strongly quenched. The suppression of jet yields increases with centrality (down to $R_{AA} \simeq 0.5$), and continues to $p_T \simeq 400$ GeV. No strong flavor (b-quark) dependence of suppression is seen at high transverse momenta. Jet fragmentation is modified in PbPb collisions. ATLAS and CMS observe enhancements at low and high values of longitudinal and transverse momenta of jet fragments, and a suppression at intermediate values. CMS finds that the jet energy is distributed in PbPb collisions to more particles with lower p_T and going to large angles as compared to pp jets. In electroweak boson production, ATLAS observes a scaling of cross-sections with the number of elementary NN collisions. In pPb collisions, jets are not strongly suppressed. However, ATLAS observes no scaling-like variation of yields with centrality at forward rapidities. Latest results from pPb collisions allow more precise tests of parton distribution functions and indicate that EPS09 nPDF is preferred.

Acknowledgments

This work was supported in part by the National Science Center grants DEC-2011/03/B/ST/02631, by DEC-2013/08/M/ST2/00320 and by PL-Grid Infrastructure.

References

[1] ATLAS Collaboration, JINST 3 (2008) S08003.
[2] CMS Collaboration, JINST 3 (2008) S08004.
[3] ATLAS Collaboration, ATLAS-CONF-2014-025, http://cds.cern.ch/record/1702988.
[4] CMS Collaboration, CMS-PAS-HIN-12-004, http://cds.cern.ch/record/1472722.
[5] ATLAS Collaboration, arXiv:1406.2979 [hep-ex] (2014).
[6] CMS Collaboration, Phys. Rev. **C90** 024908 (2014).
[7] CMS Collaboration, CMS-PAS-HIN-14-010, http://cds.cern.ch/record/1703014.
[8] CMS Collaboration, Phys. Lett. **B730** 243 (2014).
[9] ATLAS Collaboration, ATLAS-CONF-2014-024, http://cds.cern.ch/record/1702986.
[10] CMS Collaboration, CMS-PAS-HIN-14-001, http://cds.cern.ch/record/1703004.
[11] CMS Collaboration, CMS-PAS-HIN-14-007, http://cds.cern.ch/record/1703013.
[12] CMS Collaboration, CMS-HIN-14-004, http://cds.cern.ch/record/1703520.
[13] CMS Collaboration, arXiv:1312.4198 [nucl-ex] (2013).
[14] CMS Collaboration, CMS-PAS-HIN-13-006, http://cds.cern.ch/record/1631991.
[15] CMS Collaboration, Eur. Phys. J. **C74** 2951 (2014).
[16] CMS Collaboration, Phys. Lett. **B718** 773 (2013).
[17] ATLAS Collaboration, ATLAS-CONF-2014-026, http://cds.cern.ch/record/1702992.
[18] ATLAS Collaboration, ATLAS-CONF-2014-023, http://cds.cern.ch/record/1702982.
[19] ATLAS Collaboration, ATLAS-CONF-2014-020, http://cds.cern.ch/record/1702971.
[20] CMS Collaboration, CMS-PAS-HIN-14-003, http://cds.cern.ch/record/1703012.
[21] CMS Collaboration, CMS-PAS-HIN-13-007, http://cds.cern.ch/record/1703270.

Hot and dense matter at RHIC and LHC

Eugenio Scapparone

INFN-Bologna, Via Irnerio 46, 40126 Bologna, Italy

DOI: http://dx.doi.org/10.3204/DESY-PROC-2014-04/288

The results obtained by RHIC and LHC experiments in the study of nucleus-nucleus collisions shed light on the behaviour of the hot and dense matter produced in heavy ion interactions at high energy. The recent p-Pb run at the LHC added another piece of information, showing p-nucleus interactions provide interesting and unexpected features. The most recent results, the open questions and the perspectives will be discussed.

1 Introduction

During the last decades, high energy heavy ion physics provided impressive and outstanding results. RHIC experiments produced several fascinating discoveries: the hot and dense matter created in the nuclei collisions at a centre of mass energy $\sqrt{s_{\rm NN}}$=200 GeV behaves as a nearly viscosity-free fluid. The nuclear medium, opaque to hadrons but transparent to photons, suppresses the away-side jet in events with two back-to-back jets. Later LHC experiments showed that increasing the energy to $\sqrt{s_{\rm NN}}$=2.76 TeV gives a fireball hotter, larger and lasting longer. New phenomena manifest or become more pronounced: the suppression of the J/ψ in head-on central collisions (low impact parameter) and/or at low p_T is less pronounced compared to RHIC and this vector meson shows a non-zero elliptic flow. Charmed meson nuclear modification factor is larger than ordinary hadron one, and it looks smaller than that measured with b-quark hadrons. In addition the study of p-Pb interactions showed an unexpected collective behaviour and one cannot exclude yet the quark gluon plasma is created in this lighter system too.

Although these exciting results provided a remarkable step forward in the comprehension of this new state of matter, a precise measurement of the parameters characterizing this fluid is still missing; as an example the shear viscosity (η/s) has an uncertainty as large as a factor four and a similar uncertainty affects the jet transport parameter ($\hat{q}$) measurement. The above discoveries raised a number of compelling questions. What is the mechanism behind a so fast quark thermalization ? Does the QGP contain quasi-particle or long lived excitations are cancelled by the strong field ? What is the origin of the ridge, observed in p-p collision too ? These questions can be answered in the next years when a plenty of new data will be available: LHC will offer the opportunity to study the QGP at the highest temperatures ($\sqrt{s_{\rm NN}}$= 5.5 TeV) and RHIC will improve the beam energy scan (BES) to study the phase transition boundary and to search for the phase space critical point.

Given the available space I will not try to give a comprehensive review of heavy ion results at RHIC and LHC, but I will focus on few subjects. Jets and high p_T events will not be discussed

here, since a dedicated talk on this subject was presented at this conference.

2 Global properties

The Hanbury-Brown and Twiss(HBT) [1] correlation played an important role in astrophysics in the '50s, when it was used to measure the star angular size. Years later, particle physicists relied on this method to assess the spatial scale of the emitting source size by studying identical bosons, as charged pion pairs. The two particle correlation function can be defined as the ratio of two measured distributions based on two different samples, using pion pairs from the same event and from different events, respectively. The pair three-momentum difference **q** can be decomposed into the three components (q_{out}, q_{side}, q_{long}), where the *out* axis points along the pair transverse momentum, the *side* axis is perpendicular to the transverse momentum plane and the *long* axis points along the beam. The three-dimensional correlation function is fitted to an expression accounting for the Bose-Einstein enhancement, containing a term $G(q) = e^{-q^2R^2}$, where $R = (R_{out}, R_{long}, R_{side})$ is the HBT radius of the production region.

The ALICE results[2] give at the LHC a source volume $V \simeq 300\ fm^3$, a factor 2 larger than the volume measured at RHIC and a lifetime $\tau \simeq 10$ fm/c, a 20% larger than the one measured at RHIC. As pointed out by PHENIX [3], the fireball shines, emitting direct photon with a temperature T=221±19(sta)±19(sys) MeV [3]. ALICE measured a 30% hotter medium, obtaining T = 304±51 (sta+sys) MeV [4]. It is worth noting this is the average fireball temperature: hydro-dynamical models predict the highest temperature reached in the early stage is expected up to a factor 3 higher. The energy density can be estimated by using the Bjorken-formula approximation. At the LHC the hot and dense matter reaches ≃15 GeV/fm^3 [5], a factor 3 larger than the energy density measured at RHIC. In summary, the increase in centre of mass energy from $\sqrt{s_{\rm NN}}$=200 GeV to 2.76 TeV reflects in a fireball with a factor 2 larger volume, a factor 3 larger energy density, lasting 20% longer and with a temperature 30% hotter, equivalent to ($3{\cdot}10^{12}$K). Compared to this temperature record, the interior of the sun is an almost cold place, reaching a modest $2{\cdot}10^{7}$K !

3 Collectivity

The azimuthal momentum distribution of the emitted particles is usually expressed as

$$\frac{dN}{d\Phi} \propto 1 + \sum_n 2v_n \cos(2n(\Phi - \Psi_n) \tag{1}$$

where v_n is the magnitude of the $n-th$ order harmonic term relative to the angle of the plane Ψ_n.

One of the most exciting results obtained at the RHIC was the evidence that the bulk of the produced hot matter is well described by fluid-dynamics, predicting a non vanishing elliptic flow v_2. At the LHC the p_T integrated v_2 showed an increase of about 30% compared to RHIC, mainly due to the increase of the average transverse momentum of the produced particles. Recently, the ALICE collaboration, taking advantage of the detector powerful particle identification, published a paper focused on identified hadron elliptic flow [6]: a clear mass ordering was observed, with heavier particles showing a smaller v_2. This not-trivial result,

predicted by fluid-dynamic models, indicates the radial flow boosts heavier particles to higher p_T, $\Delta p_T \simeq \Delta \mathrm{m}\beta$.

One of the most urgent questions to be answered is how perfect this fluid is, that is to provide a precise measurement of the shear viscosity η/s. Initial system condition, feeding the hydro models, are a very important source of uncertainty, when extracting the medium parameters from data. As pointed out in [7], the comparison of PHOBOS elliptic flow with hydro-models gives a best fit η/s ranging from 0.08 to 0.16 when applying initial conditions based on the Colour Glass Condensate or the Glauber model, respectively. Improving our knowledge on the initial conditions is therefore mandatory to reduce the uncertainties on the shear viscosity η/s. STAR studied the U-U interactions at $\sqrt{s_{\mathrm{NN}}}$= 193 GeV. The prolate shape of this nucleus, provides the possibility to study the initial condition effect on the azimuthal distributions: interactions may occur in a body-body configuration (giving large v_2 and a relatively small number of charged particles) or tip-tip (characterized by a small v_2 and a large number of charged particles). To minimize the effect due to the impact parameter, the analysis has to be restricted to events with top 0.1% centrality. Zeta Degree Calorimeters tag these two different configurations, measuring the energy of spectator nuclei. The elliptic flow was measured as a function of the normalized multiplicity(mult/<mult>): while the Glauber model predicted a too step dependence, the IP-Glasma model [8] gives a satisfactory prediction. This model provides initial conditions for systematic flow studies. It combines the IP-Sat (impact parameter saturation) model of high energy nucleon (and nuclear) wave functions with the classical SU(3) Yang-Mills (CYM) dynamics of the Glasma fields produced in a heavy-ion collision. Event by event fluctuations studied by ATLAS [9] at the LHC provide another successful test for the IP-Glasma model. The eccentricity ϵ_2, ϵ_3, ϵ_4 are expected to be proportional to v_2 ,v_3, v_4 in most hydrodynamic calculations. It is worth nothing recently few studies showed this statement hardly applies to v_4 [10]. Any deviation of the proportionality constant can be used to constrain the shear viscosity and the initial system geometry. In the ATLAS analysis, for each event, the v_2,v_3,v_4 are extracted. The v_n probability distributions are compared to the eccentricity, rescaled to match the $<v_n>$ of the data. Initial condition were provided by two different models: the Glauber model and the MC-KLN model, the latter including gluon saturation effect. Both the Glauber and the MC-KLN models predict correctly the data at low centrality, but fail for peripheral collisions [9], underestimating the probability for large v_n. On the contrary, as pointed out in ref. [11], the IP Glasma model, coupled to the MUSIC code, a 3+1 dimensional relativistic viscous hydrodinamic simulation model, predicts quite well these distributions for peripheral events too. Fluctuations are a gold mine in modern physics: as an example temperature fluctuations in the microwave background provided invaluable informations on the universe composition. Geometric nucleon position and intrinsic subnucleon scale colour charge fluctuations are quenched by the shear viscosity: their magnitude gives therefore a direct indication on how perfect this fluid is. One of the most remarkable effects of the fluctuations is the generation of harmonics of order higher than v_2(v_n,$n \geq$3). It was shown in [12] the higher orders are very sensitive to the shear viscosity. Several experiments at the LHC measured v_n in different intervals of centrality [13, 14]. In Fig. 1 the PHENIX data [15] are compared to the IP-Glasma+Music prediction for harmonics of any order. A satisfactory agreement is obtained, with η/s=0.12 as favourite parameter. Applying the fit to the ATLAS [13] or ALICE [14] results gives a nice fit too, with a preferred η/s=0.2. The above result may suggest η/s is changing from RHIC to LHC energies. An attempt to fit all the data with a η/s temperature (and hence energy) dependent was attempted. The fit at $p_T > 1.5$ GeV/c poorly reproduces the RHIC data(fig. 2, left panel). The η/s(T) functional

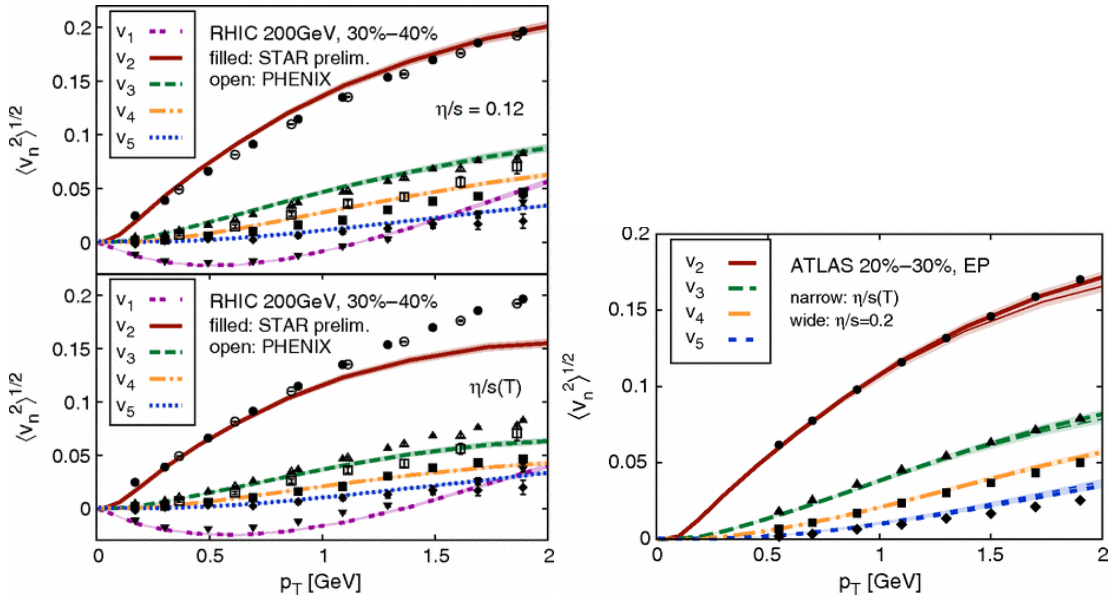

Figure 1: Comparison of $v_n(p_T)$ at RHIC (left) using constant η/s=0.12 and a temperature dependent $(\eta/s)(T)$, and at the LHC(right) using constant η/s=0.20 and a temperature dependent $(\eta/s)(T)$

form should be improved and more data at different energies, as those coming from RHIC BES, are required. Ultra central collisions are marginally dependent on initial conditions: Luzum and Ollitreatus showed [16] the root mean square of the harmonic eccentricity decreases with centrality. In addition the predictions obtained by using several different models get closer. The shear viscosity can be extracted comparing the ATLAS p_t integrated v_n data [17] to different model predictions. As a result a shear viscosity $0.07 \leq \eta/s \leq 0.43$ was obtained. The large allowed interval (factor 6) is mostly due to a tension between the v_2 and the v_3 constrain. G. Denicol et al. [18] included in the simulation the repulsive effect of nucleon-nucleon correlation, playing a non negligible role for the most central events. The fit of the IP-Glasma+Music model to the ATLAS v_n data, improves the v_2 and v_3 predictions, reduce their mutual tension and gives a preferred value of η/s=0.21. Further improvements may came from the recent data published by CMS, studying v_n at centrality as small as 0-0.2% [19].

4 Nuclear modification factor

The energy loss of scattered partons traversing the hot and dense medium can be quantified using the nuclear modification factor R_{AA}, defined as

$$R_{AA}(p_T) = \frac{Yield_{AA}(p_T)}{< N_{coll} >_{AA} \; Yield_{pp}(p_T)}, \tag{2}$$

where $Yield_{AA}$ is the yield obtained in nucleus-nucleus collisions, $Yield_{pp}$ is the yield obtained in pp collisions and $< N_{coll} >_{AA}$ is the average number of nucleon-nucleon collisions in A-A events.

A nuclear modification factor close to unit indicate that nucleus-nucleus collisions are equivalent to the superposition of nucleon-nucleon collisions, properly normalized. Partons are expected to lose energy in the hot and dense medium via gluon radiation and elastic collisions, leading to $R_{AA} < 1$. The QCD picture of parton energy loss in high energy heavy ion interactions predicts a gluon energy loss higher than the quark energy loss. In addition heavy quarks are expected to lose less energy compared to ligher quarks, due to the lack of gluon radiation in a forward cone (Casimir cone), whose angle $\theta = M_q/E_q$. Hints for a charged mesons (D^0, D^+, D^-) R_{AA} larger than that of charged particles has been reported by the ALICE experiment [20]. CMS showed the nuclear modification factor for non prompt J/Ψ(coming from b decay) is larger than D meson R_{AA}. These are clear indications the energy loss in the hot and dense matter follows the expected quark hierarchy.

The beam energy scan performed at RHIC is a nice opportunity to study the parton energy loss at different temperatures. At $\sqrt{s_{\rm NN}}$=200 GeV PHENIX found[21] a strong suppression for heavy flavour electrons compared to pp interactions (R_{AA} <1), while at $\sqrt{s_{\rm NN}}$=62 GeV the nuclear modification factor is compatible or larger than unit [22]. Although an higher statistics and a pp run at the same energy is required, this result indicates a change in the competition between the Cronin enhancement, that is prevalent in lower energy collisions, and the suppressing effects of the hot medium, that dominates at high energies. Another remarkable result obtained during the RHIC BES comes from STAR, measuring [23] the central-to-peripheral nuclear modification factor R_{CP} as a function of the centre of mass energy, where R_{CP} is defined as

$$R_{CP}(p_T) = \frac{< N_{Coll} >^{60-80\%}}{< N_{Coll} >^{0-5\%}} \frac{Yield_{AA}^{0-5\%}(p_T)}{Yield_{AA}^{60-80\%}(p_T)} \quad (3)$$

where $< N_{Coll} >^{60-80\%}$ is the average number of nucleon-nucleon collisions in events with centrality 60-80%, $< N_{Coll} >^{0-5\%}$ is the average number of nucleon-nucleon collisions in events with centrality 0-5%. While at $\sqrt{s_{\rm NN}}$=200 GeV $R_{CP} < 1$, as expected for partonic energy loss, at $\sqrt{s_{\rm NN}}$=7.7 GeV it exceeds 5 at p_T= 3 GeV/c. These two opposite trends show a smooth transition, with $R_{CP} \simeq 1$ reached between $\sqrt{s_{\rm NN}}$=27 GeV and $\sqrt{s_{\rm NN}}$=39 GeV: is the phase transition boundary within this energy interval ?

5 Quarkonia

The evidence for J/ψ suppression was a smoking gun of QGP formation at CERN-SPS experiments. Years later the RHIC experiments showed an unexpected result: the amount of suppression at $\sqrt{s_{\rm NN}}$=200 GeV was almost unchanged with respect to the SPS energies. The J/ψ suppression measured by ALICE at the LHC, was less pronounced at small centrality compared to RICH, both at forward and mid-rapidity. A possible explanation is provided by the recombination mechanism, playing an important role in J/ψ formation in heavy ion collisions at high energy. On average 70-80 $c\bar{c}$ pairs/events are expected at the LHC, to be compared to $\simeq$10 pairs at RHIC. J/ψ from $c\bar{c}$ recombination are expected to show a softer p_T spectrum and hence the J/ψ suppression should be stronger at higher p_T. Indeed ALICE results confirms this interpretation, as shown in Fig. 2(left panel). Moreover, in contrast to primordial J/ψ, the J/ψs from recombination are expected to inherit from c and $\bar{c}$ quarks their elliptic flow, due to the c quark thermalization. At RHIC a J/ψ elliptic flow consistent with zero was reported [24], while at the LHC ALICE [25] and CMS showed [26] a non zero v_2, with a $\simeq 4\sigma$ significance.

Due to the lower b$\bar{b}$ production cross section compared to the $c\bar{c}$ one, Υ is a powerful tool to study colour screening at the LHC. Nevertheless the feed-down from higher mass bottomonia, complicates data interpretation. Lattice QCD predicts a vector meson sequential suppression pattern with temperature: large uncertainties exist in the absolute calibration of this thermometer: Υ is expected to melt at a temperature 2-5 T_C, depending on the model considered, while the J/ψ melting temperature ranges from $1.5T_C$ to $3T_C$. STAR and PHENIX at RHIC showed hints for a Υ suppression in Au-Au interactions at $\sqrt{s_{\rm NN}}$=200 GeV. This suppression is compatible with the suppression reported at the LHC by CMS [27], suggesting the measured Υ suppression is consistent, both at RHIC and at the LHC, with the $\Upsilon(2s)$, $\Upsilon(3s)$ and χ_B full melting only, suggesting the $\Upsilon(1s)$ melting threshold was not reached yet. CMS measured the suppression of the three excited state: the $\Upsilon(1s)$ suppression increases with the centrality and is not suppressed in very peripheral collisions. On the contrary $\Upsilon(2s)$ is suppressed in peripheral collisions too. Finally the suppression of $\Upsilon(3s)$ is quite strong: an upper limit in the $\Upsilon(3s)/\Upsilon(1s)$ ratio <0.04 was set.

The ratio of $\Upsilon(2s)/\Upsilon(1s)$ is quite similar in pp (0.26 ± 0.01(sta) $\pm$ 0.01(sys) $\pm$ 0.02(glob))) and p-Pb interactions (0.22 ± 0.01(sta)$\pm$ 0.01(sys) $\pm$ 0.01(glob)) [27]. As a consequence, the strong $\Upsilon(2s)$ suppression seen in Pb-Pb collision (0.09 ± 0.02(sta) $\pm$ 0.02(sys) $\pm$ 0.01(glob)) cannot be explained by cold matter effects.

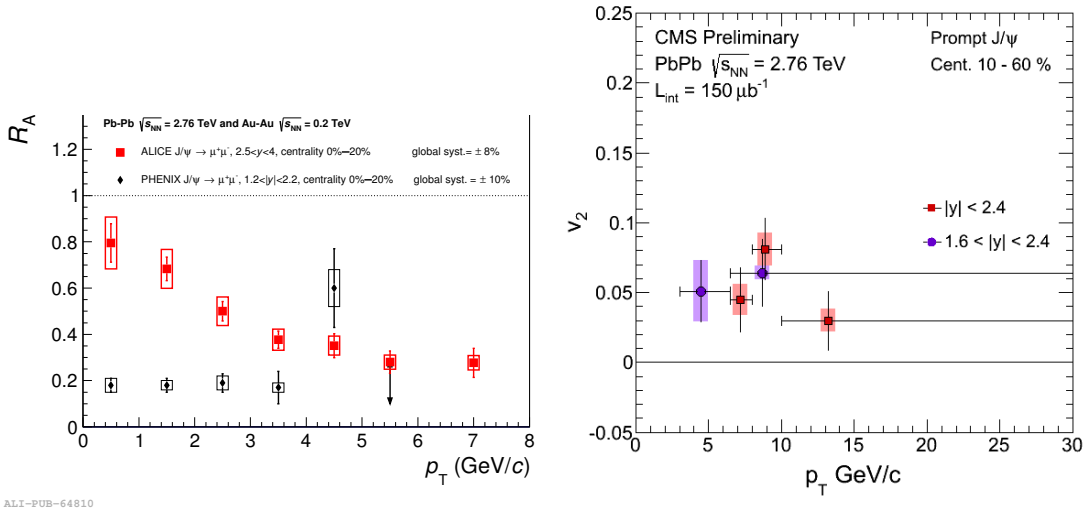

Figure 2: Left: comparison of J/ψ suppression as a function of the transverse momentum measured at the RHIC and at the LHC in the centraliy bin 0-20%. ALICE points show a less pronounced suppression at low p_T. Right: the elliptic flow measured by CMS. Both the result support a J/ψ recombination scenario.

6 The Ridge

Is Cold Nuclear Matter produced in p-Pb collisions at the LHC really cold ? Looking at electrons produced in heavy flavour decay (R_{pPb} $\simeq$1), to be compared with a much smaller

nuclear modification factor obtained in Pb-Pb collisions, the answer is affirmative. A similar conclusion can be drawn considering D meson production [28] or inclusive jet production [29] in p-Pb collisions. In addition the study of J/ψ in p-Pb collisions shows a modest to zero suppression, depending on the considered rapidity region; this result can be fully explained by initial state effects, as gluon shadowing. CMS discovered a ridge-like structure in events with a large number of produced charged particles in pp collisions [30]. A similar structure was previously found in Au-Au collisions by the RHIC experiments. The p-Pb collisions showed a ridge-like structure too, very similar, at a first look, to that observed in Pb-Pb collisions. This unexpected feature triggered a large amount of experimental [31, 32, 33] and theoretical studies. The ridge-like structure in pp and p-Pb collisions is surprisings, since these systems were not expected to produce a fireball dense and hot enough to produce strong collective effects. Several methods to separate the jet and the ridge components have been used. Namely ALICE subtracted the sample with a centrality 60-100% from the most 0-20% central events. As a result a double ridge-like structure was obtained [31]. The projection in the $\Delta\Phi$ plane can be fitted to a function:

$$\frac{1}{N_{trig}}\frac{dN}{d\Delta\Phi} = a_0 + 2\sum_{n>1} a_n \cos(n\Delta\Phi), \tag{4}$$

with v_n=$\sqrt{a_n/b}$, where b is the function baseline. As a result most of the Φ dependence comes from v_2 component, but higher orders are present too. ATLAS studied the v_n harmonics (n=1,2,3,4,5) in events with high multiplicity (220≤N<260) [33]: the results are fully consistent with the CMS analysis using the same charged particle intervals [34]. The v_n harmonics (n=1,2,3,4,5) distributions show an impressive similarities to those obtained in Pb-Pb collisions with similar multiplicity (20-30% centrality) [17]. To quantify this evidence CMS used multiparticle correlation in p-Pb interactions [35]: any effect coming from a genuine cumulative dynamics should not depend on the number of particles used to compute the v_2. The v_2 coefficient was extracted from the cumulant ($v_2(4)$,$v_2(6)$,$v_2(8)$ and $v_2(LYZ)$). For a given multiplicity range in either the Pb-Pb or p-Pb system, the values of $v_2(4)$,$v_2(6)$,$v_2(8)$ and $v_2(LYZ)$ are found to be in agreement within ±10%. The data support the multiparticle nature of the observed long-range correlations in p-Pb collisions. In addition ALICE and CMS measured the elliptic flow for identified hadrons in p-Pb collisions[36]: a mass ordering was observed (softer hadrons show larger v_2), as expected by hydro models. The above results give a convincing evidence that a large collectivity exist in p-Pb data. We cannot conclude Quark Gluon Plasma is formed in p-Pb collisions too, but this system looks hotter than expected. Another interesting effect reported in p-Pb collisions is the possible enhancement of R_{pPb} reported by ATLAS and CMS at high transverse momentum, ($p_T \geq 20$ GeV/c): more data are required and a dedicated pp run at $\sqrt{s_{\rm NN}}$=5 TeV is mandatory to have a firm conclusion on this effect.

7 Conclusions

An integrated luminosity as high as $1nb^{-1}$ will be delivered at the LHC during Run 2(2015-2018) for Pb-Pb collisions. The pp centre of mass energy will reach 13 TeV ($\simeq$ 5.1 TeV in Pb-Pb collisions). During Run 3 (2019-2026) an integrated luminosity $10nb^{-1}$ will be available to perform high statistic Pb-Pb studies; major detector upgrades during the Long Shutdown 2 will allow a reduction of the systematic error and an increase of the data samples.

After a successful Au-Au run in 2014, RHIC will provide p-Au collisions in 2015. A new beam energy scan (BES II) will be performed starting from 2018, with $\sqrt{s_{\rm NN}}\leq$ 20 GeV, focusing

on the critical point search and on a detailed study of the phase transition. The main goal of the electron-ion collider at BNL(eRHIC) is the exploration of the nucleus structure with the precision of electromagnetic probes at high energy and with sufficient intensity to access the gluon-dominated regime. The project foresees a startup on 2025 and new experiments, as sPHENIX and eSTAR [37].

References

[1] R. Hanury and R.Q.Twiss, Nature(London) 178, 1046 (1956).
[2] The ALICE Collaboration, Phys. Lett. **B696** (2011) 328.
[3] The PHENIX Collaboration, Phys. Rev. Lett **104** (2010) 132301.
[4] M. Wilde on behalf of the ALICE Collaboration, Nucl. Phys. **A904-905** (2013) 573c.
[5] The ALICE Collaboration *et al.*, Phys. Rev. Lett. (2010) 252301.
[6] The ALICE Collaboration, arXiv: 1405.4632, Submitted to JHEP.
[7] M. Luzum and R. Romantschke, Phys. Rev. **C78** (2008) 034915.
[8] B. Schenke *et al.*, Phys. Rev. **C86** (2012) 034908.
[9] The ATLAS Collaboration, JHEP 11(2013) 183.
[10] Z. Qiu and U. Heinz, arXiv:1104.0650v3.
[11] G. Gale *et al.*,Phys. Rev., Lett. **110** (2013) 012302.
[12] S. Schenke *et al.*, Phys. Rev. **C85** (2012) 024901.
[13] The ATLAS Collaboration, Phys. Rev. **C86** (2012) 014907.
[14] The ALICE Collaboration, Phys. Rev. Lett. **107** (2011) 032301
[15] The PHENIX Collaboration, Phys. Rev. Lett. **107** (2011) 2523
[16] M. Luzum and J. V. Ollitreaut, Nucl. Phys **904-905** (2013) 377c.
[17] The ATLAS Collaboration, Phys. Rev. **C86** (2012) 014907.
[18] G. Denicol *et al*, Proc. of Quark Matter 2014, in preparation.
[19] The CMS Collaboration, JHEP **02** (2014) 088.
[20] The ALICE Collaboration, JHEP 09 (2012) 112.
[21] The PHENIX Collaboration, Phys. Rev. Lett.**C84**(2011)044905.
[22] The PHENIX Collaboration, arXiv:1405.3301.
[23] the STAR Collaboration, Nucl. Phys.**A**905 (2013) 771c.
[24] The STAR Collaboration, Phys. Rev. Lett. **111** (2013) 52301.
[25] The ALICE Collaboration,Phys. Rev. Lett. **111** (2013) 162301.
[26] D. Manu on behalef of the CMS Collaboration, Proceedings of the Conference Quark Matter 2014, in press.
[27] The CMS Collaboration, JHEP 04 (2014) 103.
[28] The ALICE Collaboration, arXiv:1405.3452.
[29] E. A. Appelt on behalf of the CMS Collaboration, Proc. of Quark Matter 2014, in preparation.
[30] The CMS Collaboration, JHEP **1009** (2010) 091.
[31] The ALICE Collaboration, Phys. Lett. **B 719** (2013) 29.
[32] The CMS Collaboration, Phys. Lett. **B 724** (2013) 213.
[33] The ATLAS Collaboration, ATLAS-CONF-2014-021.
[34] The CMS Collaboration, CMS-HIN-014-006.
[35] The CMS Collaboration, CMS-HIN-014-006.
[36] The CMS Collaboration, Phys. Lett. **B 726** (2013) 164.
[37] The EIC White Paper, $https://wiki.bnl.gov/eic/index.php/Main_Page$.

Quark gluon plasma studies within a partonic transport approach

Florian Senzel[1], *Moritz Greif*[1], *Jan Uphoff*[1], *Christian Wesp*[1], *Zhe Xu*[2], *Carsten Greiner*[1]

[1]Goethe-Universität, Max-von-Laue-Str. 1, 60438 Frankfurt am Main, Germany
[2]Tsinghua University, Beijing 100084, China

DOI: http://dx.doi.org/10.3204/DESY-PROC-2014-04/289

Aiming for the simultaneous description of the hard and the soft regime of ultra-relativistic heavy-ion collisions, we present our recent findings within the partonic transport model BAMPS (Boltzmann Approach to Multi-Parton Scatterings). While using both elastic and radiative interactions provided by perturbative QCD, BAMPS allows the full 3+1D simulation of the quark-gluon plasma (QGP) at the microscopic level by solving the relativistic Boltzmann equation for quarks and gluons. BAMPS facilitates investigations of jet quenching, heavy flavor and elliptic flow within the partonic phase of heavy-ion collisions as well as studies of QGP medium properties in terms of e.g. transport coefficients like η/s and the electric conductivity.

1 Introduction

When heavy nuclei collide at ultra-relativistic energies, a system of hot and dense matter is created. Due to the enormous available energy densities within these collisions, quasi-free quarks and gluons represent the relevant degrees of freedom. Therefore the produced medium is commonly called the "quark-gluon plasma" (QGP). Experiments at both the Relativistic Heavy-Ion Collider (RHIC) at BNL and the Large Hadron Collider (LHC) at CERN show that the created medium exhibits interesting properties [1]: While high energy particles traversing the medium are quenched, the system shows at the same time a collective behavior similar to a nearly perfect liquid. Among the most prominent observables for quantifying these properties are the nuclear modification factor, R_{AA}, and the elliptic flow, v_2. While R_{AA} measures the suppression of inclusive particle yields compared to scaled p+p collisions, the elliptic flow v_2, defined in terms of the second Fourier coefficient of the azimuthal particle distribution, gives insight to the collectivity of the medium.

Although both phenomena are commonly attributed to the partonic phase of the heavy-ion collision, a simultaneous understanding of jet quenching and bulk phenomena on the microscopic level remains a challenge. In this paper we report on our progress in understanding the QGP within the partonic transport model *Boltzmann Approach to Multi-Parton Scatterings* (BAMPS). Based on cross sections calculated in perturbative quantum chromodynamics (pQCD), soft and hard particles are treated on the same footing in a common framework. While we take explicitly the running of the coupling into account, we study the energy loss of highly energetic [2, 3] and heavy flavor particles [4, 5] as well as the collective behavior in terms of the elliptic flow [3] and the electric conductivity of the underlying QGP medium [6].

2 The BAMPS framework

The partonic transport model *Boltzmann Approach to Multi-Parton Scatterings* (BAMPS) [7, 8] describes the full 3+1D evolution of both the QGP medium as well as high energy particles traversing it by numerically solving the relativistic Boltzmann equation,

$$p^\mu \partial_\mu f(\vec{x},t) = \mathcal{C}_{22} + \mathcal{C}_{2\leftrightarrow 3}\,, \tag{1}$$

for on-shell partons, quarks and gluons, and perturbative quantum chromodynamics (pQCD) interactions. To this end, a stochastical modeling of the collision probabilities together with a test-particle ansatz is employed.

Within BAMPS, both elastic $2 \to 2$ scattering processes calculated in leading-order pQCD, like e.g. $g\,g \to g\,g$, and inelastic $2 \leftrightarrow 3$ interactions, like e.g. $g\,g \leftrightarrow g\,g\,g$, are considered. The inelastic cross sections are calculated within an *improved Gunion-Bertsch (GB) approximation* [9, 10],

$$\left|\overline{\mathcal{M}}_{X\to Y+g}\right|^2 = 48\pi\alpha_s(k_\perp^2)\,(1-\bar{x})^2\,\left|\overline{\mathcal{M}}_{X\to Y}\right|^2 \left[\frac{\mathbf{k}_\perp}{k_\perp^2} + \frac{\mathbf{q}_\perp - \mathbf{k}_\perp}{(\mathbf{q}_\perp - \mathbf{k}_\perp)^2 + m_D^2\,(\alpha_s(k_\perp^2))}\right]^2 , \tag{2}$$

which agrees well with the exact pQCD matrix element over a wide phase space region [10]. As a remark, $\left|\overline{\mathcal{M}}_{X\to Y}\right|$ denotes the matrix element of the respective elastic process, while $k_\perp$ and $q_\perp$ are the transverse momentum of the emitted and internal gluons, respectively.

The running of the QCD coupling $\alpha_s(k_\perp^2)$ is considered within BAMPS by setting the scale of the coupling to the momentum transfer of the considered channel and thereby evaluating it for each collision at the microscopic level.

For modeling the Landau-Pomeranchuk-Migdal (LPM) effect, which is an important quantum effect within a partonic QCD medium, an effective cutoff function $\theta\,(\lambda - X_{LPM}\,\tau_f)$ in the radiative matrix elements is used, where λ is the mean free path of the radiating particle, τ_f the gluon formation time and X_{LPM} a parameter that effectively controls the independence between consecutive gluon emissions. The value $X_{LPM} = 0.3$ is fixed by comparing to R_{AA} data of neutral pions at RHIC [3]. Any further divergences occurring in the integration of the pQCD matrix elements are cured by a screening Debye mass m_D^2, which is dynamically computed on the basis of the current quark and gluon distribution [7].

3 Jet quenching within heavy-ion collisions

While employing PYTHIA [11] initial conditions together with a Monte Carlo Glauber sampling as described in detail in Ref. [7, 12], Fig. 1 (left) shows the nuclear modification factor R_{AA} obtained by BAMPS for gluons, light quarks and charged hadrons at the LHC [3]. Due to their larger QCD color factor, gluons are stronger suppressed than light quarks over the whole p_t range. For comparison with data, we also show the R_{AA} for charged hadrons resulting from fragmentation via AKK fragmentation functions [13]. According to this fragmentation functions, hadrons at low p_t are dominated by fragmenting gluons, while at higher p_t the quark contribution increases. Together with the rising shape of the R_{AA} this effect leads to a hadronic R_{AA} that is close to the quark R_{AA}.

Another method for characterizing the energy loss of high p_t partons within the QGP is the reconstruction of jets within heavy-ion collisions. Both the ATLAS [14] and CMS experiments

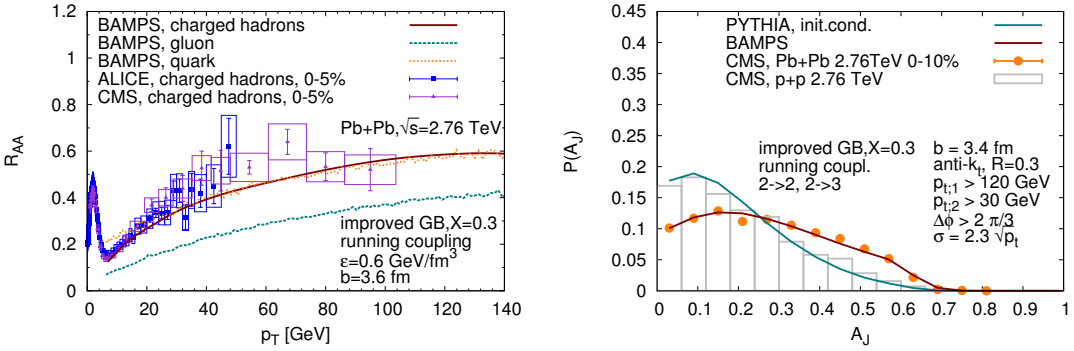

Figure 1: Left: Nuclear modification factor R_{AA} of gluons, light quarks, and charged hadrons at LHC (left) for a running coupling and LPM parameter $X = 0.3$ together with data of charged hadrons [16] as published in Ref. [3]. Right: A_J distribution calculated by BAMPS [2] with impact parameter $b_{\text{mean}} = 3.4$ fm together with PYTHIA initial conditions in comparison with $\sqrt{s} = 2.76$ TeV p+p and $\sqrt{s} = 2.76$ ATeV 0-10% Pb+Pb data measured by CMS [15] as published in Ref. [2].

[15] reported the measurement of an enhanced number of events with an asymmetric pair of back-to-back reconstructed jets in comparison to p+p events, which is quantified in terms of the momentum imbalance $A_J\,(p_{t;1}, p_{t;2}) = \frac{p_{t;1}-p_{t;2}}{p_{t;1}+p_{t;2}}$, where $p_{t;1}$ ($p_{t;2}$) is the transverse momentum of the leading (subleading) jet—the reconstructed jet with the highest (second highest) transverse momentum per event. While employing all experimental trigger conditions, Fig. 1 (right) shows the momentum imbalance A_J calculated within BAMPS together with data. Consistent with the R_{AA} studies the momentum imbalance of reconstructed jets within BAMPS is in agreement with data. For more details about the studies of reconstructed jets within BAMPS we refer to Ref. [2].

4 Heavy flavor within heavy-ion collisions

Quantitative studies of heavy flavor within BAMPS [17, 18, 4] show that, although elastic processes with a running coupling and an improved screening procedure contribute significantly to the energy loss of heavy quarks, they alone cannot reproduce the data of the nuclear modification factor or the elliptic flow of any heavy flavor particle species. Therefore, before radiative heavy quark processes have been implemented in BAMPS, we mimicked their influence by effectively increasing the elastic cross section by a factor $K = 3.5$, which is tuned to the v_2 data of heavy flavor electrons at RHIC [4]. With this fixed parameter it is furthermore possible to describe the R_{AA} of heavy flavor electrons at RHIC as well as the experimentally measured R_{AA} and v_2 of all heavy flavor particles at LHC (see Fig. 2). However, the need of the phenomenological K factor is rather unsatisfying from the theory perspective. Therefore, the question arises whether radiative processes can account for the missing contribution parameterized by the K factor. To this end, we present in the left panel of Fig. 3 the nuclear modification factor at LHC calculated within BAMPS while treating both heavy and light partons on the same footing consisting of radiative processes based on the improved GB matrix element, a running

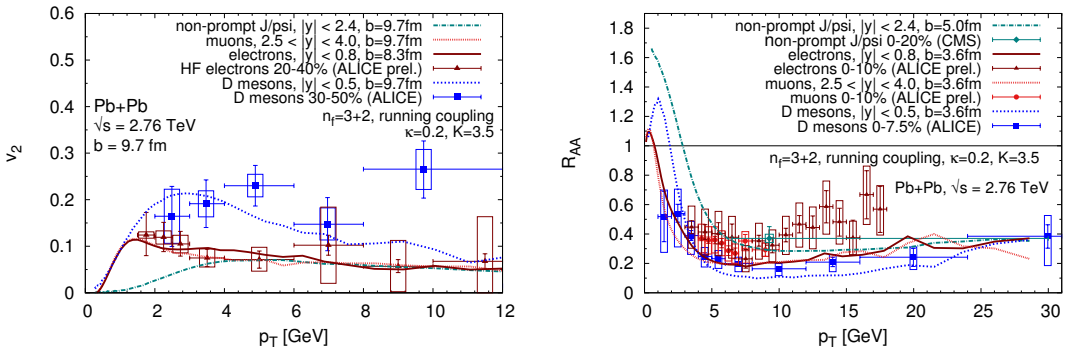

Figure 2: Elliptic flow v_2 (left) and nuclear modification factor R_{AA} (right) of various heavy flavor particles at LHC as published in Ref. [4] together with data [19, 20, 21, 22, 23, 24]. Only binary heavy flavor processes are considered and multiplied with $K = 3.5$.

coupling and an effective modeling of the LPM effect ($X_{LPM} = 0.3$) [5]. A good agreement between the BAMPS calculations and the nuclear modification factor of D mesons at LHC is found. As shown in Ref. [5] the energy loss of light and charm quarks is similar what explains why the nuclear modification factors of charged hadrons and D mesons in heavy-ion collisions have also the same values. Furthermore, mass effects in the fragmentation of gluons and light quarks to charged hadrons and charm quarks to D mesons lead to a similar suppression of charged hadrons and D mesons in BAMPS.

5 Properties of the underlying QGP medium

After presenting results on jet quenching and heavy flavor, we investigate the bulk evolution by employing the same setup as already described above together with the fixed LPM parameter $X_{LPM} = 0.3$ and a freeze-out energy density $\epsilon_c = 0.6\,\mathrm{GeV/fm}$ [26]. Since the microscopic hadronization processes within the soft regime are not fully understood yet, we show in Fig. 3 (right) our results for the integrated, partonic v_2 as a function of the number of participants N_{part} in comparison with LHC data.

Remarkably, by using the same microscopic pQCD interactions for both the hard and the soft momentum regime, BAMPS media build up a sizable amount of flow within the partonic phase. The reason for this lies in the isotropization of inelastic $2 \leftrightarrow 3$ processes as well as the running coupling, which affects the elliptic flow of particles with small p_T and the R_{AA} of particles with large p_T differently. The difference of the integrated, partonic v_2 of BAMPS and the measured, hadronic v_2 both at LHC is about $10-20\%$ and is supposed to be caused by the missing hadronic phase.

As advocated in dissipative hydrodynamic fits, an important quantity for the bulk medium in heavy-ion collisions is the shear viscosity to entropy density ratio η/s. In Fig. 4 (left) the temperature dependence of this value in a static medium allowing all $2 \to 2$ and $2 \leftrightarrow 3$ processes is shown. The shear viscosity is calculated via the Green-Kubo relation, which links the autocorrelation function of the medium energy-momentum tensor of the medium to the transport coefficient η [27]. The ratio η/s decreases with decreasing temperature and reaches

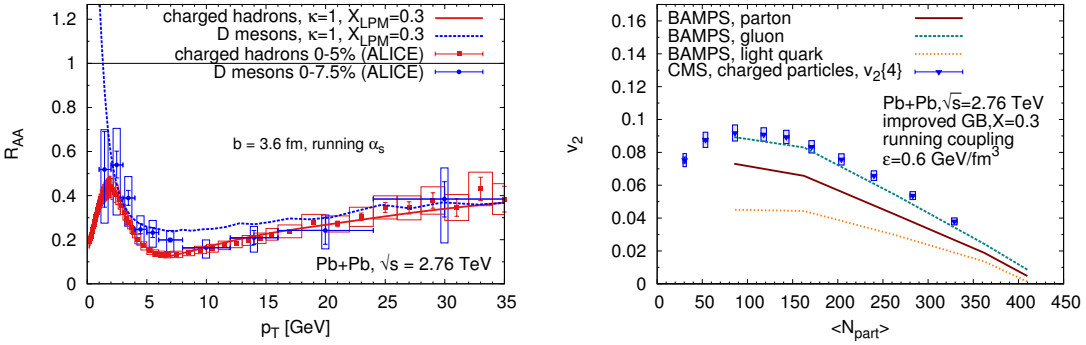

Figure 3: Left: Nuclear modification factor R_{AA} of charged hadrons and D mesons at LHC as published in Ref. [5] in comparison to data [16, 23]. Both binary and radiative processes with a LPM parameter set to $X_{LPM} = 0.3$ are considered. Right: Elliptic flow v_2 of gluons, light quarks, and both together (light partons) within $|\eta| < 0.8$ at LHC as a function of the number of participants N_{part} for a running coupling and LPM parameter $X = 0.3$ as published in Ref. [3]. As a comparison we show experimental data by CMS for charged hadrons within $|\eta| < 0.8$ [25].

a minimum at the phase transition. The value of η/s in the region around $T = 0.2\,\text{GeV}$ that is most important for the elliptic flow is approximately 0.2 for $n_f = 0$, which agrees very well with the shear viscosity extraction from dissipative hydrodynamic models employing a constant $\eta/s = 0.2$ together with initial fluctuations modeled by IP-Glasma [28]. Thus our calculation employing pQCD cross sections can give a microscopic explanation of the small shear viscosity to entropy density ratio extracted from hydrodynamics.

Besides the shear viscosity it is also possible to study other transport coefficients of the QGP medium, like e.g. the heat conductivity κ [39] or the electric conductivity σ_{el} [6]. The electric conductivity is related to the soft dilepton production rate and the diffusion of magnetic fields in the medium. Studies of the electric conductivity allows to compare the effective cross sections of medium constituents between several theories, including transport models [29, 40], lattice gauge theory [32, 33, 34, 35, 36, 37, 38] and Dyson-Schwinger calculations [41].

The longitudinal static electric conductivity σ_{el} relates the response of the electric diffusion current density $\vec{j}$ to an externally applied static electric field $\vec{E}$, $\vec{j} = \sigma_{\text{el}}\vec{E}$. Additionally, the electric conductivity can also be obtained by the Green-Kubo [42, 43] formula for the electric current density in x-direction $j_x(t)$,

$$\sigma_{\text{el}} = \beta V \int_0^\infty \langle j_x(0) j_x(t) \rangle \, \mathrm{d}t \quad \text{with} \quad j^x(t) = \frac{1}{V N_{\text{test}}} \sum_{k=1}^{M} q_k \sum_{i=1}^{N_k} \frac{p_i^x}{p_i^0}\bigg|_t \,, \tag{3}$$

where V denotes the volume, $\beta = T^{-1}$ the inverse temperature, M the number of particle species and N_k the number of particles of species k. The electric current autocorrelation function $\langle j_x(0) j_x(t) \rangle$ can be obtained numerically, as it has been done in e.g. Ref. [27] for the shear stress tensor correlation function.

By employing BAMPS with the described pQCD cross sections, it is possible to extract

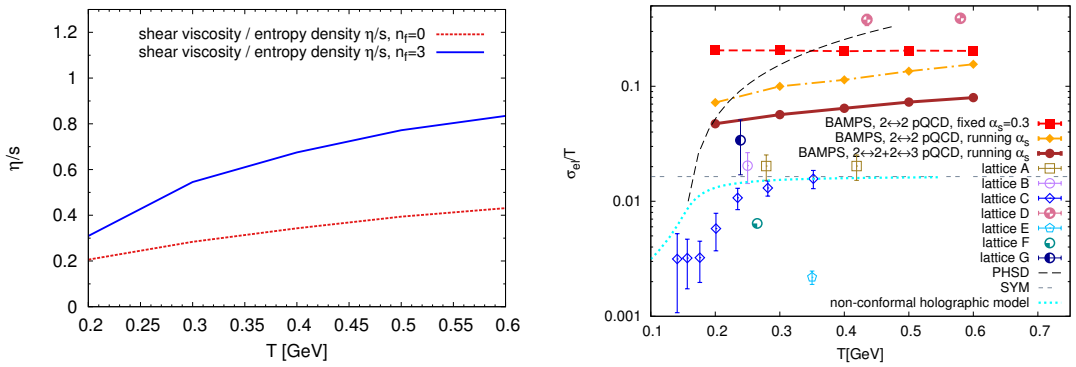

Figure 4: Left: Shear viscosity over entropy density η/s for running coupling and $X_{\mathrm{LPM}} = 0.3$ in a static medium of temperature T with number of quark flavors n_f as published in Ref. [3]. Right: Electric conductivity σ_{el} within BAMPS (filled symbols) as published in Ref. [6] compared to recent results from literature. The open symbols represent results from lattice QCD. PHSD: [29], SYM: [30], non-conformal holographic model: [31], lattice A: [32], lattice B: [33], lattice C: [34], lattice D: [35], lattice E: [36], lattice F: [37], lattice G: [38]. The electric charge is explicitly multiplied out, $e^2 = 4\pi/137$.

the electric conductivity of a plasma consisting of quarks and gluons in the massless limit using both approaches, via the response of the electric diffusion current density and the Green-Kubo relation. These studies have shown that both methods show identical results [6], what has been additionally justified by comparison with analytically formulas employing constant, isotropic cross sections. Figure 4 depicts the results for the electric conductivity using pQCD cross sections together with either a running coupling or a fixed coupling $\alpha_s = 0.3$. The electric conductivity reflects in a profound way the effect of inelastic pQCD scatterings and the running of the coupling α_s. The presented results from the BAMPS transport simulation lie between $0.04 \leq \sigma_{\mathrm{el}}/T \leq 0.08$ for temperatures 0.2 GeV $\leq T \leq$ 0.6 GeV. As a remark, the quantitative comparison with lattice QCD data is difficult since the published results from lattice QCD for the electric conductivity vary widely between $0.001 \leq \sigma_{\mathrm{el}}/T \leq 0.1$.

6 Conclusions

By solving the relativistic Boltzmann equation for on-shell partons, the partonic transport approach BAMPS allows the full 3+1D microscopic simulation of the QGP created in ultra-relativistic heavy-ion collisions. Consequently, investigations of both the suppression of high p_t particles and the collectivity of the bulk medium within a common framework are possible within BAMPS. By employing an improved Gunion-Bertsch matrix element and a running coupling evaluated at the microscopic level, we are able to describe high p_t and heavy flavor observables at LHC. Furthermore, the same microscopic pQCD interactions lead to a sizable elliptic flow of the bulk medium within the partonic phase. Furthermore, we investigated medium properties of the QGP in terms of the shear viscosity to entropy density ratio η/s and the electric conductivity σ_{el} from a microscopic perspective.

Acknowledgments

This work was supported by the Bundesministerium für Bildung und Forschung (BMBF), HGS-HIRe, H-QM, and the Helmholtz International Center for FAIR within the framework of the LOEWE program launched by the State of Hesse. Numerical computations have been performed at the Center for Scientific Computing (CSC).

References

[1] Berndt Müller, Jurgen Schukraft, and Boleslaw Wyslouch. First Results from Pb+Pb collisions at the LHC. *Ann.Rev.Nucl.Part.Sci.*, 62:361–386, 2012.

[2] Florian Senzel, Oliver Fochler, Jan Uphoff, Zhe Xu, and Carsten Greiner. Influence of multiple in-medium scattering processes on the momentum imbalance of reconstructed di-jets. arXiv:1309.1657, 2013.

[3] Jan Uphoff, Oliver Fochler, Florian Senzel, Christian Wesp, Zhe Xu, et al. Elliptic flow and nuclear modification factor in ultra-relativistic heavy-ion collisions within a partonic transport model. arXiv:1401.1364, 2014.

[4] Jan Uphoff, Oliver Fochler, Zhe Xu, and Carsten Greiner. Open Heavy Flavor in Pb+Pb Collisions at $\sqrt{s} = 2.76$ TeV within a Transport Model. *Phys.Lett.*, B717:430–435, 2012.

[5] Jan Uphoff, Oliver Fochler, Zhe Xu, and Carsten Greiner. Elastic and radiative heavy quark interactions in ultra-relativistic heavy-ion collisions. arXiv:1408.2964, 2014.

[6] Moritz Greif, Ioannis Bouras, Zhe Xu, and Carsten Greiner. Electric Conductivity of the Quark-Gluon Plasma investigated using a pQCD based parton cascade. arXiv:1408.7049, 2014.

[7] Zhe Xu and Carsten Greiner. Thermalization of gluons in ultrarelativistic heavy ion collisions by including three-body interactions in a parton cascade. *Phys.Rev.*, C71:064901, 2005.

[8] Zhe Xu and Carsten Greiner. Transport rates and momentum isotropization of gluon matter in ultrarelativistic heavy-ion collisions. *Phys.Rev.*, C76:024911, 2007.

[9] J.F. Gunion and G. Bertsch. Hadronization by color bremsstrahlung. *Phys.Rev.*, D25:746, 1982.

[10] Oliver Fochler, Jan Uphoff, Zhe Xu, and Carsten Greiner. Radiative parton processes in perturbative QCD – an improved version of the Gunion and Bertsch cross section from comparisons to the exact result. *Phys.Rev.*, D88:014018, 2013.

[11] Torbjorn Sjostrand, Stephen Mrenna, and Peter Skands. PYTHIA 6.4 physics and manual. *JHEP*, 05:026, 2006.

[12] Jan Uphoff, Oliver Fochler, Zhe Xu, and Carsten Greiner. Heavy quark production at RHIC and LHC within a partonic transport model. *Phys.Rev.*, C82:044906, 2010.

[13] S. Albino, B.A. Kniehl, and G. Kramer. AKK Update: Improvements from New Theoretical Input and Experimental Data. *Nucl.Phys.*, B803:42–104, 2008.

[14] Georges Aad et al. Observation of a Centrality-Dependent Dijet Asymmetry in Lead-Lead Collisions at $\sqrt{s_{NN}} = 2.77$ TeV with the ATLAS Detector at the LHC. *Phys.Rev.Lett.*, 105:252303, 2010.

[15] Serguei Chatrchyan et al. Jet momentum dependence of jet quenching in PbPb collisions at $\sqrt{s_{NN}} = 2.76$ TeV. *Phys.Lett.*, B712:176–197, 2012.

[16] Betty Abelev et al. Centrality Dependence of Charged Particle Production at Large Transverse Momentum in Pb–Pb Collisions at $\sqrt{s_{\rm NN}} = 2.76$ TeV. *Phys.Lett.*, B720:52–62, 2013.

[17] Jan Uphoff, Oliver Fochler, Zhe Xu, and Carsten Greiner. Heavy quarks at RHIC and LHC within a partonic transport model. *Nucl.Phys.*, A855:444–447, 2011.

[18] Jan Uphoff, Oliver Fochler, Zhe Xu, and Carsten Greiner. Elliptic flow and energy loss of heavy quarks in ultra-relativistic heavy ion collisions. *Phys.Rev.*, C84:024908, 2011.

[19] B. Abelev et al. D meson elliptic flow in non-central Pb-Pb collisions at $\sqrt{s_{\rm NN}} = 2.76$TeV. *Phys.Rev.Lett.*, 111:102301, 2013.

[20] Shingo Sakai. Measurement of R_{AA} and ν_2 of electrons from heavy-flavour decays in Pb-Pb collisions at $\sqrt{s_{NN}} = 2.76$ TeV with ALICE. *Nucl.Phys.*, A904-905:661c–664c, 2013.

[21] Zaida Conesa del Valle. Heavy-flavor suppression and azimuthal anisotropy in Pb-Pb collisions at $\sqrt{(}s_{NN}) = 2.76$ TeV with the ALICE detector. *Nucl.Phys.*, A904-905:178c–185c, 2013.

[22] Betty Abelev et al. Production of muons from heavy flavour decays at forward rapidity in pp and Pb-Pb collisions at $\sqrt{s_{NN}} = 2.76$ TeV. *Phys.Rev.Lett.*, 109:112301, 2012.

[23] Alessandro Grelli. D meson nuclear modification factors in Pb-Pb collisions at $\sqrt{s_{NN}} = 2.76$ TeV with the ALICE detector. *Nucl.Phys.*, A904-905:635c–638c, 2013.

[24] Serguei Chatrchyan et al. Suppression of non-prompt J/psi, prompt J/psi, and Y(1S) in PbPb collisions at $\sqrt{s_{NN}} = 2.76$ TeV. *JHEP*, 1205:063, 2012.

[25] Serguei Chatrchyan et al. Measurement of the elliptic anisotropy of charged particles produced in PbPb collisions at nucleon-nucleon center-of-mass energy = 2.76 TeV. *Phys.Rev.*, C87:014902, 2013.

[26] Zhe Xu and Carsten Greiner. Elliptic flow of gluon matter in ultrarelativistic heavy- ion collisions. *Phys.Rev.*, C79:014904, 2009.

[27] C. Wesp, A. El, F. Reining, Z. Xu, I. Bouras, et al. Calculation of shear viscosity using Green-Kubo relations within a parton cascade. *Phys.Rev.*, C84:054911, 2011.

[28] Charles Gale, Sangyong Jeon, Bjorn Schenke, Prithwish Tribedy, and Raju Venugopalan. Event-by-event anisotropic flow in heavy-ion collisions from combined Yang-Mills and viscous fluid dynamics. *Phys.Rev.Lett.*, 110:012302, 2013.

[29] W. Cassing, O. Linnyk, T. Steinert, and V. Ozvenchuk. Electrical Conductivity of Hot QCD Matter. *Physical Review Letters*, 110(18):182301, May 2013.

[30] Simon C Huot, Pavel Kovtun, Guy D Moore, Andrei Starinets, and Laurence G. Yaffe. Photon and dilepton production in supersymmetric Yang-Mills plasma. *Journal of High Energy Physics*, 2006(12):015–015, December 2006.

[31] S. I. Finazzo and Jorge Noronha. Holographic calculation of the electric conductivity of the strongly coupled quark-gluon plasma near the deconfinement transition. *Physical Review D*, 89(10):106008, May 2014.

[32] Gert Aarts, Chris Allton, Justin Foley, Simon Hands, and Seyong Kim. Spectral functions at small energies and the electrical conductivity in hot quenched lattice QCD. *Physical Review Letters*, 99(2):022002, 2007.

[33] Bastian B. Brandt, Anthony Francis, Harvey B. Meyer, and Hartmut Wittig. Thermal correlators in the ρ channel of two-flavor QCD. *Journal of High Energy Physics*, 2013(3):100, March 2013.

[34] Alessandro Amato, Gert Aarts, Chris Allton, Pietro Giudice, Simon Hands, and Jon-Ivar Skullerud. Electrical Conductivity of the Quark-Gluon Plasma Across the Deconfinement Transition. *Physical Review Letters*, 111(17):172001, October 2013.

[35] Sourendu Gupta. The electrical conductivity and soft photon emissivity of the QCD plasma. *Physics Letters B*, 597(1):57–62, September 2004.

[36] P. V. Buividovich, M. N. Chernodub, D. E. Kharzeev, T. Kalaydzhyan, E. V. Luschevskaya, and M. I. Polikarpov. Magnetic-Field-Induced Insulator-Conductor Transition in SU(2) Quenched Lattice Gauge Theory. *Physical Review Letters*, 105(13):132001, September 2010.

[37] Y Burnier and M Laine. Towards flavour-diffusion coefficient and electrical conductivity without ultraviolet contamination. *The European Physical Journal C*, 72(2):1–8, 2012.

[38] H.-T. Ding, A. Francis, O. Kaczmarek, F. Karsch, E. Laermann, and W. Soeldner. Thermal dilepton rate and electrical conductivity: An analysis of vector current correlation functions in quenched lattice QCD. *Physical Review D*, 83(3):034504, February 2011.

[39] M. Greif, F. Reining, I. Bouras, G.S. Denicol, Z. Xu, and C. Greiner. Heat conductivity in relativistic systems investigated using a partonic cascade. *Physical Review E*, 87(3):033019, March 2013.

[40] T. Steinert and W. Cassing. Electric and magnetic response of hot QCD matter. *Physical Review C*, 89(3):035203, March 2014.

[41] Si-xue Qin. A Divergence-Free Method to Extract Observables from Meson Correlation Functions. arXiv:1307.4587, 2013.

[42] Melville S. Green. Markoff Random Processes and the Statistical Mechanics of Time-Dependent Phenomena. II. Irreversible Processes in Fluids. *The Journal of Chemical Physics*, 22(3):1281, 1952.

[43] Ryogo Kubo. Statistical-Mechanical Theory of Irreversible Processes. I. General Theory and Simple Applications to Magnetic and Conduction Problems. *Journal of the Physical Society of Japan*, 12(6):570–586, June 1957.

New Accelerator Projects: Rare Isotope Facilities and Electron Ion Colliders

Thomas Roser
BNL, Upton, NY, 11973, USA

DOI: http://dx.doi.org/10.3204/DESY-PROC-2014-04/291

Presently there are two major areas of new accelerator projects in particle physics: a next generation of Rare Isotope facilities in the field of Nuclear Structure Physics and high luminosity Electron Ion Colliders as next generation QCD faciliies in the field of Hadron Physics. This paper presents a review of the present and future facilities and the required novel accelerator technologies for these two types of accelerator projects.

1 Introduction

Over the last century progress in accelerator technology is motivated by and has driven advances in both particle and nuclear physics. This started with Ernest Lawrence's first cyclotron built in 1932, small enough to fit in one's hand, and continues today with large hadron collider such as Brookhaven's Relativistic Heavy Ion Collider (RHIC) (Fig. 1) and CERN's Large Hadron Collider (LHC). Presently there are two major areas of new accelerator projects in particle physics: a next generation of Rare Isotope facilities in the field of Nuclear Structure Physics and high luminosity Electron Ion Colliders a next generation QCD facilities in the field of Hadron Physics.

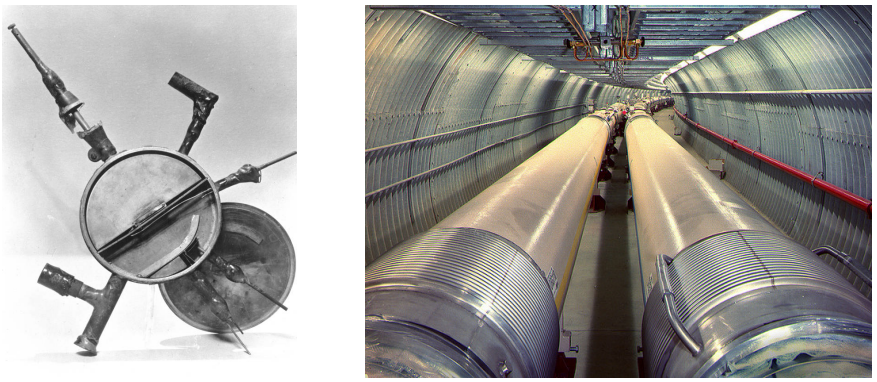

Figure 1: Accelerators used for nuclear and particle physics spanned an enormous range of scales form Ernest Lawrence's cyclotron that fit into one's hand to large hadron colliders such as the 3.8 km circumference Relativistic Heavy Ion Collider at BNL

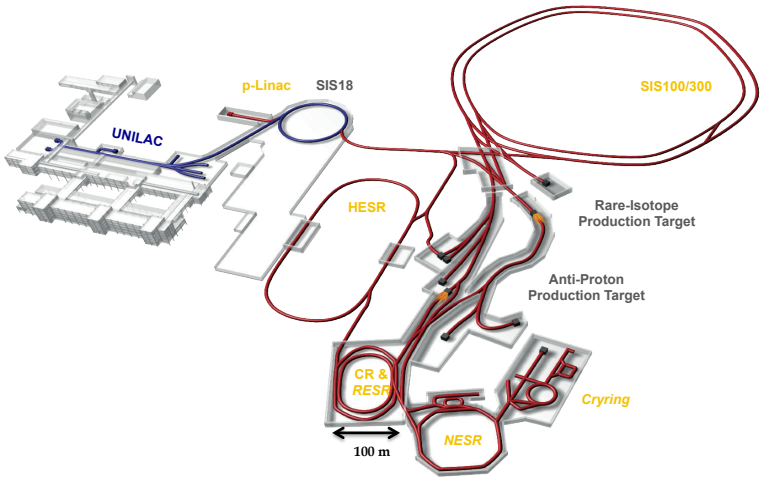

Figure 2: Layout of the FAIR facility near Darmstadt, Germany

2 Next generation of Rare Isotope facilities

The next generation of Rare Isotope facilities will dramatically increase the intensity of the driver accelerator. The three facilities under construction or close to the start of construction use a heavy ion driver beam. Enabling technologies are: Continuous Wave (CW), superconducting RF (SRF) Linear accelerators for partially stripped heavy ion beams; radiation hardened devices to strip electrons from the beams such as high speed rotating Carbon disks, liquid Lithium films or stable plasma windows; highly efficient heavy ion sources and charge breeders such as high intensity Electron Beam Ion Sources (EBIS) and high intensity Electron Cyclotron Resonance (ECR) sources; and acceleration of high intensity, partially stripped heavy ion beams in synchrotrons using Ultra High Vacuum (UHV) together with continuous collimation.

Three new Rare Isotope facilities are under construction or close to the start of construction:

- Construction has started for the Facility for Rare Isotope Beams (FRIB), a 0.2 GeV/n, 400 kW heavy ion driver that will produce beams of radioactive isotopes through fragmentation of uranium beam on a high power target. This will be the first installation of a large, CW SRF linac for hadron beams. It requires cavities for non-relativistic particle with a high quality factor to minimize the cryogenic cooling power. The heavy ion beams are produced partially stripped and then pass through an ion stripper for additional charge stripping as they gain energy. The ion stripper for the high intensity beams will be implemented either with a liquid metal film or a high pressure gas target. The construction period is planned from 2014 to 2020.

- The GSI laboratory near Darmstadt, Germany, is expanding its facility with a 30 GeV proton-equivalent heavy ion driver plus multiple accumulation and storage rings. The new facility will be called "Facility for Antiproton and Ion Research" (FAIR) (Fig. 2). The new 30 GeV synchrotron will be using fast cycling super-ferric magnets and will be optimized for the acceleration and storage of high intensity, partially stripped uranium ions. Construction has started and is now planned to be completed by about 2020.

- At the Institute of Modern Physics (IMP) in Lanzhou, China, preparations have started for a high intensity Heavy Ion Accelerator Facility (HIAF). The focus will also be on the production of rare isotopes and of high density plasma. The planned intensity of uranium beams in the SRF linac will be four times the planned intensity at FRIB. Construction is planned for the 2015 - 2021 period.

3 Electron Ion Colliders

There is renewed interest in a electron-ion collider with dramatically increased luminosity compared to the very successful electron-proton HERA facility at DESY. Most of the new proposals would also use polarized proton and light ion beams as well as heavy ion beams. Fig. 3 gives an overview of the peak luminosity versus center-of-mass energy for past, existing and future electron-proton facilities. Past and present facilities are indicated in black. The two proposals in the U.S. (MEIC at JLab and eRHIC at BNL) focus on the collision of polarized electrons with polarized protons at very high luminosity to measure the gluon spin structure at low x and electrons colliding with heavy ions for high-resolution imaging of gluon-dominated matter.

Two types of schemes to reach very high electron-ion luminosities are being pursued:

- The first scheme has the electron and hadron beam both circulating in a storage ring. In this case the beam-beam effects of the hadron beam on the lower energy electron beam severely limits the brightness of the hadron beam in order to keep the electron beam stable. To reach high luminosity many lower intensity bunches, with bunch spacing as short as 1 ns, are then needed, which then requires the operation with a large crossing angle to

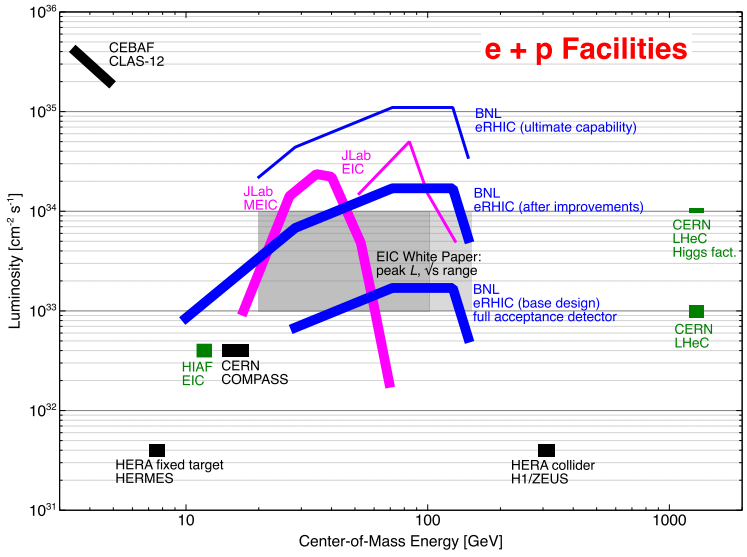

Figure 3: History and plans of the peak luminosity vs center-of-mass energy of lepton-hadron colliders

avoid parasitic collisions. This scheme is pursued for MEIC at JLab and HIAF-EIC at IMP.

- The second scheme uses an electron beam accelerated in a Energy Recovery Linac (ERL) to collide with a hadron beam in a storage ring. Since there is only a single collision of an electron bunch with the hadron beam a much higher beam-beam effect and therefore luminosity is possible. However the electron beam has to be continuously replenished from the source. This requires a new high intensity polarized electron source. This scheme is planned for eRHIC at BNL and LHeC at CERN.

3.1 MEIC at JLab

The first stage EIC proposal at JLab is called Medium Energy Electron-Ion Collider (MEIC) and would add a 3 - 12 GeV electron storage ring, using the present CEBAF as a full energy injector, and a new polarized proton (20 - 100 GeV) and heavy ion (12 - 40 GeV/n) accelerator complex (Fig. 4). The high luminosity of about $10^{34} cm^{-2} s^{-1}$ would be achieved with a very short bunch spacing of 1.3 ns as well as strong electron cooling of the ion beams. The whole complex would be laid out in the shape of a figure-8 to preserve beam polarization, including polarized deuteron beams, without needing Siberian snakes. Construction of this first stage could start after the present 12 GeV CEBAF upgrade is completed. A second stage would include a 20 GeV electron ring and a 250 GeV proton ring.

3.2 HIAF-EIC at IMP

The IMP laboratory in Lanzhou, China, also has plans to upgrade its HIAF to a Electron-Ion Collider by adding Figure-8 shaped polarized electron and proton rings. The electron energy will be 3 GeV, colliding with a 12 GeV polarized proton beam. With electron cooling of the proton beam a luminosity of $3 - 5 \times 10^{32} cm^{-2} s^{-1}$ could be reached.

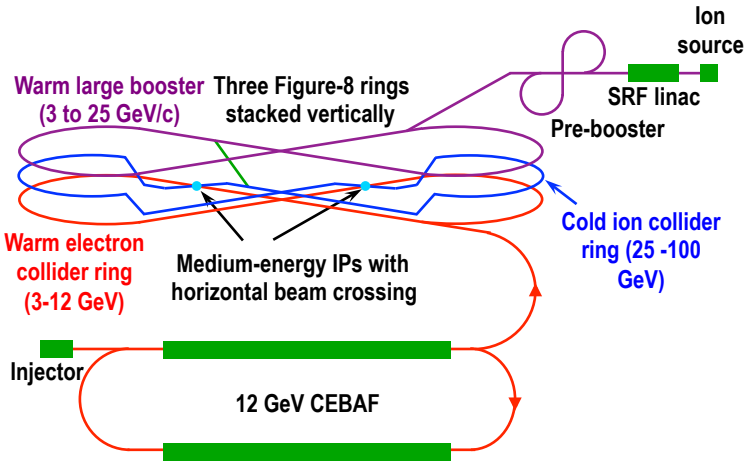

Figure 4: Layout of the proposed MEIC facility at JLab.

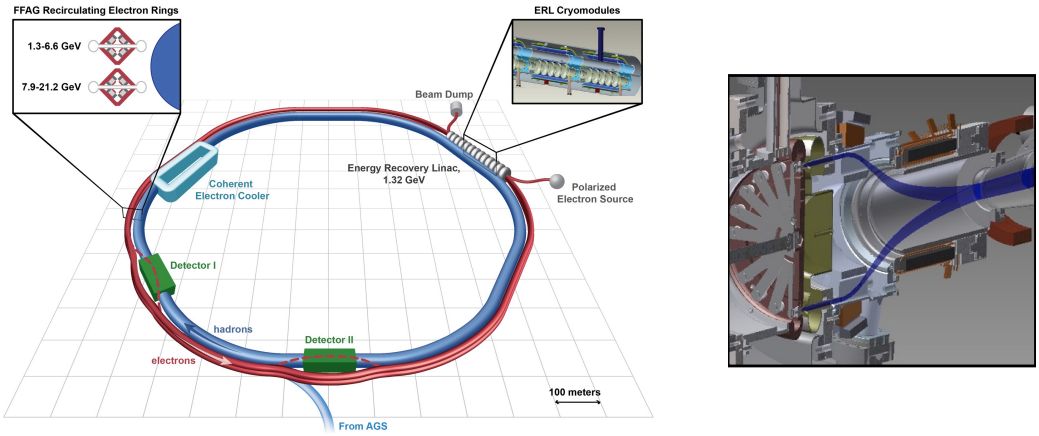

Figure 5: Layout of the proposed eRHIC facility at BNL (left) and schematic view of the high current, polarized "Gatling" electron source (right).

3.3 eRHIC at BNL

eRHIC at BNL would add a 21.2 GeV electron accelerator, based on an Energy Recovery Linac (ERL) with up to 16 recirculating passes inside the existing RHIC tunnel, to collide with the existing RHIC beams of 250 GeV polarized protons and 100 GeV/n heavy ions (Fig. 5). The 16 beam passes will be transported around the RHIC tunnel with two Fixed Field Alternating Gradient (FFAG) arcs. With the ERL the electron bunches would collide with the ion bunches only once and would allow for a very large disruption from the beam-beam interaction, which results in luminosities of about $2 \times 10^{33} cm^{-2} s^{-1}$. With modest upgrades (such as coating of the RHIC vacuum chambers) the luminosity could be increased ten-fold to about $2 \times 10^{34} cm^{-2} s^{-1}$. Because of the single pass nature of the collider a very intense (50 mA) polarized electron gun is required, which is about a factor of ten beyond the state-of-the-art. R&D is underway to build such an electron source that houses 24 individual cathodes that can be used one after the other in the style of a "Gatling" machine gun. A schematic view of this Gatling gun is shown on the right side of Fig. 5. To reach the high luminosity the ion beam will also have to be strongly cooled using coherent electron cooling. Construction of the eRHIC facility could be completed by 2024.

3.4 LHeC at CERN

There is also a proposal to collide a polarized electron beam from a 60 GeV ERL with the high energy LHC proton or heavy ion beam. Such a facility, called LHeC, would continue the search for lepton-quarks, started at HERA, but also could produce a copious number of Higgs particles if the luminosity could be increased to $10^{34} cm^{-2} s^{-1}$. The 60 GeV ERL would be the highest energy device of its kind and would use three recirculation arcs and a 20 GeV CW SRF Linac. The ERL would be in a tunnel separate from the LHC tunnel and the electron beam would collide with the LHC beam in a single interaction region. The highest luminosities would require that the electron bunch is captured by the space charge of the hadron beam at the collision point. The layout of the LHeC facility is shown in Fig. 6. Construction could occur

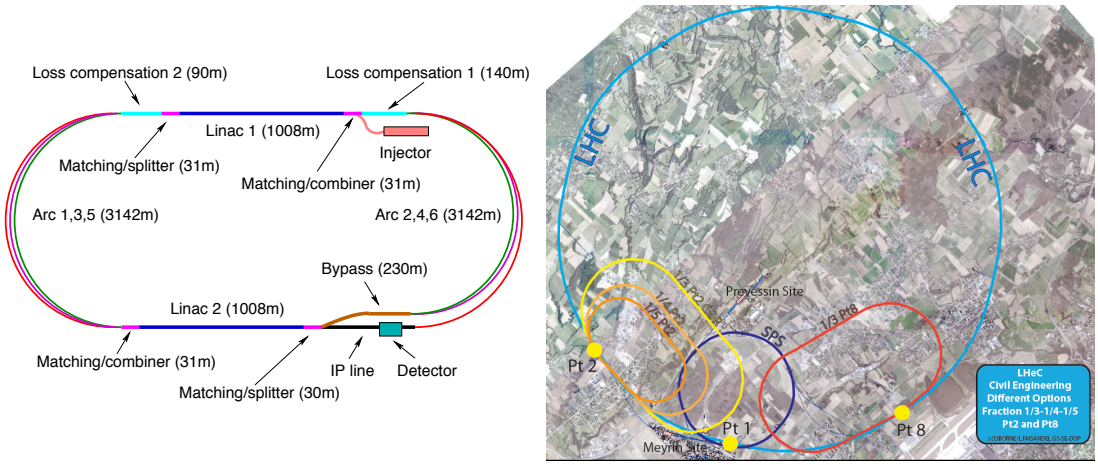

Figure 6: The 60 GeV ERL for LHeC is shown on the left. On the right are the possible locations for the electron ERL in the LHC ring.

during the 2020s.

4 Acknowledgments

I gratefully acknowledge Max Klein (Liverpool), Edgar Mahner (GSI/FAIR), Jie Wei (FRIB), Yuhong Zhang (JLab), Hongwei Zhao (IMP/Lanzhou), and Frank Zimmermann(CERN) for providing me with information on the status and plans of these projects.

Low-Energy Tests of the Standard Model - $(g-2)_\mu$ and Dark Photons

Achim Denig

Institute for Nuclear Physics and PRISMA Cluster of Excellence, Johannes Gutenberg University Mainz, Johann-Joachim-Becher-Weg 45, D-55099 Mainz, Germany

DOI: http://dx.doi.org/10.3204/DESY-PROC-2014-04/293

Low-energy tests of the Standard Model provide complementary insights to Beyond Standard Model Physics. We review two topical issues, namely the status of the anomalous magnetic moment of the muon $(g-2)_\mu$ as well as searches for a hypothetical extra-U(1) GeV-scale particle beyond the Standard Model - the so-called Dark Photon.

1 Introduction

The discovery of the Higgs boson in 2012[1] represents an impressive confirmation of the concepts of the Standard Model (SM) of particle physics. The last particle of the SM is now finally discovered, the production rate as well as the decay pattern of the Higgs particle seem to follow the predictions of the theory[2]. While searches for Beyond Standard Model (BSM) physics are of course continued at the *high-energy frontier*[3] and stringent mass bounds up to the TeV scale are established, measurements at the *precision frontier*[1] provide compementary insights. By loop-induced processes, the experimental values of low-energy observables might indeed be affected by particles with very high masses. It was found that the mass scales of BSM particles, which are tested in low-energy experiments, do indeed exceed the mass scales tested at high energies by large factors in many cases.

In this paper we are going to discuss two topical subjects of the *precision frontier*, which have triggered an enormous amount of work both in experiment and theory in the past years. The **anomalous magnetic moment of the muon** $(\mathbf{g-2})_\mu$ is one of the few physics observables, in which for more than a decade a deviation between the SM theory and the direct experiment persists. New and improved measurements of $(g-2)_\mu$ at FNAL[4] and JPARC[5] are upcoming and it is hence a good moment to review the status of this precision quantity. Originally motivated by the dark sector and their relation to dark matter, it was realized that extra-*U(1)* gauge bosons beyond the ordinary photon - therefore often called **Dark Photons** - could indeed explain the deviation in the $(g-2)_\mu$ system mentioned above. Low-energy searches for the dark photon have been carried out as a consequence and will be presented in chapter 3.

There are of course many more low-energy tests of the SM ongoing beyond the ones covered in this paper. Flavour physics (see Ref.[6]) played for instance an important role in particle

[1] often also denoted as the intensity frontier

physics in the first decade of the 21^{st} century and is continuing to do so in the LHC era . Searches for lepton flavour violation (LFV) have been carried out at flavour factories and at dedicated muon beam lines [7]. New LFV experiments are upcoming with the potential to improve upon existing results by orders of magnitude. As a legacy of the LEP-SLC era, there remain precision measurements of the electroweak mixing angle, $\sin^2\Theta_W$, which plays a central role in the SM. Unfortunately, a discrepancy between LEP and SLC could never be clarified [8]. New low-energy experiments are currently being performed or are in the design stage with the goal to measure $\sin^2\Theta_W$ at very low momentum transfer. Measurements of that kind do not only have the potential to resolve the LEP-SLC discrepancy, but have also the resolving power for New Physics contributions up to the highest mass scales in the multiple TeV range. Different measurements of $\sin^2\Theta_W$, for instance in electron-electron scattering or electron-proton scattering, are also testing complementary BSM models.

2 The anomalous magnetic moment of the muon $(g-2)_\mu$

The gyromagnetic factors of the electron and muon (g_l, l=e,μ) belong to the best known quantities in physics, both experimentally and theoretically. [9] The high accuracy is indeed motivated by the fact, that calculations of g_l are very sensitive to loop corrections and hence allow for very accurate tests of the underlying theory.

The anomalous magnetic moment of the electron $a_\mu \equiv (g-2)_e/2$ – i.e. one half of the

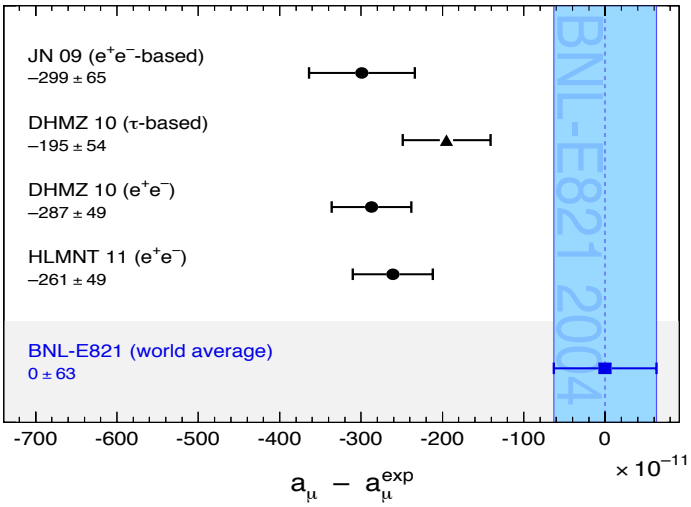

Figure 1: Comparison between the direct measurement of $(g-2)_\mu$ (BNL-E821, blue) and several theoretical evaluations within the Standard Model (black). A discrepancy larger than 3 standard deviations is found.

deviation of the g-factor from the Dirac value $g_e = 2$ – has been measured a few years ago by Gabrielse with an accuracy of 1 part in 10^{13} [10]. This accuracy is a test of the theory of quantum electrodynamics QED with unprecedented precision. The anomalous magnetic moment of the muon, $(g-2)_\mu$, is known with less accuracy. It allows, however, to resolve effects not only of QED but also of weak and strong interactions and eventually of BSM contributions.

Presently, the experimental and Standard Model values of $(g-2)_\mu$ differ by more than 3 standard deviations [11] [12], see Fig. 1, which triggered many speculations whether this might be an indication of a missing contribution due to New Physics. In the following two subchapters we will briefly review the status ot theory and experiment. We stress that the physics of $(g-2)_\mu$ is indeed testing an extremely wide class of New Physics models. Supersymmetric theories (SUSY), in which the masses of the SUSY particles are on the weak scale, could a priori explain the presently seen deviation in $(g-2)_\mu$ very nicely. There is however an increasing tension with SUSY mass limits from the LHC reaching now the TeV scale . Nevertheless, non-traditional SUSY models are still viable [13]. We will show later that light particles with very weak coupling to the SM, so-called Dark Photons, could explain the $(g-2)_\mu$ deviation very elegantly as well.

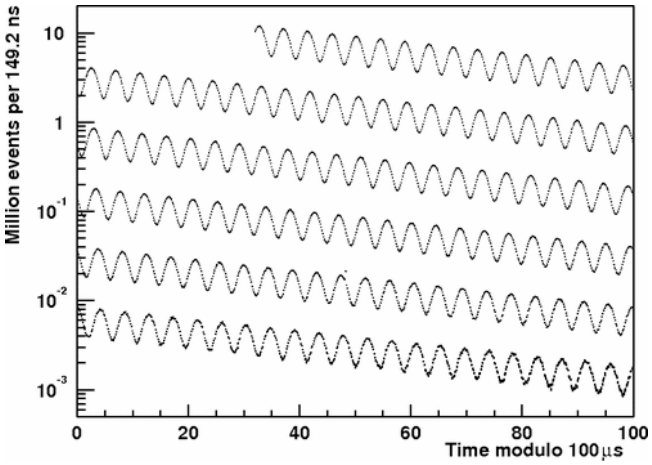

Figure 2: Measured event yield of positrons by the BNL-E821 experiment. From the modulation the value of $(g-2)_\mu$ can be extracted.

2.1 Experimental value

The most recent and most accurate experimental value of $(g-2)_\mu$ stems from a measurement at BNL. The E821 collaboration has improved the accuracy of the previous CERN measurement by a factor 14 and finds the following value:

$$a_\mu^{\text{exp}} = (11659208.9 \pm 5.4_{\text{stat}} \pm 3.3_{\text{syst}}) \cdot 10^{-10} \text{ [14]}. \quad (1)$$

To achieve such an accuracy a high-intensity polarized muon beam is injected into a storage ring with known magnetic field. The muon spin is rotating around the momentum vector due to the $\approx 0.1\%$ difference between the cyclotron and spin precession frequencies. After circling the ring many times, the muon decays into electrons plus neutrinos. Weak interaction guarantees a correlation between the electron flight direction and the original muon spin direction. As the decay electrons are detected in the experiment, the measured event yield shows a modulation proportional to the difference between the cyclotron and spin precession frequencies, i.e. proportional to $(g-2)_\mu$, see Fig. 2. Electric fields are required for a focussing of the muon beam, which complicates a precise extraction of $(g-2)_\mu$. As realized already in previous experiments

at CERN, these effects cancel if a so-called magic relativistic gamma value of the muon beam is used, which corresponds to a muon beam momentum of 3.09 GeV/c.
In 2013 the BNL $(g-2)_\mu$ ring was shipped to FNAL, where a new experiment is presently set up with the overall goal to improve the accuracy by a factor of 4 [4]. Apart from a higher muon flux compared to BNL, a series of additional improvements will lead to smaller systematic uncertainties. A second new experiment is in preparation at JPARC [5]. Differently from the BNL/FNAL approach, here the magic muon momentum will not be used, as no electric focussing fields are needed for the experiment. The solution of JPARC is the production of ultracold muons, which are then reaccelerated and injected into a 3 Tesla MRT magnet. The muon flux will be higher compared to the FNAL experiment and the overall goal is to achieve a similar accuracy as in the FNAL project.

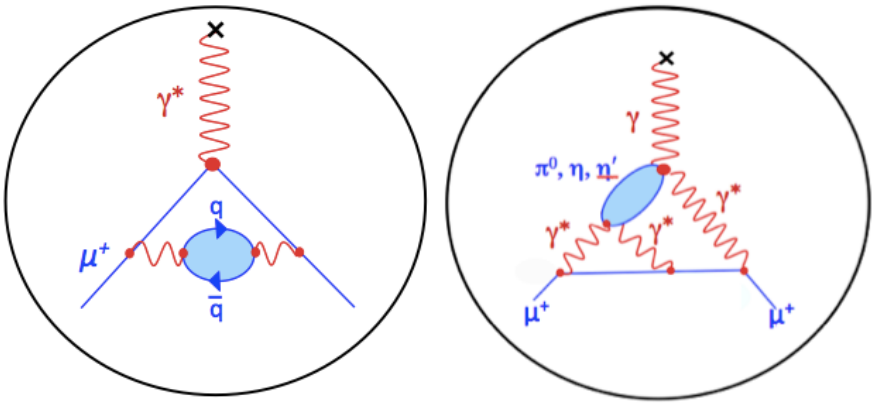

Figure 3: Hadronic contributions to $(g-2)_\mu$: the hadronic vacuum polarization (left) and the hadronic Light-by-Light contribution (right).

2.2 Standard Model prediction

Given the experimental accuracy reported above, there are measurable contributions to a_μ not only from QED, but also from weak and strong interactions. These individual contributions are listed below:

$$\begin{aligned} a_\mu^{\mathrm{SM}} &= a_\mu^{\mathrm{QED}} + a_\mu^{\mathrm{weak}} + a_\mu^{\mathrm{hadr}} \\ &= [11658471.808_{\pm 0.015} + 15.4_{\pm 0.2} + 693.0_{\pm 4.9}] \cdot 10^{-10} \\ &= [11659182.8_{\pm 4.9}] \cdot 10^{-10} \end{aligned} \tag{2}$$

The calculation of the by far dominating QED contribution was a heroic effort and has been pursued by Kinoshita and co-workers in the past decades [15]. An evaluation of up to 5 loops requires the calculation of more than 12,000 Feynman diagrams. The weak contribution has been computed up to NLO and is found to be many orders of magnitude smaller than the QED one [16]. Both the uncertainties of the QED and weak contributions are negligible in comparison to the experimental uncertainty. As can be seen from Equation 2, the bottleneck of the Standard Model prediction of $(g-2)_\mu$ is the hadronic contribution. It is split into two

parts, namely the Hadronic Vacuum Polarization HVP (see left Feynman diagram in Fig. 3) and the Hadronic Light-by-Light Scattering HLbL (Fig. 3, right) contributions. It should be noted that both contribute to only 60 ppm of the absolute contribution, they however dominate completely the uncertainty.

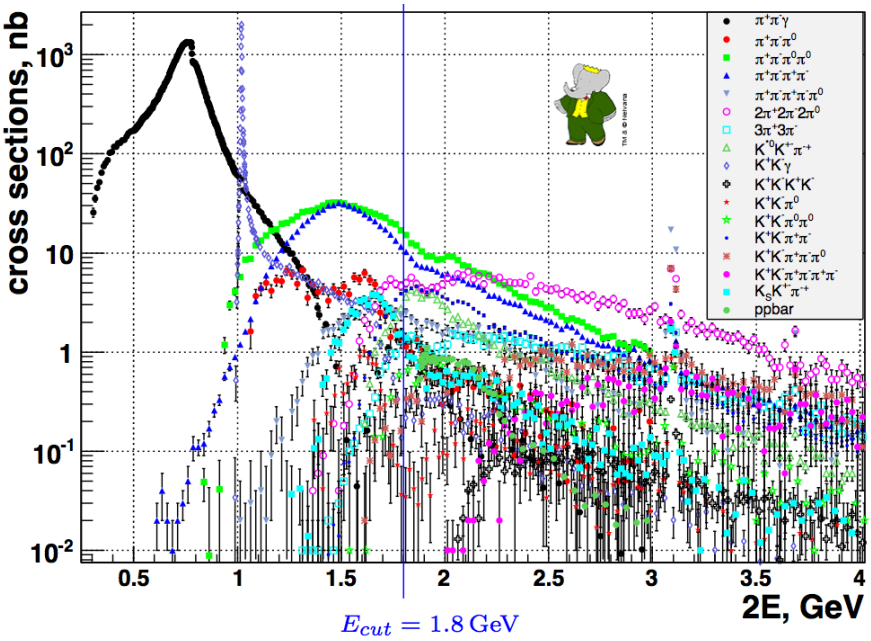

Figure 4: Exclusive hadronic final states measured by BaBar via Initial State Radiation (ISR).

The leading order HVP contribution is related via a dispersion integral to experimental data on the cross section $e^+e^- \to$ hadrons. Such a relation is based on unitarity and analyticity and is hence theoretically on safe grounds. Due to a kernel function in the dispersion integral, it comes out that low energy data of the hadronic cross section is particularily important. Indeed, the hadronic cross section below approximately 3 GeV is required with an accuracy on the level of 1%. This quest for accuracy triggered a series of cross section measurements at electron-positron facilities and led to the construction of the Novosibirsk colliders VEPP-2M and more recently of VEPP-2000 with the detectors CMD-2/CMD-3 and SND.
Major new results on hadronic cross section data were achieved at the particle factories DAΦNE (experiment KLOE) and PEP-II (experiment BaBar). As those particle factories were designed to operate at a fixed center-of-mass energy, a classical energy scan is therefore impossible. A new and very successful method has however been worked out, which allows for cross section measurements by using events, in which one of the beam electrons/positrons has emitted a high-energetic photon (intial state radiation, ISR) [17]. Depending on the energy of the ISR photon, the available hadronic mass is reduced and the hadronic cross section can be extracted for all masses below the center-of-mass energy of the collider. A good knowledge of the QED radiative corrections is required for this radiative approach. These are calculated up to next-to-leading order within the PHOKHARA [18] Monte-Carlo event generator. An overview of hadronic cross section measurements of various exclusive hadronic states via ISR by the BaBar

experiment is shown in Fig. 4. Essentially all channels up to 6 hadrons in the final state have been measured with systematic accuracies of few percent [17]. The two-pion final state $e^+e^- \to \pi^+\pi^-$ plays a special role for $(g-2)_\mu$. As can be seen in Fig. 4, the ρ resonance, which is almost entirely decaying into two pions, is dominating the cross section and hence is also playing a leading role in the dispersion integral for the HVP contribution to $(g-2)_\mu$ with approximately 75% of the total contribution steming from this channel. Unfortunately, the BaBar measurement of $\sigma(e^+e^- \to \pi^+\pi^-)$ [20], which has a claimed systematic accuracy of 0.5%, shows quite some deviation from ISR-measurements of KLOE kloe, which claims a 0.8% accuracy for the most precise of its data sets. The deviation is in the order of 3% on the ρ peak and increases towards higher masses. Precision data points from Novosibirsk [21] [22] have larger statistical and systematic uncertainties and hence can confirm neither the BaBar nor the KLOE results. As a matter of fact, this deviation is dramatically limiting our knowledge of the HVP contribution and hence a_μ^{SM}. Presently, an average of the world data set for hadronic cross section measurements yields the following value for the LO-HVP contribution to $(g-2)_\mu$: $a_\mu^{\mathrm{HVP}} = (692.3)_{\pm 4.2} \cdot 10^{-10}$.

The next important contribution beyond HVP is the HLbL contribution shown in Fig. 3, right. Here the leading subdiagram is shown, namely the coupling of photons to the pseudoscalar mesons π^0, η, or η'. So far hadronic models have been used for the calculation of the HLbL diagram. Although most groups report similar values for the absolute size of the HLbL contribution, the assumed uncertainties differ largely. The calculation with the lowest uncertainties stems from Prades, de Rafael, and Vainshtein [23]. They find the following value: $a_\mu^{\mathrm{HLbL}} = (10.5)_{\pm 2.6} \cdot 10^{-10}$. In most compilations of $(g-2)_\mu$ this result is used.
Very recently new theoretical approaches have been proposed by two groups from Bern and Mainz, namely the use of dispersion relations [24] [25]. Form factor measurements of the two-photon coupling $\gamma\gamma \to$ P, where P is a one hadron or two hadron system, are therefore of special interest for the dispersive approaches. The B-factory experiments BELLE [26] and BaBar [27] have recently measured so-called single-tag form factors for the lightest pseudoscalar mesons, however data has been reported only at very large momentum transfer above 4 GeV^2, while for the HLbL contribution measurements at low momentum transfer are required. In that kinematic range new spacelike measurements are expected from KLOE-II in Frascati and the BESIII experiment in Beijing. Important timelike measurements of the η form factor have recently been performed by the A2 collaboration in Mainz [28].

2.3 Conclusions $(\mathbf{g-2})_\mu$

With the persisting deviation between the SM prediction and the direct measurement of $(g-2)_\mu$, an interpretation in terms of BSM physics is very tempting. It is good to know that new direct measurements of $(g-2)_\mu$ with a factor 4 improved accuracy are underway at FNAL and JPARC and hopefully these projects will be able to report their results around the end of this decade. For the final interpretation of these experiments a reduction of the uncertainty of the SM prediction of $(g-2)_\mu$ is highly desirable. Fortunately, new cross section measurements via the ISR rechnique are ongoing at the BESIII facility in China and new energy scan campaigns are performed at Novosibirsk. This will eventually help to clarify the discrepancies seen between hadronic cross section measurements from BaBar and KLOE for the 2π cross section and will hence improve our knowledge of the HVP contribution. Moreover, measurements of transition form factors are ongoing at several hadron and electron facilities around the world and together

with the new developments in theory will lead to a significant progress in the HLbL contribution, which otherwise might be the leading uncertainty of the SM on the long run. As discussed in a recent whitepaper [29], there is very good hope that all these developments will lead to a further reduction of a factor 2 of the SM prediction of $(g-2)_\mu$. The combined effort in theory and experiment will therefore tell us in few years from now, whether the hint for BSM physics becomes evidence.

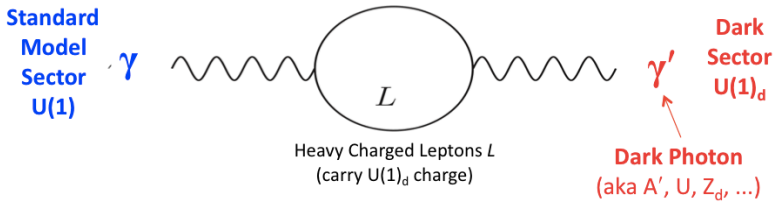

Figure 5: Dark Photon coupling to the ordinary photon in a kinetic mixing model.

3 Dark Photons

Extra U(1) gauge bosons beyond the Standard Model photon appear in essentially all string compactifications as they result naturally from symmetry breaking mechanisms towards lower gauge symmetries. A search for such kind of hypothetical particles is carried out from the lowest energies – e.g. the search for axion or axion-like particles – up to the highest energies at the LHC. More recently, particles at the GeV mass scale were proposed by several authors as they might be connected with the following puzzles in particle and astroparticle physics:

- It was shown by Arkani-Hamed and collaborators [30] that a GeV-scale particle – which was dubbed Dark Photon – could explain a surprisingly large number of astrophysical anomalies such as for instance the positron excess in the cosmic ray spectrum.
- A Dark Photon of a very similar mass scale [31] could also explain the discrepancy seen between the Standard Model predicition of $(g-2)_\mu$ and the direct measurement, see previous chapter.

The simplest mechanism with which a Dark Photon could couple to SM matter – the kinetic mixing model – was proposed by Holdom [32] already in the eighties. As depicted in Fig. 5 such a coupling can be realized by introducing a loop of charged leptons, which couple to the Standard Model U(1) photon as well to the Dark Photon. Hereby a portal between the hypothetical Dark Sector and the Standard Model is established. Of course the coupling α' must be extremely weak - much weaker than the coupling given by the electromagnetic fine structure constant $\alpha_{\rm em}$. There remain two unknown parameters of the model: the mass of the Dark Photon $m_{\gamma'}$ and the coupling constant α', which is also often expressed as $\epsilon' = \sqrt{\alpha'/\alpha_{\rm em}}$. In case dark matter particles couple to a Dark Photon, it would couple according to the kinetic mixing model to the Standard Model photon, which in turn decays into electron-positron pairs. Like this, a very elegant explanation for the positron excess is given. Regarding the $(g-2)_\mu$ puzzle, the Dark Photon would give rise to an additional exchange term, see Fig. 6, which is

missing in the SM calculation. The currently seen deviation in $(g-2)_\mu$ can be expressed as a well-constraint parameter range for $m_{\gamma'}$ and ϵ'. Taking into account constraints from various precision observables and from old beam dump experiments at FNAL and SLAC, the following parameter range would allow for a solution of the $(g-2)_\mu$ discrepancy: 20 MeV $< m_{\gamma'} <$ 200 MeV and $\epsilon' \approx 2-4 \cdot 10^{-3}$.

The possible existence of a GeV-scale Dark Photon triggered an enormous theoretical and experimental interest in the particle and nuclear physics community. In the following we will distinguish between electron scattering experiments and results from various hadron and e^+e^- accelerators. No significant signal of a Dark Photon has been found before and only 90% confidence limits have been published.

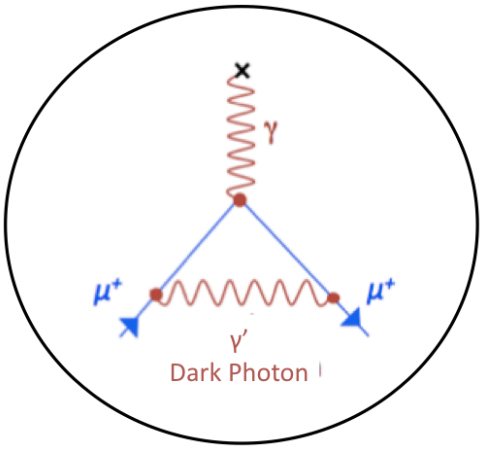

Figure 6: Hypothetical Dark Photon contribution to $(g-2)_\mu$.

3.1 Electron accelerator fixed target experiments

As Bjoerken and collaborators [33] have pointed out, low-energy electron accelerators in combination with high-resolution detectors are very well suited for Dark Photon searches. By scattering the electron beam on a nuclear target, the Dark Photon may be emitted in the initial or final state, see Fig. 7. Its coupling to an e^+e^- pair allows for an identification by looking for a bump in the e^+e^- invariant mass. The huge background is almost entirely given by QED processes, such as for instance Bethe-Heitler processes.

Successful pilot experiments have been carried out in 2011 at MAMI [34] (experiment A1) and JLAB [35] (APEX experiment) with electron beam energies of 0.9 GeV and 2.3 GeV, respectively. These runs could improve upon exisiting Dark Photon limits from BaBar (2009 results) in the mass range around 200 MeV. More recently, a very wide parameter range between approximately 40 MeV and 200 MeV was tested by MAMI with the high resolution spectrometer (HRS) setup A1 [36]. No significant signal was found and the ϵ' parameter range down to 10^{-3} was excluded, constraining a large part of the parameter range motivated by $(g-2)_\mu$, see Fig. 8.
For the near and mid-term future several dedicated experiments are in preparation at JLAB.

The APEX experiment [37], which is using an existing HRS setup at JLAB, will extend the mass range covered by A1/MAMI towards higher masses and lower ϵ' values. The HPS experiment [38] will exploit a displaced vertex technique, which allows to test even lower values of ϵ'. Finally, the Dark Light [39] experiment at the FEL accelerator at JLAB aims for testing the low mass region below the results already covered by A1. A new spectrometer setup at the MESA accelerator [40] in Mainz will also be able to cover this mass range.

3.2 Results from hadron and e^+e^- accelerators

A search for the Dark Photon is of course possible in physics environments beyond the ones tested in electron scattering. We list here the most recent results, which have been obtained in the past five years. All these results are displayed in Fig. 8 and have been obtained by looking for a bump in the e^+e^- or $\mu^+\mu^-$ invariant mass spectrum.

- The KLOE experiment at the ϕ factory DAΦNE in Frascati has searched for a bump in $\phi \to \eta e^+e^-$ events [41]. A constraint at higher masses existed already before from BaBar by similarily investigating Υ decays (BaBar 2009 [42]).

- The WASA@COSY collaboration has produced a huge statistics of π^0 events in proton proton scattering and has looked for the Dark Photon in $\pi^0 \to e^+e^-\gamma$ Dalitz events [43].

- A similar search strategy is possible in heavy ion collission and has been pursued by the HADES experiment at GSI. In addition to Dalitz decays of the π^0 also η Dalitz decays as well as decays of baryons are used [44].

- The most stringent Dark Photon limits have recently been published by the BaBar collaboration at SLAC [45]. Using ISR events and investigating the $e^+e^-\gamma$ and $\mu^+\mu^-\gamma$ final states, a very competitive search for the Dark Photon becomes available. BaBar has analyzed the full data set of approximately 500 fb^{-1} for this analysis and has obtained limits in the extremely wide mass range from 10 GeV down to threshold. Again no Dark Photon has been found and stringent constraints have been placed for the Dark Photon coupling to SM matter down to few 10^{-4}, see Fig. 8. A similar strategy had been followed already before by KLOE below 1 GeV.

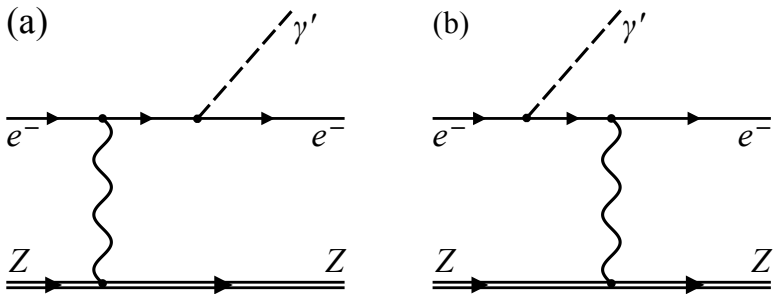

Figure 7: Feynman diagrams depicting the production of the Dark Photon in electron-nucleus scattering.

In the meantime also the Phenix experiment at RHIC has produced competitive exclusion limits by analyzing Dalitz decays of π^0 and η [46]. Those results are not yet displayed in Fig. 8 and are further constraining the favoured parameter range of $(g-2)_\mu$, such that after five years of active research the Dark Photon seems to be excluded as an explanation of the $(g-2)_\mu$ discrepancy. Of course, this range may change with new results for the direct measurement of $(g-2)_\mu$ and its SM prediction. It should be noted, that the relation of the Dark Photon to Dark Matter is still a very strong motivation. For this all the uncovered parameter space of Fig. 8 is of interest. In this context also more involved models are discussed in which either the Dark Photon is ligher than twice the electron mass or in which the Dark Photon coupling to SM matter is different from the one known from the ordinary photon. Also proposals have been brought forward to use electron accelerators as a source to produce a Dark Photon beam. This would be a unique way to search for light Dark Matter particles [47].

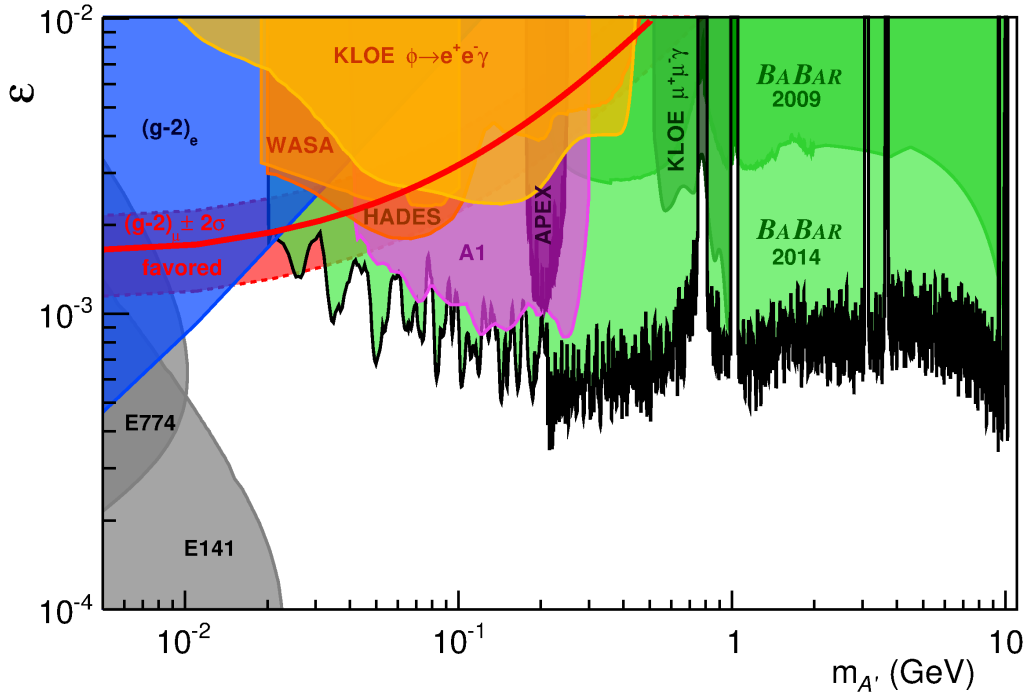

Figure 8: Dark Photon exclusion limits from various experiments.

Acknowledgments

We acknowledge support for this work from Deutsche Forschungsgemeinschaft DFG within the collaborative research center SFB-1044 and the PRISMA cluster of excellence. The author would like to thank the organizers of PANIC2014 for the invitation and for an exciting and successful conference.

References

[1] S. Chatrchyan *et al.* [CMS Collaboration], Phys. Lett. B **716** (2012) 30;
G. Aad *et al.* [ATLAS Collaboration], Phys. Lett. B **716** (2012) 1.

[2] see contribution of D. Rousseau, these proceedings.

[3] see contribution of K. Hatakeyama, these proceedings.

[4] see contribution of K. David, these proceedings.

[5] The J-PARC. 2009. g-2 collaboration, proposal submitted to J-PARC PAC (P34).

[6] see contribution of T. E. Latham, these proceedings.

[7] W. J. Marciano, T. Mori and J. M. Roney, Ann. Rev. Nucl. Part. Sci. **58** (2008) 315.

[8] The ALEPH, DELPHI, L3, OPAL, SLD Collaborations, the LEP Electroweak Working Group, the SLD Electroweak and Heavy Flavour Groups, Phys. Rept. 427 (2006) 257.

[9] F. Jegerlehner and A. Nyffeler, Phys. Rept. **477** (2009) 1.

[10] D. Hanneke, S. Fogwell and G. Gabrielse, Phys. Rev. Lett. **100** (2008) 120801.

[11] M. Davier, A. Hoecker, B. Malaescu and Z. Zhang, Eur. Phys. J. C **71** (2011) 1515 [Erratum-ibid. C **72** (2012) 1874].

[12] K. Hagiwara, R. Liao, A. D. Martin, D. Nomura and T. Teubner, J. Phys. G **38** (2011) 085003.

[13] H. Fargnoli, C. Gnendiger, S. Paehr, D. Stckinger and H. Stckinger-Kim, JHEP **1402** (2014) 070.

[14] G. W. Bennett *et al.* [Muon G-2 Collaboration], Phys. Rev. D **73** (2006) 072003.

[15] T. Aoyama, M. Hayakawa, T. Kinoshita and M. Nio, Phys. Rev. Lett. **109** (2012) 111808.

[16] M. Knecht, S. Peris, M. Perrottet and E. De Rafael, JHEP **0211** (2002) 003.

[17] V. P. Druzhinin, S. I. Eidelman, S. I. Serednyakov and E. P. Solodov, Rev. Mod. Phys. **83** (2011) 1545.

[18] S. Binner, J. H. Kühn and K. Melnikov, Phys. Lett. B **459** (1999) 279;
http://ific.uv.es/ rodrigo/phokhara/.

[19] D. Babusci *et al.* [KLOE Collaboration], Phys. Lett. B **720** (2013) 336;
F. Ambrosino *et al.* [KLOE Collaboration], Phys. Lett. B **700** (2011) 102
F. Ambrosino *et al.* [KLOE Collaboration], Phys. Lett. B **670** (2009) 285;
A. Aloisio *et al.* [KLOE Collaboration], Phys. Lett. B **606** (2005) 12.

[20] J. P. Lees *et al.* [BaBar Collaboration], Phys. Rev. D **86** (2012) 032013;
B. Aubert *et al.* [BaBar Collaboration], Phys. Rev. Lett. **103** (2009) 231801.

[21] R. R. Akhmetshin *et al.* [CMD-2 Collaboration], Phys. Lett. B **648** (2007) 28; R. R. Akhmetshin, V. M. Aulchenko, V. S. Banzarov, L. M. Barkov, N. S. Bashtovoy, A. E. Bondar, D. V. Bondarev and A. V. Bragin *et al.*, JETP Lett. **84** (2006) 413; R. R. Akhmetshin *et al.* [CMD-2 Collaboration], Phys. Lett. B **578** (2004) 285.

[22] M. N. Achasov, K. I. Beloborodov, A. V. Berdyugin, A. G. Bogdanchikov, A. V. Bozhenok, A. D. Bukin, D. A. Bukin and T. V. Dimova *et al.*, J. Exp. Theor. Phys. **103** (2006) 380.

[23] J. Prades, E. de Rafael and A. Vainshtein, (Advanced series on directions in high energy physics. 20) [arXiv:0901.0306 [hep-ph]].

[24] G. Colangelo, M. Hoferichter, B. Kubis, M. Procura and P. Stoffer, Phys. Lett. B **738** (2014) 6;
G. Colangelo, M. Hoferichter, M. Procura and P. Stoffer, JHEP **1409** (2014) 091.

[25] V. Pauk and M. Vanderhaeghen, arXiv:1409.0819 [hep-ph].

[26] S. Uehara *et al.* [Belle Collaboration], Phys. Rev. D **86** (2012) 092007.

[27] B. Aubert *et al.* [BaBar Collaboration], Phys. Rev. D **80** (2009) 052002.

[28] P. Aguar-Bartolome *et al.* [A2 Collaboration], Phys. Rev. C **89** (2014) 044608.

[29] T. Blum, A. Denig, I. Logashenko, E. de Rafael, B. Lee Roberts, T. Teubner and G. Venanzoni, arXiv:1311.2198 [hep-ph].

[30] N. Arkani-Hamed, D. P. Finkbeiner, T. R. Slatyer and N. Weiner, Phys. Rev. D **79** (2009) 015014.

[31] M. Pospelov, Phys. Rev. D **80** (2009) 095002.

[32] B. Holdom, Phys. Lett. B **166** (1986) 196.

[33] J. D. Bjorken, R. Essig, P. Schuster and N. Toro, Phys. Rev. D **80** (2009) 075018.

[34] H. Merkel *et al.* [A1 Collaboration], Phys. Rev. Lett. **106** (2011) 251802.

[35] S. Abrahamyan *et al.* [APEX Collaboration], Phys. Rev. Lett. **107** (2011) 191804.

[36] H. Merkel *et al.* [A1 Collaboration], Phys. Rev. Lett. **106** (2011) 251802.

[37] R. Essig, P. Schuster, N. Toro and B. Wojtsekhowski, JHEP **1102** (2011) 009.

[38] http://nuclear.unh.edu/HPS/HPS_proposal.pdf.

[39] http://dmtpc.mit.edu/DarkLight/DarkLightProposal_PAC39.pdf.

[40] K. Aulenbacher, M. Dehn, H. J. Kreidel, R. Heine and R. Eichhorn, ICFA Beam Dyn. Newslett. **58** (2012) 145.

[41] D. Babusci *et al.* [KLOE-2 Collaboration], Phys. Lett. B **720** (2013) 111.

[42] B. Aubert *et al.* [BaBar Collaboration], Phys. Rev. Lett. **103** (2009) 081803.

[43] P. Adlarson *et al.* [WASA-at-COSY Collaboration], Phys. Lett. B **726** (2013) 187.

[44] G. Agakishiev *et al.* [HADES Collaboration], Phys. Lett. B **731** (2014) 265.

[45] J. P. Lees *et al.* [BaBar Collaboration], arXiv:1406.2980 [hep-ex].

[46] A. Adare *et al.* [PHENIX Collaboration], arXiv:1409.0851 [nucl-ex].

[47] E. Izaguirre, G. Krnjaic, P. Schuster and N. Toro, Phys. Rev. D **90** (2014) 014052.

Dark Matter: experimental results and theory

Marco Cirelli[1]

[1]Institut de Physique Théorique, CNRS, URA 2306 & CEA/Saclay,
F-91191 Gif-sur-Yvette, France

DOI: http://dx.doi.org/10.3204/DESY-PROC-2014-04/295

I discuss four recent anomalies in Dark Matter Indirect Detection (the positron excess, the 130 GeV line, the GeV GC excess and the 3.5 KeV line) and some relevant constraints.

1 Introduction

Indirect searches for Dark Matter (DM) aim at detecting the signatures of the annihilations or decays of DM particles in the fluxes of Cosmic Rays (CRs), intended in a broad sense: charged particles (electrons and positrons, protons and antiprotons, deuterium and antideuterium), photons (gamma rays, X-rays, synchrotron radiation), neutrinos. In general, a key point of all these searches is to look for channels and ranges of energy where it is possible to beat the background from ordinary astrophysical processes. This is for instance the basic reason why searches for charged particles focus on fluxes of antiparticles (positrons, antiprotons, antideuterons), much less abundant in the Universe than the corresponding particles, and searches for photons or neutrinos have to look at areas where the DM-signal to astro-noise ratio can be maximized (typically the Galactic Center and DM-dominated structures such as dwarf satellite galaxies).

Pioneering works have explored indirect detection (ID) as a promising avenue of discovery since the late-70's. Since then, innumerable papers have explored the predicted signatures of countless particle physics DM models. In the past 6 years or so, however, the field has experienced a significant burst of activity, mainly due to the results presented by a few very well performing experiments, above all the Pamela satellite, the Fermi satellite and the Hess telescope. It is fair to say that the field has passed, for better or for worse, from a theory-driven state to a data-driven phase.

In this presentation I intend to briefly review the current status of the field, using the pretext of discussing four recent experimental 'anomalies' and the ensuing phenomenological activity. The four anomalies are: 1) the positron and electron excesses, first soundly detected by Pamela in 2008 in the positron fraction and then corroborated by many results from Fermi, Hess and recently Ams-02; 2) the '130 GeV line' from the Galactic Center (GC), first identified in 2012 by Christoph Weniger and collaborators in Fermi data; 3) the 'GeV Galactic Center γ-ray excess', promoted since 2010 most notably by Dan Hooper; 4) the 3.5 KeV X-ray line, supposedly detected in march 2014 in data from the Xmm-Newton satellite from several galaxy clusters and the Andromeda galaxy (M31).

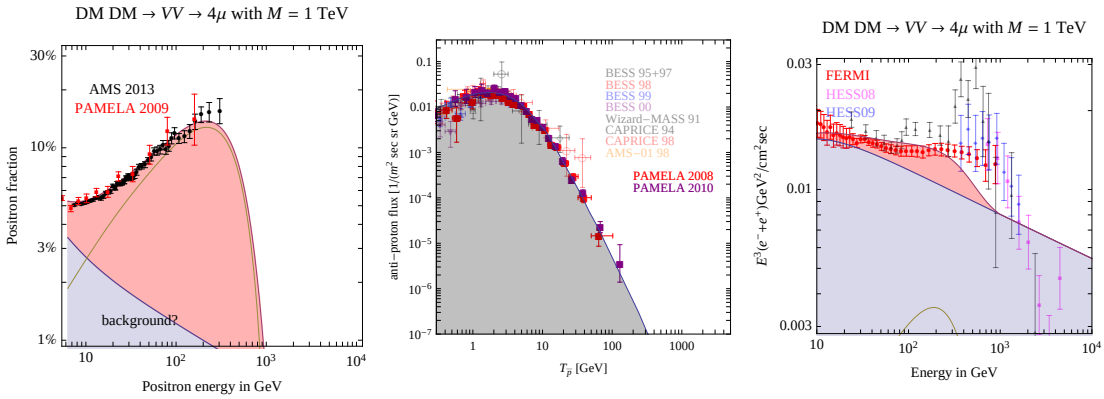

Figure 1: A compilation of recent and less recent data in charged cosmic rays, superimposed on plausible but uncertain astrophysical backgrounds from secondary production and on the flux produced by Dark Matter annihilations for a specific model. Left: positron fraction. Center: antiproton flux. Right: sum of electrons and positrons. Figures from ref. [9].

2 The positron and electron excesses

There has been a flurry of positive results from a few indirect detection experiments looking at the fluxes of charged cosmic rays. In particular, the signals pointed to an excess of electrons and positrons at the TeV and sub-TeV scale:

- Notorius data from the PAMELA satellite [1] showed, back in 2008, a steep increase in the energy spectrum of the positron fraction $e^+/(e^+ + e^-)$ above 10 GeV up to 100 GeV, compatibly with previous hints from HEAT [2] and AMS-01 [3]. These findings have later been confirmed with independent measurements by the FERMI satellite [4] and, recently, by the AMS-02 experiment [5] and extended to about 430 GeV.

- Data from PAMELA [6] also showed no excess in the $\bar{p}$ energy spectrum compared with the predicted background.

- In the $e^+ + e^-$ energy spectrum, the results of the FERMI satellite [7], combined with the results from the HESS telescope [8], hint to an excess (with respect to the expected background) reproduced by a simple power law up to about 1 TeV and eventually a steepening at energies of a few TeVs.

The data are displayed in fig. 1, together with the expected astrophysical 'backgrounds' and with the contribution from an annihilating DM particle which fits them reasonably well (see below). The properties of such a particle are pin-pointed quit precisely by the data. The DM has to be:

- With a mass of *1 to few TeV*, in order to reproduce the feature in the $e^+ + e^-$ spectrum. Actually, the hint of a flattening in the positron fraction suggested by AMS-02 favours a DM mass below about 1 TeV with about 3σ statistical significance, depending on the DM annihilation channel, so that a little bit of a tension is present with the $e^+ + e^-$ spectrum, which requires a slightly larger value.

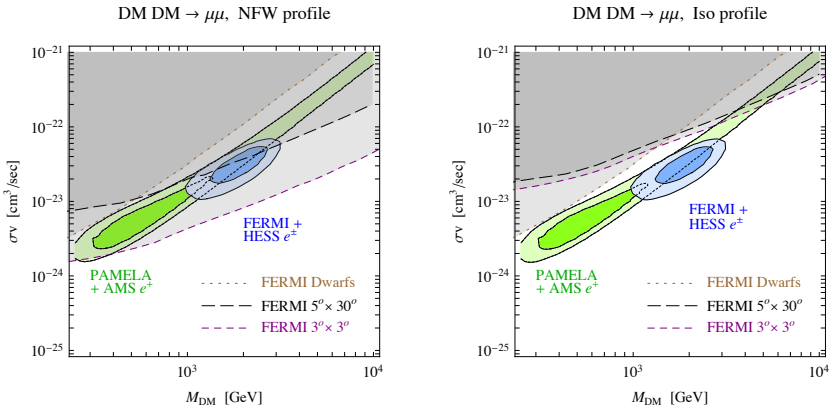

Figure 2: Best fit regions for the positron and electron excesses, together with some representative γ-ray constraints. Figure from ref. [9].

- ▷ *Leptophilic*, i.e. annihilating almost exclusively into leptonic channels, otherwise the antiproton measurements would be exceeded.
- ▷ With a *very large annihilation cross section*, of the order of $10^{-23}\,\mathrm{cm}^3/\mathrm{sec}$ or more (for the masses under consideration), much larger than the thermal one, in order to produce a large enough flux that can fit the positron rise and the $e^+ + e^-$ bump.

As tantalizing as these hints of DM can be, they have to be confronted with associated constraints. Many possible constraints can be considered, but here I will focus on two classes only. The first one is observations of γ-rays. In fig. 2 we show representative γ-ray bounds (the constraints are taken from [10, 11], more recent analyses find similar or slightly more stringent bounds). We see that the fit region shows some tension with γ-ray data (or it is rather clearly excluded) if (left) we have chosen a benchmark NFW galactic Dark Matter profile. Choosing the shallower isothermal profile (right), however, makes the constraints looser. It is therefore difficult to get a final answer from γ-rays. The second class of constraints comes from observations of the cosmic microwave background (CMB), which imposes bounds on DM annihilations (based on the fact that they would have re-ionized the primordial universe) that disfavor at various degrees and for most channels the DM interpretation of the positron excess [12].

3 The 130 GeV line

The '130 GeV line' claim has gathered a lot of attention in the past two years (for a more thorough review see [13]). Originally spotted by [14] and, above all, by [15] in the publicly available FERMI data from an extended region including the GC (fig. 3 left reports the most evocative of the original analysis' figures), it has later found support in other analyses [16, 17, 18, 19], with varying degrees of accuracy and claimed significance. [16, 19] have seen it in what could possibly be DM subhaloes of the MW, and there might be two lines, at 111 GeV and 129 GeV [20, 17]. [18] has seen it in galaxy clusters too. For a response, [21, 22, 23] challenged the analyses in a number of ways, suggesting that the line(s) could be due to unidentified

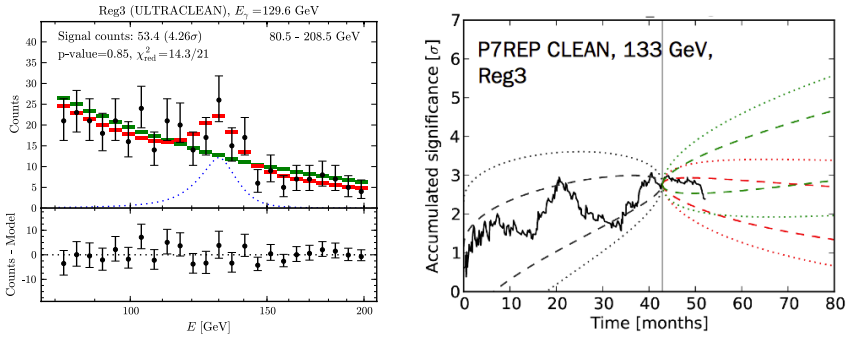

Figure 3: Left: FERMI γ-ray data and fits pointing to a line at about 130 GeV. Right: behavior with time of the accumulated significance for this signal. Figures from ref. [15] and ref. [24].

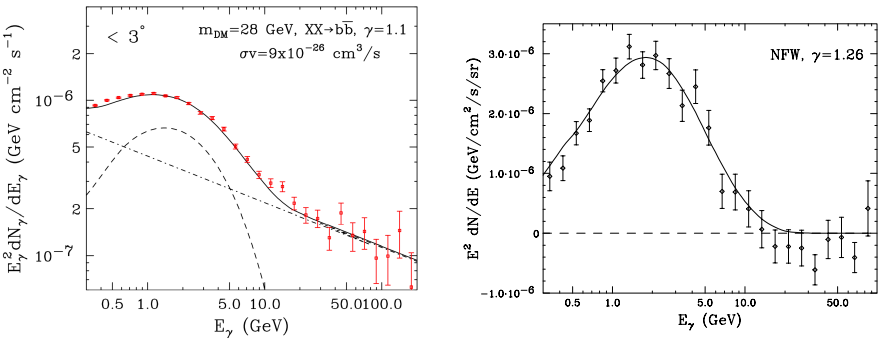

Figure 4: Earliest and latest fits to the GeV excess at the GC. From ref. [25] and ref. [27].

instrumental, statistical or astrophysical origin. Although it is probably too early for a final conclusion on this claim, it is fair to say that the current consensus seems to be that the line has been a rather unfortunate combination of an instrumental effect and a statistical fluctuation. The right panel of fig. 3 illustrates that, as more data are accumulated, the significance of the signal lowers, hence pointing at something which is probably not an actual signal.

4 The GeV Galactic Center excess

Several authors have reported since 2009 the detection of a gamma-ray signal from the inner few degrees around the GC [25, 26], with the most notable early claims by Dan Hooper. Its spectrum and morphology are found to be compatible with those expected from annihilating DM particles: to fix the ideas, the results of one of the most recent analysis [27] confirm the presence of this excess at an incredibly high level of significance (if taken at face value) and find this signal to be best fit by 31-40 GeV DM particles distributed according to a (contracted) NFW profile and annihilating into $b\bar{b}$ with $\langle\sigma v\rangle = 1.4 \div 2 \times 10^{-26}$ cm^3/s. Fig. 4 displays the earliest fit to the data (from [25]) and one of the most recent ones (from [27]).

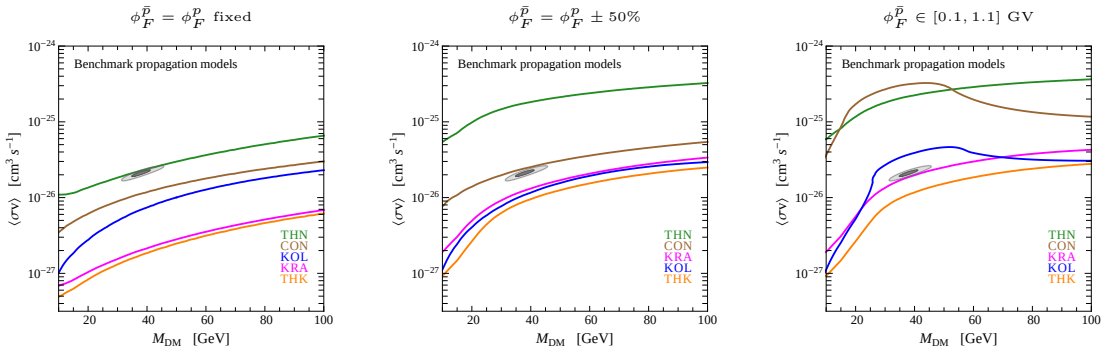

Figure 5: 3-σ exclusion contours on $\langle \sigma v \rangle$ for 100% DM annihilation into $b\bar{b}$, for the three approaches to solar modulation briefly discussed in the text. The grey area is the best-fit region. Fig. from ref. [32].

Of course, one should not forget that, in very general terms, the identification of an 'excess' strongly relies on the capability of carefully assessing the background over which the excess is supposed to emerge. The claim under scrutiny constitutes no exception, quite the contrary. The extraction of the residuals strongly relies on the modeling of the diffuse gamma-ray background (in particular the one publicly made available by the FERMI collaboration) as well as on additional modeling of astrophysical emissions, e.g. from FERMI bubbles, isotropic component, unresolved point sources, molecular gas... While this is probably the best that can be done, it is not guaranteed to be (and in general is not expected to be) the optimal strategy. Also, one should not forget that there might be alternative astrophysical explanations for the excess. A population of milli-second pulsars has been extensively discussed since the beginning [28], as well as the possibility of a spectral break in the emission of the central Black Hole [29]. More recently, the possibility has been suggested that isolated injections of charged particles (electrons [30] or protons [31]) sometime in the past, possibly connected with the activity of the central Black Hole, can produce secondary radiation able to account for the anomalous signal. While reproducing with these models all the details of the observed emission might be not easy, they represent plausible and useful counterexamples to the DM interpretation.

Still, it is interesting to insist on the tantalizing DM hypothesis and to explore ways to confirm or disprove the result within the DM framework. In particular, given the alleged hadronic origin of the signal, it is very useful to analyze the antiproton channel to put constraints on the DM interpretation of such excess. Ref. [32] delved precisely into this issue, and the condensed results are displayed in fig. 5. It considered several galactic propagation models for antiprotons (THN, CON, KOL, KRA, THK, roughly distinguished by the thickness of the diffusive halo, the diffusion properties and the presence of side effects such as convection) and several assumptions for the so-called solar modulation, i.e. the complicated effect of the magnetic field and solar cosmic ray wind of the heliosphere on the last segment of the antiproton journey. More precisely, it considered a solar force field for $\bar{p}$ fixed and equal to p one (left panel of fig. 5), variable within 50% (central panel) or free within a wide range (right panel). The overall conclusions are the following: adopting the most realistic propagation models and well motivated choices for the solar modulation potential, the hadronic ($b\bar{b}$) DM interpretation for the GeV excess is definitely in strong tension with the antiproton data. Nevertheless, given

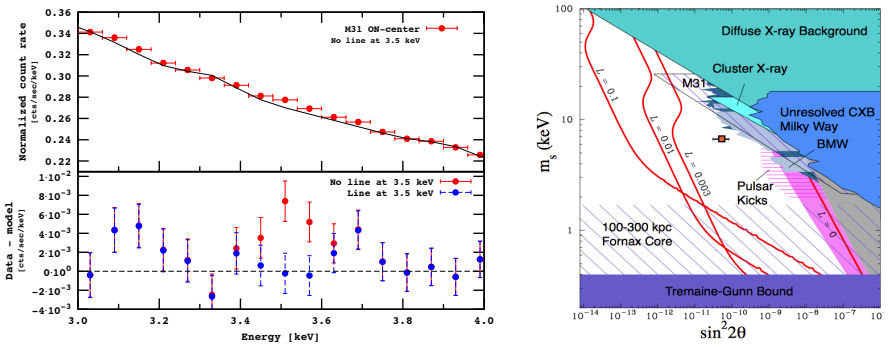

Figure 6: Identification of the 3.5 KeV line in XMM-NEWTON data (left) and the parameter space of its interpretation in terms of a decaying sterile neutrino. From ref. [35] and ref. [34].

that our knowledge of CR diffusion both in the Galaxy and in the heliosphere is far from being accurate and complete, there are still conservative choices of the parameters involved that do not result in ruling it out, namely thin halo models and large solar modulation potentials. The authors of ref. [33] have also discussed the antiproton bounds, reaching somewhat different conclusions.

5 The 3.5 KeV X-ray line

One of the latest claims in the field of indirect detection comes from a different range of energies: X-rays. In datasets from the XMM-NEWTON satellite, two independent groups [34, 35] have found evidence for an unexplained line at 3.5 KeV. The former group found it in observations of a set of 73 galaxy clusters with redshift between 0.01 and 0.35. The latter one in observations both of the Perseus cluster and of Andromeda, with no detection in "blank sky" measurements. Fig. 6, left, displays an extraction of the spectrum showing the line, from [35].

The complication is that the X-ray spectrum in this range of energies is crowded with atomic de-excitation lines from elements such as Cr, Mn, K, Fe, Ni, Ca, Cu... Ref. [36] has indeed very recently argued that previously-unaccounted-for potassium lines can well explain the signal. Ref. [37] reiterates, however, that data from Andromeda are instead solid and make the potassium interpretation problematic. On another side, ref. [38] has argued that no line is seen in Chandra data from the GC, although this conclusion depends on how one models the local background. The discussion is currently unfolding and probably more data from independent instruments will be needed.

If confirmed, however, the most straightforward explanation of the line in terms of new physics is of great interest for the field of DM indirect detection as it consists of a sterile neutrino of mass 7 KeV decaying into an ordinary ν and a photon (the detected X-ray). The decay rate turns out to be $\mathcal{O}(10^{-29})$ sec^{-1}. This, translated in terms of particle physics parameters by the effective mixing angle, lies in a region of parameter space still allowed by other constraints, as illustrated by the right panel of fig. 6. The production mechanism of a population of sterile neutrinos in the early universe would involve active-sterile oscillations helped by the presence of a sizable leptonic asymmetry, quite uncompelling, but possible.

6 Conclusions

There are arguably no firm conclusions in this field at this moment in time. There are tantalizing hints (the positron and electron excess, the gamma-ray line, the GeV GC excess and the X-ray line) and there are stringent constraints. Such constraints, however, are often relaxed by appropriate assumptions, which can be extreme or not (the illustration with the antiproton constraints on the GeV excess in section 4 is exemplar). The only firm albeit generic conclusions seem to be that:

- ◇ current experiments are clearly reaching (and in some cases have already reached) the sensitivities for which they were designed, and hence they probe very promising regions of the parameter space;
- ◇ astrophysics, in different manifestations, is the main killjoy, introducing alternative compelling explanation, irreducible uncertainties, unbeatable background noise...;
- ◇ hence, it is important to pursue a multi-messenger approach in all instances, investigating associated signals in other channels, cross-checking constraints and confirmations from independent targets etc;
- ◇ in any case, the profusion of data from the recent experiments have spurred a remarkable proliferation of DM models, so that 'traditional' DM models (such as SuSy DM) have, for better or for worse, been joined by many other possibilities.

Acknowledgments

I thank my collaborators on the papers which led to the results presented here and who helped me with many useful discussions. I acknowledge the hospitality of the Institut d'Astrophysique de Paris, where part of this work was done. Funding and research infrastructure acknowledgements: European Research Council (ERC) under the EU Seventh Framework Programme (FP7/2007-2013)/ERC Starting Grant (agreement n. 278234 — 'NEWDARK' project); French national research agency ANR under contract ANR 2010 BLANC 041301.

References

[1] O. Adriani *et al.* [PAMELA Collaboration], Nature 458, 607-609, 2009, arXiv:0810.4995.

[2] S. W. Barwick *et al.* [HEAT Coll.], Astrophys. J. **482** (1997) L191 [astro-ph/9703192].

[3] M. Aguilar *et al.* [AMS-01 Coll.], Phys. Lett. B **646** (2007) 145 [astro-ph/0703154].

[4] M. Ackermann *et al.* [The Fermi LAT Collaboration], arXiv:1109.0521 [astro-ph.HE].

[5] M. Aguilar *et al.* [AMS Collaboration], Phys. Rev. Lett. **110** (2013) 141102.
(An updated measurement has only been presented in a talk by S. Ting (and subsequent talks elsewhere).)

[6] O. Adriani *et al.* [PAMELA Coll.], Phys. Rev. Lett. **105** (2010) 121101 [arXiv:1007.0821].

[7] A. Abdo *et al.* [Fermi-LAT Coll.], Phys. Rev. Lett. **102** (2009) 181101, arXiv:0905.0025.
M. Ackermann *et al.* [Fermi LAT Coll.], Phys. Rev. D **82** (2010) 092004, arXiv:1008.3999.

[8] F. Aharonian *et al.* [H.E.S.S. Coll.], Phys. Rev. Lett. **101** (2008) 261104 [arXiv:0811.3894].
F. Aharonian *et al.* [H.E.S.S. Coll.], Astron. Astrophys. **508** (2009) 561 [arXiv:0905.0105].

[9] M. Cirelli, M. Kadastik, M. Raidal and A. Strumia, Nucl. Phys. B **813** (2009) 1 [Addendum-ibid. B **873** (2013) 530] [arXiv:0809.2409 [hep-ph]].

[10] M. Cirelli, P. Panci and P. D. Serpico, Nucl. Phys. B 840 (2010) 284 [arXiv:0912.0663]. M. Papucci and A. Strumia, JCAP 1003 (2010) 014 [arXiv:0912.0742].

[11] Fermi-LAT collaboration, Phys. Rev. Lett. 107 (2011) 241302 [arXiv:1108.3546]. Fermi-LAT collaboration, Astrophys. J. 761 (2012) 91 [arXiv:1205.6474]. For this figure we used the dwarfs data presented by A. Drlica-Wagner at the 2012 Fermi symposium.

[12] S. Galli, F. Iocco, G. Bertone and A. Melchiorri, Phys. Rev. D 80 (2009) 023505 [arXiv:0905.0003]. T.R. Slatyer, N. Padmanabhan, D.P. Finkbeiner, Phys. Rev. D 80 (2009) 043526, 0906.1197. G. Huetsi, A. Hektor, M. Raidal, Astron. Astrophys. 505 (2009) 999, arXiv:0906.4550. M. Cirelli, F. Iocco and P. Panci, JCAP 0910 (2009) 009, arXiv:0907.0719. See also: T. Kanzaki, M. Kawasaki and K. Nakayama, Prog. Theor. Phys. 123 (2010) 853, arXiv:0907.3985. Q.Yuan, B.Yue, X.-J.Bi, X.Chen, X.Zhang, JCAP 1010 (2010) 023, arXiv:0912.2504. G. Hutsi, J. Chluba, A. Hektor and M. Raidal, arXiv:1103.2766. S.Galli, F.Iocco, G.Bertone, A.Melchiorri, Phys. Rev. D 84 (2011) 027302, arXiv:1106.1528. A. Natarajan, arXiv:1201.3939. G. Giesen, J. Lesgourgues, B. Audren and Y. Ali-Haimoud, JCAP 1212 (2012) 008 [arXiv:1209.0247]. J. M. Cline and P. Scott, JCAP 1303 (2013) 044 [arXiv:1301.5908].

[13] T. Bringmann and C. Weniger, arXiv:1208.5481 [hep-ph].

[14] T. Bringmann, X. Huang, A. Ibarra, S. Vogl and C. Weniger, arXiv:1203.1312 [hep-ph].

[15] C. Weniger, JCAP **1208** (2012) 007 [arXiv:1204.2797 [hep-ph]].

[16] E. Tempel, A. Hektor and M. Raidal, arXiv:1205.1045 [hep-ph].

[17] M. Su and D. P. Finkbeiner, arXiv:1206.1616 [astro-ph.HE].

[18] A. Hektor, M. Raidal and E. Tempel, arXiv:1207.4466 [astro-ph.HE].

[19] M. Su and D. P. Finkbeiner, arXiv:1207.7060 [astro-ph.HE].

[20] A. Rajaraman, T. M. P. Tait and D. Whiteson, arXiv:1205.4723 [hep-ph].

[21] A. Boyarsky, D. Malyshev and O. Ruchayskiy, arXiv:1205.4700 [astro-ph.HE].

[22] N. Mirabal, arXiv:1208.1693 [astro-ph.HE].

[23] A. Hektor, M. Raidal and E. Tempel, arXiv:1208.1996 [astro-ph.HE].

[24] C. Weniger, presentation at the FERMI meeting for alternative observations, 25 Jul 2013.

[25] L. Goodenough and D. Hooper, arXiv:0910.2998 [hep-ph].

[26] V. Vitale *et al.* [Fermi-LAT Collaboration], arXiv:0912.3828 [astro-ph.HE]. D. Hooper and L. Goodenough, Phys. Lett. B **697** (2011) 412 [arXiv:1010.2752 [hep-ph]]. D. Hooper and T. Linden, Phys. Rev. D **84** (2011) 123005 [arXiv:1110.0006 [astro-ph.HE]]. D. Hooper, Phys. Dark Univ. **1** (2012) 1 [arXiv:1201.1303 [astro-ph.CO]]. K. Abazajian, M. Kaplinghat, Phys. Rev. D **86** (2012) 083511 [arXiv:1207.6047. D. Hooper, T. Slatyer, Phys. Dark Univ. **2** (2013) 118 [arXiv:1302.6589 [astro-ph.HE]]. C. Gordon and O. Macias, Phys. Rev. D **88** (2013) 083521 [arXiv:1306.5725 [astro-ph.HE]]. W.-C. Huang, A. Urbano and W. Xue, arXiv:1307.6862 [hep-ph]. K. N. Abazajian, N. Canac, S. Horiuchi and M. Kaplinghat, arXiv:1402.4090 [astro-ph.HE].

[27] T. Daylan, D. P. Finkbeiner, D. Hooper, T. Linden, S. K. N. Portillo, N. L. Rodd and T. R. Slatyer, arXiv:1402.6703 [astro-ph.HE].

[28] K. N. Abazajian, JCAP **1103** (2011) 010 [arXiv:1011.4275 [astro-ph.HE]]. D. Hooper, I. Cholis, T. Linden, J. Siegal-Gaskins and T. Slatyer, Phys. Rev. D **88** (2013) 083009 [arXiv:1305.0830 [astro-ph.HE]]. Q. Yuan and B. Zhang, arXiv:1404.2318 [astro-ph.HE].

[29] A. Boyarsky, D. Malyshev and O. Ruchayskiy, Phys. Lett. B **705** (2011) 165 [arXiv:1012.5839 [hep-ph]].

[30] J. Petrovic, P. D. Serpico and G. Zaharijas, arXiv:1405.7928 [astro-ph.HE].

[31] E. Carlson and S. Profumo, arXiv:1405.7685 [astro-ph.HE].

[32] M. Cirelli, D. Gaggero, G. Giesen, M. Taoso and A. Urbano, arXiv:1407.2173 [hep-ph].

[33] T. Bringmann, M. Vollmann and C. Weniger, arXiv:1406.6027 [astro-ph.HE].

[34] E. Bulbul, M. Markevitch, A. Foster, R. K. Smith, M. Loewenstein and S. W. Randall, Astrophys. J. **789** (2014) 13 [arXiv:1402.2301 [astro-ph.CO]].

[35] A. Boyarsky, O. Ruchayskiy, D. Iakubovskyi and J. Franse, arXiv:1402.4119 [astro-ph.CO].

[36] T. E. Jeltema and S. Profumo, arXiv:1408.1699 [astro-ph.HE].

[37] A. Boyarsky, J. Franse, D. Iakubovskyi and O. Ruchayskiy, arXiv:1408.4388 [astro-ph.CO].

[38] S. Riemer-Sorensen, arXiv:1405.7943 [astro-ph.CO].

Searching for New Physics in b-hadron decays

Thomas Latham on behalf of the LHCb collaboration

Department of Physics, University of Warwick, Coventry, CV4 7AL, United Kingdom

DOI: http://dx.doi.org/10.3204/DESY-PROC-2014-04/297

Recent results from the realm of b-hadron physics are presented, with a focus on anomalous results and *CP* violation studies. Results are shown from the B-factories: *BABAR* and Belle; the Tevatron experiments: CDF and D0; and the LHC experiments: ATLAS, CMS and LHCb. Together these give some tantalising hints of cracks in the Standard Model.

1 Introduction

One of the primary goals of the field of flavour physics is to uncover evidence of physics beyond the Standard Model (SM) of particle physics — so called "New Physics". This is achieved by looking for discrepancies between the SM predictions and experimental results in observables such as decay rates and *CP*-violating asymmetries. It is therefore essential to have good precision in both experiment and theory. The searches that can be performed using flavour observables are complementary to the searches for New Physics (NP) particles at the energy frontier. Indeed, they can potentially probe higher energy scales than those that are currently directly accessible. The study of b-hadrons and their decays provides an excellent laboratory in which to make such measurements. Such studies are a world-wide effort, with experiments in the USA, Europe and Japan all contributing. Some of latest results from these experimental collaborations will be presented here.

2 Measurements of *CP*-violating phases

2.1 CKM angle γ

Of the three angles of the UT, the angle γ is the least well determined. Of particular importance is that the angle γ can be determined from purely tree-level processes. In addition, these determinations are theoretically extremely clean; the correspondence between the experimental measurements and the SM value of γ is accurate to the level of 10^{-7} [1]. Such measurements are therefore a "standard candle" for the SM and can be compared with measurements from loop-dominated processes to look for discrepancies. Hence, it is very important to achieve the best possible experimental precision.

The two tree-level diagrams $b \to c\bar{u}s$ and $b \to u\bar{c}s$ have a relative weak phase of γ. For this phase to be measurable the two diagrams must interfere. This can happen in the decays $B^+ \to \overline{D}^0 K^+$ and $B^+ \to D^0 K^+$ if the D^0 and $\overline{D}^0$ decay to the same final state. The experimental method depends on the nature of the D decay. The most recent results from LHCb use the decays $D \to K^0_S \pi^+\pi^-$ and $K^0_S K^+ K^-$, and hence the so-called GGSZ method [2, 3]. The strong

phase difference between the D^0 and $\overline{D}^0$ decays can be determined as a function of the position in the Dalitz plot, either by using a model of the decay amplitudes, e.g. from *BABAR* [4], or via a model-independent approach that uses measurements of the phase difference in bins of the Dalitz plot provided by the CLEO-c experiment [5]. The LHCb collaboration have recent results using both of these approaches. The model-dependent analysis [6] uses the data sample collected in 2011, corresponding to an integrated luminosity of $1\,\text{fb}^{-1}$. The model-independent analysis [7], described here, uses the $3\,\text{fb}^{-1}$ Run 1 dataset (from 2011 and 2012).

The model-independent nature of the method essentially reduces the analysis to counting the number of B^+ and B^- signal events in each bin of the Dalitz plot. The binning scheme is symmetric about $m^2_+ = m^2_-$, the bins in one half are labelled $+i$, while the corresponding bin in the other half is labelled $-i$. The signal yields are related to the quantities of interest via

$$\begin{aligned} N^+_{\pm i} &= h_{B^+}\left[F_{\mp i} + (x_+^2 + y_+^2)F_{\pm i} + 2\sqrt{F_i F_{-i}}(x_+ c_{\pm i} - y_+ s_{\pm i})\right] , \\ N^-_{\pm i} &= h_{B^-}\left[F_{\pm i} + (x_-^2 + y_-^2)F_{\mp i} + 2\sqrt{F_i F_{-i}}(x_- c_{\pm i} - y_- s_{\pm i})\right] , \end{aligned} \tag{1}$$

where F_i is the fraction of events in bin i in the flavour-specific $D^0 \to K^0_S\pi^+\pi^-$ Dalitz plot (obtained from semileptonic $B^+ \to \overline{D}^0\mu^+\nu_\mu$ data), $h_{B^\pm}$ are normalisation factors, c_i and s_i are the cosine and sine of the strong phase difference in bin i measured by CLEO-c, and $x_\pm \equiv r_B\cos(\delta_B \pm \gamma)$ and $y_\pm \equiv r_B\sin(\delta_B \pm \gamma)$, where r_B and δ_B are the ratio of magnitudes and strong phase difference of the two B decay diagrams. A simultaneous fit to the B candidate invariant mass in each Dalitz-plot bin is used to determine $x_\pm$ and $y_\pm$. Interpreting these results in terms of the physical parameters gives

$$r_B = 0.080^{+0.019}_{-0.021}\,, \quad \delta_B = \left(134^{+14}_{-15}\right)^\circ\,, \quad \gamma = \left(62^{+15}_{-14}\right)^\circ\,,$$

which constitutes the single most precise measurement of γ.

2.2 B^0_s-$\overline{B}^0_s$ mixing phase

The neutral B mesons exhibit mixing between B and $\overline{B}$ through a box diagram. Decays to *CP* eigenstates, which are accessible for both B and $\overline{B}$, therefore allow the mixing phase to be probed via interference between the direct decay process and decay after mixing. In the B^0_s system, the SM prediction for the mixing phase is small, $\phi_s \approx (-0.0363 \pm 0.0016)\,\text{rad}$, while many NP models enhance this value.

The decay mode $B^0_s \to J/\psi\,\phi$ is experimentally very clean. However, the vector-vector final state is an admixture of *CP* eigenstates. An angular analysis is required to disentangle the *CP*-odd and *CP*-even components. The signal model is then a sum of terms containing both angular and time dependence. It is necessary to determine the flavour of the signal B meson at production. This can be achieved by using either flavour-specific decays of the other b-hadron in the event or particles (such as charged kaons) associated with the hadronisation of the signal B. It is also necessary to account for the efficiency as a function of both the decay time and the angular variables, as well as the experimental resolution on the same quantities. The ATLAS, CMS and LHCb collaborations have all recently reported new or improved measurements of ϕ_s, which are shown in Fig. 1. The ATLAS [8] and CMS [9] results use the decay $B^0_s \to J/\psi\,\phi$, while LHCb have a combination of the channels $B^0_s \to J/\psi\,\pi^+\pi^-$ and $B^0_s \to J/\psi\,K^+K^-$ using $1\,\text{fb}^{-1}$ of data [10], as well as an update of the $B^0_s \to J/\psi\,\pi^+\pi^-$ channel using the $3\,\text{fb}^{-1}$ data set [11]. This latest LHCb results constitutes the single most precise measurement of

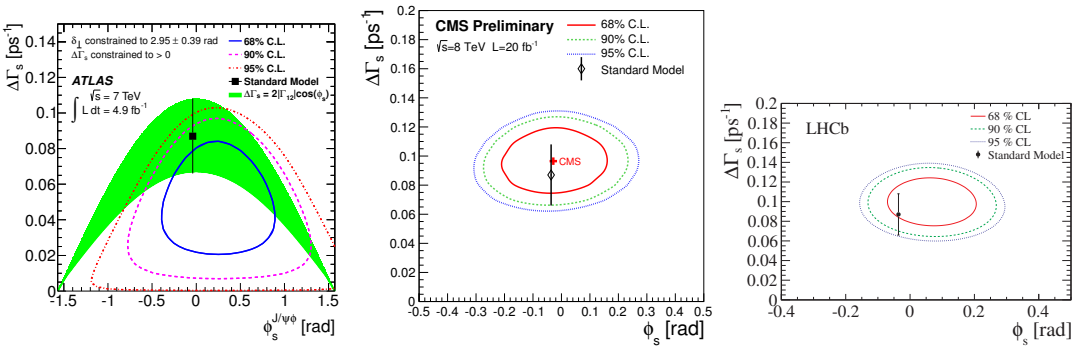

Figure 1: Results from (left) ATLAS, (middle) CMS, and (right) LHCb in the $\Delta\Gamma_s$ vs ϕ_s plane.

$\phi_s = (70 \pm 68 \pm 8)$ mrad. All of these results are consistent with the SM prediction. More precise measurements are needed to search for small deviations.

3 Semi-leptonic B decays

Semi-leptonic decays of b hadrons can be used to measure the sides of the UT by determining the absolute values of the CKM elements V_{cb} and V_{ub}. There are some persistent puzzles in this area. Firstly, poor consistency between the values of V_{xb} measured in inclusive and exclusive decays, and secondly, the sum of the measured branching fractions of exclusive semi-leptonic B to charm decays falls well short of the well measured inclusive rate (inclusive − exclusive $= (1.57 \pm 0.26)\%$). More precise measurements and measurements of extra decay channels are needed to either resolve these issues or to determine if they arise from NP contributions.

3.1 Anomalies in $\overline{B} \to D^{(*)}\tau\overline{\nu}_\tau$

In addition to the above puzzles, the *BABAR* experiment sees a large deviation from the SM in semi-tauonic B to charm decays [12, 13]. Measurements are made of the ratio of branching fractions

$$R(D^{(*)}) = \frac{\mathrm{BF}(\overline{B} \to D^{(*)}\tau^-\overline{\nu}_\tau)}{\mathrm{BF}(\overline{B} \to D^{(*)}\ell^-\overline{\nu}_\ell)} = \frac{N_{\mathrm{sig}}}{N_{\mathrm{norm}}} \times \frac{\varepsilon_{\mathrm{norm}}}{\varepsilon_{\mathrm{sig}}}\,. \tag{2}$$

The results are $R(D) = 0.440 \pm 0.072$ and $R(D^*) = 0.332 \pm 0.030$, which are 2.0σ and 2.7σ larger than the SM predictions 0.297 ± 0.017 and 0.252 ± 0.003, respectively. The combined significance of the deviation is 3.4σ. Including also the results from Belle [14, 15] increases the significance. Additionally, the *BABAR* results are incompatible (at the level of 3.1σ) with Type-II 2-Higgs-Doublet models of the possible charged Higgs contributions to these decays. The $R(D)$ and $R(D^*)$ results prefer different values of $\tan\beta/m_{H^+}$ in these models. In addition, *BABAR* and Belle results of the branching fraction of $B^- \to \tau^-\overline{\nu}_\tau$ prefer further different values of $\tan\beta/m_{H^+}$. The results can, however, be accommodated in more general 2-Higgs-Doublet models. The final results from the full Belle dataset are awaited with much anticipation.

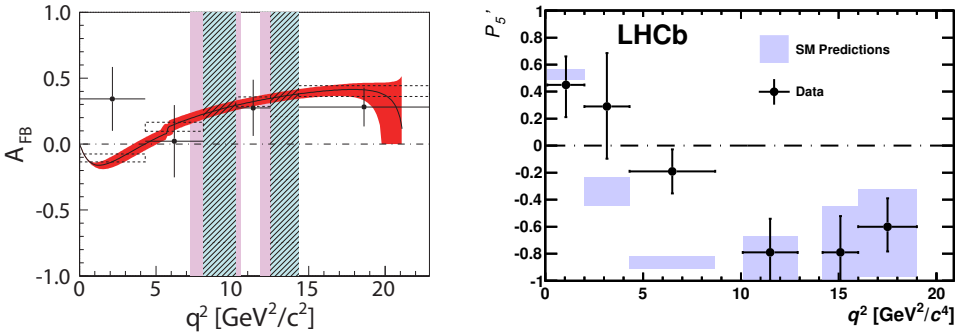

Figure 2: (left) Forward backward asymmetry as a function of q^2 for inclusive $B \to X_s \ell^+ \ell^-$. The red band is the SM prediction. (right) Distribution of the P_5' angular observable for $B^0 \to K^{*0} \mu^+ \mu^-$ decays.

3.2 Improved understanding of $\overline{B} \to D^{**} \ell \overline{\nu}_\ell$

The largest systematic uncertainty on the *BABAR* $\overline{B} \to D^{(*)} \tau^- \overline{\nu}_\tau$ results is due to the modelling of backgrounds from $B \to D^{**} \ell \nu_\ell$ decays. Many of these decays are not measured and this lack of knowledge could also be contributing to the "gap" between the inclusive and sum of exclusive branching fraction measurements mentioned earlier. Branching fractions of both charged and neutral B mesons decaying to $D^{(*)} \pi^\pm \ell \nu_\ell$ and $D^{(*)} \pi^+ \pi^- \ell \nu_\ell$ final states are measured by the *BABAR* experiment. For the latter class of decay, these are all first measurements, while those of the first type greatly improve their precision. The combined significance of the $D \pi^+ \pi^- \ell \nu_\ell$ decays is 5.1σ, while that of the $D^* \pi^+ \pi^- \ell \nu_\ell$ decays is 3.5σ. The inclusive–exclusive branching fraction gap is reduced from $\sim 7\sigma$ to $\sim 3\sigma$. These new results should also help to improve the systematic uncertainties on future analyses of $\overline{B} \to D^{(*)} \tau \overline{\nu}_\tau$. A journal paper describing the analysis and its results is in preparation.

4 Rare decays

Decays of the type $b \to s \ell^+ \ell^-$ proceed either via electroweak penguin or box diagrams. The Wilson coefficients C_7, C_9 and C_{10} encode the strength of the short-distance interactions. Many NP models predict additional contributions to the decay amplitudes at a similar level to the SM. Complementary information can be gained from branching fractions, *CP* asymmetries and angular moments, which are generally determined as a function of the 4-momentum transfer to the dimuon system, q^2.

The Belle collaboration have made the first measurements of the forward-backward asymmetry for inclusive $B \to X_s \ell^+ \ell^-$ decays [16]. The analysis uses a sum of 10 exclusive final states: 3 B^0 decays to a charged kaon and 1–3 pions, and 7 B^+ decays to a charged kaon and 0–3 pions or a K^0_S and 1–3 pions. The data sample used comprises 772 million $B\overline{B}$ pairs. The results are shown in Fig. 2 (left), where the red band is the SM prediction. Everything looks consistent with the SM at this level of precision, with the largest deviation being 1.8σ in the first bin.

The LHCb collaboration have performed an analysis of angular observables that have been

optimised to reduce their dependence on form factors [17] in the decay $B^0 \to K^{*0}\mu^+\mu^-$ [18]. The analysis uses the $1\,\text{fb}^{-1}$ data sample from 2011 and the results exhibit a large local deviation (3.7σ) in one bin of the P_5' distribution, as can be seen in Fig. 2 (right). The probability to observe a fluctuation $\geq 3.7\sigma$ in the 24 bins is 0.5%. The residual degree of dependence on form factors and hence the size of the theoretical uncertainties is a hot topic in the theory community. Improved determination of these as well as increased precision from the experimental side will help to determine if this is a genuine effect from NP contributions.

Including this result in global fits to the Wilson coefficients [19, 20, 21] indicates that it can be accommodated if the value of the C_9 coefficient is reduced. If this is indeed the case then one would expect the branching fractions of decays such as $B \to K^{(*)}\mu^+\mu^-$ and $B_s^0 \to \phi\mu^+\mu^-$ to be lower than predicted. LHCb measurements of these quantities [22, 23, 24] are indeed lower than the predictions from both Lattice QCD [25, 26] and Light Cone Sum Rules [27, 28].

One possible explanation for a low value of C_9 is contributions from a Z' particle, see for example Ref. [29]. Some NP models that include a Z' have preferred coupling to muons over electrons [30]. Due to destructive interferences this means that the branching fraction of $B^+ \to K^+\mu^+\mu^-$ should be lower than that for $B^+ \to K^+e^+e^-$. LHCb also has results for this ratio of branching fraction using the full Run 1 data sample [31]

$$R_K = \frac{\text{BF}(B^+ \to K^+\mu^+\mu^-)}{\text{BF}(B^+ \to e^+e^-)} = 0.745^{+0.090}_{-0.074} \pm 0.036\,, \tag{3}$$

which deviates from the SM prediction of unity by 2.6σ.

It would seem therefore that there is a reasonably consistent picture. However, there is much still to be understood, such as the importance of $c\bar{c}$ resonances at high q^2 [32, 33]. It is important to update all measurements to the full Run 1 data sample and to include additional decay modes, such as $\Lambda_b \to \Lambda\mu^+\mu^-$ and $B^+ \to K^+\pi^+\pi^-\ell^+\ell^-$, to further increase the sensitivity.

5 Dimuon charge asymmetry

Measurements of the dimuon charge asymmetry are sensitive to possible *CP* violation in the mixing of the neutral B mesons, which would imply $\Gamma(B \to \overline{B} \to \mu^- X) \neq \Gamma(\overline{B} \to B \to \mu^+ X)$. The D0 experiment measures the inclusive dimuon asymmetry

$$A_{sl} = \frac{N(\mu^+\mu^+) - N(\mu^-\mu^-)}{N(\mu^+\mu^+) + N(\mu^-\mu^-)}\,, \tag{4}$$

which is related to both the semi-leptonic charge asymmetries of B^0 and B_s^0 mesons.

Corrections for backgrounds have been applied (the single muon asymmetry is used to help reduce systematic uncertainties), as well as those for *CP* violation that occurs in the interference between mixing and decay. After this, the result obtained by D0 [34] is $A_{sl} = (-0.496 \pm 0.153 \pm 0.072)\,\%$, which differs from the SM prediction, $A_{sl}^{\text{SM}} = (-0.023 \pm 0.004)\,\%$, at the level of 2.8σ. Comparing separately each bin of the impact parameter distribution with the SM, the level of disagreement rises to 3.6σ.

The interpretation of the result in terms of the individual semi-leptonic asymmetries depends strongly on the assumed value of $\Delta\Gamma_d/\Gamma_d$, the discrepancy with the SM varying between 1.9σ and 3.6σ. This highlights the importance of improved measurements of $\Delta\Gamma_d/\Gamma_d$. Indeed, a recent LHCb result [35] based on $1\,\text{fb}^{-1}$ of data and using the decay modes $B^0 \to J/\psi\, K^{(*)0}$ gives a value $-0.044 \pm 0.025 \pm 0.011$, which is becoming competitive with the B-factory results.

6 Direct CP violation in charmless three-body B decays

In general, CP asymmetries can arise when there is more than one contributing amplitude to a decay and where those amplitudes have both different weak and strong phases. In charmless B^+ decays there are contributing tree and loop diagrams, which have similar magnitudes and a relative weak phase of γ. In three-body decays, the strong phase difference could arise from an intrinsic difference in the two decay diagrams, from rescattering or from interference between intermediate resonances in the Dalitz plot.

6.1 Large CP violation in $B^+ \to h^+h^+h^-$

The LHCb experiment has performed an analysis of CP violation in the phase-space of three-body charmless decays of B^+ mesons to $h^+h^+h^-$ final states ($h = K/\pi$) [36]. The measured raw asymmetries are corrected for the effects of production, detection and matter-interaction asymmetries using data control modes. The inclusive asymmetries for each mode are determined to be between $2-13\%$ in magnitude and positive (negative) for $B^\pm \to K^\pm\pi^+\pi^-$ and $\pi^\pm\pi^+\pi^-$ ($B^\pm \to K^\pm K^+K^-$ and $\pi^\pm K^+K^-$) decays. The local asymmetries in regions of the phase space are much more pronounced. Figure 3 shows the raw asymmetry as a function of the position in the Dalitz plot for the decays to $K^\pm K^+K^-$ and $K^\pm\pi^+\pi^-$. There are regions of very large positive (negative) asymmetry at low values of the $\pi^+\pi^-$ (K^+K^-) invariant mass. A similar pattern is seen for the other two decay modes.

The larger data sample than the previous analyses [37, 38] allows a more detailed examination of the variation of the asymmetries in the phase space. Figure 4 shows the $m_{\pi^+\pi^-}$ dependence of the difference between the B^- and B^+ signal yields in the $B^\pm \to \pi^\pm\pi^+\pi^-$ decay. The distributions are shown separately for the two regions $\cos\theta > 0$ and $\cos\theta < 0$, where θ is the angle between the like-sign pions in the $\pi^+\pi^-$ rest frame. The most striking features are the change in sign of the asymmetry on either side of the $\rho(770)$ resonance pole and that the sign is opposite for the two regions of $\cos\theta$. This indicates that the interference between the $\rho(770)$ and an underlying S-wave component is playing a significant role in generating the CP asymmetry. In addition, it is possible that $\pi\pi \leftrightarrow KK$ rescattering is contributing in the region between 1.2 and 1.5 GeV/c^2. Amplitude analyses of these decays will be required to fully understand the origin of these very large asymmetries.

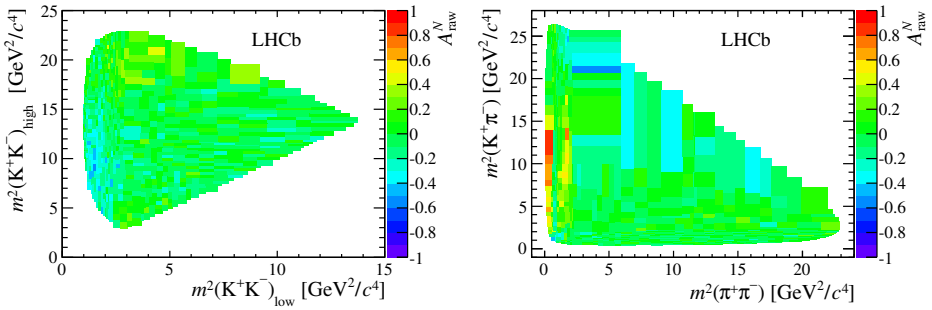

Figure 3: Raw asymmetries as a function of the DP position for $B^\pm$ decays to (left) $K^\pm K^+K^-$, and (right) $K^\pm\pi^+\pi^-$ final states.

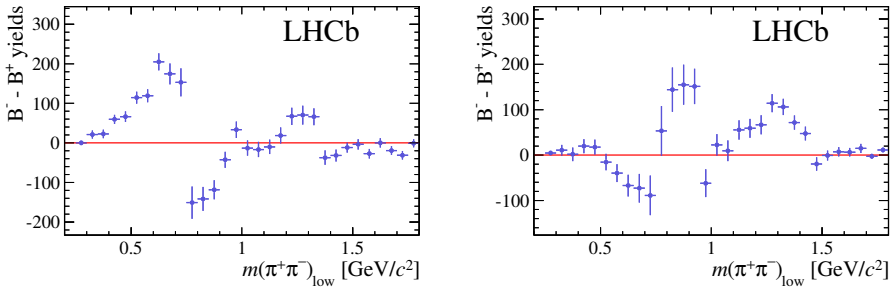

Figure 4: Difference of the B^- and B^+ signal yields as a function of the $\pi^+\pi^-$ invariant mass in the $B^\pm \to \pi^\pm\pi^+\pi^-$ decay. The yields have been background-subtracted and efficiency-corrected.

6.2 Amplitude analysis of $B^+ \to K^0_S\pi^+\pi^0$

The *BABAR* experiment has recently performed an amplitude analysis of the decay $B^+ \to K^0_S\pi^+\pi^0$. In addition to providing measurements of the branching fractions and *CP* asymmetries of the various intermediate states, a Dalitz-plot analysis allows the determination of their relative phases. Of particular interest are the relative phases of the two $K^*\pi$ components, which can be used to determine the CKM angle γ [39, 40].

A maximum likelihood fit is performed to separate signal from background and to determine the signal Dalitz-plot amplitudes. The fitted signal yield is 1014 ± 63, where the uncertainty is statistical only. The signal Dalitz-plot model follows the isobar model formalism, where the total amplitude is formed from the sum of the amplitudes for the various intermediate states. The complex coefficient for each contributing amplitude is determined from the fit. The branching fractions, *CP* asymmetries and relative phases are derived from these fitted coefficients. The signal model includes contributions from both the charged and neutral $K^*(892)$ resonances and the corresponding $K\pi$ S-wave as well as the $\rho(770)^+$ resonance.

The *CP* asymmetry of $B^+ \to K^*(892)^+\pi^0$ has a very large, negative central value (-52%) and is found to have a significance of 3.4σ, corresponding to first evidence of *CP* violation in this decay. The projection of the fit onto the $K^0_S\pi^+$ invariant mass can be seen in Figure 5, separated by the charge of the B candidate, where the asymmetry in the $K^*(892)^+$ region can be clearly seen. A journal paper describing the analysis and its results is in preparation.

7 Conclusion

With increasingly precise and sophisticated measurements, some anomalies have started to appear within the realm of b-hadron physics. Whether these are true hints of contributions from physics beyond the Standard Model will only become apparent with improved measurements and theoretical understanding. The coming years will provide better experimental precision as the LHC Run 1 data is fully exploited and the samples from Run 2 are collected and analysed. With the start of the Belle II experiment and the upgrade of the LHCb experiment both expected within the next few years, we look forward to the unprecedented precision that these complementary experiments will offer across the whole range of b-hadron physics.

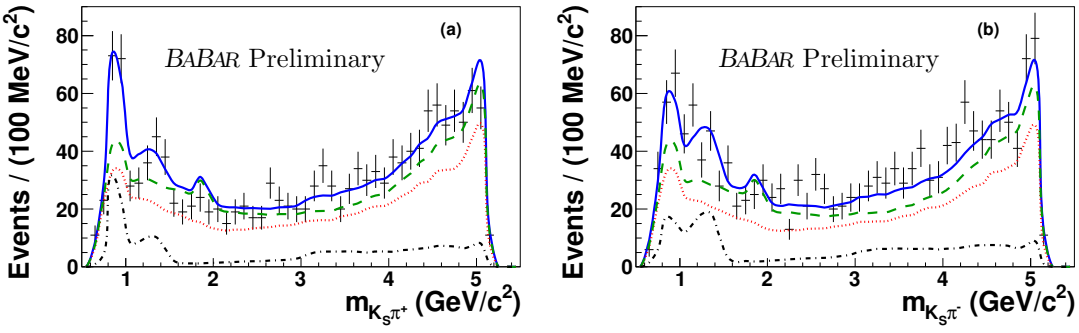

Figure 5: Data distributions of $m_{K^0_S\pi^+}$ and the corresponding fit projections for (a) B^+, and (b) B^- candidates. Points with error bars are the data, the solid (blue) lines are the total fit result, the dashed (green) lines are the total background contribution, and the dotted (red) lines are the $q\bar{q}$ component. The dash-dotted lines represent the signal contribution.

Acknowledgments

Work supported by the European Research Council under FP7 and by the Science and Technology Facilities Council.

References

[1] J. Brod and J. Zupan, JHEP **1401** (2014) 051.
[2] A. Bondar, Proceedings of BINP special analysis meeting on Dalitz analysis, 24-26 Sept, 2002. Unpublished.
[3] A. Giri, Y. Grossman, A. Soffer and J. Zupan, Phys. Rev. D **68** (2003) 054018.
[4] P. del Amo Sanchez *et al.* [BaBar Collaboration], Phys. Rev. Lett. **105** (2010) 081803.
[5] J. Libby *et al.* [CLEO Collaboration], Phys. Rev. D **82** (2010) 112006.
[6] R. Aaij *et al.* [LHCb Collaboration], Nucl. Phys. B **888** (2014) 169.
[7] R. Aaij *et al.* [LHCb Collaboration], Submitted to JHEP, arXiv:1408.2748 [hep-ex].
[8] G. Aad *et al.* [ATLAS Collaboration], Phys. Rev. D **90** (2014) 052007.
[9] CMS Collaboration, CMS-PAS-BPH-13-012 (2014).
[10] R. Aaij *et al.* [LHCb Collaboration], Phys. Rev. D **87** (2013) 112010.
[11] R. Aaij *et al.* [LHCb Collaboration], Phys. Lett. B **736** (2014) 186.
[12] J. P. Lees *et al.* [BaBar Collaboration], Phys. Rev. Lett. **109** (2012) 101802.
[13] J. P. Lees *et al.* [The BaBar Collaboration], Phys. Rev. D **88** (2013) 072012.
[14] I. Adachi *et al.* [Belle Collaboration], arXiv:0910.4301 [hep-ex].
[15] A. Bozek *et al.* [Belle Collaboration], Phys. Rev. D **82** (2010) 072005.
[16] Y. Sato *et al.* [Belle Collaboration], arXiv:1402.7134 [hep-ex].
[17] J. Matias, F. Mescia, M. Ramon and J. Virto, JHEP **1204** (2012) 104.
[18] R. Aaij *et al.* [LHCb Collaboration], Phys. Rev. Lett. **111** (2013) 191801.
[19] S. Descotes-Genon, J. Matias and J. Virto, Phys. Rev. D **88** (2013) 074002.
[20] W. Altmannshofer and D. M. Straub, Eur. Phys. J. C **73** (2013) 2646.

[21] F. Beaujean, C. Bobeth and D. van Dyk, Eur. Phys. J. C **74** (2014) 2897.
[22] R. Aaij *et al.* [LHCb Collaboration], JHEP **1307** (2013) 084.
[23] R. Aaij *et al.* [LHCb Collaboration], JHEP **1308** (2013) 131.
[24] R. Aaij *et al.* [LHCb Collaboration], JHEP **1406** (2014) 133.
[25] C. M. Bouchard, G. P. Lepage, C. J. Monahan, H. Na and J. Shigemitsu, arXiv:1310.3207 [hep-lat].
[26] R. R. Horgan, Z. Liu, S. Meinel and M. Wingate, Phys. Rev. Lett. **112** (2014) 212003.
[27] C. Bobeth, G. Hiller and D. van Dyk, JHEP **1107** (2011) 067.
[28] C. Bobeth, G. Hiller, D. van Dyk and C. Wacker, JHEP **1201** (2012) 107.
[29] R. Gauld, F. Goertz and U. Haisch, JHEP **1401** (2014) 069.
[30] W. Altmannshofer, S. Gori, M. Pospelov and I. Yavin, Phys. Rev. D **89** (2014) 095033.
[31] R. Aaij *et al.* [LHCb Collaboration], Phys. Rev. Lett. **113** (2014) 151601.
[32] R. Aaij *et al.* [LHCb Collaboration], Phys. Rev. Lett. **111** (2013) 112003
[33] J. Lyon and R. Zwicky, arXiv:1406.0566 [hep-ph].
[34] V. M. Abazov *et al.* [D0 Collaboration], Phys. Rev. D **89** (2014) 012002.
[35] R. Aaij *et al.* [LHCb Collaboration], JHEP **1404** (2014) 114.
[36] R. Aaij *et al.* [LHCb Collaboration], Submitted to Phys. Rev. D, arXiv:1408.5373 [hep-ex].
[37] R. Aaij *et al.* [LHCb Collaboration], Phys. Rev. Lett. **111** (2013) 101801.
[38] R. Aaij *et al.* [LHCb Collaboration], Phys. Rev. Lett. **112** (2014) 011801.
[39] M. Ciuchini, M. Pierini and L. Silvestrini, Phys. Rev. D **74** (2006) 051301.
[40] M. Gronau, D. Pirjol, A. Soni and J. Zupan, Phys. Rev. D **75** (2007) 014002.

Search for beyond the standard model physics at the LHC

Kenichi Hatakeyama for the CMS and ATLAS collaborations
Baylor University, One Bear Place #97316, Waco, TX, U.S.A.

DOI: http://dx.doi.org/10.3204/DESY-PROC-2014-04/316

Both CMS and ATLAS collaborations have performed searches for physics beyond the standard model of particle physics in a variety of final states using the proton-proton collision data collected during the LHC Run 1 at the center-of-mass energy of $\sqrt{s}$ = 7–8 TeV. In this paper, a review of recent results from these searches are presented. Future prospects for these searches from the LHC experiments are also discussed.

1 Introduction

The Run 1 operation of the Large Hadron Collider (LHC) from 2009 to 2012 was extremely successful. The long-sought Higgs boson was discovered by the CMS and ATLAS collaborations, which completed the standard model (SM). However, there are still many open questions in particle physics, such as the gauge hierarchy problem and the identify of dark matter, and the standard model is often considered as a low-energy approximation of a more complete theory. Both CMS and ATLAS have performed a variety of new physics searches using the Run 1 data, and more than 100 results based on the 2012 data of 8 TeV proton-proton collisions are made public [1, 2]. In this conference proceedings, I will present only some highlights of these results.

2 Search for resonances

Mass resonances are simple yet powerful probes to discover new particles, and new particles that will produce mass resonance signatures are predicted in many beyond-the-standard-model (BSM) scenarios. Single mass resonances are predicted by, e.g., extended gauge theories [W'/Z'], compositeness [excited fermions], Randall-Sundrum (RS) model [Kaluza-Klein gravitons/gluons], and paired mass resonances may be produced by, e.g., gluinos/squarks in the case of supersymmetry, and also by leptoquarks, vector-like quarks, and colorons. Searches for new physics in dilepton mass spectra were performed by both CMS [3] and ATLAS [4]. The m_{ee} spectrum measured by ATLAS is shown in Fig. 1(a). No resonant structure is observed and Z's with the SM Z couplings are excluded up to 2.9 TeV [3, 4].

The forward-backward asymmetry of dielectron pairs in the same dataset, $A_{\mathrm{FB}} = (N_{\mathrm{F}} - N_{\mathrm{B}})/(N_{\mathrm{F}} + N_{\mathrm{B}})$ where N_F (N_B) is the number of events with $\cos\theta^* > 0$ ($\cos\theta^* < 0$) and θ^* is the dielectron decay angle, provides extra handles to search for non-resonant new physics signatures originating from contact interactions or large extra spatial dimensions. No significant

deviations from the SM background expectations are observed as shown in Fig. 1(b) and lower limits are set on the contact interaction scale Λ up to 26 TeV [5].

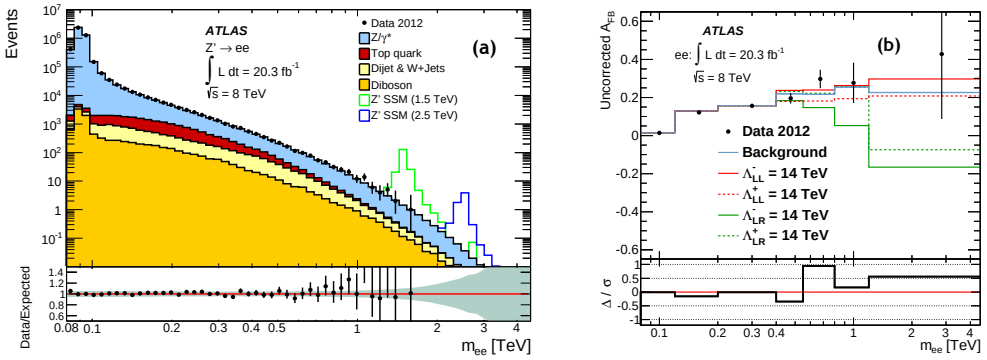

Figure 1: (a) The m_{ee} distributions with two selected Z' signals overlaid, compared to the stacked sum of all expected backgrounds, and the ratios of data to the background expectation [4]. (b) Reconstructed A_{FB} distributions for data and the SM background estimation versus m_{ee} together with the predictions of different Λ values for the contact interaction model [5].

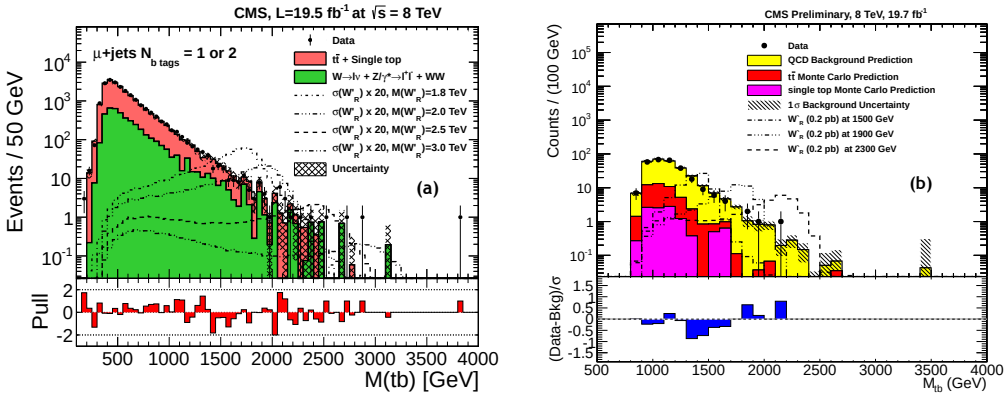

Figure 2: The m_{tb} distributions in the (a) semi-leptonic [6] and (b) all-hadronic [7] channel together with simulated W' signal distributions.

Searches for W's decaying to the top-bottom quark pairs have been performed by both CMS [6, 7] and ATLAS [8, 9]. The m_{tb} mass spectra measured in the semi-leptonic ($\mathrm{W}' \to \mathrm{tb}, \mathrm{t} \to \mathrm{Wb} \to (\mathrm{l}\nu)\mathrm{b}$) and all-hadronic ($\mathrm{W}' \to \mathrm{tb}, \mathrm{t} \to \mathrm{Wb} \to (\mathrm{q}\bar{\mathrm{q}}')\mathrm{b}$) channels by CMS are shown in Fig. 2. The right-handed W' is excluded up to about 2 TeV. For the all-hadronic searches [7, 9], the jet substructure technique is used to identify hadronically-decaying boosted top quarks from W' decays. New physics searches at the LHC often involve high-p_{T} boosted top/W's, and jet substructure tools based on "fat" jets with the size parameters $R = 0.8$–1.5 are widely used.

New heavy vector-like quarks emerge as a characteristic feature of some BSM models, including extra dimensions and composite Higgs models. They have been extensively searched for by CMS [10, 11] and ATLAS [12, 13, 14]. A new charge +2/3 quark, T, undergo three decay modes: T → Zt, Ht, and Wb. Searches have been performed in different channels to cover various branching fraction hypotheses. Searches in the opposite-sign dileptons and ≥ 3 leptons + b-tags channels are sensitive to the T → Zt decay [12]. A search with boosted W + b-tags [13] provides sensitivities to T → Wb, and a search with the same-sign dileptons + b-tags [14] is sensitive to T → Zt and T → Ht. As shown in Fig. 3, these complementary searches provide sensitivities to a wide range of branching fractions. The current lower bounds on the T mass are about 690–780 GeV from CMS [10] and 550–850 GeV from ATLAS [12, 13, 14].

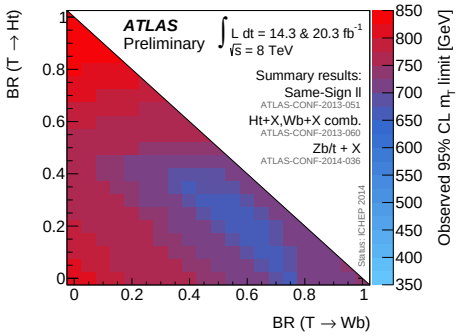

Figure 3: Observed lower limits on the mass of vector-like T quarks from ATLAS searches in the branching-ratio plane.

3 Search for dark matter

Currently one of the most important questions in particle physics is the identify of dark matter (DM). There are strong indications from many astronomical observations that there are DM particles which do not interact via strong or electromagnetic forces and are heavy enough so that they move slowly compared to the speed of light; however, such particles have not been observed in the laboratory yet. Many ground-based experiments looking for DM-nucleon scattering (direct searches) and experiments in space looking for signals from DM annihilation or decays (indirect searches) have been built. At the LHC, DM particles may be pair-produced in proton-proton collisions either directly or through cascade decays of heavier new particles. The DM particles do not interact with the CMS and ATLAS detectors; however, they can still be observed when they are boosted against initial state radiation of gluons, quarks, vector-bosons, and photons. If these radiated particles have high p_{T}, they result in the final state of mono-"X" and large missing E_{T}. Since particles that mediate interactions between SM particles and DM particles are not known, the effective field theory (EFT) is often used to model these interactions as contact interactions in interpretation of LHC DM search results. This is considered as a good model for heavy mediator masses ($>$ 3 TeV); however, a special care is necessary for lighter mediators.

CMS and ATLAS have searched for DM particles in mono-jet [15], mono-photon [16], mono-W/Z [17, 18, 19, 20], mono-top [21, 22], and di-top [23] final states associated with large missing E_T in the 8 TeV data. The mono-jet search results from CMS are shown in Fig 4(a). Searches in different final states provide the information about couplings of mediator particles to different flavors of quarks and gluons. Limits are set on the EFT contact interaction scale Λ using effective operators, and they are further translated to limits on elastic DM-nucleon cross section as a function of DM particle mass as shown in Fig. 4(b). Compared to results from direct dark matter searches, LHC results are more independent of DM masses up to kinematic limits of a few hundred GeV, more stringent at low DM masses, and less sensitive to the spin-dependence of the couplings.

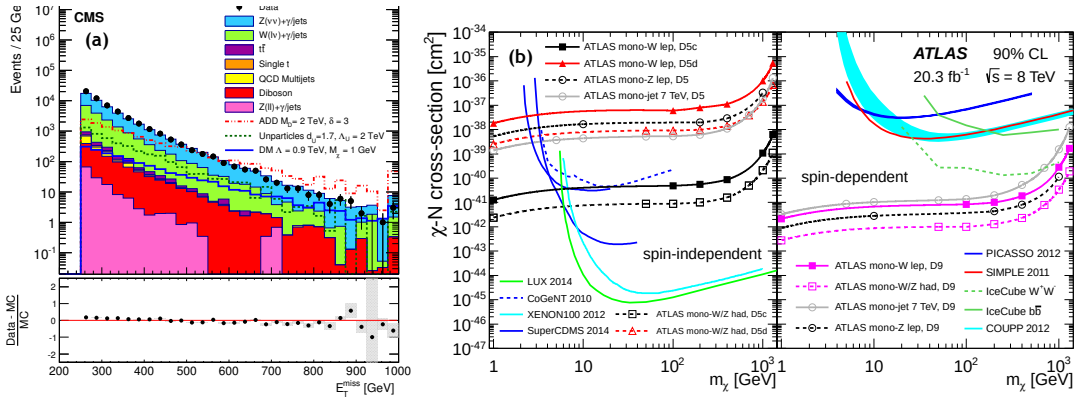

Figure 4: (a) Missing E_{T} distributions from the mono-jet search [15]. (b) The upper limits on the DM-nucleon cross section as a function of DM particle mass from searches in the mono-jet, mono-W, and mono-Z channels [19] for the spin-independent and spin-dependent EFT operators, together with limits from other experiments.

Some class of BSM models, called Higgs portal DM models, predict that a DM particle ($\tilde{\chi}$) interacts with SM particles only through the Higgs exchange process and the Higgs decays in the $\mathrm{H} \to \tilde{\chi}\tilde{\chi}$ mode. CMS searched for this signature in the vector boson fusion (VBF) channel and the $\mathrm{Z}(\to \ell\ell, \mathrm{b\bar{b}})$ + H channel [24]. The limit was placed on $\mathrm{Br}(\mathrm{H} \to \tilde{\chi}\tilde{\chi}) < 0.68$ (0.81) from the VBF (ZH) channel search, and the results are also presented in terms of the DM-nucleon cross section as shown in Fig. 5.

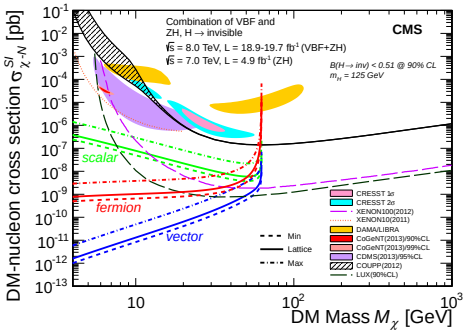

Figure 5: The upper limits on the DM-nucleon cross section versus DM particle mass from the $\mathrm{H} \to \tilde{\chi}\tilde{\chi}$ searches [24].

4 Search for supersymmetry

Supersymmetry (SUSY) is a well motivated BSM theory. In SUSY, the lightest supersymmetric particle (LSP) is considered a valid DM candidate. A broad class of SUSY scenarios with light third generation squarks and gluiness, known as natural models, can address the gauge hierarchy problem.

An extensive program to search for SUSY was carried out by CMS and ATLAS. Searches in the jets + missing E_{T} final state provide sensitivities to a wide class of SUSY models [25, 26]. Search results from ATLAS in this channel [25] are shown in Fig. 6(a). Mass exclusions reach up to about 1.4 TeV for gluinos ($\tilde{\mathrm{g}}$) and 0.9 TeV for the first- and second-generation squarks ($\tilde{\mathrm{q}}$). The inclusive searches with b-tags test natural SUSY models with TeV-scale gluinos, lighter top and bottom squarks, and nearly mass-degenerate charginos/neutralinos [27, 28]. Results from CMS [27] are shown in Fig. 6(b) for models with various gluino decay modes. The sensitivities generally degrade when there are more top quarks in the final state due to complex top quark decays.

The top squark ($\tilde{\mathrm{t}}_1$) is extensively searched for by CMS [29, 30, 31] and ATLAS [32, 33, 34, 35]

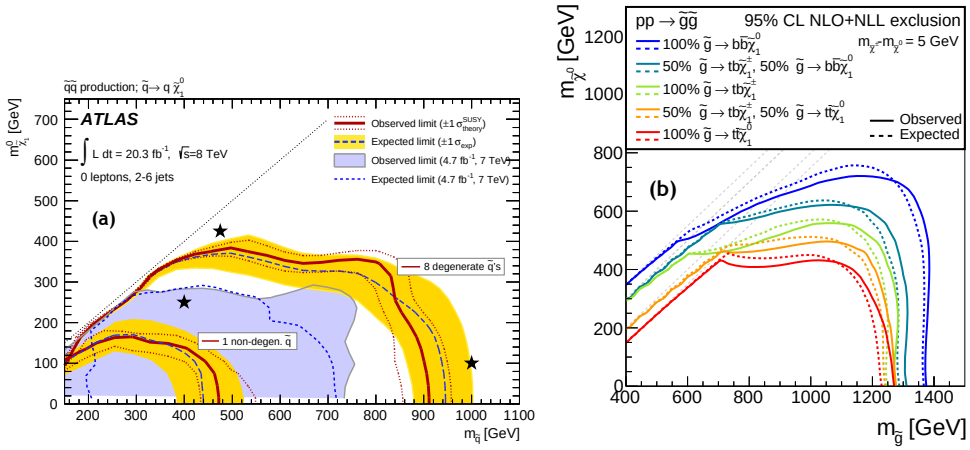

Figure 6: (a) Squark mass limits in the $m_{\tilde{q}}$-$m_{\tilde{\chi}_1^0}$ plane [25], and (b) gluino mass limits in the $m_{\tilde{g}}$-$m_{\tilde{\chi}_1^0}$ plane obtained for different gluino branching fraction models [27].

given its important role for addressing the gauge hierarchy problem. The dominant decay channel of the top squark varies over different SUSY scenarios and largely depends on available phase space for each decay mode. Results of complementary searches by ATLAS in different final states targeting different top squark decay modes are summarized in Fig. 7(a). The $\tilde{t}_1 \to t\tilde{\chi}_1^0$ decay mode is searched for in the 0-, 1-, and 2-lepton final states [32, 33, 34], and the mass exclusion extends up to about 700 GeV in the top squark mass. If $m_b + m_W + m_{\tilde{\chi}_1^0} < m_{\tilde{t}_1} < m_t + m_{\tilde{\chi}_1^0}$, the top squark often decays through $\tilde{t}_1 \to Wb\tilde{\chi}_1^0$, and searches in the 1- and 2-lepton channels provide sensitivities. If $m_{\tilde{t}_1} < m_b + m_W + m_{\tilde{\chi}_1^0}$, the top squark often decays through

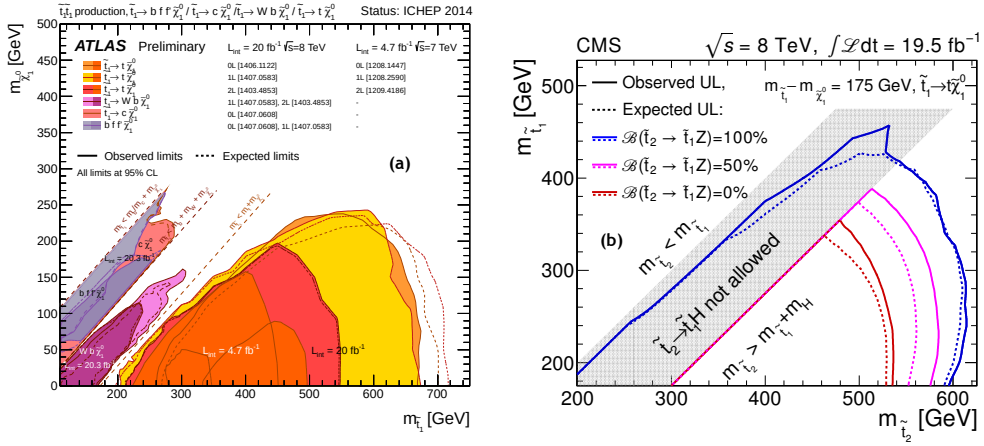

Figure 7: (a) Exclusion limits for top squark pair production from ATLAS [32, 33, 34, 35] shown in the $m_{\tilde{t}_1}$-$m_{\tilde{\chi}_1^0}$ plane. (b) Exclusion limits for $\tilde{t}_2$-pair production for different branching fractions of $\tilde{t}_2 \to Z(H)\tilde{t}_1$ [37].

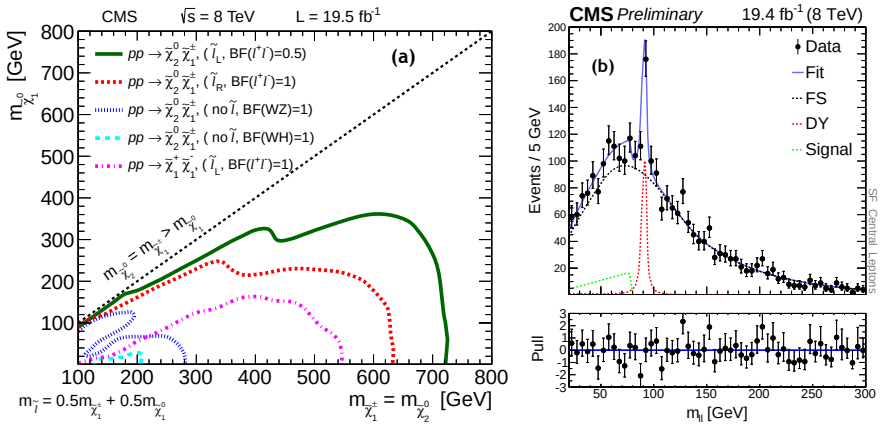

Figure 8: (a) Mass exclusions for $\tilde{\chi}_1^{\pm}\tilde{\chi}_2^0$ production with different decays, and for $\tilde{\chi}_1^{\pm}\tilde{\chi}_1^{\mp}$ production [38]. (b) Measured dilepton mass distributions with fits with the signal + background hypothesis in a dilepton mass spectrum endpoint search [44].

$\tilde{t}_1 \to c\tilde{\chi}_1^0$ or $\tilde{t}_1 \to bff'\tilde{\chi}_1^0$. In the case of $\tilde{t}_1 \to c\tilde{\chi}_1^0$ with the small mass splitting $m_{\tilde{t}_1} - m_{\tilde{\chi}_1^0}$, searches in the mono-jet + missing E_T final state provide sensitivities [31, 35]; however, as the mass splitting increases, mono-jet searches lose sensitivities and ATLAS performed a dedicated search with a charm-tagging [35] to fill this gap.

Gaining sensitivities to the top squark production remains difficult especially if $m_{\tilde{t}_1} - m_{\tilde{\chi}_1^0} \sim m_t$. If $m_{\tilde{\chi}_1^0}$ is small, the expected signal looks very similar to the SM $t\bar{t}$ production. ATLAS used the $t\bar{t}$ cross section measurement to place limits on the pair-production of top squarks with each top squark decaying to the top quark and LSP [36]. For higher $m_{\tilde{\chi}_1^0}$ values, CMS considered accessing such scenarios via the cascade decay of the heavier top squark ($\tilde{t}_2$), i.e., $\tilde{t}_2 \to \tilde{t}_1(H/Z) \to t(H/Z)\tilde{\chi}_1^0$ [37]. The results are shown in Fig. 7(b).

The production of charginos and neutralinos are also vigorously searched for by CMS and ATLAS. Searches for chargino-neutralino ($\tilde{\chi}_1^{\pm}\tilde{\chi}_2^0$) pair production were performed in a variety of final states with leptons and W, Z, and Higgs bosons [38, 39, 40, 41, 42]. These complementary searches provide sensitivities to $\tilde{\chi}_1^{\pm}\tilde{\chi}_2^0$ production with decays to left-handed sleptons ($\tilde{\ell}_L$), right-handed sleptons ($\tilde{\ell}_R$), or direct decays to Higgs and vector bosons as shown in Fig 8(a). The sensitivities and mass exclusions strongly depend on the branching fraction of $\tilde{\chi}_1^{\pm}$ and $\tilde{\chi}_2^0$. If $m_{\tilde{\ell}}$ is inbetween $m_{\tilde{\chi}_1^{\pm}}/m_{\tilde{\chi}_2^0}$ and $m_{\tilde{\chi}_1^0}$, the leptonic decay fractions of $\tilde{\chi}_1^{\pm}$ and $\tilde{\chi}_2^0$ increase, which enhances the sensitivities. For the scenarios in which $\tilde{\chi}_1^{\pm}/\tilde{\chi}_2^0$ decays to W/Z/H, sensitivities from the Run 1 searches are still modest, and the future LHC running will be essential to explore up to the TeV scale as shown in Fig. 9(c).

Searches are also performed in the HH and HZ final states [43]. A signal in these final states is expected from, e.g., the gauge-mediated SUSY model with the higgsino-like $\tilde{\chi}_{1,2}^0$ and $\tilde{\chi}_1^{\pm}$. A pair of $\tilde{\chi}_1^0$ with each $\tilde{\chi}_1^0$ decaying to H/Z and LSP (gravitino $\tilde{G}$), lead to these final states. The covered channels include $HH \to b\bar{b}b\bar{b}, \gamma\gamma(b\bar{b}, ZZ, WW, \tau\tau)$, and $HZ \to \gamma\gamma jj, \gamma\gamma\ell\ell, b\bar{b}\ell\ell$, and searches in these channels provide complementary sensitivities. Exclusions are set on the higgsino mass up to about 380 GeV in case the $\tilde{\chi}_1^0$ dominantly decays to Z and $\tilde{G}$; however, no exclusion is set on scenarios with high $\tilde{\chi}_1^0 \to H\tilde{G}$ branching fractions.

CMS has also performed a generic search for a kinematic endpoint in dilepton (e^+e^- and $\mu^+\mu^-$) mass spectra. If there is a decay process, e.g., $\tilde{\chi}_2^0 \to \ell\tilde{\ell} \to \tilde{\chi}_1^0\ell^+\ell^-$, opposite-sign same-flavor dilepton mass spectra are expected to show an endpoint (edge) at $m_{\rm edge} = \sqrt{(m^2_{\tilde{\chi}_2^0} - m^2_{\tilde{\ell}})(m^2_{\tilde{\ell}} - m^2_{\tilde{\chi}_1^0})}/m_{\tilde{\ell}}$. For this search, the signal and background contributions are determined from a kinematic fit where the dominant flavor-symmetric background is constrained with opposite-sign opposite-flavor ($e^+\mu^-$ and $e^-\mu^+$) leptons. A likelihood fit shown in Fig. 8(b) yields the observed significance of 2.4σ, which is not statistically significant, but it will be interesting to study it further with future runs.

5 Future prospects

The LHC will resume its operation in 2015 with the 13 TeV proton-proton collision energy, and the energy will go up to 14 TeV in the coming years. The energy increase from 8 to 13/14 TeV improves discovery sensitivities for high mass resonances, gluinos, and squarks drastically. The LHC is expected to deliver about 300 fb^{-1} of data by 2022, and the high-luminosity LHC (HL-LHC) will accumulate 10 times more data (i.e., about 3000 fb^{-1}) for the following 10 years after major upgrades of the LHC and CMS/ATLAS detectors. Such high luminosities help improving sensitivities particularly for weakly interacting massive particles produced with low cross sections. As examples, the estimated discovery sensitivities for gluino, top squark, and $\tilde{\chi}_1^\pm\tilde{\chi}_2^0$ production with 300 and 3000 fb^{-1} of data are shown in Fig. 9.

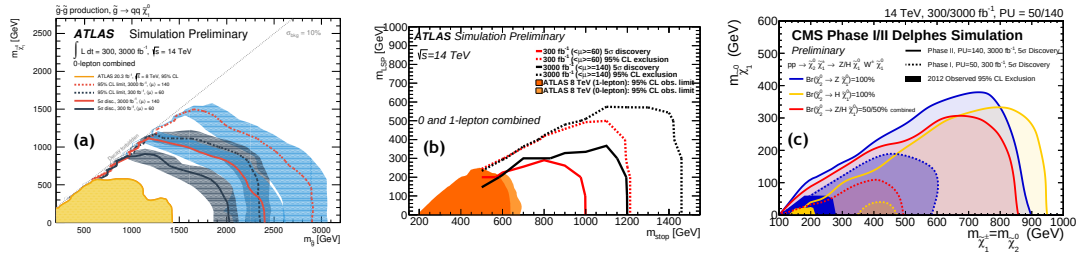

Figure 9: Discovery reaches for supersymmetry with 300 fb^{-1} (LHC Run 2+3) and 3000 fb^{-1} (HL-LHC) for (a) $\tilde{g}$-pair [45], (b) $\tilde{t}_1$-pair [45], and (c) $\tilde{\chi}_1^\pm\tilde{\chi}_2^0$ production [46].

6 Summary

The CMS and ATLAS collaborations have performed a wide variety of searches for physics beyond the standard model in the LHC Run 1 data. No new physics signature has not been observed yet, and only exclusion limits have been presented. However, our journey of new physics searches at the ∼TeV scale have just begun, and the LHC operation in the coming years will provide exciting opportunities to find new physics beyond the standard model.

References

[1] https://twiki.cern.ch/twiki/bin/view/CMSPublic/PhysicsResultsEXO
https://twiki.cern.ch/twiki/bin/view/CMSPublic/PhysicsResultsB2G

https://twiki.cern.ch/twiki/bin/view/CMSPublic/PhysicsResultsSUS
https://twiki.cern.ch/twiki/bin/view/CMSPublic/PhysicsResultsHIG
[2] https://twiki.cern.ch/twiki/bin/view/AtlasPublic/ExoticsPublicResults
https://twiki.cern.ch/twiki/bin/view/AtlasPublic/SupersymmetryPublicResults
https://twiki.cern.ch/twiki/bin/view/AtlasPublic/HiggsPublicResults
[3] CMS Collaboration, arXiv:1412.6302.
[4] ATLAS Collaboration, Phys. Rev. D **90**, no. 5, 052005 (2014) [arXiv:1405.4123].
[5] ATLAS Collaboration, Eur. Phys. J. C **74**, no. 12, 3134 (2014) [arXiv:1407.2410].
[6] CMS Collaboration, JHEP **05**, 108 (2014) [arXiv:1402.2176].
[7] CMS Collaboration, CMS-PAS-B2G-12-009.
[8] ATLAS Collaboration, arXiv:1410.4103.
[9] ATLAS Collaboration, arXiv:1408.0886.
[10] CMS Collaboration, Phys. Lett. B **729**, 149 (2014) [arXiv:1311.7667].
[11] CMS Collaboration, CMS-B2G-14-002.
[12] ATLAS Collaboration, JHEP **11**, 104 (2014) [arXiv:1409.5500].
[13] ATLAS Collaboration, ATLAS-CONF-2013-060.
[14] ATLAS Collaboration, ATLAS-CONF-2013-051.
[15] CMS Collaboration, arXiv:1408.3583.
[16] CMS Collaboration, arXiv:1410.8812.
[17] ATLAS Collaboration, Phys. Rev. Lett. **112**, no. 4, 041802 (2014) [arXiv:1309.4017].
[18] ATLAS Collaboration, Phys. Rev. D **90**, no. 1, 012004 (2014) [arXiv:1404.0051].
[19] ATLAS Collaboration, JHEP **09**, 037 (2014) [arXiv:1407.7494].
[20] CMS Collaboration, arXiv:1408.2745.
[21] CMS Collaboration, arXiv:1410.1149.
[22] ATLAS Collaboration, arXiv:1410.4031.
[23] CMS Collaboration, CMS-PAS-B2G-13-004.
[24] CMS Collaboration, Eur. Phys. J. C **74**, no. 8, 2980 (2014) [arXiv:1404.1344].
[25] ATLAS Collaboration, JHEP **09**, 176 (2014) [arXiv:1405.7875].
[26] CMS Collaboration, JHEP **06**, 055 (2014) [arXiv:1402.4770].
[27] CMS Collaboration, arXiv:1502.00300.
[28] ATLAS Collaboration, JHEP **10**, 24 (2014) [arXiv:1407.0600].
[29] CMS Collaboration, Eur. Phys. J. C **73**, no. 12, 2677 (2013) [arXiv:1308.1586].
[30] CMS Collaboration, CMS-PAS-SUS-13-015.
[31] CMS Collaboration, CMS-PAS-SUS-13-009.
[32] ATLAS Collaboration, JHEP **09**, 015 (2014) [arXiv:1406.1122].
[33] ATLAS Collaboration, JHEP **11**, 118 (2014) [arXiv:1407.0583].
[34] ATLAS Collaboration, JHEP **11**, 094 (2012) [arXiv:1209.4186].
[35] ATLAS Collaboration, Phys. Rev. D **90**, no. 5, 052008 (2014) [arXiv:1407.0608].
[36] ATLAS Collaboration, Eur. Phys. J. C **74**, no. 10, 3109 (2014) [arXiv:1406.5375].
[37] CMS Collaboration, Phys. Lett. B **736**, 371 (2014) [arXiv:1405.3886].
[38] CMS Collaboration, Eur. Phys. J. C **74**, no. 9, 3036 (2014) [arXiv:1405.7570].
[39] ATLAS Collaboration, JHEP **04**, 169 (2014) [arXiv:1402.7029].
[40] ATLAS Collaboration, JHEP **05**, 071 (2014) [arXiv:1403.5294].
[41] ATLAS Collaboration, JHEP **10**, 96 (2014) [arXiv:1407.0350].
[42] ATLAS Collaboration, arXiv:1501.07110.
[43] CMS Collaboration, Phys. Rev. D **90**, no. 9, 092007 (2014) [arXiv:1409.3168].
[44] CMS Collaboration, CMS-PAS-SUS-12-019.
[45] ATLAS Collaboration, ATL-PHYS-PUB-2013-011; ATL-PHYS-PUB-2014-010.
[46] CMS Collaboration, CMS-PAS-FTR-13-014; CMS-PAS-SUS-14-012.

Chapter 2

Quarks and gluons in hadrons, the hadron spectrum

Heavy Flavour Production in ATLAS with a focus on inclusive onia

R. W. L. Jones for the ATLAS Collaboration

Department of Physics, Lancaster University, Lancaster LA1 4YB, UK

DOI: http://dx.doi.org/10.3204/DESY-PROC-2014-04/218

ATLAS has a wide programme to study the production cross section and decay properties of particles with beauty, as well as charmonium and bottomonium states. This paper covers only the ATLAS results in the domain of charmonium production, including J/ψ, $\psi(2S)$ and χ_c states, B^+ production, a brief discussion of the Υ states and updates on the $D^{(*)}$ meson cross-section analysis. The analyses discussed include double-differential production cross-section measurements of the J/ψ, $\psi(2S)$ and P-wave charmonium states χ_{cJ}, extending upon previous measurements in precision and kinematic reach. Prompt and non-prompt modes are distinguished, as well as J/ψ vs $\psi(2S)$ and the contribution to J/ψ production from χ_c feed-down. Alongside the latter analysis, a competitive measurement of the branching fraction $B^{\pm} \to \chi_{c1} K^{\pm}$ was also performed. Results of these measurements are compared with the latest theoretical predictions from a variety of theoretical approaches.

1 Heavy flavour production in ATLAS

The ATLAS experiment at the Large Hadron Collider has copious heavy flavour production in pp collisions. It has the advantage of very high integrated luminosities, but largely relies on multi-muon triggers to select heavy flavour events. This paper will concentrate on the production of b and c hadrons in jets and has a focus on onium production. The two key sub-detector systems for the measurements here presented are the inner tracker immersed in a 2T solenoidal field, which has a coverage out to $|\eta| < 2.5$, and the muon system with coverage $|\eta| < 2.7$. The resultant tracking has a p_T resolution $\sim 0.05\% p_T(\text{GeV}) \oplus 1.5\%$ and $\sim 10 \mu m$ impact parameter resolution, which are important for the mass and lifetime resolutions in the analyses.

2 Open charm production

ATLAS has published results on $D^{*\pm}$ and D^0 production in jets [1]. It was found that neither leading order nor p_T and angular-ordered models give a good description of the momentum fraction carried but the charmed hadrons in jets, especially at low values of the fraction. A subsequent study of the $D^{*\pm}$, $D^{\pm}$ and D^0 differential cross sections as a function of the η and p_T of the charmed hadron show that these are described within the large uncertainty bands by models based on perturbative QCD [2].

3 Beauty hadron production

D^* mesons can be combined with muons as a signature of beauty hadron production in jets. ATLAS has used this technique to extract the single differential cross-sections for beauty hadrons in terms of the p_T and η of the hadron [3]. The results show that Next to Leading Order (NLO) models tend to underestimate the observed rates, despite the shapes of the distributions being reasonably reproduced by the several Monte Carlo models.

The production of B^+ hadrons has been studied using the decay to $J/\psi(\mu\mu)K^+$, where the double differential cross-sections in terms of p_T and rapidity y have been obtained [4]. The predictions from Monte Carlo and Fixed Order Next-to-Leading-Logarithm (FONNL) models [5] agree reasonably with the data, but again have a tendency to underestimate the cross-section.

4 Onium production

4.1 Prompt and non-prompt J/ψ production

ATLAS has made extensive studies of the production of heavy onia, using the production of dimuons in their decays to trigger the events. The J/ψ provides the template for the analyses [6]; the prompt and non-prompt components are separated using the pseudo-proper time of the decay candidates. The studies are in principle complicated by the different spin alignments possible, although recent CMS studies have indicated that there is little polarisation in the J/ψ production.

The production of prompt J/ψ agrees between the four main LHC experiments, though with some differences in the rapidity dependence. A multitude of models: Colour Singlet (CS); Colour Evaporation (CE); Colour Octet (CO), in various forms give a reasonable description of the observed ATLAS data, but none are perfect. It is clear that p_T spectra alone cannot distinguish between the models. (Please see the references in the ATLAS paper for the detailed models compared to the data.)

The fraction of non-prompt J/ψs is below 10% at low p_T and central rapidity, but rises with p_T to $\sim 70\%$; however, this increase is slower for forward rapidities. There is little evidence of an energy dependence in the behaviour, and comparing with CDF data, even the underlying process can have little effect. The non-prompt production with respect to p_T and rapidity is well described by perturbative QCD FONLL models with no free parameters.

4.2 Prompt and non-prompt $\psi(2S)$ production

A recent ATLAS study of the production of $\psi(2S)$ mesons has been published [7]. This study has many similarities with that of the J/ψ, except that instead of using the lower purity $\psi(2S) \to \mu\mu$ decays, the more copious $\psi(2S) \to J\psi(\mu\mu)\pi\pi$ mode is used instead. Again the prompt and non-prompt components are studied, the non-prompt fraction still rising to $\sim 70\%$ but less at high rapidity, see Figure 1. There is negligible feed-down to the $\psi(2S)$ from heavier states. ATLAS has extended the kinematic range of the studies of the prompt and non-prompt production as a function of p_T and rapidity; in the regions of overlap with studies by other LHC experiments, the agreement is good. For the prompt production, NLO combined with Non Relativistic QCD (NRQCD) predictions describe the data well across the range. However, Next-to-Next-to-Leading Order (NNLO) colour singlet models undershoot the data at higher p_T values, and k_T factorisation models undershoot the data for all values of p_T and rapidity.

The non-prompt production reveals a softer p_T spectrum and less variation with p_T than the NLO and FONLL approximation predictions. For the details of the all the predictions used for comparison, please see the references in [7].

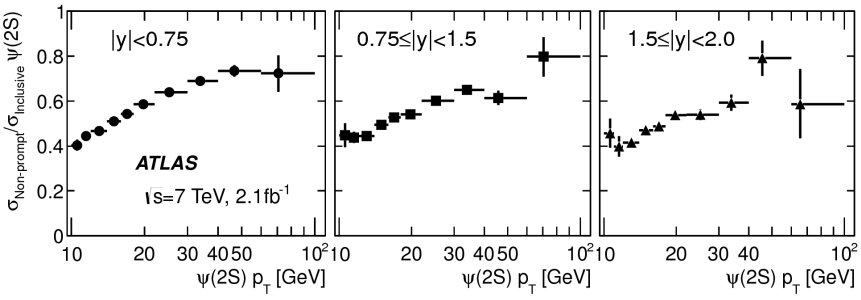

Figure 1: The non-prompt fraction with respect to the p_T of the $\psi(2S)$ for three regions of rapidity.

4.3 Prompt and non-prompt $\chi_{c1,2}$ production

ATLAS has recently studied the production of the $\chi_{c1,2}$ by reconstructing their de-excitation decays to $J/\psi\gamma$ [8]. The production differential cross-sections have been measured for both states in terms of the p_T of the χ_c and of the J/ψ. The prompt production for both states and p_T definitions is well predicted by NLO NRQCD models [9] . However, the non-prompt production shows a tendency to fall below the FONNL prediction at higher p_T. The relative production of χ_{c1} to χ_{c2} has been studied, and, under the assumption of isotropic decay, the measurements agree with NLO NRQCD predictions, though less so at higher p_T, see Figure 2. The figure also shows the fraction of prompt J/ψ produced from χ_c radiative decays, which again agrees with the NLO NRQCD predictions within the uncertainties. The relative fraction of non-prompt production shows that the production of the $\chi_{c1,2}$ is mostly prompt, even at high p_t, in contrast to the J/ψ and $\psi(2S)$ cases. Finally, ATLAS has also extracted a branching

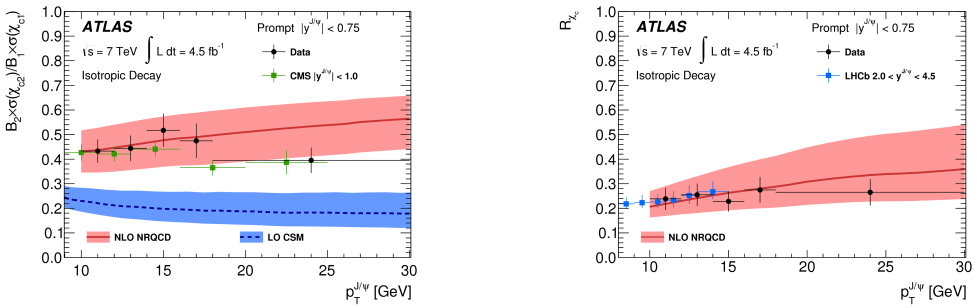

Figure 2: The relative production of prompt χ_{c1} and χ_{c2} with respect to the p_T of the J/ψ (left) and fraction of J/ψ produced from χ_c radiative decays (right).

fraction $B(B^+ \to \chi_{c1}K^+) = 4.9 \pm 0.9\,stat. \pm 0.6\,sys. \times 10^{-4}$; this is both in agreement with and

a significant improvement on measurements at previous hadron collider experiments, and is in agreement with existing B-factory measurements, thus showing good prospects for improved precision in Run 2.

4.4 The $\Upsilon(1S), \Upsilon(2S)$ and $\Upsilon(3S)$ production

Finally, ATLAS has produced double-differential cross-sections for $\Upsilon(1,2,3S)$ states[10], extending the available p_T range and providing finer detail than previous measurements from CMS and LHC. The measurements agree well with the previous measurements in the regions of overlap. Colour Singlet, Octet and Evaporation models all agree reasonably with the measured p_T spectra. The ratios of $\Upsilon(2S)/\Upsilon(1S)$ and $\Upsilon(3S)/\Upsilon(1S)$ production are dependent on the p_T of the upsilon, see Figure 3, confirming the existence of multiple mechanisms.

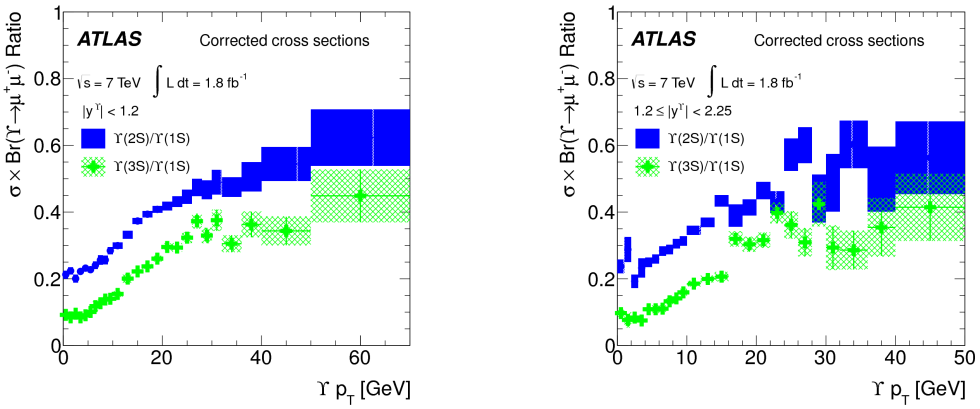

Figure 3: The relative production of prompt $\Upsilon 2S$ to $\Upsilon 1S$ and $\Upsilon 3S$ to $\Upsilon 1S$ with respect to the p_T of the Υ in the central (left) and forward (right) regions.

References

[1] ATLAS Collaboration, Phys. Rev. **D85** 052005 (2011).

[2] ATLAS Collaboration, ATLAS-CONF-2011-017 (2011); ATLAS-PUB-2011-012 (2011).

[3] ATLAS Collaboration, Nucl. Phys. **B864** 341 (2012).

[4] ATLAS Collaboration, JHEP **10** 042 (2013).

[5] M. Cacciari *et al.*, JHEP **10** 137 (2012);
M. Cacciari, M. Greco and P. Nason, JHEP **05** 007 (1998) .

[6] ATLAS Collaboration, Nucl. Phys. **B850** 387 (2011).

[7] ATLAS Collaboration, JHEP **1409** 79 (2014).

[8] ATLAS Collaboration, JHEP **1407** 154 (2014).

[9] Y.-Q. Ma, K. Wang and K.-T. Chao, Phys. Rev. **D 83** 111503 (2011);
H.-S. Shao, Comput. Phys. Commun. **184** 2562 (2013);
Y.-Q. Ma, K. Wang and K.-T. Chao, Phys. Rev. Lett. **106** 042002 (2011).

[10] ATLAS Collaboration, Phys. Rev **D87** 052004 (2013).

Medium-heavy Nuclei from Lattice Quantum Chromodynamics

Takashi Inoue[1] for the HAL QCD Collaboration

[1] Nihon University, College of Bioresource Sciences, Kanagawa 252-0880, Japan

DOI: http://dx.doi.org/10.3204/DESY-PROC-2014-04/26

Mass and structure of ^{16}O and ^{40}Ca are deduced from the quantum chromodynamics (QCD), the fundamental theory of the strong interaction. We derive two-nucleon potentials in lattice QCD simulations by the HAL QCD method. Then we apply the potentials to the nuclei using the Brueckner-Hartree-Fock theory. We find that these two nuclei are bound and possess shell structures, for a heavy quark mass corresponding to a pseudo-scalar meson mass of 469 MeV (a nucleon mass of 1161 MeV). Obtained total binding energies, 35 MeV for ^{16}O and 113 MeV for ^{40}Ca, are rather smaller than the experimental data indeed, but it is due to the unrealistic quark mass in our lattice QCD simulations.

1 Introduction

It is established that QCD is the fundamental theory of the strong interaction. However, explaining properties of nuclei starting from QCD still remains one of the most challenging problem in physics. There are several attempts to obtain mass of nuclei from lattice QCD simulations at heavy quark masses [1, 2], but direct calculations are limited only to very light nuclei, *i.e.* mass number $A \leq 4$, due to computation costs and, more severely, due to several fundamental difficulties. In this paper, we employ an alternative approach to study mass and structure of medium heavy nuclei starting from QCD.

The HAL QCD method was proposed to extract the nucleon-nucleon interaction from lattice QCD [3]. In this method, a non-local but energy independent potential of the interaction is defined and determined through the Nambu-Bethe-Salpeter wave function of the system which can be measured in lattice QCD numerical simulations. This method has been developed further and applied to many other systems [4]. The HAL QCD approach has several advantages over the direct calculations for multi-hadron system. First of all, this method does not require the ground-state saturation, which is unavoidable in the direct calculation but is usually very difficult or even impossible to achieve for multi-baryon systems, in particular on a large spacial-volume. Secondly, this method does not require the infinite-volume extrapolation, since the potential is insensitive to the lattice volume, as long as the spatial extension is larger than the interaction range between hadrons. On top of these advantages, there is one significant advantage, namely, one can extract many physical observables in this approach. For example, solving the two-body Schrödinger equation with the potential, one can obtain scattering phase-shifts as a function of energy as well as the scattering length. Moreover, combining the lattice QCD potentials with sophisticated many-body theories, one can study nuclei or even nucleon

matters based on QCD [5]. In this paper, we investigate ^{16}O and ^{40}Ca nuclei starting from QCD for the first time in history.

2 Method

There are several methods to investigate nuclei based on a free-space nucleon-nucleon interaction. The Green's function Monte Carlo method and the no-core shell model are successfully applied to nuclei around ^{12}C, but exact application to nuclei with $A > 14$ seems difficult at this moment. To study larger A nuclei, the Hartree-Fock mean field approximation has been applied traditionally. Since the Brueckner theory explains the independent particle nature of nuclei, which is a foundation of the mean field theory and shell models, the Brueckner-Hartree-Fock (BHF) theory became a standard framework for heavy nuclei [6]. In this paper, we adopt the lowest order BHF theory for our first study of medium heavy nuclei from QCD.

To study finite nuclei in the BHF theory, G matrix in a single-particle-orbit basis is needed and obtained by solving the integral Bethe-Goldstone equation

$$G(\omega)_{ij,kl} = V_{ij,kl} + \frac{1}{2}\sum_{m,n}^{>e_F} \frac{V_{ij,mn}\, G(\omega)_{mn,kl}}{\omega - e_m - e_n + i\epsilon} \tag{1}$$

where indices i to n stands for a single-particle energy-eigenstate and V is the two-nucleon interaction potential and the sum runs over excluding occupied states of the nucleus. With G matrix, single-particle potential U is given by $U_{ab} = \sum_{c,d} G(\tilde{\omega})_{ac,bd}\ \rho_{dc}$, where indices a, b, c, d corresponds to a basis-function for which we use a harmonic-oscillator wave function, and ρ is the density matrix in this basis, which is given with the wave function of energy-eigenstate Ψ^i by $\rho_{ab} = \sum_i^{occ} \Psi_a^i \Psi_b^{i*}$, where the sum runs over occupied states of the nucleus. While, the energy-eigenstates are given by solution of the Hartree-Fock equation $[K + U]\,\Psi^i = e_i \Psi^i$ with the potential U and the kinetic energy operator K. These equations are highly coupled, and self-consistent G, U, ρ, Ψ^i and e_i are determined in the iterative procedure. Finally, the Hartree-Fock ground state energy of the nucleus is given with the self-consistent U and ρ by,

$$E_0 = \sum_{a,b} \left[K_{ab} + \frac{1}{2} U_{ab} \right] \rho_{ba} - K_{\rm cm} \tag{2}$$

where $K_{\rm cm}$ is the kinetic energy of the spurious center-of-mass motion in the potential rest flame which is included in the first term.

The two-nucleon potential which we adopt at eq.(1) is the one which we derived from lattice QCD in ref. [5]. There, dynamical lattice QCD simulations ware carried out at five degenerated u, d, s-quark masses. Measured hadron masses $\{M_{\rm PS}\ ,\ M_{\rm B}\}$ ranges from $\{1171, 2274\}$ MeV to $\{469, 1161\}$ MeV, where PS and B abbreviate the pseudo-scalar meson and the octet baryon, respectively. Extracted two-nucleon potentials in $^1S_0$, $^3S_1$ and $^3D_1$ channels, share common features with phenomenological ones, *i.e.* the strong repulsive core at short distance, the attractive pocket at intermediate distance, and the strong $^3S_1$-$^3D_1$ coupling, and accordingly, reproduce experimental phase-shifts qualitatively [5]. In this paper, we include two-nucleon interaction in these three channels and omit that in higher partial waves due to a lack of lattice QCD data. We ignore the Coulomb force between protons for simplicity. For details of numerical procedure of BHF calculation, we follow ref. [7].

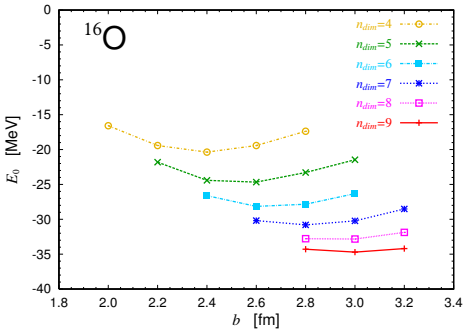

Figure 1: Ground state energy of ^{16}O at a quark mass of $M_{\rm PS} \simeq 469$ MeV

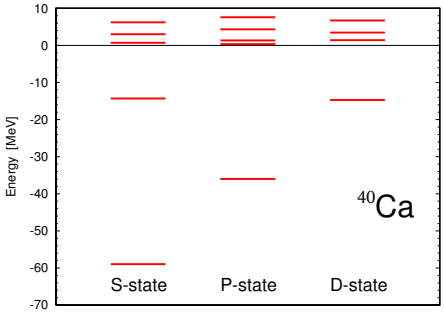

Figure 2: Single particle levels in the ^{40}Ca at a quark mass of $M_{\rm PS} \simeq 469$ MeV.

3 Results and discussion

Figure 1 shows obtained ground state energy of ^{16}O at the lightest quark mass corresponding to $M_{\rm PS} \simeq 469$ MeV, as a function of parameter b and number n_{dim} of the harmonic-oscillator wave function used as basis. We obtain a similar figure for ^{40}Ca at this quark mass. Consequently, we confirm that there are bound nuclei at this quark mass. While, we do not obtain any negative E_0 for both ^{16}O and ^{40}Ca at the other four quark masses, which at least exclude existence of tightly bound nucleus at these quark masses. In the following, we therefore consider only the lightest quark mass case, where pion mass is 469 MeV and nucleon mass is 1161 MeV. Since a computation of ^{40}Ca with $n_{dim} = 10$ is already tough on PC, we adopt $b = 3.0$ fm and $n_{dim} = 9$ for both ^{16}O and ^{40}Ca, according to the figure. Figure 2 shows obtained single particle levels of ^{40}Ca, where we can see a regular shell structure. These levels are already in good agreement with experimental data, but it could be accidental since quark masses are different.

Table 1 shows mass and structure of ^{16}O and ^{40}Ca nuclei obtained at the lightest quark, where single particle levels, total energy, and mean radius are given. Experimental data of the total energies are -127.62 MeV for ^{16}O and -342.05 MeV for ^{40}Ca. We see that the obtained binding energies are rather smaller than the experimental ones, but this is principally due to the large u, d-quark mass in our calculation. The root-mean-square radii are calculated without taking nucleon form factor and correction for the center-of-mass motion. Contrary to large discrepancies of E_0 from experimental data, these radii are more of less similar to experimental charge radius, 2.73 fm for ^{16}O and 3.48 fm for ^{40}Ca, probably due to an accidental cancellation between contributions from weaker attraction of the nuclear force and heavier nucleon mass than experimental values in this study.

In our previous papers [5], we studied the ^{4}He nucleus and the symmetric nuclear matter (SNM) from lattice QCD. We obtained energy per particle E_0/A as -1.3 MeV for ^{4}He and -5.4 MeV for SNM at the same lightest quark mass. We can see in Table 1 that the present E_0/A of ^{16}O and ^{40}Ca lie between these two values, which means that obtained E_0 are consistent with the previous results and reasonable for the nuclei at the quark mass. Moreover, in the real world, it is known that binding energy of nuclei are well described by the semi-empirical Bethe-Weizsäcker formula $E_0(A) = a_V A + a_S A^{2/3} + \cdots$. We find that E_0/A obtained from QCD at the quark mass are well described by the formula with $a_V = -5.46$ MeV and $a_S = 6.56$ MeV, when $E_0(n_{dim})$ of ^{16}O and ^{40}Ca are extrapolated for $n_{dim} \to \infty$ with $E_0(n_{dim}) = E_0(\infty) + c/n_{dim}$.

	Single particle level [MeV]				Total energy [MeV]		Radius [fm]
	$1S$	$1P$	$2S$	$1D$	E_0	E_0/A	$\sqrt{\langle r^2 \rangle}$
^{16}O	-35.8	-13.8			-34.7	-2.17	2.35
^{40}Ca	-59.0	-36.0	-14.7	-14.3	-112.7	-2.82	2.78

Table 1: Mass and structure of ^{16}O and ^{40}Ca nuclei obtained from QCD at a quark mass corresponding to pseudo-scalar meson mass of 469 MeV and octet baryon mass of 1161 MeV. Single particle levels, total energy, and root-mean-square radius are listed.

In this paper, we've obtained mass and structure of ^{16}O and ^{40}Ca nuclei from QCD at a heavy quark mass for the first time in history. This success is certainly a significant progress in theoretical nuclear physics, and demonstrates that the HAL QCD approach is quite promising.

In this study, we neglected P, F and higher partial-wave nuclear forces, in particular the LS force. It is known that the LS force is important for structures of nuclei, such as the magic number, especially at the region of heavy nuclei $A > 40$. We will include in our next study the LS force recently extracted in lattice QCD [8]. It is also known that three-nucleon force is necessary for quantitative explanation of mass and structure of nuclei. Study toward three-nucleon force from QCD is in progress [9]. Masses of u, d-quark in this study are much heavies than physical values, but this limitation will be removed in a few years, as lattice QCD simulations at the physical quark mass are currently underway on the K-computer at RIKEN AICS in Japan. Nuclear force obtained in such simulations by the HAL QCD approach will open a new connection between QCD and nuclear physics.

Acknowledgments

This research is supported in part by Grant-in-Aid of MEXT-Japan for Scientific Research (C) 23540321. Author thank ILDG/JLDG for providing storage to save our lattice QCD data.

References

[1] T. Yamazaki *et al.* [PACS-CS Coll.], Phys. Rev. D **81**, 111504 (2010); T. Yamazaki, K. Ishikawa, Y. Kuramashi and A. Ukawa, Phys. Rev. D **86**, 074514 (2012).

[2] S. R. Beane *et al.* [NPLQCD Coll.], Phys. Rev. D **85**, 054511 (2012); S. R. Beane, *et al.* [NPLQCD Coll.], Phys. Rev. D **87**, no. 3, 034506 (2013); W. Detmold and K. Orginos, Phys. Rev. D **87**, no. 11, 114512 (2013)

[3] N. Ishii, S. Aoki and T. Hatsuda, Phys. Rev. Lett. **99**, 022001 (2007); S. Aoki, T. Hatsuda and N. Ishii, Prog. Theor. Phys. **123**, 89 (2010); N. Ishii *et al.* [HAL QCD Coll.], Phys. Lett. B **712** (2012) 437.

[4] H. Nemura, N. Ishii, S. Aoki and T. Hatsuda, Phys. Lett. B **673**, 136 (2009); Y. Ikeda *et al.* [HAL QCD Coll.], EPJ Web Conf. **3**, 03007 (2010); K. Sasaki *at al.* [HAL QCD Coll.], Nucl. Phys. A **914**, 231 (2013).

[5] T. Inoue *et al.* [HAL QCD Coll.], Phys. Rev. Lett. **106**, 162002 (2011); T. Inoue *et al.* [HAL QCD Coll.], Nucl. Phys. A **881**, 28 (2012); T. Inoue *et al.* [HAL QCD Coll.], Phys. Rev. Lett. **111**, 112503 (2013).

[6] P. Ring and P. Schuck, *The Nuclear Many-Body Problem*, (Springer, 1980). G.E. Brown, T.T.S. Kuo, *et al.*, *The Nucleon-Nucleon Interaction And The Nuclear Many-Body Problem*, (World Scientific, 2010).

[7] K. T. R. Davies, M. Baranger, R. M. Tarbutton and T. T. S. Kuo Phys. Rev. **177**, 1519 (1969); P. U. Sauer, Nucl. Phys. A **150**, 467 (1970).

[8] K. Murano *et al.* [HAL QCD Coll.], Phys. Lett. B **735**, 19 (2014).

[9] T. Doi *et al.* [HAL QCD Coll.], Prog. Theor. Phys. **127**, 723 (2012).

Diquark and Baryon Masses in Composite Fermion Approach

A. Bhattacharya[1], *R.Ghosh*[1], *B.Chakrabarti*[2]

[1]Department of Physics, Jadavpur University,Calcutta 700032, India.
[2] Jogamaya Devi College, Kolkata, India.

DOI: http://dx.doi.org/10.3204/DESY-PROC-2014-04/128

A model for diquark has been suggested describing it as a Composite Fermion. The masses of the light [Λ^0, Σ^-, Ξ^-, Ω^-], heavy [Λ_c^+, Σ_c^+, Ξ_c^0, Ω_c^- and Λ_b^0, Σ_b^0, Ξ_b^0, Ω_b^-], doubly heavy [Ξ_{cc}^{++}, Ξ_{cc}^+, Ξ_{cb}^+, Ξ_{cb}^0, Ξ_{bb}^0, Ξ_{bb}^-, Ω_{cc}^+, Ω_{cb}^0, Ω_{bb}^-] and triply heavy [Ω_{ccc}, Ω_{ccb}, Ω_{bbc}, Ω_{bbb}] baryons have been studied for $J^P = \frac{1}{2}^+$ and $\frac{3}{2}^+$ states. The results are found to be in good agreement with available experimental data and other theoretical works.

1 Diquark and Baryon Masses in Composite Fermion Approach

At low energies the quark dynamics can be revisited in the light of new results of baryon and exotics spectroscopy. The regularities in hadons spectroscopy, parton distribution function, spin dependent structure function of hadrons etc hint at the existence of diquark correlation. In QCD both the gluon exchange interaction and Instanton Induced Interaction favour the spin singlet and colour anti-symmetric diquark combination. A deeply bound diquark system is one of the most important candidate for describing the baryonic and exotic system. The exact nature of the diquark correlation is under extensive study. In the present work diquarks have been described in the frame work of Composite Fermion (CF) model of quasi particle in an analogy with the electrons in strong magnetic field. The masses of the light, single heavy, doubly heavy and triply heavy baryons have been studied for $J^P = \frac{1}{2}^+$ and $\frac{3}{2}^+$ states considering the diquark-quark configuration with the suggested CF model of diquark. It has been suggested that the CFs can be described in gauge invariant way in the system of gauge interaction like the two dimensional electron gas in high magnetic field where electrons can be described as Composite Fermions [1]. This in turn may form Fermi liquid like state near the Fermi surface. CFs can have fractional charges and their spin is frozen. Such CFs are described as the stable quasi particles in the system. In the context of degenerate electron gas Raghavchari et al [2] have studied the quasi particle mass which is fully gauge invariant and can be expressed as a response function of the system. It has been observed that the strongly interacting particles sometimes behave like weekly coupled system and form a system of particles of new kind. The quasi particle behaviour of electron in a crystal is an example of such system. The electron in the lattice changes in behaviour and exists as an independent object. In the present work we have applied the idea of CF model describing a diquark as a composite fermion and have computed the masses of diquarks considering Fermi momentum (p_f) as cut off parameter.

Starting from the Hamiltonian of a CF with a momentum cut off λ the expression for the quasi particle mass in gauge invariant system can be obtained as [2] (with potential V=0):

$$\frac{1}{m^*} = \frac{1}{m}(1 + \frac{\Lambda^4}{2p_F^4}) \tag{1}$$

where m^* is the effective mass of the CF, m be the mass of each component, (p_f) is the Fermi momentum of CF and Λ is the cut off parameter. We have applied this CF picture for diquarks and computed the effective mass of diquarks. The Fermi momentum of corresponding diquarks have been estimated using the work of Bhattacharya et al [3, 4]. Considering baryon as a system of a quark and a diquark, under the influence of suitable binding energy and spin interaction the mass of heavy or light baryons can be expressed as :

$$M_B = m_q + m_D^* + E_{BE} + E_S \tag{2}$$

where m_q is quark mass, m_D^* is the diquark mass and E_{BE} is the binding energy of the quark-diquark corresponding to the potential expressed as V(r)= ar^2, where 'a' is the interaction parameter and 'r' is the baryon radius. We have used the wave function from the Statistical Model [3, 4] and the spin interaction term is expressed as :

$$E_S = \frac{8}{9}\frac{\alpha_S}{m_q m_D}\vec{S}_q \cdot \vec{S}_D|\psi(0)|^2 \tag{3}$$

where the symbols have their usual meanings. The masses of the respective baryons have been estimated by using the relation (2) and displayed in Tables 1 to 5. We have obtained very good results for Λ^0,but higher results for Σ^- and lower values for Ξ^- and Ω^-. For Σ_c^+, Λ_b^0 and Ω_c^- there is a very good agreement between our results and experimentalfindings [5, 6]. For Ξ_{cc}^{++} our proposed mass [3.5308 GeV for $J^P = \frac{1}{2}^+$] agrees reasonably with experimental value 3.5189 ± 0.0009 GeV. For doubly heavy and triply heavy Ω sectors the results have been compared with other theoretical works and there is a reasonable agreement. However it may be pointed out that the most uncertainty comes from the radii parameters which is not exactly known.

CF model is found to be quiet successful in reproducing the masses of the baryons over a wide range. Diquark in presence of chromo magnetic QCD vacuum may behave like a CF as an electron in strong magnetic field. The diquark as CF may throw some light on the understanding of structure and dynamics of the baryons.

Baryon	*Baryon* $Our-work$ $J^p=\frac{1}{2}^+$	$mass(GeV)$ $Expt.$[5, 6] $J^p=\frac{1}{2}^+$	*Baryon* $Our-work$ $J^p=\frac{3}{2}^+$	$mass(GeV)$ $Expt.$[5, 6] $J^p=\frac{3}{2}^+$
$\bigwedge^0$	1.1188	1.1156	1.3086	–
Σ^-	1.3295	1.1974	1.449	1.387
Ξ^-	1.2137	1.3217	1.3948	1.535
Ω^-	1.551	–	1.5200	1.672

Table 1: Mass Spectrum ($J^p=\frac{1}{2}^+$ and $\frac{3}{2}^+$) of Light baryons

$Baryon$	$Baryon$	$mass(GeV)$	$Baryon$	$mass(GeV)$
	$Our-work$	$Expt.$[5, 6]	$Our-work$	$Expt.$[5, 6]
	$J^p=\frac{1}{2}^+$	$J^p=\frac{1}{2}^+$	$J^p=\frac{3}{2}^+$	$J^p=\frac{3}{2}^+$
$\bigwedge_c^+$	2.9377	2.2864 ± 0.00014	3.04477	–
$\bigwedge_b^0$	5.5891	5.6202 ± 0.0016	5.7168	–
Σ_c^+	2.4577	2.4529 ± 0.0004	2.5690	2.518
Σ_b^0	5.5751	5.808	5.7169	5.829
Ξ_c^0	2.2687	$2.4708^{+0.00034}_{-0.0008}$	2.4464	2.646
Ξ_b^0	5.5069	5.7924 ± 0.003	5.7201	–
Ω_c^0	2.6724	2.6952 ± 0.0017	2.63122	2.768
Ω_b^-	5.9631	6.165 ± 0.023	5.9176	–

Table 2: Mass Spectrum ($J^p=\frac{1}{2}^+$ and $\frac{3}{2}^+$) of Heavy baryons

$Baryon$	$Baryon$	$mass$	(GeV)	$Baryon$	$mass$	(GeV)
	for	$J^p=$	$\frac{1}{2}^+$	for	$J^p=$	$\frac{3}{2}^+$
	$Ours$	$Expt.$[5, 6]	$Others$	$Ours$	$Expt.$	$Others$
Ξ_{cc}^{++}	3.9496	–	3.579	3.9807	–	3.708
			3.730			3.800
			3.480			3.610
Ξ_{cc}^+	3.5308	3.5189	3.584	3.6222	–	3.713
		± 0.0009	3.755			3.828
			3.480			3.610
Ξ_{cb}^0	6.9065	–	6.95	6.9205	–	7.02
			7.01			7.10
Ξ_{cb}^+	7.2534	–	6.965	7.2569	–	7.06
			± 0.09			± 0.09
Ξ_{bb}^0	10.6764	–	10.339	10.6873	–	10.468
			10.114			10.165
			10.093			10.330
Ξ_{bb}^-	10.5389	–	10.23	10.551	–	10.28
			10.344			10.473
			10.30			10.34

Table 3: Mass Spectrum ($J^p=\frac{1}{2}^+$ and $\frac{3}{2}^+$) of the Doubly Heavy Ξ baryon

$Baryon$	$Baryon$	$mass(GeV)$	$Baryon$	$mass(GeV)$
	$Our-work$	$Other-works$	$Our-work$	$Other-works$
	$J^p=\frac{1}{2}^+$	$J^p=\frac{1}{2}^+$	$J^p=\frac{3}{2}^+$	$J^p=\frac{3}{2}^+$
Ω_{cc}^+	3.6843	3.74 ± 0.07	3.8590	3.82 ± 0.08
		3.76		3.89
		3.718		3.847
Ω_{cb}^0	7.0225	7.045 ± 0.09	7.0769	7.12 ± 0.09
		7.05		7.11
		7.05		7.13
Ω_{bb}^-	10.6455	10.37 ± 0.1	10.6581	10.40 ± 0.1
		10.32		10.36
		10.34		10.38

Table 4: Mass Spectrum ($J^p=\frac{1}{2}^+$ and $\frac{3}{2}^+$) of the Doubly Heavy Ω baryon

$Baryon$	$Baryon$	$mass(GeV)$	$Baryon$	$mass(GeV)$
	$Our-work$	$Other-works$	$Our-work$	$Other-work$
	$J^p=\frac{1}{2}^+$	$J^p=\frac{1}{2}^+$	$J^p=\frac{3}{2}^+$	$J^p=\frac{3}{2}^+$
Ω_{ccc}	4.8508	–	$4,8916$	4.803
		–		4.925
		–		4.9(0.25)
Ω_{ccb}	8.355	8.229	8.3575	8.358
		8.018		8.025
		–		8.200
Ω_{bbc}	11.695	11.280	11.6974	11.287
		–		11.48
		11.609		11.738
Ω_{bbb}	15.0329	–	15.0449	15.118
		–		14.760
		–		14.7(0.3)

Table 5: Mass Spectrum ($J^p=\frac{1}{2}^+$ and $\frac{3}{2}^+$) of the Triply Heavy baryons

Acknowledgements

Authors are thankful to University Grant Commission, Govt. of INDIA for financial support.

References

[1] B.I.Helperin et al., Phys.Rev. **B47** 7312 (1993).

[2] A. Raghavchari et al., arXiv:cond.matt./9707055.

[3] A.Bhattacharya et al., Int. J. Mod. Phys. **A 15** 2053 (2003).

[4] A. Bhattacharya et al.,Eur. Phys. J. **C 2** 671 (1998).

[5] J. Beringer et al (PDG) Phys. Rev. **D 86** 010001 (2012).

[6] K. Nakamura et al (PDG)"Review of Particle Physics" Journal of Physics **G 37**(7A): 075021 (2010).

Polarised Drell-Yan measurement in the COMPASS experiment at CERN

Márcia Quaresma[1] for the COMPASS Collaboration

[1]LIP - Laboratório de Instrumentação e Física Experimental de Partículas, Av. Elias Garcia 14-1, 1000-149 Lisboa, Portugal, marcia@lip.pt

DOI: http://dx.doi.org/10.3204/DESY-PROC-2014-04/117

The COMPASS experiment at CERN has been contributing to the description of the nucleon spin structure, namely the transverse momentum dependent parton distribution functions (TMDs), through the Semi-Inclusive Deep Inelastic Scattering (SIDIS) using a muon beam impinging on polarised targets. These TMD functions are also accessible via the transversely polarised Drell-Yan (DY) process, which will be studied in the next COMPASS data taking, starting this Autumn. This process, in which the proton valence region will be explored, will be studied in collisions of a 190 GeV/c negative pion beam with a transversely polarised ammonia target. The QCD prediction that Sivers TMD change sign when accessed through SIDIS or via DY will be checked by the new COMPASS measurement. Considering one year of data taking, the Sivers azimuthal asymmetry statistical error is expected to be less than 2%. In addition to the polarised target, other nuclear targets will give the possibility to study unpolarised DY subjects. The experimental setup will be presented, and predictions and expectations will be discussed.

1 Introduction

The nucleon structure in leading order QCD, taking into account the quarks intrinsic transverse momentum, is described by 8 PDFs for each quark flavour. These so called TMD PDFs are accessible via either the single transversely polarised Drell-Yan measurement or the transversely polarised Semi-Inclusive DIS. The latter has been already measured in COMPASS and published [1]. The DY cross-section is written in terms of angular modulations, each containing a convolution of two PDFs, whereas in the SIDIS cross-section the amplitude of each modulation contains the convolution of one PDF and one fragmentation function. Because of that, DY is considered an excellent tool to access TMD PFDs. In addition, the TMD PDFs are expected to be sizeable in the valence quark region, being this region dominant in the foreseen COMPASS DY measurement regarding the use of a negative pion beam impinging on an ammonia target. Furthermore, the QCD TMD approach is valid in the region Q ($M_{\mu\mu} > 4$ GeV/c^2) $\gg \langle p_T \rangle \sim$ 1 GeV/c, which is also dominate in the COMPASS DY measurement.

The amplitudes present in the DY cross-section are accessed via the measurement of the azimuthal asymmetries between the two oppositely transversely polarised target cells. Each asymmetry contains the convolution of two TMD PDFs, giving access to Sivers, Boer-Mulders, transversity and pretzelosity functions.

The Sivers measurement is the main goal of the first polarised DY data. Theory predicts its sign should change when accessed through DY or SIDIS processes [2]. This is considered a crucial test of the QCD TMD approach. Figure 1 shows the phase space coverage of the two processes in COMPASS. The SIDIS result was extracted from the 2010 data and the DY from a MC simulation. The statistical error selecting just the overlap between the two measurements, i.e. with $Q^2 > 16$ GeV/c, is $\sim 1\%$ for both.

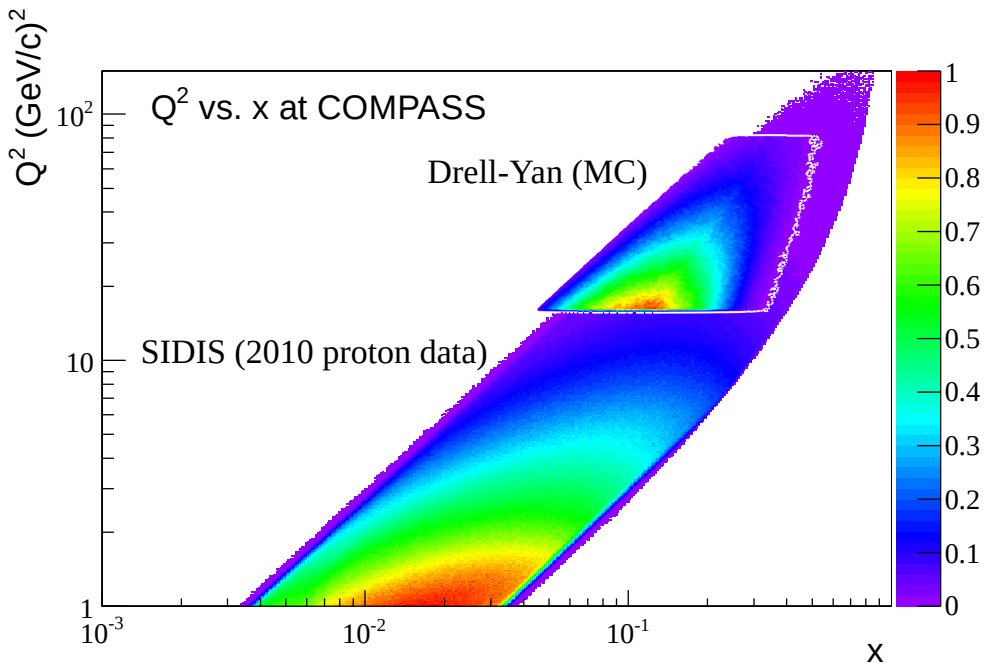

Figure 1: Q^2 versus x phase space coverage at COMPASS. Superposition of the SIDIS 2010 proton data with the DY MC simulation.

In addition to the azimuthal asymmetries measurements, several studies beyond the polarised DY measurement are possible, including the study of the flavour dependent EMC effect [3]. This will be possible by the use of nuclear targets in addition to the polarised ammonia target.

2 Experimental setup and feasibility of the experiment

COMPASS is a CERN experiment located at the end of the SPS M2 beam line. It is a fixed target experiment that consists in a two stage spectrometer giving the possibility to measure a wide angular and momentum range. The spectrometer is equiped with several tracking detectors, one hadron and one electromagnetic calorimeter in each spectrometer stage, two dedicated stations to identify muons and hodoscopes to perform the trigger. A complete description can be found in [4]. For the DY measurement, there is a hadron absorber with a beam plug in its central part, just downstream of the target, to stop the hadrons and the non-interacting beam.

The DY muons will suffer multiple scattering when crossing the absorber and this is responsible for a resolution degradation. Thus a scintillating fibre vertex detector is placed at the beginning of the absorber to improve the spatial resolution of the interaction vertex. Figure 2 shows a sketch of the hadron absorber and the vertex detector. The location of the aluminium nuclear target, necessary for the unpolarised DY studies is also shown. The polarised target is made of two target cells of ammonia which will be oppositely transversely polarised with respect to the beam direction. This polarisation will be reversed several times during the data taking, in order to cancel some systematic errors. A negative pion beam with an intensity of $10^9\pi$/s will be used.

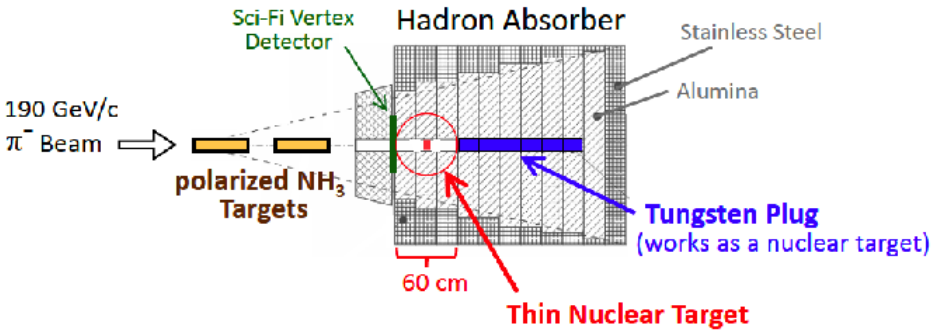

Figure 2: Sketch of the hadron absorber. In blue is visible the beam plug, in red the Al nuclear target and in green the vertex detector.

The DY pilot run has started in October. This is the opportunity to tune the experiment and analysis software before the next year's physics run. Prior to this pilot run, a beam test with a duration of three days was preformed in 2009 with success. At that time, a hadron absorber prototype was used, the trigger was based on calorimeter signals and the negative pion beam had a lower intensity, $1.5 \times 10^7\pi$/s. Now, for the pilot run everything is as it will be next year, which means the optimised absorber is installed, the trigger will be based on hodoscopes with a high efficiency, purity and target pointing capability, and we will have a high intensity pion beam available.

Figure 3 shows the dimuon mass distribution and the Z vertex distribution for the 2009 DY beam test. The J/ψ is visible and both its mass pole as well as the mass resolution are in agreement with the MC simulations. The expected J/ψ yields were confirmed regarding the involved efficiencies. The Z vertex distribution shows the separation between the two target cells and the beam plug, even in the absence of a vertex detector and the optimised absorber.

3 Event rates and statistical accuracy

The expected event rate in the mass region $4 < M_{\mu\mu} < 9$ GeV/c^2 of the polarised DY measurement is expected to be 2000 events/day. Being one year of data taking approximately 140 days, 285000 events are expected. For such a rate, the statistical errors of the asymmetries are expected to be less than 2%.

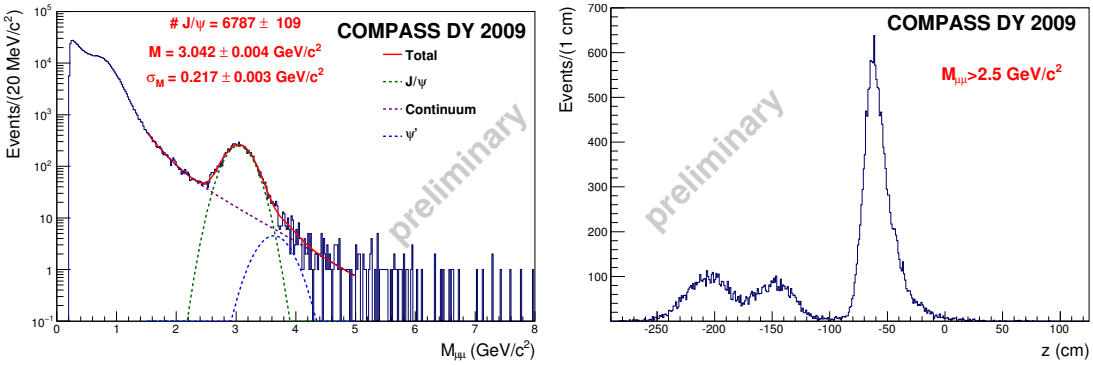

Figure 3: On the left hand side, the dimuon mass distribution is plotted. On the right hand side, the Z vertex distribution is plotted.

4 Conclusions

The DY pilot run has started in the beginning of October 2014 and will last for about two months. This is the opportunity to test the whole concept of the measurement and work out the data taking strategy for the next year's data taking. The main goals for next year are to extract the azimuthal asymmetries, in particular to check the Sivers function sign change when comparing the COMPASS SIDIS results and DY ones. By the use of nuclear targets, COMPASS also aims to contribute to the unpolarised DY studies, namely the EMC effect. Concerning the future, a second year of DY data taking before the Long Shut Down 2 at CERN, taking place in 2019, will be discussed soon. COMPASS will collect the first ever DY polarised data.

Acknowledgments

This work was partially supported by the Portuguese Fundação para a Ciência e a Tecnologia.

References

[1] C. Adolph *et al.* [COMPASS Coll.], Phys. Lett. **B717** 10 (2012).

[2] J.C. Collins, Phys. Lett. **B536** 43 (2002).

[3] D. Dutta *et al.*, Phys. Rev. **C83** 042201 (R) (2011).

[4] P. Abbon *et al.* [COMPASS Coll.], Nucl. Inst. Meth. **A577** 455 (2007).

Nucleon Transverse Structure at COMPASS

Nour Makke[1]

[1]Trieste University and INFN section of Trieste, Via A. Valerio 2, 34127 Trieste, Italy

DOI: http://dx.doi.org/10.3204/DESY-PROC-2014-04/140

COMPASS is a fixed target experiment at CERN. Part of its physics programme is dedicated to study the transverse spin and the transverse momentum structure of the nucleon using SIDIS. For these measurements, data have been collected using transversely polarised proton and deuteron targets. A selection of recent measurements of azimuthal asymmetries using data collected with transversely polarised protons is presented.

1 Introduction

The description of the partonic structure of the nucleon remains one of the main challenges in hadron physics. In the last few decades, a considerable theoretical and experimental progress has been accomplished and the relevance of the quark transverse spin and transverse momentum to study its structure has been assessed. The nucleon constituents are not only collinear moving objects but they may also have a momentum component transverse to the nucleon direction of motion. In the present theoretical framework, eight transverse momentum dependent parton distribution functions (TMD PDFs) are required for each quark flavour at leading twist, describing all possible correlations between the transverse momentum and spin of the quarks, and the spin of the nucleon. The most famous and studied one is the Sivers PDF. Integrating over the quark intrinsic transverse momentum, five among these functions vanish and three survive giving the well known number ($q(x, Q^2)$), helicity ($\Delta q(x, Q^2)$) and transversity ($\Delta_\perp q(x, Q^2)$) distribution functions. Experimentally, the latter is the least known one. Beside these, many other twist-2 distributions can be introduced, correlating the spin and the transverse momentum.

Many processes are being, and will be, studied to access the TMD PDFs, namely transversely polarised hard proton-proton collisions, Drell-Yan processes and semi-inclusive deep inelastic scattering (SIDIS). Although they are complementary, the last channel is nowadays the major source of information. Its main advantage is that TMD effects generate different azimuthal modulations in its cross section, which can be separately explored and extracted from the same experimental data set. The modulations depend on two angles, ϕ_S and ϕ_h which define the azimuthal angle of the initial nucleon spin and the produced hadron momentum respectively. These angles are defined in the so called gamma nucleon system in which the direction of the virtual photon is the z axis and the xz plane is defined by the lepton scattering plane. The modulation amplitudes are different structure functions, proportional to the convolution of the TMD PDFs and fragmentation functions (FFs).

The transversity distributions $\Delta_\perp q(x)$ can not be measured in inclusive DIS due to their chirally odd nature. They can instead be extracted from measurements of single-spin azimuthal

asymmetries in cross-sections for SIDIS of leptons on transversely polarised nucleons, in which a hadron is also detected. The measurable asymmetry, the Collins asymmetry, is due to a combined effect of $\Delta_\perp q$ and the chiral-odd Collins TMD-FF $\Delta_T^0 D_q^h$, which describes the spin-dependent part of the hadronization of a transversely polarised quark into a hadron with transverse momentum p_T. At leading order, the Collins mechanism leads to a modulation in the azimuthal distribution of the produced hadrons given by:

$$N(\phi_C) = \alpha(\phi_C) \cdot N_0(1 + A_{Coll} \cdot P_T \cdot f \cdot D_{NN} \sin\phi_C) \quad (1)$$

where α contains the apparatus efficiency and acceptance, P_T is the target polarisation, D_{NN} is the spin transfer coefficient and f is the fraction of polarisable nuclei in the target, $\phi_C = \phi_h - \phi_{S'} = \phi_h + \phi_S - \pi$ is the Collins angle, with ϕ_h the hadron azimuthal angle, $\phi_{S'}$ the final azimuthal angle of the quark spin and ϕ_S the azimuthal angle of the nucleon spin in the gamma-nucleon system.

2 The COMPASS experiment

COMPASS [1] (COmmon Muon and Proton Apparatus for Structure and Spectroscopy) is a fixed target experiment located at the CERN SPS taking data since 2002. Semi-inclusive DIS data have been collected using a 160 GeV longitudinally polarised muon beam and longitudinally or transversely polarised proton (NH_3) and deuteron (^{6}LiD) targets. The spectrometer comprises a variety of different tracking detectors, and allows to detect charged tracks in a broad momentum and angular range. Calorimeters, muon filters and a gas radiator RICH detector are available for particle identification.

3 Data Analysis and Results

Collins and Sivers asymmetries have been extracted as a function of x, z and p_T for positive and negative hadrons, pions and kaons, using lepton scattering off transversely polarised deuterons (2002-04) and protons (2007,2010). Using a deuteron target, the resulting Collins and Sivers asymmetries turned out to be compatible with zero [2],[3], an observation which has been interpreted as a cancellation between the u and d quark contributions in the isoscalar target. Using a proton target, a first measurement was performed separately versus x, z and p_T for unidentified hadrons, pions and kaons [4],[5],[6]. The Collins asymmetry is small, compatible with zero, except for $x \geq 0.05$ where a significant signal (up to 10 %) appears with opposite sign for positive and negative hadrons, pions and kaons. The results for the Sivers asymmetry are compatible with zero for negative hadrons and exhibit small positive values (up to 3%) for positive hadrons both at small and at large x. Compared with HERMES results measured at smaller Q^2, the results were found to be slightly smaller. A further investigation showed that the signal is concentrated at small W while at larger W, it tends to zero. Thus COMPASS data highlights a possible W dependence of the Sivers asymmetry for positive hadrons. The other six asymmetries were extracted from deuteron and proton data and were found to be compatible with zero.

Recently, further investigation of the previous observations has been performed by studying the x, z, p_T and W dependencies in different Q^2 regions: $Q^2 \in$ [1,4], [4,6.25], [6.25,16] and $Q^2 \geq 16$ (GeV/c)^2, using the data set collected in 2010 on a transversely polarised proton.

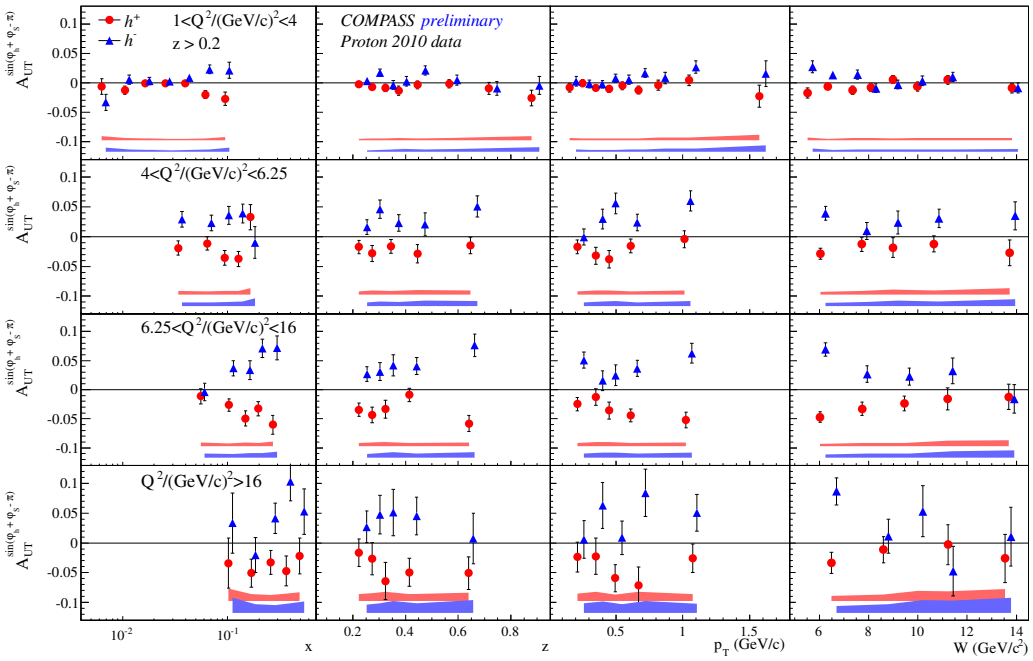

Figure 1: Collins asymmetry vs. x, z, p_T, W in four Q^2 ranges.

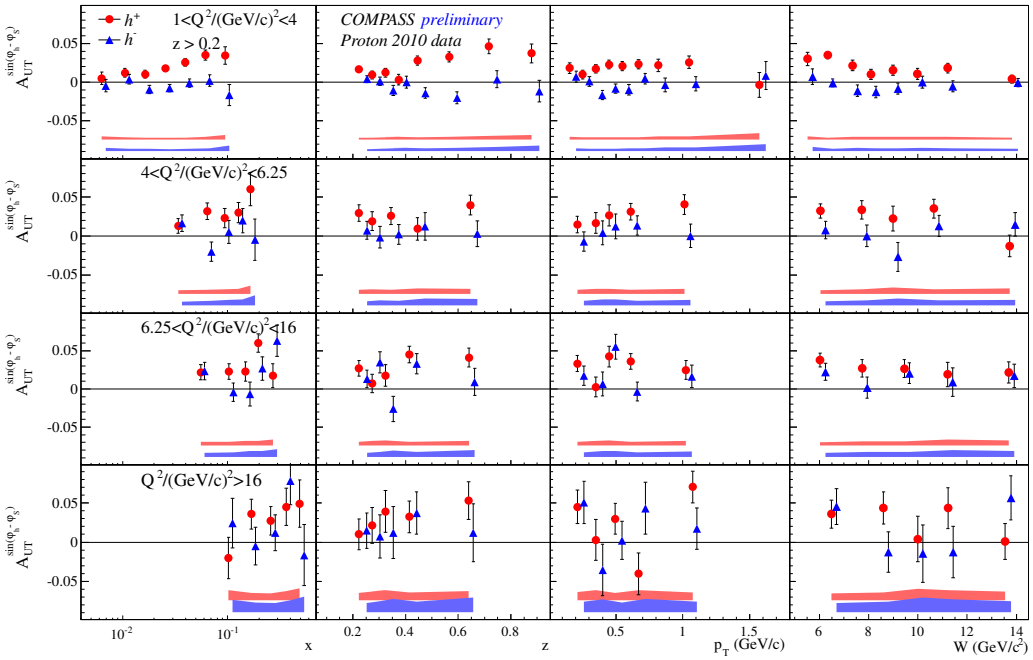

Figure 2: Sivers asymmetry vs. x, z, p_T, W in four Q^2 ranges.

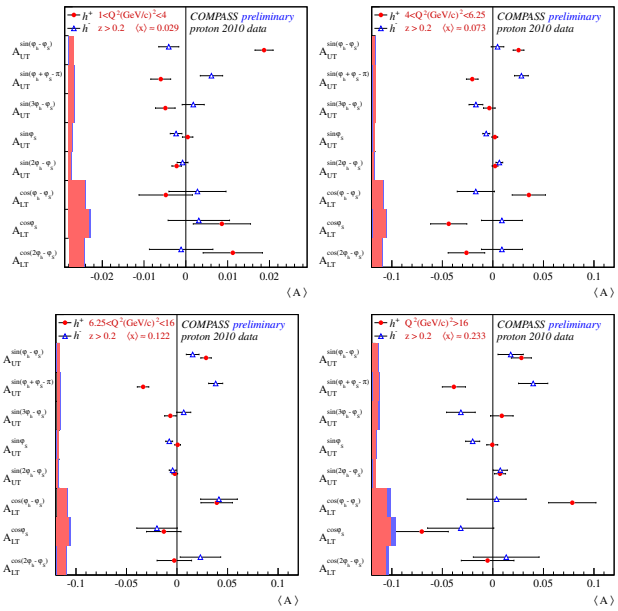

Figure 3: Mean of the eight asymmetries in four Q^2 regions.

These new results for Collins and Sivers asymmetries are shown in Fig. 1-2 versus x, z, p_T and W and the mean of the eight asymmetries are shown in Fig. 3. Error bars show only statistical uncertainties. The systematic uncertainties, estimated separately for each asymmetry and hadron charge, are shown by the bands. The increase of Collins asymmetry at large x and small W increases with Q^2. For Sivers asymmetry, the non-negligible signal for positive hadrons at large x is clearly visible, also at large Q^2, which is important for the Drell-Yan measurement foreseen by COMPASS in 2015. The other six asymmetries are compatible with zero.

4 Conclusions

A first study of the dependence of Collins, Sivers and the other six asymmetries upon kinematic variables x, z, p_T and W in different Q^2 regimes is performed, showing a non negligible Q^2 dependence of the Collins asymmetry. A more detailed multidimensional analysis of the eight asymmetries in simultaneous bins of (x,Q^2) and (x,z,p_T) is close to be finalised.

References

[1] P. Abbon *et al.* [COMPASS Collaboration], Nucl. Instrum. Meth. A **577** 455 (2007).
[2] Ageev E *et al.* [COMPASS Collaboration], Nucl. Phys. B **766** 31 (2007).
[3] Alekseev *et al.* [COMPASS Collaboration], Phys. Lett. B **673** 127 (2009).
[4] C. Adolph *et al.* [COMPASS Collaboration], Phys. Lett. B **717** 376 (2012).
[5] C. Adolph *et al.* [COMPASS Collaboration], Phys. Lett. B **717** 383 (2012).
[6] C. Adolph *et al.* [COMPASS Collaboration], hep-ex/1408.4405.

Timelike Compton Scattering off the Proton: beam and/or target spin asymmetries.

Marie Boër[1], *Michel Guidal*[1]

[1]Institut de Physique Nucléaire, CNRS-IN2P3, Université Paris-Sud F-91406 Orsay, France

DOI: http://dx.doi.org/10.3204/DESY-PROC-2014-04/256

We present a sample of results of our work to be published soon on Timelike Compton scattering off the proton, in the framework of the Generalized Parton Distributions formalism.

1 Introduction

More than 40 years after the discovery of point-like components within the proton, its quarks and gluons structure is still not well understood and is still intensively studied. Hard exclusive processes on the proton provide access to the Generalized Parton Distributions (GPDs) [1, 2, 3, 4] which contain informations about the longitudinal momentum and the spatial transverse distributions of partons inside the proton (in a frame where the nucleon has an "infinite" momentum along its longitudinal direction). Such a hard exclusive process is the Deeply Virtual Compton scattering process which corresponds to the reaction $\gamma^{(*)}P \to \gamma^{(*)}P$ and to the scattering of a high-energy virtual photon off a quark inside the proton. There are two particular cases of deep Compton processes. "Spacelike" Deeply Virtual Compton Scattering (DVCS) corresponds to the case where the incoming photon is emitted by a lepton beam and has a high spacelike virtuality and and where the final photon is real. The DVCS process has been studied for the past ∼15 years and is still intensively studied both theoretically and experimentally. The second particular case of deep Compton scattering is the Timelike Compton Scattering (TCS) process. It corresponds to the case where the incoming photon is real and the final photon has a high timelike virtuality and decays into a lepton pair (see Fig. 1). Contrary to DVCS, there is no published experimental data yet for TCS. Both DVCS and TCS give access to the same proton GPDs in the QCD leading twist formalism. The study of TCS in parallel to DVCS is a very powerful way to check the universality of GPDs and/or to study higher twist effects. The reaction $\gamma P \to e^+e^-P$ also involves the Bethe-Heitler process, where the incoming real photon creates a lepton pair, which then interacts with the proton. It is not sensitive to the GPDs but to the form factors. It can be calculated with a few percent accuracy.

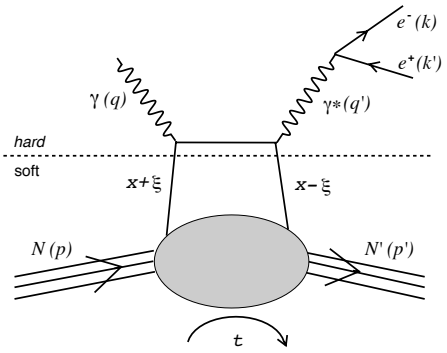

Figure 1: Leading twist TCS diagram.

2 Amplitudes and observables

The four vectors involved are indicated in Fig. 1. According to QCD factorization theorems, at sufficiently large $Q'^2 = (k + k')^2$ (photon's virtuality), we can decompose the TCS amplitude into a soft part, parameterized by the GPDs, and a hard part, exactly calculable by Feynman diagrams techniques. We work in a frame where the average protons and the average photons momenta, respectively P and $\bar{q}$, are collinear along the z-axis and in opposite directions. We define the lightlike vectors along the positive and negative z directions as $\tilde{p}^\mu = P^+/\sqrt{2}(1, 0, 0, 1)$ and $n^\mu = 1/P^+ \cdot 1/\sqrt{2}(1, 0, 0, -1)$, with $P^+ \equiv (P^0 + P^3)/\sqrt{2}$. We have the properties $\tilde{p}^2 = n^2 = 0$ and $\tilde{p} \cdot n = 1$. In this frame, the TCS amplitude can be written in the asymptotic limit (mass terms are neglected with respect to Q'^2) with the Ji convention for GPDs [5]:

$$
\begin{aligned}
T^{TCS} = & -\frac{e^3}{q'^2}\, \bar{u}(k)\, \gamma^\nu\, v(k')\, \epsilon^\mu(q) \\
& \left[\frac{1}{2}\, (-g_{\mu\nu})_\perp \int_{-1}^{1} dx\, \left(\frac{1}{x - \xi - i\epsilon} + \frac{1}{x + \xi + i\epsilon} \right) . \left(H(x,\xi,t) \bar{u}(p') \not{n} u(p) + E(x,\xi,t) \bar{u}(p') i\sigma^{\alpha\beta} n_\alpha \frac{\Delta_\beta}{2M}\, u(p) \right) \right. \\
& \left. - \frac{i}{2} (\epsilon_{\nu\mu})_\perp \int_{-1}^{1} dx\, \left(\frac{1}{x - \xi - i\epsilon} - \frac{1}{x + \xi + i\epsilon} \right) . \left(\tilde{H}(x,\xi,t) \bar{u}(p') \not{n} \gamma_5\, u(p) + \tilde{E}(x,\xi,t) \bar{u}(p') \gamma_5 \frac{\Delta . n}{2M}\, u(p) \right) \right] \quad (1)
\end{aligned}
$$

where x is the quark longitudinal momentum fraction, $\Delta = (p' - p)$ is the momentum transfer, $t = \Delta^2$ and ξ is defined as

$$\xi = -\frac{(p - p').(q' + q)}{(p + p').(q' + q)}. \quad (2)$$

In Eq. 1, we used the metric

$$(-g_{\mu\nu})_\perp = -g_{\mu\nu} + \tilde{p}_\mu n_\nu + \tilde{p}_\nu n_\mu \ , \quad (\epsilon_{\nu\mu})_\perp = \epsilon_{\nu\mu\alpha\beta}\, n^\alpha\, \tilde{p}^\beta. \quad (3)$$

The Bethe-Heitler amplitude reads:

$$T^{BH} = -\frac{e^3}{\Delta^2} \bar{u}(p') \left(\gamma^\nu F_1(t) + \frac{i\sigma^{\nu\rho}\Delta_\rho}{2\,M} F_2(t) \right) u(p)\, \epsilon^\mu(q) \bar{u}(k) \left(\gamma_\mu \frac{\not{k} - \not{q}}{(k-q)^2} \gamma_\nu + \gamma_\nu \frac{\not{q} - \not{k}'}{(q-k')^2} \gamma_\mu \right) v(k'), \quad (4)$$

where $F_1(t)$ and $F_2(t)$ are the proton Dirac and Pauli form factors. At fixed beam energy, the cross section of the photoproduction process depends on four independant kinematic variables, which we choose as: Q'^2, t and the two angles θ and ϕ of the decay electron in the γ^* center of mass. The 4-differential unpolarized cross section reads:

$$\frac{d^4\sigma}{dQ'^2 dt d\Omega}(\gamma p \to p' e^+ e^-) = \frac{1}{(2\pi)^4} \frac{1}{64} \frac{1}{(2ME_\gamma)^2}\, |\, T^{BH} + T^{TCS}\, |^2, \quad (5)$$

where $|\, T^{BH} + T^{TCS}\, |^2$ is averaged over the target proton and beam polarizations and summed over the final proton spins.

We define the single and double spin asymmetries as:

$$A_{\odot U}\ (A_{Ui}) = \frac{\sigma^+ - \sigma^-}{\sigma^+ + \sigma^-}, \quad A_{\odot i} = \frac{(\sigma^{++} + \sigma^{--}) - (\sigma^{+-} + \sigma^{-+})}{\sigma^{++} + \sigma^{--} + \sigma^{+-} + \sigma^{-+}}, \quad (6)$$

where the first index of A corresponds to the polarization state of the beam and the second one corresponds to the polarization state of the target. $A_{\odot U}$ is the circularly polarized beam spin

asymmetry. The + and − superscripts in σ correspond to the two photon spin states, right and left polarized. A_{Ui} are the single target spin asymmetries where the + and − superscripts refer to the target spin orientations along the axis $i = x, y, z$. The axis x and y are perpendicular to the incoming proton direction (along the z-axis) in the γP center of mass frame and are respectivelly in the scattering plane and perpendicular to this plane. $A_{\odot i}$ are the double spin asymmetries with a circularly polarized beam and with a polarized target. We finally define the single linearly polarized beam spin asymmetry as

$$A_{\ell U}(\Psi) = \frac{\sigma_x(\Psi) - \sigma_y(\Psi)}{\sigma_x(\Psi) + \sigma_y(\Psi)}, \tag{7}$$

where Ψ is the angle between the photon polarization vector and the $\gamma P \to \gamma^* P'$ plane and where σ_x (σ_y) indicate a photon polarized in the x-(y-)direction.

3 Numerical results and sensitivity to GPDs

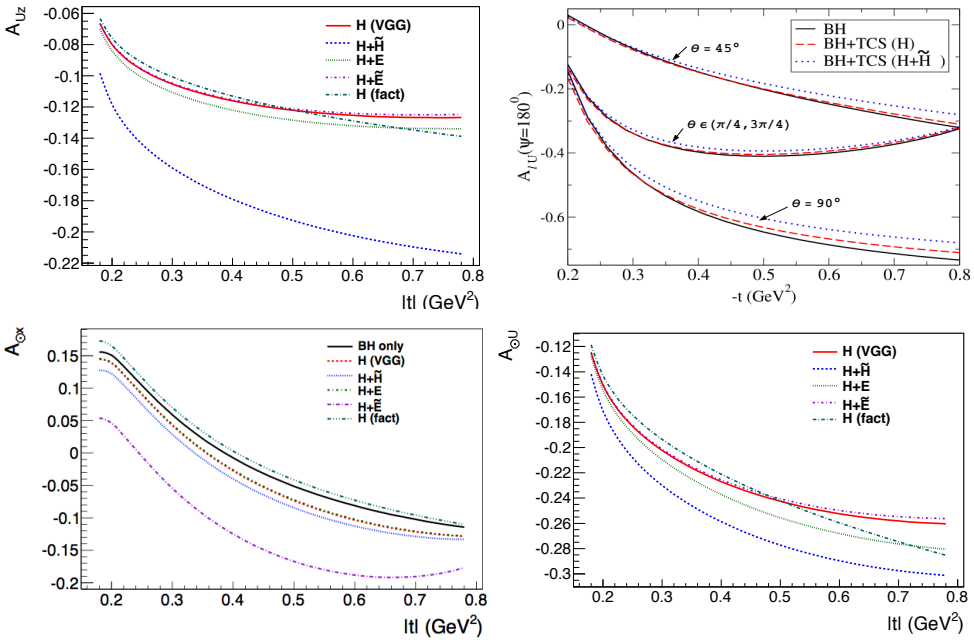

Figure 2: Spin asymmetries as a function of $-t$. Top left: $A_{\odot U}$ for BH+TCS. Top right: $A_{\ell U}$ for BH and BH+TCS. Bottom left: A_{Uz} for BH+TCS. Bottom right: $A_{\odot x}$ for BH and BH+TCS. All calculations are done at $\xi = 0.2$, $Q'^2 = 7$ GeV^2, $\phi = 90°$ and θ integrated over $[45°, 135°]$. $A_{\ell U}$ is also shown for $\theta = 45°$ and $\theta = 90°$.

We performed our calculations using the GPD parameterization of the VGG model [6, 7, 8]. We focus here on the spin asymmetries. Figure 2 shows the circularly (top row left) and linearly (top row right) polarized beam spin asymmetries as a function of t. One should note that $A_{\odot U}$

is particularly sensitive to the GPDs as it is exactly 0 for BH alone. It comes from the fact that this asymmetry is sensitive to the imaginary part of the amplitudes and the BH amplitude is purely real. We also show $A_{\odot U}$ with a factorized-t ansatz instead of a Reggeized-t ansatz for the H GPD which illustrates the sensitivity to the GPD modeling. In contrast, the $A_{\ell U}$ asymmetry, which is strong, is dominated by the BH and the TCS makes up only small deviations. Indeed, this asymmetry is sensitive to the real part of the amplitudes.

We display in Fig. 2 (bottom row) two examples of asymmetries with a polarized target: A_{Uz} and $A_{\odot x}$ (double spin asymmetry). We present the results for TCS+BH with different GPDs contributions and parameterizations. All single target spin asymmetries are zero for the BH alone as they are proportional to the imaginary part of the amplitudes. This makes the A_{Ui} asymmetries privileged observables to study GPDs. On the contrary, it is more difficult to access GPDs with double spin asymmetries as the BH alone produces a strong double spin asymmetry.

4 Discussion

We have presented a sample of our results to be published soon, namely the t-dependence of single and double spin asymmetries for the $\gamma P \to e^+e^-P$ reaction which we analyzed in the framework of the GPD formalism. We didn't discuss this here due to lack of space but we also compared our unpolarized cross sections and our single beam spin asymmetries with those of the earlier work of Refs [9, 10] and they are in agreement at the few percent level. We have introduced in our work the target polarization in order to define the single and double spin asymmetries with polarized targets. We have also introduced some higher twist corrections and gauge invariance restoration terms.

As the BH contribution alone doesn't contribute to single target spin asymmetries and to circularly polarized beam spin asymmetries, these observables are good candidates to study GPDs. Such measurements can be envisaged at the JLab 12 GeV facility. In particular, a proposal has been accepted for the CLAS12 experiment (JLab Hall B) to measure the unpolarized BH+TCS cross section [11]. The work that we presented here can open the way to new complementary experimental programs with polarized beams and/or targets.

References

[1] K. Goeke, M. V. Polyakov and M. Vanderhaeghen, Prog. Part. Nucl. Phys. **47**, 401 (2001).

[2] M. Diehl, Phys. Rept. **388**, 41 (2003).

[3] A.V. Belitsky, A.V. Radyushkin, Phys. Rept. **418**, 1 (2005).

[4] M. Guidal, H. Moutarde and M. Vanderhaeghen, Rept. Prog. Phys. **76**, 066202 (2013).

[5] X. Ji, Phys.Rev.Lett. **78**, 610 (1997); Phys.Rev.D **55**, 7114 (1997).

[6] M. Vanderhaeghen, P.A.M. Guichon and M. Guidal, Phys. Rev. Lett. **80** 5064 (1998)

[7] M. Vanderhaeghen, P. A. M. Guichon and M. Guidal, Phys. Rev. D **60** 094017 (1999).

[8] M. Guidal, M. V. Polyakov, A. V. Radyushkin and M. Vanderhaeghen, Phys. Rev. D **72** 054013 (2005).

[9] E. R. Berger, M. Diehl and B. Pire, Eur. Phys. J. C **23**, 675 (2002).

[10] A. T. Goritschnig, B. Pire and J. Wagner, Phys. Rev. D **89** (2014) 094031

[11] I. Albayrak et al. and the CLAS Collaboration, JLab PAC 39 Proposal, (2012).

Measurements of the Form Factor in VPγ^* Transitions and Study of the $\eta \to \pi^+\pi^-\pi^0$ Dalitz Plot at KLOE

Li Caldeira Balkeståhl[1] on behalf of KLOE-2 collaboration

[1]Department of Physics and Astronomy, Uppsala University, Box 516, SE-751 20 Uppsala, SWEDEN

DOI: http://dx.doi.org/10.3204/DESY-PROC-2014-04/141

The Vector→Pseudoscalar γ^* decays $\phi \to \eta e^+e^-$ and $\phi \to \pi^0 e^+e^-$ have been measured based on 1.7 pb^{-1} of data collected with the KLOE experiment, for extracting the branching ratios and transistion form factors.

With 1.6 pb^{-1} of data from the same experiment, we measure the Dalitz plot distribution of the $\eta \to \pi^+\pi^-\pi^0$ decay. Preliminary values are given for the Dalitz plot parameters a, b, d, f.

1 Transition form factors of VPγ^*

The differential decay rate of Vector→Pseudoscalar γ^*, with the virtual photon decaying in a lepton pair, is described by [1]:

$$\frac{d}{dq^2}\frac{\Gamma(\mathrm{V}\to \mathrm{P}l^+l^-)}{\Gamma(\mathrm{V}\to \mathrm{P}\gamma)} = \frac{\alpha}{3\pi}\frac{|F_{\mathrm{VP}}(q^2)|^2}{q^2}\sqrt{1-\frac{4m^2}{q^2}}\left(1+\frac{2m^2}{q^2}\right)\left[\left(1+\frac{q^2}{m_{\mathrm{V}}^2-m_{\mathrm{P}}^2}\right)^2-\frac{4m_{\mathrm{V}}^2q^2}{(m_{\mathrm{V}}^2-m_{\mathrm{P}}^2)^2}\right]^{\frac{3}{2}} \tag{1}$$

where q is the invariant mass of the lepton pair, F_{AB} is the transition form factor, m is the lepton mass and m_{A}, m_{B} are the masses of the mesons A and B. In the one pole approximation, the transition form factor is

$$F_{\mathrm{VP}}(q^2) = \frac{1}{1-q^2/\Lambda^2} \tag{2}$$

where Λ is the characteristic mass relevant to the process. The slope of the transition form factor is defined as

$$b_{\mathrm{VP}} = \frac{dF_{\mathrm{VP}}(q^2)}{dq^2}|_{q^2=0}$$

which for the one pole approximation gives $b_{\mathrm{VP}} = \Lambda^{-2}$.

The simple vector meson dominance model (VMD) can be used to calculate transistion form factors. This model is in general quite sucessful, but it puzzlingly fails for the decay $\omega \to \mu^+\mu^-\pi^0$, as shown by the Lepton-G [2] and NA60 [3, 4] experiments. Therefore it is important to verify other Vector→Pseudoscalar γ^* processes.

Recently, new theoretical approaches have been proposed to describe these deviations from VMD: one based on dispersion theory [5], one based on an effective field theory including light vector mesons as degrees of freedom [6] and one based on chiral effective field theory with resonances [7]. To descriminate between these models, more data on VPγ^* transition form factors, for different vector and pseudoscalar mesons, is needed.

1.1 $\phi \to \eta e^+ e^-$

The existing experimental data on the $\phi \to \eta e^+ e^-$ decay are very scarce. The branching ratio has been measured by two experiments, in units of 10^{-4} the world average is equal to 1.15 ± 0.10 (PDG [8], the result comes from SND [9] and CMD-2 [10] experiments). The slope of the transition form factor was determined only by the SND experiment with very large error, $b_{\phi\eta} = 3.8 \pm 1.8$ GeV^{-2} [9], while the value expected from VMD is $b_{\phi\eta} \simeq 1$ GeV^{-2}.

With the KLOE detector, using 1.7 pb^{-1} of data, we have measured $\phi \to \eta e^+ e^-$ with $\eta \to 3\pi^0$, with a total of 29 626 $\pm$178 events in the final sample. This results in a branching ratio of $\left(1.075 \pm 0.038_{\rm norm} \pm 0.007_{\rm stat}{}^{+0.006}_{-0.002\ \rm syst}\right) \cdot 10^{-4}$, where the normalization error comes from the uncertainty in the ϕ meson production cross-section and in the luminosity measurement. A fit of the lepton pair invariant mass spectrum to Equation 1 using Equation 2 is shown in Figure 1. This gives $b_{\phi\eta} = 1.17 \pm 0.10(\text{stat})^{+0.07}_{-0.11}(\text{syst})$.

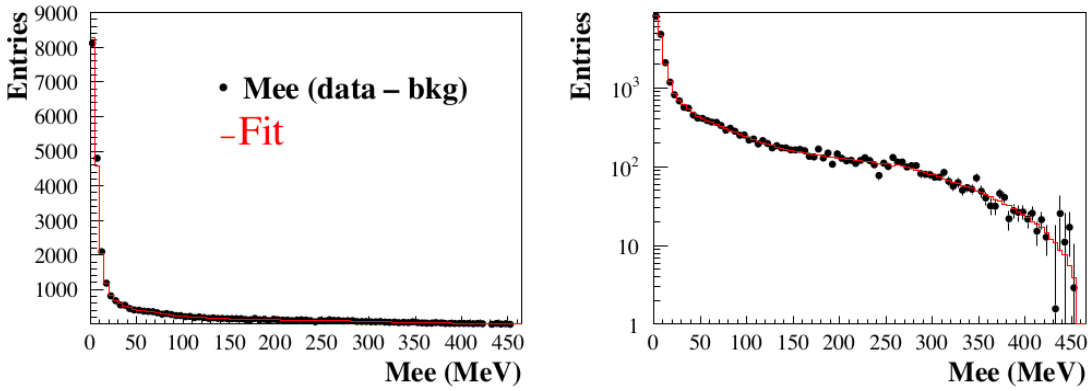

Figure 1: Observed (not corrected for acceptance) experimental distribution of invariant mass of the lepton pair for the $\phi \to \eta e^+ e^-$ signal after background subtraction. The red lines represent the best fit using Eq. 1 with single pole form factor paremetrization Eq. 2.

The modulus squared of the transition form factor as a function of the lepton pair invariant mass can be extracted by dividing, for each bin in q, the data by the number of reconstructed events simulated with $F_{\phi\eta} = 1$. This is shown in Figure 2, where the Monte Carlo data sample has been normalized to the experimental data in the first bin. A fit of this distribution to the one-pole approximation formula (Eq. 2) results in $b_{\phi\eta} = (1.25 \pm 0.10)$ GeV^{-2}, in agreement with the slope extracted directly from the acceptance uncorrected differential decay distribution.

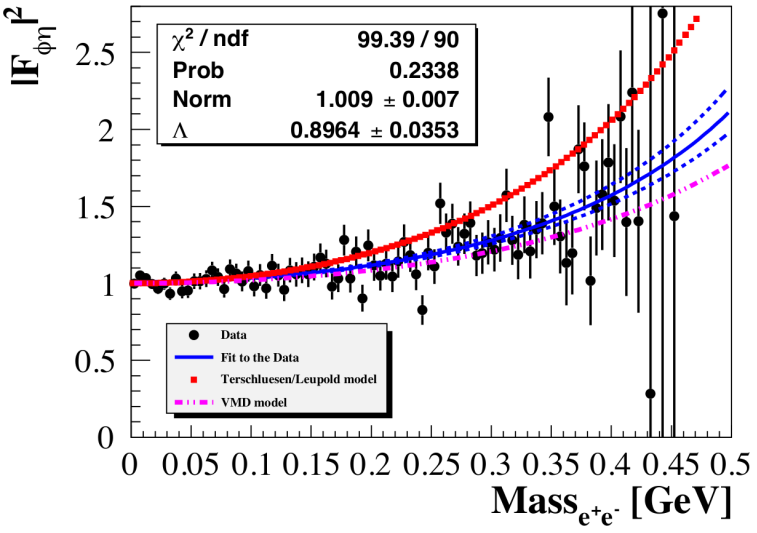

Figure 2: $|F_{\phi\eta}|^2$ as a function of the invariant mass of the lepton pair. In blue (full line with dashed error band) the result from the fit to Equation 2, in pink (dash dot line) the VMD prediction and in red (full line) the theoretical calcualtion of [6].

1.2 $\phi \to \pi^0 e^+ e^-$

For the decay $\phi \to \pi^0 e^+ e^-$ there is no data on the transition form factor slope, and the branching ratio measurements have large errors: the world average is $(1.12 \pm 0.28) \cdot 10^{-5}$ (PDG [8], the result comes from SND [11] and CMD-2 [12] experiments).

An analysis of this decay using 1.7 pb^{-1} of data collected at KLOE is underway. At the end of the analysis chain there are 14 680 events, of which Monte Carlo simulation shows about 22% are $e^+e^- \to e^+e^-\gamma\gamma$ background and 20% are $\phi \to \pi^0\gamma$ background (with conversion of the photon in the detector). The background could be subtracted bin by bin in order to extract the invariant mass distribution of the lepton pair. Results on both branching ratio and transition form factor are forthcoming.

2 Decay dynamics of $\eta \to \pi^+\pi^-\pi^0$

The isospin breaking decay $\eta \to \pi^+\pi^-\pi^0$ is sensitive to the difference of the up and down quarks, since electromagnetic effects in this decay are small [13, 14, 15, 16]. The decay width

$$\Gamma(\eta \to \pi^+\pi^-\pi^0) \propto Q^{-4} \quad \text{where } Q^2 \equiv \frac{m_s^2 - \hat{m}^2}{m_d^2 - m_u^2} \quad \text{and } \hat{m} = \frac{1}{2}(m_d + m_u),$$

allows to determine Q, thus setting an elliptical constraint in the light quark mass plane $\frac{m_u}{m_d}$ *vs* $\frac{m_s}{m_d}$ [17]. The chiral perturbation theory calculations for the decay width show a slow converge ($\Gamma_{LO} = 66$ eV, $\Gamma_{NLO} = 160 \pm 50$ eV [18] and $\Gamma_{NNLO} = 295 \pm 17$ [19], $\Gamma_{exp} = 295 \pm 16$ eV [8]). This indicates the importance of the final state interactions between pions, which can be taken

into account by the use of dispersive theory [20, 21]. Calculations have also been performed in a non-relativistic effective field theory approach [22].

A more complete comparison between theory and experiment is facilitated by the Dalitz plot, containing full information on the dynamics of the decay. For the $\eta \to \pi^+\pi^-\pi^0$ decay, the normalized variables X and Y are used

$$X = \sqrt{3}\frac{T_{\pi^+} - T_{\pi^-}}{Q_\eta} \qquad Y = \frac{3T_{\pi^0}}{Q_\eta} - 1 \qquad (Q_\eta = T_{\pi^+} + T_{\pi^-} + T_{\pi^0})$$

where T_{π^i} is the kinetic energy of the π^i in the η rest frame. The squared amplitude of the decay can be expanded around $X = Y = 0$ as

$$|A(X,Y)|^2 \simeq N(1 + aY + bY^2 + cX + dX^2 + eXY + fY^3 + gX^2Y)$$

and the coefficients a, b, c, d, e, f, g are called Dalitz plot parameters.

Using 1.6 pb^{-1} of data collected at KLOE we extract the Dalitz plot distribution for $\eta \to \pi^+\pi^-\pi^0$. The preliminary results for the Dalitz plot parameters are shown in Table 1, compared to earlier experimental results. Note that the present analysis includes only statistical errors as the systematic effects are under investigation.

Experiment	-a	b	d	f
Gormley[23]	1.17(2)	0.21(3)	0.06(4)	-
Layter[24]	1.080(14)	0.03(3)	0.05(3)	-
CBarrel[25]	1.22(7)	0.22(11)	0.06(fixed)	-
KLOE[26]	$1.090(5)(^{+19}_{-8})$	0.124(6)(10)	$0.057(6)(^{+7}_{-16})$	0.14(1)(2)
WASA[27]	1.144(18)	0.219(19)(47)	0.086(18)(15)	0.115(37)
This work	1.104(3)	0.144(3)	0.073(3)	0.155(6)

Table 1: Experimental results for the Dalitz plot parameters of $\eta \to \pi^+\pi^-\pi^0$.

References

[1] L. G. Landsberg, Phys. Rept. **128**, 301 (1985).

[2] R. I. Dzhelyadin *et al.*, Phys. Lett. **B102**, 296 (1981).

[3] R. Arnaldi *et al.* (NA60 Collaboration), Phys. Lett. **B677**, 260 (2009).

[4] G. Usai (NA60 Collaboration), Nucl. Phys. A **A855**, 189 (2011).

[5] S. P. Schneider, B. Kubis and F. Niecknig, Phys. Rev. **D86**, 054013 (2012).

[6] C. Terschlusen and S. Leupold, Phys. Lett. **B691**, 191 (2010).

[7] S. Ivashyn, Prob. Atomic Sci. Technol. **2012N1**, 179 (2012).

[8] J. Beringer *et al.* (Particle Data Group), Phys. Rev. **D86**, 010001 (2012).

[9] M. N. Achasov *et al.*, Phys. Lett. **B504**, 275 (2001).

[10] R. R. Akhmetshin *et al.* (CMD-2 Collaboration), Phys. Lett. **B501**, 191 (2001).

[11] M. N. Achasov *et al.*, JETP Lett. **75**, 449 (2002).

[12] R. R. Akhmetshin *et al.* (CMD-2 Collaboration), Phys. Lett. **B503**, 237 (2001).

[13] D. G. Sutherland, Phys. Lett. **23**, 384 (1966).

[14] J. S. Bell and D. G. Sutherland, Nucl. Phys. **B4**, 315 (1968).

[15] R. Baur, J. Kambor and D. Wyler, Nucl. Phys. **B460**, 127 (1996).
[16] C. Ditsche, B. Kubis and U.-G. Meißner", Eur. Phys. J. **C60**, 83 (2009).
[17] H. Leutwyler, Phys. Lett. **B378**, 313 (1996).
[18] J. Gasser and H. Leutwyler, Nucl. Phys. **B250**, 539 (1985).
[19] J. Bijnens and K. Ghorbani, JHEP **0711**, 030 (2007).
[20] G. Colangelo, S. Lanz, H. Leutwyler and E. Passemar, POS **EPS-HEP2011**, 304 (2011)
[21] K. Kampf, M. Knecht, J. Novotný and M. Zdráhal, Phys. Rev. **D84**, 114015 (2011).
[22] S. P. Schneider, B. Kubis and C. Ditsche, JHEP **1102**, 028 (2011)
[23] M. Gormley *et al.*, Phys. Rev. **D2**, 501 (1970).
[24] J.G. Layter *et al.*, Phys. Rev. **D7**, 2565 (1973).
[25] A. Abele *et al.* (Crystal Barrel Collaboration), Phys. Lett. **B471**, 197 (1998).
[26] F. Ambrosino *et al.* (KLOE collaboration), JHEP **0805**, 006 (2008).
[27] P. Adlarson *et al.* (WASA-at-COSY collaboration), Phys. Rev. **C90**, 045207 (2014).

Generalized Parton Distributions at COMPASS: Present Results and Future Perspectives

Eric Fuchey[1] on behalf of COMPASS collaboration

[1]CEA Saclay, IRFU/SPhN 91191 Gif-sur-Yvette, France

DOI: http://dx.doi.org/10.3204/DESY-PROC-2014-04/103

Understanding the nucleon structure remains one of the key challenges of nuclear physics. The Generalized Parton Distributions (GPDs) grant a new insight for the study of the nucleon structure, as they provide a three-dimensional picture of the nucleon. COMPASS at CERN has a great potential for GPD studies, with its forthcoming measurement of deeply virtual Compton scattering and exclusive meson production off the proton with both μ^+ and μ^-. The current COMPASS GPD program will be discussed, as well as an overview of the investigation on future possible developments. Existing results of exclusive meson production will also be presented.

1 Reminder on Generalized Parton Distributions

The Generalized Parton Distributions (GPDs) constitute a new, three dimensional parametrization of the nucleon structure. They correlate the momentum distribution of the partons inside the proton, parametrized by the parton distribution functions, to the transverse spatial distribution of those partons, parametrized by the form factors. As such, those objects grant access to the orbital angular momentum of the quarks [1, 2, 3].

GPDs can be accessed thanks to exclusive processes such as Deeply Virtual Compton Scattering (DVCS $\ell p \to \ell p \gamma$), or exclusive meson production off the nucleon. In such reactions, the virtual photon (with a high virtuality Q^2) emitted by the lepton selects a quark in the nucleon with a longitudinal momentum fraction $x + \xi$, which re-emits a photon (in the case of DVCS) or produces a hadron (in the case of meson production), and is reabsorbed in the proton with a momentum $x - \xi$. During the reaction, a quadrimomentum t is transferred to the nucleon (Figure 1).

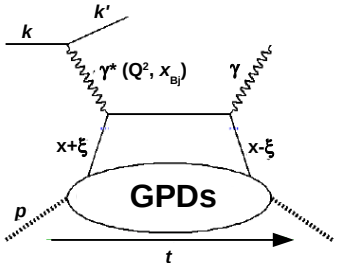

Figure 1: Feynman diagram of DVCS at lowest order.

We count four chiral-even GPDs (which do not involve quark-helicity flip), H, E, $\tilde{H}$, $\tilde{E}$, and as many chiral-odd GPDs (which involve quark-helicity flip). Those GPDs are functions of x, ξ, and t. The second moment in x of the sum of H and E for a given quark flavor gives the quark total angular momentum. This property is called the Ji sum rule [3]. As a consequence, the study of H and E are of first importance to understand the content of the proton in spin, and COMPASS at CERN has the ability to study them both.

2 The COMPASS experiment at CERN

2.1 COMPASS experimental setup

COMPASS (Common Muon Proton Apparatus for Structure and Spectroscopy) at CERN is a large acceptance magnetic spectrometer dedicated to the study of hadronic physics. It is installed on one of the Super-Proton-Synchrotron beam lines, and is able to receive beams of various types: protons, pions, and both positive and negative polarized muons (polarization $\simeq$ 80 %).

The experimental setup is composed of two dipoles and of a large number of tracking detectors for charged particle reconstruction and momentum measurement. A ring imaging Cherenkov detector provides particle identification, and two calorimeters provide energy measurement. A more complete description of the detectors is provided in [4]. Such an apparatus grants COMPASS with a wide kinematic range.

The experimental setup described above can be modified or completed to measure a specific process. Let us review the modifications that have been done for DVCS measurement.

2.2 Compass configuration for DVCS measurement

At COMPASS, the DVCS ($\mu p \to \mu p \gamma$) will be measured using the high intensity ($\sim 4 \times 10^7\,\mu\,\mathrm{s}^-1$) polarized muon beam. DVCS is a relatively low cross section process, so the luminosity will be maximized with a 2.5 meter long liquid hydrogen target. In the DVCS kinematics, the photon is produced at forward angle, and the proton recoils at very large angle. To measure and identify the recoil proton, a 4-meter long Time-Of-Flight detector called CAMERA is surrounding the target. To extend the kinematic coverage of DVCS detection to the higher x_{Bj}, a large angle electromagnetic calorimeter has also been added. With such an apparatus, COMPASS can measure the DVCS process on a wide x_{Bj} range (from 0.005 to $\simeq 0.3$) with a Q^2 up to $\simeq 20\,\mathrm{GeV}^2$ (limited by integrated luminosity).

3 The COMPASS GPD program

Thanks to several advantageous features, which we are going to discuss, COMPASS has the ability to study both GPD H [5] and GPD E. First, both μ^+ and μ^- beams are available at COMPASS (Sec. 2.1), each having one polarization direction. This feature is currently unique, and will provide useful additional information for the extraction of GPDs thanks to DVCS measurement (see Secs. 3.1 and 3.2). In addition to this, the x_{Bj} range covered by COMPASS ($0.005 < x_{Bj} < 0.3$) spans over the existing gap between the DVCS data from HERA in the gluon region ($x_{Bj} \leq 10^{-2}$) on the one hand, and the data from HERMES and Jefferson Lab in the valence region ($x_{Bj} \geq 0.1$). COMPASS is also a versatile detector, in this sense that it is able to measure simultaneously DVCS and several exclusive neutral meson channels, such as π^0, ρ^0, ϕ, ω.

3.1 Study of GPD H

The GPD H is studied with DVCS measurements on unpolarized hydrogen. A 10-day long test run, recorded in 2009 at COMPASS with a reduced DVCS setup (40 cm liquid hydrogen target, short recoil proton calorimeter, no additional calorimetry), proved the capability of such

a setup to measure exclusive photon production, but also the capability to isolate, at high x_{Bj} values, a DVCS signal among the total $\mu p \to \mu p \gamma$ signal (composed of the interference of DVCS and Bethe-Heitler, where the photon is radiated by the incident or the scattered lepton).

In 2012, a four-week long pilot run has been recorded, with a mostly complete DVCS setup (full scale recoil proton detector, full luminosity, partially equipped large angle calorimeter). This run, which is still under analysis, has proved that the recoil proton detector is able to detect and identify protons. The results from this run will be available soon.

The full DVCS run will occur in 2016 and 2017 [5]. Interesting information will come from the $\mu p \to \mu p \gamma$ cross sections measurements with both muon charge states ($d\sigma(\mu^{+,\to})$ and $d\sigma(\mu^{-,\leftarrow})$) both from their sum $\mathcal{S}_{CS,U}$ and their difference $\mathcal{D}_{CS,U}$.50.0 The DVCS cross section can be isolated from $\mathcal{S}_{CS,U}$. Its t-dependence, expected to be in $\exp(-Bt)$, provides the size of the proton $r_\perp$ at the measured x_{Bj}, knowing that $\langle r_\perp^2(x_{Bj})\rangle \simeq 2B(x_{Bj})$. The t-slope parameter B has been measured at HERA at $x_{Bj} < 0.01$ (square and triangles on Fig. 2). In this region, B is measured to be constant. In the x_{Bj} range covered by COMPASS, the proton size is expected to shrink (solid and dashed lines on Fig. 2), and the projected COMPASS uncertainties with two years of data (circles on Fig. 2) should be able to determine the x_{Bj}-slope, α' of this shrink.

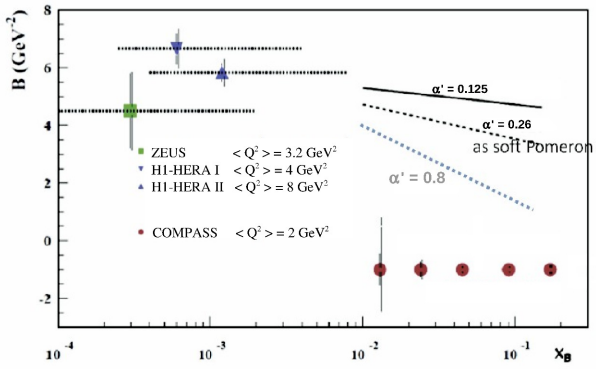

Figure 2: t-slope parameter as a function of x_{Bj} measured by HERA (square and triangles), and projected statistical uncertainty with two years of data at COMPASS (circles).

The study of the ϕ modulation of the Bethe-Heitler-DVCS interference term in $\mathcal{S}_{CS,U}$ and $\mathcal{D}_{CS,U}$ allow to isolate their first ϕ moment (respectively $s_1^{Int}\sin(\phi_{\gamma\gamma})$ and $c_1^{Int}\cos(\phi_{\gamma\gamma})$), which depend respectively on the imaginary part and real part of $F_1 \times \mathcal{H}$. ($\mathcal{H}$ being the observable of the GPD H, called Compton form factor).

3.2 Study of GPD E

The measurements of DVCS and exclusive channels on polarized hydrogen allow to study the GPD E, which allows for nucleon spin flip.

The exclusive production of ρ^0 meson on a transversely polarized hydrogen target (without recoil detection) has been performed with muon data recorded at COMPASS between 2007 and 2010. Eight target spin asymmetries, depending on ϕ and ϕ_S (ϕ_S being the angle between muon scattering plane and proton polarization) have been extracted [6, 7] and successfully interpreted in terms of GPDs [8].

Among these quantities (available on Fig. 3), the $\sin(\phi - \phi_S)$ term sets a good constraint on GPDs E, confirming that the *total* contribution of E for *all* quark flavors and gluons are small [7]. The combined information of the $\sin(2\phi - \phi_S)$ and $\sin\phi_S$ terms also indicate that the chiral-odd GPD H_T should not be small.

In the future, COMPASS might also be able to measure DVCS on a transversely polarized target, with recoil proton detection. The measurement of first moment in $\phi - \phi_s$ of the charge spin cross section difference on a transversely polarized target, $\mathcal{D}_{CS,T}$, provides access to both Compton form factors $\mathcal{H}$ and $\mathcal{E}$ on the same footing. With two years of data, COMPASS could improve by a factor 2 the statistical accuracy on this quantity compared to its previous measurement by HERMES [9], [5]. This challenging prospect is still under investigation, as it is currently technically limited by the combination of a transversely polarized target (which, by order, is surrounded by a magnet) with recoil proton detection.

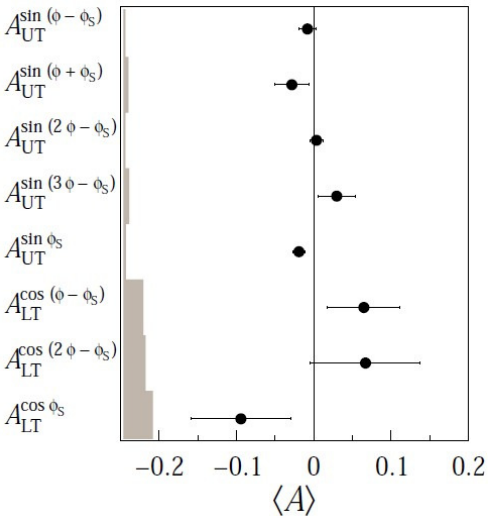

Figure 3: Target spin asymmetries on $\mu p^{\uparrow\downarrow} \to \mu p \rho^0$ measured at COMPASS [6, 7].

4 Summary

The study of the GPDs is one of the hot topics in the structure of the nucleon. The COMPASS experiment, with its unique features (Sec. 3), offers a very promising GPD program. The few existing results (Secs. 3.1 and 3.2) are very encouraging to go forward the forthcoming full DVCS run (2016-2017), which will provide a good accuracy for the measurement of several observables of interest (proton size, Compton form factor $\mathcal{H}$). The possibility to measure DVCS on transversely polarized target at COMPASS, though being a technical challenge, is also being investigated.

Acknowledgments

We would like to acknowledge the P2IO Excellence Laboratory for its financial support.

References

[1] D. Mller, D. Robaschik, B. Geyer, F.-M. Dittes and J. Hoeji, Fortsch. Phys. **42** (1994) 101 [hep-ph/9812448].

[2] A. V. Radyushkin, Phys. Rev. D **56** (1997) 5524 [hep-ph/9704207].

[3] X. D. Ji, Phys. Rev. Lett. **78** (1997) 610 [hep-ph/9603249].

[4] P. Abbon *et al.* [COMPASS Collaboration], Nucl. Instrum. Meth. A **577** (2007) 455 [hep-ex/0703049].

[5] F. Gautheron *et al.* [COMPASS Collaboration], CERN-SPSC-2010-014.

[6] C. Adolph *et al.* [COMPASS Collaboration], Phys. Lett. B **731** (2014) 19 [arXiv:1310.1454 [hep-ex]].

[7] C. Adolph *et al.* [COMPASS Collaboration], Nucl. Phys. B **865** (2012) 1 [arXiv:1207.4301 [hep-ex]].

[8] S. V. Goloskokov and P. Kroll, Eur. Phys. J. C **74** (2014) 2725 [arXiv:1310.1472 [hep-ph]].

[9] A. Airapetian *et al.* [HERMES Collaboration], JHEP **0806** (2008) 066 [arXiv:0802.2499 [hep-ex]].

Deeply pseudoscalar meson electroproduction with CLAS and Generalized Parton Distributions

Michel Guidal[1], *Valery Kubarovsky*[2]

[1]Institut de Physique Nucléaire Orsay, CNRS-IN2P3, Université Paris-Sud, France
[2]Thomas Jefferson National Accelerator Facility, Newport News, Virginia 23606

DOI: http://dx.doi.org/10.3204/DESY-PROC-2014-04/33

We discuss the recent data of exclusive π^0 (and π^+) electroproduction on the proton obtained by the CLAS collaboration at Jefferson Lab. It is observed that the cross sections, which have been decomposed in $\sigma_T + \epsilon\sigma_L$, σ_{TT} and σ_{LT} structure functions, are dominated by transverse amplitude contributions. The data can be interpreted in the Generalized Parton Distribution formalism provided that one includes helicity-flip transversity GPDs.

The formalism of Generalized Parton Distributions (GPDs) which has appeared in the last two decades (Refs. [1, 2, 3] for the original articles and Ref. [4] for a recent review) allows to interpret the exclusive electroproduction of photons or mesons on the nucleon in terms of quarks and gluons (i.e. partons), the fundamental degrees of freedom of Quantum Chromodynamics (QCD). It has been shown [5] that for these processes, at sufficiently large virtuality of the photon $Q^2 = (e-e')^2$, there is a factorization between a "hard" elementary scattering part at the quark or gluon level, exactly calculable in perturbative QCD, and a non-perturbative nucleon structure part, which encodes all the complex partonic structure of the nucleon and which is parametrized by GPDs. This factorization is illustrated in Fig. 1 for the case of π^0 electroproduction on the proton, on which we will focus in this article. For pseudoscalar meson production, it is shown that, at leading-twist QCD, this factorization is valid only for longitudinal incoming photons, that the longitudinal part of the cross section σ_L should dominate at asymptotically large Q^2 valuse and that two quark helicity-conserving GPDs contribute to the process: $\tilde{H}$ and $\tilde{E}$. These two GPDs correspond to the amplitudes where the nucleon spin remains unchanged or has been flipped respectively. At QCD leading-order, the GPDs depend on three independent variables: x, ξ and t. In simple terms, GPDs represent, in a frame where the nucleon goes to the speed of light in a certain direction, the probability amplitude of finding a quark in the nucleon with a longitudinal momentum fraction $x+\xi$ and of putting it back

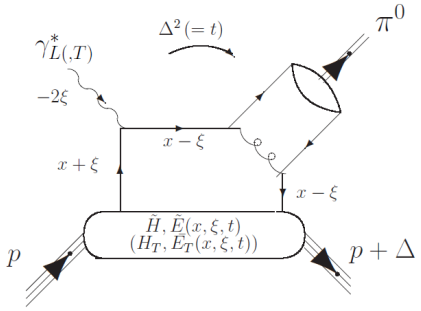

Figure 1: The "handbag" diagram for exclusive π^0 electroproduction on the proton in terms of GPDs. When longitudinal photons are involved, only the helicity-conserving GPDs $\tilde{H}$ and $\tilde{E}$ enter, while for transverse photons, the helicity-flip GPDs H_T and $\tilde{E}_T$ also enter the process. The various kinematical variables are explained in the text.

into the nucleon with a different longitudinal momentum fraction $x - \xi$, plus some transverse momentum "kick", which is represented by t. For the particular case of $\xi = 0$, the momentum transfer Δ (with $\Delta^2 = t$) is the conjugate variable of the impact parameter $b_\perp$ so that the GPDs encode both the longitudinal momentum distributions of partons inside the nucleon through their dependence on x and their transverse position distributions through their dependence on t. This allows for a sort of tomography of the nucleon where one can probe the transverse size of the nucleon for different quark momentum slices.

Recently, the CLAS collaboration has measured at Jefferson Lab with a 5.75-GeV electron beam the 4-fold differential cross sections $d^4\sigma/dtdQ^2dx_Bd\phi_\pi$ [1] of the $ep \to ep\pi^0$ reaction, thus extracting the structure functions $\sigma_T + \epsilon\sigma_L, \sigma_{TT}$ and σ_{LT} as functions of t over a wide range of Q^2 and x_B [6]. Fig. 2 shows a sample of these results (1800 kinematic points in bins of Q^2, x_B, t and ϕ_π were measured in all). These results are in agreement with the results of Ref. [7], which published high accuracy cross sections in a limited kinematical range in the lower Q^2, W and $|t|$ regions of the present experiment. One observes that the $d\sigma_{TT}/dt$ structure function (which is negative) is comparable in magnitude with the unpolarized structure function $d\sigma_U/dt = d\sigma_T/dt + \epsilon d\sigma_L/dt$). Furthermore, $d\sigma_{LT}/dt$ is small in comparison with $d\sigma_U/dt$ and $d\sigma_{TT}/dt$. In the same vein, in an earlier CLAS measurement [8], sizeable beam-spin asymmetries (proportional to the fifth structure function $\sigma_{LT'}$), were found for this same channel. Such non-zero asymmetries imply that both transverse and longitudinal amplitudes participate in the process. Similarly, at higher energies, the HERMES collaboration measured the transverse target spin asymmetry in the "cousin" channel of π^+ electroproduction [9]. The sizeable results can also only be explained by significant transverse amplitude contributions.

All these experimental observations point to the model-independent conclusion that the asymptotic leading-order handbag approach for which the longitudinal part of the cross section is dominant is not applicable at the present values of Q^2. Although model-dependent, this is confirmed by theoretical calculations of the handbag diagram for longitudinal virtual photons based solely on the $\tilde{H}$ and $\tilde{E}$ GPDs which are found to underestimate the measured cross sections by more than an order of magnitude, even after including finite–size corrections through Sudakov form factors[10].

This failure to describe these experimental results for exclusive pseudo-scalar meson electroproduction with quark helicity-conserving GPDs recently stimulated the consideration of the role of the chiral-odd quark helicity-flip contributions (i.e. where the active quark in Fig. 1 undergoes a helicity-flip), in particular through the introduction of so-called transversity GPDs; namely: H_T, which characterizes the quark distributions involved in nucleon helicity-flip, and $\bar{E}_T (= 2\widetilde{H}_T + E_T)$ which characterizes the quark distributions involved in nucleon helicity-non-flip processes [11, 12].

Pseudoscalar meson electroproduction, and in particular π^0 production, was identified [10, 13, 14] as especially sensitive to the quark helicity-flip subprocesses. The produced meson has no intrinsic helicity so that the angular momentum of the incident photon is either transferred to the nucleon via a quark helicity-flip or involves orbital angular momentum processes. In addition, for π^0 production the structure of the amplitudes further suppresses the quark helicity-conserving amplitudes relative to the helicity-flip amplitudes [10].

The results of two GPD-based models which include transversity GPDs [14, 15] are superimposed in Fig. 2. The GL and GK approaches, though employing different models of GPDs,

[1] The standard x_B Bjorken variable is related to ξ: $\xi \simeq x_B/(2 - x_B)$ and ϕ_π is the azimuthal angle between the leptonic and hadronic planes.

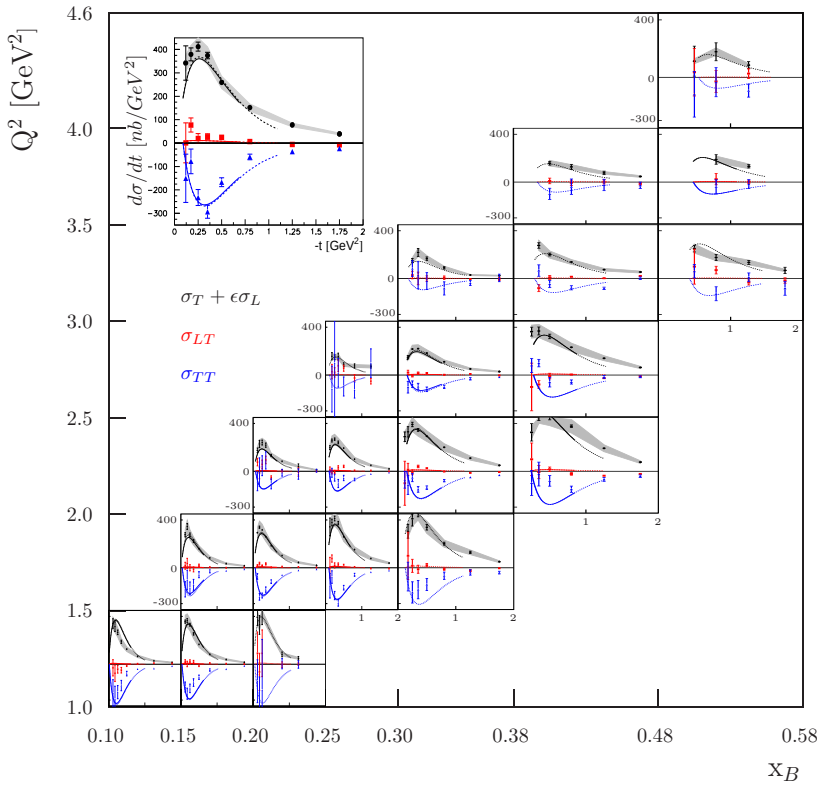

Figure 2: The extracted structure functions vs. t as measured by CLAS. The data and curves are as follows: black (filled circles) - $d\sigma_U/dt = d\sigma_T/dt + \epsilon d\sigma_L/dt$, blue (triangles) - $d\sigma_{TT}/dt$, and red (squares) - $d\sigma_{LT}/dt$. The curves are theoretical predictions produced with the models of Refs. [14] (solid) and [15] (dashed).

lead to transverse photon amplitudes that are much larger than the longitudinal amplitudes. These latter account for only a small fraction (typically less than 10%) of the unseparated structure functions $d\sigma_T/dt + \epsilon d\sigma_L/dt$ in the kinematic regime under investigation. With such inclusion of the quark-helicity non-conserving chiral-odd GPDs, which contribute primarily to $d\sigma_T/dt$ and $d\sigma_{TT}/dt$ and, to a lesser extent, to $d\sigma_{LT}/dt$, the model of Ref. [14] agrees rather well with the data. Deviations in shape become greater at smaller $-t$ for the unseparated cross section $d\sigma_U/dt$. The behavior of the cross section as $|t| \to |t|_{min}$ is determined by the interplay between H_T and $\bar{E}_T$. For the GPDs of Ref. [14] the parameterization was guided by the lattice calculation results of Ref. [12], while Ref. [15] used a GPD Reggeized diquark-quark model to obtain the GPDs. The results in Fig. 2 for the model of Ref. [14] (solid curves), in which $\bar{E}_T$ is dominant, agree rather well with the data. In particular, the structure function σ_U begins to decrease as $|t| \to |t|_{min}$, showing the effect of $\bar{E}_T$. In the model of Ref. [15] (dashed curves) H_T is dominant, which leads to a large rise in cross section as $-t$ becomes small so that the contribution of $\bar{E}_T$ relative to H_T appears to be underestimated. One can make a similar conclusion

from the comparison between data and model predictions for σ_{TT}. This shows the sensitivity of the measured π^0 structure functions for constraining the transversity GPDs.

We also mention that π^+ electroproduction has also been measured by the CLAS collaboration [16] in the same phase space. It is found that the GK model describes also qualitatively the low-t unseparated cross sections over the whole (x_B, Q^2) domain, when the same transversity GPDs are included. In π^+ production, the role of transversity GPDs is less apparent because of the presence and dominance of the longitudinal π^+-pole term (which is absent in π^0 production). However, this latter contribution has an important contribution only in the low $|t|$ domain and only for the lowest x_B and the largest Q^2 values, leaving sensitivity to other contributions, namely transversity GPDs.

In conclusion, differential cross sections of exclusive π^0 (and π^+) electroproduction on the proton have been obtained in the few-GeV region in a wide Q^2, x_B, t, ϕ_π phase space with the CLAS detector at JLab, from which the structure functions $d\sigma_U/dt$, $d\sigma_{TT}/dt$ and $d\sigma_{LT}/dt$ could be extracted. It is found that $d\sigma_U/dt$ and $d\sigma_{TT}/dt$ are comparable in magnitude with each other, while $d\sigma_{LT}/dt$ is very much smaller than either pointing to the dominance of transverse amplitude contributions to the process.

Within the handbag interpretation, there are two independent theoretical calculations [14, 15] which confirm that the measured unseparated cross sections are much larger than expected from leading-twist handbag calculations which are dominated by longitudinal photons. When including transversity GPDs, the general shapes and magnitudes of the various structure functions are reproduced. Extensive new CLAS measurements of beam spin, target spin and double-spin asymmetries for exclusive pseudo-scalar electroproduction on the proton are currently under analysis. Comparison of these results with theoretical models will allow to confirm (or not) the GPDs interpretations that we have outlined here.

This material is based upon work supported by the U.S. Department of Energy, Office of Science, Office of Nuclear Physics under contract DE-AC05-06OR23177.

References

[1] D. Mueller, D. Robaschik, B. Geyer, F. M. Dittes and J. Horejsi, Fortsch. Phys. **42** (1994) 101.

[2] X. D. Ji, Phys. Rev. Lett. **78** (1997) 610, Phys. Rev. D **55** (1997) 7114.

[3] A. V. Radyushkin, Phys. Lett. B **380** (1996) 417, Phys. Rev. D **56** (1997) 5524.

[4] M. Guidal, H. Moutarde and M. Vanderhaeghen, Rept. Prog. Phys. **76** (2013) 066202.

[5] J. C. Collins, L. Frankfurt and M. Strikman, Phys. Rev. D **56** (1997) 2982.

[6] I. Bedlinskiy *et al.* [CLAS Collaboration], arXiv:1405.0988 [nucl-ex].

[7] E. Fuchey, A. Camsonne, C. Munoz Camacho, M. Mazouz, G. Gavalian, E. Kuchina, M. Amarian and K. A. Aniol *et al.*, Phys. Rev. C **83** (2011) 025201.

[8] R. De Masi *et al.* [CLAS Collaboration], Phys. Rev. C **77** (2008) 042201.

[9] A. Airapetian *et al.* [HERMES Collaboration], Phys. Lett. B **682** (2010) 351.

[10] S. V. Goloskokov and P. Kroll, Eur. Phys. J. C **65** (2010) 137.

[11] M. Diehl and P. Hagler, Eur. Phys. J. C **44** (2005) 87.

[12] M. Gockeler *et al.* [QCDSF and UKQCD Collaborations], Phys. Rev. Lett. **98** (2007) 222001.

[13] S. Ahmad, G. R. Goldstein and S. Liuti, Phys. Rev. D **79** (2009) 054014.

[14] S. V. Goloskokov and P. Kroll, Eur. Phys. J. A **47** (2011) 112.

[15] G. R. Goldstein, J. O. Hernandez and S. Liuti, Phys. Rev. D **84** (2011) 034007, Int. J. Mod. Phys. Conf. Ser. **20** (2012) 222, J. Phys. G **39** (2012) 115001.

[16] K. Park *et al.* [CLAS Collaboration], Phys. Rev. C **85** (2012) 035208.

New JLab/Hall A Deeply Virtual Compton Scattering results

Maxime Defurne[1] for the Hall A DVCS collaboration

[1]CEA, Centre de Saclay, IRFU/SPhN/LSN, F-91191 Gif-sur-Yvette, France

DOI: http://dx.doi.org/10.3204/DESY-PROC-2014-04/32

New data points for unpolarized Deeply Virtual Compton Scattering cross sections have been extracted from the E00-110 experiment at Q^2=1.9 GeV^2 effectively doubling the statistics available in the valence region. A careful study of systematic uncertainties has been performed.

Generalized Parton Distributions (GPDs) correlate the spatial and momentum distributions of partons inside the nucleon. They are nowadays the main way to study the orbital angular momentum of quarks via the Ji's sum rule. As GPDs are accessible through deep exclusive processes, a worldwide experimental program has been developped to study them [1]. Experiment E00-110 has been designed to investigate the electroproduction of photons ($ep \rightarrow ep\gamma$). Beam helicity dependent cross sections at x_B=0.36 and Q^2 = {1.5,1.9,2.3} GeV^2 have been published by Munoz *et al.* in 2006 [2]. An additional unpolarized cross section at the highest value of Q^2 was extracted at 2.3 GeV^2. Here we present the extraction of the unpolarized cross section at the intermediate Q^2= 1.9 GeV^2.

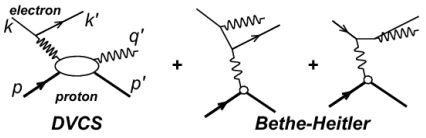

Figure 1: Lowest order QED diagrams for DVCS and Bethe Heilter processes. Defining $q = k - k'$, Q^2=$-|q|^2$ and t=$|p - p'|^2$. x_B is given by $\frac{Q^2}{2p \cdot q}$.

1 Phenomenological framework

Photon electroproduction in the deep inelastic kinematics includes the coherent contribution of Bethe-Heitler, where the photon is emitted by the incoming or scattered electron, and Deeply Virtual Compton Scattering (DVCS) where the photon is emitted by the proton (see figure 1). The amplitude for DVCS is parametrized by Compton form factors (CFF) which are complex integral of GPDs. The interference between these two processes makes the photon electroproduction a golden channel because it gives access to the real and imaginary parts of CFFs. Kumericki and Muller [3] performed a Fourier expansion of the different contributions according to ϕ, the angle between the leptonic and the hadronic plane. The information about the GPD is embedded in the Fourier coefficients of the DVCS amplitude and the interference term. The

amplitude of photon electroproduction $A_{ep\to ep\gamma}$ is given by:

$$\begin{aligned} |A_{ep\to ep\gamma}|^2 &= |A_{DVCS}|^2 + |A_{BH}|^2 + I_{BH/DVCS}, \text{ with} \\ |A_{DVCS}|^2 &\propto c_0^{DVCS} + \sum_{n=1}^{2} \Big(c_n^{DVCS} cos(n\phi) + s_n^{DVCS} sin(n\phi) \Big) \\ I_{BH/DVCS} &\propto c_0^{I} + \sum_{n=1}^{2} \Big(c_n^{I} cos(n\phi) + s_n^{I} sin(n\phi) \Big) \end{aligned} \tag{1}$$

Indeed c_n^{DVCS} and s_n^{DVCS} (respectively c_n^I and s_n^I) are bilinear (respectively linear) combinations of CFFs. The amplitude of the Bethe Heitler is exactly known assuming a reliable parameterization of the form factors of the nucleon. The beam helicity independent cross section is mostly sensitive to $\mathcal{H}\mathcal{H}^*$ and Re$\mathcal{H}$, and the difference of beam helicity dependent cross sections to Im$\mathcal{H}$.

2 Experimental setup

The experiment ran in the Hall A of Jefferson Laboratory [4] in the spring of 2004, using the 80%-polarized 5.75 GeV continuous electron beam provided by CEBAF impinging on a 15-cm long liquid hydrogen target. The left high resolution spectrometer was dedicated to the scattered electron detection.

A dedicated electromagnetic calorimeter made of $11 \times 12 = 132$ lead fluoride blocks read by photomultiplier tubes (PMTs) was used to detect the outgoing photon.

A recoil detector was built for the proton detection but it was demonstrated that a cut on the squared missing mass associated to the reaction $ep \to e\gamma X$ was enough to ensure the exclusivity. As the proton detector was limiting the acceptance, it was not used in this analysis.

3 Subtraction of π^0 contamination

In their center-of-mass frame, π^0 isotropically decay into two photons, emited back-to-back. While, in the laboratory frame, due to the directionality of the Lorentz boost, the decay photons share the energy asymetrically in most cases. As a result, one of them may get most of the energy and the other one almost nothing, impossible to detect because of the 1 GeV threshold imposed on the calorimeter. In that case, as exclusive π^0 have an energy close to the one of an exclusive photon, we will interpret it as an exclusive photon.

To subtract this contamination, The sample of π^0's whose two photons have been detected is used. Knowing their 4-momenta, we simulate their decay N_{gen}=5000 times thanks to a Monte Carlo simulation. Among the N_{gen} decays, there are:

- n_0 events where none of the photons have been detected, or only one photon detected but with an associated missing mass not compatible with an exclusive photon event.
- n_2 events where the two photons are detected.
- n_1 events where one photon is detected with a missing mass compatible with an exclusive photon event.

For each of the n_1 decays, the kinematic variables t, ϕ are computed as if it was an exclusive photon event. Then this event is considered with the weight $\frac{1}{n_2}$ in the corresponding experimental bin. At the end of the day, the contamination is estimated in all the experimental bins.

This method naturally includes the π^0 electroproduction cross section in the subtraction. Since it relies strongly on our ability to detect the two photons of the decay, we apply a geometrical cut on the calorimeter surface to remove its edges and corners.

4 Monte Carlo simulation

The Monte Carlo simulation has been upgraded to Geant4. Radiative corrections are applied following the method described in [5]. Emission of soft photons from internal bremmstrahlung is handled using the equivalent radiator method.

Because of radiation damage, blocks close to the beam have a poorer energy resolution than the ones far from the beam. As a consequence, the exclusivity peak in the $M^2_{ep\to e\gamma X}$ will be larger close to the beam than far from it. Since binning in t and ϕ translates into geometrical cuts in the calorimeter, it is vital to have a good match between the Monte Carlo and the experimental missing mass spectrum.

To estimate the error due to the exclusivity cut, we studied the cross section variations when changing the missing mass cut.

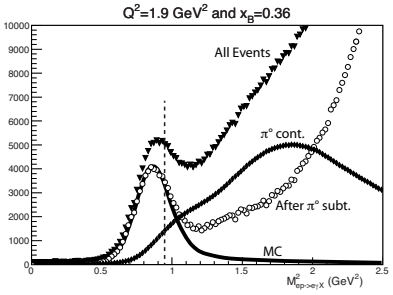

Figure 2: Missing mass spectrum associated to $ep \to e\gamma X$. To ensure exclusivity, we require a value below 0.95 GeV^2.

5 Cross section and CFF extraction

Using the formalism developped in [3], we parameterize the cross section in terms of CFFs. However there are too many unknowns with respect to our data. By assuming twist-2 dominance and a sizeable $|DVCS|^2$ contribution (as hinted in [2]), we end up using three parameters in order to fit each data bin in ϕ and t (equation 4). We studied 5 bins in t, each of them with 24 bins in ϕ, giving a total number of bins N_{bin}=120.

To fit each of the 5 t-bins, we minimize the following χ^2:

$$\chi^2 = \sum_{k=0}^{N_{bin}} \left(\frac{N_k^{exp} - N_k^{sim}}{\sigma_k^{exp}} \right)^2 \tag{2}$$

where N_k^{exp} is the number of counts in bin k from data after subtraction of contamination, and σ_k^{exp} represents the statistical uncertainty on the number of counts in the bin k. N_k^{sim} the

number of counts in the bin k expected with the Monte Carlo simulation and is given by:

$$N_k^{sim} = L \int_{\Phi_k} \frac{d^4\sigma}{d\Phi} d\Phi_k, \quad (3)$$

$$\frac{d^4\sigma}{d\Phi} = \frac{d^4\sigma_{BH}}{d\Phi} + \Gamma^{\mathcal{C}^{DVCS}_{unp}} \times \mathcal{C}^{DVCS}_{unp} + \Gamma^{\mathcal{C}^I(\mathcal{F})} \times Re\mathcal{C}^I(\mathcal{F}) + \Gamma^{\mathcal{C}^I(\mathcal{F}_{eff})} \times Re\mathcal{C}^I(\mathcal{F}_{eff}), \quad (4)$$

with L the integrated luminosity of the experiment and Φ_k the phase space of the experimental bin.

The coefficients Γ in equation 4 are given by [3] and depend on ϕ, t, x_B and Q^2. Their integral is performed using the Monte Carlo simulation and help us to take into account most of the kinematic dependences. Finally, by evaluating the coefficients Γ at the vertex and applying selection cuts on the variables reconstructed by the detectors, we correct for bin migration.

At the end of the day, we obtain unpolarized photon electroproduction cross sections at x_B=0.36 and Q^2=1.9 GeV^2. The photon electroproduction cross sections will be published at the end of the year 2014.

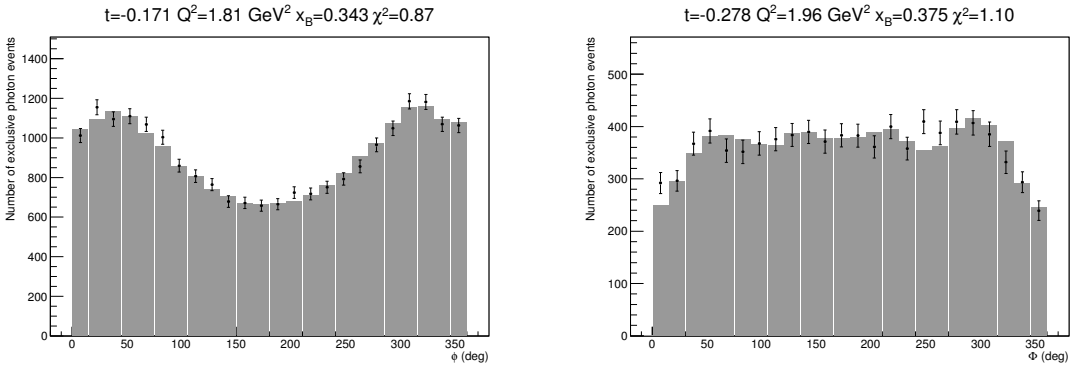

Figure 3: The markers are the number of counts from experiment. The histograms represent the number of counts expected by the Monte Carlo simulation once the cross section has been extracted by the fitting procedure.

References

[1] M. Guidal, H. Moutarde, and M. Vanderhaeghen, "Generalized Parton Distributions in the valence region from Deeply Virtual Compton Scattering," *accepted in Rep. Prog. Phys.*, vol. 76, 2013.

[2] C. Muñoz Camacho *et al.*, "Scaling tests of the cross-section for deeply virtual compton scattering," *Phys.Rev.Lett.*, vol. 97, p. 262002, 2006.

[3] A. Belitsky and D. Mueller, "Exclusive electroproduction revisited: treating kinematical effects," *Phys.Rev.*, vol. D82, p. 074010, 2010.

[4] J. Alcorn *et al.*, "Basic instrumentation for hall a at jefferson lab," *Nucl. Instrum. Meth.*, vol. A522, pp. 294–346, 2004.

[5] M. Vanderhaeghen, J. M. Friedrich, D. Lhuillier, D. Marchand, L. Van Hoorebeke, and J. Van de Wiele, "Qed radiative corrections to virtual compton scattering," *Phys. Rev.*, vol. C62, p. 025501, 2000.

COMPASS Polarized Target for Pion-Induced Drell–Yan Experiment

Jan Matoušek[1] on behalf of the COMPASS collaboration

[1]Charles University, Faculty of Mathematics and Physics, Prague, Czech Republic

DOI: http://dx.doi.org/10.3204/DESY-PROC-2014-04/35

The first ever polarized Drell–Yan (DY) measurement is under preparation at COMPASS experiment at CERN. One of the key parts is the low-temperature polarized target. Modifications are required to cope with the intense pion beam that will be used. Solid NH_3 will serve as a transversely-polarized target. Polarization is expected to be up to 90%. Two 55 cm long target cells give the target volume of about 690 cm^3. The data taking is expected to start on fall 2014 and to continue in 2015 (approximately 180 days). Current status of the target, the modifications and future plans are presented.

1 Introduction

COMPASS [1] is a fixed-target experiment situated at CERN Super Proton Synchrotron (SPS) North Area. For physics data taking it uses either hadron or muon beams[1]. The beam interacts with a target, which can be polarized. COMPASS detector is a universal spectrometer with good particle tracking and identification capability.

COMPASS experiment focuses on spin structure studies and hadron spectroscopy [2]. The first ever measurement of a single-polarized Drell–Yan (DY) process using a pion beam and a transversely-polarized proton target was proposed [3]. Its goal is to test some crucial predictions of QCD, namely a change of sign of the Sivers and Boer–Mulders TMDs when measured in Semi-Inclusive Deep-Inelastic Scattering (SIDIS) and in DY processes.

As the DY cross section is small, the luminosity should be as high as possible. In the case of COMPASS this corresponds to the beam intensity of about 10^8 pions/s. That is the highest hadron beam intensity COMPASS has used so far, which leads to several challenges for the detection, data acquisition and the polarized target.

2 Polarized target

The low-temperature polarized target [1, 4] is a key instrument for COMPASS spin structure studies. It is one of the biggest systems of its kind in the world[2] and can provide degree of polarization higher than 80% in the case of H in NH_3 and 50% in the case of D in ^{6}LiD [5].

[1]Produced by proton beam from the SPS hitting a Be target. The beam can be either positive or negative with momentum up to 280 GeV/c. Muons are naturally longitudinally polarized.

[2]The target volume has cylindrical shape with about 4 cm in diameter and is about 120 cm long.

The target material is polarized by Dynamic Nuclear Polarization (DNP) method [6] at about 0.5 K. When the optimal polarization is reached, the target is switched to a *frozen spin* mode at about 50 mK. A long spin-lattice relaxation time at such temperature (in order of 10^3 hours) allows to perform reasonably efficient experiment. Two microwave systems for DNP allow to have target cells with opposite polarization to reduce systematic errors in measured asymmetries.

The polarization is measured by a continuous-wave NMR. The cooling is provided by a dilution refrigerator, which has a power of about 5 mW at 75 mK [7]. A large-aperture superconducting magnet provides a field up to 2.5 T parallel and 0.64 T perpendicular to the beam axis. Homogeneity of the longitudinal field is about 10^{-5} T. Combination of the two fields allows measurement with transverse polarization and polarization rotation.

3 Drell–Yan program at COMPASS

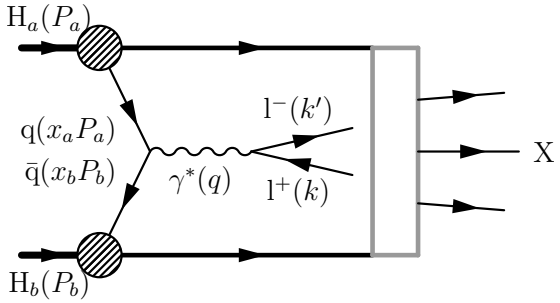

Figure 1: The Drell–Yan process. A quark-antiquark pair from the two hadrons annihilate, producing a lepton-antilepon pair in final state. The grey box denotes hadronization.

The Feynman graph on Fig. 1 shows the Drell–Yan (DY) process, which has lately attracted much attention as a tool for polarized hadron structure studies. Its main advantage is that only leptons are measured in the final state, which means that the cross section does not involve any fragmentation function but only convolution of structure functions of both hadrons. The process is well calculable, dedicated calculations of the pion-induced DY process for the COMPASS kinematics were recently published [8].

The disadvantage of the DY process is a small cross section. To collect a good statistics a beam with intensity up to 10^8 pions/s will be used resulting in a large secondary-hadron flux. A special hadron absorber was designed to stop the non-interacting beam and all secondary particles except muons right after the target to avoid a spectrometer flooding-up [3]. It is made of stainless steel and alumina, with a tungsten beam plug in the centre to stop the beam.

The high intensity pion beam together with the hadron absorber will cause slightly higher radiation dose in the experimental building than in previous runs. Because of that the control room will be moved to another building.

4 Modifications of the target for the DY program

The DY program, namely the intense hadron beam and the presence of the absorber brought need for modification of the target. New target cells were made. There are two cells (4 cm in diameter, 55 cm long) with 20 cm long microwave stopper in between[3]. The gap between the cells prevents event migration between oppositely-polarized cells. It is wider than in the SIDIS runs since the hadron absorber introduces significant multiple scattering, which worsens the vertex resolution. A special adapter was designed for the microwave cavity to accommodate two cells with one stopper instead of two.

The NMR system for polarization measurement has 10 coils. Three coils are placed outside of each cell and are oriented for measurement in the longitudinal field. Two coils are placed inside each cell near the ends for polarization homogeneity monitoring.

The target superconducting magnet was refurbished by CERN magnet group. In addition to the fixed trim coils it got various upgrades, e. g. better thermal insulation and new control and safety system.

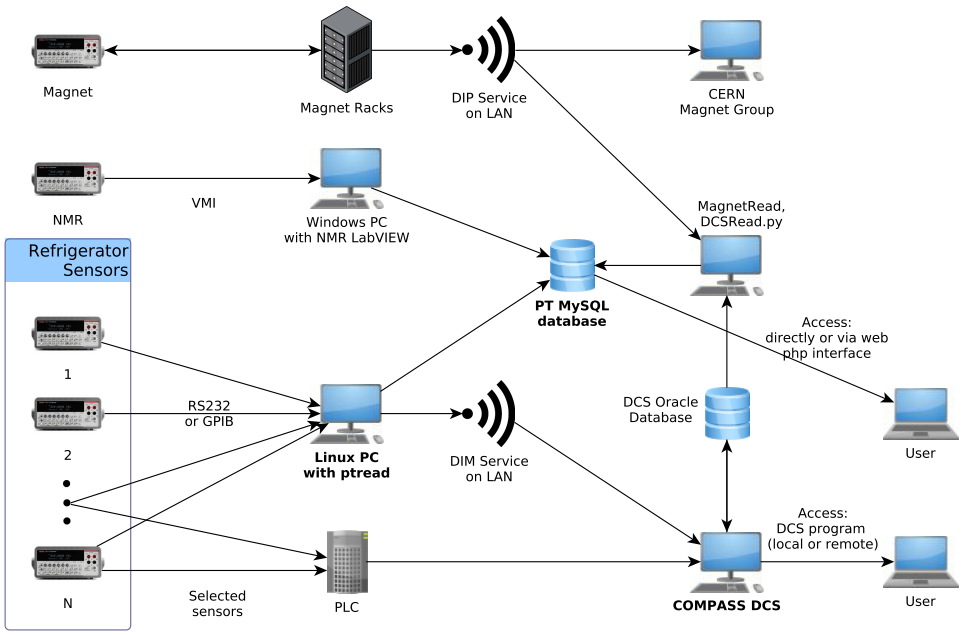

Figure 2: Diagram of target monitoring. The Linux computer with ptread package reads refrigerator sensors. Data can be stored locally in SQLite database, sent to MySQL database and published by DIM server for COMPASS DCS. The magnet is monitored by CERN experts and NMR by a LabVIEW^{TM} program.

Since the control room was moved from the experimental building, a remote control is necessary. For most systems the current COMPASS centralised Detector Control System (DCS) was working well, but the dilution refrigerator was only partly monitored by it. It was decided

[3]The SIDIS design was three cells (30-60-30 cm long, 4 cm in diameter) with 5 cm long stoppers.

to abandon the old LabVIEW^{TM} system [9] for refrigerator monitoring and to develop a new, more robust, Linux-based software called *ptread* instead. It can communicate with the DCS using DIM library [10] and insert data into MySQL and SQLite databases. These features are important for the remote monitoring. The main advantage is that the software package is modular and easily adjustable. Figure 2 shows how various subsystems of the target (including the refrigerator) are monitored.

In addition to the *ptread* PC there is a Programmable Logic Controller (PLC) unit that monitors the most important parameters of the refrigerator [9]. It is powered from a source insensitive to power failures.

5 Conclusion

The magnet was refurbished and is being cooled down and commissioned. Dilution refrigerator was tested and mounted in place. Its sensors are connected to the new Linux-based monitoring system. The new target cells are ready. The target will be prepared for the physics data taking, that is scheduled from the beginning of November 2014. Second run is planned for 2015. In total there should be about 180 days of data taking.

Acknowledgements

This work was supported in part by the European Community-Research Infrastructure Activity under the FP7 programme (Hadron Physics 3), Czech Republic MEYS grants.

References

[1] P. Abbon *et al.*, NIM **A 577** 455 (2007).

[2] The COMPASS Collaboration, *List of COMPASS publications*, `http://wwwcompass.cern.ch/compass/publications/`

[3] The COMPASS Collaboration, *COMPASS-II Proposal*, CERN SPSC **014** 340 (2010).

[4] J. H. Koivuniemi *et al.*, JPCS **150** 012023 (2009).

[5] K. Kondo *et al.*, NIM **A 526** 70 (2004).

[6] A. Abragam, M. Goldman, Rep. Prog. Phys. **41** 395 (1978).

[7] N. Doshita *et al.*, NIM **A 526** 138 (2004).

[8] M. Aicher, A. Schäfer and W. Vogelsang, Phys. Rev. **D 83** 114023 (2011).

[9] F. Gautheron *et al.*, NIM **A 526** 147 (2004).

[10] C. Gaspar *et al.*, *Distributed information management system*, `http://dim.web.cern.ch/dim/`.

Soft QCD Measurements at LHCb

A. T. Grecu on behalf of the LHCb Collaboration

Horia Hulubei National Institute for Physics and Nuclear Engineering (IFIN-HH),
30 Reactorului, RO-077125, Bucharest-Măgurele, Romania

DOI: http://dx.doi.org/10.3204/DESY-PROC-2014-04/249

Its forward acceptance puts the LHCb in a unique position at the LHC to measure soft QCD phenomena at large rapidities and low transverse momenta. Recent results on charged particle multiplicities, energy flow, and inclusive cross-sections are presented.

1 The LHCb experiment at LHC

The LHCb experiment at LHC was designed to test the flavour aspect of the Standard Model through precision measurements of rare b and c hadron decays [1]. The LHCb detector [2] is built as a single arm forward spectrometer fully instrumented for measurements in the forward pseudorapidity (η) region $2 < \eta < 5$. The primary pp interaction region is located within a silicon-strip vertex detector (VELO) which allows reconstruction of tracks without momentum information also in the backward pseudorapidity interval $-3.5 < \eta < -1.5$. The high-precision tracking system [3] continues with a large area silicon tracker located upstream of a magnetic dipole with a bending power of 4 Tm and three stations of silicon-strip detectors and straw drift tubes situated downstream of the magnet. A calorimetry system is used to measure the neutral component and muons are detected by a dedicated system of alternating layers of iron and multi-wire proportional chambers [4]. The LHCb experiment is operated at a low and consistent number of visible proton-proton (pp) interactions.

Monte Carlo (MC) simulated events were used to compute detection efficiencies, estimate systematic uncertainties and compare model predictions with respect to the measurements. Full simulation samples are produced using PYTHIA6.4 [6] configured according to established tunes [7] or the LHCb specific tune [8].

2 Vector meson central exclusive production

Exclusive vector meson photoproduction provides a rich testing ground for QCD. At high meson masses the process can be predicted using perturbative calculations [9]. The light meson production is best described in the frame of the Regge theory [10]. The elastic pp interaction is mediated by the exchange of a colourless object such as a gamma photon or a pomeron, which is replaced by two gluons at hard scales. The colliding protons propagate undetected in the beam pipe. Here, we review the central elastic exclusive production of the J/ψ and $\psi(2S)$ vector mesons decaying to two muons [11] as an update of a previous measurement [12] where a smaller data sample was analysed. The main difference is in the method for determining the background due to production of J/ψ and $\psi(2S)$ mesons in inelastic pp collisions where

the additional particles leave the LHCb acceptance and remain undetected. This is the main source of background. It is determined from a fit of the squared momentum of the muon pair (p_T^2) distribution that follows closely HERA measurement [13] extrapolations according to Regge theory. Additional non-resonant background (muon pairs created in the QED process) is estimated from side-bands in the invariant mass spectrum and feed down background from exclusive production of heavier meson decays is evaluated from simulation. The cross-section times the branching fraction of the decay mode to two muons, each inside the LHCb fiducial range ($2.0 < \eta_{\mu^\pm} < 4.5$), is in good agreement with various theoretical predictions. Figure 1 shows the comparison to the LO and NLO predictions from a fit on a combined HERA and LHCb data sample. The NLO prediction tends to better reproduce the differential cross-section shape in data.

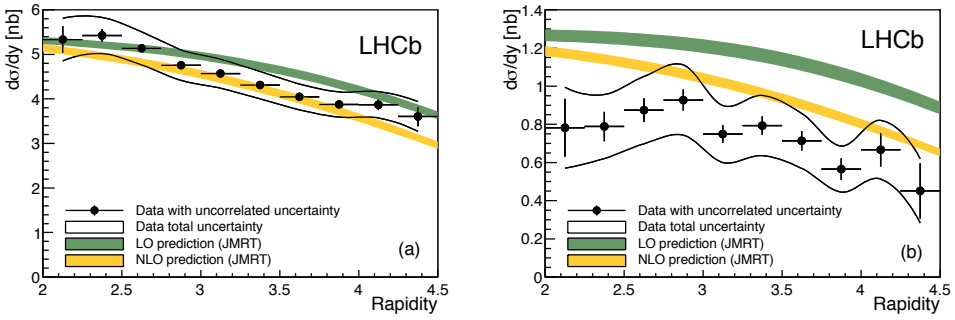

Figure 1: Differential cross-section for (a) J/ψ and (b) $\psi(2S)$ central exclusive production compared to LO and NLO predictions of [14]. The bands indicate the total uncertainties which are mostly correlated between bins. Errors bars contain only the statistical uncertainty.

The measured photoproduction cross-section shows a deviation from the power law established at HERA [15] which can be accounted to higher order or saturation effects. In the low parton fractional momentum (x) domain accessible to the LHCb detector saturation effects manifest due to gluon recombination. Thus, theoretical saturation models can be constrained by measurement through their dependence on the gluon parton density function. The considered models [16] are found in good agreement with the LHCb data.

3 Energy flow and charged particle multiplicities

The final state of an inelastic hadron-hadron collision can be described in QCD as the combined effect of hard and soft scattering processes of the hadron constituents, initial- and final-state radiation and the fragmentation of coloured final state into colour-neutral hadrons. While the hard scattering is well predicted by perturbative QCD, the theoretical modelling of the soft component, also called the underlying event (UE), remains a challenge. The phenomenological approach to this issue is done differently in various generators leading to model parameters to be constrained by experiment for specific beam particles and energies. Recently, LHCb studied two basic observables describing the UE in the forward region, the energy flow [17] which is sensitive to the multi-parton interactions arising especially at low x where the parton densities are high, and the prompt charged particle multiplicities and densities [18, 19] as physical quantities characterizing the overall UE activity.

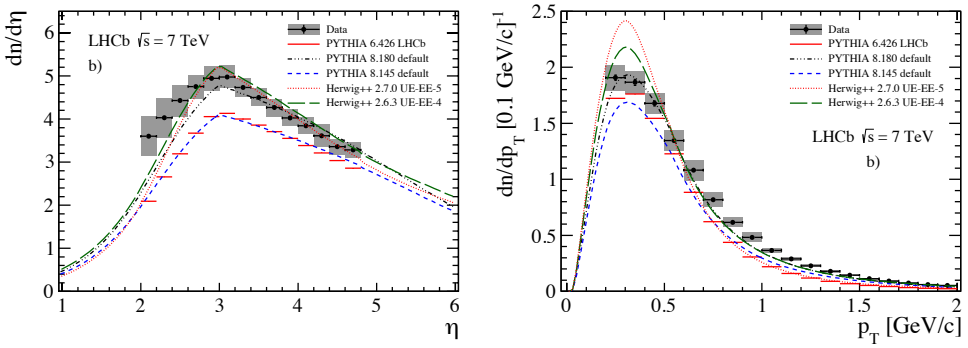

Figure 2: Charged particle density as function of (left) η and (right) p_T compared to PYTHIA8 and HERWIG++ predictions. Error bars represent the statistical negligible uncertainty. Grey bands give the extent of the combined uncertainties.

The energy flow is defined as the average energy created in a particular η range normalised by the range size. The charged forward energy flow measurement was performed using only tracking information, approximating the energy with the value of the momentum. The total energy flow is computed using data-constrained estimates from simulation corrected with informations from the calorimeter system to get the neutral component. The events are split in four classes: inclusive minimum bias, hard scattering with at least one high p_T track, diffractive enriched events requiring that there be no track in the backward region ($-3.5 < \eta < -1.5$) and the alternative non-diffractive enriched ones. Corrections are done in each η bin using MC. The dominant uncertainties come from the simulation model uncertainty on the bin-by-bin correction factors. The energy flow distributions are compared to the predictions of a series of PYTHIA tunes [7, 20] and cosmic-ray interaction models [21]. PYTHIA 8.135 emulates best the data in all event classes except for the hard scattering interactions. Among the cosmic-ray interaction models SYBILL closely follows the PYTHIA8 behaviour. The hard scattering events are better described by QGSJET. Experimental uncertainties are lowest in the forward region where the largest divergences between models are seen. This aspect confirms the energy flow as an important observable for generator tuning.

The measurement of charged particle multiplicities and densities follows closely a previously published measurement [18] adding the measurement of momentum. Prompt charged particles are defined as particles originating from PV or a decay chain in which the sum of the mean lifetimes is below 10 ps, thus the decay products of b and c hadrons are prompt. Only events with at least one track in $2.0 < \eta < 4.8$ having $p_T > 0.2$ GeV/c and $p > 2$ GeV/c are considered. Furthermore only tracks traversing the full tracking system are included in the analysis. The analysis kinematic range is $0.2 < p_T < 2.0$ GeV/c; $2.0 < \eta < 4.5$. Distributions are corrected in each bin for reconstruction artefacts and non-prompt particle contamination, the effect of unobserved events especially at low multiplicities, pile-up events and various other detection inefficiencies. The systematic uncertainties are dominated by the uncertainty on the amount of detector material contributing to the production of non-prompt particles.

Charged particle densities and multiplicities are compared to estimates obtained for various PYTHIA6 tunes and PHOJET [22] which fail to match the magnitude of the distributions. Overall data shape is well described qualitatively by all the generators including PYTHIA8 and HERWIG++ [23] tuned to central region measurements (see Fig. 2). Never-

theless, HERWIG++ largely overestimates at low p_T and PYTHIA8 underestimate the data at large p_T, so none of the considered event generators can describe the entire range of the measurements which make these results valuable reference points toward a successful tuning of generators in the forward region.

Acknowledgements

The author kindly acknowledges financial support through grant PN-II-ID-PCE-2011-3-0749 (56/07.10.2011), IDEI program and contract LHCb 3/03.01.2012, program PN-II:Capacităţi-3.

References

[1] B. Adeva *et al.* arXiv:hep-ex/0912.4179 (2009).

[2] A. A. Alves Jr. *et al.*, JINST **3** S08005 (2008).

[3] R. Aaij *et al.*, JINST **9** 09007 (2014);
R. Aaij *et al.* arXiv:hep-ex/1408.1251 (2014).

[4] A.A. Alves Jr. *et al.*, JINST **8** P02022 (2013);
F. Archilli *et al.*, JINST **8** P10020 (2013).

[5] R. Aaij *et al.*, JINST **8** P04022 (2013).

[6] T. Sjostrand, S. Mrenna, and P. Z. Skands, JHEP **0605** 026 (2006).

[7] P. Z. Skands, Phys. Rev. **D82** 074018 (2010).

[8] I. Belyaev *et al.*, J. Phys.: Conf. Ser. **331** 032047 (2011).

[9] A.D. Martin, C. Nockles, M. G. Ryskin, and T. Teubner, Phys. Lett. **B662** 252–258 (2008).

[10] P.D.B. Collins, *An Introduction to Regge Theory and High-Energy Physics* (Cambridge Univ. Press, Cambridge, 1977).

[11] R. Aaij *et al.*, J. Phys. G: Nucl. Part. Phys. **40** 045001 (2013).

[12] R. Aaij *et al.*, J. Phys. G: Nucl. Part. Phys. **41** 055002 (2014).

[13] C. Adloff *et al.*, Phys. Lett. **B541** 251-264 (2002); arXiv:hep-ex/0205107.

[14] S.P. Jones, A.D. Martin, M.G. Ryskin, and T. Teubner, JHEP **1311** 085 (2013).

[15] C. Alexa *et al.*, Eur. Phys. J. **C73** 2466 (2013).

[16] L. Motyka and G. Watt, Phys. Rev. **D78** 014023 (2008);
M. B. Gay Ducati, M.T. Griep, and M.V.T. Machado, Phys. Rev. **D88** 017504 (2013).

[17] R. Aaij *et al.*, Eur. Phys. J. **C73** 2421 (2013).

[18] R. Aaij *et al.*, Eur. Phys. J. **C72** 1947 (2012).

[19] R. Aaij *et al.*, Eur. Phys. J. **C74** 2888 (2014).

[20] T. Sjostrand, S. Mrenna, and P. Z. Skands. Comput. Phys. Commun. **178** 852–867 (2008).

[21] T. Pierog and K. Werner, Nucl. Phys. Proc. Suppl. **196** 102–105 (2009);
S. Ostapchenko, AIP Conf. Proc. **928** 118–125 (2007);
E.-J. Ahn, R. Engel, T. K. Gaisser, P. Lipari, and T. Stanev, Phys. Rev. **D80** 094003 (2009).

[22] R. Engel, Z. Phys. **C66** 203–214 (1995).

[23] M. Bahr *et al.*, Eur. Phys. J. **C58** 639–707 (2008);
J. Bellm *et al.*, arXiv:hep-ph/1310.6877 (2013).

Polarization Observables T and F in single π^0- and η-Photoproduction off quasi-free Nucleons

Thomas Strub

Department of Physics, University of Basel, Klingelbergstrasse 82, 4056 Basel, Switzerland

DOI: http://dx.doi.org/10.3204/DESY-PROC-2014-04/175

Meson photoproduction has developed into a powerful tool to study the nucleon excitation spectrum and test effective quark models which operate in the non-perturbative regime of QCD. An insight into the J^P configurations and isospin decompositions of the contributing resonances is gained by measuring a minimal set of polarization observables on both the proton and the neutron.

Single π^0- and η-photoproduction off a transversally polarized d-butanol target has been measured with circularly polarized bremsstrahlung photons generated by the MAMI-C electron microtron. With the nearly 4π acceptance of the combined Crystal Ball/TAPS setup the double polarization observable F and the target asymmetry T can be extracted for the first time for polarized, quasi-free neutrons over a wide energy and angular range.

1 Introduction

The nucleon and its excitation spectrum has been of great interest since many decades in order to study quantum chromodynamics in the non-perturbative regime. Due to the fact that many broad, overlapping resonances contribute to the excitation spectrum within a small energy range it cannot be understood from differential cross sections alone. While, for a long time, the method of choice to explore nucleon resonances was pion scattering with its large cross sections the attention came to photo- and electroproduction experiments when reaching higher intensity polarized electron beams, highly polarized targets with long relaxation times, and modern detector systems.

In the most general relativistic approach single pseudoscalar meson photoproduction gives access to four complex production amplitudes from which 16 real-valued polarization observables can be constructed [1]. These observables depend on beam, target and recoil polarization, and are, as well as the production amplitudes, functions of the invariant mass W and the production angle of the meson θ. The θ-dependence can be expanded in a partial-waves series by means of the electric and magnetic multipols $E_{l\pm}$ and $M_{l\pm}$, respectively, where l denotes the angular momentum. Thus, high statistic measurements of these observables in the (W, θ)-space allow to construct a uniquely determined solution of the production amplitudes up to a global phase through the partial wave analysis (PWA). It can be shown that eight carefully chosen observables have to be measured in order to find such a unique solution, which is called *complete experiment* [2].

Since the electromagnetic interaction does not conserve isospin the production vertex for single pseudoscalar meson photoproduction decomposes, in general, into three isospin ampli-

tudes, namely one isoscalar ($\Delta I = 0$), A^{IS}, and two isovector ($\Delta I = 0, \pm 1$), A^{IV} and A^{V3} (cf., e.g., [3]). Due to the fact that pions form an isospin triplet ($I = 1, I_3 = 0, \pm 1$) all three amplitudes contribute to π-photoproduction. In contrast, since η is an isospin singlet state, the isospin changing amplitude A^{V3} will not contribute to η-photoproduction. This makes photoproduction of isoscalar mesons especially interesting because it is selective to $N^*(I = 1/2)$ resonances only, whereas $\Delta(I = 3/2)$ resonances will not contribute. Nevertheless, in both cases, it is necessary to measure not only photoproduction off the proton but also off the neutron in order to fix all isospin amplitudes. A second reason for the interest in η-photoproduction off the neutron is the recent observation of a narrow structure around $W = 1670$ MeV which is not seen for the proton channel [4].

Due to the lack of free neutron targets photoproduction measurements off the neutron have always to be made with neutrons (weakly) bound in light nuclei within the quasi-free approximation. This gives rise to additional nuclear effects such as final state interactions (FSI). Indeed, a suppression of the free total cross section of about 25% is observed in π^0-photoproduction off quasi-free protons from the deuterium target [5]. However, η-photoproduction off quasi-free protons from the deuterium target does not show a significant difference [6]. In any case, it is reasonable to assume that this effect cancels out when measuring polarization observables.

In the following we present a preliminary analysis of the polarization observables T and F for single π_0- and η-photoproduction. Following the notation of [7] the differential cross section for a circularly polarized photon beam and a transversally polarized target reads

$$\frac{d\sigma}{d\Omega} = \frac{1}{2}\frac{d\sigma_0}{d\Omega}\left(1 + T P_T \sin\phi + F P_\odot P_T \cos\phi\right),$$

where P_T and $P_\odot$ denote the target and beam degree of polarization, respectively and ϕ is the angle between the target spin an the reaction plane.

2 Experiment and analysis

The experiment was performed at the MAMI-C accelerator in Mainz, Germany, which delivered a longitudinally polarized electron beam with energy of 1.557 GeV and a polarization degree of about 80%. Circularly polarized bremsstrahlung photons were produced in a radiator foil and were energy tagged with the Glasgow-Mainz photon tagger with energies between 0.47 GeV and 1.45 GeV. The resulting degree of polarization of bremsstrahlung photons from relativistic electrons depends on the photon energy E_γ and is described by Olsen and Maximon [8]. Transversally polarized target nucleons were provide by polarized deuterons of a frozen spin d-butanol (C_4D_9OD) target with a mean degree of polarization of about 80%.

The target was surrounded by the cylindrical particle identification detector (PID) made of 24 plastic scintillator strips, each covering an azimuthal angle of 15°. The PID was surrounded by a multi-wire proportional chamber (MWPC), which was not used in the current analysis. The spherical Crystal Ball calorimeter (CB) surrounding the MWPC consists of 672 NaI(Tl) crystals and covers polar angles from 20° to 160°. The forward direction was covered by the hexagonal two arm photon spectrometer (TAPS) built from 72 $PbWO_4$ (inner two rings) and 366 BaF_2 crystals (ring 3 to 11). A VETO wall in front of TAPS was used for particle identification. The combined CB/TAPS setup gives an almost 4π acceptance in the center of mass frame with a high angular and energy resolution.

The fist step of the data analysis was to select only events with the correct number of charged and neutral hit information from the detector. For the neutron channel the photons were

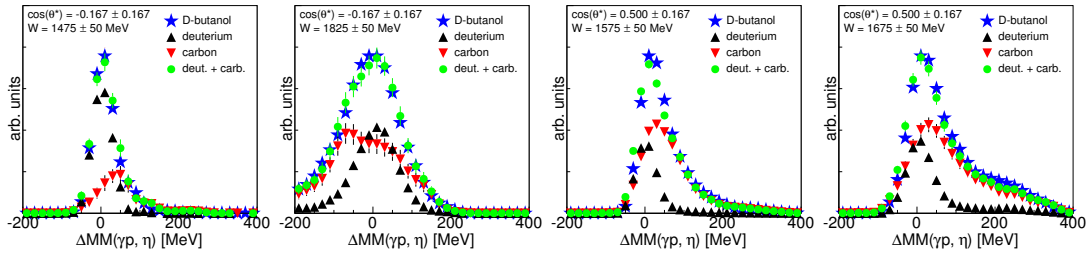

Figure 1: (Color online) Missing mass spectra for $\gamma p \to \eta p \to 2\gamma p$ for the carbon background subtraction. The spectra for deuterium and carbon are fitted to the d-butanol spectra. The ratio of carbon and deuterium, withing the missing mass cuts, is equal to the dilution factor.

identified by a χ^2-test finding the best combination for the meson invariant mass. Coincidence time cuts were applied to all photons and to eliminate accidentally coincident tagger photons, a random background subtraction was performed.

In order to separate the background channels kinematic cuts were applied separately for each W-θ-bin. Since all relevant events come from the polarized deuterons from the d-butanol target all cuts were determined from deuterium data. First, a coplanarity cut on the meson-nucleon system was applied. Then, an invariant mass cut on the reconstructed meson was performed. Finally, a γp-η missing mass cut was used to eliminate most of the background. The last step was to reconstruct the full event using four-momentum conservation, i.e., the Fermi momentum of the initial nucleon was determined from the knowledge of the incident photon energy and the complete final state. With this, the kinematics was transferred into the center of mass frame.

The observables were extracted using two opposite spin states for both, the photon helicity and nucleon spin. The above definition of the polarization observables can then be rewritten and reads, for F (and analogous for T),

$$F\cos\phi = \frac{1}{P_\odot}\frac{1}{P_T}\frac{d\sigma^+ - d\sigma^-}{d\sigma_0} = \frac{1}{P_\odot}\frac{1}{P_T}\frac{d\sigma^+ - d\sigma^-}{d\sigma^+ + d\sigma^-} = \frac{1}{P_\odot}\frac{1}{P_T}\frac{N^+_{\rm db} - N^-_{\rm db}}{N^+_{\rm db} + N^-_{\rm db}}\frac{1}{1-d}.$$

Here, the superscripts $(+,-)$ refer to the two photon helicity states, $N^\pm_{\rm db}$ denotes the count rate from d-butanol data and $d = d\sigma_0^{\rm carbon}/d\sigma_0^{\rm deuterium}$ is the dilution factor.

The last equality in the above equation holds for the following two reasons. First, flux normalization and efficiency corrections cancel out. Second, the cross sections refer to the reaction on the deuteron. However, unpolarized carbon and oxygen contributions only cancel in the numerator. Therefore, the additional contribution in the denominator has to be factorized out by the determination of the dilution factor. Figure 1 shows, for some selected bins, missing mass spectra of deuterium and carbon data fitted to the spectrum of d-butanol data. From this we can determine the unwanted contribution of events from carbon and oxygen from the d-butanol data.

3 Preliminary results and conclusion

Figure 2 shows some selected preliminary results for the polarization observables T and F for single π^0- and η-photoproduction off quasi-free protons and neutrons, respectively. Moreover, preliminary results for the reaction off the free proton and some model results are included.

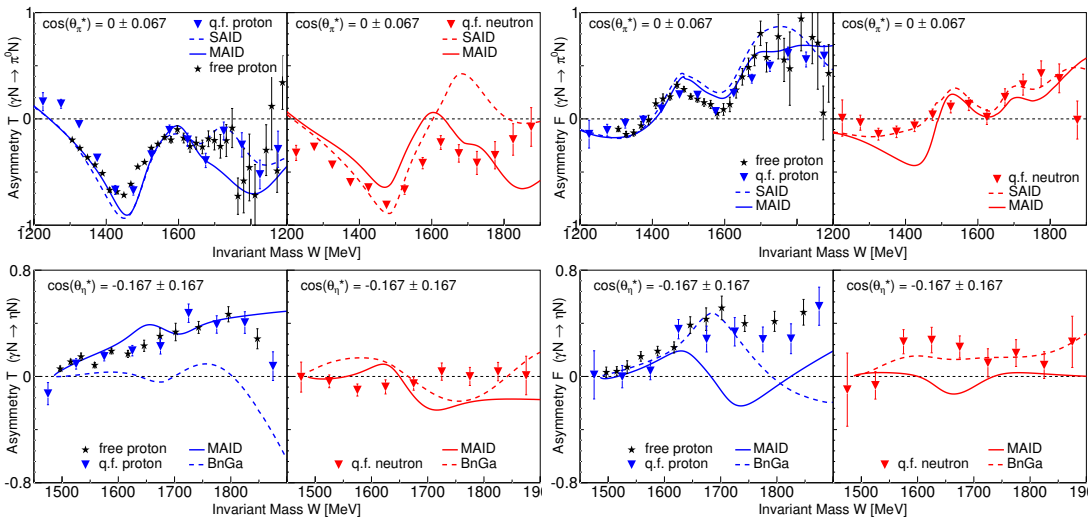

Figure 2: (Color online) Preliminary results for the polarization observables T and F. Top (bottom) row: π^0- (η-)photoproduction. Left (right) side: observable T (F) off free/quasi-free proton and quasi-free neutron. *Free proton data:* V. Kashevarov (preliminary); for final free proton $\gamma p \to \eta p$ results c.f. [9].

The free and quasi-free proton data are in nice agreement. The main contribution to the systematic uncertainties comes from the determination of the dilution factors caused by poorly matching missing mass spectra (only statistical errors are shown).

The best agreement with model predictions is found for π^0-photoproduction off the proton at lower energies, which is the best-known channel. There, the different models also make the same predictions. However, for higher energies the models deviate from each other and cannot reproduce the data consistently for both observables. For π^0-photoproduction off the quasi-free neutron the models already disagree at lower energies and for η-photoproduction off quasi-free protons and neutrons, respectively, the models even disagree down to the production threshold.

The final results will contribute to the complete experiment and will hopefully help to improve the model predictions and give a better understanding of the underlying physics.

References

[1] G.F. Chew, M.L. Goldberger, F.E. Low and Y. Nambu, Phys. Rev. **106** 1345 (1957).

[2] W.-T. Chiang and F. Tabakin, Phys. Rev. **C55** 2054 (1997).

[3] B. Krusche and S. Schadmand, Prog. Part. Nucl. Phys. **51** 399 (2003).

[4] D. Werthmüller *et al.*, Phys. Rev. Lett. **111** 232001 (2013).

[5] M. Dieterle *et al.*, Phys. Rev. Lett. **112** 142001 (2014).

[6] D. Werthmüller *et al.*, Phys. Rev. **C90** 015205 (2014).

[7] A.M. Sandorfi *et al.*, J. Phys. **G38** 053001 (2011).

[8] H. Olsen and L.C. Maximon, Phys. Rev. **114** 887 (1959).

[9] C.S. Akondi *et al.*, Phys. Rev. Lett. **113** 102001 (2014).

Measurement of $\sigma_{1/2}$ and $\sigma_{3/2}$ in Photoproduction of $\pi^0\pi^0$ Pairs off Neutrons in the Nucleon Resonance Region

Manuel Dieterle[1]

[1] Department of Physics, University of Basel, Klingelbergstrasse 82, 4056 Basel, Switzerland

DOI: http://dx.doi.org/10.3204/DESY-PROC-2014-04/168

Helicity dependent cross sections $\sigma_{1/2}$ and $\sigma_{3/2}$ of photoproduction of $\pi^0\pi^0$ meson pairs off quasi-free protons and off quasi-free neutrons in the second and third nucleon resonance region have been measured for the first time at the Mainzer Mikrotron (MAMI) electron accelerator facility. The knowledge of $\sigma_{1/2}$ and $\sigma_{3/2}$ will put stringent constraints on the different resonances that contribute to the nucleon excitation spectrum and will clearly help to improve its theoretical understanding.

1 Introduction

Meson photoproduction offers unique possibilities to investigate the nucleon and its excited states. Double meson photoproduction has the great advantage of enabling access to higher lying nucleon resonances that have no significant decay mode to the nucleon ground state via photoproduction of single mesons. Among the different meson pairs $2\pi^0$ is in particular interesting as non-resonant background terms (i.e. pion-pole, Kroll-Rudermann) are strongly suppressed because photons couple only weakly to neutral pions. Whereas for the reactions on the proton a lot of experimental data is available, data for the reactions on the neutron are sparse. In addition, even though in recent years much progress in the theoretical description of the results was achieved, the available models are still controversial even at low energies where only few resonances contribute. From the total cross sections of e.g. π^0 or η meson photoproduction off quasi-free protons and neutrons it is well known that rather different resonances contribute to the reactions on the proton compared to those on the neutron [1, 2, 3, 4]. The measurement of single and double polarization observables will help to reveal the different resonance contributions and thereby serve as an important input for the theoretical description of the structure and the excitation spectrum of the nucleon.
The double polarization observable E is defined as the asymmetry of the two helicity dependent cross sections $\sigma_{1/2}$ and $\sigma_{3/2}$ (1/2 (3/2): photon and target spins anti- (parallel)) normalized by the sum of both:

$$E = \frac{\sigma_{1/2} - \sigma_{3/2}}{\sigma_{1/2} + \sigma_{3/2}} = \frac{\sigma_{1/2} - \sigma_{3/2}}{2 \cdot \sigma_{\text{unpol}}} \tag{1}$$

2 Experiment

The experiment was performed at the MAMI electron accelerator at Mainz, Germany. The primary longitudinally polarized electron beam of 1.557 GeV was directed onto a 10 μm thick cobalt-iron radiator foil where a cirularly polarized photon beam of energies in the range of 0.45 GeV and 1.5 GeV was produced by the bremsstrahlung process. In order to determine the energy of the photons, the scattered electrons were detected in the focal plane of the Glasgow-Mainz Tagged Photon Spectrometer to analyze their momentum. The produced photon beam impinged on a longitudinally polarized deuterated Butanol (C_4D_9OD) target of 2 cm length and 2.2 cm diameter which was mounted in the center of the Crystal Ball (CB) detector. An additional electromagnetic calorimeter, the TAPS detector, was placed as forward wall downstream of the target. A charged particle identification detector (PID) mounted around the target inside CB and plastic scintillators (Vetos) in front of each of the crystals of TAPS allowed for the identification of charged particles. The experiment provided almost 4π angular coverage. The degree of target polarization was up to 60% and of the photon beam, depending on the energy, up to 80%.

3 Analysis

Double π^0 photoproduction was analyzed in coincidence with recoil protons and neutrons in the reactions $\gamma p(n) \rightarrow \pi^0\pi^0 p(n)$ and $\gamma n(p) \rightarrow \pi^0\pi^0 n(p)$. The nucleon in brackets is treated as undetected spectator nucleon. The photons, protons and neutrons have been identified in an analysis that combined the energy deposited in CB and the PID, the Vetos, the time-of-flight versus energy and a pulse-shape analysis in TAPS. The π^0 pairs were identified from the measured invariant mass of the photon pairs. In order to achieve a clean identification of the reaction, conditions on the coplanarity of the two-meson system and the recoil nucleon as well as a missing mass analysis have been determined on data from a comparable experiment with a liquid deuterium (LD_2) target. In the latter case, no background contribution from unpolarized nuclei inside carbon or oxygen contribute to the spectra, allowing for a much more precise determination of the kinematical limits. The data from deuterated butanol were then analyzed and only the events within these limits have been accepted and resulted in nearly background free invariant mass distributions (see figure 1).

To subtract the contribution from reactions on the unpolarized carbon and oxygen nuclei inside the deuterated butanol target, an additional experiment using the same setup and target but filled with carbon foam (^{12}C) of identical geometry and of about the same density was performed and analyzed in the same way as the deuterated butanol data.

In order to determine the double polarization observable E according to equation (1) either the sum of the two helicity dependent cross sections or the unpolarized cross section can be used for the normalization of the asymmetry. Both calculations have been carried out to ensure that the contributions from unpolarized nuclei are well under control. The contribution of reactions on such unpolarized nuclei was determined by a comparison of the missing mass spectra of the three datasets: deuterated butanol, liquid deuterium and carbon. The result is presented in figure 2. It is clearly visible that in each spectrum the yield from the LD_2 and ^{12}C data perfectly add up to the C_4D_9OD data, as expected.

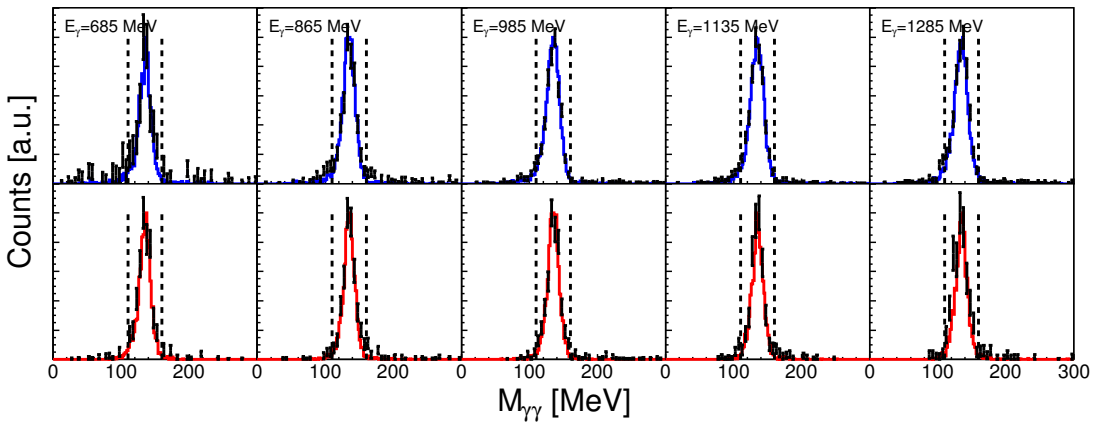

Figure 1: Final invariant mass spectra for five selected energy bins of one selected angular bin. Upper row: Reaction $\gamma p(n) \rightarrow \pi^0\pi^0 p(n)$, Lower row: Reaction $\gamma n(p) \rightarrow \pi^0\pi^0 n(p)$. Points: data, solid line: MC yield. Vertical dashed lines: region of the invariant mass cut.

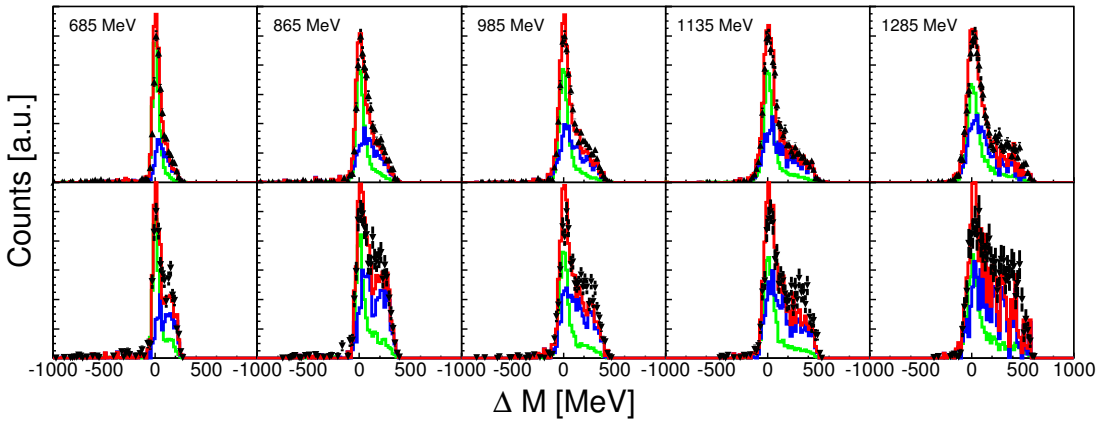

Figure 2: Carbon subtraction method using missing mass for five selected energy bins of one selected angular bin. Upper row: Reaction $\gamma p(n) \rightarrow \pi^0\pi^0 p(n)$, Lower row: Reaction $\gamma n(p) \rightarrow \pi^0\pi^0 n(p)$. Solid triangles: dButanol data. Solid lines: LD_2 (green), Carbon (blue) and sum of both (red).

4 Preliminary Results

Preliminary results for the helicity dependent cross sections $\sigma_{1/2}$ and $\sigma_{3/2}$ (middle and right) as well as the double polarization observable E (left) are presented in figure 3 and are compared to the model predictions from Bonn-Gatchina [5] (currently only available for the reaction $\gamma p(n) \rightarrow \pi^0\pi^0 p(n)$) and MAID [6]. It is clearly visible that both normalization methods are in perfect agreement with each other indicating that the subtraction of the contributions from reactions on the unpolarized nuclei from carbon and oxygen is well understood. The comparison of the data with the theoretical descriptions again reveal the impact of the helicity dependent

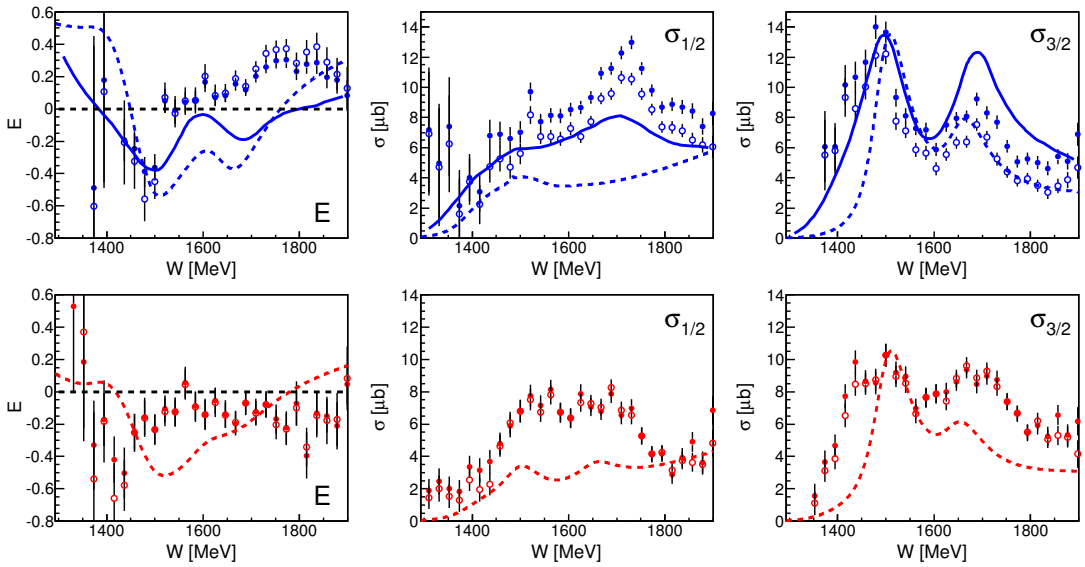

Figure 3: Preliminary results of the helicity dependent cross sections $\sigma_{1/2}$, $\sigma_{3/2}$ and double polarization observable E. Upper row: Reaction $\gamma p(n) \rightarrow \pi^0\pi^0 p(n)$, Lower row: Reaction $\gamma n(p) \rightarrow \pi^0\pi^0 n(p)$. Solid circles: normalized with carbon subtracted dButanol data, open circles: normalized with unpolarized total cross section. Solid line: BnGa model[5], dashed line: MAID model[6].

cross sections. Whereas the $\sigma_{1/2}$ cross section on the proton is better described by the BnGa model than by the MAID model, the opposite is true for the $\sigma_{3/2}$ cross section. Consequently neither one manages to describe the double polarization observable E, although the BnGa is closer to the result. Also for the neutron, the MAID model predicts a much better result for $\sigma_{3/2}$ than for $\sigma_{1/2}$. Obviously these results will clearly help to improve the models and to constrain the different resonance contributions.

References

[1] M. Dieterle *et al.*, Phys. Rev. Lett. **112**, 142001 (2014) [10.1103/PhysRevLett.112.142001].

[2] D. Werthmüller *et al.*, Phys. Rev. C **90**, 015205 (2014) [10.1103/PhysRevC.90.015205].

[3] D. Werthmüller *et al.*, Phys. Rev. Lett. **111**, 232001 (2013) [10.1103/PhysRevLett.111.232001].

[4] L. Witthauer *et al.*, Eur. Phys. J. A **49**, 154 (2013)

[5] *private communication*, A. Sarantsev, Bonn-Gatchina partial wave analysis $BG2014-02$.

[6] A. Fix and H. Arenhovel, Eur. Phys. J. A **25**, 115 (2005) [nucl-th/0503042].

Update on the OLYMPUS two-photon exchange experiment

Noaryr Akopov[1] for the OLYMPUS Collaboration

[1]Yerevan Physics Institute, Alikhanyan Br. 2, 0036 Yerevan, Armenia

DOI: http://dx.doi.org/10.3204/DESY-PROC-2014-04/143

The OLYMPUS experiment performed on the DORIS accelerator at DESY was designed to measure the e^-p to e^+p elastic cross sections ratio with high accuracy (<1%) in order to determine the effect of the two-photon exchange. Presence of such effect can explain the existing difference in electric to magnetic elastic form factors ratio measured in unpolarized and polarized ep elastic scattering.

1 Introduction

The nucleon electric and magnetic elastic form factors $G_E^{(p,n)}$ and $G_M^{(p,n)}$ are fundamental observables reflecting the composite structure of the nucleon consisting of quarks and gluons. More than fifty years, since the famous measurements, performed by Hofstadter [1] the only experimental information on these form factors and their ratios was available with the unpolarized cross section measurements using the Rosenbluth separation method [2]. During the last fifteen years thanks to polarization techniques developed at JLab [3], independent experimental measures of the form factor ratio were obtained, and the ratio of $G_{E(p)}/G_{M(p)}$ as a function of squared four-momentum transfer Q^2 was found to be distinctly different from that measured before with the Rosenbluth method: $G_E^p/G_M^p \approx 1/\mu_p$, with μ_p being the proton anomalous magnetic moment. Such a difference (see Fig. 1) is puzzling and it suggests the two photon exchange contribution to the elastic ep cross section could explain this puzzle. The only direct way to estimate experimentally the two photon exchange contribution is the measurements of the ratio of e^+p/e^-p elastic cross sections. The OLYMPUS experiment performed on the DORIS accelerator at DESY has collected huge sample of data (more than 4.4 fb^-1 of integrated luminosity) with e^+p and e^-p elastic scattering, and will provide very precise results on the cross section ratio (less than 1% of total uncertainties).

2 The OLYMPUS experiment

The OLYMPUS experiment was designed to measure the ratio of the elastic cross sections e^+p/e^-p over a wide kinematic range with the high precision. The experiment used the intense e^-, e^+ beams stored in the DORIS ring at 2 GeV interacting with an internal windowless hydrogen gas target [4] with the scattered/recoiling e/p measured in the range of $(20^o < \theta < 80^o, -15^o < \phi < 15^o)$. The spectrometer [5] (see Fig. 2) consists of the following main components: the time-of-flight (ToF) scintillation detectors to provide the elastic trigger

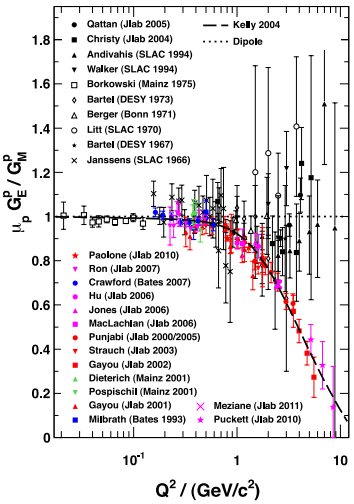

Figure 1: Proton electric to magnetic form factor ratio from unpolarized measurements (data points slightly deviated around unity) using the Rosenbluth method and from double polarization experiments (data points rapidly decreasing with Q^2). Also shown are two recent parametrization.

as well the particle identification, the drift chambers to provide the tracking and second level

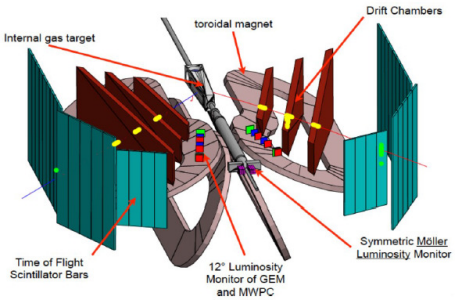

Figure 2: Schematic overview of the OLYMPUS spectrometer

trigger, and toroidal magnet to define the track momentum. To determine the relative e^+p/e^-p luminosity three sets of monitors were used, the first based on slow control information on target density and beam current, the second based on MWPC+GEMs tracking telescopes at 12^o, and the third based on symmetric Mőller-Bhabha calorimeters installed at 1.3^o. The high efficiency of the spectrometer operating together with the excellent performance of the accelerator, both provided the successful data taking. The DORIS accelerator was operated in top-up injection mode, which allowed the target density to be increased beyond the design value. An integrated luminosity of 4.4 fb^{-1} was achieved, the collected data consists of about equal amount of e^+

(44.1%) and e^- (43.3%) beam luminosities for positive toroid polarity. Due to the high background smaller data sets: 5.4% with the e^- beam and 7.2% with the e^+ beam were taken with the negative polarity, which are mainly used for systematic studies.

3 Data Analysis

The analysis framework is based on ROOT C^{++}/Geant4 providing the opportunities to analyze the real data as well the Monte Carlo samples equivalently. The radiative corrections which are very important to define the final ratio of $\frac{\sigma(e^+p)}{\sigma(e^-p)}$ are implemented in Monte Carlo generator, also a pion generator to estimate the inelastic background has been developed and tested. The digitization for all detector components to perform a realistic Monte Carlo studies to estimate possible systematic uncertainties is done. The calibration constants for the ToF are well advanced which allows the lepton/proton separation (see Fig. 3) based on particle squared mass distribution defined with:

$$M^2 = p^2[(cT/L)^2 - 1],$$

where p is the track momentum, c is the speed of light, T is the time of ToF hit and L is the track path length from the interaction point to the ToF hit. The algorithm for the reconstruction

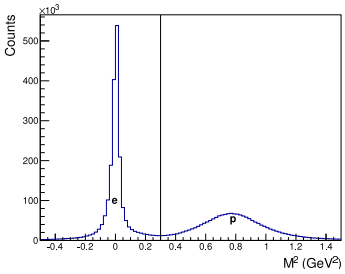

Figure 3: Particle squared mass distribution

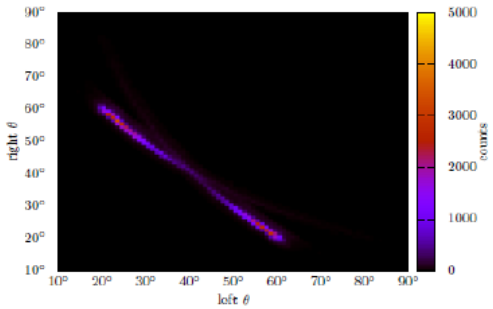

Figure 4: Polar left-right angles correlation with all elastic cuts applied

code is essentially improved, the massive production of the reconstructed runs is started. The set of kinematic and geometric constraints to select the elastic events such as the left and right

tracks vertex difference, momentum balance, coplanarity is developed and optimized for certain bins over Q^2 and virtual photon polarization ϵ. The typical "elastic" picture with the left-right polar angles correlation after all cuts applied is shown on Fig. 4. The present level of the Monte Carlo data agreement can be seen in Fig. 5. One should note that still the data are

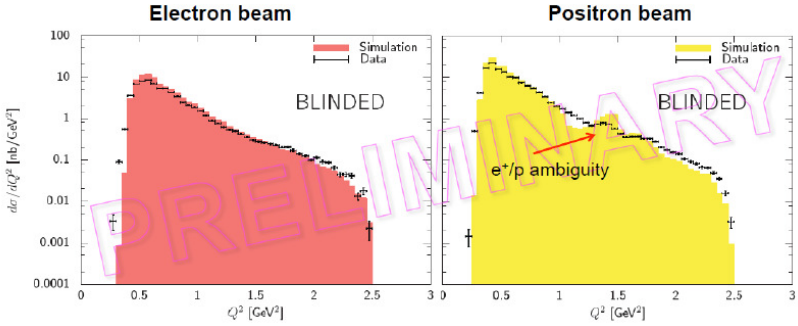

Figure 5: Q^2 distributions for selected elastic events for e^- sample (left panel) and e^+ sample (right panel). The dashed area on both panels is the Monte Carlo simulation.

blinded in order to prevent a bias in several independent analyzes. The data analysis is close to be completed. Two other experiments [6, 7] are close to publish the final results with the measured $\frac{\sigma(e^+p)}{\sigma(e^-p)}$ ratio. The preliminary results from the OLYMPUS collaboration are expected to be released at the end of 2014.

References

[1] R. Hofstadter, Rev. Mod. Phys. **28**, 214 (1956).

[2] M.N. Rosenbluth, Phys. Rev. **79**, 615 (1950).

[3] V. Punjabi et al., Phys. Rev. **C71**, 055202 (2005); Erratum-ibid. Phys. Rev. **C71**, 069902(E) (2005);
M. Jones et al., Phys. Rev. Lett. **84**, 1398 (2000);
O. Gayou et al., Phys. Rev. Lett. **88**, 092301 (2002);
G. MacLachlan et al.,Nucl. Phys. **A764**, 261 (2006).

[4] J.C. Bernauer et al., NIM **A755**, 20 (2014).

[5] R. Milner et al., NIM **A741**, 1 (2014).

[6] B.A. Raue for the CLAS Collaboration, AIP Conf.Proc. **1257**, 617 (2010);P. Bennett dor the CLAS Collaboration, AIP Conf.Proc. **1441**, 156 (2912).

[7] A.V. Gramolin et al., Nucl.Phys.Proc.Suppl. **225-227**, 316 (2012).

Helicity Dependent Cross Sections in η Photoproduction off Quasi-Free Protons and Neutrons

Lilian Witthauer[1]

[1] Department of Physics, University of Basel, Klingelbergstrasse 82, 4056 Basel, Switzerland

DOI: http://dx.doi.org/10.3204/DESY-PROC-2014-04/169

Preliminary results for the double polarisation observable E and the corresponding helicity dependent cross sections $\sigma_{1/2}$ and $\sigma_{3/2}$ of η photoproduction off quasi-free protons and neutrons have been obtained by a recent experiment at the MAMI electron accelerator at Mainz, Germany. The results will help to constrain the origin and quantum numbers of the bump-like structure in the η cross section off the neutron.

1 Introduction

The identification of the relevant effective degrees of freedom of QCD is the most important step in order to understand the structure of the nucleon. Since the resonances which contribute to the excitation spectrum are often broad and overlapping, the comparison of experimental data and theoretical models is rather difficult. Single and double polarization observables allow for the determination of the quantum numbers of the contributing resonances and are therefore an ideal tool to investigate the excitation spectrum of the nucleon.
A very selective channel in this context is the photoproduction of η mesons. Due to the isoscalar property of the η, Δ ($I = 3/2$) resonances cannot decay to the ground state by emitting an η. Furthermore $P_{11}(1440)$ and $D_{13}(1520)$ resonances have a very small branching ratio into the Nη final state (close to threshold high orbital angular momenta are strongly suppressed). Especially, the investigation of this photoproduction channel is very interesting as the resulting cross section on the neutron shows a large resonance-like structure, beyond the dominating $S_{11}(1535)$, which is not seen on the proton. The structure has been reported by different collaborations [1, 2, 3, 4] and is visible on different nucleon systems (deuterium and helium), excluding origin from nuclear effects [5, 6]. Theoretical model descriptions have not yet lead to consistent results.
Using a circularly polarised photon beam and a longitudinally polarised target, the double polarisation observable E can be determined:

$$E = \frac{\sigma_{1/2} - \sigma_{3/2}}{\sigma_{1/2} + \sigma_{3/2}} = \frac{\sigma_{1/2} - \sigma_{3/2}}{2\sigma_{tot}^{unpol}} \tag{1}$$

The corresponding helicity dependent cross-sections $\sigma_{1/2}$ (photon and target spin anti-parallel) and $\sigma_{3/2}$ (photon and target spin parallel) give direct hints to the spin of the underlying resonances and are therefore ideally suited to reveal the origin of the narrow structure on the neutron.

2 Experiment and Analysis

The experiment was carried out by the A2 collaboration at the electron accelerator facility MAMI in Mainz, Germany. A circularly polarised, tagged photon beam with energies up to 1.557 GeV impinged onto the longitudinally polarised deuterated Butanol target. The target had a diameter of 2.2 cm, a length of 2 cm and an effective density of 0.66 g/cm^3. A deuteron polarisation of around 60% was reached, the photons had a polarisation degree of up to 80%. The almost 4π covering detector system consisted of the two electromagnetic calorimeters Crystal Ball and TAPS. The particle identification detector surrounding the target and the plastic vetos in front of the TAPS detector were used to distinguish charged from neutral particles. To determine the contribution of the unpolarised carbon and oxygen nuclei inside the deuterated butanol target, additional background measurements using a dedicated carbon foam target have been performed.
Both decay channels, $\eta \to 2\gamma$ and $\eta \to 3\pi^0 \to 6\gamma$, have been analysed using standard invariant mass and χ^2-techniques. Additional cuts have been applied to the missing mass of the nucleon and to the coplanarity of the meson-nucleon system. Using the two different scintillation components of the TAPS BaF_2 crystals, a Pulse-Shape-Analysis has been performed to distinguish neutrons from photons. The Fermi motion of the deuteron has been removed, the procedure is explained in detail in [5].

Two different methods have been used to determine the double polarisation observable E.

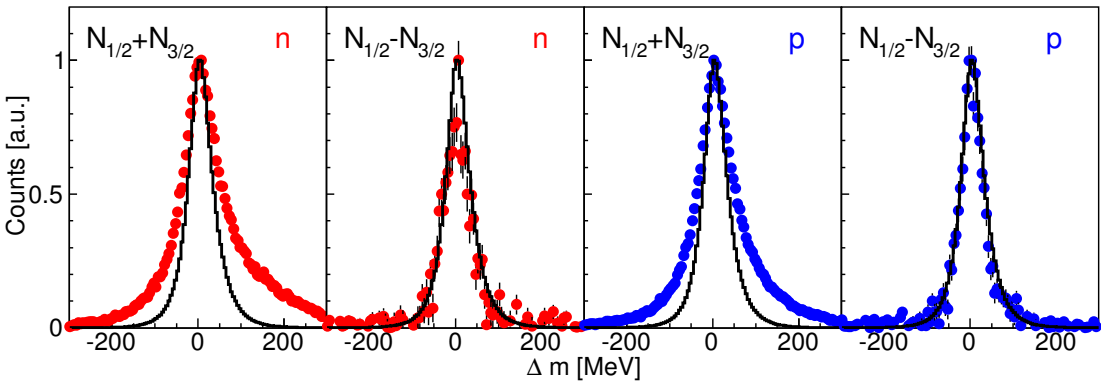

Figure 1: The missing mass of the sum (first and third figure) and the difference (second and fourth figure) of the two helicity states. Data (dots) are compared to simulation (line). The two left-hand figures show the situation for the neutron, the two right-hand for the proton. In both cases the carbon contribution in the sum of the two helicity states is clearly visible and leads to a broadening of the peak compared to the simulation. In the countrate difference, the carbon contribution automatically drops out and the data are consistent with the simulation.

First, a direct approach was chosen, the difference of the two helicity states has been divided by the known unpolarised total cross section (second part of equation 1). In this case the unpolarised carbon automatically drops out (see figure 1), but a accurate total normalisation is needed. In the second approach the carbon background measurement was used and the difference was divided by the carbon subtracted sum of the two helicity states (first part in equation 1). Whereas in this case the overall normalisation cancels out, the carbon contribution has to

be known exactly. The contribution of the carbon is determined by fitting the missing mass spectra of the deuteron and carbon data to the one of butanol, see Figure 2. The fitting procedure was performed for every bin of photon energy and polar angle. In the range of the missing mass cut (vertical black lines) the contribution of unpolarised carbon and oxygen nuclei is well under control.

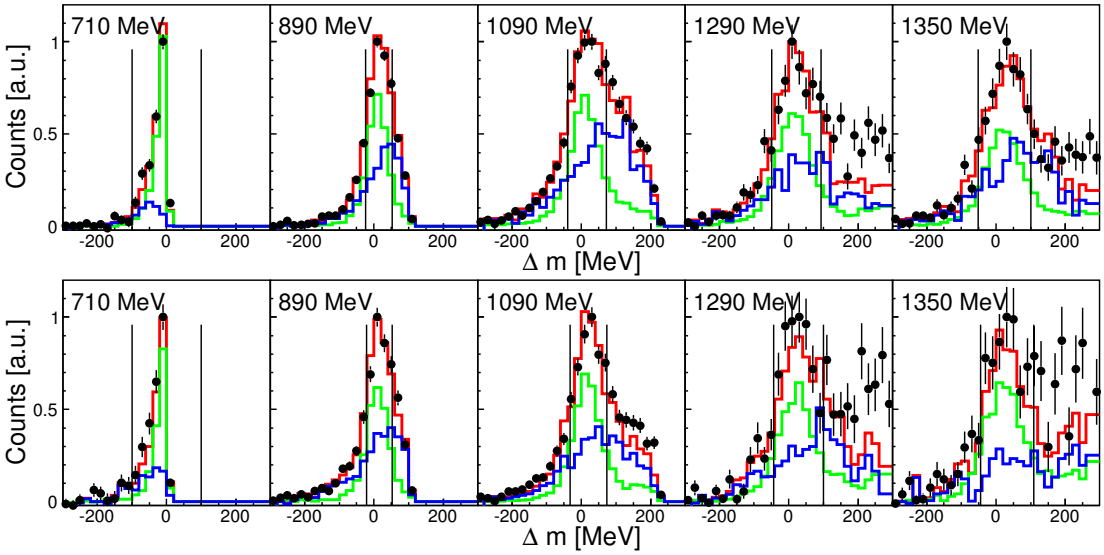

Figure 2: Upper (lower) row: the missing mass distribution of the proton (neutron) for the $\eta \to 2\gamma$ channel for five different photon energy bins intergrated over all angular bins. Solid lines: The contributions of the reactions on the deuteron (green) and the carbon (blue) and the sum of both (red). Within the range of the missing mass cut (vertical black lines), the sum is consistent with the measured distribution on the deuterated butanol (black dots).

3 Preliminary Results

The preliminary results of the double polarisation observable E as well as the helicity dependent cross sections $\sigma_{1/2}$ and $\sigma_{3/2}$ as a function of the center-of-mass energy W are shown in figure 3. The direct method (open circles) and the carbon subtraction method (solid circles) are in good agreement. As predicted by the models, the contribution from the helicity 1/2 state is significantly larger than the contribution from 3/2. This is mainly caused by the dominating $S_{11}(1535)$ resonance. Even at higher energies, the contribution of the helicity 3/2 state is very small. The resonance like structure on the neutron only appears in $\sigma_{1/2}$, as predicted by the BnGa model [7]. The MAID model [8] with the strong contributing $D_{15}(1675)$ in $\sigma_{3/2}$ does not reproduce the helicity dependent cross-sections for the neutron. For the proton the overall situation seems to be well understood by the models.

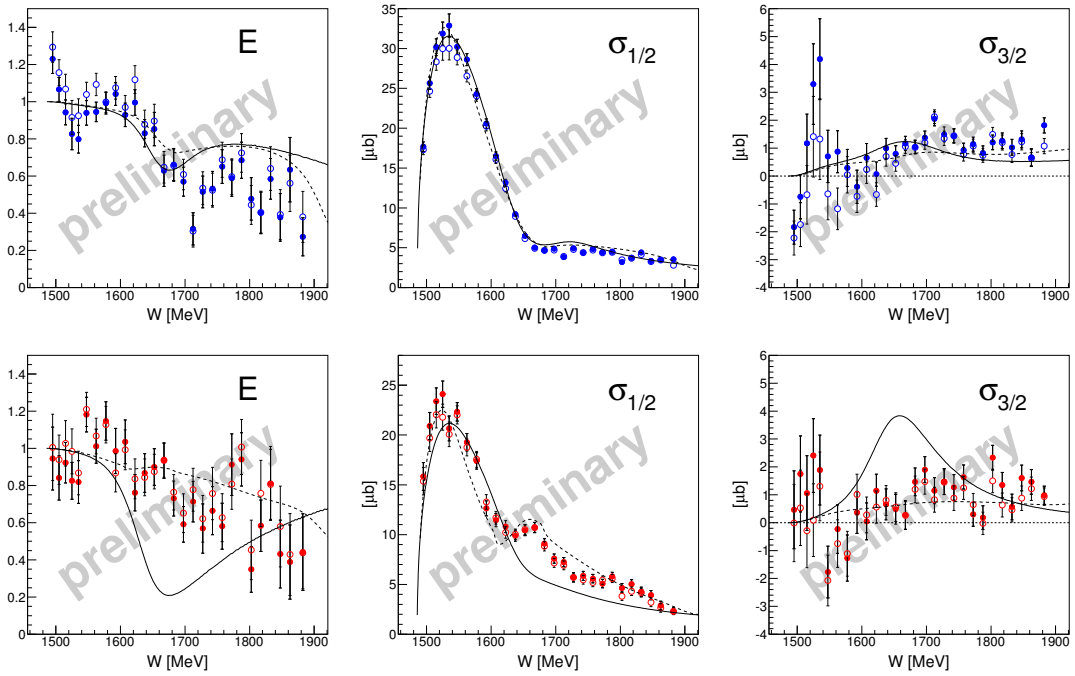

Figure 3: Preliminary Results. Double polarisation observable E and helicity dependent cross sections $\sigma_{1/2}$, $\sigma_{3/2}$ for η photoproduction on the proton (upper row) and on the neutron (lower row). Solid circles: normalised with carbon subtracted deuterated butanol, open circles: normalised with unpolarised total cross section. The results are compared to the BnGa model [7] (dashed line) and the MAID model [8] (solid line).

References

[1] V. Kuznetsov *et al.*, Phys. Lett. B **647**, 23 (2007) [10.1016/j.physletb.2007.01.041].

[2] I. Jaegle *et al.*, Eur. Phys. J. A **47**, 11 (2011) [10.1140/epja/i2011-11011-x].

[3] F. Miyahara et al., Prog. Theor. Phys. Suppl. 168, 90 (2007) [10.1143/PTPS.168.90].

[4] D. Werthmüller *et al.*, Phys. Rev. Lett. **111**, 232001 (2013) [10.1103/PhysRevLett.111.232001].

[5] D. Werthmüller *et al.*, Phys. Rev. C **90**, 015205 (2014) [10.1103/PhysRevC.90.015205].

[6] L. Witthauer *et al.*, Eur. Phys. J. A **49**, 154 (2013) [10.1140/epja/i2013-13154-0].

[7] A.V. Anisovich *et al.*, Eur. Phys. J. A, **48**, 15 (2012) [10.1140/epja/i2012-12015-8].

[8] W.-T. Chiang *et al.*, Nucl. Phys. A **700**, 429-453 (2002) [nucl-th/0110034].

Physics opportunities in electron-hadron collisions at the future eRHIC

Salvatore Fazio

Brookhaven National Laboratory, PO BOX 5000, 11973 Upton NY, USA

DOI: http://dx.doi.org/10.3204/DESY-PROC-2014-04/113

Our understanding of the structure of nucleons is described by the properties and dynamics of quarks and gluons in the theory of quantum chromodynamics. With advancements in theory and the development of phenomenological tools we are preparing for the next step in subnuclear tomographic imaging at a future electron-ion collider. A large range of center-of-mass energies ($\sqrt{s} \approx 45 - 150$ GeV) in combination with extremely high luminosities ($> 10^{33}$ cm^{-2}s^{-2}) will open a unique opportunity for very high precision measurements, allowing for a detailed investigation of the proton and nuclear hadronic substructure in multi-dimensions. In addition, highly polarized nucleon ($P \approx 70\%$) and electron ($P \approx 80\%$) beams can probe the parton polarizations in previously unexplored kinematic regions and with unprecedented accuracy, as well as address the role of orbital angular momentum with respect to the nucleon spin. This talk will summarize the eRHIC physics case for electron-proton collisions, the expected impact over the current knowledge and some of the technical challenges of such a versatile experimental endeavor.

1 Introduction

The BNL proposal for a future Electron-Ion Collider, eRHIC [1], is a major new research facility that builds on the existing RHIC accelerator complex to advance the long-term vision for Nuclear Physics to discover and understand the emergent phenomena of QCD, i.e. the creation of mass and spin of the visible matter. Its design concept incorporates new and innovative accelerator techniques to provide a cost-effective design to add a polarized electron beam colliding with the full array of RHIC hadron beams at a luminosity beyond 10^{33}cm^{-2}s^{-1}.

Such a facility will address directly and with high precision questions that relate to our fundamental understanding of QCD:

- How are the sea quarks and gluons, and their spins, distributed in space and momentum inside the nucleon?
- Where does the saturation of gluon densities set in?
- How does the nuclear environment affect the distribution of quarks and gluons and their interactions in nuclei?

eRHIC will address the above questions with the highest, unprecedented precision and at one facility.

2 electron-proton scattering at eRHIC

eRHIC will open up the unique opportunity to go far beyond our current largely one-dimensional picture of the nucleon. It will enable partonic "tomographic images", providing essential insight into QCD dynamics inside hadrons. Moreover it can unravel how the proton spin derives from its constituents: the quarks and the gluons, a formidable challenge that goes directly to the heart of exploring and understanding the QCD dynamics of matter.

2.1 Proton's helicity structure

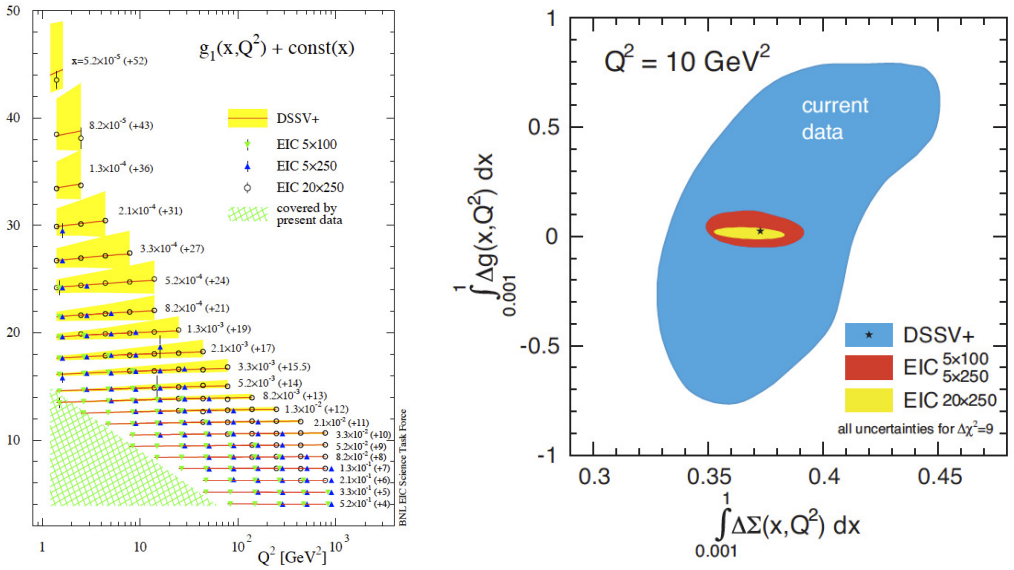

Figure 1: (*left*)Projected eRHIC data for the structure function g_1 for different combinations of electron and proton beam energies; (*right*) Correlated uncertainties for the flavor singlet combination $\Delta\Sigma$ and the gluon helicity density Δg.

Helicity-dependent parton densities encode the information to what extent quarks and gluons with a given momentum fraction x tend to have their spins aligned with the spin direction of a nucleon and are related to how the spin of a nucleon is composed of the spins and orbital angular momenta of quarks and gluons. The integrals of helicity PDFs over all momentum fractions x at a resolution scale Q^2, $\Delta f(Q^2) = \int_0^1 \Delta f(x, Q^2) dx$, provide information about the contribution of a given parton flavor f to the spin of the nucleon. A precise determination of the polarized gluon $\Delta g(x, Q^2)$ and quark $\Delta q(x, Q^2)$ distribution functions in a broad kinematic regime is a primary goal of eRHIC.

Current determinations of Δg suffer from both a limited $x - Q^2$ coverage and fairly large theoretical scale ambiguities in polarized p+p collisions for inclusive (di)jet and pion production [2]. Several channels are sensitive to Δg in e+p scattering at collider energies such as DIS jet or charm production, but QCD scaling violations in inclusive polarized DIS have been identified as the golden measurement.

Figure 1(*left*) illustrates the simulated data sets for inclusive polarized DIS at eRHIC for the three different choices of c.m. energies. The error bars reflect the expected statistical accuracy for a integrated luminosity of 10fb^{-1} and assuming 70% beam polarizations.

The simulated data are used in a fit to study what can be achieved for the first moments of the flavor singlet combination $\Delta\Sigma$ and the gluon helicity density Δg, which both enter the proton spin sum rule $\frac{1}{2} = \frac{1}{2}\Delta\Sigma + \Delta g + \Sigma_q L_q^z + L_g^z$, with $L_{q,g}^z$ denoting the contribution from orbital angular momentum (not accessible in inclusive DIS). Figure 1(*right*) shows how eRHIC will greatly reduce the uncertainties, in particular for Δg which is largely unconstrained so far.

2.2 Multidimensional imaging of quarks and gluons

With its wide range in energy, nuclear beams and high luminosity, eRHIC will offer an unprecedented opportunity for precision measurements, allowing us to study the momentum and space-time distribution of gluons and sea quarks in nucleons and nuclei.

One of the main goals will be a precise determination of the Generalized Parton Distribution functions (GPDs), which describe the distribution of quarks and gluons in the nucleon with respect to both position and momentum. Moreover, GPDs allow us to study how the orbital motion of quarks and gluons in the nucleon contributes to the nucleon spin, completing the spin sum role (see Sec. 2.1).

A golden measurement toward the determination of the whole set of GPDs is Deeply Virtual Compton Scattering (DVCS), which is the exclusive production of a real photon. This theoretical and experimentally clean process is sensitive to both quarks and gluons (via evolution).

Presently available DVCS measurements provide some limited information on GPDs and more precise data, in a wider phase space and including transversely polarized target spin asymmetry, are required to pin them down [3].

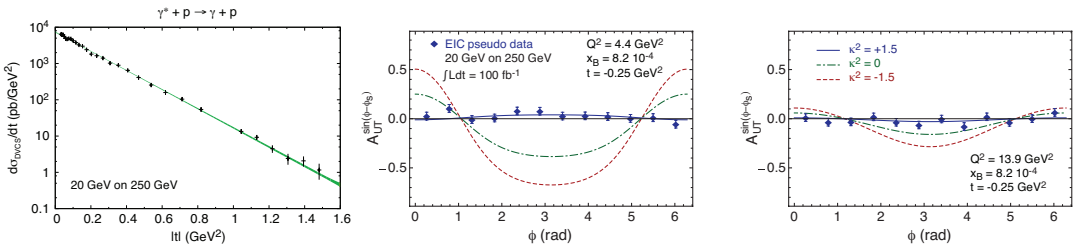

Figure 2: Expected uncertainties for a DVCS $|t|$-differential cross section (*left*) measurement in a particular x, Q^2 bin, and for A_{UT} (*center-right*) compared to theory model with large positive (*solid*), vanishing (*dot − dashed*), and large negative (*dashed*) E^{sea} contributions.

An access to GPDs requires a large data set with small errors. As an example of the precision achievable at eRHIC, Fig. 2 (*left*) shows the expected uncertainty for a measurement of the DVCS $|t|$-differential cross section in a particular x, Q^2 bin. Figure 2(*center-right*) shows the expected uncertainty for the transverse target-spin asymmetry (A_{UT}) as a function of the azimuthal angle ϕ between the production and the scattering planes for a particular $x_{Bj}, Q^2, |t|$ bin, compared to theoretical expectations. The simulation proves that eRHIC can perform accurate measurements of cross sections and asymmetries in a very fine binning and with a very low statistical uncertainty.

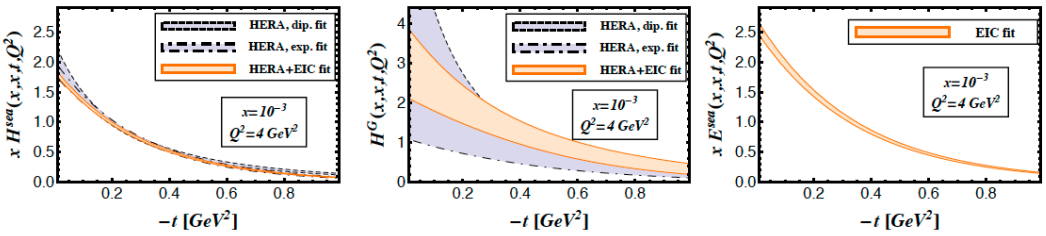

Figure 3: Extraction of GPD H for sea quarks ($left$) and gluons ($center$) and GPD E for sea quarks ($right$) in a particular x, Q^2 bin. The violet band is the uncertainty obtained excluding the eRHIC pseudo-data to the global fit procedure.

A global fit, including the eRHIC simulated data together with all the data presently available has been done. Figure 3 shows how eRHIC can largely improve the knowledge on GPD H for gluons. Moreover, a precise measurement of the transversely polarized target spin asymmetry A_{UT}, which allows for a decomposition of GPD H and E contributions, leads to the accurate extraction of GPD E, which at the moment remains almost unconstrained [3], providing an estimate of the angular momentum carried by sea quarks.

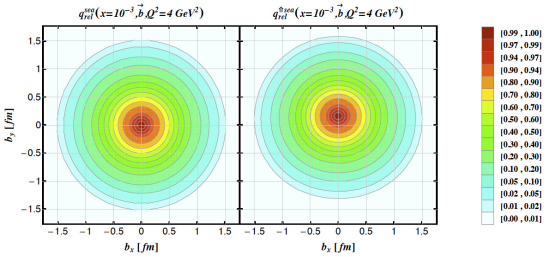

Figure 4: Tomographical picture of the sea-quuarks distribution in the impact parameter space for an unpolarized ($left$) and a polarized ($right$) proton beam.

Fourier-transforming the GPDs, it is possible to obtain the quarks and gluons distributions in the impact parameter space. Fig. 4 shows an example of a tomographic (2+1 D) picture of the see-quarks distribution as resulting from eRHIC pseudo-data analysis, in a particular bin, for the case of an unpolarized and a polarized proton-beam. The shift observed in the polarized case comes from the GPD E contribution.

References

[1] E.C. Aschenauer *et al.*, "eRHIC Design Study: An Electron-Ion Collider at BNL", arXiv:1409.1633

[2] E.C. Aschenauer, "The RHIC Spin Program: Achievements and Future Opportunities, arXiv:1304.0079

[3] E.C. Aschenauer, S. Fazio, K. Kumericki, and D. Mueller, JHEP 09 (2013) 093

Transverse single-spin asymmetries in $W^{\pm}$ and Z^0 bosons production in p+p collisions at RHIC

Salvatore Fazio

Brookhaven National Laboratory, PO BOX 5000, 11973 Upton NY, USA

DOI: http://dx.doi.org/10.3204/DESY-PROC-2014-04/112

The non universality of the quark Sivers function is a fundamental prediction from the gauge invariance of QCD. The experimental test of the Sivers function sign change between semi-inclusicve DIS and Drell-Yan processes is one of the open questions in hadronic physics, and can provide a direct verification of TMD factorization. While a precise measurement of asymmetries in Drell-Yan production is challenging, $W^{\pm}/Z^0$ production is equally sensitive to the predicted sign change. We present the preliminary measurement of the transverse single spin asymmetry of weak bosons by the STAR experiment at RHIC using transversely polarized proton-proton collisions at $\sqrt{s} = 500$ GeV.

1 Introduction

Transversely polarized spin effects are connected to transverse momentum dependent (TMD) distributions, leading to a multi-dimensional picture of the proton and a possible test of the framework and the underlying theory of perturbative QCD. For a quantitative application of the TMD framework to transverse single-spin asymmetries measured in proton-proton collisions, the required two scales (typically Q^2 and P_T) are not well defined, with Drell-Yan di-lepton (DY) and $W^{\pm}/Z^0$ boson production two of the exceptions. Thus, DY and weak boson production can be used to test the so-called Sivers TMD function [1], $f_{1T}^{\perp}$, which describes the correlation of parton transverse momentum with the transverse spin of the nucleon. There is evidence of a quark Sivers effect in semi-inclusive DIS (SIDIS) measurements [2] where the quark Sivers function is associated with a final state effect from the gluon exchange between the struck quark and the target nucleon remnants. On the other hand, for the virtual photon production in the DY process, the Sivers asymmetry originates from the initial state of the interaction. As a consequence, the quark Sivers functions are of opposite sign in SIDIS and in DY [3]

$$f_{q/h^{\uparrow}}^{\mathrm{SIDIS}}(x, k_{\perp}) = -f_{q/h^{\uparrow}}^{\mathrm{DY}}(x, k_{\perp}), \tag{1}$$

and this non-universality is a fundamental prediction from the gauge invariance of QCD.

The experimental test of this sign change is one of the open questions in hadronic physics, and can provide insights on the TMD factorization. While luminosity and experimental requirements for a meaningful measurement of asymmetries in Drell-Yan production are challenging, weak boson production is equally sensitive to the predicted sign change and can be well measured at STAR. The results can also provide essential input to study the TMD evolution effects, because of the high Q^2 in the $W \to e\nu$ production due to the large boson mass. The STAR experiment at RHIC is currently the best place where these effects can be tested.

The transverse single spin asymmetry, A_N, solely calculated from the lepton decay is predicted to be diluted [4] due to smearing, thus a full reconstruction of the produced boson kinematics is crucial for a meaningful measurement. Based on the transversely polarized data sample collected in the year 2011 at $\sqrt{s} = 500$ GeV ($L_{int} = 25$ pb^{-1}), an analysis has been performed at STAR to fully reconstruct the $W^{\pm}$ bosons from the lepton decay and all other particles in the recoil from the initial hard scattering. This analysis also includes a first look at A_N in Z^0 production. A proposed measurement with increased statistics will be directly competitive with a Drell-Yan measurement in pion-proton scattering at CERN.

2 Weak boson selection and asymmetry measurement

A data sample characterized by the $W \to e\nu$ signature as in Ref. [5], requires an isolated high $P_T > 25$ GeV electron and a total recoil $P_T > 18$ GeV. In order to fully reconstruct the W kinematics, the momenta of all decay products must be measured. The momentum of the neutrino produced in the leptonically decayed W can only be indirectly deduced from conservation of the transverse momentum.

We define the missing transverse energy as a vector restoring the balance in the event

$$\vec{\not{E}}_T = - \sum_{\substack{i \in \text{tracks,} \\ \text{clusters}}} \vec{P}_{i,T}. \tag{2}$$

At the STAR detector, due to a limited tracker acceptance of $|\eta| \sim 1$, the problem with measuring the missing momentum from the hadronic recoil is that particles with high rapidities escape the detector. At the same time, the beam remnants with high longitudinal momentum carry away only a little portion of the total transverse momentum. We accounted for the unmeasured tracks and clusters by using an event-by-event Monte Carlo correction to the data, using PYTHIA 6.4 with "Perugia 0" tune. Knowing its transverse momentum, the longitudinal component of the neutrino's momentum can be reconstructed solving the quadratic equation for the invariant mass of the produced boson

$$M_W^2 = (E_e + E_\nu)^2 - (\vec{P}_e + \vec{P}_\nu)^2, \tag{3}$$

where we assumed the nominal value of the W-mass. Eq. 3 leads to two possible solutions for P_L^ν, and we chose the smaller one in magnitude which, as shown by a Monte Carlo study, leads to a more truthful reconstruction of the original kinematics.

Background sources coming from $W^{\pm} \to \tau^{\pm}\nu_\tau$, $Z^0 \to e^+e^-$ and QCD events have been estimated to be at most a few percent of the selected sample, as shown in table 1.

Proc.	$W^{\pm} \to \tau^{\pm}\nu_\tau$	$Z^0 \to e^+e^-$	QCD
B/S	1.88% (W^+); 1.39% (W^-)	0.88% (W^+); 2.94% (W^-)	1.59% (W^+); 3.40% (W^-)

Table 1: Background over signal in the W^+ and W^- samples respectively.

The transverse single spin asymmetry is expressed as: $A_N = \frac{\sigma_\uparrow - \sigma_\downarrow}{\sigma_\uparrow + \sigma_\downarrow}$. We bin our data sample in three observables: the rapidity y, the azimuthal angle ϕ, and the P_T of the produced boson. Thus, we calculate A_N using the formula in Eq. 4, which helps to cancel out unwanted effects due to geometry and luminosity [6].

$$A_N \sin(\phi) = \frac{1}{< P >} \frac{\sqrt{N_\uparrow(\phi_i) N_\downarrow(\phi_i + \pi)} - \sqrt{N_\uparrow(\phi_i + \pi) N_\downarrow(\phi_i)}}{\sqrt{N_\uparrow(\phi_i) N_\downarrow(\phi_i + \pi)} + \sqrt{N_\uparrow(\phi_i + \pi) N_\downarrow(\phi_i)}}, \tag{4}$$

where N is the number of recorded events in the $i-th$ bin with a certain spin ($\uparrow\downarrow$) configuration in the "left" (ϕ_i) or in the "right" ($\phi_i + \pi$) side of the detector and $< P > \simeq 53\%$ is the average RHIC beam polarization for 2011 transverse p+p run.

The STAR preliminary results for the A_N measurement of the W^+ and W^- boson production are shown separately in Fig. 1 as a function of y^W and P_T^W. The systematic uncertainties, added in quadrature, have been evaluated via a Monte Carlo challenge using a theoretical prediction for the asymmetry from [7]. The 3.4% overall systematic uncertainty on beam polarization measurement is not shown in the plots.

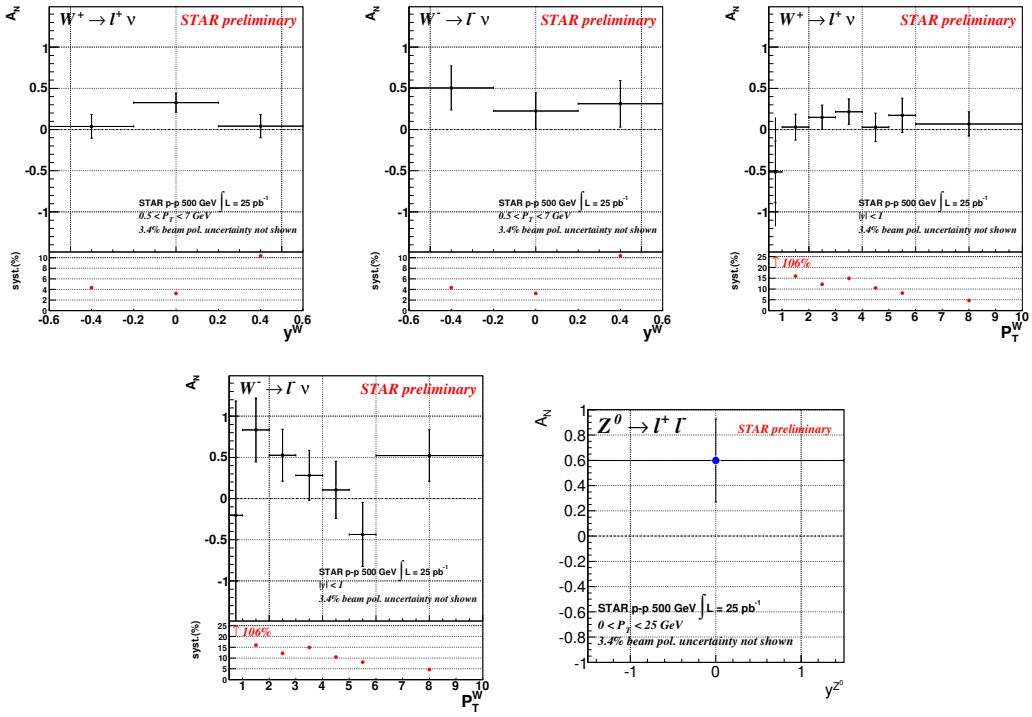

Figure 1: Transverse single spin asymmetry amplitude for $W^{\pm}$ and Z^0 boson production measured at STAR in a pilot run at $\sqrt{s} = 500$ GeV with a recorded luminosity of 25 pb^{-1}.

The $Z^0 \to e^+e^-$ process has many advantages: it is experimentally very clean and the boson kinematics are easy to reconstruct since there is no neutrino in the final decay (thus it carries only the overall systematics coming from the polarization measurement), it is background free and the asymmetry is expected to be the same size as the $W^{\pm}$ one. The only big disadvantage is the much lower cross section which makes the measurement very statistics hungry.

A data sample characterized by the Z^0 signature has been selected, requiring two isolated high $P_T > 25$ GeV electrons, of opposite charge and with an invariant mass within $\pm 20\%$ of

the nominal value. The STAR preliminary result for the A_N measurement of the Z^0 boson production in a single y^Z, P_T^Z bin is shown in Fig. 1.

3 Conclusions and outlook

This preliminary study, based on a pilot run of transverse polarized p+p collisions at $\sqrt{s}$ = 500 GeV with a recorded integrated luminosity of 25 pb^{-1}, is a proof-of-principle which shows that STAR is capable of measuring the transverse single spin asymmetry for fully reconstructed $W^{\pm}$, Z^0 bosons. The preliminary results from Fig. 1 can be compared with the most up-to-date theoretical A_N predictions for $W^{\pm}$, Z^0 boson production including TMD-evolution from reference [7], shown in Fig. 2, where the error bands have been updated accounting for the current almost complete uncertainty on sea-quark functions in the fits [8]. RHIC is capable of delivering 900 pb^{-1} in 14 weeks running using a dynamic β* squeeze [9] through the fill. Future STAR measurements of weak boson production , with a much higher collected luminosity (for projections see [10]), can lead to the first experimental test of the sign change of the Sivers function. Furthermore, it will provide an ideal tool to study the spin-flavor structure of sea quarks inside the proton, in an x-range where the measured asymmetry in the $\bar{u}$ and $\bar{d}$ unpolarized sea quark distribution [11] can only be explained by strong non-pQCD contributions.

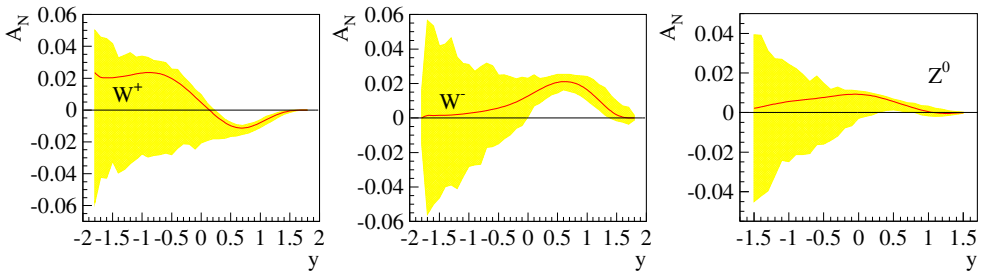

Figure 2: Theoretical prediction of A_N for $W^{\pm}$ and Z^0 boson production in p+p collisions at $\sqrt{s}$ = 500 GeV including TMD-evolution [7].

References

[1] D. W. Sivers, Phys. Rev. **D41**, 83 (1990), 43, 261 (1991)
[2] M. Anselmino *et al.*, Eur. Phys. J. **A39**, 89 (2009)
[3] J. C. Collins, Phys. Lett. **B536**, 43 (2002)
[4] Z.-B. Kang and J. -W. Qiu, *Phys. Rev. Lett.* **103**, 172001 (2009)
[5] L. Adamczyk *et al.*,The STAR Collaboration, arXiv:1404.6880 [nucl-ex]
[6] Bültmann S *et al.*, Phys. Lett. **B632** 167 (2006)
Bültmann S *et al.*, Phys. Lett. **B647** 98 (2007)
Ohlsen G G and Keaton Jr P W, Nucl. Instr. Meth. **109** 41 (1973)
[7] M. G. Echevarria, A. Idilbi, Z.-B. Kang, I. Vitev, Phys. Rev. D**D89**, 074013 (2014)
[8] Z.-B. Kang, private communication
[9] D. Trbojevic, J. Yichao, Y. Luo, BNL-102458-2013-CP
[10] S. Fazio and D. Smirnov (for the STAR Collaboration), PoS (DIS2014) 237
[11] E. A. Hawker *et al.*, Phys. Rev. Lett. **80**, 3715 (1998)

The OZI Rule and Spin Alignment of Vector Mesons at COMPASS

Karin Schönning[1] for the COMPASS collaboration

[1]Dept. of Physics and Astronomy, Uppsala University, Box 516, 751 20 Uppsala, Sweden and CERN, 1211 Geneve 23, Switzerland

DOI: http://dx.doi.org/10.3204/DESY-PROC-2014-04/36

The reaction $pp \to pVp$ ($V = \omega$, ϕ) has been studied with the COMPASS spectrometer in 2008 and 2009, using a 190 GeV/c proton beam impinging on a liquid hydrogen target. The measured cross section ratio ratio violates the OZI prediction by a factor of ≈4. Its kinematic dependence of the Feynman x_F and the M_{pV} mass is discussed in terms of diffractive production of baryon resonances in competition with central production. The $M_{p\omega}$ spectrum has a rich structure, indicating the importance of baryon resonances decaying into $p\omega$, in sharp contrast to the structureless $M_{p\phi}$ spectrum. Outside the resonant region, the OZI violation factor is about 8, independently of x_F. The spin density matrix element ρ_{00} of the vector mesons is studied in selected reference frames. Dependences of the vector meson spin alignment on x_F and M_{pV} are found.

The Okubo-Zweig-Iizuka (OZI) rule [1] states that all hadronic processes with disconnected quark lines are suppressed. As a consequence, the production of ϕ mesons from non-strange hadrons would only be allowed due to its deviation from ideal mixing with the ω meson. Using the known deviation of the mixing angle, $\delta_{\mathrm{V}} = 3.7^{\circ}$, the cross section ratio for ϕ and ω production is predicted to be $\sigma(AB \to X\phi)/\sigma(AB \to X\omega) = \tan^2 \delta_{\mathrm{V}} = 0.0042$, where A, B and X are non-strange hadrons [2]. At low energies, the ratio can be expressed in terms of meson-meson or meson-nucleon couplings: $g^2_{\phi\rho\pi}/g^2_{\omega\rho\pi} = g^2_{\phi NN}/g^2_{\omega NN} = \tan^2 \delta_{\mathrm{V}} = 0.0042$, assuming the coupling ratios $g_{\phi\rho\pi}/g_{\omega\rho\pi}$ and $g_{\phi NN}/g_{\omega NN}$ are equal [3].

The OZI rule has been tested in several experiments and has been found to be remarkably well fulfilled [4, 5]. Apparent violations of the OZI rule – observed in $p\bar{p}$ annihilations at rest and in nucleon-nucleon collisions – can be interpreted either as a true violation due to gluonic intermediate states [6] or as an evasion from the OZI rule because of a hidden strangeness component in the nucleon [7].

The COMPASS collaboration here presents a study of the OZI violation in $p_{\mathrm{beam}}\, p_{\mathrm{target}} \to p_{\mathrm{fast}}\, V\, p_{\mathrm{recoil}}$ at a beam momentum of 190 GeV/c. For simplicity, this will from now on be denoted $p\,p \to p\,V\,p$. Unless otherwise stated explicitly, p without subscript and the Feynman variable $x_{\mathrm{F}} = p_L/p_{L\mathrm{max}}$, p_L denoting the longitudinal momentum, will refer to the fast proton. The reduced 4-momentum transfer squared is $t' = |t| - |t|_{\mathrm{min}}$, where $t = (p_{p\mathrm{beam}} - (p_{p\mathrm{fast}} + p_V))^2$. In the region where the COMPASS data are collected, *i.e.* $t' > 0.1$ (GeV/c)^2, production of vector mesons occur either by resonant production, where the beam proton dissociates diffractively to an intermediate baryon resonance, or non-resonant production, which can be either central Pomeron-Reggeon fusion or a shake-out of a $q\bar{q}$ pair [7] from the sea of the beam nucleon when interacting with a Pomeron or a Reggeon emitted from the

target. In resonant production, the dynamics of the vector meson depends on the intermediate baryon resonance whereas in non-resonant production it depends on the exchange object(s).

The production mechanism is reflected in the decay angular distributions which can be expressed in terms of the spin density matrix [8]. When the inital state is unpolarised, symmetries leave one independent element of the spin density matrix, ρ_{00}, which is a measure for spin alignment (tensor polarisation). It can be extracted from distributions of the angle between the decay plane (3-body decay) or decay axis (2-body decay) of the vector meson and a well-chosen reference axis [9].

The COMPASS spectrometer set-up [10] is suitable for this kind of measurements due to the large angular acceptance and high momentum resolution. COMPASS is a two-stage fixed-target magnetic spectrometer at the CERN SPS. The analysis is based on the 2008 and 2009 data taking with a positively charged hadron beam impinging on a liquid hydrogen target. The hadron beam contains 75% protons which are tagged by CEDARs (differential Cherenkov detectors). Pions, protons and kaons in the final state are identified with a RICH detector in the first stage and electromagnetic (ECAL) and hadronic calorimeters in both stages of the set-up. The trigger system selects events with a recoiling proton in a cylindrical time-of-flight detector surrounding the target (RPD) which results in a minimum bias on the forward kinematics. Since the ω and ϕ mesons are measured simultaneously with the same set-up and triggers, many systematic uncertainties cancel.

For the analysis, events from the reactions $pp \rightarrow p\,\omega\,p$, $\omega \rightarrow \pi^+\pi^-\pi^0$ and $pp \rightarrow p\,\phi\,p$, $\phi \rightarrow K^+K^-$ are selected. The recoil proton is detected in the RPD, whereas charged pions, kaons and fast protons are detected in the spectrometer. RICH identification is required for the π^+ from the ω decay and the K^+ from the ϕ decay. The π^0 mesons from the ω decays are identified from the invariant mass distribution of two photons detected in the ECAL's. The ω mesons are identified from the $\pi^+\pi^-\pi^0$ invariant mass distribution and the ϕ mesons from the K^+K^- mass distribution. Additional cuts on exclusivity and coplanarity are applied. The x_F is required to lie within the interval 0.6-0.9 and t' within 0.1-1.0 $(\mathrm{GeV/c})^2$ to assure that the ϕ and the ω samples belong to the same phase space region. To separate signal from background, a Breit-Wigner function folded by a gaussian on top of a polynomial background has been fitted to the data. The acceptance is corrected for event-by-event using a 3-dimensional acceptance matrix in t', $M_{p\mathrm{V}}$ and x_F. The systematic uncertainties are estimated to 12%, where the largest contributions come from the RICH and ECAL efficiencies. More details on the analysis is given in Refs. [11, 12].

The invariant mass of the pV system, M_{pV}, has been studied for ω and ϕ. In the case of the ω, the data are divided into four different ranges in x_F (0.2-0.6, 0.6-0.7, 0.7-0.8 and 0.8-0.9). Several structures are then discernible in the $M_{p\omega}$ spectrum, located at about 1800 $\mathrm{MeV/c^2}$, 2200 $\mathrm{MeV/c^2}$ and 2600 $\mathrm{MeV/c^2}$. These can be interpreted as N^* resonances that have been observed in other experiments, mainly in $N\pi$ final states [13]. The $M_{p\phi}$ spectrum appears structureless.

The cross section ratio $R_{\phi/\omega} = \frac{d\sigma(p\,p \rightarrow p\,\phi\,p)/dx_\mathrm{F}}{d\sigma(p\,p \rightarrow p\,\omega\,p)/dx_\mathrm{F}}$ has been measured in three x_F intervals: 0.6-0.7, 0.7-0.8 and 0.8-0.9. The OZI violation factor is defined as the cross section ratio divided by the value predicted by the OZI rule: $F_\mathrm{OZI} = R_{\phi/\omega}/\tan^2\delta_\mathrm{V}$, with $\tan^2\delta_\mathrm{V} = 0.0042$. The results are shown in Figure 1. The ratio is between 2.9 and 4.5 and depends on x_F. The abundance of intermediate baryon resonances in ω production, observed in the $p\omega$ mass spectrum, suggests that resonant production is dominant in the case of ω but not for ϕ. In order to compare ω and ϕ samples produced with the similar mechanisms, the resonant region was removed by imposing a cut in the momentum of the vector meson in the rest frame of the

proton - vector meson system, p_V. This is shown in the left panel of Fig. 1. Since no structures are observed in the $M_{p\omega}$ spectrum above $M_{p\omega} = 3.3$ GeV/c^2, which corresponds to $p_V = 1.4$ GeV/c, the F_{OZI} factor was measured for $p_V > 1.4$ GeV/c. In this region, the value of F_{OZI} converges to about 8, independent of x_F. The SPHINX collaboration used $p_V > 1.0$ GeV/c [14] and we therefore carried out the same measurement for comparison. The COMPASS result is consistent with SPHINX [11].

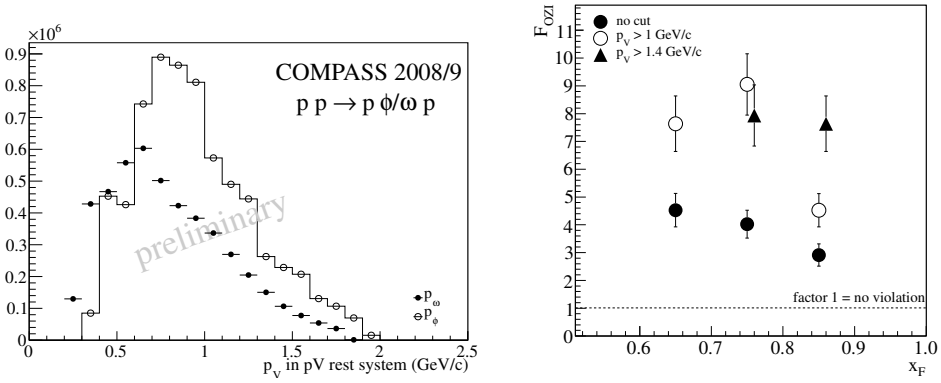

Figure 1: Left: The vector meson momentum p_V in the rest frame of the pV system, where V refers to ϕ (white dots) or ω (black dots. The ϕ histogram has been scaled by a factor of 100. Right: OZI violation factor F_{OZI} as a function of x_{F} for different p_V cuts.

The spin alignment, quantified by the first element of the spin denisty matrix, ρ_{00}, has also been measured. The differential cross section can be parameterised in terms of ρ_{00} and the angle between the analyser (the normal of the decay plane in the case of the $\omega \to \pi^+\pi^-\pi^0$ decay and the direction of one of the decay kaons in the case of the $\phi \to K^+K^-$ decay) and some reference axis. Two different reference axes have been tested: the direction of the pV system in the rest system of V (the helicity frame) and the direction of the transferred momentum from the beam proton to the fast proton, $\Delta\vec{P}$ (the transferred momentum frame). The ω meson is significantly aligned in the helicity frame and the value of ρ_{00} depends strongly on $M_{p\omega}$, as shown in the left panel of Figure 2. This is in line with the abundance of structures in the $M_{p\omega}$ spectrum and emphasises the importance of intermediate baryon resonances in the production of ω mesons. Above the resonant region, ρ_{00} approaches 1/3 which corresponds to an unaligned ω spin. The ϕ meson spin is unaligned in the helicity frame in the two measured $M_{p\phi}$ intervals, consistent with the absence of resonances in the $M_{p\phi}$ spectrum [11]. In non-resonant production, the helicty frame becomes irrelevant since the pV system does not correspond to a resonant state. In such cases, the transferred momentum frame should be a more natural choice. The results, presented in the right panel of Figure 2, show that this is indeed the case for both ω and ϕ. The ϕ meson spin is strongly aligned in this frame and the alignment becomes stronger with increasing x_F, *i.e.* when the contribution from central production increases. The results for the ω meson spin show the same behavious though the alignment is weaker than for ϕ. After removing the resonant region in the ω data, the results are consistent with those of the ϕ meson.

To summarise, this study shows that intermediate baryon resonances play a very important role in the production of ω mesons. This is supported by structures in the $M_{p\omega}$ spectrum, the p_V dependence of the OZI violation factor and the strong $M_{p\omega}$ dependence of the ω meson spin alignment in the helicity frame. The corresponding measurement for ϕ indicates an absence

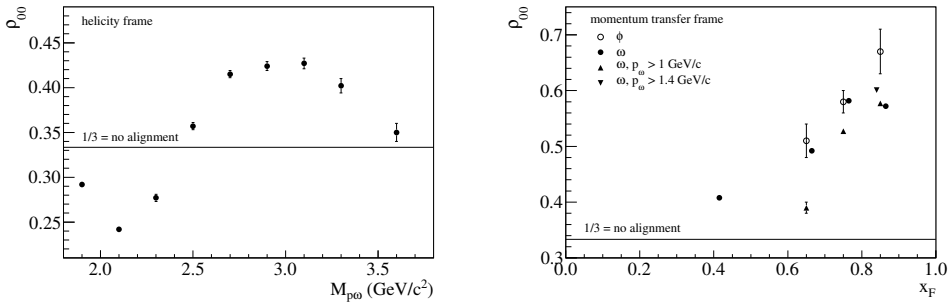

Figure 2: Left: Spin alignment ρ_{00} as a function of $M_{p\omega}$. Right: Spin alignment ρ_{00} extracted using $\Delta\vec{P}$ as reference axis as a function of x_F for different p_V cuts.

of baryon resonances in ϕ production. Other processes, *e.g.* central Reggeon-Pomeron fusion or the shake-out of a $q\overline{q}$ state in the nucleon sea may instead contribute here. The strong x_F dependence of the spin alignment with respect to the transferred momentum from the beam proton to the fast proton speaks in favour of the former. The latter could be investigated by comparing the results presented here, obtained with a proton beam, to results obtained with a pion beam. With a pion beam, no contribution from a $q\overline{q}$ shake-out can occur.

Another interesting finding is that outside the $p\omega$ resonant region, the OZI violation factor converges to a value of about 8, independently of x_F. This is in remarkable agreement not only with the SPHINX analysis [14] after removal of the low-$M_{p\omega}$ region, but surprisingly also with data close to threshold from ANKE [15], DISTO [16] and COSY-TOF [17, 18].

References

[1] S. Okubo, Phys. Lett. **5** (1963) 165; G. Zweig, Developments in the Quark Theory of Hadrons, Volume 1. Edited by D. Lichtenberg and S. Rosen. pp. 22-101; J. Iizuka, Prog. Theor. Phys. Suppl. **37** (1966) 21.

[2] H. J. Lipkin, Int. J. Mod. Phys. E **1** (1992) 603.

[3] H. J. Lipkin, Phys. Lett. B **60** (1976) 371.

[4] V. P. Nomokonov and M. G. Sapozhnikov, Phys. Part. Nucl. **34** (2003) 94 [Fiz. Elem. Chast. Atom. Yadra **34** (2003) 189].

[5] A. Sibirtsev and W. Cassing, Eur. Phys. J. A **7** (2000) 407.

[6] S. J. Lindenbaum, Nuovo Cim. A **65** (1981) 222.

[7] J. R. Ellis, M. Karliner, D. E. Kharzeev and M. G. Sapozhnikov, Phys. Lett. B **353** (1995) 319; J. R. Ellis, M. Karliner, D. E. Kharzeev and M. G. Sapozhnikov, Nucl. Phys. A **673** (2000) 256.

[8] K. Gottfried and J. D. Jackson, Nuovo Cim. **33** (1964) 309.

[9] K. Schilling, P. Seyboth and G. E. Wolf, Nucl. Phys. B **15** (1970) 397 [Erratum:ibid. B **18** (1970) 332].

[10] P. Abbon *et al.* [COMPASS Collaboration], Nucl. Instrum. Meth. A **577** (2007) 455.

[11] C. Adolph *et al.* [COMPASS Collaboration], Nucl. Phys. B **886** (2014) 1078.

[12] J. Bernhard, Ph.D. thesis, Mainz University (2014).

[13] J. Beringer *et al.* [Particle Data Group Collaboration], Phys. Rev. D **86** (2012) 010001.

[14] S. V. Golovkin *et al.*, Z. Phys. A **359** (1997) 435.

[15] M. Hartmann *et al.* [ANKE Collaboration] Phys. Rev. Lett. **96** (2006) 242301

[16] F. Balestra *et al.* [DISTO Collaboration], Phys. Rev. C **63** (2001) 024004

[17] S. Abd El-Samad *et al.* [COSY-TOF Collaboration], Phys. Lett. B **522** (2001) 16

[18] M. Abdel-Bary *et al.* [COSY-TOF Collaboration], Phys. Lett. B **647** (2007) 351

Studies of light Mesons at COMPASS

Sebastian Uhl on behalf of the COMPASS Collaboration

Technische Universität München, James-Franck-Straße, 85748 Garching, Germany

DOI: http://dx.doi.org/10.3204/DESY-PROC-2014-04/118

The COMPASS experiment has taken a large data set with a negative pion beam impinging on a liquid-hydrogen target to study the spectrum of light mesons in diffractive dissociation reactions. The properties of known resonances are studied, and new, possibly spin-exotic states are searched in three-pion final states. A new state at about $1.4\,\mathrm{GeV}/c^2$ with a_1 quantum numbers is observed in the decay to $f_0\,(980)\,\pi$. The spin-exotic 1^{-+} wave is investigated in order to search for the controversial $\pi_1\,(1600)$.

1 Introduction

The **Co**mmon **M**uon and **P**roton **A**pparatus for **S**tructure and **S**pectroscopy (COMPASS) is a fixed-target experiment located at CERN's Super Proton Synchrotron (SPS). It is aimed to study the structure and dynamics of hadrons. The spectrum of light mesons is investigated using reactions of a negative hadron beam, consisting mostly of pions, with a liquid-hydrogen target. Isovector states are diffractively produced and dissociate into multi-particle final states. The decay products are detected in a two-stage magnetic spectrometer equipped with an electromagnetic and hadronic calorimeter in each spectrometer stage [1]. The apparatus provides full coverage for charged and neutral particles, resulting in a homogenous acceptance over a rather wide kinematic range.

The diffractive dissociation of a beam pion into a three-pion final state is the dominant reaction in the data COMPASS collected by impinging a $190\,\mathrm{GeV}/c$ pion beam on a liquid-hydrogen target. A recoil-proton detector in the trigger selected events with a reduced four-momentum transfer squared t' from the beam to the target between 0.1 and $1.0\,\mathrm{GeV}^2/c^2$. In COMPASS the three-pion final state can be detected simultaneously in two different channels, $\pi^-\pi^-\pi^+$ and $\pi^-\pi^0\pi^0$. About 50 million exclusive $\pi^- p \to \pi^-\pi^-\pi^+ p$ and 3.5 million exclusive $\pi^- p \to \pi^-\pi^0\pi^0 p$ have been recorded.

The process is sketched in Fig. 1. The beam pion is excited to an intermediate state X^-, which subsequently decays into three pions. In order to study the intermediate state a partial-wave analysis using the isobar model is employed, decomposing the three-pion spectrum into its spin-parity components. In the isobar model the decay of the state X^- happens via successive two-body decays. In the case of the three-pion final state, X^- first decays to a bachelor pion and an isobar $R_{\pi\pi}$, which then decays to two pions. The $\rho\,(770)$, $f_0\,(980)$, $f_2\,(1270)$, $f_0\,(1500)$, $\rho_3\,(1690)$, and a broad $(\pi\pi)_S$ component are used as isobars in the present analysis. The fit model considers partial waves with the spin J of X^- up to 6. Also the relative orbital angular momentum L between the isobar $R_{\pi\pi}$ and the bachelor pion can go up to 6. Of the possible combinations, 87 waves with non-negligible intensity are kept for the final analysis:

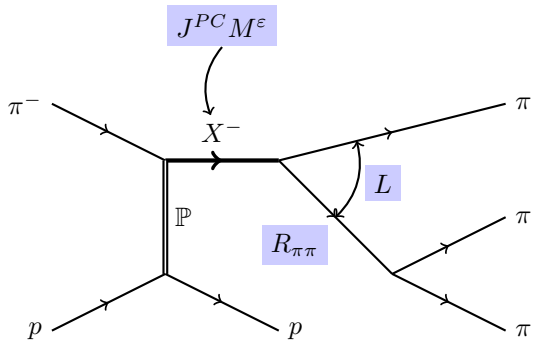

Figure 1: Sketch of the diffractive dissociation process under study.

80 with a positive reflectivity $\varepsilon = +1$ and 7 with $\varepsilon = -1$. In addition one incoherent wave with an isotropic angular distribution is included. The wave names $J^{PC}M^{\varepsilon}R_{\pi\pi}\pi L$ encode the quantum numbers of the intermediate state X^- and the information on the decay channel. The three-pion mass range between 500 and 2500 MeV/c^2 is divided into bins of 20 MeV/c^2 for the $\pi^-\pi^-\pi^+$ channel, and 40 MeV/c^2 for the $\pi^-\pi^0\pi^0$ channel. In addition the data are also divided into eleven bins of t' for $\pi^-\pi^-\pi^+$ and eight bins for $\pi^-\pi^0\pi^0$, such that all bins contain approximately the same number of events. The general features of this partial-wave analysis fit have been described before [2, 3].

2 The spin-exotic $J^{PC} = 1^{-+}$ wave

The existence of the $\pi_1(1600)$ is disputed. Previous experiments have claimed its observation [4], but could not reproduce this result on a larger sample with an extended set of waves in a limited range of t' [5]. COMPASS has also observed this state scattering a pion beam off a lead disk [6].

The partial-wave intensity of the spin-exotic $1^{-+}1^+\rho(770)\pi P$ wave found in the liquid-hydrogen data used for the present analysis is depicted in Fig. 2 (blue points) for the $\pi^-\pi^-\pi^+$ channel. A strong dependence of the intensity on the squared four-momentum transfer t' is observed. At lower values of t' only a broad structure is found, whereas when going towards higher t' a bump above 1600 MeV/c^2 is becoming more evident. This behavior is also observed in the $\pi^-\pi^0\pi^0$ channel.

Such a behavior could be caused by the interference of a genuine resonance with a large non-resonant contribution, for which the Deck effect [7] is a possible explanation. In order to study this Monte Carlo events were generated using the model from [8]. The same partial-wave decomposition was performed as for real data. The contribution to the exotic wave is displayed in Fig. 2 (green points). The intensity of the Deck model has been rescaled such that the total intensities in this wave over all mass and t' bins match. At lower values of t' a large part of the intensity can be described as coming from the Deck effect by this ansatz, at higher t' it is almost negligible.

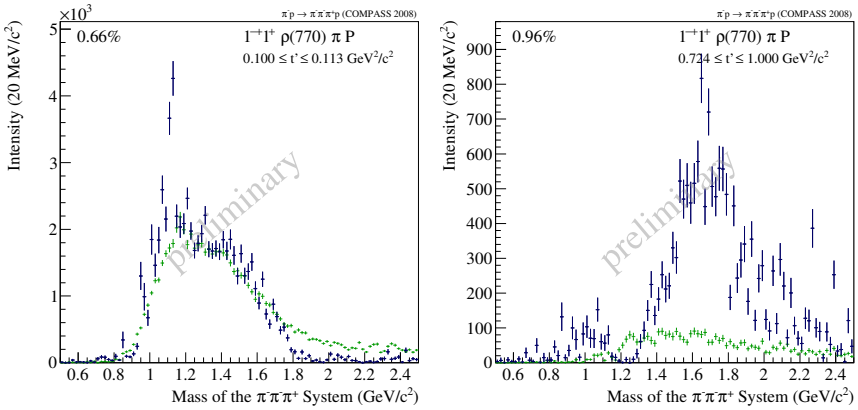

Figure 2: Partial-wave intensity of the spin-exotic $1^{-+}1^{+}\rho\,(770)\,\pi P$ wave (blue points) overlaid with a projection of a simulated Deck-effect into this wave (green points) for the lowest (left) and the highest (right) t' bin.

3 A new axial-vector state $a_1\,(1420)$

Compared to the previous COMPASS analysis [6] the number of partial-waves has almost been doubled. This is owed to the huge number of events allowing us to search also for smaller signals. One particularly interesting signal was found in the $1^{++}0^{+}f_0\,(980)\,\pi P$ wave. Fig. 3 shows the intensity of this wave for the two channels $\pi^-\pi^-\pi^+$ and $\pi^-\pi^0\pi^0$. A narrow structure around $1400\,\mathrm{MeV}/c^2$ is observed in both channels. In addition to the peak in the intensity spectrum, also rapid phase-motions with respect to the other waves are observed. This previously unobserved signal would correspond to a new state $a_1\,(1420)$. Different parameterizations for the isobar, in particular for the $f_0\,(980)$ and the broad $(\pi\pi)_S$ component have been tested in order to exclude a possible artifact from the used model.

Resonance parameters for this state and some well-known resonances are extracted from a fit of Breit-Wigner amplitudes to a subset of the spin-density matrix for the $\pi^-\pi^-\pi^+$ channel. This fit does not only describe the intensities of the individual waves, but also takes into account the interference between them. In the current analysis six waves are used, at least one resonant contribution is put into each wave: the $a_1\,(1260)$ and an a_1' in the $1^{++}0^{+}\rho\,(770)\,\pi S$ wave, the $a_2\,(1320)$ and an a_2' in the $2^{++}1^{+}\rho\,(770)\,\pi D$, the $\pi_2\,(1670)$ and $\pi_2\,(1880)$ in the $2^{-+}0^{+}f_2\,(1270)\,\pi S$, the $\pi\,(1800)$ in the $0^{-+}0^{+}f_0\,(980)\,\pi S$, the $a_4\,(2040)$ in the $4^{++}1^{+}\rho\,(770)\,\pi G$, and finally the new $a_1\,(1420)$ in the $1^{++}0^{+}f_0\,(980)\,\pi P$ wave. In addition there is one non-resonant contribution in each wave. The Breit-Wigner parameters are obtained from a simultaneous χ^2 fit to the spin-density submatrix of the six waves in all t' bins.

The extracted parameters of the major resonances are in agreement with previous measurements by COMPASS and other experiments [6]. Fig. 3 shows the result from this fit for the new $a_1\,(1420)$. A well determined mass of $M = 1412 - 1422\,\mathrm{MeV}/c^2$ and a narrow width of $\Gamma = 130 - 150\,\mathrm{MeV}/c^2$ is obtained. This is in contrast to other signals of similar magnitude like the a_1', the a_2' or the $\pi_2\,(1880)$ for which a larger uncertainty in mass and width is retrieved from the same fit.

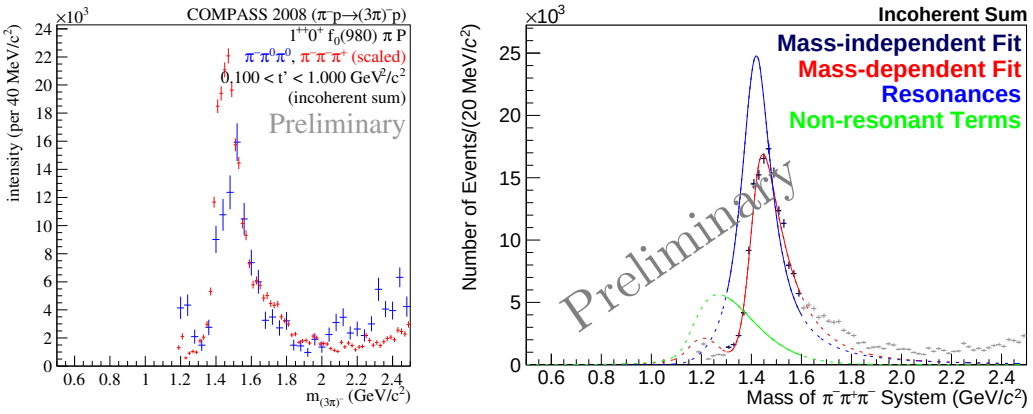

Figure 3: Left: Partial-wave intensity of the $1^{++}0^+ f_0\,(980)\,\pi P$ wave for the $\pi^-\pi^0\pi^0$ (blue) and the $\pi^-\pi^-\pi^+$ (red) channel. Right: Mass-dependent fit for the $\pi^-\pi^-\pi^+$ channel.

4 Conclusions

COMPASS has collected a huge data set of three-pion events to study the spectrum of light mesons. A possible new resonance with a_1 quantum numbers with a mass around $1420\,\mathrm{MeV}/c^2$ and a width below $150\,\mathrm{MeV}/c^2$ is found in the $f_0\,(980)\,\pi P$ decay mode. Compared to other small resonances the parameters are well constrained. The corresponding wave shows a rapid phase-motion with respect to the reference waves. The t'-resolved analysis provides valuable insight into the spin-exotic candidate $\pi_1\,(1600)$. Large parts of the intensity found in the corresponding wave at lower t' can be described with the Deck effect, which vanishes at higher t'. Work is ongoing to make a statement on the resonant nature of this state.

Acknowledgments

The author acknowledges financial support by the German Bundesministerium für Bildung und Forschung (BMBF), by the Maier-Leibnitz-Laboratorium der Universität und der Technischen Universität München, and by the DFG Cluster of Excellence "Origin and Structure of the Universe" (Exc153).

References

[1] COMPASS collaboration, P. Abbon *et al.*, Nucl. Instrum. Meth. A **577**, 455 (2007), arXiv:hep-ex/0703049; COMPASS collaboration, P. Abbon *et al.*, submitted to Nucl. Instrum. Meth. A, arXiv:1410.1797.

[2] S. Paul on behalf of the COMPASS Collaboration, proceedings of the MENU 2013, arXiv:1312.3678.

[3] S. Uhl on behalf of the COMPASS Collaboration, PoS(Hadron 2013)087, arXiv:1401.4943.

[4] S.U. Chung *et al.*, Phys. Rev. D **65**, 072001 (2002).

[5] A.R. Dzierba *et al.*, Phys. Rev. D **73**, 072001 (2006).

[6] COMPASS collaboration, M.G. Alekseev *et al.*, Phys. Rev. Lett. **104**, 241803 (2010).

[7] R.T. Deck, Phys. Rev. Lett. **13**, 169 (1964).

[8] C. Daum *et al.*, Nucl. Phys. B **182**, 269 (1981).

Measuring Luminosity at OLYMPUS

Dmitry Khaneft[1] for the OLYMPUS Collaboration[1]

[1]Johannes Gutenberg-Universität Mainz, Mainz, Germany

DOI: http://dx.doi.org/10.3204/DESY-PROC-2014-04/144

The OLYMPUS experiment [1] seeks to provide a high-precision measurement (<1% error) of the positron-proton versus electron-proton elastic scattering cross-section ratio. This requires fine control of all systematic uncertainties, including the calculation of the luminosity. For this purpose, multiple independent subsystems were operated alongside the main spectrometer during data taking to allow for empirical determination of the luminosity as a function of time. An approximate value is computed based on the parameters of the lepton beam and gaseous target, while small-angle elastic scatters of known cross-section are counted by two sets of ionization-based detector systems. The most precise value comes from counting coincidences of high-rate (pure QED) lepton-lepton scatters using a pair of calorimetric lead fluoride Cherenkov detectors.

1 Introduction

The OLYMPUS experiment was equipped with an eight-coil toroidal magnet and detectors located in two horizontal sectors on both sides of the beamline (see Fig. 1). Each side consisted of drift chambers for particle tracking and a set of time-of-flight scintillator bars for triggering and measurements of energy deposition, particle position, and timing. Two luminosity monitors were used: symmetric Møller/Bhabha (SYMB) calorimeters at $\theta = 1.291^\circ$ and detector telescopes at 12° in both sectors, each consisting of three gas electron multiplier (GEM) detectors interleaved with three multi-wire proportional chambers (MWPCs). In additional the luminosity could be measured using the slow control system.

2 Slow control system

The slow control system (see Fig. 2a) was used to control the gas feed to the target [2]. Together with the beam current measurements and the detector live time the slow control system allowed for a luminosity measurement using the following equation:

$$\mathcal{L} = I \cdot \rho \cdot \Delta t,$$

where I is the beam current, ρ is the target density, and Δt is the measurement time. Although the slow control was not precise enough ($\pm 15\%$ absolute and $\pm 3\%$ relative uncertainty) for the cross-section ratio determination, it made possible an on-line luminosity measurement that proved useful during the data taking period.

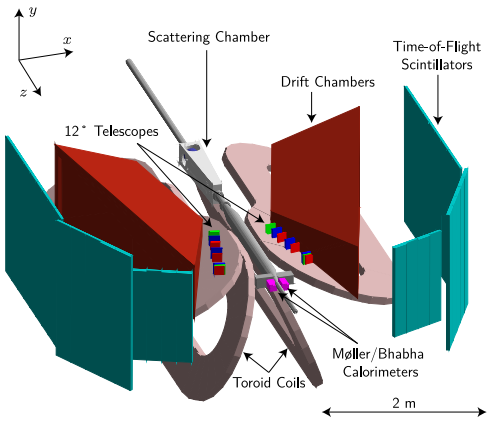

Figure 1: A solid-model representation of the OLYMPUS detector with the top four magnet coils removed to show the instrumented horizontal sectors

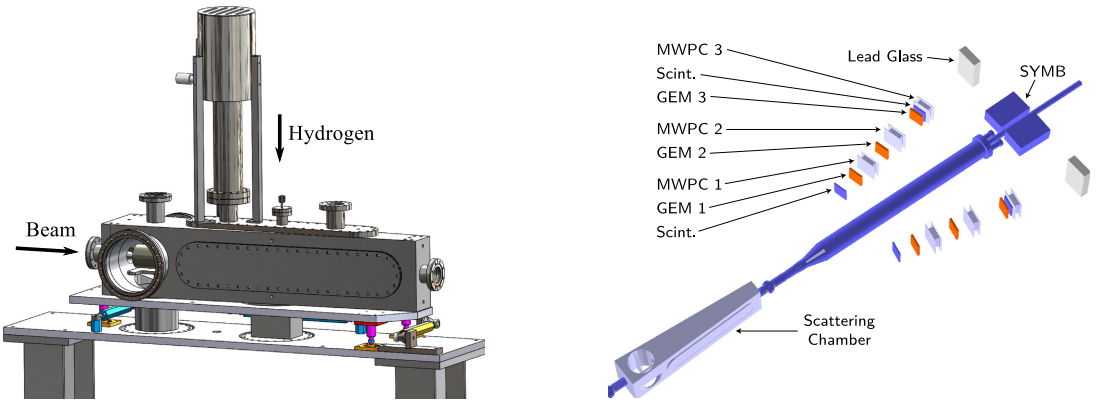

(a) (b)

Figure 2: CAD model of the OLYMPUS scattering chamber (a) and the layout of the $\theta = 12°$ luminosity monitors and the symmetric Møller/Bhabha calorimeters (b).

3 12° monitors

The 12° luminosity monitors (see Fig. 2b) measured elastic lepton-proton scattering in coincidence with the recoil proton detected in drift chambers. With a designed statistical precision of less than 1% per hour of data taking it is capable to measure the electron-proton to positron-proton elastic scattering cross-section ratio, as well as serve as a cross check for other luminosity monitors.

Fig. 3a and Fig. 3b show lepton reconstructed vertex and scattering angle. One can see that acceptance is similar for opposite beam charge and toroid polarity combinations but because the most of data were taken using positive magnet polarity a correction using a Monte Carlo simulation has to be performed.

Fig. 3c and Fig. 3d show lepton reconstructed vertex and scattering angle together with

corresponding Monte Carlo simulations, for a positive magnet polarity. The Monte Carlo results reproduce the data very well with only a small difference in scaling.

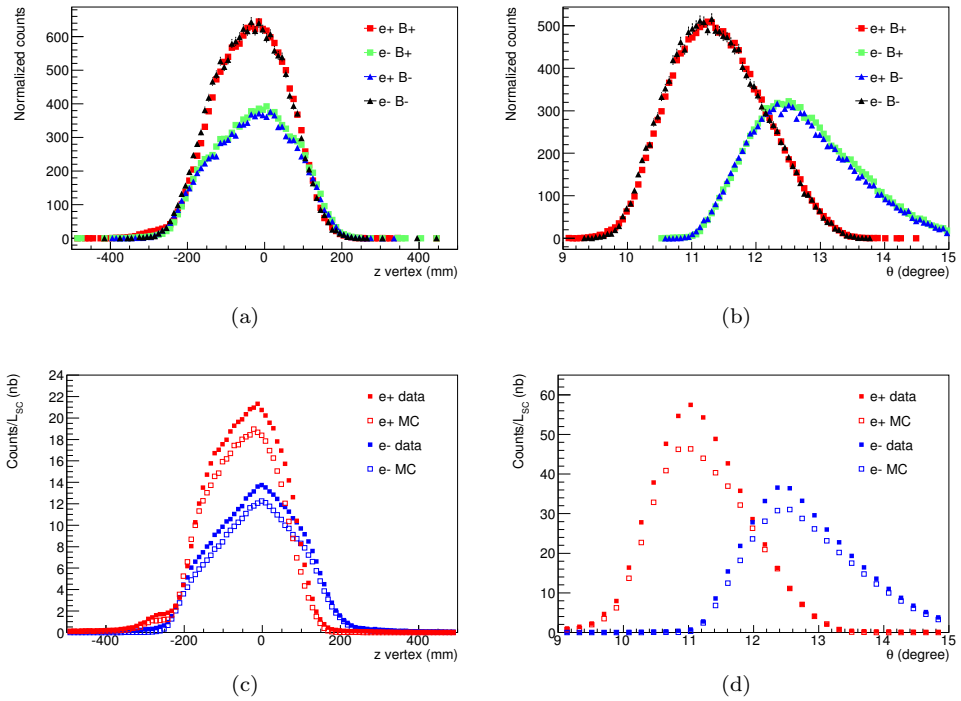

Figure 3: Lepton reconstructed vertex (a,c) and scattering angle (b,d).

4 Symmetric Møller/Bhabha monitor

Symmetric Møller/Bhabha monitor was designed for a high precision luminosity measurements. It detected lepton pairs from symmetric ($\theta = 1.29°$ for a beam energy of 2 GeV) Møller/Bhabha scattering. High event rates made possible to measure a luminosity on the timescale of minutes.

Fig. 4a shows SYMB signal in the coincidence (central crystal in both detectors should had the highest signal amplitude, i.e., contained the center of the electromagnetic shower) mode. Møller/Bhabha events can be seen as a red ellipse in the top right corner. Lines going out of the ellipse correspond to events when one of the leptons lost part of it's energy due to a collision with a collimator. Fig. 4b shows the data taken in the Master/Slave (central crystal in one of the detectors should have the highest signal amplitude) mode. In this mode electronics allowed to detect leptons from lepton-proton elastic scattering that can be seen as a yellow area at the right bottom edge of the figure.

As Møller/Bhabha cross-sections strongly depend on a scattering angle, it is crucial to know the exact position of detectors in respect to the target, as well as the offset and slope of the beam. Monte Carlo simulation (see Fig. 5a and Fig. 5b) shows counts dependency from

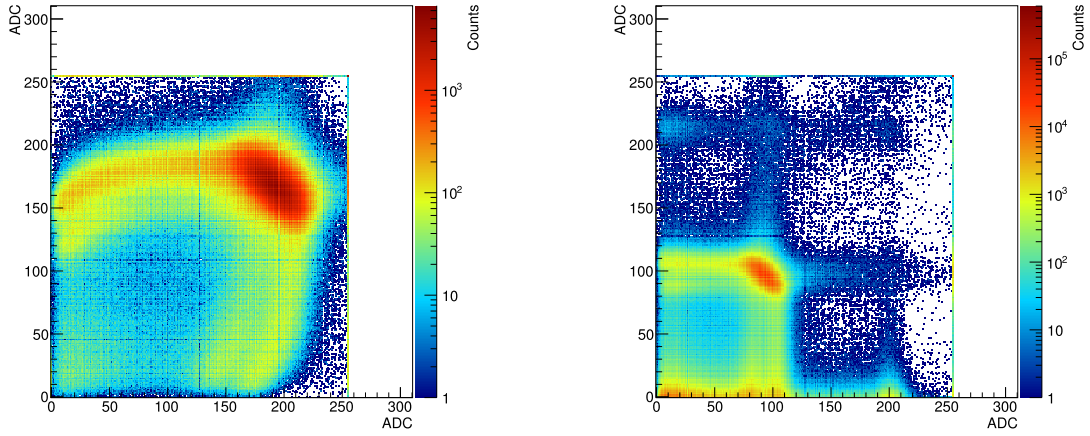

(a) (b)

Figure 4: Typical signal of the SYMB in the coincidence mode (a) and Master/Slave mode (b).

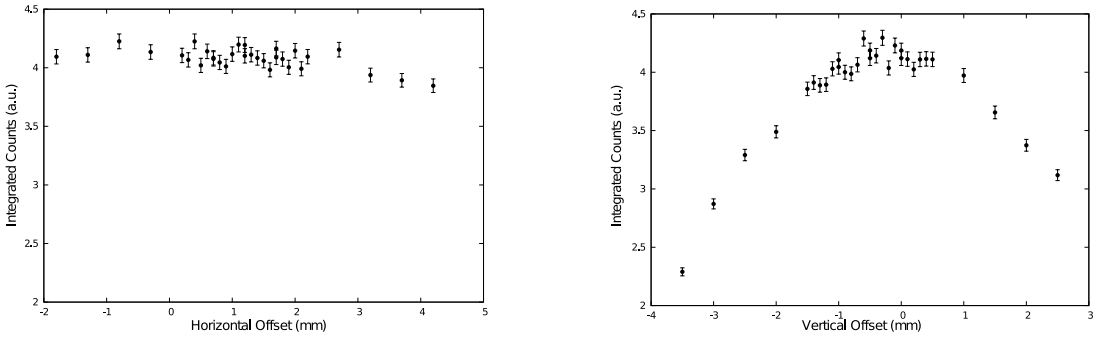

(a) (b)

Figure 5: Counts dependency from horizontal (a) and vertical (b) beam offsets.

horizontal and vertical beam offsets. It can be seen that the SYMB detector is very sensitive to the vertical beam offset, while changing horizontal position has much smaller effect.

References

[1] R. Milner, D. Hasell, M. Kohl, U. Schneekloth, N. Akopov, et al. The OLYMPUS experiment. *Nuclear Instruments and Methods in Physics Research Section A*, 741:1–17, 2014.

[2] J. C. Bernauer, V. Carassiti, G. Ciullo, et al. The OLYMPUS internal hydrogen target. *Nuclear Instruments and Methods in Physics Research Section A*, 755:20–27, 2014.

Elastic Electron and Muon Scattering Experiment Off the Proton at PSI

Steffen Strauch for the MUSE Collaboration

University of South Carolina, Columbia, SC 29208

DOI: http://dx.doi.org/10.3204/DESY-PROC-2014-04/76

While consistent results for the charge radius of the proton have been extracted from elastic electron-scattering data and through the spectroscopy of atomic hydrogen, recent high-precision studies of muonic hydrogen found notably smaller values for the charge radius. This so-called proton-radius puzzle raises questions ranging from experimental and methodological issues to physics beyond the Standard Model. The puzzle certainly calls for new measurements. The MUon Scattering Experiment (MUSE) at the Paul Scherrer Institute is being developed to provide elastic scattering data off the proton with electron and muon beams of positive and negative charge. Each of the four sets of data will allow the extraction of the proton charge radius; in combination, the data test possible differences of the electron and muon interactions and additionally two-photon exchange effects. The experiment will cover a four-momentum-transfer range from 0.002 to 0.07 GeV^2.

1 The Proton-Radius Puzzle

The electric and magnetic structure of the proton can be probed in electron-proton scattering experiments. In the one-photon exchange approximation, the experimental cross section depends on the electric and magnetic form factors, G_E and G_M, respectively. The form factors are functions of the four-momentum transfer squared, $-Q^2$, and can be determined in a Rosenbluth separation at fixed Q^2 in a series of measurements with varying electron scattering angles, θ. The slope of the electric form factor at $Q^2 = 0$ defines the proton charge radius, r_p,

$$r_p^2 = -6\hbar^2 \left.\frac{dG_E}{dQ^2}\right|_{Q^2=0} .$$

In a recent such measurement the A1 Collaboration in Mainz found a value of $r_p = 0.879 \pm 0.008$ fm [1]. The polarization transfer in electron-proton scattering experiments does not allow for a separation of the electric and magnetic form factors, but only depends on the form factor ratio, G_E/G_M. Polarization data, however, give independent constraints and a recent measurement and analysis of the LEDEX Collaboration at Jefferson Lab found a value of $r_p = 0.875 \pm 0.010$ fm [2]. An alternative method to determine the proton radius is the spectroscopy of atomic hydrogen. The electron wave function in the S states has overlap with the proton wave function and their interaction modifies the Lamb shift in hydrogen by an amount, which depends on the proton radius, $\Delta E \propto |\psi_S(0)|^2 r_p^2$. Radius extractions by CODATA from electronic hydrogen spectroscopy data give a value of $r_p = 0.8775 \pm 0.0051$ fm. Due to the larger muon mass, the overlap of the lepton wave function with the proton in

muonic hydrogen is 8×10^6 times larger than in electronic hydrogen, making the spectroscopy of muonic hydrogen that much more sensitive. While the electronic data have been consistent, recent measurements of the Lamb shift in the muonic hydrogen atom obtained a significantly smaller value of the proton radius of 0.84087 ± 0.00039 fm [3, 4]. That these precise results differ by seven standard deviations from the combined results of all electronic data is the so called *proton radius puzzle*. Figure 1 shows this obvious disagreement.

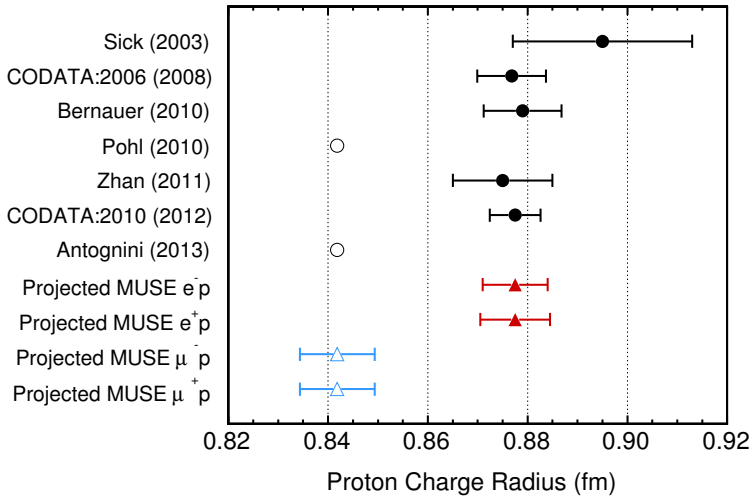

Figure 1: Previous results (circles) and projected MUSE results (triangles) of proton-radius measurements and extractions of electronic (full symbols) and muonic (open symbols) data [1, 2, 3, 4, 5, 6, 7].

This discrepancy has triggered a lively discussion. A recent review article [8] discusses many ideas, which were brought forward as possible solutions to the puzzle. The explanations can be grouped as follows. First, there may be problems with the experiment, including underestimation of uncertainties, difficulties in fitting the slope of the electric form factor for the radius extraction [9], or issues in QED calculations in the analysis of spectroscopy data. Second, novel hadronic physics may be important for μp but not for ep systems; suggested effects include proton polarizability effects proportional to m_ℓ^4 [10], off-shell corrections, and two-photon proton-structure corrections. Finally, the discrepancy may be an indication of the violation of μ/e universality and hint at physics beyond the standard model; *e.g.* [11]. Several ideas have been ruled out and none have gained universal acceptance.

Clearly, new data are needed. New spectroscopy measurements have been performed, including also experiments on deuterium and on helium [12]. New electron scattering experiments will try to improve on the precision of the form factor extraction and to reach lower values of Q^2 [12]. The proposed MUSE experiment [13] at the Paul Scherrer Institute (PSI), however, is unique. It is the only experiment, which will directly compare ep and μp in an elastic scattering experiment.

2 The MUSE Experiment at PSI

The MUSE experiment will measure $e^{\pm}p$ and $\mu^{\pm}p$ elastic scattering cross sections for lepton scattering angles between $\theta = 20^{\circ}$ and 100° and beam momenta of $p = 115, 153$, and 210 MeV with a low beam flux of up to 5 MHz. The experiment will cover a range in Q^2 between 0.002 and 0.07 GeV^2. Measurements with both charges for the lepton allow for studies of possible two-photon exchange mechanisms. The use of both e and μ beams allows for a direct test of lepton-type dependent effects.

The experiment will be set up at PSI's πM1 secondary beam line. A schematic diagram of the proposed large-acceptance setup is shown in Fig. 2. In the absence of inelastic reactions off the

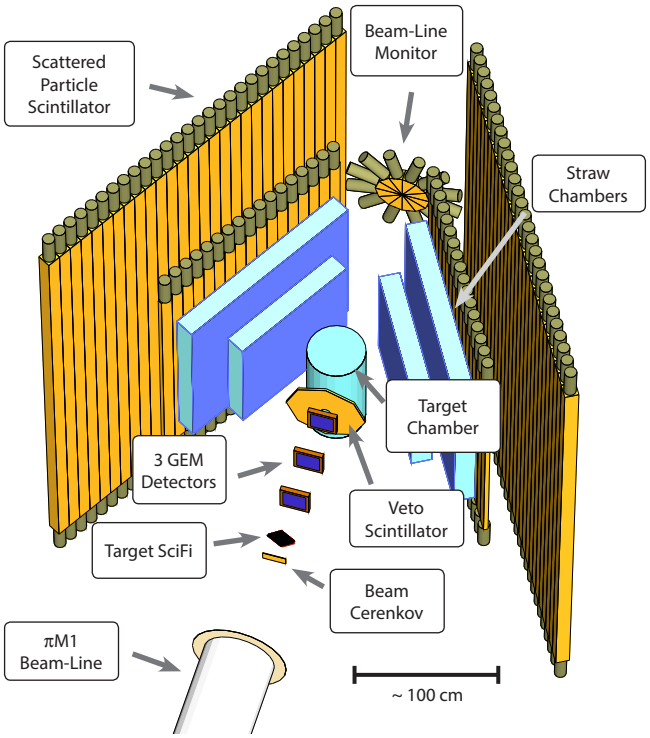

Figure 2: Schematic view of the planned detector setup for the MUSE experiment.

proton, the determination of the lepton scattering angle at a given beam momentum completely determines the kinematics of the reaction. A magnetic spectrometer to determine the scattered particle momentum is not needed. The beam Čerenkov detector measures the beam particle time relative to the radio-frequency of the accelerator. Test measurements have shown that the particle types (e, μ, and π) can be well separated by their time-of-flight. The quite large emittance of the incident beam requires to track each incoming particle in a scintillator fiber detector and a set of three gas-electron multiplier (GEM) chambers. The scattered particles are tracked in a series of straw chambers and are detected in the fast scintillators, which are

included in the trigger for the experiment. The veto scintillator, just upstream of the scattering chamber, allows a reduction of the trigger rate due to background tracks. The stability of the beam properties will be monitored with a downstream beam-line monitor. That detector also serves as an efficient veto for Møller scattering events.

Detailed Geant4 [14] based Monte-Carlo simulations of the experiment are underway to help optimize the detector setup and to study the parameters of the experiment. Items being studied include the resolution of the scattering-angle and vertex reconstructions, the muon decay-in-flight background, which is a source of electron tracks, and the Møller scattering background. Beam- and scattered-particle momentum distributions including radiative tails are necessary ingredients for radiative corrections of the experimental cross sections. These distributions are determined in full simulations of the experiment. The simulation results are being validated to the extent possible with experimental data.

Preliminary estimates of the total relative cross-section uncertainties for muon and electrons are 0.4% and 0.6%, respectively. The sensitivity of the experiment to differences in the extracted proton radius from e and μ scattering data is expected to be ± 0.009 fm.

Acknowledgments

R&D work on the MUSE experiment is funded by the U.S. NSF and DOE. This work has also been supported in parts by NSF PHY-1205782.

References

[1] J.C. Bernauer *et al.*, Phys. Rev. Lett. **105**, 242001 (2010).

[2] X. Zhan *et al.*, Phys. Lett. **B705**, 59–64 (2011).

[3] R. Pohl *et al.* Nature **466**, 213–216 (2010).

[4] A. Antognini *et al.*, Science **339**, 417–420 (2013).

[5] I. Sick, Phys. Lett. **B576**, 62–67, (2003).

[6] P.J. Mohr, B.N. Taylor, and D.B. Newell, Rev. Mod. Phys. **84**, 1527–1605 (2012).

[7] P.J. Mohr, B.N. Taylor, and D.B. Newell, Rev. Mod. Phys. **80**, 633–730 (2008).

[8] R. Pohl, R. Gilman, G.A. Miller, and K. Pachucki, Ann. Rev. Nucl. Part. Sci. **63**, 175–204 (2013).

[9] E. Kraus, K.E. Mesick, A. White, R. Gilman, and S. Strauch, arXiv:1405.4735 [nucl-ex] (2014).

[10] G.A. Miller, Phys. Lett. **B718**, 1078–1082, (2013).

[11] C.E. Carlson and B.C. Rislow, Phys. Rev. **D86**, 035013 (2012).

[12] Mainz Institute for Theoretical Physics. Proton Radius Puzzle Workshop, (2014). `https://indico.mitp.uni-mainz.de/conferenceDisplay.py?ovw=True&confId=14`.

[13] R. Gilman *et al.*, arXiv:1303.2160 [nucl-ex] (2013).

[14] S. Agostinelli *et al.*, Nucl. Instrum. Meth. **A506**, 250–303 (2003).

Constraining Transversity and Nucleon Transverse-polarization Structure Through Polarized-proton Collisions at STAR

James L. Drachenberg for the STAR Collaboration

Valparaiso University, Valparaiso, IN 46383, United States of America

DOI: http://dx.doi.org/10.3204/DESY-PROC-2014-04/78

Studies of jet and di-hadron production from polarized-proton collisions can expand current knowledge of nucleon transverse-polarization structure. In data collected in 2006 at $\sqrt{s} =$ 200 GeV, STAR observes for the first time in $p^{\uparrow} + p$ nonzero asymmetries from transversity coupled to Collins and di-hadron fragmentation functions. Measurements at 500 GeV allow sensitivity to different mixes of partonic subprocesses; and comparisons of all measurements at 200 and 500 GeV may enlighten theoretical questions concerning evolution, universality, and factorization-breaking in non-collinear formulations of pQCD. Results from analyses of STAR data collected in 2011 at $\sqrt{s} = 500$ GeV are presented, including first-ever measurements offering constraints on models involving gluon linear polarization.

1 Introduction

Azimuthal transverse single-spin asymmetries, A_{UT}, from polarized-proton collisions present a challenge and an opportunity. To account for nonzero A_{UT} from high-p_T hadroproduction (e.g. Ref. [1]) one is challenged to understand pQCD beyond the collinear formulation at leading twist [2]. By so doing, one gains the opportunity for insight into the transverse polarization structure of the nucleon.

Two approaches that can generate nonzero A_{UT} in pQCD are to formulate collinear pQCD to account for higher twist multi-parton correlators (twist-3 formalism) [3, 4] or to formulate pQCD to account for intrinsic transverse momentum dependence (TMD formalism) [5, 6]. In the twist-3 formalism one can obtain asymmetries, in principle, from both the parton distribution functions or the fragmentation functions (e.g. Refs. [7, 8]). Similarly, in the TMD formalism one can obtain asymmetries, in principle, from both the parton distribution functions (the so-called "Sivers effect") [5, 6] and the fragmentation functions, e.g. the so-called "Collins effect" [9]. Furthermore, it has been shown that the intrinsic transverse momentum integrals of the TMD functions are closely related to the twist-3 functions (e.g. Ref. [10]).

One avenue to enrich understanding of nucleon spin structure is through jet production from high-energy polarized-proton collisions [11]. By measuring the spin-dependent, azimuthal asymmetry in the jet production ($A_{UT}^{\sin\phi_S}$), one can access the twist-3 parton distribution function, sensitive to the Sivers function. Additionally, by measuring different spin-dependent, azimuthal modulations in the distribution of hadrons within a jet ($A_{UT}^{\sin(\phi_S-\phi_H)}$ or $A_{UT}^{\sin(\phi_S-2\phi_H)}$), one can gain sensitivity to transversity or gluon linear polarization coupling to spin-dependent Collins

or "Collins-like" [12] fragmentation functions, respectively. Similarly to the Collins effect, one can also access transversity coupled to polarized "interference fragmentation functions" (IFF) through spin-dependent, azimuthal asymmetries in the relative orientation of two hadrons from the same parton (e.g. Ref. [13]). While IFFs survive in the leading-twist, collinear formulation of pQCD with factorization expected to hold, the Collins effect depends upon TMD-factorization that is broken, in general, for high-p_T hadroproduction [14]. Thus, by studying both Collins and IFF asymmetries for overlapping kinematics, one opens the possibility to enlighten deep theoretical questions, such as TMD factorization-breaking and universality.

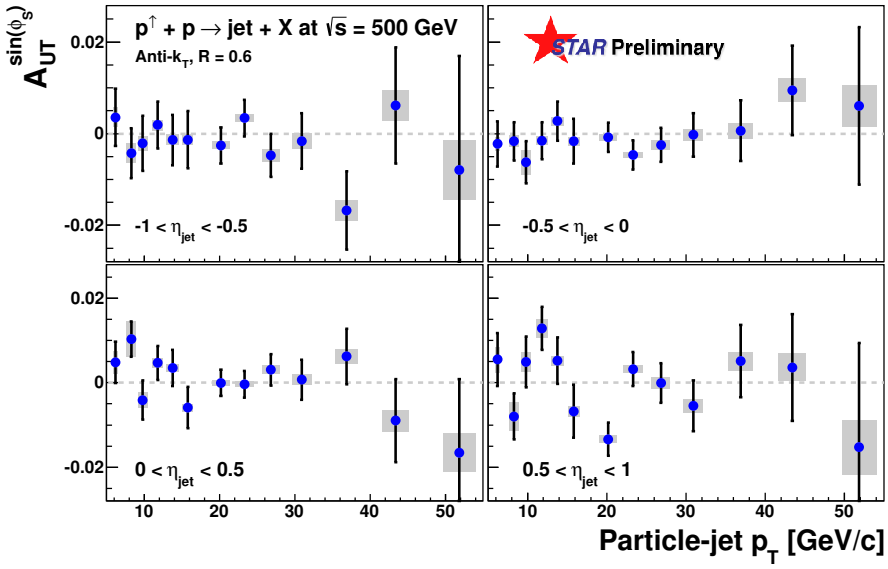

Figure 1: Inclusive jet azimuthal transverse single-spin asymmetries as a function of particle-jet transverse momentum for four bins of jet pseudorapidity relative to the polarized beam. Statistical uncertainties are shown by error bars and systematic uncertainties by error boxes. Measurements show no sign of large asymmetries and may suggest further constraints on the gluon Sivers function through the sensitivity of the twist-3 parton distribution function.

The STAR detector [15] at RHIC has seen the first signatures of transversity in polarized-proton collisions from charged-pion Collins [16] and IFF [17] asymmetries at $|\eta| < 1$ from 2.4 pb^{-1} at $\sqrt{s} = 200$ GeV collected in 2006. In 2011 STAR integrated 25 pb^{-1} of luminosity from $p^{\uparrow} + p$ at $\sqrt{s} = 500$ GeV with 53% polarization. This dataset allows the first measure of these asymmetries at $\sqrt{s} = 500$ GeV, including the first-ever measurement of the "Collins-like" asymmetry, with sensitivity to gluonic subprocesses enhanced relative to $\sqrt{s} = 200$ GeV. Comparison of all asymmetry modulations across $\sqrt{s} = 200$ and 500 GeV is expected to extend the current knowledge of these effects to broader kinematics as well as inform questions about the evolution of transversity and the TMD functions.

2 Analysis

The present data were collected with a minimum-bias trigger (VPDMB), requiring a coincidence in STAR's vertex position detector (VPD) [18], as well as with "jet-patch" triggers, requiring patches of energy in STAR's barrel (BEMC) and endcap (EEMC) electromagnetic calorimeters [15]. Jets are reconstructed using the "anti-k_T" algorithm [19] with a radius of 0.6 and utilize energy deposition in the BEMC and EEMC as well as charged-particle tracks from STAR's time projection chamber (TPC) [15].

Descriptions of the analysis techniques and simulation studies are given in Ref. [20]. The dominant systematic uncertainties arise from jets reconstructed at the detector level that fail to match to one at the parton-jet level. Additional systematic uncertainties come from the contamination of kaons, protons, and electrons to the charged-pion signal; trigger bias; the "leak-through" of competing effects coupling to non-uniform detector acceptance; uncertainties from calorimeter gains, efficiencies, and response to charged hadrons; tracking efficiency; and Monte Carlo simulation statistics. Measured asymmetries are corrected for smearing due to finite azimuthal-angle resolution.

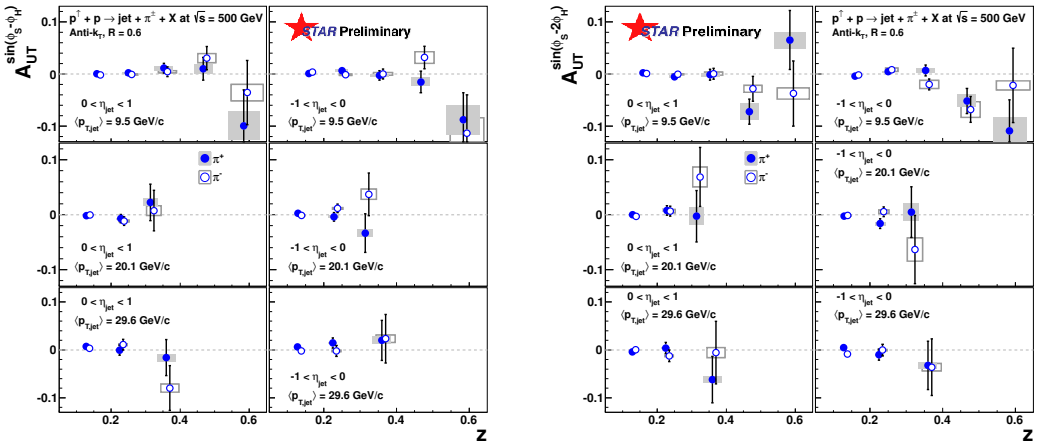

Figure 2: (left) Collins and (right) "Collins-like" asymmetries as a function of pion z for three bins of jet p_T and two bins of jet pseudorapidity relative to the polarized beam. Collins asymmetries are consistent with zero at low jet p_T, where gluonic subprocesses dominate, and are statistics limited at high jet p_T, where the best sensitivity to quark subprocesses is expected. The present "Collins-like" asymmetries should provide the first experimental constraints on model predictions utilizing linearly polarized gluons.

3 Results

In Fig. 1 the measured azimuthal asymmetries in the inclusive jet production are presented as a function of particle-jet p_T for four bins of jet pseudorapidity relative to the polarized beam. No large asymmetries are observed, consistent with expectation from measurements at $\sqrt{s} = 200$ GeV [21, 22, 23] as well as model predictions [7]. The present data may suggest

further constraints on the gluon Sivers function through the sensitivity of the twist-3 parton distribution function.

The left-hand panel of Fig. 2 shows Collins asymmetries as a function of $z = p_\pi/p_{jet}$ for three bins of jet p_T and two bins of jet psuedorapidity relative to the polarized beam. At low p_T, Collins asymmetries are expected to be quite small due to the prevalence of gluonic subprocesses [24], and this is consistent with the present measurement. For the higher two bins of jet p_T, quark-gluon scattering is expected to begin to dominate the underlying partonic cross section [24]. Thus, one may expect sensitivity to a nonzero Collins effect at higher p_T, however, the present data are statistics limited in this kinematic region. Analysis of STAR's high-statistics dataset at $\sqrt{s} = 200$ GeV, collected in 2012, will provide good sensitivity to effects from quark subprocesses in a region where nonzero signals are already observed [16, 25].

The right-hand panel of Fig. 2 shows the "Collins-like" asymmetries as a function of z for three bins of jet p_T and two bins of jet psuedorapidity relative to the polarized beam. Existing model predictions are unconstrained by measurement and suggest a maximum possible upper-limit of $\approx 2\%$ [11]. The present data fall well below this maximum with the best precision at lower values of z, where models suggest the largest effects may occur. Thus, the present data should allow for the first experimental constraints beyond the positivity bounds.

References

[1] B. I. Abelev et al. *Phys. Rev. Lett.*, 101:222001, 2008.

[2] G. Kane, J. Pumplin, and W. Repko. *Phys. Rev. Lett.*, 41:1689, 1978.

[3] A. Efremov and O. Teryaev. *Yad. Fiz.*, 36:242, 1982. [Sov. J. Nucl. Phys. 36, 140 (1982)].

[4] J. Qiu and G. Sterman. *Phys. Rev.*, D59:014004, 1998.

[5] D. Sivers. *Phys. Rev.*, D41:83, 1990.

[6] D. Sivers. *Phys. Rev.*, D43:261, 1991.

[7] K. Kanazawa and Y. Koike. *Phys. Lett.*, B720:161, 2013.

[8] K. Kanazawa, Y. Koike, A. Metz, and D. Pitonyak. *Phys. Rev.*, D89:111501, 2014.

[9] J. Collins. *Nucl. Phys.*, B396:161, 1993.

[10] D. Boer, P.J. Mulders, and F. Pijlman. *Nucl. Phys.*, B667:201, 2003.

[11] U. D'Alesio, F. Murgia, and C. Pisano. *Phys. Rev.*, D83:034021, 2011.

[12] M. Anselmino et al. *Phys. Rev.*, D73:014020, 2006.

[13] A. Bacchetta and M. Radici. *Phys. Rev.*, D70:094032, 2004.

[14] T.C. Rogers and P.J. Mulders. *Phys. Rev.*, D81:094006, 2010.

[15] K.H. Ackermann et al. *Nucl. Instr. Meth.*, A499:624, 2003. and references therein.

[16] R. Fatemi. *AIP Conf. Proc.*, 1441:233, 2012.

[17] A. Vossen. *AIP Conf. Proc.*, 1560:519, 2013.

[18] W.J. Llope et al. *Nucl. Instr. Meth.*, A759:23, 2014.

[19] M. Cacciari, G. P. Salam, and G. Soyez. *J. High Energy Phys.*, 04:063, 2008.

[20] J.L. Drachenberg. *EPJ Web Conf.*, 73:02009, 2014.

[21] B. Abelev et al. *Phys. Rev. Lett.*, 99:142003, October 2007.

[22] L. Adamczyk et al. *Phys. Rev.*, D86:032006, August 2012.

[23] A. Adare et al. arXiv:1312.1995.

[24] A. Mukherjee and W. Vogelsang. *Phys. Rev.*, D86:094009, 2012.

[25] E.C. Aschenauer et al. The RHIC Spin Program: Achievements and Future Opportunities. 2013. arXiv:1304.0079.

Partial Wave Analyses of the $\pi^+\pi^-\pi^-$ System at upgraded VES Setup

Igor Kachaev[1], *V. Dorofeev*[1], *A. Ekimov*[1], *V. Gotman*[1], *A. Ivashin*[1], *V. Kalendarev*[1], *Yu. Khokhlov*[1,2], *M. Kholodenko*[1], *V. Konstantinov*[1], *V. Matveev*[1], *M. Mikhasenko*[1], *V. Nikolaenko*[1], *A. Plekhanov*[1], *D. Ryabchikov*[1], *Yu. Salomatin*[1], *V.Sugonyaev*[1], *E. Volkov*[1], *A. Zaitsev*[1,2]

[1] IHEP, Pobedy street 1, 142280 Protvino, Russia
[2] MIPT, Kerchenskaya street 1A, 117303 Moscow, Russia

DOI: http://dx.doi.org/10.3204/DESY-PROC-2014-04/200

Partial Wave Analysis of the $\pi^+\pi^-\pi^-$ system produced by 29 GeV/c π^- beam on berillium target is presented. About $30 \cdot 10^6$ events in the wide $|t'|$ range $0 \ldots 0.8$ GeV^2/c^2 are collected with upgraded VES setup. The size of the data sample is 2.5 times larger than that previously analyzed by VES. Data are analyzed using formalism of density matrix with unlimited rank. We discuss status of the $a_1(1420)$, $a_2(1700)$, $a_3(1875)$ states, structure of exotic $\rho(770)\pi$ P-wave with $J^{PC} = 1^{-+}$.

1 VES setup and events selection

We present preliminary results of mass independent PWA of the $\pi^+\pi^-\pi^-$ system on the data obtained after VES upgrade. We compare them with data obtained before upgrade and discuss structures which can be considered resonant. Currently we do not claim any numerical results.

VES setup is full featured magnetic spectrometer which operates on mostly π^- beam (2% of K^-) with energy 37 GeV/c before upgrade and 29 GeV/c after upgrade. It is equipped with electromagnetic calorimeter and multicellular Cherenkov counter for particle identification. Description of VES setup before upgrade can be found in [1] and after upgrade in [2]. For charged 3π system net result of the upgrade is severely large acceptance (see Fig. 1) due to taking out of trigger hodoscope and severely large statistics due to upgraded DAQ.

Diffractive production of charged 3π final state dominates at VES energies, so data selection is simple and background is negligible. We require beam particle identified as π^-, 3 tracks with charges $+--$ (identification as π mesons is done for old data only), total energy for charged tracks 27–31 (36–38) GeV, free (not associated with tracks) energy in the electromagnetic calorimeter less than 0.5 GeV and vertex of interaction inside the target. Analysis is done for $M(3\pi) = 0.6$–2.6 GeV/c^2 in 20 MeV/c^2 bins and four $|t'|$ intervals 0–0.03–0.15–0.30–0.80 GeV^2/c^2. We have about $30 \cdot 10^6$ 3π events after upgrade and about $12 \cdot 10^6$ 3π events before upgrade.

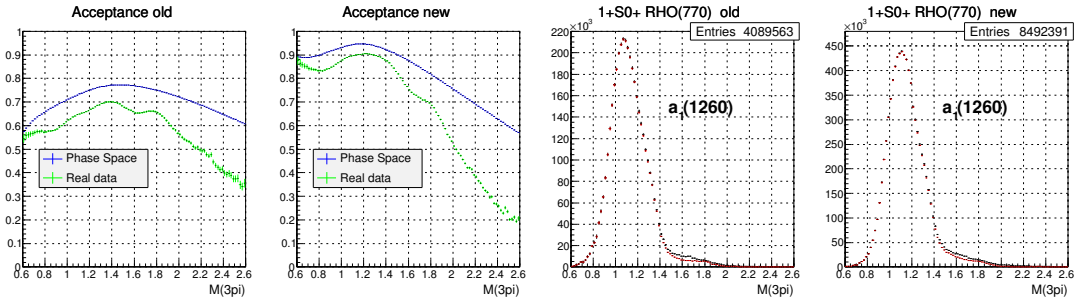

Figure 1: VES geometric acceptance before and after upgrade; largest wave $1^+S0^+\rho(770)$ for $|t'| < 0.03\ GeV^2/c^2$ in old and new data.

2 Method of the analysis

Our method of the analysis is based on Illinois PWA [3]. We are using extended likelihood event by event fit with positive definite density matrix as parameters. No restrictions are placed on the rank of the matrix. Amplitudes are constructed using isobar model, sequential decay of 3-particle system via $\pi\pi$ subsystem, with relativistic corrections according to [4]. Wave has quantum numbers $J^P L M^\eta$ R where J^P is spin-parity for 3π system, M^η is projection of spin and exchange naturality, R is the known resonance in $\pi\pi$ system and L is orbital momentum in Rπ decay. Isospin and G-parity $I^G = 1^-$ are the same for all 3π charged states. To describe broad part of $\pi\pi$ S-wave we use modified M solution from [5]. To make this amplitude broad we drop 4-th order terms and coupling to $K\bar{K}$. We name this pseudo state ε, it should describe among other things $f_0(1400)$ and possible $\sigma(600)$. Narrow $f_0(975)$ and $f_0(1500)$ are included separately. Purely geometric (not GEANT) model of the acceptance is used.

2.1 Coherent part of density matrix

Coherent part of the density matrix ρ is the largest part of the matrix which has rank one and behaves like vector of amplitudes. Let us decompose ρ with dimension d into its eigenvalues and eigenvectors:

$$\rho = \sum_{k=1}^{d} e_k V_k V_k^+ \quad \text{where} \quad \begin{cases} e_k \text{ is k-}th \text{ eigenvalue} \\ V_k \text{ is k-}th \text{ eigenvector} \end{cases}$$

Let $e_1 \gg e_2 > \ldots > e_d > 0$. This condition is often met for 3π system. Leading term $\rho_L = e_1 V_1 V_1^+$ is coherent part of density matrix and $\rho_S = \rho - \rho_L$ is the rest, incoherent part. This decomposition is stable with respect to variations of ρ matrix elements. Experience shows that resonances tend to concentrate in ρ_L while ρ_S can contain non-leading exchanges, albeit it often contains garbage. Results for full ρ are drawn below as black points with errors, for ρ_L as red one.

3 Fit results

In Fig. 1 one can see wave $1^+S0^+\rho(770)$ for low $|t'|$ region in both old $37\,GeV/c$ and new $29\,GeV/c$ data. The wave contains huge contribution from $a_1(1260)$ and a shoulder at $M(3\pi) \approx$

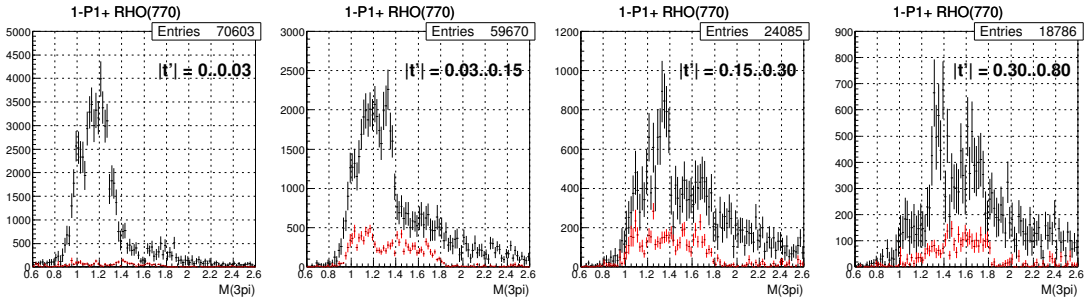

Figure 2: Exotic wave $1^-P1^+\rho(770)$ in all four $|t'|$ regions, old 37 GeV/c data.

$1.7\,GeV/c^2$ which can correspond to $a_1(1700)$. Two conclusions can be drawn here — first, the structure of the wave is approximately the same in both old and new data; next, data for the coherent part of the density matrix fill the whole wave. The same is true for all other largest waves, like $0^-S0^+\varepsilon$ and $2^-S0^+f_2(1270)$ (not shown here).

Probably the wave with exotic quantum numbers $J^{PC} = 1^{-+}$ has the most controversial status in the whole 3π PWA. Corresponding objects $\pi_1(1300)$ and $\pi_1(1600)$ are long discussed. The wave $1^-P1^+\rho(770)$ is shown in Fig. 2, 3 for all four $|t'|$ intervals both for old and new data. The wave is small — no more than 2–5% on the total number of events for old and new data in all $|t'|$ regions. This wave does not correspond to coherent part of density matrix — results for ρ_L are 2–10 times smaller than for the whole ρ. Prominent feature of the new data is that this wave is two times larger than in old data with respect to total number of events for $|t'| < 0.03\ GeV^2/c^2$ and is slightly more structured in other $|t'|$ regions. We think that our model of the setup is still too crude. Given this data existence of both π_1 objects looks questionable.

Now we will discuss some other possibly resonant waves. To save space only new 29 GeV/c data are shown. As it was shown in the presentation new data have better quality although old data mostly lead us to the same conclusions. In Fig. 4 (a) one can see wave $2^+D1^+\rho(770)$ for medium $|t'| = 0.03 \ldots 0.15\ GeV^2/c^2$ region with well known $a_2(1320)$. State $a_2(1700)$ is discussed in this wave. One can see that the state $a_2(1320)$ is in the coherent part of the density matrix ρ_L and there is nothing in this wave outside $a_2(1320)$ region, especially in its

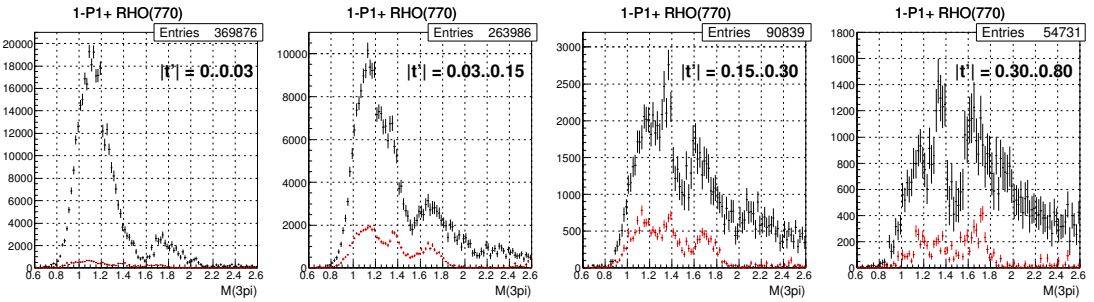

Figure 3: Exotic wave $1^-P1^+\rho(770)$ in all four $|t'|$ regions, new 29 GeV/c data.

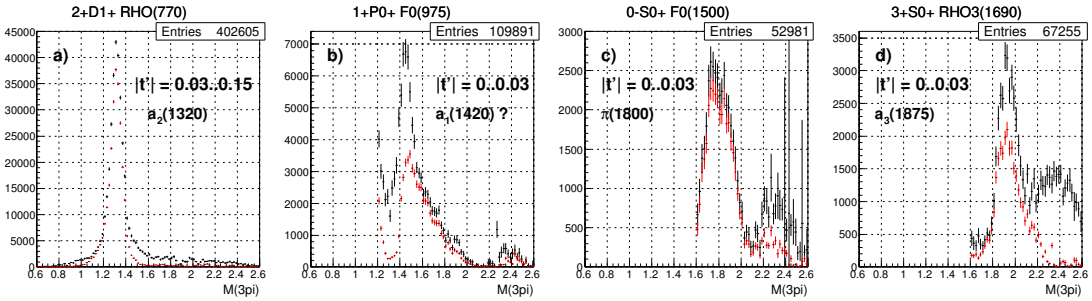

Figure 4: Waves $2^+D1^+\rho(770)$, $1^+P0^+f_0(975)$, $0^-S0^+f_0(1500)$, $3^+S0^+\rho_3(1690)$, new data.

coherent part. We can't see anything which can be interpreted as $a_2(1700)$.

Until the end of this section all waves are shown for $|t'| < 0.03\ GeV^2/c^2$. In Fig. 4 (b) the wave $1^+P0^+f_0(975)$ with discussed $a_1(1420)$ is shown. Good narrow resonant like structure can be seen at $M(3\pi) \approx 1.45\ GeV/c^2$. The same structure, albeit less prominent and never reported, can be seen in our old data. This structure has some peculiarities — its coherent and incoherent parts are approximately of the same magnitude; coherent part is severely wider than the peak itself. These features make difficult resonant interpretation of given structure.

In Fig. 4 (c) the wave $0^-S0^+f_0(1500)$ is shown. This is probably a decay mode $\pi(1800) \to f_0(1500)\pi$ which was studied before but is much more pronounced in new data. For this wave at $M(3\pi) \sim 1.8GeV/c^2$ coherent part fills the whole wave which supports resonant interpretation of the peak. In Fig. 4 (d) one can see the wave $3^+S0^+\rho_3(1690)$. A peak at $M(3\pi) \sim 1.9\ GeV/c^2$ is clearly seen. The peak is even more pronounced in ρ_L. We think this is a decay mode $a_3(1875) \to \rho_3(1690)\pi$. The object $a_3(1875)$ is listed as "further states" in [6] and was last observed in [7]. Our analysis can be a ground to re-establish this state.

4 Conclusions

Mass-independent PWA is done for old 37 GeV and new 29 GeV $\pi^+\pi^-\pi^-$ data collected with VES setup. Preliminary results are shown. Large PWA waves look alike for 37 GeV and 29 GeV data. Some small waves are seen much better in new data. Decay modes $\pi(1800) \to f_0(1500)\pi$, $a_3(1875) \to \rho_3(1690)\pi$ are seen in 0^-S and 3^+S waves. State $a_2(1700)$ is not seen in $2^+D1^+\,\rho\pi$. Interpretation of $f_0(975)\pi$ in 1^+S wave at $M \sim 1.4\ GeV/c^2$ is controversial. The wave $1^-P1^+\rho(770)$ with $J^{PC} = 1^{-+}$ is small, no more than 2–4% from total number of events in all $|t'|$ regions both in old and new data. Its coherent part is 2–10 times smaller.

Acknowledgments

This research was supported in part by Presidential grant NSh-999.2014.2 and RFBR grant 13-02-00576.

References

[1] S.I. Bityukov *et al.*, Phys. Lett. **B268** 137 (1991)

[2] Yu. Khokhlov *et al.*, EPJ Web of Conferences **37**, 01029 (2012)
[3] J.D. Hansen *et al.*, Nucl. Phys. **B81** 403 (1974)
[4] S.U. Chung *et al.*, Phys. Rev. **D48**, N3 1225 (1993)
[5] Au, Morgan, Pennington, Phys. Rev. **D35** 1633 (1987)
[6] K. Nakamura *et al.*, Particle Data Group, **JP G** 37, 075021 (2010)
[7] S.U. Chung *et al.*, Phys. Rev. **D65** 07 (2001)

Chapter 3

Quarks and gluons in hot and dense matter

Upsilon Production at the STAR Experiment with a Focus on New U+U Results

Róbert Vértesi for the STAR Collaboration

Nuclear Physics Institute ASCR, 25 068 Řež, Czech Republic

DOI: http://dx.doi.org/10.3204/DESY-PROC-2014-04/91

We report recent Υ measurements in p+p, d+Au and Au+Au collisions at $\sqrt{s_{NN}} = 200$ GeV, and detail the analysis in U+U collisions at $\sqrt{s_{NN}} = 193$ GeV. Results on Υ production versus rapidity are consistent with pQCD predictions in p+p collisions. However, Υ production in mid-rapidity ($|y|<0.5$) d+Au collisions is suppressed with respect to p+p collisions beyond model predictions that take into account modification of parton distribution functions and initial parton energy loss inside nuclei. The nuclear modification factor R_{AA} shows a significant suppression in central Au+Au and U+U collisions, consistent with model calculations including color screening effects in a deconfined medium.

1 Introduction

Due to color screening, the production of quarkonia in high energy heavy ion collisions is expected to be sensitive to the energy density of the medium. Sequential suppression of different quarkonium states may therefore serve as a thermometer of the medium [1]. Although the suppression of charmonia was anticipated as a key signature of the Quark Gluon Plasma (QGP), the observed energy dependence of J/ψ suppression is rather weak [2]. This phenomenon is explained by J/ψ production via recombination (coalescence) of $c\bar{c}$ pairs in the QGP. Bottomonia, on the other hand, are less affected by recombination and can provide a cleaner probe of the strongly interacting medium. While p+p measurements provide a benchmark for pQCD and serve as a baseline for nuclear modification, d+Au collisions are generally considered as suitable to study cold nuclear matter (CNM) effects such as shadowing of the parton distribution functions and initial state parton energy loss. Central U+U data at $\sqrt{s_{NN}} = 193$ GeV, which is estimated to have a 20% higher average energy density than that of Au+Au [3], allow for further tests of the sequential suppression hypothesis.

2 Experiment and analysis

The STAR experiment at RHIC is a complex detector that provides a full azimuthal coverage at mid-rapidity ($|\eta|<1$). A detailed description of the STAR detector is in Ref. [4]. The $\Upsilon \to \mathrm{e}^-\mathrm{e}^+$ decay channel, with a branching ratio $B_{\mathrm{ee}} \approx 2.4$ %, was studied. Analysis of year 2012 $\sqrt{s_{NN}} =$ 193 GeV U+U data was done in a similar way to recently published Υ measurements in p+p, d+Au and Au+Au collisions at $\sqrt{s_{NN}} = 200$ GeV [5], with differences highlighted below. A total of 17.2 million *high-tower* triggered U+U events were collected requiring an energetic hit

in the Barrel Electromagnetic Calorimeter (BEMC), corresponding to an integrated luminosity of 263.4 μb^{-1}. Momentum measurement and electron identification based on the energy loss dE/dx were done in the Time Projection Chamber (TPC). The projected position of the track is required to match the position of the hit in the BEMC to the extent $\Delta R = (\Delta\varphi^2 + \Delta\eta^2)^{1/2} < 0.04$ in the azimuth–pseudorapidity space. The three most energetic adjacent BEMC towers including the hit tower were combined into *cluster*s. Electron candidates were required to have similar cluster energy and momentum ($0.75 < E_{cluster}/p < 1.35$ c) with most of the energy in one tower ($E_{tower}/E_{cluster} > 0.7$ for those candidates that fired the trigger, $E_{tower}/E_{cluster} > 0.5$ for other candidates). They were then paired, and required to have an opening angle $\theta > 90°$. Fig. 1 shows the invariant mass distribution of the paired candidates. The combinatorial background was subtracted using like-sign combinations. In the peak region there is also a significant contribution from Drell-Yan and open $b\bar{b}$ processes. Templates of the $\Upsilon(nS)$ peaks and the Drell-Yan contributions obtained from simulations, and the $b\bar{b}$ contribution from pQCD model calculations were fitted simultaneously to determine their relative contributions. The reconstruction efficiency was determined using simulations and electron-enriched data samples as $\epsilon \approx 3\%$. The corrected $p_{\rm T}$-spectrum is shown in Fig. 2. Bin-shift correction was done using a Boltzmann function with a slope $T = 1.16$ GeV, extracted from a parametrized interpolation over ISR, CDF and CMS data. A fit to the spectrum yiels a slope $T = 1.32\pm0.21$ GeV, consistent with the interpolation. The measured Υ cross section in U+U collisions is $B_{\rm ee} \left.\frac{d\sigma^{\Upsilon}_{\rm AA}}{dy}\right|_{|y|<1} = 4.37\pm1.09(stat)\pm^{+0.65}_{-1.01}(syst)$ μb. The major systematic uncertainties are from signal extraction ($^{+4.8}_{-18}\%$), tracking efficiency (11.8%), electron identification in the TPC ($^{+4.0}_{-6.4}\%$) and in the BEMC (5.9%), TPC-BEMC matching (5.4%), trigger efficiency ($^{+1.1}_{-3.6}\%$), geometrical acceptance ($^{+1.7}_{-3.0}\%$) and input $p_{\rm T}$ and y spectrum in the simulations (2.1%).

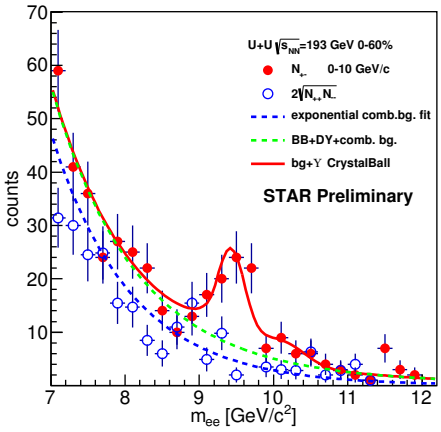

Figure 1: Invariant mass distribution of like-sign (filled dots) and unlike-sign (open points) electron pairs in $\sqrt{s_{NN}}$=193 GeV U+U collisions of 0–60% centrality at mid-rapidity, with background and peak fits.

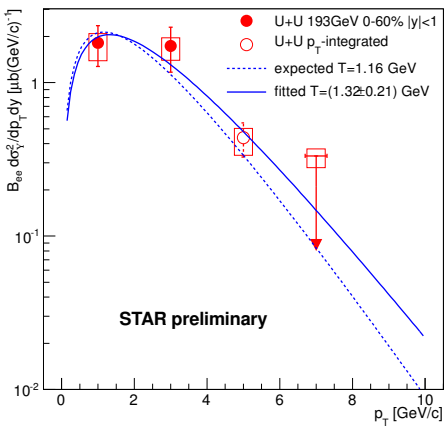

Figure 2: Υ $p_{\rm T}$-spectrum in $\sqrt{s_{NN}}$=193 GeV U+U collisions of 0–60% centrality at mid-rapidity. The fit (solid line) to the data is compared to the expected slope (dashed).

3 Upsilon production in p+p and d+Au collisions

Fig. 3 shows the cross sections for Υ production in $\sqrt{s_{NN}}$=200 GeV p+p and d+Au collisions [5]. The data are compared to NLO pQCD color evaporation model predictions [6]. In Fig. 4 the nuclear modification factor in d+Au is compared to calculations including shadowing and/or parton energy loss [6, 7]. While the p+p data are consistent with pQCD, CNM effects alone may not be enough to explain the suppression in the d+Au mid-rapidity bin ($|y|$<0.5).

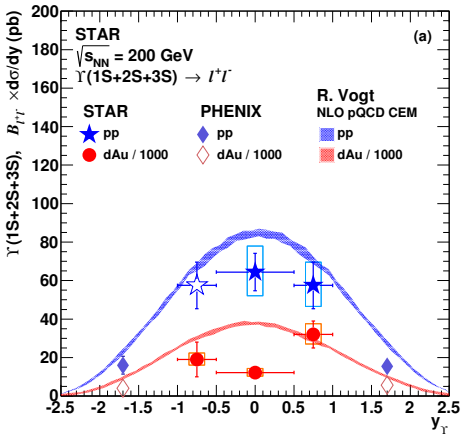

Figure 3: Υ yield $B_{\rm ee}\frac{d\sigma}{dy}$ for p+p and d+Au collisions [5] compared to a pQCD model [6].

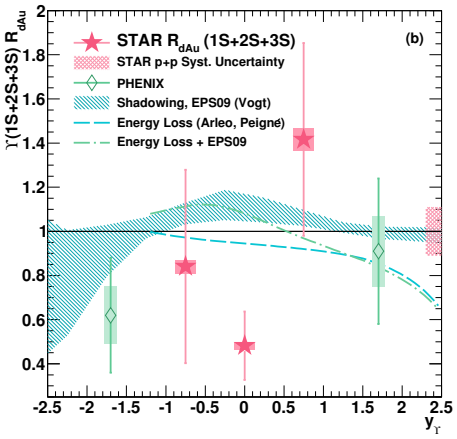

Figure 4: $R_{\rm dAu}$ versus y of Υ mesons [5] compared to theoretical calculations [6, 7].

4 Upsilon suppression in heavy ion collisions

Nuclear modification factors of the Υ(1S+2S+3S) in d+Au, Au+Au and U+U collisions are presented in Fig. 5 with respect to the number of participants, and compared to model calculations [8, 9], as well as $\sqrt{s_{NN}}$=2.76 TeV Pb+Pb data from the CMS experiment [10]. The trend observed in Au+Au is generally continued in the U+U data, with an $R_{\rm AA} = 0.35 \pm 0.17(stat.)^{+0.03}_{-0.13}(syst.)$ in the 10% most central U+U collisions. The model of Strickland and Bazow [8] incorporates lattice QCD results on screening and broadening of bottomonium, as well as the dynamical propagation of the Υ meson in the colored medium. The scenario with a potential based on heavy quark internal energy is consistent with the observations, while the free energy based scenario is disfavoured. The strong binding scenario in a model proposed by Emerick, Zhao, and Rapp [9], which includes possible CNM effects in addition, is also consistent with STAR results. The measured $R_{\rm AA}$ at RHIC and at LHC are consistent within the sizeable uncertainties. However, the LHC data, which corresponds to higher energy densities, shows a trend that differs from RHIC: a strong suppression is present at all but the lowest $N_{\rm part}$ values.

Fig. 6 shows Au+Au $R_{\rm AA}$ for the ground state Υ(1S) and the excited states Υ(2S+3S) separately, compared to the $R_{\rm AA}$ of high-$p_{\rm T}$ J/ψ mesons in $\sqrt{s_{NN}}$ = 200 GeV Au+Au collisions [11]. The Υ(1S) shows a suppression similar to that of high-$p_{\rm T}$ J/ψ mesons, more than if only cold nuclear matter effects were present [5]. The excited state yields are consistent with a complete suppression within the precision of the measurement.

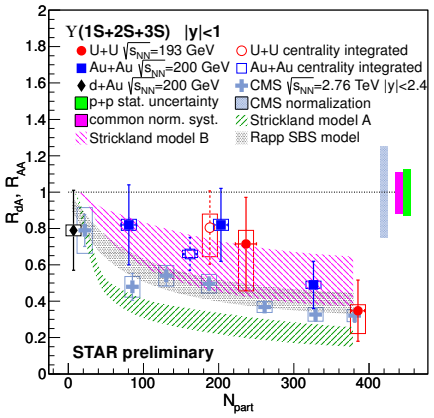

Figure 5: $R_{\rm AA}$ vs. $N_{\rm part}$ in $\sqrt{s_{NN}}$=200 GeV d+Au, Au+Au and 193 GeV U+U collisions, compared to models [8, 9] and LHC data [10].

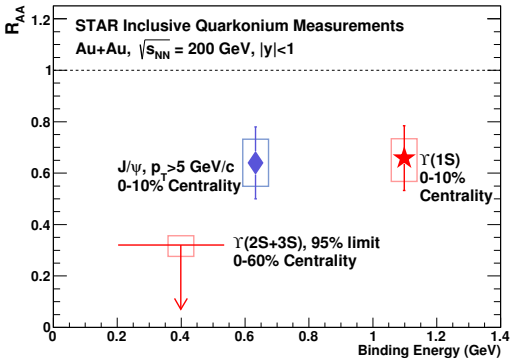

Figure 6: $R_{\rm AA}$ of the Υ(1S) and the Υ(2S+3S) states compared to high-$p_{\rm T}$ J/ψ $R_{\rm AA}$ [11], plotted against binding energy, in $\sqrt{s_{NN}}$=200 GeV Au+Au collisions.

5 Summary and outlook

We reported recent measurements of Υ production in p+p, d+Au and Au+A collisions at $\sqrt{s_{NN}}$ = 200 GeV, as well as U+U at 193 GeV. The slope of the $p_{\rm T}$-spectrum in U+U collisions is consistent with interpolations from other experiments. We see a significant suppression in $|y|$<1 central Au+Au and U+U collisions, which attests to the presence of a deconfined medium and support the sequential melting hypothesis. However, the $|y|$<0.5 d+Au data also shows a suppression beyond model predictions, suggesting that CNM effects may also play an important role. The new Muon Telescope Detector has been completed by 2014, and will allow for a precise reconstruction of the three Υ states separately, through the dimuon channel. Future high-statistics p+Au collisions from 2015 will help us gain a deeper insight to the CNM effects.

This work has been supported by the grant 13-20841S of the Czech Science Foundation (GAČR), and by the MSMT grant CZ.1.07/2.3.00/20.0207 of the European Social Fund (ESF) in the Czech Republic: Education for Competitiveness Operational Programme (ECOP).

References

[1] A. Mócsy and P. Petreczky, Phys. Rev. Lett. **99**, 211602 (2007).
[2] A. Adare *et al.* [PHENIX Collaboration], Phys. Rev. Lett. **98**, 232301 (2007).
[3] D. Kikola, G. Odyniec and R. Vogt, Phys. Rev. C **84**, 054907 (2011).
[4] K. H. Ackermann *et al.* [STAR Collaboration], Nucl. Instrum. Meth. A **499**, 624 (2003).
[5] L. Adamczyk *et al.* [STAR Collaboration], Phys. Lett. B **735**, 127 (2014).
[6] R. Vogt, R. E. Nelson and A. D. Frawley, PoS ConfinementX, **203** (2012).
[7] F. Arleo and S. Peigne, JHEP **1303**, 122 (2013).
[8] M. Strickland and D. Bazow, Nucl. Phys. A **879**, 25 (2012).
[9] A. Emerick, X. Zhao and R. Rapp, Eur. Phys. J. A **48**, 72 (2012).
[10] S. Chatrchyan *et al.* [CMS Collaboration], Phys. Rev. Lett. **109**, 222301 (2012).
[11] L. Adamczyk *et al.* [STAR Collaboration], Phys. Lett. B **722**, 55 (2013).

Recent Highlights from the PHENIX Heavy-Ion Program at RHIC

Baldo Sahlmueller[1] for the PHENIX collaboration

[1] Goethe University, Max-von-Laue-Str. 1, 60438 Frankfurt, Germany

DOI: http://dx.doi.org/10.3204/DESY-PROC-2014-04/318

Over the last decade it has been established that a quark-gluon plasma (QGP) is formed in ultrarelativistic A+A collisions at RHIC energies. In recent years, detector upgrades have enabled the detailed study of this hot and dense matter. Important probes, among others, are direct photons and heavy flavor observables. Although the RHIC d+Au program was originally undertaken to study initial state and cold nuclear matter effects, recent measurements at both RHIC (d+Au) and the LHC (p+Pb) have found evidence for collective phenomena in these small systems.

1 Direct Photons

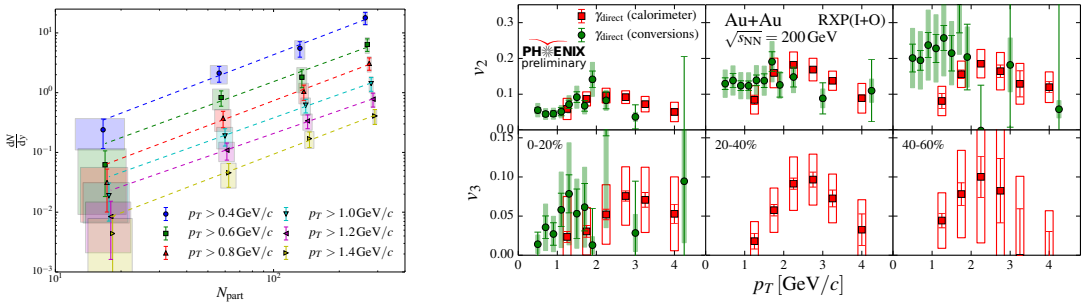

Figure 1: a) Integrated thermal photon yields as a function of N_{part} for different lower p_T integration limits. The dashed lines are independent fits to a power-law. b) Azimuthal anisotropy v_2 and v_3 of direct photons, for three different centrality selections.

Earlier PHENIX measurements established a surprising behavior of direct photon production and elliptic flow at low transverse momenta [1]. Current theoretical models cannot explain this so-called direct photon puzzle, a large excess of direct photon production over the $p+p$ baseline in Au+Au collisions at $\sqrt{s_{\mathrm{NN}}} = 200$ GeV, together with a large azimuthal anisotropy of direct photons.
A new measurement, using data taken in 2010, offers a significantly improved precision for both the direct photon spectra and the azimuthal anisotrop [2]. This new measurement uses the conversion of real photons in the detector material for the measurement, it confirms the previously

published data and extends the transverse momentum range towards lower p_T. The new data furthermore allow the analysis in finer centrality bins than before. The thermal photon yield is extracted as the excess of the direct photon production over the binary-scaled $p+p$ baseline. It is fit with an exponential, the slopes of these functions are independent of the centrality selection within the uncertainties of the measurement, with an average slope of $\sim$240 MeV/c.

The integrated thermal photon yield has been calculated in four centrality bins for different p_T ranges, it is shown in Figure 1a as a function of N_{part}. We observe a scaling of the integrated yield with a power law function AN_{part}^{α}. The exponent α was found to be common for all p_T integration ranges, with $\alpha = 1.48 \pm 0.08(\text{stat.}) \pm 0.04(\text{syst.})$. This is in the range of recent theoretical models describing direct photon emission in Au+Au collisions at this energy (see references in [2]).
The new methods have also been used to measure the direct photon azimuthal anisotropy, for the first time, the triangular flow v_3 has also been measured. The p_T range and the precision of v_2 have been improved compared to the previously published data. The direct photon v_2 and v_3 are shown in Figure 1b. The result on both v_2 and v_3 puts strong new constraints on the modeling of the hydrodynamic time evolution and the modeling of radiation emission in heavy ion collisions.

2 Quarkonia and Heavy Flavor

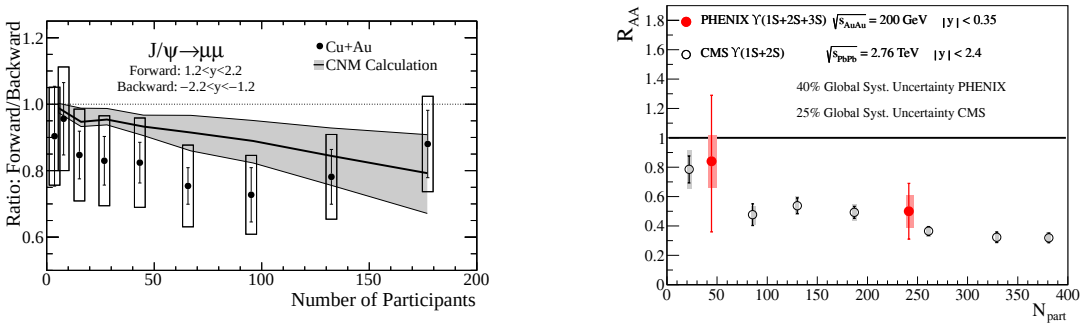

Figure 2: a) Ratio of forward- and backward-rapidity (Cu-going/Au-going) J/ψ yields measured in Cu+Au collisions, with a model calculation for the contributions from cold nuclear matter (see [3] and references therein). b) Υ nuclear modufication factor $R_{\rm AA}$ in Au+Au collisions at $\sqrt{s_{\rm NN}}$ = 200 GeV [4], compared to CMS results at LHC energies.

Heavy quarks are produced predominantly in hard scattering processes in the early phase of the collisions and hence can be used as a probe for the evolution of the medium. Quarkonia can be used like a thermometer for the medium, for example the Υ dissolves at a lower temperature than the J/ψ. PHENIX has excellent capabilities to measure heavy flavor production and quarkonia through leptonic channels.
One result of the J/ψ measurement in Cu+Au collisions at $\sqrt{s_{\rm NN}} = 200$ GeV is the ratio of the yields in the Cu-going direction and the Au-going direction [3]. This ratio is shown in Figure 2a as a function of centrality, represented by the number of participants. The suppression of the

J/ψ is stronger in the Cu-going direction which is consistent with more low-x shadowing in the Au nucleus than the Cu nucleus. The result is also consistent with observations in d+Au collisions at the same energy where the suppression is stronger in the d going direction.
The Υ has been measured in Au+Au collisions at the same energy [4]. The resulting $R_{\rm AA}$ is shown in Figure 2b, a suppression of the Υ is seen in more central collisions. The suppression is consistent with the disappearance of the $2s$ and $3s$ states of the meson. A similar suppression within uncertainties can be seen in Pb+Pb collisions at the LHC.

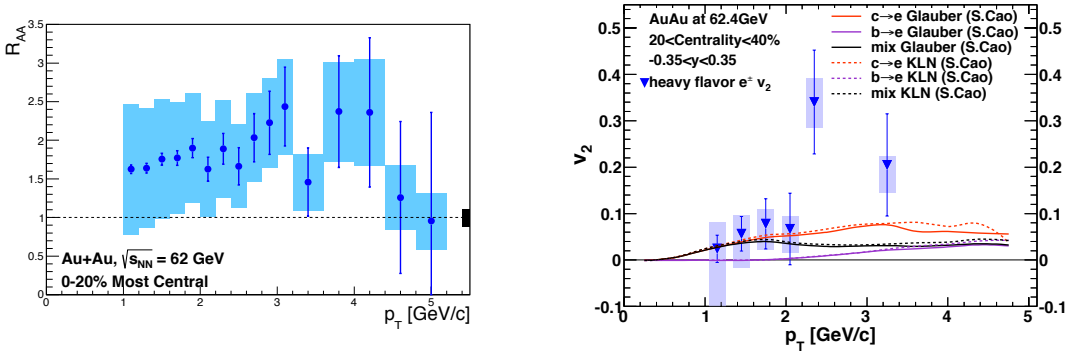

Figure 3: a) Nuclear modification factor $R_{\rm AA}$ of heavy-flavor electrons in 0-20% central Au+Au collisions at $\sqrt{s_{\rm NN}}$ = 62.4 GeV. b) Heavy-flavor electron v_2, compared to model calculations, at the same energy (see [5] and references therein)
.

Heavy flavor production and its azimuthal anisotropy was measured via single electrons in Au+Au collisions at a lower energy of $\sqrt{s_{\rm NN}}$ = 62.4 GeV. [5] Surprisingly, $R_{\rm AA}$ of these single electrons shows an enhancement over the $p+p$ reference at this energy, as seen in Figure 3a. This is opposite to the measurement of the same observable at $\sqrt{s_{\rm NN}}$ = 200 GeV. The v_2 measurement, shown in Figure 3b, hints at a small but positive v_2 for heavy-flavor electrons which is also predicted by theoretical models. With the currently large uncertainties, no final conclusion can be drawn, hence it is important to improve the measurement with a new dataset that should be obtained in the future.

3 Initial State Effects

LHC analyses on p+Pb collisions at $\sqrt{s_{\rm NN}}$ = 5.02 TeV have indicated strong azimuthal long-range correlations of hadron pairs, PHENIX has complemented these results with a measurement of the charged particle v_2 in d+Au collisions at $\sqrt{s_{\rm NN}}$ = 200 GeV, using a small rapidity gap of $\Delta\eta$ = 0.47 to 0.7 [6]. So far, the reason for these anisotropies is now known.
A new analysis of the azimuthal angular correlations between charged hadrons at central rapidity and the energy deposited in a calorimeter at forward (Au-going direction) rapidity, with a pseudorapidity gap of $\Delta\eta > 2.75$, shows an enhanced near-side angular correlation [7]. Figure 4a depicts this ridge-like correlation in central d+Au collisions. This result confirms the earlier PHENIX measurement with a smaller rapidity gap.
The azimuthal anisotropy v_2 has been measured as well with a large rapidity gap of $\Delta\eta > 2.75$

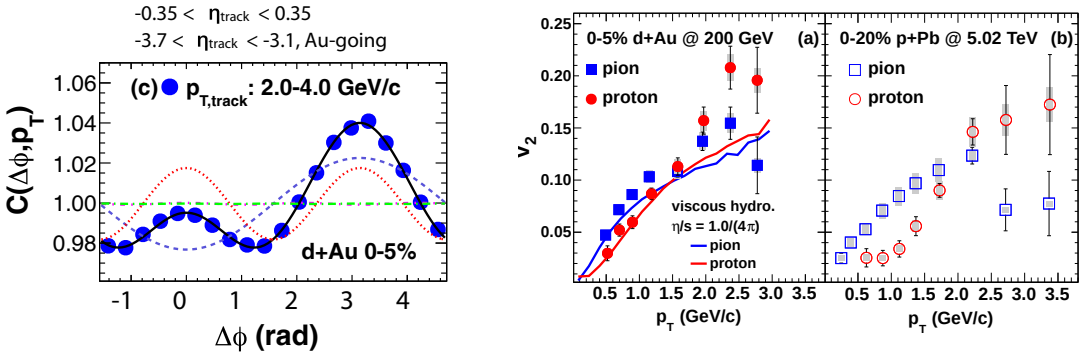

Figure 4: a) Azimuthal correlation function $C(\Delta\phi, p_T)$ for track-tower pairs in 0-5% central d+Au collisions at $\sqrt{s_{\rm NN}}$ = 200 GeV, together with a four-term Fourier expansion fit. The individual components are drawn as well. b) v_2 of identified pions and (anti-)protons in the same collisions. The PHENIX data are compared with a hydrodynamic calculation in the left panel [9], and with LHC data for central p + Pb collisions in the right panel of the figure [8].

between the event plane and the observed particles. The measurement has been done with identified charged particles (pions and protons). The result of this measurement can be seen in Figure 4b, compared with results in p+Pb collisions at the LHC. At both energies, the same mass ordering as in heavy-ion collisions is observed. The PHENIX data are compared to a calculation with Glauber initial conditions for viscous hydrodynamics with $\eta/s = 1.0/(4\pi)$, starting at $\tau = 0.5$ fm/c, followed by a hadronic cascade [9]. The mass splitting at lower p_T is seen in the calculation as well, the mass splitting is larger at the LHC which might indicate a larger radial flow in the higher energy regime.

4 Future

Currently, the PHENIX collaboration is working on the construction of a new detector for future RHIC runs. It will cover 2π in azimuth and include excellent capabilities to measure jets with electromagnetic and hadronic calorimetry. It is described in more detail in [10].

References

[1] A. Adare *et al.*, Phys. Rev. Lett. **104**, 132301 (2010), Phys. Rev. Lett. **109**, 122302 (2012).
[2] A. Adare *et al.*, arXiv:1405.3940 (2014).
[3] C. Aidala *et al.*, arXiv:1404.1873 (2014).
[4] A. Adare *et al.*, arXiv:1404.2246 (2014).
[5] A. Adare *et al.*, arXiv:1405.3301
[6] A. Adare *et al.* Phys. Rev. Lett. **111**, 212301 (2013).
[7] A. Adare *et al.*, arXiv:1404.7461 (2014).
[8] B. B. Abelev *et al.* (ALICE Collaboration), Phys. Lett. **B 726**, 164 (2013).
[9] J. Nagle *et al.*, arXiv:1312.4565 (2013), M. Luzum, P. Romatschke, Phys. Rev. **C 78**, 034915 (2008).
[10] C. Aidala *et al.*, arXiv:1207.6378 (2012).

ALICE Results on Vector Meson Photoproduction in Ultra-peripheral p–Pb and Pb–Pb Collisions

Evgeny Kryshen for the ALICE Collaboration
CERN, 1211 Geneva 23, Switzerland

DOI: http://dx.doi.org/10.3204/DESY-PROC-2014-04/198

Lead nuclei, accelerated at the LHC, are sources of strong electromagnetic fields that can be used to measure photon-induced interactions in a new kinematic regime. These interactions can be studied in ultra-peripheral p–Pb and Pb–Pb collisions where impact parameters are larger than the sum of the nuclear radii and hadronic interactions are strongly suppressed. Heavy quarkonium photoproduction is of particular interest since it is sensitive to the gluon distribution in the target. The ALICE Collaboration has studied J/ψ and ψ(2S) photoproduction in ultra-peripheral Pb–Pb collisions and exclusive J/ψ photoproduction off protons in ultra-peripheral p–Pb collisions at the LHC. Implications for the study of gluon density distributions and nuclear gluon shadowing are discussed. Recent ALICE results on ρ^0 photoproduction are also presented.

1 Introduction

Lead nuclei, accelerated at the LHC, are sources of strong electromagnetic fields, which are equivalent to a flux of quasi-real photons, thus p–Pb and Pb–Pb collisions can be used to measure γp, γPb and $\gamma\gamma$ interactions in a new kinematic regime. These interactions are usually studied in ultra-peripheral collisions (UPC), characterised by impact parameters larger than the sum of the radii of the incoming hadrons, in which hadronic interactions are strongly suppressed. Heavy quarkonium photoproduction is of particular interest since, in leading order perturbative QCD, its cross section is proportional to the squared gluon density of the target. LHC kinematics corresponds to Bjorken-x ranging from $x \sim 10^{-2}$ down to $x \sim 10^{-5}$, while the heavy-quark mass requires a virtuality Q^2 larger than a few GeV^2, hence introducing a hard scale. Thus quarkonium photoproduction off protons in p–Pb UPC can be used to probe the behaviour of the gluon density at low x and to search for gluon saturation in the proton. On the other hand, quarkonium photoproduction in Pb–Pb UPC provides a direct tool to study nuclear gluon shadowing effects, which are poorly known and play a crucial role in the initial stages of heavy-ion collisions. Light vector meson photoproduction measurements would also help to shed light on underlying photoproduction mechanisms at a soft scale.

The ALICE experiment [1] measured J/ψ, ψ(2S) and ρ^0 photoproduction in Pb–Pb UPC at $\sqrt{s_{\rm NN}} = 2.76$ TeV and exclusive J/ψ photoproduction off protons in p–Pb UPC at $\sqrt{s_{\rm NN}} = 5.02$ TeV [2, 3, 4]. These results are briefly reviewed in the following sections.

2 J/ψ, ψ(2S) and ρ^0 photoproduction in Pb–Pb collisions

The ALICE detector consists of a central barrel covering the pseudorapidity range $|\eta| < 0.9$ and a muon spectrometer in the forward direction. Central barrel detectors, relevant for UPC measurements, include an Inner Tracking System (ITS), a Time Projection Chamber (TPC) and a Time-Of-Flight detector (TOF). The muon spectrometer consists of a set of absorbers, a dipole magnet, five tracking and two trigger stations used to detect muons in the range $-4 < \eta < -2.5$. The VZERO-A ($2.8 < \eta < 5.1$) and the VZERO-C ($-3.7 < \eta < -1.7$) scintillator arrays are used for triggering and multiplicity measurements. The Zero-Degree Calorimeters (ZDC), located at ± 114 m from interaction point, are used to detect neutrons in the very forward regions.

ALICE measured J/ψ photoproduction in ultra-peripheral Pb–Pb collisions at forward rapidity in the dimuon channel [2] and at central rapidity both in the dimuon and dielectron channels [3]. The forward UPC trigger required a single muon with $p_{\rm T} > 1$ GeV/c in the muon spectrometer, at least one hit in VZERO-C and a veto on VZERO-A activity. For the measurement at central rapidity, the trigger required two back-to-back hits in TOF, two hits in a Silicon Pixel Detector (SPD, two innermost ITS layers) and vetoes on both VZERO detectors. Events with only two unlike sign dileptons and a neutron ZDC signal below 6 TeV were then selected in the offline analysis. The energy deposition in the TPC was used to separate dielectron and dimuon channels at mid-rapidity.

The reconstructed J/ψ signal includes contributions from coherent and incoherent production mechanisms. Coherent J/ψ photoproduction, when a photon interacts coherently with the whole nucleus, is characterized by a narrow transverse momentum distribution with $\langle p_{\rm T} \rangle \sim 60$ MeV/c. In the incoherent case the photon couples to a single nucleon so that the $p_{\rm T}$ distribution becomes much broader with $\langle p_{\rm T} \rangle \sim 400$ MeV/c. The transverse momentum distributions for dileptons with an invariant mass around the J/ψ mass were fitted with templates corresponding to different production mechanisms. Contributions from continuum dilepton production, feed-down from ψ(2S) decays and a possible contamination from hadronically produced J/ψ's were also taken into account in the fits. The results on the coherent J/ψ photoproduction cross section are compared with various model calculations in Fig. 1 (left). The best agreement was found for the model [5], which incorporates gluon shadowing according to EPS09 global fits [6]. A similar conclusion was obtained in Ref. [7] where the gluon shadowing factor $R_g(x \sim 10^{-3}, Q^2 \sim 2.4\ \text{GeV}^2) = 0.61^{+0.05}_{-0.04}$ was extracted from the ALICE measurement at mid-rapidity.

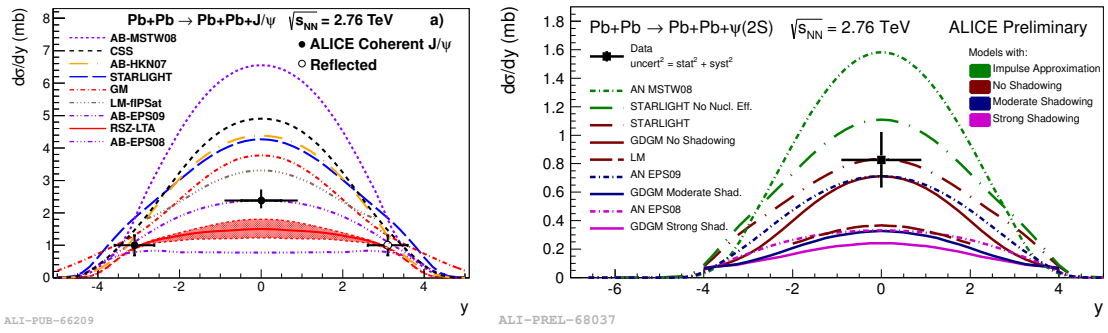

Figure 1: ALICE results on coherent J/ψ (left) and ψ(2S) (right) photoproduction cross section in Pb–Pb collisions at $\sqrt{s_{\rm NN}} = 2.76$ TeV in comparison with model predictions [2, 3].

ALICE also measured coherent $\psi(2S)$ cross section at mid-rapidity via the dilepton (l^+l^-) decay and in the channel $\psi(2S) \to J/\psi + \pi^+\pi^-$ followed by $J/\psi \to l^+l^-$ decay. The measured cross section, shown in Fig. 1 (right), disfavours models with no nuclear effects and those with strong gluon shadowing, however different predictions rely on different reference $\gamma + p \to \psi(2S) + p$ cross sections, thus preventing stronger conclusions. Many uncertainties on the measurement and on the γp reference cancel in the ratio of the coherent $\psi(2S)$ and J/ψ cross sections. The measured ratio $\sigma^{coh}_{\psi(2S)}/\sigma^{coh}_{J/\psi} = 0.344^{+0.076}_{-0.074}$ appears to be a factor two larger than in γp measurements at HERA [8] indicating that nuclear effects may affect differently 1S and 2S charmonium states.

Measurement of the coherent ρ^0 photoproduction at the LHC is important for verification of ρ^0 photoproduction models, which differ by factor two in the predicted cross sections [9, 10, 11]. ALICE measured coherent ρ^0 photoproduction cross section in the $\pi^+\pi^-$ channel at mid-rapidity in ultra-peripheral Pb–Pb collisions at $\sqrt{s_{NN}} = 2.76$ TeV. ALICE results, shown in Fig. 2 (left), disfavour the standard Glauber approach (GDL1 curve) [11], but appear to be in agreement with STARLIGHT, which is also based on the Glauber formalism, but neglects the elastic part of the total ρN cross section [9]. It is worth noting that a similar trend has been already revealed at lower energies by the STAR experiment [12]. The ALICE measurement is also consistent with the GM model [10] based on the colour-dipole approach and the Color Glass Condensate formalism.

3 Exclusive J/ψ photoproduction in p–Pb collisions

The large photon flux produced by the lead nucleus in p–Pb collisions at the LHC offers a possibility to measure exclusive J/ψ photoproduction off protons and to probe the gluon density distribution in the proton in a new kinematic regime. J/ψ photoproduction has been previously studied at HERA at γp centre-of-mass energies $W_{\gamma p}$ ranging from 20 to 305 GeV [13]. HERA cross sections are well described by a power law $\sigma(W_{\gamma p}) \sim W^{\delta}_{\gamma p}$, reflecting the fact that the underlying gluon distribution follows a power law in x down to $x \sim 10^{-4}$. A deviation from the power law for $\sigma(W_{\gamma p})$ at higher energies could indicate a change in the evolution of the gluon density function at lower x, as expected at the onset of saturation.

ALICE utilized three options to trigger on J/ψ decays in ultra-peripheral p–Pb collisions:

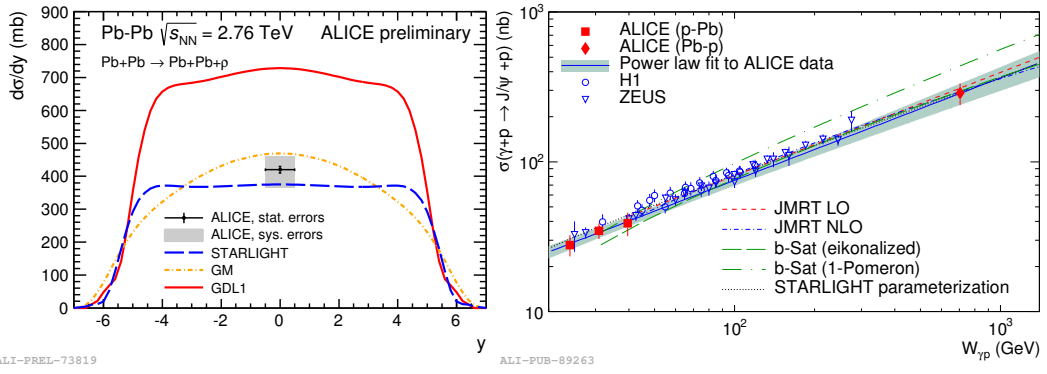

Figure 2: Left: ALICE results on coherent ρ^0 photoproduction cross section in Pb–Pb collisions at $\sqrt{s_{NN}} = 2.76$ TeV. Right: exclusive J/ψ photoproduction cross section off protons measured by ALICE in comparison with HERA data and model predictions [4].

dimuon in the muon spectrometer ($-4.0 < \eta < -2.5$), dimuon or dielectron in the central barrel ($|\eta| < 0.9$) and intermediate case with a muon in the muon arm and another one in the barrel. In addition, the LHC provided collisions of protons on lead ions in two configurations: p–Pb (the proton moves towards the muon spectrometer) and Pb–p (the lead ion moves towards the muon spectrometer). This allowed ALICE to study exclusive J/ψ photoproduction in a rapidity range $-4 < y < 4$, extend accessible $W_{\gamma\mathrm{p}}$ energies up to almost 1 TeV and to probe Bjorken-x down to $x \sim 2 \times 10^{-5}$ where saturation effects might already play an important role.

The first ALICE results on exclusive J/ψ photoproduction off protons measured in p–Pb collisions via dimuon channel at forward rapidity were published in [4]. J/ψ decays were reconstructed in $2.5 < y < 4.0$ (p–Pb) and $-3.6 < y < -2.6$ (Pb–p) rapidity intervals, corresponding to γp centre-of-mass energies of $21 < W_{\gamma\mathrm{p}} < 45$ GeV and $577 < W_{\gamma\mathrm{p}} < 952$ GeV respectively. Exclusive J/ψ events were selected by vetoing activity in SPD, VZERO-A and ZDC. The remaining non-exclusive J/ψ, e.g. diffractive events accompanied by the proton dissociation, were subtracted out by fitting p_{T} distributions with templates corresponding to exclusive and non-exclusive event samples. Photoproduction cross sections $\sigma(W_{\gamma\mathrm{p}})$ were extracted from the exclusive cross sections $\frac{\mathrm{d}\sigma}{\mathrm{d}y}(\mathrm{p} + \mathrm{Pb} \to \mathrm{p} + \mathrm{Pb} + \mathrm{J}/\psi)$ at the corresponding rapidity intervals by dividing out the photon flux from Pb nuclei. ALICE results on $\sigma(W_{\gamma\mathrm{p}})$ are shown in Fig. 2 (right) in comparison with previous measurements and various theoretical models based on extrapolations of HERA data. ALICE photoproduction cross sections are consistent with a power law with $\delta = 0.68 \pm 0.06$ (stat + syst), similar to the trend obtained from HERA, thus indicating no significant change in the power-law x-dependence of the gluon density in the proton down to $x \sim 2 \times 10^{-5}$.

4 Conclusions

ALICE results on the coherent J/ψ photoproduction in ultra-peripheral Pb–Pb collisions are in good agreement with models based on the moderate gluon shadowing from the EPS09 global fit. The measured coherent ψ(2S) photoproduction cross section disfavours models with no nuclear effects and those with strong gluon shadowing. Coherent ρ^0 photoproduction in Pb–Pb collisions at the LHC cannot be described in the standard Glauber formalism, but is in agreement with STARLIGHT and the colour-dipole approach. ALICE results on the exclusive J/ψ photoproduction off a proton measured in p–Pb collisions indicate no significant change in the power-law x-dependence of the gluon density in the proton between HERA and LHC energies.

References

[1] K. Aamodt *et al.* [ALICE Collaboration], J. Instrum. **3**, S08002 (2008).
[2] B. Abelev *et al.* [ALICE Collaboration], Phys. Let. **B718**, 1273 (2013).
[3] E. Abbas *et al.* [ALICE Collaboration], Eur. Phys. J. **C73**, 2617 (2013).
[4] B. Abelev *et al.* [ALICE Collaboration], arXiv:1406.7819 [nucl-ex] (2014).
[5] A. Adeluyi and C. A. Bertulani, Phys. Rev. **C85**, 044904 (2012).
[6] K. J. Eskola, H. Paukkunen and C. A. Salgado, JHEP **0904**, 065 (2009).
[7] V. Guzey, E. Kryshen, M. Strikman and M. Zhalov, Phys. Lett. **B726**, 290 (2013).
[8] C. Adloff *et al.* [H1 Collaboration], Phys. Lett. **B541**, 251 (2002).
[9] S. R. Klein and J. Nystrand, Phys. Rev. **C60**, 014903 (1999).
[10] V. P. Goncalves and M. V. T. Machado, Phys. Rev. **C84**, 011902 (2011).
[11] V. Rebyakova, M. Strikman and M. Zhalov, Phys. Lett. **B710**, 647 (2012).

[12] G. Agakishiev *et al.* [STAR Collaboration], Phys. Rev. **C85**, 014910 (2012).
[13] S. Chekanov *et al.* [ZEUS Collaboration], Eur. Phys. J. **C24**, 345 (2002).
C. Alexa *et al.* [H1 Collaboration], Eur. Phys. J. **C73**, 2466 (2013).

J/ψ production at the STAR experiment

Petr Chaloupka for the STAR collaboration

Czech Technical University in Prague, Zikova 1903/4, 16636, Praha 6, Czech Republic

DOI: http://dx.doi.org/10.3204/DESY-PROC-2014-04/89

This paper reports on STAR measurements of J/ψ production at mid-rapidity. We present results on the ψ(2S) to J/ψ yield ratio in p+p collisions at $\sqrt{s}$=500 GeV. We also report results from Au+Au collisions at $\sqrt{s_{NN}}$ = 39 GeV, 62.4 GeV, 200 GeV together with results from U+U collisions at $\sqrt{s_{NN}}$=193 GeV. Nuclear modification factors are presented as a function of centrality and p_T.

1 Introduction

Suppression of quarkonium production in heavy-ion collisions due to Debye color screening of quark and antiquark potential in the deconfined medium, has been proposed as a signature of quark-gluon plasma (QGP) formation. Since the Debye screening length depends on the temperature attained by the QGP medium, systematic measurements of production of various quarkonium states can provide insight into thermodynamic properties of the QGP. However, there are other effects that may alter the observed yields, such as cold nuclear matter effects (CNM) including shadowing/anti-shadowing of parton distribution functions and final state nuclear absorption, and statistical coalescence of quark-antiquark pairs in the QGP. Measurements of J/ψ yields at different collision energies, collision systems, and centralities help to disentangle the interplay of these effects on the J/ψ production.

2 Data analysis and results

The STAR experiment is a large-acceptance detector which excels at tracking and identification of charged particles at mid-rapidity ($|\eta| < 1$) with full azimuthal coverage. In the bellow discussed analyses J/ψ's are reconstructed at mid-rapidity in the di-electron decay channel, $J/\psi \to e^+ + e^-$ (branching ratio $B_{ee} = 5.9\%$). Electrons and positrons are reconstructed using the Time Projection Chamber (TPC) which also provides particle identification by measuring ionization energy loss (dE/dx). Furthermore, the particle identification is enhanced by the Time of Flight detector (TOF) in the low-p_T region and by the Barrel Electromagnetic Calorimeter (BEMC) in the high-p_T region.

In order to correctly interpret results from heavy-ion collisions we first need to understand the J/ψ production in elementary p+p collisions. STAR has measured production of J/ψ in p+p collisions at $\sqrt{s}$=500 GeV, the highest collision energy achievable in p+p collisions at RHIC. A p_T-dependent differential cross section for inclusive J/ψ production is shown in Fig. 1. The high precision results at the new collision energy reaching up to p_T = 20 GeV/c provide additional information that can be used to discriminate among different production models.

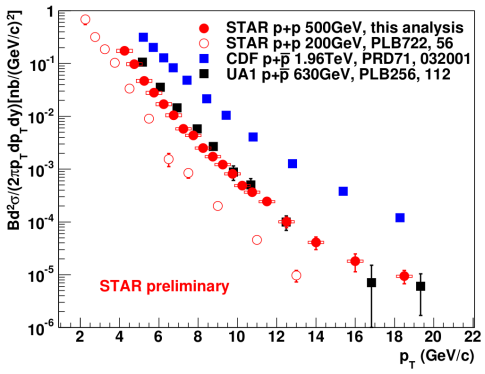

Figure 1: The J/ψ invariant cross section in p+p collisions at $\sqrt{s_{NN}}$=200 and 500 GeV, compared to results from other experiments.

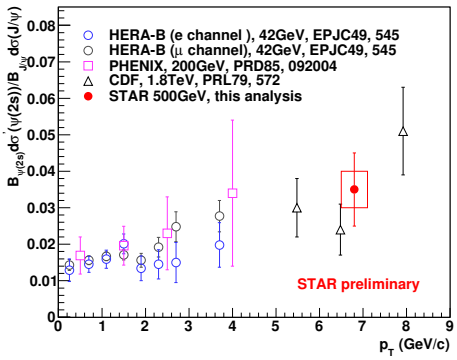

Figure 2: Ratio of ψ(2S) to J/ψ yields in p+p at $\sqrt{s}$=500 GeV, compared to results from HERA-B, PHENIX and CDF experiments.

Moreover, the high statistics data recorded in year 2011 allowed to measure for the first time the production of ψ(2S) state in p+p collisions at $\sqrt{s}$=500 GeV. The STAR result on the ψ(2S) to J/ψ yield ratio at mid-rapidity presented in Fig. 2 is in agreement with results from other experiments which exhibit an increasing trend with p_T with no significant dependence on the collision energy.

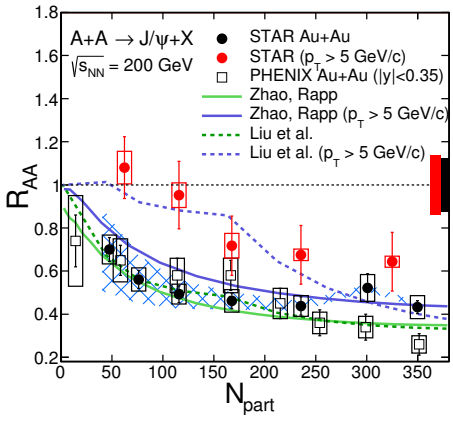

Figure 3: J/ψ R_{AA} as a function of centrality in Au+Au collisions at $\sqrt{s_{NN}}$=200 GeV from STAR [1, 2] and PHENIX [3], compared to model calculations [4, 5].

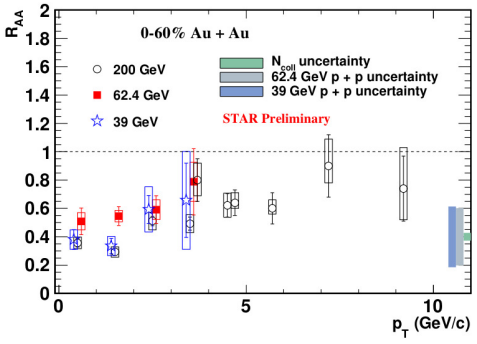

Figure 4: STAR results on J/ψ R_{AA} from 0-60% Au+Au collisions at $\sqrt{s_{NN}}$= 39, 62.4 and 200 GeV as a function of p_T. Open boxes represent systematic uncertainties. The boxes on the vertical axis represent uncertainties from CEM [6] baseline estimation for 39 and 62.4 GeV and $\langle N_{coll} \rangle$ uncertainties.

STAR results [1, 2] on modification of J/ψ production in Au+Au collisions at $\sqrt{s_{NN}}$=200 GeV are presented in Fig. 3. The nuclear modification factor R_{AA} is shown as a function of centrality (represented by number of participants, N_{part}) and compared to PHENIX [3] results. Strong suppression in the most central collisions is observed for both the low-p_T dominated

result [1] (shown in black) and the high-p_T (p_T>5 GeV/c) results [2] (shown in red). R_{AA} at high-p_T are systematically higher than the low-p_T ones. For high-p_T J/ψ the suppression is observed only in central collisions (0-30%) while in peripheral and mid-peripheral collisions the R_{AA} is consistent with unity. Since d+Au results[7] indicate that at $p_T>$ 5 GeV/c the CNM effects are negligible, the observed suppression in Au+Au collisions is likely to come from suppression in the QGP (due to color screening or other dynamical effects). However, it should be noted that the data are not corrected for B$\rightarrow J/\psi$ feed-down which can be, based on p+p data, as high as 15-25% in this p_T range. The data in Fig. 3 are compared to models of Zhao and Rapp [5] and Liu et al. [4]. These models contain not only suppression due to the color screening effect, but also secondary production of J/ψ via recombination of thermalized c and $\bar{c}$ quarks. The interplay between direct production and recombination can be studied by varying collision energy. Fig. 4 shows STAR results on p_T dependence of J/ψ R_{AA} in Au+Au collisions at $\sqrt{s_{NN}}$=200, 62.4 and 39 GeV. Centrality dependence of the low-p_T ($p_T<$ 5 GeV/c) part of the data is shown in Fig. 5. At all three energies a similar suppression pattern is observed. The centrality dependence in Fig. 5 is compared to the model by Zhao and Rapp [5]. These calculations, in agreement with the data, predict rather small dependence of the suppression on the collision energy. In these models, the suppression of primordial J/ψ is more significant at a higher collision energy, but it is compensated by the increased contribution from regeneration due to larger charm quark production cross section.

It should be noted that STAR did not measure p+p data at 62.4 and 39 GeV and hence the Color Evaporation Model (CEM) [6] was used as a reference instead. The resulting uncertainties are shown as boxes in Fig. 4 and 5.

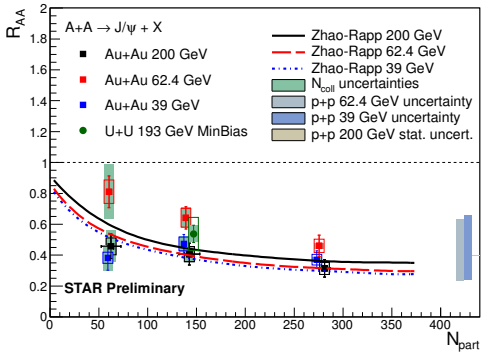

Figure 5: Centrality dependence of J/ψ R_{AA} for p_T<5 GeV/c in Au+Au collisions at different collision energies and U+U (p_T<6 GeV/c) at $\sqrt{s_{NN}}$=193 GeV.

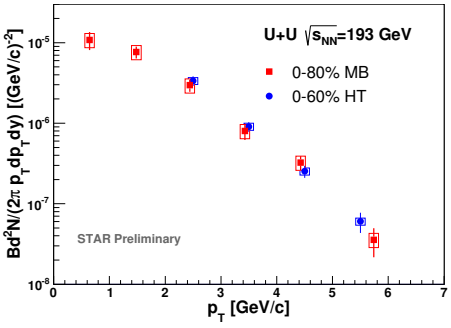

Figure 6: J/ψ invariant yield versus transverse momentum in U+U collisions at $\sqrt{s_{NN}}$=193 GeV from minimum bias (red) events and events triggered by high-p_T electron in BEMC (blue).

To further study the pattern of quarkonium suppression STAR recorded collisions of non-spherical Uranium nuclei at $\sqrt{s_{NN}}$=193 GeV in which an approximately 20% higher energy density can be reached. STAR results on J/ψ invariant yield at mid-rapidity in U+U collisions at $\sqrt{s_{NN}}$=193 GeV are shown in Fig. 6 with p_T reaching up to 6 GeV/c. The presented data are from 0-80% minimum bias (in red) and at high-p_T from events triggered by a signal from high-p_T electron in Electromagnetic Calorimeter (in blue). Spectra from p+p collisions at $\sqrt{s_{NN}}$=200 GeV are used to obtain J/ψ R_{AA} in U+U at $\sqrt{s_{NN}}$=193 GeV. The p_T dependence

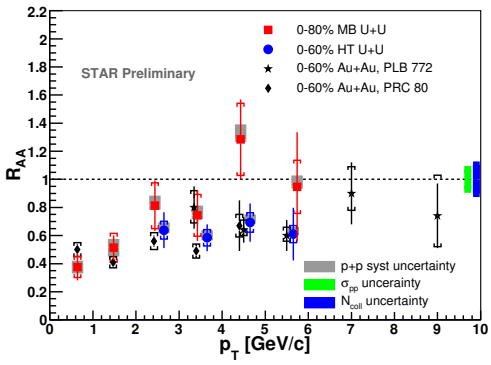

Figure 7: J/ψ nuclear modification factor in U+U collisions at $\sqrt{s_{NN}}$=193 GeV as a function of p_T, compared to results form Au+Au collisions at $\sqrt{s_{NN}}$=200 GeV.

of the R_{AA} shown in Fig. 7 is within uncertainties similar to Au+Au collisions. The data show a strong suppression at low-p_T with a non-negligible suppression remaining even in the high-p_T region. The R_{AA} obtained from the low-p_T dominated 0-80% minimum bias events are compared to the centrality (N_{part}) dependence of R_{AA} at different Au+Au collision energies in Fig. 5. The U+U results are consistent within uncertainties with the suppression pattern observed in Au+Au.

3 Summary

STAR has measured ratio of ψ(2S) to J/ψ in p+p collisions at $\sqrt{s}$=500 GeV and found it consistent with the results at other collision energies. The J/ψ suppression in Au+Au collisions at lower energies of $\sqrt{s_{NN}}$=39 and 62.4 GeV is similar to those at 200 GeV suggesting an important interplay of suppression of primordial J/ψ and regeneration. STAR has also measured J/ψ R_{AA} in U+U collisions at $\sqrt{s_{NN}}$=193 GeV. The U+U data are consistent within uncertainties with the suppression pattern observed in Au+Au collisions.

References

[1] L. Adamczyk et al. J/ψ production at low p_T in Au+Au and Cu+Cu collisions at $\sqrt{s_{NN}}$ = 200 GeV at STAR. *Phys.Rev.*, C90:024906, 2014.

[2] L. Adamczyk et al. J/ψ production at high transverse momenta in p+p and Au+Au collisions at $\sqrt{s_{NN}}$ = 200 GeV. *Phys.Lett.*, B722:55–62, 2013.

[3] A. Adare et al. J/ψ Production vs Centrality, Transverse Momentum, and Rapidity in Au+Au Collisions at $\sqrt{s_{NN}}$ = 200 GeV. *Phys.Rev.Lett.*, 98:232301, 2007.

[4] Yun-peng Liu, Zhen Qu, Nu Xu, and Peng-fei Zhuang. J/psi Transverse Momentum Distribution in High Energy Nuclear Collisions at RHIC. *Phys.Lett.*, B678:72–76, 2009.

[5] Xingbo Zhao and Ralf Rapp. Charmonium in Medium: From Correlators to Experiment. *Phys.Rev.*, C82:064905, 2010.

[6] R. E. Nelson, R. Vogt, and A. D. Frawley. Narrowing the uncertainty on the total charm cross section and its effect on the j/ψ cross section. *Phys. Rev. C*, 87:014908, 2013.

[7] A. Adare et al. Transverse-Momentum Dependence of the J/ψ Nuclear Modification in d+Au Collisions at $\sqrt{s_{NN}}$ = 200 GeV. *Phys.Rev.*, C87(3):034904, 2013.

Elliptic Flow of Thermal Photons in Chemically Non-Equilibrated QCD Medium

Akihiko Monnai[1]

[1]RIKEN BNL Research Center, Brookhaven National Laboratory, Upton, NY 11973, USA

DOI: http://dx.doi.org/10.3204/DESY-PROC-2014-04/87

Heavy-ion experiments have recently revealed that azimuthal momentum anisotropy – elliptic flow – of direct photons from a QCD medium is a few times larger than hydrodynamic predictions. I present a possible explanation for the enhancement based on late quark chemical equilibration. The color glass theory indicates that the medium is initially gluon-rich. Thermal photons are then mainly produced after quarks are produced, at which point large flow anisotropy is developed. The numerical estimations indicate that slow chemical equilibration visibly enhances the elliptic flow of thermal photons.

1 Introduction

The quark-gluon plasma (QGP) is a deconfined phase of quantum chromodynamics (QCD). After its experimental realization at BNL Relativistic Heavy Ion Collider (RHIC) [1] and CERN Large Hadron Collider (LHC) [2], there have been extensive studies on its properties. Large azimuthal momentum anisotropy, heavy quark diffusion and jet quenching observed in the experiments indicate that the quarks and gluons are strongly-coupled. The bulk medium follows the description of a relativistic fluid with small viscosity [3]. On the contrary, photons and leptons are weakly coupled to the medium as they are not sensitive to the strong interaction. The transparency makes them unique probes to investigate the hot medium. Heavy particles, such as weak bosons, are mostly created at the time of collision while photons and dileptons can be produced thermally, which implies the existence of collectivity in those observables.

In this study, I focus on thermal photons. The photons created in the hard process are called prompt photons and those emitted softly from the medium are called thermal photons. One of the most useful observables for the quantification of the collectivity is elliptic flow v_2, which is defined in Fourier expansion of particle spectra with respect to the azimuthal angle

$$\frac{dN}{d\phi} = \frac{N}{2\pi}[1 + 2v_1\cos(\phi - \Psi_1) + 2v_2\cos(\phi - \Psi_2) + 2v_3\cos(\phi - \Psi_3) + ...], \tag{1}$$

where ϕ is the angle in momentum space and Ψ_n are the respective reaction planes. The quantity is sensitive to the magnitude of medium interaction as they are non-vanishing only when non-central geometry and/or fluctuation in the collision is converted into momentum anisotropy. Hadronic v_2 and v_3 are found large, which is considered as an evidence for the aforementioned strongly-coupled QGP. Surprisingly, on the other hand, direct photon v_2 is found large at RHIC [4] and LHC [5]. It is a few times larger than hydrodynamic predictions and almost comparable to pion v_2, even though the quantity should reflect the small flow anisotropy in early stages

of the time-evolution. This phenomenon is now recognized as "photon v_2 puzzle". Recent experimental data also indicate the existence of large direct photon v_3 comparable to the pionic counterpart, which implies that the enhancement is at least partially due to the properties of the medium itself.

2 Chemically non-equilibrated fluid

A heavy-ion system before the collision is described as the color glass condensate, a state of saturated gluons [6]. The system locally equilibrates in a short time ~ 1 fm/c after the collision and form the quark-gluon plasma, which behaves as a fluid until it reaches freeze-out. An important observation is that thermalization and chemical equilibration do not necessarily occur simultaneously [7]. When the system is chemically non-equilibrated at the onset of hydrodynamic evolution, thermal photon emission is suppressed because of the scarcity of quarks. This can lead to enhancement of photon v_n as the contribution of later stages where the flow anisotropy is already large becomes effectively large [8].

The inviscid hydrodynamic equations of motion of a chemically non-equilibrated system are energy-momentum conservation and rate equations for the energy momentum tensor and the number currents in the QGP phase:

$$\partial_\mu T_q^{\mu\nu} + \partial_\mu T_g^{\mu\nu} = 0, \tag{2}$$

$$\partial_\mu N_q^\mu = 2r_b n_g - 2r_b \frac{n_g^{\rm eq}}{(n_q^{\rm eq})^2} n_q^2, \tag{3}$$

$$\partial_\mu N_g^\mu = (r_a - r_b) n_g - r_a \frac{1}{n_g^{\rm eq}} n_g^2 + r_b \frac{n_g^{\rm eq}}{(n_q^{\rm eq})^2} n_q^2 + r_c n_q - r_c \frac{1}{n_g^{\rm eq}} n_q n_g, \tag{4}$$

where r_a, r_b and r_c are reaction rates for (a) gluon splitting, (b) the quark pair production and (c) gluon emission from a quark, respectively. The subscript *eq* denotes that the variable is in chemical equilibrium. Local thermalization of the quark and the gluon components is assumed and the total energy density and the total pressure are defined as $e = e_q + e_g$ and $P = P_q + P_g$. n_q and n_g are the number densities for quarks and gluons, respectively. Late quark chemical equilibration corresponds to $r_b < r_a, r_c$ because the pair creation is the process which changes the quark number density. Here the matter-antimatter degrees of freedom is included in N_q^μ. It is note-worthy that the inverse of the reaction rate gives the chemical relaxation time τ_i. Since the parton picture is no longer applicable in the hadronic phase, the system is simply assumed to be in chemical equilibrium below the crossover temperature.

The hydrodynamic medium is characterized by the equation of state and the chemical reaction rates. The former is given by a hyperbolic interpolation of the parton gas of u, d, g and the resonance gas of hadrons with mass up to 2.5 GeV as $s = c(T)s_{\rm par} + [1 - c(T)]s_{\rm had}$ where the interpolation function is $c(T) = \{1 + \tanh[(T - T_c)/\Delta T]\}/2$. The connecting temperature $T_c = 0.17$ GeV and the crossover width $\Delta T = 0.017$ GeV are chosen. This preserves the consistency with the parton gas model used to estimate the equilibrium parton densities $n_q^{\rm eq}$ and $n_g^{\rm eq}$. The latter is parametrized as $r_i = c_i T$ $(i = a, b, c)$ where c_i is the dimensionless parameter. The initial conditions for the energy density is based on an analytical Glauber model [9]. The numerical estimation is performed in the (2+1)-dimensional boost invariant geometry. Thermal photon emission rate is based on the hyperbolic interpolation of the rates in the hadronic [10] and the QGP phases [11]. Note that the parameters are chosen for demonstration of the chemical equilibration effects and precision analyses will be discussed elsewhere.

3 Numerical results

Elliptic flow of thermal photons is shown in Fig. 1 along with the time-evolution of the quark number density for different quark chemical equilibration parameters. $c_b = 0.2, 0.5$ and 2.0 roughly corresponds to $\tau_{\rm chem} = 1/c_b T \sim 5.0, 2.0$ and 0.5 fm/c when the average medium temperature is $T \sim 0.2$ GeV. Au-Au collisions at $\sqrt{s_{NN}}$ =200 GeV are considered. The impact parameter is set to $b = 7$ fm at the thermalization time $\tau_{\rm th} = 0.4$ fm/c. One can see that late quark chemical equilibration leads to enhancement of thermal photon v_2. It is note-worthy that the typical chemical equilibration time suggested in a pre-equilibrium model [7] is 2 fm/c.

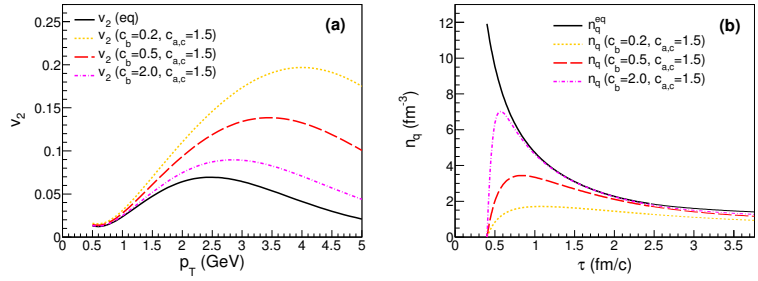

Figure 1: (a) Elliptic flow of thermal photons and (b) time-evolution of the quark number density for different quark chemical equilibration rates. Thin lines for the number density indicate that the medium temperature is near the crossover $T < T_c + \Delta T$.

Figure 2 shows the dependence of thermal photon v_2 and that of the time-evolution of the gluon number density on gluon-involved equilibration parameters for a fixed c_b. The elliptic flow is slightly reduced for late gluon equilibration because gluons are initially overpopulated and larger number of gluons in the early stage leads to earlier production of quarks with small anisotropy. Quantitatively, it can be seen that the quark equilibration process plays bigger role in the thermal photon v_2 modification than the gluon one.

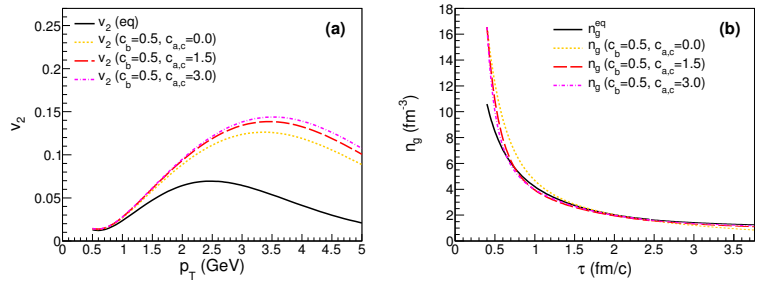

Figure 2: (a) Elliptic flow of thermal photons and (b) time-evolution of the gluon number density for different gluon chemical equilibration rates. Thin lines for the number density indicate that the medium temperature is near the crossover $T < T_c + \Delta T$.

Transverse-momentum spectra of thermal photons show slight reduction for the late chemical equilibration cases due to the suppression in the photon emission. The magnitude is found to

be not significant for the current parameter settings, but the introduction of more sophisticated photon emission rate and the dynamical equation of state would be important for quantitative discussion as the spectra and v_2 would both be sensitive to the input [12].

4 Conclusion and outlook

Thermal photon elliptic flow from a chemically non-equilibrated QGP fluid is estimated by the newly-developed hydrodynamic model coupled to the rate equations for the parton number densities. This is motivated by the fact that a high-energy heavy-ion system is initially gluon-rich because the colliding nuclei are described as the color glass condensate. The numerical analyses indicate that thermal photon v_2 is visibly enhanced by late quark chemical equilibration, contributing positively to the resolution of the "photon v_2 puzzle". The fact that the difference in thermalization and chemical equilibration times affects phenomenology implies that the interplay of pre- and post-equilibrium physics is important, which is in good analogy to the fact that thermal and chemical freeze-out have to be treated separately at the end of a hydrodynamic estimation for hadronic spectra. Future prospects include introduction of more quantitative photon emission rate, initial conditions, equation of state and transport processes as well as estimation of the contribution of prompt photons, which are naively believed to have almost vanishing anisotropy, for the comparison to the experimental data of direct photons. It would also be important to investigate the effects of other mechanisms, *e.g.*, Ref. [13] for the comprehensive understanding of photon physics in heavy-ion collisions.

Acknowledgments

The work is inspired by fruitful discussion with B. Müller. The author would like to thank for valuable comments by Y. Akiba and L. McLerran on the paper. The work of A.M. is supported by RIKEN Special Postdoctoral Researcher program.

References

[1] K. Adcox *et al.* [PHENIX Collaboration], Nucl. Phys. **A757**, 184 (2005); J. Adams *et al.* [STAR Collaboration], Nucl. Phys. **A757**, 102 (2005); B. B. Back *et al.* [PHOBOS Collaboration], Nucl. Phys. **A757**, 28 (2005); I. Arsene *et al.* [BRAHMS Collaboration], Nucl. Phys. **A757**, 1 (2005).

[2] K. Aamodt *et al.* [The ALICE Collaboration], Phys. Rev. Lett. **105**, 252302 (2010).

[3] B. Schenke, S. Jeon and C. Gale, Phys. Rev. Lett. **106**, 042301 (2011).

[4] A. Adare *et al.* [PHENIX Collaboration], Phys. Rev. Lett. **109**, 122302 (2012).

[5] D. Lohner [ALICE Collaboration], J. Phys. Conf. Ser. **446**, 012028 (2013).

[6] L. D. McLerran and R. Venugopalan, Phys. Rev. **D49**, 2233 (1994); **D49**, 3352 (1994).

[7] A. Monnai and B. Müller, arXiv:1403.7310 [hep-ph].

[8] A. Monnai, Phys. Rev. C **90**, 021901 (2014).

[9] P. F. Kolb, J. Sollfrank and U. W. Heinz, Phys. Rev. **C62**, 054909 (2000).

[10] C. T. Traxler and M. H. Thoma, Phys. Rev. **C53**, 1348 (1996).

[11] S. Turbide, R. Rapp and C. Gale, Phys. Rev. **C69**, 014903 (2004); F. Arleo, P. Aurenche, F. W. Bopp, I. Dadic, G. David, H. Delagrange, D. G. d'Enterria and K. J. Eskola *et al.*, hep-ph/0311131.

[12] F. Gelis, H. Niemi, P. V. Ruuskanen and S. S. Rasanen, J. Phys. **G30**, S1031 (2004).

[13] A. Monnai, arXiv:1408.1410 [nucl-th].

Results on Heavy-Flavour Production in pp, p–Pb and Pb–Pb Collisions with ALICE at the LHC

Grazia Luparello[1] for the ALICE Collaboration

[1]Università di Trieste and INFN - Trieste, via A. Valerio 2, Trieste, Italy

DOI: http://dx.doi.org/10.3204/DESY-PROC-2014-04/92

The ALICE Collaboration has measured heavy-flavour production through the reconstruction of hadronic decays of D mesons at mid-rapidity and via semi-electronic (at mid-rapidity) and semi-muonic (at forward rapidity) decays of charm and beauty hadrons in pp, p–Pb and Pb–Pb collisions. A summary of the most recent results from p–Pb collisions at $\sqrt{s_{NN}} = 5.02$ TeV and Pb–Pb collisions at $\sqrt{s_{NN}} = 2.76$ TeV is presented in this paper.

1 Introduction

Heavy quarks are effective probes of the Quark Gluon Plasma (QGP) formed in high-energy nucleus-nucleus collisions, since they are produced on a short time scale with respect to that of the QGP. They traverse the strongly interacting medium and lose energy through radiative [1] and collisional [2] processes. Theoretical calculations predict a dependence of the energy loss on the colour charge and on the mass of the parton traversing the medium, resulting in a hierarchy in the energy loss with beauty quarks losing less energy than charm quarks, and charm quarks losing less energy than light quarks and gluons [3, 4]. The energy loss is experimentally investigated via the nuclear modification factor $R_{\rm AA}$, defined as the ratio of the yield in nucleus-nucleus collisions to that observed in pp collisions scaled by the number of binary nucleon-nucleon collisions. In the absence of medium effects, $R_{\rm AA}$ is expected to be unity for heavy flavours, since the production yields are proportional to the number of binary nucleon-nucleon collisions. The expected hierarchy in the energy loss described above can be verified comparing the $R_{\rm AA}$ of different particle species, namely $R_{\rm AA}({\rm B}) > R_{\rm AA}({\rm D}) > R_{\rm AA}(light)$. For this comparison it should be considered that the $R_{\rm AA}$ of the different hadronic species are also affected by the different production kinematics and fragmentation function of gluons, light and heavy quarks. The $R_{\rm AA}$ can be modified also due to initial-state effects, since the nuclear environment affects the quark and gluon distributions as described either by calculations based on phenomenological modifications of the Parton Distribution Functions (PDF) [5] or by the Colour Glass Condensate (CGC) effective theory [6]. Partons can also lose energy in the initial stages of the collision via initial-state radiation [7], or they can experience transverse momentum broadening due to multiple soft collisions prior to the hard scattering [8]. Initial-state effects are addressed by studying p–Pb collisions. Finally, in nucleus-nucleus collisions the charmed hadron azimuthal anisotropy, quantified via the second order coefficient of the Fourier decomposition of the particle momentum azimuthal distribution (v_2), tests whether also charm quarks participate in the collective expansion dynamics and possibly thermalize in the QGP.

2 Open heavy-flavour measurements in ALICE

The excellent performance of the ALICE detector [9] allows open heavy-flavour measurements in several decay channels and in a wide rapidity range. At mid-rapidity ($|y| < 0.5$) D mesons are reconstructed via their hadronic decay channels: $D^0 \to K^-\pi^+$, $D^+ \to K^-\pi^+\pi^+$, $D^{*+} \to D^0\pi^+ \to K^-\pi^+\pi^-$, $D_s^+ \to \phi\pi^+ \to K^-K^+\pi^+$ and their charge conjugates. D-meson selection is based on the reconstruction of decay vertices displaced by a few hundred μm from the interaction vertex, exploiting the high track-position resolution close to the interaction vertex provided by the Inner Tracking System (ITS). The large combinatorial background is reduced by selections applied on the decay topology and by the identification of charged kaons and pions in the Time Projection Chamber (TPC) and Time-Of-Flight (TOF) detector. Electrons are identified at mid-rapidity through their specific energy loss in the TPC gas combined with the information from the TOF and from the electromagnetic calorimeter (EMCal). At forward rapidity, open heavy-flavour production is studied in the semi-muonic decay channel. Muons are reconstructed in the five tracking stations of the Muon Spectrometer ($-4 < \eta < -2.5$). The reconstructed tracks are matched with tracklets measured in the trigger stations to reject punch-through hadrons.

3 Results

Figure 1 shows the nuclear modification factor ($R_{\rm pPb}$) measured in p–Pb collisions at $\sqrt{s_{\rm NN}}$=5.02 TeV as a function of $p_{\rm T}$ for heavy-flavour decay electrons (left) and muons (right). The measurement of D-meson $R_{\rm pPb}$ is reported in [10]. The results are compatible with unity within

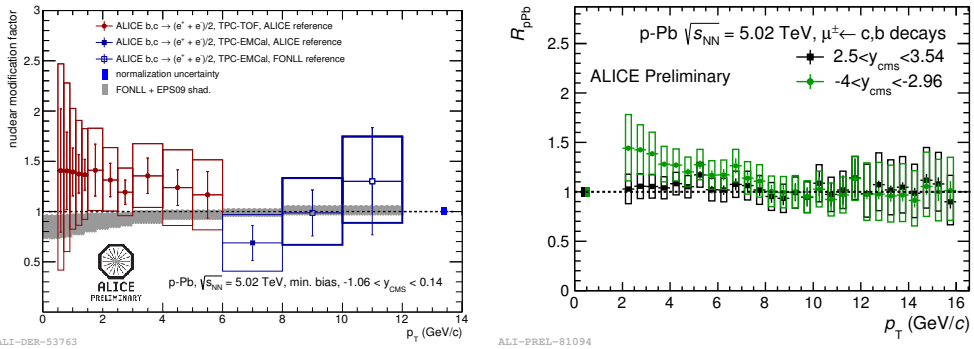

Figure 1: $R_{\rm pPb}$ of heavy-flavour decay electrons at mid-rapidity and heavy-flavour decay muons at forward (p-going direction) and backward (Pb-going direction) rapidities in minimum-bias p–Pb collisions, as a function of $p_{\rm T}$.

uncertainties without any significant dependence on the rapidity interval investigated. The measurements confirm that initial-state effects due to the presence of cold-nuclear matter are small in the measured $p_{\rm T}$ range. Theoretical predictions based on pQCD calculations including the EPS09 [5] nuclear modification of the PDF can describe the measurements. The D-meson $R_{\rm pPb}$ is also compatible with calculations based on the CGC [6] and with a model including cold-nuclear-matter energy loss, nuclear shadowing and $k_{\rm T}$-broadening [11].

Open heavy-flavour production is also studied in p–Pb collisions as a function of the event activity. The ratio $Q_{\rm pPb}^{\rm mult}(p_{\rm T}) = \frac{{\rm d}N_{\rm pPb}^{\rm mult}/{\rm d}p_{\rm T}}{<N_{\rm coll}^{\rm mult}>{\rm d}N_{\rm pp}/{\rm d}p_{\rm T}}$ is used to study the possible multiplicity-dependent modification of the p_T-differential yields in p–Pb collisions with respect to the binary-scaled yields measured in pp collisions. Events are divided in classes based on the energy measured in the Zero Degree Calorimeters located in the Pb-going direction (ZNA). The average number of nucleon-nucleon collisions for the considered ZNA energy event class, $< N_{\rm coll}^{\rm mult} >$, is calculated with the hybrid approach described in [12]. Figure 2 demonstrates that the $Q_{\rm pPb}^{\rm mult}$ of prompt D mesons for events with high and low multiplicities is compatible with unity within uncertainties, thus no multiplicity-dependent modification of D-meson production in p–Pb collisions relative to the binary-scaled pp production is observed.

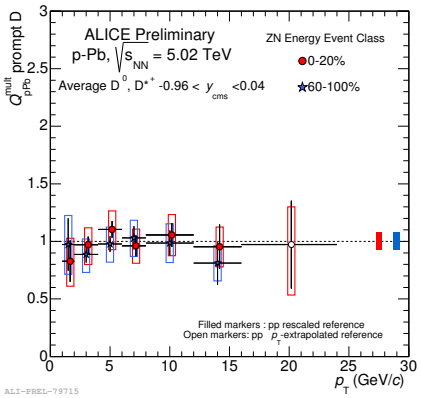

Figure 2: Prompt D-meson $Q_{\rm pPb}^{\rm mult}$ in the 0-20% and 60-100% ZNA energy classes.

In Pb–Pb collisions, the open heavy-flavour $R_{\rm AA}$ measured with ALICE in the different channels [13] shows a strong reduction of the yields at large trasverse momenta ($p_{\rm T} > 5$ GeV/c) in the most central collisions relative to a binary-scaled pp reference. This suppression is interpreted as due to charm quark in-medium energy loss. The expected mass ordering of the energy loss is also investigated: Fig. 3 (left) shows the D-meson $R_{\rm AA}$ as a function of centrality, represented as the average number of nucleons participating in the interaction, compared to the one of J/ψ from beauty-hadron decays measured by CMS [14]. The D-meson $p_{\rm T}$ range was chosen in order to obtain a significant overlap with the $p_{\rm T}$ distribution of B mesons decaying to J/ψ with $6.5 < p_{\rm T} < 30$ GeV/c, thus allowing a consistent comparison. A similar trend as a function of centrality is observed, but the D-meson $R_{\rm AA}$ is systematically lower than the one of J/ψ from B decays. This is consistent with the expectation of a smaller in-medium energy loss for beauty than for charm quarks. A comparison with the $R_{\rm AA}$ of charged hadrons and pions is also done (not shown): a similar suppression is observed, although the uncertainties do not allow yet to draw a conclusion on the colour-charge dependence of the in-medium energy loss. Figure 3 (right) shows the v_2 of heavy-flavour decay electrons and muons in the centrality interval 20-40%. The two results are compatible within uncertainties. For $2 < p_{\rm T} < 3$ GeV/c a positive v_2 is observed ($> 3\sigma$ effect). The D-meson v_2 measured in the 30-50% centrality class is larger than zero with a 5.7σ significance in the interval $2 < p_{\rm T} < 6$ GeV/c and comparable in magnitude to the one of charged hadrons [15] (not shown). These results indicate that heavy quarks participate in the collective motion of the system. At high $p_{\rm T}$, v_2 results could give insight into the path-length dependence of the in-medium energy loss, but the present statistics

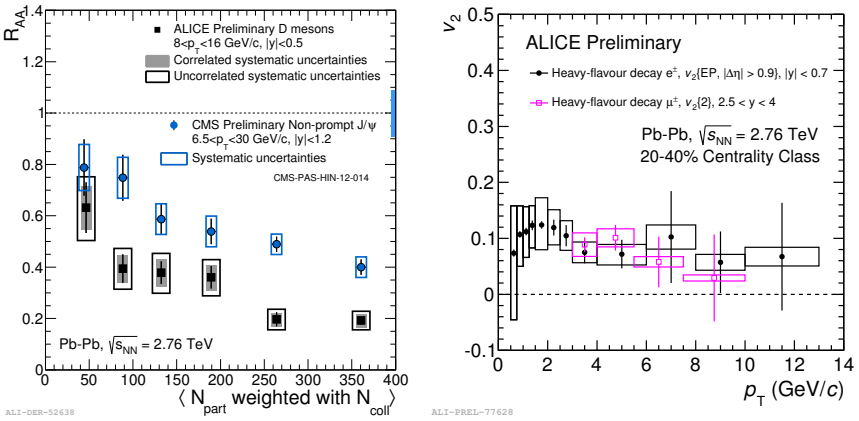

Figure 3: Left: $R_{\rm AA}$ of prompt D mesons and of non-prompt J/ψ measured by CMS [14] as a function of centrality, expressed in terms of the number of nucleons participating in the interaction. Right: Heavy-flavour decay electron and muon v_2.

does not allow to conclude on this.

In summary, in p–Pb collisions the open heavy-flavour $R_{\rm pPb}$ is consistent with unity indicating that initial-state effects are small. In Pb–Pb collisions a large suppression of open heavy-flavour yields is observed at intermediate and high $p_{\rm T}$. Since initial-state effects are small, these results can be interpreted as a final-state effect due to the interaction of the charm quarks with the hot and dense medium. The v_2 measured in Pb–Pb semi-central collisions is larger than zero at low $p_{\rm T}$, suggesting that heavy quarks participate in the collective motion of the system.

References

[1] M. Gyulassy and M. Plumer, Phy. Lett. **B243**, 432 (1990); R. Baier, Y. L. Dokshitzer, A. H. Mueller, S. Peigne and D. Schiff, Nucl. Phys. **B484**, 265 (1997).

[2] M. H. Thoma and M. Gyulassy, Nucl. Phys. **B351**, 491 (1991); E. Braaten and M. H. Thoma, Phys. Rev. **D44**, 1298; (1991); Phys. Rev. **D44**, 2625 (1991).

[3] Y. L. Dokshitzer, D. E. Kharzeev, Phys. Lett. **B519**, 199-206 (2001).

[4] N. Armesto, C. A. Salgado, U. A. Wiedemann, Phys. Rev. **D69** 114003 (2004).

[5] K. Eskola, H. Paukkunen, C. Salgado, JHEP **04** 065 (2009).

[6] H. Fujii and K. Watanabe, arXiv:1308.1258.

[7] I. Vitev, Phys. Rev. **C 75** 064906 (2007).

[8] M. Lev and B. Petersson, Z. Phys. **C21** 155 (1983); X. N. Wang, Phys. Rev. **C61** 064910 (2000).

[9] B. B. Abelev *et al.* [ALICE Collaboration], arXiv:1402.4476 [nucl-ex].

[10] B. Aberlev *et al.* [ALICE Collaboration], arXiv:1405.3452 [nucl-ex].

[11] R. Sharma, I. Vitev and B. W. Zhang, Phys. Rev. **C 80** 054902 (2009).

[12] A. Toia, arXiv:1410.0481 [nucl-ex].

[13] B. Abelev *et al.* [ALICE Collaboration], PRL 109 112301 (2012); JHEP **9** 112 (2012).

[14] CMS Collaboration, CMS-PAS-HIN-12-014 (2013).

[15] B. Abelev *et al.* [ALICE Collaboration], PRL 111 102301 (2013); Phys. Rev. **C90** 034904 (2014).

Search for Muonic Atoms at RHIC

Kefeng Xin[1] for the STAR Collaboration

[1]Rice University, 6100 Main St MS-315, Houston, Texas, USA

DOI: http://dx.doi.org/10.3204/DESY-PROC-2014-04/39

We present the search results for muonic atoms on $\sqrt{s_{NN}} = 200$ GeV Au+Au collisions collected by the STAR experiment at RHIC. With the muon identification at low momentum, the invariant mass spectra were reconstructed. Clear signals are observed at the expected atom masses. Two particle correlations show that the production of the daughter particles happens at the same space-time point, presenting the signature of atom ionization. The fraction of primordial muons is extracted from π-μ correlations.

1 Introduction

Muonic atoms are like ordinary atoms except that the electrons are replaced with muons. These atoms have been studied in many fundamental physics experiments, such as precision measurements of proton size [1] and nuclear quadrupole moments [2]. Muonic atoms with pions in the core have been produced from intense K_l beam at Brookhaven National Lab [3] and Fermilab [4]. However hydrogen-like muonic atoms with more exotic particles in the core (kaons or antiproton) have never been observed. Heavy-ion experiments, with large amount of thermal muons and hadrons produced, make an ideal environment for the production of such exotic atoms. This provides us a great opportunity to make these discoveries.

Muons that are involved in the atom production make the study particularly interesting in heavy-ion experiments, because thermal leptons are considered to be ideal penetrating probes of hot QCD matter as their production rates rapidly increase with the temperature of the medium. However, one difficulty of measuring the thermal leptons is that they are mixed with a large amount of leptons from weak hadronic decays, which carry little information of the hot and dense matter. Muonic atoms are only produced by particles right after freeze-out, i.e. hadrons and thermal muons or muons from resonance decays like $\rho \to \mu^+\mu^-$, not by the muons from the weak hadronic decays, which are produced at a relatively late stage. Thus the idea of measuring the distributions of muonic atoms in heavy-ion collisions has been suggested by several theorists, Melvin Schwartz, Gordon Baym, Gerald Friedman, [5], Joseph Kapusta, Agnes Mocsy, [6] etc.

2 Analysis and Results

The dataset used in this analysis is from Au+Au collisions at $\sqrt{s_{NN}} = 200$ GeV collected by the STAR detector in year 2010. Central triggered events are selected to maximize the particle multiplicities. A total of 231 million events passed the event level selections. Particles are identified from the time-of-flight detector and the time projection chamber. The muon momentum

is limited to 0.15-0.25 GeV/c to ensure the purity of the sample. The corresponding momenta for kaons and protons/antiprotons are 0.7-1.17 GeV/c and 1.33-2.22 GeV/c respectively.

The invariant mass reconstruction is done with the combinatorial method. The combinatorial signal is constructed by pairing a hadron and a muon with opposite electric charges (unlike-sign method) from the same event. The background is constructed in two ways: a mixed-event method, in which a hadron and a muon with opposite electric charges from two different events are paired; and a like-sign method, in which a hadron and a muon with the same electric charge from a same event are paired.

Note that the Coulomb effect becomes stronger when the two charged particles are close in phase space. In the unlike-sign method, two particles carry opposite charges, which produce attractive Coulomb force and thus enhance the mass distributions, especially at the low mass region. In contrast, in the like-sign method, the repulsive Coulomb force from the same charge suppresses the mass distributions at the low mass region. In the mixed-event method, there is no Coulomb effect for hadron-muon pairs. Therefore, the mixed-event backgrounds are used for acceptance correction of like-sign backgrounds:

$$LS_{+-}(corrected) = \sqrt{LS_{++}LS_{--}}\frac{ME_{+-}}{\sqrt{ME_{++}ME_{--}}}, \tag{1}$$

where LS and ME stands for like-sign and mixed-event respectively, and the index stands for the charges for hadrons and leptons. Details of this correction are discussed in [7] [8].

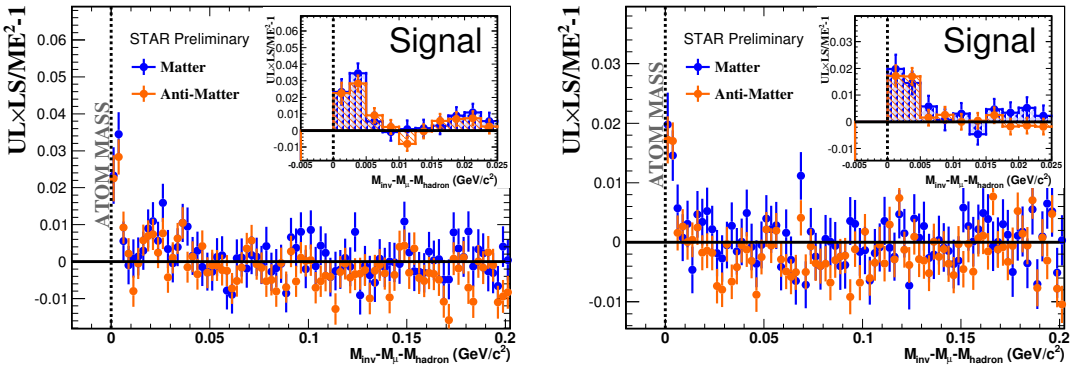

(a) p-μ^- and $\bar{p}$-μ^+ pairs.

(b) K^--μ^+ and K^+-μ^- pairs.

Figure 1: The pair invariant mass distributions of $UL \times LS/ME^2 - 1$ show peaks at the atom masses.

We adopted the following observable to cancel the trivial Coulomb effect and preserve the signal:

$$UL \times LS/ME^2 - 1 \tag{2}$$

where $UL \times LS$ stands for unlike-sign × like-sign, to cancel the Coulomb effect, and ME stands for mixed-event for normalization. After the rejection of the Coulomb force, we observe the sharp peaks at the expected zero net mass in Fig. 1. The error bars show the statistical uncertainties. The signal is robust in both K-μ and p-μ systems and their antimatter systems.

Femtoscopic correlations between two particles have also been used as a probe of muonic atoms. The correlation as a function of k^*, which is the magnitude of the momentum of either particle in the pair rest frame, shows how the interactions of the two particles change with respect to their distance in phase space. STAR has thoroughly studied the K-π system [9], in which only Coulomb interation dominates. For non-identified particles, a leading particle can be selected, and two cases can be distinguished by $C_+(k^*)$ and $C_-(k^*)$, which stand for the leading particle travels faster and slower, respectively. Then the double ratio $C_+(k^*)/C_-(k^*)$ can be calculated to show the difference of the two cases. This method was successfully used in previous measurements to probe the space-time asymmetry of the emission of two particles [9].

The measurement of K-π system is performed from the dataset and kinetic region similar as K-μ system which we used for muonic atom signal extraction. The origin of the non-unity in double ratio comes from the Coulomb interactions between the kaons and pions, which are later on enhanced in $C_+(k^*)$ and suppressed in $C_-(k^*)$ because of the space-time emission asymmetries of kaons and pions. The double ratio of $K-\mu$ system, overlaid on top of K-π system, can be separated in two regions as shown in Fig. 2. On the right of the dashed line, where only Coulomb interactions are expected in both systems, the double ratios of the two systems are consistent. This is consistent with the existence of the Coulomb force, which is a necessary condition to form muonic atoms. On the left of the dashed line, where the muonic atoms are expected to appear, when getting to very low k^*, instead of divergence, the double ratios of $K-\mu$ system show convergence to unity. The unity double ratio provides a signature of muonic atoms disassociation at the detector beam pipe, where the hadrons and the muons are separated from the bound state at the same space-time point.

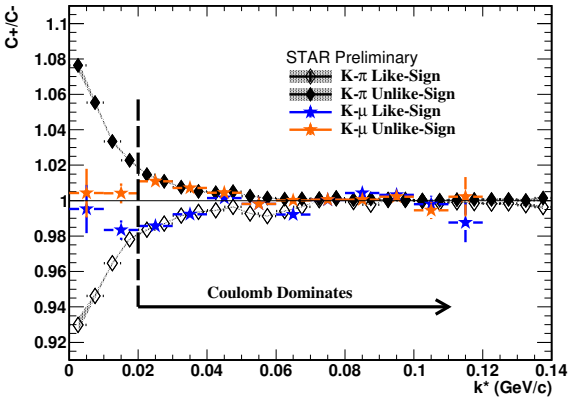

Figure 2: The double ratio of the K-π and K-μ systems show significant difference at low k*. The convergence to unity of K-μ suggests the ionization at the beam pipe after the production of muonic atoms.

The π-μ correlations are also studied. A large amount of muons from weak decays can pass the track selections, and mix with the primordial muons. Thus these π-μ interactions inherit the interactions from π-π interactions, which have two major sources, the electrostatic Coulomb interactions and quantum interference from identical pions [10]. The later factor generates a strong enhancement on the correlation functions. We denote the three correlation functions as the follows:

- A for correlations between pions and muons from simulated weak decays from real pions.
- B for correlations between pions and inclusive muons, which is measured from data.
- C' for correlations between pions and primordial muons.

The three functions satisfy the linear relationship: $B = \alpha \times C' + \beta \times A$, where α stands for the fraction of primordial muons from inclusive muons produced from the collisions. C' is then estimated by π-π correlations, because of the fact that pion mass and muon mass are fairly close. To avoid quantum statistics enhancement, the correlation function from Coulomb between like-sign pairs is estimated from reversed unlike-sign pairs C. The relation then becomes: $B = \alpha \times 1/C + \beta \times A$. The minimum χ^2 fitting is performed in Fig. 3. If two particles have similar trajectories and orientation, implying that they are close in momenta space, the detector will not be able to have enough spacial resolution to distinguish them and will merge the two tracks. The fitting range is selected between 0.02-0.2 GeV/c, discarding the very low k^* where the missing track problem is significant. The fitting results show that the fraction of primordial muons is 22.0±0.4%.

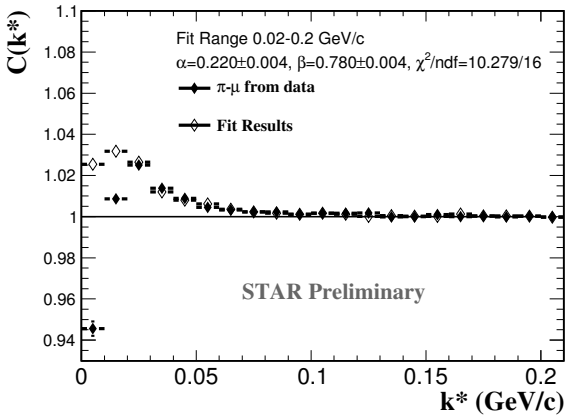

Figure 3: Measured π-μ correlation function, fitted by π-π correlation function and simulated π-$\mu_{\rm prim}$.

3 Conclusions

Au+Au collisions at $\sqrt{s_{NN}}$ = 200 GeV collected by the STAR experiment are used in this measurement to search for muonic atoms. The invariant mass distributions show clear signals at the expected mass position for K^+-μ^-, K^--μ^+, p-μ^-, and antiproton-μ^+. The signal is robust after long-range Coulomb effect is rejected. The double ratio of K-μ system indicates the kaons and muons that are very close in phase space are emitted at the same space and time, which is consistent with muonic atom ionization. The fraction of primordial muons is extracted from the correlation method.

References

[1] Aldo Antognin, *et al.*, Science **339** 417 (2013).
[2] Y. Tanaka and B. M. Steffen, Phys. Rev. Lett. **51** 18 (1983).
[3] R. Coombes, *et al.*, Phys. Rev. Lett. **37** 5 (1976).
[4] S. H. Aronson, *et al.*, Phys. Rev. Lett. **48** 16 (1982).
[5] G. Baym, G. Freidman, R. J. Hughes, and B. Jack, Phys. Rev. **D48** 9 (1993).
[6] J. Kapusta and A. Mocsy, Phys. Rev. C **59** 5 (1999).
[7] A. Adare, *et al.*, Phys. Rev. C **81** 5 (2010).
[8] L. Adamczyk, *et al.*, Phys. Rev. C **86** 5 (2012).
[9] J. Adams, *et al.*, Phys. Rev. Lett. **91** 26 (2003).
[10] J. Adams, *et al.*, Phys. Rev. C **71** 044906 (2005).

Relativistic heavy ion physics at JINR: status of the BM@N and MPD experiments

Alexander Zinchenko for the MPD and BM@N Collaborations
JINR, 141980 Dubna, Moscow region, Russia

DOI: http://dx.doi.org/10.3204/DESY-PROC-2014-04/177

The future accelerator facility NICA (JINR, Dubna) will supply ion species ranging from polarized proton to heavy ions with design luminosity of up to 10^{27} cm^{-2}c^{-1} for Au nuclei in the region of the collider energy up to $\sqrt{s_{NN}} = 11$ GeV. It will complement the existing accelerator Nuclotron, which is being currently upgraded in order to be able to accelerate Au nuclei up to $E_{kin} = 4.65$A GeV ($\sqrt{s_{NN}} = 3.5$ GeV). These machines will host two heavy ion experiments: BM@N (Baryonic Matter at Nuclotron) and MPD (MultiPurpose Detector), which are described in this paper.

1 NICA complex

The Nuclotron-based Ion Collider fAcility (NICA) [1], shown in Fig. 1, is a new accelerator complex being constructed at JINR, Dubna, Russia. NICA's aim is to provide collisions of heavy ions over a wide range of atomic masses, from Au+Au collisions at $\sqrt{s} = 4 - 11$A GeV (for Au^{79+}) and an average luminosity of L = 10^{27} cm^{-2}s^{-1} to proton-proton collisions with $\sqrt{s_{pp}} = 20$ GeV and L = 10^{32} cm^{-2}s^{-1}.

Study of heavy ion collisions at the collider with the MultiPurpose Detector (MPD) will be complemented by spin physics research with polarized beams of protons and deuterons with the Spin Physics Detector (SPD) as well as a fixed-target program at center of mass energy from 1 to 4 GeV at the BM@N (Baryonic Matter at Nuclotron) detector.

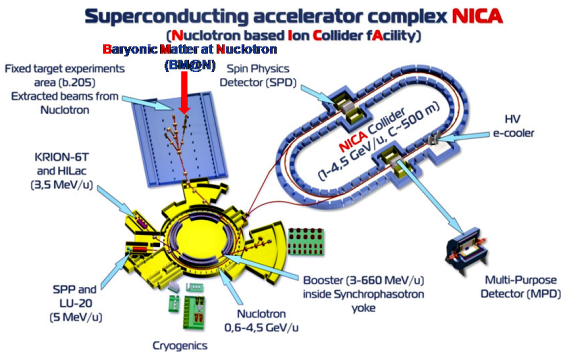

Figure 1: NICA complex.

2 MPD experiment

The main goal of the NICA/MPD program [2] is a comprehensive experimental investigation of the properties and dynamics of the hot and dense nuclear matter in a poorly explored region of the QCD phase diagram, with a main emphasis on such QCD subjects as

properties of deconfinement phase transition, critical phenomena and chiral symmetry restoration.

The NICA/MPD experimental program includes simultaneous measurements of observables that are presumably sensitive to high nuclear density effects and phase transitions. In the first stage of the project are considered - multiplicity and spectral characteristics of the identified hadrons including strange particles, multi-strange baryons and antibaryons; event-by-event fluctuations in multiplicity, charges and transverse momentum; collective flows (directed, elliptic and higher ones) for observed hadrons. In the second stage the electromagnetic probes (photons and dileptons) will be measured.

The detector for exploring phase diagram of strongly interacting matter in a high track multiplicity environment has to cover a large phase space, be functional at high interaction rates and comprise high efficiency and excellent particle identification capabilities. The MPD detector [3, 4], shown in Fig. 2, matches all these requirements. It consists of a barrel part and two end caps. The barrel part is a set of various subdetectors. The main tracker is the time projection chamber (TPC) supplemented by the inner tracker (IT). IT and TPC have to provide precise tracking, momentum determination and vertex reconstruction. The time of flight (TOF) system must be able to identify charged hadrons and nuclear clusters in a broad pseudorapidity range. The electromagnetic calorimeter (ECAL) should identify electrons, photons and measure their energy with high precision. The zero degree calorimeter (ZDC) should provide event centrality and event plane determination, and also measurement of the energy deposited by spectators. There are also a straw-tube tracker (ECT) and a fast forward detector (FFD).

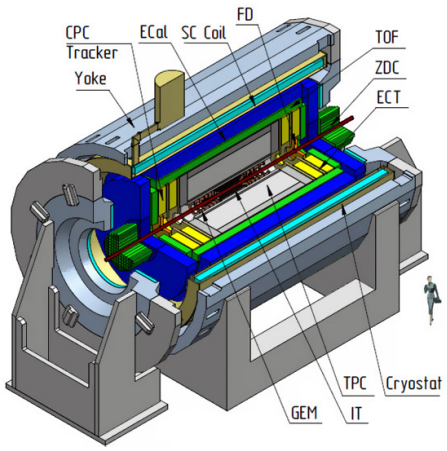

Figure 2: MPD detector.

The magnet of MPD is a solenoid with a thin superconducting NbTi winding and a flux return iron yoke. The magnet should provide a homogeneous magnetic field of 0.5 T. The field inhomogeneity in the tracker area of the detector is about 0.1%.

The MPD time projection chamber (TPC) is the main tracking detector that has to provide charged particles momentum measurement with sufficient resolution (about 2% at p_t = 300 MeV/c), two track separation (with a resolution <1 cm), vertex determination and dE/dx measurement (dE/dx resolution better than 8%) at pseudorapidities $|\eta| < 2.0$ and $p_t > 100$ MeV/c. TPC readout system is based on Multi-Wire Proportional Chambers (MWPC) with cathode readout pads.

The identification of charged hadrons (PID) at intermediate momentum ($0.1 - 3$ GeV/c) is achieved by the time-of-flight (TOF) measurements which are complemented by the energy loss (dE/dx) information from the TPC and IT detector systems. TOF system should provide a large phase space coverage $|\eta| < 3.0$, high combined geometrical and detection efficiency (better than 80%), identification of pions and kaons with $0.1 < p_t < 2$ GeV/c and (anti)protons with $0.3 < p_t < 3$ GeV/c. The choice for the TOF system is multigap Resistive Plate Counters (mRPC) which have good time resolution of $\sigma < 70$ ps. The barrel covers the pseudorapid-

ity region $|\eta| < 1.5$ with the average efficiency above 90%. The end cap system covers the pseudorapidity region $1.5 < |\eta| < 3.0$.

Currently, the MPD physics program is under careful evaluation through the extensive feasibility studies. As they show, the MPD detector will provide good conditions for the strangeness measurements in heavy ion collisions, both in the hyperon [6] and hypernuclei sectors (Fig. 3 left panel).

Electromagnetic probes (electron-positron pairs) will also be accessible (Fig. 3 right panel) [7] for studies, e.g., of the low-mass dilepton enhancement in heavy ion collisions.

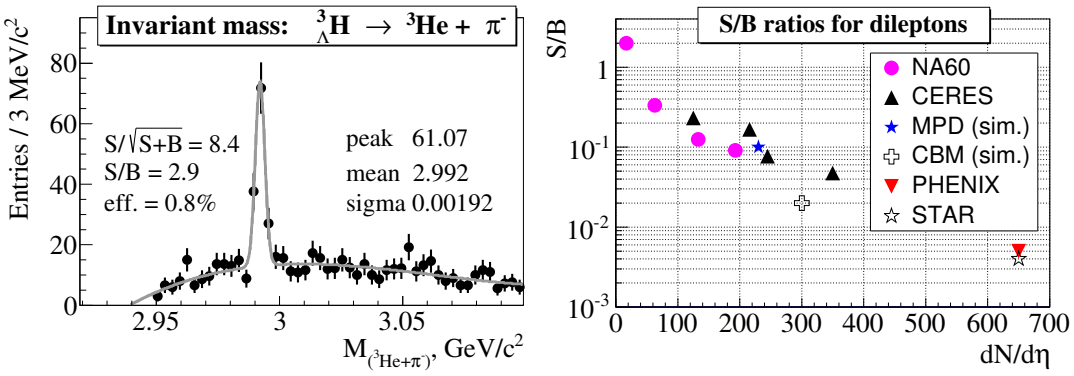

Figure 3: Some results from MPD feasibility studies: left - reconstructed invariant mass of ^{3}He and π^-; right - signal-to-background ratios obtained in different experiments for low-invariant mass region of lepton pairs versus charged particle density.

3 BM@N experiment

A successful operation of the NICA complex will require the existing machine Nuclotron to be upgraded in order to accelerate Au nuclei. After that, the improved Nuclotron beams will also be used to run a fixed target experiment BM@N [5]. The detector will allow to study A+A collisions by measuring a variety of observables.

Particle yields, ratios, transverse momentum spectra, rapidity and angular distributions, as well as fluctuations and correlations of hadrons will be studied as a function of the collision energy and centrality. A sketch of the proposed experimental set-up is shown in Fig. 4. It combines high precision track measurements with time-of-flight information for particle identification and total energy measurements for event characterization. The charged track multiplicity will be measured with the set of GEM (Gas Electron Multipliers) detectors located downstream of the target inside the analyzing magnet of 0.8 T

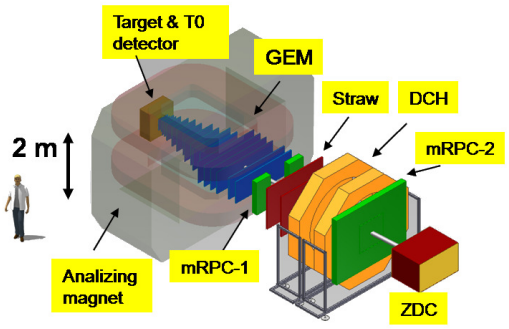

Figure 4: BM@N detector.

and drift chambers (Straw, DCH) situated outside the magnetic field. Design parameters of the time-of-flight detectors based on multigap Resistive Plate Chambers (mRPC-1,-2) with a strip read-out allow efficient discrimination between particle species with momentum up to a few GeV/c. The Zero Degree Calorimeter (ZDC) is designed for the collision centrality analysis by measuring the energy of forward going particles. The Recoil detector, partially covering the backward hemisphere (-1< η <1.2) near the target, is planned for the independent analysis of the collision centrality by the measurement of the energy of the target fragments.

The BM@N project is being realized by a Collaboration of more than 100 physicists and engineers from 12 countries. According to the project realization plan, the first elements of the BM@N detector will be installed at the Nuclotron beam line in early 2015 to perform test beam measurement. The physics data taking is planned to start in 2016. At present, an active R&D program and beam line development works are complemented with intensive Monte Carlo simulation studies for optimization of the detector design. Figure 5 illustrates the quality of hyperon reconstruction in the BM@N detector with the GEM tracker. The obtained results indicate that even in high multiplicity central Au+Au collisions the proposed set-up has very good reconstruction capability for strange hyperons.

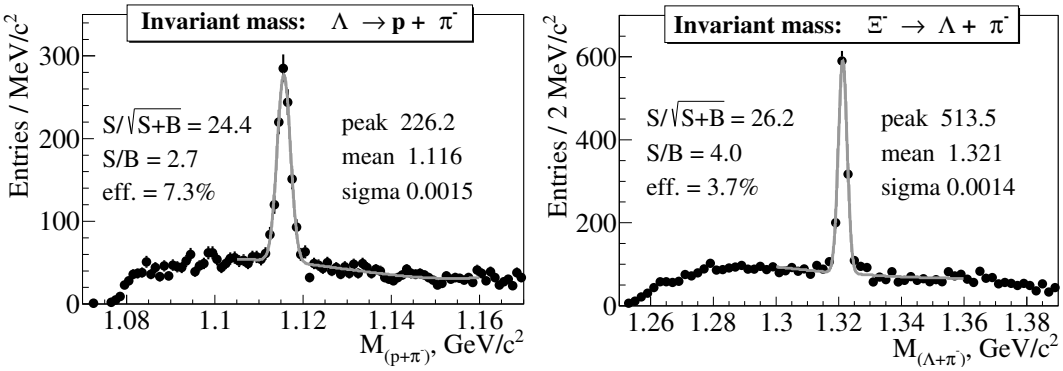

Figure 5: Some results from BM@N feasibility studies: reconstructed Λ (left) and Ξ^- (right) hyperon invariant mass peaks.

References

[1] http://nica.jinr.ru

[2] NICA White Paper, https://indico.cern.ch/event/275003/contribution/1/material/paper/0.pdf.

[3] K. U. Abraamyan et al., Nucl. Instrum. Meth. **A628**, 99 (2011)

[4] http://nica.jinr.ru/files/CDR_MPD/MPD_CDR_en.pdf.

[5] http://nica.jinr.ru/files/BM@N/BMN_CDR.pdf

[6] V. Vasendina, A. Zinchenko, these Proceedings.

[7] V. Vasendina et al., Phys. Part. Nucl. Lett. **10**, 769 (2013).

LHCb results in proton-nucleus collisions at the LHC

Katharina Müller

Winterthurerstr. 190, CH-8057 Zurich, Switzerland

DOI: http://dx.doi.org/10.3204/DESY-PROC-2014-04/251

The forward acceptance of the LHCb detector allows it to probe proton-ion collision in a unique kinematic range, complementary to the other LHC experiments. The production of J/Ψ and Υ-mesons decaying into two muons is studied at the LHCb experiment in proton-lead collisions at a proton-nucleon centre-of-mass energy $\sqrt{s_{NN}} = 5$ TeV. The analysis is based on a data sample corresponding to an integrated luminosity of 1.6 nb^{-1}. The nuclear modification factor and the forward-backward production ratio are determined for J/Ψ and Υ(1S) mesons. Clear suppression of prompt J/Ψ production is observed with respect to the production in pp collisions at large rapidity, while the suppression of J/Ψ from b-hadron decays is less pronounced. The nuclear modification factor for Υ(1S) mesons in the forward region is found to be similar to those for J/Ψ from b-hadron decays. Furthermore a first observation of Z bosons in proton-lead collisions is reported.

1 Introduction

In ultra-relativistic heavy-ion collisions, the production of heavy quarkonia or electroweak bosons are expected to be suppressed with respect to proton-proton collisions, if a quark-gluon plasma, QGP, is created [1]. The suppression of heavy quarkonia and Z boson production with respect to pp collisions can also take place in proton-nucleus (pA) collisions, where a quark-gluon plasma is not expected to be created and only cold nuclear matter effects, such as nuclear absorption, parton shadowing and parton energy loss in initial and final states occur [2, 3, 4]. The study of pA collisions therefore provides important input to disentangle the QGP effects from cold nuclear effects, probe nuclear parton distribution functions which are poorly constrained, and provide a reference sample for nucleus-nucleus collisions.

In early 2013, the LHCb detector [5] collected two data samples corresponding to 1.6 nb^{-1} of proton-lead collisions at a centre-of-mass energy per proton-nucleon pair of $\sqrt{s_{NN}} = 5$ TeV. The two data samples correspond to two different beam configurations, with the proton (lead) beam into the direction of LHCb, referred to as forward (backward). Owing to the asymmetric beam configuration the LHCb acceptance corresponds to $1.5 < y < 4.0$ ($-5.0 < y < -2.5$) for the forward (backward) configuration. Results on J/Ψ [6], Υ [7] and Z [8] production are reported below.

2 J/Ψ and Υ production

J/Ψ [6] and Υ [7] mesons are reconstructed in the di-muon final states with the transverse momentum, p_T, of the di-muon system restricted to $p_T < 14$ GeV/c ($p_T < 15$ GeV/c) for J/Ψ (Υ). The excellent vertexing capability of LHCb allows a separation of prompt J/Ψ mesons and J/Ψ mesons from b-hadron decays (J/Ψ from b). The number of prompt J/Ψ and J/Ψ from b candidates are determined by a combined fit to the di-muon invariant mass and pseudo-proper time distributions. The pseudo-proper time is defined as $t_z = (z_{J/\Psi} - z_{PV}) \times M_{J/\Psi}/p_z$, where $z_{J/\Psi}$ is the z position of the J/Ψ decay vertex, z_{PV} that of the primary vertex, p_z the z component of the measured J/Ψ momentum, and $M_{J/\Psi}$ the mass of the J/Ψ.

Figure 1 shows the projections of the combined fit in two rapidity (y) bins in the forward and the backward region. The number of candidates for J/Ψ from b is about a factor of 10 smaller than for prompt J/Ψ.

The invariant di-muon mass distribution for the Υ candidates of the two samples are shown in Fig. 2. Higher combinatorial background in the backward region is observed for J/Ψ and Υ production due to the larger multiplicity in lead-proton collisions. Measurements for J/Ψ production are performed in three bins of rapidity; the low statistics of the Υ sample do not allow a differential measurement.

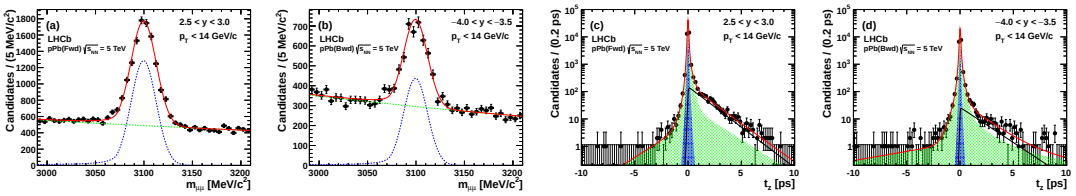

Figure 1: Projections of the combined fit: di-muon invariant mass (left two plots) and pseudo-proper time (right two plots) in the forward and backward region [6].

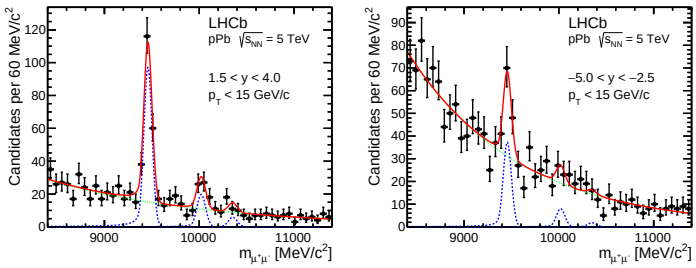

Figure 2: Di-muon invariant mass distribution for Υ candidates in the forward (left) and backward (right) region [7].

3 Cold nuclear effects

Nuclear effects are usually characterised by the nuclear modification factor R_{pA} and the forward-backward production ratio R_{FB},

$$R_{pA} = \frac{d\sigma_{pA}/dy}{Ad\sigma_{pp}/dy}, \qquad R_{FB} = \frac{d\sigma_{pA(y>0)}/dy}{d\sigma_{pA(y<0)}/dy}, \tag{1}$$

which depend on the production cross-section of a given particle in pA collisions and for R_{pA} also on the cross-section in pp collisions at the same centre-of-mass energy as well as the atomic number A. The advantage of measuring the R_{FB} is that it does not rely on the knowledge of the production cross-section in pp collisions and that experimental systematic uncertainties and theoretical scale uncertainties cancel partially.

To determine the nuclear modification factor R_{pA}, the reference cross-sections in pp collisions at $\sqrt{s_{NN}} = 5$ TeV are needed [9, 10]. These are obtained by a power-law fit to the previous LHCb measurements of J/Ψ and Υ production at 2.76 TeV, 7 TeV and 8 TeV. Figure 3 shows the nuclear modification factors (left two plots) and the forward-backward production ratios (right two plots), for prompt J/Ψ mesons and J/Ψ from b as functions of rapidity [6], compared to different theoretical predictions [2, 11, 3, 4]. A clear suppression of about 40% at large rapidity is observed for prompt J/Ψ production. The measurements agree with most predictions. The data show a modest suppression of J/Ψ from b production in the forward region, with respect to that in pp collisions. This is the first indication of the suppression of b hadron production in proton-lead collisions. The nuclear modification factor and forward-backward production ratio for J/Ψ from b reflect that cold nuclear matter effects on b hadrons are less pronounced than for J/Ψ.

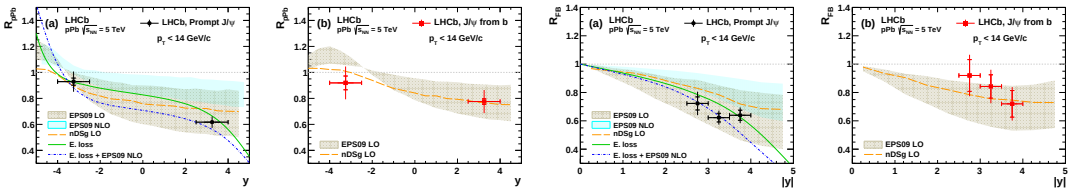

Figure 3: Forward-backward production ratios (R_{FB}, left two plots) and nuclear modification factor (R_{pA}, right two plots) for prompt J/Ψ and J/Ψ from b as functions of rapidity [6] together with theoretical predictions from (yellow dashed line and brown band) [2, 11], (blue band) [3], and (green solid and blue dash-dotted lines) [4].

Figure 4 shows R_{pA} and R_{FB} for Υ(1S) [7] together with the LHCb results of prompt J/Ψ and J/Ψ from b with theoretical predictions. The data are consistent with a suppression in the forward region and a possible enhancement in the backward region. In the forward region, the suppression of $\Upsilon(1S)$ mesons is smaller than that of prompt J/Ψ mesons and similar to J/Ψ from b, indicating that the cold nuclear matter effects on Υ(1S) mesons and J/Ψ from b are similar. Data and theoretical predictions which include coherent energy loss and nuclear shadowing as parametrised with EPOS09 [4] agree within the large experimental uncertainties.

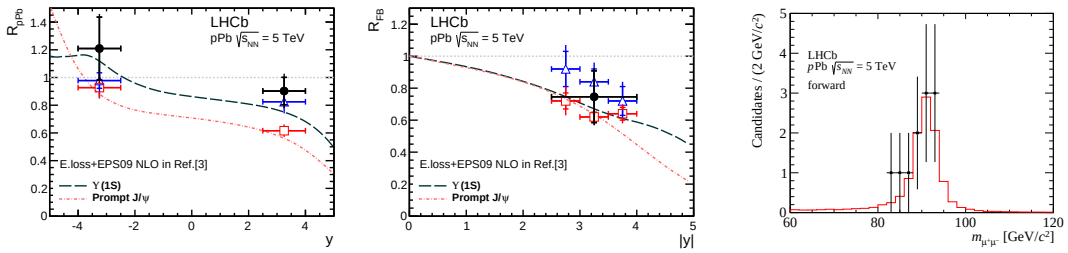

Figure 4: R_{FB} and R_{pA} for Υ, prompt J/Ψ and J/Ψ from b as functions of rapidity [7] (left two plots) with theoretical predictions including energy loss and nuclear shadowing [4]. Di-muon invariant mass for the Z candidates in the forward sample (right plot) [8].

4 Inclusive Z boson production in proton-lead collisions

The Z candidates are reconstructed in the di-muon final state [8]. Background contributions from muon mis-identification and the decay of heavy flavour mesons are determined from data. A total of 15 candidates are selected with a purity of above 99%, corresponding to a significance of $10.4\sigma(6.8\sigma)$ for the Z signal in the forward (backward) direction. Figure 4 (right plot) shows the di-muon invariant mass of the Z candidates in the forward direction. The inclusive Z boson production cross-section is measured to be $\sigma(Z \to \mu\mu) = 13.5^{+5.4}_{-4.0} \pm 1.2$ nb in the forward and $\sigma(Z \to \mu\mu) = 10.7^{+8.4}_{-5.1} \pm 1.0$ nb in the backward configuration, where the first uncertainty is statistical and the second systematic. The large experimental uncertainties do not allow definite conclusions on the presence of nuclear effects.

References

[1] T. Matsui and H. Satz. J/ψ Suppression by Quark-Gluon Plasma Formation. *Phys.Lett.*, B178:416, 1986.

[2] E.G. Ferreiro, F. Fleuret, J.P. Lansberg, and A. Rakotozafindrabe. Impact of the Nuclear Modification of the Gluon Densities on J/ψ production in pPb collisions at $\sqrt{s_{NN}} = 5$ TeV. *Phys.Rev.*, C88(4):047901, 2013.

[3] J.L. Albacete, N. Armesto, R. Baier, G.G. Barnafoldi, J. Barrette, et al. Predictions for $p + Pb$ Collisions at $\sqrt{s_{NN}} = 5$ TeV. *Int.J.Mod.Phys.*, E22:1330007, 2013.

[4] Francois Arleo and Stephane Peigne. Heavy-quarkonium suppression in p-A collisions from parton energy loss in cold QCD matter. *JHEP*, 1303:122, 2013.

[5] Jr. Alves, A. Augusto et al. The LHCb Detector at the LHC. *JINST*, 3:S08005, 2008.

[6] R Aaij et al. Study of J/ψ production and cold nuclear matter effects in pPb collisions at $\sqrt{s_{NN}} = 5$ TeV. *JHEP*, 1402:072, 2014.

[7] Roel Aaij et al. Study of Υ production and cold nuclear matter effects in pPb collisions at $\sqrt{s_{NN}} = 5$ TeV. *JHEP*, 1407:094, 2014.

[8] R. Aaij et al. Observation of Z production in proton-lead collisions at LHCb. *JHEP*, 1409:030, 2014.

[9] ALICE and LHCb Collaborations. Reference pp cross-sections for J/ψ studies in proton-lead collisions at $\sqrt{s_{NN}} = 5.02$ TeV and comparisons between ALICE and LHCb results. 2013.

[10] The LHCb Collaboration. Reference pp cross-sections for $\Upsilon(1S)$ studies in proton-lead collisions at $\sqrt{s_{NN}} =$ 5.02 TeV and comparisons between ALICE and LHCb results. 2014.

[11] Z. Conesa del Valle, E.G. Ferreiro, F. Fleuret, J.P. Lansberg, and A. Rakotozafindrabe. Open-beauty production in pPb collisions at $\sqrt{s_{NN}}$=5 TeV: effect of the gluon nuclear densities. *Nucl.Phys.*, A926:236–241, 2014.

On Parton Number Fluctuations

Stéphane Munier

Centre de physique théorique, École polytechnique, CNRS, Palaiseau, France

DOI: http://dx.doi.org/10.3204/DESY-PROC-2014-04/163

Parton evolution with the rapidity essentially is a branching diffusion process. We describe the fluctuations of the density of partons which affect the properties of QCD scattering amplitudes at moderately high energies. We arrive at different functional forms of the latter in the case of dipole-nucleus and dipole-dipole scattering.

1 Quantum chromodynamics at high density

Quantum chromodynamics in the high-energy/high-density regime is a very rich field from a theoretical viewpoint since it involves genuinely nonlinear physics, and nontrivial fluctuations. The latter are deemed *a goldmine for modern physics* [1]. From a phenomenological viewpoint, there is a wealth of data from different experiments which await interpretation. (For a review, we refer the reader to the recent textbook by Kovchegov and Levin [2]).

Electron-proton (or better, nucleus) scattering is maybe the best experiment to probe QCD in this regime, as was done at HERA, an $e^{\pm}p$ facility. The electron interacts with the proton through a quark-antiquark pair, which appears as a quantum fluctuation of a (virtual) photon of the Weizsäcker-Williams field of the electron. The probability amplitudes for these fluctuations follow from a simple QED calculation. The $q\bar{q}$ pair is a color dipole, and hence electron-hadron scattering may be related to dipole-hadron scattering. If one looks at events in which the $q\bar{q}$ pair has a small-enough size (as compared to the typical size of a hadron), as is possible by selecting longitudinally-polarized highly-virtual photons, then perturbative QCD may be used as a starting point to compute some properties of the dipole-hadron scattering amplitudes.

As for the interaction of protons and/or nuclei as is currently performed at the LHC, the observables need to be carefully chosen if one wants to be able to predict cross sections from first principles – at least in the present state of the art of the theory. Indeed, one needs a hard momentum scale to justify the use of perturbation theory, and the latter must be found in the final state in the form of e.g. the transverse momentum of a jet. It turns out that an observable such as $p_\perp$-broadening in proton-nucleus collisions, namely the transverse momentum distribution of single jets, may also be related to the dipole-nucleus amplitude.

We will first review the formulation of the rapidity evolution of the dipole-nucleus scattering amplitude in QCD in the high-energy limit. The latter is given by the Balitsky-Kovchegov (BK) equation. We will relate the known shape of its solution to gluon-number fluctuations in the quantum evolution of the dipole. We will then be able to predict the form of geometric scaling for dipole-dipole scattering, which turns out to be different from the solution to the BK equation.

2 Dipole-nucleus scattering

Let us start with the scattering of a dipole off a nucleus at relatively low energy. The forward elastic amplitude T is a function of the dipole size r_0, which is given by the McLerran-Venugopalan model:

$$T(r_0) = 1 - e^{-\frac{r_0^2 Q_A^2}{4}}. \tag{1}$$

This formula resums multiple exchanges of pairs of gluons between the bare dipole and the nucleus (see Fig. 1a). Q_A is the saturation momentum of the nucleus. Equation (1) essentially means that a dipole of size larger than $\sim 1/Q_A$ is absorbed ($T \sim 1$), while the nucleus is transparent to dipoles of size smaller than $\sim 1/Q_A$. For our purpose, we may approximate $T(r_0)$ by the step function $\Theta(\ln r_0^2 Q_A^2/4)$.

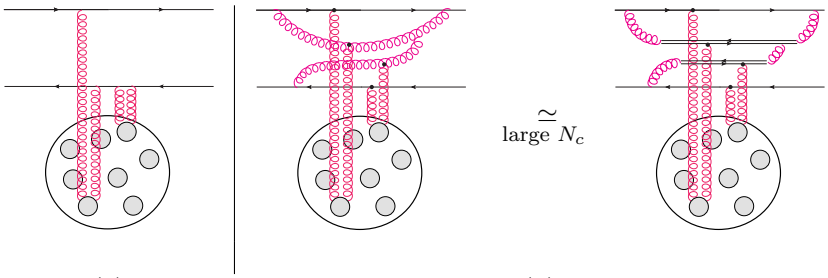

Figure 1: Particular graphs contributing to the dipole-nucleus scattering amplitude at low (a) and high (b) energy in the restframe of the nucleus.

Going to higher energies $\sqrt{s}$ by increasing the rapidity of the dipole, the scattering process gets dominated by high-occupancy quantum fluctuations of the initial dipole (see Fig. 1b). The rapidity ($y \equiv \ln s$) dependence of the amplitude is given by the Balitsky-Kovchegov (BK) equation

$$\partial_y T(r_0, y) = \bar{\alpha} \int \frac{d^2 r_1}{2\pi} \frac{r_0^2}{r_1^2 (r_0 - r_1)^2} \left[T(r_1, y) + T(r_0 - r_1, y) - T(r_0, y) - T(r_1, y) T(r_0 - r_1, y) \right] \tag{2}$$

($\bar{\alpha} \equiv \frac{\alpha_s N_c}{\pi}$), whose large-$y$ solutions are traveling waves, namely fronts which translate (almost) unchanged in shape towards negative values of the $\ln r_0^2$ variable as the rapidity increases. The linear part of this equation (the first three terms in the r.h.s.) form the BFKL equation, whose kernel possesses as eigenfunctions the power functions $|r_0|^{2\gamma}$, the corresponding eigenvalues being $\bar{\alpha}\chi(\gamma)$, where $\chi(\gamma) \equiv 2\psi(1) - \psi(\gamma) - \psi(1-\gamma)$. Introducing the particular eigenvalue $\chi(\gamma_0)$, where γ_0 is such that $\chi'(\gamma_0) = \chi(\gamma_0)/\gamma_0$, the shape of T as a function of the dipole size r_0 in the region $T \ll 1$ and the y-dependence of the saturation scale read

$$T(r_0, y) \underset{r_0 \ll 1/Q_s(y)}{\sim} \ln \frac{1}{r_0^2 Q_s^2(y)} e^{\gamma_0 \ln(r_0^2 Q_s^2(y))} \quad \text{and} \quad Q_s^2(y)/Q_A^2 \simeq e^{\bar{\alpha}\chi'(\gamma_0) y}. \tag{3}$$

The BK equation (2) can be established in the framework of the dipole model (see e.g. [2]), where gluons are replaced by zero-size $q\bar{q}$ pairs. In this model, the Fock state of the incoming

dipole which is "seen" by the nucleus at the time of the interaction is built from successive independent splittings of dipoles. At a given rapidity y, the latter Fock state can be thought of as a collection of n dipoles, generated by a splitting process which belongs to a class of processes generically called *branching diffusion*.

The main point we wanted to make at this conference and in Ref. [3] was that T has an elegant and useful probabilistic interpretation in the dipole picture: *It represents the probability that the largest dipole present in the Fock state of the incoming $q\bar{q}$ pair at the time of the interaction has a size which is larger than the inverse nuclear saturation momentum, $1/Q_A$.* Indeed, according to the McLerran-Venugopalan model, a given dipole interacts with the nucleus only if its size is larger than $1/Q_A$, hence it is necessary and sufficient that at least one of the dipoles in the Fock state be larger than $1/Q_A$ for the scattering to take place. Thus solving the BK equation amounts to understanding the statistics of the extremal particles in a branching random walk (BRW). Our first task is to recover the shape of the amplitude (3), previously obtained through a analysis of the BK equation, from the latter statistics.

We observe that the extremal particle in a BRW has fluctuations which can originate only from two places: From the first stages of the rapidity evolution, when the overall number of dipoles is small and thus subject to large statistical fluctuations (we shall call this type of stochasticity "front fluctuations"), and from the tip of the distribution, where by definition, particle numbers keep small. Elsewhere, the evolution is essentially deterministic since it acts on a large number of objects. The effect of the front fluctuations is to shift the particle distribution

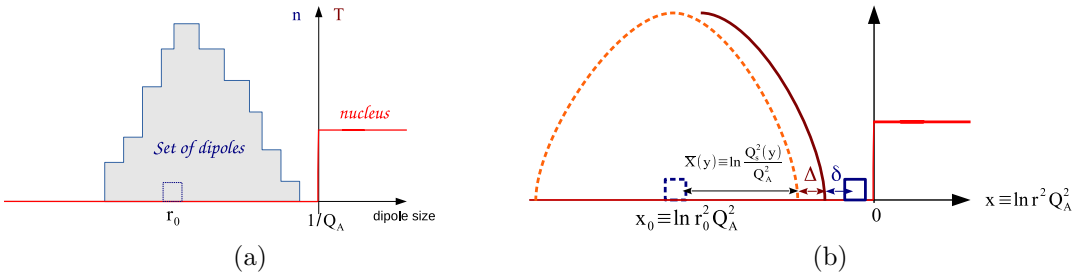

Figure 2: (a) Sketch of the dipole distribution (as seen at a given impact parameter) in a particular realization of the evolution to the rapidity y of an initial dipole of size r_0. (b) Model for the evolution of a given realization, with the "front" and "tip" fluctuations described in the text.

by Δ. We conjecture[1] that the distribution of Δ is $\propto e^{-\gamma_0 \Delta}$. The effect of the tip fluctuations is instead to send randomly particles ahead of the front by δ. We conjecture the same exponential law $\propto e^{-\gamma_0 \delta}$.

We introduce our notations in Fig. 2. According to the previous discussion, in a particular event, the scattering occurs if $x_0 + \bar{X}(y) + \Delta + \delta \geq 0$. Hence the amplitude T simply is the average of this condition over Δ and δ:

$$T \propto \int_0^{+\infty} d\delta\, e^{-\gamma_0 \delta} \int_0^{+\infty} d\Delta\, e^{-\gamma_0 \Delta} \Theta(x_0 + \bar{X}(y) + \Delta + \delta) \propto (-x_0 - \bar{X}(y)) e^{\gamma_0 (x_0 + \bar{X}(y))}. \quad (4)$$

[1] Arguments in favor of this conjecture were presented in Ref. [4].

Switching back to the QCD variables, we recover the expression of T given in Eq. (3). We conclude that *the shape of the dipole-nucleus scattering amplitude as a function of the dipole size is directly related to the event-by-event fluctuations of the size of the largest dipole*, which in turn stem from the fluctuations of the numbers of gluons produced in the QCD evolution.

3 Dipole-dipole scattering

While the dipole-nucleus amplitude probes the statistics of the largest dipole in the quantum evolution, the physics of dipole-dipole scattering is a bit different: Indeed, since the elementary amplitude (for dipoles of respective sizes r_0 and R_0) at zero rapidity is essentially $T(r_0, R_0) \sim \alpha_s^2 \delta(\ln r_0^2/R_0^2)$, it is the very shape of the dipole number distribution that is actually probed (Fig. 3). So in order to compute the shape of the amplitude, we need on one hand the probability distribution of the front fluctuations used before, and on the other hand the shape of the dipole number density from the deterministic evolution. We also need to implement *saturation* in the evolution (see Fig. 3c) to comply with the unitarity constraint $T \leq 1$. All in all, we obtain

$$T(r_0, y) \underset{r_0 \ll 1/Q_s(y)}{\sim} \ln^2 \frac{1}{r_0^2 Q_s^2(y)} e^{\gamma_0 \ln(r_0^2 Q_s^2(y))} \quad \text{where} \quad Q_s^2(y) R_0^2 \simeq e^{\bar{\alpha}\chi'(\gamma_0) y}. \tag{5}$$

Interestingly enough, it differs from the dipole-nucleus case; compare Eq. (3) to Eq. (5). This is the main prediction of the way of looking at QCD evolution we have promoted at this conference and in Ref. [3].

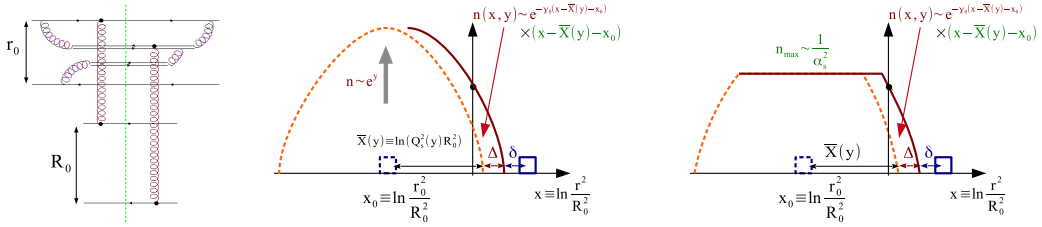

(a) (b) (c)

Figure 3: (a) Graph contributing to dipole-dipole scattering at high energies. (b) Sketch of the evolution of the dipole number density, model including fluctuations. (c) The same, but with saturation.

We refer the reader to [3] for the details, references, and more results, in particular on the finite-y corrections to the saturation scale in both the dipole-dipole and dipole-nucleus cases.

References

[1] E. Scapparone, plenary talk at this conference.

[2] Y.V. Kovchegov and E. Levin. *Quantum Chromodynamics at High Energy.* Cambridge Monographs on Particle Physics, Nuclear Physics and Cosmology. Cambridge University Press, 2012.

[3] A. H. Mueller and S. Munier, Phys. Lett. B **737** (2014) 303.

[4] A. H. Mueller and S. Munier, "Phenomenological picture of fluctuations in branching random walks," arXiv:1404.5500 [cond-mat.dis-nn] to appear in Phys. Rev. E (2014).

Proton-lead measurements using the ATLAS detector

Martin Spousta for the ATLAS Collaboration

Charles University in Prague

DOI: http://dx.doi.org/10.3204/DESY-PROC-2014-04/275

Measurements of soft and hard particle production in proton-lead collisions at the LHC have provided surprising results. Measurements of jets and high-p_{T} hadrons have shown an unexpected enhancement in the production of high-p_{T} charged particles and a similarly unexpected variation of the jet yield with proton-lead collision centrality. Studies of correlations in the production of soft particles have provided results that suggest strong collective behavior similar to that observed in lead-lead collisions. We give a brief report on the latest proton-lead measurements done by ATLAS.

1 Introduction

Proton-nucleus collisions at high energies provide an opportunity to study the effect of an extended nuclear target on the dynamics of soft and hard scattering processes and subsequent particle production. This involves extraction of nuclear parton distribution functions as well as disentangling the potential interplay between the soft and hard processes. In this short report we summarize the recent measurements done by ATLAS [1, 2, 3, 4, 5, 6, 7] that may improve our understanding of the physics of proton-nucleus collisions.

The analyses summarized here use the data from proton-lead (p+Pb) collisions measured by the ATLAS experiment. The LHC provided p+Pb collisions in two runs. During the first run in September 2012 and the second run in early 2013 ATLAS has recorded integrated luminosity of approximately 1 $\mu\mathrm{b}^{-1}$ and 29 nb^{-1}, respectively. The LHC was configured with a 4 TeV proton beam and a 1.57 TeV per-nucleon Pb beam that together produced collisions with a nucleon-nucleon centre-of-mass energy of $\sqrt{s_{\mathrm{NN}}} = 5.02$ TeV. The higher energy of the proton beam results in a net rapidity shift of the nucleon-nucleon centre-of-mass frame relative to the ATLAS rest frame. This rapidity shift is 0.47 towards the proton beam direction.

Some of the measurements are evaluated for several intervals in collision centrality characterized by the total transverse energy measured from the section of ATLAS forward calorimeter (FCal) spanning the pseudorapidity interval $3.2 < \eta < 4.9$, $\sum E_{\mathrm{T}}^{\mathrm{Pb}}$. Centrality intervals were defined in terms of percentiles of $\sum E_{\mathrm{T}}^{\mathrm{Pb}}$ determined using standard techniques [8]. The Glauber model [9] and its Glauber-Gribov extension [10] were used to estimate $\langle N_{\mathrm{part}} \rangle$ or the average value of the nuclear thickness function, $\langle T_{\mathrm{Pb}} \rangle$, for each centrality interval. The Glauber-Gribov model takes into account event-to-event fluctuations in the nucleon-nucleon cross-section, σ_{NN}. Two sets of Glauber-Gribov $\langle N_{\mathrm{part}} \rangle$ results were obtained for two different values of the parameter, Ω, that determines the width of the assumed Gaussian fluctuations in σ_{NN}.

2 Charged particle multiplicities and p_{T} spectra

Historically, the basic experimental observables quantifying the particle production are the charged particle multiplicity and pseudorapidity distributions. Previous measurements at RHIC have shown that the rapidity integrated particle multiplicity in d+Au collisions scales with number of inelastically interacting, or "participating", nucleons, N_{part}. This scaling behaviour has been interpreted as a result of coherent multiple soft interactions of the projectile nucleon in the target nucleus, the so called wounded-nucleon model. The characteristic centrality dependence of charged hadron pseudorapidity distributions showing a strong increase in the yields of nucleus-going direction that was previously observed can be explained by the phenomenology of soft hadron production or in parton saturation models.

Similar features as those seen previously are observed in the charged particle multiplicities measured by ATLAS [2]. In the most peripheral collisions (centrality interval 60-90%), $\mathrm{d}N_{\mathrm{ch}}/\mathrm{d}\eta$ has what appears to be a double-peak structure, similar to that seen in proton-proton (pp) collisions [11]. In more central collisions, the shape of $\mathrm{d}N_{\mathrm{ch}}/\mathrm{d}\eta$ becomes progressively more asymmetric, with more particles produced in the Pb-going direction than in the proton-going direction. The increase in the particle production in central relative to the most peripheral collisions is roughly linear in pseudorapidity. The N_{part} scaling of multiplicities exhibits a strong sensitivity to the Glauber modeling: while the standard Glauber modeling leads to a strong increase in the multiplicity per participant pair with increasing N_{part}, the Glauber-Gribov approach leads to a much milder centrality dependence.

The expected particle production rate in p+Pb collisions is determined by the product of the inelastic nucleon-nucleon cross-section, σ_{NN}, and the nuclear thickness function, $\langle T_{\mathrm{Pb}} \rangle$, which is averaged over a distribution of proton impact parameters incident on the nuclear target. The "nuclear modification factor" R_{pPb} can be therefore written as

$$R_{\mathrm{pPb}}(p_{\mathrm{T}}, y^{\star}) = \frac{1}{\langle T_{\mathrm{Pb}} \rangle} \frac{1/N_{\mathrm{evt}}\ \mathrm{d}^2 N_{\mathrm{pPb}}/\mathrm{d}y^{\star}\mathrm{d}p_{\mathrm{T}}}{\mathrm{d}^2\sigma_{\mathrm{pp}}/\mathrm{d}y\,\mathrm{d}p_{\mathrm{T}}}, \tag{1}$$

where nucleon-nucleon cross-section is approximated by pp cross-section, σ_{pp}, neglecting isospin effects. In the absence of nuclear effects at high-p_{T}, the R_{pPb} will be unity. The nuclear modification factor was extracted in two measurements, see Refs.[3, 4]. The reference pp cross-section was determined using the interpolation of cross-sections measured at the centre-of-mass energy of 2.76 and 7 TeV. The nuclear modification factors increase with momentum in the region $0.1 < p_{\mathrm{T}} < 2$ GeV, then they reach a maximum and decrease up to $p_{\mathrm{T}} \approx 8$ GeV and stay constant within the experimental uncertainties until p_{T} of ≈ 20 GeV. The magnitude of the peak strongly depends both on rapidity and centrality. It increases from the proton-going to Pb-going direction and from peripheral to central collisions. The constant region is less sensitive to the different centrality and rapidity intervals. The absolute magnitude of the R_{pPb} and its centrality behaviour strongly depend on the choice of the geometric model.

The nuclear modification factor of charged particles show signs of increasing in the region of $p_{\mathrm{T}} \gtrsim 30$ GeV. This trend does not have a strong rapidity dependence but is more pronounced in peripheral events. This result seems to show the same unexpected trend as was observed by the CMS Collaboration [12].

3 Jets and Z bosons

The nuclear modification factor R_{pPb} was measured also for jets [5] using as a reference the inclusive jet cross-section in $\sqrt{s} = 2.76$ TeV pp collisions x_T-interpolated to 5.02 TeV using previous ATLAS measurements of jet production at 2.76 and 7 TeV. Results were also reported for the central-to-peripheral ratio R_{CP}, made with respect to the 60-90% centrality bin. The centrality-inclusive R_{pPb} results for 0-90% collisions indicated only a modest enhancement over the geometric expectation. This is generally consistent with predictions from the modification of the parton distribution functions in the nucleus.

The results of the R_{CP} measurement indicate a strong, centrality-dependent reduction in the yield of jets in central collisions relative to that in peripheral collisions. The reduction becomes more pronounced with jet p_{T} and at more forward (p-going) rapidities. These two results are reconciled by the centrality-dependent R_{pPb} results, which show a suppression in central collisions and enhancement in peripheral collisions which is systematic in p_{T} and y^*. The R_{CP} and R_{pPb} data at forward rapidities were replotted as a function of $p_{\mathrm{T}} \cosh(y^*)$, the approximate total jet energy. When plotted this way, the results from different rapidity bins fall into roughly a single trend. This suggests that the mechanism responsible for the observed effects may depend only on the total jet energy or, more generally, on the underlying parton-parton kinematics such as the fractional longitudinal momentum of the parton originating in the proton x_p. If the relationship between the centrality intervals and proton-lead collision impact parameter determined within the geometric models is correct, these results imply large, impact parameter-dependent changes in the number of partons available for hard scattering. However, they may also be the result of a correlation between the kinematics of the scattering and the soft interactions resulting in particle production at backward (Pb-going) rapidities.

The influence of nuclear environment on the production of high-p_{T} particles was further tested by measuring the production of Z bosons [6]. The Z bosons were reconstructed via the di-electron and di-muon decay channels. Results from the two channels are consistent and combined to obtain a total cross-section of 144.1 $\pm$ 10.8 nb within the fiducial acceptance region. The total measured cross-section is compared to a baseline pQCD model in which nuclear binding and motion effects are neglected. The p_{T} dependence of the cross-section is in a good agreement with baseline pQCD, however the rapidity dependence shows significant asymmetry compared to the baseline pQCD. A relative excess in the Z boson differential cross-section is seen in the backward (Pb-going) part of the rapidity distribution. This asymmetry is more pronounced in central events and is apparently absent in peripheral events which are roughly symmetric about the centre of mass. Whether the relative asymmetry in central events compared to peripheral events is interpreted as an excess at backward rapidity or a deficit at forward rapidity depends on the choice of Glauber model centrality implementation. This centrality ordering is similar to that observed by ATLAS in high-p_{T} forward jets in p+Pb. The Z boson yield is expected to scale with number of binary collisions, $N_{\mathrm{coll}} = N_{\mathrm{part}} - 1$, however deviations from this scaling are observed, similarly as in the case of the charged particle yields. The charged particle yields are expected to scale with N_{part} and so the ratio $(\mathrm{d}N_Z/\mathrm{d}\eta)/(\mathrm{d}N_{\mathrm{ch}}/\mathrm{d}y)$ was fitted by a function of the form $a \cdot (N_{\mathrm{part}} - 1)/N_{\mathrm{part}}$ which describes the data well. The agreement in the geometric scaling trends between these two very different observables suggests that both are reflecting the consequences of the initial state conditions of the nucleus.

4 Ridge and flow

One striking observation in high-energy nucleus-nucleus collisions is the large anisotropy of particle production in the azimuthal angle ϕ. This anisotropy is often studied via a two-particle correlation of particle pairs in relative pseudorapidity ($\Delta\eta$) and azimuthal angle ($\Delta\phi$). The anisotropy manifests itself as a strong excess of pairs at $\Delta\phi \sim 0$ and π, and the magnitude of the excess is relatively constant out to large $|\Delta\eta|$. The azimuthal structure of this "ridge-like" correlation is commonly characterized by its Fourier harmonics, $\mathrm{d}N_{pairs}/\mathrm{d}\Delta\phi \sim 1+\sum_n 2v_n^2 \cos n\Delta\phi$. The v_n values are commonly interpreted as the collective hydrodynamic response of the created matter to the collision geometry and its density fluctuations in the initial state. For a small collision system, such as pp or p+A collisions, it was assumed that the transverse size of the produced system is too small for the hydrodynamic flow description to be applicable. Thus, it came as a surprise that ridge-like structures were also observed in two-particle correlations in high-multiplicity pp and p+Pb collisions.

Recent measurement done by ATLAS [7] explores the detailed properties of the ridge-like correlations and the flow via the two particle correlation (2PC) method. The two-particle correlations and v_n coefficients are obtained as a function of p_{T} for pairs with $2 < |\Delta\eta| < 5$ in different intervals of event activity, defined by either N_{ch}, the number of reconstructed tracks, or total transverse energy measured in FCal on the Pb-fragmentation side, $\sum E_{\mathrm{T}}^{\mathrm{Pb}}$. Significant long-range correlations (extending to $|\Delta\eta| = 5$) are observed for pairs at the near-side ($|\Delta\phi| < \pi/3$). A similar long-range correlation is also observed on the away-side ($|\Delta\phi| > 2\pi/3$), after subtracting the recoil contribution estimated using the 2PC in low activity events. The v_n, ($n = 2, 3, 4, 5$) values increase with p_{T} to $3-4$ GeV and then decrease for higher p_{T}, but remain positive in the measured p_{T} range. The $v_1(p_{\mathrm{T}})$ function is observed to change sign at $p_{\mathrm{T}} \approx 1.5-2.0$ GeV and to increase to about 0.1 at $p_{\mathrm{T}} > 4$ GeV. The magnitudes of v_n increase with both N_{ch} and $\sum E_{\mathrm{T}}^{\mathrm{Pb}}$. The extracted $v_2(p_{\mathrm{T}})$, $v_3(p_{\mathrm{T}})$, and $v_4(p_{\mathrm{T}})$ are compared to the v_n coefficients in p+Pb collisions at $\sqrt{s_{\mathrm{NN}}} = 2.76$ TeV with similar N_{ch}. After applying a scale factor of $K = 1.25$ that accounts for the difference of mean p_{T} in the two collision systems, the shape of the $v_n(p_{\mathrm{T}}/K)$ distribution in Pb+Pb collisions is found to be similar to the shape of $v_n(p_{\mathrm{T}})$ distribution in p+Pb collisions. This suggests that the long-range ridge correlations in high-multiplicity p+Pb collisions and peripheral Pb+Pb collisions are driven by similar dynamics.

Acknowledgments

This work was supported by Charles University in Prague, projects INGOII LG13009, PRVOUK P45, and UNCE 204020/2012.

References

[1] ATLAS Collaboration. *JINST*, 3:S08003, 2008.

[2] ATLAS Collaboration. ATLAS-CONF-2013-096. https://cds.cern.ch/record/1599773.

[3] ATLAS Collaboration. ATLAS-CONF-2013-107. https://cds.cern.ch/record/1624333.

[4] ATLAS Collaboration. ATLAS-CONF-2014-029. http://cds.cern.ch/record/1704978.

[5] ATLAS Collaboration. ATLAS-CONF-2014-024. http://cds.cern.ch/record/1702986.

[6] ATLAS Collaboration. ATLAS-CONF-2014-020. http://cds.cern.ch/record/1702971.

[7] ATLAS Collaboration. arXiv:1409.1792.

[8] ATLAS Collaboration. *Phys.Lett.*, B710:363–382, 2012.

[9] M. Miller, K. Reygers, S. Sanders, and P. Steinberg. *Ann. Rev. Nucl. Part. Sci.*, 57:205–243, 2007.

[10] V. Guzey and M. Strikman. *Phys. Lett.*, B633:245–252, 2006.

[11] ATLAS Collaboration. *Phys. Lett.*, B688:21–42, 2010.

[12] CMS Collaboration. CMS-PAS-HIN-12-017. http://cds.cern.ch/record/1625865.

Soft Probes of the Quark-Gluon Plasma in ATLAS

Krzysztof W. Wozniak[1] on behalf of the ATLAS Collaboration

[1]Institute of Nuclear Physics, PAS, ul. Radzikowskiego 152, 31-342 Krakow, Poland

DOI: http://dx.doi.org/10.3204/DESY-PROC-2014-04/230

Measurements of low-p_{T} (< 5 GeV) particles in Pb+Pb collisions at the LHC provide valuable insight in the production and evolution of the quark-gluon plasma. In particular, measurements of the elliptic and higher order flow harmonics imprinted on the azimuthal angle distributions of low-p_T particles directly probe the strongly-coupled dynamics of the quark gluon plasma and test hydrodynamic model descriptions of its evolution. The large acceptance ATLAS detector makes it possible to measure flow event-by-event and to determine the correlations between different event planes and different flow harmonics.

In collisions of lead nuclei from two beams accelerated in the Large Hadron Collider (LHC) to the energy in the centre-of-mass of $\sqrt{s_{\mathrm{NN}}} = 2.76$ TeV a very high energy density is achieved in a relatively large volume. This leads to creation of a dense, strongly interacting matter - the Quark-Gluon Plasma (QGP). Such matter undergoes first an expansion and then a hadronization leading to particles observed in detectors. While the properties of most energetic partons (observed as jets) are affected mostly by the initial conditions of QGP, the production of particles with lower momenta is also sensitive to the later evolution of QGP. Detailed studies of various correlations between low-p_{T} particles were performed by the ATLAS experiment. In these analyses information from several parts of the ATLAS detector [1] was used. In the Inner Detector covering over 5 pseudorapidity units ($|\eta| < 2.5$) tracks of charged particles are reconstructed. The calorimeters register energy of hadrons, electrons and photons in the $|\eta| < 4.9$ range. The signal registered in the $3.1 < |\eta| < 4.9$ range (i.e. from Forward Calorimeters) is used as a measure of the centrality of Pb+Pb collisions.

In heavy-ion collisions, with an exception of the most central ones, the area of the overlap of nuclei has an elongated shape. The asymmetry of the QGP volume leads in hydrodynamical models to different pressure gradients and then to the azimuthal asymmetry of particle emission (flow). The asymmetry is studied using the Fourier expansion:

$$\frac{\mathrm{d}N_{\mathrm{ch}}}{\mathrm{d}\phi} \sim 1 + 2\sum_{n=1}^{\infty} v_n(p_{\mathrm{T}}, \eta)\cos(n(\phi - \Phi_n)),$$

where azimuthal angles ϕ and Φ_n of the charged particles and the reaction planes, respectively, are used.

The second Fourier harmonic, v_2, called elliptic flow, represents the magnitude of correlations connected with the elongated shape of the overlap of the nuclei. In the LHC experiments it is usually measured using particles with $p_{\mathrm{T}} > p_{\mathrm{T,min}}$, with $p_{\mathrm{T,min}} = 0.3 - 0.5$ GeV, with a model dependent extrapolation to $p_{\mathrm{T}} \approx 0$. No extrapolation is needed in ATLAS if *tracklets*, defined as two hits registered in the innermost pixel detector, compatible with the primary vertex position, are used to reconstruct particles with p_{T} down to 0.07 GeV. In Fig. 1 the dependence of the

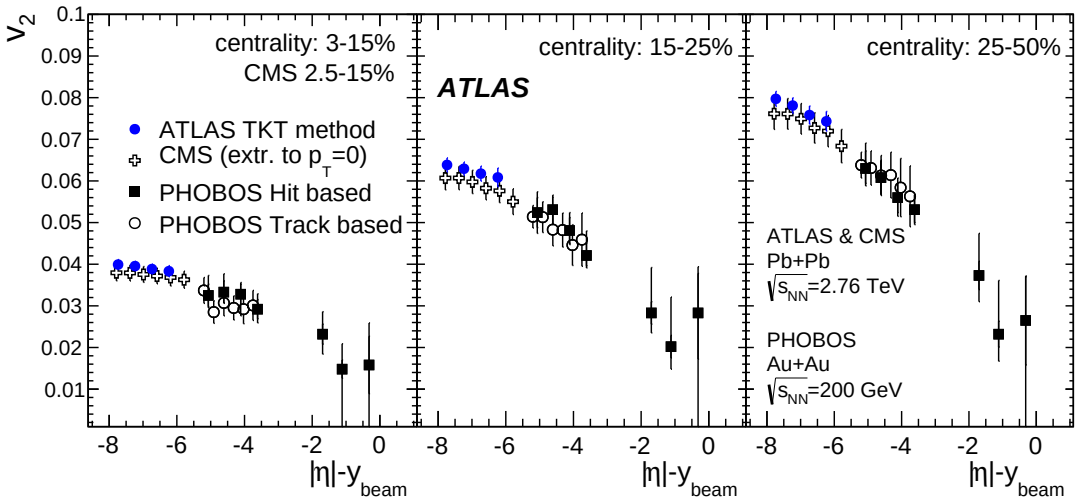

Figure 1: Integrated elliptic flow, v_2, presented as a function of $|\eta| - y_{beam}$ for three centrality intervals obtained by the ATLAS [2] and CMS [3] experiments for Pb+Pb collisions at $\sqrt{s_{\rm NN}} = 2.76$ TeV and by the PHOBOS experiment [4] for Au+Au collisions at $\sqrt{s_{\rm NN}} = 200$ GeV.

integrated elliptic flow, v_2, on pseudorapidity, shifted by the rapidity of the beam, $y_{\rm beam}$, is presented. This shift corresponds to the Lorentz transformation of rapidity to the rest frame of one of the colliding nuclei. After such transformation the PHOBOS experiment observed an extended longitudinal scaling of v_2 at energies $\sqrt{s_{\rm NN}} = 19.6 - 200$ GeV [4]. The data points from ATLAS follow the trend seen by PHOBOS, unfortunately, the acceptance of the ATLAS detector is too small, to obtain any overlap with PHOBOS,

Flow harmonics can be also measured without determination of the event plane angle, Φ_n, using two-particle or many-particle correlations. If flow is the only source of the two-particle correlations, flow harmonics can be calculated as $v_n\{2\} = \sqrt{\langle\cos(n(\phi_a - \phi_b))\rangle}$. For $2k$-particle correlations ($k > 1$) especially useful are *cumulants*, which measure genuine $2k$-particle correlations. A comparison of flow harmonics obtained by ATLAS using the event plane method, $v_n\{\rm EP\}$, two-particle correlations, $v_n\{2\}$, four-particle cumulants, $v_n\{4\}$, and mean values of $p(v_n)$ distributions from event-by-event measurements, $v_n\{\rm EbyE\}$ is shown in Fig. 2 [5]. For all measured harmonics we observe $v_n\{2\} > v_n\{\rm EP\} > v_n\{\rm EbyE\} > v_n\{4\}$ relation. $v_n\{2\}$ are the largest beacuse of the non-flow contributions from short range correlations (for example resonance decays), suppressed in all other methods. The differences between $v_n\{\rm EP\}$, $v_n\{\rm EbyE\}$ and $v_n\{4\}$ are mainly due to flow fluctuations affecting each of them in a different way. In addition to four-particle cumulants, also six- and eight-particle cumulants are used by ATLAS to measure $v_2\{6\}$ and $v_2\{8\}$, respectively. They are very similar to $v_2\{4\}$, which means that already by using the four-particle cumulants non-flow contributions are efficiently suppressed [5].

Another comparison of the data and models of heavy-ion collisions is possible in a study of correlations between two or more event plane angles, Φ_n, measured in different η intervals for different harmonics [6]. The correlators are defined as $\langle\cos(c_1\Phi_1 + 2c_2\Phi_2 + ... + lc_l\Phi_l)\rangle$ with the constants c_n fulfilling the constraint $c_1 + 2c_2 + ... + lc_l = 0$. In Fig. 3 eight correlators with two event planes measured by ATLAS are presented [6]. Usually the correlations are positive,

especially for $4(\Phi_2 - \Phi_4)$, $6(\Phi_2 - \Phi_6)$ and $6(\Phi_3 - \Phi_6)$, but for one of three plane correlations, $2\Phi_2 - \Phi_3 + 4\Phi_4$, it is negative [6]. The values and centrality dependence of correlators from the data and predicted by Glauber model are distinctly different. However, a good qualitative agreement with the data is seen for predictions from the AMPT model [7], which starting from the same initial state as the Glauber model in addition simulates final-state dynamics.

The correlations between magnitudes of flow harmonics measured by ATLAS [8] are presented in Figs. 4 and 5. The data points were obtained in narrow bins of flow vector, q_2 (defined in Ref. [8]), and centrality. The flow vector characterises the asymmetry of the particle production and is directly related to the shape of the initial volume of the QGP, while the centrality reflects its size mostly. For v_2 measured in different p_{T} intervals, linear correlations within fixed centrality are observed (Fig. 4) and only the slope of the linear fit changes with centrality. This suggests presence of viscous effects which are controlled by the overall system size and not its shape. Negative, approximately linear correlations between v_3 and v_2 are observed (Fig. 5 left), similar to anti-correlations between corresponding eccentricities calculated from the positions of participating nucleons. However, the correlations between v_4 and v_2 (Fig. 5 right) are non-linear and thus are not completely eccentricity driven [8].

Detailed studies of several aspects of flow phenomena in ATLAS provide a better understanding of the QGP initial state and evolution. In the flow harmonics calculated from multi-particle cumulants non-flow contributions are suppressed. Effects of final-state dynamics have large impact on correlations between event plane angles. The analysis of correlations between elliptic flow and other flow harmonics reveals viscous effects, anti-correlation of v_3 versus v_2 and non-linear terms in v_4 and v_5 dependence on v_2.

Acknowledgments:

This work was supported in part by the National Science Center grant DEC-2011/03/B/ST/02631 and by PL-Grid Infrastructure.

References

[1] ATLAS Collaboration, JINST 3, S08003 (2008).

[2] ATLAS Collaboration, arXiv:1405.3936v2 [hep-ex] (2014), accepted by Eur. Phys. J. C.

[3] CMS Collaboration, Phys. Rev. C 87, 014902 (2013).

[4] PHOBOS Collaboration, B.B. Back et al., Nucl. Phys. A757, 28 (2005).

[5] ATLAS Collaboration, arXiv:1408.4342 [hep-ex] (2014).

[6] ATLAS Collaboration, Phys. Rev. C80, 024905 (2014).

[7] Z.-W. Lin, C. M. Ko, B.-A. Li, B. Zhang, and S. Pal, Phys. Rev. C 72, 064901 (2005).

[8] ATLAS Collaboration, ATLAS-CONF-2014-022, http://cdsweb.cern.ch/record/1702980 (2014).

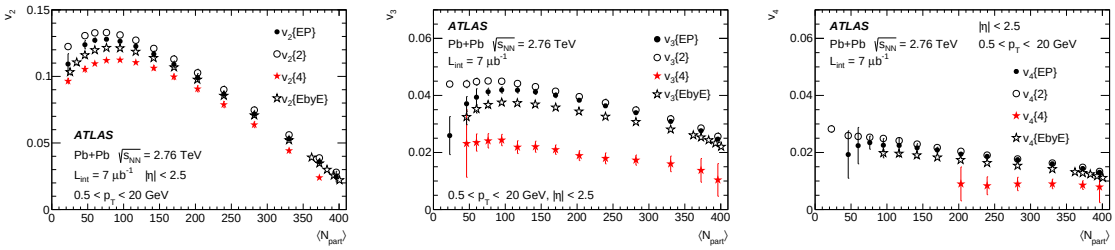

Figure 2: N_{part} dependence of flow harmonics: v_2 (left), v_3 (middle) and v_4 (right) obtained using several different methods [5].

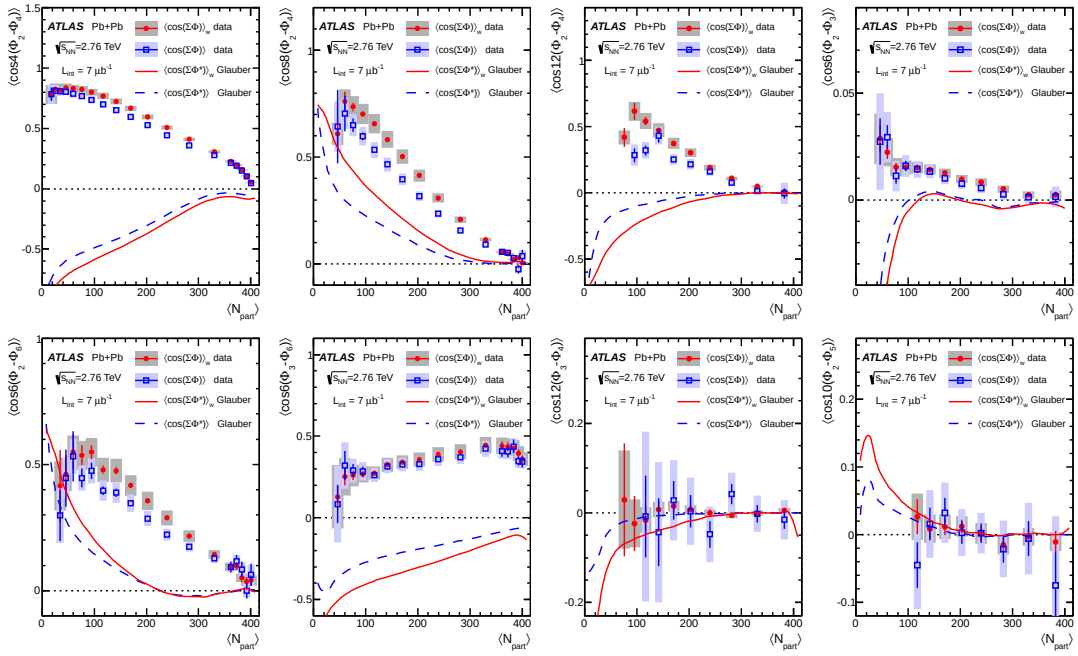

Figure 3: Centrality dependence of two-plane correlators (points) compared with correlations among participant-plane angles expected from the Glauber model (lines) [6].

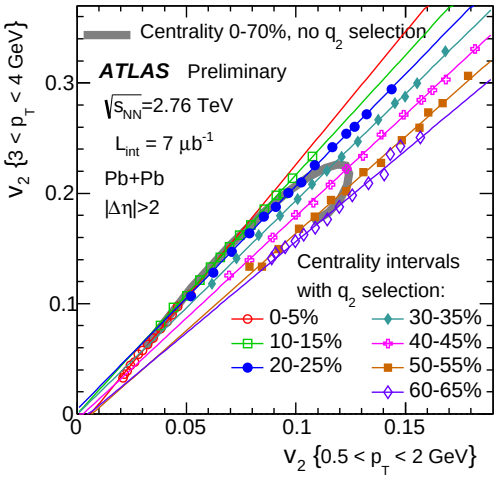

Figure 4: The correlation between values of v_2 measured in 3-4 GeV p_T range and in 0.5-2 GeV p_T range for several centrality and q_2 intervals, overlaid with the centrality dependence without q_2 selection (grey band) [8]. Linear fits to the data points in each centrality are shown as straight lines.

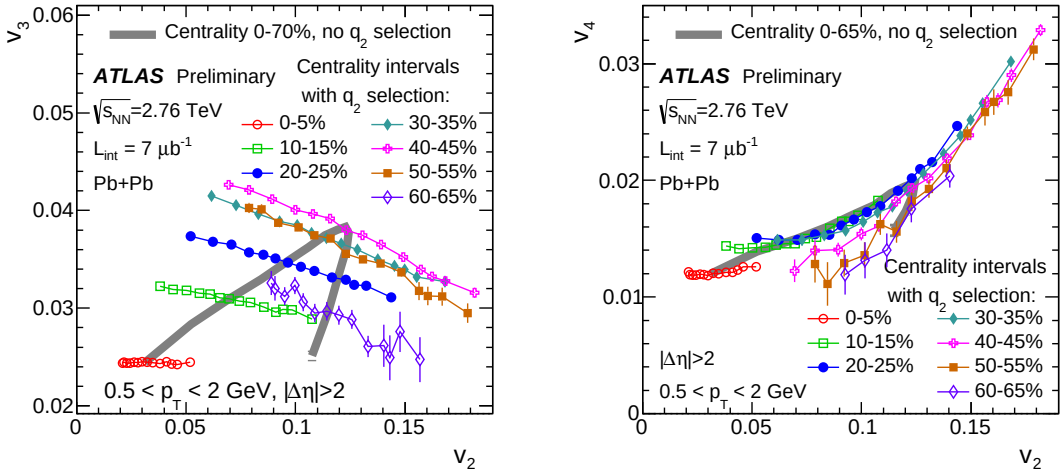

Figure 5: The correlation (left) between v_3 and v_2 and (right) between v_3 and v_2, all measured in 0.5-2 GeV p_T range [8]. Several different centrality selections (denoted by different symbols and colours) and q_2 intervals are used and overlaid with the centrality dependence without q_2 selection (grey band).

Measuring the gluon distribution in nuclei at an Electron-Ion Collider

Matthew A. C. Lamont

Brookhaven National Lab, Upton, NY, 11973, USA

DOI: http://dx.doi.org/10.3204/DESY-PROC-2014-04/44

Despite the successes of the HERA accelerator, where much information was gained on the structure of the nucleon, data on the structure of the nucleus at moderate-to-small x remains elusive, as only fixed-target high-x data currently exist. The small-x region, however, is of great interest. The nucleon structure in this region is dominated by gluons which show a rapid rise with decreasing x. At low-x, this growth must be tamed and the gluon distribution will be saturated. However, only tantalising hints of this have been observed so far. Therefore, the construction of an Electron-Ion Collider (EIC), colliding polarised electrons with polarised protons and also a wide variety of nuclei, will allow an exploration of the region of small-x in great detail, answering questions on both the spatial and momentum distributions of gluons and sea quarks in nuclei. In particular, the saturation region is more accessible in nuclei due to the amplification of the saturation scale with nuclear size ($Q_S \propto \mathrm{A}^{1/3}$). In this paper I present the current status of measuring the gluon distribution in nuclei in e+A collisions at an EIC.

1 Introduction

As the HERA measurements of structure functions showed, at small x, the gluon and sea-quark distributions dominate the structure of the nucleon [1]. In fact, if the structure functions continued to grow untamed with decreasing x, through a process of hard gluons splitting into softer gluons, then the cross-section would become larger than the black-disk limit. Therefore, this growth must be tamed at small x, when soft gluons can recombine into harder gluons. Saturation is achieved when these two processes match each other. This saturation phenomena is expected to be universal, appearing in both nucleons and nuclei. However, its effect is amplified in nuclei, where the saturation scale is expected to grow with nuclear size ($Q_S \propto \mathrm{A}^{1/3}$). Therefore, saturation effects should be visible at higher values of x than in nucleons. A review of saturation physics can be found in the literature [2]. A knowledge of this regime is of vital importance to understanding the underlying physics which governs the initial conditions of heavy-ion collisions at both RHIC and in particular, the LHC, where particle production is dominated by gluons from this unknown region. To that end, eRHIC is a machine that is being designed at Brookhaven National Lab that utilizes the current $2B hadron facility of RHIC and would provide e+A collisions at high energy and high luminosity [3]. eRHIC would also provide polarized electrons and protons for the study of the spin structure of nucleons.

In this paper, I will not discuss the spin capabilities of an electron-ion collider, but rather focus on measurements that can be made in e+A collisions which will provide further insight

into the structure of nuclei. For a detailed review of both the spin capabilities and a more in-depth coverage of the e+A physics than is allowed in this manuscript, please refer to the EIC White Paper [4].

2 Structure Functions

One of the first measurements that will be made in nuclear DIS collisions is of the cross-section as a function of (x,Q^2). Although this is one of the easiest measurements to make, it contains a lot of important information. This cross-section can be written in terms of structure functions:

$$\sigma_r(x,Q^2) = F_2^A(x,Q^2) - \frac{y^2}{Y+} F_L^A(x,Q^2) \tag{1}$$

The two structure functions of importance are F_2 and F_L, which reflect the quark and gluon momentum distributions respectively. In order to measure F_L directly, it is necessary to have high-statistics datasets over a number of energies. This was not possible at HERA and hence the gluon distribution in nucleons was inferred from the scaling violation of the F_2 distribution [1].

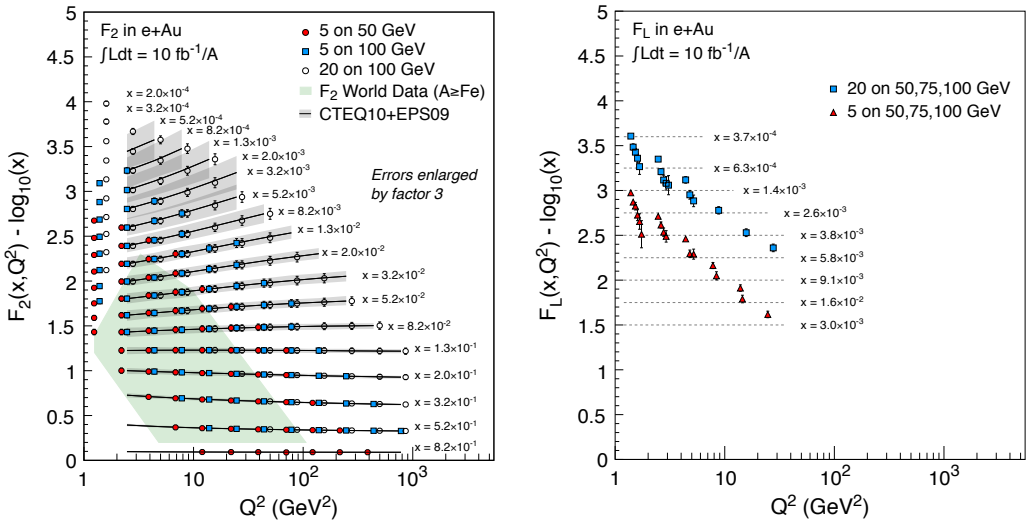

Figure 1: The F_2 (left) and F_L (right) distributions at eRHIC for e+Au collisions. The uncertainties on the pseudo-data are overwhelmingly systematic and represent an integrated luminosity of 10 fb^{-1}/A.

The left side of Figure 1 shows the (x, Q^2) coverage of the F_2 distribution according to the pseudo-data generated for three different eRHIC energies. These pseudo-data were generated using PYTHIA with EPS09 NLO PDFs and represent 10 fb^{-1}/A of data, corresponding to approximately 6 months running time. The highest energy (20x100 GeV beams) extend the phase-space to the lowest (x, Q^2) region while the lowest energy (5x50 GeV beams) extends this measurement to high-x. Also shown on the plot are the EPS09 predictions and their associated uncertainties, together with existing data from fixed target e+A collisions. At small-x, these

uncertainties are very large and the data from eRHIC will have a significant impact on the EPS09 uncertainties. For clarity, both the errors coming from EPS09 and the pseudo-data have been enlarged by a factor of 3.

The right side of Figure 1 shows the corresponding F_L measurement. The F_L data were extracted using a Rosenbluth Separation analysis technique where, for each (x, Q^2) bin, a minimum of 3 data points were fit and were required to have a separation of at least 0.1 units of y^+. This technique, however, leads to large uncertainties and these are represented in the plot. Although these are significant, this will be a first measurement of F_L in nuclei.

3 Diffraction in $e + A$ collisions

One of the interesting results to come out of HERA was that a large fraction of events (10-15%) were diffractive. That is, in a significant fraction of collisions at very high energies, the nucleon stayed intact. Whilst this, in and of itself, is a large fraction of events, it is predicted that in nuclei, where saturation effects may be observed at eRHIC, this number could be a factor of 2 or 3 higher.

One of the most promising methods for observing saturation in diffractive collisions, other than the cross-section, is that of vector meson production. Figure 2 shows the cross-section for vector meson production in both coherent and incoherent diffractive collisions, as a function of the Mandelstam variable t, where the uncertainties correspond to an integrated luminosity of 10 fb^{-1}/A. Note that the Q^2 range is above the photo-production threshold. This is shown for both the J/ψ and the ϕ vector mesons. Both of these distributions were generated using the SARTRE MC event generator which has recently been developed for diffractive physics in e+A collisions [5].

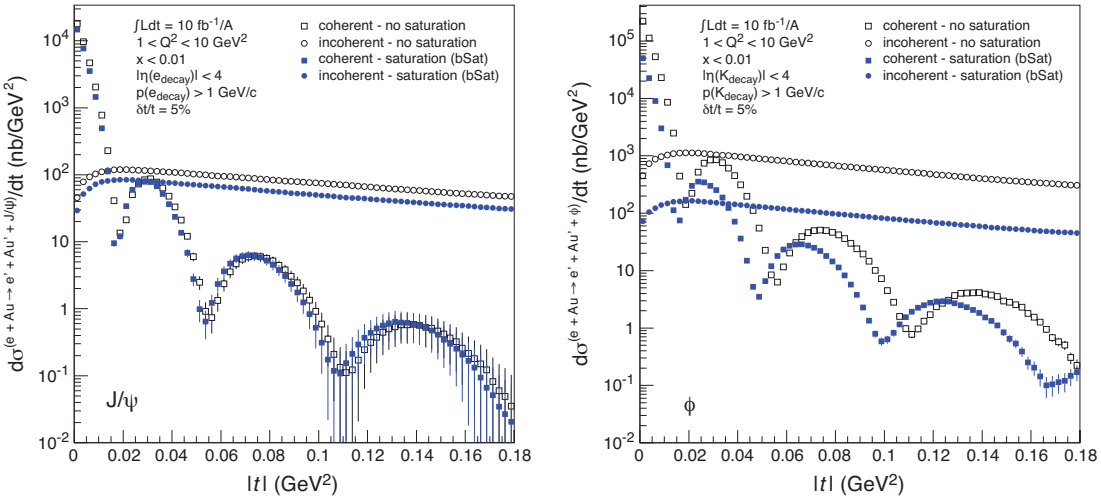

Figure 2: The coherent and incoherent diffractive distributions for the J/ψ (left) and the ϕ (right) vector mesons for an integrated luminosity of 10 fb^{-1}/A, respectively. All distributions were calculated using the SARTRE event generator.

This shows that in the case of the J/ψ, then there is very little difference between the

distributions for the saturated and unsaturated case. However, for the ϕ, there is a very significant difference. This comes about because of the size of the wave-functions, where the ϕ wave function is much larger than that of the J/ψ and hence it is more sensitive to saturation effects. In fact, one can take these distributions and perform a Fourier Transform to obtain the input source distribution. Figure 3 shows examples of this for the saturated and unsaturated case for both the J/ψ and the ϕ mesons, which plots both the input Woods-Saxon distribution and the Fourier Transform of the coherent diffractive distribution. As can be seen in the figure, there is little difference between the cases for the J/ψ whereas there is a large difference in the two scenarios for the ϕ meson.

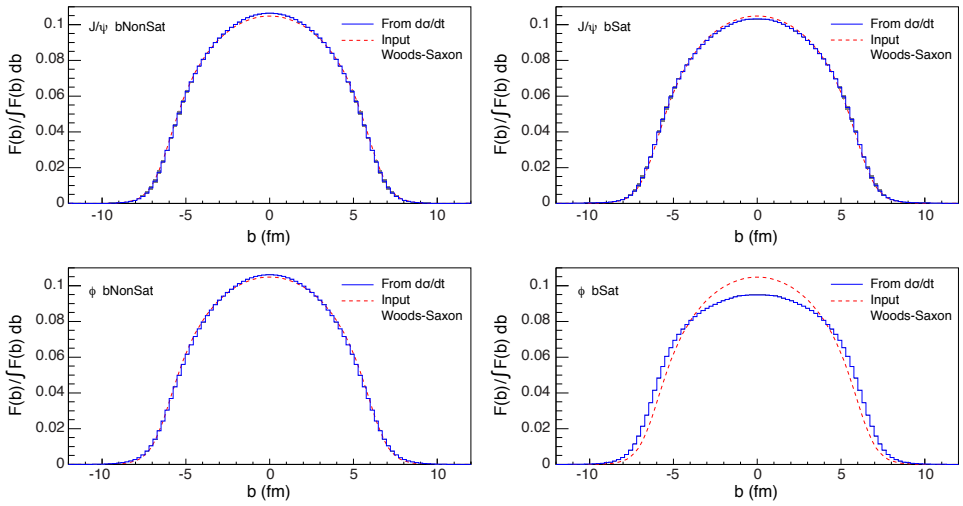

Figure 3: The Fourier Transform of the coherent diffraction distribution in the case of a saturated and unsaturated wave function for the J/ψ (top) and the ϕ (bottom) vector mesons presented in Figure 2. Also shown in each case are the input Woods-Saxon distributions.

Without an Electron-Ion Collider, these measurements cannot be made. Therefore, it is imperative that if we are to more fully understand the par tonic structure of the nucleus, an electron-ion collider is built.

References

[1] S. Aid *et al.*, (H1 Collaboration) Phys. Lett. **B354** (1995) 494-505.

[2] J. Jalilian-Marian and Y. V. Kovchegov, Prog. Part. Nucl. Phys. **56**, 104 (2006).

[3] E.-C. Aschenauer *et al.*, ArXiv:1409.1633.

[4] A. Accardi *et al.*, ArXiv:1212.1701.

[5] T. Toll and T. Ullrich, Phys. Rev. **C 87**, 024913 (2013).

Transverse Momentum Distributions of Charged Particles and Identified Hadrons in p–Pb Collisions at the LHC

Jacek Otwinowski [1] for the ALICE Collaboration

[1] IFJ PAN, Radzikowskiego 152, 31-342 Krakow, Poland

DOI: http://dx.doi.org/10.3204/DESY-PROC-2014-04/142

The transverse momentum distributions (p_{T}) of charged particles and identified hadrons in p–Pb collisions at $\sqrt{s_{\mathrm{NN}}} = 5.02$ TeV have been measured by ALICE at the LHC. Charged-particle tracks are reconstructed at mid-rapidity over a large momentum range $0.15 < p_{\mathrm{T}} < 50$ GeV/c. Light-flavour hadrons and resonances are identified in the various momentum regions, ranging from 0.15 GeV/c to 15 GeV/c, using specific energy loss (dE/dx), time-of-flight, topological particle-identification and invariant-mass reconstruction techniques. p_{T} spectra are measured for different charged particle multiplicity intervals. Results from p–Pb collisions are compared with pp and Pb–Pb results, and with theoretical models.

1 Introduction

Production of light-flavor hadrons in high energy p–Pb collisions at the LHC is used to study the cold nuclear matter effects (Cronin effect [1], shadowing and gluon saturation [2]), which might influence particle production. It is also possible to search for collective phenomena or indication of the final state effects, which might modify the measured hadron spectra. Here, the question is whether the p–Pb can be considered as a reference system for measurements in Pb–Pb collisions, where the quark-gluon plasma (QGP) [3] is expected to be produced.

In these proceedings, we present results on primary charged particles (98% hadrons) and identified light-flavor hadrons ($\pi^{\pm}$, $\mathrm{K}^{\pm}$, $\mathrm{K}^{0}_{\mathrm{s}}$, p, $\bar{\mathrm{p}}$, Λ, $\bar{\Lambda}$, Ξ^{-}, $\bar{\Xi}^{+}$) obtained by ALICE. Primary charged particles are defined in ALICE as all charged particles produced in the collision and their decay products, except for particles from weak decays of strange hadrons.

In order to quantify nuclear effects, the particle production in p–Pb collisions is compared to pp with use of nuclear modification factor,

$$R_{\mathrm{pPb}}(p_{\mathrm{T}}) = \frac{\mathrm{d}^2 N_{\mathrm{ch}}^{\mathrm{pPb}}/\mathrm{d}\eta\mathrm{d}p_{\mathrm{T}}}{\langle T_{\mathrm{pPb}}\rangle \mathrm{d}^2\sigma_{ch}^{\mathrm{pp}}/\mathrm{d}\eta\mathrm{d}p_{\mathrm{T}}}, \tag{1}$$

where $N_{\mathrm{ch}}^{\mathrm{pPb}}$ is the particle multiplicity in minimum-bias p–Pb collisions, $\sigma_{\mathrm{ch}}^{\mathrm{pp}}$ is the pp cross section, and $\langle T_{\mathrm{pPb}}\rangle = 0.0983 \pm 0.0035$ mb^{-1} is the average nuclear overlap function calculated for minimum bias p–Pb collisions [4] based on Glauber Monte Carlo simulations [5]. The pp reference spectra are constructed [6] using pp measurements at $\sqrt{s} = 2.76$ and 7 TeV at the LHC.

2 ALICE experiment

ALICE [7] is the dedicated heavy-ion experiment at the LHC. The particle tracks are reconstructed using the hit information from the six silicon layers of the Inner Tracking System (ITS) and up to 159 space points from the Time Projection Chamber (TPC). The relative p_{T} resolution obtained with the ITS and TPC combined tracking amounts to $\sigma_{p_{\mathrm{T}}}/p_{\mathrm{T}} = 1$–$5\%$ for $p_{\mathrm{T}} = 0.1$–20 GeV/c. ALICE has excellent particle identification (PID) capabilities in the broad transverse momentum range $p_{\mathrm{T}} = 0.1$–20 GeV/c, which is unique at the LHC. Charged hadrons with $p_{\mathrm{T}} = 0.1$–5 GeV/c are identified using the energy loss (dE/dx) from the ITS and TPC detectors, the time-of-flight measurement with TOF detector, and Cherenkov light from the high momentum particle identification detector (HMPID). Above $p_{\mathrm{T}} = 5$ GeV/c, they are identified based on the dE/dx in the relativistic rise range of the Bethe-Bloch curve in the TPC. Strange hadrons which decay into charged particles ($\mathrm{K}^0_{\mathrm{s}} \to \pi\pi$, $\Lambda \to \pi p$ and $\Xi \to \pi\Lambda$) are identified via their decay topology and invariant mass analysis. In addition, the PID information for their decay products is used to improve signal to background ratio. More details about tracking and particle identification can be found in [8].

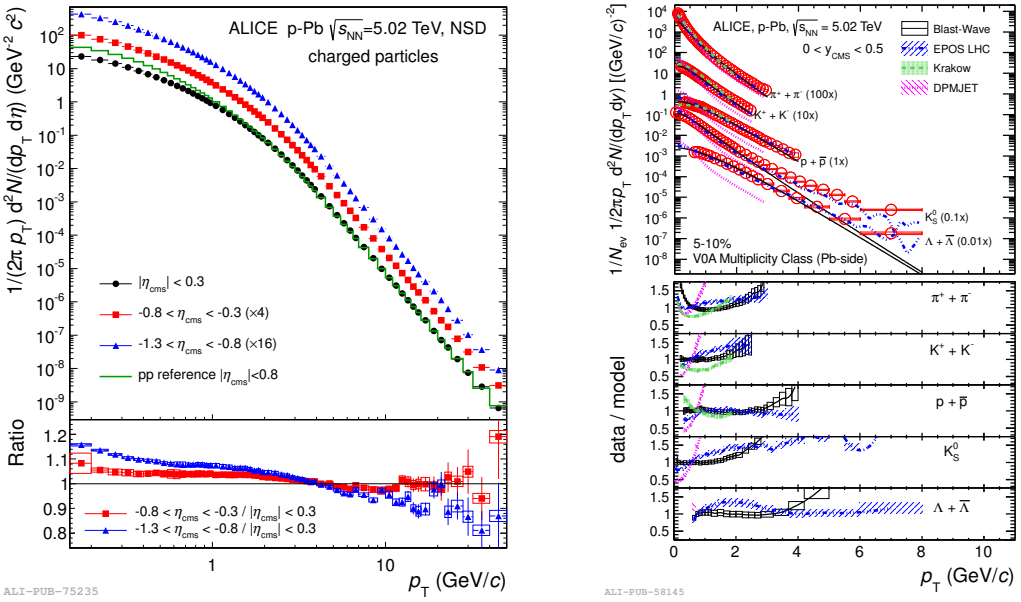

Figure 1: Left: p_{T} spectra measured in p–Pb collisions in three pseudorapidity ranges [4]. The pp reference spectrum is also shown [6]. Right: p_{T} spectra of identified hadrons measured in high multiplicity p–Pb collisions [9] compared to hydrodynamic models (see text for details).

3 Results

Figure 1 (left) shows the p_{T} spectra measured for charged particles in p–Pb collisions in three pseudorapidity ranges [4]. The constructed pp reference [6] at central rapidity is also shown. In the bottom panel, the ratios of the p_{T} spectra measured in two forward pseudorapidity regions with respect to central-pseudorapidity production are shown, indicating that the spectral shape is changing (spectra become softer) with increasing psedorapidity. The effect is particularly visible for p_{T} spectra measured in the most forward pseudorapidity interval, $-1.3 < \eta_{\mathrm{cms}} < -0.8$.

Figure 1 (right) shows the p_{T} spectra of identified hadrons measured in high multiplicity p–Pb collisions [9] in comparison to hydrodynamic (Blast-Wave [10], Kraków [11], EPOS LHC [12]) and QCD-inspired (DPMJET [13]) models. The hydrodynamic models describe data reasonably well for $p_{\mathrm{T}} < 2$ GeV/c while DPMJET fails in describing data for all p_{T}. This might indicate that collective phenomena (e.g. flow etc.) are present in high multiplicity p–Pb collisions.

Figure 2 shows p/π and $\Lambda/\mathrm{K}^0_{\mathrm{s}}$ ratios measured in low and high multiplicity p–Pb collisions [9] in comparison to measurements in peripheral and central Pb–Pb collisions [14]. Similar to Pb–Pb, the baryon-to-meson ratio increases with event multiplicity, however, the increase is smaller compared to Pb–Pb.

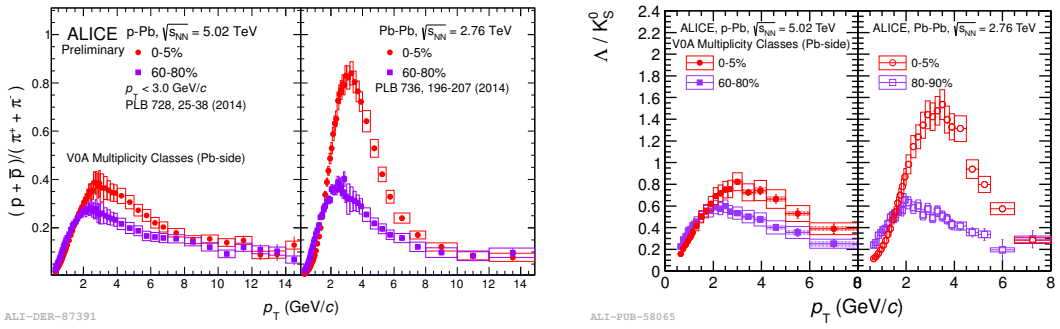

Figure 2: p/π (left) and $\Lambda/\mathrm{K}^0_{\mathrm{s}}$ (right) ratios measured in low (60-80%) and high (0-5%) multiplicity p–Pb collisions [9] in comparison to measurements in peripheral (60-80%) and central (0-5%) Pb–Pb collisions [14].

Figure 3 (left) shows the nuclear modification factor R_{pPb} measured in minimum bias p–Pb collisions [4] in comparison to nuclear modification factors measured in central Pb–Pb collisions ([4] and references therein). The results, showing a strong suppression in central Pb–Pb collisions and almost no suppression in p–Pb, indicate that the effect observed in Pb–Pb collisions is related to interaction with the matter in the final state. Figure 3 (right) shows R_{pPb} for identified hadrons measured in minimum bias p–Pb collisions. At low $p_{\mathrm{T}} < 2$ GeV/c, similar depletion is observed for all particle species. At intermediate $2 < p_{\mathrm{T}} < 7$ GeV/c, enhanced production of protons and Ξ is observed with the characteristic mass dependence, which might be related to collective phenomena (e.g. flow etc.). At high $p_{\mathrm{T}} > 7$ GeV/c, no modification of hadron production is observed, $R_{\mathrm{pPb}} \approx 1$.

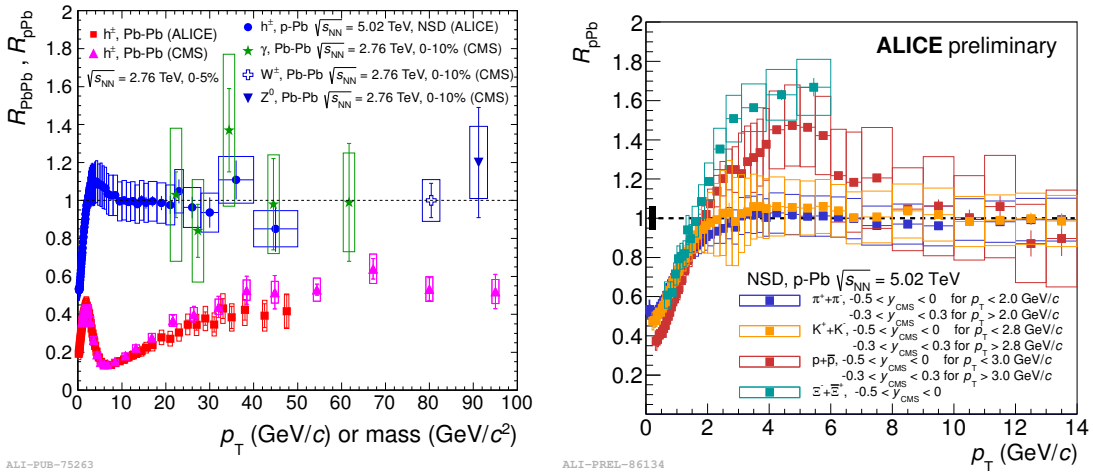

Figure 3: Left: Nuclear modification factors measured as a function of p_{T} in minimum-bias p–Pb collisions [4] and central Pb–Pb collisions ([4] and references therein). Right: R_{pPb} for identified hadrons measured in minimum-bias p–Pb collisions.

In summary, p_{T} spectra measured for light-flavor hadrons in minimum-bias p–Pb collisions, when compared to the reference pp spectrum, show a depletion at low p_{T} (similar for all hadron species), mass dependent enhancement at intermediate p_{T}, and no modification at high p_{T}. The study of the p_{T} spectra measured as a function of multiplicity in p–Pb collisions suggests that collective-like phenomena might develop in high multiplicity p–Pb events.

References

[1] J.W. Cronin *et al.*, Phys. Rev. **D11** 3105 (1975).

[2] C. Salgado *et al.*, J. Phys. **G39** 015010 (2012).

[3] B. Muller, J. Schukraft, and B. Wyslouch, Annu. Rev. Nucl. Part. Sci. **62** 361 (2012).

[4] ALICE Collaboration, Eur. Phys. J. **C74** 3054 (2014).

[5] M. Miller *et al.*, Annu. Rev. Nucl. Part. Sci. **57** 205 (2007).

[6] ALICE Collaboration, Eur. Phys. J. **C73** 2662 (2013).

[7] ALICE Collaboration, JINST **3** S08002 (2008).

[8] ALICE Collaboration, Int. J. Mod. Phys. **A29** 1430044 (2014).

[9] ALICE Collaboration, Phys. Lett. **B728** 25 (2014).

[10] P. Huovinen *et al.*, Phys. Lett. **B503** 58 (2001).

[11] P. Bozek, Phys. Rev. **C85** 014911 (2012).

[12] T. Pierog *et al.*, hep-ph/1306.0121 (2013).

[13] S. Roesler, R. Engel, and J. Ranft, hep-ph/0012252 (2000).

[14] ALICE Collaboration, Phys. Lett. **B736** 196 (2014).

Light (Hyper)Nuclei production at the LHC with ALICE

Ramona Lea[1] for the ALICE Collaboration

[1]Dipartimento di Fisica dell'Universita and Sezione INFN, Trieste, Italy

DOI: http://dx.doi.org/10.3204/DESY-PROC-2014-04/77

The excellent particle identification and momentum measurement capabilities of the ALICE detector allows for the identification of dueterons and ^{3}He and and their corresponding anti-nuclei. This is achieved via the measurement of their specific energy loss in the Time Projection Chamber and the velocity measurement by the Time Of Flight detector. Moreover, thanks to the Inner Tracking System capability to separate primary from secondary vertices, it is possible to identify (anti-)hypertritons exploiting their mesonic weak decay ($^3_\Lambda$H $\rightarrow$ ^{3}He + π^-). Results on the production yields of light nuclei and anti-nuclei in Pb–Pb and p–Pb are presented, together with the measurement of hypertriton production rates in Pb–Pb and upper limits for the production of lighter exotica candidates. The experimental results are compared with the predictions of both thermal (statistical) and coalescence models.

1 Introduction

High energy heavy-ion collisions offer the opportunity to measure light anti-nuclei and search for hypermatter. In fact, although the measurement is challenging as the production probability decreases with increasing mass, the data collected at the LHC allows for the measurement of such particles. Thanks to its unique performance for particle identification, the ALICE detector [1, 2] allows for the identification and the measurements of (anti-)nuclei (deuterons and ^{3}He and their corresponding anti-nuclei) and (anti-)hypertriton and gives the opportunity to search for predicted particles such as the H-Dibaryon and the Λn bound state. Usually two different approaches are used to describe the production yield of these particles: they can be formed at the kinetic freeze-out via the coalescence of nucleons (hyperons) close in phase-space, or their can born in thermal equilibrium [3, 4, 5]. In the thermal models the chemical freeze-out temperature $T_{\rm chem}$ is the key parameter at LHC energies: the production yields depend exponentially on this temperature and on the mass of the particle m ($\mathrm{d}N/\mathrm{d}y \sim \exp(-m/T_{\rm chem})$).
For the present analysis, the data of Pb–Pb collisions at $\sqrt{s_{\rm NN}}$ = 2.76 TeV recorded in two periods during the years 2010 and 2011 and the data of p–Pb collisions at $\sqrt{s_{\rm NN}}$ = 5.02 TeV recorded at the beginning of 2013 were used.

2 (Anti-)Nuclei

Nuclei and anti-nuclei are identified over a wide range of momentum using the combined information of the specific energy loss ($\mathrm{d}E/\mathrm{d}x$) measurement in the Time Projection Chamber (TPC) [6], the velocity measured by the Time Of Flight detector (TOF) [7] and the measurement of the Cherenkov radiation angle measured with the High Momentum Particle Identification Detector (HMPID) [7]. The measured energy loss signal in the TPC of a track is required to be within a 3σ region around the expected value for a given mass hypothesis: with this method it possible to provide a pure sample of ^{3}He in the (2-8) GeV/c transverse momentum interval, while it is limited to 1.4 GeV/c for deuterons. In order to extend deuteron identification, the measured time-of-flight and Cherenkov radiation allows for deuteron identification up to 8 GeV/c. The measured raw spectra were corrected for efficiency and acceptance. Figure 1 shows the deuteron transverse momentum p_{T} spectra in different centrality (multiplicity) classes in Pb–Pb (left panel) and p–Pb (right panel) collisions. In both colliding systems, a hardening of the spectrum with increasing centrality is observed as expected in a hydrodynamic description of the fireball as a radially expanding source. In order to extrapolate the yield in the regions where it is not measured, the spectra were fitted with a Blast-Wave function [8].

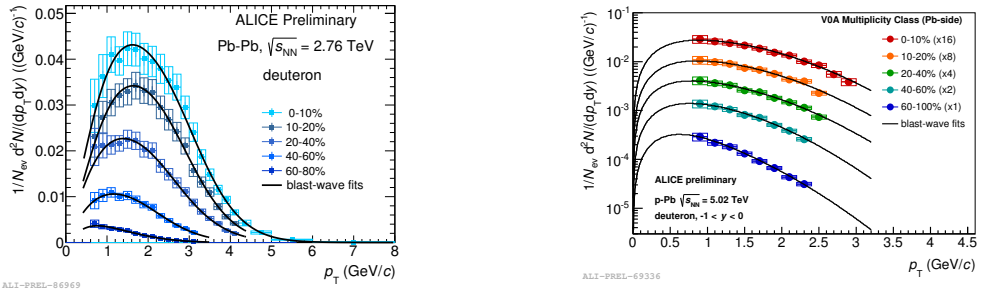

Figure 1: Transverse momentum spectra in different centrality (multiplicity) classes for deuterons in Pb–Pb (left) and in p–Pb (right) collisions at LHC energies.

Figure 2 shows the coalescence parameter $\mathrm{B}_2 = E_{\mathrm{deuteron}} \frac{d^3N_{\mathrm{deuteron}}}{dp^3_{\mathrm{deuteron}}} / \left(E_{\mathrm{proton}} \frac{d^3N_{\mathrm{proton}}}{dp^3_{\mathrm{proton}}} \right)^2$, for Pb–Pb (left) and p–Pb (right) collisions. In a simple coalescence model the B_2 parameter is independent of p_{T}: this is observed in peripheral Pb–Pb and p–Pb. More sophisticated models show that B_2 scales like the HBT radii [9]: the decrease with centrality in Pb–Pb can be explained as an increase in the source volume and the increasing with p_{T} in central Pb–Pb reflects the $\mathrm{k_T}$-dependence of the homogeneity volume in HBT.

3 (Anti-)Hypertriton

The hypertriton $^3_\Lambda$H is the lightest known hypernucleus and is formed by a proton, a neutron and a Λ. Its mass is 2.991 $\pm$ 0.002 GeV/c^2 and it has a lifetime comparable with the free Λ one (few hundreds of picoseconds) [10]. The ($^3_\Lambda\overline{\mathrm{H}}$) $^3_\Lambda$H production yield was measured in Pb–Pb by exploiting its weak mesonic decay ($^3_\Lambda\mathrm{H} \rightarrow {}^3\mathrm{He} + \pi^-$) (($^3_\Lambda\overline{\mathrm{H}} \rightarrow {}^3\overline{\mathrm{He}} + \pi^+$)), via the topological identification of secondary vertices and the analysis of the invariant mass distributions of the

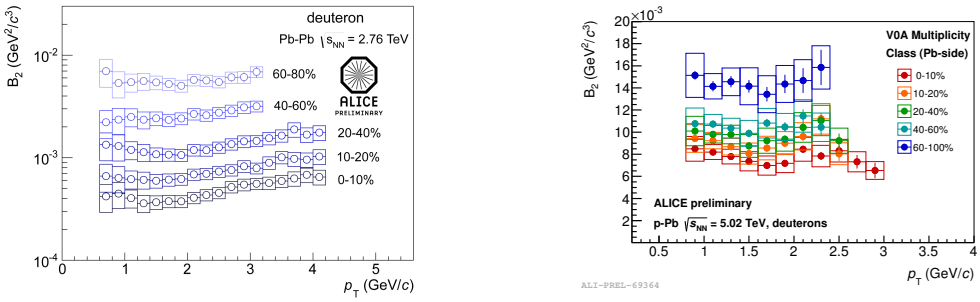

Figure 2: Coalescence parameter B_2 as a function of p_T for deuterons in in Pb–Pb (left) and p–Pb (right) collisions.

decay daughters. The measured $^3_\Lambda$H production yield $\mathrm{d}N/\mathrm{d}y$ is compared to different models as a function of the branching ratio ($B.R.$) in Figure 3 (left panel). At the theoretical value ($B.R.$ = 25 %) [11], the model which describes better the obtained value is the equilibrium thermal model [3] with a temperature T_{chem} =156 MeV. This temperature is the one which best describes all the particle yields measured at LHC.

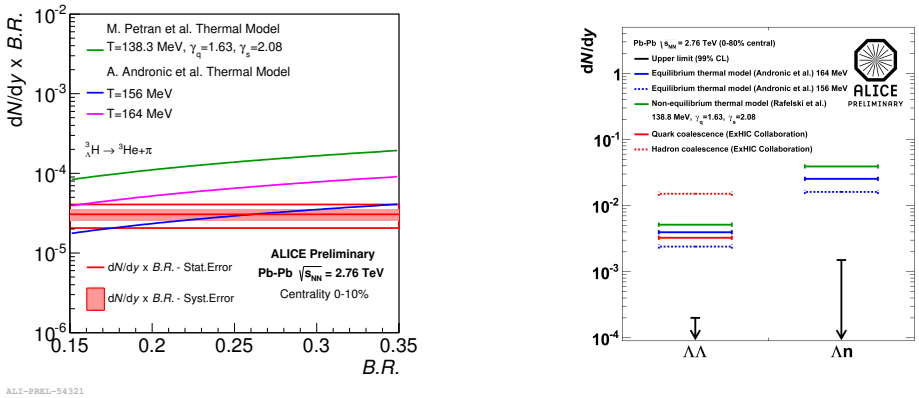

Figure 3: Left: $\mathrm{d}N/\mathrm{d}y$ comparison to different models for the hypertriton measurement. Right: upper limits for H-Dibaryon and Λn $\mathrm{d}N/\mathrm{d}y$ compared with several theoretical models.

4 Exotic Bound State

The H-Dibaryon is a hypothetical *uuddss* bound state (ΛΛ) first predicted by Jaffe in a bag model calculation [12]. Recent lattice calculations [13, 14, 15, 16] suggest that H-Dibaryon should be a bound state, with a binding energy of around 1 MeV/c^2. The same binding energy is also favored from the observed double-Λ hypernuclei, which gives the current constraints on the ΛΛ interaction (for a recent review see [17] and the references therein). In this analysis the decay of the H-Dibaryon into Λpπ was investigated. In the measured invariant mass distribution

no evidence of a signal for the H-Dibaryon was found [18], and an upper limit of dN/dy 2×10^{-4} (99 %CL) was obtained. The HypHI collaboration at GSI found evidence for a possible Λn bound state with a mass of 2.054 GeV/c^2, decaying into a deuteron and a pion [19]. The invariant mass distribution of deuterons and pions from displaced vertices, where a possible Λn bound state is expected to be visible, was studied but no signal was observed [18]. This led to an upper limit of dN/dy 1.5×10^3 (99 %CL). The extracted limits are a factor of 10 lower than the thermal model predictions used to estimate the expected signal while this successfully describes the measured yields of deuterons, ^{3}He and $^3_\Lambda$H nuclei. Figure3 (right) shows the upper limits on the dN/dy of H-Dibaryon and Λn and are compared with several theoretical models.

5 Summary and Conclusions

The $p_{\rm T}$ spectra of deuteron and ^{3}He (not shown here) were measured in p–Pb and Pb–Pb collisions: a hardening of the spectra with increasing centrality is observed in both the colliding systems. The coalescence parameter B_2 was also determined; it was found to be independent from $p_{\rm T}$ in p–Pb and peripheral Pb–Pb collisions, while it increases with $p_{\rm T}$ in central Pb–Pb collisions. A decrease with centrality is also observed in Pb–Pb collisions. The production yield of deuterons, ^{3}He and $^3_\Lambda$H nuclei is in agreement with the current best thermal fit from equilibrium thermal model with a $T_{\rm chem} = 156$ MeV. On the other hand, the upper limits for exotica (H-Dibaryon and Λn) are lower than the thermal model expectation by at least an order of magnitude, therefore the existence of such states with the assumed decay branching fraction, mass and lifetime is questionable.

Acknowledgments

The author acknowledges financial support from Consorzio per la Fisica, Trieste.

References

[1] K. Aamodt *et al.* (ALICE collaboration), J. Phys. G: Nucl. Part. Phys. **32** 1295 (2006)
[2] K. Aamodt *et al.* (ALICE collaboration), JINST **3** S08002 (2008)
[3] A. Andronic *et al.*, Phys. Lett. **B697** 203 (2011)
[4] J. Cleymans *et al.*, Phys. Rev. **C84** 054916 (2011)
[5] M. Petráň *et al.*, CERN-PH-TH/2012-262, arXiv:1303.2098v2 [hep-ph] (2013)
[6] J. Alme *et al.*, Nucl. Instrum. Meth. **A622** 316-367 (2010)
[7] B. I. Abelev *et al.*, (ALICE Collaboration), arXiv:1402.4476 [nucl-ex]
[8] E. Schnedermann, J. Sollfrank and U. Heinz, Phys. Rev. C **48**, (1993) 2462
[9] R. Scheibl, U. Heinz, Phys. Rev. **C59** 1585 (1999)
[10] B. I. Abelev *et al.* (STAR Collaboration) 2010 *Science* **328** 58
[11] W. Gloeckle *et al.*, Nucl. Phys. **A639** 297 (1998)
[12] R. Jaffe, Phys. Rev. Lett. **38** 195 and erratum ibid 1977 **38** 617 (1977)
[13] S. R. Beane *et al.* (NPLQCD Collaboration), Phys. Rev. Lett. **106** 162001 (2011)
[14] T. Inoue *et al.* (HAL QCD Collaboration), Phys. Rev. Lett. **106** 162002 (2011)
[15] P. E. Shanahan, A. W. Thomas, R. D. Young, Phys. Rev. Lett. **107** 092004 (2011)

[16] J. Heidenbauer, U. G. Meiner, Phys. Lett. **B706** 100 (2011)
[17] E. Botta, T Bressani, G. Garbarino, Eur. Phys. J. **A48** 41 (2012)
[18] B. Dönigus (for the ALICE Collaboration), Nucl. Phys. **A904905** (0) 547c (2013)
[19] C. Rappold *et al.* (HypHI collaboration), Phys. Rev. **C88**, 041001(R) (2013)

The QCD critical end point driven by an external magnetic field in asymmetric quark matter

Pedro Costa[1], *Márcio Ferreira*[1], *Constança Providência*[1], *Hubert Hansen*[2], *Débora P. Menezes*[2]

[1]Centro de Física Computacional, Department of Physics, University of Coimbra, P-3004-516 Coimbra, Portugal
[2]IPNL, Université de Lyon/Université Lyon 1, CNRS/IN2P3, 4 rue E.Fermi, F-69622 Villeurbanne Cedex, France
[2]Departamento de Física, CFM, Universidade Federal de Santa Catarina, Florianópolis, SC, CP 476, CEP 88.040-900, Brazil

DOI: http://dx.doi.org/10.3204/DESY-PROC-2014-04/75

The effect of the isospin/charge asymmetry and an external magnetic field in the location of the critical end point (CEP) in the QCD phase diagram is investigated. By using the 2+1 flavor Nambu–Jona-Lasinio model with Polyakov loop (PNJL), it is shown that the isospin asymmetry shifts the CEP to larger baryonic chemical potentials and smaller temperatures, and in the presence of a large enough isospin asymmetry the CEP disappears. Nevertheless, a sufficiently high external magnetic field can drive the system into a first order phase transition again.

The QCD phase diagram under extreme conditions of density, temperature and magnetic field is the subject of intense studies [1]. Understanding the effect of an external magnetic field on the structure of the QCD phase diagram is very important: these extremely strong magnetic fields are expected to affect the measurements in heavy ion collisions (HIC) at very high energies, to influence the behavior of the first stages of the Universe and are also relevant to the physics of compact astrophysical objects like magnetars.

On the other hand, the effect of the isospin/charge asymmetry in the QCD phase diagram is also very interesting due to its role on the location of the critical end point (CEP): it was shown that for a sufficiently asymmetric system the CEP is not present [2, 3].

In the present work we describe quark matter subject to strong magnetic fields within the 2+1 PNJL model. The PNJL Lagrangian with explicit chiral symmetry breaking where the quarks couple to a (spatially constant) temporal background gauge field, represented in terms of the Polyakov loop and in the presence of an external magnetic field is given by [4]:

$$\mathcal{L} = \bar{q}\left[i\gamma_\mu D^\mu - \hat{m}_f\right] q \;+\; G\sum_{a=0}^{8}\left[(\bar{q}\lambda_a q)^2 + (\bar{q}i\gamma_5\lambda_a q)^2\right]$$
$$-K\left\{\det\left[\bar{q}(1+\gamma_5)q\right] + \det\left[\bar{q}(1-\gamma_5)q\right]\right\} + \mathcal{U}\left(\Phi,\bar{\Phi};T\right) - \frac{1}{4}F_{\mu\nu}F^{\mu\nu}, \qquad (1)$$

where the quark sector is described by the SU(3) version of the Nambu–Jona-Lasinio model which includes the scalar-pseudoscalar (chiral invariant) and the t'Hooft six fermion interactions that breaks the axial $U_A(1)$ symmetry. The $q = (u, d, s)^T$ represents a quark field with three

flavors, $\hat{m}_f = \mathrm{diag}_f(m_u^0, m_d^0, m_s^0)$ is the corresponding (current) mass matrix, $\lambda_0 = \sqrt{2/3}I$ where I is the unit matrix in the three flavor space, and $0 < \lambda_a \leq 8$ denote the Gell-Mann matrices. The coupling between the magnetic field B and quarks, and between the effective gluon field and quarks is implemented *via* the covariant derivative $D^\mu = \partial^\mu - iq_f A^\mu_{EM} - iA^\mu$ where q_f represents the quark electric charge ($q_d = q_s = -q_u/2 = -e/3$), A^{EM}_μ and $F_{\mu\nu} = \partial_\mu A^{EM}_\nu - \partial_\nu A^{EM}_\mu$ are used to account for the external magnetic field and $A^\mu(x) = g_{strong}\mathcal{A}^\mu_a(x)\frac{\lambda_a}{2}$ where $\mathcal{A}^\mu_a$ is the $\mathrm{SU}_c(3)$ gauge field. We consider a static and constant magnetic field in the z direction, $A^{EM}_\mu = \delta_{\mu 2}x_1 B$. In the Polyakov gauge and at finite temperature the spatial components of the gluon field are neglected: $A^\mu = \delta^\mu_0 A^0 = -i\delta^\mu_4 A^4$. The trace of the Polyakov line defined by $\Phi = \frac{1}{N_c}\langle\langle \mathcal{P}\exp i\int_0^\beta d\tau\, A_4(\vec{x},\tau)\,\rangle\rangle_\beta$ is the Polyakov loop which is the *exact* order parameter of the $\mathbb{Z}_3$ symmetric/broken phase transition in pure gauge.

To describe the pure gauge sector an effective potential $\mathcal{U}\left(\Phi, \bar{\Phi}; T\right)$ is chosen in order to reproduce the results obtained in lattice calculations [5]:

$$\frac{\mathcal{U}\left(\Phi, \bar{\Phi}; T\right)}{T^4} = -\frac{a(T)}{2}\bar{\Phi}\Phi + b(T)\ln\left[1 - 6\bar{\Phi}\Phi + 4(\bar{\Phi}^3 + \Phi^3) - 3(\bar{\Phi}\Phi)^2\right], \tag{2}$$

where $a(T) = a_0 + a_1\left(\frac{T_0}{T}\right) + a_2\left(\frac{T_0}{T}\right)^2$, $b(T) = b_3\left(\frac{T_0}{T}\right)^3$. The standard choice of the parameters for the effective potential $\mathcal{U}$ is $a_0 = 3.51$, $a_1 = -2.47$, $a_2 = 15.2$, and $b_3 = -1.75$. T_0 is the critical temperature for the deconfinement phase transition within a pure gauge approach: it was fixed to a constant $T_0 = 270$ MeV, according to lattice findings. The parameters of the model are $\Lambda = 602.3\,\mathrm{MeV}$, $m_u^0 = m_d^0 = 5.5\,\mathrm{MeV}$, $m_s^0 = 140.7\,\mathrm{MeV}$, $G\Lambda^2 = 1.385$ and $K\Lambda^5 = 12.36$.

The thermodynamical potential for the three flavor quark sector, Ω, in the mean field approximation is written as

$$\Omega(T,\, B,\, \mu_f) = 2G\sum_{f=u,\,d,\,s}\langle\bar{q}_f q_f\rangle^2 - 4K\,\langle\bar{q}_u q_u\rangle\langle\bar{q}_d q_d\rangle\langle\bar{q}_s q_s\rangle + \left(\Omega_f^{vac} + \Omega_f^{mag} + \Omega_f^{med}\right), \tag{3}$$

where the vacuum Ω_f^{vac}, the magnetic Ω_f^{mag}, the medium contributions Ω_f^{med} and the quark condensates $\langle\bar{q}_f q_f\rangle$ have been evaluated with great detail in [6, 7]. The mean field equations are obtained by minimizing the thermodynamical potential (3) with respect to the order parameters $\langle\bar{q}_f q_f\rangle$, Φ and $\bar{\Phi}$.

We start the discussion of our results by the location of the CEP when no external magnetic field is present.

It has been shown that the location of the CEP depends on the isospin [8]: as an example, in $\beta-$equilibrium matter the CEP occurs at larger baryonic chemical potentials and smaller temperatures [8]. Indeed, we are interested in d-quark rich matter as it occurs in neutron stars and in HIC: isospin asymmetry in neutron matter has $\mu_d \sim 1.2\mu_u$, and presently the attained isospin asymmetry in HIC corresponds to $\mu_u < \mu_d < 1.1\mu_u$. In the present work the effect of isospin on the CEP is studied: we increase systematically μ_d with respect to μ_u taking the s-quark chemical potential equal to zero ($\mu_s = 0$ leads to all CEP's occur at $\rho_s = 0$).

The results for the CEP in the previous conditions are presented in Fig. 1. For reference we also show the red full point that corresponds to the CEP with $\mu_u = \mu_d = \mu_s$. When the isospin asymmetry is increased the CEP moves to smaller temperatures and larger baryonic chemical potentials.

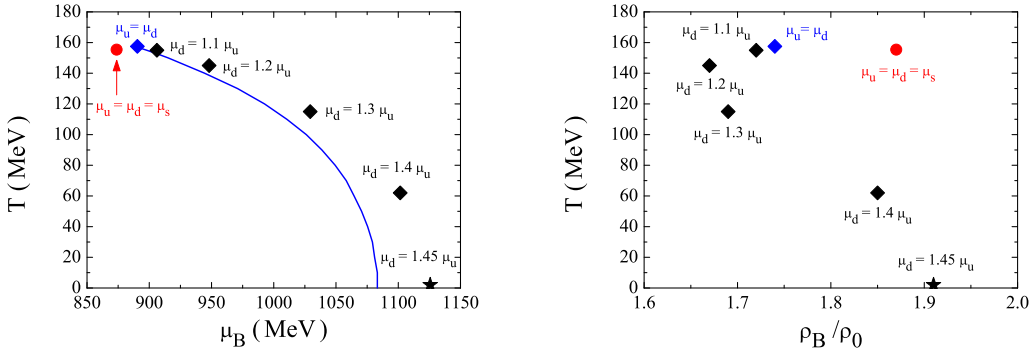

Figure 1: The influence of the isospin in the location of the CEP within the PNJL model: the full line is the first order phase transition line for zero isospin matter ($\mu_u = \mu_d$, $\mu_s = 0$). The chemical potential for the strange quark is always taken equal to zero, except the for the red point ($\mu_u = \mu_d = \mu_s$) which is given for reference. When $\mu_d > 1.45\mu_u$ the CEP doesn't exist anymore.

When the asymmetry is large enough, $\mu_d = 1.45\mu_u$, the CEP disappears (this CEP is represented in Fig. 1 by a star at $T = 0$). This scenario leads to $|\mu_u - \mu_d| = |\mu_I| = |\mu_Q| = 130$ MeV, below the pion mass and, accordingly, no pion condensation occurs under these conditions.

The CEP for (T, ρ_B) plane is shown in the right panel of Fig. 1. When $\mu_u < \mu_d < 1.2\mu_u$ the baryonic density of the CEP decreases with asymmetry but for $\mu_d \gtrsim 1.2\mu_u$ the opposite occurs and at the threshold ($\mu_d = 1.45\mu_u$) $\rho_B \sim 1.91\rho_0$.

Now, we investigate how a static external magnetic field will influence the localization of the CEPs previously calculated. The results are plotted in Fig. 2. In the left panel of Fig. 2 the red dots correspond to symmetric matter ($\mu_u = \mu_d = \mu_s$) and reproduce qualitatively the results previously obtained within the NJL model [9] being the trend qualitatively similar: the increasing of the intensity of the magnetic field leads to an increase of the CEP's temperature and to a decrease of the CEP's baryonic chemical potential until the critical value $eB \sim 0.4$ GeV^2; for stronger magnetic fields, both T and μ_B increase. In the right panel of Fig. 2 the CEP is given in a T vs. ρ_B plane. The results show that when eB increases from 0 to 1 GeV^2 the baryonic density at the CEP increases from $2\rho_0$ to $14\rho_0$.

Taking the isospin symmetric matter scenario $\mu_u = \mu_d$ and $\mu_s = 0$, the effect of the magnetic field on the CEP is very similar to the previous one (see blue diamonds in Fig. 2): the CEP's temperature is only slightly larger and the CEP's baryonic density is slightly smaller.

Also interesting is the case that occurs for the very asymmetric matter scenario: a first order phase transition driven by the magnetic field takes place if $\mu_d \gtrsim 1.45\mu_u$. Taking the threshold value $\mu_d = 1.45\mu_u$ it is seen that for eB <0.1 GeV^2 two CEPs may appear. Indeed, for sufficiently small values of eB the T^{CEP} is small and the Landau level effects are visible.

A magnetic field affects in a different way u and d quarks due to their different electric charge. A consequence is the possible appearance of two or more CEPs for a given magnetic field intensity. Two critical end points occur at different values of T and μ_B for the same magnetic field intensity for fields $0.03 \lesssim eB \lesssim 0.07$ GeV^2. Above 0.07 GeV^2 only one CEP remains. For stronger fields we get $T^{CEP} > 100$ MeV: Landau level effects are completely

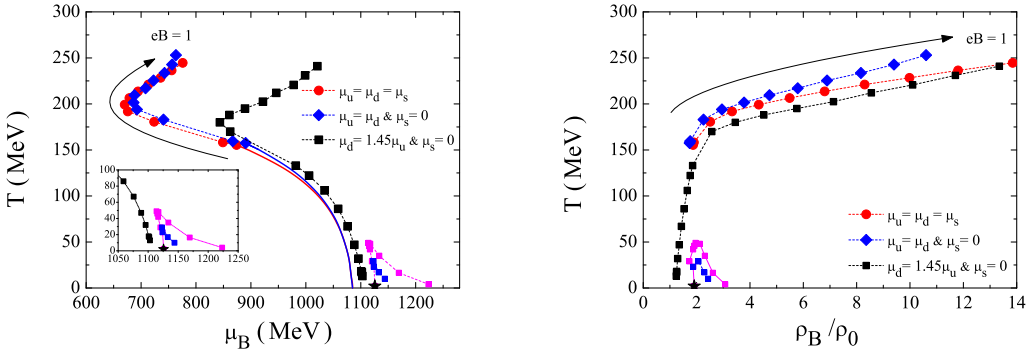

Figure 2: Effect of an external magnetic field on the location of the CEP: T^{CEP} vs μ_B^{CEP} (left panel) and T^{CEP} vs ρ_B^{CEP} (right panel). The full lines correspond to the first order transitions at $eB = 0$. Three scenarios are shown: $\mu_u = \mu_d = \mu_s$ (red dots), $\mu_u = \mu_d$; $\mu_s = 0$ (blue diamonds) and $\mu_d = 1.45\mu_u$, $\mu_s = 0$ (black squares) corresponding to the threshold isospin asymmetry above which no CEP occurs. In the last scenario for strong enough magnetic fields and low temperatures two or more CEP exist at different temperatures for a given magnetic field intensity (pink and blue squares).

washed out at these temperatures.

Acknowledgments

This work was supported by C.F.C., by Project No. CERN/FP/123620/2011 developed under the initiative QREN financed by the UE/FEDER through the program COMPETE "Programa Operacional Factores de Competitividade" by Grant No. SFRH/BD/51717/2011, by CNPq/Brazil and by FAPESC/Brazil.

References

[1] M. Ferreira, P. Costa and C. Providência, Phys. Rev. D **89**, 036006 (2014); D. P. Menezes, M. B. Pinto, L. B. Castro, P. Costa and C. Providência, Phys. Rev. C **89**, 055207 (2014); M. Ferreira, P. Costa, O. Loureno, T. Frederico and C. Providência, Phys. Rev. D **89**, 116011 (2014); M. Ferreira, P. Costa and C. Providência, Phys. Rev. D **90**, 016012 (2014).

[2] H. Ueda, T. Z. Nakano, A. Ohnishi, M. Ruggieri, and K. Sumiyoshi, Phys. Rev. D **88**, 074006 (2013).

[3] H. Abuki, Phys. Rev. D **87**, 094006 (2013).

[4] K. Fukushima, Phys. Lett. **B591**, 277 (2004); C. Ratti, M. A. Thaler, and W. Weise, Phys. Rev. D **73**, 014019 (2006).

[5] S. Roessner, C. Ratti and W. Weise, Phys. Rev. D **75**, 034007 (2007).

[6] D.P. Menezes, M.B. Pinto, S.S. Avancini, A. P. Martínez, and C. Providência, Phys. Rev. C **79**, 035807 (2009); D.P. Menezes, M.B. Pinto, S.S. Avancini and C. Providência, Phys. Rev. C **80**, 065805 (2009).

[7] S.S. Avancini, D.P. Menezes and C. Providência, Phys. Rev. C **83**, 065805 (2011).

[8] P. Costa, M. Ferreira, H. Hansen, D. P. Menezes and C. Providência, Phys. Rev. D **89**, 056013 (2014).

[9] Sidney S. Avancini, Débora P. Menezes, Marcus B. Pinto, and Constança Providência, Phys. Rev. D **85**, 091901 (2012).

Anisotropic flow from hard partons in ultra-relativistic nuclear collisions

Boris Tomášik[1,2], *Martin Schulc*[2]

[1]Univerzita Mateja Bela, Tajovského 40, 97401 Banská Bystrica, Slovakia
[2]Czech Technical University in Prague, FNSPE, Břehová 7, 11519 Prague 1, Czech Republic

DOI: http://dx.doi.org/10.3204/DESY-PROC-2014-04/96

Anisotropies of hadronic distribution in nuclear collisions are used for determination of properties of the nuclear matter. At the LHC it is important to account for the contribution to the flow due to momentum transferred from hard partons to the quark-gluon plasma.

In ultrarelativistic nuclear collisions, hadron momentum distributions are azimuthally anisotropic and parametrised with the help of Fourier expansion with amplitudes of individual modes usually denoted as v_n's. If spectra are summed over a large number of events, symmetry constraints dictate all odd amplitudes to vanish. In individual events, however, these constraints are not realised, because the event shapes fluctuate.

In general, the mechanism behind the modification of hadronic spectra is the blue-shift. Transverse expansion of the fireball enhances production of hadrons with higher p_t. If the normalisation and the slope of p_t spectrum depend on azimuthal angle, this indicates different transverse expansion velocity in different directions. Expansion is caused by pressure gradients in the initial state. We thus have a link between the initial state of the fireball and the observed hadronic spectra. (In fact, here we propose a mechanism which can break this link.)

The link is described by relativistic hydrodynamics. The scheme is based on fundamental conservation laws complemented by the equation of state. In non-ideal hydrodynamics it also involves transport coefficients, e.g. shear and bulk viscosity. The goal is to tune them so that hydrodynamic modelling yields results in accord with the observations.

Unfortunately, there are some problems. The initial conditions are unknown. They are set by energy depositions in early partonic interactions. Various models predict energy and momentum density profiles with different levels of spikiness. One can get the same result on flow anisotropies with different initial conditions if one re-tunes the transport coefficients [1]. This hinders the determination of viscosities from comparisons to data. The extracted values would depend on the assumptions that are made about *unknown* initial conditions.

This problem might be settled with the help of flow anisotropy fluctuations [2]. Simulations indicate that the values of v_n's in individual events follow to large extent the corresponding spatial anisotropies of the initial state [3, 4]. The departure from this proportionality has also been studied [4, 5]. The mechanism proposed in the present paper would break this proportionality since it produces flow anisotropy *during* the hydrodynamic evolution *without* the need for any anisotropy in the initial state.

We point out [6] that in nuclear collisions at LHC energies there is more than one dijet pair per event. (We might have to lower the threshold for what we count as hard parton; here we use $p_t > 3$ GeV/c.) They deposit most—if not all—of their energy and momentum into

the plasma and are fully quenched. Since momentum must be conserved, the wakes behind the partons must stream and carry it. Such streams would generate anisotropy of collective expansion in every individual event. This leads to elliptic anisotropy even after a summation over large number of events. Indeed, isotropically produced jets generate elliptic anisotropy. The important detail is the possibility that the induced streams can interact and merge.

Suppose that two dijet pairs are produced in a non-central collision. The elliptic flow due to spatial deformation is directed parallel to the reaction plane. If both pairs are aligned with this plane, then all streams contribute to positive v_2, see Fig. 1 (left). On the other hand, if the jets are oriented under large angle with respect to the reaction plane, then the two streams directed inwards can meet, merge into one, and continue in a direction given by the sum of their two momenta. They do not contribute to the collective flow in their original direction. The chance of merger is higher in the latter case than in the former one since there the jets pass each other within a narrower path. Perpendicularly to the reaction plane the fireball is wider so the streams parallel to the reaction plane can well proceed without bothering each other. In addition to this mechanism, Fig. 1 (right) also suggests that contribution to triangular flow is created by the merger of two streams.

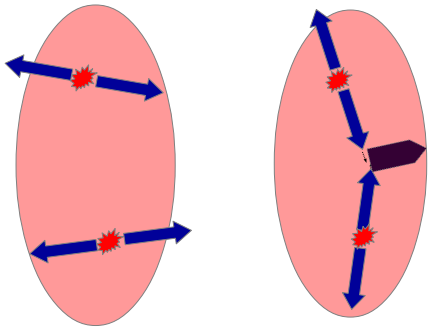

Figure 1: Transverse cross-section through the fireball with two dijet pairs produced. Reaction plane is horizontal. Left: two dijets both emitted in the direction of the reaction plane both contribute positively to the elliptic flow, which is dominant in the same direction. Right: if hard partons are produced off the reaction plane, some of their streams can come together and merge.

This picture is supported by our simulations. We developed 3+1D ideal hydrodynamic simulation code [7, 8] using the SHASTA scheme to handle shocks. We include force term J^μ

$$\partial_\mu T^{\mu\nu} = J^\nu \tag{1}$$

which represents the dragging of the fluid by hard partons [9]

$$J^\nu = -\sum_i \frac{1}{(2\,\pi\,\sigma_i^2)^{\frac{3}{2}}}\,\exp\left(-\frac{(\vec{x}-\vec{x}_{\mathrm{jet},i})^2}{2\,\sigma_i^2}\right)\left(\frac{dE_i}{dt},\frac{d\vec{P}_i}{dt}\right) \tag{2}$$

where the sum goes through all hard partons in the system and the width σ_i was set to 0.3.

We first checked that indeed the streams are induced behind the partons and that they flow even after the partons are fully quenched (as was also observed in [9]). In a simulation with static medium we could see that the streams merge when they meet. Then, until their energy is spread over a larger volume, they continue flowing in common direction [7].

The mechanism has been included into more realistic simulation of nuclear collisions. In these studies it was not our aim to reach the complete description of data. We rather wanted to gain realistic estimate of the influence of our mechanism on the observed anisotropies. Therefore, we started our simulations always with smooth initial conditions calculated within the optical Glauber model. Any fluctuation on top of non-zero event-averaged flow harmonics is then

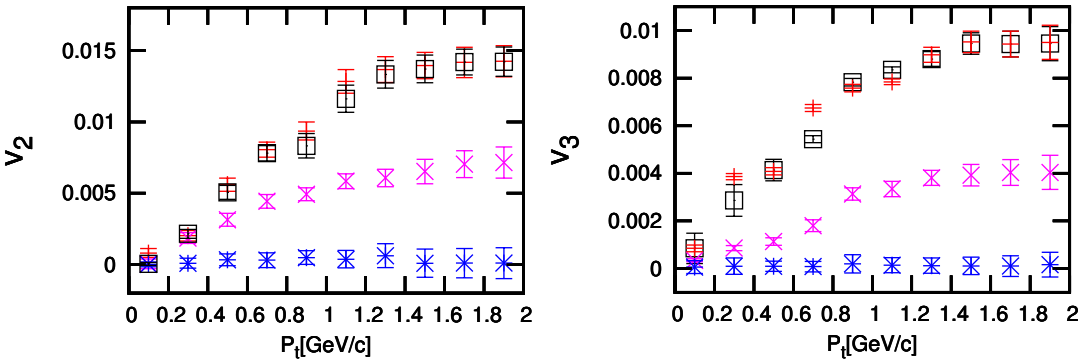

Figure 2: Anisotropy coefficients from central collisions. Two simulations with hard partons with different energy loss. One simulation with only energy and no momentum deposition (hot spots). One simulation with smooth initial conditions.

clearly a consequence of hard partons inducing flow anisotropies. We start our simulation with uniform profile in longitudinal rapidity stretched over 10 units and cut by half-Gaussian tails at both ends. This feature represents the approximate boost-invariance at highest LHC energies. Note that the use of 3+1D hydrodynamic model, which makes our simulation distinct from those reported in [10, 11], is important because the hard partons injected into plasma break the boost invariance and thus the possibility to reduce the dimensionality of the hydrodynamic model.

At the beginning of each event simulation we generate the positions and directions of the hard parton pairs. Their number fluctuates according to Poissonian and their p_T's follow from [6]

$$E\frac{d\sigma_{NN}}{d^3p} = \frac{1}{2\pi}\,\frac{1}{p_T}\,\frac{d\sigma_{NN}}{dp_T\,dy} = \frac{B}{(1+p_T/p_0)^n} \tag{3}$$

with $B = 14.7$ mb/GeV^2, $p_0 = 6$ GeV and $n = 9.5$. Momenta in a pair are back-to-back. The initial positions are generated from the distribution of the binary collisions calculated within optical Glauber model.

In an expanding fireball we assume that the energy loss of a parton scales with the entropy density as $dE/dx = dE/dx|_0\,(s/s_0)$ where $s_0 = 78.2/\text{fm}^3$ (corresponds to energy density 20 GeV/fm^3). Hydrodynamic description of the collision is finished at the freeze-out hypersurface specified by temperature 150 MeV. Generation of final state hadrons is done with the help of THERMINATOR2 [12] Monte Carlo model.

In Fig. 2 we show the v_n's calculated in central collisions. To study the effect of momentum deposition we simulated 100 evolutions for every setting and generated 5 THERMINATOR2 events for each of them. For the momentum loss we made simulations with $dE/dx|_0$ set to 4 GeV/fm and 7 GeV/fm and they lead to the same momentum anisotropies. Their magnitude indicates that the effect is important and should be included in realistic simulations. Finally, we also simulated events where we put in hot spots with the same energy on top of the smooth initial conditions instead of hard partons. They deposit only energy and no momentum, and the generated flow anisotropies are about half of those initiated by hard partons.

Simulations of non-central collisions clearly show that the contribution enhances the observed anisotropies. In Fig. 3 we see about 50% addition to v_2 as compared to the case with smooth initial conditions. Triangular anisotropy is absent in the initial conditions and thus any v_3 is exclusively due to hard partons.

The presented results clearly demonstrate the necessity to include this mechanism into realistic hydrodynamic simulations which aim at extracting the properties of quark matter. For the alignment of the studied effect with the geometry of the fireball it is crucial to include more than one dijet pair into the simulation, unlike done in [13]. The interplay of many generated streams appears important.

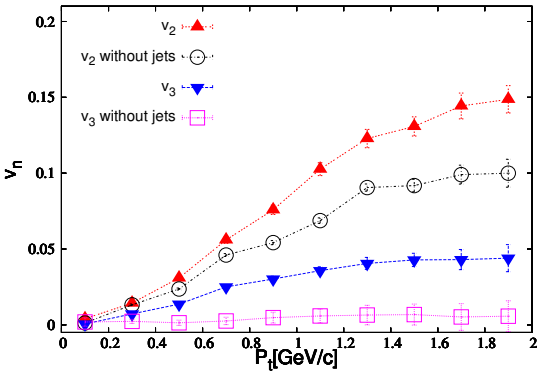

Figure 3: Coefficients v_2 and v_3 from 30–40% centrality events. Results of simulations with hard partons are compared with results from smooth initial conditions.

Acknowledgments

This work was supported in parts by APVV-0050-11, VEGA 1/0457/12 (Slovakia) and MŠMT grant LG13031 (Czech Republic).

References

[1] M. Luzum and P. Romatschke, Phys. Rev. C **78** (2008) 034915 [Erratum-ibid. C **79** (2009) 039903]
[2] U. Heinz, J. Phys. Conf. Ser. **455** (2013) 012044
[3] C. Gale, *et al.*,Phys. Rev. Lett. **110** (2013) 012302
[4] H. Niemi, G. S. Denicol, H. Holopainen and P. Huovinen, Phys. Rev. C **87** (2013) 5, 054901
[5] S. Floerchinger and U. A. Wiedemann, Phys. Rev. C **89** (2014) 034914
[6] B. Tomášik and P. Lévai, J. Phys. G **38** (2011) 095101
[7] M. Schulc and B. Tomášik, J. Phys. G **40** (2013) 125104
[8] M. Schulc and B. Tomášik, Phys. Rev. C **90** (2014) 064910
[9] B. Betz, *et al.*,Phys. Rev. C **79** (2009) 034902
[10] R. P. G. Andrade, J. Noronha and G. S. Denicol, Phys. Rev. C **90** (2014) 024914
[11] S. Floerchinger and K. C. Zapp, Eur. Phys. J. C **74** (2014) 3189
[12] M. Chojnacki, A. Kisiel, W. Florkowski and W. Broniowski, Comput. Phys. Commun. **183** (2012) 746
[13] Y. Tachibana and T. Hirano, Phys. Rev. C **90** (2014) 021902

Chapter 4

Hadrons in medium - hyperons and mesons in nuclear matter

Hyperon-nucleon interaction in chiral effective field theory

Johann Haidenbauer

Institute for Advanced Simulation, Forschungszentrum Jülich GmbH, D-52425 Jülich, Germany

DOI: http://dx.doi.org/10.3204/DESY-PROC-2014-04/134

Results of a study of the hyperon-nucleon system within chiral effective field theory are reported. The investigation is based on the scheme proposed by Weinberg which has been applied rather successfully to the nucleon-nucleon interaction in the past. Results for the ΛN and ΣN interactions in free space and nuclear matter, obtained up to next-to-leading order, are presented and discussed.

1 Introduction

Chiral effective field theory (EFT) as proposed in the pioneering works of Weinberg [1] is a powerful tool for the derivation of baryonic forces. In this scheme there is an underlying power counting which allows to improve calculations systematically by going to higher orders in a perturbative expansion. In addition, it is possible to derive two- and corresponding three-body forces as well as external current operators in a consistent way.

Recently, a hyperon-nucleon (YN) interaction has been derived up to next-to-leading order (NLO) in chiral EFT by the Jülich-Bonn-Munich group [2]. At that order there are contributions from one- and two-pseudoscalar-meson exchange diagrams and from four-baryon contact terms without and with two derivatives. SU(3) flavor symmetry is imposed for constructing the YN interaction in order to reduce the number of free parameters, in particular the number of low-energy constants (LECs) associated with the arising contact terms. In the actual calculation the SU(3) symmetry is broken, however, by the mass differences between the involved mesons (π, K, η) and between the baryons (N, Λ, Σ).

An excellent description of available ΛN and ΣN scattering data could be achieved at NLO. Corresponding results are reported in Sect. 3. In addition the in-medium properties of the EFT YN interaction have been investigated. Specifically, binding energies of the Λ and Σ hyperons in nuclear matter have been calculated, based on a conventional first-order Brueckner calculation, and these are also presented.

2 The YN interaction in chiral EFT

The derivation of the chiral baryon-baryon potentials for the strangeness sector at leading order (LO) using the Weinberg power counting is outlined in Refs. [3, 4]. Details for the NLO case can be found in Ref. [2], see also [5]. The LO potential consists of four-baryon contact terms without derivatives and of one-pseudoscalar-meson exchanges while at NLO contact terms with

two derivatives arise, together with contributions from (irreducible) two-pseudoscalar-meson exchanges. The contributions from pseudoscalar-meson exchanges (π, η, K) are completely fixed by the assumed SU(3) flavor symmetry. On the other hand, the strength parameters associated with the contact terms, the LECs, need to be determined in a fit to data. How this is done is described in detail in Ref. [2]. Note that we impose also SU(3) symmetry for those contact terms which reduces the number of independent LECs that can contribute.

The reaction amplitudes are obtained from the solution of a coupled-channels Lippmann-Schwinger (LS) equation for the interaction potentials:

$$T^{\rho'' \rho', J}_{\nu'' \nu'}(p'', p'; \sqrt{s}) = V^{\rho'' \rho', J}_{\nu'' \nu'}(p'', p') + \sum_{\rho, \nu} \int_0^\infty \frac{dpp^2}{(2\pi)^3} V^{\rho'' \rho, J}_{\nu'' \nu}(p'', p) \frac{2\mu_\nu}{q_\nu^2 - p^2 + i\eta} T^{\rho \rho', J}_{\nu \nu', J}(p, p'; \sqrt{s}) \ .$$

The label ν indicates the particle channels and the label ρ the partial wave. μ_ν is the pertinent reduced mass. The on-shell momentum in the intermediate state, q_ν, is defined by $\sqrt{s} = \sqrt{m^2_{B_{1,\nu}} + q^2_\nu} + \sqrt{m^2_{B_{2,\nu}} + q^2_\nu}$. Relativistic kinematics is used for relating the laboratory energy $T_{\rm lab}$ of the hyperons to the c.m. momentum.

We solve the LS equation in the particle basis, in order to incorporate the correct physical thresholds. Depending on the total charge, up to three baryon-baryon channels can couple. The Coulomb interaction is taken into account appropriately via the Vincent-Phatak method [6]. The potentials in the LS equation are cut off with a regulator function, $f_R(\Lambda) = \exp\left[-\left(p'^4 + p^4\right)/\Lambda^4\right]$, in order to remove high-energy components [7]. We consider cutoff values in the range $\Lambda = 500$ – $650\,\text{MeV}$, similar to what was used for chiral NN potentials [7].

3 Results for ΛN and ΣN in free space and nuclear matter

Our results for ΛN and ΣN scattering are presented in Fig. 1. The bands (black/red for NLO and grey/green bands for LO) represent the variation of the cross sections based on chiral EFT within the considered cutoff region, i.e. 550-700 MeV in the LO case [3] and 500-650 MeV at NLO. For comparison also results for the Jülich '04 [8] meson-exchange model are shown (dashed line).

Obviously, the available ΛN and ΣN scattering data are very well described by our NLO EFT interaction. In particular, and as expected, the energy dependence exhibited by the data is visibly better reproduced within our NLO calculation than at LO. This concerns in especially the $\Sigma^+ p$ channel. But also for Λp the NLO results are now well in line with the data even up to the ΣN threshold. Furthermore, one can see that the dependence on the cutoff mass is strongly reduced in the NLO case. Additional results, for differential cross sections and for phase shifts, can be found in Ref. [2].

Besides an excellent description of the YN data the chiral EFT interaction yields a satisfactory value for the hypertriton binding energy, see Ref. [2]. Calculations for the four-body hypernuclei ${}^4_\Lambda$H and ${}^4_\Lambda$He based on the EFT interactions can be found in Ref. [9].

Recently, we have also investigated the properties of our YN interactions in nuclear matter [10]. Specifically, we performed a conventional first-order Brueckner calculation based on the standard choice of the single-particle (s.p.) potentials. Table 3 summarizes preliminary results for the Λ and Σ potential depths, $U_\Lambda(p_\Lambda = 0)$ and $U_\Sigma(p_\Sigma = 0)$, evaluated at the saturation point of nuclear matter, i.e. for $k_F = 1.35$ fm^{-1}. Corresponding results obtained for the Jülich

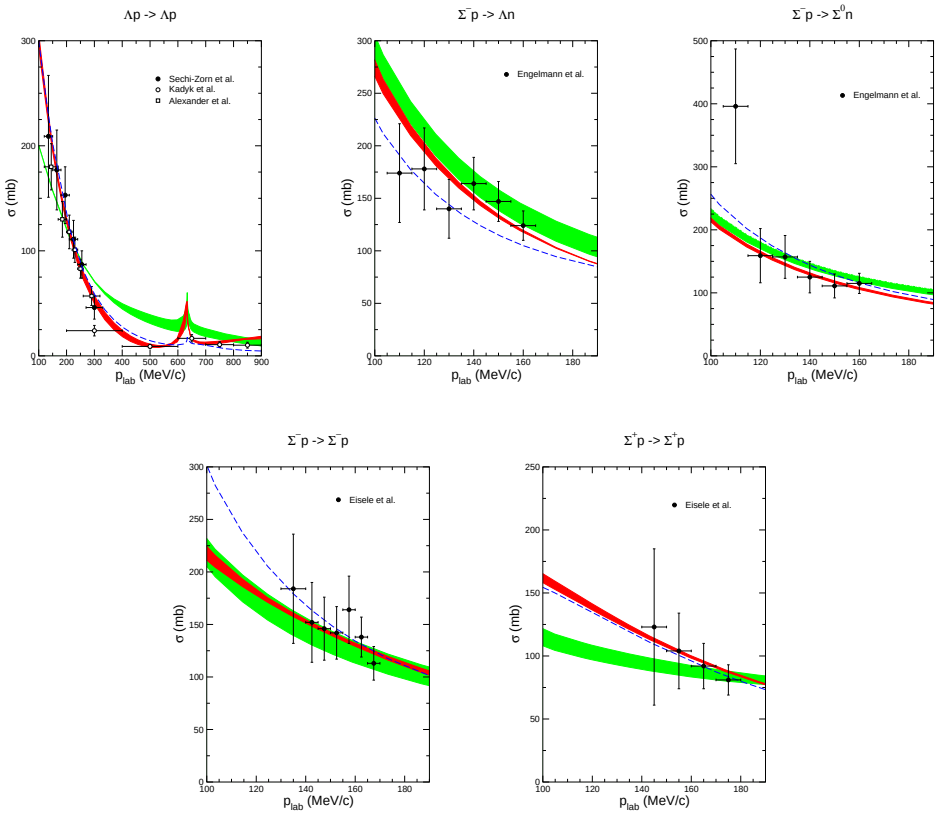

Figure 1: Total cross sections for ΛN, and ΣN scattering as a function of p_{lab}. The grey/green band shows the chiral EFT results to LO for variations of the cut-off in the range $\Lambda = 550$–700 MeV, while the black/red band are results to NLO for $\Lambda = 500$–650 MeV. The dashed curve is the result of the Jülich '04 [8] meson-exchange potential.

meson-exchange potentials from 2004 [8] and 1994 [11] are also included. In case of the EFT results we show the variation with the cutoff. These are comparable for U_Λ at LO and NLO, but noticeably reduced for U_Σ at NLO. The predictions for $U_\Lambda(0)$ are well in line with the 'empirical' value for the Λ binding energy in nuclear matter of about -27 to -30 MeV, deduced from the binding energies of finite Λ hypernuclei [12].

As already emphasized in Ref. [2] the interaction in the $^3S_1$ partial wave of the Σ^+p channel is repulsive, for the LO potential but also for the NLO interaction. As a consequence the predicted Σ s.p. potential is likewise repulsive, see Table 3. Such a repulsion is in accordance with evidence from the analysis of level shifts and widths of Σ^- atoms and from recently measured (π^-, K^+) inclusive spectra related to Σ^--formation in heavy nuclei [13, 14].

Table 1: Results for the s.p. potentials $U_\Lambda(0)$ and $U_\Sigma(0)$ (in MeV) based on our EFT interactions and the Jülich meson-exchange interactions.

	EFT LO	EFT NLO	Jülich '04 [8]	Jülich '94 [11]
Λ [MeV]	$550 \cdots 700$	$500 \cdots 650$		
$U_\Lambda(0)$	$-38.0 \cdots -34.4$	$-29.3 \cdots -22.9$	-51.2	-29.8
$U_\Sigma(0)$	$28.0 \cdots 11.1$	$17.4 \cdots 12.1$	-22.2	-71.45

4 Summary

Chiral effective field theory, successfully applied in Ref. [7] to the NN interaction, also works well for the baryon-baryon interactions in the strangeness sector [2, 15, 16]. In particular, the results for the YN interaction presented here, obtained to next-to-leading order in the Weinberg counting, are very encouraging. First there is a visible improvement in the quantitative reproduction of the available data on ΛN and ΣN scattering and, secondly, the dependence on the regularization scheme is strongly reduced as compared to the LO result. Indeed the description of the YN system achieved at NLO is now on the same level of quality as the one by the most advanced meson-exchange YN interactions.

Acknowledgements

I would like to thank N. Kaiser, U.-G. Meißner, A. Nogga, S. Petschauer, and W. Weise for collaborating on the topics covered by my talk. Work supported in part by DFG and NSFC (CRC 110).

References

[1] S. Weinberg, Phys. Lett. B **251** (1990) 288.
[2] J. Haidenbauer, S. Petschauer, N. Kaiser, U.-G. Meißner, A. Nogga, W. Weise, Nucl. Phys. A **915** 24 (2013).
[3] H. Polinder, J. Haidenbauer, U.-G. Meißner, Nucl. Phys. A **779** 244 (2006).
[4] J. Haidenbauer, U.-G. Meißner, A. Nogga, H. Polinder, Lect. Notes Phys. **724** 113 (2007).
[5] S. Petschauer, N. Kaiser, Nucl. Phys. A **916** 1 (2013).
[6] C.M. Vincent, S.C. Phatak, Phys. Rev. C **10** 391 (1974).
[7] E. Epelbaum, W. Glöckle, U.-G. Meißner, Nucl. Phys. A **747** 362 (2005).
[8] J. Haidenbauer, U.-G. Meißner, Phys. Rev. C **72** 044005 (2005).
[9] A. Nogga, Few Body Syst. **55**, 757 (2014).
[10] J. Haidenbauer, U.-G. Meißner, Nucl. Phys. A **936** 29 (2015).
[11] A. Reuber, K. Holinde, J. Speth, Nucl. Phys. A **570** 543 (1994).
[12] D.J. Millener, C.B. Dover, A. Gal, Phys. Rev. C **38** 2700 (1988).
[13] M. Kohno, Y. Fujiwara, Y. Watanabe, K. Ogata and M. Kawai, Phys. Rev. C **74** 064613 (2006).
[14] J. Dabrowski and J. Rozynek, Phys. Rev. C **78** 037601 (2008).
[15] H. Polinder, J. Haidenbauer, U.-G. Meißner, Phys. Lett. B **653** 29 (2007).
[16] J. Haidenbauer, U.-G. Meißner, Phys. Lett. B **684** 275 (2010).

Strangeness in the Universe? Advances and perspectives in the low-energy kaon-nucleon/nuclei interaction studies at the DAΦNE collider

C. Curceanu[1], *M. Bazzi*[1], *G. Beer*[2], *C. Berucci*[1,3], *D. Bosnar*[4], *A.M. Bragadireanu*[1,5], *M. Cargnelli*[3], *A. d'Uffizi*[1], *L. Fabietti*[6], *C. Fiorini*[7,8], *F. Ghio*[9], *C. Guaraldo*[1], *R.S. Hayano*[10], *M.Iliescu*[1], *T. Ishiwatari*[3], *M. Iwasaki*[11], *P. Levi Sandri*[1], *J. Marton*[3], *S. Okada*[11], *D. Pietreanu*[1,5], *K. Piscicchia*[1], *M. Poli Lener*[1], *T. Ponta*[5], *R. Quaglia*[7,8], *A. Romero Vidal*[12], *E. Sbardella*[1], *F Schembari*[7,8], *A. Scordo*[1], *H. Shi*[3], *D.L. Sirghi*[1,5], *F. Sirghi*[1,5], *H. Tatsuno*[11], *I. Tucakovic*[1], *O. Vazquez Doce*[6], *E. Widmann*[3], *J. Zmeskal*[3]

[1]INFN, Laboratori Nazionali di Frascati, Via Enrico Fermi 40, I-00044, Frascati (Roma), Italy
[2]Department of Physics and Astronomy, University of Victoria, Victoria, BC, Canada
[3]Stefan-Meyer-Institut für subatomare Physik, Vienna, Austria
[4]University of Zagreb, Zagreb, Croatia
[5]Horia Hulubei National Institute of Physics and Nuclear Engineering, Magurele, Romania
[6]Excellence Cluster Universe, Technische Universität München, Garching, Germany
[7]Politecnico di Milano, Dipartimento di Elettronica, Informazione e Bioingegneria, Milano, Italy
[8]INFN Sezione di Milano, Milano, Italy
[9]INFN Sezione di Roma I and Istituto Superiore di Sanità, Roma, Italy
[10]The University of Tokyo, Tokyo, Japan
[11]RIKEN, The Institute of Physics and Chemestry Research, Saitama, Japan
[12]University of Santiago de Compostela, Santiago de Compostela, Spain

DOI: http://dx.doi.org/10.3204/DESY-PROC-2014-04/21

The DAΦNE electron-positron collider at the Laboratori Nazionali di Frascati of INFN, Italy, has made available a unique quality low-energy negatively charged "kaons beam", which is used to study the kaon-nucleon/nuclei interactions at low energies, by the SIDDHARTA and AMADEUS collaborations. SIDDHARTA has already performed unprecedented precision measurements of kaonic atoms, and is being presently upgraded, as SIDDHARTA-2, to approach new frontiers. The AMADEUS experiment plans to perform in the coming years precision kaon-nuclei interactions at low-energies measurements, to study the possible formation of kaonic nuclei and of the Λ(1405) and many other processes involving strangeness. These studies have implications going from particle and nuclear physics to astrophysics, helping to understand the role of strangeness in the Universe.

1 Low energy kaon-nucleon/nuclei studies at DAΦNE

The recently upgraded DAΦNE [1, 2] electron-positron collider at the Frascati National Laboratory of INFN produces the ϕ-resonance, which decays with a probability of about 50% in K^+ K^-, providing an excellent quality low-energy kaon "beam". This beam is intensively used

for the study of the low-energy kaon-nucleon/nuclei interactions, a field still lacking experimental data. By making use of this beam, in 2009 the SIDDHARTA (SIlicon Drift Detector for Hadronic Atom Research by Timing Application) experiment performed a precision measurement of the strong interaction induced energy shift and width of the 1s level, via the measurement of the X-ray transitions of kaonic hydrogen, and high precision measurements of the kaonic helium3 and 4 X-ray transitions to the 2p level. The first exploratory measurement of kaonic deuterium was performed too. SIDDHARTA-2, a major upgrade of SIDDHARTA, presently under preparation, will measure the kaonic deuterium transitions to the 1s level. The final goal is to extract, for the first time, the isospin-dependent antikaon-nucleon scattering lengths, fundamental quantities to understand the chiral symmetry breaking mechanism. The AMADEUS (Antikaon Matter at DAΦNE: an Experiment with Unraveling Spectroscopy) experiment will perform the first complete study of the low-energy kaon-nuclei interactions by using a series of cryogenic gaseous targets, as d, ^{3}He, ^{4}He , 4He, and solid targets.

Among the aims of AMADEUS there are: the measurement of the $\Lambda(1405)$ decaying to Σ π in all possible charge combinations, and to give a definite answer to the debated question of the existence of the kaonic nuclei. If such states exist we will measure their properties (binding energies, width and decay channels). Presently, as a first step towards AMADEUS realization, we are analyzing the 2004-2005 KLOE data.

2 The SIDDHARTA and SIDDHARTA-2 experiments

In the SIDDHARTA experiment the monochromatic low-energy charged kaons produced at the DAΦNE collider are degraded in energy and stopped in a cryogenic gaseous target, where kaonic atoms are efficiently produced. An important element of the apparatus is the charged kaon trigger, which is based on the coincidence of the signals from two plastic scintillation counters mounted top and bottom of the e^+ e^- interaction point. The trigger system takes advantage of the back-to-back topology of the produced low-energy kaons: $\Phi \rightarrow K^+ K^-$ and its use drastically increases the signal-to-background ratio, because most of the background is generated by non interacting e^+ and e^- beam particles, uncorrelated in time with the collisions.

The kaons which are stopped inside the target produce highly excited kaonic atoms which deexcite to the fundamental level, emitting X rays. These X rays were detected by 144 Silicon Drift X-ray Detectors (SDDs) mounted around the target. A detailed description of the experimental setup is given in Ref. [3]. The setup was installed above the electron-positron interaction point at the DAΦNE collider in 2009. The following measurements were performed:

- kaonic hydrogen X-ray transitions to the 1s level, the most precise measurement ever [3];
- kaonic helium4 transitions to the 2p level, the first measurement using a gaseous target [3, 4];
- kaonic helium3 transitions to the 2p level, the first measurement ever [5, 6];
- kaonic deuterium X-ray transitions to the 1s level - as an exploratory measurement [7].

The 1s-state strong-interaction shift ϵ and width Γ of kaonic hydrogen were determined to be: $\epsilon = -283 \pm 36(\text{stat}) \pm 6(\text{syst})$ eV and $\Gamma = 541 \pm 89(\text{stat}) \pm 22(\text{syst})$ eV.

These are the most precise results ever compared to the previous measurements [8, 9]. The values of ϵ and Γ are consistent with the theoretical predictions [10]. The SIDDHARTA results

allow the most precise evaluation of the K^-p scattering length, which yields strong constraints on the theoretical description of the low-energy antikaon-nucleon interactions [11, 12, 13]. For a more complete study of the isospin dependent antikaon-nucleon interaction, the measurement of the shift and width of kaonic-deuterium 1s state is mandatory. Presently, a major upgrade of the apparatus, SIDDHARTA-2, is undergoing. The upgrade is going to improve the signal/background ratio by a factor about 20 in order to perform the measurement of kaonic deuterium X-ray transitions to the 1s level and of other types of kaonic atoms transitions [14]

3 The AMADEUS experiment

The low-energy (p $\leq$ 100 MeV/c) kaon-nuclei interaction studies represent the main aim of the AMADEUS experiment [15, 16]. These type of measurements require detecting all charged and neutral particles coming from the K^- interactions with various targets with an almost 4π acceptance. The AMADEUS collaboration plans to implement the existent KLOE detector [17, 18] in the free internal region between the beam pipe and the Drift Chamber inner wall (having a diameter of 50 cm) with a dedicated setup. The dedicated setup includes: the target, which can be either solid or a gaseous cryogenic one, a tracker system (TPC-GEM) and a trigger (scintillating fibers read by SiPM detectors). The negatively charged kaons may stop inside the target or interact at low energies, initiating a series of processes. Among these, a key-role is played by the generation of $\Lambda(1405)$ which can decay into Σ^0 π^0, Σ^+ π^- or $\Sigma^-\pi^+$ We plan to study all these three channels in the same data sample. We plan as well to verify the possible existence of "kaonic nuclear cluster" by studying the Λp and Λd channels. Many other kaon-nuclei processes will be investigated, either for the first time, or in order to obtain more accurate results than those actually reported in literature. In the summer of 2012 a half cylinder carbon target was built and installed inside the Drift Chamber of KLOE as a first step towards the AMADEUS realization. The target thickness was optimized to have a maximum of stopped kaons (about 24% of generated) without degrading too much the energy of resulting charged particles inside the target material. The experiment run from October to the end of 2012. The analysis of these data is ongoing; it will provide new insights in the low-energy interactions of charged kaons in the nuclear matter.

4 Conclusions

The DAΦNE collider delivers an excellent quality low-energy charged kaons beam. Such a beam was intensively used by the SIDDHARTA collaboration to perform unique quality measurements of kaonic atoms (kaonic hydrogen and kaonic helium). SIDDHARTA-2 will perform the kaonic deuterium and other types of kaonic atoms transitions measurements in the near future. The kaonic-nuclei interactions at low-energies are being investigated by the AMADEUS collaboration to search for the possible formation and decay of "kaonic nuclear cluster" and of yet un-measured kaon-nuclei low-energy processes. SIDDHARTA, SIDDHARTA(-2) and AMADEUS are and will continue to provide unique quality results, which will help to understand the role of strangeness in the Universe.

Acknowledgments

We thank C.Capoccia, G.Corradi, B.Dulach and D.Tagnani from LNF-INFN and H.Schneider, L.Stohwasser and D.Stückler from Stefan-Meyer-Institut for their fundamental contribution in designing and building the SIDDHARTA setup. We thank the DAΦNE staff for the great working conditions and permanent support. Part of this work was supported by Hadron Physics I3 FP6 European Community program, Contract No.RII3 CT-2004-506078; the European Community-Research Infrastructure Integrating Activity Study of Strongly Interacting Matter (Hadron Physics 2, Grant Agreement No.227431 and HadronPhysics 3, Contract No.283286 under the Seventh Framework Programme of EU); Austrian Federal Ministry of Science and Research BMBWK 650962/0001 VI/2/2009; Romanian National Authority for Scientific Research,Contract No.2-CeX 06-11-11/2006; the Grant in-Aid for Specially Promoted Research (20002003), MEXT, Japan; the Austrian Science Fund (FWF):[P20651-N20]; the DFG Excellence Cluster Universe of the Technische Universität München and the Croatian Science Foundation under Project No. 1680

References

[1] C. Milardi *et al.*, Int. J. Mod. Phys.**A24**, 360 (2009).

[2] M. Zobov *et al.*, Phys. Rev. Lett **104**, 174801 (2010).

[3] M. Bazzi *et al.*, Phys. Lett.**B704**, 113 (2011).

[4] M. Bazzi *et al.*, Phys. Lett. **B681**, 310 (2009).

[5] M. Bazzi *et al.*, Phys. Lett. **B714**, 40 (2012).

[6] M. Bazzi *et al.*, Phys. Lett. **B697**, 199 (2011).

[7] M. Bazzi *et al.*, Nucl. Phys.**A907**, 69 (2013).

[8] M. Iwasaki *et al.*, Phys. Rev. Lett. **78**, 3067 (1997); T.M. Ito *et al.*, Phys. Rev. **C58**, 2366 (1998).

[9] G. Beer *et al.*, DEAR Collaboration, Phys. Rev. Lett. **94**, 21230 (2005).

[10] B. Borasoy, R. Nißler, W.Weise, Phys. Rev. Lett.**94**, 213401 (2005); B. Borasoy, U.-G. Meißner, R. Nißler, Phys. Rev.**C74**, 055201 (2006).

[11] A. Cieply, E. Friedman, A. Gal, D. Gazda, J. Mares, Phys. Lett. **B702**, 402 (2011).

[12] Y. Ikeda, T. Hyodo, W. Weise, Phys. Lett. **B706**, 63 (2011).

[13] Y. Ikeda, T. Hyodo, W. Weise, Nucl. Phys. **A881**, 98 (2012).

[14] The SIDDHARTA-2 Collaboration, SIDDHARTA-2 Proposal, https://www.lnf.infn.it/committee/private/documenti/SIDDHARTA2-proposal FINAL.pdf

[15] The AMADEUS Collaboration, Letter of Intent - Study of deeply bound kaonic nuclear states at DAΦNE2, http://www.lnf.infn.it/esperimenti/siddharta/LOI AMADEUS March2006.pdf

[16] The AMADEUS Collaboration, AMADEUS Phase-1: Physics, setup and Roll-in Proposal, LNF- 07-24(IR), 2007. (http://www.lnf.infn.it/sis/preprint/pdf/getfile.php?filename=LNF-07 24(IR).pdf)

[17] M. Napolitano, Nucl. Phys. Proc. Supp. **61B**, 589 (1998); KLOE and KLOE2 Collaboration, Nucl. Phys Proc. Suppl. **B249**, 225 (2012).

[18] The AMADEUS Collaboration, Nucl. Phys. **A804**, 286 (2008).

Cascade production in antikaon reactions with protons and nuclei

V.K. Magas[1,2], *A. Feijoo*[1], *A. Ramos*[1,2]

[1]Dept. d'Estructura i Constituents de la Matèria, Universitat de Barcelona,
Martí Franquès 1, E08028 Barcelona, Spain
[2]Institut de Ciències del Cosmos, Universitat de Barcelona,
Martí Franquès 1, E08028 Barcelona, Spain

DOI: http://dx.doi.org/10.3204/DESY-PROC-2014-04/170

We study the meson-baryon interaction in S-wave in the strangeness S=-1 sector using a chiral SU(3) Lagrangian extended to next-to-leading order (NLO). Our model has 7 new parameters, coming from NLO terms in the chiral Lagrangian, which are fitted to the large set of experimental data available for different two-body channels. We pay particular attention to the $K^- p \to K\Xi$ reactions, where the effect of the NLO terms in the Lagrangian is very important. In order to improve our model in these particular channels, we take into account phenomenologically the effects of the high spin hyperonic resonances, namely $\Sigma(2030)\ \left(\frac{7}{2}^+\right)$ and $\Sigma(2250)\ \left(\frac{5}{2}^-\right)$. Finally, the developed model is applied to simulate the Ξ production in nuclei.

1 Introduction

Chiral perturbation theory (χPT) is a powerful effective theory [1] that respects the chiral symmetry of the QCD Lagrangian and describes successfully the low energy hadron phenomenology. Unitary extensions of the theory ($U\chi PT$) permit to describe hadron dynamics in the vicinity of resonances, as in the case of the $\Lambda(1405)$ baryon located only 27 MeV below the $\bar{K}N$ threshold. In the last years interest in this problem is renewed due to the availability of more precise data coming from the measurement of the energy shift and width of the 1s state in kaonic hydrogen by the SIDDHARTA collaboration [2], which has permitted to better constrain the parameters of the meson-baryon Lagrangian at next-to-leading order (NLO) [3, 4, 5, 6].

In this work we attempt a study of the meson-baryon interaction in the $S = -1$ sector, paying a especial attention to the Ξ hyperon production reactions $K^- p \to K^+\Xi^-\,, K^0\Xi^0$, not employed in the NLO fits of earlier works, in spite of being especially sensitive to the NLO terms of the Lagrangian since the lowest-order tree level term does not contribute. A complete approach to Ξ production reactions must also implement the effect of high-spin resonances [7, 8, 9], which we also incorporate in our fit. Finally, we explore the Ξ hyperon production reaction on several nuclei.

2 Meson-baryon amplitudes from the chiral Lagrangian at NLO

The meson-baryon interaction up to NLO can be derived from the chiral Lagrangian [1] and reads $V_{ij}^{\rm NLO} = V_{ij}^{(1)} + V_{ij}^{(2)}$ with:

$$V_{ij}^{(1)} = -\frac{C_{ij}(2\sqrt{s} - M_i - M_j)}{4f^2}\sqrt{\frac{M_i + E_i}{2M_i}}\sqrt{\frac{M_j + E_j}{2M_j}}\,, V_{ij}^{(2)} = \frac{D_{ij} - 2(k_\mu k'^\mu)L_{ij}}{f^2}\sqrt{\frac{M_i + E_i}{2M_i}}\sqrt{\frac{M_j + E_j}{2M_j}}\,, \tag{1}$$

where the indices i, j run over the allowed coupled channels, which in the present $S = -1$ study are K^-p, $\bar{K}^0n$, $\pi^0\Lambda$, $\pi^0\Sigma^0$, $\pi^+\Sigma^-$, $\pi^-\Sigma^+$, $\eta\Lambda$, $\eta\Sigma^0$, $K^+\Xi^-$ and $K^0\Xi^0$, C_{ij} is a matrix of numerical coefficients, f is the pion decay constant, and D_{ij} and L_{ij} are coefficient matrices that depend on the NLO parameters: b_0, b_D, b_F, d_1, d_2, d_3, d_4. The unitarized amplitude is determined from the solution of a Bethe-Salpeter equation $T_{ij} = V_{ij} + V_{il}G_lT_{lj}$, where the loop function G_l is properly regularized using dimensional regularization and depends on a subtraction constant a_l at a given energy scale which we take here to be $\mu = 1$ GeV (see [3, 4, 5, 6, 10] for more details). Therefore, at the lowest order, the unitarized amplitudes depend on 7 parameters: the decay constant f of the Weinberg-Tomozawa term, which is taken as a free parameter to partly simulate higher-order terms, plus the loop subtraction constants which, applying isospin symmetry arguments, reduce to 6. At next-to-leading order, there are 7 additional parameters to be fitted.

We present our results in the following, very brief, way: Fig. 1 shows the $K^-p \to K^0\Xi^0$ cross section obtained from our fits; Table 1 shows the corresponding threshold branching ratios.

Let us concentrate on the left subplot of Fig. 1. The first fit we perform is a *classical* WT fit to the cross section of different channels, excluding Ξ production channels, and to the threshold branching ratios. Obviously, the results for the $K^-p \to K^0\Xi^0$ reactions are rather bad, see *WT (no Ξ channels)* dotted line. When we force our WT model to fit also the Ξ production data - *WT* dashed line - some strength is built for the $K^-p \to K^0\Xi^0$ cross section, although the agreement is far from perfect. Now if we and into the game NLO terms of the chiral Lagrangian the progress is obvious - *NLO* line. Also we would like to comment that including NLO terms we improve the agreement in all the channels although for the $K^0\Xi^0$ and $K^+\Xi^-$ ones the changes are most drastic.

3 Inclusion of high spin resonances

The shape of the $\bar{K}N \to K\Xi$ cross sections reflects that terms of the type $\bar{K}N \to Y \to K\Xi$, where Y stands for some hyperon resonance, may also come into play. From the eight three- and four-star candidates listed in the PDG, the $7/2^+$ $\Sigma(2030)$ and the $5/2^-$(estimated) $\Sigma(2250)$ seem more appropriate, according to the phenomenological model of [8] and our previous fit [6] . As in [11, 7], we follow the Rarita-Schwinger scheme to describe the resonance fields and build up their contribution to the amplitude, which depends on four new parameters for each resonance: its mass M_R, width Γ_R, product of couplings to the initial and final states, $g_{R\bar{K}N}g_{RK\Xi}$, and a cut-off Λ_R which suppresses high-momentum contributions. The final amplitude for initial $i = K^-p, \bar{K}^0n$ and final $j = K^+\Xi^-, K^0\Xi^0$ channels reads $T_{ij} = \sqrt{4M_pM_\Xi}T_{ij} + T_{ij}^{5/2^-} + T_{ij}^{7/2^-}$.

The cross sections for the $K^-p \to K^0\Xi^0$ reaction, obtained from different fits that considers the effect of these two hyperon resonances, are shown on the right subplot of Fig. 1. The dotted

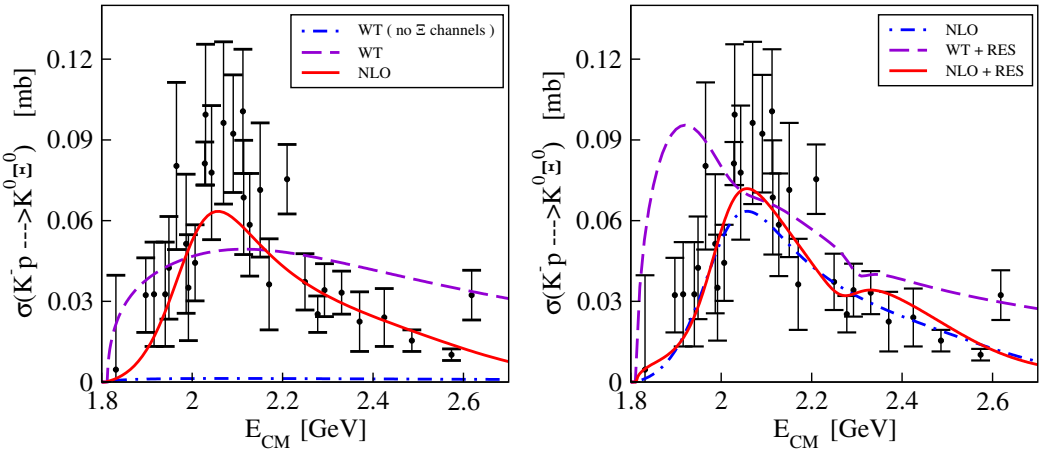

Figure 1: **Left subplot:** $K^- p \to K^0 \Xi^0$ cross section as a function of the center-of-mass energy for the NLO different fits, see text for more details. **Right subplot:** $K^- p \to K^+ \Xi^-$ cross section as a function of the center-of-mass energy for different fits, in particular including the contribution from high spin resonances. For both sub-figures the experimental data are taken from [12, 13, 14, 15, 16, 17, 18].

NLO line (the Ξ production data are now included in all fits) repeats the best fit without resonance contribution, i.e. it is the same as in Fig. 1A and should be used for more clear comparison. We have tried to fit the data adding the resonance terms to the WT model - *WT+Res* dashed line. Such a test clearly shows the absolute necessity of the NLO term to reproduce data on Ξ production. The full line *NLO+Res* corresponds to our best fit, where we take into account the simultaneous effect of the NLO Lagrangian and two hyperon resonances.

We note that our fit reproduces very satisfactorily all other elastic and inelastic cross sections in the $S = -1$ channel. The inclusion of resonances affect these other channels indirectly through their fine tuning effect on the parameters of the chiral Lagrangian at NLO. An example of the quality of the fit is shown in Table 1, where the threshold branching ratios between several channels are shown for different fitting schemes.

Table 1: Threshold branching ratios for different fitting schemes:

Model	γ	R_n	R_c
WT (no Ξ)	2.34	0.185	0.665
WT	2.30	0.185	0.665
NLO	2.31	0.186	0.660
WT+Res	2.48	0.202	0.667
NLO+Res	2.50	0.188	0.664
Exp.	2.36	0.189	0.664
data	±0.04	±0.015	±0.011

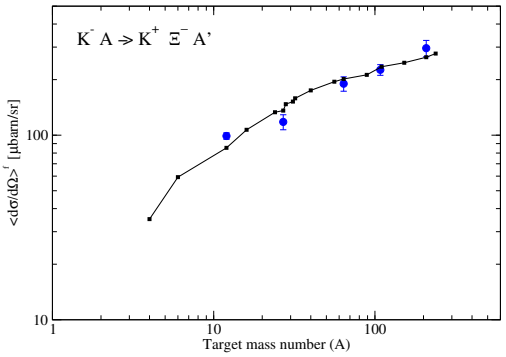

Figure 2: Cross section for Ξ hyperon production in (K^-, K^+) reaction on various nuclei [19].

4 Ξ production in nuclei

Finally, we perform an exploratory study on Ξ hyperon production in nuclei as a precursor reaction to form double-Λ hypernuclei. We employ a local density approach to describe the different nuclear targets. The propagation of antikaons before they reach the interaction point and that of the produced kaons as they leave the nucleus is taken within an eikonal approximation, which we consider to be a fair choice given the high momentum value of the incoming K^- ($p_{K^-} = 1.65$ GeV/c) and emitted K^+ ($0.95 < p_{K^+} < 1.30$ GeV/c; $1.7^\circ < \Theta_{K^+,Lab} < 13.6^\circ$). Our results for the calculated Ξ production cross section on several nuclei are shown by the square symbols joined by the solid line in Fig. 2. We obtain a good agreement with data [19], a fact that stimulates us to continue our investigations focussing on the production of bound Ξ states, much in line to what other theoretical works have attempted before [20, 21, 22].

Acknowledgement

This work is supported by the European Community-Research Infrastructure Integrating Activity *Study of Strongly Interacting Matter* (HadronPhysics3, Grant Agreement 283286) under the Seventh Framework Programme, by the contract FIS2011-24154 from MICINN (Spain), and by the Generalitat de Catalunya contract 2014SGR-401.

References

[1] J. Gasser and H. Leutwyler, Nucl. Phys. **B250** 465 (1985).

[2] M. Bazzi, G. Beer, L. Bombelli, A. M. Bragadireanu, M. Cargnelli, G. Corradi, C. Curceanu (Petrascu) and A. d'Uffizi *et al.*, Phys. Lett. **B704** 113 (2011).

[3] Y. Ikeda, T. Hyodo, W. Wiese, Nucl. Phys. **A881** 98 (2012).

[4] Zhi-Hui Guo, J. A. Oller, Phys. Rev. **C87** 035202 (2013).

[5] M. Mai and U. -G. Meissner, Nucl. Phys. **A900** 51 (2013).

[6] V. K. Magas, A. Feijoo and A. Ramos, AIP Conf. Proc. **1606** 208 (2014); arXiv:1311.5025 [hep-ph]; A. Feijoo, V.K. Magas, A. Ramos, Proceedings of the 13th International Workshop on Meson Production, Properties and Interaction, Krakow, Poland (2014).

[7] K. Shing Man, Y. Oh and K. Nakayama,, Phys. Rev. **C83** 055201 (2011).

[8] D. A. Sharov, V. L. Korotkikh, D. E. Lanskoy, Eur. Phys. J. **A47** 109 (2011).

[9] B. Jackson, Y. Oh, H. Haberzettl and K. Nakayama, Phys. Rev. **C89** 025206 (2014).

[10] B. Borasoy, R. Nissler, W. Wiese, Eur. Phys. J. **A25** 79 (2005).

[11] K. Nakayama, Y. Oh and H. Habertzettl, Phys. Rev. **C74** 035205 (2006).

[12] G. Burgun *et al.*, Nucl. Phys. **B8** 447 (1968)

[13] J. R. Carlson *et al.*, Phys. Rev. **D7** 2533 (1973).

[14] P. M. Dauber *et al.*, Phys. Rev. **179** 1262 (1969).

[15] M. Haque *et al.*, Phys. Rev. **152** 1148 (1966).

[16] G. W. London *et al.*, Phys. Rev. **143** 1034 (1966).

[17] T. G. Trippe, P. E. Schlein, Phys. Rev. **158** 1334 (1967).

[18] W. P. Trower *et al.*, Phys. Rev. **170** 1207 (1968).

[19] T. Iijima *et al.*, Nucl. Phys. **A546** 588 (1992).

[20] C. B. Dover and A. Gal, Annals Phys. **146** 309 (1983).

[21] C. B. Dover, D. J. Millener and A. Gal, Nucl. Phys. **A572** 85 (1994).

[22] T. Harada, Y. Hirabayashi and A. Umeya, Phys. Lett. **B690** 363 (2010).

Energy and density dependence of the $\bar{K}N$ and ηN amplitudes near threshold

Aleš Cieplý[1], *Jaroslav Smejkal*[2]

[1]Nuclear Physics Institute, 250 68 Řež, Czech Republic
[2]Institute of Experimental and Applied Physics, Czech Technical University in Prague, Horská 3a/22, 128 00 Praha 2, Czech Republic

DOI: http://dx.doi.org/10.3204/DESY-PROC-2014-04/102

Chirally motivated model is used to describe meson-baryon interactions at low energies. After fixing free parameters to available experimental data on reactions in the free space the model is extrapolated to subthreshold energies and to nonzero nuclear densities. The impact of nuclear matter on the elastic $\bar{K}N$ and ηN amplitudes is discussed.

1 Introduction

The modern approach to low-energy meson baryon interactions is based on chiral dynamics that implements the QCD symmetries in a nonperturbative region infested by presence of baryon resonances. There, the standard perturbation theory fails but the higher order contributions can be (at least in their major part) accounted for by using coupled channels and resummation techniques based on Lippmann-Schwinger or Bethe-Salpeter equation.

In our contribution we demonstrate the effects of nuclear medium on the $\bar{K}N$ and ηN amplitudes. We employ effective separable potentials that match the meson-baryon amplitudes up to NLO order in the chiral perturbative expansion. These potentials are then inserted into Lippmann-Schwinger equation to get the amplitudes which are then used to calculate the measurable quantities, typically cross sections or branching ratios of specific processes. The separable potentials are particularly useful for in-medium applications where the off-shell form factors provide a natural extension to account for two-body inelasticities related to many particle dynamics. This feature represents an advantage over more popular on-shell approaches based on dispersion relation for the inverse of the scattering T-matrix or on the so called N/D method.

2 The model

In the present work we consider low energy s-wave interactions of the basic 0^- meson octet (π, K, $\bar{K}$, η) with the $1/2^+$ octet of baryons (N, Λ, Σ, Ξ). The separable potential model adopted by us was invented by Kaiser, Siegel and Weise [1] who related the kernel of the Lippmann-Schwinger equation to the scattering amplitude constructed from an effective chiral Lagrangian.

The potential matrix reads as

$$V_{ij}(k,k';\sqrt{s}) = g_i(k^2)\, v_{ij}(\sqrt{s})\, g_j(k'^2) \quad (1)$$

$$v_{ij}(\sqrt{s}) = -\frac{C_{ij}(\sqrt{s})}{4\pi f_i f_j}\sqrt{\frac{M_i M_j}{s}} \quad (2)$$

where the indexes i, j run over the space of involved meson-baryon coupled channels and the off-shell form factors are taken in the Yamaguchi form, $g_j(k) = 1/[1+(k/\alpha_j)^2]$, with the inverse ranges α_j introduced as free parameters of the model. The central inter-channel couplings C_{ij} are energy dependent and determined by the chiral SU(3) symmetry, k (k') denotes the CMS meson momenta in the initial (final) state, $\sqrt{s}$ is the total CMS energy and M_j stand for baryon masses. f_j represents a meson decay constant and we allow for its different physical values f_π, f_K and f_η depending on the meson in a specific j-th channel. The transition amplitudes obtained as simple algebraical solutions of the Lippmann-Schwinger equation are also separable,

$$F_{ij}(k,k';\sqrt{s}) = g_i(k^2)\, f_{ij}(\sqrt{s})\, g_j(k'^2) \quad (3)$$

$$f_{ij}(\sqrt{s}) = \left[(1 - v\cdot G(\sqrt{s}))^{-1}\cdot v\right]_{ij} \quad (4)$$

where the Green function $G(\sqrt{s})$ is diagonal in the channel space and becomes density dependent in nuclear medium. In general, the intermediate state Green function can be written as

$$G_n(\sqrt{s},\rho) = -4\pi \int_{\Omega_n(\rho)} \frac{d^3p}{(2\pi)^3}\frac{g_n^2(p^2)}{k_n^2 - p^2 - \Pi_n(\sqrt{s},p;\rho) + \mathrm{i}0} \quad (5)$$

Here the impact of nuclear medium is twofold. Foremostly, for channels involving nucleons the Pauli exclusion principle restricts the integration space to a domain Ω_n of allowed nucleon momenta. In addition, the in-medium hadron selfenergies shift the pole of the propagator by a sum of meson and baryon selfenergies represented by the $\Pi_n(\sqrt{s},p;\rho)$ in Eq. (5). In a free space, when the integration goes over the whole momentum space and $\Pi_n(\sqrt{s},p;\rho) = 0$, the integral has an analytical form while in nuclear matter the integration has to be performed numerically. Normally, one also constructs the meson selfenergies from the in-medium meson-baryon amplitudes, so a selfconsistent treatment is required (see Ref. [2] for details).

The model was successfully applied to describe the available low energy experimental data for K^-p reactions including the recent precise measurement of the kaonic hydrogen characteristics by the SIDDHARTA collaboration. Later on, the same methodology was used to describe the data on πN scattering and $\pi p \longrightarrow \eta n$ reaction. We refer the reader to our previous publications [3] and [4] for the details of the fitting procedure, the quality of the fits, and for all other relevant information including references to the experimental data. In general, the quality of the fits in the $\bar{K}N$ sector is quite good when only the TW term is accounted for while the inclusion of higher order NLO contributions is mandatory to achieve realistic description of the experimental data in the $\pi N - \eta N$ sector.

3 $\bar{K}N$ and ηN amplitudes

In Figure 1 we demonstrate the impact of nuclear medium on the elastic K^-p amplitude as obtained with the NLO30 model from Ref. [3]. The energy dependence of the amplitude in vacuum (shown by the dotted lines) is clearly affected by the presence of the $\Lambda(1405)$ resonance

with a peak of the imaginary part $\Im F_{K^-p}$ located around 1400 MeV. We note in passing that the NLO30 model generates poles of the amplitude at energies $z_{\bar{K}N} = (1418 - \mathrm{i}44)$ MeV and $z_{\pi\Sigma} = (1355 - \mathrm{i}86)$ MeV, so the peak and poles positions are not trivially related. The Pauli blocking shifts the $\Lambda(1405)$ structure above the $\bar{K}N$ threshold and the resonance is partially dissolved in nuclear matter. However, the incorporation of hadron selfenergies has an opposing effect moving the structure back below the threshold and leading to a rapid increase of attraction in the real part of the amplitude for energies about 30 MeV below the $\bar{K}N$ threshold. Since the K^-n amplitude is much smaller in magnitude and its energy dependence is not so profound, the overall effect on K^- propagation in nuclear matter is as follows. While antikaon feels a moderate attraction at energies around and above the threshold much larger attraction is anticipated at subthreshold energies. This result is in line with phenomenological analysis of kaonic atoms, though even more attraction is required by the data, apparently due to $\bar{K}NN$ absorption [5].

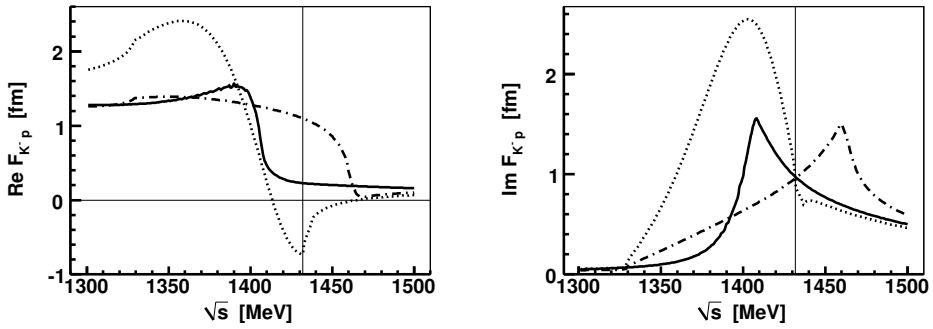

Figure 1: Energy dependence of the real (left panel) and imaginary (right panel) parts of the K^-p amplitude generated with the NLO30 model of Ref. [3]. The dotted lines show the free-space amplitude, the dot-dashed lines demostrate the effect of Pauli blocking and the dashed lines show the combined effect of Pauli blocking and hadron selfenergies. The $\bar{K}N$ threshold is marked by the thin vertical line.

While the subthreshold energy dependence of the $\bar{K}N$ amplitude is strongly affected by nuclear medium, the effect on the ηN amplitude is much less profound at least at subthreshold energies. This can be seen in Fig. 2 where the impacts of Pauli blocking and hadron selfenergies are visualized. The peak structure observed in the figure can be assigned to the $N^*(1535)$ resonance generated dynamically by the model. It is shifted to higher energies due to Pauli blocking and made more pronounced. The implementation of hadron selfenergies spreads the resonance structure over a large interval of energies and it practically dissolves in the nuclear matter. The main difference with respect to the $\bar{K}N$ case may be related to a different origin of the dynamically generated resonances. While the $\Lambda(1405)$ results from a quasi-bound $\bar{K}N$ molecular state the $N^*(1535)$ originates from a virtual $K\Xi$ state that is shifted to much lower energies by inter-channel dynamics. In effect, the in-medium dynamics of the $N^*(1535)$ resonance is not so strongly correlated with the ηN system as it is in the $\bar{K}N$ sector. Still, the ηN scattering length is reduced from $a_{\eta N} = (0.65 + \mathrm{i}0.15)$ fm in a free space to about $a_{\eta N} = (0.35 + \mathrm{i}0.13)$ fm in nuclear matter. This results into a sizeable reduction of η-nuclear attraction at the ηN threshold. However, the effect is much smaller at energies about 20-30

MeV below the threshold that are relevant for a possible existence of η-nuclear bound states.

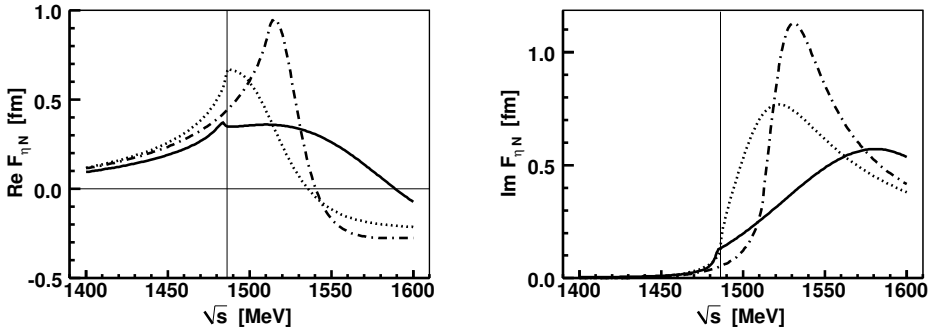

Figure 2: Energy dependence of the real (left panel) and imaginary (right panel) parts of the ηN amplitude obtained with the NLO30$_\eta$ model from Ref. [4]. The dotted lines show the free-space amplitude, the dot-dashed lines demostrate the effect of Pauli blocking and the dashed lines show the combined effect of Pauli blocking and hadron selfenergies. The ηN threshold is marked by the thin vertical line.

4 Summary

We have looked at an impact of nuclear medium on the energy dependence of the $\bar{K}N$ and ηN amplitudes. The most striking feature of the in-medium $\bar{K}N$ amplitude is represented by a sharp increase of the $\bar{K}N$ attraction at energies about $30 - 40$ MeV below the threshold. As it was shown in Refs. [2], [5] an anticipated energy shift from threshold to subthreshold $\bar{K}N$ energies provides a link between the shallow $\bar{K}$-nuclear optical potentials obtained microscopically from threshold $\bar{K}N$ interactions and the phenomenological deep ones deduced from kaonic atoms data. On the contrary, the ηN attraction is reduced in nuclear matter, both by the Pauli blocking and by the hadron selfenergies. Nevertheless, the subthreshold energy region is affected only moderately and it was shown in [6] that the in-medium ηN attraction appears sufficient to bind the η mesons in nuclei.

Acknowledgments

The work of A. C. was supported by the Grant Agency of Czech Republic, Grant No. P203/12/2126.

References

[1] N. Kaiser, P. B. Siegel, W. Weise, Nucl. Phys. **A594** 325 (1995).
[2] A. Cieplý, E. Friedman, A. Gal, D. Gazda, J. Mareš, Phys. Rev. **C84** 045206 (2011).
[3] A. Cieplý, J. Smejkal, Nucl. Phys. **A881** 115 (2012).
[4] A. Cieplý, J. Smejkal, Nucl. Phys. **A919** 46 (2013).
[5] E. Friedman, A. Gal, Nucl. Phys. **A881** 150 (2012).
[6] A. Cieplý, E. Friedman, A. Gal, J. Mareš, Nucl. Phys. **A925** 126 (2014).

Search for a $\pi\Lambda N - \pi\Sigma N$ dibaryon in p+p@3.5 GeV

J.C. Berger-Chen[1,2], *L. Fabbietti*[1,2] for the HADES Collaboration

[1]Physik Department E12, Technische Universität München, 85748 Garching, Germany
[2]Excellence Cluster 'Origin and Structure of the Universe', 85748 Garching, Germany

DOI: http://dx.doi.org/10.3204/DESY-PROC-2014-04/101

This work is dedicated to the search for a $\pi\Lambda N - \pi\Sigma N$ resonance $\mathcal{Y}$ with the quantum numbers $(Y, I, J^P) = (1, \frac{3}{2}, 2^+)$. The double charged $\Sigma(1385)N - \Delta(1232)Y$ quasibound state was looked for in the reaction $pp \to \mathcal{Y}^{++}K^0$ with its unique decay into Σ^+ and proton measured with the HADES setup at a kinetic beam energy of 3.5 GeV. The analysis including background determination and a description of the data with a K^0_S Monte Carlo cocktail are presented.

1 Introduction

Recently, a relativistic three-body Fadeev formalism suitable for two-body p-wave interactions was applied to calculate the $\pi\Lambda N - \pi\Sigma N$ coupled channel system with $I = \frac{3}{2}$ and $J^P = 2^+$ [1]. Dominant p-wave interactions in the πN and $\pi\Lambda - \pi\Sigma$ channels were found with a large contribution of the $\Delta(1232)$ and $\Sigma(1385)$ resonances. A rather robust $\pi\Lambda N$ resonance located around 10-20 MeV/c^2 below the $\pi\Sigma N$ threshold was obtained, which can be viewed as an s-wave dibaryon $\mathcal{Y}$ with $(Y, I, J^P) = (1, \frac{3}{2}, 2^+)$ equivalent to an $\Sigma(1385)N - \Delta(1232)Y$ quasibound state bound by over 50 MeV. The double charged state can be uniquely measured in p+p collisions at energies above the $\Sigma(1385)$ production threshold ($pp \to \mathcal{Y}^{++}K^0 \to \Sigma^+ pK^0$), whereas the $\mathcal{Y}^+$ formed together with a K^+ ($\mathcal{Y}^+ \to \Sigma^+ n/\Sigma^0 p$) may not be distinguishable from the decay of a $\bar{K}NN$ quasibound state ($K^- pp \to \Sigma^+ n/\Sigma^0 p$). Thus, the HADES p+p data measured at 3.5 GeV, which is well above $\Sigma(1385)$ production threshold [2], are perfectly suited to search for the $\mathcal{Y}^{++}$ dibaryon in its unique decay. Thereby, knowledge gained by a previous analysis [3] on exclusive K^0 production channels in the same data set were incorporated meaning that the determined cross sections and angular anisotropies were included in this work. The main result of that analysis was the finding of predominant contributions by K^0 channels associated with resonances ($\Delta(1232)$ and $\Sigma(1385)$) thus confirming earlier observations made in the study of resonance contributions ($\Lambda(1405)$, $\Sigma(1385)^0$, $\Lambda(1520)$, $\Delta(1232)$, N^*, K^{*0}) to the $\Sigma^\pm\pi^\pm pK^+$ final states [4].

2 The HADES experiment

The **H**igh-**A**cceptance **D**i-**E**lectron **S**pectrometer (HADES) [5] is a versatile detector system located at GSI Helmholtzzentrum (Darmstadt, Germany) and is provided by the SIS18 with heavy ion beams of 1-2 AGeV or proton beams up to 3.5 GeV impinging on a fixed target. The

HADES setup has an azimuthal coverage of 85% and an acceptance in polar angles from 18° to 85°. The momentum resolution was determined to be $\Delta p/p \approx 3\%$.

The most important detector components used in the presented analysis are first of all the Multi-Wire Drift Chambers (MDCs), where two layers are mounted in front of the superconducting magnet with a toroidal field and two layers behind it to help in track finding, momentum reconstruction and particle identification via the specific energy loss information. Furthermore, a Time-Of-Flight wall at the end of the setup allows for online multiplicity triggering to enhance inelastic events in the recorded data sample.

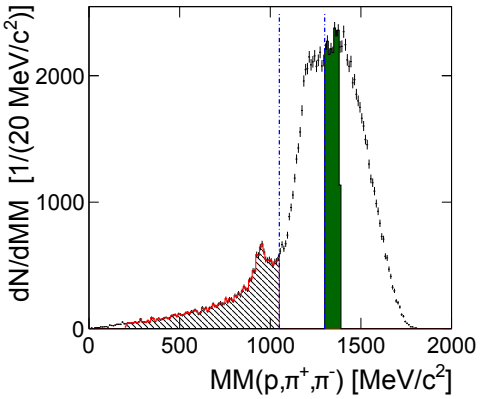

Figure 1: Missing mass spectrum with respect to the proton, π^+ and π^-. The red-hatched and green-filled areas indicate the mass regions used for the low mass (LM) and the high mass (HM) sideband sample. The blue dash-dotted lines show the cut on the Σ^+ mass.

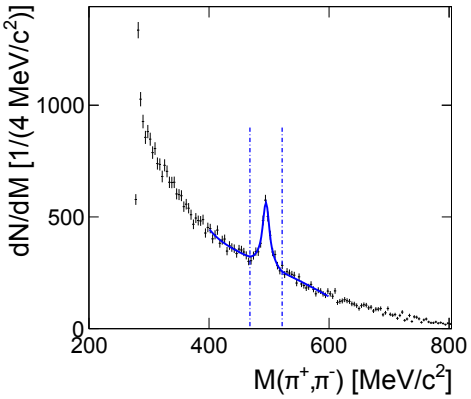

Figure 2: $\pi^+\pi^-$-invariant mass spectrum including secondary vertex cuts [3] and fitted with the sum of two Gaussians, a Landau and a polynomial. The blue dash-dotted lines indicate the 3σ-cut region on the K^0_S mass.

3 The analysis and preliminary results

As mentioned above the $\pi\Lambda N - \pi\Sigma N$ resonance, which can be denoted as $\mathcal{Y}$, can be uniquely measured through the reaction $pp \to \mathcal{Y}^{++}K^0 \to \Sigma^+ pK^0$. Since the long-lived K^0_L cannot be detected by the HADES setup, this analysis concentrates on the short-lived K^0_S and its charged decay into π^+ and π^- ($BR \approx 69.20\%$). A four particle selection was implemented to enhance the above reaction by choosing events with a proton, π^+, π^+ and a π^-. The proton is thereby assumed to be produced directly, whereas one of the π^+ should originate from the decay of the Σ^+. This way, only the decay of the Σ^+ into a neutron and a π^+ ($BR \approx 48.31\%$) was considered neglecting the branching into proton and π^0 ($BR \approx 51.57\%$), since the heavier baryon is more likely to be boosted into the forward region, where HADES has no acceptance.

3.1 Background determination

The background determination in the four particle data sample is a crucial step in this analysis and consists mainly of combinatorial background generated by non-strange reactions. Contri-

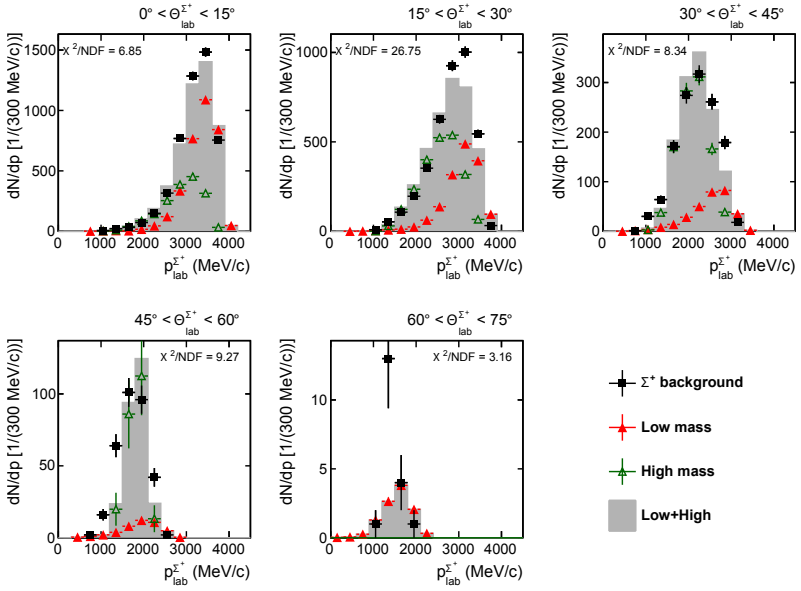

Figure 3: Momentum distribution of the Σ^+ background in five bins of $\Theta^{\Sigma^+}_{lab}$ with the cuts: MM(p,π^+,π^-) = 1050-1300 MeV/c^2 and 810 MeV/c^2 > MM(p,π^+,π^+,π^-) > 1045 MeV/c^2. Overlayed are the spectra for the LM and HM sideband samples with their sum in gray.

butions from other K^0_S production channels can be modeled in a first attempt by an incoherent Monte Carlo cocktail, which individual cross sections were obtained in a separate analysis of the same data set [3]. To emulate the background, a so-called sideband analysis was performed on the missing mass distribution to the proton, π^+ and π^- (Fig. 1). Only a rough cut on the primary vertex was applied here to reject off-target events. Furthermore, no additional mass cut, e.g. on the K^0_S, was applied to keep enough statistics for the sideband analysis. A data sample was defined in this spectrum, which contains data with missing masses lower (LM) and higher (HM) than the Σ^+ (1050 MeV/c^2 > MM(p,π^+,π^-) > 1300 MeV/c^2) and thus include only background. They are indicated as red-hatched and green-filled areas in the plot and are chosen such to have about the same integral. This background sample needs to reproduce the kinematics, which remains in the Σ^+ mass region. Therefore, the momentum distributions of the sideband samples LM and HM were fitted in five individual Θ_{lab} bins to describe the momentum distribution of a Σ^+ background sample, which was obtained through a cut on the missing mass spectrum to the four particles proton, π^+, π^+ and π^- (810 MeV/c^2 > MM(p,π^+,π^+,π^-) > 1045 MeV/c^2). From the exclusive analysis discussed in [3] it is known that the reaction $pp \to \Sigma^+ p K^0_S$ does not contribute in these mass regimes. Figure 3 shows the mentioned momentum distributions of Σ^+ candidates and quotes the achieved χ^2/NDF for each Θ_{lab} bin, which mostly stays below 10 except for $\Theta_{lab} = 15° - 30°$ with $\chi^2/NDF = 26.75$. The conclusion is, that the sideband sample does not fully describe the Σ^+ background and further work is necessary here. However, the description is good enough to use the so determined relative contributions of the LM and HM samples to the full background model for a first try to search for a signal of the $\mathcal{Y}^{++}$ dibaryon, which should be located around 10-20 MeV/c^2 below the $\pi\Sigma N$ threshold (2267 MeV/c^2) [1].

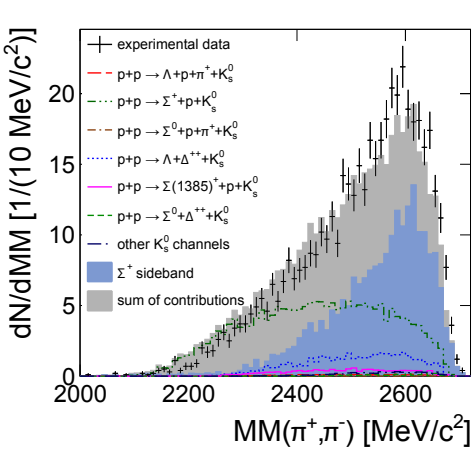

Figure 4: Missing mass spectrum with respect to the π^+ and π^- with a cut on the K^0_S and the Σ^+ mass. The contributions of the K^0_S reactions are according to the findings of [3].

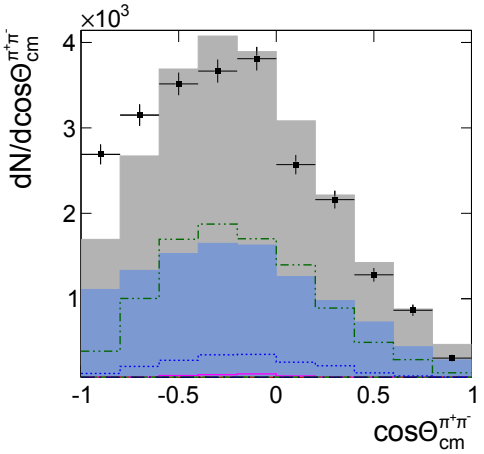

Figure 5: Angular distribution of the $\pi^+\pi^-$-system in the center-of-mass with a cut on the K^0_S and on the Σ^+ mass. The color code is the same as written in the label of Figure 4.

3.2 Preliminary results

In Figure 4 the MM(π^+,π^-) distribution is depicted, which contains a cut on the Σ^+ mass (1050 MeV/c^2 < MM(p,π^+,π^-) < 1300 MeV/c^2) and a 3σ-cut on the K^0_S mass determined in the $\pi^+\pi^-$-invariant mass distribution (Fig. 2) by a fit with a sum of two Gaussians for the signal and a Landau plus a polynomial function for the background. However, no enhancement is seen in the interesting region below the $\pi\Sigma N$ threshold. The missing mass spectrum is rather well described by the incoherent K^0_S cocktail determined in [3] and the background model, from which the relative contribution was obtained by a simultaneous fit to this missing mass spectrum and the $\pi^+\pi^-$-angular distribution $cos\Theta^{\pi^+\pi^-}_{cm}$ (Fig. 5) with fixed cross sections and angular anisotropies for the K^0_S reactions. Although the χ^2/NDF extracted from the simultaneous fit to the two spectra of 5.07 is rather good, some disagreement between model and data is observed at $cos\Theta^{\pi^+\pi^-}_{cm} < -0.5$, which can be due to the imperfect background model.

4 Summary and outlook

The $\pi\Lambda N - \pi\Sigma N$ resonance $\mathcal{Y}$ with $(Y, I, J^P) = (1, \frac{3}{2}, 2^+)$ was searched for in the reaction $pp \to \mathcal{Y}^{++}K^0 \to \Sigma^+ pK^0 \to n\pi^+ pK^0$. Thereby, a sideband analysis was performed to model the Σ^+ background in the distribution MM(p,π^+,π^-). A satisfactory description was achieved to use this background model in the further study of the missing mass spectrum MM(π^+,π^-) with help of the K^0_S reaction cocktail determined in [3]. No obvious enhancement is seen in the MM(π^+,π^-) below the $\pi\Sigma N$ threshold, in fact the data is described rather well by the model. However, no interference effects were taken into account, which can be only studied with help of a Partial Wave Analysis (PWA) similar as for the search of the K^-pp quasibound state in the same data set [6].

Acknowledgements

The authors gratefully acknowledge the support of the TUM Graduate School's Faculty Graduate Center Physics at Technische Universität München, Germany, PTDC/FIS/113339/2009 LIP Coimbra, NCN grant 2013/10/M/ST2/00042 SIP JUC Cracow, Helmholtz Alliance HA216/EMMI GSI Darmstadt, VH-NG-823, Helmholtz Alliance HA216/EMMI TU Darmstadt, 283286, 05P12CRGHE HZDR Dresden, Helmholtz Alliance HA216/EMMI, HIC for FAIR (LOEWE), GSI F&E Goethe-University, Frankfurt VH-NG-330, BMBF 06MT7180 TU München, Garching BMBF:05P12RGGHM JLU Giessen, Giessen UCY/3411-23100, University Cyprus CNRS/IN2P3, IPN Orsay, Orsay MSMT LG 12007, AS CR M100481202, GACR 13-06759S NPI AS CR, Rez, EU Contract No. HP3-283286.

References

[1] H. Garcilazo and A. Gal. Relativistic three-body calculations of a Y=1, I=3/2, JP=2+ $\pi\Lambda N - \pi\Sigma N$ dibaryon. *Nucl. Phys.*, A897:167–178, 2013.

[2] G. Agakishiev et al. Baryonic resonances close to the $\bar{K}$-N threshold: The Case of $\Sigma(1385)^+$ in pp collisions. *Phys. Rev.*, C85:035203, 2012.

[3] G. Agakishiev et al. Associate K^0 production in p+p collisions at 3.5 GeV: The role of $\Delta(1232)^{++}$. *Phys. Rev.*, C90:015202, 2014.

[4] G. Agakishiev et al. Production of $\Sigma^{\pm}\pi^{\pm}pK^+$ in p+p reactions at 3.5 GeV beam energy. *Nucl. Phys.*, A881:178–186, 2012.

[5] G. Agakishiev et al. The High-Acceptance Dielectron Spectrometer HADES. *Eur. Phys. J.*, A41:243–277, 2009.

[6] E. Epple. Experimental news from a theoretical state: The 'ppK^-'. *PoS*, BORMIO2014:049, 2014.

η' mesic nucleus spectroscopy with (p, d) reaction at GSI

Yoshiki K. Tanaka[1], *Yassid Ayyad*[2], *Jose Benlliure*[3], *Kai-Thomas Brinkmann*[4], *Stefan Friedrich*[4], *Hiroyuki Fujioka*[5], *Hans Geissel*[4,6], *Jnaneswari Gellanki*[7], *Chenlei Guo*[8], *Eric Gutz*[4], *Emma Haettner*[6], *Muhsin N. Harakeh*[7], *Ryugo S. Hayano*[1], *Yuko Higashi*[9], *Satoru Hirenzaki*[9], *Christine Hornung*[4], *Yoichi Igarashi*[10], *Natsumi Ikeno*[11,12], *Kenta Itahashi*[13], *Masahiko Iwasaki*[13], *Daisuke Jido*[14], *Nasser Kalantar-Nayestanaki*[7], *Rituparna Kanungo*[15], *Ronja Knoebel*[4,6], *Nikolaus Kurz*[6], *Volker Metag*[4], *Ivan Mukha*[6], *Tomofumi Nagae*[5], *Hideko Nagahiro*[9], *Mariana Nanova*[4], *Takahiro Nishi*[1], *Hooi Jin Ong*[2], *Stephane Pietri*[6], *Andrej Prochazka*[6], *Christophe Rappold*[6], *Moritz P. Reiter*[6], *Jose Luis Rodríguez Sánchez*[3], *Christoph Scheidenberger*[4,6], *Haik Simon*[6], *Branislav Sitar*[16], *Peter Strmen*[16], *Baohua Sun*[8], *Ken Suzuki*[17], *Imrich Szarka*[16], *Maya Takechi*[18], *Isao Tanihata*[2,8], *Satoru Terashima*[8], *Yuni N. Watanabe*[1], *Helmut Weick*[6], *Eberhard Widmann*[17], *John S. Winfield*[6], *Xiaodong Xu*[6], *Hiroki Yamakami*[5], *Jianwei Zhao*[8]

[1]The University of Tokyo, 7-3-1 Hongo, Bunkyo, 113-0033 Tokyo, Japan
[2]RCNP, Osaka University, 10-1 Mihogaoka, Ibaraki, 567-0047 Osaka, Japan
[3]Universidade de Santiago de Compostela, 15782 Santiago de Compostela, Spain
[4]Universität Giessen, Heinrich-Buff-Ring 16, 35392 Giessen, Germany
[5]Kyoto University, Kitashirakawa-Oiwakecho, Sakyo-ku, 606-8502 Kyoto, Japan
[6]GSI, Planckstrasse 1, 64291 Darmstadt, Germany
[7]KVI-CART, University of Groningen, Zernikelaan 25, 9747 AA Groningen, the Netherlands
[8]Beihang University, Xueyuan Road 37, Haidian District, 100191 Beijing, China
[9]Nara Women's University, Kita-Uoya Nishi-Machi, 630-8506 Nara, Japan
[10]KEK, 1-1 Oho, Tsukuba, 305-0801 Ibaraki, Japan
[11]Tohoku University, 6-3 Aoba, Aramaki, Aoba, Sendai, 980-8578 Miyagi, Japan
[12]YITP, Kyoto University, Kitashirakawa-Oiwakecho, Sakyo-ku, 606-8502 Kyoto, Japan
[13]Nishina Center, RIKEN, 2-1 Hirosawa, Wako, 351-0198 Saitama, Japan
[14]Tokyo Metropolitan University, 1-1 Minami-Osawa, Hachioji, 192-0397 Tokyo, Japan
[15]Saint Mary's University, 923 Robie Street, Halifax, Nova Scotia B3H 3C3, Canada
[16]Comenius University Bratislava, Mlynská dolina, 842 48 Bratislava, Slovakia
[17]Stefan-Meyer-Institut für subatomare Physik, Boltzmangasse 3, 1090 Vienna, Austria
[18]Niigata University, 8050 Ikarashi 2-no-cho, Nishi-ku, 950-2181 Niigata, Japan

DOI: http://dx.doi.org/10.3204/DESY-PROC-2014-04/106

We have performed a spectroscopic experiment using the ^{12}C(p, d) reaction at 2.5 GeV incident energy to search for η' mesic nuclei for the first time. A missing-mass spectrum of the reaction was obtained around the η' emission threshold using the fragment separator FRS at GSI. An overview of the experiment including the status of the analysis is given.

1 Introduction

One feature of the η' meson is its large mass compared with other pseudoscalar mesons. This is theoretically understood as a consequence of the $U_A(1)$ anomaly, which contributes to the η' mass only with spontaneous and/or explicit breaking of chiral symmetry in the low-energy region of QCD [1, 2]. In the nuclear medium, in which chiral symmetry is partially restored, the mass of the η' meson can be reduced. Such a mass reduction induces an attraction between an η' and a nucleus, and η' meson-nucleus bound states (η' mesic nuclei) may exist [3, 4, 5].

So far, there are some theoretical and experimental studies for the η' meson in the nuclear medium. For example, in Nambu–Jona-Lasinio model calculations, around 150 MeV mass reduction is predicted at normal nuclear density [3, 6]. Experimentally, the CBELSA/TAPS collaboration claimed an attractive potential of about -37 MeV and an absorption width of $15-25$ MeV at nuclear matter density for an average η' momentum of 1050 MeV/c [7]. This small width implies that the decay width of η' mesic nuclei can be small as well.

In order to search for η' mesic nuclei and study in-medium properties of the η' meson, we performed an inclusive measurement of the $^{12}\mathrm{C}(p, d)$ reaction for the first time in August 2014 [8]. A proton beam with kinetic energy of 2.5 GeV was used potentially to produce η' mesic states in ^{11}C nuclei, and the missing-mass for the reaction was measured by analyzing the momentum of the ejectile deuteron. In such an inclusive measurement, the signal-to-noise ratio is expected to be very small due to other background processes such as multi-pion production ($p + N \to d + \pi$'s). Thus a measurement with good statistics is required. Our simulation shows that observation of peak structures in an inclusive spectrum is feasible with the experimental conditions prevailing at the Fragment Separator (FRS) of GSI [9], if the mass reduction of the η' meson at normal nuclear density is as large as 150 MeV and the in-medium width is around 20 MeV [8].

2 Experiment

2.1 Experimental setup

Figure 1 shows the detector setup in the initial experiment carried out at the FRS. A 2.5 GeV proton beam with an intensity of the order of 10^{10} per a 4-second spill accelerated in SIS-18 synchrotron impinged onto a 4 g/cm^2 thick carbon target, and the ejectile deuterons were momentum-analyzed by the FRS used as a spectrometer. The tracks of the deuterons were measured by two sets of multi-wire drift chambers (MWDC's) at a dispersive focal plane (S4) with the dispersion of 3.6 cm/% to derive their momenta. The overall missing-mass resolution is expected to be about $\sigma \sim 1.6$ MeV/c^2, which is dominated by the straggling of the energy loss in the target. This is much smaller than the expected decay width of η' mesic nuclei and is sufficient for the measurement.

With this setup, a large amount of protons produced by the (p, p') inelastic scattering reach the S4 focal plane as a background. Thus, particle identification is necessary based on the velocity difference between the signal deuterons ($\beta_d \sim 0.83$) and the background protons ($\beta_p \sim 0.95$). Plastic scintillators (SC2H, SC2V, SC41, and SC42) were installed at the S2 and S4 areas for time-of-flight (TOF) measurements. Moreover, high-refractive-index aerogel Čerenkov detectors (HIRAC and mini-HIRAC) with silica aerogel radiators of a refractive index of $1.17-1.18$ [10] and a total-reflection Čerenkov detector (TORCH) with an Acrylite radiator were placed for further rejection of the background protons.

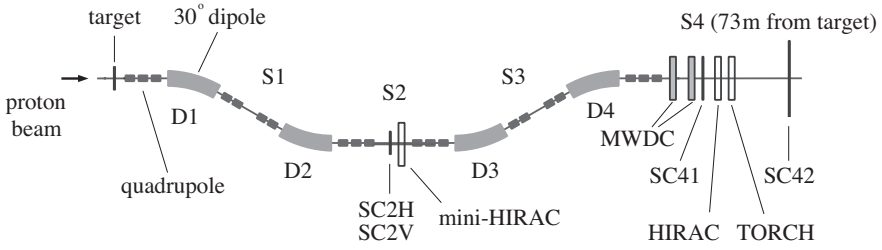

Figure 1: A schematic view of the experimental setup at the FRS. See the text for details.

2.2 Particle identification

A measured TOF spectrum between S2 and S4 with an unbiased trigger is shown in Figure 2. The smaller peak on the right side corresponds to the signal deuterons, and the higher peak on the left side is the background protons. The TOF difference between these two peaks is about 20 ns, which is consistent with our calculation. The ratio of the deuterons to the protons was about 1 to 200, and the total particle rate at the S4 focal plane was about 8×10^5/spill.

In the production measurements, we used a hardware trigger based on the S2-S4 TOF to reject the background protons and reduce the acquisition rate to the order of 10^3/s. Figure 3 shows the S2-S4 TOF and the TOF between the two scintillators at S4 (SC41-SC42) under this trigger condition. The proton peak seen in Figure 2 is rejected without influencing the signal deuterons. In Figure 3, accidental multi-proton events are still visible, whose amount is about the same as that of the signal deuterons. These can be rejected in the offline analysis by the TOF between the two S4 scintillators as shown in Figure 3, a waveform analysis of the S2 scintillator signals, and an analysis of the three Čerenkov detectors.

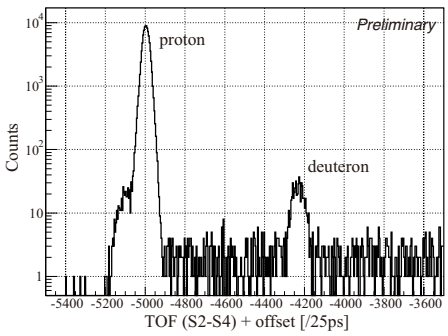

Figure 2: A measured TOF histogram between S2 and S4 by SC2H and SC41 with an unbiased trigger.

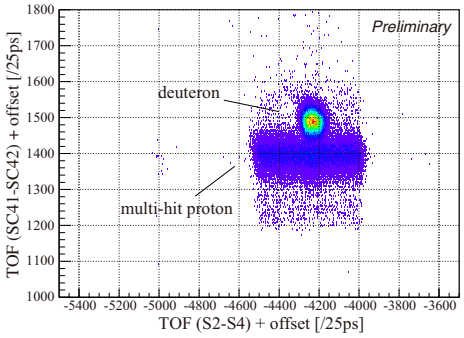

Figure 3: Measured TOF between S2 and S4 by SC2H and SC41 and TOF between two scintillators (SC41-SC42) at S4 with the TOF(S2-S4) trigger.

2.3 Momentum calibration

The momentum calibration was carried out by measuring the $d(p, d)p$ backward elastic scattering using a 1.6 GeV proton beam and a CD_2 target. In this reaction, monochromatic deuterons with the momentum of 2.8 GeV/c are emitted, which is at the middle of the momentum range in the production measurement. By measuring these deuterons at the S4 focal plane, the proper functionality of the whole system was confirmed and the ion-optical properties of the spectrometer were obtained.

2.4 Summary of measurements

We measured the $^{12}C(p, d)$ reaction with a 2.5 GeV proton beam for about 5 days. The excitation energy from roughly -90 MeV to $+40$ MeV from the η' emission threshold was investigated by measurements with several scaling factors for the FRS magnetic fields from 0.98 to 1.02. High statistical significance was achieved by measuring about $(5–10)\times10^6$ deuterons for each setting.

As a reference, the $d(p, d)$ reaction was also measured in the same momentum range of the deuterons using a 2.5 GeV proton beam and a CD_2 target. In this measurement, peak structures related to η' mesic states are not expected. Thus, it provides information for understanding the background processes in this inclusive measurement.

3 Summary and future prospects

We have performed an inclusive measurement of the $^{12}C(p, d)$ reaction with a 2.5 GeV proton beam to search for η' mesic nuclei for the first time. A missing-mass spectrum of the $^{12}C(p, d)$ reaction was measured around the η' emission threshold with the expected spectral resolution of $\sigma \sim 1.6$ MeV/c^2. The analysis of the spectrum is now in progress.

For FAIR, we are planning a semi-exclusive measurement of the (p, dp) reaction as well as an inclusive measurement of the (p, d) reaction with better statistics. The R&D is on-going.

Acknowledgements

The experiment was performed in the framework of the Super-FRS collaboration for FAIR. This work is partly supported by a Grant-in-Aid for JSPS Fellows (No. 258155).

References

[1] D. Jido, H. Nagahiro, and S. Hirenzaki, Phys. Rev. C **85** 032201(R) (2012).
[2] S. H. Lee and T. Hatsuda, Phys. Rev. D **54** 1871 (1996).
[3] H. Nagahiro, M. Takizawa, and S. Hirenzaki, Phys. Rev. C **74** 045203 (2006).
[4] H. Nagahiro and S. Hirenzaki, Phys. Rev. Lett. **94** 232503 (2005).
[5] H. Nagahiro *et al.*, Phys. Rev. C **87** 045201 (2013).
[6] P. Costa, M. C. Ruivo, and Yu. L. Kalinovsky, Phys. Lett. B **560** 171 (2003).
[7] M. Nanova *et al.*, Phys. Lett. B **727** 417 (2013); M. Nanova *et al.*, *ibid.* **710** 600 (2012).
[8] K. Itahashi *et al.*, Prog. Theor. Phys. **128** 601 (2012).
[9] H. Geissel *et al.*, Nucl. Instr. Meth. B **70** 286 (1992).
[10] M. Tabata *et al.*, Nucl. Instr. Meth. A **623** 339 (2010).

Dilepton Production in Transport-based Approaches

Janus Weil[1], *Stephan Endres*[1], *Hendrik van Hees*[1], *Marcus Bleicher*[1], *Ulrich Mosel*[2]

[1]Frankfurt Institute for Advanced Studies , Ruth-Moufang-Str. 1, 60438 Frankfurt, Germany
[2]Institut für Theoretische Physik, JLU Giessen, Heinrich-Buff-Ring 16, 35392 Giessen, Germany

DOI: http://dx.doi.org/10.3204/DESY-PROC-2014-04/173

We investigate dilepton production in transport-based approaches and show that the baryon couplings of the ρ meson represent the most important ingredient for understanding the measured dilepton spectra. At low energies (of a few GeV), the baryon resonances naturally play a larger role and affect already the vacuum spectra via Dalitz-like contributions, which can be captured well in an on-shell-transport scheme. At higher energies, the baryons mostly affect the in-medium self energy of the ρ, which is harder to tackle in transport models and requires advanced techniques.

1 Introduction

Lepton pairs are known to be an ideal probe for studying phenomena at high densities and temperatures. They are created at all stages of a heavy-ion collision, but unlike hadrons they can escape the hot and dense zone almost undisturbed (since they only interact electromagnetically) and thus can carry genuine in-medium information out to the detector. Dileptons are particularly well-suited to study the in-medium properties of vector mesons, since the latter can directly convert into a virtual photon, and thus a lepton pair [1, 2]. One of the groundbreaking experiments in this field was NA60 at the CERN SPS, which revealed that the ρ spectral function is strongly broadened in the medium. Calculations by Rapp et al. have shown that this collisional broadening is mostly driven by baryonic effects, i.e., the coupling of the ρ meson to baryon resonances (N^*, Δ^*) [3]. In the low-energy regime, the data taken by the DLS detector have puzzled theorists for years and have recently been confirmed and extended by new measurements by the HADES collaboration [4, 5, 6, 7, 8, 9]. At such low energies, it is expected that not only the in-medium properties are determined by baryonic effects, but that already the production mechanism of vector mesons is dominated by the coupling to baryons (even in vacuum).

2 The model: hadronic transport + VMD

Already our previous investigations [10] based on the GiBUU transport model [11] have shown that the baryonic N^* and Δ^* resonances can give important contributions to dilepton spectra at SIS energies, both from pp and AA collisions, via Dalitz-like contributions. This finding was based on the assumption that these resonances decay into a lepton pair exclusively via an intermediate ρ meson (i.e. strict vector-meson dominance). In the transport simulation, the Dalitz decays $R \to e^+e^-N$ are treated as a two-step process, where the first part is an $R \to \rho N$

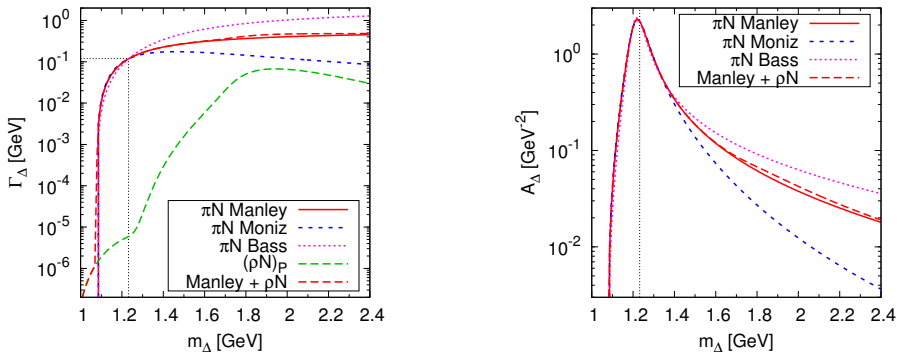

Figure 1: Partial widths for the πN and ρN decay channels (left) and spectral function (right) of the Δ resonance as a function of the off-shell mass.

decay, followed by a subsequent conversion of the ρ into a lepton pair ($\rho \to e^+e^-$). The branching ratios for the $R \to \rho N$ decay are taken from the partial-wave analysis by Manley et al. [12], while the decay width for the second part is calculated under the strict-VMD assumption as $\Gamma_{ee}(m) = \Gamma_0 \cdot (M/m)^3$. For the present study we extend the VMD assumption also to the $\Delta(1232)$ state, whose dilepton contribution has been subject to much controversy recently. Since the Δ is too light to decay into an on-shell ρ meson, it is difficult to determine its coupling to the ρ experimentally, and consequently Manley and other analyses do not find any sign of a $\Delta \to \rho N$ decay. Nevertheless the Δ has a photonic decay mode, which means that also a dilepton Dalitz decay channel must exist. The latter has been claimed to be particularly significant for dilepton spectra at SIS energies [13]. However, this argument was based on the continuation of the photon decay into the time-like region neglecting the involved electromagnetic transition form factor [14]. Unfortunately this form factor is essentially unknown in the time-like region from the experimental point of view. However, it is clear that it can significantly alter the dilepton yield from the Δ (easily by an order of magnitude) [15]. In order to deal with this situation, we choose to apply the assumption of strict VMD not only to the N^* and Δ^* resonances, but also to the Δ itself, assuming a p-wave (i.e. $L = 1$) decay into ρN. Together with the other resonance channels, this results in a consistent model with clear assumptions, which can be tested against experiment. One free parameter that is left to fix in this approach is the on-shell branching ratio of $\Delta \to \rho N$. We use a value of $5 \cdot 10^{-5}$, in order to produce dilepton yields which are roughly equivalent to the radiative decay for small Δ masses and compatible with the HADES data at low energies. Fig. 1 shows the partial decay width into ρN, which is extremely small at the Δ pole mass, but grows significantly when going to larger masses. But even in the very high-mass tail, the additional decay mode has only little influence on the overall width and spectral function of the Δ (even less than the different parametrizations of the πN width).

3 Dilepton spectra from p+p collisions

Fig. 2 shows a comparison of our simulation results for p+p collisions (inside the detector acceptance) to the dilepton mass spectra measured by the HADES collaboration at three different beam energies. Since the mesonic decay channels have not changed with respect to earlier works [10], we concentrate here on the discussion of the baryonic contributions. The Δ is shown in two

approaches, a QED-like radiative decay [14] (neglecting the occurring form factor), and a VMD decay $\Delta \to \rho N \to e^+e^-N$. While both give rather similar results at low energies (where the form-factor effects are still small), the differences get larger at higher energies. There the VMD curve develops a clear peak at the ρ mass and a bump around $m_\Delta - m_N \approx 300$ MeV (from the on-shell Δs), while the QED curve is flat and structureless (due to the absence of a form factor). However, both models agree on the fact that the Δ contribution becomes sub-dominant at higher energies and is exceeded by other contributions (in particular the higher resonances N^* and Δ^* become more significant). Thus the data can not distinguish between both models.

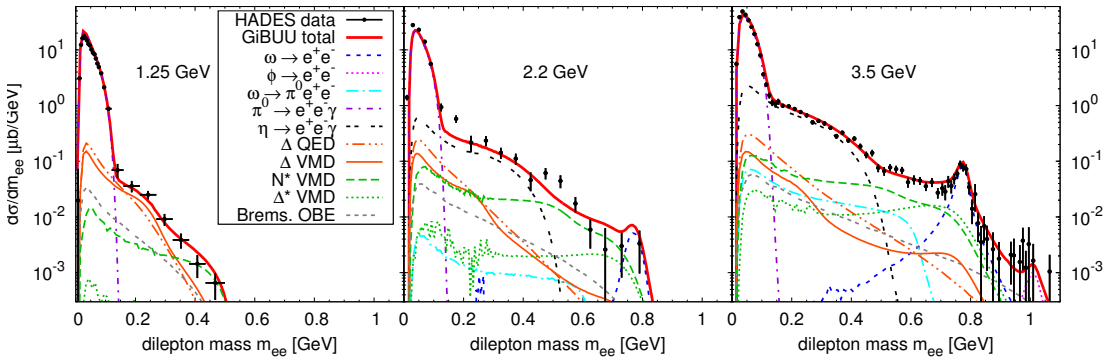

Figure 2: Dilepton mass spectra for pp collisions, in comparison to the data from [4, 5, 6].

4 Dilepton spectra from A+A collisions

Fig. 3 shows our results of dilepton spectra from nucleus-nucleus collisions compared to the HADES data. The light CC system has been measured at two different energies (1 and 2 AGeV) and the heavier ArKCl at the intermediate energy of 1.76 AGeV. The best agreement with data is achieved in the CC system at 2 AGeV, where the spectrum above the pion mass is dominated by the η Dalitz and the baryonic VMD channels. In the 1 AGeV reaction, we see some underestimation at intermediate masses around 300 MeV, despite the inclusion of OBE Bremsstrahlung according to Shyam et al. [16]. Since there are many channels contributing with similar strength here, it is hard to tell where the underestimation originates from. In the medium-size ArKCl system, we see a similar underestimation at intermediate masses and a slight excess in the vector-meson pole region. One may be surprised that a pure (on-shell) transport approach without explicit inclusion of in-medium spectral functions achieves such a good agreement here, but that just shows the importance of Dalitz-like contributions of the baryons, which are captured well by our transport treatment.

5 Conclusions

We have shown that the HADES dilepton data from pp and AA collisions can be described rather well with a combination of a resonance-model-based transport approach with a strict-VMD coupling of the baryons to the em. sector, where a mix of different baryonic resonances contributes to the total dilepton yield. We can not reproduce the dominant contribution of

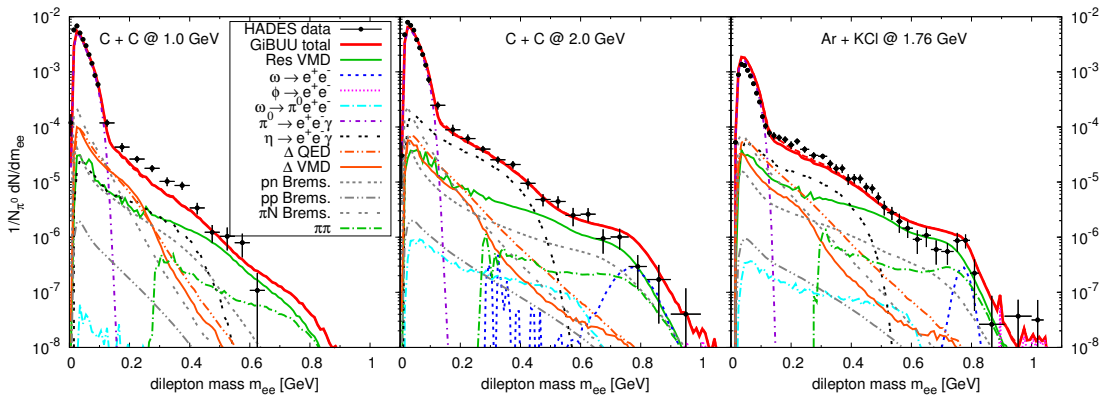

Figure 3: Dilepton mass spectra for AA collisions, in comparison to the data from [7, 8, 9].

the $\Delta(1232)$, which was claimed in other models [13]. In order to improve the description of heavy systems and to make the connection to higher energies, a proper dynamic treatment of in-medium spectral functions is required, which may be provided by the so-called "coarse-graining" approach, which is subject of ongoing investigations [17].

Acknowledgments

This work was supported by the Hessian Initiative for Excellence (LOEWE) through the Helmholtz International Center for FAIR and by the Federal Ministry of Education and Research (BMBF). J.W. acknowledges funding of a Helmholtz Young Investigator Group VH-NG-822 from the Helmholtz Association and GSI.

References

[1] S. Leupold, V. Metag, U. Mosel, Int. J. Mod. Phys. E 19, 147 (2010)
[2] R. Rapp, J. Wambach, H. van Hees, Landolt-Börnstein I/23, 4 (2010)
[3] H. van Hees, R. Rapp, Phys. Rev. Lett. 97, 102301 (2006)
[4] G. Agakishiev et al. (HADES Collaboration), Phys. Lett. B 690, 118 (2010)
[5] G. Agakishiev et al. (HADES Collaboration), Eur. Phys. J. A 48, 64 (2012)
[6] G. Agakishiev et al. (HADES Collaboration), Phys. Rev. C 85, 054005 (2012)
[7] G. Agakichiev et al. (HADES Collaboration), Phys. Rev. Lett. 98, 052302 (2007)
[8] G. Agakishiev et al. (HADES Collaboration), Phys. Lett. B 663, 43 (2008)
[9] G. Agakishiev et al. (HADES Collaboration), Phys. Rev. C 84, 014902 (2011)
[10] J. Weil, H. van Hees, U. Mosel, Eur. Phys. J. A 48, 111 (2012)
[11] O. Buss, T. Gaitanos, K. Gallmeister, H. van Hees, M. Kaskulov et al., Phys. Rep. 512, 1 (2012)
[12] D. Manley, E. Saleski, Phys. Rev. D 45, 4002 (1992)
[13] E. Bratkovskaya, J. Aichelin, M. Thomere, S. Vogel, M. Bleicher, Phys. Rev. C 87(6), 064907 (2013)
[14] M.I. Krivoruchenko, A. Faessler, Phys. Rev. D 65, 017502 (2002)
[15] G. Ramalho, M. Pena, Phys. Rev. D 85, 113014 (2012)
[16] R. Shyam, U. Mosel, Phys. Rev. C 82, 062201 (2010)
[17] S. Endres, H. van Hees, J. Weil, M. Bleicher, J. Phys. Conf. Ser. 503, 012039 (2014)

Chapter 5

Neutrinos and related astrophysical implications

Non-relativistic Majorana neutrinos in a thermal bath and leptogenesis

Simone Biondini

Technische Universität München, James-Franck-Str. 1, 85747 Garching, Germany

DOI: http://dx.doi.org/10.3204/DESY-PROC-2014-04/13

Neutrino oscillations, the evidence of dark matter and the baryon asymmetry in the universe can not be explained by the standard model of particle physics. Majorana fermions enter in many scenarios of physics beyond the standard model. For example, in the simplest leptogenesis framework, heavy Majorana neutrinos are at the origin of the baryon asymmetry. In the strong wash-out regime non-relativistic Majorana neutrinos produce the lepton asymmetry that is partially reprocessed into a baryon asymmetry. Moreover, all the interactions occur in a thermal medium, namely the universe in its early stage. We discuss an effective field theory approach to study the dynamics of non-relativistic Majorana particles in a thermal bath made of standard model particles. In particular, the decay width of Majorana neutrinos and the CP asymmetries are key ingredients for most leptogenesis models. We address the derivation of such quantities at finite temperature. We provide a formalism to calculate the thermal corrections to the CP asymmetry in the case of a hierarchical mass spectrum for heavy Majorana neutrinos.

1 Motivation and introduction

The standard model (SM) of particle physics can explain almost all the available experimental data and observations. However, few remarkable evidences, such as the dark matter and the baryon asymmetry in the universe, demand for new physics. Let us focus on the existing imbalance between matter and anti-matter in the universe that may be expressed in terms of the baryon to photon ratio [1]

$$\eta \equiv \frac{n_B - n_{\bar{B}}}{n_\gamma} = (6.21 \pm 0.16) \times 10^{-10} \,. \tag{1}$$

It is not possible to reproduce such a value within the SM, being its CP violating source too small [2]. Many models for the dynamical generation of the baryon asymmetry have been proposed. Among those leptogenesis [3] is both theoretically and phenomenologically interesting since one can make some connections with the low-energy neutrino physics [4]. In the leptogenesis framework a lepton asymmetry is generated by the CP violating decays of heavy Majorana neutrinos into leptons and anti-leptons in different amounts. These heavy states can in principle explain the smallness of the SM neutrinos via the see-saw mechanism. The net lepton asymmetry is then partially reprocessed into a baryon asymmetry through the so called sphalerons transitions.

In the simplest realization of leptogenesis, the lepton asymmetry is generated by the decay of the lightest heavy Majorana neutrino. The heavier ones decouple earlier from the entire dynamics. One may characterize the properties of the heavy neutrinos in the thermal bath by exploiting the definition of the *decay parameter* [4], that reads

$$K = \frac{\Gamma(T=0)}{H(T=M_1)} = \frac{\frac{M_1|F_1|^2}{8\pi}}{\sqrt{g_*}1.66\frac{M_1^2}{M_{\rm Pl}}} = \frac{\frac{|F_1|^2 v^2}{M_1}}{8\pi\sqrt{g_*}1.66\frac{v^2}{M_{\rm Pl}}} = \frac{\tilde{m_1}}{m_*} \ . \tag{2}$$

The $\Gamma(T=0) \equiv \Gamma_0$ is the in-vacuum total decay width of the heavy Majorana neutrino and $H(T=M_1)$ the Hubble rate evaluated at a temperature of the order of the heavy neutrino mass, M_1. As shown in (2), the decay parameter can be also written in terms of low-energy neutrino quantities where F_1 is the Yukawa coupling between the heavy Majorana neutrino and SM Higgs and lepton doublet, g_* is the effective number of relativistic particles at $T \sim M_1$, $M_{\rm Pl}$ is the Planck scale, v^2 is the electroweak vacuum expectation value and $m_* \simeq 1.1$ eV. According to the neutrino oscillation experiments, one can choose the scale for $\tilde{m}_1$ to be $\mathcal{O}(10)$ eV (according to solar neutrino mass difference). This estimation provides an important information: the lightest heavy neutrinos remain coupled with the SM bath even after the temperature of the cooling system has dropped below the scale M_1. Therefore, the final lepton asymmetry is generated when the heavy neutrinos are non-relativistic. We refer to this scenario as strong wash-out regime [4]. In the next two sections, we show how the effective field theory (EFT) approach may help to address the dynamics of non-relativistic Majorana fermions in a thermal bath. Indeed we may explore the following hierarchy of scales $M_1 \gg T \gg M_W$, where the M_W represents the electroweak scale. The last inequality is well satisfied in the leptogenesis scenario under consideration.

2 Thermal width in the EFT framework

In this section we derive the heavy neutrino thermal width, already calculated in [5] and [6], by using an EFT approach. The thermal corrections to the width are induced by the SM particles in the thermal bath and the calculation in a fully relativistic thermal field theory framework requires the evaluation of two-loop diagrams at finite temperature. On the other hand, by exploiting the EFT, one can split the calculation into two steps: the first one-loop computation is required to match the full theory with the EFT. This can be done setting the temperature to zero, so it amounts at the calculation of typical in-vacuum matrix elements. The second one-loop computation is required to calculate the thermal corrections in the EFT. At the accuracy of the result presented here, only tadpole diagrams are involved.

The low-energy Lagrangian contains SM particles and non-relativistic excitations of Majorana neutrinos at typical energies and momenta smaller than M_1. For heavy neutrinos at rest, up to fluctuation much smaller than M_1, the EFT Lagrangian reads

$$\mathcal{L}_{\rm EFT} = N^\dagger \left(i\partial_0 - i\frac{\Gamma_0}{2} \right) N + \frac{\mathcal{L}^{(1)}}{M_1} + \frac{\mathcal{L}^{(2)}}{M_1^2} + \frac{\mathcal{L}^{(3)}}{M_1^3} + \mathcal{O}\left(\frac{1}{M_1^4}\right) , \tag{3}$$

where $\mathcal{L}^{(1)}$, $\mathcal{L}^{(2)}$ and $\mathcal{L}^{(3)}$ contain dimension five, six and seven operators respectively. To show the procedure, we consider the dimension five operator in $\mathcal{L}^{(1)}$. On symmetry grounds, only the operator $a\, N^\dagger N \phi^\dagger \phi$ contributes, where a is the corresponding matching coefficient.

The operator describes the interaction between heavy Majorana neutrinos and SM Higgs at low energies. In order to determine the coefficient a, we consider the heavy neutrino-Higgs scattering both in the fundamental theory and the low-energy, as shown in figure 1. A one-loop calculation at $T = 0$ is necessary to fix $a = -(3/8\pi)\lambda|F_1|^2$, where λ is the Higgs self-coupling.

Finally we compute the thermal correction to the neutrino width by considering the tadpole diagram in the EFT. It describes the thermal modification induced by thermal Higgs bosons. The leading order thermal width reads

$$\Gamma_\phi = 2\frac{\mathrm{Im}\, a}{M_1}\langle\phi^\dagger(0)\phi(0)\rangle_T = -\frac{\lambda|F|^2 M_1}{8\pi}\left(\frac{T}{M_1}\right)^2 \tag{4}$$

where relativistic and thermal corrections factorize as a result of the EFT treatment.

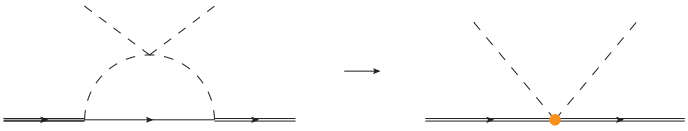

Figure 1: Matching of the dimension five operator. The one-loop process in the fundamental theory is matched onto the effective low-energy interaction. The solid double line stands for the heavy Majorana neutrino, dashed line for Higgs bosons and solid line for SM leptons.

3 CP violating parameter at finite temperature

In this section we want to show how to compute thermal corrections to the CP asymmetry at leading order in the SM couplings. The unflavoured CP asymmetry is defined as follows

$$\epsilon_1 = \sum_f \frac{\Gamma(N_1 \to \ell_f + X) - \Gamma(N_1 \to \bar{\ell}_f + X)}{\Gamma(N_1 \to \ell_f + X) + \Gamma(N_1 \to \bar{\ell}_f + X)} \tag{5}$$

and it arises from the interference between one-loop and tree level diagrams [3]. We focus only on the vertex diagram shown in figure 2 (left diagram). We consider the case of a hierarchically ordered heavy neutrino mass spectrum with two mass eigenstates, M_1 and M_2, such that $M_2 \gg M_1$. At least two neutrinos are needed as one can easily see from the combination of the Yukawa couplings appearing in the $T = 0$ expression for the unflavoured CP asymmetry

$$\epsilon_1 = \frac{\mathrm{Im}\left[(F_1^* F_2)^2\right]}{16\pi|F_1|^2}\left(\frac{M_1}{M_2}\right) + \mathcal{O}\left(\frac{M_1}{M_2}\right)^3, \tag{6}$$

where we have expanded the known result in [7] according to the hierarchy $M_2 \gg M_1$.

We calculate the leading order thermal correction to the quantity in (6) that arises from the effective low-energy interaction between non-relativistic Majorana neutrino and SM Higgs at energy scales of order $T \ll M_1$. This is done in complete analogy with the thermal width by considering the matching in figure 2. However, there is an important difference with respect to the previous case: we need to construct two subsequent effective theories. We have to integrate

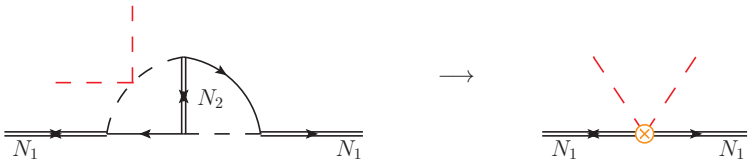

Figure 2: The matching of the fundamental process onto the effective low-energy interaction is shown. The red-dashed lines stand for thermal Higgs bosons from the plasma.

out the energy modes of order M_2 as a first step and integrate out the energy modes of order M_1 in a second stage. Therefore, one is finally left with the proper degrees of freedom: non-relativistic heavy neutrinos that decay and generate the CP asymmetry in a SM thermal bath. The final result is organized according to the power counting of the two effective theories: an expansion in M_1/M_2 and an expansion in T/M_1. It has the form

$$\epsilon_{1,T} \sim \epsilon_1 \, \lambda \left(\frac{T}{M_1} \right)^2 + \cdots , \tag{7}$$

where the dots stand for higher orders terms.

Acknowledgements

I would like to thank N. Brambilla, M. Escobedo and A. Vairo for the collaboration on the work presented here based on [8], [9], and the organizers of *PANIC 2014*.

References

[1] E. Komatsu *et al.* [WMAP Collaboration], Astrophys. J. Suppl. **180** (2009) 330 [arXiv:0803.0547 [astro-ph]].

[2] C. Jarlskog, Phys. Rev. Lett. **55** (1985) 1039.

[3] M. Fukugita and T. Yanagida, Phys. Lett. B **174** (1986) 45.

[4] W. Buchmuller, P. Di Bari and M. Plumacher, Annals Phys. **315** (2005) 305 [hep-ph/0401240].

[5] A. Salvio, P. Lodone and A. Strumia, JHEP **1108** (2011) 116 [arXiv:1106.2814 [hep-ph]].

[6] M. Laine and Y. Schröder, JHEP **1202** (2012) 068 [arXiv:1112.1205 [hep-ph]].

[7] L. Covi, E. Roulet and F. Vissani, Phys. Lett. B **384** (1996) 169 [hep-ph/9605319].

[8] S. Biondini, N. Brambilla, M. A. Escobedo and A. Vairo, JHEP **1312** (2013) 028 [arXiv:1307.7680, arXiv:1307.7680].

[9] S. Biondini, N. Brambilla, M. A. Escobedo and A. Vairo, "Thermal corrections to the CP asymmetry in leptogenesis for hierarchical neutrino masses"

The OPERA Experiment: Latest Results

Annika Hollnagel[1] on behalf of the OPERA Collaboration

[1]Hamburg University, Luruper Chaussee 149, D-22761 Hamburg, Germany

DOI: http://dx.doi.org/10.3204/DESY-PROC-2014-04/54

The long-baseline neutrino oscillation experiment OPERA has been designed for the direct observation of ν_τ appearance in the CNGS ν_μ beam. The OPERA detector is located at the LNGS underground laboratory, with a distance of 730 km from the neutrino source at CERN. It is a hybrid detector, combining the micrometric precision of emulsion cloud chambers with electronic detector elements for online readout.

While CNGS beam data taking lasted from 2008 to 2012, the neutrino oscillation analysis is still ongoing. Updated results with increased statistics are presented, including the recent observation of ν_τ appearance at $4.2\,\sigma$.

1 Introduction

During the last decades, neutrino oscillations have been studied by many experiments, and a standard picture of 3-flavour oscillations via the mixing of neutrino mass eigenstates has emerged. However, most experiments - such as the first observation of atmospheric neutrino oscillations by Super-Kamiokande [1] - work in disappearance mode. The observation of neutrino oscillations in appearance mode is required to firmly establish this 3-flavour framework.

Similar to DONuT [2] in its capability to identify τ leptons from ν_τ CC interactions on an event-by-event basis, the goal of OPERA[1] [3] is to provide the first direct observation of ν_τ appearance via $\nu_\mu \to \nu_\tau$ oscillations in a long-baseline beam of ν_μ. Although the detector is not optimised for other purposes, ν_e appearance in the sub-leading channel of $\nu_\mu \to \nu_e$ oscillations has also been studied.

2 The OPERA Experiment

2.1 Detector and neutrino beam

Due to the low cross sections involved, the detection of neutrino interactions in general requires a large target mass, while on the other hand, micrometric precision is needed for the observation of the short-lived τ leptons. The OPERA detector was designed as a hybrid apparatus to fulfill both requirements.

High-resolution ($\mathcal{O}$ (μm)) AgBr nuclear emulsions on plastic bases are interleaved with Pb plates to form *Emulsion Cloud Chamber* (ECC) modules called *bricks* - see Figure 1(a) for a schematic view and dimensions. At the downstream side of each brick, extra *Changeable Sheet* (CS) emulsion doublets act as an interface between ECC and *Electronic Detector* (ED)

[1]**OPERA: O**scillation **P**roject with **E**mulsion T**r**acking **A**pparatus.

components [4]. Altogether, the detector comprises about 150 000 bricks, resulting in a total target mass of 1.25 kt.

The bricks are arranged in two *target* regions of 31 vertical walls, perpendicular to the neutrino beam direction. Each wall is followed by planes of horizontal and vertical *Target Tracker* (TT) scintillator strips, allowing the location of neutrino interactions within the target, i.e. the identification of the respective brick. Downstream of each target region, a magnetic *spectrometer* - made from iron core dipole magnets, *Resistive Plate Chamber* (RPC & XPC) detectors, and *Precision Tracker* (PT) drift tubes - is used for the identification of μ momentum and charge. Upstream of these two identical *Super Modules* (SM), a RPC *VETO* system is installed. Figure 1(b) shows a lateral view of the detector.

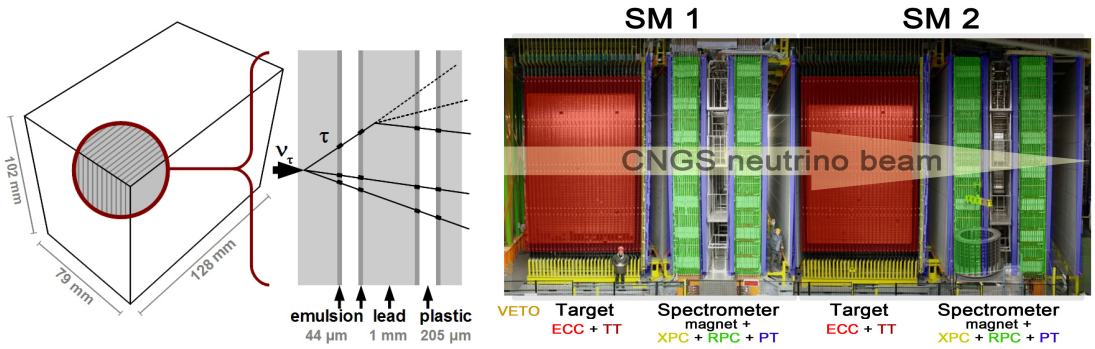

(a) ECC brick module.

(b) Lateral view (whole detector).

Figure 1: The OPERA detector.

The CNGS[2] ν_μ beam [5, 6] is a conventional neutrino beam, using 400 GeV-p from the CERN-SPS[3], a graphite target, and a magnetic horn focusing system. The resulting average ν_μ energy is ~ 17 GeV - well-above the threshold for τ lepton production in ν_τ CC interactions. While negligible for ν_τ, the contaminations with other flavours are 2.1 % for $\overline{\nu}_\mu$ and 1 % for $\nu_e + \overline{\nu}_e$, respectively. Between 2008 and 2012, a total of 17.97×10^{19} p.o.t. have been delivered.

With the detector location at the LNGS[4] underground laboratory, the baseline of the experiment is 730 km.

3 Neutrino oscillation results

3.1 $\nu_\mu \to \nu_\tau$ oscillations

The data sample used for the present results on $\nu_\mu \to \nu_\tau$ oscillations consists of 4685 fully analysed neutrino interactions with predefined selection criteria [7]: 0μ events and 1μ events with μ momentum of less than 15 GeV were searched for ν_τ appearance in the 1st and 2nd most probable bricks of 2008 + 2009 data, as well as in the 1st most probable bricks of 2010 + 2011 + 2012. In this sample, 4 ν_τ candidate events have been confirmed, their ECC reconstructions are shown in Figure 2.

[2]**CNGS: C**ERN **N**eutrinos to **G**ran **S**asso.
[3]**SPS: S**uper **P**roton **S**ynchrotron.
[4]**LNGS: L**aboratori **N**azionali del **G**ran **S**asso.

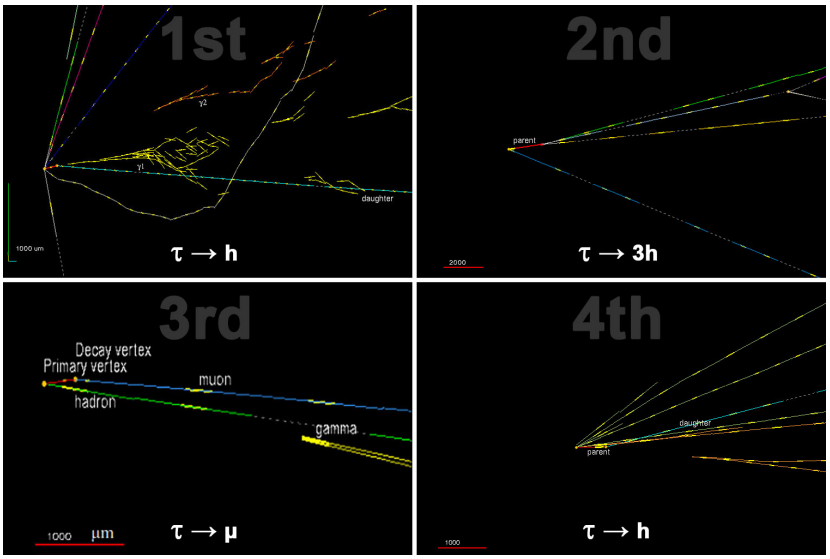

Figure 2: ECC reconstructions of the four confirmed ν_τ candidates.

With an expected signal of 2.11 ± 0.42 events[5] and a background of 0.233 ± 0.041, the 4 observed events correspond to a p-value of 1.24×10^{-5} (Fisher method) or 1.03×10^{-5} (likelihood analysis) for the no-oscillation hypothesis, both giving a significance of $4.2\,\sigma$ for the first observation of ν_τ appearance. A measurement of Δm^2_{23} has also been performed, resulting in intervals of $[1.8, 5.0] \times 10^{-3}\,\mathrm{eV}^2$ (Feldman-Cousins) and $[1.9, 5.0] \times 10^{-3}\,\mathrm{eV}^2$ (Bayes) at 90 % C.L., respectively.

Further details on the analysis procedure, the kinematics of the ν_τ candidate events, and the backgrounds can be found in [8, 9, 10].

3.2 $\nu_\mu \to \nu_e$ oscillations

With the possibility of electron identification, OPERA is also able to perform an appearance search in the sub-leading channel of $\nu_\mu \to \nu_e$ [11].

In the unbiased 2008+2009 data sample of 5255 located ν CC interactions (corresponding to 5.25×10^{19} p.o.t.), 19 ν_e candidate events have been found, while 19.8 ± 2.8 background events are expected from beam contamination and 1.4 events from standard 3-flavour oscillations (see Figure 3(a)). A cut on the reconstructed energy $E_{\nu,rec}$ of the ν_e candidates at $< 20\,\mathrm{GeV}$ to increase the signal-to-noise ratio results in 4 remaining ν_e candidates, with an expected signal of 1 event and a background expectation of 4.6. The number of observed events is compatible with the no-oscillation hypothesis, allowing to derive an upper limit of $\sin^2(2\theta_{13}) < 0.44$ at 90 % C.L.[6]

For non-standard oscillations in the parameter space of large $\Delta m^2_{new} > 0.1\,\mathrm{eV}^2$ suggested by the LSND and MiniBooNE experiments, new limits could be derived by introducing a cut of $E_{\nu,rec} < 30\,\mathrm{GeV}$, reducing the number of observed ν_e candidate events to 6. With an expected

[5] Assumptions: $\Delta m^2_{23} = 2.32 \times 10^{-3}\,\mathrm{eV}^2$, $\sin^2(2\theta_{23}) = 1$.
[6] Assumptions: $\sin^2(2\theta_{13}) = 0.098$, $\sin^2(2\theta_{23}) = 1$, $\Delta m^2_{23} = \Delta m^2_{31} = 2.32 \times 10^{-3}\,\mathrm{eV}^2$, $\delta_{CP} = 0$.

background of 9.4 events (incl. 1.3 events from 3-flavour oscillations), the Bayesian upper limit on large $\sin^2(2\theta_{new})$ is 7.2×10^{-3}. Figure 3(b) shows the exclusion plot in the Δm^2_{new} vs. $\sin^2(2\theta_{new})$ plane.

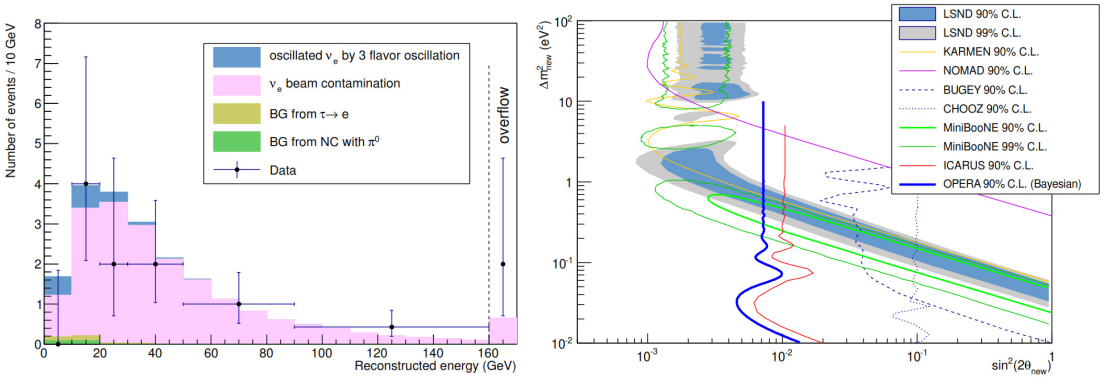

(a) Reconstructed energy of the ν_e candidates.

(b) Exclusion plot (non-standard scenario).

Figure 3: $\nu_\mu \to \nu_e$ oscillation analysis.

4 Conclusion

OPERA is a long-baseline neutrino oscillation experiment. Data taking in the CNGS beam lasted from 2008 to 2012, with a total exposure of 17.97×10^{19} p.o.t.

In the main analysis of $\nu_\mu \to \nu_\tau$ oscillations, 4 ν_τ interactions have been confirmed within the current data sample of 4685 fully analysed events. Using statistical methods, this result constitutes the first observation of ν_τ appearance in a ν_μ beam at $4.2\,\sigma$ significance.

In the sub-leading channel of $\nu_\mu \to \nu_e$ oscillations, new limits could be derived in the parameter space of non-standard neutrino oscillations.

References

[1] Y. Fukuda et al. [Super-Kamiokande Collaboration]. *Phys.Rev.Lett.*, 81:1562–1567, 1998.

[2] K. Kodama et al. [DONuT Collaboration]. *Phys.Rev.*, D78:052002, 2008.

[3] R. Acquafredda et al. [OPERA Collaboration]. *JINST*, 4:P04018, 2009.

[4] A. Anokhina et al. [OPERA Collaboration]. *JINST*, 3:P07005, 2008.

[5] G. Acquistapace et al. CERN-98-02, INFN-AE-98-05, CERN-YELLOW-98-02. 1998.

[6] R. Baldy et al. CERN-SL-99-034-DI, CERN-SL-99-34-DI, INFN-AE-99-05, INFN-AE-99-5. 1999.

[7] N. Agafonova et al. [OPERA Collaboration]. *PTEP*, 2014(10):101C01, 2014.

[8] N. Agafonova et al. [OPERA Collaboration]. *Phys.Lett.*, B691:138–145, 2010.

[9] N. Agafonova et al. [OPERA Collaboration]. *JHEP*, 1311:036, 2013.

[10] N. Agafonova et al. [OPERA Collaboration]. *Phys.Rev.*, D89(5):051102, 2014.

[11] N. Agafonova et al. [OPERA Collaboration]. *JHEP*, 1307:004, 2013.

Initial probe of δ_{CP} by T2K with combined electron neutrino appearance and muon neutrino disappearance.

H.M. O'Keeffe[1] on behalf of the T2K collaboration

[1]Physics Department, Lancaster University, Lancaster, UK, LA1 4YB

DOI: http://dx.doi.org/10.3204/DESY-PROC-2014-04/164

T2K is a long-baseline neutrino oscillation experiment in which a ν_μ beam is produced at the J-PARC facility and detected 295 km away by the Super-Kamiokande, water Cherenkov detector. Up to May 2013, T2K has accumulated 6.57×10^{20} protons on target, approximately 8% of the experimental goal. T2K has observed 120 ν_μ candidates, which show a clear disappearance oscillation pattern, and 28 ν_e candidates, with which ν_e appearance was established. The measurement of ν_e appearance is particularly important because it enables us to determine $\delta_{\rm CP}$ when θ_{23} and θ_{13} are known. Using values of θ_{23} determined by T2K disappearance measurements and θ_{13} measured by reactor $\bar{\nu}_e$ experiments, T2K has obtained the first constraint on $\delta_{\rm CP}$ from a ν_e appearance measurement.

1 The Tokai to Kamioka experiment

The Tokai to Kaimoka (T2K) experiment is a long-baseline neutrino oscillation experiment located in Japan. An intense, high purity ν_μ beam is produced (at J-PARC) by colliding a 30 GeV proton beam with a stationary graphite target, resulting in a beam of secondary hadrons. Three magnetic horns are used to select π^+, which decay to produce an almost pure beam of ν_μ (approximately 1% ν_e contamination). The neutrino beam is directed 2.5° away from the axis between the target and the far detector 295 km away. This off-axis technique produces a narrow band beam with a peak energy around 0.6 GeV. This corresponds to the energy of the first $\nu_\mu \to \nu_e$ oscillation maximum.

The near detector complex is located 280 m downstream from the neutrino production point and consists of an on-axis Interactive Neutrino GRID (INGRID) detector and an off-axis near detector (ND280). INGRID is used to monitor the beam intensity and direction. ND280 is used to measure the neutrino flux and interaction cross-sections, which reduces systematic uncertainties on the oscillation analyses. The off-axis detector consists of several sub-detectors inside a 0.2 T magnet, namely a π^0 detector, two active fine grain detectors, three gaseous argon time projection chambers, an electromagnetic calorimeter and a side muon range detector.

The far detector, located 295 km from the neutrino production point, is the Super-Kamiokande water Cherenkov detector. Super-Kamiokande is divided into an inner and outer detector. The inner detector has a 22.5 kton water fiducial volume that is surrounded by 11,129 photomultiplier tubes (PMTs). The inner detector and PMTs are surrounded by a 2 m wide outer detector. Neutrino interactions with water produce Cherenkov light which can be used to distinguish be-

tween electron and muon-like events. Good separation between ν_e and ν_μ candidates is achieved via a particle identification variable, with a probability of misidentifying a μ as an e of $< 1\%$.

T2K was optimised to perform a high precision measurement of the mixing parameters θ_{23} and Δm^2_{32} via ν_μ disappearance and to search for the mixing angle θ_{13} via ν_e appearance in the far detector. Recent work from the collaboration has provided the first hints that the parameter δ_{CP} may not be zero. Up to May 2013 T2K has collected 6.57×10^{20} protons on target.

2 Joint ν_μ and ν_e analysis

Charged current (CC) ν_μ interactions in the near detector are used to constrain the energy spectrum of the neutrino beam and neutrino interaction cross section parameters. Details of this analysis are given in [1]. CC interactions that pass the selection criteria are divided into three classes: CC-0π, which is dominated by CC quasi elastic scattering (CCQE) interactions; CC$-1\pi^+$, from CC resonant pion production; and finally CC-other which covers all remaining CC topologies that are selected. The three samples are fitted with a total of 25 beam parameters, 21 cross section parameters and 210 parameters that describe ND280 detector systematics. The fit to the ND280 data gives estimates for 22 beam flux parameters at the far detector (Super-Kamiokande), 5 common cross section parameters and their covariance. Inclusion of information from ND280 reduces the uncertainty on the expected number of electron-like events at the far detector from 27.2% to 8.8%.

At Super-Kamiokande, candidate events are selected if they are in time with the T2K neutrino beam, the energy of the Cherenkov ring is above 30 MeV, the ring occurs in the inner detector and there is low activity in the outer detector. A further cut is applied to ensure that the event vertex is at least 2 m from the wall of the inner tank and such events are "fully contained fiducial volume" (FCFV). Full details are given in [1]. Candidate ν_e interactions in the FCFV sample are identified by looking for events with a single electron-like Cherenkov ring with a reconstructed electron momentum above 100 MeV/c and reconstructed neutrino energy below 1250 MeV. The momentum cut is necessary to eliminate decay-electrons from stopping muons generated by CC interactions in the detector. Finally, additional contamination from π^0 events, which can mimic ν_e interactions is reduced by using a new reconstruction algorithm based upon the work in [2]. The application of this cut removes 69% of the π^0 background events relative to previous T2K ν_e appearance selections [3].

A binned extended maximum likelihood fit is used to determine the neutrino oscillation parameters. The likelihood comprises of four components: a normalization term ($\mathcal{L}_{norm}$), a spectral shape term ($\mathcal{L}_{shape}$), a systematics term ($\mathcal{L}_{syst}$) and a constraint term ($\mathcal{L}_{const}$) from other measurements. The likelihood is therefore:

$$\mathcal{L}(N_{obs}, \overrightarrow{x}, \overrightarrow{o}, \overrightarrow{f}) = \mathcal{L}_{norm}(N_{obs}; \overrightarrow{o}, \overrightarrow{f}) \times \mathcal{L}_{shape}(\overrightarrow{x}; \overrightarrow{o}, \overrightarrow{f}) \times \mathcal{L}_{syst}(\overrightarrow{f}) \times \mathcal{L}_{const}(\overrightarrow{o}),$$

where N_{obs} is the number of observed events, $\overrightarrow{x}$ is a set of kinematic variables, $\overrightarrow{o}$ represents the oscillation parameters and $\overrightarrow{f}$ describes the systematic uncertainties. Full details of the likelihood fit used in the T2K analysis is given in [1]. In the fit, values for several oscillation parameters are fixed as follows: $\sin^2\theta_{12} = 0.306, \Delta m^2_{21} = 7.6 \times 10^{-5}\text{eV}^2$ [4], $\sin^2\theta_{23} = 0.5, |\Delta m^2_{32}| = 2.4 \times 10^{-3}\text{eV}^2$ [5] and $\delta_{\text{CP}} = 0$. For the normal (inverted) hierarchy case, the best-fit value (68% confidence level) is $\sin^2 2\theta_{23} = 0.140^{+0.038}_{-0.032}(0.170^{+0.045}_{-0.037})$. In total, 28 candidate ν_e events were observed, which is significantly larger than the predicted background of 4.92 ± 0.55. Figure 1 shows the best fit reconstructed neutrino energy for the 28

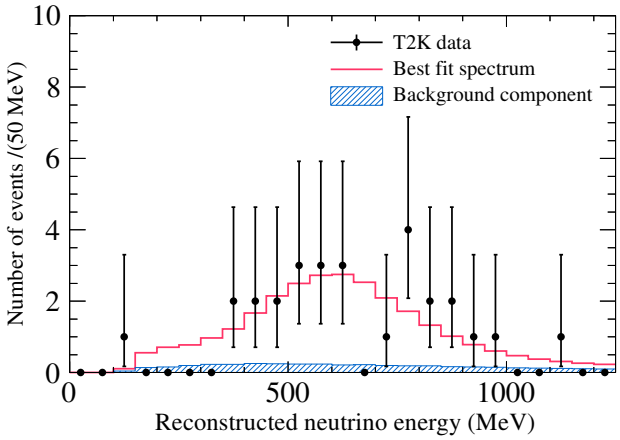

Figure 1: The $E_\nu^{\rm rec}$ distribution for ν_e candidates with the MC prediction at the best fit of $\sin^2\theta_{13} = 0.144$ (normal hierarchy).

observed ν_e events. The significance for a non-zero value of θ_{13} is calculated to be 7.3σ using the difference of log likelihood values between the best-fit value of θ_{13} and $\theta_{13} = 0$ and using a test statistic having fixed values of θ_{23} and $\delta_{\rm CP}$.

Using any value of the parameters θ_{23} and $\delta_{\rm CP}$ consistent with their present uncertainties returns a significance of greater than 7σ. The uncertainty associated with θ_{23} and Δm^2_{32} are taken into account via the $\mathcal{L}_{const}$ term in the fit and marginalising the likelihood over θ_{23} and Δm^2_{32}. Values of $\sin^2\theta_{23}$ and Δm^2_{32} are taken from the T2K ν_μ disappearance results [5]. Performing the fit for all values of $\delta_{\rm CP}$ results in the allowed contours shown in Figure 2

Constraints on the parameter $\delta_{\rm CP}$ can be obtained by combining the T2K results with the measured θ_{13} value from reactor anti-neutrino experiments. Details of the constraint are given in [1]. The combined T2K and reactor neutrino measurement indicates a preferred value of $-\pi/2$ for $\delta_{\rm CP}$. The Feldman-Cousins method is used to determine the 90% C.L. limits shown in Figure 3. The data excludes values of $\delta_{\rm CP}$ between 0.19π and 0.80π at 90% C.L. for the normal hierarchy. For the inverted hierarchy values between $-\pi$ and -0.97π and -0.04π and π are excluded at 90%C.L.

3 Conclusions

The T2K experiment has made the first observation of ν_e appearance in a ν_μ beam at a baseline of 295 km and peak beam energy of 0.6 GeV. A best fit value for $\sin^2 2\theta_{13} = 0.140^{+0.038}_{-0.032}$ ($0.170^{+0.045}_{-0.037}$) for the normal (inverted) neutrino mass hierarchy and assuming fixed values of $|\Delta m^2_{32}| = 2.4 \times 10^3$ eV^2, $\sin^2\theta_{23} = 0.5$ and $\delta_{\rm CP} = 0$. This best fit value has a significance of 7.3σ over the hypothesis of $\sin^2 2\theta_{13} = 0$. By combining the T2K result with the world average value of θ_{13} from reactor experiments, $\delta_{\rm CP}$ between 0.19π and 0.80π at 90% C.L. for the normal hierarchy. For the inverted hierarchy values between $-\pi$ and -0.97π and -0.04π and π are excluded at 90% C.L. The T2K experiment will continue to take data and investigate

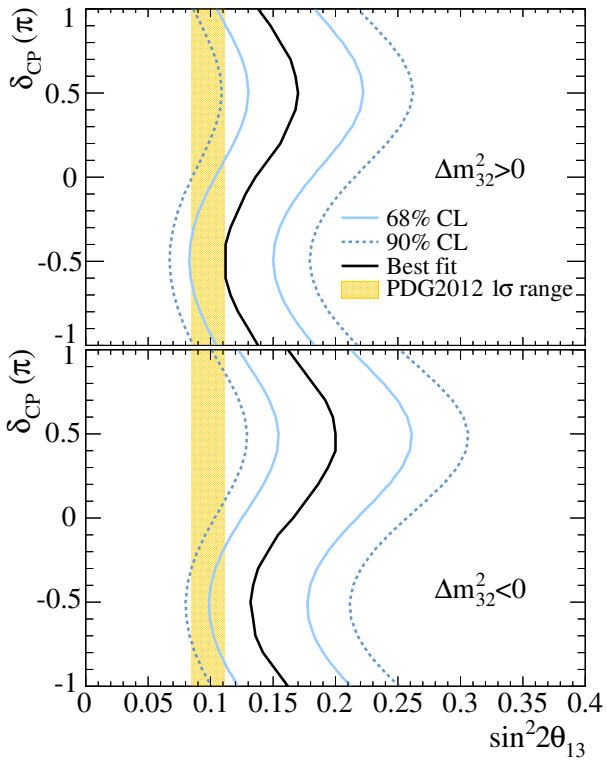

Figure 2: Allowed region of 68% (thin, solid, light blue) and 90% C.L. (dashed, blue) for $\sin^2 2\theta_{13}$ for each value of $\delta_{\rm CP}$. The thick (black) solid line is the best fit value for each value of $\delta_{\rm CP}$. Run1-4 data, marginalized over $\sin^2\theta_{23}$ and Δm^2_{32}. The values of $\sin^2\theta_{23}$ and Δm^2_{32} are varied in the fit with the constraint from [5]. The shaded region shows the average value of θ_{13} from the PDG 2012 [6].

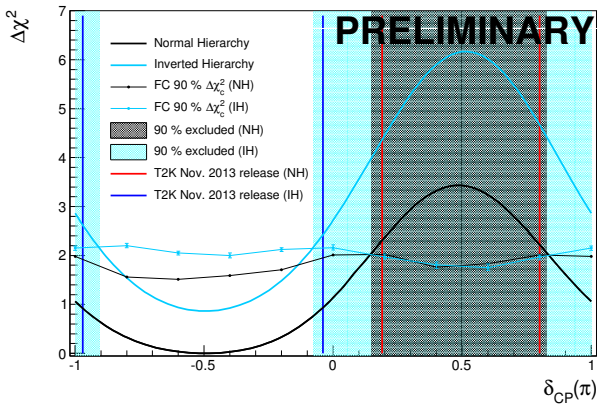

Figure 3: Profiled $\Delta\chi^2$ as a function of δ_{CP} for the combined reactor neutrino results and T2K joint three flavour frequentist analysis. The critical $\Delta\chi^2$ values and excluded regions obtained at the 90% C.L. for the normal and inverted hierarchies are overlaid.

CP violation in the lepton sector more precisely.

References

[1] K. Abe *et al.* (T2K Collaboration), Phys. Rev. Lett. **112**, 061802 (2014).

[2] R.B. Patterson *et al.*, Nucl.Instrum.Meth. **A608**, 206 (2009).

[3] K. Abe *et al.* (T2K Collaboration), Phys.Rev.Lett **107**, 041801 (2011).

[4] G.L. Fogli *et al.*, Phys.Rev. **D84**, 053007 (2011).

[5] K. Abe *et al.* (T2K Collaboration), arXiv:1308.0465 [hep-ex], (2013).

[6] J. Beringer *et al.* (Particle Data Group), Phys.Rev. **D86, 010001, (2012).**

Status of the Karlsruhe Tritium Neutrino Experiment KATRIN

Kathrin Valerius[1] for the KATRIN Collaboration

[1]Institut für Kernphysik, Karlsruher Institut für Technologie, Karlsruhe, Germany

DOI: http://dx.doi.org/10.3204/DESY-PROC-2014-04/80

Precision measurements of the kinematics of weak decays represent the only model independent approach to address the still unknown absolute scale of neutrino masses in a laboratory experiment. The KATRIN experiment, currently under construction at the Karlsruhe Institute of Technology, aims to improve the neutrino mass sensitivity obtained through precision spectroscopy of tritium β decay by an order of magnitude to 200 meV/c^2 (90% CL). In this contribution we present an overview of the status of the major components of the experimental set-up and report results from first commissioning measurements.

1 Introduction

Neutrino properties, and in particular the open question regarding the scale of neutrino rest masses, bear fundamental relevance to many current research topics in cosmology, theoretical particle physics, and astroparticle physics. Neutrino oscillation experiments, while providing us with a consistent neutrino mixing scheme and accurate measurements of two independent neutrino mass differences, cannot address the absolute mass scale.

Precision cosmology and the search for neutrinoless double beta decay can be used as sensitive probes of neutrino masses. However, these methods rely on multi-parameter cosmological models or on the assumption of neutrinos being of Majorana nature, respectively. By contrast, precision measurements of the kinematics of β decays (^{3}H, ^{187}Re) or electron capture processes (^{163}Ho) allow for a direct, i.e. model independent, neutrino mass search (see [1] for a recent review). The most mature technique relies on the spectroscopy of tritium β decay near its kinematic endpoint at 18.6 keV. Due to the phase space factor, the shape of the β-decay energy spectrum $\mathrm{d}N/\mathrm{d}E$ carries an imprint of the neutrino mass values m_i ($i = 1, 2, 3$):

$$\frac{\mathrm{d}N}{\mathrm{d}E} \propto F(Z,E) \cdot p_\mathrm{e} \cdot (E + m_\mathrm{e}) \cdot (E_0 - E) \cdot \sum_{i=1}^{3} |U_{\mathrm{e}i}|^2 \sqrt{(E_0 - E)^2 - m_i^2} \cdot \Theta(E_0 - E - m_i). \quad (1)$$

Here, p_e and E are the electron momentum and energy, the Fermi function $F(Z,E)$ describes the Coulomb interaction of the outgoing electron with the daughter nucleus, and E_0 is the Q-value of the decay. Given the smallness of neutrino mass splittings, typical experimental resolution will not be sufficient to resolve the individual m_i. Hence, the observable is an effective squared "electron type" neutrino mass, $m^2_{\nu,\beta} = \sum_{i=1}^{3} |U_{\mathrm{e}i}|^2 \, m_i^2$, where the $U_{\mathrm{e}i}$ denote elements of the PMNS mixing matrix.

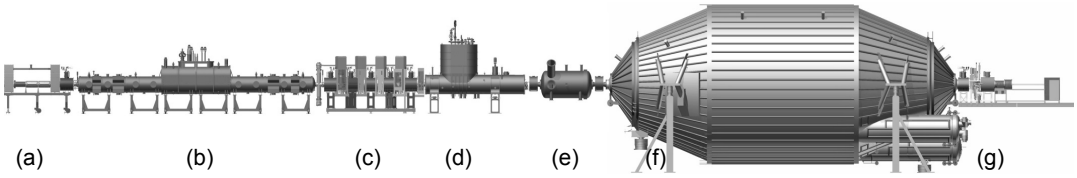

Figure 1: Overview of the KATRIN set-up: (a) calibration and monitoring system, (b) windowless gaseous tritium source, (c) differential and (d) cryogenic pumping sections, (e) pre-spectrometer, (f) main spectrometer, (g) detector system.

The present state of the art of tritium β-decay experiments is defined by electrostatic spectrometers using magnetic adiabatic collimation (MAC-E filters), a technique which allowed two experiments at Mainz and Troitsk to place upper limits on $m_{\nu,\beta}$ at about 2 eV/c^2 [2, 3]. Using the same basic principle, the upcoming KArlsruhe TRItium Neutrino experiment (KATRIN) will push the sensitivity on $m_{\nu,\beta}$ further by an order of magnitude. KATRIN is currently in its construction and commissioning phase at the Karlsruhe Institute of Technology. In the following we review the status of the major components and present results from the initial commissioning runs of the spectrometer and detector section.

2 The KATRIN Experiment

Main components An overview of the KATRIN set-up, spanning about 70 m in length, is presented in Fig. 1. The principal components can be grouped into the tritium-bearing Source and Transport Section (**a**–**d**) and the tritium-free Spectrometer and Detector Section (**e**–**g**).

Source and Transport Section. A high-luminosity windowless gaseous tritium source delivers 10^{11} β-decay electrons per second. The active volume consists of a 10 m long beam tube of 90 mm diameter. Molecular tritium gas is injected at the center and differentially pumped and recycled at both ends. The closed loops of the tritium processing system circulate about 40 g of T_2 per day. A complex cryostat system utilising a novel two-phase neon cooling concept will allow to maintain an extremely stable operating temperature inside the beam tube ($\Delta T <$ 30 mK at $T = 30$ K). Tests of the refrigeration system validated the concept, even surpassing the stringent stability requirement [4]. A comprehensive control and monitoring apparatus has been developed [5] to ensure the stability and to monitor minute fluctuations of the column density – a key parameter of the experiment which critically affects both the statistical accuracy of the measurement and the energy loss of the electrons traversing the source.

Electrons starting in the source are adiabatically guided through the pumping units and towards the spectrometer via a strong magnetic field produced by a chain of superconducting solenoids. The purpose of the successive differential (DPS) and cryogenic (CPS) pumping sections is to reduce the tritium flow rate by a combined factor of 10^{14}, thus preventing tritium from entering the spectrometer section. Manufacturing of both pumping sections is scheduled to be completed in 2015; the five superconducting solenoids of the DPS have already been delivered and are currently being tested on site. Likewise, the assembly of the source cryostat is under way and scheduled to be finished in mid-2015, when all components of the Source and Transport Section will be integrated and subject to a staged commissioning process.

Spectrometer and Detector Section. The KATRIN beam line features a pre-spectrometer to select the upper few 100 eV portion of the tritium β spectrum, and a large, high-resolution main spectrometer ($\Delta E = 0.93$ eV at $E \approx 18.6$ keV). With its length of 23 m, diameter of 10 m and volume of about 1240 m^3, the main spectrometer is one of the largest ultra-high vacuum recipients ever built. The spectrometer vessel has been on site at Karlsruhe since end of 2006. Since then, in a multi-year effort, an elaborate two-layer inner electrode made up of $\sim$ 22,000 wires has been installed inside the main spectrometer, which allows to apply a screening electric potential to shield against cosmics-induced background electrons. After completion of the wire electrode installation, the spectrometer was prepared for UHV conditions by performing a baking cycle at $T \approx 300°$C. The detector system [6], comprising a 148-pixel PIN diode, passive and active background shielding, calibration devices and two superconducting magnets, was installed and commissioned together with the data acquisition unit in 2011-12.

Neutrino mass sensitivity. The aim of improving the neutrino mass sensitivity by a factor 10 demands an improvement by a factor of 100 in the experimental observable $m^2_{\nu,\beta}$ (cf. Eq. 1). It also implies that a background level of 10^{-2} cps is required – similar to what has been achieved at previous, much smaller experiments. KATRIN is expected to reach its full sensitivity potential after 3 net years of measurement (corresponding to about 5 calendar years of running), at which point statistical and systematic uncertainties will contribute about equally to the total measurement uncertainty [7]. At its full sensitivity, KATRIN can discover a neutrino mass as small as 350 meV at 5σ significance, or place an upper limit at 200 meV (90% CL).

3 Results of the first commissioning phase

In summer 2013, an extensive campaign of commissioning runs was conducted, with two major objectives: (a) to test the transmission properties of the main spectrometer, and (b) to investigate the overall background rate and validate the background model based on simulations and on previous tests with the smaller pre-spectrometer. For this measurement programme, a high-definition calibration electron source (small energy spread, angular selectivity, fast-pulse operation; see [9] for a general concept) was attached to one end of the main spectrometer, and the detector system was connected at the opposite side.

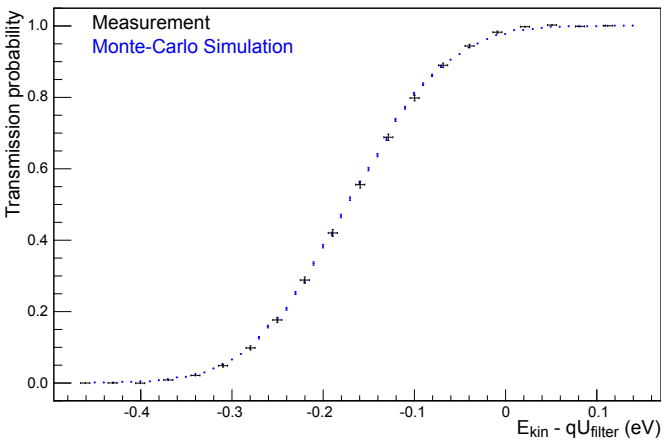

Figure 2: Transmission test of the KATRIN main spectrometer at filter potential $U_{\mathrm{filter}} = 18.6$ kV [8].

These first commissioning measurements successfully validated the design concepts of the KATRIN Spectrometer and Detector section: Firstly, they demonstrated that the main spectrometer indeed acts as a precision MAC-E filter. Figure 2 shows that the shape of the high-pass transmission characteristics is well

understood by Monte-Carlo simulations taking into account the small residual energy spread of the calibration electron source. Furthermore, the thorough simulation-optimised electromagnetic design of the main spectrometer paid off, as the spectrometer did not exhibit any signs of elevated background rates caused by Penning trap-type storage conditions. Such effects had plagued previous experiments and also the KATRIN pre-spectrometer in its initial configuration [10]. First investigations regarding background composition have been carried out; in compliance with the expectation from simulation models [11], a considerable portion was found to originate from stored electrons deposited by ^{219}Rn and ^{220}Rn decays in the spectrometer volume. Countermeasures have been implemented successfully [12] and will be tested further in the upcoming second round of commissioning runs, along with additional passive and active background suppression methods.

4 Summary

While components of the Source and Transport Section are still in the construction phase, commissioning of the already completed Spectrometer and Detector Section has commenced. Important concepts employed in the realisation of the experiment have been proven to be successful (e.g., vacuum and precision high-voltage systems, electromagnetic design of the spectrometers). As of fall 2014, a second commissioning campaign is ongoing to investigate details of the transmission characteristics and to test further background reduction mechanisms. Integration of the Source and Transport components into the beam-line are foreseen for 2015, and data-daking with the completed KATRIN set-up is expected to begin in 2016.

References

[1] G. Drexlin, V. Hannen, S. Mertens, and C. Weinheimer. Current direct neutrino mass experiments. *Advances in High Energy Physics*, 2013:293986, 2013.

[2] C. Kraus, B. Bornschein, L. Bornschein, J. Bonn, B. Flatt, A. Kovalik, B. Ostrick, E.W. Otten, J.P. Schall, T. Thümmler, and C. Weinheimer. Final results from phase II of the mainz neutrino mass search in tritium β decay. *The European Physical Journal C - Particles and Fields*, 40(4):447–468, 2005.

[3] V.N. Aseev, A.I. Belesev, A.I. Berlev, E.V. Geraskin, A.A. Golubev, N.A. Likhovid, V.M. Lobashev, A.A. Nozik, V.S. Pantuev, V.I. Parfenov, A.K. Skasyrskaya, F.V. Tkachov, and S.V. Zadorozhny. Upper limit on the electron antineutrino mass from the Troitsk experiment. *Physical Review D*, 84:112003, 2011.

[4] S. Grohmann, T. Bode, M. Hötzel, H. Schön, M. Süßer, and T. Wahl. The thermal behaviour of the tritium source in KATRIN. *Cryogenics*, 55-56(0):5–11, 2013.

[5] M. Babutzka, M. Bahr, J. Bonn, B. Bornschein, A. Dieter, G. Drexlin, K. Eitel, S. Fischer, F. Glück, S. Grohmann, M. Hötzel, T.M. James, W. Käfer, M. Leber, B. Monreal, F. Priester, M. Röllig, M. Schlösser, U. Schmitt, F. Sharipov, M. Steidl, M. Sturm, H.H. Telle, and N. Titov. Monitoring of the operating parameters of the KATRIN windowless gaseous tritium source. *New Journal of Physics*, 14(10):103046, 2012.

[6] J.F. Amsbaugh, J. Barrett, A. Beglarian, T. Bergmann, H. Bichsel, L.I. Bodine, J. Bonn, N.M. Boyd, T.H. Burritt, Z. Chaoui, S. Chilingaryan, T.J. Corona, P.J. Doe, J.A. Dunmore, S. Enomoto, J. Fischer, J.A. Formaggio, F.M. Fränkle, D. Furse, H. Gemmeke, F. Glück, F. Harms, G.C. Harper, J. Hartmann, M.A. Howe, A. Kaboth, J. Kelsey, M. Knauer, A. Kopmann, M.L. Leber, E.L. Martin, K.J. Middleman, A.W. Myers, N.S. Oblath, D.S. Parno, D.A. Peterson, L. Petzold, D.G. Phillips II, P. Renschler, R.G.H. Robertson, J. Schwarz, M. Steidl, D. Tcherniakhovski, T. Thümmler, T.D. Van Wechel, B.A. VanDevender, S. Vöcking, B.L. Wall, K. L. Wierman, J.F. Wilkerson, and S. Wüstling. Focal-plane detector system for the KATRIN experiment. *ArXiv e-prints*, April 2014.

[7] KATRIN collaboration. KATRIN design report. *FZKA scientific report*, 7090, 2005.

[8] S. Groh. PhD thesis, Karlsruhe Institute of Technology, in preparation.

[9] M. Beck, K. Bokeloh, H. Hein, S. Bauer, H. Baumeister, J. Bonn, H.-W. Ortjohann, B. Ostrick, S. Rosendahl, S. Streubel, K. Valerius, M. Zboril, and C. Weinheimer. An angular-selective electron source for the KATRIN experiment. *ArXiv e-prints*, November 2014.

[10] F.M. Fränkle, F. Glück, K. Valerius, K. Bokeloh, A. Beglarian, J. Bonn, L. Bornschein, G. Drexlin, F. Habermehl, M.L. Leber, A. Osipowicz, E.W. Otten, M. Steidl, T. Thümmler, C. Weinheimer, J.F. Wilkerson, J. Wolf, and S.V. Zadorozhny. Penning discharge in the KATRIN pre-spectrometer. *Journal of Instrumentation*, 9(7):P07028, 2014.

[11] S. Mertens, G. Drexlin, F.M. Fränkle, D. Furse, F. Glück, S. Görhardt, M. Hötzel, W. Käfer, B. Leiber, T. Thümmler, N. Wandkowsky, and J. Wolf. Background due to stored electrons following nuclear decays in the KATRIN spectrometers and its impact on the neutrino mass sensitivity. *Astroparticle Physics*, 41:52–62, 2013.

[12] S. Görhardt. *Background Reduction Methods and Vacuum Technology at the KATRIN Spectrometers*. PhD thesis, Karlsruhe Institute of Technology, 2014.

Neutrino Physics with the Precision IceCube Next Generation Upgrade (PINGU)

Tomasz Palczewski[1] for the IceCube/PINGU Collaboration

[1]Department of Physics and Astronomy, The University of Alabama, Tuscaloosa, AL, 35487

DOI: http://dx.doi.org/10.3204/DESY-PROC-2014-04/84

The IceCube Neutrino Observatory at the geographic South Pole is the largest neutrino telescope on Earth. IceCube and its low energy extension, DeepCore, were fully assembled at the end of 2010. DeepCore lowered the IceCube neutrino energy threshold to about 10 GeV, allowing access to a rich variety of atmospheric neutrino oscillation physics, and further improving sensitivity to indirect searches for WIMP dark matter and other phenomena. The recent measurements of a relatively large θ_{13} mixing angle and the first observations of atmospheric neutrino oscillations in the tens of GeV region in DeepCore open the possibility to determine the Neutrino Mass Hierarchy (NMH) in the proposed new in-fill array called Precision IceCube Next Generation Upgrade (PINGU). PINGU would lower the neutrino energy threshold and significantly increase the sensitivity to the NMH. For every year of the PINGU detector operation, on the order of one hundred thousand atmospheric neutrinos will be collected. These high statistics will allow PINGU to distinguish between the normal and inverted NMH at 3σ significance with an estimated 3.5 years of data.

1 Introduction

In the past 15 years, the neutrino oscillations have been studied in many different experiments, using neutrinos from man-made neutrino sources (beams, reactors), from the Sun, and from the atmosphere [1]. Neutrino oscillations occur because the neutrino flavor eigenstates are different than neutrino mass eigenstates. This phenomenon can be described in the standard three-flavor mixing scheme (3 x 3 "PMNS" mixing matrix) [2]. Recently, the last unknown mixing angle θ_{13} was measured by reactor and accelerator experiments [3, 4, 5]. The moderately large value of $\theta_{13}(\simeq 9^\circ)$ opens a new epoch in the studies of CP violation and determination of the neutrino mass hierarchy [6]. The measurement of the NMH with PINGU relies on the fact that Earth has an average density close to that of MSW resonance for neutrinos in the few GeV energy range. Therefore, significant oscillation probability modifications will occur for atmospheric neutrinos passing through Earth. The character of those modifications strongly depends on the sign of the NMH. This effect can be studied in a detector with a neutrino energy threshold of a few GeV and a large fiducial volume to acquire sufficient statistics. In addition, flavor identification and directional reconstruction in the same energy regime is required. The NMH determination depends on oscillations of both the neutrinos and anti-neutrinos. The survival probability distribution for muon neutrinos and muon anti-neutrinos in Normal Hierarchy (NH) and Inverted Hierarchy (IH) are shown in Fig. 1.

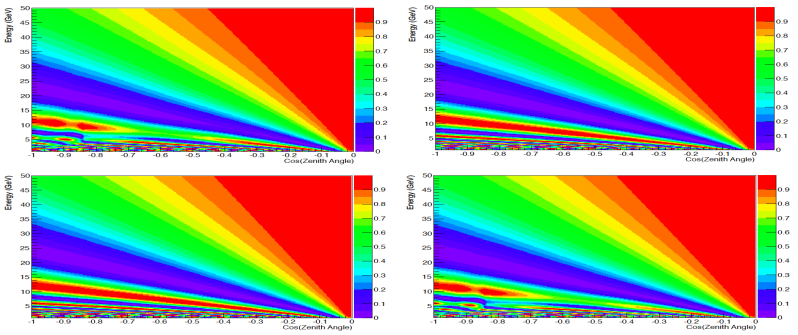

Figure 1: Survival probabilities for muon neutrinos passing through the Earth as a function of energy and zenith angle. A value of Cos(Zenith Angle) = -1 is a directly up going neutrino which is passing through the Earth's core. Muon neutrinos and NH (top left), muon neutrinos and IH (top right), muon anti-neutrinos and NH (bottom left), muon anti-neutrinos and IH (bottom right).

2 IceCube/DeepCore and proposed PINGU detector

IceCube consists of 86 cables ("strings"), each instrumented with 60 Digital Optical Modules (DOMs). The DOM consists of a 10 inch photomultiplier tube (PMT), calibration light sources and digitizing electronics. The DOMs are deployed at depths between 1450m and 2450m below the surface. The horizontal distance between most of the IceCube strings is 125 m and the vertical spacing between DOMs is 17 m. Eight strings near the center are more densely spaced with 42 - 72 m horizontal spacing and 7 m vertical spacing. Most DOMs on these eight strings contain PMTs with 35% higher quantum efficiency than standard IceCube DOMs. These eight densely instrumented strings in conjunction with the twelve IceCube strings surrounding them make up the DeepCore detector. IceCube also includes 81 surface stations, called IceTop. A sketch of IceCube and DeepCore strings, and IceTop stations is shown in Fig. 2. This

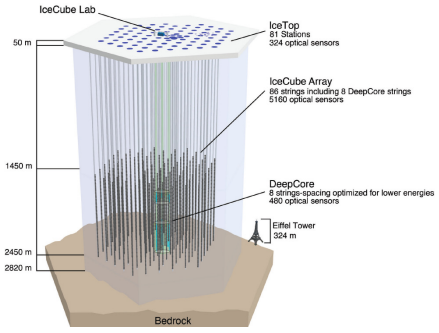

Figure 2: A sketch of IceCube and DeepCore strings, and IceTop stations.

configuration lowered the neutrino energy threshold to 10 GeV. The PINGU design follows closely that which was used for IceCube and DeepCore. PINGU will consist of 40 new strings with 20 m horizontal distance between strings and 5 m vertical distance between DOMs.

3 Neutrino Mass Hierarchy with PINGU

The proposed PINGU detector, described in Sec. 2, has no ability to distinguish between neutrinos and anti-neutrinos. However, atmospheric neutrinos in a few GeV energy region have an interaction cross section with matter almost two times larger than anti-neutrinos. Furthermore, the atmospheric neutrino flux is larger than the atmospheric anti-neutrino flux. Therefore, a potentially measurable effect, connected with significant oscillation probability modifications (see Fig. 1), remains. The distinguishability metric defined as follows [7]:

$$S_{tot} = \sqrt{\frac{(N_{i,j}^{IH} - N_{i,j}^{NH})^2}{N_{i,j}^{IH}}}$$

where $N_{i,j}$ is the number of muon neutrino events in the i and jth bin in neutrino energy and cosine of zenith angle, can be used to quantify the observable difference between the NH and IH. The distinguishability metrics for one year of simulated PINGU data after applying the selection criteria and event reconstruction described in [8] are shown in Fig. 3.

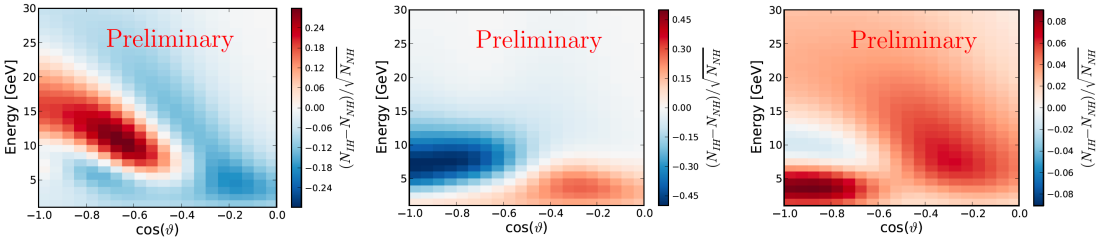

Figure 3: Distinguishability metrics for one year of simulated PINGU data: ν_μ CC (left), ν_e CC (middle), ν_τ CC events (right).

Three independent methods of determining the NMH significance in PINGU were developed: the log likelihood ratio method, the Asimov approach, and the Fisher information matrix method. Full details of these statistical methods are given in [8]. The first method is the most detailed, but it is too computationally intensive to incorporate the full range of systematics. Therefore, it was used mainly as a statistical error estimation benchmark to the other methods. The results from different methods were validated with each other and also agree well with external studies [9]. The main systematic error sources come from the energy calibration scale and physics-related uncertainties from limited knowledge of flux normalization and neutrino cross sections, and known precision of oscillation parameters. The systematic error studies connected with particle identification, cross section details, and ice model are not conducted. The significance of the neutrino mass hierarchy determination as a function of time, using the Fisher/Asimov approach including particle ID performance and a full complement of systematics (reconstruction errors are not included), under assumption of IH and θ_{23} in the first octant is shown in Fig. 4 (left). The influence of the change of the θ_{23} octant is shown in Fig 4(right).

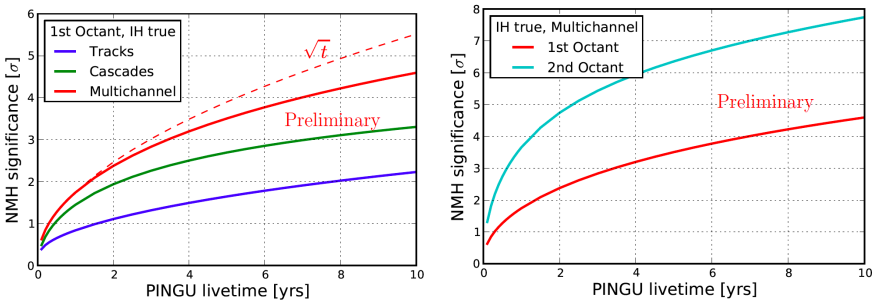

Figure 4: The significance of the neutrino mass hierarchy determination as a function of time for the IH and the first octant (left) and compared to the second octant (right) for multichannel case. The red dashed line (left) shows the expectation for a $\sqrt{t}$ dependence.

4 Conclusions

PINGU has the potential to answer one of the most important questions in the fundamental neutrino physics, namely what the sign of the Neutrino Mass Hierarchy is. We expect PINGU to be very competitive with the significance and timescale quoted for the other proposed experiments (INO, HyperK, LBNF/NOνA, JUNO) [10]. PINGU will be able to distinguish between the normal and inverted NMH at 3 σ level in 3.5 years. Beyond the measurement of the NMH, PINGU has a rich physics program. PINGU will have highly competitive sensitivity to ν_μ disappearance, θ_{23} octant and maximal mixing, and ν_τ appearance. Furthermore, PINGU will extend IceCube's and DeepCore's dark matter searches to WIMP masses below 20 GeV and improve sensitivity in the detection of low-energy supernova neutrinos.

Acknowledgments

The full IceCube/PINGU Collaboration author list and acknowledgments page can be found online here: https://icecube.wisc.edu/collaboration/authors/pingu

References

[1] J. Beringer *et al.* (PDG), PR **D86**, 010001 (2012).
[2] Z. Maki, M. Nakagawa and S. Sakata, Prog. Theor. Phys. **28**, 870, (1962).
[3] K. Abe *et al.*, Phys. Rev. Lett. **107**, 041801, (2011).
[4] F.P. An *et al.*, Phys. Rev. Lett. **108**, 171803 (2012).
[5] R.P. Litchfield, SLAC-eConf-C**120521**, (2012).
[6] H. Minakata, arXiv, 1209.1690, (2012).
[7] E. K. Akhmedov, S. Razzaque and A.Y. Smirnov, JHEP **1302**, 082 (2013).
[8] M.G. Aartsen *et al.*, arXiv, 1401.2046, (2014).
[9] W. Winter, Phys. Rev. **D88**, 013013, (2013).
[10] M. Blennow *et al.*, arXiv, 1311.1822, (2014).

Search for Sterile Neutrinos with the Borexino Detector

Mikko Meyer[1]

[1]Institut für Experimentalphysik, Universität Hamburg, Luruper Chaussee 149, D-22761 Hamburg, Germany

on behalf of the Borexino/SOX Collaboration:
M. Agostini, K. Altenmüller, S. Appel, G. Bellini, J. Benziger, N. Berton, D. Bick, G. Bonfini, D. Bravo, B. Caccianiga, L. Cadonati, F. Calaprice, A. Caminata, P. Cavalcante, A. Chavarria, A. Chepurnov, M. Cribier, D. D'Angelo, S. Davini, A. Derbin, L. di Noto, M. Durero, A. Empl, A. Etenko, S. Farinon, V. Fischer, K. Fomenko, D. Franco, F. Gabriele, J. Gaffiot, C. Galbiati, S. Gazzana, C. Ghiano, M. Giammarchi, M. Göger-Neff, A. Goretti, L. Grandi, M. Gromov, C. Hagner, Th. Houdy, E. Hungerford, Aldo Ianni, Andrea Ianni, N. Jonquères, M. Kaiser, V. Kobychev, D. Korablev, G. Korga, D. Kryn, T. Lachenmaier, T. Lasserre, M. Laubenstein, B. Lehnert, T. Lewke, J. Link, E. Litvinovich, F. Lombardi, P. Lombardi, L. Ludhova, G. Lukyanchenko, I. Machulin, S. Manecki, W. Maneschg, S. Marcocci, J. Maricic, Q. Meindl, G. Mention, E. Meroni, M. Meyer, L. Miramonti, M. Misiaszek, M. Montuschi, P. Mosteiro, V. Muratova, R. Musenich, B. Neumair, L. Oberauer, M. Obolensky, F. Ortica, K. Otis, M. Pallavicini, L. Papp, L. Perasso, A. Pocar, G. Ranucci, A. Razeto, A. Re, A. Romani, N. Rossi, R. Saldanha, C. Salvo, S. Schönert, L. Scola, H. Simgen, M. Skorokhvatov, O. Smirnov, A. Sotnikov, S. Sukhotin, Y. Suvorov, R. Tartaglia, G. Testera, C. Veyssière, D. Vignaud, M. Vivier, R. B. Vogelaar, F. von Feilitzsch, H. Wang, J. Winter, M. Wojcik, A. Wright, M. Wurm, O. Zaimidoroga, S. Zavatarelli, K. Zuber, G. Zuzel

DOI: http://dx.doi.org/10.3204/DESY-PROC-2014-04/7

Several observed anomalies in the neutrino sector could be explained by a fourth (sterile) neutrino with a squared mass difference in the order of $1\,\mathrm{eV}^2$ to the other three standard neutrinos. This hypothesis can be tested with an artificial MCi neutrino (^{51}Cr) or a kCi anti-neutrino (^{144}Ce$-^{144}$Pr) source deployed near or inside a large low background detector like Borexino. The SOX project (Short baseline neutrino Oscillation with BoreXino) aims for the detection of sterile neutrinos and will also allow to measure the neutrino magnetic moment, the electroweak mixing angle as well as the g_V and g_A coupling constants at low energy.

1 Introduction

The leptonic flavor mixing of neutrinos has been well established by a number of experiments. In the common picture, the three neutrino flavors $(\nu_e, \nu_\mu, \nu_\tau)$ are linear combinations of the three neutrino mass eigenstates (ν_1, ν_2, ν_3) separated by the two squared mass differences of $\Delta m^2_{21} = 8 \cdot 10^{-5}\,\mathrm{eV}^2$ and $\Delta m^2_{31} = 2.4 \cdot 10^{-3}\,\mathrm{eV}^2$.

However, a number of short baseline experiments have measured a neutrino deficit with respect to the expectations. These results are commonly defined as *neutrino anomalies*. From the historical point of view the LSND result has been the first result which was inconsistent with the standard scenario and pointed to the possibility of the existence of a fourth (sterile) neutrino (3+1 model). Recently, the re-calculation of the $\bar{\nu}_e$ flux from reactors together with the re-evaluation of the inverse beta decay cross section (due to the change of the neutron life-time), resulted in an observed anti-neutrino deficit of about 7% for experiments within 100 m of the reactors. This discrepancy is known as the reactor anomaly and could be explained by a fourth (sterile) neutrino [1].

In the nineties, two solar neutrino experiments (GALLEX and SAGE) performed calibration campaigns with artificial neutrino sources (^{51}Cr and ^{37}Ar) to check their detector efficiencies. Both experiments observed independently a lower neutrino flux than expected and a recent global re-analysis confirmed the anomaly at 3σ [2].

One powerful method to probe the neutrino anomaly is to repeat similar source experiments with more intense ν_e and $\bar{\nu}_e$ sources at a large low background detector like Borexino [3, 4, 5]. Thanks to the good energy and vertex resolution, it might even be possible to observe the characteristic neutrino oscillation pattern within the detector, if the Δm^2 is in the favored range of $1\,\mathrm{e}V^2$ and the mixing angle is not to small.

2 The Borexino detector

Borexino is a 300 t liquid scintillator detector designed for the real-time detection of solar neutrinos at the LNGS in Italy [6]. The detection of the solar ν_e is performed by neutrino electron scattering (NC+CC) and via the inverse beta decay (IBD) for the $\bar{\nu}_e$ geo-neutrinos. Borexino has provided a precise spectroscopy of solar neutrinos [7], including recently the first direct detection of the primary pp neutrinos from the Sun [8].

The Borexino detector consists of a nylon vessel with an diameter of 9.5 m (target area) surrounded by the buffer and water tank as shielding. The scintillation light originating from neutrino interactions are detected by 2,214 PMTs mounted on the so-called *stainless steel sphere*.

The inner nylon vessel contains the liquid scintillator composed from PC (pseudocumene, 1,2,4-trimethylbenzene) and PPO (2,5-diphenyloxazole) as a wavelength shifter. As part of a R&D effort, Borexino has reached an unprecedented radio-purity. Currently, the ^{238}U and ^{232}Th concentration is as low as 10^{-19} g/g. Other backgrounds include ^{85}Kr, ^{210}Bi and most importantly ^{210}Po. The energy response throughout the detector volume was carefully measured and calibrated by radioactive sources. At 1 MeV the energy resolution was determined to 4.5% and the vertex resolution is about 15 cm at 0.7 MeV [5].

3 Search for sterile neutrinos with the Borexino detector

The search for possible light sterile neutrinos can be performed by using either monochromatic neutrino sources like ^{51}Cr or ^{37}Ar, or by using intense anti-neutrino sources (^{144}Ce, ^{106}Ru or ^{90}Sr) with a continuous β-spectrum. The size of the source used by an experiment should be as compact as possible to observe the characteristic (anti-)neutrino oscillation pattern. The Borexino experiment will use the ^{144}Ce anti-neutrino source and possibly the ^{51}Cr neutrino source.

3.1 Anti-neutrino emitters in Borexino

During the first phase of the SOX project an anti-neutrino source with a continuous β-spectrum will be placed underneath the Borexino detector (8.25 m from the detector center). The detection of the $\bar{\nu}_e$ is then performed via the inverse beta decay (IBD), $p+\bar{\nu}_e \rightarrow e^+ + n$. The signature is provided by the positron annihilation (prompt signal) followed by the neutron capture on hydrogen (delayed signal). This coincidence allows an efficient way to suppress background and is often referred to as the golden channel of neutrino physics. The anti-neutrino detection was successfully applied for the geo-neutrino analysis [9] and is also widely used by other experiments [10]. A suitable $\bar{\nu}_e$ source must have $Q_\beta > 1.806\,\mathrm{MeV}$ (above the IBD threshold) and a half life long enough to allow the production and transportation of the source to the detector [11]. The Borexino collaboration has decided to use ^{144}Ce–^{144}Pr, which features $Q_\beta\left(^{144}Pr\right)$ of 2.996 MeV. ^{144}Ce can be extracted from spent nuclear fuel followed by column chromatography. Due to the high IBD cross-section [12] the source activity can be in the order of 100 kCi.

3.2 Neutrino emitters in Borexino

As a further option the deployment of a neutrino source underneath the Borexino detector is under consideration. For that purpose the ^{51}Cr source used by the GALLEX experiment could be refurbished. ^{51}Cr is an electron capture source, $^{51}\mathrm{Cr} + e^- \rightarrow {}^{51}\mathrm{V} + \nu_e$, featuring four monochromatic neutrino lines. In 81.6% (8.5%) of the time it decays to the ground state of ^{51}V and emits a 747 keV (752 keV) ν_e, while in 9% (0.9%) of the time a 427 keV (432 keV) ν_e is emitted to the first excited state of ^{51}V followed by the emission of a 320 keV γ. The dominant ν_e line is very similar to the 0.862 MeV ν_e from the radioactive decay of ^{7}Be in the Sun. The ^{51}Cr source will be produced by neutron irradiation of ^{50}Cr at nuclear reactors. Natural chromium consists mainly of ^{52}Cr (83.9%) and ^{53}Cr (9.5%). Since ^{53}Cr has a relatively large thermal neutron cross section of 18.7 barn, enriched ^{50}Cr has has to be used in order to reach the desired activity of 5-10 MCi.

3.3 Sensitivity and expected results

The analysis of short baseline neutrino oscillation in Borexino can be performed in two ways. The standard disappearance procedure is a rate analysis. If neutrino oscillation occur, the expected number of events with respect to the non-oscillation scenario will be lower. This technique relies on a precise knowledge of the source activity and background estimation. The second technique is called oscillometry and is an almost unique feature of the Borexino experiment or of a similar large liquid scintillator detector [5]. The physics potential of the SOX concept is shown in Figure 1. During the first phase the cerium source and possibly the chromium source will be placed underneath the detector. This will allow testing the parameter region currently favored by global fits. Depending on the results, the cerium source might also be placed inside the water tank or in the center of the detector.

4 Conclusion

The Borexino detector is an ideal candidate to search for sterile neutrinos. During the first phase of the experimental setup, an anti-neutrino source will be placed in a tunnel underneath the large low background detector Borexino. The source will arrive at the end of 2015 at the

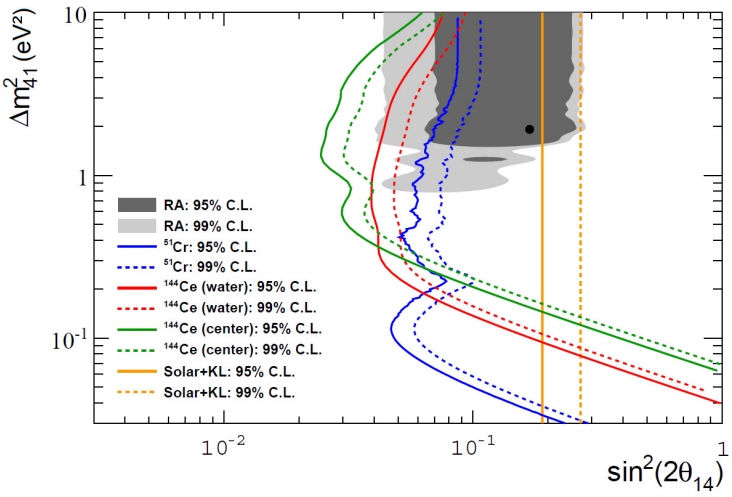

Figure 1: Sensitivity for the SOX project [3]. The cerium source sensitivity for the first phase (see text for details) is similar to the sensitivity of the shown chromium source.

Laboratori Nazionali del Gran Sasso. First results are expected in 2016. Additional physics of the SOX concept includes studies of the magnetic moment of the neutrino as well as the measurement of the Weinberg angle [3].

References

[1] G. Mention, M. Fechner, Th. Lasserre, Th.A. Mueller, D. Lhuillier, et al. The Reactor Antineutrino Anomaly. *Phys.Rev.*, D83:073006, 2011.

[2] C. Giunti, M. Laveder, Y.F. Li, Q.Y. Liu, and H.W. Long. Update of Short-Baseline Electron Neutrino and Antineutrino Disappearance. *Phys.Rev.*, D86:113014, 2012.

[3] G. Bellini et al. SOX: Short distance neutrino Oscillations with BoreXino. *JHEP*, 1308:038, 2013.

[4] B. Ricci N. Ferrari, G. Fiorentini. The Cr-51 neutrino source and Borexino: a desirable marriage. *Phys. Letters B*, 387:427–431, 1996.

[5] M. Pallavicini. The SOX project: a search for sterile neutrinos with BoreXino. *PoS*, Neutel2013:026, 2013.

[6] G. Alimonti et al. The Borexino detector at the Laboratori Nazionali del Gran Sasso. *Nucl.Instrum.Meth.*, A600:568–593, 2009.

[7] G. Bellini et al. Final results of Borexino Phase-I on low energy solar neutrino spectroscopy. *Phys.Rev.*, D89:112007, 2014.

[8] G. Bellini et al. Neutrinos from the primary proton-proton fusion process in the Sun. *Nature*, 512(7515):383–386, 2014.

[9] G. Bellini et al. Measurement of geo-neutrinos from 1353 days of Borexino. *Phys.Lett.*, B722:295–300, 2013.

[10] Y. Abe et al. First Measurement of θ_{13} from Delayed Neutron Capture on Hydrogen in the Double Chooz Experiment. *Phys.Lett.*, B723:66–70, 2013.

[11] Th. Lasserre. Testing the Reactor and Gallium Anomalies with Intense (Anti)Neutrino Emitters. *Nucl.Phys.Proc.Suppl.*, 235-236:214–219, 2013.

[12] P. Vogel and John F. Beacom. The angular distribution of the neutron inverse beta decay, $\bar{\nu}_e + p \to e^+ + n$. *Phys. Rev.*, D60:053003, 1999.

The Hunt for neutrinoless double beta decay with the NEXT experiment

David Lorca[1] on behalf of the NEXT Collaboration

[1]Instituto de Fisica Corpuscular (IFIC), CSIC & Univ. de Valencia, E-46071 Valencia, Spain

DOI: http://dx.doi.org/10.3204/DESY-PROC-2014-04/65

The NEXT-100 detector will search for the neutrinoless double beta decay of ^{136}Xe using an electroluminescent high-pressure xenon gas TPC filled with 100 kg of enriched Xe. An observation of this hypothetical process would establish a Majorana nature for the neutrino and prove the violation of lepton number. A scaled-down prototype, NEXT-DEMO, has been built to demonstrate the feasibility of the technology. NEXT-DEMO includes an energy plane made of PMTs and a tracking plane made of SiPMs. X-ray energy depositions, produced by the de-excitation of xenon atoms after their interaction with gamma rays, have been used to characterize the detector response. With this method, the released energy by gammas coming from ^{22}Na source has been corrected, achieving an energy resolution of 5.691% FWHM and 1.62% FWHM at the 29.7 keV and 511 keV peaks respectively, which extrapolate to 0.62% FWHM and 0.73% FWHM at $Q_{\beta\beta}$ value of Xenon.

1 Introduction

Double beta decay ($\beta\beta$) is a very rare nuclear transition in which a nucleus with Z protons decays into a nucleus with Z+2 protons and same mass number A. It can only be observed in those isotopes where the β decay mode is forbidden due to the energy of the daughter nuclei being higher than the energy of the parent nuclei, or highly suppressed. Two decay modes are usually considered: the standard two-neutrino mode ($\beta\beta2\nu$), which has been observed in several isotopes with typical half-lives in the range of $10^{18} - 10^{21}$ years [1], and the neutrinoless mode ($\beta\beta0\nu$), which violates lepton-number conservation, and is therefore forbidden in the Standard Model of particle physics.

An observation of $\beta\beta0\nu$ would prove that neutrinos are Majorana particles, that is, identical to their antiparticles [2], and would provide direct information on neutrino masses [1]. Besides, it would demonstrate that total lepton number is violated, a result that can be linked to the cosmic asymmetry between matter and antimatter through the process known as leptogenesis [3].

The half-life of $\beta\beta0\nu$, if mediated by light, Majorana neutrino exchange, can be written as

$$(T^{0\nu}_{1/2})^{-1} = G^{0\nu} \left|M^{0\nu}\right|^2 m^2_{\beta\beta} \tag{1}$$

where $G^{0\nu}$ is an exactly-calculable phase-space integral for the emission of two electrons; $\left|M^{0\nu}\right|$ is the nuclear matrix element of the transition, which has to be evaluated theoretically; and $m_{\beta\beta}$ is the effective Majorana mass of the electron neutrino:

$$m_{\beta\beta} = \left|\sum U^2_{ei} m_i\right| \tag{2}$$

where m_i are the neutrino mass eigenstates and U_{ei} are elements of the neutrino mixing matrix.

The aim of all $\beta\beta0\nu$ experiments is to measure the decay rate of this disintegration. However, the measurement is limited by the experimental sensitivity of the detector employed, which can be expressed as

$$T_{1/2} \propto a \cdot \epsilon \cdot \sqrt{\frac{M \cdot t}{\Delta E \cdot B}} \tag{3}$$

where M is the isotope mass, ΔE is the energy resolution, B is the background rate, ϵ is the detection efficiency and a is a term which includes nuclear matrix elements [1].

Due to the presence of the two neutrino mode, together with background events which can fall in the energy Region of Interest (ROI) where the neutrinoless mode is expected, ΔE is a must to resolve the possible $\beta\beta0\nu$ events. In addition, an appropriate selection of detector components and surroundings should be done in such a way to reduce background rate as low as possible. Besides, current generation of $\beta\beta0\nu$ experiments have explored the region of neutrino masses corresponding to 160-250 meV (depending of n.m.e.) [4] by using from tens to a few hundred kilos of isotope mass. The non detection of a signal creates the necessity of increase the isotope mass in the new generation up to the ton scale to explore new areas.

2 The NEXT Concept

The NEXT experiment combines good energy resolution, a low background rate and the possibility to scale-up the detector to large masses of $\beta\beta$ isotope by using a high-pressure xenon gas (HPXe) electroluminescent (EL) time projection chamber (TPC) to search for $\beta\beta0\nu$ in ^{136}Xe.

Whit this technology, an energy resolution better than 1% FWHM can be achieved in NEXT at $Q_{\beta\beta}$ of Xe thanks to the small Fano Factor of gaseous xenon ($F_{HPXe} = 0.15 \pm 0.02$) [5], compared with other media such as liquid xenon (LXe) ($F_{LXe} \sim 20$), together with the low fluctuations introduced by an EL-based amplification. Besides, HPXe provides topological information of the events, allowing to discriminate between signal events (a twisted track of about 10 cm long, with two energy depositions at both ends) from background events (single electrons with only one blob at the end and most of the time accompanied by an X-ray [6]). Furthermore, ^{136}Xe constitutes 8.86% of all natural xenon, but the enrichment process is relatively simple and cheap compared to that of other $\beta\beta$ isotopes, thus making ^{136}Xe the most obvious candidate for a future multi-ton experiment.

The detection process in NEXT implies independent systems for tracking and calorimetry. Particles interacting in the HPXe transfer their energy to the medium ionizing and exciting its atoms. The excitation energy is manifested in the prompt emission of VUV ($\sim$ 178 nm) scintillation light. The ionization electrons drift toward the TPC anode thanks to the presence of a moderate electric field, entering in a region with an even more intense electric field. There, secondary VUV photons are generated isotropically by electroluminescence. Therefore both scintillation and ionization produce an optical signal, to be detected with a plane of PMTs (the energy plane) located behind a transparent cathode. The detection of the primary scintillation light constitutes the start-of-event, whereas the detection of EL light provides an energy measurement. Electroluminescent light provides tracking as well, since it is detected a few millimeters away from production at the anode plane, via an array of MPPCs (the tracking plane).

3 NEXT-DEMO: R&D and results

To demonstrate that the NEXT concept is feasible, a scaled prototype, NEXT-DEMO, was developed. NEXT-DEMO is a cylindrical pressure vessel made of stainless steel, able to withstand up to 20 bar of internal pressure. It is 60 cm long and 30 cm in diameter, and holds $\sim$ 1.5 kg of Xe at 10 bar. Three wire grids, the cathode, gate and anode, limit the two active regions of the TPC. The primary scintillation light is directly detected by a plane of 19 Hamamatsu R7378A PMTs behind the cathode grid. Electroluminescent light produced by ionization electrons, is once again detected in the energy plane but the forward going photons are also detected in an array of 256 tetraphenyl butadiene (TPB) coated Hamamatsu S10362-11-050P SiPMs. The tracking plane is used to reconstruct the position of energy deposits and, ultimately, the topology of an event as a whole.

In this prototype, the abundance of xenon K-shell X-ray emission during data taking with a ^{22}Na source has been identified as a multitool for the characterisation of the fundamental parameters of the gas as well as the equalisation of the response of the detector [7]. The advantage of using these events is that they are distributed all over the volume of the detector and the range of the $\sim$30 keV electrons produced is small, around 0.6 mm at 10 bar [8], releasing almost all their energy in a single point. Such depositions have been used to extract correction factors which describe the detector geometry effects. In addition, both loss of charge due to electron attachment with gas impurities and temporal fluctuations during the EL generation due to temperature and pressure oscillations have been corrected.

The mentioned corrections have been applied to the reconstructed energy released by gammas coming from a ^{22}Na (see [7]), where an energy resolution for the K_α peak (29.7 keV) and photopeak (511 keV) of (5.691 $\pm$ 0.003)% FWHM and (1.62 $\pm$ 0.01)% FWHM were extracted respectively. Independently extrapolating these two values to the ^{136}Xe $Q_{\beta\beta}$ assuming the dominance of photon shot noise Poisson statistics results in a predicted energy resolution at $Q_{\beta\beta}$ of 0.6256% FWHM and 0.7353% FWHM respectively.

4 NEXT-100

Following the previous ideas, the NEXT collaboration plans to build the NEXT-100 detector, described in [6], which will be formed by a HPXe TPC containing 100 kg of xenon, enriched at 90% in its ^{136}Xe isotope, at 15 bar. The pressure vessel is built with low activity stainless steel, and contains an inner copper shield, 12 cm thick and made of radio pure copper, to attenuate the radiation coming from the high-energy gammas emitted in the decays of ^{208}Tl and ^{214}Bi, present in the external detector. The energy measurement in NEXT-100 is provided by a total of 60 Hamamatsu R11410-10 photomultipliers (PMTs) covering 32.5% of the cathode area constitute the energy plane. This PMT model has been specially developed for radiopure, xenon-based detectors. The tracking function is provided by an array of around 7200 SiPMs, 1 cm pitch, located behind the EL region, and coated with TPB.

All materials present in the NEXT-100 detector have been chosen according to rigorous radiopurity requirements, which together with the detection technique employed by NEXT, produce an expected background rate of $5{\cdot}10^{4}$ counts/(kg·keV·year) [6]. After 5 years of data taking, a sensitivity of $5.9{\cdot}10^{25}$ years is predicted or, in terms of the effective neutrino Majorana mass $m_{\beta\beta}$, a value of around 100 meV, making NEXT one of the most competitive experiments in the field [9].

NEXT-100 is approved for operation in the Laboratorio Subterráneo de Canfranc (LSC), in Spain, where the installation of seismic platform, lead castle, gas system, emergency recovery system and vessel are already completed. Underground operations with non-enriched xenon will start in 2015 and the physics case with enriched xenon is planned for early 2016.

5 Conclusions

The search for $\beta\beta0\nu$ is one of the major current challenges in neutrino physics. Due to the high sensitivity provided by a HPXe TPC with EL amplification, NEXT-100 promises to be one of the leading experiments in the field, exploring the region of neutrino mass down to 100 meV. One of its prototypes, NEXT-DEMO, has demonstrated the main issues of such technology, helping in the design of the final detector. In addition, xenon K-shell X-ray depositions have been identified as a useful tool for the characterization of this type of detectors, providing the spatial calibration needed for close-to-optimal energy resolution.

Acknowledgments

This work was supported by the following agencies and institutions: the European Research Council under the Advanced Grant 339787-NEXT; the Ministerio de Economía y Competitividad of Spain under grants CONSOLIDER-Ingenio 2010 CSD2008-0037 (CUP), FPA2009-13697-C04 and FIS2012-37947-C04; the Director, Office of Science, Office of Basic Energy Sciences, of the US Department of Energy under contract no. DE-AC02-05CH11231; and the Portuguese FCT and FEDER through the program COMPETE, project PTDC/FIS/103860/2008.

References

[1] J. J. Gomez-Cadenas, J. Martin-Albo, M. Mezzetto, F. Monrabal and M. Sorel, "The Search for neutrinoless double beta decay," Riv. Nuovo Cim. **35**, 29 (2012) [arXiv:1109.5515 [hep-ex]].

[2] J. Schechter and J. W. F. Valle, "Neutrinoless Double beta Decay in SU(2) x U(1) Theories," Phys. Rev. D **25**, 2951 (1982).

[3] S. Davidson, E. Nardi and Y. Nir, "Leptogenesis," Phys. Rept. **466**, 105 (2008) [arXiv:0802.2962 [hep-ph]].

[4] A. Gando and others, "Limit on Neutrinoless $\beta\beta$ Decay of Xe-136 from the First Phase of KamLAND-Zen and Comparison with the Positive Claim in Ge-76," Phys.Rev.Lett., 110 (2013) [arXiv:1211.3863 [hep-ex]].

[5] David Nygren, "High-pressure xenon gas electroluminescent TPC for 0-ν $\beta\beta$-decay search," NIM A, 603, 337-348, (2009), [doi = "http://dx.doi.org/10.1016/j.nima.2009.01.222"].

[6] [NEXT Collaboration], "NEXT-100 Technical Design Report (TDR): Executive Summary," arXiv:1202.0721 [physics.ins-det].

[7] David Lorca and others, "Characterisation of NEXT-DEMO using xenon K_α X-rays," [arXiv:1407.3966 [hep-ex]].

[8] M. J. Berger and others, "Computer Programs for Calculating Stopping-Power and Range Tables for Electrons, Protons, and Helium Ions (version 1.2.3)," ESTAR, PSTAR and ASTAR (2005) ["http://physics.nist.gov/Star"].

[9] J. J. Gomez-Cadenas, J. Martin-Albo, M. Sorel, P. Ferrario, F. Monrabal, J. Munoz-Vidal, P. Novella and A. Poves, "Sense and sensitivity of double beta decay experiments," JCAP **1106**, 007 (2011), [arXiv:1010.5112 [hep-ex]].

The effect of Quantum Gravity on astrophysical Neutrino flavor observables.

Jonathan Miller[1], *Roman Pasechnik*[2]

[1]Departamento de Física Universidad Técnica Federico Santa María
Casilla 110-V, Valparaíso, Chile
[2]Theoretical High Energy Physics, Department of Astronomy and Theoretical Physics, Lund University, Sölvegatan 14A, SE 223-62 Lund, Sweden

DOI: http://dx.doi.org/10.3204/DESY-PROC-2014-04/180

At the quantum level, an interaction of a neutrino with a graviton may trigger the collapse of the neutrino flavor eigenstate to a neutrino mass eigenstate. We will present that such an essentially quantum gravity effect may have strong consequences for neutrino oscillation phenomena in astrophysics due to the relatively large scattering cross section of relativistic neutrinos off massive sources of gravitational fields (the case of gravitational Bethe-Heitler scattering). This results in a new technique for the indirect detection of gravitons by measuring the flavor composition of astrophysical neutrinos.

A theoretical extrapolation of fundamental Quantum Mechanics concepts to Einstein's gravity suffers from major difficulties with quantization of space-time, ultraviolet behavior and non-renormalizability of the resulting theory. Typically quantum gravity effects are disregarded as being irrelevant at energy scales smaller than the Planck scale, $M_{Pl} \sim 10^{19}$ GeV. Due to suppression, quantum gravity effects are referred to as unobservable [1, 2].

We propose a new approach for indirect experimental studies of (local) quantum gravity interactions based upon an effect on neutrino oscillation observables of a neutrino interaction with an energetic graviton. This may happen in large-angle energetic gravitational Bremsstrahlung off an astrophysical neutrino passing through an external classical gravitational potential. This gravitational Bethe-Heitler (GBH) process can be considered in the quasi-classical approxi-

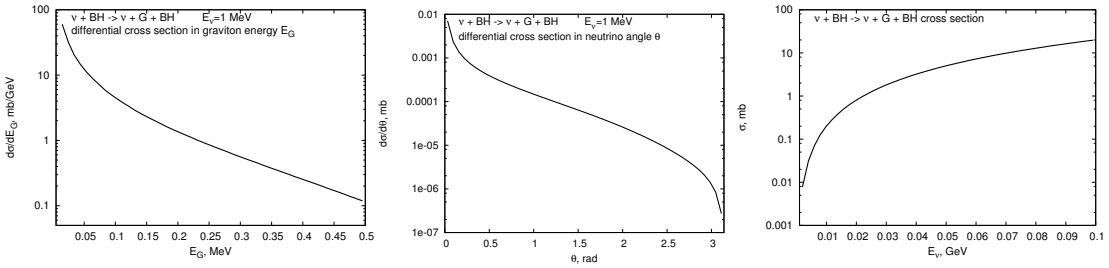

Figure 1: Differential cross section versus radiated graviton energy E_G (left), polar angle of the final-state neutrino θ_ν, and the integrated cross section as a function of incoming neutrino energy E_ν for GBH scattering of a neutrino off a massive object.

mation for large angle and/or large energy graviton emission (Born approximation). Such a process may happen with high probability, such as in the case of scattering off a massive source of gravitational field (star or a black hole). The neutrino interaction serves as a direct *quantum measurement* of the microscopic properties of the gravitational field at astrophysical scales.

Weakly-interacting neutrinos are an efficient carrier of information at astrophysical scales due to not being absorbed or scattered by interstellar mediums. This property of neutrinos enables us to utilize them for large-scale astrophysical *experiments*. In the identified experiment neutrinos *change* their quantum state due to a local quantum gravity process (in terms of local graviton coupling to a fundamental matter particle) and convey information about this process through the cosmological medium to Earth. Elementary particles in the mass basis are eigenstates of the Hamiltonian of quantum-gravitational interactions similar to how leptons and quarks are weak eigenstates in the flavor and CKM bases. The second important neutrino property that neutrino mass and flavor eigenstates are not the same.

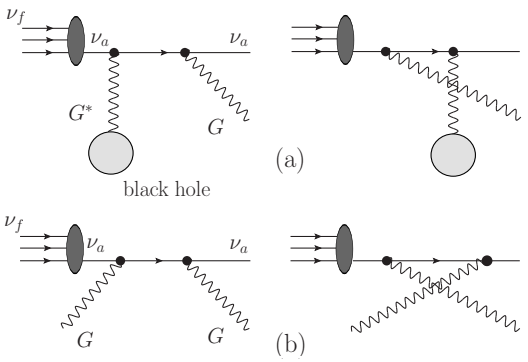

Figure 2: The quantum gravity processes which causes the decoherence of the neutrino flavor eigenstate ($f = e, \mu, \tau$) effectively converting it to a mass eigenstate ($a = 1, 2, 3$) – GBH scattering of neutrino off a massive object (a), and gravitational Compton scattering (b). The ellipse is a projection to a mass state and the circle is a classical source of gravitational field.

Consider a relativistic neutrino propagating in the gravitational potential of a static black hole. At the quantum level a graviton interacts only with a definite mass state (or gravitational mass eigenstate) $a = 1, 2$ or 3. Expressed equivalently definite mass eigenstates (propagating states) are conserved by the quantum gravity hamiltonian while superpositions, such as the flavor eigenstates, are not. Astrophysical neutrinos are initially produced in electroweak processes in a definitive flavor state, $f = e, \mu$ or τ, which are coherent superpositions of mass eigenstates. This neutrino is quantum mechanically observed by the energetic graviton as being in a definite mass state. This means that between the production in an astrophysical source and the detection in an Earth based detector, the neutrino exists in a definite mass state and has experienced *quantum decoherence*.

The neutrino is *converted* to mass state with a probability $P_{\nu_f \to \nu_a} = |\Psi_{\nu_f \to \nu_a}|^2$, given in terms of the corresponding wave function $\Psi_{\nu_f \to \nu_a}$ which projects out a flavor state ν_f onto a mass state ν_a and is typically expressed in terms of the corresponding PMNS mixing matrix element, $\Psi_{\nu_f \to \nu_a} = V_{af} e^{-i \frac{m_a^2}{2E_\nu} L}$.

We consider the case shown in Fig. 2(a), the graviton exchange is with negative momentum transfer squared $t = -q^2 < 0$ in the t-channel with the propagator stretched between the relativistic neutrino of mass m_ν and energy $E_\nu \gg m_\nu$ and a massive classical gravitational field source with mass $M \gg E_\nu$. The cross section has been calculated for the gravitational scattering of scalar particles with $M \gg m$ in [3]. We use their formula as a good approximation to estimate the neutrino-solar mass cross section numerically. In this case, as an order-of-

magnitude estimate, the GBH cross section at the Born level behaves as

$$\sigma_{\rm GBH} \sim \frac{M^2 E_\nu^2}{M_{Pl}^6}\,, \quad M \gg E_\nu \gg m_\nu\,, \tag{1}$$

and thus may not be very small since the Planck scale suppression can be largely eliminated by having a mass M of a heavy classical source in numerator. In particular, for a solar mass object $M \sim 10^{57}$ GeV, we have $M^2/M_{Pl}^6 \sim 1$ GeV^{-4}, so there is no significant suppression of the cross section for relativistic neutrinos.

Note that the Bethe-Heitler calculation in QED to first order gives the correct cross section for photon Bremsshtrahlung for extended objects such as a nucleus as shown in Ref. [4]. Similarly, we expect that the GBH result for a point-like classical source should be roughly correct to first order for extended objects, like a star or dark matter distribution.

The traditional source of decoherence typically referred to in astrophysical neutrino oscillations studies can be called *propagation decoherence*. Here the neutrino mass states have separated or dispersed so that they no longer interfere at large distances from the production point. This source of decoherence depends on the energy resolution of the detection process, the energy of the neutrino, the masses of the neutrino mass states, and details of the production and detection processes. Beyond the characteristic length the propagating neutrino mass states no longer interfere during the interaction process [5].

Note that while the flux due to *quantum decoherence* is a flux of pure mass eigenstates, that in the propagation decoherence case the flux is not of pure mass eigenstates, but rather decoherent (spatially separated) mass eigenstates. No quantum measurement of the state of these neutrinos has taken place, and the neutrino still exists as a superposition of mass states. These two situations are the same when detected in the case where the flux does not pass through matter; in the case where the flux passes through matter, the effect due to matter is different for the two cases. In the *quantum decoherence* case, the neutrino flux experiences regeneration as fluxes of neutrinos in pure mass eigenstates. In the propagation decoherence case, the neutrino flux experiences regeneration as a superposition of mass eigenstates.

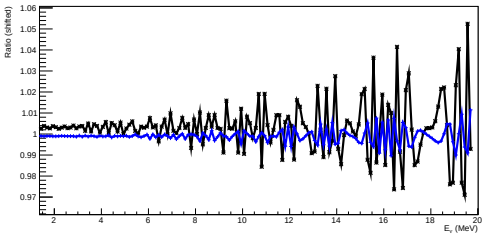

Figure 3: Ratio for neutrinos which have undergone propagation decoherence (blue) and neutrinos which have undergone graviton induced decoherence (black).

The theory of neutrino propagation, including neutrino propagation in medium and neutrino propagation where the neutrino experiences propagation decoherence, is well presented in [5] [6]. These papers give the essentials of neutrino propagation in matter and propagation decoherence, but no explicit formula is given for a neutrino which undergoes propagation decoherence and then experiences the Earth matter effect.

For simplicity consider just two regimes, the vacuum and the earth (with constant density) and two neutrino flavors. Due to the discontinuity at the earth's surface, the flavor amplitudes should be matched at the border between the two regimes. The flavor at the point before the density jump is used to determine the initial state [6].

The condition for the wave packet separation to be complete is given explicitly by [7]. They note that this is different than the effect due to averaging (Section 2.1) over the energy, despite the effect being computationally the same for vacuum[5]. We expect significant (> 1 km) wave packet separation for supernova more than 10 kpc distant.

The amplitude of the state at the boundary between regimes can be given by $A_{ee}^{dec} = \cos^2(\theta)\, e^{i\frac{3\pi}{4}} + \sin^2(\theta)\, e^{-i\frac{3\pi}{4}}$ and $A_{e\mu}^{dec} = \sin(\theta)\cos(\theta)\left(e^{-i\frac{3\pi}{4}} - e^{i\frac{3\pi}{4}}\right)$. These give the flavor amplitudes of a neutrino produced in a ν_e state which has travelled through vacuum and experienced wave packet separation when it reaches the Earth vacuum transition. An amplitude which depends on the phase between the wave packets would be incorrect for large wave packet separations. This amplitude is then projected to the new matter basis.

The ratio of neutrinos which have undergone *propagation decoherence* and at the same time propagated through a region of constant density to those which have only propagated through the vacuum is given by the following expression

$$\begin{aligned} R_p &= \Big(\cos(x_m)^2\,(3+\cos(4\theta)) + (2+\cos(4\theta_m-8\theta)+\cos(4\theta_m-4\theta))\sin(x_m)^2 \\ &- 2\sin(2x_m)\sin(2\theta_m-2\theta)\sin(2\theta)\Big)/(3+\cos(4\theta))\,. \end{aligned} \tag{2}$$

Analogically, the ratio of neutrinos which have undergone *quantum decoherence* in the presence of the matter effect (medium of constant density) to those which have propagated through the vacuum takes a different form

$$R_q = \frac{5+\cos(4\theta_m)+\cos(4\theta_m-4\theta)+\cos(4\theta)+4\cos(2x_m)\cos(2\theta)\sin(2\theta_m-2\theta)}{6+2\cos(4\theta)}\,. \tag{3}$$

A difference between the ratios R_p and R_q could be measurable and indicates the difference between *propagation decoherence* and *quantum decoherence* in the presence of the matter effect. Measurement of such a difference could serve as a clear example of graviton detection. In the presence of an additional jump in matter density the corresponding numerical results are presented in Fig.3, demonstrating that measurement of graviton induced decoherence is possible.

More details of this work can be found at [8] and this research was supported in part by the National Science Foundation under Grant No. NSF PHY11-25915 and by PROYECTO BASAL FB 0821 CCTVal and by Fondecyt (Grant No. 11130133).

References

[1] F. Dyson, *The World on a String*, review of *The Fabric of the Cosmos: Space, Time, and the Texture of Reality* by Brian Greene, New York Review of Books, Volume 51, Number 8, May 13, (2004);
F. Dyson, *Is a Graviton Detectable?*, Poincare Prize Lecture International Congress of Mathematical Physics Aalborg, Denmark, Aug. 6, 2012.

[2] T. Rothman and S. Boughn, Found. Phys. **36**, 1801 (2006).

[3] B. M. Barker, S. N. Gupta, J. Kaskas, Phys. Rev. 182 (1969) 1391-1396.

[4] H.K. Tseng, R.H. Pratt, Phys. Rev. A 19, 1525 (1979).

[5] M. Beuthe, Phys. Rept. **375**, 105 (2003) [hep-ph/0109119].

[6] M. Blennow and A. Y. Smirnov, Adv. High Energy Phys. **2013**, 972485 (2013) [arXiv:1306.2903].

[7] Y. Farzan and A. Y. Smirnov, Nucl. Phys. B **805**, 356 (2008) [arXiv:0803.0495].

[8] J. Miller and R. Pasechnik, [arxiv:1305.4430].

CANDLES – Search for Neutrino-less Double Beta Decay of ^{48}Ca –

S. Umehara[1], *T. Kishimoto*[1,2], *M. Nomachi*[1], *S. Ajimura*[1], *T. Iida*[1], *K. Nakajima*[1], *K. Ichimura*[1], *K. Matsuoka*[1], *T. Ishikawa*[1], *D. Tanaka*[1], *M. Tanaka*[1], *T. Maeda*[1], *S. Yoshida*[2], *K. Suzuki*[2], *H. Kakubata*[2], *W. Wang*[2], *V. T. T. Trang*[2], *W. M. Chan*[2], *M. Doihara*[2], *T. Ohata*[2], *K. Tetsuno*[2], *Y. Tamagawa*[3], *I. Ogawa*[3], *S. Tomita*[3], *G. Fujita*[3], *A. Kawamura*[3], *T. Harada*[3], *Y. Inukai*[3], *K. Sakamoto*[3], *M. Yoshizawa*[3], *K. Fushimi*[4], *R. Hazama*[5], *N. Nakatani*[5], *H. Ohsumi*[6], *K. Okada*[7]

[1]Research Center for Nuclear Physics, Osaka University, Ibaraki 567-0047, Japan
[2]Graduate School of Science, Osaka University, Toyonaka, Osaka 560-0043, Japan
[3]Graduate School of Engineering, University of Fukui, Fukui 910-8507, Japan
[4]Faculty of Integrated Arts and Science, The University of Tokushima, Tokushima 770-8502, Japan
[5]Faculty of Human Environment, Osaka Sangyo University, Osaka 574-8530, Japan
[6]Faculty of Culture and Education, Saga University, Saga 840-8502, Japan
[7]Department of Computer Science and Engineering, Kyoto Sangyo University, Kyoto 603-8555, Japan

DOI: http://dx.doi.org/10.3204/DESY-PROC-2014-04/97

CANDLES is the project to search for neutrino-less double beta decay of ^{48}Ca. Now we installed the CANDLES III system at the Kamioka underground laboratory. The CANDLES III system realizes the low background condition by a characteristic structure and data analyses for background rejection. Here we report performances of the CANDLES III system.

1 Double beta decay of ^{48}Ca

The neutrino-less double beta decay ($0\nu\beta\beta$) is acquiring great interest after the confirmation of neutrino oscillation which demonstrated nonzero neutrino mass. Measurement of $0\nu\beta\beta$ provides a test for the Majorana nature of neutrinos and gives an absolute scale of the effective neutrino mass. Many experiments have been carried out so far and many projects have been proposed.

Among double beta decay nuclei, ^{48}Ca has an advantage of the highest $Q_{\beta\beta}$-value (4.27 MeV). This large $Q_{\beta\beta}$-value gives a large phase-space factor to enhance the $0\nu\beta\beta$ rate and the least contribution from natural background radiations in the energy region of the $Q_{\beta\beta}$-value. Therefore good signal to background ratio is ensured in a $0\nu\beta\beta$ measurement. For the $0\nu\beta\beta$ measurement of ^{48}Ca, we proposed CANDLES(CAlcium fluoride for the study of Neutrinos and Dark matters by Low Energy Spectrometer) system[1].

2 CANDLES III at Kamioka observatory

We installed the detector system CANDLES III at the Kamioka underground laboratory (2700 m.w.e.). The CANDLES III system consists of 96 CaF_2(pure) scintillators with total mass of 305 kg and liquid scintillator with total volume of 2 m^3. The CaF_2(pure) scintillators, which are main detectors, are immersed in the liquid scintillator. The liquid scintillator acts as a 4 π active shield to veto external backgrounds. Scintillation lights from the CaF_2(pure) and the liquid scintillator are viewed by 62 large photomultiplier tubes (13" $\times$ 48 and 20" $\times$ 14). The signal of the CaF_2(pure) scintillator has a decay time of 1 μsec although the liquid scintillator has a width of around a few tens nsec. Thus the signals from the CaF_2(pure) can be discriminated against the background signals on the liquid scintillator by observing pulse shapes.

3 Background in the $Q_{\beta\beta}$ region

As mentioned above, backgrounds can be strongly limited because of the highest $Q_{\beta\beta}$-value of ^{48}Ca. The remaining backgrounds are following processes:
(a) ^{212}Bi $\xrightarrow[\beta]{}$ ^{212}Po $\xrightarrow[\alpha]{}$ ^{208}Pb (Th-chain)
(b) ^{208}Tl $\xrightarrow[\beta]{}$ ^{208}Pb(Th-chain)
(c) γ-ray from neutron capture
In this section we mention about study for the rejection of process (a) and (b).

^{212}Po nucleus in process (a) has short half-life 0.299 μsec. On the other hand, the CaF_2(pure) scintillator has long decay constant ($\sim$ 1 μsec). Thus radiations emitted by consecutive decays of ^{212}Bi and ^{212}Po are measured as one event in ADC gate (4 μsec) for the CaF_2(pure) scintillator. Energy deposited by the consecutive decays in the CaF_2(pure) scintillator is $E_{max} = 5.3$ MeV, because a quenching factor for α-ray is around 35%. Thus the process is serious backgrounds in a interesting energy window for the $0\nu\beta\beta$ measurement. In order to reject the events, we measured the pulse shape of the consecutive events by using the characteristic 500 MHz flash ADC. Details of the analyses are described in [2, 3]. As the result of the analyses, the background from process (a) will be reduced by the 3 orders of magnitude.

The other background candidate is process (b) of ^{208}Tl events. ^{208}Tl has large Q_β-value through it emits 2.6 MeV γ-ray. The probability which the high energy γ-rays are contained in a single CaF_2(pure) scintillator is small. However the $0\nu\beta\beta$ decay is extremely the rare process. Thus the background has to be seriously considered.

In order to reject the ^{208}Tl events, we applied a time correlation analysis. The ^{208}Tl events has a preceding α-decay with a half life of 3 minutes (^{212}Bi : $E_\alpha = 6.1$ MeV). Thus we can reject the ^{208}Tl events by identifying the preceding α-ray. For identifying the α-ray, we need the good position resolution and the pulse shape discrimination between α- and γ-rays. Details of the analyses are shown in [4]. Based on techniques of the position reconstruction and the pulse shape discrimination, we applied the time correlation analysis for ^{208}Tl. The energy spectrum of the candidate events of the preceding α-rays is shown in figure 1-a). The peak at 1.7 MeV was likely due to the α-rays coming from the preceding ^{212}Bi decays. To confirm origin of the peak, we analyzed the distribution of time lag Δt between the preceding and the delayed events. The time lag Δt distribution of the preceding events with energy of 1.6 - 1.8 MeV is shown in figure 1-b). In order to obtain the half-life, we fitted the time spectrum with two exponential function. The half-life derived from the Δt distribution was 187 $\pm$ 56 sec. The half-life nearly agreed with one of ^{208}Tl(183 sec). Thus it was concluded that the peak at 1.7 MeV was due to

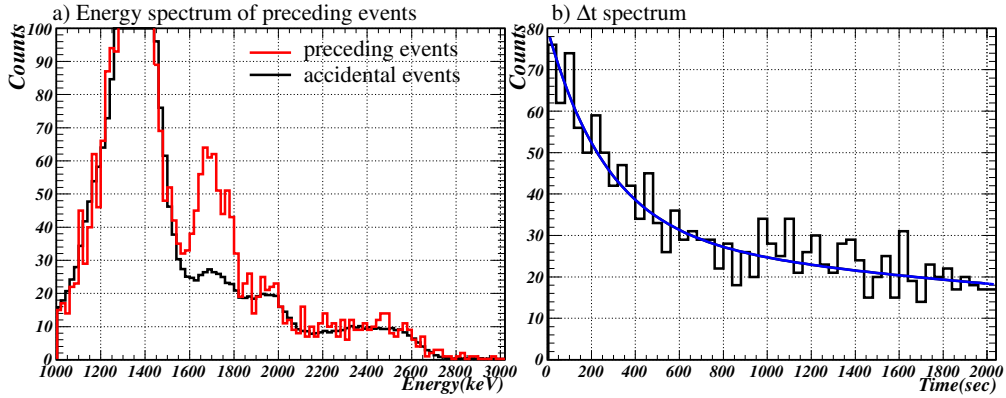

Figure 1: a) The energy spectra of the preceding events of ^{208}Tl. Red (black) line corresponds to the preceding (accidental) events. The peak at 1.7 MeV was due to ^{212}Bi decay (E_α = 6.1 MeV). b) Δt distribution between the preceding and delayed events. By fitting with two exponential function, we obtained the half-life of 187 ± 56 sec.

^{212}Bi α-rays and we found that ^{208}Tl can be rejected by the time correlation analysis.

As mentioned above, it is important to detect the preceding ^{212}Bi. Thus installation of a fast read-out DAQ system leads the good rejection efficiency for ^{208}Tl, because of least detecting loss in dead time. In early 2013 we installed a new DAQ system, of which read-out speed was improved 2.4 times as high as the previous one[5]. The dead time was decreased from 21% to 2%. As the result the event rate of the selected ^{212}Bi events was improved from 8.9±0.9 events/day to 12.7±0.7 events/day. This means that the rejection efficiency of ^{208}Tl was improved by 30%.

4 Analysis

In order to check the background rejection, we performed a pilot run. The criteria to select candidate events for $0\nu\beta\beta$ are given as follows.
(1) CaF_2(pure) scintillators fire.
(2) No liquid scintillator fires.
(3) The events are not process (a) events.
(4) The events are not candidate of the ^{208}Tl events of process (b).
As mentioned in section 2, criteria (1) and (2) are applied by using the pulse shapes difference between the CaF_2(pure) and liquid scintillators. Criteria (3) and (4) are described in section 3.

A selection of the candidate events was made for 4987 kg·days of data from Jun. to Sep. 2013. The energy spectrum using the 26 CaF_2(pure) scintillators, which are the high purity scintillators, is shown in figure 2. As the result, we observed 6 events in the $0\nu\beta\beta$ window of 4.17 - 4.48 MeV.

Here we estimated background rate in the $Q_{\beta\beta}$-value region. As mentioned above, the 3 processes are expected as the backgrounds in the $Q_{\beta\beta}$-value region. The background rate from process (a) and (b) was estimated by radioactivities of the CaF_2(pure) scintillators. The background rate was $\sim$ 1 event/4987 kg·days. In the CANDLES system, the other background candidate is γ-rays from neutron capture in the surrounding materials of the detector (process (c)). In order to estimate the background rate from neutron capture γ-rays, we performed a

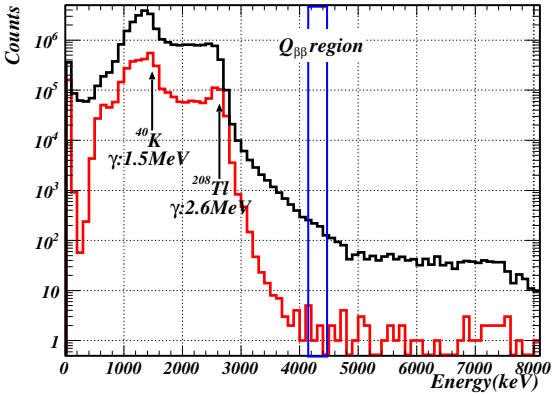

Figure 2: Energy spectra with/without the event selection. Black line represents an experimental data without the event selection. After the event selection, 6 events are seen in the $0\nu\beta\beta$ window.

special run using a ^{252}Cf neutron source. Based on the result of the special run and Monte-Carlo simulation, we estimated that the event rate from the γ-rays is 3.4 event/4987 kg·days. By using the expected background rate, we present an experimental sensitivity. The sensitivity with the 90 % C.L. is 0.8×10^{22} year.

5 Future perspective

In order to reduce the γ-rays from neutron capture, we plan to install a shielding system in the CANDLES III system in early 2015. The shielding system consists of boron/cadmium sheet and Pb blocks. We estimate to reduce the γ-ray rate by ~ 2 orders of magnitude.

Other improvement for the CANDLES III system is a cooling system. The CaF_2(pure) scintillator is known that amount of light output increases with low temperature. The increasing rate of the light yield is 2%/°C. We have already installed the cooling system and will start operation of the system. We estimate to increase the light yield by 30%.

6 Conclusion

Now the CANDLES III system was installed at the Kamioka underground laboratory. By improvement of the detector system and the pulse shape analyses, we can reduce the background events from Bi $\rightarrow$ Po and ^{208}Tl. We performed the pilot run in order to check the background rate. The sensitivity of the $0\nu\beta\beta$ half-life is 0.8×10^{22} year with the pilot run . In near future we will upgrade the CANDLES III system to reduce the background rate. After the upgrade the sensitivity will be $\sim 10^{24}$ year for the $0\nu\beta\beta$ half-life.

References

[1] T. Kishimoto et al. In *Proc. of 4th Workshop on Neutrino Oscillations and their Origin*, page 338, 2003.

[2] S. Umehara et al. *Phys. Rev. C*, 78:058501, 2008.

[3] S. Umehara et al. *Physics Procedia*, in press.

[4] S. Umehara et al. *EPJ Web of Conferences*, 66:08008, 2014.

[5] K. Suzuki et al. *IEEE 19th REAL-TIME conference proceeding*, in press.

Precision measurement of ν_μ disappearance by T2K

Erez Reinherz-Aronis

Colorado State University, Fort Collins, Colorado, USA

DOI: http://dx.doi.org/10.3204/DESY-PROC-2014-04/165

T2K is a long-baseline neutrino oscillation experiment, where a muon neutrino beam is produced at the J-PARC facility and after traveling 295 km it is detected by Super-Kamiokande, a water Cherenkov detector with a 22.5 kton fiducial mass. One aim of the experiment is to precisely determine the mixing angle θ_{23} and the mass squared difference Δm^2_{23} using a measurement of muon neutrino disappearance. The T2K accumulated dataset is 6.57×10^{20} protons on target, which is 8% of the experimental goal. Here we present an analysis of the T2K muon neutrino disappearance data and the worlds best constraint on the value of the mixing angle θ_{23} obtained by this analysis.

1 Introduction

Neutrinos can be characterized by two different eigenstates states: Flavor eigenstates and Mass eigenstates. On one hand neutrinos production and detection is described by their flavor eigenstates, on the other hand neutrinos propagation through space is determined by their mass eigenstates. The relation between the flavor and mass states is given by the PMNS matrix [1, 2, 3, 4], which is a 3×3 unitary matrix, parametrized by 3 mixing angles and one phase. Moreover, it can be written as a multiplication of three 2D rotation matrixes. This commonly representation have been driven by the challenge to detect neutrinos.

The PMNS matrix has been tested by various experiments, different techniques, with different neutrino sources (such as solar, atmospheric, accelerator/reactor) and has been found to describe the relation between Flavor and Mass states to a good accuracy.

The probability of a muon neutrino with energy E_ν to remain a muon neutrino after traveling a distance L is given by

$$P(\nu_\mu \to \nu\mu) \simeq 1 - 4\cos^2\theta_{13}\sin^2\theta_{23}\cdot\left[1 - \cos^2\theta_{13}\cdot\sin^2\theta_{23}\right]\cdot\sin^2(1.267\Delta m^2 L/E_\nu) \quad (1)$$

where θ_{13} and θ_{23} are the PMNS mixing angles and $\Delta m^2(eV^2/c^4)$ is the neutrino mass-squared splitting. We note that the PMNS matrix depends on the difference between the neutrino masses (Δm^2) not on their absolute masses. Hence the absolute neutrino mass ordering is unknown. This is called the mass hierarch problem in neutrinos. In the case of three neutrinos there are two ways to order the masses, i.e the Normal Hierarchy (NH) and the Inverted Hierarchy (IH). In Eq. (1) the mass-squared split depends on the mass order and is $\Delta m^2_{32} = m^2_3 - m^2_2$

for the NH and $\Delta m^2_{13} = m^2_1 - m^2_3$ for the IH.

In these proceedings we present the recent T2K muon neutrino disappearance oscillation measurement with an accumulated data of 6.57×10^{20} protons on target (POT). This data has doubled since our previous measurement [5] and utilized the new near-detector selections samples which better constrain the measured neutrino charged current (CC) interactions.

2 T2K

Tokai-to-Kamioka (T2K) [6] is a neutrino oscillation experiment, located in Japan, with a baseline of 295 km. The experiment consists of a neutrino beam produced by the J-PARC lab, a near detector complex 280 m downstream of the target (ND280), and the well known Super-Kamiokande (SK) as its far detector (Figure (1) shows a profile of the T2K experiment setup) The neutrino beam is produced by colliding 30 GeV protons with a thick graphite target,

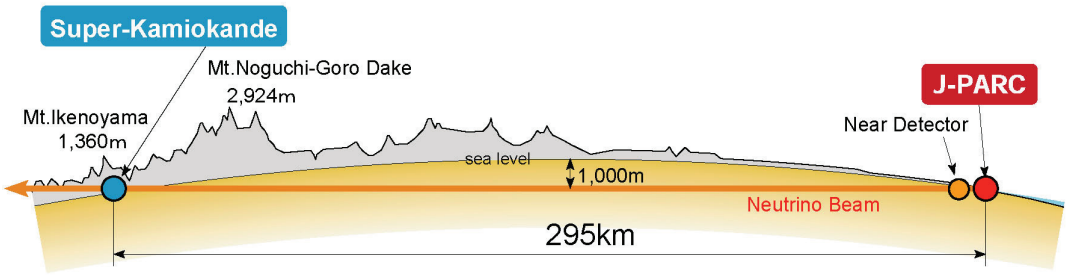

Figure 1: A schematic of a neutrinos traveling from the neutrino beamline at J-PARC, through the near detectors (green dot) which are used to determine the properties of the neutrino beam, and then 295 km underneath the main island of Japan to Super-Kamiokande.

creating charged mesons. The charged pions and kaons are then focused towards the axis of the proton beam by three magnetic horns and are directed into a decay volume, where they decay in-flight to muon neutrinos.

T2K is an off-axis experiment, where its beam is directed 2.5˚ away from the target-SK line, this results and with neutrino energies that are peaked around the oscillation maximum (∼650 MeV) [7] and a smaller high energy tail, which are one of the main sources of backgrounds.

In the near detector complex the direction and stability of the beam is monitored by the on-axis INGRID detector [8]. The ND280 off-axis detectors [6], which have a similar opening angle as SK from the beam, are design to measure the unoscillated beam flux and energy spectrum for the SK (far detector) oscillation measurements.

3 Oscillation Analysis

The T2K analysis extracts the oscillation parameters using the near and far detector measurements. The near detector primarily measures and constrains the produced neutrino flux in order to predict the unoscillated neutrino rate at the far detector. Then the neutrino disappearance is determined by comparing the observed far detector neutrino rates to the predicted unoscillated neutrino rates. Fig. 2 shows the unoscillated expected numbers of events (blue) and the measured number of events (black) as a function of the neutrino energy. The far detector

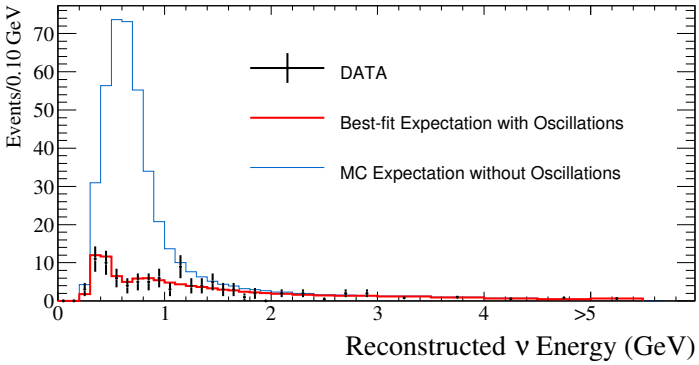

Figure 2: Reconstructed ν energy spectrum at the far detector for data (black), best-fit MC spectrum (red), and spectrum without oscillations (blue).

predictions depend on the input oscillation parameters, the unoscillated incident neutrino flux, the neutrino interaction cross sections and the detector response. A measurement of ν_μ CC events in ND280 is used to tune both the initial flux estimates and parameters of the neutrino interaction models. The measurement also estimates the uncertainties in the predicted neutrino spectrum at the far detector.

In this analysis, the ND280 measurement provides better constraints on the flux and interaction model parameters by using improved event selections, reconstruction, and higher ND280 statistics. This enhanced was achieved by dividing CC events into three categories based on the number of pions in the final state (for more detailed please see J. Perkin in these proceedings).

Source of uncertainty (number of parameters)	$\delta n_{SK}^{exp}/n_{SK}^{exp}$
ND280-independent cross section (11)	4.9%
Flux and ND280-common cross section (23)	2.7%
SK detector and FSI+SI systematics (7)	5.6%
$\sin^2\theta_{13}$, $\sin^2\theta_{12}$, Δm^2_{21}, δ_{CP}	0.2%
Total (45)	8.1%

Table 1: The effect of 1 σ systematic parameter variation on the number of μ-like events, computed for oscillations with $\sin^2\theta_{23} = 0.5$ and $|\Delta m^2_{32}| = 2.40 \times 10^{-3}$ eV^2/v^4.

We estimated oscillation parameters using an unbinned maximum likelihood fit to the SK spectrum for the parameters $\sin^2\theta_{23}$ and either Δm^2_{32} or Δm^2_{13} for the NH and IH respectively. Oscillation probabilities are calculated using the full three-flavor oscillation framework with the other oscillation parameters are fit with constraints $\sin^2\theta_{13} = 0.0251 \pm 0.0035$, $\sin^2\theta_{12} = 0.312 \pm 0.016$, and $\Delta m^2_{21} = (7.50 \pm 0.20) \times 10^{-5}\mathrm{eV}^2/\mathrm{c}^4$ [9]. In addition, we have fitted 45 nuisance parameters (systematic uncertainties related to flux, cross section, final state nuclear effects and detector performance) which are summarized in Table 1 for the different uncertainties categories. Fig. 3 presents the ratio of the observed spectrum (points) to the unoscillation hypothesis, and our best fit (solid red line) to the data.

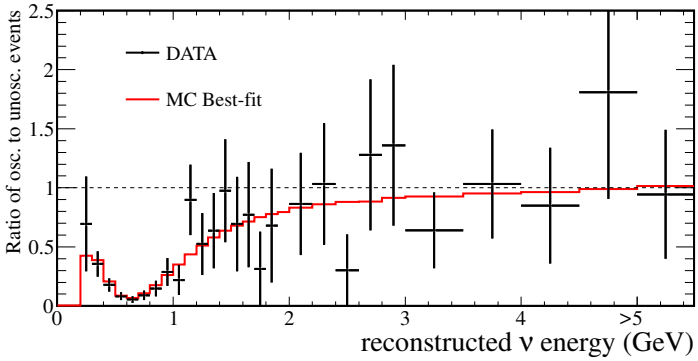

Figure 3: Ratio of far detector neutrino rates over the unoscillated neutrino rates as a function of neutrino energy for data (points) and MC expectations (red line) using the best-fitted neutrino parameters.

In Fig. 4 we present both the 68% and 90% C.L. confidence regions which were achieved using a Feldman-Cousins [12] and Cousins-Highland [13] alike methods which marginalizes over the second oscillation parameter. These limits are overlaid and compared to both MINOS [11] (hatch brown) and SK-atmospheric [10] (hatch blue) disappearance results.

4 Conclusion

T2K has made the most precise measurement of $\sin^2\theta_{23}$ using a data set based on 6.57×10^{20} POT. This measurement of $\sin^2\theta_{23} = 0.514^{+0.055}_{-0.056}$ ($\sin^2\theta_{23} = 0.511 \pm 0.055$) for the NH (IH) is consistent with maximal mixing. The best-fit mass-squared splitting is $\Delta m^2_{32} = 2.51 \pm 0.10$ ($\Delta m^2_{32} = 2.48 \pm 0.10$) $\times 10^{-3}\mathrm{eV}^2/\mathrm{c}^4$ for the case of the NH (IH).

References

[1] B. Pontecorvo, Sov. Phys. JETP **6**, 429 (1957) [Zh. Eksp. Teor. Fiz. **33**, 549 (1957)].

[2] B. Pontecorvo, Sov. Phys. JETP **7**, 172 (1958) [Zh. Eksp. Teor. Fiz. **34**, 247 (1957)].

[3] B. Pontecorvo, Sov. Phys. JETP **26**, 984 (1968) [Zh. Eksp. Teor. Fiz. **53**, 1717 (1967)].

[4] Z. Maki, M. Nakagawa and S. Sakata, Prog. Theor. Phys. **28**, 870 (1962).

[5] K. Abe *et al.* [T2K Collaboration], Phys. Rev. Lett. **111**, no. 21, 211803 (2013) [arXiv:1308.0465 [hep-ex]].

[6] K. Abe *et al.* [T2K Collaboration], Nucl. Instrum. Meth. A **659**, 106 (2011) [arXiv:1106.1238 [physics.ins-det]].

[7] K. Abe *et al.* [T2K Collaboration], Phys. Rev. D **87**, 012001 (2013) [arXiv:1211.0469 [hep-ex]].

[8] K. Abe, N. Abgrall, Y. Ajima, H. Aihara, J. B. Albert, C. Andreopoulos, B. Andrieu and M. D. Anerella *et al.*, Nucl. Instrum. Meth. A **694**, 211 (2012) [arXiv:1111.3119 [physics.ins-det]].

[9] J. Beringer *et al.* [Particle Data Group Collaboration], Phys. Rev. D **86**, 010001 (2012).

[10] A. Himmel [Super-Kamiokande Collaboration], AIP Conf. Proc. **1604**, 345 (2014) [arXiv:1310.6677 [hep-ex]].

[11] P. Adamson *et al.* [MINOS Collaboration], Phys. Rev. Lett. **112**, 191801 (2014) [arXiv:1403.0867 [hep-ex]].

[12] G. J. Feldman and R. D. Cousins, Phys. Rev. D **57**, 3873 (1998) [physics/9711021 [physics.data-an]].

[13] R. D. Cousins and V. L. Highland, Nucl. Instrum. Meth. A **320**, 331 (1992).

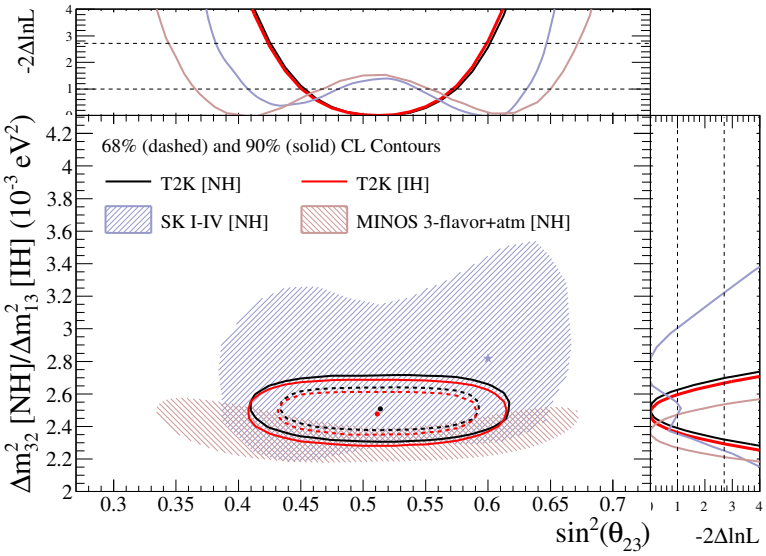

Figure 4: The 68% and 90% C.L. confidence regions for $\sin^2\theta_{23}$ and Δm^2_{32} (NH) or Δ^2_{13} (IH). The SK [10] and MINOS [11] 90% C.L. regions for NH are shown for comparison.

Recent Results from the T2K ND280 Detector

Jonathan Perkin[1] on behalf of the T2K collaboration

[1]The University of Sheffield, Department of Physics and Astronomy, Sheffield, S3 7RH, England

DOI: http://dx.doi.org/10.3204/DESY-PROC-2014-04/166

The T2K near detector complex, ND280, is located at the J-PARC accelerator facility in Tokai, Japan, 280 m downstream from the target. These proceedings will summarise recent physics results from ND280.

1 Introduction

T2K is a long-baseline neutrino oscillation experiment based in Japan designed to look for $\nu_\mu \to \nu_\mu$ disappearance and $\nu_\mu \to \nu_e$ appearance. In 2013 T2K reported [1] the discovery of ν_e appearance from a pure ν_μ beam. The beam is produced from the in-flight decay of pions and exploits the pion decay kinematics by positioning its detectors 2.5° off the beam axis. This improves the monochromaticity of the resulting ν_μ energy spectrum, reduces its high energy tail and selects a peak energy close to the ν_μ oscillation maximum for the 295 km T2K baseline. In order to quantify oscillations one must first predict the expected neutrino interaction rate and flavour composition, in the absence of oscillations, at some fixed baseline from the beam origin. In T2K this is facilitated by a near detector complex at 280 m from the graphite target used to produce the ν_μ beam. The off-axis near detector, ND280 and on-axis near detector, INGRID are used to constrain the neutrino flux and cross section parameters of the JPARC neutrino beam. Additionally, due to the large number of target materials present in the ND280 complex, it can provide information on neutrino-nucleon cross sections at energies around 1 GeV.

2 Off-axis near detector: ND280

The near detector at 280 m, ND280, illustrated in Figure 1, sits 2.5° from the beam axis and comprises a dedicated upstream, scintillator-based, π^0 detector (P0D) followed by a tracker region composed of three gaseous time projection chambers (TPCs) interleaved with two 0.8 ton fine grained scintillator detectors (FGDs). The P0D, TPCs and FGDs are surrounded by hermetic electromagnetic lead/scintillator sampling calorimeters (ECALs). A large electromagnet surrounds these sub-detectors, providing a 0.2 T field. The gaps in the flux-return are instrumented with scintillating paddles for muon tagging and constitute the side muon-range detector (SMRD). The P0D can be operated with or without a passive water target in order to permit on-water or on-carbon rate and cross section measurements. Additional target materials can be found in the two scintillator/brass sampling calorimeter sub-modules either side of the central P0D fiducial volume. The FGDs are scintillator based calorimeters with FGD1 having a pure hydrocarbon target mass and FGD2 containing a passive water target, again permitting on-carbon and on-water rate and cross section measurements. The large fiducial mass of lead

in the ECALs can further be exploited for cross section studies, investigations into interactions on gaseous argon atoms in the TPC are currently underway.

3 T2K near detector constraint

Before ND280 can constrain the neutrino flux and cross section parameters, models of each must first be constructed. The T2K flux prediction [2] is derived from *in-situ* measurements of the proton beam and on-axis measurements of the neutrino beam, coupled with Monte Carlo (MC) simulations of the neutrino flux. The GEANT3/FLUKA based flux simulation is itself tuned using external data from hadron production experiments including NA61/SHINE. The official T2K MC event generator (NEUT) takes the flux prediction as an input and is subsequently used to predict neutrino interaction rates and flavour composition at the near and far detectors. NEUT cross section models are tuned to external lepton and pion scattering data. Uncertainties on NEUT cross section models are calculated [1] by varying model parameters such as axial-mass, fermi-momentum and binding energy (and their respective shapes and normalisations) in fits to external data from experiments such as MiniBooNE.

The ND280 constraint makes use of an inclusive charged current (CC) event sample which is classified according to three final state topologies: CC0π, CC1π^+ and CCOther. The CC0π subsample is predominantly composed of CC quasi-elastic (CCQE) events (i.e. the $\nu_l + n \rightarrow l^- + p$ signal channel at the far detector), the CC1π^+ sample is 40% resonant pion production ($\nu_l + p \rightarrow l^- + \pi^+ + p$) and CCOther, which is dominated by the deep inelastic scattering ($\nu_l + N \rightarrow l^- + N' + \pi^\pm + \pi^0 + ...$) component, covers all remaining toplogies. In each case the events require a reconstructed muon track in the fiducial volume of FGD1, which is identified by tagging the scattered lepton according to its energy loss in the TPCs. The efficiency (purity) of selecting CC0π, CC1π^+ and CCOther events are 50.1% (72.6%), 29.5% (49.4%) and 35.2% (73.8%) respectively. The inclusive CC selection, measured by ND280, is subsequently used to reweight the flux prediction at the far detector. The effect of applying the ND280 constraint on T2K systematic uncertainties is shown in Table 1. Contributions to the flux and cross section uncertainty that are correlated between near and far detectors are constrained by ND280. Systematics arising from differences in near and far detector target nuclei and hadronic interactions are not. In total there are 25 beam parameters, 21 cross section parameters and 210 ND280 systematic parameters in the fit. The far detector systematic is independent of the ND280 constraint. The ND280 constraint reweights 22 far detector flux parameters and 5 shared cross section parameters. After ap-

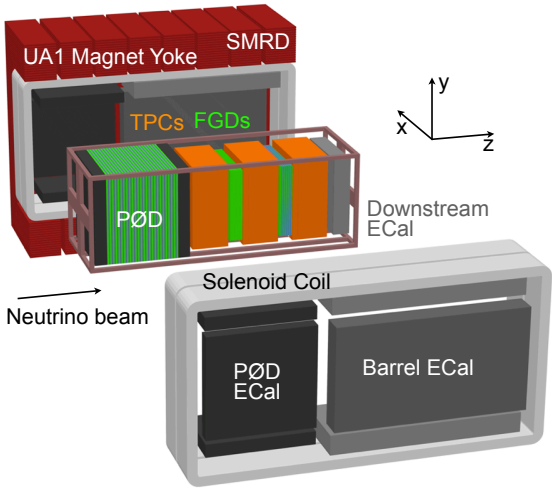

Figure 1: ND280: the T2K off-axis near detector at 280 m.

plying the ND280 constraint, the uncorrelated flux and cross section uncertainties remain the dominant contribution to the total T2K systematic.

Source	$\delta N_{\nu_\mu}/N_{\nu_\mu}$	$\delta N_{\nu_e}/N_{\nu_e}$
ND280 constrained flux + cross section	21.8%(2.7%)	26.0%(3.1%)
Uncorrelated flux + cross section	5.0%	4.7%
Hadronic interactions	3.0%	2.4%
Far detector systematic	4.0%	2.7%
Total	23.5%(7.7%)	26.8%(6.8%)

Table 1: Fractional error ($\delta N/N$) of the predicted number of ν_μ and ν_e events at the T2K far detector without (with) the near detector constraint.

4 Measuring the intrinsic ν_e component of the beam

There is an irreducible ν_e contamination of the JPARC ν_μ beam arising from muon and kaon decays. It is important to measure and constrain this effect using ND280 as it affects the predicted ν_e rate at the far detector. The CC inclusive ν_e selection, using particle identification in the TPCs and ECALs, is split into two different event classifications: CCQE-like and CCnonQE-like, with a constraint imposed using *in-situ* $e^{\pm}$ control samples. The T2K MC prediction is of a 1.2% ν_e component in the ν_μ beam [3]. The number of measured ν_e events $N_{\nu_e}^{\text{meas}}$ compared to the number predicted by MC $N_{\nu_e}^{\text{MC}}$ gives a ratio $N_{\nu_e}^{\text{meas}}/N_{\nu_e}^{\text{MC}} = 1.01 \pm 0.10$. Electron neutrinos coming from muon and kaon decay are also measured separately, resulting in ratios of $N_{\nu_e}^{\text{meas}}/N_{\nu_e}^{\text{MC}} = 0.68 \pm 0.30$ and $N_{\nu_e}^{\text{meas}}/N_{\nu_e}^{\text{MC}} = 1.10 \pm 0.14$, respectively.

5 Cross section measurements

T2K has performed the first measurement of CC inclusive ν_μ interactions on carbon at neutrino energies of ∼1 GeV [4]. The measurement is reported as a flux-averaged double-differential cross section, binned in muon momentum and angle. The data used were taken in 2010 and 2011, with a total of 10.8×10^{19} protons-on-target (POT). The analysis is performed on 4485 inclusive CC candidate events selected in FGD2. The flux-averaged total cross section is measured to be $\langle \sigma_{\text{CC}} \rangle_\Phi = (6.91 \pm 0.13(\text{stat}) \pm 0.84(\text{syst})) \times 10^{-39} \text{cm}^2/\text{nucleon}$ for a mean ν_μ energy of 0.85 GeV.

Additionally, ND280 has made the first differential cross-section measurements of CC inclusive ν_e interactions on carbon at neutrino energies of ∼1 GeV [5]. The measurement is reported as a function of electron momentum, electron scattering angle and four-momentum transfer of the interaction. The flux-averaged total cross section measured to be $\langle \sigma_{\text{CC}} \rangle_\Phi = (1.11 \pm 0.09(\text{stat}) \pm 0.18(\text{syst})) \times 10^{38} \text{cm}^2/\text{nucleon}$ for a mean ν_e energy of 1.3 GeV. A data sample with a total of 5.90×10^{20} POT was analysed. The differential and total cross section measurements agree with the predictions of the NEUT and GENIE MC event generators. The NEUT prediction is 1.23×10^{38} cm^2/nucleon and the GENIE prediction is 1.08×10^{38} cm^2/nucleon. The total ν_e charged-current cross section result is in agreement with data from the Gargamelle experiment. The total flux-averaged cross sections for ν_μ and ν_e on carbon, along with their respective NEUT and GENIE MC expectations are plotted in Figure 2.

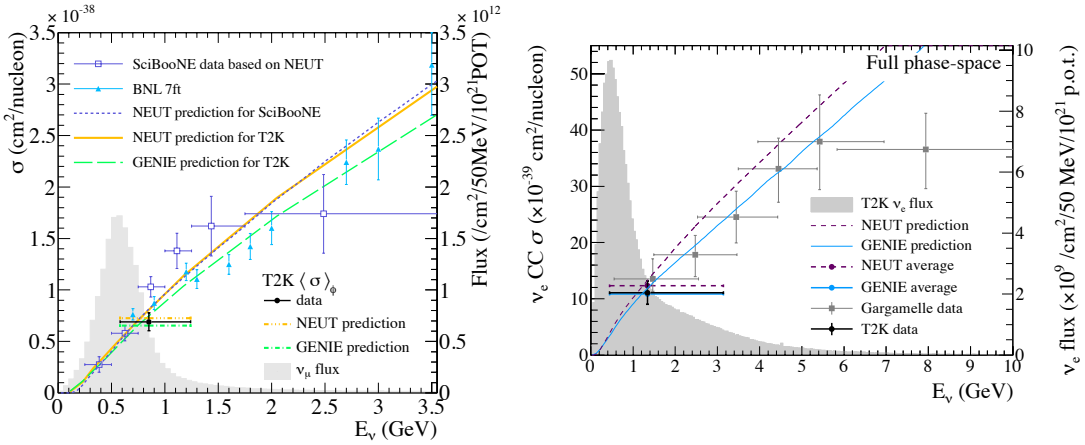

Figure 2: Total flux-averaged cross section for ν_μ *(left)* and ν_e *(right)* on carbon with MC expectations from NEUT and GENIE.

The on-axis interactive neutrino grid (INGRID), also located at the ND280 complex has measured the CC inclusive ν_μ cross section on iron and hydrocarbon [6] for a mean neutrino energy of 1.51 GeV. The flux-averaged total cross sections are $\langle\sigma_{CC}\rangle_\Phi = (1.444\pm0.002(\text{stat})^{+0.189}_{-0.157}(\text{syst}))\times 10^{38}\text{cm}^2/\text{nucleon}$ and $\langle\sigma_{CC}\rangle_\Phi = (1.379\pm0.009(\text{stat})^{+0.178}_{-0.147}(\text{syst}))\times10^{38}\text{cm}^2/\text{nucleon}$ respectively, with a ratio of $1.047 \pm 0.007(\text{stat}) \pm 0.035(\text{syst})$.

6 Conclusions and outlook

The T2K near detector complex is essential to constrain the flux and cross section parameters that are correlated between the near and far detectors. Additionally, it provides an accurate measurement of the intrinsic, irreducable ν_e contamination. As more data are acquired, a rich sample of neutrino-nucleon cross section measurements are becoming accessible. Such measurements not only enhance the precision of T2K oscillation results, but also provide important constraints for other experiments in the field.

References

[1] K. Abe *et al.* (T2K Collaboration), Phys. Rev. Lett. **112**, 061802 (2014).

[2] K. Abe *et al.* (T2K Collaboration), Phys. Rev. D **87**, 012001 (2013).

[3] K. Abe *et al.* (T2K Collaboration), Phys. Rev. D **89**, 092003 (2014).

[4] K. Abe *et al.* (T2K Collaboration), Phys. Rev. D **87**, 092003 (2013).

[5] K. Abe *et al.* (T2K Collaboration), arXiv:1407.7389 (2014).

[6] K. Abe *et al.* (T2K Collaboration), Phys. Rev. D **90**, 052010 (2014).

Recent Results from MINERvA

Jonathan Miller[1] for the MINERvA Collaboration

[1]Departamento de Física Universidad Técnica Federico Santa María
Casilla 110-V, Valparaíso, Chile

DOI: http://dx.doi.org/10.3204/DESY-PROC-2014-04/158

MINERvA (Main INjector ExpeRiment for v-A) is a few-GeV neutrino nucleus scattering experiment at Fermilab using various nuclei as targets. The experiment provides measurements of neutrino and anti-neutrino cross sections off of nuclear targets which are important for neutrino oscillation experiments and the probing of the nuclear medium. Presented are recent results from MINERvA on quasi-elastic, inclusive charged-current neutrino scattering, and pion production processes.

The MINERvA physics program is a broad based particle and nuclear physics program to measure important cross sections and channels for other particle physics experiments like IceCube and NOvA, and to use the neutrino to probe the weak component of nucleon and nuclear structure. For both, measurements in the range of 1-20 GeV are necessary, as this is where the complementary electromagnetic and hadronic data exists from nuclear physics and is the energy range that many neutrino experiments are sensitive. The results presented in these proceedings are available [1, 2, 3], where more detail on the analysis and the results may be obtained.

These first results from MINERvA include coherent pion production [1], charged pion production [2], and inclusive charged current cross section ratios [3]. These results are relevant for the analyses of neutrino experiments such as T2K and provide important input into understanding the effects of nuclear structure.

MINERvA is an experiment situated at Fermilab, near Chicago in the United States. It utilises the NuMI beam line in order to measure neutrino-nuclear cross sections at neutrino energies of between 1.5 and 20 GeV. The results presented here include data from the Low Energy (LE) run with median energy of 3.5 GeV, future results will include data from the Medium Energy (ME) run with median energy of 5.7 GeV.

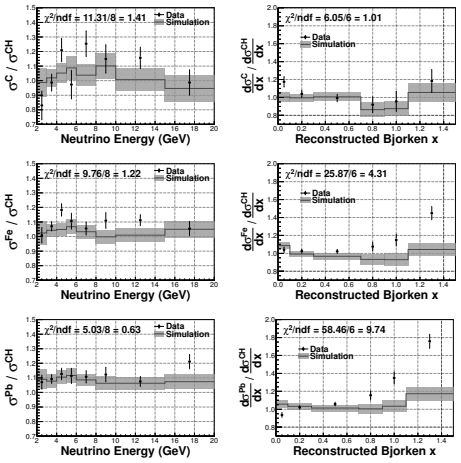

Figure 1: The ratios of the differential cross section per nucleon with respect to reconstructed bjorken x and of the cross section per nucleon depending on reconstructed energy (E_ν) for Pb, Fe, and C relative to CH. The error bars in data are statistical and in simulation are systematic. The calculation for χ^2 includes correlations. Events not shown with $x > 1.5$.

The MINERvA detector[4] consists of a target region with 5 nuclear targets. Each target consists of a module with passive targets consisting of lead (Pb), iron (Fe), and graphite (C) and is separated by 4 active tracker modules. Downstream is an active tracker region. Active modules are made up of strips of plastic scintillator (CH) aligned in three orientations. Down stream of this region are the electromagnetic and hadronic calorimeters, with scintillator surrounded by iron and lead to induce energy loss. Downstream (2m) of the MINERvA detector is the MINOS near detector, a magnetised iron spectrometer.

The recent results from MINERvA have utilised charged current interactions in the neutrino and anti-neutrino datasets. The selection of charged current events are those where the muon travels from the interaction vertex through the MINERvA detector (leaving a minimum ionising track) and into the MINOS detector. MINOS serves as a muon spectrometer, and is used for a precise measurement of the muon momentum and charge. Two of the results presented here have charged pions in the final state. Charged pions may be identified using the deposited energy along the track, and by the observation of a Michel electron ($\pi \to \mu \to e$) at the end of the track in the tracker or electromagnetic calorimeter region. Details about basic tracking and vertex determination may be found in [4].

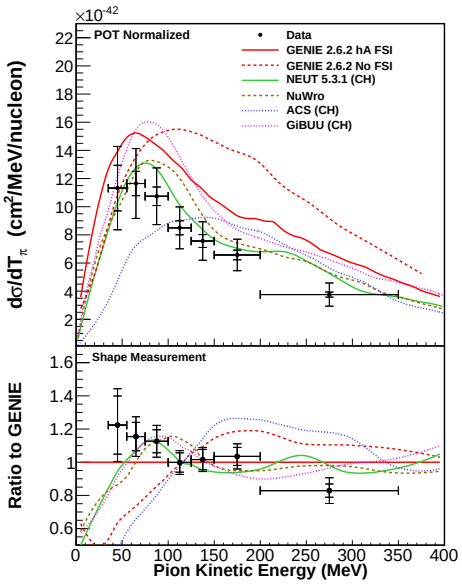

Figure 2: The charged pion differential cross section with respect to pion kinetic energy (top) and the ratio of this cross section to that predicted by GENIE with FSI normalised to the measured integral (bottom). Included are predictions from GENIE, ACS[7], NEUT[8], GiBUU[9] and NuWro[10]. Shown are the statistical uncertainty (inner error bars) and total uncertainty (outer error bars).

The charged current cross section, where a lepton (in MINERvA's case, a muon) is in the final state, are the most important cross sections to the neutrino physics program. Measuring the inclusive ratio of the cross sections of the main nuclear targets in MINERvA (0.628 tons of Fe, 0.711 tons of Pb, 0.159 tons of C, and 5.48 tons of CH), provides a flux independent probe of the structure of the nucleus. To have a well understood acceptance at all nuclear targets, the reconstructed neutrino energies are restricted to being above 2 GeV and the reconstructed muon angles to being less than 17°. The hadronic energy of the event E_h is calculated by the calorimetric sum not associated with the muon track. This allows the reconstruction of the kinematic variables $E_\nu = E_\mu + E_h$, $Q^2 = 4E_\nu E_\mu \sin^2(\theta_\mu/2)$, and $x = Q^2/(2M_N E_h)$. In this inclusive event selection, the GENIE sample is not dominated by any one process or classification (such as deep inelastic scattering (DIS)). The data used for this analysis consisted of 2.94e20 protons on target (pot) in the neutrino configuration.

The results of this inclusive charged current ratios are shown in Fig. 1. The ratios of the cross section depending on reconstructed neutrino energy show broad agreement with the GENIE simulation, however, the differential cross section with respect to reconstructed bjorken x shows disagreement. This disagreement is a suppression at low x and enhancement at high

x, and the overall level changes as a function of the number of nucleons in the nucleus with the high x point showing agreement for the C over CH ratio and the low x point showing agreement for the Pb over CH ratio. The difference between data and simulation at low x may be due to poorly modelled nuclear shadowing effects. At high x most of the events are quasielastic, and so improvements in nuclear scaling models from the quasielastic to the deeply inelastic regime may be required.

A common case of charged current scattering is where a pion is produced. This is important to current and future long baseline experiments. Charged current pion production becomes convoluted with quasielastic scattering due to final state interactions (FSI) possibly causing the absorption of the pion in the nucleus causing the signature to appear quasielastic like. Models for the nuclear interactions which the produced pion may undergo are included in various generators/models including GENIE, ACS, NEUT, GiBUU and NuWro and the pion may undergo absorption, scattering, and charge exchange. The MiniBooNE measurement of this cross section shows agreement with the generators when they do not include FSI for pions with kinetic energy of 20 to 400 MeV (pions likely produced by delta decays)[5]. The charged current pion production differential cross section with respect to pion kinetic energy was measured by selecting events with a charged muon and at least one pion. The reconstructed pion provides the pion kinetic energy and the angle the pion travels with respect to the beam. To select events with only a single produced pion, a cut on the invariant mass (W) is used. The muon energy (E_μ), angle (θ_μ), and hadron energy (E_h) were used to reconstruct the invariant mass using the equations: $E_\nu = E_\mu + E_h$,$Q^2 = 2E_\nu(E_\mu - |\vec{p}_\mu|\cos\theta_\mu) - m_\pi^2$, and $W^2 = M_p^2 - Q^2 + 2M_pE_h$.

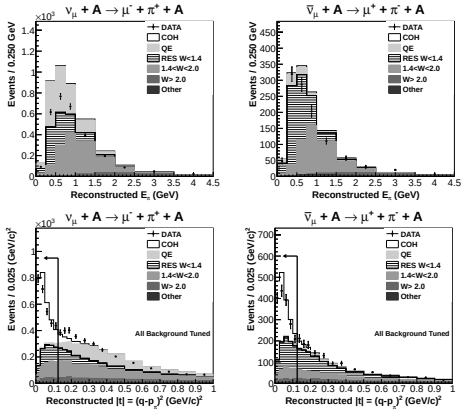

Figure 3: The top two plots show reconstructed energy in the $0.2 < t < 0.6$ (GeV/c)^2 sideband for the ν and $\bar{\nu}$ datasets. On the bottom is reconstructed t after background tuning. The shape in t near 0 is determined by the resolution.

The results of the measurement of charged pion production are shown in Fig. 2. Models of interactions within the nucleus cause pions to *migrate* to lower energies through scattering or be suppressed due to absorption or charge exchange. The shape is particular sensitive to such effects, and demonstrates that the models included in the favoured generators give broad agreement with the data when the generators include FSI for pions for pions with kinetic energy between 20 and 400 MeV. These results come from 3.04e20 pot in the neutrino configuration.

Coherent pion production is the production of a pion after the neutrino scatters off the entire nucleus leaving the nucleus unchanged. It is characterised by a small momentum exchange between the nucleus and the system of the leptons and produced pion. The theory in this regime is not well understood, and many different approaches are included in neutrino event generators. This process is important in the analysis of accelerator neutrino experiments where this process is a background to the desired quasielastic signal, in these experiments the analyses use neutrino event generators to interpret their data and understand their background. A measurement of coherent charged pion production constrains the neutrino event generators for these processes and so improves the aforementioned analyses.

The coherent pion events were selected by requiring a charged pion and muon in the final

state and little activity in the vertex region. The measured transferred four momentum (t) is required to be small. Other backgrounds are constained by use of a high t sideband. This provides a selection of model independent coherent pion production events and allows the study of the differential cross section with respect to pion angle and energy. As shown in Fig. 3, the background in the sideband region was tuned to the data correcting the incoherent background which was subtracted from the low t sample providing a sample of coherent pion events.

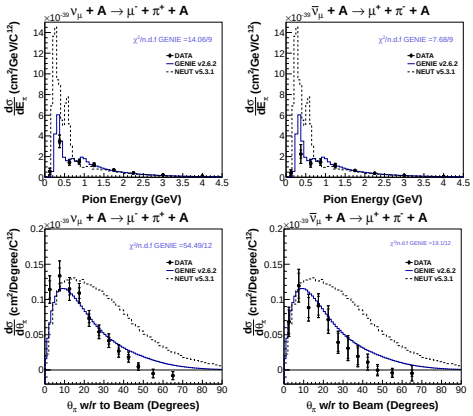

Figure 4: Shown is $\frac{d\sigma}{dE_\pi}$ on top and $\frac{d\sigma}{d\theta_\pi}$ on bottom with inner error bars showing the statistical uncertainty and outer error bars showing the total uncertainty. The χ^2 compares the data versus bin averaged cross sections from GENIE[6].

The coherent pion differential cross section is shown in Fig. 4 versus both pion angle and pion energy. Here the pion angle with respect to the beam is more forward than that of the commonly used Rein-Sehgal model in GENIE[6].

In conclusion, MINERvA has made important contributions to understanding the neutrino-nucleon interactions in the moderate energies (1-10 GeV) which are crucial to accelerator and atmospheric based neutrino experiments. Measurements of the pion production cross section and the ratio of the inclusive scattering cross section show broad agreement with the generators. The behaviour of the ratio of the cross section with respect to Bjorken x is not well modelled in the generator and requires theoretical input. Also, the pions produced in coherent pion production are more forward scattering than what exists within the generators. The start of the ME run has provided much larger statistics for future measurements studying nuclear structure and neutrino cross sections.

J.M. was supported by the National Science Foundation under Grant No. NSF PHY11-25915 and by PROYECTO BASAL FB 0821 CCT-Val and by Fondecyt (Grant No. 11130133) during the completion of this report.

References

[1] A. Higuera, A. Mislivec, L. Aliaga, O. Altinok, A. Bodek, A. Bravar, A. Butkevich and M. F. Carneiro *et al.*, arXiv:1409.3835.

[2] B. Eberly *et al.* [MINERvA Collaboration], arXiv:1406.6415.

[3] B. G. Tice *et al.* [MINERvA Collaboration], Phys. Rev. Lett. **112**, 231801 (2014) [arXiv:1403.2103].

[4] L. Aliaga *et al.* [MINERvA Collaboration], Nucl. Instrum. Meth. A **743**, 130 (2014) [arXiv:1305.5199].

[5] A. A. Aguilar-Arevalo *et al.* [MiniBooNE Collaboration], Phys. Rev. D **83**, 052007 (2011) [arXiv:1011.3572].

[6] C. Andreopoulos, A. Bell, D. Bhattacharya, F. Cavanna, J. Dobson, S. Dytman, H. Gallagher and P. Guzowski *et al.*, Nucl. Instrum. Meth. A **614**, 87 (2010) [arXiv:0905.2517].

[7] M. Sajjad Athar, S. Chauhan and S. K. Singh, Eur. Phys. J. A **43**, 209 (2010) [arXiv:0908.1443 [nucl-th]].

[8] Y. Hayato, Acta Phys. Polon. B **40**, 2477 (2009).

[9] U. Mosel, O. Lalakulich and K. Gallmeister, Phys. Rev. D **89**, 093003 (2014) [arXiv:1402.0297 [nucl-th]].

[10] T. Golan, C. Juszczak and J. T. Sobczyk, Phys. Rev. C **86**, 015505 (2012) [arXiv:1202.4197 [nucl-th]].

INO-ICAL detector sensitivity for the measurement of atmospheric neutrino mixing parameters

Daljeet Kaur, Md. Naimuddin, Sanjeev Kumar

Department of physics and Astrophysics, University of Delhi, Delhi, 110007, India

DOI: http://dx.doi.org/10.3204/DESY-PROC-2014-04/202

Neutrino oscillation physics is now enriched with various compelling evidences of neutrino oscillations and their masses from several experiments but measurement of correct neutrino mass hierarchy, octant of θ_{23} and determination of value CP violating phase δ_{CP} are still unknown puzzles. The recently measured substantially large third mixing angle θ_{13} from the reactor experiments [1, 2] has opened up new opportunities in the neutrino physics sector [3, 4]. Atmospheric neutrino experiments have potential to explain these unknown mysteries through their wide coverage of baseline and with energies in the range from MeV to TeV. The magnetised Iron CALorimeter detector (ICAL) at India-based Neutrino Observatory (INO) [5] is a proposed atmospheric neutrino experiment, located at Theni district in South India. The main goals of INO experiment is to measure the correct neutrino mass hierarchy and the precise measurement of neutrino mixing parameters through the observation of atmospheric ν_μ and $\bar{\nu}_\mu$ events. A 50 kton magnetised Iron CALorimeter (ICAL) detector will be the main detector at INO where Resistive Plate Chamber (RPC) will be used as an active detector to trace the particle tracks on their passage through the detector. The unique feature of ICAL is to separate the atmospheric ν_μ and $\bar{\nu}_\mu$ with its excellent charge identification capabilities. We have performed a χ^2 analysis for the precision measurement using the simulated neutrino data generated for the ICAL detector using NUANCE [6] neutrino generator. Here, we present INO-ICAL capability for measuring the atmospheric neutrino oscillation parameters $|\Delta m^2_{32}|$ and $\sin^2\theta_{23}$ using neutrino energy and muon direction as observables in presence of actual detector resolutions and efficiencies.

Interaction of atmospheric neutrinos with the detector produce associative lepton and hadrons through Quasi-Elastic (QE), Single pion production (Resonance) and Deep Inelastic scattering (DIS) processes. Muons are produced due to Charged Current interactions of muon neutrinos ant anti-neutrinos while single pion along with one lepton produced due to resonance interactions. Hadrons are produced due to deep inelastic scattering (DIS) at high energies. Muons create a long track on their passage through detector and their charge and momenta can be identified through the track bending and curvature in presence of magnetic field whereas hadrons produce bunch of hits in form of shower. The energy and direction resolutions of muons and hadrons based on GEANT4 detector [8] simulation are provided by the INO collaboration as a function of their true energies and true directions [7, 9]. Since the muon direction reconstruction is well known for ICAL we have used the reconstructed muon directions in the final analysis. In the present analysis, muon energy and angular resolutions are implemented by smearing true muon energy and direction of each μ^+ and μ^- event using the ICAL muon resolution functions [7]. True hadron energies are smeared using ICAL hadron resolution functions [9].

The neutrino energy can be reconstructed from reconstructed muon and hadron energy. We use reconstructed neutrino energy as the sum of reconstructed muon and hadron energy and muon direction as observables for binned χ^2 analysis.

For the analysis, we simulate 1000 year unoscillated NUANCE data generated using Honda et al. 3D flux [10]. The implementation of oscillation effects to these unoscillated data have been done using a well known re-weighting algorithm as presented in earlier ICAL analyses [11, 12]. We use the fixed values of solar mixing parameters $\sin^2(2\theta_{12}) = 0.86$, $\Delta m^2_{21} = 7.6 \times 10^{-5} eV^2$ and $\delta_{cp} = 0$ where as the atmospheric mixing parameters are marginalised within their 3σ range with the best fit values $\sin^2(\theta_{23}) = 0.5$ and $\Delta m^2_{32} = 2.4 \times 10^{-3} eV^2$. Here, we assume normal hierarchy is true. The oscillation re-weighted events with detector resolutions and efficiencies are then binned into neutrino energy and muon direction. The data is divided into neutrino energy bins in the range of 0.8 - 10.8 GeV. We use 15 bins in the range 0.8-5.8 GeV with bin size of 0.33 GeV and from 5.8-10.8 GeV 5 bins with bin size of 1 GeV. 20 $\cos\theta_\mu$ direction bins are used in the range of -1 to 1. Finally, for χ^2 estimation, the data has been scaled down for 10 years of exposure to minimising the statistical fluctuations. The definition of atmospheric mass square splitting as $|\Delta m^2_{eff}|$ following the Ref. [12] has been considered for the analysis. We have used the poissonian definition of χ^2 given as

$$\chi^2(\nu_\mu) = \sum_{min} \left(2N^{th'}_{ij}(\nu_\mu) - 2N^{ex}_{i,j}(\nu_\mu) + 2N^{ex}_{i,j}(\nu_\mu) \ln \left(\frac{N^{ex}_{i,j}(\nu_\mu)}{N^{th^{prime}}_{i,j}(\nu_\mu)} \right) \right) + \sum_k \zeta_k^2, \tag{1}$$

where

$$N^{th'}_{ij}(\nu_\mu) = N^{th}_{i,j}(\nu_\mu) \left(1 + \sum_k \pi^k_{ij} \zeta_k \right). \tag{2}$$

In Eq.(1), N^{ex}_{ij} is the observed number of the ν_μ events in i^{th} E_ν and j^{th} $\cos\theta_\mu$ bin generated using true values of the oscillation parameters. In Eq.(2), N^{th}_{ij} is the number of theoretically predicted events generated by varying oscillation parameters without including systematic errors, $N^{th'}_{ij}$ shows shifted events spectrum due to different systematic uncertainties, π^k_{ij} is the systematic shift due to k^{th} systematic error. A total five systematic uncertainties are considered for our analysis; these are 20% overall flux normalisation uncertainty, 10% cross-section uncertainty, 5% uncertainty on the zenith angle dependence of the flux. 5% energy dependent tilt error and 5% overall statistical uncertainty. All the systematic uncertainties are applied using the method of "pulls" as described in [11, 13]. ζ_k is the univariate pull variable corresponding to the π^k_{ij} uncertainty. An expression similar to Eq.(1) can be obtained for $\chi^2(\bar{\nu}_\mu)$ using reconstructed μ^+ event samples. We have calculated $\chi^2(\nu_\mu)$ and $\chi^2(\bar{\nu}_\mu)$ separately and then these two are added to get total χ^2_{total} as

$$\chi^2_{total} = \chi^2(\nu_\mu) + \chi^2(\bar{\nu}_\mu). \tag{3}$$

We impose a 10% prior while marginalising over $\sin^2\theta_{13}$ as

$$\chi^2_{ical} = \chi^2_{total} + \left(\frac{\sin^2\theta_{13}(true) - \sin^2\theta_{13}}{\sigma_{\sin^2\theta_{13}}} \right)^2. \tag{4}$$

Finally, in order to obtain the experimental sensitivity for θ_{23} and $|\Delta m^2_{eff}|$, we minimise the χ^2_{ical} function by varying oscillation parameters within their allowed ranges over all systematic

uncertainties. The precision on the oscillation parameters can be defined as:

$$Precision = \frac{P_{max} - P_{min}}{P_{max} + P_{min}}, \tag{5}$$

where P_{max} and P_{min} are the maximum and minimum values of the concerned oscillation parameters at the given confidence level.

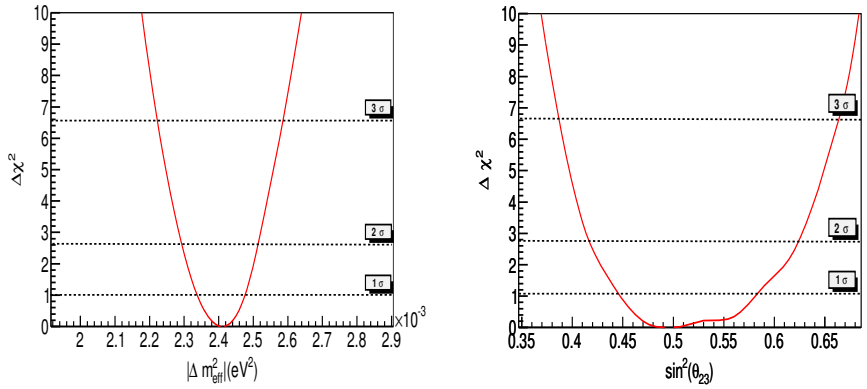

(a) (b)

Figure 1: (a) $\Delta\chi^2$ as a function of $|\Delta m^2_{32}|$ (b) $\Delta\chi^2$ as a function of $\sin^2\theta_{23}$.

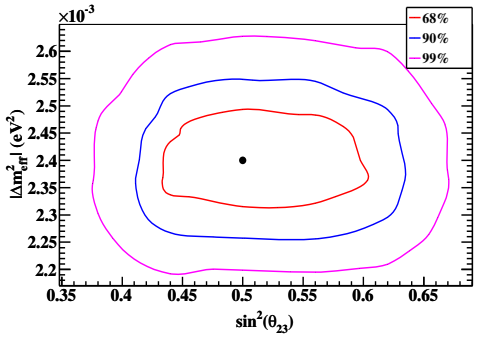

Figure 2: Contour plot for 68%, 90% and 99% confidence level for 10 years exposure of ICAL detector

The sensitivity for the measurement of test parameters $|\Delta m^2_{eff}|$ and for $\sin^2\theta_{23}$ at 1σ, 2σ and 3σ confidence intervals are shown in Figure 1(a) and Figure 1(b) respectively. The final contour plots in $|\Delta m^2_{eff}|$ and $\sin^2\theta_{23}$ plane assuming $\Delta\chi^2_{ical} = \chi^2_{min} + m$ has been obtained,

where χ^2_{min} is the minimum value of χ^2_{ical} for each set of oscillation parameters and values of m are taken as 2.30, 4.61 and 9.21 corresponds to 68%, 90% and 99% confidence levels. The ($|\Delta m^2_{eff}|$, $\sin^2\theta_{23}$) contour plot is shown in Figure 2. We find that for 10 years of exposure of ICAL detector with detector resolutions and efficiencies, INO-ICAL is able to measure $|\Delta m^2_{32}|$ and $\sin^2\theta_{23}$ with a precision of 4.15% and 16% at 1σ confidence level using neutrino energy and muon direction binning. Present results show an imrovement of 18.62 % and 5 % on the precision of $|\Delta m^2_{32}|$ and $\sin^2\theta_{23}$ over the earlier ICAL analysis with muon energy and muon direction observables [11].

Acknowledgements

We thank INO physics and simulation group for continuous support throughout this work. We would also like to thank Department of Science and Technology (DST) and Council for Scientific and Industrial Research (CSIR) for providing us financial support for this research.

References

[1] F. P. An et al. [Daya-Bay Collaboration], Phys. Rev. Lett. 108, 171803 (2012), arXiv:hep-ex/1203.1669.

[2] J. K. Ahn et al. [RENO Collaboration], Phys. Rev. Lett. 108, 191802 (2012), arXiv:hep-ex/1204.0626.

[3] H. Minakata, Nucl. Phys. Proc. Suppl. 235-236, 173 (2013), arXiv:hep-ph/1209.1690.

[4] M C Gonzalez-Gracia, Physics of the Dark Universe **4**1-5 (2014).

[5] The Technical Design Report of INO-ICAL Detector (2006), http://www.ino.tifr.res.in/ino/.

[6] D. Casper, Nucl.Phys. Proc.Suppl. **112**, 161 (2002), arXiv:hep-ph/0208030.

[7] A. Chatterjee et al. [arXiv:1405.7243v1][physics.ins-det](2014).

[8] GEANT simulation toolkit wwwasd.web.cern.ch/wwwasd/geant/

[9] M. M. Devi et al., JINST **8** P11003 (2013).

[10] M. Honda et al., Phys. Rev. **D70**, 043008 (2004), arXiv:astro-ph/0404457.

[11] T. Thakore et al. JHEP **05**, 058 (2013).

[12] A. Ghosh et al., JHEP **04**, 009 (2013).

[13] M. C. Gonzalez-Garcia, M. Maltoni et al, Phys.Rev. **D70**, 033010 (2004), arXiv:hep-ph/0404085v1.

IsoDAR and DAEδALUS

Joshua Spitz

Massachusetts Institute of Technology, Cambridge, MA 02139, USA

DOI: http://dx.doi.org/10.3204/DESY-PROC-2014-04/124

The DAEδALUS collaboration seeks to construct a number of high-intensity cyclotrons for use throughout neutrino physics, including searching for a sterile neutrino, sensitivity to non-standard neutrino interactions, measurements of coherent neutrino-nucleus scattering and ultimately, a determination of CP violation in neutrinos. This proceedings focusses on the physics goals of the DAEδALUS project.

1 Introduction

We don't know if neutrinos obey Charge-Parity (CP) symmetry and we don't know how many neutrinos there are. Answers to these questions are vital for understanding the neutrino's place amongst the fundamental particles as well as its role in the evolution of the universe. The DAEδALUS collaboration has set out to produce cyclotron-based neutrino sources for, among other things, answering these questions. The experimental concept calls for two classes of cyclotrons in producing isotope and pion/muon decay-at-rest sources of neutrinos, an injector cyclotron and a Superconducting Ring Cyclotron (SRC). The injector cyclotron can be combined with a liquid scintillator based neutrino detector for trying to answer the question of how many neutrinos there are [1], and a set of SRC devices, located at various distances from an ultra-large free-proton-based detector, can be used to measure CP violation in neutrinos [2]. While there are a number of technological challenges associated with constructing these devices (e.g., see Ref. [3]), the focus of this work is on the physics capabilities of these unique experiments.

2 IsoDAR

The Isotope Decay-at-Rest experiment (IsoDAR), doubling as the injector cyclotron design for the DAEδALUS neutrino CP violation project, will use a 600 kW resistive cyclotron to accelerate 5 mA of 60 MeV/amu H_2^+. For IsoDAR, a dedicated experiment that will utilize this source, the ions will be directed onto a ^{9}Be target to produce a large flux of neutrons emanating from the target. These MeV-scale neutrons, produced at the level of $\sim$0.1 neutron per incoming proton [4], will slow down and eventually capture inside of a surrounding ^{7}Li ($\geq$99.99% isotopically pure) sleeve. The product of this capture, ^{8}Li, beta decays with a half-life of 840 ms to produce an electron antineutrino with energy in the 3-14 MeV range. There are about 15 $\overline{\nu}_e$ per 1000 protons on target expected. The cyclotron-target configuration can be placed within $\sim$10 m of a planned or existing liquid scintillator based detector, such as KamLAND [5], for

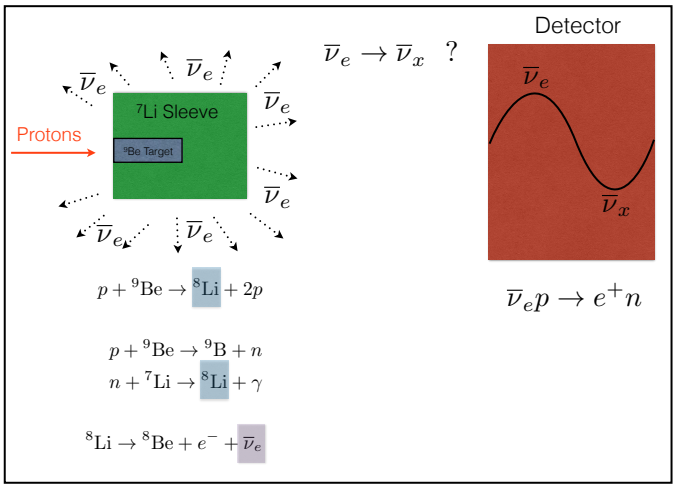

Figure 1: The IsoDAR idea for an intense source of electron antineutrinos source near a planned or existing liquid scintillator detector.

collecting electron antineutrino induced inverse beta decay (IBD) interactions ($\overline{\nu}_e p \to e^+ n$) and $\overline{\nu}_e$-electron elastic scatters ($\overline{\nu}_e e^- \to \overline{\nu}_e e^-$). The collected electron antineutrino IBD events can provide sensitivity to high-Δm^2 neutrino oscillations, a signal which would be indicative of the existence of at least one light sterile neutrino. The approximately 800,000 IBD events expected in 5 years running IsoDAR 16 m away from the 897 ton fiducial mass KamLAND detector would allow a sensitivity of $>10\sigma$ to electron antineutrino disappearance at $\Delta m^2 \sim 1$ eV^2. Such a large sample would even provide the ability to distinguish between the existence of one or two sterile neutrinos in many mixing scenarios [6]. Further, the $\approx$2500 $\overline{\nu}_e$-electron elastic events expected would provide a unique test of non-standard neutrino interactions and physics beyond the Standard Model in general [7]. The IsoDAR idea, with a focus on the oscillation concept, is shown in Figure 1.

3 DAEδALUS

The neutrino CP violating parameter δ_{CP} can be measured by studying $\overline{\nu}_\mu \to \overline{\nu}_e$ oscillations at medium baseline (tens of km for neutrino energies in the 20-50 MeV range). For DAEδALUS, the muon antineutrino flux is produced with 800 MeV protons striking a carbon target to create charged pions. The pions quickly come to rest in the target and decay to a muon and a muon neutrino ($\pi^+ \to \mu^+ \nu_\mu$). The positively charged muon subsequently comes to rest as well and decays to a positron and two neutrinos ($\mu^+ \to e^+ \nu_e \overline{\nu}_\mu$) with energies from 0-52.8 MeV. Electron antineutrino appearance from the muon antineutrino component of this source can be studied, via the IBD interaction at medium baseline, to provide a measurement of δ_{CP}. A set of cyclotrons, at distances of 1 km, 8 km, and 20 km away from a single ultra-large detector are envisioned by DAEδALUS for this purpose. In general, the near cyclotron will be used to constrain the initial flux via ν_e-electron scattering, the middle-distance cyclotron will constrain the rise probability, and the far cyclotron(s) will be used to power the fit for electron antineutrino appearance. Neutrinos from the different sources are differentiated at the

single detector with pulse timing. DAEδALUS requires the power of the cyclotrons at each site to be 0.8, 1.6 and 4.8 MW, from near to far. These tentative requirements are set such that DAEδALUS can match the sensitivity of the Long Baseline Neutrino Experiment (LBNE) 2011 baseline design [8]. Notably, the contamination of intrinsic $\overline{\nu}_e$, from the source rather than from appearance, is at the $\sim 4\times10^{-4}$ level because almost all of the (grand)parent π^- capture on nuclei before they have a chance to decay. The DAEδALUS experimental concept, in consideration of the CP violation measurement, is shown in Figure 2.

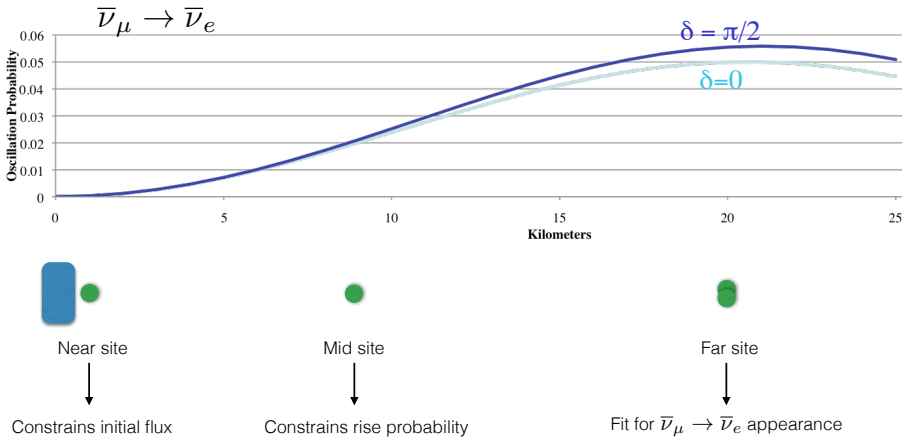

Figure 2: The DAEδALUS experimental concept, depicting the various accelerator locations and their general purposes, with respect to an ultra-large detector. A set of example oscillation probabilities, for two different values of $\delta_{\rm CP}$, is also shown.

Along with contributing information about the initial composition of the un-oscillated source, the first "near" cyclotron can be used for a set of of short-baseline measurements, especially when considered in combination with smaller detectors located near the accelerator. Specifically, a coherent neutrino-nucleus scattering experiment with a dark-matter-style detector sensitive to nuclear recoils at the keV-scale is possible [9]. Such a detector could be located tens of meters from the source in order to search for the well-predicted, but as-yet-unseen, coherent interaction of a neutrino with an entire nucleus. In case the accelerator is located at a deep underground lab, a dedicated dark matter experiment nearby could also make the discovery. Further, a multi-detector configuration could provide a unique neutral current based sterile neutrino oscillation search using the coherent events [10]. Such a neutral current based disappearance search would be uniquely sensitive to the sterile flavor component of the fourth neutrino mass eigenstate, a measurement which is not directly accessible using charged current based searches.

The near cyclotron can also be used to look for high-Δm^2 oscillations, $\overline{\nu}_\mu \rightarrow \overline{\nu}_e$ appearance as well as the disappearance of ν_e, in combination with the envisioned nearby ultra-large detector [11]. Both of these measurements can be considered complimentary to IsoDAR's low(er) energy electron antineutrino disappearance probe. In the case that a new oscillatory frequency consistent with a sterile neutrino is confirmed, we will want to measure its properties, including precise determinations of its characteristic mass splitting and mixing angles. Such measurements are best accomplished, of course, using multiple flavors in both appearance and disappearance modes and with both neutrinos and antineutrinos. It is also worth noting that

the envisioned short baseline electron antineutrino appearance search with DAEδALUS can be considered a direct test of the LSND and MiniBooNE antineutrino anomalies [12, 13, 14].

4 Status and conclusion

DAEδALUS is working within a four-phase program for surmounting the technological obstacles associated with building and operating these megawatt-class cyclotrons and establishing their cost-effectiveness and ability. The currently underway Phase 1 aims to deploy and test an intense H_2^+ ion source; Phase 2 will demonstrate a full-scale version of the low energy beam transport and injector cyclotron systems, and use this system to definitively address the sterile neutrino; Phase 3 will continue with the production of an actual full superconducting ring cyclotron accelerator module at a near location from an ultra-large water or scintillator based detector for sterile neutrino and coherent neutrino-nucleus scattering physics; and Phase 4 involves the deployment of the complete DAEδALUS experiment featuring cyclotrons at three distances for a measurement of δ_{CP}. This program of research and development and measurements relevant for accelerator science, producing medical isotopes for industry [15], and neutrino physics is ongoing. Among other physics goals, this program will help to answer two of the most profound and important questions in physics today: 1) How many neutrinos are there? and 2) Do neutrinos and antineutrinos behave the same?

Acknowledgments

This work was done with support from the National Science Foundation under Grant Number PHY-1205175.

References

[1] A. Bungau *et al.*, Phys. Rev. Lett **109** 141802 (2012).

[2] J.M. Conrad and M.H. Shaevitz, Phys. Rev. Lett. **104** 141802 (2010).

[3] A. Adelmann, J. Alonso, W.A. Barletta, J.M. Conrad, M.H. Shaevitz, J. Spitz, M. Toups, and L.A. Winslow, Adv. High Energy Phys. **2014** 347097 (2014).

[4] A. Adelmann *et al.*, 1210.4454 [physics.acc-ph] (2012).

[5] S. Abe *et al.* [KamLAND Collaboration], Phys. Rev. Lett. **100** 221803 (2008).

[6] M. Sorel, J. M. Conrad, and M. H. Shaevitz, Phys. Rev. D **70** 073004 (2004).

[7] J.M. Conrad, M.H. Shaevitz, I. Shimizu, J. Spitz, M. Toups, and L. Winslow, Phys. Rev. D **89** 072010 (2014).

[8] V. Barger *et al.*, "Report of the US long baseline neutrino experiment study", arXiv:0705.4396 [hep-ph] (2007).

[9] A.J. Anderson, J.M. Conrad, E. Figueroa-Feliciano, K. Scholberg, and J. Spitz, Phys. Rev. D **84** 013008 (2011).

[10] A.J. Anderson, J.M. Conrad, E. Figueroa-Feliciano, C. Ignarra, G. Karagiorgi, K. Scholberg, M.H. Shaevitz, and J. Spitz, Phys. Rev. D **86** 013004 (2012).

[11] S.K. Agarwalla, J.M. Conrad, and M. Shaevitz, arXiv:1105.4984 [hep-ph] (2011).

[12] A. Aguilar *et al.* [LSND Collaboration], Phys. Rev. D **64** 112007 (2001).

[13] A.A. Aguilar-Arevalo *et al.* [MiniBooNE Collaboration], Phys. Rev. Lett. **105** 181801 (2010).

[14] A. A. Aguilar-Arevalo *et al.* [MiniBooNE Collaboration], Phys. Rev. Lett. **110** 161801 (2013).

[15] J.R. Alonso, arXiv:1209.4925 [nucl-ex] (2012).

Chapter 6

Dark matter and cosmology

XENON100 and XENON1T Dark Matter Search with Liquid Xenon

Gaudenz Kessler on behalf of the XENON collaboration
Physics Department, University of Zurich

DOI: http://dx.doi.org/10.3204/DESY-PROC-2014-04/109

The XENON100 detector is a dual-phase (liquid-gas) xenon time-projection chamber for dark matter particle detection containing 161 kg liquid xenon and 242 photomultiplier tubes to detect the scintillation light produced by particle interactions with xenon nuclei.

XENON1T, the next generation dark matter experiment, is being under construction and will house a total amount of 3.2 t of xenon. The designed background level is 100 times lower than that in XENON100. It is surrounded by a water tank that acts as an active muon veto. It is planned to upgrade the experiment to XENONnT with 7 t of liquid xenon.

1 Particle Detection with a Dual-Phase Time-Projection Chamber

The XENON project aims to detect Weakly Interactive Massive Particles (WIMPs) with a dual-phase time-projection chamber (TPC) filled with liquid and gaseous xenon. There are two types of particle interaction with the xenon inside the TPC. Charged particles (like electrons or muons) or γ would interact electromagnetically with an electron of the xenon atom shell. This kind of interaction is referred to as electronic recoil (ER). WIMPs would scatter off the xenon nuclei and cause a nuclear recoil (NR). Neutrons as well interact via nuclear recoil.

Figure 1 shows a schematic description of particle detection in such a detector. An energy deposition due to a particle interaction inside the TPC causes both direct scintillation light and ionisation of the xenon atoms. The direct scintillation light (S1) is promptly detected by two arrays of photomultiplier tubes (PMTs) that are located at the top and at the bottom of the TPC. The ionised electrons are extracted upwards by an electric field. They drift with a constant velocity upwards until they reach the liquid-gas surface. After being extracted into the gas phase of the TPC they produce scintillation light (S2) that is proportional to the number of extracted electrons. Since the electron extraction into the gas phase is very close to the top PMT array, the xy position can be reconstructed using the hit-pattern of photons on the top PMTs. The z coordinate of the interaction can be calculated from the drift time between the S1 and the S2 signals. This allows for a full 3D event position reconstruction. Because the ionisation density is higher for NRs than for ERs, the recombination is stronger for NR. This leads to a different ratio between S2/S1 for NRs and ERs and can be used to discriminate between these types of interaction.

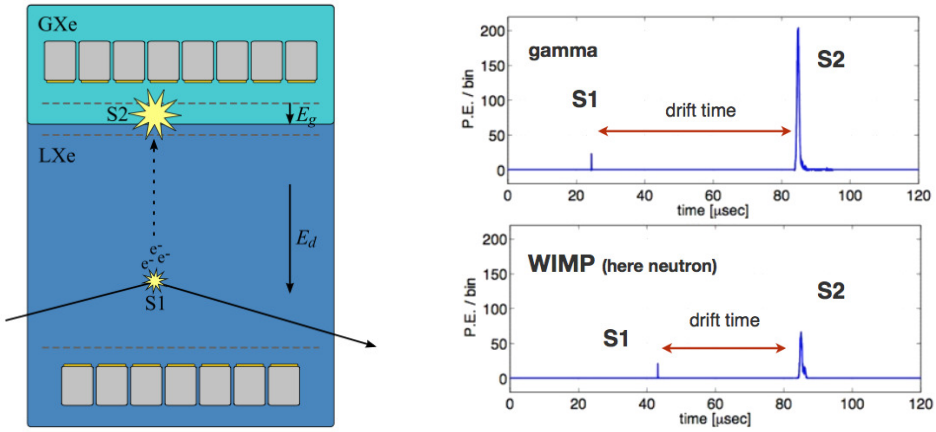

Figure 1: Working principle of a dual-phase time-projection chamber. Left: a particle interaction in the liquid xenon causes direct scintillation light (S1) and free electrons that drift to the gas phase and produce electroluminescence signal (S2). Right: the ratio between S1 and S2 is used to discriminate between ERs (electromagnetic background) and NRs (WIMPs or neutrons). The drift time between S1 and S2 peaks is used to determine the z position of the interaction.

2 XENON100

The XENON100 experiment is located at the Laboratori Nazionali del Gran Sasso (LNGS) in Italy, in which the flux of cosmic muons is reduced by a factor of 10^6 by 1400 meters of rock. The experiment consists of dual-phase time-projection chamber filled with 62 kg of liquid xenon (30 cm height $\times$ 30 diameter). The TPC is surrounded by other 99 kg of liquid xenon that act as an active veto. There are two arrays of PMTs on the top (in the gas phase) and the bottom of the TPC (242 in total). The drift field inside the liquid xenon is 530 V/cm and the field to extract drifting electrons into the gas phase is 12 kV/cm [1]

To probe the recoil behaviour of the background and signal high statistic calibrations have been performed. A ^{60}Co and a ^{232}Th source was used for the ER and an AmBe neutron source for the NR. For a good understanding of the background appearing in the experiment all components of the detector were screened for their radioactivity with high-purity Ge detectors. The obtained data was used to perform a full Monte Carlo simulation of all radioactive materials in all components of the experiment. The energy spectrum obtained in the Monte Carlo simulation fits very well to the background spectrum measured in the detector [2]. At the time of the publication, XENON100 is one of the experiments with the lowest background. The expected background rate in the signal region was determined to be only 1.0 ± 0.2 events for 224.6 live days, 0.79 ± 0.16 of which coming from γ events leaking to lower (S2/S1) values and $0.17^{+0.12}_{-0.07}$ coming from neutrons [3, 4]. In the signal region two events were observed, which means that there is no significant excess about the expected background due to a signal in the XENON100 data. There is a 26.4 % probability that the background fluctuates to two events. This result lead to the most stringent limit for the elastic spin-independent WIMP-nucleon cross-section at that time above 8 GeV/c^2, with a minimum of 2×10^{-45} cm^2 at 55 GeV/c^2 at 90% confidence

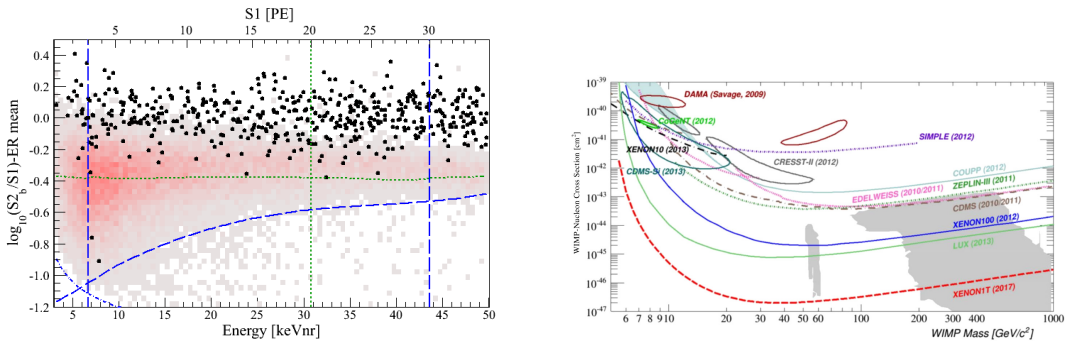

Figure 2: Left: event distribution observed during 224.6 live days using $\log_{10}(S2_b/S1)$ flattened by subtracting the ER band mean, as a function of NR energy. There are two events in the signal region, Right: exclusion limit on the WIMP-nucleon cross section obtained by XENON100 and expected sensitivity of XENON1T.

level [4]. Figure 2 shows the event distribution measured during 224.6 live days (left) and the limit for spin-independent WIMP-nucleon scattering that as achieved with XENON100 (right). 50% of the xenon nuclei have a non-zero spin. The natural abundance of ^{129}Xe and ^{131}Xe is 26.4% and 21.3%, respectively. XENON100 contains 26.2% ^{129}Xe and 21.8% ^{131}Xe. Hence also the spin-dependent elastic interaction was studied and XENON100 still holds the most stringent limit on the spin-dependent WIMP-neutron cross-section [5].

A search for axions and axion-like particles has been performed with the XENON100 data of 224.6 live days $\times$ 34 kg exposure. The axion-electric coupling constant, g_{Ae}, could be rejected for values larger than 7.7×10^{-12} (90% C.L.) [6].

An alternative way to directly detect Dark Matter is to observe inelastic WIMP-nucleus scattering, in which the nuclear recoil excites the nucleus to a low-level excited state [7]. There are two xenon isotopes for which this process is possible: ^{129}Xe has an excitation energy of 39.6 keV to the lowest-lying state, the excitation energy of ^{131}Xe is 80.3 keV. In the analysis of inelastic events ^{129}Xe is considered. The excited state has a lifetime of 0.97 ns which is too short for the nuclear recoil and the photon emission from the deexcitation to be distinguished in time. Hence the expected signal is a nuclear recoil simultaneous with a 40 keV photon. The expected sensitivity in the XENON100 detector is 5×10^{-38} cm^2 for a mass of 100 GeV/c^2 at 90% confidence level.

An annual modulation analysis and low-mass WIMP search are being performed. At the moment 154 live days of new data is available that will be unblinded soon. Currently the XENON100 detector is used to probe the recoil behaviour with various calibration sources.

3 XENON1T

The next generation detector, XENON1T, is currently under construction in Hall B of the Gran Sasso Underground Laboratory. It will house a total amount of 3.2 tons of liquid xenon with 2 tons inside the sensitive region of the TPC. The TPC is a cylinder of 1 meter diameter and 1 meter height and contains in total 248 3-inch PMTs that are designed to have an especially low radioactivity and to operate in liquid xenon environment [8] The experiment will have 100

times lower background than its predecessor XENON100. Therefore it is embedded inside a 10 meter diameter water shield that is instrumented with 84 8-inch PMTs and acts as a Cherenkov muon veto [9]. The sensitive volume is shielded by 10 cm of liquid xenon. The required level of ^{85}Kr will be below 0.5 ppt (a few ppt in XENON100), and the contamination of ^{222}Rn will be only 1 μBq/kg whereas it was 65 μBq/kg in XENON100. The goal is to achieve only 0.5 events per ton per year. The operation is planned to start in 2015. The expected sensitivity is 2×10^{-47} cm^2 for 55 GeV/c^2.

After two years of operation it is planned to upgrade XENON1T to XENONnT, the next stage with a total mass of 7 tons of liquid xenon, which would allow to increase the sensitivity by another order of magnitude. For a fast upgrade most of the systems XENON1T will be reused.

References

[1] E. Aprile et al. (XENON100), Astropart. Phys. 35, 573-590 (2012)

[2] E. Aprile et al. (XENON100), Phys. Rev. D 83, 082001 (2011).

[3] E. Aprile et al. (XENON100), J. Phys. G: Nucl. Part. Phys. 40, 115201 (2013)

[4] E. Aprile et al. (XENON100), Phys. Rev. Lett. 109, 181301 (2012).

[5] E. Aprile et al. (XENON100), Phys. Rev. Lett. 111, 021301 (2013)

[6] E. Aprile et al. (XENON100), Phys. Rev. D 90, 062009

[7] L. Baudis et al., Phys. Rev. D 88, 115014, (2013)

[8] L. Bauids et al., JINST 8 P04026 (2013)

[9] E. Aprile et al. (XENON100), arxiv:1406.2374

Current Status of the Dark Matter Search Experiment CRESST

Holger Kluck[1,2] for the CRESST Collaboration

[1]Institute of Atomic and Subatomic Physics, Vienna University of Technology, 1020 Wien, Austria
[2]Institute of High Energy Physics of the Austrian Academy of Sciences, 1050 Wien, Austria

DOI: http://dx.doi.org/10.3204/DESY-PROC-2014-04/240

CRESST is a cryogenic direct Dark Matter search experiment based on phonon-light technique. It is aiming for the detection of *weakly interacting massive particles* (WIMPs) via their scattering off nuclei in $CaWO_4$ target crystals. Significant improvements have been achieved with respect to previous measurement campaigns in terms of intrinsic radiopurity of $CaWO_4$ crystals and rejection of nuclear recoil events from alpha decays near surfaces. In this contribution, the related changes in the detector design will be discussed. Based on the first ~ 30 kg-live-days of data acquired by a single $CaWO_4$ detector module with a new design, we present limits for the spin-independent WIMP-nucleon cross section, which exclude new parameter space below $3\,\mathrm{GeV}/c^2$.

1 Introduction

Various observations point to the existence of particle-like Dark Matter [1]. However, the actual particle candidate, which may be a *weakly interacting massive particle* (WIMP), has not yet been discovered undoubtedly: Some experiments, e.g. LUX [2] and SuperCDMS [3], obtained null results, whereas other experiments, e.g. DAMA/LIBRA [4] and previously also CRESST [5], observed a potential signal.

CRESST recently published the result of a new search for WIMP-nucleon scattering based on a single upgraded detector module, *TUM40* [6]. After a short introduction of the CRESST experiment in sec. 2, we will present the improvements of this upgraded module (sec. 3) and the obtained result (sec. 4) before we conclude in sec. 5.

2 The CRESST experiment

The cryogenic Dark Matter search CRESST is looking for nuclear recoils induced by the elastic scattering of WIMPs off the nuclei in $CaWO_4$ targets. The energy deposited by a potential WIMP-nucleon scattering is only in the order of a few 10 keV, therefore a sufficient background suppression is crucial [5]. To discriminate e^-/γ background events, CRESST simultaneously reads out signals from two channels: the scintillation light emitted by the $CaWO_4$ crystal (*light signal*) and the non-thermal phonon excitation of the crystal lattice (*phonon signal*). The rejection of *near-surface α events* will be outlined in sec. 3. A detailed description of the

experimental set-up, the data acquisition, and analysis can be found in earlier publications [7, 8].

The phonon signal, which is independent of the interacting particle type, is used to measure the deposited energy E. Contrary, for the same E, the light signal of nuclear recoils is suppressed with respect to the light signal of e^-'s/γ's, and decreases with the mass of the nucleus.

This *quenching effect* is evident in the plane of *light yield* (LY), i.e. the ratio of light signal over phonon signal, versus E as schematically shown in fig. 1: The e^-/γ-band is normalized to $LY = 1$ at 122 keV via calibration with a ^{57}Co source. At decreasing values of LY, bands for α recoils and recoils of the O, Ca, and W nuclei are located [9].

Due to the overlapping of the bands at low energies, see fig. 1, a low background activity and a low experimental threshold are necessary for dedicated low-mass WIMP searches. CRESST made progress in both aspects with an upgraded detector module, resulting in a WIMP sensitivity down to $\sim 1\,\mathrm{GeV}/c^2$ [6].

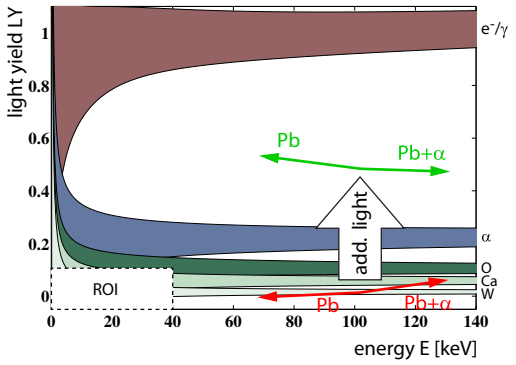

Figure 1: Illustration of the various bands in the light yield−energy-plane for a $CaWO_4$ detector and the region of interest (ROI) for the WIMP search with the TUM40 detector module. Additional scintillation light shifts near-surface α and Pb events out of the vicinity of the nuclear recoil bands [12], for details see text.

3 The upgraded detector module TUM40

CRESST runs with 18 detector modules of various designs and a total target mass of roughly 5 kg [6] in its current data taking period (CRESST-II Phase 2). Here, we will focus on 29.35 kg d recorded with only one module, *TUM40*, based on a $CaWO_4$ crystal with a mass of ~ 250 g [6]. This module shows three improvements: a decreased intrinsic e^-/γ background, a fully efficient rejection of near-surface α background, and a high phonon resolution allowing to set a low trigger threshold.

The intrinsic e^-/γ background is reduced by growing the crystal in a dedicated furnace at the TU Munich [10]. Figure 2 compares the background spectrum of TUM40 (*filled blue histogram*) with the one of a commercial $CaWO_4$ crystal (*open black histogram*). Whereas the spectrum of the com-

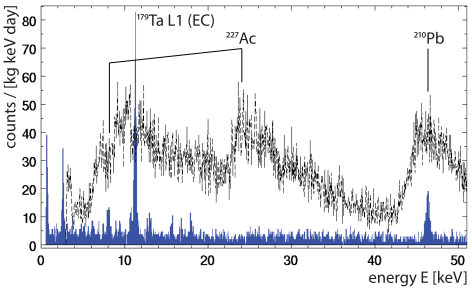

Figure 2: Background spectra for a commercial $CaWO_4$ crystal (*open black histogram*) and TUM40 (*filled blue histogram*). Prominent features are the beta decays of ^{227}Ac and ^{210}Pb, and the electron capture of cosmogenic ^{179}Ta [6, 11].

mercial crystal is dominated by beta decays of internal ^{227}Ac and ^{210}Pb contaminations, these are strongly reduced in the TUM40 spectrum: The background rate of TUM40 is with ~ 3.5 counts/kg/d/keV up to 10 times lower than the one of a comparable commercial crystal. A detailed discussion of the remaining background of TUM40 can be found in [11].

Near-surface α decays are mostly $^{210}\mathrm{Po} \rightarrow {}^{206}\mathrm{Pb} + \alpha$ decays near surrounding surfaces and contribute to the background in two ways: If the resulting α particle hits the crystal after having already lost most of its energy, it can leak as *degraded* α into the nuclear recoil bands. In case the resulting ^{206}Pb nucleus hits the crystal, such an event can leak from its band closely below the W band to the ROI. To actively veto this α (Pb) background, already previously each crystal was encapsulated by a scintillating and reflecting foil which is hit by the remaining α particle. The additional scintillation light of the foil shifts the event to a higher LY value as illustrated in fig. 1. However, previously not the complete surrounding of the crystals was scintillating due to the bronze clamps that hold the crystal. This results in an unexpected high rate of non-vetoed near-surface α decays in the previous data taking period (CRESST-II Phase 1) [5]. The TUM40 module holds the target crystal by sticks made of scintillating $CaWO_4$, therefore it is nearly fully surrounded by scintillating surfaces, which strongly increase the veto efficiency against near-surface α events. So far, TUM40 found no near-surface α events which are not vetoed. A detailed evaluation of the *$CaWO_4$-stick-design* will be given in [12].

The TUM40 module features also an excellent trigger threshold: Measured with electronic calibration pulses, the trigger efficiency reaches 50 % already at ~ 600 eV. Furthermore, a very good energy resolution of ~ 100 eV has been achieved. This is validated by the widths of the γ lines in fig. 2 [6]. The good energy resolution together with the very low threshold predestines the TUM40 module for a low-mass WIMP search.

4 Results of a dedicated low-mass WIMP search

The TUM40 module alone collected an exposure of 29.35 kg d, before all cuts and corrections for detection efficiencies in 2013 [6]. The *region of interest* (ROI) for WIMPs on the $LY-E$-plane includes all events with a LY lower than the central LY of the O recoil band and within an energy interval starting at the trigger threshold of 600 eV and ending at 40 keV [6], see fig. 1.

Applying Yellin's optimum interval method [13] on the events in the ROI results in an exclusion limit at 90 % CL for elastic spin-independent WIMP-nucleon scattering as shown in fig. 3 (*red line*) [6]. We emphasize three features of this limit:

First, it is a leading limit and excludes new parameter space for $m_\chi \leq 3\,\mathrm{GeV}/c^2$. Second, compared to other

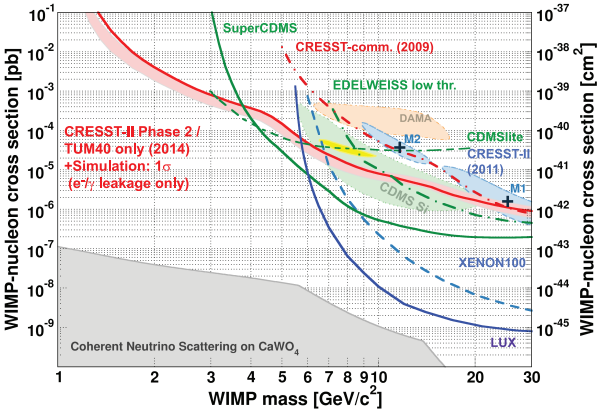

Figure 3: Limit on elastic spin-independent WIMP-nucleon scattering reported in [6] (red solid line) compared to selected results of current Dark Matter searches, see [6] for the references.

limits, this limit is relatively flat: Due to the multi-element target $CaWO_4$, CRESST is sensitive to the scattering of WIMPs at low and high masses via O ($A = 15.999\,\mathrm{u}$), and W ($A = 183.84\,\mathrm{u}$). Therefore, this limit is also relevant at higher WIMP masses. For instance, the TUM40 results exclude the low-mass maximum M2 and constrain the higher mass maximum M1 where CRESST-II Phase 1 previously reported an event excess over expected background [5]. Third, the experimental limit agrees with the expected 1σ limit due to the assumed leakage of e^-/γ background in the ROI (fig. 3, *light red region*). Therefore, no additional background component is necessary to explain the observed events [6].

5 Conclusion and outlook

With $\sim 30\,\mathrm{kg\,d}$ of data, CRESST could show the improved performance of the upgraded TUM40 detector module: a decreased intrinsic e^-/γ background by a factor of up to 10, an improved rejection power against near-surface α events, and a low trigger threshold of $\sim 600\,\mathrm{eV}$. Combined, these improvements result in a leading limit on elastic spin-independent WIMP-nucleon scattering below $3\,\mathrm{GeV}/c^2$ and in the exclusion of the M2 maximum of CRESST-II Phase 1.

It is planned to continue data taking with CRESST-II Phase 2 until reaching an exposure sufficient to clarify the nature of M1, probably mid of 2015. As all of the recent progress is well understood, projections based on reasonable further improvements indicate the possibility to reach $\sim 10^{-6}\,\mathrm{pb}$ at $\sim 3\,\mathrm{GeV}/c^2$. Therefore, CRESST is especially predestined to test new parameter space at low WIMP masses.

Acknowledgments

This work was supported by funds of the German Federal Ministry of Science and Education (BMBF), the Munich Cluster of Excellence (Origin and Structure of the Universe), the Maier-Leibnitz-Laboratorium (Garching), the Science and Technology Facilities Council (STFC) UK, and the Helmholtz Alliance for Astroparticle Physics. We gratefully acknowledge the work of Michael Stanger from the crystal laboratory of the TU Munich. We are grateful to LNGS for their generous support of CRESST, in particular to Marco Guetti for his constant assistance.

References

[1] G. Bertone, ed. *Particle Dark Matter.* Cambridge University Press, 2010.
[2] D.S. Akerib *et al.*, Phys. Rev. Lett. **112** 091303 (2013), arXiv:1310.8214[astro-ph.CO].
[3] R. Agnese *et al.*, Phys. Rev. Lett. **112** 241302 (2014), arXiv:1402.7137[hep-ex].
[4] R. Bernabei *et al.*, Eur. Phys. J. **C73** 2648 (2013), arXiv:1308.5109[astro-ph.GA].
[5] G. Angloher *et al.*, Eur. Phys. J. **C72** 1971 (2012), arXiv:1109.0702[astro-ph.CO].
[6] G. Angloher *et al.*, Eur. Phys. J. **C74** 3184 (2014), arXiv:1407.3146[astro-ph.CO].
[7] G. Angloher *et al.*, Astropart. Phys. **23** 325 (2005), arXiv:astro-ph/0408006.
[8] G. Angloher *et al.*, Astropart. Phys. **31** 270 (2009), arXiv:0809.1829[astro-ph].
[9] R. Strauss *et al.*, Eur. Phys. J. **C74** 2957 (2014), arXiv:1401.3332[astro-ph.IM].
[10] A. Erb and J.-C. Lanfranchi, Cryst. Eng. Comm. **15** 2301 (2013).
[11] R. Strauss *et al.*, arXiv:1410.4188[physics.ins-det] (2014), submitted to J. Cosmol. Astropart. Phys.
[12] R. Strauss *et al.*, arXiv:1410.1753[physics.ins-det] (2014), submitted to Eur. Phys. J. **C**.
[13] S. Yellin, Phys. Rev. **D66** 032005 (2002), arXiv:physics/0203002.

Dark matter annihilation and local warming in the core of a neutron star

M. Ángeles Pérez-García[1], *Joseph Silk*[2,3,4]

[1] Department of Fundamental Physics, University of Salamanca, Plaza de la Merced s/n 37008 Salamanca, Spain
[2]Institut d'Astrophysique, UMR 7095 CNRS, Université Pierre et Marie Curie, 98bis Blvd Arago, 75014 Paris, France
[3]Department of Physics and Astronomy, The Johns Hopkins University, Homewood Campus, Baltimore MD 21218, USA
[4]Beecroft Institute of Particle Astrophysics and Cosmology, Department of Physics, University of Oxford, Oxford OX1 3RH, UK,

DOI: http://dx.doi.org/10.3204/DESY-PROC-2014-04/30

In this contribution we propose that the possible existence of a component of self-annihilating dark matter in the universe may result in a local inner core warming of medium-age neutron stars on a time-scale of $\sim 10^2$ yr. The energy released from annihilation of a massive ($m_\chi \gtrsim$ TeV) dark matter particle in the central regions of the star could be capable of injecting an extra neutrino/photon component allowing a positive emissivity, opposed to the usual negative values for the standard cooling processes. As a result, an enhanced early warming era in the neutron star coolig scenario may result.

In the ΛCDM paradigm, current indications from recent Planck data [1] show that the current total matter content of the Universe is roughly 27%, more precisely Planck data yield (at 68% CL) a physical baryonic content $\Omega_b h^2 = 0.02207 \pm 0.00033$ and a physical dark matter (DM) content of $\Omega_c h^2 = 0.1196 \pm 0.0031$. DM, being about five times more abundant than baryonic matter, has not yet been thoroughly taken into account in our current understanding of microscopic processes occurring inside stars. Namely, for neutron stars (NSs), the physical description of the interior has mostly been attempted only taking into account ordinary standard model species. Even if a tiny fraction, it remains to be determined at what extent the DM component may play a role and, consequently, trigger observable effects that could have been missidentified entangled in the, already complex, description of these objects.

Provided DM could be a Majorana particle, the emission of radiation in the final states from self-annihilation could be used as indirect evidence of its existence as we will argue. Althouh we should keep in mind that there is not yet consensus on basic DM properties such as bosonic or fermionic nature or, as mentioned, whether it is a Majorana or Dirac particle. To try to shed light on these aspects there is an international multi-messenger effort involving collider, direct or indirect searches where DM signals may be detected. Typically, globular clusters or the galactic center seem regions where a vast amount of this type of matter is expected. Some partial hints of an extra photon component coming from the galactic center have already arised [2]. The actual interaction strength in this dark sector is not clearly determined so far

and candidates in the weak sector (WIMPs) seem favoured in light of cosmological arguments. Regarding fundamental properties such as the mass of the DM candidate, favoured values in the range $m_\chi \sim \mathcal{O}(\ 10\ \mathrm{GeV/c^2} - 10\,\mathrm{TeV/c^2})$ are under current scrutiny.

In our galaxy a DM density distribution can be described under the form of a power-law density profile as already pointed out in the seminal work of [3]. Assuming this prior, the possibility of gravitational accretion of the dark component into massive compact stars comes naturally. In particular, the very dense environments of planets and stars seem capable to resonantly capture DM [4].

More in detail, in a NS with radius R and baryonic number N_B the large opacity of its internal dense core to incoming WIMPs seems capable to stabilize an inner distribution of these, given a scattering cross-section with nucleons around the value of the geometrical cross-section $\sigma_{\mathrm{geom}} \simeq 2.4 \times 10^{-45}\ \mathrm{cm}^2 \left(\frac{1.4\mathrm{M}_\odot}{\mathrm{M}}\right)\left(\frac{\mathrm{R}}{11.5\,\mathrm{km}}\right)^2$. For possibly larger cross-sections than this and in order to preserve unitarity, the NS opacity saturates providing no enhancement of DM capture. On the other hand, for cross-sections smaller than the geometrical value there is a fundamental limit given by the escape velocity of the NS, that on the Newtonian approximation is $v_{esc} \simeq 0.6c\sqrt{2G\left(\frac{M}{1.4M_\odot}\right)\left(\frac{11.5\,\mathrm{km}}{R}\right)}$. In this case, the NS gravitational potential well could bound the WIMPs kinematically although to form an inner thermalized distribution they must further interact with a nucleus/nucleon with mass M' losing an energy fraction $\frac{\Delta E_k}{E_k} \lesssim \frac{4M'm_\chi}{(M'+m_\chi)^2}$ of the incoming kinetic energy E_k every time.

The internal thermalized DM distribution can be parametrized by a particle number density $n_\chi(r,T) = n_{0,\chi}e^{-\left(\frac{r}{r_{\mathrm{th}}}\right)^2}$ where r_{th} is the thermal radius and $n_{0,\chi}$ is the central value normalized to the DM population number inside the star of radius R [5] at a given time in a local environment density similar to our solar system value of about $\rho_\chi \simeq 0.3\ \mathrm{GeV/cm^3}$.

The population at a given time inside the NS, $N_\chi(t)$, is obtained from the solution of an ordinary differential equation $\dot{N}_\chi = C_\chi - C_a N_\chi^2$ including competing processes by means of a capture rate C_χ and an annihilation rate C_a yielding [4]

$$N_\chi(t) = \sqrt{\frac{C_\chi}{C_a}}\coth\left[\frac{(\mathrm{t}-\mathrm{t_{col}})}{\tau} + \coth^{-1}\left(\sqrt{\frac{\mathrm{C_a}}{\mathrm{C_\chi}}}\mathrm{N_\chi(t_{col})}\right)\right], \tag{1}$$

with $\tau^{-1} = \sqrt{C_\chi C_a}$ the relaxation time to achieve equilibrium and $N_\chi(t_{\mathrm{col}})$ is the number of DM particles inside the progenitor core at the time of the collapse (NS birth). This population is esentially inherited from the progenitor star in its lifetime.

The energetics of the dynamical microscopic processes must include the heating and cooling possibilities. First, considering the specific emissivity (energy released per unit volume and unit time) in the photon and neutrino channels arising from the annhilation channels it could be written as

$$\varepsilon_\chi(r,T) \simeq n_\chi^2(r,T) m_\chi \langle\sigma_a v\rangle \sum_{i=\nu,\gamma} f_i, \tag{2}$$

with $\langle\sigma_a v\rangle \simeq 3 \times 10^{-26}\,\mathrm{cm^3/s}$ the velocity averaged annihilation cross-section and $f_i \simeq \int \frac{E}{m_\chi}\frac{dN_i}{dE}dE$ the energy fraction from the spectrum $\frac{dN_i}{dE}$. We must note that the quantity $f = f_\nu + f_\gamma$ is a positive number, *injecting* net energy into the system.

In the typical scenarios for NS cooling [6] standard-model (anti)neutrinos and photons are in charge of cooling efficiently the system. From observations, effective external temperatures

can be measured for a dozen isolated NSs [7]. In the so-called direct URCA process a very efficient neutrino cooling mode is triggered if the proton fraction in the core is large enough, in excess of $(9-11)\%$. Since this requires large central densities it is uncertain whether this mode is switched on. However, if the existence of a spectator neutron is allowed, reactions $p+e+n \to n+n+\nu_e$, $n+n \to p+n+e+\bar{\nu}_e$ under the so-called modified URCA (MURCA) process can proceed. Its emissivity is given by

$$\varepsilon_\nu^{MURCA} \simeq -8.55 \times 10^{21} \left(\frac{T}{10^9\, K}\right)^8 \mathrm{erg\,s^{-1}cm^{-3}}, \tag{3}$$

where the minus sign means that they are cooling modes, effectively removing energy from the system. In addition to this mode and at late times ($\gtrsim 10^5$ yr) the standard photon mode overtakes the cooling as a black-body emitter with a luminosity $L_\gamma \simeq 4\pi R^2 \sigma_{SB} T_e^4$ and $T_e \simeq T^{0.5+\alpha}$, $\alpha \simeq 0.1$ is the effective temperature with $T_e \simeq 0.87 \times 10^6 (T/10^8\, K)^{0.55}$. This yields $\varepsilon_\gamma \simeq -L_\gamma / \frac{4}{3}\pi R^3$ [6].

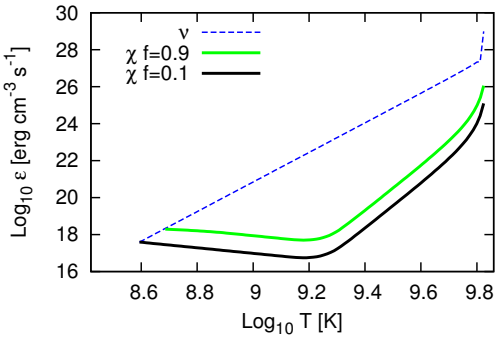

Figure 1: Emissivities in the inner NS core as a function of internal temperature for $m_\chi = 10$ TeV. Dashed line is the MURCA neutrino process while the solid green and black lines denote the effect of a DM energy deposit of $f = 0.9, 0.1$ respectively.

If we now consider the dynamical heat-energy flow the equations for the luminosity L and local temperature T (including redshift factors e^Φ in a curved static spacetime) read [8]

$$\frac{1}{4\pi r^2}\sqrt{1-\frac{r_s}{r}}\frac{\partial}{\partial r}\left(e^{2\Phi}L\right) = -\varepsilon - \frac{C_v}{e^\Phi}\frac{\partial T}{\partial t}, \quad \frac{L}{4\pi r^2} = \kappa\sqrt{1-\frac{r_s}{r}}e^{-\Phi}\frac{\partial}{\partial r}\left(Te^\Phi\right), \tag{4}$$

where $\varepsilon = \sum_{j=\nu,\gamma} \varepsilon_j$ is the contribution of the emissivities, $r_s = 2GM$ is the Schwarzschild radius, C_v is the heat capacity per unit volume and κ is the thermal conductivity. C_v is the sum of the contribution of partial heat capacities from particle constituents (we take protons, neutrons, electrons) $C_v = \sum_{i=p,n,e} C_{v,i}$. For a degenerate core with fermions we have (per unit volume) $C_{v,i} = N_i(0)\frac{\pi^2}{3}k_B^2 T$ and $N_i(0) = \frac{m_i^* c^2 p_{F,i}}{\pi^2}$ is the density of states for a degenerate quantum system, being $p_{F,i}$ the ith-Fermi momentum and $m_{p,n}^* < m_n$ the in-medium nucleon mass, that can be a reduced with respect to vacuum values due to many-body effects [9]. Consistently, we

take $m_e^* = m_e$. Let us note that in the Newtonian limit (the one we are going to analyze in this contribution) the solution is obtained from solving in the isothermally flat limit. This is a consequence of the large thermal conductivity in the system. Relativistic corrections to time and distance scales are set to unity. Then the equation simplifies to

$$C_v \frac{dT}{dt} = -|\varepsilon_\nu| - |\varepsilon_\gamma| + \varepsilon_\chi. \tag{5}$$

In Fig.(1) we show the emissivities in the NS inner core as a function of internal temperature T. We suppose neutrinos, photons and DM particles in a flat, Newtonian space. We assume an initial temperature of $T \simeq 1$ MeV. We depict with a dashed line the MURCA neutrino process while the solid green and black lines denote the effect of an energy deposit of $f = 0.9, 0.1$, respectively. We can see that at a $T \simeq 10^{8.6-8.7}$ K the emissivities are comparable. This T drop corresponds to $\sim 10^2$ yr assuming a central core density of 3.5 times that of nuclear saturation density for a 10 TeV particle. Let us remind here that we have supposed that the core is isothermal at very early times. Standard approaches show that isothermality in the core takes about $\Delta t \simeq 10$ yr to be achieved, however this correction should not change much the results obtained here. In a previous work [10] it was determined that the possible effect on the cooling pattern in a NS was a flattening of the temperature of the star around $\sim 10^4$ K at times larger than $\sim 10^7$ yrs, making this a challenging experimental confirmation, especially if looking towards central galactic locations where DM fraction may be enhanced. We find here that, for existing models of DM candidates with masses in the $\gtrsim$TeV range this is, in principle, a viable measurement that could test the proposed mechanism. This is subject of ongoing work and results will appear elsewhere. As a final remark let us mention that we have supposed that the fate of the NS is to remain as a nucleon-matter object, but if, however, a nucleation massive event is triggered, furhter consequences may result. This has been partially explored in [11][12][13]. M. A. P. G. would like to thank useful conversations with J. Pons and C. Kouvaris and the kind hospitality of IAP where part of this work was developed and the Spanish MICINN MULTIDARK, FIS2012-30926 projects.

References

[1] P. A. R. Ade et al. [Planck Collaboration], arXiv: 1303.5075.

[2] T. Daylan et al., arXiv:1402.6703.

[3] J. E. Gunn and J. R. Gott ApJ, **176** (1972) 1.

[4] A. Gould, ApJ **321** 571 (1987).

[5] M. A. Pérez-García and J. Silk, arXiv: 1403.6111, in press in Phys. Lett. B

[6] D. Page et al, ApJ **155** (2004) 623.

[7] D. G. Yakovlev et al, Advances in Space Research **33** (2004) 523.

[8] K. S. Thorne, *The General Relativistic Theory of Stellar Structure and Dynamics*, in C. Dewitt, E. Schatzman, P. Véron, editor, High Energy Astrophysics, Volume 3, (1967).

[9] M. A. Pérez-García , C. Providencia and A. Rabhi, Phys Rev C **84** (2011) 045803.

[10] C. Kouvaris, Phys. Rev. D **77** (2008) 023006.

[11] M. A. Pérez-García, Silk, J., Stone, J. R. , Phys. Rev. Lett. **105** (2010) 141101.

[12] M. A. Pérez-García and J. Silk, Physics Letters B **711** (2012) 6.

[13] M. A. Pérez-García, F. Daigne and J. Silk, ApJ **768** (2013) 145.

DarkSide-50: results from first argon run

Davide D'Angelo for the DarkSide collaboration

Università degli Studi di Milano e I.N.F.N., via Celoria 16, 20133 Milano, Italy

DOI: http://dx.doi.org/10.3204/DESY-PROC-2014-04/315

DarkSide (DS) at Gran Sasso underground laboratory is a direct dark matter search program based on TPCs with liquid argon from underground sources. The DS-50 TPC, with 50 kg of liquid argon is installed inside active neutron and muon detectors. DS-50 has been taking data since Nov 2013, collecting more than 10^7 events with atmospheric argon. This data represents an exposure to the largest background, beta decays of ^{39}Ar, comparable to the full 3 y run of DS-50 with underground argon. When analysed with a threshold that would give a sensitivity in the full run of about 10^{-45} cm^2 at a WIMP mass of 100 GeV, there is no ^{39}Ar background observed. We present the detector design and performance, the results from the atmospheric argon run and plans for an upscale to a multi-ton detector along with its sensitivity.

The DarkSide (DS) project [1] aims to direct Dark Matter detection via WIMP-nucleus scattering in liquid Argon. The detectors are dual phase Time Projection Chambers (TPCs) located at Laboratori Nazionali del Gran Sasso in central Italy under a rock coverage of $\sim$3800 m w.e. DS aims to a background-free exposure via three key concepts: (1) very low intrinsic background levels, (2) discrimination of electron recoils and (3) active suppression of neutron background.

DS has a multi-stage approach: after the operation of a 10 kg detector [2], we are now running DarkSide-50 (DS-50) detector with a 45 kg fiducial mass TPC and a projected sensitivity of $\sim 10^{-45}$ cm^2 for a 100 GeV WIMP. The project will continue with a multi-ton detector and a sensitivity improvement of two orders of magnitude.

The DS-50 TPC is depicted in Fig. 1. The scattering of WIMPs or background in the active volume induces a prompt scintillation light, called S1, and ionization. Electrons which do not recombine are drifted by an electric field applied along the z-axis. The maximum drift time across the 35.6 cm height is $\sim$375 μs at the operative field of 200 V/cm. Electrons are then extracted into gaseous argon above the extraction grid, where a secondary larger scintillation emission takes place, called S2. Two arrays of 19 3"-PMTs collect the light on each side of the TPC.

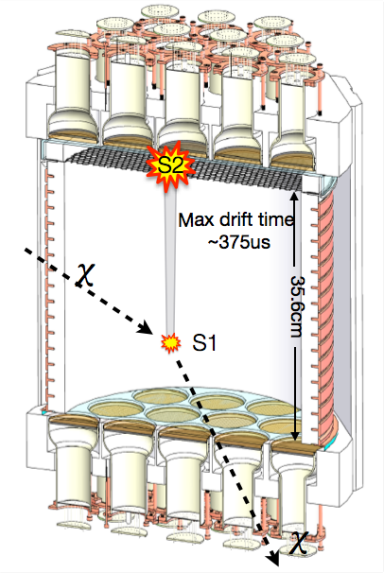

Figure 1: DS-50 TPC principle of operation.

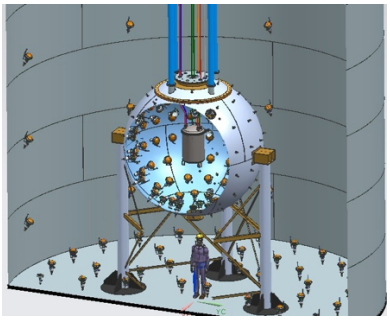

Figure 2: DS-50 Schematics. TPC, ND and MD are visible.

The TPC is housed inside an organic liquid scintillator Neutron Detector (ND) and a water Cherenkov Muon Detector (MD) [3], designed to host also a larger TPC with up to 5 t of Liquid Argon, see Fig. 2. The ND is made by a 4 m diameter steel sphere filled with a 1:1 mixture of Pseudocumene (PPO doped) and Trimethyl Borate (TMB) for enhanced neutron detection. The scintillation light is captured by 110 8"-PMTs mounted on the sphere inner surface. In addition of acting as a veto it also features independent trigger capabilities for an in-situ measurement of the neutron background. Boron has a high n-capture cross section which allows a compact veto size and reduces the capture time to 2.3 μs, two orders of magnitude below pure PC. The n-capture on ^{10}B results in recoiling ^{7}Li and α particle. In 94% of the cases a 0.48 MeV-γ accompanies the process and is brightly visible. In the remaining cases the recoil energy of 1.47 MeV must be detected and this is typically quenched to $\sim$ 50 keV. Simulations indicate an efficiency $>$ 99% for radiogenic neutrons and $>$ 95% for cosmogenic neutrons [4]. The MD is a cylindrical tank, 11 m in diameter and 10 m high, filled with ultra-pure water and instrumented with 80 8" PMTs on the floor and inner walls. In addition of acting as water Cherenkov detectors for through-going muons with >99% efficiency, it also serves as passive shielding again gammas and neutrons from the rocks. DS-50 has been commissioned and is taking data since Nov. 2013. After circulatimg Argon through charcoal filters for about 5 months, the electron lifetime was brought a stable value of $\sim$ 5 ms, much larger then the maximum drift time in the TPC.

Operating Argon detectors implies dealing with the intrinsic cosmogenic background from ^{39}Ar, a β-emitter with a Q=565 keV and $\tau_{1/2} = 269$ y. In Atmospheric Argon (AAr) its activity can be as high as $\sim$ 1 Bq/kg. However we have identified a source of Underground Argon (UAr) where the contamination is $<$ 6.5 mBq/kg. A cryogenic distillation plant is producing the UAr at a rate of $\sim$ 0.5 kg/d. We are currently operating with AAr and we will switch to UAr at the beginning of 2015. Argon has an intrinsic capability to distinguish Electron Recoils (ER) such as ^{39}Ar decays from Nuclear Recoils (NR). Prompt scintillation light in Argon comes from the de-excitation of singlet and triplet states of Ar_2^*, having very different mean lives: $\tau_{\text{singlet}} \sim 7$ ns while $\tau_{\text{triplet}} \sim 1.6\,\mu$s. Since NRs tend to populate more the singlet state, they result in significantly faster signals compared to ERs. We define the parameter F90 as the ratio of charge collected in the first 90ns over the total S1 charge. NRs are distributed around F90 $\sim$ 0.7 while ERs around F90 $\sim$ 0.3.

We have characterised our detector in terms of Light Yield (LY). At null field we have used the LY from the ^{39}Ar shoulder at 565 keV, obtaining $\text{LY}_{\text{null}} \sim 8$ pe/keV, assumed energy independent within 3%. With the application of the drift field, the LY becomes energy dependent and ^{39}Ar is way beyond or region of interest. Therefore we spiked argon by adding gaseous ^{83m}Kr in the recirculation system. ^{83m}Kr decays fast ($\tau_{1/2} \sim 1.8$ h) and yields a good monochromatic line at 41.5 keV. We have used the relative position of this line with and without drift field to scale the LY, obtaining $\text{LY}_{200V} \sim 7.2$ pe/keV at 200 V/cm.

Compared to ERs, NRs are quenched by a factor that depends on energy and field. We have used the data from SCENE [5] to determine the quenching factor. SCENE features a small TPC with a concept similar to DS and has been measuring recoils from a neutron beam, whose energy can be selected. SCENE has measured quenching factors at different neutron energies

and drift field with respect to ERs from ^{83m}Kr. We have processed SCENE raw data using the DS reconstruction code and we have obtained the quenching factors as well as the distributions of the F90 parameter.

The ND has been also commissioned. The LY has been estimated exploiting ^{60}Co contamination present in the cryostat. The LY has been found to be ~ 0.5 pe/keV, sufficient to detect recoils following a neutron capture on Boron of the order of 50 keV$_{ee}$. Unfortunately we have observed a high rate due to the intrinsic biogenic isotope ^{14}C in the TMB, at the level of $\sim 10^{-13}$ g/g. We have therefore successfully distilled the scintillator mixture and replaced TMB with pure Pseudocumene. Meanwhile we have identified a supplier of TMB coming from an underground oil batch which is low in ^{14}C, $< 10^{-15}$ g/g. We will restore the design scintillator mixture before the end of 2014.

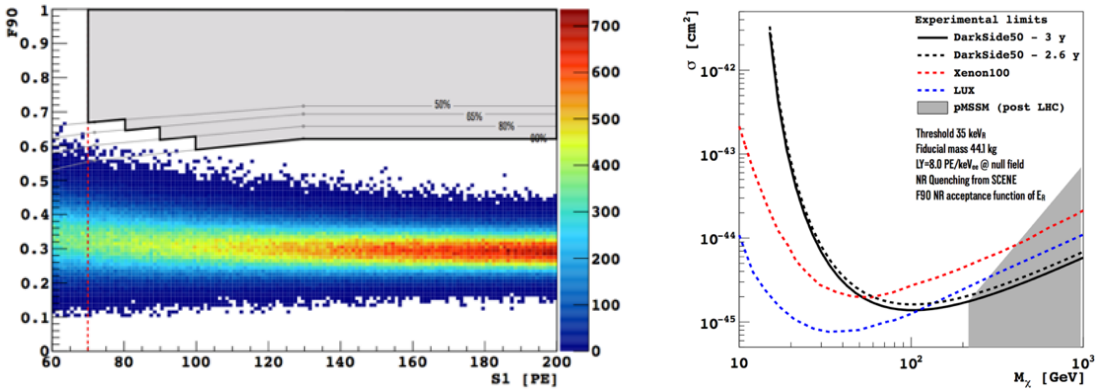

Figure 3: DS-50 exposure of 280 kg-days, F90 vs S1 energy in PE units with the NR acceptance curves and the WIMP search region superimposed (left). DS-50 projected sensitivity for 2.6 y and 3 y running with UAr compared to rejection curves from LUX and Xenon100 experiments (right).

In Fig. 3 (left) are shown events corresponding to 280 kg-days in the parameter plane of F90 vs S1 Energy in photoelectrons. Only single hit events are selected. A z-cut is applied to remove the regions close to the cathode and to the extraction grid. Events which show a coincident energy deposition in the ND are removed. The high ^{39}Ar content of AAr allows us to calibrate our S1-PSD with an exposure equivalent to 2.6 y of operation with UAr at a contamination as high as the present upper limit. In this energy scale 70 pe and 125 pe correspond to ~ 35 keV and ~ 57 keV NRs according to the quenching factors determined from the SCENE data. 70 pe is also our choice of energy threshold. We have also superimposed the F90 NR acceptance curves derived from SCENE, a conservative choice as DS has a higher LY and hence narrower F90 distributions. This plot proves that PSD at 200 V/cm can efficiently suppress the dominant ER background that we expect in 2.6 y of DS-50 UAr run, while maintaining high acceptance for WIMPs. We have then proceeded to define a WIMP search region as in Fig. 3. Assuming no candidate WIMP event, this allows us to project the sensitivity of DS-50 in the parameter plane of WIMP-nucleus cross-section vs WIMP mass, as it can be seen in Fig. 3 (right), and compare it to the existing Xenon100 and LUX rejection curves. Systematics on NR quenching factors and F90 curves contribute about 10% variation at 100 GeV WIMP mass.

We have also modelled F90 using the statistical distributions of the underlying processes with parameters taken from data. The model accounts for macroscopic effects related to argon micro-physics, detector properties, reconstruction and noise effects. We have simulated F90 distributions for a DS upgrade of 3.8 t fiducial mass and for 5 y of run, assuming the ER background will be dominated by ^{39}Ar at its present upper limit. Figure 4 shows the agreement of the simulated distribution for a sample energy bin to real DS-50 data, after normalization. Similar plots are obtained for all energy slices. Figure 5 (left) shows the simulated exposure in analogy to the DS-50 data plot of Fig. 3. In this case the energy threshold would be 120 pe although 100 pe could be considered too. The projected sensitivity is shown in Fig. 5 (right). An increase in sensitivity of two orders of magnitude is expected in comparison with DS-50.

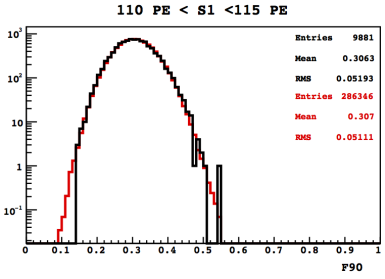

Figure 4: F90 distributions in the [110,115] pe sample energy bin. Simulation (red) compared to data (black) after normalization.

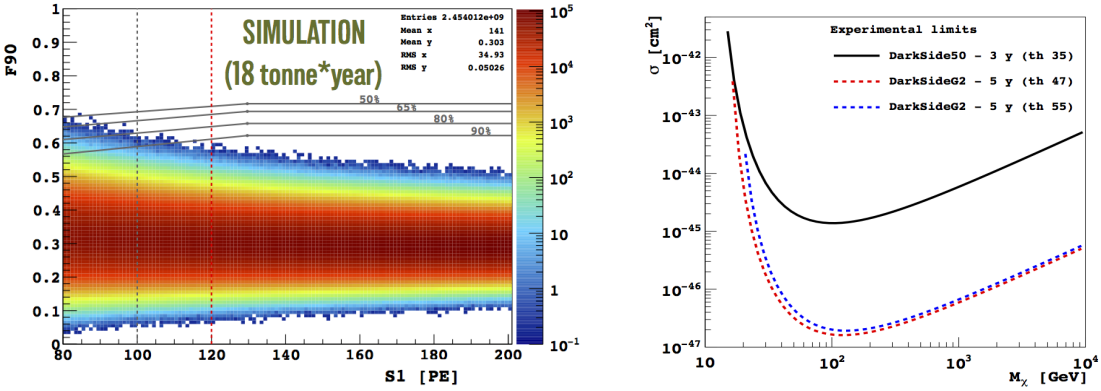

Figure 5: DS multi-ton upscale. Simulated exposure of 5 y, F90 vs S1 energy in PE units (left). Projected sensitivity with 120 pe (blue) and 100 pe (red) compared to DS-50 (right).

DS-50 has now acquired ∼5000 kg-day of AAr data. The analysis is ongoing [6] in order to improve your understanding of backgrounds and study the S2 signal. The latter would bring x-y position reconstruction, hence a full 3D volume fiducialization, and additional ER/NR discrimination from the S2/S1 ratio. We are also planning a detailed source calibration campaign in fall 2014. In January 2015 we foresee to switch to UAr and start the physics run.

References

[1] T. Alexander *et al.* [DarkSide Collaboration], JINST **8** (2013) C11021.
[2] T. Alexander *et al.* [DarkSide Collaboration], Astropart. Phys. **49** (2013) 44 [arXiv:1204.6218 [astro-ph.IM]].
[3] L. Pagani, D. D'Angelo and S. Davini, PoS EPS **-HEP2013** (2013) 062.
[4] A. Wright, P. Mosteiro, B. Loer and F. Calaprice, Nucl. Instrum. Meth. A **644** (2011) 18 [arXiv:1010.3609].
[5] H. Cao *et al.* [SCENE Collaboration], arXiv:1406.4825 [physics.ins-det].
[6] P. Agnes *et al.* [DarkSide Collaboration], arXiv:1410.0653 [astro-ph.CO].

Searching for Dark Matter with the LUX experiment

J. E. Y. Dobson[1] for LUX Collaboration

[1]School of Physics & Astronomy, University of Edinburgh, Edinburgh, UK, EH9 3JZ

DOI: http://dx.doi.org/10.3204/DESY-PROC-2014-04/95

The Large Underground Xenon (LUX) experiment completed its first physics run in 2013 and produced a world-leading limit for spin-independent scattering of Weakly Interacting Massive Particles using 85.3 live-days of data. After presenting these first results we discuss the detector development work and calibrations following the first physics run, the current status of LUX and plans for the future multi-ton LUX-ZEPLIN experiment.

1 Introduction

First postulated more than 80 years ago to address the missing mass of the Milky Way galaxy, dark matter remains one of the best motivations for physics beyond the Standard Model. The Λ-Cold Dark Matter standard model of Big Bang cosmology is now well established and presents a clear and consistent picture of a universe in which non-baryonic cold dark matter makes up around four fifths of the total matter content. The evidence in support of this is both abundant and varied and includes galactic rotation curves, precise measurements of the cosmic microwave background, weak lensing studies of galaxy clusters, primordial nucleosynthesis and the characteristics of large scale structure in the universe [1]. Despite considerable knowledge concerning the impact of dark matter on these astrophysical phenomena very little is known about its fundamental nature. Direct search experiments aim to change this by detecting individual interactions of particles of dark matter that are hypothesised to permeate our galaxy. Many experiments focus on the search for Weakly Interacting Massive Particles (WIMPs), the leading candidates for dark matter. They look for the low energy nuclear recoils expected when WIMPs scatter elastically off target nuclei in the experiment. The small interaction cross sections and low velocities expected for galactic WIMPs impose the challenging requirement that dark matter detectors need to be sensitive to ∼few keV recoiling nuclei and at the same time be capable of amassing exposures of many kg · years.

2 The LUX Experiment

The Large Underground Xenon (LUX) experiment [2] is a 370 kg dual-phase liquid xenon time projection chamber (TPC) located 4850 feet underground (4300 m w.e.) at the Sanford Underground Research Facility (SURF) in Lead, South Dakota. The active region of the TPC is 47 cm in diameter and 48 cm in height comprising 250 kg of xenon. Interactions in the liquid xenon produce both prompt scintillation light (S1) and ionisation electrons that drift in an applied

electric field (181 V/cm) to the liquid-gas interface at the top of the detector. The electrons are then extracted into the gas phase (6.0 kV/cm), where they produce electroluminescence (S2). The S1 and S2 signals are used to reconstruct the deposited energy and their ratio is used to discriminate WIMP-like nuclear recoils (NR) from background electron recoils (ER) at the 99.6% level at a 50% NR acceptance in the energy range of the LUX analysis. The TPC is read out from the top and bottom by two arrays of 61 photomultiplier tubes (PMTs) which image the central liquid xenon region and record the S1 and S2 signals. The x-y position of an interaction is determined to better than 4–6 mm from the localisation of the hit pattern of S2 light in the top PMT array. The depth of the interaction is given—to similar precision—based on the measured drift speed of the electrons (1.51 ± 0.01 mm/μs) and the time interval between the S1 and S2 light. This knowledge of the precise 3D position of an interaction means the full self-shielding capability of the liquid xenon can be utilised by only considering interactions in an inner radioactively-quiet fiducial volume.

An extensive screening campaign imposed stringent requirements on the levels of radioactivity for materials used to build the detector. Before being used in LUX, the full contingent of research grade xenon was purified at a dedicated research facility using a novel technique based on chromatographic separation. In addition to shielding against cosmic rays provided by the rock overburden, the LUX detector sits within a 6.1 m tall and 7.6 m in diameter water tank, instrumented with 20 8-inch PMTs, which acts as both an active veto for any penetrating cosmic rays and as a further shield to any remaining γ-rays and neutrons. Backgrounds from these particles are thereby rendered subdominant to those from radioactivity of internal detector components. A full description of LUX can be found in [2].

3 First results from LUX

LUX completed its first physics run in 2013, collecting a total of 85.3 live-days of WIMP search data between late April and early August. During this period the ER background rate inside the 118 kg fiducial volume was measured to be 3.6 ± 0.3 mDRU (mDRU= 10^{-3} counts/day/kg/keV) in the energy range of interest, to date the lowest achieved by any xenon TPC. Full details of the radiogenic and muon-induced backgrounds in LUX can be found in [3]. To reduce the scope for bias, a non-blind analysis was conducted in which only a minimal set of high-acceptance data quality cuts were used. Single scatter events containing exactly one S1 within the maximum drift time (324 μs) preceding a single S2 were selected for further analysis. The single scatter ER and NR acceptance was measured with dedicated tritium (β^-), AmBe, and ^{252}Cf (neutron) datasets. All the cuts and efficiencies combined to give an overall WIMP-detection efficiency of 17, 50 and $> 95\%$ at 3.0, 4.3 and 7.5 keV recoil energies respectively.

In total 160 events were observed in the energy range of interest for WIMPs, between 2–30 photoelectrons (phe) S1, with all observed events being consistent with the predicted background of electron recoils. The p-value for the background-only hypothesis was 0.35. Confidence intervals on the spin-independent WIMP-nucleon cross section were set using a profile likelihood ratio (PLR) test statistic which exploits the separation of signal and background distributions in radius, depth and S1 and S2. For the signal model we conservatively assumed no signal below 3 keV, the lowest energy for which direct light yield measurements in xenon existed. The 90% upper C.L. are shown in figure 1 (left) with a minimum of 7.6×10^{-46}cm^2 at a WIMP mass of 33 GeV/c^2, making LUX the first experiment to probe sub-zeptobarn WIMP-nucleon cross sections. We see in figure 1 (right) that the LUX limit fully excludes nearly all

the anomalous results at low WIMP masses claimed by a number of experiments. Full details of the analysis can be found in [4].

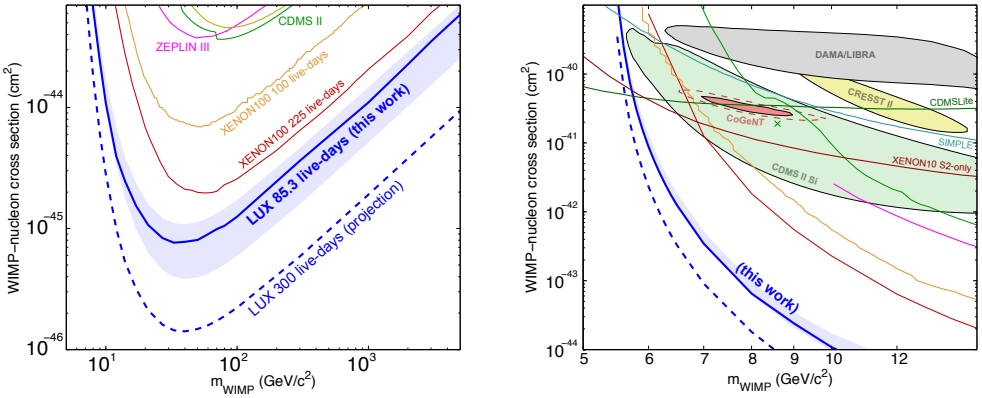

Figure 1: *Left:* The LUX 90% confidence limit on the spin-independent elastic WIMP-nucleon cross section for the 85.3 live-day exposure (blue) and projected limit for the upcoming 300-day run (dashed blue). *Right:* Close-up of low-mass region.

Following the first WIMP-search result LUX underwent a period of upgrades and maintenance in preparation for the final 300-day WIMP-search run. This included a campaign of cathode and grid wire conditioning aimed at increasing the applied drift and extraction fields and improvements to the krypton calibration system and the xenon controls and recovery system. Finally, a D-D neutron generator providing an almost monochromatic source of neutrons was used to make an in-situ calibration (down to 0.7 keV for the ionization channel) of the low-energy nuclear recoil response of LUX through an analysis of multiple-scatter events [5].

Final preparations for the 300-day run are now underway and it is expected to start before the end of 2014. The sensitivity for the 300-day run is expected to surpass that of the first WIMP-search result by a factor of around five and the sensitivity at low masses will benefit from the confirmation of the detector response to low-energy recoils.

4 LUX-ZEPLIN

Looking to the future, designs for the LUX-ZEPLIN (LZ) experiment are well underway. At the heart of LZ is a scaled up version of the LUX TPC with an active region containing about 7 tonnes (at least 5 tonnes fiducial). LZ will replace LUX on the 4850' level at SURF and will reuse the LUX water tank. Figure 2 shows the overall detector concept.

In addition to the considerable increase in target mass ($\sim$40 $\times$ LUX fiducial) LZ features a more sophisticated veto system which includes an optically separated and instrumented xenon *skin* layer between the inner TPC and the walls of the cryostat and an external liquid scintillator veto (gadolinium loaded linear alkyl benzene). The combination of skin readout and the outer detector creates a highly efficient integrated veto system providing powerful rejection of γ-rays and neutrons from internal sources (e.g. PMTs) that could otherwise scatter once in the TPC and then escape, thus potentially posing a problematic background.

With a projected sensitivity of 10^{-48}cm^2 for its full 1000-day exposure, LZ reaches faster and further than any competing experiment being proposed on a similar timescale, exploring

a significant fraction of the parameter space remaining above the irreducible background from coherent scattering of neutrinos from astrophysical sources [6]. Earlier this year LZ was selected by the US Department of Energy as one of three approved *Generation 2* dark matter experiments and plans to begin its construction phase in 2015 with a projected start of physics data taking in 2018.

5 Conclusions

With its first WIMP search data LUX set the world's most stringent limit for spin-independent WIMP-nucleon elastic scattering, becoming the first direct search experiment to probe the sub-zeptobarn regime. The LUX 300-day run is due to start soon and will further increase this sensitivity by a factor of five with discovery still possible. In the longer term the LUX-ZEPLIN experiment will improve on the LUX 300-day sensitivity by almost two orders of magnitude, enabling significantly deeper probing of parameter space for discovery if necessary, or giving the capability to characterise a dark matter signal if found.

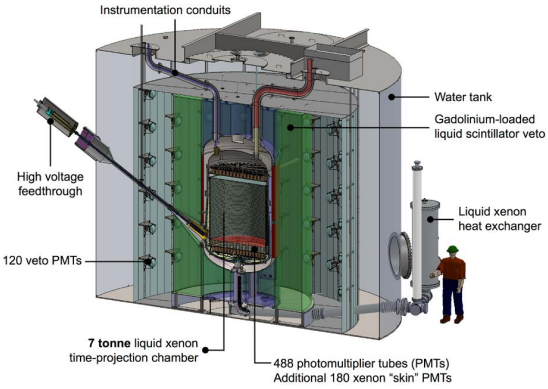

Figure 2: Schematic of the LZ experiment as housed in the reused LUX water-tank.

Acknowledgments

This work was partially supported by the U.S. Department of Energy (DOE) under award numbers DE-FG02-08ER41549, DE-FG02-91ER40688, DE-FG02-95ER40917, DE-FG02-91ER40674, DE-NA0000979, DE-FG02-11ER41738, DE-SC0006605, DE-AC02-05CH11231, DE-AC52-07NA27344, and DE-FG01-91ER40618; the U.S. National Science Foundation under award numbers PHYS-0750671, PHY-0801536, PHY-1004661, PHY-1102470, PHY-1003660, PHY-1312561, PHY-1347449; the Research Corporation grant RA0350; the Center for Ultra-low Background Experiments in the Dakotas (CUBED); and the South Dakota School of Mines and Technology (SDSMT). LIP-Coimbra acknowledges funding from Fundação para a Ciência e Tecnologia (FCT) through the project-grant CERN/FP/123610/2011. Imperial College and Brown University thank the UK Royal Society for travel funds under the International Exchange Scheme (IE120804). The UK groups acknowledge institutional support from Imperial College London, University College London and Edinburgh University, and from the Science & Technology Facilities Council for PhD studentship ST/K502042/1 (AB). The University of Edinburgh is a charitable body, registered in Scotland, with registration number SC005336.

References

[1] K.A. Olive et al. Review of Particle Physics. *Chin.Phys.*, C38:090001, 2014.

[2] D.S. Akerib et al. The Large Underground Xenon (LUX) Experiment. *Nucl.Instrum.Meth.*, A704:111–126, 2013.

[3] D.S. Akerib et al. Radiogenic and Muon-Induced Backgrounds in the LUX Dark Matter Detector. *Astropart.Phys.*, 62:33–46, 2014.

[4] D.S. Akerib et al. First results from the LUX dark matter experiment at the Sanford Underground Research Facility. *Phys.Rev.Lett.*, 112:091303, 2014.

[5] J. Verbus. Recent Results from the LUX Dark Matter Search, in: Lake Louise Winter Institute 2014.

[6] J. Billard, L. Strigari, and E. Figueroa-Feliciano. Implication of neutrino backgrounds on the reach of next generation dark matter direct detection experiments. *Phys.Rev.*, D89:023524, 2014.

The EDELWEISS-III Dark Matter Search: Status and Perspectives

Lukas Hehn[1] on behalf of the EDELWEISS Collaboration

[1]Karlsruhe Institute of Technology (KIT), Institut für Kernphysik

DOI: http://dx.doi.org/10.3204/DESY-PROC-2014-04/235

EDELWEISS is a direct Dark Matter search program looking for WIMPs in the GeV-TeV mass range. For that purpose, an array of cryogenic Ge mono-crystals read out simultaneously by NTD thermal sensors and by surface electrodes is installed in the Modane underground laboratory. We present a summary of EDELWEISS-II results including limits on axion couplings. For EDELWEISS-III a major upgrade of the setup was undertaken. 36 new FID800 Ge bolometers are currently installed, as well as a new DAQ system and improved shielding to lower the background.

1 The EDELWEISS experiment

1.1 Experimental setup at LSM

The EDELWEISS experiment is situated in the deepest underground laboratory in Europe, the *Laboratoire Souterrain de Modane* (LSM). A 4800 mwe rock overburden reduces the cosmic muon flux by a factor of $O(10^6)$ to only $5\,\mu/\mathrm{m}^2/\mathrm{day}$ [1]. In the LSM, the experiment is housed in a clean room with a deradonized air supply and a remaining activity from Rn-decay of a few tens of $\mathrm{mBq/m}^3$. The surrounding active muon veto system of 48 plastic scintillator modules and $100\,\mathrm{m}^2$ with a geometric coverage of $>98\,\%$ tags throughgoing muons. Next is a 50 cm thick polyethylene (PE) layer to moderate the neutron flux, followed by 20 cm lead for the suppression of γ-activity. Inside is a dilution copper cryostat which cools down several tens of kg of detectors to stable cryogenic temperatures of a few mK.

1.2 Cryogenic bolometer detectors

The detectors used in EDELWEISS are germanium mono-crystal bolometers (see Fig. 1 left). Particles can interact with the Ge atoms via elastic scattering on either the nucleus or the electron shell and thereby produce both $\mathrm{e}^-/\mathrm{h}^+$-pairs and phonons. By comparing the ionization yield Q, the fraction of created charge vs. heat energy, it is possible to discriminate *Electronic Recoils* (ER) from *Nuclear Recoils* (NR) on an event-by-event basis. *ER*s from β's and γ's have $Q = 1$ by definition while *NR*s from neutrons and expected from WIMPs produce significantly less charge with $Q \approx 0.3$. This allows to efficiently reject background radiation from possible WIMP candidate events. To read out the two signals, the cylindrical detectors are equipped with phonon sensors and electrodes on the surface. At an operating temperature of $T = 18\,\mathrm{mK}$ the

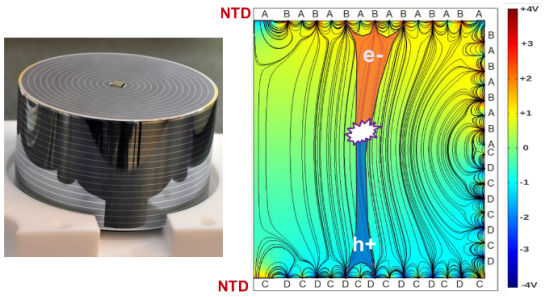

Figure 1: Left: FID800 detector with concentric ring electrodes and NTD phonon sensor. Width = 7 cm and height = 4 cm. Right: Axial symmetric electric field map with the charges of a fiducial event drifted to electrode sets B and D.

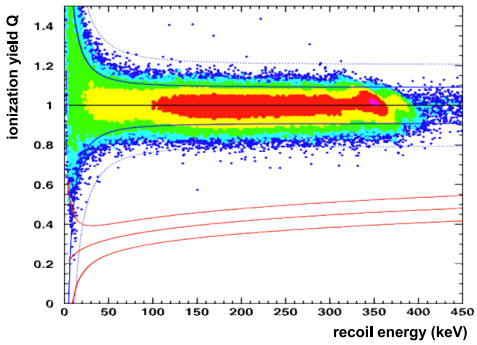

Figure 2: ^{133}Ba calibration data with electron recoils from $>400,000\,\gamma$'s. No event above 20 keV populates the 90 % C.L. nuclear recoil band.

Neutron Transmutation Doped (NTD) germanium transistors measure a minuscule temperature increase of $\approx 1\,\mu$K for a 10 keV recoil. Concentric rings of Al electrodes are connected such, that interleaved rings form two different sets on top and bottom [2]. These sets are biased with different voltages $O(1\,\text{V})$, drifting charges to top and bottom of the detector and along the surface (see Fig. 1 right). The set of *fiducial electrodes* (here B and D) has the higher potential difference and collects charges from the inner bulk volume of the crystal, while a signal on the *veto* electrodes (A,C) efficiently rejects events near the surface. Detectors used in EDELWEISS-II had masses of 400 g and a so called *InterDigit* (ID) design with ring electrodes only on top and bottom, while the outer sides had planar electrodes. The resulting electric field configuration led to an inner *fiducial mass* of 40 % or 160 g. For the 800 g crystals used in EDELWEISS-III a *Fully InterDigit* (FID) design with ring electrodes also on the sidewalls leads to a much higher fiducial mass of 75 % or 600 g, while at the same time improving the rejection of surface events due to better charge collection.

2 Results from the EDELWEISS-II phase

Phase II of the EDELWEISS experiment was running under stable low temperature conditions from April 2009 to May 2010, for a continuous data taking of more than 400 days. Installed were 10 ID-detectors with masses around 400 g each.

2.1 Standard WIMP analysis

The standard analysis [3], optimized for WIMPs of masses $O(100\,\text{GeV})$, used a total effective exposure of 384 kg.days after all cuts. In the 90 % C.L. nuclear recoil band [20, 200 keV] (the WIMP search region), 5 candidate events were observed, which was compatible with the expected background of 3.0 events. This result was interpreted in terms of a spin-independent WIMP-nucleon scattering cross section, leading to $\sigma_{\text{SI}} < 4.4 \times 10^{-8}$ pb (90 % C.L.) for a WIMP mass of 85 GeV. Constraints were also set on scenarios with inelastic scattering mechanisms.

Due to their similarities, the results of EDELWEISS-II and the CDMS experiment could be combined and the two collaborations published an exclusion limit of $\sigma_{\mathrm{SI}} < 3.3 \times 10^{-8}$ pb for a WIMP mass of 90 GeV, derived from a combined exposure of 614 kg.days [4].

2.2 Low mass WIMP analysis

A dedicated analysis was performed on a reduced data set to search for low mass WIMPs between 7 and 30 GeV [5]. The 4 ID detectors with the best resolutions were used and stronger quality cuts allowed to lower the analysis threshold to 5 $\mathrm{keV_{nr}}$, therefore making the experiment sensitive to low WIMP masses. With an upper recoil energy limit set to 20 keV, the results are independent from the standard WIMP analysis. For a reduced effective exposure of 113 kg.days a maximum of 3 candidate events (depending on the WIMP mass) were found, which was compatible with the expected background from neutrons and γ's of 2.9 events. At a WIMP mass of 10 GeV and with only one candidate event, the resulting limit derived with Poisson statistics is $\sigma_{\mathrm{SI}} < 1.0 \times 10^{-5}$ pb (90 % C.L.) which significantly constrains a possible CoGeNT signal and excludes signals reported by DAMA/LIBRA and CRESST.

2.3 Search for Axions and ALPs

Complimentary to WIMP search in nuclear recoil events, the search for axions in EDELWEISS-II was performed on data of electron recoils only [6]. Axions and *Axion Like Particles* (ALPs) could lead to such recoils after producing photons via the Primakoff effect (enhanced by Bragg diffraction in the mono-crystals) or electrons via the axio-electric effect. For these type of events the surface rejection with the ID design provided very low backgrounds down to 0.3 evts/kg/day/keV and energy thresholds down to 2.5 $\mathrm{keV_{ee}}$, in a data set with 484 kg.days exposure. For 3 different solar production mechanisms and the assumption of an axion Dark Matter halo limits could be set on axion-photon and axion-electron couplings to exclude mass ranges of $0.92\,\mathrm{eV} < m_{\mathrm{A}} < 80\,\mathrm{keV}$ for DFSZ axions and $5.78\,\mathrm{eV} < m_{\mathrm{A}} < 40\,\mathrm{keV}$ for KSVZ axions.

3 Improvements for EDELWEISS-III

The EDELWEISS-II sensitivity goal was reached in 2010 with the experiment eventually limited by backgrounds. To probe spin-independent cross sections down to $\sigma_{\mathrm{SI}} \approx 10^{-9}$ pb, EDELWEISS-III will employ a higher exposure at a significantly reduced background level.The 36 FID 800-g detectors currently installed in the cryostat do not only increase the fiducial mass from 1.6 kg in EDELWEISS-II to > 20 kg, but also have reduced background due to their improved design. The rejection of γ's was shown to be 5$\times$ better than for ID400 detectors. This was measured with calibration data from a ^{133}Ba γ-source (see Fig. 2). Out of $> 4 \times 10^5\,\gamma's$ no event leakage into the 90 % C.L. nuclear recoil band above 20 keV was observed, giving a rejection factor of $< 6 \times 10^{-6}$ NRs/γ. Rejection of surface events was also improved: With a ^{210}Pb source implanted in its copper casing, a detector was exposed to 10^5 α's, β's and γ's of the Pb decay chain. Only one event in the 90 % C.L. NR-band above 15 keV was observed after the fiducial volume cut, giving a rejection of 4×10^{-5} misidentified evts/kg.day. Both improvements are attributed to the better charge collection due to the additional electrode rings, which decreases the misreconstruction of double scatter events.

Enhancements were also made to the experimental setup. Within the cryostat additional PE at the 1 K stage has been added between detectors and cold electronics, while new PE pieces outside the shield against the warm electronics. Coaxial cabling in the cryostat has been replaced with more radiopure Kapton cabling. New thermal screens for the cryostat itself are now made from NOSV copper with higher radiopurity. The combined neutron suppression compared to EDELWEISS-II improved by a factor of 100. In order to reduce microphonic noise, the pulse tubes close to the cryostat have been replaced by GM thermal machines outside the complete shielding, which are connected by a cryoline. To avoid Johnson noise, resistors in the electronics have been removed and the active feedback system was replaced by a relay system. Altogether these changes lead to improvements of $\approx 30\,\%$ in resolutions, lowering the average FWHM baselines of the ionization channels from 900 eV to 600 eV and from 1.2 keV to 1.0 keV for the heat channel. Multiple R&D efforts are currently ongoing to improve the sensitivity of the experiment: Replacing the JFET based amplifiers with a HEMT readout could improve the resolution on the ionization channel down to 300 eV, with a significant benefit for low mass WIMP search. The recent installation of an integrated DAQ system is accompanied by tests with an event triggered 40 MHz readout of the ionization channel, which gives additional spatial information on the z-axis of the detector. The channel upscaling due to the new DAQ system is a crucial requirement for the next phase after EDELWEISS-III, the proposed cryogenic 1-ton scale multi-target experiment EURECA [7].
With the 36 FID800 detectors installed, EDELWEISS-III is currently on the way to take a first data set of 3000 kg.days exposure, expected to be background free. The final goal is then an exposure of 12 000 kg.days which should reach a sensitivity of $\sigma_{\mathrm{SI}} \approx 10^{-9}$ pb with background limitation setting in.

Acknowledgments

The help of the technical staff of the Laboratoire Souterrain de Modane and the participant laboratories is gratefully acknowledged. The EDELWEISS project is supported in part by the Helmholtz Association, by the French Agence Nationale pour la Recherche, by Science and Technology Facilities Council (UK) and the Russian Foundation for Basic Research (grant No. 07-02-00355-a). R&D activities towards EURECA are supported in part by the German ministry of science and education (BMBF Verbundforschung ATP Proj.-Nr. 05A11VK2) and by the Helmholtz Alliance for Astroparticle Phyics (HAP), funded by the Initiative and Networking Fund of the Helmholtz Association,

References

[1] B. Schmidt *et al.* Astrop. Phys. 44, 28 (2013).

[2] A. Broniatowski *et al.* Phys. Lett. **B681** 305 (2009)

[3] E. Armengaud *et al.* Phys. Lett. **B702** 329 (2011).

[4] Z. Ahmed *et al.* Phys. Rev. **D84** 011102(R) (2011).

[5] E. Armengaud *et al.* Phys. Rev. **D86** 051701(R) (2012).

[6] E. Armengaud *et al.* JCAP 11, 67 (2013).

[7] G. Angloher *et al.* Physics of the Dark Universe 3, 41 (2014)

Searching a Dark Photon with HADES

Romain Holzmann[1], *Malgorzata Gumberidze*[2] for the HADES collaboration

[1]GSI Helmholtzzentrum für Schwerionenforschung, 64291 Darmstadt, Germany
[2]Technical University Darmstadt, 64289 Darmstadt, Germany

DOI: http://dx.doi.org/10.3204/DESY-PROC-2014-04/9

The existence of a photon-like massive particle, the γ' or dark photon, is postulated in several extensions of the Standard Model. Such a particle could indeed help to explain the puzzling behavior of the observed cosmic-ray positron fraction as well as to solve the so far unexplained deviation between the measured and calculated values of the muon $g-2$ anomaly. The dark photon, unlike its conventional counterpart, would have mass and would be detectable via its mixing with the latter. We present a search for the e^+e^- decay of such a hypothetical dark photon, also named U boson, in inclusive dielectron spectra measured with HADES in the p (3.5 GeV) + p, Nb reactions, as well as in the Ar (1.756 GeV/u) + KCl reaction. A new upper limit on the kinetic mixing parameter squared (ϵ^2) at 90% CL has been obtained in the mass range $M_U = 0.02 - 0.55$ GeV and is compared here with the present world data set. For masses 0.03 – 0.1 GeV, the limit has been lowered with respect to previous results, allowing to exclude a large part of the parameter space favored by the muon $g-2$ anomaly.

1 Introduction

Observations of the cosmic-ray electron and/or positron flux by ATIC [1], PAMELA [2], HESS [3], Fermi [4], and recently the AMS02 collaboration [5] have revealed an unexpected excess at momenta above 10 GeV, in particular in the positron fraction $e^+/(e^- + e^+)$. These observations cannot easily be reconciled in a consistent way with known astrophysical sources [6] and alternative theoretical explanations have therefore been put forward. In particular, scenarios in which the excess radiation stems from the annihilation of weakly interacting dark matter particles [6, 7] might offer an enticing solution to the puzzle.

To accommodate DM in elementary particle theory and to allow it to interact with visible matter, it has been proposed to supplement the Standard Model (SM) with an additional sector characterized by another $U(1)'$ gauge symmetry [8, 9, 10]. The corresponding vector gauge boson — called U boson, A', γ', or simply dark photon — would thereby mediate the annihilation of DM particles into charged lepton pairs. Indeed, from theoretical arguments a kinetic mixing of the $U(1)'$ and $U(1)$ symmetry groups would follow [11], providing a natural connection between the dark and SM sectors. For that purpose, a mixing parameter ϵ has been introduced [8] relating the respective coupling strengths α‘ and α of the dark and SM photons to visible matter via $\epsilon^2 = \alpha'/\alpha$. Through the $U(1) - U(1)'$ mixing term the U boson would be involved in all processes which include real or virtual photons [12]. On the other hand, any search for a U boson will have to deal with the large unavoidable background from standard QED radiative processes [13], namely any electromagnetic decay leading to lepton pairs. In

recent years, a number of such searches have been conducted in various experiments done in the few-GeV beam energy regime, looking either at e^+e^- pair distributions produced in electron scattering [14, 15] or in the electromagnetic decays of the neutral pion [16] and the ϕ meson [17]. Analyzing data obtained from high-flux neutrino production experiments at CERN [18] and at Serpukhov [19], regions in parameter space ϵ^2 vs. M_U corresponding to a long-lived U have been excluded as well. Note finally, that from the very precisely measured value of the anomalous gyromagnetic factors $(g-2)$ of the muon and electron [20], additional constraints are put on the allowed range of the mixing parameter ϵ and the mass M_U [21, 22].

2 The HADES experiment

The High-Acceptance DiElectron Spectrometer (HADES) operates at the GSI Helmholtzzentrum für Schwerionenforschung in Darmstadt where it uses the few-GeV beams from the heavy-ion synchrotron SIS18. A detailed description of HADES can be found in [23]. In the experiments discussed here a proton beam with a kinetic energy of $E_p = 3.5$ GeV and an average intensity of about 2×10^6 particles per second was used to bombard either a solid 12-fold segmented niobium target (with 2.8% nuclear interaction probability) [24] or a liquid hydrogen target (1% interaction probability) [25]. Likewise, a 1.76 GeV/u Ar beam was used to bombard KCl targets [26]. In the data analysis, electrons and positrons were identified by applying selection cuts to the RICH patterns, pre-shower and energy-loss signals. Charged particles were tracked through the HADES magnetic field and indentified leptons were combined two-by-two to reconstruct the 4-momentum of e^+e^- pairs. A detailed description of this analysis is given in [23, 26].

3 The U-boson search

The search for the U boson can be performed with HADES using all electromagnetic decays typically populated in few-GeV hadronic interactions, that is mostly $\pi^0 \to \gamma U$, $\eta \to \gamma U$, and $\Delta \to NU$, followed by $U \to e^+e^-$. In contrast to previous experiments focusing on a specific decay channel, our search was based on the inclusive measurement of all e^+e^- pairs produced in a given mass range. Because of the expected long lifetime of the U boson, the width of an observable signal is solely determined by the detector resolution.

The present analysis is based on the raw dilepton mass spectra, i.e. spectra not corrected for efficiency and acceptance. The low invariant-mass region of the spectra ($M_{ee} < 0.13\ GeV/c^2$) is dominated by π^0 Dalitz decays, at intermediate masses ($0.13\ GeV/c^2 < M_{ee} < 0.55\ GeV/c^2$), η and Δ Dalitz decays prevail, and the high-mass region is populated mostly by low-energy tails of vector-meson decays [24, 25]. However, as the electromagnetic decay branching ratios decrease with increasing particle mass, resulting in low sensitivity, we restrict our search to $M_U < 0.6\ GeV/c^2$.

Our search for a narrow resonant state in the e^+e^- mass distributions has been conducted in the following way: The dN/dM_{ee} spectra, measured in either of the analyzed reactions, was fitted piece-wise with a model function consisting of a 5^{th}-order polynomial and a Gauss peak of fixed position M_{ee} and fixed width. The adjustment was done by sliding a fit window of width $\pm 4\sigma(M)$ over the spectrum in steps of 3 MeV/c^2. In each step, the fit delivered a parameterization of the local background in presence of a possible Gaussian signal of given width $\sigma(M)$. Consequently, a statistical likelihood-based test must be performed to determine

at a given Confidence Level (CL) an upper limit (UL) for a possible U-boson signal [27]. In our case, background and e^+e^- efficiency corrections are needed to extract an absolute signal yield, and as both are known with limited accuracy only, we have used the method proposed by Rolke, Lopez and Conrad [28] to compute the UL at a confidence level CL=90%. A pair efficiency and acceptance correction factor, $eff \times acc$, has been obtained from detailed simulations and, after having corrected the UL for this factor, the procedure detailed in [29] was used to compute a corresponding upper limit $UL(\epsilon^2)$ on the relative coupling strength ϵ^2 of a hypothetical dark vector boson. Finally, in Fig. 1 we show the HADES result together with a compilation of limits from the searches conducted by KLOE-2 [17], APEX [15], WASA at COSY [16], A1 at MAMI [14], and BaBar [30].

At low masses ($M_U < 0.1\ GeV/c^2$) we clearly improve on the recent result obtained by WASA [16], excluding now to a large degree the parameter range allowed by the muon $g-2$ anomaly. At higher masses, the sensitivity of our search is compatible with, albeit somewhat lower than the combined KLOE-2 analysis of ϕ decays. Our data probe, however, the U-boson coupling in η decays and add hence complementary information. At masses above the η mass, the inclusive dilepton pectrum is fed by Δ (and to some extent heavier baryon resonance) decays which offer only small sensitivity, partly due to the small electromagnetic branching ratio ($BR_{N\gamma} \simeq 10^{-3} - 10^{-2}$) and partly due to the decreasing $BR_{U\to ee}$ at high M_U. Recently, the UL in the high-mass region has been largely improved by an analysis of data obtained by the BaBar experiment, namely $e^+e^- \to e^+e^-$ and $e^+e^- \to \mu^+\mu^-$ [31] (not shown in Fig. 1). On the other hand, at low masses, we expect to lower substantially the UL by including recent HADES data from the 1.23 GeV/u Au+Au reaction in our search.

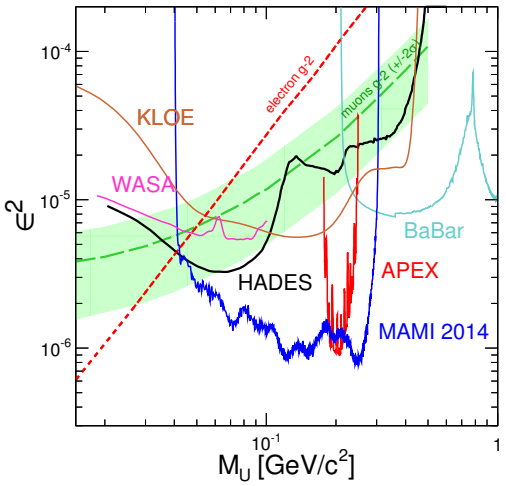

Figure 1: The 90% Cl upper limit on ϵ^2 versus the U-boson mass obtained from the combined analyses of the HADES data (solid black line) in comparison with existing limits from the MAMI/A1, APEX, BaBar, WASA, and KLOE-2 experiments (various colored lines). In addition, the constraints from the muon g-2 anomaly are indicated (green shaded band).

Acknowledgement

The HADES Collaboration gratefully acknowledges support by BMBF grants 06DR9059D, 05P12CRGHE, 06FY171, 06MT238 T5, and 06MT9156 TP5, by HGF VH-NG-330, by DFG

EClust 153, by GSI TMKRUE, by the Hessian LOEWE initiative through HIC for FAIR (Germany), by EMMI GSI, TU Darmstadt (Germany): VH-NG-823, Helmholtz Alliance HA216/ EMMI, by grant GA CR 13-067595 (Czech Rep.), by grant NN202198639 (Poland), Grant UCY/3411-23100 (Cyprus),by CNRS/IN2P3 (France), by INFN (Italy), and by EU contracts RII3-CT-2005-515876 and HP2 227431.

References

[1] J. Chang *et al.*, Nature **456**, 362 (2008).
[2] O. Adriani *et al.*, Nature **458**, 607 (2009).
[3] F. Aharonian *et al.*, Astron. Astrophys. **508**, 561 (2009).
[4] A. Abdo *et al.*, Phys. Rev. Lett. **102**, 181101 (2009).
[5] L. Accardo *et al.* (AMS Collaboration), Phys. Rev. Lett. **113**, 121101 (2014).
[6] I. Cholis, L. Goodenough, N. Weiner, Phys. Rev. D **79**, 123505 (2009).
[7] I. Cholis *et al.*, Phys. Rev. D **80**, 1123518 (2009).
[8] P. Fayet, Phys. Lett. B **95**, 285 (1980).
[9] C. Boehm, P. Fayet, Nucl. Phys. B **683**, 219 (2004).
[10] M. Pospelov, A. Ritz, M. B. Voloshin, Phys. Lett. B **662**, 53 (2008).
[11] B. Holdom, Phys. Lett. B **166**, 196 (1986).
[12] M. Reece, L.-T. Wang, JHEP **0907**, 051 (2009).
[13] L. Landsberg, Phys. Rept. **128**, 301 (1985).
[14] H. Merkel *et al.* (A1 Collaboration), Phys. Rev. Lett. **112**, 221802 (2014).
[15] S. Abrahamyan *et al.* (APEX Collaboration), Phys. Rev. Lett. **107**, 191804 (2011).
[16] P. Adlarson *et al.* (WASA-at-COSY Collaboration), Phys. Lett. B **726**, 187 (2013).
[17] D. Babuski *et al.* (KLOE-2 Collaboration), Phys. Lett. B **720**, 111 (2013).
[18] S. Gninenko, Phys. Rev. D **85**, 055027 (2012).
[19] J. Blümlein, J. Brunner, Phys. Lett. B **731**, 320 (2014).
[20] G.W. Bennett *et al.* (Muon (g-2) Collaboration), Phys. Rev. D **73**, 072003 (2006).
[21] M. Pospelov, Phys. Rev. D **80**, 095002 (2009).
[22] M. Endo, K. Hamaguchi, G. Mishima, Phys. Rev. D **86**, 095029 (2012).
[23] G. Agakishiev *et al.* (HADES Collaboration), Eur. Phys. J. A **41**, 243 (2009).
[24] G. Agakishiev *et al.* (HADES Collaboration), Phys. Lett. B **715**, 304 (2012).
[25] G. Agakishiev *et al.* (HADES Collaboration), Eur. Phys. J. A **48**, 64 (2012).
[26] G. Agakishiev *et al.* (HADES Collaboration), Phys. Rev. C **84**, 014902 (2011).
[27] G. Cowan, K. Cranmer, E. Gross, O. Vitells, Eur. Phys. J. C **71**, 1554 (2011).
[28] W.A. Rolke, A.M. Lopez, J. Conrad, Nucl. Inst. Meth. Phys. Res. A **551**, 493 (2005).
[29] G. Agakishiev *et al.* (HADES Collaboration), Phys. Lett. B **731**, 265 (2014).
[30] B. Aubert *et al.* (BaBar Collaboration), arXiv:0902.2176.
[31] J. P. Lees *et al.* (BaBar Collaboration), arXiv:1406.2980

Chapter 7

Nuclear and particle astrophysics

Magnetic horizons of ultra-high energy cosmic rays

Rafael Alves Batista, Günter Sigl

II. Institute for Theoretical Physics, University of Hamburg
Luruper Chaussee, 149, 22761 Hamburg, Germany

DOI: http://dx.doi.org/10.3204/DESY-PROC-2014-04/127

The propagation of ultra-high energy cosmic rays in extragalactic magnetic fields can be diffusive, depending on the strength and properties of the fields. In some cases the propagation time of the particles can be comparable to the age of the universe, causing a suppression in the flux measured on Earth. In this work we use magnetic field distributions from cosmological simulations to assess the existence of a magnetic horizon at energies around 10^{18} eV.

1 Introduction

During their propagation ultra-high energy cosmic rays (UHECRs) can be deflected by the intervening cosmic magnetic fields, namely the extragalactic and galactic. The extragalactic magnetic field has different strengths in different regions of the universe. For instance, in the center of clusters of galaxies it is $\sim$10 μG, with coherence length of the order of 10 kpc. The existence of magnetic fields in the voids is still controversial [1], but there are some indications that they can be $\sim 10^{-15}$-10^{-12} G, with typical coherence lengths of the order of 1 Mpc [1].

The propagation of cosmic rays in the extragalactic magnetic fields can be diffusive if the scattering length is much smaller than the distance from the source to the observer. Depending on the magnetic field strength and diffusion length, a significant fraction of these particles can have trajectory lengths comparable to the Hubble radius. In this case, a suppression in the flux of cosmic rays is expected compared to the case in which magnetic fields are absent, leading to the existence of a magnetic horizon for the propagation of cosmic rays. This effect has been previously studied by many authors, including Mollerach & Roulet [2], who developed a parametrization for it, under the assumption of Kolmogorov turbulence. In this work we generalize their result for the case of inhomogeneous extragalactic magnetic fields.

2 Magnetic suppression

The diffusive cosmic ray spectrum for an expanding universe can be written as [3]

$$j(E) = \frac{c}{4\pi} \int_0^{z_{max}} dz \left|\frac{dt}{dz}\right| Q(E_g(E,z),z) \frac{dE_g}{dE} \left(\int_0^{\infty} dB \frac{1}{N_s} \sum_{i=0}^{N_s} \frac{\exp\left(-\frac{r_g^2}{\lambda^2}\right)}{(4\pi\lambda^2)^{3/2}} p(B) \right), \quad (1)$$

where $p(B)$ is the probability distribution of the magnetic field strength B, r_g is the comoving distance of the source and λ is the so-called Syrovatskii variable, given by:

$$\lambda^2(E,z,B) = \int_0^z dz' \left|\frac{dt}{dz'}\right| \frac{1}{a^2(z')} \left[\frac{c l_c(z)}{3} \left(a_L \left(\frac{E}{E_c(z,B)} \right)^{\frac{1}{3}} + a_H \left(\frac{E}{E_c(z,B)} \right)^2 \right) \right], \quad (2)$$

with $a = 1/1+z$ being the scale factor of the universe and $l_c(z) = l_{c,0}a(z)$ the coherence length of the field at redshift z. The parameters a_L and a_H are, respectively, 0.3 and 4. E_c is the critical energy, defined as the energy for which a particle has a Larmor radius equal to the coherence length of the magnetic field. The probability distribution functions can be obtained from magnetohydrodynamical (MHD) simulations of the local universe. In this work we considered four different cosmological simulations, namely the ones performed by Miniati [4], Dolag *et al.* [5], Das *et al.* [6], Donnert *et al.* [7].

If the term in parentheses in equation 1 is equal to 1, then the magnetic field dependence will vanish and the shape of the spectrum will be independent of the modes of propagation. This result is known as the propagation theorem [8], and states that if the separation between the sources in a uniform distribution is much smaller than the characteristic propagation lengths, the UHECR spectrum will have a universal shape. This spectrum (j_0) will be henceforth called universal.

We have not considered the actual time evolution of these cosmological simulations. Instead we assume a magnetic field distribution at $z = 0$ and extrapolate it to higher redshifts: $B = B_0(1+z)^{2-m}$, with m designating the evolution parameter. Moreover, we assume a Kolmogorov magnetic field with strengths taken from the simulations.

The suppression factor G can be written as:

$$G = \frac{j(E)}{j_0(E)} \approx \exp\left[-\frac{(aX_s)^\alpha}{x^\alpha + bx^\beta} \right], \quad (3)$$

with $x \equiv E/\langle E_c \rangle$, α, β, a and b the best fit parameters obtained by fitting $j(E)/j_0(E)$ with the function in the right-hand side of the equation. The complete list of best fit parameters for these extragalactic magnetic field models can be found in ref. [9]. In this expression $X_s = d_s/\sqrt{R_H l_c}$, where d_s is the source separation and R_H the Hubble radius.

3 Magnetic horizons

In this work the magnetic horizon is defined as the mean distance that a cosmic ray can propagate away from the source in a Hubble time. In figure 1 $\lambda/\sqrt{R_H l_c}$ is displayed as a function of the redshift. In this case λ can be understood as the average distance a particle can

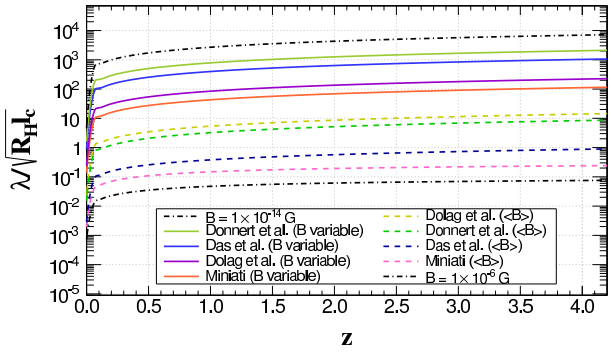

Figure 1: Volume-averaged Syrovatskii variable for an E/Z =10^{16} eV, m =1, γ =2 and z_{max} =4. Solid lines correspond to the extragalactic magnetic field distribution, dashed lines correspond to the values obtained using the mean magnetic field strengths obtained from these models, and dotted dashed lines are two limiting cases with high and low magnetic field strengths.

propagate away from the source in a time interval corresponding to a redshift z. In this figure we notice that the magnetic horizons for the case of extragalactic magnetic field distributions from cosmological simulations are larger compared to the case of a Kolmogorov turbulent field with B_{rms} equal to the mean magnetic field strength from the distributions. This happens due to the fact that the voids fill most of the volume, dominating the magnetic field distribution and hence the volume-averaged Syrovatskii variable.

We can calculate the energy (E_e) for which the suppression factor is $G = 1/e \approx 0.37$ of its original value, as a function of the coherence length. The results are shown in figure 2.

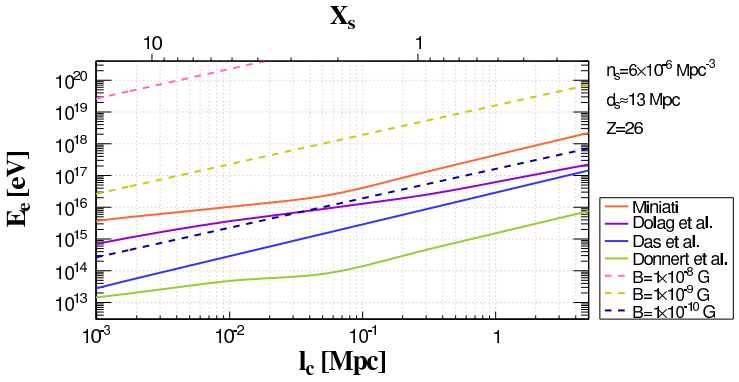

Figure 2: Upper limit on the energy for which the flux of cosmic rays is suppressed to $1/e$ (≈37%) of its former value, as a function of the coherence length. Solid lines correspond to the indicated extragalactic magnetic field model, and dashed lines to constant magnetic field strengths. This particular case is for a source density of 6×10^{-6} Mpc^{-3} and Z=26.

The magnetic suppression due to magnetic horizon effects starts to become relevant for $E \lesssim 10^{17}$ eV, for the most optimistic choice of parameters (heavy composition, large coherence

length and low source density). The curves in figure 2 reflect the behavior of the diffusion coefficient, shown in equation 2 within square brackets, which is proportional to l_c^{-1} for small values of the coherence length, and to $l_c^{2/3}$ for large l_c.

4 Discussion and outlook

We have parametrized the suppression of the cosmic ray flux at energies $\lesssim$Z$\times 10^{18}$ eV. The method to obtain this parametrization can be adapted to any magnetic field distribution from cosmological simulations (for details see ref. [9]). Moreover, we have also derived upper limits for this suppression to occur, as a function of the coherence length.

The results here described suggest that the suppression sets in at energies below $\sim 10^{17}$ eV. This has profound implications for the interpretation of current experimental data. For instance, recently there has been several attempts [10, 11] to perform a combined spectrum-composition fit to data from the Pierre Auger Observatory [12, 13]. These results indicate that the spectral indexes of the sources are hard ($\gamma \sim$1.0-1.6), which contradicts the current acceleration paradigm, in which UHECRs are accelerated to the highest energies through Fermi-like mechanisms ($\gamma \sim$2.0-2.2). In ref. [2] it was shown that the existence of a magnetic horizon around 10^{18} eV can affect the results of these combined fits, softening the spectral index to $\gamma \sim 2$. We have shown that if one considers a more realistic extragalactic magnetic field model, the contribution of the voids is dominant and since the field strengths in these regions are low, the suppression will also be small compared to the case of a simple Kolmogorov turbulent magnetic field. In this case, the combined spectrum-composition fits would again favor scenarios in which the sources have hard spectral index.

Acknowledgements

RAB acknowledges the support from the Forschungs- und Wissenschaftsstiftung Hamburg. GS was supported by the State of Hamburg, through the Collaborative Research program "Connecting Particles with the Cosmos" and by BMBF under grant 05A11GU1.

References

[1] A. Neronov and I. Vovk, Science **328** 73 (2010)
[2] S. Mollerach and E. Roulet, JCAP **10** 13 (2013)
[3] V. Berezinsky and A. Z. Gazizov, Astrophys. J. **643** 8 (2013)
[4] F. Miniati, MNRAS **337** 199 (2002)
[5] K. Dolag *et al.*, JCAP **1** 9 (2005)
[6] S. Das *et al.*, Astrophys. J. **682** 29 (2008)
[7] J. Donnert *et al.*, MNRAS **392** 1008 (2009)
[8] R. Aloisio and V. Berezinsky, Astrophys. J. **612** 900 (2004)
[9] R. Alves Batista and G. Sigl, JCAP **11** 031 (2014)
[10] R. Aloisio, V. Berezinsky and P. Blasi. JCAP **10** 020 (2014)
[11] A. Taylor, Astropart. Phys. **54** 48 (2014)
[12] Pierre Auger Collaboration, Phys. Lett. B **685** 239 (2010)
[13] Pierre Auger Collaboration. arXiv:1409.5083 (*to appear in Phys. Rev. D*)

Core-collapse supernova simulation using Λ hyperon EoS with density-dependent couplings

Sarmistha Banik[1], *Prasanta Char*[2]

[1]BITS Pilani, Hyderabad Campus, Shamirpet Mondal, Hyderabad-500078, India
[2]Astroparticle Physics & Cosmology Division,Saha Institute of Nuclear Physics, 1/AF Bidhan nagar, Kolkata-700064, India.

DOI: http://dx.doi.org/10.3204/DEFY-KROC-2014-04/115

Recently we generated an equation of state (EoS) table of dense matter relevant to neutron star and supernova with Λ hyperons. We use this EoS to investigate the role of strange hyperons in the dynamical collapse of a non-rotating massive star to a black hole(BH) using 1D General relativistic simulation $GR1D$. We follow the dynamical formation and collapse of the protoneutron star (PNS) from the gravitational collapse of a massive progenitor, adopting this EoS table.

1 Introduction

Neutron stars are born in the aftermath of massive stars ($> 8M_{\odot}$) through the core-collapse supernova (CCSN) explosions in the penultimate stage of their evolution. The fate of the compact object depends on the EoS and the amount of infalling material. In addition to the nucleons and nuclear matter, several novel phases with large strangeness fraction such as, hyperon matter, and quark phase, and Bose-Einstein condensates of antikaons are theoretically predicted in the early post-bounce phase of a core-collapse supernova. There are several exotic EoS, including quark and hyperons, for supernova simulations. However, none of them are within the observational constraints of $2M_{\odot}$ neutron stars [1, 2].

The Banik, Hempel and Bandyopadhyay (BHB) EoS is the first realistic EoS table involving hyperons [3] that is compatible with the recent observations. It is based on the density-dependent relativistic mean field model (DD2). The model is exploited to describe the uniform and non-uniform matter in a consistent manner. Further, light and heavy nuclei along with interacting nucleons are treated in the nuclear statistical equilibrium (NSE) model of Hempel and Schaffner-Bielich (HS) which includes excluded volume effects and DD relativistic interactions [4]. We considered only Λ hyperons and exclude other hyperons such as Σ and Ξ, due to scarcity of experimental data about their potential depth values in nuclear matter.

The presence of exotic particles may have considerable effect on the core collapse supernova explosions. It was earlier reported that hyperons appear just after the core bounce. And they trigger the BH formation, but fail to generate the second shock because the EoS is softened too much with their appearance [5]. These studies were carried out with the hyperonic EoS of Shen et. al. [6], which do not conform to the the observational mass limit of neutron star.

In this paper, we follow the dynamical formation and evolution of a PNS beginning from the onset of core collapse adopting our BHB EoS table[3]. We report the effect of hyperons on the

black hole formation using the spherically-symmetric general relativistic hydrodynamic code, $GR1D$[7]. We use both the variants of BHB hyperonic EoS tables. In one case the repulsive hyperon-hyperon interaction is mediated by the strange ϕ mesons [BHB$\Lambda\phi$] and in the second case ϕ mesons are not considered [BHBΛ]. We also compare these results with nucleon-only EoS, that we denote by HS(DD2).

2 The equation of state and the numerical simulations

The BHB EoS table is based on a density dependent (DD2) relativistic hadron field theory [8, 9], where baryon-baryon interaction is mediated by σ, ω, ρ mesons. The additional ϕ mesons take care of the hyperon-hyperon couplings. The density-dependence of the couplings gives rise to a rearrangement term in baryon chemical potential that on the other hand, changes the pressure. Thus the EoS is significantly changed at higher densities. Nuclear symmetry energy is another important parameter that controls the stiffness of the EoS. The symmetry energy and its density dependence near the saturation density n_0 are denoted by $S_\nu = E_{sym}(n_0)$ and slope parameter $L = 3n_0 dE_{sym}/dn|_{n=n_0,T=0}$. The DD2 model, with $S_\nu = 31.67$ MeV and $L = 55.04$ MeV, are fully consistent with the experimental and observational constraints [8]. The BHB$\Lambda(\phi)$ EoS table covers a broad range of density ($\sim 10^{3.22} - 10^{15.22(15.3)}$ g/cm^3), temperature($T =$ 0.01 to 158.48 MeV) and charge-to-baryon number ratio ($Y_p = 0$ to 0.60) [3].

The matter consists of nuclei, (anti)neutrons , (anti)protons, (anti) Λ hyperons, and photons at different regions. Electrons and positrons form a uniform background; contribution of neutrinos and muons are not taken into account in the calculations. In the DD2 parameter set, the nuclear matter saturation density is 0.149065fm^{-3}, binding energy 16.02MeV, incompressibility of matter 242.7MeV and symmetry energy 31.67MeV. The effective Dirac mass (m*/m) of neutron and proton are 0.5628 and 0.5622 respectively. For the Λ, the experimental mass value is 1115.7MeV, and the potential depth in nuclear matter is -30MeV.

We use the open source code $GR1D$ [7] for the supernova simulations. $GR1D$ is a spherically-symmetric, general-relativistic Eulerian hydrodynamics code for low and intermediate mass progenitors. It is designed to follow the evolution of stars beginning from the onset of core collapse to black hole formation for different zero age main sequence(ZAMS) progenitors.

3 Result & Discussions

We report our simulation results for a $40M_\odot$ progenitor model of Woosley et. al [10] using GR1D [7] for BHB EoS. We solved the Tolman-Oppenheimer-Volkov equation for zero temperature (T=0) β-equilibrated matter. The maximum mass of the neutron star for nucleon-only HS(DD2) EoS is $2.42M_\odot$, whereas for BHB$\Lambda(\phi)$ EoS, the maximum mass reduces to $1.95(2.1)M_\odot$. The corresponding radii are 11.9 km and 11.7(11.6) km respectively [9, 3].

Fig. 1 shows the plot of the baryonic and gravitational mass of PNS, obtained from simulations. The maximum mass is higher than that of NS. When accretion pushes PNS over its maximum mass, a BH is formed. The spike in the gravitational mass correspond to a blow-up and the BH formation. For the HS(DD2) EoS(solid line), this happens for a $2.47M_\odot$ star at 0.94 sec after bounce, whereas for BHB$\Lambda(\phi)$ EoS (the dashed line, colour online) this happens much earlier at 0.55 sec after bounce for a $2.25M_\odot$ star.

Figs. 2 and 3 show the evolution of central density (ρ_c) and temperature (T) for the nucleon-only HS(DD2) (solid lines) and BHB$\Lambda(\phi)$ EoS (dashed lines) respectively. The bounce

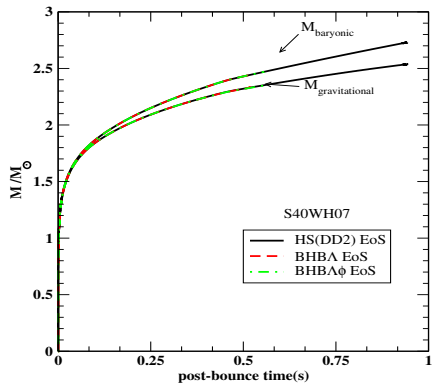

Figure 1: Post-bounce evolution of baryonic mass and gravitational mass.

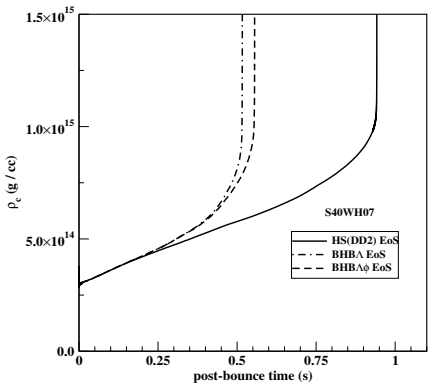

Figure 2: Central density as a function of post-bounce time.

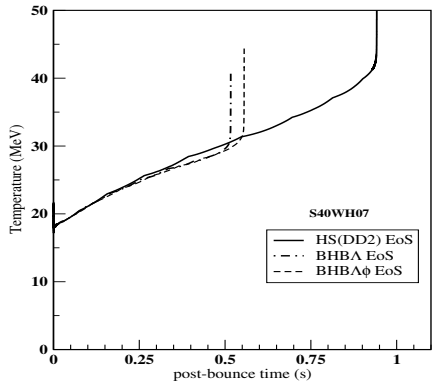

Figure 3: Temperature as a function of post-bounce time.

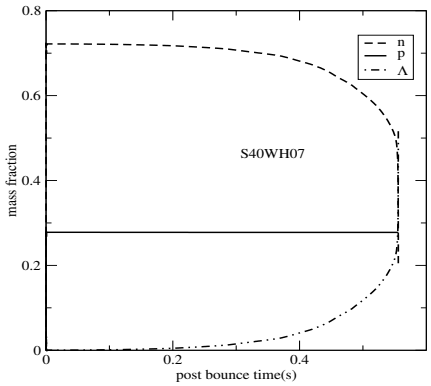

Figure 4: Mass fractions of various species are plotted as a function of post-bounce time.

corresponds to the spikes at real timeline $t_{bounce} = 0.321$sec, which we take as t=0 in the figure. The value of t_{bounce} is same for the HS(DD2) and BHBΛ(ϕ) cases; the hyperons do not appear at that density as evident from the mass fraction graph (Fig. 3). The onset of BH formation is marked by a sharp rise in the value of central density as well as the temperature profile. Owing to the hyperon emergence, the contraction of PNS is accelerated, which leads to quicker rise in temperature and central density. Or in other words, the stiffer EoS leads to larger post-bounce time to BH-formation.

In Fig. 4, we show the compositions of PNS. Initially at core bounce the system consists of neutron and protons only, hyperons appears first at 0.16 sec after core bounce. As soon as the Λ hyperons populate, they replace the neutrons. And the central density that was just above normal nuclear matter density at bounce rises to $\sim 4 \times 10^{14} gm/cm^{-3}$ and the temperature rises to $\sim$ 23MeV.

4 Summary

We studied the effect of hadron-hyperon phase transition in core-collapse supernova using general relativistic hydrodynamic simulation GR1D [7]. By following the dynamical collapse of a new-born proto-neutron star from the gravitational collapse of a $40M_{\odot}$ star adopting the BHB hyperonic EoS table [3], we noticed that hyperons appear just before bounce. It appears off center at first due to high temperature and prevails at the center just before the black hole formation, when the density becomes quite high. Also the presence of hyperons triggers the early BH formation, compared to nucleon-only case.

Acknowledgments

SB acknowledges the financial support from Department of Science & Technology, India, BITS Pilani, Hyderabad and Alexander von Humboldt Foundation.

References

[1] P. B. Demorest, T. Pennucci,S. M. Ransom, M. S. E. Roberts & J. W. T. Hessels, Nature **467** 1081 (2010).

[2] J. Antoniadis et. al., Science **340**, 6131 (2013).

[3] S. Banik, M. Hempel, D. Bandyopadhyay, Astrophy. Suppl. J, **214** 22 (2014).

[4] M. Hempel and J. Schaffner-Bielich, Nucl. Phys. A **837** 210 (2010).

[5] S. Banik, Phy. Rev. **C 89** 035807 (2014).

[6] H. Shen, H. Toki, K. Oyamatsu, K. Sumiyoshi, Astrophy. Suppl. J, **197**, Issue 2, 14 pp. (2011).

[7] C. D. Ott and E. O'Connor, Class. Quant. Grav.**27** 114103 (2010).

[8] S. Typel, G. Röpke, T. Klähn, D. Blaschke and H.H. Wolter, Phys. Rev.**C 81** 015803 (2010).

[9] P. Char, S. Banik, Phy Rev **C90** 015801 (2014).

[10] S. E. Woosley, A. Heger, and T. A. Weaver, Rev. Mod. Phys. **74** 1015 (2002).

Investigation of the rotation effects on high–density matter in hybrid stars

Tomoki Endo

Division of Physics, Department of General Education, National Institute of Technology, Kagawa College, 355 Chokushi-cho, Takamatu, Kagawa 761-8058, Japan

DOI: http://dx.doi.org/10.3204/DESY-PROC-2014-04/98

The equation of state (EOS) of high-density matter is still not clear and several recent observations indicate restrictions to EOSs. Theoretical studies should thus elucidate EOSs at high density and/or high temperature. Many theoretical studies have attempted to account for the effect of rotation of rapidly rotating neutron stars (pulsars), which are commonly observed astronomical objects having high-density interiors. Furthermore, neutron stars generate a strong magnetic field. Several recent studies indicate that this magnetic field exerts some restrictions on the EOS. Theoretical studies should thus incorporate these effects. In this paper, we focus on the effect of rotation. We find that one of our EOSs is consistent with these observations, and another is inconsistent. We also find an important relation between radius and rotation.

1 Introduction

It is widely believed that quark matter exists in high-temperature and/or high-density environments such as those of relativistic heavy-ion collisions [1] or the cores of neutron stars [2, 3], and the "deconfinement transition" has been actively searched. Theoretical studies using model calculations or based on the first principle, lattice QCD [4] have been also carried out by many authors to find the critical temperature of the deconfinement transition. Although many exciting results have been reported, the deconfinement transition is not yet clearly understood. Many theoretical studies have suggested that the deconfinement transition is of first order in high-density cold matter [5, 6]. We thus assume that it is a first-order phase transition in the present work. We have given the equation of state (EOS) for the hadron–quark mixed phase taking into account the charge screening effect [7] without making any approximations. We have investigated the inner structures of neutron stars as environments of quark matter [8, 9]. Recently, many theoretical studies have attempted to account for the effect of the rotation of neutron stars [10, 11, 12, 13]. The results suggest that observations restrict the EOSs of theoretical calculations. Other studies have given the effect of the magnetic field [14, 15, 16, 17] and it would thus be interesting to account for the magnetic effect in our EOS. However, as a first step, we focus on the effect of rotation. We thus apply our EOS to a stationary rotating star in this paper.

2 Formalism and Numerical Results

Our formulation was presented in detail in Ref. [7, 8] and is only briefly explained here. The quark phase consists of u, d, and s quarks and the electron. We incorporate the MIT bag model and assume a sharp boundary at the hadron–quark interface. u and d quarks are treated as massless and s as having mass ($m_s = 150$MeV), and the quarks interact with each other via a one-gluon-exchange interaction inside the bag. The hadron phase consists of the proton, neutron and electron. The effective potential is used to describe the interaction between nucleons and to reproduce the saturation properties of nuclear matter. In treating the phase transition, we have to consider the thermodynamic potential. The total thermodynamic potential ($\Omega_{\rm total}$) consists of hadron, quark and electron contributions and the surface contribution:

$$\Omega_{\rm total} = \Omega_{\rm H} + \Omega_{\rm Q} + \Omega_{\rm S}, \tag{1}$$

where $\Omega_{\rm H(Q)}$ denotes the contribution of the hadron (quark) phase. We here introduce the surface contribution $\Omega_{\rm S}$, parameterized by the surface tension parameter σ, $\Omega_{\rm S} = \sigma S$, with S being the area of the interface. Note that $\Omega_{\rm S}$ may be closely related with the confining mechanism and unfortunately we have no definite idea about how to incorporate it. Many authors have treated its strength as a free parameter and investigated how its value affects results [18, 19, 20]. We take the same approach in this study. To determine the charge screening effect, we also make calculations without the screening effect [7, 21, 22]. We then apply the EOS derived in our paper [7] to the Tolman–Oppenheimer–Volkoff equation [8, 9]. We finally apply our EOS to a stationary rotating star. However, it is difficult to consider the rotation effect in general relativity. We therefore make assumptions of 1) stationary rigid rotation ("uniform rotation"), 2) axial symmetry with respect to the spin axis; and 3) the matter being a perfect fluid. Stationary rotation in general relativity has been reviewed in [23] and [10]; we follow their calculation. We then apply our EOS to a stationary rotating star.

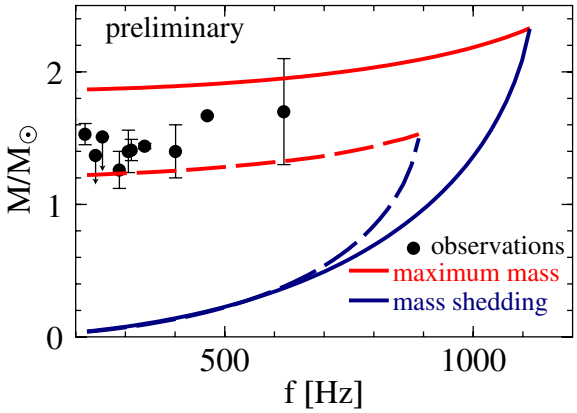

Figure 1: (Color online) Mass–frequency relation obtained with our models plotted against the observational data listed in [10]. The solid and dashed curves represent the results obtained with and without screening, respectively.

Figure 1 shows the result for a rotating star obtained using our EOSs with and without screening. The red curve shows the maximum mass of the star and the blue curve shows

the mass-shedding curve, which corresponds to the Kepler frequency. The Kepler frequency indicates that the centrifugal force is equal in magnitude to gravity. Therefore, the area on the right-hand side of the blue curve is physically invalid. If the red curve is lower than the observations, the EOS should be ruled out. Our EOS in the screening case is thus consistent with these observations. However, our EOS without screening is not consistent and therefore inappropriate. This could be due to the softness of the EOS [10], although further studies are required.

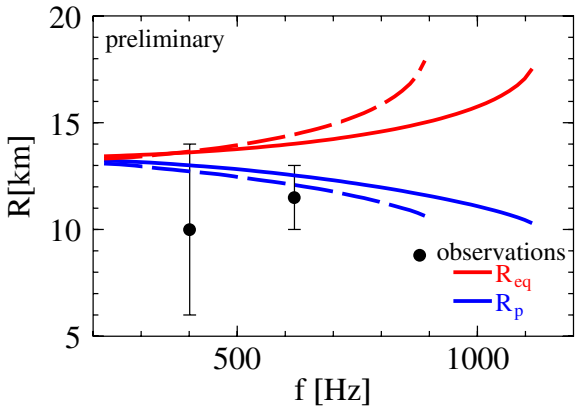

Figure 2: (Color online) Radius–frequency relation of our model plotted against observational data (SAXJ1808.4-3658 and 4U1608-52). The solid and dashed curves represent the results obtained with and without screening, respectively.

Figure 2 suggests an important relation between the radius and rotation. The radius of a star is considered a single value because we ordinarily consider a star approximately spherical. However, if the star is rapidly rotating, it is an ellipse rather than a sphere, and we have to recognize the different radii. Therefore, we introduce two values, R_{eq} and $R_{\rm p}$, which are the equatorial radius and polar radius, respectively. Figure 2 shows R_{eq} and $R_{\rm p}$ with respect to rotation. If the rotation rate is 400 Hz or higher, the two radii are different. We thus have to note the effects of rotation on rapidly rotating stars.

3 Summary and Concluding Remarks

We presented the difference between EOSs with and without charge screening taking into account rotation effects. We used a simple model for quark matter and hadron matter. To obtain a more realistic picture of the hadron–quark phase transition, we need to take into account color superconductivity [20, 24, 25] and relativistic mean field theory [26]. A neutron star has another interesting feature—its magnetic field. The origin of the magnetic field is still unknown. A magnetic field can be explained by the spin-polarization of quark matter [27, 28], but whether quark matter exists strongly depends on the EOS. In this paper, we did not include magnetic fields. Several recent studies have investigated the effect of the magnetic field on the EOS [14, 15, 16, 17]. Interesting results would be obtained if we took into account both the magnetic field and rotation effects.

Acknowledgments

This work was supported in part by a Principal Grant from the National Institute of Technology, Kagawa College.

References

[1] K. Adcox *et al.*, (PHENIX collaboration), Phys. Rev. Lett. **88** 022301 (2002); C. Adler *et al.*, (STAR collaboration), Phys. Rev. Lett. **90** 082302 (2003).

[2] J. Madsen, Lect. Notes Phys. **516** 162 (1999).

[3] K. S. Cheng, Z. G. Dai and T. Lu, Int. Mod. Phys. **D7** 139 (1998).

[4] For review, D. H. Rischke, Prog. Part. Nucl. Phys. **52** (2004) 197; J. Macher and J. Schaffner-Bielich, Eur. J. Phys. **26** 341 (2005) and references therein.

[5] R. D. Pisalski and F. Wilczek, Phys. Rev. Lett. **29** 338 (1984).

[6] R. V. Gavai, J. Potvin and S. Sanielevici, Phys. Rev. Lett. **58** 2519 (1987).

[7] T. Endo, T. Maruyama, S. Chiba and T. Tatsumi, Prog. Theor. Phys. **115** 337 (2006); hep-ph/0510279.

[8] T. Endo, Phys. Rev. **C83** 068801 (2011).

[9] T. Endo, arXiv:1310.0913[astro-ph.HE].

[10] A. Kurkela, P. Romatschke, A. Vuorinen and B. Wu, arXiv:1006.4062[astro-ph.HE].

[11] M. Orsaria, H. Rodrigues, F. Weber and G.A. Contrera, Phys. Rev. **D87** 023001 (2013).

[12] F. Weber, M. Orsaria and R. Negreiros, arXiv:1307.1103[astro-ph.SR]

[13] R. Belvedere, K. Boshkayev, J. A. Rueda, and R. Ruffini, arXiv:1307.2836[astro-ph.SR]

[14] V. Dexheimer, R. Negreiros and S. Schramm, arXiv:1108.4479[astro-ph.HE].

[15] C. Chirenti, and J. Skakalala, Phys. Rev. **D88** 104018 (2013).

[16] R. Aguirre, E. Bauer and I. Vidana, Phys. Rev. **C89** 035809 (2014).

[17] R. Mallick and S. Schramm, Phys. Rev. **C89** 045805 (2014).

[18] H. Heiselberg, C. J. Pethick and E. F. Staubo, Phys. Rev. Lett. **70** 1355 (1993).

[19] N. K. Glendenning and S. Pei, Phys. Rev. **C52** 2250 (1995).

[20] M. Alford, K. Rajagopal, S. Reddy, and F. Wilczek, Phys. Rev. **D64** 074017 (2001).

[21] Toshiki Maruyama, T. Tatsumi, D.N. Voskresensky, T. Tanigawa, T. Endo and S. Chiba, Phys. Rev. **C73** 035802 (2006); nucl-th/0505063.

[22] T. Maruyama, T. Tatsumi, T. Endo and S. Chiba, Recent Res. Devel. Phys. **7** 1 (2006); nucl-th/0605075

[23] N. Stergioulas and J.L. Friedman, Astrophys. J. **444** 306 (1995).

[24] For reviews, M. Alford, A. Schmitt, K. Rajagopal and T. Schäfer, Rev. Mord. Phys. **80** 1455 (2008).

[25] M. Alford and S. Reddy, Phys. Rev. **D67** 074024 (2003).

[26] H. Shen, H. Toki, K. Oyamatsu and K. Sumiyoshi, Nucl. Phys. **A637** 435 (1998).

[27] T. Tatsumi, Phys. Lett. **B489** 280 (2000).

[28] T. Tatsumi, arXiv:1107.0807[hep-ph].

LHCf: Very forward measurement at LHC p-p and p-Pb

H. Menjo[1], *O. Adriani*[2,3], *E. Berti*[2,3], *L. Bonechi*[2], *M. Bongi*[2,3], *G. Castellini*[4], *R. D'Alessandro*[2,3], *M. Del Prete*[2,3], *M. Haguenauer*[5], *Y. Itow*[6,7], *K. Kasahara*[8], *K. Kawade*[6], *Y. Makino*[6], *K. Masuda*[6], *E. Matsubayashi*[6], *G. Mitsuka*[6], *Y. Muraki*[6], *P. Papini*[2], *A-L. Perrot*[9], *D. Pfeiffer*[9], *S. Ricciarini*[2,4], *T. Sako*[6,7], *Y. Shimizu*[10], *Y. Sugiura*[6], *T. Suzuki*[8], *T.Tamura*[11], *A. Tiberio*[2,3], *S. Torii*[8], *A. Tricomi*[12,13], *W.C. Turner*[14], *Q. Zhou*[6]

[1] Graduate school of Science, Nagoya University, Japan
[2] INFN Section of Florence, Italy
[3] Physics and Astronomy Department, University of Florence, Italy
[4] IFAC-CNR, Italy
[5] Ecole-Polytechnique, France
[6] Solar-Terrestrial Environment Laboratory, Nagoya University, Japan
[7] Kobayashi-Maskawa Institute for the Origin of Particles and the Universe, Nagoya University, Japan
[8] RISE, Waseda University, Japan
[9] CERN, Switzerland
[10] JAXA, Japan
[11] Kanagawa University, Japan
[12] INFN Section of Catania, Italy
[13] University of Catania, Italy
[14] LBNL, Berkeley, USA

DOI: http://dx.doi.org/10.3204/DESY-PROC-2014-04/94

The LHCf experiment is an LHC experiment dedicated to measurement of very forward neutral-particle spectra with the aim of improving hadronic interaction model used in MC simulation of cosmic-ray induced air showers. The LHCf have completed the physics plans for $\sqrt{s}$ = 0.9 and 7 TeV p-p collisions in 2010 and for $\sqrt{s_{NN}}$ = 5.02 p-Pb collisions in 2013. The LHCf have another operation with the increased collision energy of 13 TeV in 2015. The recent LHCf result of forward neutron energy spectra at 7 TeV p-p and forward π^0 spectra at p-Pb are presented in this paper.

1 LHCf experiment

The LHCf experiment is one of the LHC forward experiments. The aim is to provide critical calibration data of hadronic interaction models used in MC simulation of air showers induced by cosmic-rays with measuring the production spectra of neutral secondary particles at the very forward region of LHC collisions. The most of energetic particles produced at collisions emit into the forward region and the energy flux of secondaries concentrates on the region although the multiplicity concentrates on the central region of collisions which are covered by the central

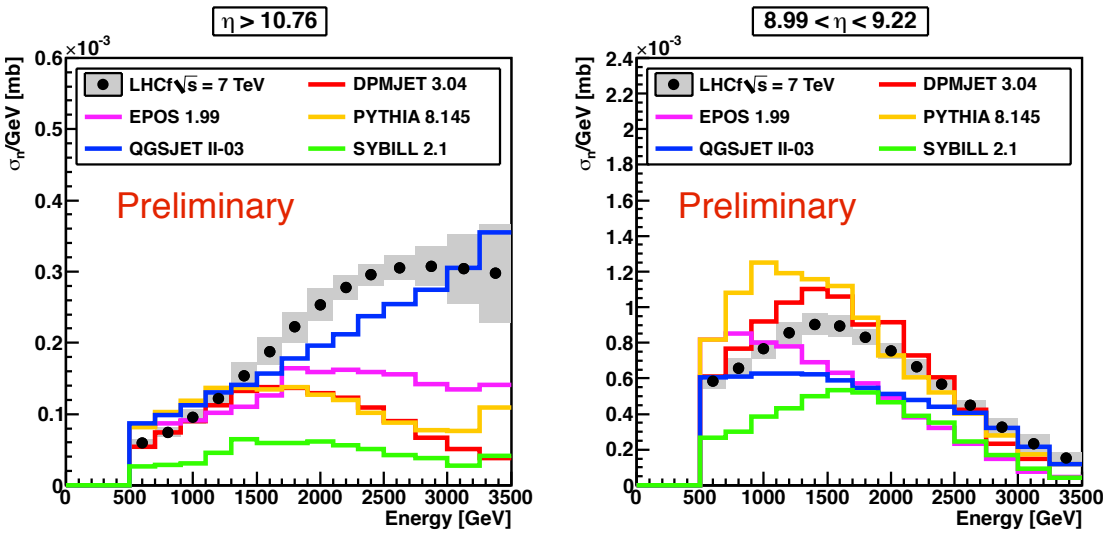

Figure 1: Forward neutron energy spectra at $\sqrt{s} = 7$ TeV p-p collisions measured in $\eta > 10.76$ (left) and $8.99 < \eta < 9.22$ (right) [6]. The black dots and the shaded area show LHCf data and the uncertainties. The color lines indicate the predictions by several hadron interaction models[7, 8, 9, 10, 11].

detectors like ATLAS.
The LHCf have two independent detectors, so called Arm1 and Arm2, which were installed +/- 140m from the ATLAS interaction point (IP1). Each detector has two sampling and imaging calorimeter towers which are consisted of tungsten plates, 16 scintillator layers for shower sampling and four position sensitive layers for measurement of shower position. The position sensitive layers were developed with deferent techniques of X-Y scintillating fiber hodoscopes and X-Y silicon strip detectors for Arm1 and Arm2, respectively. The transverse cross sections of calorimeters are $20{\times}20\,\mathrm{mm}^2$ and $40{\times}40\,\mathrm{mm}^2$ in Arm1 and $25{\times}25\,\mathrm{mm}^2$ and $32{\times}32\,\mathrm{mm}^2$ in Arm2. The energy resolution of detectors are about 5 % for photons and 40 % for neutrons. The position resolution is better than $200\,\mu$m for photons and a few mm for neutrons. More details of the detector performance were reported elsewhere [1, 2].
The LHCf have successfully completed the operation with proton-proton collisions at $\sqrt{s} = 0.9$, 7 TeV in 2010 and the operation with proton-lead collisions at $\sqrt{s_{NN}} = 5.02$ TeV in 2013. The forward photon and π^0 spectra at proton-proton collisions has been published [3, 4, 5].

2 Neutron spectrum in $\sqrt{s} = 7$ TeV p-p collisions

The measurement of neutron energy spectum is a way to access one of the key parameters for air-shower development, inelasticity of hadronic interaction. The parameter is estimated from the energy of leading baryons in collisions. The LHCf detectors are able to measure neutral hadrons, mostly neutrons, with 40% energy resolution and 1 mm position resolution. Events with hadron induced showers are well identified with parameters calculated from longitudinal developments of showers. Figure 1 shows the preliminary result of neutron energy spectra after

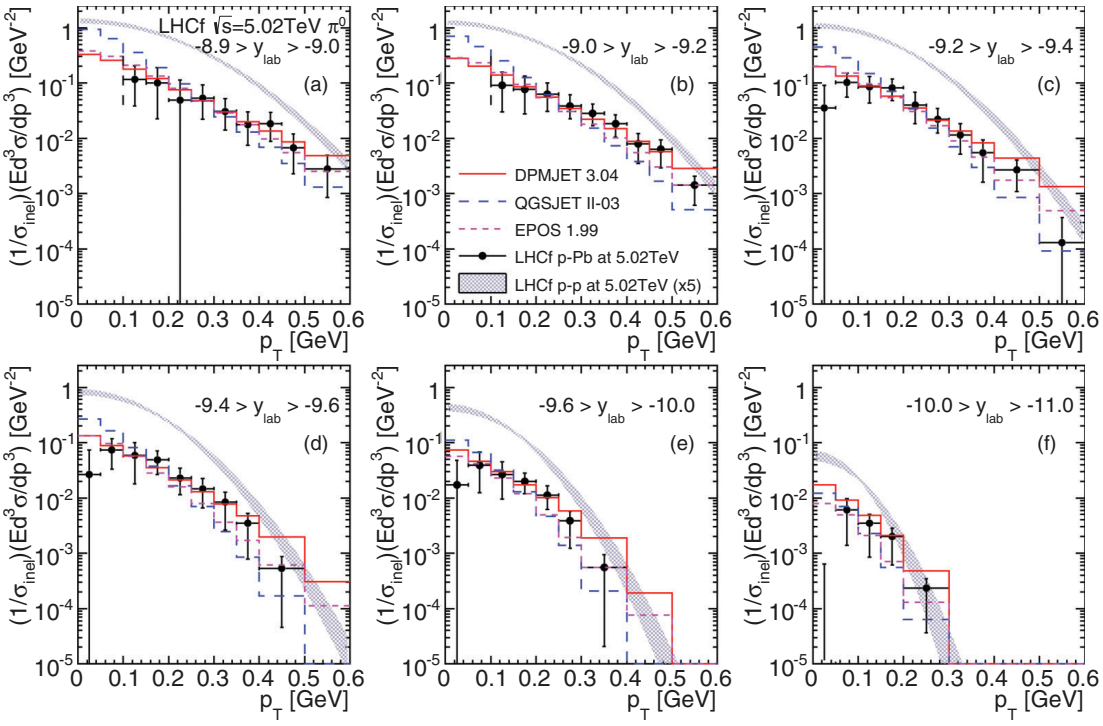

Figure 2: Transverse momentum spectra of forward π^0s at p-Pb [12]. The black dots and the shaded area show LHCf data and the uncertainties. The color lines indicate the predictions by several hadron interaction models[7, 8, 9, 10, 11].

unfolding procedure for detector response [6]. The left and the right figures are for the pseudo-rapidity bins of $\eta > 10.76$ and $8.99 < \eta < 9.22$, respectively. The colored lines indicate the predictions of several hadronic interaction models [7, 8, 9, 10, 11]. We found that the spectrum in $\eta > 10.76$ was very hard like QGSJET2 and the spectrum in $8.99 < \eta < 9.22$ was in the middle of model predictions.

3 π^0 P_T spectrum in $\sqrt{s_{NN}} = 5.02$ TeV p-Pb collisions

In the bingeing of 2013, LHC had proton-lead collisions at the center-of-mass collision energy per nucleus of $\sqrt{s_{NN}} = 5.02$ TeV. LHCf have installed one of the LHCf detectors (Arm2) into the LHC tunnel and had an operation. In the most of our operation time, the Arm2 detector was located on the p-remnant side where proton beams passed from IP1. The LHCf had an operation at the Pb-remnant side only for some hours. In that time, the detector was located 4 cm up from zero degree of collisions to avoid too high multiplicity on the calorimeter towers. Figure 2 shows the transverse momentum spectra of π^0s in p-Pb collisions (the p-remnant side) [12]. The expected contribution of ultra peripheral collisions (UPCs) was already subtracted in these spectra. The thin lines indicate the predictions from the hadronic interaction models, DPMJET3, QGSJET2 and EPOS1.99. The transverse momentum spectra at proton-

proton collisions with the equivalent energy of $\sqrt{s} = 5.02\,\mathrm{TeV}$ were derived from the LHCf data taken at $\sqrt{s} =$ 0.9 2.76 and 7 TeV proton-proton collisions and are shown as the gray hatched lines in Fig.2. Comparing the measured transverse momenta with the estimated spectra in proton-proton collisions give us new information of nuclear modification effect. The nuclear modification factor, $\mathbf{R_{pPb}}$, was defined as the ratio of the p-Pb result to the p-p result. $\mathbf{R}_{pPb}$ varies from 0.1 at P_T 0.1 GeV/c to 0.3 at P_T 0.3 GeV/c. This tendency is found in the all rapidity bins of Fig2. The hadronic interaction model reproduce the small factor of $\mathbf{R_{pPb}}$ 0.1 constantly in the P_T range. They are in good agreement with the LHCf result within the errors.

4 Future prospects

The LHC will restart the operation in 2015. In the beginning of LHC physics run, a run with very low-luminosity of $10^{30} cm^2 s^{-1}$ is planed. The LHCf will have an operation for one week in that period at proton-proton collisions with $\sqrt{s} = 13\,\mathrm{TeV}$. The collision energy is about 10^{17} eV. It will be unique data point of forward spectra at the highest collision-energy of collider experiment in the next decades. Comparing with the date taken at proton-proton collisions of $\sqrt{s} = 0.9$, 2.76 and 7 TeV in the past operations, the energy scaling of forward particle production can be checked. The test with the wide collision energy of $10^{14} - 10^{17}$ eV in the laboratory frame is important because it covers the energy of well-known Knee kink of the cosmic-ray spectrum around 10^{15} eV. Additionally the operation in 2015 will be important to study the diffractive physics thanks to the common operation with the ATLAS experiment. The LHCf sends its final trigger signals to ATLAS trigger system and they trigger ALTAS after pre-scaling of the signals. It was confirmed by a simple simulation study that an event cut with the number of particle tracks in the ATLAS central tracker works well to select only diffractive events. Forward production spectra with such event categorization help us to understand the particle production mechanism in the soft hadronic interactions.
After the operation in 2015, we are proposing to bring one of the detectors to RHIC and to have an operation at proton-proton collisions with $\sqrt{s} = 0.5\,\mathrm{TeV}$. It provides an opportunity of measuring forward production spectra with much wider P_T coverage than the operation at LHC 0.9 TeV proton-proton collisions. It will be much useful to test the energy scaling.

References

[1] O. Adriani, et al., JINST **3** (2008) S08006.
[2] K. Kawade, et al., JINST **9** (2014) P03016.
[3] O. Adriani, et al., PLB 715 (2012) p. 298-303.
[4] O. Adriani, et al., Phys. Lett. B **703** (2011) 128.
[5] O. Adriani, et al., PRD **86** (2012) 092001.
[6] O. Adriani, et al., in preparation.
[7] F. W. Bopp, J. Ranft R. Engel and S. Roesler, Phys. Rev. C **77** (2008) 014904.
[8] T. Sjostand, S. Mrenna and P. Skands, JHEP **05** (2006) 026.
[9] K. Werner, F.-M. Liu and T. Pierog, Phys. Rev. C **74** (2006) 044902.
[10] S. Ostapchenko, Phys. Rev. D **74** (2006) 014026.
[11] E.-J. Ahn, et al., Phys. Rev. D **80** (2009) 094003.
[12] O. Adriani, et al., Phys. Rev. C **89** (2014) 065209.

Numerical Analysis of the $^1S_0$ Pairing Gap in Neutron Matter

S. Maurizio[1], *J. W. Holt*[2], *P. Finelli*[3]

[1] Albert Einstein Center for Fundamental Physics, Institute for Theoretical Physics, CH-3012 Bern, Switzerland
[2] Department of Physics, University of Washington, Seattle, WA 98195-1560
[3] Department of Physics and Astronomy, University of Bologna, I-40126 Bologna, Italy and INFN, Bologna section, I-40127 Bologna, Italy

DOI: http://dx.doi.org/10.3204/DESY-PROC-2014-04/66

In a recent paper [1] we studied the behavior of the pairing gaps Δ_F as a function of the Fermi momentum k_F for neutron and nuclear matter in all relevant angular momentum channels where superfluidity is believed to naturally emerge. The calculations employed realistic chiral nucleon-nucleon potentials [2, 3] with the inclusion of three-body forces and self-energy effects. In this contribution we perform a numerical analysis of Khodel's method [6] for the singlet case.

1 Khodel's method

In this section we explain the method employed to solve the BCS equations by partial-wave decomposition. The BCS equation reads in terms of the NN potential $V(\mathbf{k},\mathbf{k}') = \langle \mathbf{k}\,|V|\,\mathbf{k}'\rangle$ as follows

$$\Delta\left(\mathbf{k}\right) = -\sum_{\mathbf{k}'}\langle \mathbf{k}\,|V|\,\mathbf{k}'\rangle \frac{\Delta\left(\mathbf{k}'\right)}{2E\left(\mathbf{k}'\right)}\,, \tag{1}$$

with $E(\mathbf{k})^2 = \xi(\mathbf{k})^2 + |\Delta(\mathbf{k})|^2$ and where $\xi(\mathbf{k}) = \varepsilon(\mathbf{k}) - \mu$, $\varepsilon(\mathbf{k})$ denotes the single-particle energy and μ is the chemical potential. We can decompose both the interaction and the gap function

$$\langle \mathbf{k}\,|V|\,\mathbf{k}'\rangle = 4\pi\sum_l (2l+1) P_l(\hat{\mathbf{k}}\cdot\hat{\mathbf{k}}') V_l(k,k') \tag{2}$$

$$\Delta(\mathbf{k}) = \sum_{lm}\sqrt{\frac{4\pi}{2l+1}} Y_{lm}(\hat{\mathbf{k}})\Delta_{lm}(k)\,, \tag{3}$$

where $Y_{lm}(\hat{\mathbf{k}})$ denotes the spherical harmonics, l and m are the quantum numbers associated with the orbital angular momentum and its projection along the z axis and $P_l(\hat{\mathbf{k}}\cdot\hat{\mathbf{k}}')$ refers to the Legendre polynomials. After performing an angle-average approximation we have the following equation for any value of l

$$\Delta_l^j(k) = \sum_{l'}\frac{(-1)^\Lambda}{\pi}\int dk'\; V_{ll'}^j(k,k')\frac{\Delta_{l'}^j(k')}{E(k')}k'^2\,, \tag{4}$$

where $\Lambda = 1 + (l - l')/2$, j refers to the total angular momentum ($\boldsymbol{J} = \boldsymbol{l} + \boldsymbol{S}$) quantum number including spin $\boldsymbol{S}$ and now $E(k)^2 = \xi(k)^2 + \sum_{jl} \Delta_l^j(k)^2$. Gaps with different l and j are coupled due to the energy denominator but we assume that different components of the interaction mainly act on non-overlapping intervals in density. To solve Eq. (4), we follow the approach suggested by Khodel *et al.* [6] that has been proven to be stable even for small values of the gap and to require only the initial assumption of a scale factor δ (results will be δ-independent, as will be shown in Sect. 2). We define an auxiliary potential W according to

$$W_{ll'}(k,k') = V_{ll'}(k,k') - v_{ll'}\phi_{ll'}(k)\phi_{ll'}(k') \,, \tag{5}$$

where $\phi_{ll'}(k) = V_{ll'}(k,k_F)/V_{ll'}(k_F,k_F)$ and $v_{ll'} = V_{ll'}(k_F,k_F)$ so that $W_{ll'}(k,k')$ vanishes on the Fermi surface. The coupled gap equations can be rewritten as

$$\Delta_l(k) - \sum_{l'} (-1)^{\Lambda} \int d\tau' \; W_{ll'}(k,k') \frac{\Delta_{l'}(k')}{E(k')} = \sum_{l'} D_{ll'}\phi_{ll'}(k) \,, \tag{6}$$

where $d\tau = k^2 dk/\pi$ and the coefficients $D_{ll'}$ satisfy

$$D_{ll'} = (-1)^{\Lambda} v_{ll'} \int d\tau \; \phi_{ll'}(k) \frac{\Delta_{l'}(k)}{E(k)} \,. \tag{7}$$

The gap is defined as follows

$$\Delta_l(k) = \sum_{l_1 l_2} D_{l_1 l_2} \chi_l^{l_1 l_2}(k) \,, \tag{8}$$

where

$$\chi_l^{l_1 l_2}(k) - \sum_{l'} (-1)^{\Lambda} \int d\tau' \; W_{ll'}(k,k') \frac{\chi_{l'}^{l_1 l_2}(k')}{E(k')} = \delta_{ll_1}\phi_{l_1 l_2}(k) \,, \tag{9}$$

and $\delta_{ll'}$ is the scale factor. The property that $W_{ll'}(k,k')$ vanishes on the Fermi surface ensures a very weak dependence of $\chi_l^{l_1 l_2}(k)$ on the exact value of the gap so that, in first approximation, it is possible to rewrite the previous equation (9) as

$$\chi_l^{l_1 l_2}(k) - \sum_{l'} (-1)^{\Lambda} \int d\tau' \; W_{ll'}(k,k') \frac{\chi_{l'}^{l_1 l_2}(k')}{\sqrt{\xi^2(k') + \delta^2}} = \delta_{ll_1}\phi_{l_1 l_2}(k) \,. \tag{10}$$

We use this equation to evaluate $\chi_l^{l_1 l_2}(k)$ initially by matrix inversion, then we use this function to self-consistently evaluate $D_{ll'}$. Finally, we solve the system given by Eqs. (7)–(9) in a self-consistent procedure as shown in Fig. 1 (left panel). We always assumed $\mu = \varepsilon_F$ and adopted the relativistic version of the single-particle energy $\varepsilon(k) = \sqrt{k^2 + M_N^2}$, where M_N is the nucleon mass. For the pairing potential $V(p,k)$ we introduce the following ansatz:

$$V(p,k) = V_{2\mathrm{B}}(p,k) + \sum_m V_{3\mathrm{B}}(p,k,m) \simeq V_{2\mathrm{B}}(p,k) + V_{2\mathrm{B}}^{\mathrm{eff}}(k_F,p,k) \,, \tag{11}$$

where $V_{2\mathrm{B}}$ is the NN potential [2] at N3LO order in the chiral expansion and the three-body potential is approximated by an effective two-body density-dependent potential V_{2B}^{eff} derived by Holt *et al.* in Refs. [4, 5]. When considering self-energy effects, we simply perform the transformation $M_N \to M_N^*$ using the effective mass obtained by Holt *et al.* in Ref. [7] using a density matrix expansion technique.

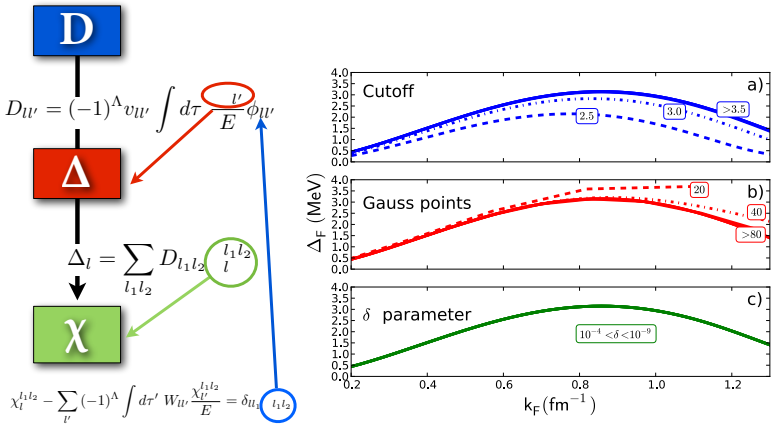

Figure 1: **Left**: Self-consistent procedure (Eqs. 7–9) for the solution of the gap equation according to Khodel's prescription [6]. **Right**: Numerical analysis of Khodel's procedure for the singlet channel in neutron matter: **a)** cutoff, **b)** Gaussian integration points and **c)** δ dependence. This method is a very stable procedure if satisfactory values of n_{gauss} and Λ_k are employed.

2 Results and Numerical analysis

In the neutron matter case, at the two-body level, there is good agreement with the gap computed from well known realistic potentials like the CD-Bonn or Nijmegen interactions [9], except for larger densities where the N3LO gap exhibits a higher value (phase shifts from the chiral N3LO potential exhibit more attraction than the CD-Bonn potential for high momenta [8]). We tested Khodel's method [6] against the variation of the following three parameters: n_{gauss} (number of Gauss integration points), Λ_k (cutoff for integrals in the momentum space, see Eq. (4)) and δ (the scale factor). In Fig. 1 (right side) we summarise our results. In the upper panel (**a**) we calculated Δ_F for different values of the momentum cutoff (using $n_{gauss} = 200$ and $\delta = 1 \times 10^{-10}$ MeV) where in the second panel (**b**) we varied n_{gauss} (keeping $\Lambda_k = 4.5$ fm^{-1} and $\delta = 1 \times 10^{-10}$ MeV) and in the lower panel (**c**) we changed δ (with $n_{gauss} = 200$ and $\Lambda_k = 4.5$ fm^{-1}) by orders of magnitude. Our conclusion is that the method proposed by Khodel [6] is a very stable procedure to study nuclear superfluidity if a reasonable number of Gaussian points (≥ 100) and a realistic momentum cutoff (≥ 4 fm^{-1}) are employed. In Fig. 2 we compare our full calculation for the gap, i.e., with the complete potential in Eq. (11) and the density-dependent effective mass, with recent results by Hebeler *et al.* [8], where the authors started from a chiral N3LO interaction and evolved to a sharp low-momentum interaction. Also presented for comparison are *ab-initio* results obtained in the last several years: Auxiliary Field Diffusion Monte Carlo (AFDMC) [10] with AV8' + UIX potentials, Quantum Monte Carlo (QMC) [11], where the authors have retained the S-wave part of the AV18 interaction, and Correlated Basis Functions (CBF) [12] still with AV8' plus UIX. We observe that at low densities the gap behaviors are very similar, with the exception of QMC, but beyond Fermi momenta

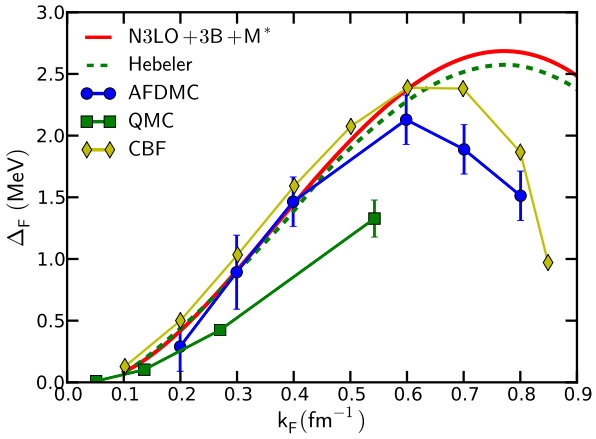

Figure 2: The $^1S_0$ gap for neutron matter computed with the realistic chiral potential of [2] at N3LO plus the three-body contribution of Eq. (11) and the inclusion of the effective mass in comparison with *ab-initio* simulations.

of $k_F \approx 0.6$ fm^{-1} the gaps computed with the Argonne potentials decrease rapidly in contrast to those from chiral interactions. At the present time, it is hard to assess if disagreement is due to different choices in the nuclear Hamiltonian or different many-body methods.

Acknowledgments

Work supported in part by US DOE Grant No. DE-FG02-97ER-41014.

References

[1] S. Maurizio, J. W. Holt and P. Finelli, Phys. Rev. C **90** (2014) 044003.
[2] R. Machleidt and D. R. Entem, Phys. Rept. **503** (2011) 1 and references therein.
[3] E. Epelbaum, H.-W.Hammer and Ulf-G. Meissner, Rev. Mod. Phys. **81** (2009) 1773 and references therein.
[4] J. W. Holt, N. Kaiser and W. Weise, Phys. Rev. C **79** (2009) 054331.
[5] J. W. Holt, N. Kaiser and W. Weise, Phys. Rev. C **81** (2010) 024002.
[6] V. V. Khodel, V. A. Khodel and J. W. Clark, Nucl. Phys. A **598** (1996) 390.
[7] J. W. Holt, N. Kaiser, and W. Weise, Eur. Phys. J. A **47** (2011) 128.
[8] K. Hebeler, A. Schwenk and B. Friman, Phys. Lett. B **648** (2007) 176.
[9] M. Hjorth-Jensen and D. J. Dean, Rev. Mod. Phys. **75** (2003) 607.
[10] S. Gandolfi, A. Y. .Illarionov, F. Pederiva, K. E. Schmidt and S. Fantoni, Phys. Rev. C **80** (2009) 045802.
[11] A. Gezerlis and J. Carlson, Phys. Rev. C **77** (2008) 032801(R).
[12] A. Fabrocini, S. Fantoni, A. Y. Illarionov and K. E. Schmidt, Phys. Rev. Lett. **95** (2005) 192501.

Recent Results from the Telescope Array Experiment

Thomas Stroman for the Telescope Array Collaboration
University of Utah, Salt Lake City, United States

DOI: http://dx.doi.org/10.3204/DESY-PROC-2014-04/62

The Telescope Array Experiment (TA) is the northern hemisphere's largest detector of ultra-high-energy cosmic rays (UHECRs). Built to measure the UHECR chemical composition, arrival-direction anisotropy, and energy spectrum for $E > 1$ EeV, TA's instrumentation includes both an array of scintillator-based particle counters and three fluorescence detector stations overlooking the ground array. This presentation highlights recent composition, spectrum, and anisotropy measurements based on UHECR data collected since TA operations began in 2007, including preliminary results for $E > 10$ PeV from the newly commissioned TA Low-energy Extension (TALE). The expected impact of planned expansions to the experiment will also be described.

1 Introduction

Ultra-high-energy cosmic rays (UHECRs) are subatomic particles that have been accelerated elsewhere in the cosmos to energies in excess of 10^{18} eV. Primary UHECR particles incident on Earth's atmosphere undergo inelastic collisions with gas nuclei, producing extensive air showers. These cascades of secondary particles produce ultraviolet light (via fluorescence emissions of excited nitrogen as well as the Cherenkov mechanism) en route to the ground, where the shower's electromagnetic and muonic footprint can be several kilometers wide in the case of the most energetic primary interactions.

The cosmic-ray flux is a steeply falling function over many orders of magnitude in energy, so that a detector with very large exposure is necessary for any experimental investigation of especially the highest-energy UHECRs' properties. The Telescope Array (TA) experiment is the northern hemisphere's largest UHECR detector, built on over 700 km^2 centered at approximately 39.3° N, 112.9° W in west-central Utah. The original TA instrumentation consists of 38 ultraviolet telescopes located at three fluorescence detector (FD) stations, operating since 2007, and 507 surface detectors (SDs) located every 1.2 km on a square grid, operating since 2008. The SD array and each FD station operate independently, as well as allowing hybrid SD+FD or stereoscopic FD+FD observation of individual showers.

Telescope Array's design facilitates the study of several distinct but interrelated aspects of the nature of UHECRs, and we present some recent highlights of these investigations here. After a brief review of the data analysis in Section 2, we report measurements of an intermediate-scale anisotropy we call the *hotspot* (Section 3), a proton-dominated chemical composition at all energies $E > 10^{18.2}$ eV (Section 4), and the differential energy spectrum manifesting four

distinct spectral features in the range $15.9 \leq \log_{10}(E/\mathrm{eV}) < 20.5$ (Section 5). Finally, we preview the present and future operations to enlarge the TA scientific program in Section 6.

2 Data analysis

The principle underlying TA data analysis is the reconstruction of the air shower properties responsible for the observed signal. The shower trajectory is first determined from an appropriate combination of signal timing and/or detector geometry, which enables the reconstruction of shower energy and, in the case of FD observations, the longitudinal development. The details of the analysis depend on whether the data being analyzed originated in SD or FD observation [1, 2].

A shower observed via direct detection of secondary particles by SDs has its impact position and zenith angle θ determined from the respective distribution of signal sizes and times. The observed signals are then projected onto a lateral distribution model, from which the shower density 800 m from the axis (s_{800}) is interpolated. A lookup table provides an estimate, determined from Monte Carlo simulation and calibrated to the FD energy scale via common events, of the primary shower energy for the observed combination of s_{800} and θ.

In the case of a shower observed via atmospheric fluorescence, the pattern of illuminated photomultiplier tubes (PMTs) constrains the shower trajectory to a plane including the position of the FD. Within this shower-detector plane, the shower's inclination angle and impact parameter determine the relative timing of the signals observed in each PMT.

An inverse-Monte Carlo technique determines the energy and atmospheric slant depth of shower maximum (X_{max}) by varying the longitudinal profile parameters of simulated showers, until reaching the best agreement in detector response between simulation and data.

3 Anisotropy above 57 EeV

Based on five years of SD observation, a directional excess in the flux of UHECRs with $E >$ 57 EeV has been observed in the constellation Ursa Major [3]. Given the exposure of the SD array, the expected number of events within a 20° radius was 4.5, but 19 were observed, a 5.1σ excess (see Fig. 1). The chance probability of our observing an excess of this size from an isotropic flux, given intermediate-scale event oversampling in 5° steps from 15° to 35°, is 3.7×10^{-4}, for a post-trials significance of 3.4σ. Preliminary analysis including a sixth year of data increases the significance of the observation to 4.0σ.

4 Mass composition

It is possible to estimate the mean mass of primary cosmic rays as a function of energy by comparison of the observed X_{max} distribution to model predictions for known compositions. Using the hybrid combination of data from the SD array and the Middle Drum FD (consisting of equipment refurbished from the High Resolution Fly's Eye experiment), we find our observations compatible with a predominantly protonic composition at all energies $E > 10^{18.2}$ eV regardless of the choice of hadronic interaction model used in simulation [4].

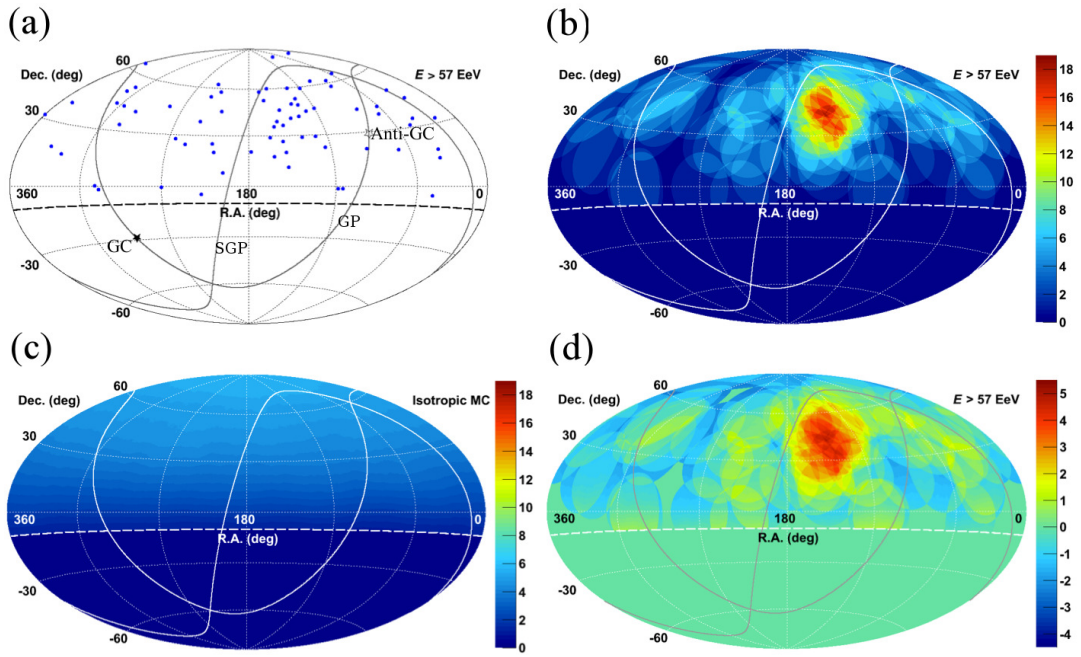

Figure 1: Anisotropy above 57 EeV: (**a**) arrival directions; (**b**) arrival directions with 20° oversampling; (**c**) expected number of events assuming isotropic null hypothesis; (**d**) Li-Ma significance of excess.

5 Energy spectrum

Using six years of data from the SD array, we observe two features in the UHECR spectrum: a hardening *ankle* at $10^{18.70\pm0.02}$ eV and a suppression above $10^{19.74\pm0.04}$ eV compatible with the *GZK cutoff* predicted for protons. The suppression represents a 6.59σ deficit relative to a spectrum maintaining the post-ankle spectral slope without cutoff.

The newly commissioned TA Low-energy Extension (TALE) includes ten FD telescopes observing at higher elevation angles than the main FD configuration, complemented by an array of closely-spaced ($\sim$ 400 m) SDs, to reduce the energy threshold for shower detection [5]. A preliminary analysis using fluorescence and Cherenkov light seen by the TALE FD extends the observed spectrum to below 10 PeV and reveals two additional spectral breaks.

6 Future operations

A number of operations are being pursued to upgrade Telescope Array in the coming years. A quadrupling of the TA exposure above 10^{19} eV (TA$\times$4) will be accomplished by adding another 500 SDs with greater spacing, overlooked by two additional FD stations. The detection threshold will be pushed further down into the PeV decade via a Non-Imaging Cherenkov Experiment (NICHE [6]) cross-calibrated with TALE events. Progress continues toward UHECR detection via bistatic radar (TARA [7]), and we are exploring claims of a connection between thun-

derstorms and high-energy radiation with a lightning-mapping array (TALMA). The science program at Telescope Array continues to grow increasingly expansive and robust.

Acknowledgments

The Telescope Array experiment is supported by the Japan Society for the Promotion of Science through Grants-in-Aid for Scientific Research on Specially Promoted Research (21000002) "Extreme Phenomena in the Universe Explored by Highest Energy Cosmic Rays," and the Inter-University Research Program of the Institute for Cosmic Ray Research; by the U.S. National Science Foundation awards PHY-0307098, PHY-0601915, PHY-0703893, PHY-0758342, PHY-0848320, PHY-1069280, and PHY-1069286 (Utah) and PHY-0649681 (Rutgers), and through TeraGrid resources provided by Purdue University and Indiana University [8]; by the National Research Foundation of Korea (2006-0050031, 2007-0056005, 2007-0093860, 2010-0011378, 2010-0028071, R32-10130); by the Russian Academy of Sciences, RFBR grants 10-02-01406a and 11-02-01528a (INR), IISN project No. 4.4509.10, and Belgian Science Policy under IUAP VI/11 (ULB). The foundations of Dr. Ezekiel R. and Edna Wattis Dumke, Willard L. Eccles, and George S. and Dolores Doré Eccles all helped with generous donations. The State of Utah supported the project through its Economic Development Board, and the University of Utah through the Office of the Vice President for Research. The experimental site became available through the cooperation of the Utah School and Institutional Trust Lands Administration (SITLA), the U.S. Bureau of Land Management, and the U.S. Air Force. We also wish to thank the people and the officials of Millard County, Utah, for their steadfast and warm support. We gratefully acknowledge the contributions from the technical staffs of our home institutions as well as the University of Utah Center for High Performance Computing (CHPC).

References

[1] T. Abu-Zayyad et al. The Cosmic-Ray Energy Spectrum Observed with the Surface Detector of the Telescope Array Experiment. *Astrophys. J. Letters*, 768:L1, May 2013.

[2] T. Abu-Zayyad et al. The energy spectrum of ultra-high-energy cosmic rays measured by the Telescope Array FADC fluorescence detectors in monocular mode. *Astroparticle Physics*, 48:16–24, August 2013.

[3] R. U. Abbasi et al. Indications of Intermediate-scale Anisotropy of Cosmic Rays with Energy Greater Than 57 EeV in the Northern Sky Measured with the Surface Detector of the Telescope Array Experiment. *Astrophys. J. Letters*, 790:L21, August 2014.

[4] R. U. Abbasi et al. Study of Ultra-High Energy Cosmic Ray Composition Using Telescope Array's Middle Drum Detector and Surface Array in Hybrid Mode. *ArXiv e-prints*, August 2014.

[5] G. Thomson. The Telescope Array Low Energy Extension (TALE). *International Cosmic Ray Conference*, 3:338, 2011.

[6] J. Krizmanic, D. Bergman, and Pierre Sokolsky for the TA/TALE Collaboration. The Non-Imaging CHErenkov Array (NICHE): A TA/TALE Extension to Measure the Flux and Composition of Very-High Energy Cosmic Rays. *ArXiv e-prints*, July 2013.

[7] R. Abbasi et al. Telescope Array Radar (TARA) observatory for Ultra-High Energy Cosmic Rays. *Nuclear Instruments and Methods in Physics Research A*, 767:322–338, December 2014.

[8] C. Catlett et al. *TeraGrid: Analysis of Organization, System Architecture, and Middleware Enabling New Types of Applications*. IOS Press, 2007.

Results and prospects on registration of reflected Cherenkov light of EAS from cosmic particles above 10^{15} eV

R.A. Antonov[1], *T.V. Aulova*[1], *E.A. Bonvech*[1], *D.V. Chernov*[1], *T.A. Dzhatdoev*[1,*], *Mich. Finger*[2,3], *Mir. Finger*[2,3], *V.I. Galkin*[4,1], *D.A. Podgrudkov*[4,1], *T.M. Roganova* [1]

[1] Skobeltsyn Institute of Nuclear Physics, Lomonosov Moscow State University, Leninskie gory 1-2, 119991 Moscow, Russia

[2] Charles University in Prague, Faculty of Mathematics and Physics, V Holesovickach 2, 18000 Prague, Czech Republic

[3] Joint Institute for Nuclear Research, Joliot-Curie 6, 141980 Dubna, Moscow region, Russia

[4] Faculty of Physics, Lomonosov Moscow State University, Leninskie gory 1-2, 119991 Moscow, Russia

[*] timur1606@gmail.com

DOI: http://dx.doi.org/10.3204/DESY-PROC-2014-04/152

We give an overview of the SPHERE experiment based on detection of reflected Vavilov-Cherenkov radiation ("Cherenkov light") from extensive air showers in the energy region E>10^{15} eV. A brief history of the reflected Cherenkov light technique is given; the observations carried out with the SPHERE-2 detector are summarized; the methods of the experimental datasample analysis are described. The first results on the primary cosmic ray all-nuclei energy spectrum and mass composition are presented. Finally, the prospects of the SPHERE experiment and the reflected Cherenkov light technique are given.

1 Introduction

Despite several decades of intensive research, experimental results on the superhigh energy ($E > 10^{15}$ eV = 1 PeV) cosmic ray spectrum and composition are still somewhat controversial. An uncertainty of the spectral shape is considerable (see, e.g., [1]), and the results on the nuclear composition obtained by different experiments are often contradictory (e.g. [2]). A scatter of results is especially large for the composition studies: various measurements of the mean logarithmic mass number, $< lnA >$, at some energy region span almost the full range of masses from proton to Iron. For some extensive air shower (EAS) experimental techniques the uncertainty of the primary composition might translate into an additional error of the reconstructed all-nuclei spectrum, and this latter systematic uncertainty may dominate the total error of the spectrum measurement.

The experimental situation clearly calls for development of new EAS observation and data analysis methods. In the present paper we describe one such method based on reflected Vavilov-Cherenkov radiation ("Cherenkov light") registration. Many details could be found in [3].

The first proposal to use a compact device lifted over a snow surface to observe reflected

Cherenkov light of EAS was made by A.E. Chudakov [4]. The first detector of such kind was developed by C. Castagnoli et al. [5]. The first balloon-borne apparatus capable of reflected Cherenkov light observation was the SPHERE-1 detector [6]; it had a mosaic of only 19 PMTs and could not register details of light impulse shape. The next generation, and currently the most advanced experiment with reflected Cherenkov light, employed the SPHERE-2 detector.

2 The SPHERE-2 detector and the datasample

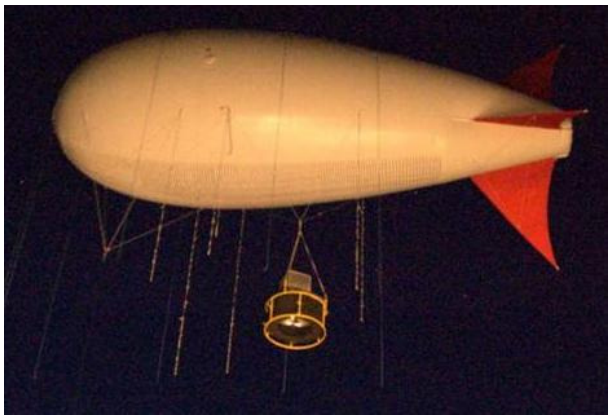

Figure 1: The SPHERE-2 detector carried by the BAPA tethered balloon.

The SPHERE-2 balloon-borne detector [3] had a mosaic of 109 PMTs and 12.5 ns time sampling (25 ns until the 2012 experimental run). A general view of the SPHERE-2 detector together with by the BAPA tethered balloon is shown in Fig. 1. Observations were typically carried out in February-March at altitude H= 400–900 m above the surface of Lake Baikal. Total observation time for the 2008–2013 runs was about 140 h; about 1100 EAS were detected.

3 Simulations, data analysis and results

The detector response simulations were carried out by means of Monte Carlo (MC) approach using the CORSIKA code with the QGSJET-I high energy hadronic model and the GHEISHA low energy hadronic model [7], and the Geant4 code [8]. The first step of experimental data analysis is reconstruction of lateral distribution function (LDF) of detected showers. An example of reconstructed LDF is shown in Fig. 2, left. LDF reconstruction is a quite complex procedure; it is important to have several independent techniques to ensure robustness of this procedure. An example of LDF obtained with the second technique is shown in Fig. 2, right. The next step of analysis, estimation of EAS primary energy, was performed by normalising the experimental LDFs to the model LDFs with known energy [9]. Finally, the sample of the estimated primary energy values together with the model of the instrumental acceptance allowed the all-nuclei spectrum reconstruction [10],[3].

Simulated energy distributions for the 2013 experimental run data, power-law primary spectrum $J \sim E^{-\gamma}$ with slope $\gamma = 3$, and different types of primary nuclei, are shown in Fig. 3,

left. The lowest curve corresponds to the primary Iron case, upper concentric curves are calculated for the Nitrogen, Helium and proton cases, correspondingly. The thick curve that fits the experimental histogram (circles) is drawn for the energy distribution with mixed composition. Information about the LDF steepness, that is sensitive to the primary composition, was utilized to build a model of energy distribution for mixed composition (see [10],[3] for more details).

The combined all-nuclei spectrum for the 2011–2013 runs is shown in Fig. 3 (right) by stars with statistical uncertainies (bars); systematic uncertainties are shown as well. For comparison the results of the KASCADE-Grande (triangles with associated statistical and systematic uncertainties) [11] and the Akeno (circles) [12] experiments are shown. For the Akeno case statistical uncertainties are small and comparable to the diameter of the circles, and systematic uncertainties are unknown. For other results on the all-nuclei spectrum see [13].

The primary composition for the 2012 run was reconstructed using the LDF steepness parameter [14],[3], that allows an event-by-event composition study. The reconstructed composition for the 2012 run is shown in Fig. 2 of [14]. It is in general agreement to the KASCADE-Grande result [15]; the estimated fraction of light nuclei averaged over the 30–150 PeV energy region is 0.21 ± 0.11.

4 Prospects and conclusions

Uncertainty of results on the primary spectrum and composition discussed in sec. 3 at E>50 PeV is dominated by statistical errors. Two possible extensions of the SPHERE experiment to the energy region E>100 PeV were proposed [3]:
1) A SPHERE-type detector with $N>10^3$ channels that would allow to perform an event-by-event study of the primary CR composition at E>100 PeV with statistical uncertainty comparable to the KASCADE-Grande's one given ∼500 h of exposition at H= 2–3 km;
2) A detector with $N>10^3$ channels aimed for study of the all-nuclei spectrum of Ultrahigh Energy Cosmic Rays (UHECR, $E>10^{18}$ eV) during a long-duration high-altitude (H≈30–40 km) Antarctic flight, or, alternatively, a detector with $N>10^4$ channels that would allow to study the UHECR primary composition under similar experimental conditions.

To conclude, we have reviewed a novel technique to study CR at E>1 PeV using reflected Cherenkov light. The method is currently mature enough to be competitive with other EAS observation methods, given sufficient observation time. For the first time, a detailed reconstruction of the all-particle CR spectrum at E= 3-300 PeV was performed using reflected Cherenkov light. This technique allows the CR nuclear composition study on event-by-event basis. Reflected Cherenkov light is a promising signal to study CR at E>100 PeV, either with tethered balloon at H= 2–3 km, or during a high-altitude Antarctic flight.

Acknowledgements

The authors are grateful to the technical collaborators of the SPHERE-2 experiment. The work was supported by the Russian Foundation for Basic Research (grants 11-02-01475-a, 12-02-10015-k, 13-02-00470-); the Russian President grants LSS-871.2012.2; LSS-3110.2014.2; the Program of basic researches of Presidium of Russian Academy of Sciences "Fundamental properties of a matter and astrophysics". Calculations were performed using the SINP MSU space monitoring data center computer cluster; we are grateful to Dr. V.V. Kalegaev for permission to use the hardware and to V.O. Barinova, M.D. Nguen, D.A. Parunakyan for technical support.

References

[1] R. Abbasi et al. (ICETOP), astro-ph/1202.3039 (2012).

[2] Y. Tsunesada et al. (BASJE), Proc. 30th ICRC **4** 127 (2008); K.-H. Kampert & M. Unger, APh **35** 660 (2012).

[3] R.A. Antonov et al., Phys. Part. Nucl. (2015) (In press).

[4] A.E. Chudakov, Proc. All-USSR Symp. on Exp. Meth. of UHECR (Yakutsk) (In Russian) 69 (1974).

[5] C. Castagnoli et al., Proc. 17th ICRC **6** 103 (1981).

[6] R.A. Antonov et al., Nucl. Phys. (Proc. Suppl.) **B52** 182 (1997); R.A. Antonov et al., Proc. 27th ICRC **1** 59 (2001).

[7] D. Heck et al., FZKA Report 6019 (1998); N. Kalmykov et al., Nucl. Phys. (Proc. Suppl.) **B52** 17 (1997); H.C. Fesefeldt, Technical Report No. PITHA 85-02 RWTH (1985).

[8] S. Agostinelli et al., NIM **A506** 250 (2003).

[9] L.G. Dedenko et al., Nucl. Phys. (Proc. Suppl.) **B136** 1217 (2004).

[10] R.A. Antonov et al., 33^{rd} ICRC (Rio), id. 1185 (2013).

[11] W.D. Apel et al. (KASCADE-Grande), APh **36** 183 (2012).

[12] M. Nagano et al., J. Phys. G **18** 423 (1992).

[13] M.G. Aartsen et al., Phys. Rev. D **88** 042004 (2013); S.P. Knurenko et al., 33^{rd} ICRC (Rio), id. 53 (2013); S.P. Knurenko, A. Sabourov, EPJ Web of Conf. **53** 04004 (2013); M. Fukushima, Talk at ISVHECRI-2014 (2014).

[14] Antonov et al., J. Phys. Conf.Ser. **409** 012088 (2013).

[15] W.D. Apel et al. (KASCADE-Grande), Phys. Rev. D. (2013).

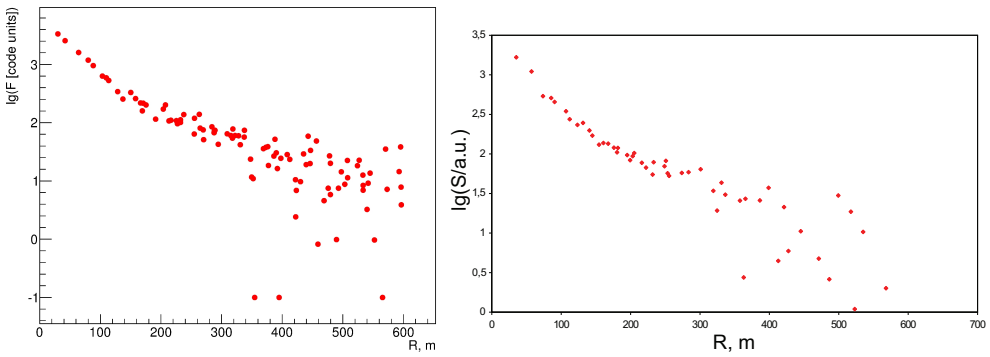

Figure 2: Two examples of reconstructed experimental LDFs: left — for the first analysis, right — for the second analysis.

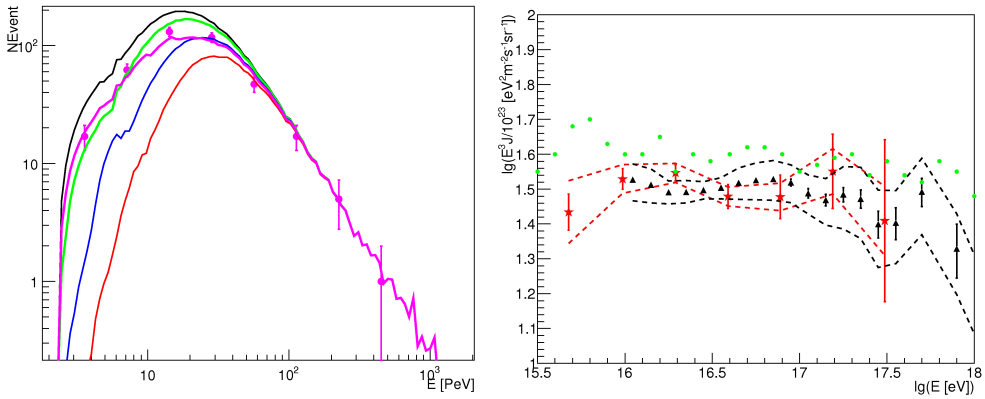

Figure 3: Left — model energy distribution for different composition assumptions (curves) and experimental energy distribution for the 2013 run data (circles). Right — the all-nuclei spectrum reconstructed for the 2011–2013 runs (stars) along with the KASKADE-Grande and Akeno results.

Chapter 8

Tests of symmetries and conservation laws

^{3}He/^{129}Xe Clock Comparison Experiment: Search for Spin-Dependent Short-Range Interaction

Kathlynne Tullney[1], *Fabian Allmendinger*[2], *Werner Heil*[1], *Sergei Karpuk*[1], *Yuri Sobolev*[1], *Ulrich Schmidt*[2]

[1]Institut für Physik, Johannes Gutenberg-Universität Mainz, Germany
[2]Physikalisches Institut, Ruprecht-Karls-Universität Heidelberg, Germany

DOI: http://dx.doi.org/10.3204/DESY-PROC-2014-04/69

We report on the search for a new spin–dependent interaction $\vec{\sigma}\cdot\hat{r}$ which causes a shift in the precession frequency of nuclear spin polarized gases. Therefore we use a comagnetometer that is based on the detection of freely precessing nuclear spins from ^{3}He and ^{129}Xe gas samples using SQUIDs as low–noise magnetic flux detectors. As result we could improve the upper bounds of the dimensionless product $g_s g_p$ of the monopole–dipole coupling of an axion to the spin of a bound neutron in the mass range between 2 μeV and 500 μeV (corresponding to force ranges between $3 \cdot 10^{-4}$ m and 10^{-1} m) by up to 4 orders of magnitude.

The existence of a new spin–dependent short–range force may be a signature of pseudoscalar boson particles like the axion, which was proposed by Peccei and Quinn to solve the strong *CP* problem [1]. This hypothetical particle could have been created in early stages of the universe and since it is a light and weak interacting particle, it is an attractive candidate to the cold dark matter that could compose up to 1/3 of the ingredients of the universe [2]. An axion or any axion–like particle mediates an interaction between a fermion f and the spin of another fermion f_σ which in case of monopole-dipole coupling violates parity and time symmetries. The Yukawa-type potential of this monopole-dipole interaction with range λ is given by [3]

$$V_{\mathrm{sp}}(r) = \frac{\hbar^2 g_s^f g_p^{f_\sigma}}{8\pi m}(\vec{\sigma}\cdot\hat{r})\left(\frac{1}{\lambda r}+\frac{1}{r^2}\right)e^{-r/\lambda}\ , \tag{1}$$

where g_s^f and $g_p^{f_\sigma}$ are dimensionless scalar and pseudoscalar constants for the axion-fermion vertices, which in our case correspond to the scalar coupling of an axion or an axion-like particle to a nucleon ($g_s^f = g_s^N$) and its pseudoscalar coupling to a polarized bound neutron ($g_p^{f_\sigma} = g_p^n$). $\hat{r}$ is the unit distance vector pointing from the polarized fermion to the unpolarized fermion, respectively from the polarized sample to the unpolarized sample. λ is the range of the Yukawa force with $\lambda = \hbar/m_a c$, m_a is the mass of the axion and m is the mass of the fermion which carries the spin $\vec{\sigma}$. The potential given by Eq. 1 effectively acts near the surface of a massive unpolarized sample ($r \leq \lambda$) as a pseudo-magnetic field and gives rise to a shift $\Delta\omega_{\mathrm{sp}} = 2\pi\Delta\nu_{\mathrm{sp}} = V_\Sigma/\hbar$ in the precession frequency of nuclear spin polarized gases. The potential V_Σ is obtained by integration of $V_{\mathrm{sp}}(r)$ from Eq. 1 over the volume of the massive unpolarized sample averaged over the volume of the polarized sample.

Our approach to search for non-magnetic spin-dependent interactions is to use an ultrasensitive low-field comagnetometer which is based on simultaneous detection of free spin precession of

gaseous, nuclear spin polarized ^{3}He and ^{129}Xe atoms. The Larmor frequencies of helium and xenon in a constant magnetic guiding field B are given by $\omega_{\mathrm{L,He(Xe)}} = \gamma_{\mathrm{He(Xe)}} \cdot B$, whereby $\gamma_{\mathrm{He(Xe)}}$ are the gyromagnetic ratios of the according gas species. Hence, the influence of ambient magnetic fields cancels in the weighted difference of Larmor frequencies, respectively, the corresponding time integral, the weighted difference of Larmor phases

$$\Delta\omega = \omega_{\mathrm{He}} - \frac{\gamma_{\mathrm{He}}}{\gamma_{\mathrm{Xe}}} \cdot \omega_{\mathrm{Xe}} = 0\,, \quad \Delta\Phi(t) = \Phi_{\mathrm{He}}(t) - \frac{\gamma_{\mathrm{He}}}{\gamma_{\mathrm{Xe}}} \cdot \Phi_{\mathrm{Xe}}(t) = const\,. \tag{2}$$

For the gyromagnetic ratios of helium and xenon we took the literature values given by $\gamma_{\mathrm{He}}/\gamma_{\mathrm{Xe}} = 2.75408159(20)$ [5, 6]. The quantities $\Delta\omega$ and $\Delta\Phi(t)$ are sensitive to anomalous frequency shifts due to non–magnetic spin interactions. According to the Schmidt model [4], in the nuclei of helium and xenon the spin of 1/2 is carried by a neutron only. Thus, the frequency shift $\Delta\nu_{\mathrm{sp}}$ due to the spin–dependent short–range force (Eq. 1) is expected to be similar for ^{3}He and ^{129}Xe. Hence, the frequency shift $\Delta\nu_{\mathrm{sp}}$ does not drop out in the the weighted frequency, respectively, weighted phase difference (Eq. 2). A detailed description of this comagnetometer can be found in [7].

1 Experimental Setup and Principle of Measurements

The experiment was performed inside the magnetically shielded room BMSR-2 at the Physikalisch Technische Bundesanstalt Berlin (PTB). BMSR-2 has a passive shielding factor, which exceeds 10^8 above 6 Hz. A homogeneous guiding magnetic field of about 350 nT - with maximum field gradients of about 33 pT/cm - was provided inside the shielded room by means of a square coil pair (B_x-coils). With a second square coil pair (B_y-coils) which was arranged perpendicular to the first one it was possible to manipulate the precession of the spin samples, e.g., $\pi/2$ spin flip by nonadiabatic switching [7]. For detection of the spin precession we used a low-T_c DC–SQUID vector magnetometer system [8, 9]. The pick-up coils of the SQUIDs were sensitive to the vertical magnetic field component of the two precessing nuclear spin species (^{3}He, ^{129}Xe). The system noise of the SQUIDs was about 2.3 fT/$\sqrt{\mathrm{Hz}}$ in the range of the precession frequencies. Most part of the environmental noise was caused by dewar vibrations relative to the B_x-coils. Here, combining two SQUIDs to a gradiometer helps to suppress this effect down to a level of 2.5 fT/$\sqrt{\mathrm{Hz}}$. As gas container we used a cylindrical cell made of aluminosilicate glass (GE180) with a diameter of 58 mm and a length of 60 mm. ^{3}He and ^{129}Xe were nuclear spin polarized outside the shielding by means of optical pumping. Afterwards the cell was filled with a mixture of polarized ^{3}He, polarized ^{129}Xe (≈ 2 mbar, ≈ 8 mbar) and N_2 (≈ 35 mbar). The nitrogen was added to suppress xenon relaxation due to the van der Waals molecular coupling. After transportation of the measurement cell into the BMSR-2 the cell was mounted directly beneath the dewar which houses the SQUIDs. A cylindrical glass tube with a length of 1 m and an inner diameter of 60 mm was placed on a separate support with its axis aligned with the axis of the cylindrical measurement cell. At its open end towards the polarized sample cell a BGO–crystal (BGO = $Bi_4Ge_3O_{12}$, ρ=7.13 g/cm^3, diameter 60 mm and length 70 mm) was installed. The tube and with it the BGO–crystal could be moved horizontally from "close"–position to "distant"–position and vice versa, whereby the movement of the glass tube was possible without opening the door of the magnetic shielded room, i.e., without interruption of the ^{3}He and ^{129}Xe spin precession. At "close"–position we had a minimum gap of 2.2 mm between the BGO–crystal and the polarized gases. The BGO–crystal was used, since a non-conducting material prevented us from additional noise sources.

If the spin–dependent axion fermion interaction exist it will cause a shift $\Delta\omega_{\rm sp}^{w}$ in the weighted precession frequency difference (Eq. 2) when the BGO–crystal is close ("close"–position) to the measurement cell. If the BGO–crystal is far away ("distant"–position) from the measurement cell this frequency shift should vanish. To measure this frequency shift $\Delta\omega_{\rm sp}^{w}$ the measurement procedure was as follows: The spin precession signals were measured whereby the BGO-crystal was installed close to the cell ("close"–position). After 10800 s the BGO–crystal was moved away ("distant"–position). The spin precession signals were then measured again for about 21500 s. It was also possible to do measurements where the BGO-crystal was first in the "distant"–position and in the second part of the measurement in the "close"-position. These measurements were repeated several times whereby for systematic checks, the BGO–crystal could be placed left and right with respect to the ^{3}He/^{129}Xe sample cell.

2 Data Analysis and Results

A detailed despription of the data analysis is described in [10, 11]. Briefly, for each measurement run – in total we did 10 runs – the accumulated phases and with it the corresponding phase difference $\Delta\Phi(t)$ was determined, which is not a constant in time, as Eq. 2 may suggest. Instead higher order effects, as Earth rotation, chemical shift and the generalized Ramsey-Bloch-Siegert-Shift [11], have to be taken into account. These effects can be parameterized by

$$\Delta\Phi(t) = \Phi_0 + \Delta\omega_{\rm lin}\cdot t - \epsilon_{\rm He}\cdot T^{*}_{2,\rm He}\cdot A_{\rm He}\cdot e^{-\frac{t}{T^{*}_{2,\rm He}}} + \epsilon_{\rm Xe}\cdot T^{*}_{2,\rm Xe}\cdot A_{\rm Xe}\cdot e^{-\frac{t}{T^{*}_{2,\rm Xe}}} \ . \qquad (3)$$

If the pseudoscalar Yukawa potential $V_{\rm sp}(r)$ would occur at an instant $t = t_0$ due to the movement of the BGO–crystal, an additional linear phase drift $\Delta\omega_{\rm sp}^{w}\cdot(t-t_0) = 2\pi\cdot\Delta\nu_{\rm sp}^{w}\cdot\Theta(\pm(t-t_0))\cdot(t-t_0)$ in Eq. 3 is expected[1]. The frequency shift $\Delta\nu_{\rm sp}$ is then extracted from

$$\Delta\nu_{\rm sp} = \frac{\Delta\omega_{\rm sp}^{w}}{2\pi\cdot(1-\frac{\gamma_{\rm He}}{\gamma_{\rm Xe}})} \ . \qquad (4)$$

For each measurement run $\Delta\nu_{\rm sp}$ was determinded. From the calculation of the weighted mean, one gets $\overline{\Delta\nu}_{\rm sp} = (-2.9\pm2.3\pm0.1)$ nHz. The last value corresponds to the systematic error[2]. The $\chi^2/d.o.f$ of the data to their weighted mean $\overline{\Delta\nu}_{\rm sp}$ gives 2.29, indicating that the errors on the measured frequency shifts are somewhat underestimated. In order to take this into account, the errors were scaled to obtain a χ^2/d.o.f of one, as recommended, e.g., by [12, 13]. At the 95% C.L., our result for the measured frequency shift is

$$\overline{\Delta\nu}_{\rm sp} = (-2.9\pm6.9\pm0.2)\ \text{nHz}\ . \qquad (5)$$

The result of $\overline{\Delta\nu}_{\rm sp}$ indicates that we find no evidence for a pseudoscalar short–range interaction mediated by axions or axion–like particles.
From the total error $\delta(\overline{\Delta\nu}_{\rm sp}) = \pm7.1$ nHz exclusion bounds for $\left|g_s^N g_p^n\right|$ can be derived by calculating V_Σ and using $|\delta(\overline{\Delta\nu}_{\rm sp})| \geq 2\cdot V_\Sigma/h$. The results are shown in Fig.1. We substantially improved the bounds on a spin–dependent short–range interaction between polarized (bound) neutrons and unpolarized nucleons over most of the axion window. Existing constraints on axions or axion–like particles heavier than 20 μeV could be tightened by up to four orders of magnitudes.

[1] $(\pm)$ in the argument of the Heaviside step function has to be set (-) for the sequence c→d and (+) for the reverse one d→c.

[2] A detailed description of the calculation of the systematic error is given in [11].

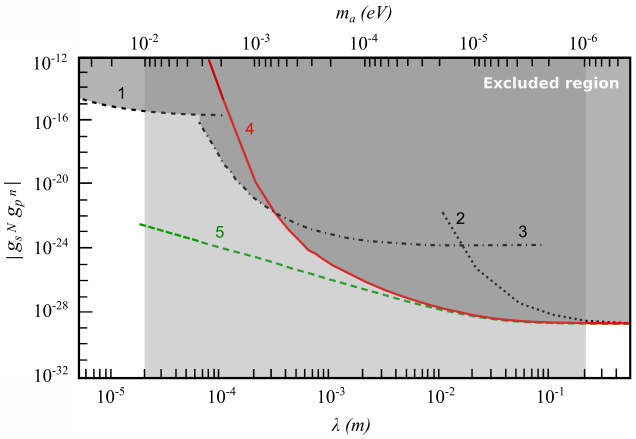

Figure 1: The experimental 95% confidence upper limit on $\left|g_s^N g_p^n\right|$ plotted versus the range λ of the Yukawa-force with $\lambda = \hbar/(m_a c)$. The light gray area indicates the axion window. (1): result of [14], (2): result of [15], (3): result of [16], (4): this experiment ($\Delta x = 2.2$ mm), (5): expected results for Δx≈ 0 mm using $\delta(\overline{\Delta\nu}_{\rm sp}) = \pm 7.1$ nHz demonstrates the gain in measurement sensitivity for $\lambda < 10^{-3}$ m. For bounds on the pseudoscalar short–range force between polarized electrons and unpolarized nucleons see [17].

References

[1] C.D. Peccei, H.R. Quinn, Phys. Rev. Lett. **38**, 1440 (1977)

[2] J. Jaeckel, A. Ringwald, Annu. Rev. Nucl. Part. Sci. **60**, 405 (2010)

[3] J.E. Moody, F. Wilczek, Phys. Rev. D **30**, 130 (1984)

[4] Th. Schmidt, Zeitschrift für Physik A Hadronen und Kerne **10**6, 358 (1937)

[5] International council for Science: Committee on Data for Science and Technology (CODATA), www.codata.org (2007)

[6] M. Pfeffer and O. Lutz, J. Magn. Res. A **108**, 106 (1994)

[7] C. Gemmel *et al.*, Eur. Phys. Journal D **57**, 303 (2010)

[8] D. Drung, Physica C **368**, 134 (2002)

[9] M. Burghoff *et al.* IEEE Trans. App. Supercon. **17**, 846 (2007)

[10] C. Gemmel *et al.* Phys. Rev. D **82**, 111901(R) (2010).

[11] K. Tullney *et al.* Phys. Rev. Lett. **111**, 100801 (2013)

[12] The Particle Data Group Phys. Lett. B **592**, 14 (2004)

[13] W.H. Press, S.A. Tenkolsky, W.T. Vetterling and B.P. Flannery *Numerical Recipes 3rd Edition: The Art of Scientific Computing.*, Cambridge University Press, New York (2007)

[14] T. Jenke *et al.* Phys. Rev. Lett. **112**, 151105 (2014)

[15] A.N. Youdin *et al.* Phys. Rev. Lett. **77**, 2170 (1996)

[16] M. Bulatowicz *et al.* Phys. Rev. Lett. **111**, 102001 (2013)

[17] S.A. Hoedel Phys. Rev. Lett. **106**, 041801 (2011)

Search for T-invariance Violation in the Proton-Deuteron Scattering

Azamat Temerbayev[1], *Yury Uzikov*[2]

[1]ENU, Kazhymukhan 5, Astana, 010008 Kazakhstan
[2]JINR, Joliott-Curie 6, Dubna, 141890 Russia

DOI: http://dx.doi.org/10.3204/DESY-PROC-2014-04/86

The spin-dependent Glauber theory is used to calculate differential observables and integrated polarized cross sections of the *pd* scattering at proton beam energy 135 MeV. In addition to the pure strong NN interactions, the Coulomb effects and T-invariance violating but P-parity conserving interactions are considered. This study is motivated by the TRIC experiment planned at COSY to test time-reversal symmetry.

1 Introduction

Under assumption of CPT-symmetry, CP violation established in physics of kaons and B-mesons implies existence of T-odd P-odd interactions. These interactions are parametrized in the standard model by CP violating phase of the Cabibbo-Kobayashi-Maskawa matrix. On the contrary, time-invariance-violating (T-odd) P-parity conserving (P-even) flavor conserving (TVPC) interactions do not arise on the fundamental level within the standard model. This type of interaction can be generated by radiative corrections to the T-odd P-odd interaction. However in such a case its intensity is too small to be observed in experiments at present [1]. Thus, observation of TVPC effects would be considered as indication to physics beyond the standard model.

The goal of the TRIC experiment [2] is the measurement of the total polarized cross section $\widetilde{\sigma}$ of the proton-deuteron scattering with vector polarization of the proton p_y^p and tensor polarization of the deuteron P_{xz} (see below Eq. (4)). As it was shown in Ref. [3], this observable constitutes a null-test of TVPC effects. According to [4], the experiment [2] will be done at beam energy 135 MeV. The aim of this experiment is to improve the results of previous measurement [5] on $\vec{n}^{167}$Ho scattering by one order of magnitude. In this case, detailed information on the ordinary T-even P-even spin observables at this energy is required in order to determine magnitude of possible false-effects caused by pure strong and Coulomb interaction due to non-ideal conditions of the experiment. However, experimental data on these observables at this energy are not complete. In the present work we use the Glauber theory to calculate unpolarized differential cross section and spin observables of the elastic *pd* scattering and total polarized *pd* cross sections. The spin-dependent formalism of the pd-elastic scattering is recently developed in Ref. [6]. The formalism includes full spin dependence of elementary pN-amplitudes and S- and D-components of the deuteron wave function. We further develop the formalism to account for Coulomb effects and TVPC interactions.

2 Elements of formalism

Assuming P-invariance the transition operator for the process $pd \to pd$ can be written as [7]

$$\begin{aligned} M = (A_1 + A_2\boldsymbol{\sigma}\hat{\mathbf{n}}) + (A_3 + A_4\boldsymbol{\sigma}\hat{\mathbf{n}})(\mathbf{S}\hat{\mathbf{q}})^2 + (A_5 + A_6\boldsymbol{\sigma}\hat{\mathbf{n}})(\mathbf{S}\hat{\mathbf{n}})^2 + A_7(\boldsymbol{\sigma}\hat{\mathbf{k}})(\mathbf{S}\hat{\mathbf{k}}) + \\ A_8(\boldsymbol{\sigma}\hat{\mathbf{q}})\left[(\mathbf{S}\hat{\mathbf{q}})(\mathbf{S}\hat{\mathbf{n}}) + (\mathbf{S}\hat{\mathbf{n}})(\mathbf{S}\hat{\mathbf{q}})\right] + (A_9 + A_{10}\boldsymbol{\sigma}\hat{\mathbf{n}})(\mathbf{S}\hat{\mathbf{n}}) + A_{11}(\boldsymbol{\sigma}\hat{\mathbf{q}})(\mathbf{S}\hat{\mathbf{q}}) + \\ A_{12}(\boldsymbol{\sigma}\hat{\mathbf{k}})\left[(\mathbf{S}\hat{\mathbf{k}})(\mathbf{S}\hat{\mathbf{n}}) + (\mathbf{S}\hat{\mathbf{n}})(\mathbf{S}\hat{\mathbf{k}})\right] \\ +(T_{13} + T_{14}\boldsymbol{\sigma}\hat{\mathbf{n}})\left[(\mathbf{S}\hat{\mathbf{k}})(\mathbf{S}\hat{\mathbf{q}}) + (\mathbf{S}\hat{\mathbf{q}})(\mathbf{S}\hat{\mathbf{k}})\right] + T_{15}(\boldsymbol{\sigma}\hat{\mathbf{q}})(\mathbf{S}\hat{\mathbf{k}}) + T_{16}(\boldsymbol{\sigma}\hat{\mathbf{k}})(\mathbf{S}\hat{\mathbf{q}}) + \\ T_{17}(\boldsymbol{\sigma}\hat{\mathbf{k}})\left[(\mathbf{S}\hat{\mathbf{q}})(\mathbf{S}\hat{\mathbf{n}}) + (\mathbf{S}\hat{\mathbf{n}})(\mathbf{S}\hat{\mathbf{q}})\right] + T_{18}(\boldsymbol{\sigma}\hat{\mathbf{q}})\left[(\mathbf{S}\hat{\mathbf{k}})(\mathbf{S}\hat{\mathbf{n}}) + (\mathbf{S}\hat{\mathbf{n}})(\mathbf{S}\hat{\mathbf{k}})\right], \end{aligned} \tag{1}$$

were $\boldsymbol{\sigma}$ is the Pauli matrix acting on the spin state of the proton beam, $\mathbf{S}$ is the spin operator of the deuteron; the unit vectors $\hat{\mathbf{q}}$, $\hat{\mathbf{k}}$, $\hat{\mathbf{n}}$ are defined through initial $\mathbf{p}$ and final $\mathbf{p}'$ momenta as $\hat{\mathbf{q}} = (\mathbf{p} - \mathbf{p}')/|\mathbf{p} - \mathbf{p}'|$, $\hat{\mathbf{k}} = (\mathbf{p} + \mathbf{p}')/|\mathbf{p} + \mathbf{p}'|$, $\hat{\mathbf{n}} = [\hat{\mathbf{k}} \times \hat{\mathbf{q}}]/|[\hat{\mathbf{k}} \times \hat{\mathbf{q}}]|$; $A_1 \div A_{12}$ are T-even P-even invariant amplitudes introduced in Ref. [6], $T_{13} \div T_{18}$ are T-odd P-even (TVPC) amplitudes. The reference frame is defined as $OZ \uparrow\uparrow \hat{\mathbf{k}}$, $OX \uparrow\uparrow \hat{\mathbf{q}}$, $OY \uparrow\uparrow \hat{\mathbf{n}}$. Under T-invariance conditions $T_{13} = T_{14} = T_{15} = T_{16} = T_{17} = T_{18} = 0$ the following relations between spin transfer coefficients are valid [7]

$$\begin{aligned} K_x^z(\vec{p} \to \vec{p}) = -K_z^x(\vec{p} \to \vec{p}),\ K_x^z(\vec{p} \to \vec{d}) = -K_z^x(\vec{d} \to \vec{p}), \\ K_x^z(\vec{d} \to \vec{p}) = -K_z^x(\vec{p} \to \vec{d}),\ K_x^z(\vec{d} \to \vec{d}) = -K_z^x(\vec{d} \to \vec{d}). \end{aligned} \tag{2}$$

In addition the relations $A_y^p = P_y^p$ and $A_y^d = P_y^d$ are also valid, where A_y^p (A_y^d) is the vector analyzing power for the proton (deuteron) and P_y^p (P_y^d) is the polarization of the final proton (deuteron) for the case of unpolarized initial particles.

In general case TVPC NN interaction contains 18 different terms [8]. We consider here only following terms which were under discussion in Ref. [4]:

$$\begin{aligned} t_{pN} = h[(\boldsymbol{\sigma} \cdot \mathbf{p})(\boldsymbol{\sigma}_N \cdot \mathbf{q}) + (\boldsymbol{\sigma}_N \cdot \mathbf{p})(\boldsymbol{\sigma} \cdot \mathbf{q}) - (\boldsymbol{\sigma}_N \cdot \boldsymbol{\sigma})(\mathbf{p} \cdot \mathbf{q})] + \\ +g[\boldsymbol{\sigma} \times \boldsymbol{\sigma}_N] \cdot [\mathbf{q} \times \mathbf{p}] + g'(\boldsymbol{\sigma} - \boldsymbol{\sigma}_N) \cdot i\,[\mathbf{q} \times \mathbf{p}][\boldsymbol{\tau} \times \boldsymbol{\tau}_N]_z. \end{aligned} \tag{3}$$

Here $\boldsymbol{\sigma}$ ($\boldsymbol{\sigma}_N$) is the Pauli matrix acting on the spin state of the proton (nucleon $N = p, n$), $\boldsymbol{\tau}$ ($\boldsymbol{\tau}_N$) is the corresponding matrix acting on the isospin state, $\mathbf{q} = \mathbf{p} - \mathbf{p}'$. In the framework of the phenomenological meson exchange interaction the term g' corresponds to $\rho-$meson exchange, and h-term provides the axial meson exchange. In the single scattering approximation accounting S- and D- waves of the deuteron we obtain only two non-zero amplitudes: T_{15} and T_{16} [7]. Other TVPC amplitudes vanish in this case: $T_{13} = T_{14} = T_{17} = T_{18} = 0$. The charge-exchange g'-term gives zero-contribution because the corresponding isospin matrix element equals zero for the single scattering mechanism of the $pd \to pd$ process.

In collinear kinematics the transition operator (1) contains only four terms (invariant spin amplitudes) for the case of T-even P-even interaction and one additional term for T-odd P-even interactions. Consequently, the total cross section of the pd interaction takes the form

$$\sigma_{tot} = \sigma_0 + \sigma_1 \mathbf{p}^p \cdot \mathbf{p}^d + \sigma_2 (\mathbf{p}^p \cdot \hat{\mathbf{k}})(\mathbf{p}^d \cdot \hat{\mathbf{k}}) + \sigma_3 P_{zz} + \widetilde{\sigma} p_y^p P_{xz}^d, \tag{4}$$

where $\mathbf{p}^p$ ($\mathbf{p}^d$) is the vector polarization of the initial proton (deuteron) and P_{zz} and P_{xz} are the tensor polarizations of the deuteron. The OZ axis is directed along the proton beam

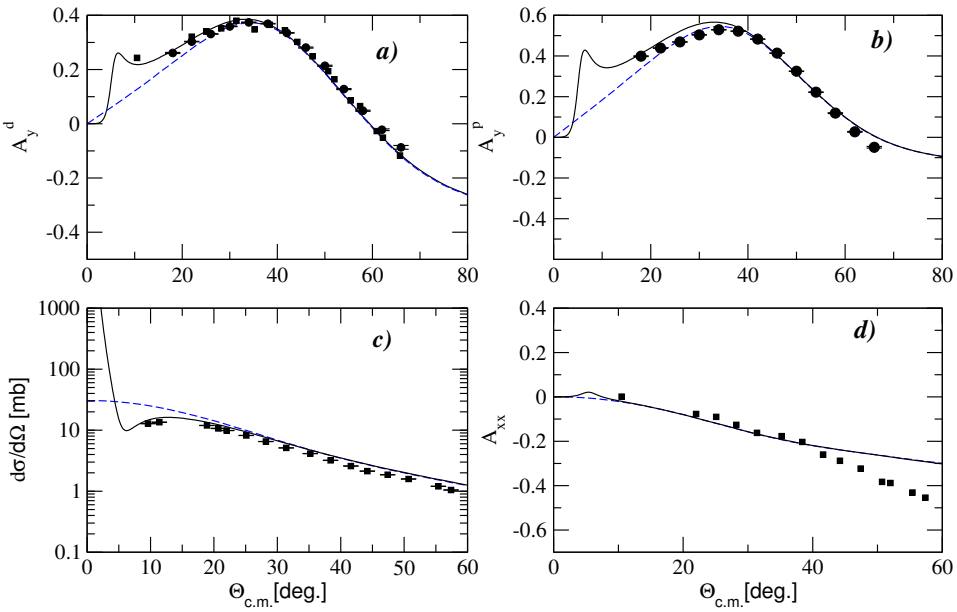

Figure 1: Result of our calculations [10] of spin observables A_y^d(a), A_y^p (b), $d\sigma/d\Omega$ (c) and A_{xx} (d) of the *pd* elastic scattering in comparison with the data [11] (squares) and [12] (circles) at 135 MeV: without Coulomb (dashed line) and with Coulomb included (full).

momentum. In Eq. (4) the terms σ_i with $i = 0, 1, 2, 3$ are non-zero only for T-even P-even interaction and the last term $\widetilde{\sigma}$ is non-zero if the T-odd P-even interaction effects occur. Thus, this term constitutes a null-test signal of T-invariance violation with P-parity conservation. The total hadronic polarized cross sections σ_1 and σ_3 are calculated using the optical theorem, whereas Coulomb effects are taken into account in the line of Ref. [9].

3 Numerical results and discussion

The detailed formalism for T-even P-even amplitudes $A_1 \div A_{12}$ was developed within the Glauber model in Ref. [6] taking into account single and double scattering mechanisms, S- and D-components of the deuteron wave function and full spin dependence of the elementary pN scattering amplitudes. We use this formalism to calculate spin observables of the *pd*-elastic scattering at energy of the TRIC experiment, i.e. $T = 135$ MeV. In addition to Ref. [6] we take into account the Coulomb interaction, as explained in [10] within the single scattering mechanism. Some results of numerical calculations performed with the Cd Bonn wave function of the deuteron are shown in Fig. 1. One can see from this figure, that the Glauber model allows to explain data on unpolarized cross section, vector analyzing powers A_y^p, A_y^d and tensor analyzing power in forward hemisphere. Accounting for the Coulomb interaction is very important at these energies and considerably improves the agreement with the experimental data [11, 12] at small c.m.s. scattering angles $\theta_{cm} < 20^\circ - 30^\circ$. We can show [10] that good agreement was obtained also between this theory and the data [12] on spin-correlation coefficients $C_{xz,y}$, $C_{y,y}$,

$C_{x,z}$, and $C_{z,x}$ of the pd elastic scattering at 135 MeV in forward hemisphere.

The constants g and h in Eq. (3) are chosen here in such a way that the absolute value of the integrated cross section $\tilde{\sigma}$ in Eq. (4) would be $\tilde{\sigma}/\sigma_0 = 10^{-6}$. One should note that the aim of the TRIC experiment is to get an upper limit for the TVPC signal $\tilde{\sigma}$ just at this level. We show [7] that in this case the maximal magnitudes of the violation of the relations (2) (in forward hemisphere, $\theta_{cm} < 50^\circ$) are $2 \div 3 \times 10^{-4}$ for $|K_x^z(p \to d) + K_z^x(d \to p)|$, $|A_y^p - P_y^p| \sim 3 \times 10^{-5}$ and much more lower for others relations. Thus, $|K_x^z(p \to d) + K_z^x(d \to p)|$ is by two orders of magnitude higher than $\tilde{\sigma}/\sigma_0$. Nevertheless, the null-test observable $\tilde{\sigma}$ can be measured in one experiment, whereas measurement of $|A_y^p - P_y^p|$ and $|K_x^z(pd) + K_z^x(dp)|$ requires two or more experiments with measurement of polarizations of final particles.

Let us consider possible problems in measurement of the null-test observable $\widetilde{\sigma}$. One source of false-effects is connected with non-zero projection of the vector polarization of the deuteron $p_y^d \neq 0$ onto direction of the vector polarization of the proton beam p_y^p. In this case the term $\sigma_1 p_y^p p_y^d$ in Eq. (4) contributes to the asymmetry $A_{xz,y}$ which is planned to be measured in the TRIC experiment [2] and corresponds to the cases $p_y^p P_{xz}^d > 0$ and $p_y^p P_{xz}^d < 0$. According to our calculation, at beam energy 135 MeV the total cross sections are $\sigma_0 = 78.5$ mb, $\sigma_1 = 3.7$ mb, $\sigma_2 = 17.4$ mb, and $\sigma_3 = -1.1$ mb. Therefore, the ratio $r = \sigma_1/\sigma_0$ is equal to ≈ 0.05. If the TRIC project is going to measure the ratio $R_T = \widetilde{\sigma}/\sigma_0$ with an uncertainty about $\leq 10^{-6}$ (an upper limit for R_T), then one can find from this ratio r that the vector polarization of the deuteron p_y^d has to be less than $\approx 2 \times 10^{-6}$. When making this estimation, we assume that the ratio of the background-to-signal is $p_y^d \sigma_1/\widetilde{\sigma} \sim 10^{-1}$.

4 Summary

We found that the Glauber model with Coulomb interaction taken into account reasonably explains existing data on unpolarized differential cross section and some spin observables of pd elastic scattering at 135 MeV in forward hemisphere. This provides a theoretical basis for estimation of possible false-effects in the TRIC experiment [2] planned at this energy.

References

[1] I.B. Khriplovich, Nucl. Phys. **B352** 385 (1991).

[2] COSY Proposal N 215, "Test of Time reversal invariance in proton-deuteron scattering at COSY", Spokespersons: D. Eversheim, B. Lorentz, Yu. Valdau, available from http://donald.cc.kfa-juelich.de/wochenplan/List of all COSY-Proposals.shtml.

[3] H.E. Conzett, Phys. Rev. **C48** 423 (1993).

[4] M. Beyer, Nucl. Phys. **A560** 906 (1993).

[5] P.R. Huffman *et al.*, Phys. Rev. **C55** 2684 (1997).

[6] M.N. Platonova, V.I. Kukulin, Phys. Rev. **C81** 014004 (2010).

[7] A.A. Temerbayev, Yu.N. Uzikov, Izv. Ross. Akad. Nauk Ser. Fiz. (2015) (in press).

[8] P. Herczeg, Nucl. Phys. **75** 655 (1966).

[9] Yu.N. Uzikov, J. Haidenbauer, Phys. Rev. **C79** (2009) 024617.

[10] A.A. Temerbayev, Yu.N. Uzikov, Yad. Fiz. **78** 38 (2015).

[11] K. Sekiguchi *et al.*, Phys. Rev. **C65** 034003 (2002).

[12] B. von Przewoski *et al.*, Phys. Rev. **C74** 064003 (2006).

Parity Violation Inelastic Scattering Experiments at 6 GeV and 12 GeV Jefferson Lab

Vincent Sulkosky[1] for the JLab PVDIS and SoLID collaborations

[1]University of Virginia, Charlottesville, Virginia 22904, USA

DOI: http://dx.doi.org/10.3204/DESY-PROC-2014-04/257

We report on the measurement of parity-violating asymmetries in the deep inelastic scattering and nucleon resonance regions using inclusive scattering of longitudinally polarized electrons from an unpolarized deuterium target. The effective weak couplings C_{2q} are accessible through the deep-inelastic scattering measurements. Here we report a measurement of the parity-violating asymmetry, which yields a determination of $2C_{2u}$ - C_{2d} with an improved precision of a factor of five relative to the previous result. This result indicates evidence with 95% confidence that the $2C_{2u}$ - C_{2d} is non-zero. This experiment also provides the first parity-violation data covering the whole resonance region, which provide constraints on nucleon resonance models. Finally, the program to extend these measurements at Jefferson Lab in the 12 GeV era using the Solenoidal Large Intensity Device was also discussed.

1 Introduction

In parity-violating electron scattering (PVES), the PV asymmetry is given by the expression: $A_{PV} = \frac{\sigma_R - \sigma_L}{\sigma_R + \sigma_L}$, where σ_R (σ_L) represents the cross-section for scattering longitudinally polarized right-handed (left-handed) electrons. This observable is highly sensitive to studies beyond the standard model physics and the structure of both nuclei and nucleons [1]. In deep inelastic scattering (DIS), the asymmetry can be expressed (mostly model-independent) in terms of the variables $a_{1,3}\left(x, Q^2\right)$, which are related to the subatomic structure of the nucleus and the neutral-weak axial and vector coupling of the electron and the quark. Here, x is the Bjorken scaling variable, and Q^2 is the four-momentum transferred squared.

In the approximation where the electron exchanges only a single photon or Z boson with the target, simple expressions for $a_{1,3}$ can be expressed for a deuteron target in the valence quark model:

$$a_1 = \frac{6}{5}\left(2C_{1u} - C_{1d}\right), a_3 = \frac{6}{5}\left(2C_{2u} - C_{2d}\right).$$

The $C_{1u(1d)}$ and $C_{2u(2d)}$ represent the effective weak couplings between electrons and up (down) quarks. Sometimes, they are collectively expressed as C_{1q} and C_{2q}. The indices 1 and 2 correspond to if the coupling to the electron or quark is vector or axial-vector. C_{1q} is the (AV) combination of the electron's axial-vector weak charge and the quark's vector weak charge. Then C_{2q} is the (VA) combination of the electron's vector weak charge and the quark's axial-vector weak charge. The C_{2q} is sensitive to PV due to the quark chiral states and can only be direclty accessed in DIS, whereas, C_{1q} can also be obtained from elastic PVES. SLAC E122 [2] was

the first PVES experiment and provided the first measurement for $\sin^2\theta_w$. It also established the gauge model of Weinberg, Glashow, and Salam as the correct theory for the electroweak interactions.

2 Experimental Procedure

The measurements reported at the conference were conducted using a 5−6 GeV longitudinally-polarized electron beam at Jefferson Lab. The beam current was ~ 100 μA with approximately 90% polarization. The electron beam was incident on a 20-cm long liquid deuterium target controlled at a temperature of 22 K. The scattered electrons were detected in a pair of spectrometers [3] that provided high precision measurements of their momentum and angle. For the majority of the run period, the spectrometers were set to detect DIS electrons [4]. However, additional data were also collected in four kinematic settings, which covered the entire nucleon resonance region [5]. Besides providing constraints on nucleon resonance models, these data also exhibited a feature known as "quark-hadron duality" [6] for electroweak observables for the first time.

3 Results

3.1 Nucleon resonance region

Figure 1 shows the measured PV asymmetries, scaled by $1/Q^2$, from $\vec{e}$-^{2}H scattering in the resonance region versus W. The vertical error bars represent the statistical uncertainties, whereas the horizontal bars indicate the RMS value of the W coverage for each bin. The shaded band near the bottom of the graph shows the experimental systematic uncertainties. The measured asymmetries are consistent with the three resonance models [7, 8, 9]. In Fig. 1, theory A (dashed lines), theory B (dotted lines) and theory C (solid lines) correspond to Refs. [7], [8] and [9], respectively. In the case of Theories B and C, there are three curves, which indicate the upper and lower bands and central values of the two calculations. These data also agree well with the DIS estimation (dash-double-dotted lines) using CTEQ-Jefferson Lab (CJ) [10] parton distribution fuction (PDF) fits. This agreement with the DIS calculation indicates that quark-hadron duality holds at the 10−15% level throughout the entire resonance region.

3.2 Deep inelastic region

In Fig. 2, the correlation plot of $2C_{2u}$ - C_{2d} versus $2C_{1u}$ - C_{1d} at $Q^2 = 0$ is shown as extracted from the measured asymmetry. The details of the extraction are presented in Ref. [4]. The new results are represented by the ellipse labeled "This measurement", and the results on $2C_{2u}$ - C_{2d} deviate from zero by 2σ. The yellow ellipse shows the results from the SLAC 122 experiment. The vertical band is the latest C_{1q} results [11]. The red ellipse is the combined result from all published measurements. The standard model expected value is represented by the black dot, which is in good agreement with all measured results.

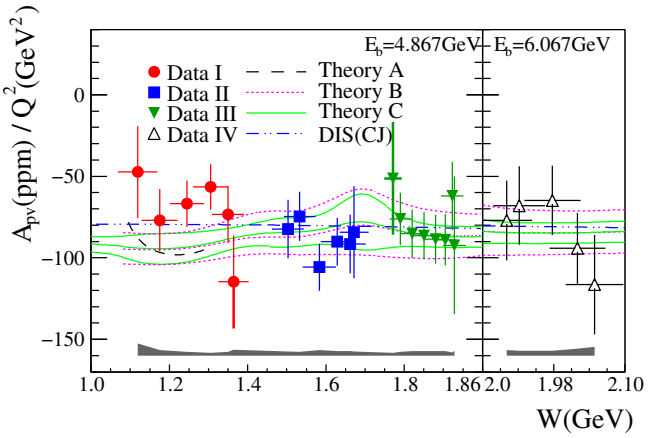

Figure 1: Invariant mass dependence of the measured $\vec{e}$-^{2}H parity-violating asymmetries in the nucleon resonance region. See text for details. Reproduced from Ref. [5].

4 Future Perspectives

With the upgrade of the Jefferson Lab electron beam, the PVDIS program will continue with the Solenoidal Large Intensity Device (SoLID) [12]. This device is a multi-purpose spectrometer with physics topics including PVDIS on proton and deuteron targets, semi-inclusive DIS on polarized proton and ^{3}He targets and threshold J/ψ production. The main motivation for the PVDIS experiment is to investigate possible new interactions beyond the Standard Model and to measure the PDF ratio d/u at high x. The experiment will obtain data over a wide kinematic range: $x > 0.2$, 2 GeV^2 $< Q^2 <$ 10 GeV^2 and will improve the measurement of the effective weak couplings by one order of magnitude compared with the 6 GeV results presented here.

5 Summary

In conclusion, recent results on the parity-violating asymmetries over the whole nucleon resonance region and in the deep-inelastic regime are reported. We have improved our knowledge on the electron-quark VA effective coupling term $2C_{2u}$ - C_{2d} by a factor of five. Our result is in agreement with the standard model prediction and is the first evidence that $2C_{2u}$ - C_{2d} deviates from zero at the 2σ level. Additionally, the nucleon resonance asymmetries agree with DIS-based calculations, indicating for the first time that quark-hadron duality may also exists in electroweak observables. The resonance data provide constraints on nucleon resonance models, which are relevant for background estimations to elastic PVES measurements. Finally, the construction of SoLID, to be used with the upgraded Jefferson Lab 12-GeV electron beam, will allow us to continue these measurements and improve our knowledge on C_{2q} by another order of magnitude.

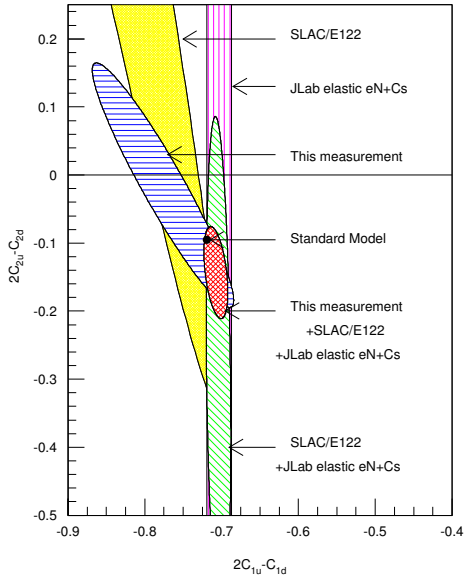

Figure 2: (color online) Comparison of current results (blue ellipse) compared with earlier experiments for the effective weak couplings. See text for details. Reproduced from Ref. [4].

Acknowledgments

This work was supported in part by the Jeffress Memorial Trust under Grant no. J-836, the U.S. National Science Foundation under grant no. 0653347, and the U.S. Department of Energy under award nos. DE-SC0003885 and DE-AC02-06CH11357. This work was authored by Jefferson Science Associates, LLC under U.S DOE contract no. DE-AC05-06OR23177. The U.S. Government retains a nonexclusive, paid-up irrevocable, world-wide license to publish or reproduce this manuscript for U.S. Government purposes.

References

[1] D.S. Armstrong and R.D. McKeown, Annu. Rev. Nucl. Part. Sci. **62** 337 (2012).
[2] C.Y. Prescott *et al.*, Phys. Lett. B **77** 347 (1978); C.Y. Prescott *et al.*, Phys. Lett. B **84** 524 (1979).
[3] J. Alcorn *et al.*, Nucl. Instrum. Meth. **A522** (2004) 294.
[4] D. Wang *et al.*, Nature **506** 7486 67 (2014).
[5] D. Wang *et al.*, Phys. Rev. Lett. **111** 082501 (2013).
[6] E.D. Bloom and F.J. Gilman, Phys. Rev. Lett. **25** (1970) 1140.
[7] K. Matsui, T. Sato, and T.-S.H. Lee, Phys. Rev. C **72** 025204 (2005).
[8] M. Gorchtein, C.J. Horowitz, and M.J. Ramsey-Musolf, Phys. Rev. C **84** 015502 (2011).
[9] N.L. Hall, P.G. Blunden, W. Melnitchouk, A.W. Thomas, and R.D. Young, Phys. Rev. D **88** 013011 (2013).
[10] J.F. Owens, A. Accardi, and W. Melnitchouk, Phys. Rev. D. **87** 094012 (2013).
[11] D. Androic *et al.*, Phys. Rev. Lett. **111** 141803 (2013).
[12] J.-P. Chen *et al.*, arXiv:1409.7741.

Latest results of MEG and status of MEG-II

Francesco Renga[1] for the MEG Collaboration

[1]INFN - Sez. di Roma, P.le A. Moro 2, 00185 Roma, Italy

DOI: http://dx.doi.org/10.3204/DESY-PROC-2014-04/38

Within the Standard Model, in spite of neutrino oscillations, the flavor of charged leptons is conserved in very good approximation, and therefore charged Lepton Flavor Violation is expected to be unobservable. On the other hand, most new physics models predict charged Lepton Flavor Violation within the experimental reach, and processes like the $\mu \to e\gamma$ decay became standard probes for physics beyond the Standard model. The MEG experiment, at the Paul Scherrer Institute (Switzerland), searches for the $\mu \to e\gamma$ decay, down to a Branching Ratio of about 5×10^{-13}, exploiting the most intense continuous muon beam in the world and innovative detectors. In this talk I will present the latest results from MEG, and the status of its upgrade (MEG-II), aiming at an improvement of the sensitivity by one order of magnitude within this decade.

1 Introduction

Charged lepton flavor conservation is an accidental symmetry in the standard model (SM), not related to the gauge structure of the theory, but following from the particle content of the model. As a consequence, this conservation is naturally violated in most of the extensions of the standard model. Indeed, LFV in the charged lepton sector (cLFV) is expected in the SM due to neutrino oscillations, but the expected branching ratios for LFV decays ($< 10^{-40}$) are predicted to be well below the current experimental sensitivities. Hence, an observation of cLFV would be an unambiguous evidence of new physics (NP) beyond the SM.

Among the NP models predicting cLFV at observable levels, Supersymmetry (SUSY) is of particular interest: even if the theory is developed to be flavor blind at the high energy scale, cLFV arises at the electroweak scale through renormalization group equations, and hence it is essentially unavoidable. Moreover, many SUSY models predict a strong correlation between cLFV and the possible deviation of the muon $g-2$ from its SM prediction. Anyway, the expected branching ratios strongly depend on the specific flavor structure of the model. Recent limits on $\mu \to e\gamma$ already rule out several scenarios still allowed by direct searches at LHC but nonetheless, even within the same models, a different flavor structure can predict rates not yet explored, and within the reach of the next generation of cLFV experiments (see [1] for a specific model with flavored gauge mediation).

I will report here the latest results for the search of $\mu \to e\gamma$ with the MEG experiment, and the status of its upgrade MEG-II.

2 The quest for $\mu^+ \to e^+\gamma$ with the MEG experiment

The MEG experiment [2], at the Paul Scherrer Institut (PSI, Switzerland), exploits the most intense continuous muon beam in the world (up to 10^8 muons per second) to search for the $\mu^+ \to e^+\gamma$ decay. Positive muons are stopped in a thin plastic target, and hence the signature of the $\mu^+ \to e^+\gamma$ decay is given by a positron and a photon, monochromatic (~ 52.8 MeV), emitted at the same time, and back-to-back. Although a prompt background is given by the radiative $\mu \to e\nu\overline{\nu}\gamma$ decay, the largely dominant background, when operating with with very high muon beam intensity, is given by the accidental coincidence of a positron from a muon decay with a photon from another muon decay (radiative decay or annihilation in flight of the positron). The background rate is then proportional to the square of the muon rate, making useless a further increase of the muon rate as soon as the background expected in the signal region becomes relevant. For this reason, the MEG experiment is operated with $\sim 3 \times 10^7$ muons per second, which is found to be an optimal value for our setup.

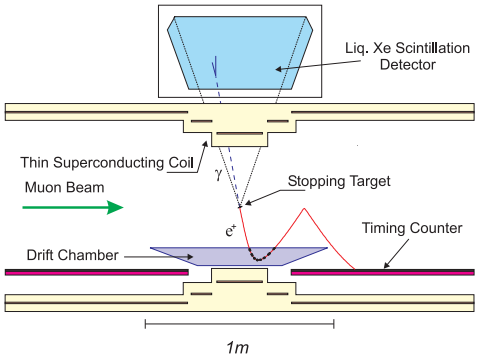

Figure 1: The MEG detector.

The MEG detector is shown in Figure 1. Positron are reconstructed in MEG by a system of 16 planar drift chamber in a gradient magnetic field, with its main component along the beam axis, and a system of 30 scintillating bars for timing and trigger. The gradient magnetic field is necessary to prevent tracks emitted at almost 90 degrees with respect to the beam axis to make several turns within the spectrometer before exiting the detector. The drift chambers reached a resolution of ~ 300 μm in the radial direction and ~ 1 mm along the beam axis, resulting into a core momentum resolution of ~ 330 keV and angular resolutions of ~ 10 mrad. The timing counter allows to measure the positron time with a resolution of ~ 70 ps. The overall positron efficiency is $\sim 30\%$, and it is largely dominated by the loss of positrons in the path from the drift chamber system to the timing counter.

Photons are reconstructed by a liquid Xenon detector instrumented with 856 PMTs. It measures the energy, the time and the conversion point of the photon, with resolutions of ~ 900 keV in the bulk region of the detector, 70 ps and $\lesssim 6$ mm.

The decay vertex is defined by the intersection of the positron track with the target, while the direction from the vertex to the photon conversion point is taken as the photon direction to determine the relative $e\gamma$ angle.

Electronic waveforms from all detectors are fully digitized at GS/s rates thanks to the DRS4 chip developed at PSI. A fully digital trigger system has been developed, exploiting energy, time and position measurements in the Xenon detector and time measurement in the timing counter.

Several calibrations are necessary to reach and measure the mentioned resolutions. Among them, it is worth to mention the use of a pion beam, along with an ancillary photon detector to select back to back photon pairs in the reaction chain $\pi^- + p \to \pi^0 + n$, $\pi^0 \to \gamma\gamma$. Kinematics make the selected positrons almost monochromatic, with an energy of about 55 MeV, very near to the signal photon energy. This is used to calibrate the absolute energy scale of the calorimeter, which is then monitored periodically with low energy photons from proton-induced nuclear reactions, in order to finally get a 0.2% accuracy on the energy scale.

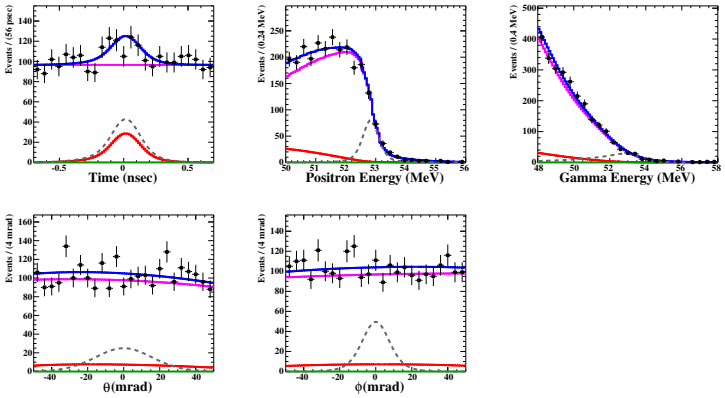

Figure 2: Result of the fit (blue) to the 2009-2011 data (black dots with error bars). Contributions from accidental background (blue), radiative decay background (red) and signal (green) are shown. The signal PDFs for a branching ratio of 3×10^{-11} are also shown for reference (gray).

A likelihood analysis is used for the search of $\mu \to e\gamma$. Five discriminating variables are used: the positron energy E_e, the photon energy E_γ, the relative time $T_{e\gamma}$ and the projections of the relative angle angle $\phi_{e\gamma}$ and $\theta_{e\gamma}$. The signal Probability Distribution Functions (PDFs) are obtained by combining the measured resolution, as well as the PDFs for the radiative muon decays. Conversely, the PDFs for the accidental background are fully extracted from data, using sideband regions defined in the E_γ vs. $T_{e\gamma}$ plane. In the construction of the PDFs we take into account several correlations in the positron PDFs, which emerge from geometrical effects and are well understood both qualitatively and quantitatively. The results of the likelihood fit, based on the data collected in the 2009-2011 period ($\sim 36 \times 10^{13}$ muons stopped in the target), are shown in Figure 2 [3]. No significant signal is observed, and an upper limit on the number of signal events has been extracted at 90% confidence level, with a frequentistic approach based on a profile likelihood ratio. This is combined with a normalization factor obtained by counting the number of Michel positrons reconstructed in the spectrometer and, including all systematics (dominated by the uncertainties on the PDFs for the relative angle), an upper limit of 5.7×10^{-13} is obtained for the $\mu \to e\gamma$ branching ratio, to be compared with an expected limit of 7.7×10^{-13} (from toy Monte Carlo studies).

The MEG experiment collected data in 2012 and 2013, and doubled the available statistics. Several improvements have been included in the on going analysis of these data: refined algorithms allowed to increase the efficiency for tracks making several turns within the spectrometer; a more accurate measurement if the magnetic field has been performed in order to

reduce the corresponding systematic uncertainties; an algorithm for the recognition of photons coming from positron annihilation in flight has been introduced, in order to suppress the main contribution to the background at large photon energies. Although the determination of the final sensitivity is still ongoing, an expected upper limit below 5×10^{-13} is foreseen.

3 Status of MEG-II

As already mentioned, many NP models predict a $\mu \to e\gamma$ branching ratio not far from the current limit. Hence, a short term upgrade to improve the sensitivity of MEG of about one order of magnitude is worth the effort. As shown in [4], the upgraded experiment will be competitive with the first phase of the experiments searching for $\mu \to e$ conversion in the field of nuclei, if cLFV arises from magnetic-moment operators, $\mathcal{L} \propto \overline{\mu}_R \sigma_{\mu\nu} e_L F^{\mu\nu}$, like in supersymmetry.

The upgrade of the MEG experiment will involve all the subdetectors. The system of 16 drift chambers will be replaced with a unique cylindrical drift chamber with stereo wires. The chamber will be operated with a light mixture of Helium and Isobutane (85%:15%) to reduce the material budget, and will cover all the path of the track to the timing counter, in order to recover the large inefficiency observed in MEG. A single hit resolution of about 120 μm is expected and confirmed by measurements with different prototypes in different environments (cosmic rays and positron beams). Given the stereo angle, it will give a resolution below 1 mm along the beam axis. A momentum resolution of 130 keV and angular resolutions of about 5 mrad are expected.

The Timing Counter will be replaced by about 500 scintillating tiles read out by Silicon Photomultipliers (SiPM). Tests with positron beams confirmed that a time resolution of about 30 ps can be reached combining the time measurements of the tiles hit by each track.

The PMTs in the inner face of the liquid Xenon calorimeter will be replaced with SiPMs, specifically developed to be sensitive to ultra-violet scintillation light of Xenon. The improved granularity will allow to improve the resolutions for photons converting just after entering the calorimeter (*shallow events*) and the capability of detecting pileup photons. Moreover, the geometry of the lateral faces will be changed in order to increase the fiducial volume and better control the reflection of the scintillation light. The energy resolution is expected to go down to 1%. Finally, a new DAQ board is under development, still based on the DRS4 chip, in order to handle the increased number of channels within the limited space of the MEG experimental hall.

The upgraded detectors are presently under construction and are expected to be ready for an engineering run at the end of 2015 and for physics runs in 2016. A three-year data taking campaign is foreseen, with an optimal muon rate which should reach 7×10^7 muons per second, thanks to the improved resolutions. An expected upper limit of about 4×10^{-14} is finally envisaged.

References

[1] L. Calibbi *et al.*, arXiv:1408.0754 [hep-ph] (2014).

[2] J. Adam *et al.*, Eur. Phys. J. **C73** 2365 (2013).

[3] J. Adam *et al.*, Phys. Rev. Lett. 110 201801 (2013).

[4] A. M. Baldini *et al.*, arXiv:1301.7225 [physics.ins-det] (2013).

Parity-Violating Electron Scattering

Krishna S. Kumar for the MOLLER collaboration

Department of Physics and Astronomy, Stony Brook University, USA

DOI: http://dx.doi.org/10.3204/DESY-PROC-2014-04/255

Measurements of parity-violating asymmetries in the scattering of longitudinally polarized electrons off unpolarized fixed targets are used to access leptonic and semi-leptonic weak neutral current amplitudes. One thrust of the current program is the measurement the elastic neutral weak amplitude at very low Q^2 from scattering off a heavy spinless nucleus, which is sensitive to the presence of a neutron skin. A second major thrust is the neutral current elastic amplitude at very low Q^2 off protons and electrons and in the DIS regime off deuterium, which allows precision measurements of the weak mixing angle at low energy and is thus sensitive to new physics beyond the Standard Model.

1 Introduction

The technique of electron scattering has been used for more than sixty years to study nuclear and nucleon structure using the experimental cleanliness and well-understood theory of electromagnetic interactions. Soon after parity-violation in the weak interactions was demonstrated, Zel'dovich noted that if an analogous neutral interaction existed, then parity violation would be manifested in longitudinally polarized lepton scattering off unpolarized nucleons due to the interference between the weak and electromagnetic amplitudes. He estimated that the parity-vioating asymmetry A_{PV} would be of order $10^{-4}Q^2$ (GeV)^2.

For typical fixed target experiments, A_{PV} ranges from roughly 10^{-4} to as small as 10^{-7}. Parity violation in deep inelastic electron nucleon scattering was first observed at SLAC [1], consituting an important test of the SU(2)×U(1) gauge theory of electroweak interactions. Over the past 30 years, the experimental techniques employed to measure these tiny left-right asymmetries have been steadily refined such that statistical and systematic errors better than 1 part per billion (ppb) are possible [2, 3].With judiciously chosen targets and kinematics, this has facilitated measurements in several important physics topics, such as many-body nuclear physics, nucleon structure and searches for physics beyond the standard model at the TeV scale. In this review, we discuss the ongoing research program and future prospects.

2 Neutron Skin of a Heavy Nucleus

In a heavy nucleus such as ^{208}Pb, the fractional difference between neutron radius R_n and proton radius R_p is believed to be several percent. Analogous to the classic measurement of R_p via elastic electron electromagnetic scattering, R_n can be measured via parity-violating electron scattering [4]. The parity violating asymmetry in elastic scattering off a heavy spinless nucleus is proportional to the ratio of the neutron to proton form factors since the weak neutral current

coupling of protons is much smaller than that of neutrons. Experimentally, there is some controversy as to how well R_n is known [5]; the best guess is $\sim 5\%$. A precise measurement of R_n can have impact on nuclear theory, atomic parity violation [6] and neutron star structure [7].

With the improvements made on the control of helicity-correlated beam fluctuations, it became feasible to make a measurement of $A_{\rm PV}$ in elastic scattering off a ^{208}Pb target. For a beam energy of 1.05 GeV and a scattering angle of 6° and $Q^2 \sim 0.01$ GeV^2, A_{PV} is of order 0.6 ppm. A 3% measurement of A_{PV} leads to a 1% measurement of R_n. A new experimental project known as PREX was approved and carried out a first data run at Jefferson Laboratory in 2010. The experiment ran for about 10 weeks in the spring of 2010. Statistics for a 9% A_{PV} measurement and a 3% R_n determination was accumulated [8]. After corrections for beam fluctuations, the grand average was found to be 594 ± 50 parts per billion (ppb). After normalizing to the beam polarization and subtracting background, the PREX result is $A_{PV} = 656 \pm 60$ (stat) ± 14 (syst) ppb.

The measured result corresponds to a value for the neutron skin of $R_n - R_p = +0.33^{+0.16}_{-0.18}$ fm. While the result demonstrates that the neutron RMS radius is 2σ larger than that of the protons the result is not yet precise enough to discriminate between various models based on mean field theory and other observables. A followup proposal to obtain the remaining statistics required for a 1% R_n measurement by the PREX collaboration has been approved and will likely run in 2016. Two other attractive nuclei to explore R_n measurements are ^{48}Ca and $^{120/124}$Sn. In general low Z nuclei tend to have a higher figure of merit due to the fact that the optimum Q^2 at which one must make the A_{PV} measurement tends to increase, and the figure of merit rises with the square of the asymmetry times the count rate [9]. ^{48}Ca is particularly interesting because microscopic calculations may soon be feasible, which would allow R_n to be related to poorly studied 3-neutron forces. It turns out that ^{48}Ca is an ideal measurement at Jefferson Laboratory with a similar configuration to that used for PREX, except that the beam energy would be raised to 2.2 GeV, and an experimental proposal has recently been approved.

It is interesting to consider measurements of Pb and Sn at Mainz in the future, adapting the apparatus that would be required for a high precision proton weak charge measurement (see Sec. 3). It looks feasible to design the require apparatus for a 0.5% R_n measurement of ^{208}Pb [10]. The loss in rate due to the lower beam energy is roughly compensated by the larger available solid angle. The momentum resolution that would be required is about 1%, and a system of baffles could be used to isolate elastic events while rejecting background from inelastics as well as from neutrals [11].

3 Precision Weak Neutral Current Measurements

Precision measurements of the properties of W and Z bosons and their couplings to leptons and quarks have allowed sensitive tests of the electroweak theory. No significant deviation from Standard Model predictions have been found. Nevertheless, experiments continue to probe for the indirect effects of new physics at the TeV scale by making more and more precise measurements of electroweak parameters. Weak neutral current (WNC) interactions at $Q^2 \ll M_Z^2$ can probe for heavy Z$'$ bosons or leptoquarks whose effects might be highly suppressed in measurements on the Z pole [12], and for dark sector mediators that have small admixtures to the Z boson [13]. Since the neutral current amplitude at the Z pole is imaginary, there are no interference terms with new, real four-fermion amplitudes. At low Q^2 on the other hand, interference effects might be measurable if sufficient accuracy is achieved [2, 3, 14, 15].

A general, model-independent way to parametrize the contributions of contact interactions of high-mass particles to low-energy measurements of electron scattering off target fermions f is to use a Lagrangian [16] parametrized by coupling constants g_{ij} (i, $j = R$, L), and a mass scale Λ. The goal of low energy neutral current measurements is to reach sufficient sensitivity to access $\Lambda/g_{ij} \geq 1$ TeV for as many different initial and final state fermions and chiral combinations as possible, similar sensitivity yet complementary to that of the highest energy colliders.

Over the past couple of decades, the three published measurements with sufficient sensitive to probe the TeV-scale were the weak charge measurement in ^{133}Cs [17], the NuTeV neutrino deep-inelastic scattering measurement [18] and the measurement of $A_{\rm PV}$ in electron-electron (Møller) scattering [19] at SLAC. As we await the restart of the Large Hadron Collider (LHC) at full beam energy and design luminosity, improving these constraints and expanding their reach to include more fermion scattering combinations takes on increased significance. This is because such measurements will help narrow down the physics mechanisms that are responsible for any observed anomalies at the LHC.

The interactions of the Z-boson at low Q^2 can be approximated by four-fermion contact interactions. The parity-violating part of the electron-hadron interaction can then be given in terms of phenomenological couplings C_{ij}, where C_{1j} (C_{2j}) gives the vector (axial-vector) coupling to the j^{th} quark. In the Standard Model, all four couplings are functions of a single parameter: the weak mixing angle $\sin^2\theta_W$. The atomic Cesium weak charge measurement measured one combination of C_{1u} and C_{1d} precisely.

At sufficiently forward angles and low Q^2, the hadronic structure uncertainty in the WNC elastic electron-proton amplitude becomes small enough such that one can measure the underlying coherent $2u + d$ e-q amplitude combination to high precision, thus precisely constraining $2C_{1u}+C_{1d}$. This combination is proportional to $1-4\sin^2\theta_W$. A 4% measurement of A_{PV} would achieve a precision of $\delta(\sin^2\theta_W) = 0.0007$. This is the goal of the Qweak experiment [20] in Hall C at Jefferson Lab, which is reported on separately in these proceedings. The experiment has completed data-taking and published their first result based on commissioning data [21].

It would be highly complementary to obtain a new measurement of the proton weak charge with a new apparatus where the beam energy is smaller than 200 MeV. The dominant theoretical uncertainty in the prediction of A_{PV} is due to higher-order radiative corrections involving $\gamma - Z$ box diagrams. In order to compensate for the lower energy, it will be necessary to obtain data over the full range of the azimuth using a solenoidal spectrometer [11]. Such an experiment would be a flagship measurement of the proposed new MESA facility at Mainz. A measurement of A_{PV} with an ultimate goal of 2% overall error is compelling and seems feasible [22]

The upgrade of Jefferson Laboratory to 11 GeV will allow precision measurements in parity-violating deep inelastic scattering (PV DIS). One measurement using a 6 GeV beam and the existing high resolution spectrometers in Hall A has recently been published, and helped establish that the axial-quark couplings of light quarks to the Z boson are indeed non-zero [23]. A new dedicated high luminosity apparatus has been propopsed centered around a large superconducting solenoidal magnet [24]. This project, known as SoLID (Solenoidal Large Intensity Device), would allow $\sim 1\%$ measurements of A_{PV} for the first time over a range of x and Q^2 values, as high as $x \sim 0.7$ (x is the fraction of the nucleon momentum carried by the struck quark). PV DIS measurements with such accuracy and kinematic range provides access to novel aspects of nucleon structure, such as charge symmetry violation and investigation of higher-twist effects. Most importantly, PV DIS allows the isolation of the linear combination $2C_{2u} + C_{2d}$, which is difficult to measure using elastic scattering. A_{PV} in DIS can be written as as functions of two parameters $a(x)$ and $b(x)$, which are functions of the parton distributions $f_i(x)$ and the elec-

tromagnetic charges. For an isoscalar target such as deuterium, the dependence on structure largely cancels out in the A_{PV} ratio of the weak and electromagnetic amplitudes.

The measurement would test the WNC amplitude in the lepton-quark sector, where there is currently a discrepancy with the theoretical prediction in the NuTeV result. Secondly, combined with other measurements in elastic electron-proton scattering, precise constraints would be possible on the lesser known axial-vector quark couplings C_{2i}. This would, among other things, provide complementary constraints on various models with new heavy leptophobic Z' bosons [25] and leptoquarks [12]. More generally, the projected result for A_{PV}^D of 0.6% translates into a measurement of a specific linear combination of the phenomenological couplings C_{ij} to an accuracy of ± 0.0083, more than a factor of 30 better than the best current constraints. This translates into contact interaction scale reach $\gtrsim 2.5$ TeV.

The Feynman diagrams for electron-electron (Møller) scattering involve both direct and exchange diagrams that interfere with each other. A_{PV} for this process was first calculated in the late 70's [26] The electroweak theory prediction at tree level in terms of the weak mixing angle is $Q_W^e = 1 - 4\sin^2\theta_W$; this is modified at the 1-loop level [27, 28] and becomes dependent on the energy scale at which the measurement is carried out, *i.e.* $\sin^2\theta_W$ "runs". It increases by $\sim$3% compared to its value at the scale of the Z^0 boson mass, M_Z. The SLAC E158 experiment carried out the first measurement of parity violation in Møller scattering [19]. The grand average result for the parity-violating asymmetry in Møller scattering at $Q^2 = 0.03$ GeV^2 was found to be: $A_{\rm PV} = -131 \pm 14(\text{stat}) \pm 10(\text{syst})$ (ppb).. From the measured result, and assuming that the only contributing chiral structure comes from the $\Lambda_{\rm LL}$ term, the 95% C.L. limit is 7 TeV or 16 TeV depending on the sign of the contact interaction term.

There is strong motivation to make further improvements in the accuracy of weak neutral current coupling constants at low energy. Improved measurements would keep pace with the improved sensitivity for discovery at the multi-TeV scale by experiments at the Large Hadron Collider. With the upgrade of Jefferson Laboratory to 12 GeV, a new project called MOLLER (Measurement of Lepton-Lepton Electroweak Reaction) is being designed to improve on the SLAC E158 measurement of the weak charge of the electron Q_W^e by a factor of five. For the 2.3% total uncertainty envisioned, the sensitivity reach is $\frac{\Lambda}{\sqrt{|g_{RR}^2 - g_{LL}^2|}} = 7.5$ TeV. The strongest constraints on four-lepton contact interactions come from LEP 2, approaching 5 TeV for specific chiral combinations. However, the parity-conserving cross-sections and forward-backward asymmetries studied at LEP 2 are blind to the parity-violating combination $g_{RR}^2 - g_{LL}^2$ probed by MOLLER.

The prediction for MOLLER A_{PV} is 35.6 parts per billion (ppb). The goal is to measure this quantity to a statistical precision of 0.74 ppb and keep systematic errors to be significantly smaller, in order to achieve a 2.3% measurement of Q_W^e. MOLLER will greatly benefit from the steady improvement in the techniques employed to measure parity-violating asymmetries to sub-ppb systematic precision and to also achieve normalization control at the sub-% level. The MOLLER collaboration, a group of $\sim$ 100 authors, is currently developing the technical design of the apparatus, and is in the process of seeking project funding of order 20M$ from IS DoE, NSF and international funding agencies. The goal is to obtain construction funding by 2017 so that experiment commissioning and first data collection can take place by 2020.

4 Summary

Parity-violating electron scattering is a mature field and addresses fundamental questions in a variety of different topics. The E158 experiment at SLAC has produced the most precise measurement of the weak mixing angle at low energy. The Qweak experiment at Jefferson Laboratory is on track to make an improved weak mixing angle measurement. The two future proposals at Jefferson Laboratory, SoLID and MOLLER, will lead to important new insights on the structure of the nucleon and yield new and more precise measurements of the weak mixing angle and constitute flagship projects after the 12 GeV upgrade. It will be greatly beneficial to design and carry out a new measurement of the proton weak charge at Mainz that will improve on the Qweak experiment by a factor of 2.

In parallel, it is greatly motivated to carry out new measurements of A_{PV} on heavy nuclei to measure the ground-state neutron distribution. The PREX measurement is on-going and should produce a 1% measurement of the neutron radius in ^{208}Pb in a few years. In the long run, it will be very important to produce comparable measurements using Ca and Sn isotopes at Jefferson Laboratory and at Mainz. Finally, the proposed new MESA facility at Mainz has the potential to add important new measurements to the impressive list of parity-violation experiments in order to probe nuclear and nucleon structure and to search for physics beyond the Standard Model.

Acknowledgments

This work has been funded by a grant from the Division of Nuclear Physics at the US Department of Energy's Office of Science.

References

[1] C.Y. Prescott, W.B. Atwood, R. Leslie Cottrell, H.C. DeStaebler, Edward L. Garwin, et al. Parity Non-conservation in Inelastic Electron Scattering. *Phys.Lett.*, B77:347–352, 1978.

[2] K.S. Kumar, Sonny Mantry, W.J. Marciano, and P.A. Souder. Low Energy Measurements of the Weak Mixing Angle. *Ann.Rev.Nucl.Part.Sci.*, 63:237–267, 2013.

[3] Jens Erler, Charles J. Horowitz, Sonny Mantry, and Paul A. Souder. Weak Polarized Electron Scattering. 2014.

[4] T.W. Donnelly, J. Dubach, and Ingo Sick. Isospin Dependences in Parity Violating Electron Scattering. *Nucl.Phys.*, A503:589, 1989.

[5] C.J. Horowitz, S.J. Pollock, P.A. Souder, and R. Michaels. Parity violating measurements of neutron densities. *Phys.Rev.*, C63:025501, 2001.

[6] S.J. Pollock, E.N. Fortson, and L. Wilets. Atomic parity nonconservation: Electroweak parameters and nuclear structure. *Phys.Rev.*, C46:2587–2600, 1992.

[7] C.J. Horowitz and J. Piekarewicz. Neutron star structure and the neutron radius of Pb-208. *Phys.Rev.Lett.*, 86:5647, 2001.

[8] S. Abrahamyan, Z. Ahmed, H. Albataineh, K. Aniol, D.S. Armstrong, et al. Measurement of the Neutron Radius of 208Pb Through Parity-Violation in Electron Scattering. *Phys.Rev.Lett.*, 108:112502, 2012.

[9] Shufang Ban, C.J. Horowitz, and R. Michaels. Parity Violating Electron Scattering Measurements of Neutron Densities. *J.Phys.*, 39:015104, 2012.

[10] M. Thiel, D. Becker, M. Ferretti, K. Kumar, and C. Sfienti. Neutron skin studies of medium and heavy nuclei. *EPJ Web Conf.*, 73:07007, 2014.

[11] P.A. Souder and R. Holmes. New spectrometers for precision measurements of parity violation with polarized electrons. 1990.

[12] M.J. Ramsey-Musolf. Low-energy parity violation and new physics. *Phys.Rev.*, C60:015501, 1999.

[13] Hooman Davoudiasl, Hye-Sung Lee, and William J. Marciano. Muon g-2, Rare Kaon Decays, and Parity Violation from Dark Bosons. *Phys.Rev.*, D89:095006, 2014.

[14] Vincenzo Cirigliano and Michael J. Ramsey-Musolf. Low Energy Probes of Physics Beyond the Standard Model. *Prog.Part.Nucl.Phys.*, 71:2–20, 2013.

[15] Jens Erler and Shufang Su. The Weak Neutral Current. *Prog.Part.Nucl.Phys.*, 71:119–149, 2013.

[16] E. Eichten, Kenneth D. Lane, and Michael E. Peskin. New Tests for Quark and Lepton Substructure. *Phys.Rev.Lett.*, 50:811–814, 1983.

[17] S.C. Bennett and Carl E. Wieman. Measurement of the 6S to 7S transition polarizability in atomic cesium and an improved test of the Standard Model. *Phys.Rev.Lett.*, 82:2484–2487, 1999.

[18] G.P. Zeller et al. A Precise determination of electroweak parameters in neutrino nucleon scattering. *Phys.Rev.Lett.*, 88:091802, 2002.

[19] P.L. Anthony et al. Precision measurement of the weak mixing angle in Moller scattering. *Phys.Rev.Lett.*, 95:081601, 2005.

[20] D.S. Armstrong, A. Asaturyan, T. Averett, J. Benesch, J. Birchall, et al. The Qweak Experiment: A Search for New Physics at the TeV Scale via a Measurement of the Proton's Weak Charge. 2012.

[21] D. Androic et al. First Determination of the Weak Charge of the Proton. *Phys.Rev.Lett.*, 111(14):141803, 2013.

[22] D. Becker, K. Gerz, S. Baunack, K.S. Kumar, and F.E. Maas. P2 - The weak charge of the proton. *AIP Conf.Proc.*, 1563:78–81, 2013.

[23] D. Wang et al. Measurement of parity violation in electron–quark scattering. *Nature*, 506(7486):67–70, 2014.

[24] J.P. Chen, H. Gao, T.K. Hemmick, Z. E. Meziani, and P.A. Souder. A White Paper on SoLID (Solenoidal Large Intensity Device). 2014.

[25] Matthew R. Buckley and Michael J. Ramsey-Musolf. Precision Probes of a Leptophobic Z' Boson. *Phys.Lett.*, B712:261–265, 2012.

[26] Emanuel Derman and William J. Marciano. Parity Violating Asymmetries in Polarized Electron Scattering. *Annals Phys.*, 121:147, 1979.

[27] Andrzej Czarnecki and William J. Marciano. Electroweak radiative corrections to polarized Moller scattering asymmetries. *Phys.Rev.*, D53:1066–1072, 1996.

[28] Jens Erler and Michael J. Ramsey-Musolf. The Weak mixing angle at low energies. *Phys.Rev.*, D72:073003, 2005.

Precision Tests of the Standard Model with Kaon Decays at CERN

Tommaso Spadaro[1] for the NA62 collaboration

[1]Laboratori Nazionali di Frascati dell'INFN, Via E. Fermi 40, 00044 Frascati, Italy

DOI: http://dx.doi.org/10.3204/DESY-PROC-2014-04/14

Selected precision Standard Model tests performed in the recent past or possible in the near future using kaon decays are discussed, with a focus on unambiguous signatures, such as those for Lepton-Flavor violation (LFV) and Lepton-Number violation (LNV) transitions, and on the physics reach at the high-intensity beams produced at the CERN SPS for the NA48/2 and NA62 experiments. Recent results on the search for the LNV process $K^{\pm} \to \pi^{\mp}\mu^{\pm}\mu^{\pm}$ and for LFV-induced deviations from the SM expectation for the ratio of decays widths for $K^{+} \to e^{+}\nu$ and $K^{+} \to \mu^{+}\nu$ are briefly discussed. Sensitivity improvements with the new phase of NA62 on a variety of observables are outlined.

1 The Kaon physics framework

The Standard Model appears remarkably simple at a c.m. energy around the kaon mass, with few unknown parameters in the QCD dynamics, namely light and strange quark masses and e.m.- or QCD-induced isospin-breaking effects. This leaved room for a thouough study of the symmetry of the electro-weak lagrangian performed in the last decades. Searches with kaons have been competitive with those with B-mesons for lepton-flavor (LF) or CP violation transitions (most notably, the precise measurements of CPV in the mixing ϵ [1] and of the direct CPV in the decay [2]) and reached the highest sensitivity in the search for CPT and quantum mechanics violation effects. The most precise gauge-universality test comes for the unitarity of the first row of the CKM matrix, thanks to the results from kaon decays giving V_{us}, and from super-allowed nuclear transitions giving V_{ud} [3]. This translated into a severe constraint for every new-physics extension of the SM [4].

2 Search for lepton number violation from kaon decays

The lepton-number violation transition $K^{\pm} \to \pi^{\mp}\mu^{\pm}\mu^{\pm}$ is forbidden in the SM. It might be possible in new-physics models, if mediated by a Majorana neutrino. For neutrino masses ranging from 100 to 300 MeV, the cited channel would be that with the highest sensitivity [5].

The search for this decay has been performed at the NA48/2 experiment. The main goal of NA48/2 was the search for direct CPV from precise measurement of the charge asymmetry in the Dalitz-plot density slopes between the decays $K^{+} \to \pi^{+}\pi^{0\pm}\pi^{0,\mp}$ and their charge conjugates [6]. NA48/2 operated with high-intensity, unseparated, simultaneous, highly-collimated, 60-GeV momentum $K^{\pm}$ beams, with a 3.8% momentum bite. The beams entered a decay region in

vacuum instrumented with a magnetic spectrometer to measure the momentum of charged decay products, a fast scintillator hodoscope establishing the event time and initiating the trigger, and a liquid Krypton calorimeter downstream the hodoscope with high transversal segmentation and an excellent energy and spatial resolution. The LKr calorimeter was followed by a hadron calorimeter and a muon-veto system (MUV) used both for muon identification and for muon triggering. For details on the apparatus, see [7].

Samples were acquired in 2003-2004 by requiring the presence of three tracks at the trigger level using both the hodoscope and the spectrometer information. A single vertex was reconstructed from the three tracks, and for two of them associated hits in the MUV were required. The sample left for normalization had the same angular acceptance and vertex requests for the three tracks as the two-muon sample, while no request was made on the MUV system, and was equivalent to about 1.4×10^{11} kaon decays in a given fiducial volume.

Two-muon samples were divided into correct-sign (wrong-sign), candidates for the LN conserving (violating) decay $K^{\pm} \to \pi^{\pm}\mu^{\pm}\mu^{\mp}$ ($K^{\pm} \to \pi^{\mp}\mu^{\pm}\mu^{\pm}$). The three-track invariant mass distribution for the correct (wrong) sign sample, is shown in the left (right) panel of Fig. 1. A clear peak around the kaon mass is present for the correct sign events, while no peak is observed for the wrong sign sample. The number of events counted in the signal region agrees with the pure-background expectation. The corresponding upper limit, $BR(K^{\pm} \to \pi^{\mp}\mu^{\pm}\mu^{\pm}) < 1.1 \times 10^{-9}$ at 90% CL [8], improves on previous results by a factor of 3.

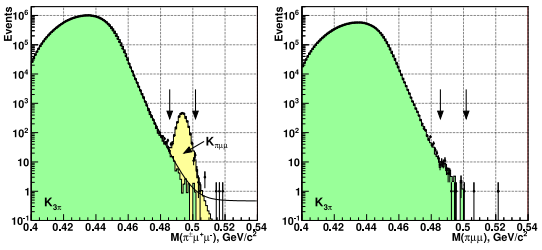

Figure 1: Three-track invariant mass from correct-sign (left-panel) and wrong-sign (right panel) $K \to \pi\mu\mu$ samples. The vertical arrows define the signal region.

3 Search for lepton flavor violation from kaon decays

Thanks to the cancellation of hadronic uncertainties, the ratio R_K of decay widths for kaon decays to $e\nu$ and $\mu\nu$ final states can be predicted with extremely high accuracy in the SM: $R_K = 2.477 \pm 0.001 \times 10^{-5}$ [9]. In large-tan β super-symmetric models R_K might deviate from the SM estimate by up to the percent [10, 11] and this NP effect should be dominated by a LFV contribution from $e\nu_\tau$ final states. After the Higgs discovery made the large-tan β scenario less probable and after the constraints from the $B \to \tau\nu$ and $B_{(s)} -> \mu^+\mu^-$ are taken into account, NP effects on R_K above the per-mil level are disfavoured [12]. Nevertheless, NP effects at the percent level might still be envisaged in scenarios with SM extensions including sterile fermions and inverse see-saw [13].

A data taking at the NA62 experiment was performed in 2007-2008, dedicated to the measurement of R_K. At that time, the most precise measurement of R_K had a total uncertainty

of 1.3% [14]. The design of NA62 was optimized for the R_K measurement with respect to that used for NA48/2, by increasing the beam momentum to 74 GeV, decreasing the momentum bite to 2.5%, and by increasing the momentum kick provided by the spectrometer magnet.The resolution on the missing mass from kaon decays from a single track was therefore significantly improved, thus increasing the kinematic separation of $K \to e\nu$ (a.k.a. K_{e2}) decays with respect to $K \to \mu\nu$ decays ($K_{\mu 2}$). Beam particles with a single charge were used and the majority of the data taking was devoted to a positively charged beam.

The main trigger for $K_{\mu 2}$ events required a single track observed at the hodoscope together with activity in the drift chambers corresponding to a single track. To trigger K_{e2} events, the request of having an energy deposition of at least 10 GeV in the LKr calorimeter was added. In the offline analysis, K_{e2} decays were identified by requiring a cluster of energy in the LKr calorimeter, geometrically associated to the kaon daughter track, and by selecting events with a ratio of energy measured by the calorimeter to momentum measured by the spectrometer around unity. Events with a squared missing mass at the K decay point around zero are considered K_{e2} candidates, see the left panel of Fig 2. The misidentification probability of high-energy muons mimicking the electron energy release in the calorimeter has been precisely evaluated comparing a muon-enriched control sample acquired by interspersing a lead bar between the two hodoscope planes. The probability was measured to be at the level of 4×10^{-6} and depends on the muon energy.

NA62 selected the largest K_{e2} data set ever, with almost 150000 events. The total background amounts to almost 11%, dominated by $K_{\mu 2}$ decays with muons mimicking the electron energy release in the calorimeter (5.64±0.20%). Radiative structure-dependent $K_{e2\gamma}$ decays contribute for 2.60±0.11%, while the beam halo due to muons from upstream in flight decay of beam pions constitute the third background source, 2.11±0.09%. The analysis for R_K was per-

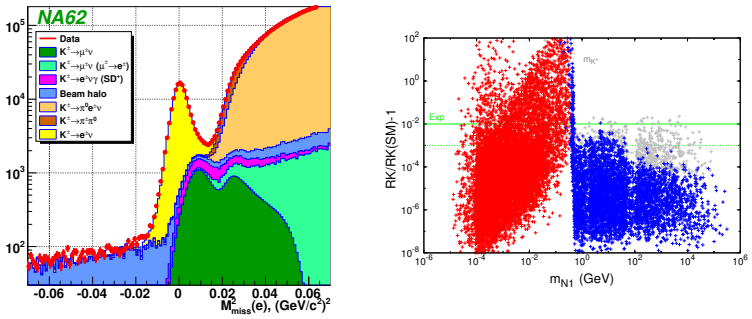

Figure 2: Left: Squared missing mass at the K decay vertex, evaluated assuming the daughter track has the electron mass, for K_{e2} candidate events. Right: fractional deviation of R_K with respect to its SM expectation as a function of the lightest sterile neutrino mass for NP models with sterile neutrinos with inverse see-saw (from Ref. [13]). Models above the solid green line representing the upper bound from the NA62 result of Eq. 1 are excluded.

formed in 10 bins of lepton momentum and separating runs according to the beam charge and to the setup (with and without the lead bar). The results are found to be mutually compatible and average to

$$R_K = (2.488 \pm 0.007_{\text{stat}} \pm 0.007_{\text{syst}}) \times 10^{-5}. \quad (1)$$

	K Mode	UL at 90% CL	Experiment
LFV	$K^+ \to \pi^+\mu^+e^-$	1.3×10^{-11}	E777/E865 [17]
LFV	$K^+ \to \pi^+\mu^-e^+$	5.2×10^{-10}	E865 [18]
LNV	$K^+ \to \pi^-\mu^+e^+$	5.0×10^{-10}	E865 [18]
LNV	$K^+ \to \pi^-e^+e^+$	6.4×10^{-10}	E865 [18]
LNV	$K^+ \to \pi^-\mu^+\mu^+$	1.1×10^{-9}	NA48/2 [8]
LNV	$K^+ \to \mu^-\nu e^+e^+$	2.0×10^{-8}	Geneva-Saclay [19]
LNV	$K^+ \to e^-\nu\mu^+\mu^+$	no data	

	π^0 Mode	Status	Experiment
LFV, ν_R	$\pi^0 \to$ inv.	$< 3 \times 10^{-7}$	E949 [20]
LFV	$\pi^0 \to e\mu$	$< 4 \times 10^{-10}$	KTeV [21]
NP scalars	$\pi^0 \to 4\gamma$	$< 2 \times 10^{-8}$ at 90% CL	Crystal box [22]
NP scalars	$\pi^0 \to e^+e^-e^+e^-$	$3.34(16)10^{-5}$	KTeV [21]
NP vectors	$\pi^0 \to U\gamma$, $U \to e^+e^-$	Various exclusions	see [23]
C violation	$\pi^0 \to 3\gamma$	$< 3.1 \times 10^{-8}$ at 90% CL	Crystal box [22]

Table 1: Upper (lower) panel: LFV/LNV K-decay modes (π^0 decay modes) possibly studied at the imminent run of NA62: the single-event sensitivity is expected to reach 10^{-12} (10^{-10}).

The residual systematic uncertainty is due to a number of different contributions [15]. Notwithstanding an uncertainty improvement on the previous data by a factor of 4, the result is in agreement with the SM expectation. Exclusion plots for NP contributions can be obtained: the right panel of Fig. 2 refers to models with sterile neutrino and inverse see-saw.

4 Near-future sensitivity from NA62 on NP searches

The NA62 collaboration developed a new detector setup, including the trigger and data acquisition systems, optimized to measure the branching fraction for the rare flavor-changing neutral current decay $K^+ \to \pi^+\nu\bar{\nu}$ with a 10% total uncertainty. For a detailed description of the new setup and of the measurement itself, see [16]. The data taking will begin in 2014 and will last for at least two years. Higher proton intensity and much larger beam accepted solid angle compared to the NA48/2 setup will allow 1.2×10^{13} K decays in a 60-meter long fiducial region to be studied, an improvement by a factor of 50. This, together with the possibility to apply flexible and dedicated trigger strategies using PID information and multi-track requests, will allow a single-event sensitivity at the level of 10^{-12} for the lepton-flavor violation channels listed in the upper panel of Table 1. The background rejection for the identification of the cited LNV decay $K^\pm \to \pi^\mp\mu^\pm\mu^\pm$ will be increased hugely, thanks to the redundant PID capability of the new setup and to the lowering of the invariant mass resolution by more than a factor of 2. The expected sentitivity will increase by a factor from 100 to 1000. Major impact on other topics are foreseen. One year of data taking at the new NA62 corresponds to more than 10^{11} π^0's produced from $K^+ \to \pi^+\pi^0$. This intense and possibly tagged π^0 *beam* will allow other interesting studies, as listed in the lower panel of Table 1. Among these, we cite the search for NP vectors, also called *dark photons* [24]. In one year of data taking $\sim 10^{15}$ $D^\pm$ will be produced, thus allowing interesting searches for long-lived exotic particles reaching the NA62 apparatus, such as the heavy neutral leptons of the NP model by Shaposhnikov and others [25].

References

[1] A. J. Buras, D. Guadagnoli and G. Isidori, Phys. Lett. B **688** (2010) 309 and references therein.

[2] V. Fanti *et al.* [NA48 Collaboration], Phys. Lett. B **465** (1999) 335 [hep-ex/9909022]. J. R. Batley *et al.* [NA48 Collaboration], Phys. Lett. B **544** (2002) 97 [hep-ex/0208009]. A. Alavi-Harati *et al.* [KTeV Collaboration], Phys. Rev. Lett. **83** (1999) 22 [hep-ex/9905060].

[3] M. Antonelli *et al.*, Phys. Rept. **494** (2010) 197 [arXiv:0907.5386 [hep-ph]].

[4] A. Czarnecki, W. J. Marciano and A. Sirlin, Phys. Rev. D **70** (2004) 093006 [hep-ph/0406324].

[5] A. Atre, T. Han, S. Pascoli and B. Zhang, JHEP **0905** (2009) 030 [arXiv:0901.3589 [hep-ph]].

[6] J. R. Batley *et al.* [NA48/2 Collaboration], EPJ C52 (2007) 875.

[7] V. Fanti *et al.* [NA48 Collaboration], Nucl. Instrum. Meth. A **574** (2007) 433.

[8] J. R. Batley *et al.* [NA48/2 Collaboration], Phys. Lett. B **697** (2011) 107.

[9] V. Cirigliano, I. Rosell, Phys. Rev. Lett. **99** (2007) 231801.

[10] A. Masiero, P. Paradisi, R. Petronzio, Phys. Rev. D **74** (2006) 011701 and JHEP 0811 (2008) 042.

[11] J. Girrbach, U. Nierste, arXiv:1202.4906.

[12] R. M. Fonseca, J. C. Romao and A. M. Teixeira Eur. Phys. J. C **72** (2012) 2228.

[13] A. Abada, *et al.* JHEP **1402** (2014) 091 [arXiv:1311.2830v2 [hep-ph]]

[14] F. Ambrosino, *et al.* [KLOE Collaboration], Eur. Phys. J. C **64** (2009) 627.

[15] C. Lazzeroni, *et al.* [NA62 Collaboration], Phys. Lett. B **719** (2013) 326.

[16] G. Ruggiero [NA62 Collaboration], proceedings of PANIC 2014 conference.

[17] A. Sher, *et al.*, Phys. Rev. D **72** (2005) 012005 [hep-ex/0502020].

[18] R. Appel, *et al.*, Phys. Rev. Lett. **85** (2000) 2877 [hep-ex/0006003].

[19] A. M. Diamant-Berger, *et al.*, Phys. Lett. B **62** (1976) 485.

[20] A.V. Artamonov, *et al.* [E949 Collaboration], [arXiv:hep-ex/0506028v2] (2005).

[21] E. Abouzaid, *et al.* [KTeV Collaboration], Phys. Rev. Lett. **100** (2008) 182001 [arXiv:0802.2064 [hep-ex]].

[22] J. McDonough, *et al.*, Phys. Rev. D 38 (1988) 2121.

[23] see Fig. 6 in arXiv:1311.0029v1 [hep-ph] and references therein.

[24] B. Holdom, Phys. Lett. B 166 (1986) 196; P. Galison and A. Manohar, Phys. Lett. B 136 (1984) 279.

[25] L. Canetti *et al.* [arXiv:1208.4607v2 [hep-ph]].

Ultracold Neutron Physics at the Los Alamos National Laboratory

Leah Broussard[1] for the UCNA, UCNB, UCNτ, and LANL nEDM collaborations

[1]Los Alamos National Laboratory, Los Alamos, NM, USA 87545

DOI: http://dx.doi.org/10.3204/DESY-PROC-2014-04/116

Los Alamos National Laboratory uses one of the highest density sources of ultracold neutrons in the world to perform precision measurements in neutron decay. The UCNA experiment's most recent dataset is expected to determine the beta asymmetry with half-percent uncertainty. Currently in progress are the UCNB experiment to measure the neutrino asymmetry, and the UCNτ experiment to measure the neutron lifetime. Finally, a new effort is underway to improve the sensitivity to the neutron EDM by an order of magnitude.

1 The UCN source at LANSCE

The ultracold neutron (UCN) facility at the Los Alamos Neutron Science Center (LANSCE) is used for a number of precision studies of the electroweak interaction through the decay of the neutron and the search for symmetry violations that could generate an electric dipole moment. UCN have energies of less than about 300 neV or 4 mK temperature, rendering them sensitive to all four of the fundamental forces at levels achievable in the laboratory. They are completely reflected by some material potentials, are constrained to heights of about 3 m by gravity, can be completely polarized by magnetic fields of about 6 T due to the neutron's magnetic moment, and decay due to the weak interaction with an experimentally convenient lifetime of about 15 minutes.

The pulsed 800 MeV proton beam from the LANSCE linear accelerator incident on a tungsten target produces spallation neutrons, which are moderated in graphite and cold polyethylene. The resulting cold neutrons can then single scatter in a solid deuterium crystal and convert into UCN. The UCN then escape the source, which is subsequently closed off by a butterfly valve, and are transported by a stainless steel guide system out of the biological shielding into the experimental area, where densities of up to 50 UCN/cc have been achieved [1].

2 UCNA

One of the most important tests of our understanding of the electroweak interaction is the unitarity of the Cabibbo-Kobayashi-Maskawa (CKM) quark-mixing matrix, which is sensitive to new physics beyond the Standard Model [2]. The matrix element V_{ud} contributes to the most precise such test. In neutron decay, two measurements are required to extract V_{ud}: the lifetime and a correlation coefficient, such as the asymmetry between the neutron spin and the emitted electron, A, to set the value of λ, the ratio of axial-vector to vector couplings. Currently, V_{ud}

is determined most precisely from the set of superallowed $0^+ \rightarrow 0^+$ Fermi decays [3]. It is extracted from neutron decay with about an order of magnitude greater uncertainty, primarily due to the uncertainty in λ. However, as the neutron is not sensitive to nuclear-structure dependent corrections, with reduced experimental error this system should be able to achieve a lower ultimate uncertainty.

The UCNA experiment is the first to determine the beta asymmetry A using UCN. The UCN are 100% polarized by a 6 T superconducting magnet and adiabatic fast passage spin flipper. The UCN are bottled by a copper guide with thin, beryllium foil end caps inside a 1 T decay spectrometer, which aligns their spins along the spectrometer axis. The decay electrons are guided along the magnetic field lines to a detection system consisting of multi-wire proportional chambers for position sensitivity and fast timing for backscatter reconstruction, and plastic scintillators for energy determination.

The most recent published result, resulting in the extraction of $\lambda = -1.2756(30)$, includes 20M beta decay events after all cuts applied, and a total systematic uncertainty of 0.8% and statistical uncertainty of 0.5% [4]. The most important uncertainties include the rate of depolarization of UCN, the backscattered fraction of electrons, and the determination of the electron energy as a function of angle. Several improvements significantly reduced the uncertainty of the 2011-2013 data set, now in analysis. A shutter installed between the polarizing 6 T magnet and the decay trap allowed for an improved determination of depolarization fraction. Thinner foils for the end caps on the decay trap reduced both the backscatter correction and uncertainty. A fast timing source using an avalanche photodiode to detect the Auger from ^{113}Sn in coincidence with the monoenergetic conversion electrons detected by the UCNA detectors improved characterization of scattering and energy loss as a function of pitch angle. Finally, calibrations using xenon and LED studies improved the uncertainty of the energy reconstruction. The systematic uncertainty is expected to improve by almost a factor of 3 in this data set, and is statistics limited. Future ventures to improve the determination of A would require a significant improvement in the neutron decay rate.

3 UCNτ

The lifetime of the neutron is a necessary input to extract V_{ud} along with the beta asymmetry, and is also a critical input for predicting the primordial helium abundance in the early universe. The accuracy of the determination of the lifetime is called into question by the current discrepancy between the lifetime as measured by either beam or bottle experiments, of about 8 s out of $\sim$880 s [5]. One important uncertainty in previous material bottle traps is the determination of the wall loss due to the material interactions. A magneto-gravitational trap eliminates all material interactions and significantly reduces this effect. The asymmetric shape also mitigates the effect of quasi-bound orbits which are not quickly cleaned and are not completely trapped, and can be lost at similar time scales to the decay lifetime. A storage time of $\tau_{store} = 860 \pm 19$ s has recently been demonstrated in the trap [6], and new methods for UCN detection within the trap are being developed. The current apparatus is being developed for a 1 s measurement of the neutron lifetime, ultimately leading to the design of a sub-1-s experiment.

4 UCNB

The correlation between the neutron spin and the neutrino direction B is sensitive to possible scalar and tensor currents predicted by theories beyond the Standard Model [7]. The neutrino direction must be determined from the decay proton and electron detected in coincidence. A greater sensitivity to b_ν, the electron energy dependent component of a scalar/tensor contribution to B, can be obtained by taking the ratio of the proton and electron asymmetry. By performing a simultaneous fit to the observed electron energy spectra for each proton/electron direction, the proton/electron asymmetries, and the spin-averaged electron energy spectrum, b, b_ν and λ can be extracted simultaneously with precision at the 10^{-3} level from 10^8 total decays [8].

The UCNB experiment uses novel 2 mm thick, large area (12 cm diameter active area), highly segmented (127 hexagonal pixels) silicon detectors installed in the UCNA spectrometer to detect the electron and proton from neutron beta decay in coincidence [9]. The detection system was developed in collaboration with the Nab experiment [10], which will measure the electron-neutrino correlation and Fierz interference term b at the Spallation Neutron Source. Custom preamplifiers are being developed which must meet the requirements of fast timing ($\sim$10 ns) for distinguishing electron backscatter events and very low noise to detect the protons. The protons are emitted with less than 800 eV and could not pass the deadlayer of the detector. Therefore they are accelerated by a -30kV high voltage bias applied to the detection system, including detector and mounting structure, preamplifiers and data acquisition system.

This detector has achieved the first direct observation of both the proton and electron from neutron beta decay in coincidence, using an 8 channel prototype preamplifier. The system can clearly resolve signals above 20 keV with 3 keV (σ) resolution, sufficient for triggering on proton events. A 24 channel prototype has been developed with improved noise characteristics and faster rise time of 20 ns, and after successful demonstration with neutron beta decay, the full 128 channel (127 pixels + ganged partial pixels) system will be implemented. The system has been operated stably at -30 kV and in the 0.6 T expansion region for 100 hours without damage to detectors or electronics. The detector connections can be mechanically damaged during installation, however. A new design using pogo-pin style connectors similar to those used in KATRIN [11] has been tested using 1 cm diameter prototype silicon detectors and have been demonstrated to be robust with many mechanical and cooling cycles. Full-size detectors fully instrumented with pogo-pins are now in development.

5 LANL nEDM

The existence of an electric dipole moment (EDM) in a non-degenerate system requires a violation of time and parity and is a clear indication of the presence of new physics, especially regarding the important question of the observed baryon asymmetry in the universe. Searches for EDMs provide sensitive tests of Beyond the Standard Model theories well beyond the reach of the LHC [12]. The most precise search for an EDM in the neutron was performed at the ILL, using Ramsey's method of separated oscillatory fields. The UCN spins were rotated into the plane perpendicular to the magnetic field, allowed to precess with an electric field aligned parallel and anti-parallel to the magnetic field, then rotated to complete the spin flip. This experiment achieved the limit $d_n < 2.9 \times 10^{-26}$ e-cm (90% C.L.) [13]. To improve this limit, an increase in density to about 100 UCN/cc is required.

With modest improvement to the LANSCE UCN source, the required UCN density for a 10^{-27} e-cm sensitivity is achievable. The most straightforward gains, of about a factor 3, come from improvement in the proton beam delivery and in increasing the current. Currently the proton pulse structure consists of a large burst every 5 s, resulting in significant UCN losses as UCN that fail to escape the source volume before the next beam burst fall back into the solid deuterium crystal when the butterfly valve reopens. Increasing the period to 30 s significantly reduces this loss, but requires an upgrade to beam safety hardware that inaccurately measures the average current, which still falls short of the design specification of 10 μA. A redesign of the UCN source, including better modeling of the moderator configuration, improved cooling, and moving the deuterium closer to the tungsten target is expected to deliver another factor of 2 improvement. Improved transport of the UCN out of the source volume and through the guide system should increase the density by a factor of 3 or more. To take advantage of the increased density, further improvements to the ILL design will be implemented. A prototype high voltage chamber is currently being constructed to test improvements to the geometry and materials used in the electrodes to permit an electric field greater than 10 kV/cm during precession. The PSI collaboration has demonstrated the required improvements to the magnetometry using a ^{199}Hg co-magnetometer to look for variations in the magnetic field over time [14].

6 Summary

The LANSCE UCN facility has a vibrant program for fundamental symmetries and precision searches for physics beyond the Standard Model. The facility was designed to allow for very low background measurements of polarized neutron decay correlations, especially the beta-asymmetry and neutrino-asymmetry, and has expanded to support efforts to determine the neutron lifetime and a search for an electric dipole moment. Planned upgrades to proton beam delivery and source performance will ensure this facility remains one of the most competitive UCN sources in the world.

References

[1] A. Saunders *et al.*, Rev. Sci. Instrum. **84** 013304 (2013).

[2] M. Antonelli *et al.*, Phys. Rep. **494**, 197 (2010).

[3] J. C. Hardy and I. S. Towner, Phys. Rev. C **79** 055502 (2009).

[4] M. P. Mendenhall *et al.*, Phys. Rev. C **87** 032501(R) (2013).

[5] A. T. Yue *et al.*, Phys. Rev. Lett. **111** 222501 (2013).

[6] D. J. Salvat *et al.*, Phys. Rev. C **89** 052501(R) (2014).

[7] T. Bhattacharya *et al.*, Phys. Rev. D **85** 054512 (2012).

[8] B. Plaster, S. J. Sjue and A. R. Young, (2014) in prep.

[9] A. Salas-Bacci *et al.*, Nucl. Instr. and Meth. in Phys. Rev. A **735** 408 (2014).

[10] S. Baessler *et al.*, AIP Conf. Proc. **1560** 114 (2013).

[11] B. A. VanDevender *et al.*, Nucl. Instr. and Meth. in Phys. Rev. A **673** 46 (2012).

[12] J. Engel, M. J. Ramsey-Musolf and U. van Kolck, Prog. Part. Nucl. Phys **71** 21 (2013).

[13] C. A. Baker *et al.*, Phys. Rev. Lett. **97** 131801 (2006).

[14] B. M. Horras, Ph.D. thesis, ETH Zürich (2012).

Measurements of Electric Dipole Moments of Charged Particles at Storage Rings

Volker Hejny for the JEDI Collaboration

Institut für Kernphysik and Jülich Center for Hadron Physics, Forschungszentrum Jülich, 52425 Jülich, Germany

DOI: http://dx.doi.org/10.3204/DESY-PROC-2014-04/156

Electric Dipole Moments (EDM) of elementary particles are considered to be one of the most powerful tools to investigate CP violation beyond the Standard Model and to find an explanation for the dominance of matter over antimatter in our universe. Up to now experiments concentrated on neutral systems (neutrons, atoms, molecules). Storage rings offer the possibility to measure EDMs of charged particles by observing the influence of the EDM on the spin motion. The Cooler Synchrotron COSY at the Forschungszentrum Jülich provides polarized protons and deuterons up to a momentum of 3.7 GeV/c and is thus an ideal starting point for such an experimental program. The JEDI (Jülich Electric Dipole moment Investigations) Collaboration has been formed to exploit the COSY facility to demonstrate the feasibility of such a measurement and to perform all the necessary investigations towards the design of a dedicated storage ring.

1 Introduction

Electric dipole moments (EDM) break parity (P), time-reversal (T) symmetry, and — via the CPT-theorem — charge-parity (CP) symmetry. The established Kobayashi-Maskawa mechanism of CP violation predicts EDMs orders of magnitude below the current experimental limits. In addition, the Standard Model Lagrangian contains a possible source of CP violation in strong interaction, which, however, does not seem to be realized in nature: the experimental bound from neutron EDM experiments (for an overview see e.g. Ref. [1]) on the strength parametrized by the vacuum angle θ_{QCD} is $|\theta_{\mathrm{QCD}}| \lesssim 10^{-10}$ and, thus, unexpectedly small. Furthermore, the universal matter/antimatter asymmetry implies that there should be CP violation from physics besides the Kobayashi-Maskawa mechanism and beyond the Standard Model. EDMs are excellent probes for these new CP-violating sources [2, 3, 4].

Once an EDM has been measured, the next goal is to identify its source. Is it, for example, caused by strong CP violation or from physics beyond the Standard Model? Experimental data on the EDMs of several light nuclei could provide an answer to this question: different classes of models predict different hierarchies of EDMs and thus can be disentangled once several light-nuclear EDM experiments (protons, deuterons and possibly ^{3}He) have been performed.

2 Basic Concept

The basic concept of measuring a permanent electric dipole moment is to place the test object into a strong electric field and to monitor the spin precession caused by the electric dipole moment. For neutral systems this can be done in a quasi-static, localized setup. Charged particles, however, are accelerated by the electric field. Therefore, it has been suggested in Ref. [5] (at that time for muons) to utilize a storage ring for such a measurement. The goal of the US-based srEDM collaboration [6] and the Jülich-based JEDI collaboration [7] is to apply this concept to protons, deuterons and ^{3}He [8].

The spin motion of a particle in a storage ring due to magnetic and electric dipole moments is described by the Thomas-BMT equation [9]

$$\frac{\mathrm{d}\vec{S}}{\mathrm{d}t} = \left(\vec{\Omega}_{\mathrm{MDM}} + \vec{\Omega}_{\mathrm{EDM}}\right) \times \vec{S} \tag{1}$$

$$\vec{\Omega}_{\mathrm{MDM}} = -\frac{q}{m_0}\left[G\vec{B} + \left(\frac{1}{\gamma^2-1} - G\right)\frac{\vec{\beta}\times\vec{E}}{c}\right] \tag{2}$$

$$\vec{\Omega}_{\mathrm{EDM}} = -\frac{dc}{\hbar S}\left[\frac{\vec{E}}{c} + \vec{\beta}\times\vec{B}\right] \tag{3}$$

with S denoting the spin of the particle, t the time in the laboratory system, q and m_0 the charge and the mass of the particle, β and γ the relativistic Lorentz factors, G the magnetic anomaly and d the electric dipole moment. Terms proportional to $\vec{\beta}\cdot\vec{E}$ and $\vec{\beta}\cdot\vec{B}$ (*i.e.*, the effect of longitudinal field components) are omitted. The general idea of the measurement is to adjust the electric and magnetic fields as well as the particle momentum such, that the term $\vec{\Omega}_{\mathrm{MDM}}$ — sensitive to the magnetic dipole moment — vanishes. For the proton with a positive anomalous magnetic moment this can be achieved with a purely electric ring by setting the momentum to $p = \frac{m_0}{\sqrt{G}}$, for deuterons and ^{3}He a suitable combination of electric and magnetic fields is necessary. Thereby, starting with the spin aligned to particle momentum, the precession caused by the transverse electric and magnetic fields (the latter creating a motional electric field $\vec{\beta}\times\vec{B}$) will lead to a vertical polarization build-up.

Assuming high intensity beams of $4\cdot10^{10}$ particles per fill, a polarization degree of 80%, electric fields of $E = 10\,\mathrm{MV/m}$, and spin coherence times of 1000 s (see below) a statistical error for an EDM of $10^{-29}\,e$cm is in reach for one year of measurement. The remaining challenge is to get the systematic uncertainty down to the same level.

While the effects from the magnetic dipole moment can only be canceled in a dedicated storage ring yet to be designed and built, the Cooler Synchrotron COSY at the Forschungszentrum Jülich is an ideal place for the necessary R&D work and a proof-of-principle experiment [7, 10]. COSY is a unique facility for spin physics with hadronic probes on a world-wide scale: it has a history of a highly successful operation of cooled polarized proton and deuteron beams and polarized targets. As a purely magnetic ring the spin precession caused by the magnetic dipole moment of the particles cannot be canceled. Instead, this spin motion is utilized to develop tools and equipment for the design and operation of the final ring. Furthermore, using an rf Wien filter the spin precession due to the magnetic dipole moment can be manipulated such that the motional electric field generates a net EDM effect [8, 10].

3 R&D at COSY

Currently various developments are under way at COSY: improved beam position monitors, electrostatic deflectors, polarimetry, the rf Wien filter, systematic studies of the influence of sextupoles, steerers and solenoids, etc. One major goal was to increase the spin coherence time of the particles: as an ensemble of about 10^{10} particles is under observation, the length of one experimental cycle is determined by the time the spins of all particles precess coherently with the same angular velocity. For this purpose a time marking system using the EDDA detector as polarimeter has been developed to monitor the horizontal spin precession — i.e. the in-plane polarization — of a deuteron beam at 0.97 GeV/c. Further information on the method, the data analysis and the results on the spin coherence time can be found in Refs. [11, 12]. Here a short summary: for deuterons in a pure magnetic ring with vertical bending fields the Thomas-BMT equation reduces to

$$\frac{\mathrm{d}S}{\mathrm{d}t} = \frac{qB}{m_0} \cdot G. \tag{4}$$

Dividing this by the cyclotron frequency $\omega_{\mathrm{cyc}} = \frac{qB}{m_0\gamma}$ one gets $\nu = \gamma G$. ν is called the spin tune and describes the number of spin revolutions per turn relative to the particle momentum. For an unbunched beam decoherence is expected within less than one second due to the spread in momentum (and, thus, in γ). To first order this spread can be compensated by a bunched beam and spin coherence times of several seconds can be achieved. Higher orders (e.g. synchrotron oscillations, dispersion effects) can be corrected by means of sextupoles. Here, spin coherence times of several hundred seconds could already be reached.

Another tool to be used for studying the effect of various ring elements like solenoids, steerer and the rf Wien filter on the spin motion is the precise measurement of the spin tune with a precision close to $\Delta\nu \approx 10^{-10}$. This has been used successfully during the last beam times and a corresponding publication is currently under preparation.

4 Summary and Outlook

At the Cooler Synchrotron COSY of the Forschungszentrum Jülich R&D work has been started towards a dedicated storage ring for measuring electric dipole moments of charged hadrons. A time marking system together with the EDDA detector has been setup to allow for high precision studies of the spin motion in COSY. As a first result large spin coherence times in the order of several hundred seconds have been achieved by tuning the standard ring sextupole magnets. There are two major milestones for the next five years: a proof-of-principle experiment at COSY with limited sensitivity and a conceptual design report for the final EDM ring.

Acknowledgments

We would like to thank the technical and administrative staff at the Forschungszentrum Jülich, especially at the COoler SYnchrotron COSY and at the participating institutes.

References

[1] S.K. Lamoreaux and R. Golub, J. Phys. G **36** 104002 (2009).

[2] J.M. Pendlebury *et al.*, Nucl. Inst. Meth. **A440** 471 (2000).

[3] T. Fukuyama, Int. J. Mod. Phys. **A27** 1230015 (2012).

[4] K. Jungmann, Ann. Phys. **525** 550 (2013).

[5] F.J.M. Farley *et al.*, Phys. Rev. Lett. **93** 052001 (2004).

[6] srEDM Collaboration, *http://www.bnl.gov/edm*

[7] JEDI Collaboration, *http://collaborations.fz-juelich.de/ikp/jedi*

[8] F. Rathmann, A. Saleev and N.N. Nikolaev, J. Phys. Conf. Ser. **447** 012011 (2013).

[9] V. Bargmann, L. Michel, and V.L. Telegdi, Phys. Rev. Lett. **2** 435 (1959).

[10] A. Lehrach *et al.*, *Search for Permanent Electric Dipole Moments at COSY Step 1: Spin coherence and systematic error studies*, COSY proposals #216 (2012) and #216.1 (2014).

[11] P. Benati *et al*, Phys. Rev. STAB **15** 124202 (2012).

[12] Z. Bagdasarian *et al.*, Phys. Rev. STAB **17** 052803 (2014).

Latest results from the *a*SPECT experiment

Alexander Wunderle[1], *Oliver Zimmer*[2], *Romain Virot*[2], *Camille Theroine*[3], *Torsten Soldner*[2], *Martin Simson*[2], *Christian Schmidt*[1], *Romain Maisonobe*[2], *Gertrud Konrad*[4], *Werner Heil*[1], *Ferenc Glück*[5], *Marcus Beck*[1], *Stefan Baeßler*[6]

[1]Johannes Gutenberg-Universität, Staudingerweg 7, 55128 Mainz, Germany
[2]Institut Laue-Langevin, 71 avenue des Martyrs, 38000 Grenoble, France
[3]European Spallation Source, Box 176, S221 00 Lund, Sweden
[4]Technische Universität Wien, Stadionallee 2, 1020 Wien, Austria
[5]Karlsruher Institut für Technologie, Hermann-von-Helmholtz-Platz 1, 76344 Eggenstein, Germany
[6]University of Virginia, 382 McCommick Rd. Charlottesville, VA, USA

DOI: http://dx.doi.org/10.3204/DESY-PROC-2014-04/72

The *a*SPECT retardation spectrometer measures the $\beta - \bar{\nu}_e$ angular correlation coefficient a in the β-decay of the free neutron. This measurement can be used to determine the ratio $\lambda = \frac{g_A}{g_V}$ of the weak coupling constants, as well as to search for physics beyond the standard electroweak model. In spring/summer 2013 *a*SPECT had a successful beam time at the Institut Laue-Langevin (ILL), Grenoble/France. The goal of this beam time is to improve the current uncertainty of a from $\frac{\Delta a}{a} \sim 5\%$ to about 1%. To achieve this goal the systematic uncertainties of *a*SPECT have to be understood accordingly. This is achieved via systematic tests, measurements of a with different systematic parameter settings during the beam time and measurements afterwards, like the work-function fluctuations of electrodes or the magnetic field ratio of our spectrometer. Sophisticated simulations of our spectrometer are used to understand and reduce the systematic uncertainties further.

1 Motivation

The β-decay of the free neutron is an ideal system to search for physics beyond the standard model. Its daughter nucleus, the proton, is the simplest possible, so no complicated nuclear corrections are necessary. Further, the system is overdetermined, which opens the possibility to determine one parameter of the standard model, λ, by measuring different correlations. With this complementarity a reduction of the systematic uncertainties of the parameter, as well as a test of the standard model itself is possible.

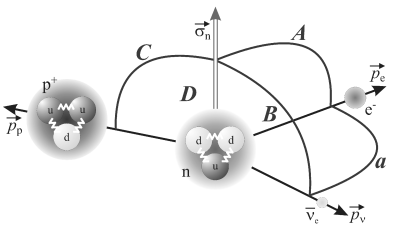

Figure 1: Graphical representation of the important angular correlations in the β-decay of the free neutron.

One of these correlations is the $\beta - \bar{\nu}_e$ angular correlation coefficient a. It describes the angular distribution between the emitted electron and electron-antineutrino and is linked to λ by $a = \frac{1-|\lambda|^2}{1+3|\lambda|^2}$. For further information about the physics of the

neutron, the reader is referred to [1].

2 The *a*SPECT Experiment

*a*SPECT is a MAC-E-filter (**M**agnetic **A**diabatic **C**ollimation combined with an **E**lectrostatic potential). In the following an overview of the measurement principle of a MAC-E filter and the systematic of *a*SPECT is given.

2.1 Measurement Principle

A schematic of the experimental setup of *a*SPECT can be seen in Fig. 2. The neutrons are collimated and guided through the Decay Volume (DV) at high magnetic field (B = 2.2 T). The protons from decays in the DV are adiabatically guided by the magnetic field to a region of 0.44 T, the Analysing Plane (AP). This adiabatic change of the magnetic field causes a momentum transfer from transversal momentum to longitudinal momentum, known as the inverse magnetic mirror effect. Between the electrodes in the DV and the AP a voltage is applied, which acts as a retardation voltage for the protons. This retardation potential performs the energy analysis of the protons. The resolution of a MAC-E filter is determined by the ratio of the magnetic field in the DV and in the AP, in case of *a*SPECT the resolution is about 20 %.

Protons with enough kinetic energy to overcome the potential barrier in the AP are accelerated by typically -15 kV and are detected by a silicon-drift-detector [2]. In this way *a*SPECT measures the integral recoil spectrum of the protons with high precision. This spectrum can be used to determine a and therefore λ with high precision.

For a detailed description of *a*SPECT the reader is referred to [3, 4].

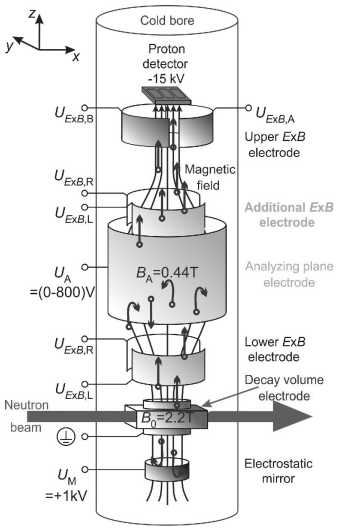

Figure 2: Schematic of the spectrometer *a*SPECT.

2.2 Beam Times and Improvements

*a*SPECT has had several beam times in the past, leading to significant improvements of the system and finally a successful beamtime in 2013. In the following a short overview of these improvements is given. A data acquisition system (DAQ) with logarithmic amplification has been designed and tested to avoid any saturation effects, as seen in 2008. The vacuum has been improved by better cleaning procedures, exchange of materials in the UHV system and the installation of additional turbo molecular and getter pumps. Further, the edges of our electrode system have been smoothed and the whole system has been recoated to reduce field emission. Also an additional dipole electrode has been installed to remove trapped charged particles from a penning-like trap in our spectrometer. These improvements proved to solve the problematic of discharges in the spectrometer and to reduce the background to a sufficiently

low level to determine a with $\frac{\Delta a}{a} \sim 1$ %. The system has been further improved by a new neutron collimation made of conductive boron nitride. Furthermore, a system to measure the beam profile inside of the DV has been designed for investigations of the so-called edge effect with high precision. This system also allows ti introduce radioactive sources into the DV, for alignment and background studies. The DV and AP have been redesigned out of flat electrode plates to obtain well-defined surfaces, which is important to determine the exact potential inside the electrodes.

In 2013 a beam time of 100 days took place with the improved system. This run includes 40 days of pure data taking. During these days no discharges occurred and a sufficiently low background has been observed. No saturation effects in the DAQ have been observed and an additional DAQ without a shaper, but with a high resolution FlashADC has been tested. With a statistical sensitivity of about 1.3 % per day and detector pad (a 3 pad detector was used) many in-depth systematic tests of the system were possible. The analysis of the data and the systematics is currently ongoing.

3 First Results

A thorough investigation of the systematic uncertainties is necessary to achieve the goal of aSPECT of $\frac{\Delta a}{a} \sim 1$ %. One of the main contributions to the systematic error is the uncertainty of the transmission-function of the MAC-E filter. The transmission-function is a function of the ratio of the magnetic field in the AP region and the DV region, as well as the potential difference between AP and DV electrodes [3]

$$f_{Trans} = f\left(\frac{B_{AP}}{B_{DV}}, \Phi_{AP} - \Phi_{DV}\right).$$

3.1 Magnetic field ratio

The magnetic field ratio $r_B = \frac{B_{AP}}{B_{DV}}$ has to be know to a level of $\frac{\Delta r_b}{r_b} \leq 10^{-4}$, which corresponds to an error contribution of $\frac{\Delta a}{a} \sim 0.1\%$ [4]. To achieve this level of precision a nuclear magnetic resonance system (NMR) has been designed, since a standard hall probe can not reach the required precision under lab conditions. The measurement of the magnetic field ratio took place immediately after the beam time at the beam place. The NMR system measured the magnetic field in the DV and AP simultaneously, determining the ratio of the magnetic fields. A small drift has been observed over time for the magnetic field in the single regions, as well as systematic influences of surrounding materials. However, the ratio of the magnetic field stays stable at a level of $\frac{\Delta r_b}{r_b} < 10^{-4}$, see Fig. 3. This is more than sufficient for our goal of $\frac{\Delta a}{a} \sim 1\%$.

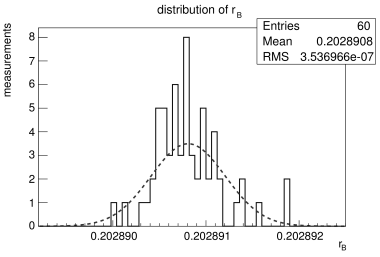

Figure 3: Histogram of the distribution of the r_B values for different settings and over time. The dashed line shows a Gaussian fit to the measured data.

3.2 Potential difference

An accuracy of the retardation potential for the decay protons $U_A = \Phi_{AP} - \Phi_{DV}$ of ~ 10 mV corresponds to an error in a of $\frac{\Delta a}{a} \sim 0.1\%$ [4]. The determination of the potential difference between the AP electrode and the DV electrode is not a trivial task. The retardation voltage is applied by a stable power supply (FUG HCN 0,8M 800) and measured by a precision digital multimeter (Agilent 3458A). However, the applied potential seen by the decay protons is changed by the shape of the electrode, field leakage from outside of the electrode and the work function of the surface material of the electrode.

The shape of the potential due to the electrode design can be simulated. The field leakage can be simulated and measured partially by changing the voltage difference between the electrode and its surrounding during the beam time. The work function, more precisely, the surface contact potential, has to be measured afterwards using eg. a Kelvin Probe. In Fig. 4 a scan of the surface contact potential at air of one of the aSPECT electrodes is shown. Clearly three different areas of different contact potential can be distinguished. These 'patches' are caused by the different crystal orientations of the gold coating of the electrodes [5]. The scanning of the electrodes with a Kelvin Probe is ongoing. First results show an average fluctuation across an electrode of 19 mV and differences of the average between different electrodes of 35 mV. The surface contact potential does not reflect the potential fluctuations, as seen by the protons, which have to be determined by simulations of the electric potential inside the electrodes. But these first results can be used for a worst case scenario, since a fluctuation of 54 mV in the retardation voltage corresponds to $\frac{\Delta a}{a} \sim 0.5\%$, which is compatible with an overall precision of $\frac{\Delta a}{a} \sim 1\%$.

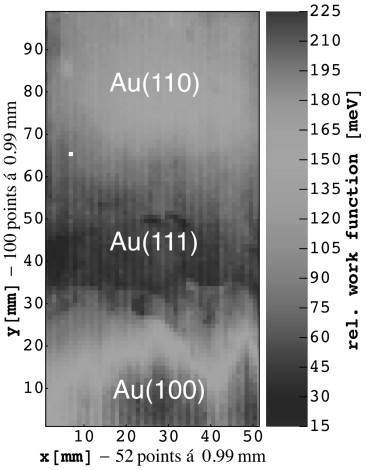

Figure 4: Scan of the surface contact potential with a Kelvin Probe of one of the aSPECT electrodes. For more details see text.

Acknowledgements

This work has been supported by the joint priority program 1491 of the Deutsche Forschungsgemeinschaft and the Austrian Science Fund, project HE2308/9-1, HE2308/9-2, ZI816/1-1, ZI816/4-1, SO1058/2-1 and I534-N20, the University of Mainz, the ILL and the Technische Universität Vienna.

References

[1] H. Abele, Prog. Part. Nucl. Phys., **60** 1 (2008).

[2] M. Simson *et al.*, NIM A, **581** 3 (2007).

[3] O. Zimmer *et al.*, NIM A, **440** 3 (2000).

[4] F. Glück *et al.*, Eur. Phys. J. A, **23** 1 (2005).

[5] Handbook of Chemistry and Physics, 95th edition, **ISBN 9781482208672**, (2014).

Limit on Lorentz-Invariance- and CPT-Violating Neutron Spin Interactions Using a ^{3}He-^{129}Xe Comagnetometer

Fabian Allmendinger[1], *Ulrich Schmidt*[1], *Werner Heil*[2], *Sergei Karpuk*[2], *Yury Sobolev*[2], *Kathlynne Tullney*[2]

[1]Physikalisches Institut, Ruprecht-Karls-Universität Heidelberg, Germany
[2]Institut für Physik, Johannes Gutenberg-Universität Mainz, Germany

DOI: http://dx.doi.org/10.3204/DESY-PROC-2014-04/41

We performed a search for a Lorentz-invariance- and CPT-violating coupling of the ^{3}He and ^{129}Xe nuclear spins to posited background fields. Our experimental approach is to measure the free precession of nuclear spin polarized ^{3}He and ^{129}Xe atoms using SQUIDs as detectors. As the laboratory reference frame rotates with respect to distant stars, we look for a sidereal modulation of the Larmor frequencies of the co-located spin samples. As a result we obtain an upper limit on the equatorial component of the background field $\tilde{b}^n_\perp < 8.4 \cdot 10^{-34}$ GeV (68% C.L.). This experiment is currently the most precise test of spin anisotropy due to the excellent long spin-coherence time.

1 Introduction and Experimental Setup

In the context of the Standard-Model Extension (SME)[1, 2, 3], couplings of the neutron or proton spin $\boldsymbol{\sigma}^{\boldsymbol{n,p}}$ to relic background fields $\tilde{\boldsymbol{b}}^{\boldsymbol{n,p}}$ are discussed. The background fields have distinct directions in space and correspond to preferred spin directions. These couplings with the potential $V = \tilde{\boldsymbol{b}}^{\boldsymbol{n,p}} \cdot \boldsymbol{\sigma}^{\boldsymbol{n,p}}$ are purely non-magnetic, but change the energy levels of spins in a magnetic field, which can be detected by changes in the Larmor frequency of precessing spins.

Nuclear spin clocks, based on the detection of free spin precession of gaseous nuclear polarized ^{3}He and ^{129}Xe atoms with LT$_C$ SQUIDs as low-noise magnetic flux detectors are used as ultra-sensitive probe for nonmagnetic spin interactions, since the magnetic interaction (Zeeman term) drops out in the case of co-located spin samples (comagnetometry). Measurements of uninterrupted precession of $T \sim 1$ day can be achieved at the present stage of investigation due to long spin-coherence times. The principle of measurement is to search for sidereal variations of the precession frequency of co-located spin species while the Earth and hence the laboratory reference frame rotates with respect to distant stars.

To give a short overview of the setup (details are given in Ref. [4]): The two polarized gas species (and N_2 as a buffer gas) are filled into a low-relaxation spherical glass cell with radius $R = 5$ cm. Typically, the optimum conditions in terms of long transverse relaxation times (T_2^*) and high Signal-to-Noise Ratio are met at a gas mixture with pressures of $p_{He} = 3$ mbar, $p_{Xe} = 5$ mbar, $p_{N2} = 25$ mbar. The cell is positioned in a homogeneous static magnetic field (about 400 nT)

that is generated by Helmholtz coils mounted inside the strongly magnetically shielded room *BMSR-2* at the *Physikalisch-Technische Bundesanstalt* in Berlin. At that field strength, the Larmor frequencies of ^{3}He and ^{129}Xe are about $\omega_{He} \approx 2\pi \cdot 13$ Hz and $\omega_{Xe} \approx 2\pi \cdot 4.7$ Hz, respectively. To measure these precession frequencies very precisely, low-noise low-temperature DC-SQUID gradiometers are used as magnetic flux detectors. Due to the very low field gradients in the order of pT/cm at the location of the cell, the transverse relaxation times reached $T_2^* = 8.5$ h for ^{129}Xe and up to $T_2^* = 100$ h for ^{3}He [4]. The measured signal amplitudes at the beginning of the measurement were up to $A_{\mathrm{He}} = 20$ pT and $A_{\mathrm{Xe}} = 8$ pT for ^{3}He and ^{129}Xe, respectively. The noise level (combination of four gradiometers) was $\rho = 3\ \mathrm{fT}/\sqrt{\mathrm{Hz}}$. Due to the long spin-coherence time and the high initial Signal-to-Noise Ratio, the spin precession could be monitored for more than one day, which improves the sensitivity remarkably (see below).

2 Data Evaluation and Results

To be sensitive to tiny nonmagnetic interactions, one has to consider the weighted difference of the respective Larmor frequencies of the co-located spin samples, or the corresponding time integral (weighted phase difference), which are defined by

$$\Delta\omega = \omega_{\mathrm{He}} - \frac{\gamma_{\mathrm{He}}}{\gamma_{\mathrm{Xe}}}\omega_{\mathrm{Xe}} \quad \text{and} \quad \Delta\Phi = \Phi_{\mathrm{He}} - \frac{\gamma_{\mathrm{He}}}{\gamma_{\mathrm{Xe}}}\Phi_{\mathrm{Xe}} \quad . \tag{1}$$

In doing so, magnetic field fluctuations are canceled, i.e. in principle $\Delta\omega = 0$ and $\Delta\Phi$ =const. if there are no further interactions. However, on a closer look, $\Delta\Phi$ is not constant in time, as higher order effects have to be take into account. These can be parameterized by

$$\Delta\Phi(t) \quad = \quad c_0 + c_1 t + E_{\mathrm{He}} e^{-t/T^*_{2,\mathrm{He}}} + E_{\mathrm{Xe}} e^{-t/T^*_{2,\mathrm{Xe}}} + F_{\mathrm{He}} e^{-2t/T^*_{2,\mathrm{He}}} + F_{\mathrm{Xe}} e^{-2t/T^*_{2,\mathrm{Xe}}} \quad . \tag{2}$$

The linear contribution stems from Earth's rotation and from chemical shift. The four exponential terms account for the Ramsey-Bloch-Siegert shift [5, 6]. These effects are discussed in Ref. [4]. Finally, the function in Eq. (2) together with the appropriate parameterization of the Lorentz-invariance-violating effect - in this case a sidereal modulation $\propto \tilde{b} \cdot \sin(\Omega_S \cdot t + \varphi_0)$ - is fitted to the combined weighted phase difference data of all measurement runs (7 in total). The resulting estimate on sidereal modulation is compatible with zero within the correlated and uncorrelated uncertainties and can be expressed as an upper limit on the magnitude of the hypothetical background field:

$$\tilde{b}^{\mathrm{n}}_{\perp} \quad < \quad 6.7 \cdot 10^{-34}\ \mathrm{GeV}\ (68\%\ \mathrm{C.L.}) \quad . \tag{3}$$

3 Frequency Stability

The benefit of long spin-coherence times can be explained on the basis of the Cramer-Rao Lower Bound (CRLB). The CRLB gives the minimum variance of an unbiased estimator of a deterministic parameter. In this case, the sensitivity of frequency measurements depends on the measurement time with coherent spin precession T, the signal amplitude at the beginning of the measurement A decaying with a time constant T_2^* and the noise level ρ (assuming white noise)[7]. The frequency uncertainty is:

$$\sigma_f \quad \geq \quad \frac{\sqrt{3}}{\pi}\frac{\rho}{A} \cdot T^{-3/2} \cdot \sqrt{C(T, T_2^*)} \tag{4}$$

with the dimensionless factor $C(T, T_2^*)$ accounting for the exponential decay of the Signal-to-Noise Ratio. The remarkable result is that the frequency uncertainty decreases with $T^{-3/2}$ for white (Gaussian) noise. The Allan Standard Deviation (ASD) is the appropriate measure to study the temporal characteristics of the ^{3}He-^{129}Xe comagnetometer with respect to phase or frequency determination. The ASD method is an established analysis technique for studying the low-frequency component of a time series and is a measure of phase and frequency stability of clocks and oscillators. In the case of the ^{3}He-^{129}Xe comagnetometer, one compares the ^{3}He precession frequency to the "scaled" ^{129}Xe precession frequency. These two oscillator frequencies are supposed to be the same if all deterministic phase shifts (chemical shift, Earth's rotation, Ramsey-Bloch-Siegert shift etc.) have been incorporated correctly. The behavior of the frequency uncertainty in the ASD plot is shown in Fig. 1 (black symbols) for two different runs. With increasing integration times τ the uncertainty in frequency decreases with $\sigma_{\mathrm{ASD}} \propto \tau^{-\frac{3}{2}}$ as expected by the CRLB in Eq. (4). This indicates the presence of pure white (Gaussian) noise. In other words: All deterministic phase shifts (chemical shift, Earth's rotation, Ramsey-Bloch-Siegert shift etc.) have been incorporated correctly. This has been tested for all measurement runs with different experimental conditions (e.g. different sample cells, partial pressures, magnetic field directions, T_2^*) and the ASD plot shows the expected behavior, leading to the conclusion that the fit model in Eq. (2) describes the behavior of the comagnetometer correctly. An incorrect fit model would immediately lead to a deviation from the CRLB power law. This is also demonstrated in Fig. 1 (gray symbols) showing the ASD as a function of τ for the residuals of a fit model where the $F_{\mathrm{He,\,Xe}}$ terms (called "cross-talk") of Eq. (2) are omitted. For run 6 (the run with largest cross-talk effect), the large deviation from the CRLB power law above $\tau \approx 500$ s is impressive. For run 3 (the run with the smallest cross-talk effect) the deviation in the ASD plot is smaller.

4 Conclusion

Freely precessing gaseous, nuclear polarized ^{3}He and ^{129}Xe samples can be used as ultra-sensitive probe for nonmagnetic spin interactions, since the magnetic interaction (Zeeman term) drops out in the case of co-located spin samples. Long spin-coherence times are highly beneficial as the uncertainty in frequency estimation decreases with $T^{-3/2}$ for Gaussian noise according to the CRLB. The ASD method can be used to verify the CRLB power law and thereby rule out the presence of further noise sources (i.e. further deterministic frequency shifts). With a similar setup, upper limits on interactions mediated by axion-like particles were obtained [8]. The next challenging step is to apply this method in the search for an electric dipole moment of ^{129}Xe.

References

[1] V. A. Kostelecký and S. Samuel, Phys. Rev. D **39**, 683 (1989).
[2] D. Colladay and V. A. Kostelecký, Phys. Rev. D **58**, 116002 (1998).
[3] V. A. Kostelecký and C. D. Lane, Phys. Rev. D **60**, 116010 (1999).
[4] F. Allmendinger *et. al*, Phys. Rev. Lett. **112**, 110801 (2014).
[5] F. Bloch and A. Siegert, Phys. Rev. **57**, 522 (1940).
[6] N. F. Ramsey, Phys. Rev. **100**, 1191 (1955).
[7] W. Heil *et al.*, Ann. Phys. (Berlin) **525**, 539 (2013).
[8] K. Tullney *et al.*, Phys. Rev. Lett. **111**, 100801 (2013).

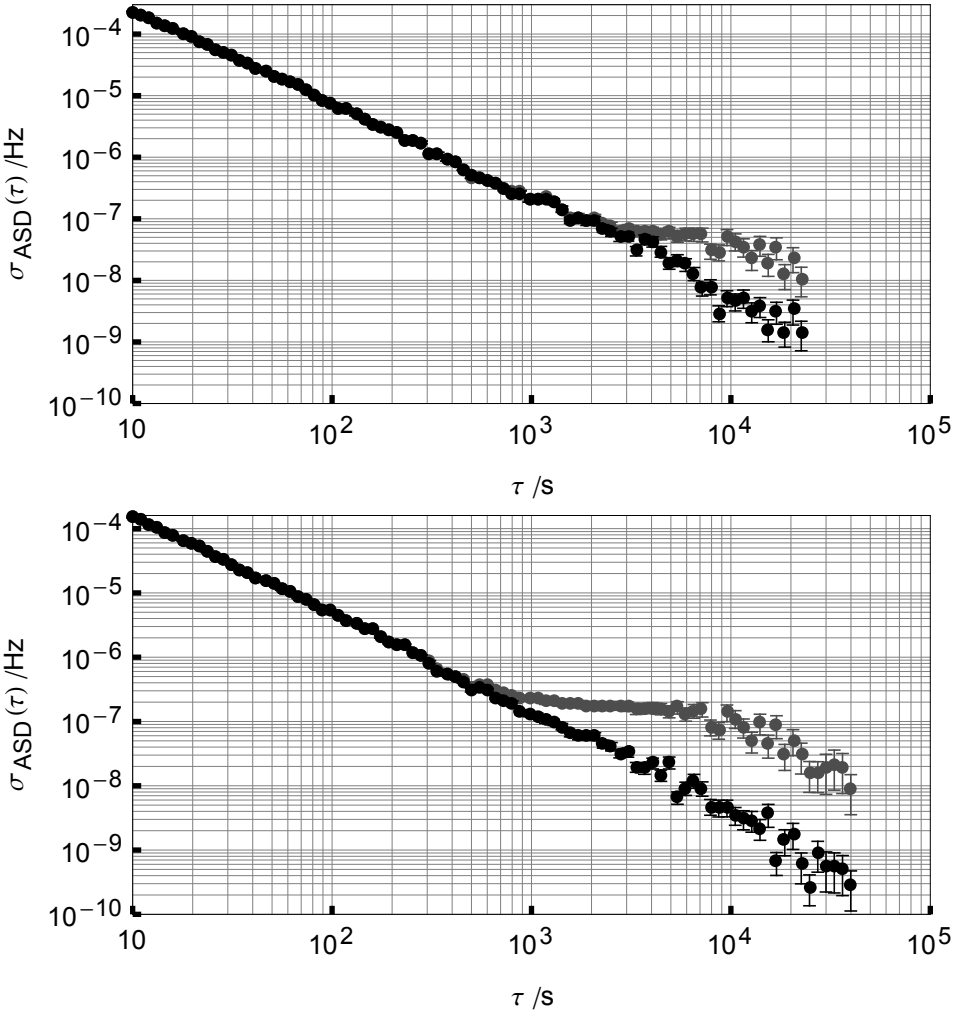

Figure 1: ASD plot of the residual frequency noise of two independent runs (Top: Run 3, Bottom: Run 6). Black symbols: ASD for the correct fit model (Eq. (2)). With increasing integration times τ the uncertainty in frequency decreases as $\sigma \propto \tau^{-\frac{3}{2}}$ indicating the presence of white (Gaussian) noise. Gray symbols: ASD for an incorrect fit model (omitting the Cross-Talk term). For run 6 (the run with largest cross-talk effect), the large deviation from the CRLB power law above a few hundred seconds is impressive. For run 3 (the run with the smallest cross-talk effect) the deviation in the ASD plot is smaller.

Laser spectroscopy of the hyperfine splitting energy in the ground state of muonic hydrogen

Masaharu Sato[1], *Katsuhiko Ishida*[1], *Masahiko Iwasaki*[1,2], *Sohtaro Kanda*[3], *Yue Ma*[1], *Yasuyuki Matsuda*[4], *Teiichiro Matsuzaki*[1], *Katsumi Midorikawa*[5], *Yu Oishi*[1], *Shinji Okada*[1], *Norihito Saito*[5], *Kazuo Tanaka*[1,4], *Satoshi Wada*[5]

[1]RIKEN Nishina Center, RIKEN, Wako, Saitama 351-0198, Japan
[2]Department of Physics, Tokyo Institute of Technology, Meguro, Tokyo 152-8551, Japan
[3]Department of Physics, The University of Tokyo, Bunkyo, Tokyo 113-0033, Japan
[4]Graduate School of Arts and Sciences, The University of Tokyo, Meguro, Tokyo 153-8902, Japan
[5]RIKEN Center for Advanced Photonics, RIKEN, Wako, Saitama 351-0198, Japan

DOI: http://dx.doi.org/10.3204/DESY-PROC-2014-04/67

A new measurement has been proposed to determine the proton Zemach radius from the ground-state hyperfine splitting energy of muonic hydrogen by mean of a laser spectroscopy. The resonance frequency corresponding to the hyperfine splitting energy difference is searched with a recently-developed mid-infrared laser. We have studied the experimental feasibility in the RIKEN-RAL muon facility.

1 Physics motivation

One of the recent hot topics in the present physics is *the proton radius puzzle*, which was stimulated by a measurement of the muonic hydrogen Lamb shift at Paul Scherrer Institute [1]. It is a discrepancy of the proton charge radius obtained by the muonic hydrogen Lamb shift from those by the ordinary methods such as electron-proton scattering and hydrogen spectroscopy [2]. The difference seems not to be attributed to the experimental uncertainty because it is more than 7σ by taking into account the new precise measurements in both sides [3, 4, 5]. To explain the discrepancy, there are several interpretations including hypotheses for physics beyond the standard model. However, none of them are still conclusive.

Meanwhile, the proton internal structure is not only related with the electric distribution, as defined as charge radius, but also with the magnetism distribution. It is a very interesting question how the magnetic distribution of the proton is determined by muons and it may give a definitive answer to understand proton radius puzzle. Therefore, we focus on the proton Zemach radius R_Z, which is defined as,

$$R_Z = \int d^3\mathbf{r}|\mathbf{r}| \int d^3\mathbf{r}' \rho_E(\mathbf{r}')\rho_M(\mathbf{r}-\mathbf{r}'), \tag{1}$$

where ρ_E and ρ_M denote the spatial distribution of the proton charge and the magnetism, respectively. To derive the proton Zemach radius, we measure the hyperfine splitting energy of

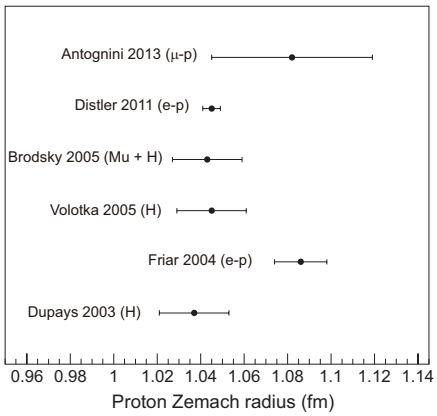

Figure 1: Summary of proton Zemach radius measurements.

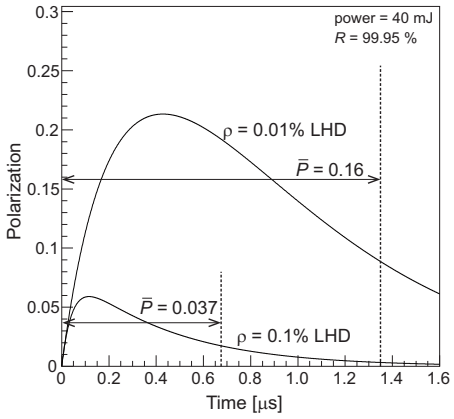

Figure 2: Time population of the muon spin polarization.

the muonic hydrogen. Theoretically, the hyperfine splitting energy is described as [6],

$$\Delta E_{HFS} = E_F(1 + \delta^{QED} + \delta^{FF} + \delta^{rec} + \delta^{pol} + \delta^{hvp}), \tag{2}$$

where E_F denotes the Fermi energy. The terms δ^{QED}, δ^{FF}, δ^{rec}, δ^{pol} and δ^{hvp} indicate the corrections related with higher order QED, proton electromagnetic form factor, recoil effect, proton polarizability and hadronic vacuum polarization, respectively. The dominant contribution is δ^{FF} and is as large as ∼7500 ppm [7]. Its leading contribution is expressed with the proton Zemach radius as, $\delta^{FF} = -2\alpha m_{\mu p} R_Z + O(\alpha^2)$, where α and $m_{\mu p}$ is the fine structure constant and the reduced mass of the muon and the proton. As same with the charge radius, the proton Zemach radius has been determined by $e - p$ scattering and the hydrogen spectroscopy [7, 8, 9, 10, 11]. Very recently, the PSI group has determined the Zemach radius from the two transitions in the 2S to 2P states of muonic hydrogen [5]. That is the first determination of the proton Zemach radius from the muonic system, however, the accuracy is still lower than the electronic determinations. A summary of the proton Zemach radius measurements is plotted in Fig. 1. Our goal is to determine proton Zemach radius from muonic hydrogen with much higher precision.

2 Principle

The experimental principle is as follows.

- *Formation of the muonic hydrogen*
  Negative muons are stopped in the hydrogen target. In the initial capture, an excited state of the muonic hydrogen is formed with a high principle quantum number of ~ 14, however, the state is quickly de-excited to the ground state. Since the nuclear capture rate in the muonic hydrogen is extremely small, muons in the atomic ground state decay with almost the same lifetime of free muons ($\tau = 2.197$ μs).

- *Laser-induced hyperfine sublevel transition*
  We irradiate a laser before muon decays to induce a transition from $^1S_0$ to $^3S_1$. The ground state hyperfine splitting energy is 0.183 eV, which corresponds to the mid-infrared wavelength of 6.78 μm. A selective excitation in a specific $^3S_1$ state ($m_Z = +1$ or -1) is realized by using a circularly-polarized laser due to the conservation rule of total angular momentum. Then the muon spin in $^3S_1$ is polarized.

- *Detection of the muon decay asymmetry*
  If polarized muons in the $^3S_1$ state decay, the emission of electrons has an asymmetry in the spatial distribution by V-A theory. Therefore, the electron emission asymmetry will be a signal to search for the resonance during the frequency scan. We detect asymmetry in the number of decay electrons in the forward and backward directions along with the laser direction.

These are the brief principle of the proposed measurement. The feasibility with the above procedure is discussed in the next section.

3 Feasibility

To accomplish the measurement, we study the two key issues; the laser-induced transition probability from $^1S_0$ to $^3S_1$ and the collisional quench rate in the $^3S_1$ state.

To detect muon decay asymmetry in the $^3S_1$ state with a limited beam time, the transition probability has to be sufficiently high to scan over a wide range of the frequency. The laser-induced transition probability P is evaluated with the laser power E [J], the cross sectional area S [m^2] and the temperature T [K] as, $P = 2\times10^{-5}E/S/\sqrt{T}$ [12]. The probability is proportional to the laser power, thus the intense mid-infrared laser is important for this measurement. Very recently mid-infrared laser system with intense and narrow band-width has been developed in RIKEN [13]. The precision of the hyperfine splitting energy is expected to be $\sim$2 ppm due to the narrow band-width. With realistic parameters of $E = 40$ mJ, $S = 4$ cm^2 and $T = 20$ K, the probability is calculated to be 4.4×10^{-4}. Since this probability is too small to perform the measurement, we adopt a multi-pass cavity installed in the hydrogen target to enhance the effective laser power by a reflection with mirrors facing each other. We assume the reflectivity of the mirror to be 99.95%. Then achievable polarization is estimated with the effect of the collisional quench rate discussed below.

The second issue is the collisional quench rate. It is known that the muon in the $^3S_1$ state is quickly de-excited to the $^1S_0$ state by a collision with a neighboring hydrogen atom and lose the polarization. If the collisional quench rate is much larger than that of the muon decay, the muon polarization made by the laser excitation is mostly lost before muon decays. Therefore, this quench rate is essential and should be comparable with the muon decay rate. Theoretically, this quench rate is calculated in Ref. [14], and it is proportional to the hydrogen density. A typical quench rate is 20 MHz with the density (ρ) of 0.1% of the liquid hydrogen density (LHD), which corresponds to the $^3S_1$ lifetime of 50 ns.

With the discussion above, we estimate the muon spin polarization taking into account the transition and quench rates. Figure 2 shows the time population of the muon spin polarization. After laser injection, the polarization increases slowly due to the small transition probability caused by each laser pass, but eventually decreases with the attenuation of the laser after the multiple reflection. The averaged polarization during the optimized time gate is 3.7 % with

ρ = 0.1% LHD. If we decease the hydrogen density to be 0.01% LHD, the polarization is increased to be 16% due to the longer lifetime of the $^3S_1$ state as shown in the figure.

Finally, we estimate the beam time for the measurement in the RIKEN-RAL muon facility. A typical intensity of 40 MeV/c negative muon beam is 2×10^4 s^{-1} with double pulse operation [15]. With the density of ρ = 0.1% LHD, about 0.1% of muons stop in the hydrogen target. For the electron counter, the acceptance and the sensitivity of spin polarization are 28% and 23%, respectively. Then the time to find the resonance with the significance of 3σ is 25 hours, where the standard deviation is defined by the statistical fluctuation in the electron counts.

We simply set the range of the scan region to be $\pm$5.7 GHz, taken from a convolution of theoretical uncertainty of δ^{FF} and δ^{pol} in Ref. [7]. The scan interval is assumed to be 100 MHz which is comparable with the resonance width of $\sim$80 MHz. We follow the three-stage scan over the frequency range above. The first and second scans are devoted to finding the resonance frequency with 3σ and 5σ significance, respectively. In the third scan, we determine the resonance frequency with fine step of 50 MHz. In total, we need 220 days for the scan sequence. With lower hydrogen density of 0.01% LHD, the time is reduced to 26 days because of the higher spin polarization. However it is very challenging to perform with such a low-density gas target against the background. We plan to follow stepwise beam studies to optimize the experimental condition in RIKEN-RAL.

4 Summary

We propose a new measurement of the hypdrefine splitting energy in the ground-state muonic hydrogen. A newly-developed intense mid-infrared laser enables us to measure it with an unprecedented accuracy of $\sim$ 2 ppm. The spin polarization in the spin triplet state is populated by a circularly-polarized laser. We search for the resonance frequency by detecting the spatial asymmetry in the polarized muon decay. From the measurement of the hyperfine splitting energy, we can derive the proton Zemach radius. The measurement is feasible at the RIKEN-RAL pulsed-muon facility.

References

[1] R. Pohl *et al.*, Nature **466** (2010) 213.
[2] P.J. Mohr, B.N. Taylor, and D.B. Newell, Rev. Mod. Phys. **80** (2008) 633.
[3] J. C. Bernauer *et al.*, Phys. Rev. Lett. **105** (2010) 242001.
[4] X. Zhan *et al.*, Phys. Lett. B**705** (2011) 59.
[5] A. Antognini *et al.*, Science **339** (2013) 417.
[6] M. I. Eides *et al.*, Phys. Rep. **342** (2001) 63.
[7] A. Dupays *et al.*, Phys. Rev. A**68** (2003) 052503.
[8] J. L. Friar and I. Sick, Phys. Lett. B**579** (2004) 285.
[9] A. V. Volotka *et al.*, Eur. Phys. J. D**33** (2005) 23.
[10] S. J. Brodsky *et al.*, Phys. Rev. Lett. **94** (2005) 022001, errutum Phys. Rev. Lett. **94** (2005) 169902.
[11] M. O. Distler *et al.*, Phys. Lett. B**696** (2011) 343.
[12] A. Adamczak *et al.*, Nucl. Instrum. Meth. B**281** (2012) 72, D. Bakalov, private communication.
[13] N. Saito *et al.*, Proc. of SPIE, vol **8526** (2012) 852605-1.
[14] J. S. Cohen, Phys. Rev. A**43** (1991) 4668.
[15] T. Matsuzaki *et al.*, Nucl. Instrum. Meth. A**465** (2001) 365.

Chapter 9

Standard model physics at the TeV scale

Recent electroweak results from ATLAS

Jochen Meyer[1] on behalf of the ATLAS collaboration

[1]CERN, 1211 Geneve 23, Switzerland

DOI: http://dx.doi.org/10.3204/DESY-PROC-2014-04/215

ATLAS measurements of multi-boson production processes involving combinations of W, Z and isolated photons are summarized. Production processes sensitive to vector-boson fusion and vector-boson scattering such as electroweak production of single vector bosons associated with two forward jets and the di-boson production at 8 TeV pp collisions are also presented. Measurements of the cross section and branching ratio for Z to four leptons are described. Standard Model parameters, such as the weak mixing angle, are measured with high precision by ATLAS and are compared to world averages. Prospects at HL-LHC are discussed as an outlook.

1 Introduction

The LHC gives amongst others the opportunity to probe the validity of the electroweak (EW) sector of the Standard Model (SM) at energies not accessible before. Deviations from the SM could indicate new physics like anomalous gauge couplings. Pair production of heavy gauge bosons are of special interest because there is an intersection with Higgs physics.

The ATLAS detector [1] installed at the LHC is able to measure and identify objects like leptons, photons and jets with its inner detector (ID) [2], hadronic and electromagnetic calorimetry [3] and muon spectrometer [4]. Neutrinos escape without any signal and are reconstructed in the transverse plane as missing energy E_T^{miss}.

2 Electroweak parameters

There are many predictions by the SM derived from just a small set of input parameters to be provided by measurements. The effective weak mixing angle, accessible via the forward-backward asymmetry A_{FB} of Z boson decays, is one of these parameters. The $Z \to e^+e^-$ (resp. $Z \to \mu^+\mu^-$) decays are analyzed with 4.8 (resp. 4.7) fb^{-1} of pp collisions at a center of mass energy of $\sqrt{s} = 7$ TeV [5]. The sensitivity of this measurement is greatly enhanced by the use of candidate electrons measured only by the calorimeters beyond the inner detector acceptance, i.e. with $2.5 < |\eta| < 4.9$. In general the invariant mass of lepton pairs is required to be 66 GeV $< m_{\ell\ell} <$ 1 TeV while if a forward electron is involved the upper bound is 250 GeV.

The background is very small with a dominant component arising from multi-jet events misidentified as prompt lepton pairs. This background is derived with data-driven techniques and is three (four) orders of magnitude smaller than the ee ($\mu\mu$) signal. Backgrounds from di-boson, $Z \to \tau\tau$ and $t\bar{t}$ are taken from Monte Carlo (MC). The angle $\cos\theta^*_{CS}$ in the Collins-Soper frame relates the final state leptons to the initial state and defines the forward ($A_{FB} > 0$)

and backward ($A_{FB} < 0$) directions. The ratio of the difference between forward and backward cross sections in a given bin of $m_{\ell\ell}$, divided by the total cross section in that bin, quantifies A_{FB}. It is determined as a function of $m_{\ell\ell}$ and unfolded for detector effects, with the main systematic uncertainties originating from the parton distribution functions (PDF) and limited MC statistics. Good agreement with the theoretical calculations is found.

The leptonic effective weak mixing angle $\sin^2\theta_W^{\text{eff}}$ is extracted from the raw A_{FB} distributions by performing χ^2 fits of templates constructed for different values of $\sin^2\theta_W^{\text{eff}}$. Only events with 70 GeV $< m_{\ell\ell} <$ 250 GeV are used. The combination of all channels results in $\sin^2\theta_W^{\text{eff}} = 0.2297 \pm 0.0004(\text{stat}) \pm 0.0009(\text{syst})$ and is the first such measurement at the Z pole from a hadron collider that combines electron and muon final states. Figure 1 presents results from other experiments as well as the ATLAS measurement separated into channels. Their combination deviates 1.8 standard deviations from the PDG best fit value.

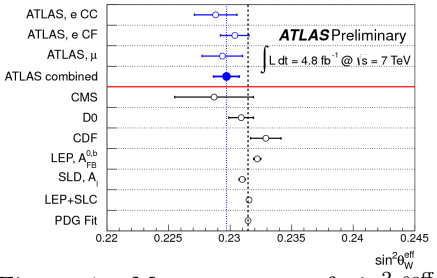

Figure 1: Measurements of $\sin^2\theta_W^{\text{eff}}$ from various experiments [5].

3 Single resonant decay to four leptons

The main contribution to the single resonant decay to four leptons at the Z pole is s-channel $Z \to \ell^+\ell^-$ production with one of the leptons emitting an off-shell Z or photon that creates another lepton pair. This final state provides a cross check for the performance of Higgs to ZZ^* to 4-lepton measurements and the branching of the Z boson to four leptons can be determined.

A dataset of pp collisions recorded at $\sqrt{s} = 7$ TeV ($\sqrt{s} = 8$ TeV) with 4.5 fb^{-1} (20.3 fb^{-1}) is analyzed [6]. Events are required with either one pair of electrons and one pair of muons, four electrons or four muons with the appropriate charge assignments. The four lepton invariant mass, $m_{4\ell}$, has to fulfill 80 GeV $< m_{4\ell} <$ 100 GeV. Each lepton pair must have an invariant mass above 5 GeV. In the same flavor modes this requirement must be fulfilled by any pairing of opposite charge. The largest dilepton invariant mass is required to be larger than 20 GeV. The overall background is determined to $< 1\%$ while there is a non resonant fraction of t-channel and gluon initial state production amounting to about 4%.

To measure $\frac{\Gamma_{Z\to 4\ell}}{\Gamma_Z}$, the expected background and non resonant contribution are subtracted from the number of observed events. Corrections for reconstruction efficiency are applied and an extrapolation to the full phase space is performed. The resulting yield is normalized to the $Z \to \mu\mu$ yield in the same dataset. The combined result $(3.20 \pm 0.25(\text{stat}) \pm 0.13(\text{syst})) \times 10^{-6}$ is in agreement with the SM value $(3.33 \pm 0.01) \times 10^{-6}$. The measurement was repeated in a fiducial volume previously introduced by CMS [7]. The results are in agreement and there is no deviation from the SM. Also cross sections at the two center of mass energies are measured and agree with the SM.

4 Di-boson production

The most recent result by ATLAS is the measurement of the W^+W^- production cross section in pp collisions at $\sqrt{s} = 8$ TeV [8]. The analyzed data amounts to 20.3 fb^{-1}. Considered events contain either one electron and one muon with $m_{e\mu} > 10$ GeV or two electrons or two muons

with $m_{ee/\mu\mu} > 15$ GeV and a deviation of 15 GeV from the Z mass. In all channels, the events are required to have opposite charge and substantial E_T^{miss}. Events with any jet with transverse momentum greater than 25 GeV reconstructed by the anti-k_t algorithm are rejected.

The main background components are W boson production with jets, Drell-Yan and $t\bar{t}$, and other di-boson modes. They are fully obtained from data, normalized to data in specific control regions, or, for the smaller components taken from MC. The total cross section is measured for all channels separately by correcting for the reconstruction efficiency and an extrapolation to the full phase space. The results are presented in Fig. 2. It shows in particular the combined cross section $71.4 \pm 1.2(\text{stat})^{+5.0}_{-4.4}(\text{syst})^{+2.2}_{-2.1}(\text{lumi})$pb, together with the theoretical predictions at NLO in QCD which are somewhat lower than the data.

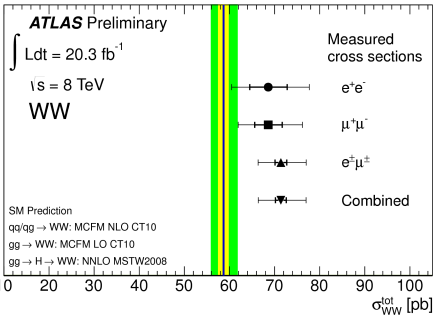

Figure 2: W^+W^- cross section [8].

5 Z boson production through vector-boson fusion

In addition to standard QCD production of Z bosons accompanied by at least two hard jets, there is the interesting production mode via vector-boson fusion referred to as EW production. This is of special interest since it gives insights into the gauge coupling structure of the EW sector of the SM.

A dataset of $20.3\,\text{fb}^{-1}$ of pp collisions recorded at $\sqrt{s} = 8$ TeV is analyzed [9]. Selected events contain a pair of electrons or muons forming an on-shell Z. At least two jets reconstructed with the anti-k_t algorithm have to be present. Five fiducial regions with different sensitivity to the EW component are studied. In the control region EW production is suppressed while the search region is optimized for this mode. The dominant background is $t\bar{t}$ which is taken from MC like WW, Wt and W plus jets. Background from multi-jet events is estimated using data driven techniques. Figure 3 presents the measured cross sections in the fiducial regions and the corresponding theory predictions.

The search region requires a di-jet invariant mass m_{jj} of at least 1 TeV and is used to probe for the EW component. The resulting m_{jj} distribution is fitted with templates to extract the EW component. The template for strong Z production is constrained by data selected in the control region. The measured cross section for the EW production is $10.7 \pm 0.9(\text{stat}) \pm 1.9(\text{syst}) \pm 0.3(\text{lumi})$fb and agrees well with the theory value of $9.38 \pm 0.5(\text{stat})^{+0.15}_{-0.24}(\text{scale}) \pm 0.24(\text{PDF}) \pm 0.09(\text{model})$fb. The background only hypothesis is rejected with more than 5 standard deviations.

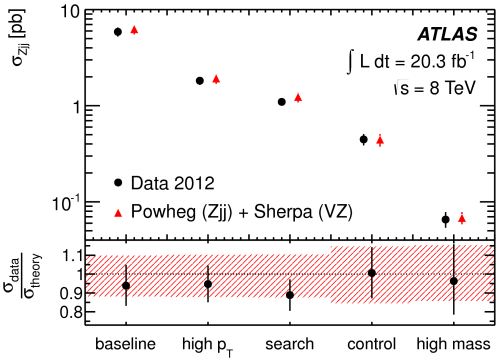

Figure 3: Z plus jets cross section [9].

The Z boson production associated with two jets gives insights into the triple gauge coupling parameters Δg_1^Z and λ_Z for which one-dimensional limits can be found in Ref. [9]. Because here the W bosons may be far off-shell the probing is complementary compared to studies in W^+W^- analyses.

6 $W^{\pm}W^{\pm}$ production via vector-boson scattering

The production of two W bosons of same charge is highly suppressed in the SM and even at the LHC only barely accessible. The final state can be created through strong production or vector-boson scattering which gives the possibility to study quartic gauge couplings.

A dataset of $20.3\,\mathrm{fb}^{-1}$ of pp collisions recorded at $\sqrt{s} = 8$ TeV is studied in two fiducial regions [10]: An inclusive region and a region where vector-boson scattering is enhanced. The inclusive region gathers events with exactly two electrons or muons of same charge and an invariant mass > 20 GeV while those with an invariant mass deviating less than 10 GeV from the Z mass are rejected. Besides substantial E_T^{miss}, there must be at least two jets reconstructed by the anti-k_t algorithm with $m_{jj} > 500$ GeV for the jets with highest transverse momentum. The region optimized for vector-boson scattering requires in addition a rapidity separation $|\Delta y_{jj}| > 2.4$ for those two jets. In both selections no jet must be identified as a b-jet.

The dominant background source arises from WZ, $W\gamma^*$ and $W\gamma$ production with photons converting into electron pairs in the ID material in the latter case. Most of the backgrounds are taken from MC and therefore the main uncertainty apart from jet reconstruction uncertainties of $11 - 15\%$ are theory uncertainties which amount to $4 - 11\%$. The combined measured cross section in the inclusive region (VBS region) is $2.1 \pm 0.5(\mathrm{stat}) \pm 0.3(\mathrm{syst})$fb ($1.3 \pm 0.4(\mathrm{stat}) \pm 0.2(\mathrm{syst})$fb) and within uncertainties compatible with the theory value of 1.52 ± 0.11fb (0.95 ± 0.06fb). The combined significance rejecting the background only hypothesis is 4.5 (3.6). The analysis provides one-dimensional as well as two-dimensional limits for quartic gauge couplings for several operator bases.

7 Prospects for HL-LHC

Facing future upgrade scenarios there are several studies for ATLAS physics performance at a high luminosity LHC at $\sqrt{s} = 14$ TeV. A variety of multi-boson channels is analyzed in their fiducial regions [11] and effective Lagrangian parameters for triple and quartic gauge couplings with cutoff unitarization are studied. Potential discovery values and expected limits are given for integrated luminosities of $300\,\mathrm{fb}^{-1}$ and $3\,\mathrm{ab}^{-1}$.

References

[1] ATLAS Collaboration, JINST **3** (2008) S08003.

[2] ATLAS Collaboration, CERN-LHCC-97-16, CERN-LHCC-97-17.

[3] ATLAS Collaboration, CERN-LHCC-96-40, CERN-LHCC-96-41, CERN-LHCC-96-42.

[4] ATLAS Collaboration, CERN-LHCC-97-22.

[5] ATLAS Collaboration, ATLAS-CONF-2013-043, http://cds.cern.ch/record/1544035.

[6] ATLAS Collaboration, Phys. Rev. Lett. **112** (2014) 231806 [arXiv:1403.5657 [hep-ex]].

[7] CMS Collaboration, JHEP **1212** (2012) 034 [arXiv:1210.3844 [hep-ex]].

[8] ATLAS Collaboration, ATLAS-CONF-2014-033, http://cdsweb.cern.ch/record/1728248.

[9] ATLAS Collaboration, JHEP **1404** (2014) 031 [arXiv:1401.7610 [hep-ex]].

[10] ATLAS Collaboration, arXiv:1405.6241 [hep-ex].

[11] ATLAS Collaboration, ATL-PHYS-PUB-2013-006, http://cdsweb.cern.ch/record/1558703.

Recent QCD Results from ATLAS

Tibor Ženiš[1] on behalf of the ATLAS collaboration

[1]Comenius University Bratislava, Slovakia

DOI: http://dx.doi.org/10.3204/DESY-PROC-2014-04/212

The ATLAS collaboration has performed studies of a wide range of QCD phenomena, from soft particle to hard photon and jet production. Recent soft-QCD measurements include studies of underlying event, vector meson production and quark confinement effects. Differential measurements of inclusive and multi-jet production provide stringent tests of high-order QCD predictions and provide input for determination of parton density functions. Measurements of isolated inclusive and di-photons cross sections for high p_{T} photons test various theoretical predictions and constrain parton density functions. In addition the total pp cross section at 7 TeV, together with the elastic and inelastic contributions, is measured and compared to various models. An overview of these results is given.

1 Introduction

The measurements described in this overview cover wide range of quantum chromodynamics (QCD) processes. The soft part of these processes characterized by low momentum transfer, comprehend processes with underlying events and is important at the total pp cross section determination. These processes cannot be calculated by the perturbative approach within the Standard Model (SM) however the obtained results test and constrain phenomenological models. The hard processes like jets, isolated prompt photon, photon and jet production provide a stringent tests for high-order theoretical QCD calculations.

The results were obtained using data produced in pp collisions at $\sqrt{s} = 7$ and 8 TeV collected by the ATLAS detector in years 2010, 2011 and 2012.

2 The ATLAS detector

The ATLAS detector is described in detail elsewhere [1]. The beam-line is surrounded by a tracking detector that uses silicon pixel, silicon strip and straw tube technologies and is embedded in a 2 T magnetic field. The tracking system covers the pseudorapidity range $|\eta| < 2.5$. It is surrounded by electromagnetic and hadronic calorimeters covering $|\eta| < 3.2$ which are complemented by a forward calorimeter covering $3.1 < |\eta| < 4.9$.

The Minimum Bias Trigger Scintillator (MBTS) detectors, the detectors used in the soft QCD measurements, are mounted in front of the endcap calorimeters on both sides of the interaction point at $z = \pm 3.56$ m and cover the range $2.09 < |\eta| < 3.84$.

The Absolute Luminosity for ATLAS (ALFA) sub-detector is located at 240 m from the interaction point in Roman Pots, its purpose is the measurement of elastic pp-scattering and small angles in the Coulomb-Nuclear Interference region.

3 Results of the ATLAS measurements

Underlying events (UE) comprise soft processes accompanying hard parton-parton interaction in pp collisions. There is no way to unambiguously distinguish between signals from the hard processes and from the UE.

The η, φ plane[1] can be divided into regions around the leading object (the highest p_{T} track or cluster in the event). Three regions are defined. The *toward* one ($\Delta\phi < 60°$) containing the leading object, the *away* one ($\Delta\phi > 120°$) containing the second leading jet in the di-jet events and the *transverse* one. The transverse region is the region most sensitive to the UE. One can distinguish the transverse region according to the leading object in this region with the maximum value of an observable into the *trans-min* and the *trans-max* sides on the event-by-event basis. Each observable has its definition of the sides.

ATLAS measured distributions sensitive to the underlying event in QCD jet events [2] using data collected at $\sqrt{s} = 7\,\mathrm{TeV}$ separately for inclusive jets and exclusive di-jet events. A sample of results is shown in Fig. 1. Comparisons to the predictions of different Monte-Carlo (MC) models show a need for further model tuning, but in general the standard approach is found to reproduce the features of the underlying event in both types of event selection.

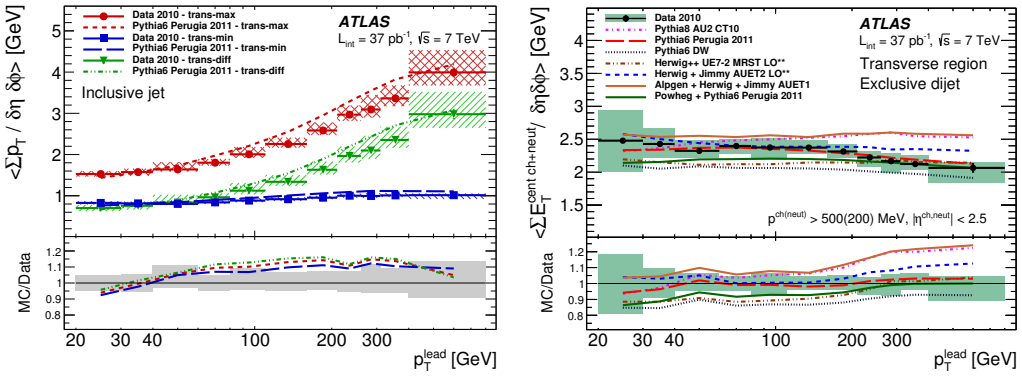

Figure 1: Comparison of profiles of charged-particle $\sum p_{\mathrm{T}}$ left (neutral and charged $\sum E_{\mathrm{T}}$ right) as a function of $p_{\mathrm{T}}^{\mathrm{lead}}$ in transverse regions for ATLAS measurements and MC predictions.

A measurement of charged-particle distributions sensitive to the properties of the underlying event for an inclusive sample of events containing a Z-boson decaying to an electron or muon pair [3] was performed using the ATLAS detector. The measured distributions are compared to the similar ones measured in jet events and to the predictions of various MC generators implementing different underlying event models.

ATLAS measured the inealistic pp cross section using the MBTS detector [4] for an acceptance region $\xi = M_{\mathrm{X}}^2/s > 5\times10^{-6}$ (M_{X} is a mass of the dissociation system) and the differential cross section for the rapidity gap size $\Delta\eta$ (central part of detector without activity) for $\Delta\eta < 8$ and $|\eta| < 4.9$ [5]. Fig. 2 left shows the ATLAS measurements with the TOTEM measurements and model predictions. The ATLAS results are consistent.

The total pp cross section measurement [6] was performed using the ALFA subdetector of

[1] ATLAS uses cylindrical coordinates (η, φ) in the transverse plane. η is the pseudorapidity, φ the azimuthal angle around the beam pipe.

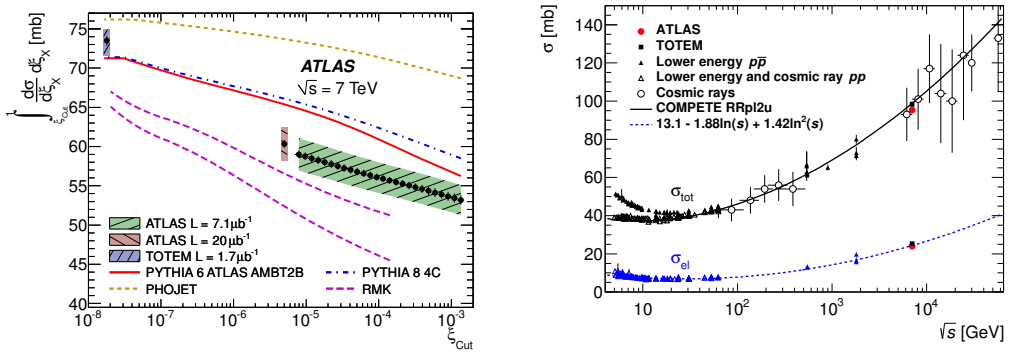

Figure 2: The differential inelastic (left) and total/elastic (right) pp cross section.

ATLAS. The total cross section is extracted using the optical theorem and its value is $\sigma_{\rm tt}(pp \to X) = 95.35 \pm 0.38(\text{stat.}) \pm 1.25(\text{exp.}) \pm 0.37(\text{extr.})\,\text{mb}$. Fig. 2 right shows this measurement compared with other published measurements.

The measurement of the $\varphi(1020)$ [7] probes strangeness production at a soft scale $Q = 1\,\text{GeV}$. It is sensitive to s-quark and low-x gluon densities. It is also sensitive to the fragmentation details. The $\varphi(1020)$ measurements can constrain phenomenological hadroproduction models.

Additional jet activity in di-jet events was measured using pp collisions at ATLAS [8]. The measurement tests the perturbative QCD theoretical predictions in extreme regions of phase space. In cases of large rapidity separation of jets or when a veto of additional jet activity is applied, higher order corrections become increasingly important. No theoretical prediction provides good agreement with the data in all observables over the whole phase space.

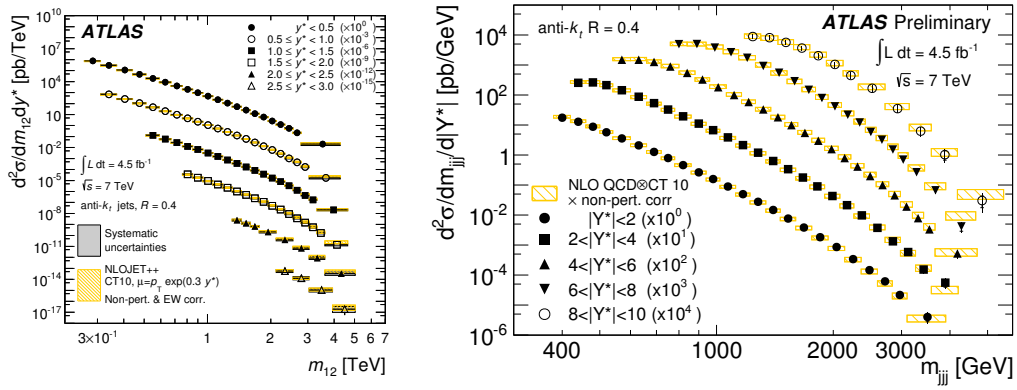

Figure 3: The differential di-jet (left) and three-jet (right) production cross section measured by the ATLAS detector compared to the NLOJet++ calculations.

ATLAS measured the inclusive-jet (not yet published) di-jet [9] and three-jet [10] production cross sections in pp collisions at $\sqrt{s} = 7\,\text{TeV}$. The measurements are in good agreement with the the NLOJet++ theoretical predictions when using the CT10, NNPDF2.1 and MSTW 2008 PDF sets as shown in Fig. 3.

An ATLAS measurement of the cross section for the production of isolated prompt photons in pp collisions at $\sqrt{s} = 7\,\text{TeV}$ [11] is compared to the LO parton-shower MC models and to the NLO perturbative QCD calculations. The prompt photon production is sensitive to the gluon content of the proton ($qg \to q\gamma$) and can be used to constrain gluon PDFs. The NLO QCD calculations agree with the ATLAS measurements.

The dynamics of isolated-photon plus jet production in pp collisions at $\sqrt{s} = 7\,\text{TeV}$ has been studied with the ATLAS detector at the LHC [12]. The production of prompt photons in association with a jet in pp collisions, $pp \to \gamma + \text{jet} + X$ provides a testing ground for perturbative QCD in a cleaner environment than in jet production, since the photon originates directly from the hard interaction. The next-to-leading-order QCD calculations are compared to the measurements and provide a good description of the data, except for the case of the azimuthal opening angle.

4 Conclusion

Various measurements sensitive to the soft and perturbative SM processes have been considered. Their characteristics like total pp cross section, characteristics of the underlying events, jets, isolated prompt photon, photon and jet production cross sections were measured by the ATLAS detector and compared to the theoretical expectations and Monte-Carlo calculations. The results of the measurements are used or have a potential to test and tune PDFs and phenomenological model parameters.

Acknowledgments

This work was supported by the Slovak funding agency (The Ministry of Education, Science, Research and Sport of the Slovak Republic).

References

[1] ATLAS Collaboration, JINST 3 (2008) S08003
[2] ATLAS Collaboration, Eur.Phys.J. C74 (2014) 2965
[3] ATLAS Collaboration, submitted to EPJC, arXiv:1409.3433
[4] ATLAS Collaboration, Nature Commun. 2 (2011) 463
[5] ATLAS Collaboration, Eur. Phys. J. C72 (2012) 1926
[6] ATLAS Collaboration, submitted to Nuclear Physics B, arXiv:1408.5778
[7] ATLAS Collaboration, Eur. Phys. J. C (2014) 74:2895
[8] ATLAS Collaboration, submitted to EPJC, arXiv:1407.5756
[9] ATLAS Collaboration, JHEP05(2014)059
[10] ATLAS Collaboration, ATLAS-CONF-2014-045
[11] ATLAS Collaboration, Phys. Rev. D 89, 052004 (2014)
[12] ATLAS Collaboration, Nucl. Phys, B 875 (2013) 483–535

Measurements of vector-boson production in ATLAS and CMS

Manuella G. Vincter[1] on behalf of the ATLAS and CMS Collaborations

[1]Carleton University, 1125 Colonel By Drive, Ottawa, ON, K1S 5B6, Canada

DOI: http://dx.doi.org/10.3204/DESY-PROC-2014-04/213

Vector-boson production in $p-p$ collisions in LHC Run-1 has been extensively studied by ATLAS and CMS. Charged and neutral-current Drell-Yan cross sections are sensitive to the parton distribution functions of the proton and electroweak corrections. The measurements of the neutral-current Drell-Yan process in three distinct kinematic regions, i.e. at the Z boson mass peak, below, and above, are performed. The results are compared to NLO Monte Carlo simulations and to NNLO QCD predictions corrected for NLO EW effects calculated using various parameterisations of the parton distribution functions. An overview of these results is given.

1 Introduction

The proton-proton collisions at the Large Hadron Collider (LHC) are in fact parton-parton collisions, where the momentum fraction x carried by a parton can be described in terms of Parton Distribution Functions (PDFs). These colliding partons may undergo a hard-scattering process producing, for example, a Z boson in the final state. The production cross section for such a process may be factorised into the hard scattering between the partons and the PDF of each of the interacting partons. Via this hard scatter, one can test perturbative QCD (pQCD). Predictions for such processes are available at next-to-next-to-leading order (NNLO).

Drell-Yan (DY) production at the LHC probes the structure of the PDFs over a wide range of x and four-momentum transfer Q^2. The quark and gluon PDFs may be parameterised by functions that describe their shapes as a function of x. One can then use such processes to feed information into global QCD fits to extract these PDFs. The cross-section measurements available at the LHC have differing sensitivity to the proton's PDFs and so much may be gained by including, for example, electroweak boson production as such processes are sensitive to both the valence and sea quark distributions.

The recent measurements presented at this PANIC Conference included the transverse momentum $p_{\mathrm{T}}^{\ell\ell}$ and invariant mass $m_{\ell\ell}$ dependence of the production of $Z/\gamma^* \to \ell\ell$, where the lepton can be either an electron or a muon, as well as the charge asymmetry of $W^{\pm}$ production. The results from QCD analyses extracting PDF information were also discussed. A subset of this presentation is summarised in these proceedings.

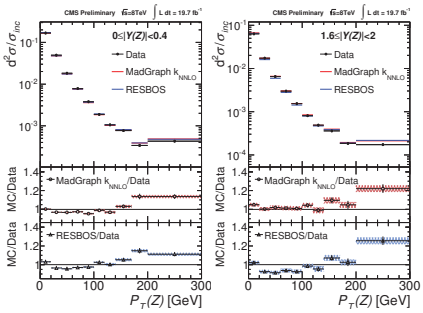

Figure 1: The CMS Z production cross section [1] as a function of $p_{\mathrm{T}}^{\ell\ell}$ in two illustrative bins of $Y_{\ell\ell}$ compared to MADGRAPH [2] normalised to NNLO (red) and RESBOS [4] (blue).

2 $p_{\mathrm{T}}^{\ell\ell}$ dependence of Z/γ^* production

Near the Z pole, single and double-differential cross-section measurements as a function of $p_{\mathrm{T}}^{\ell\ell}$ and Z-boson rapidity $Y_{\ell\ell}$ are reported. The region of low $p_{\mathrm{T}}^{\ell\ell}$ is that of initial state radiation and intrinsic k_{T} of the partons. This region may be modeled through either soft-gluon resummation or parton showers. The high $p_{\mathrm{T}}^{\ell\ell}$ region is that dominated by the radiation of high p_{T} gluons. This region may be modeled by fixed-order calculations available at NNLO. Several measurements have been made by ATLAS and CMS comparing to the predictions for a given choice of PDF. Only one example is illustrated here. Figure 1 shows the CMS measurement [1] of the double-differential cross section for DY dimuon production in two illustrative bins of the dimuon rapidity $Y_{\ell\ell}$. The ratios in these plots show comparisons of data to the leading order MADGRAPH [2] prediction scaled to NNLO with the FEWZ [3] calculation, and the NNLO RESBOS [4] prediction which models soft-gluon resummation at low $p_{\mathrm{T}}^{\ell\ell}$. Both predictions tend to overshoot the data for $p_{\mathrm{T}}^{\ell\ell}$ above approximately 80 GeV. RESBOS also tends to undershoot the data at lower $p_{\mathrm{T}}^{\ell\ell}$.

ATLAS also makes use of its differential cross-section measurements as a function of $p_{\mathrm{T}}^{\ell\ell}$ [5] and an angular variable ϕ_η^* [6] to produce a better tune for the parton shower model used (PYTHIA8 [7]) in conjunction with generators. This new tune called AZNLO is compared to an older tune labelled 4C in Figure 2. The new tune was obtained by modifying, e.g., the values of the primordial k_{T} within the proton and the value of the initial-state radiation cutoff in the parton shower. The tune shows agreement with data to better than 2% up to $p_{\mathrm{T}}^{\ell\ell}$ of 50 GeV.

3 $m_{\ell\ell}$ dependence of Z/γ^* production

Single and double-differential DY cross-section measurements as a function of $m_{\ell\ell}$ and $Y_{\ell\ell}$ are available from ATLAS and CMS in the $m_{\ell\ell}$ range of 15 GeV up to 2000 GeV. Low-mass DY production is dominated by the electromagnetic coupling of the photon γ^* to the quark-antiquark pair. This region exhibits different sensitivity to u and d-type quarks than on the Z pole which is dominated by the electroweak coupling of the Z. The measurements are compared to fixed-order calculations and to various generators and PDFs.

Figure 3 (left) shows the ATLAS measurement of the DY differential cross section at low $m_{\ell\ell}$ [8], compared to fixed-order FEWZ [3] calculations at next-to-leading order and NNLO.

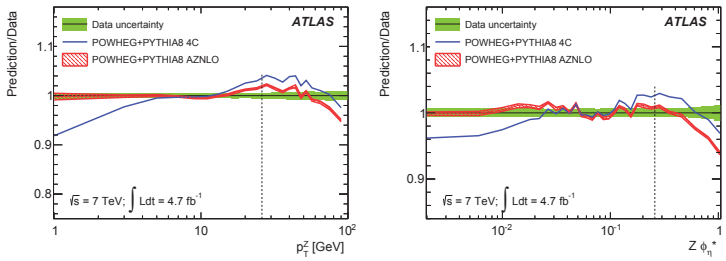

Figure 2: Comparison [5] of the tuned 4C (blue) and AZNLO (red) predictions to the $p_{\mathrm{T}}^{\ell\ell}$ (left) and ϕ_{η}^{*} (right) differential cross-section data from ATLAS.

It is evident at low $m_{\ell\ell}$ that NNLO-level calculations are needed to successfully describe the data. In this region of low $m_{\ell\ell}$, the CMS measurement [9] of the differential cross section as a function of $Y_{\ell\ell}$ is shown in Figure 3 (right) compared to a FEWZ prediction with several NNLO PDFs currently available. The agreement is good to the 10% level.

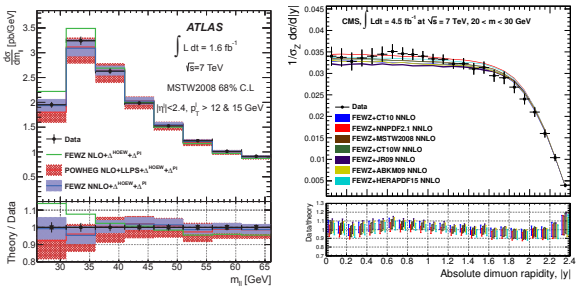

Figure 3: Left: The ATLAS cross-section measurement [8] as a function of $m_{\ell\ell}$ (points) compared to NLO and NNLO predictions. Right: Comparison of the CMS cross-section measurement [9] as a function of $|Y_{\ell\ell}|$ with theory expectations including NNLO PDF sets.

4 $W^{\pm}$ charge asymmetry

The dominant $W^{\pm}$ production mechanisms at the LHC are $d\overline{u} \to W^{-}$ and $u\overline{d} \to W^{+}$ and so the differential cross section charge asymmetry of $W^{\pm}$ production as a function of the lepton η can provide additional insight into the d/u PDF ratio as well as sea antiquark PDFs, including the poorly known strange sea. CMS has recently made a measurement of this $W^{\pm}$ charge asymmetry [10], shown in Figure 4 (left) compared to several PDF predictions. Best agreements are obtained with, e.g., the CT10 [11] PDFs while the MSTW2008 [12] family of PDFs shows significant deviations as the lepton η approaches zero. A global QCD fit was made by CMS [10], which used the HERA I inclusive data [13] and these charge-asymmetry results. Figure 4 (right) shows the prediction for d-valence quarks. Adding these new data to the global fit not only better constrains this PDF but also predicts a slight change in the shape of d_v as a function of x.

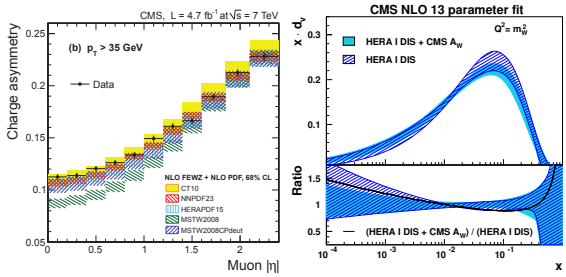

Figure 4: Left: Comparison of the CMS muon charge asymmetry [10] to predictions interfaced with several PDFs. Right: Distribution of d_v resulting from a global fit using HERA I deep inelastic scattering data [13] and CMS muon asymmetry [10] (shaded), and HERA only (hashed).

5 Conclusions

Vector-boson production at the LHC is interesting on many levels. It can be used as a probe of pQCD via the hard-scattering process as well as to better constrain PDFs, particularly valence quarks and poorly-known strange sea quarks. These proceedings presented a very brief overview of some of the ATLAS and CMS measurements that contribute to this new knowledge: the $p_{\mathrm{T}}^{\ell\ell}$ and $m_{\ell\ell}$ dependence of DY production as well as the $W^{\pm}$ production charge asymmetry.

References

[1] CMS Collaboration, CMS-PAS-SMP-13-013, cds.cern.ch/record/1700115.

[2] J. Alwall *et al.*, JHEP **06** 128 (2011).

[3] R. Gavin *et al.*, Comput. Phys. Commun. **182** 2388 (2011).

[4] G. Ladinsky and C. Yuan, Phys. Rev. **D50** 4239 (1994); F. Landry *et al.*, Phys. Rev. **D67** 073016 (2003); C. Balazs and C. Yuan, Phys. Rev. **D56** 5558 (1997).

[5] ATLAS Collaboration, arXiv:1406.3660 (2014).

[6] ATLAS Collaboration, Phys. Lett. **B720** 32 (2013).

[7] T. Sjöstrand, S. Mrenna, and P. Z. Skands, Comput. Phys. Commun. **178** 852 (2008).

[8] ATLAS Collaboration, JHEP **06** 112 (2014).

[9] CMS Collaboration, JHEP **12** 030 (2013).

[10] CMS Collaboration, Phys. Rev. **D90** 032004 (2014).

[11] H.-L. Lai *et al.*, Phys. Rev. **D82** 074024 (2010).

[12] A.D. Martin *et al.*, EPJ **C63** 189 (2009); A.D. Martin *et al.*, EPJ **C73** 2318 (2013).

[13] F.D. Aaron *et al.* (H1 and ZEUS Collaborations), JHEP **01** 109 (2010).

Higgs Boson in Lepton Decay Modes at the CMS Experiment

Somnath Choudhury[1] for the CMS collaboration

[1]DESY - Hamburg, Germany

DOI: http://dx.doi.org/10.3204/DESY-PROC-2014-04/120

The results on the standard model Higgs boson in lepton decay channels with tau pair and muon pair final states using 25 fb^{-1} of pp collision data at 7 and 8 TeV center-of-mass energies collected by the CMS detector at the LHC has been summarized. A direct evidence of the Higgs-lepton coupling is established with the tau pair decay mode. Searches for Higgs bosons decaying to leptons in scenarios beyond the standard model such as supersymmetry within the minimal extension of the model has also been reported.

1 Introduction

The ATLAS and CMS collaborations in July 2012 came out with the observation of a Higgs boson [1, 2] using proton-proton collision data from the LHC at CERN corresponding to integrated luminosities of around 5 fb^{-1} at 7 TeV and 5 fb^{-1} at 8 TeV center-of-mass energies. The LHC has completed its first run with the detectors having recorded about 95% of delivered collision data, among which about 90% were certified and used to obtain the results reported here. The final analysis is based on integrated luminosity of 20 fb^{-1} at 8 TeV in addition to the 5 fb^{-1} at 7 TeV collected by the CMS detector [3]. The observation of a Higgs boson around mass of 125 GeV in the high resolution boson decay channels motivates the search in major fermion decay modes as decays of the Higgs boson to tau pairs and bottom quark pairs have significantly large branching fraction in this mass regime. The 125 GeV Higgs boson opens an interesting avenue for its decays to fermions as this would provide an effective handle for the measurement of the Higgs coupling to fermions. The Higgs boson suffers from quadratically divergent self-energy corrections at high energies. Numerous extensions to the standard model (SM) have been proposed to address these divergences one of which is supersymmetry, a symmetry between fundamental bosons and fermions, which results in cancellation of the divergences. The Minimal Supersymmetric extension of the standard model (MSSM), outlays the introduction of 2 Higgs doublets leading to 5 physical Higgs bosons after electroweak symmetry breaking, where, h and H are the CP-even scalar bosons, A is the CP-odd pseudoscalar boson and H^+ and H^- are the charged bosons. If the discovered Higgs boson is the low mass Higgs within MSSM, then the search for its heavy partners gains a lot of interest in tau pair decay which has a branching fraction around 10% enhanced at all masses.

The CMS detector plays a crucial role in robustly identifying individual particles in the collision events. The detector subsystems employed for the analysis are the pixel detector and the silicon tracker forming the innermost component of the detector followed by the electromagnetic calorimeter of lead tungstate crystals and hadronic calorimeter of brass / scintillator

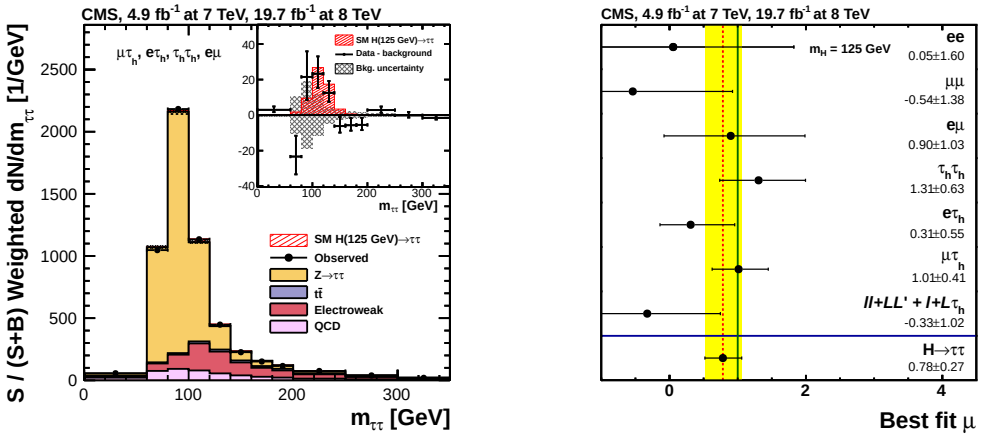

Figure 1: The di-tau invariant mass distribution combining all categories (on left) and the signal strength with respect to SM expectation in different di-tau decay channels and result of the combination (on right).

samplers which is enveloped by the 3.8 T superconducting solenoid. Outside the solenoid are the muon chambers which are gas ionization detectors in steel return yoke composed of cathode strip chambers, resistive plates and drift tubes. For the physics object reconstruction in a collision event, CMS uniquely employs a particle flow technique which provides event description in the form of mutually exclusive particles identifying all stable particles produced in the event by combining the capabilities of each sub-detector with the most precise measurement of the energy and direction for each particle and then individual measurements from each sub-detector are combined by a geometrical linking alogorithm providing particle identification on blocks of these linked elements. The experiment had to establish methods to cope with a high number of multiple collisions per beam crossing (pileup), which occurs at high luminosity. The average number of pileup events is about 9 and 21 interactions in the years 2011 and 2012 respectively. The successful mitigation of pileup was demonstrated and an almost uniform response of the missing transverse energy resolution as a function of the number of primary vertices in the event is achieved. The SM Higgs boson analysis utilises the major Higgs boson production mechanisms in pp collisions in order of decreasing cross-sections namely gluon fusion, vector boson fusion (VBF) and associated production with vector bosons (VH). The MSSM Higgs bosons search utilises the production in gluon fusion and in association with bottom quarks or in bottom quark fusion.

2 Higgs to Taus

The SM H$\rightarrow \tau\tau$ search [4] is performed using all possible decays in fully leptonic, semi-leptonic and fully hadronic states using the final-state signatures eμ, $\mu\mu$, ee, eτ_h, $\mu\tau_h$ and $\tau_h\tau_h$, where electrons and muons arise from leptonic τ-decays and τ_h denotes hadronic tau lepton decays. To enhance the sensitivity of the search, each of these categories is further divided into three exclusive sub-categories according to the nature of the associated jets in the event. The gluon-

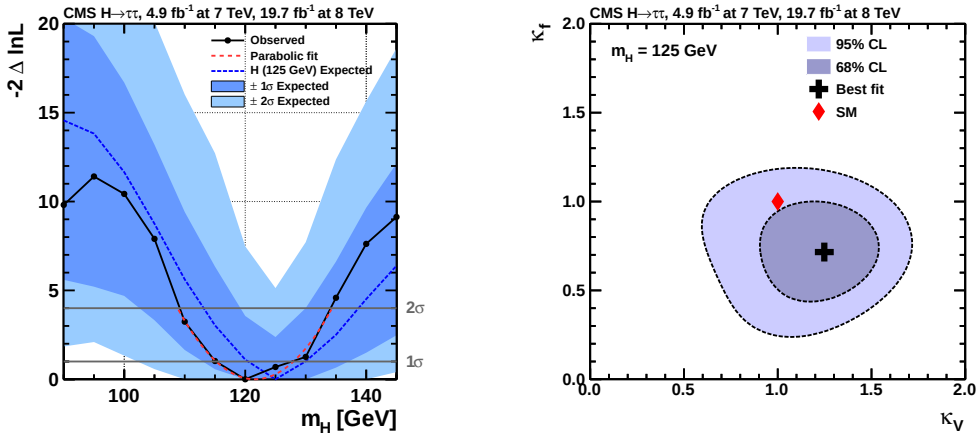

Figure 2: The measured mass from log-likelihood scan in the di-tau channel (on left) and the 2-D scan of couplings to vector bosons and fermions scaled to the SM expectation (on right).

fusion production mechanism has the largest production cross section. However, in the mass region of interest, background from Drell–Yan production of tau pairs overwhelms the expected Higgs boson signal. This search therefore relies strongly upon the signature of Higgs bosons produced via vector boson fusion (VBF) or in association with a high transverse momentum (p_T) jet recoiling against the tau pair. In the former case, the distinct topology of two jets with a large rapidity separation greatly reduces the background. In the latter, requiring a high-p_T jet both suppresses background, and improves the resolution of the tau-pair invariant mass. The search has been categorized into 0-jet, 1-jet and 2-jet VBF categories to extract the signal which are further split on the basis of hadronic tau p_T and di-tau p_T for 0 and 1 jet categories or di-tau p_T, di-jet invariant mass and di-jet pseudorapidity separation for 2-jet category. The 0-jet category constrains the background normalization, identification efficiencies and energy scales, the 1-jet category improves the resolution of Higgs boson mass and the VBF category has high signal over background ratio. The analysis is also performed in the VH category with lepton tagging from vector bosons along with the tau lepton pair.

To distinguish the Higgs boson signal from the background, the tau-pair mass is reconstructed using a maximum likelihood technique. The algorithm estimates the original momentum components of the two taus by maximizing a likelihood with respect to free parameters corresponding to the missing neutrino momenta, subject to kinematic constraints. Other terms in the likelihood take into account the tau-decay phase space and the probability density in the tau transverse momentum, parametrized as a function of the tau-pair mass. This algorithm yields a tau-pair mass with a mean consistent with the true value, and distribution with a nearly Gaussian shape. The relative $m_{\tau\tau}$ mass resolution estimated from simulation is 10–20% depending on the di-tau decay channel and category. The likelihood based mass reconstruction allows for a better separation between simulated 125 GeV Higgs signal and $Z\rightarrow \tau\tau$ background than the visible mass alone, yielding an improvement in the final expected significance of 40%.

In each of these categories, a search is performed for an excess of events in the reconstructed di-tau invariant mass distribution. The largest source of irreducible background is $Z\rightarrow \tau\tau$ which is estimated using an observed sample of $Z\rightarrow \mu\mu$ events, where the reconstructed muons are

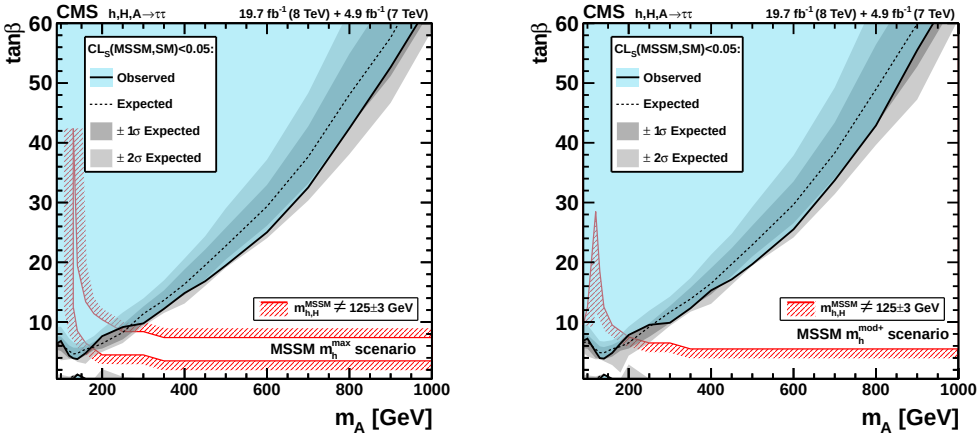

Figure 3: Region in the parameter space of tanβ versus m_A excluded at 95% CL in the context of the MSSM maximal mixing scenario (on left) and a modified mixing ${m_h}^{mod+}$ benchmark scenario (on right). The expected one- and two- standard deviation ranges and the mean expected 95% CL upper limits are shown together with the observed excluded region.

replaced by the reconstructed particles from simulated tau decays, a procedure called "embedding". The normalization for this process is determined from the measurement of the CMS measured cross section. The reducible backgrounds (W + jets, multijet production, Z + jets) are also evaluated from control samples in data. The QCD multijet background is evaluated using the ratio of opposite-sign (OS) to same-sign (SS) di-tau events and relaxed lepton isolation after an estimate of the W + jets background using the high transverse mass ($m_T^{\ell E_T^{miss}}$) side-band W boson enriched region and extrapolating it to the signal region. The Z + jets background is evaluated from fake rate and OS/SS ratio with the shape from simulation. The top pair produced events and diboson contribution are estimated using simulation.

Combining all event categories, a broad excess of events is observed in the tau pair invariant mass distribution as seen in Figure 1 over a range of the Higgs boson mass consistent with the 125 GeV scalar boson observed in the high resolution boson decay channels. The observed (expected) significance of the excess at Higgs boson mass of 125 GeV is 3.2σ (3.7σ). The best-fit value of the signal strength is μ=0.78±0.27, obtained in the global fit combining all channels included in this analysis where the H→WW process has been added as a background for the observed process. This result provides the first direct indication of the Higgs boson coupling to leptons. The mass of the Higgs boson measured in this channel is 122±7 GeV from a parabolic fit of the log-likelihood scan of the observed mass points in data shown in Figure 2. The measured couplings of the Higgs boson to vector bosons and fermions scaled with respect to SM, shows consistency within around one standard deviations from SM predictions where the H→WW process has been added as a signal for this measurement.

A Higgs-like state at 125 GeV is rather large for the light MSSM Higgs boson which can be achieved by maximizing the radiative corrections to Higgs mass at 1-loop level. The tau-pair decays of the neutral Higgs bosons in the MSSM, having a branching fraction of roughly 10%, serve as the best experimental signature for this search. The $b\bar{b}$ mode, though it has a much larger branching fraction, suffers from an overwhelming background from multi-jet production.

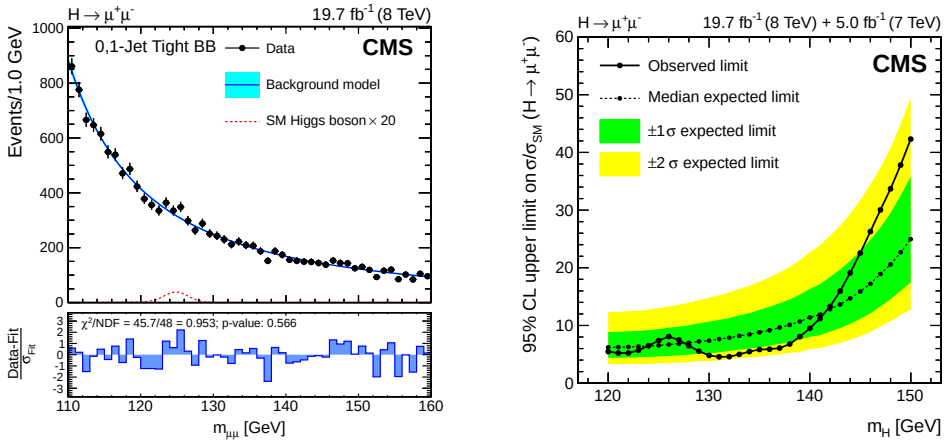

Figure 4: The di-muon invariant mass distribution combining all categories (on left) and 95% CL upper limits on cross section times the branching ratio normalized to the SM expectation as a function of Higgs boson mass (on right).

The MSSM Higgs bosons search [5] is performed using the di-tau final-state signatures eμ, $\mu\mu$, eτ_h, $\mu\tau_h$ and $\tau_h\tau_h$. The τ_h decay modes considered for the analysis are a single charged hadron, a charged hadron with neutral pion via the $\rho(770)$ resonance and three charged hadrons via the a_1 resonance. The data sample has been divided on the b-jet multiplicity into b-tag and non b-tag categories to enhance the sensitivity to bbΦ coupling:
• b-Tag category: At most one jet with p_T>30 GeV and at least one b-tagged jet with p_T>20 GeV.
• Non b-Tag category: At most one jet with p_T>30 GeV and no b-tagged jet with p_T> 20 GeV.
The di-tau invariant mass spectrum shows no evidence for a Higgs boson signal and hence 95% confidence level (CL) upper bound on the Higgs boson production cross-section times the branching fraction to tau pairs have been set using the mass shape of the tau pair mass spectrum and uncertainties from theory (parton distribution function and renormalization / factorization), normalization (luminosity and efficiency) and shape (energy scale). These limits are further interpreted in the MSSM parameter space on the m_A-tanβ plane as shown in Figure 3 in the maximal mixing scenario of the stop-top sector with a soft SUSY breaking mass of 1 TeV as the stop mass scale as well as a modified m_h mixing benchmark scenario [6]. It excludes all previously unexplored regions reaching as low as tanβ = 3.9 for mass of the pseudoscalar Higgs boson m_A=140 GeV.

3 Higgs to Muons

One of the properties of the Higgs boson that has to be checked is the couplings to first and second generation leptons. Indeed, the SM Higgs decays to fermions should not be universal. A search for H→ $\mu\mu$ [7] is performed with at total luminosity of the 7 and 8 TeV dataset from Run-1 LHC. In the SM, the decay H→ $\mu\mu$ presents a vary small branching ratio of $2.2\text{x}10^{-4}$ at m_H = 125 GeV. However, the search takes advantage of the clean signature in the detector and the excellent di-muon invariant mass resolution. The gluon fusion and VBF production

modes are utilized by the jet multiplicity of events in the final state. In addition, events are split into categories according to the p_T of the di-muon system, the properties of jets in the 2-jet category, and according to the detector regions (barrel, endcap, overlap regions) in which the two muons are reconstructed. The latter make use of the different experimental resolutions of the reconstructed di-muon mass for muons from different detector regions. The signal is extracted by means of a fit to the di-muon invariant mass distribution using signal and background shapes. The combined di-muon mass distribution is shown in Figure 4, weighted for the ratio of the signal and signal-plus-background distributions in the dfferent event categories. The background distribution is estimated using an analytic fit function, and, amongst others, systematic uncertainties are estimated by modifying the used fit function. Upper limits on the cross section times H$\rightarrow \mu\mu$ branching ratio have been derived and the observed (expected) limit is found to be 7.4 (5.1) times the SM prediction. The observed significance at 125 GeV is 1.1σ and no significant excess of events is expected in this channel at the Run-1 LHC luminosity.

4 Conclusion

A broad excess of events is observed for the SM Higgs boson search in the tau pair decay mode consistent with the 125 GeV Higgs boson signal from high resolution boson decay modes ($\gamma\gamma$ and ZZ$^\star\rightarrow 4\ell$) providing the first direct indication of the Higgs boson coupling to leptons. Combining tau pair and bottom quark pair decay modes, the significance for Higgs boson decay to fermions at 125 GeV is more than 3σ showing the first direct evidence of Higgs-fermion coupling [8] at the LHC. The mass of the Higgs boson measured in the di-tau channel is 122 ± 7 GeV from a parabolic fit of the likelihood scan of the Higgs mass. The results on the SM Higgs boson in di-tau and di-muon decays reveal lepton non-universality. The search for MSSM Higgs bosons in tau pair decay has set stringent bounds in the m_A-tanβ plane with different MSSM benchmark scenarios tested and reaching as low as tanβ=3.9 at m_A=140 GeV at a modified mixing scenario consistent with the observed Higgs boson at 125 GeV. In the Run-2 LHC, the measurement of properties of the Higgs-like state in tau decay would continue looking for deviations from SM as well as searches for Higgs bosons beyond the SM in lepton decays.

References

[1] The ATLAS Collaboration, Phys. Lett. **B 716** 1 (2012).

[2] The CMS Collaboration, Phys. Lett. **B 716** 30 (2012).

[3] The CMS Collaboration, JINST **3** S08004 (2008).

[4] The CMS Collaboration, JHEP **05** 104 (2014) and all references therein.

[5] The CMS Collaboration, arXiv: 1408.3316 [hep-ex] and all references therein.

[6] M. Carena et. al., Eur.Phys.J. **C73** 2552 (2013).

[7] The CMS Collaboration, CMS-PAS-HIG-13-007 and all references therein.

[8] The CMS Collaboration, Nat. Phys. **10**, 557 (2014) and all references therein.

The Higgs Physics Programme at the International Linear Collider

Felix Sefkow[1]

[1]DESY, Notketraße 85, 22607 Hamburg, Germany

DOI: http://dx.doi.org/10.3204/DESY-PROC-2014-04/122

The talk summarises the case for Higgs physics in e^+e^- collisions and explains how Higgs parameters can be extracted in a model-independent way at the International Linear Collider (ILC). The expected precision will be discussed in the context of projections for the experiments at the Large Hadron Collider (LHC).

1 Introduction

The discovery of a Higgs boson, honoured with the 2013 Nobel prize in physics, marks a turning point in particle physics, as the last missing building block of the Standard Model falls into place and opens the door to completely new studies of a particle unlike every other discovered before. Like in many earlier instances in the history of particle physics, it did not come as a surprise, but was anticipated and sought for. The Higgs mass had been predicted with increasing precision from the analysis of electro-weak quantum corrections, in which measurements at the previous generation of e^+e^- colliders played a prominent role.

Today, Higgs physics has been identified as one of the prime "drivers" of the field, as a compelling line of research with great promise, where surprises may be expected. The main question is to fully establish the profile of the Higgs particle, measure its quantum numbers and, above all, its precisely predicted couplings to almost all other fundmental particles, and to find out whether it fulfils its rôle in the Standard Model, or whether it holds the key to new physics beyond.

The accuracy, which is required in order to detect possible mechanisms behind electroweak symmetry breaking through deviations of the Higgs couplings from their pure Standard Model values, has been quantitatively investigated in the framework of the Snowmass study 2013 [1]. Popular models like two-Higgs doublet or composite Higgs schemes, which predict new particles at the TeV scale, and which are still compatible with recent limits from direct searches at the LHC, typically lead to such deviations in the per-cent or sub-percent range. This sets the scale of the future experimental challenges and demonstrates the discovery potential of precision measurements in the Higgs sector.

The ILC and its detectors

The ILC has been proposed as the next big high energy accelerator project. It is designed to have centre-of-mass energies ranging from 250 to 500 GeV and is upgradeable to reach 1 TeV. The delivered luminosity increases with energy and amounts to typically 100 – 300 fb^{-1}/y,

with beam polarisations of up to 80% and 30% for electrons and positrons, respectively. The superconducting technology is mature, as is demonstrated by the on-going construction of the European XFEL at DESY, which uses a very similar design at industrial scales. A technical design report (TDR) [2] for the ILC has been completed in 2012, a proposed site has been selected in the Kitakami mountains in the North of Japan, and the project is currently being discussed at ministerial levels.

Two detector concepts have been proposed [3] for the ILC, which have been optimised for precision, as radiation hardness and rate capability requirements are very relaxed with respect to those at the LHC. The detectors feature highly granular and compact calorimeters for particle flow reconstruction, ultra-thin and precise trackers, and vertex detectors capable of identifying not only beauty but also charm quarks. Detailed designs have been implemented in the simulations to evaluate the physics potential under realistic conditions, including beam-induced backgrounds.

2 Measurements of Higgs couplings

It is instructive to recall the necessary ingredients to a measurement of a coupling strength. The number of particles N observed in a given final state f, normalised to integrated Luminosity L, is given by the product of cross-section σ and branching fraction $\mathcal{B}$, which is the ratio of partial width Γ_f to total width Γ_T. The couplings to the initial and final state, g_i and g_f, enter via the production cross section and the partial width, such that one has

$$N/L = \sigma \cdot \mathcal{B} = \sigma \cdot \Gamma_f/\Gamma_T \sim g_i^2 \cdot g_f^2 \,/\, \Gamma_T \,. \tag{1}$$

In order to extract g_f, one needs a measurement of the inclusive cross section – to obtain g_i – and the total width. In the Z line shape analysis at LEP, the width of the Z resonance was directly observable, and the cross section in the e^+e^- final (and initial) state provided a normalisation of the couplings of the Z to fermions. The width of the Higgs particle, however, is expected to be about 4 MeV in the Standard Model and too narrow to be resolved experimentally, so it has to be extracted from the branching ratio of a channel, for which the coupling is already known, e.g. from a production measurement,

$$\Gamma_T = \mathcal{B}/\Gamma_f \sim \mathcal{B}/g_f^2 \tag{2}$$

At the LHC the total cross section and total width are poorly constraint, and in general the Standard Model values are assumed. At the ILC, however, one can make use of the unique features of an e^+e^- collider to obtain a self-contained set of observables.

2.1 Higgs production at the ILC

The dominant Higgs production processes at the ILC are Higgs strahlung and W fusion. [4]. Figure 1 shows the diagrams and the dependence of the cross-section on the centre-of-mass energy. Higgs strahlung as an s channel process dominates at threshold, whilst the cross section of the t channel process W fusion increases logarithmically with energy and takes over at about 450 GeV. Here, one has made use of the beam polarisation to enhance the cross section. Now, since at an e^+e^- machine one can control the energy of the incoming fermions, one can select the dominant process by tuning the beam energy.

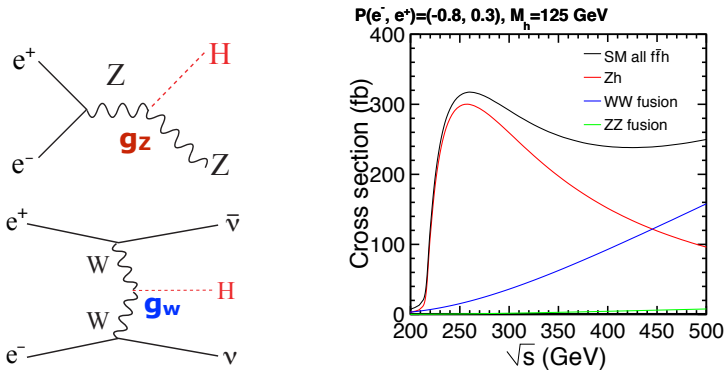

Figure 1: Higgs production diagrams and cross section vs. centre-of-mass energy.

Another consequence of the well-defined initial state is the possibility to apply kinematic constraints. In ZH events, a Higgs signal can be observed in the spectrum of recoil masses against the Z decay products,

$$M^2_{\text{recoil}} = E^2 - p^2 \text{ with } E = \sqrt{s} - E_Z \text{ and } p = p_Z$$

This works best for Z decays into muon pairs, as shown in Figure 2, but also well for the electron channel, whilst for hadronic Z decays it is more difficult. Here, no requirements whatsoever on the Higgs final state have been made, it can even be invisible, and thus the measurement is fully inclusive. It provides an absolute normalisation for all branching ratios into specific final states and a model-independent extraction of the absolute value of g_Z, the Higgs Z coupling, which is *the* central measurement of the Higgs coupling analyses.

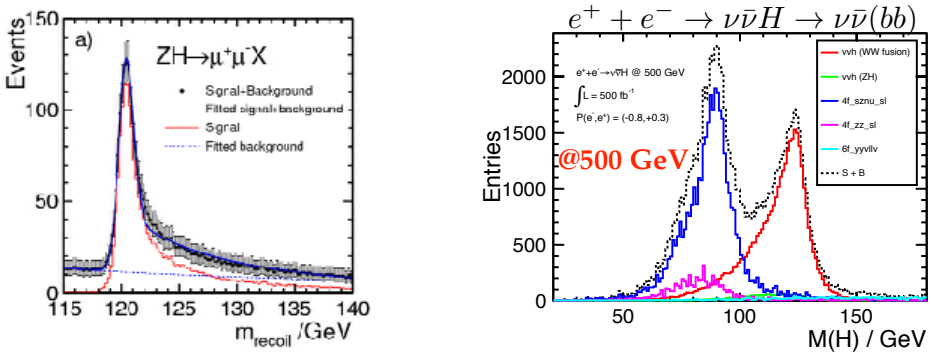

Figure 2: Higgs signal in the recoil mass spectrum (ZH production), and in the $b\bar{b}$ di-jet mass (W fusion).

2.2 The Higgs total width

The Higgs mass of 125 GeV is almost ideally suited for the study of a large number of decay modes with not too small branching ratios. However, the fraction of decays into Z pairs is only a few per-cent and the statistics for specific Z channels very small. An extraction of the total width, using Eq. 2 with g_Z and $\mathcal{B}(\mathrm{H} \to \mathrm{ZZ}^*)$ is in principle possible, but would suffer from large uncertainties of $\sim 20\%$.

It is more advantageous to use the W fusion cross section and the branching ratio $\mathcal{B}(\mathrm{H} \to \mathrm{WW}^*)$. Since in W fusion the Higgs is accompanied by two neutrinos, the recoil method cannot be applied for a decay-mode independent measurement, but a specific Higgs channel must be used. Both the $b\bar{b}$ and the WW^* channel are suited [5]; the $b\bar{b}$ signal is shown in Figure 2. Since these decay modes are also measured in HZ production, the ratio g_W/g_Z and thus g_W can be extracted and Γ_T from Eq. 2. Now one has all ingredients to convert also the other branching ratio measurements into absolute couplings,

2.3 Higgs couplings to fermions and the self-coupling

Thanks to the relatively benign beam conditions at the ILC vertex detector systems can be realised which can not only identify b flavoured hadron decays on the basis of the finite decay length, but can also tag charmed hadrons and disentangle prompt open charm from tertiary vertices, which originate from $b \to c$ decays. Particularly well suited are ZH events with Z decaying into neutrinos, such that the final state consists of the two jets from the Higgs only, giving a signal in the diet invariant mass. A multivariate analysis of the vertex topologies then yields a simultaneous measurement of $\mathcal{B}(\mathrm{H} \to b\bar{b})$, $\mathcal{B}(\mathrm{H} \to c\bar{c})$ and $\mathcal{B}(\mathrm{H} \to gg)$, and thus g_b, g_c and a model-dependent value for g_t, like the $\gamma\gamma$ mode.

The measurement of the coupling to the second quark generation is unique for testing the mass dependence of the Higgs coupling in the quark sector, since couplings to u, d and s quarks are unobservable. In the lepton sector, g_τ can be measured well, but in the H$\to \mu\mu$ channel only very few events can be observed and only at the highest energies attainable at the ILC, where luminosity and cross section are maximal.

The direct observation of the top Higgs Yukawa coupling is made though a production cross section measurement for the $t\bar{t}$H channel, where, e.g., a Higgs is radiated from one of the two quarks in a $t\bar{t}$ pair. This involves the analysis of complex 8 or 10 fermion final states, where eben after using flavour tags and di-jet masses, the signal basically consists of an excess over expectation without $t\bar{t}$H coupling. This is a particularly good example for cases where a large gain in precision can be obtained from a combined evaluation of ILC and LHC data, see below.

Finally, a measurement of the Higgs self-coupling would represent the last cornerstone in establishing the Higgs profile and demonstrating that it has the properties required for electroweak symmetry breaking. The strength g_{HHH} can be measured at the ILC, albeit with only moderate precision. This is due to the fact that ZHH events are not only produced with diagrams involving triple-Higgs coupling, but also through processes like double Higgs strahlung, which constitute an irreducible background. The situation is more favourable in the case of W fusion leading to $\nu\bar{\nu}$HH events, therefore the best precision is obtained at highest energies, where the dilution is less and luminosity and cross section are largest.

3 Global fits and achievable precision: Summary

In a staged running scenario, each centre-of-mass energy, 250, 500 and 1000 GeV, provides an independent set of measurements. Altogether, 33 measurements of $\sigma \cdot \mathcal{B}$ values are made and injected into a global fit with 10 free parameters – the couplings to W, Z and t, b, c, τ, μ fermions, indirect to gg, $\gamma\gamma$ pairs, and the total width Γ_T. The result is shown in Figure 3.

The precision has been compared to that expected for the LHC [6] and its high-luminosity upgrade [7]. In these studies consistent assumptions and constraints have been used for both colliders' data sets, which is important for a fair comparison. As the Figure 3 shows, with linear collider results the per-cent and sub-per-cent level precision can be reached, which is required to detect deviations from the Standard Model in the magnitude expected in theories for mechanisms behind electro-weak symmetry breaking.

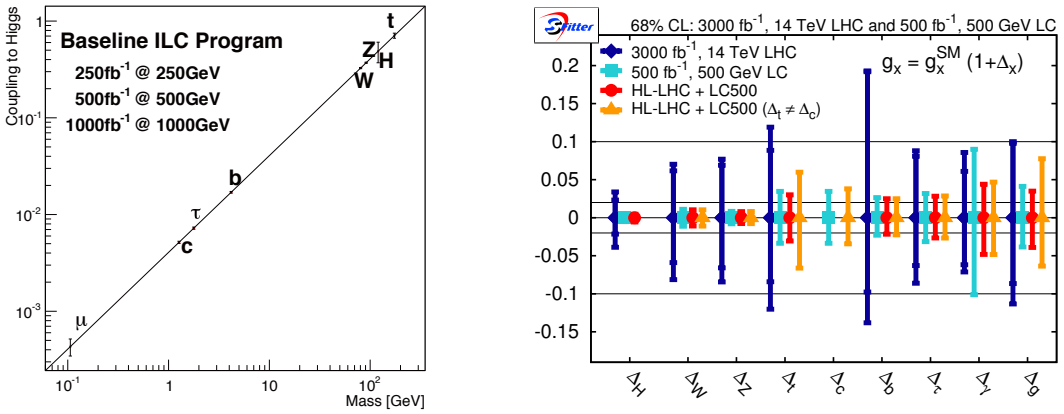

Figure 3: Higgs coupling strengts, mesurerd at the ILC, as a function of mass: relative precision for expected ILC and LHC results, including the luminosity upgrade, and combination of data.

References

[1] S. Dawson, A. Gritsan, H. Logan, J. Qian, C. Tully, R. Van Kooten, A. Ajaib and A. Anastassov *et al.*, arXiv:1310.8361 [hep-ex].

[2] C. Adolphsen, M. Barone, B. Barish, K. Buesser, P. Burrows, J. Carwardine, J. Clark and H. M. Durand *et al.*, arXiv:1306.6328 [physics.acc-ph].

[3] T. Behnke, J. E. Brau, P. N. Burrows, J. Fuster, M. Peskin, M. Stanitzki, Y. Sugimoto and S. Yamada *et al.*, arXiv:1306.6329 [physics.ins-det].

[4] H. Baer, T. Barklow, K. Fujii, Y. Gao, A. Hoang, S. Kanemura, J. List and H. E. Logan *et al.*, arXiv:1306.6352 [hep-ph].

[5] C. Dürig, K. Fujii, J. List and J. Tian, arXiv:1403.7734 [hep-ex].

[6] M. E. Peskin, arXiv:1312.4974 [hep-ph].

[7] M. Klute, R. Lafaye, T. Plehn, M. Rauch and D. Zerwas, Europhys. Lett. **101** (2013) 51001

Top Quark Precision Physics at Linear Colliders

Frank Simon[1] on behalf of the ILC Physics and Detector Study and the CLICdp Collaboration

[1]Max-Planck-Institut für Physik, Föhringer Ring 6, 80805 München, Germany

DOI: http://dx.doi.org/10.3204/DESY-PROC-2014-04/123

Linear e^+e^- colliders provide a rich set of opportunities for precision top physics, crucial for the understanding of electroweak symmetry breaking and for the search for physics beyond the Standard Model. A $t\bar{t}$ threshold scan in e^+e^- annihilation enables a precise measurement in theoretically well-defined mass schemes with small experimental and theoretical systematic uncertainties. Above the production threshold, the efficient identification of top pair events combined with polarized beams provides the potential to extract the form factors for the top quark couplings with high precision and in a model-independent way, resulting in excellent sensitivity to physics beyond the Standard Model. This contribution provides an overview of top physics at linear colliders based on results from full-simulation studies of top quark pair production in the detectors proposed for ILC and CLIC.

1 Introduction

As the heaviest particle in the Standard Model, the top quark has a special role. Due to its high mass, it has the the strongest coupling of all known particles to the Higgs field. It also takes a central role in many models of New Physics, and thus provides a high sensitivity for phenomena beyond the Standard Model.

To date, the top quark is the only quark that has been studied exclusively at hadron colliders. The clean experimental environment in e^+e^- collisions enables the study of all decay modes of the top quark with high resolution and very low background levels. The measurements at lepton colliders also profit from the high precision of theoretical calculations, which result in small overall systematic uncertainties.

At e^+e^- colliders, there are two different main programs for top physics. The first is the study of the threshold for top quark pair production, which provides access to the detailed properties of the top quark. The second is the use of the top quark as a tool for the search for physics beyond the Standard Model, for example by precisely measuring its coupling to the electroweak interactions. In the first case, collision energies at several different values around 350 GeV are necessary, while the second program requires energies substantially in excess of the threshold for top pair production, of the order of 500 GeV or higher. In particular, the energies above threshold are uniquely available at linear e^+e^- colliders.

Two such high-energy e^+e^- colliders are currently being developed in international collaboration, the International Linear Collider (ILC) [1] and the Compact Linear Collider (CLIC) [2]. They are based on different acceleration technologies, resulting in a different energy reach for the full projects. ILC is based on superconducting RF structures, and is planned as a 500 GeV collider with operation at different energies from 250 GeV to 500 GeV, including the region around the $t\bar{t}$ threshold, and the possibility for upgrades to one TeV. CLIC uses a

normal-conducting two-beam acceleration scheme, and is foreseen to be constructed in several stages. It has an ultimate energy of 3 TeV and two lower energy stages to maximise the physics potential, with the first stage covering the $t\bar{t}$ threshold. For ILC, the technical design report has been completed, while for CLIC a conceptual design report was delivered, with a technical design phase still ongoing until 2018.

In the following, the top physics program at these future colliders is illustrated based on two examples that have been studied with detailed simulations with realistic detector models, including physics and machine-related backgrounds. For the $t\bar{t}$ threshold scan, studies have been performed both in the context of ILC and CLIC, while the investigation of the physics potential for measurements of the electroweak couplings of the top quark have been performed for ILC at 500 GeV.

2 A top threshold scan at ILC and CLIC

The cross section of $t\bar{t}$ production close to the threshold strongly depends on the top quark mass. In addition, it receives contributions from the top quark width, from the strong coupling and from the top Yukawa coupling. The top width influences the shape of the would-be bound state of the $t\bar{t}$ pair. The strong coupling and the top Yukawa coupling, which both influence the interaction of the two top quarks, primarily affect the overall magnitude of the cross section. Beyond those effects connected to the $t\bar{t}$ system, the cross section also receives corrections due to initial state radiation (ISR) and due to the luminosity spectrum of the collider. The pure $e^+e^- \to t\bar{t}$ cross section can be calculated with high precision, resulting in clean theoretical predictions for the observables based on theoretically well-defined parameters, such as the 1S mass of the top quark.

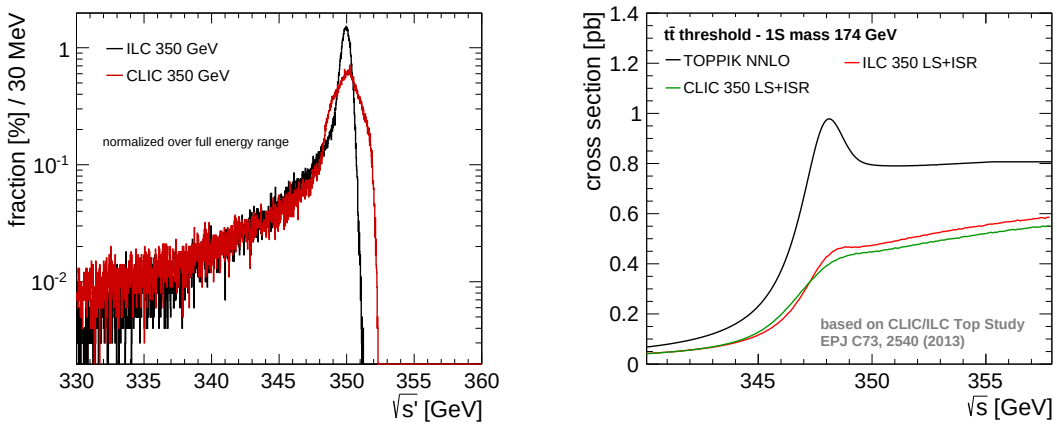

Figure 1: The luminosity spectrum for ILC and CLIC at 350 GeV (*left*) and the resulting total $t\bar{t}$ cross section in the threshold region based on TOPPIK NNLO calculations [3, 4] including ISR and luminosity spectrum effects.

Figure 1 shows the luminosity spectrum of both ILC and CLIC at an energy of 350 GeV, and illustrates the effect of these spectra together with initial state radiation on the pure $t\bar{t}$

production cross section calculated with NNLO QCD [3, 4]. The luminosity spectrum and ISR result in an overall reduction of the effective cross section since they shift a fraction of the luminosity below the threshold energy, and lead to a broadening of the threshold turn-on due to the low-energy tail and due to the width of the main luminosity peak. Since the beam energy spread is larger at CLIC than at ILC, the smearing is slightly more pronounced at CLIC.

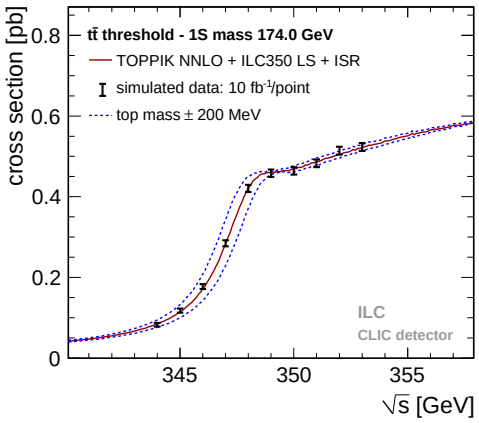

Figure 2: A simulated $t\bar{t}$ threshold scan at ILC with 10 points spaced by 1 GeV each, assuming an integrated luminosity of 10 fb^{-1} per point with unpolarised beams. For illustration purposes, the effect of a shift in the 1S top quark mass by $\pm$200 MeV is shown in addition to the simulated data points. Figure taken from [6].

With full detector simulations of the CLIC_ILD concept [5] the reconstruction efficiencies for $t\bar{t}$ events and the rejection efficiency for Standard Model background was determined in the threshold region. These efficiencies are used to simulate threshold scans at ILC and CLIC, as illustrated in Figure 2. From these scans, the top mass is determined via a template fit of the measured cross section. With a 10-point scan with a total integrated luminosity of 100 fb^{-1} assuming unpolarised beams, the top quark mass can be determined with a statistical uncertainty of 18 MeV in the case of ILC and 21 MeV in the case of CLIC [6]. The current precision of α_s of 0.0007 leads to a systematic uncertainty of equal magnitude (18 MeV for ILC, 20 MeV for CLIC), which is expected to improve in the future with a more precise determination of the strong coupling constant.

In addition, there are experimental systematic uncertainties from several sources, such as the beam energy and the reconstruction efficiency and background contamination, which are expected to have a total size below 50 MeV. On top of that, there are theoretical systematics due to the precision of the calculation of the total $t\bar{t}$ cross section. These depend on the details of the calculations, and are still being evaluated. With the simplified assumption of a 3% overall normalisation uncertainty, the resulting systematic uncertainty of the mass is around 50 MeV, making theoretical uncertainties potentially the leading source of systematics.

A potentially important source of experimental systematics is the knowledge of the luminosity spectrum. The impact of this has been studied for CLIC by reconstructing the luminosity spectrum from simulated measurements of large-angle Bhabha scattering [7]. In a preliminary study, the uncertainty resulting from the precision of the reconstructed luminosity spectrum

has been found to be of the order of 6 MeV, demonstrating that this is not a limiting factor for the overall precision of the top quark mass measurement. Since the luminosity spectrum at ILC is less complicated than the one at CLIC, even smaller uncertainties are expected for the ILC case.

Overall, a $t\bar{t}$ threshold scan at linear colliders is expected to provide the top quark mass in a theoretically well-defined mass scheme with sub-100 MeV total uncertainty, which would provide a knowledge of the $\overline{MS}$ mass of the top quark at the 100 MeV level or better. Given the dominance of systematics and the uncertainties involved in the conversion from the 1S to the $\overline{MS}$ mass, the small differences in statistical uncertainties between the different linear collider options are insignificant.

3 Electroweak couplings

The capability for polarised beams at linear colliders provides excellent conditions to probe the electroweak couplings of the top quark in $t\bar{t}$ production above threshold. These couplings are precisely determined in the Standard Model, but may receive substantial modifications in scenarios with physics beyond the Standard Model, such as extra dimensions and Higgs compositeness. The measurement of the total production cross section, the forward-backward asymmetry and the helicity angle, each for two different polarisation configurations, provides sufficient information to fully constrain the top quark couplings with high precision. Since the asymmetry and angle measurements require the identification of the top quark charge and rely on the correct association of W bosons and b jets to top candidates, these measurements profit from higher energy which provides a clean separation of the two top quarks in the $t\bar{t}$ system.

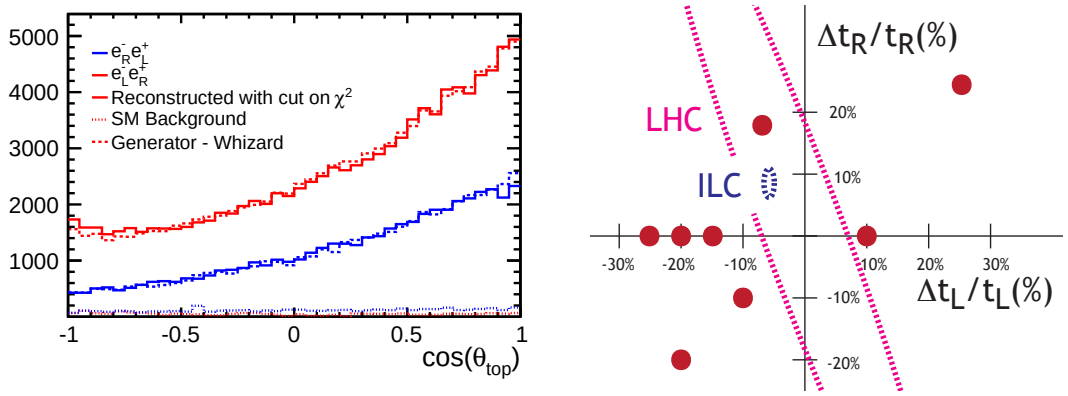

Figure 3: The forward-backward asymmetry of $t\bar{t}$ production at 500 GeV in a full simulation study for two different polarisation configurations of the beams ($\pm$ 80% e^-, $\mp$ 30% e^+ polaristion) (*left*). Figure taken from [8]. The precision achievable at ILC at 500 GeV with an integrated luminosity of 500 fb^{-1} for the left- and right-handed couplings of the top quark, compared to the expected precision achievable at the HL-LHC, together with the deviations from the Standard Model values in a variety of models with composite Higgs bosons [9, 10] (*right*).

Figure 3 *left* shows the forward-backward asymmetry in a full simulation study with the ILD

detector [11] for an integrated luminosity of 500 fb^{-1} at an energy of 500 GeV at ILC. The total integrated luminosity is equally split between two polarisation configurations of $\pm 80\%$, $\mp 30\%$ for electrons and positrons, respectively [8]. From this measurement, the forward-backward asymmetry is extracted with a $\sim$2% uncertainty including statistical and systematic contributions. Similarly, the helicity angle distribution can be extracted with a precision of 4%, and the total cross section with a 0.5% uncertainty. From these results, the left- and right-handed couplings can be extracted with a 0.7% and 1.8% precision, respectively [8, 9]. This precision is illustrated in Figure 3 *right* together with the predicted deviations from the Standard Model for several scenarios of New Physics with composite Higgs bosons and with the precision expected from the HL-LHC [9, 10]. This clearly illustrates the immense power of a polarised high-energy electron-positron collider not only to discover possible new phenomena in the top sector, but also to precisely pin down the underlying mechanism if deviations from the Standard Model are observed.

4 Summary

The future linear electron-positron colliders ILC and CLIC provide excellent opportunities for a precise study of the top quark sector. With polarised beams, the possibility for a scan of the $t\bar{t}$ production threshold and with measurements of the electroweak couplings of the top quark at energies substantially above the threshold they will provide high precision measurements of top quark properties and significant sensitivity for various physics scenarios beyond the Standard Model. A linear collider will determine the top-quark mass in the theoretically well-defined $\overline{MS}$ scheme with a total precision of 100 MeV or better, and is capable of a percent-level measurement of the top electroweak couplings, which provides sensitivity to new physics scales extending substantially beyond the direct reach of present colliders.

References

[1] T. Behnke *et al.*, arXiv:1306.6327 [physics.acc-ph].

[2] P. Lebrun *et al.*, arXiv:1209.2543 [physics.ins-det].

[3] A. H. Hoang and T. Teubner, Phys. Rev. D **60**, 114027 (1999).

[4] A. H. Hoang and T. Teubner, Phys. Rev. D **58**, 114023 (1998).

[5] L. Linssen *et al.*, arXiv:1202.5940 [physics.ins-det].

[6] K. Seidel, F. Simon, M. Tesar and S. Poss, Eur. Phys. J. C **73**, 2530 (2013).

[7] S. Poss and A. Sailer, Eur. Phys. J. C **74**, 2833 (2014).

[8] M. S. Amjad *et al.*, arXiv:1307.8102 [hep-ex].

[9] F. Richard, arXiv:1403.2893 [hep-ph].

[10] K. Agashe *et al.*, arXiv:1311.2028 [hep-ph].

[11] T. Behnke *et al.*, arXiv:1306.6329 [physics.ins-det].

Measurements with electroweak bosons at LHCb

Katharina Müller

Winterthurerstr. 190, CH-8057 Zurich, Switzerland

DOI: http://dx.doi.org/10.3204/DESY-PROC-2014-04/241

The LHCb measurements of electroweak boson production, either inclusive, or in association with a jet or a D meson at a centre-of-mass energy $\sqrt{s}$=7 TeV as well as Z boson production in proton-lead collisions are reported. The LHCb forward acceptance allows measurements complementary to the other LHC experiments.

1 Introduction

The LHCb detector [1] is a single-arm forward spectrometer instrumented in the pseudorapidity region $2 < \eta < 5$ and is optimised for the study of B and D mesons. Its unique kinematic coverage allows it perform measurements that are sensitive to both low and high values of Bjorken x and hence are complementary to those performed at the general purpose detectors, ATLAS and CMS. At energy scales typical for electroweak boson production, LHCb measurements are sensitive to values of x as low as 1.7 $\times 10^4$, where they can provide a fundamental input to parton distribution functions (PDFs) kinematic parametrisations of the partons within the colliding protons. The results presented here, except for Z production in proton-lead, are based on data collected at a centre-of-mass energy of 7 TeV with an integrated luminosity of about 1 fb^{-1}.

2 W boson production

A measurement of inclusive W boson production is performed at LHCb using the muonic decay mode of the W boson [2]. Events are selected which contain a muon with a transverse momentum, p_T, above 20 GeV/c and $2 < \eta^\mu < 4.5$. In addition, the muon is required to be isolated and consistent with production from the primary vertex. Furthermore it is required that there is no other muon in the event with $p_T > 2$ GeV/c. The signal purity is obtained by fitting the p_T distribution of the data sample in eight bins of muon pseudorapidity for both charges, simultaneously, to the expected shapes for signal and background. Background contributions are decay-in-flight of pions and kaons, semi-leptonic decays of heavy-flavour mesons, $Z \to \mu\mu$ events with one muon outside the LHCb acceptance and $Z \to \tau\tau$ events with a single muon in the final state. The templates are obtained from simulation for the signal and the electroweak backgrounds and from data for the other backgrounds. A total of about 8×10^6 W candidates are selected, with signal purities of about 77% for both charges of the muon. The signal yield is corrected for losses due to reconstruction and selection efficiency, acceptance and final-state radiation (FSR). The reconstruction and selection efficiencies are primarily estimated from data, while the acceptance and FSR corrections are determined with simulation. The total

cross-sections for W^+ and W^- production in the fiducial range defined as $p_T^\mu > 20$ GeV/c and $2 < \eta^\mu < 4.5$ are measured to be $\sigma(W^+ \to \mu\nu) = 861.0 \pm 2.0 \pm 11.2 \pm 14.7$ pb and $\sigma(W^- \to \mu\nu) = 675.8 \pm 1.9 \pm 8.8 \pm 11.6$ pb, where the first uncertainty is statistical, the second is systematic and the third is due to the luminosity. The W^+ and W^- cross-sections and the lepton charge asymmetry as a function of muon pseudorapidity are shown in Fig. 1, where many experimental and theoretical uncertainties cancel for the latter. The measurements are compared to theoretical predictions calculated at next-to-next-to-leading order (NNLO) in QCD [3] using different parameterisations of the PDFs. In general, the results are in good agreement with the predictions.

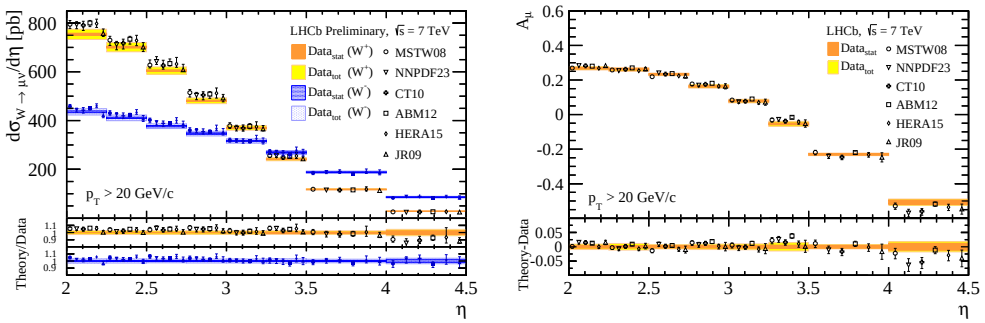

Figure 1: W^+ and W^- cross-sections (left) and lepton charge asymmetry (right) as a function of muon pseudorapidity [2]. The measurements, shown as coloured bands, are compared to NNLO predictions with different PDF sets. They are displaced horizontally for better visibility.

3 Z plus jet production

The production of a Z boson in association with a hadronic jet is studied with the Z decaying into two muons [4] with the same kinematic requirements for the muons as in the W analysis. In addition, the di-muon invariant mass is restricted to $60 < M_{\mu\mu} < 20$ GeV/c^2 and the event is required to contain a high-p$_T$ jet with $2 < \eta^{jet} < 4.5$ and $p_T^{jet} > 10$ or 20 GeV/c. The jets are reconstructed using an anti-k_T algorithm [5] with radius parameter of R=0.5. Reconstructed tracks and neutral clusters serve as charged and neutral inputs to the jet reconstruction algorithm and are selected using a particle flow algorithm. The jet energy scale is determined using simulation and cross-checked in data, with the jet energy resolution varying between 10 and 15% for the p_T^{jet} between 10 and 100 GeV/c. The fraction of $Z \to \mu\mu$ events containing a jet are determined to be $\sigma(Z + jet)/\sigma(Z) = 0.209 \pm 0.002 \pm 0.015$ for jet $p_T^{jet} > 10$ GeV/c and $\sigma(Z + jet)/\sigma(Z) = 0.083 \pm 0.001 \pm 0.007$ for jet $p_T^{jet} > 20$ GeV/c. The first uncertainty is statistical and the second systematic. The differential cross-section normalised to the inclusive Z cross-section for $p_T^{jet} > 20$ GeV/c is shown as a function of the azimuthal separation of the Z boson and the jet, $\Delta\phi$, in Fig. 2. The measurement is compared to theoretical predictions at up to $\mathcal{O}(\alpha_s^2)$ with parton showering and hadronisation effects included. As expected, the calculations performed at $\mathcal{O}(\alpha_s)$ fail to describe the distribution.

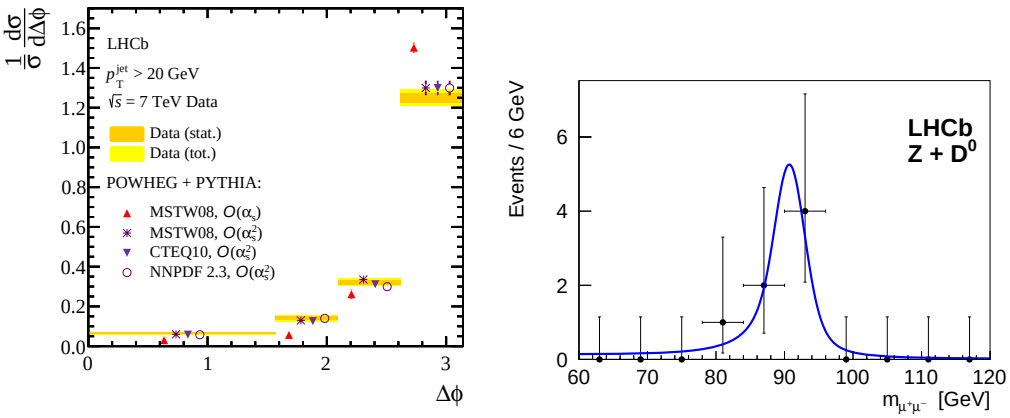

Figure 2: Z plus jet cross-section as a function of $\Delta\phi$ [4] (left). Invariant di-muon mass for the selected $Z + D^0$ candidates [6] (right).

4 Z plus D production

The $Z \to \mu\mu$ selection is also applied to search for the production of Z bosons in association with D mesons [6]. The D candidates are reconstructed using the $D^0 \to K\pi^+$ and $D^+ \to K\pi^+\pi^+$ decay modes and are restricted to the kinematic range of $2 < \eta^D < 4$ and $2 < p_T^D < 12$ GeV; together with the kinematic range of the muons of the Z decay, this also defines the fiducial volume of the measurement. The Z and the D are furthermore required to come from the same primary vertex. Backgrounds are taken into account from feed-down from beauty meson decays, which is the dominant contribution, combinatorics, and pile-up where the Z boson and the D meson are produced in different proton-proton interactions. The signal purity is determined to be about 95%. A total of 7(4) candidates are found for the $Z + D^0(Z + D^+)$ decay channel, corresponding to a combined significance of 5.1σ. The reconstructed mass of the Z boson for events in the $Z + D^0$ sample is shown in Fig. 2 (right). The production cross-sections are measured to be $\sigma(Z \to \mu\mu, D^0) = 2.50 \pm 1.12 \pm 0.22$ pb and $\sigma(Z \to \mu\mu, D^+) = 0.44 \pm 0.23 \pm 0.03$ pb, where the first uncertainty is statistical and the second systematic. The cross-sections receive contributions from single parton (SPS) and double parton scattering processes (DPS). The latter dominates in the kinematic range of the measurement. The measured cross sections are found to be in agreement with theoretical predictions[1] for the $Z + D^0$ but lower for $Z + D^{\pm}$. However, the large statistical uncertainties do not allow a firm conclusion.

5 Inclusive Z boson production in proton-lead collisions

Measurements in proton-lead collisions can serve as reference for future lead-lead collisions but can also provide significant constraining power for nuclear PDFs in unprobed regions of the phase space, at both low and high x_A, where x_A is the longitudinal momentum fraction of the parton in the nucleon. A search for Z boson production is performed based on two data samples corresponding to 1.6 nb^{-1} of proton-lead collisions at a centre-of-mass energy per

[1]The SPS contribution is calculated with MCFM [7], DPS as $\sigma = (\sigma_{Z\to\mu\mu}\sigma_D)/\sigma_{eff}$ with σ_{eff} from [8].

proton-nucleon pair of $\sqrt{s_{NN}}$ =5 TeV [9]. The two data samples correspond to two different beam configurations, with the proton (lead) beam into the direction of LHCb, referred to as forward (backward). The Z candidates are reconstructed in the di-muon final state. Background contributions from muon mis-identification and the decay of heavy flavour mesons are determined from data. A total of 15 candidates are selected with a purity of above 99%, corresponding to a significance of 10.4σ (6.8σ) for the Z signal in the forward (backward) direction. Figure 3 (left) shows the di-muon invariant mass of the Z candidates in the forward direction. The inclusive Z boson production cross-section is measured to be $\sigma(Z \to \mu\mu) = 13.5^{+5.4}_{-4.0} \pm 1.2$ nb in the forward and $\sigma(Z \to \mu\mu) = 10.7^{+8.4}_{-5.1} \pm 1.0$ nb in the backward configuration. Here, the first uncertainty is statistical and the second systematic. The measurements are compared to theoretical predictions calculated at NNLO using the FEWZ generator [3] and computed with and without considering nuclear effects based on the EPS09 nuclear PDF set [10] in Fig. 3 (right).

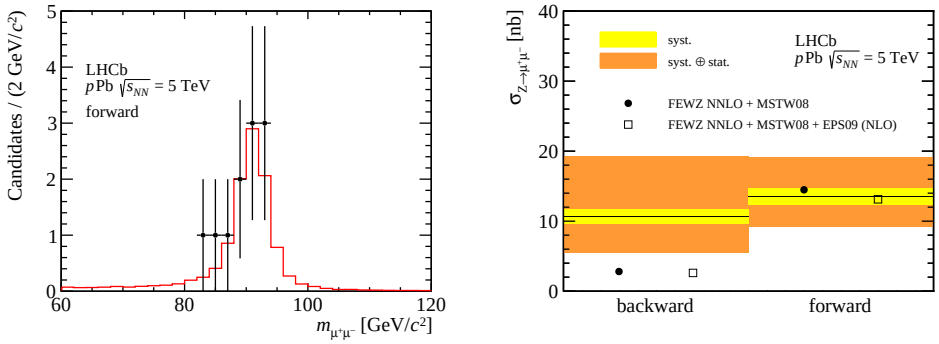

Figure 3: Left: Invariant di-muon mass of the Z candidates in proton-lead collisions. Right: Experimental results and theoretical predictions for the Z production cross-section in proton-lead collisions [9].

References

[1] Jr. Alves, A. Augusto et al. The LHCb Detector at the LHC. *JINST*, 3:S08005, 2008.

[2] R. Aaij et al. Measurement of the forward W boson cross-section in pp collisions at $\sqrt{s} = 7$ TeV. 2014.

[3] Ye Li and Frank Petriello. Combining QCD and electroweak corrections to dilepton production in FEWZ. *Phys.Rev.*, D86:094034, 2012.

[4] R. Aaij et al. Study of forward Z + jet production in pp collisions at $\sqrt{s} = 7$ TeV. *JHEP*, 1401:033, 2014.

[5] Matteo Cacciari, Gavin P. Salam, and Gregory Soyez. The Anti-k(t) jet clustering algorithm. *JHEP*, 0804:063, 2008.

[6] Roel Aaij et al. Observation of associated production of a Z boson with a D meson in the forward region. *JHEP*, 1404:091, 2014.

[7] John M. Campbell and R.K. Ellis. MCFM for the Tevatron and the LHC. *Nucl.Phys.Proc.Suppl.*, 205-206:10–15, 2010.

[8] F. Abe et al. Double parton scattering in $\bar{p}p$ collisions at $\sqrt{s} = 1.8$TeV. *Phys.Rev.*, D56:3811–3832, 1997.

[9] R. Aaij et al. Observation of Z production in proton-lead collisions at LHCb. *JHEP*, 1409:030, 2014.

[10] K.J. Eskola, H. Paukkunen, and C.A. Salgado. EPS09: A New Generation of NLO and LO Nuclear Parton Distribution Functions. *JHEP*, 0904:065, 2009.

Measurement of Properties of the Higgs Boson in Bosonic Decay Channels using the ATLAS Detector

Eleonora Benhar Noccioli[1] on behalf of the ATLAS Collaboration
[1]Université de Genève, 24 Quai Ernest-Ansermet, CH 1211 Genève 4, Switzerland

DOI: http://dx.doi.org/10.3204/DESY-PROC-2014-04/224

The paper reports the properties of the Higgs boson measured in bosonic decay channels ($H \to ZZ^* \to 4\ell$, $H \to \gamma\gamma$, $H \to WW^* \to \ell\ell\nu\nu$ and $H \to Z\gamma \to \ell\ell\gamma$) with 25 fb^{-1} of pp collision data from the LHC run-1 collected by the ATLAS detector. An improved mass measurement, as well as new fiducial and differential cross sections measurements are discussed.

1 Introduction

In the discovery of the Higgs boson, announced by ATLAS [1] and CMS [2] in July 2012, the analyses searching for bosonic decay channels played a crucial role among all channels accessible at the LHC. Since then, using two and a half times more data than was available for the discovery [3], more precise measurements of the properties of this particle have been achieved. Once again the $H \to ZZ^* \to 4\ell$, $H \to \gamma\gamma$ and $H \to WW^* \to \ell\ell\nu\nu$ decay modes have proven to be fundamental in testing the agreement between the observed results and the Standard Model (SM) predictions. Thanks to several refinements achieved in both the $H \to ZZ^* \to 4\ell$ and $H \to \gamma\gamma$ analyses, an improved measurement of the mass of the Higgs boson was recently published. The production modes and therefore the Higgs couplings were tested, and found to be in agreement with theory predictions. In addition, no significant deviations were found following new fiducial and differential cross section measurements, performed in both the $H \to ZZ^* \to 4\ell$ and $H \to \gamma\gamma$ decay channels. Furthermore, an indirect measurement of the Higgs width, Γ_H, was made exploiting the $H \to ZZ^*$ off-peak background interference effects. Finally, a combined measurement of the spin-CP properties of the boson is available. In the following sections the results obtained using approximately 25 fb^{-1} of pp collision data collected at 7 TeV and 8 TeV in 2011 and 2012 are reported.
While in the $H \to Z\gamma \to \ell\ell\gamma$ final state no signal has yet been observed, this channel will be particularly interesting in the coming years due to its sensitivity to the presence of new physics beyond the SM. The last section of this paper describes the analysis and the latest available results.

2 $H \to ZZ^* \to 4\ell$

The $H \to ZZ^* \to 4\ell$ channel provides good sensitivity to the measurement of the Higgs properties due to its high signal-to-background ratio (s/b), which is about two, and its excellent mass resolution varying from 1.6 GeV to 2 GeV depending on the final state.
The analysis searches for two pairs of same-flavor, oppositely charged electrons and muons. Only isolated leptons arising from the same vertex are considered, and they are required to fulfill kinematic cuts and identification quality criteria. In particular, the 2012 data were analysed using a more efficient electron reconstruction algorithm, and an improved likelihood-based electron identification that increased the background rejection by a factor of 2.
Photons originating from final-state radiation (FSR) are searched for and recovered. A kinematic fit is then used to constrain the mass of the leading lepton pair (including FSR photons) to the Z pole mass within the experimental resolution.
The reducible *Z+jets* and $t\bar{t}$ backgrounds are estimated using data-driven methods, while the main ZZ^* background is estimated from simulation and normalized to next-to-leading order calculations. A new boosted decision tree (BDT) discriminant is applied to suppress the ZZ^* contribution, which uses the transverse momentum and pseudorapidity of the four lepton system, and a matrix element kinematic discriminant.
An improved electromagnetic energy calibration and a reduced uncertainty on the muon momentum scale have resulted in a decrease of the systematic uncertainty on the Higgs boson mass. This is measured with a two-dimensional fit to the four lepton invariant mass $\mathrm{m}_{4\ell}$ and the ZZ^* BDT output. The new procedure provides approximately 8% extra sensitivity on the mass with respect to the past, when a simple $m_{4\ell}$ fit was used. The measured Higgs boson mass in the $H \to ZZ^* \to 4\ell$ the decay channel is: $m_H = 124.51 \pm 0.52(\mathrm{stat}) \pm 0.06(\mathrm{syst})$ GeV [4].

By categorising the events according to the characteristics of the different production modes, we can further explore the coupling structure of the Higgs and measure possible deviations from the SM expectations. Four categories are considered: VBF-like, hadronic VH-like, leptonic VH-like and ggF-like. New multivariate techniques are used in the VBF category and in the recently introduced hadronic VH, both characterised by two jets in the final state. An additional lepton is required for the leptonic VH, while the ggF category includes all events discarded by the others. The ratio between the observed and expected signal events, referred to as the signal strength, is extracted at the combined $H \to \gamma\gamma$ and $H \to ZZ^* \to 4\ell$ mass value, which will be presented in the following section. For production in gluon fusion or in association with $t\bar{t}$ or $b\bar{b}$ pairs the signal strength is found to be $1.7^{+0.5}_{-0.4}$, while for vector boson fusion combined with WH/ZH associated production it is $0.3^{+1.6}_{-0.9}$ [5].

The fiducial and differential cross sections of the Higgs boson production have been recently measured in the $H \to ZZ^* \to 4\ell$ decay channel. The extraction of the signal yield for the measurement of the fiducial cross section is performed using a fit to the $m_{4\ell}$ distribution. In the differential cross section measurements, given the low number of signal events expected in each bin, a simple cut-and-count method is used, subtracting the expected number of background events from the observed ones. The differential measurements are performed for several Higgs kinematic distributions, decay angles and jets-related variables. The measured cross sections, determined within a fiducial phase space and corrected for detection efficiency and resolution effects, are then compared to selected theoretical calculations of the SM expectations. No significant deviation from any of the tested predictions is found [6].

The measurement of the ZZ final state in the mass range above the $2m_Z$ threshold provides

a unique opportunity to measure the off-shell couplings strength of the observed Higgs boson. Assuming an identical coupling strength for on- and off-shell Higgs boson production and decay, one can reinterpret these measurements as a constraint on the total width Γ_H/Γ_H^{SM}. Given the assumptions detailed in Ref.[7], the observed 95% CL limit is found to be: $4.8 < \Gamma_H^{95\%}/\Gamma_H^{SM} < 7.7$.

3 $H \to \gamma\gamma$

The $H \to \gamma\gamma$ channel offers a clean signature due to the excellent mass resolution in the diphoton final state, allowing the observation of a narrow mass peak over a smoothly falling background determined from data. The typical mass resolution is 1.7 GeV, while the s/b is approximately 3%.
Higgs boson candidates are selected by requiring two photons fulfilling tight identification criteria based on calorimeter shower shapes, isolation requirements and kinematic cuts. The diphoton invariant mass $m_{\gamma\gamma}$ is computed using the measured energies and their opening angle, estimated from the production vertex and the photon impact points in the calorimeter. The vertex is selected by an algorithm that exploits the longitudinal segmentation of the calorimeter and information from the tracks associated to each vertex. Thanks to a revised photon energy calibration [8], a 10% improvement is achieved on the expected mass resolution.
To improve the accuracy of the mass measurement, events are separated into ten categories with different s/b, invariant mass resolutions and systematic uncertainties. The Higgs boson mass is extracted from a simultaneous signal-plus-background fit to the mass spectra of all categories where the parameters associated to the background model are allowed to vary. The measured mass in $H \to \gamma\gamma$ is found to be: $m_H = 125.98 \pm 0.42(\text{stat}) \pm 0.28(\text{syst})$ GeV [4].

The available data also allow a measurement of the fiducial and differential cross section in this channel. The general strategy is similar to that already described for the $H \to 4\ell$ channel: signal yields are extracted in a fiducial volume and then corrected for the effects of detector inefficiency and resolution. In this case, the number of signal events is estimated using a fit to $m_{\gamma\gamma}$. Differential cross sections as a function of variables related to the diphoton kinematics and the jet activity are measured and found to be broadly in line with SM expectations [9].

An improved mass measurement is obtained from the combination of the new results available for the $H \to ZZ^* \to 4\ell$ and the $H \to \gamma\gamma$ channels. The compatibility between the mass measurements from the two individual channels is now at the level of 2.0σ. The final measurement, $m_H = 125.36 \pm 0.37(\text{stat}) \pm 0.18(\text{syst})$ GeV, has significantly improved systematic uncertainty and supersedes the previous result [4].

4 $H \to WW^* \to \ell\ell\nu\nu$

The $H \to WW^* \to \ell\ell\nu\nu$ channel has the highest rate among the bosonic decays and its s/b ratio is $O(10)\%$, but it suffers from a limited mass resolution due to the presence of two neutrinos in the final state. The dominant backgrounds are WW, $t\bar{t}$ and Wt, all of which have two W bosons in their final state, *W+jets* and other diboson processes. In the analysis, events with two opposite-charge leptons and a large momentum imbalance from the neutrinos are split according to the jet multiplicity. This allows the control of the background from top quarks, as well as the extraction of the signal strengths for the ggF production process, populating mainly the 0- and 1-jet bin, and the VBF production process, ending up in the 2-jets category. An

excess of events relative to the background-only expectation is observed at $m_H = 125.5$ GeV with a local significance of 3.8σ and a measured signal strength of $\mu = 0.99^{+0.31}_{-0.28}$ [10].

Studies of the spin and parity of the Higgs boson have been carried out in all three channels introduced so far, and subsequently combined. These studies have shown that the new particle's quantum numbers are compatible with the SM spin-parity $J^P = 0^+$, whereas all alternative hypotheses are excluded at confidence levels above 97.8% [11].

5 $H \to Z\gamma \to \ell\ell\gamma$

The observation of the $H \to Z\gamma \to \ell\ell\gamma$ is extremely challenging, due to the low cross section, close to that of the $H \to 4\ell$, and the large background, which result in a s/b ratio ranging from 0.01 to 0.001. The event selection requires two opposite-sign leptons and one photon, satisfying very similar requirements to those of the $H \to \gamma\gamma$ and $H \to 4\ell$ analyses. The main backgrounds originate from continuum $Z + \gamma$, $Z + \ell\ell$ production, and from radiative $Z \to \ell\ell\gamma$ decays. To improve the signal sensitivity of this analysis, the selected events are classified into eight categories with different centre-of-mass energies, lepton flavours, s/b ratios and invariant-mass resolutions. The presence of a signal is tested using a likelihood fit to the $m_{\ell\ell\gamma}$ spectra, where the signal and the background are modelled by analytical functions independently in the eight event categories. No excess with respect to the background is found, and upper limits have been set on the cross section times branching ratio. The 95% CL limit for a Higgs mass of $m_H = 125.5$ GeV is found to be 11 times the SM expectation [12].

References

[1] ATLAS Collaboration, *The ATLAS Experiment at the CERN Large Hadron Collider*, JINST **3** S08003 (2008).

[2] CMS Collaboration, *The CMS Experiment at the CERN Large Hadron Collider*, JINST **3** S08004 (2008).

[3] ATLAS Collaboration, *Observation of a new particle in the search for the Standard Model Higgs boson with the ATLAS detector at the LHC*, Phys.Lett. **B716** 1-29 (2012).

[4] ATLAS Collaboration, *Measurement of the Higgs boson mass from the $H \to \gamma\gamma$ and $H \to ZZ^* \to 4\ell$ channels with the ATLAS detector using 25 fb^{-1} of pp collision data*, Phys.Rev. **D90** 052004 (2014).

[5] ATLAS Collaboration, *Measurements of Higgs boson production and couplings in the four-lepton channel in pp collisions at center-of-mass energies of 7 and 8 TeV with the ATLAS detector*, Submitted to Phys.Rev.D (2014).

[6] ATLAS Collaboration, *Fiducial and differential cross sections of Higgs boson production measured in the four-lepton decay channel in pp collisions at $\sqrt{s}$=8 TeV with the ATLAS detector*, Phys.Lett. **B 738** 234-253 (2014).

[7] ATLAS Collaboration, ATLAS-CONF-2014-042, https://cds.cern.ch/record/1740973

[8] ATLAS Collaboration, *Electron and photon energy calibration with the ATLAS detector using LHC Run 1 data*, Submitted to EPJC (2014).

[9] ATLAS Collaboration, *Measurement of fiducial and differential cross sections for Higgs boson production in the diphoton decay channel at $\sqrt{s} = 8$ TeV with ATLAS*, Submitted to JHEP (2014).

[10] ATLAS Collaboration, *Measurements of Higgs boson production and couplings in diboson final states with the ATLAS detector at the LHC*, Phys.Lett. **B726** 88-119 (2013).

[11] ATLAS Collaboration, *Evidence for the spin-0 nature of the Higgs boson using ATLAS data*, Phys.Lett. **B726** 120-144 (2013).

[12] ATLAS Collaboration, *Search for Higgs boson decays to a photon and a Z boson in pp collisions at $\sqrt{s}$=7 and 8 TeV with the ATLAS detector*, Phys.Lett. **B732** 8-27 (2014).

Inclusive Deep-Inelastic Scattering at HERA

Zhiqing Zhang on behalf of the H1 and ZEUS Collaborations

Laboratoire de l'Accélérateur Linéaire, Univ. Paris-Sud 11 and IN2P3/CNRS, Orsay France

DOI: http://dx.doi.org/10.3204/DESY-PROC-2014-04/259

This contribution covers three recent results on deep-inelastic scattering at HERA: (i) new measurements of the proton longitudinal structure function F_L from H1 and ZEUS experiments, (ii) a dedicated NC cross section measurement from ZEUS in the region of high Bjorken x, and (iii) preliminary combination results of all HERA inclusive data published up to now by H1 and ZEUS, taking into account the experimental correlations between measurements.

1 Introduction

At the electron-proton (ep) collider HERA, the inclusive neutral current (NC) differential cross sections in Bjorken x, the virtuality Q^2 and inelasticity y are connected with three different structure functions F_2, F_L and xF_3 as:

$$\tilde{\sigma}_{\rm NC}(x,Q^2,y) \equiv \frac{d^2\sigma_{\rm NC}}{dxdQ^2}\frac{xQ^4}{2\pi\alpha^2}\frac{1}{Y_+} = \left(F_2 - \frac{y^2}{Y_+}F_L - \frac{Y_-}{Y_+}xF_3\right) \quad (1)$$

where $Y_\pm = 1 \pm (1-y)^2$ and the fine structure constant $\alpha = \alpha(Q^2 = 0)$. The reduced cross section $\tilde{\sigma}$ differs from the full cross section by a kinematic factor. The F_2, corresponding to photon exchange, dominates. At high y, the F_L term, proportional to the absorption cross section for longitudinally polarized virtual photons by protons, is sizable. At $Q^2 \lesssim 1000\,\text{GeV}^2$, the xF_3 term, arising from Z exchange, is small. The similar relation also exists for the charged current (CC) process.

2 New F_L measurements

Using data taken with a lepton beam energy of 27.6 GeV and two proton beam energies of $E_p =$ 460 and 575 GeV corresponding to centre-of-mass energies of 225 and 252 GeV, respectively, the inclusive NC cross sections have been measured by H1 [1]. The measurements cover the region of $6.5\times10^{-4} \le x \le 0.65$ for $35 \le Q^2 \le 800\,\text{GeV}^2$ up to the highest accessible inelasticity $y = 0.85$. The measurements are used together with previously published H1 data at $E_p = 920\,\text{GeV}$ and lower Q^2 data at $E_p = 460, 575$ and 920 GeV to extract F_L in the region $1.5 \le Q^2 \le 800\,\text{GeV}^2$. The new measurement (Fig. 1(left)) extends the previous H1 measurements at low and medium Q^2 regions [2, 3] to higher Q^2 and improves the experimental precision in the region $35 \le Q^2 \le 110\,\text{GeV}^2$, thus the new measurement supersedes the previous H1 measurements [2, 3].

Similar measurements have also been performed by ZEUS but in a different kinematic region $0.13 \le y \le 0.75$ and $5 \le Q^2 \le 110\,\text{GeV}^2$ [6]. The new results supersede those in the previous

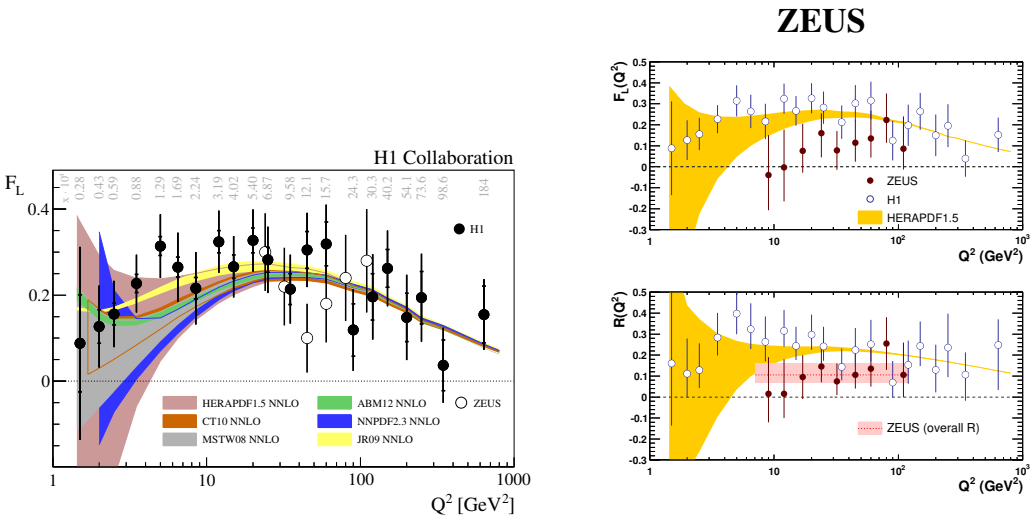

Figure 1: Left: new H1 F_L measurement (solid points) in comparison with previous ZEUS measurement (open points) [4] and a few selected NNLO predictions [5]. Right: new ZEUS F_L (a) and R (b) measurements (solid points) in comparison with H1 measurements (open points) and NNLO HERAPDF 1.5 prediction. The inner error bars represent the statistical uncertainties, the full error bars the total uncertainties. The shaded band labelled "ZEUS (overall R)" represents the 68% probability interval for the overall R.

publication [4]. The reduced cross sections were used together with those from the previous ZEUS data collected at $\sqrt{s} = 300\,\text{GeV}$ to extract F_L as well as F_2 for 27 values of x and Q^2. Relative uncertainties for F_L were in the range of $0.1 - 0.2$. In addition, F_L and the ratio, $R = F_L/(F_2 - F_L)$, have also been extracted as a function of Q^2 together with an overall value of $R = 0.105^{+0.055}_{-0.037}$. The results are shown in Fig. 1(right). The F_L measurements are lower than but compatible with those in the previous ZEUS and H1 publications and in reasonable agreement with the theoretical prediction.

3 High x measurement from ZEUS

Motivated by the large uncertainty of parton distribution functions (PDFs) at high x, NC $e^{\pm}p$ cross sections have been measured up to values of $x \simeq 1$ in a dedicated ZEUS analysis using an integrated luminosity of $187\,\text{pb}^{-1}$ of e^-p and $142\,\text{pb}^{-1}$ of e^+p collisions at $\sqrt{s} = 318\,\text{GeV}$ [7]. Differential cross sections in x and Q^2 are presented for $Q^2 \geq 725\,\text{GeV}^2$ (see Fig. 2 for the ratio of the e^-p measurements over the SM expectations based on a variety of recent PDFs). An improved reconstruction method and greatly increased amount of data allow a finer binning in the high-x region of the NC cross section and lead to a measurement with much improved precision compared to a similar earlier analysis. The agreement between the measurement and the predictions is non-trivial as the latter are mostly modeled with a $(1-x)^{\beta}$ parameterization.

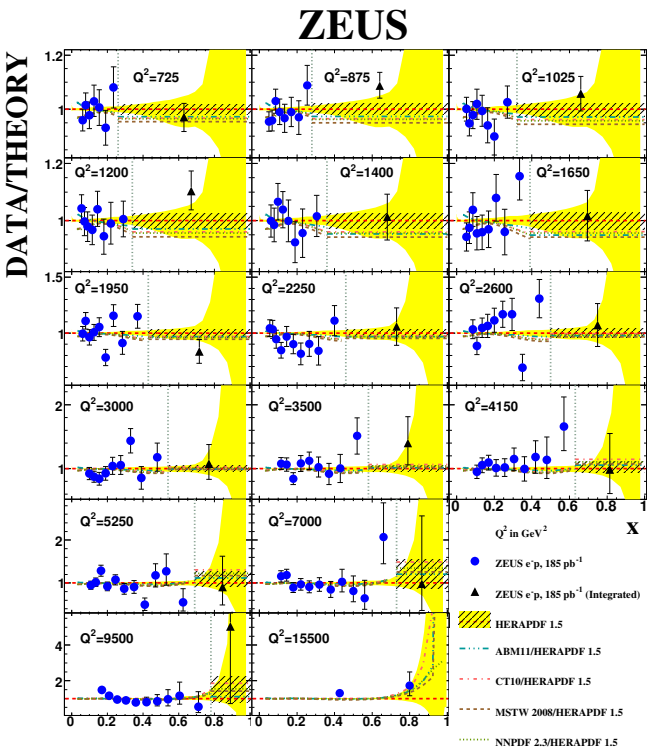

Figure 2: Ratio of the measured NC e^-p cross section over the SM expectation using the HERAPDF1.5 PDFs. The expectation for the integrated high x bin is shown as hatched box.

4 Preliminary combination results of full HERA data

A preliminary combination is performed of all inclusive deep-inelastic cross sections measured by the H1 and ZEUS collaborations in NC and CC $e^{\pm}p$ scattering [8]. The data correspond to an integrated luminosity of about $1\,\mathrm{fb}^{-1}$ and span six orders of magnitude in both Q^2 and x. They include data taken at proton beam energies of 920, 820, 575 and 460 GeV. The combination method used takes the correlations of systematic uncertainties into account, resulting in much improved accuracy. This is illustrated in Fig. 3 showing part of the combined dataset. The combined data are the inputs for the forthcoming HERAPDF 2.0 and will also have an important impact on other global PDF sets.

5 Summary

Recent results on deep-inelastic scattering at HERA have been presented. The H1 and ZEUS experiments each have determined new measurements of the proton longitudinal structure function F_L, making use of the HERA data recorded at reduced centre-of-mass energies. The results are in agreement with each other and with predictions derived from QCD fits. The region of high x is explored in a dedicated measurement by the ZEUS collaboration. All HERA inclusive

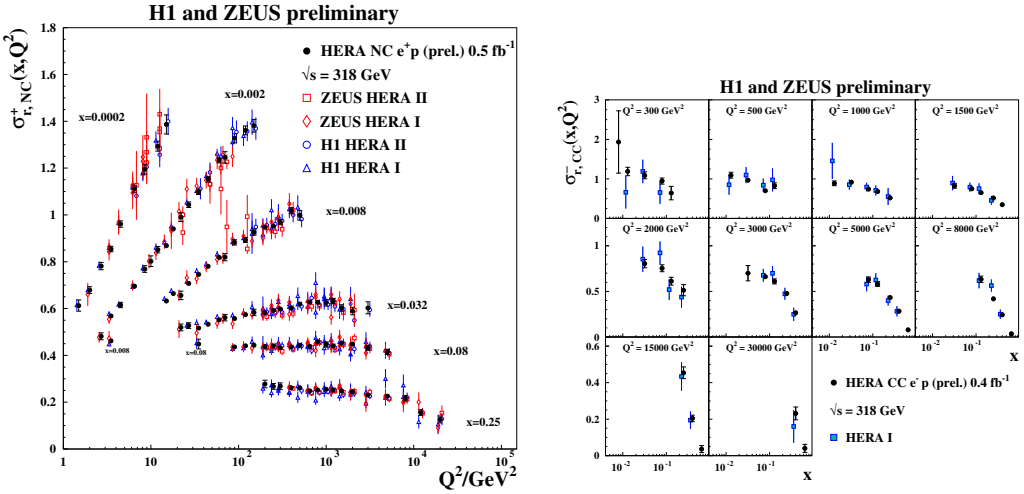

Figure 3: Left: Combined NC e^+p reduced cross section as a function of Q^2 for six selected x-bins compared to the separated H1 and ZEUS data which were input to the combination procedure. Right: Combined CC e^-p reduced cross section as a function of x for 10 Q^2 bins in comparison with the results from HERA I alone. The error bars represent the total uncertainties.

data published up to now by H1 and ZEUS are combined, taking into account the experimental correlations between measurements. The combined dataset includes measurements of neutral current and charged current cross sections recorded at different centre-of-mass energies, spanning up to six orders of magnitude both in momentum transfer Q^2 and in Bjorken x. The dataset is superior in precision compared to the previous HERA data combination which included a smaller fraction of the total integrated luminosity collected at HERA. Point-to-point uncorrelated uncertainties better than 1% are observed in certain kinematic regions.

References

[1] V. Andreev *et al.* [H1 Collaboration], Eur. Phys. J. C **74** (2014) 2814 [arXiv:1312.4821 [hep-ex]].

[2] F. D. Aaron *et al.* [H1 Collaboration], Phys. Lett. B **665** (2008) 139 [arXiv:0805.2809 [hep-ex]].

[3] F. D. Aaron *et al.* [H1 Collaboration], Eur. Phys. J. C **71** (2011) 1579 [arXiv:1012.4355 [hep-ex]].

[4] S. Chekanov *et al.* [ZEUS Collaboration], Phys. Lett. B **682** (2009) 8 [arXiv:0904.1092 [hep-ex]].

[5] HERAPDF 1.5 [H1 and ZEUS Collaborations], `http://www-h1.desy.de/publications/H1preliminary.short_list.html`; H. L. Lai *et al.*, Phys. Rev. D **82** (2010) 074024 [arXiv:1007.2241 [hep-ph]]; A. D. Martin, W. J. Stirling, R. S. Thorne and G. Watt, Eur. Phys. J. C **63** (2009) 189 [arXiv:0901.0002 [hep-ph]]; S. Alekhin, J. Bluemlein and S. Moch, Phys. Rev. D **89** (2014) 5, 054028 [arXiv:1310.3059 [hep-ph]]; R. D. Ball *et al.*, Nucl. Phys. B **867** (2013) 244 [arXiv:1207.1303 [hep-ph]]; P. Jimenez-Delgado and E. Reya, Phys. Rev. D **79** (2009) 074023 [arXiv:0810.4274 [hep-ph]].

[6] H. Abramowicz *et al.* [ZEUS Collaboration], arXiv:1404.6376 [hep-ex].

[7] H. Abramowicz *et al.* [ZEUS Collaboration], Phys. Rev. D **89** (2014) 072007 [arXiv:1312.4438 [hep-ex]].

[8] H1 and ZEUS Collaborations, *Combined measurement of inclusive $e^{\pm}p$ scattering cross sections at HERA*, H1prelim-14-041, ZEUS-prel-14-005.

Vector Boson + Jets Production at CMS

Yun-Ju Lu[1] on behalf of CMS Collaboration

[1]National Central University, No. 300, Jhongda Rd., Jhongli City, Taoyuan County 32001, Taiwan

DOI: http://dx.doi.org/10.3204/DESY-PROC-2014-04/182

Recent measurements of the production cross section of a vector boson in association with jets and a vector boson in association with heavy flavour quarks in proton-proton collision are presented. The collisions were recorded at $\sqrt{s} = 7$ and 8 TeV with the CMS detector at the LHC, for an integrated luminosity of 5.2 and 19.7 fb^{-1} respectively.

1 Introduction

Measurements of the production cross section of a vector boson in association with jets (V+jets, $V = W, Z, \gamma$) and a vector boson in association with heavy flavour quarks (V+HF) are fundamental tests of perturbative quantum chromodynamics (pQCD). These V+jets and V+HF productions also constitute important backgrounds to searches for rare standard model processes and to searches for particles predicted by new physics. With the LHC proton-proton collision data taken in 2011 and 2012, the CMS collaboration [1] measured the V+jets cross section to higher energies and jet multiplicities compared to previous results from CMS. The rapidity distributions in V+jet events and ratios of the cross sections of Z/γ^* plus jets and photon plus jets events are also measured to provide additional sensitivities to parton distribution functions (PDFs) and higher order effects.

Besides testing pQCD, measurements of W and Z production with b hadrons (Z+b and W+b) are particular important for searches of new particles. For Z+b process, both cross section and angular distribution are measured. For W+b process, previous measurements concentrating on W-boson production with at least one observed b-quark jet have shown various levels of agreement with theoretical calculation. The CMS measurement provides a complementary approach focusing on the observation of W-boson production with two well-separated b-quark jets. The study of associated production of a W boson and a charm (c) quark (W+c) production provides direct access to the strange-quark content of the proton. More precise knowledge of the PDFs is essential for many present and future precision analyses.

2 Vector boson + jets

The production cross sections of a photon and one or more jets in the final state with various angular configurations are sensitive to contributions from the QCD hard-scattering subprocesses and to PDFs of the proton. The main background for these processes comes from the decay of neutral hadrons into nearly collinear pairs of photons. These background is estimated using a data-driven method which exploits the distribution of energy in the vicinity of the photon. The

measurement is performed in four regions of pseudorapidity for the photon and two regions of pseudorapidity for the leading-transverse-momentum jet [2]. This kinematic region corresponds to x and Q^2 region of $0.002 \lesssim x \lesssim 0.4$ and $1600 \leq Q^2 \leq 9 \times 10^4$ GeV^2. Results are compared to theoretical predictions from the SHERPA [3] leading-order QCD event generator and the next-to-leading-order(NLO) perturbative QCD calculation from JETPHOX [4]. The predictions are found to be consistent with the data over most of the examined kinematic region.

Compared to γ+jets process, Z/γ^*+jets process has a much cleaner signature. Z/γ^*+jets cross sections with jet multiplicity up to six and seven for $\sqrt{s} = 7$ and 8 TeV respectively are measured [5],[6]. The differential cross section as a function of the transverse momentum of the leading jet is shown in Figure 1. The differential cross section as a function of jet multiplicity and H_T, the scalar sum of jet transverse momenta is also measured. The experimental results and their NLO theoretical predictions are generally consistent within uncertainties.

The measurements of the production cross section of W+jets events have a larger data-sample size however also higher systematic uncertainties compared to measurements of Z+jets events. The higher systematic uncertainties are mainly from a lager background contamination from $t\bar{t}$ decay. The data sample of proton-proton collisions at $\sqrt{s} = 7$ TeV was collected and corresponds to an integrated luminosity of 5.0 fb^{-1}. The measured cross sections [7] are compared to predictions from MADGRAPH [8] + PYTHIA [9] and SHERPA, and to NLO calculations from BLACKHAT+SHERPA [10]. The differential cross section as a function of the transverse momentum of the leading jet is displayed in Figure 1. The differential cross section are found to be in agreement with the predictions for most kinematic region.

The angular distributions of Z/γ^*+jet events and γ+jet events are measured with $\sqrt{s} = 7$ TeV data [11]. The rapidity of a particle is defined as $y = (1/2)\ln[(E + p_z)/(E - p_z)]$, where E is the energy and p_z is the momentum component along the direction of the counterclockwise circulating proton beam. The invariant rapidity difference can be written in terms of the measured quantities y_V and $y_{\rm jet}$ as $y_{\rm dif} = |y_V - y_{\rm jet}|/2$. The quantity $y_{\rm sum} = |y_V + y_{\rm jet}|/2$ is the boost from the laboratory frame to the center-of-mass frame of the V and jet. The distribution in $y_{\rm sum}$ depends mainly on the PDFs , while the distribution in $y_{\rm dif}$ reflects the leading order partonic differential cross section. The distribution for the sum of the V and jet rapidity is shown in Figure 1. It is best described by hybrid calculations that employ NLO PDF.

The measurement of the cross section ratio of Z/γ^*+jets and γ+jets provides an important information about possible contributions of large logs in higher-order effects. This measurement used data collected at $\sqrt{s} = 7$ TeV [12]. The results are compared to leading order prediction from MADGRAPH. The prediction agrees with data in shape, but overestimates the ratio.

3 Vector boson + heavy quarks

The measurement of the cross sections for the production of a Z boson in association with at least two b-jets is displayed in Figure 2 [13]. The measurement is of particular importance for search of higgs production associated with a Z boson. The result is compared to MADGRAPH in the five-flavour scheme, where b quarks are assumed massless, and the four-flavour scheme, where massive b quarks are used, as well as with the NLO predictions from amc@nlo [14]. With the tracker only b-tag, angular separation of the b hadrons and the Z boson is measured in [15]. The azimuthal separation($\Delta\phi$) between the b hadrons compared to theory is shown in Figure 2. Some differences are found between predictions and data in collinear region.

The production cross section for a W boson and two b-jets is measured at $\sqrt{s} = 7$ TeV [16].

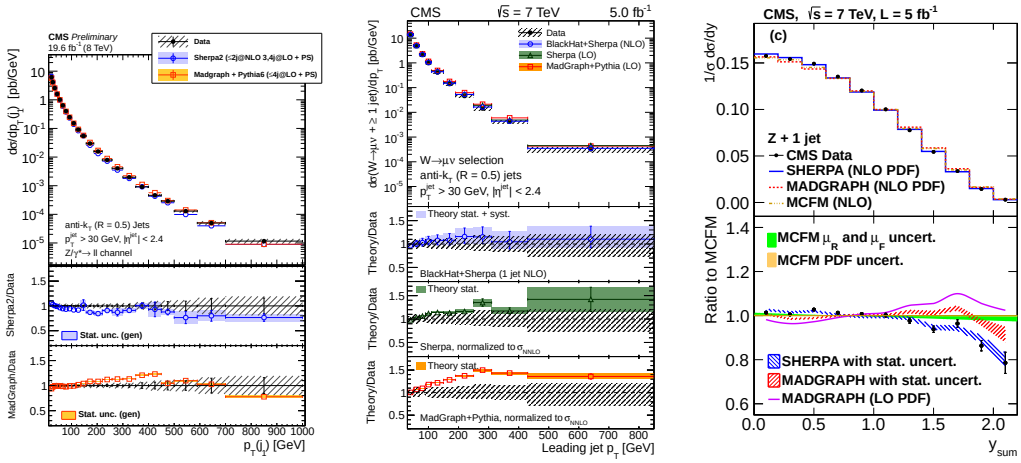

Figure 1: Differential cross sections of Z+jets at $\sqrt{s} = 8$ TeV(left) and W+jets at $\sqrt{s} = 7$ TeV(center) as a function of the transverse momentum of the leading jet. The distribution of y_{sum} in Z+jet channel(right).

Previous studies from hadron colliders are concentrated on W-boson production with at least one observed b-quark jet. Different level of agreements with theory is found in these analyses. The study of W boson and exactly two b-jets hence complements previous measurements. The measured fiducial cross section is in agreement with NLO prediction from MCFM at parton level.

The study of associated production of a W boson and a charm quark at hadron colliders provides direct access to the strange-quark content of the proton. The good measurement of charmquark jet charge is utilized in this measurement to disentangle the W+c signal component from most of the background processes [17]. The measured total cross section is compared with next-to-leading order calculation from MCFM [18] using four PDF sets, which is shown in Figure 2. Measurement of the cross section ratio of $\sigma(W^+ + \bar{c})/\sigma(W^- + c)$ is a test of $s - \bar{s}$ asymmetry hypothesis. The measured cross section ratios are around 95%. This result does not favour such hypothesis although the measurement is still dominated by experimental uncertainties.

4 Conclusion

Recent CMS results of V+jets and V+HF productions have been presented. Besides the measurements from different final states, new results also extend the kinematic coverage of previous measurements and probe additional observables. Overall, NLO predictions agree with the data rather well for most of the V+jets processes. Some disagreements exist for the variables sensitive to higher order term such as H_T. Some differences remain between theory and measurements in the production of V+HF such as angular distribution of the Z+b-jets process and differential cross section of W+chram process. These results provide input to MC tools and background estimation of different standard model measurements and beyond standard model searches.

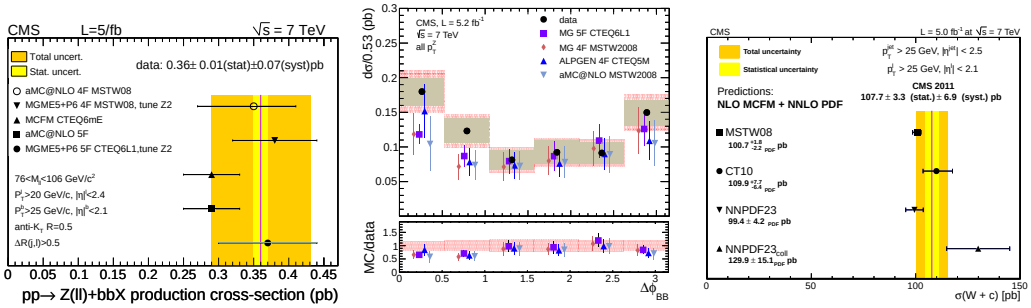

Figure 2: Cross sections for the production of a Z boson with at least two b-jets(left). Differential cross sections as a function of ϕ difference between two b quarks(center). Total cross section of W+c production compared with NLO MCFM using four different PDF sets(right).

References

[1] S. Chatrchyan et al. The CMS experiment at the CERN LHC. *JINST*, 3:S08004, 2008.

[2] Serguei Chatrchyan et al. Measurement of the triple-differential cross section for photon+jets production in proton-proton collisions at $\sqrt{s}$=7 TeV. *JHEP*, 1406:009, 2014.

[3] T. Gleisberg, Stefan. Hoeche, F. Krauss, M. Schonherr, S. Schumann, et al. Event generation with SHERPA 1.1. *JHEP*, 0902:007, 2009.

[4] S. Catani, M. Fontannaz, J.P. Guillet, and E. Pilon. Cross-section of isolated prompt photons in hadron hadron collisions. *JHEP*, 0205:028, 2002.

[5] Vardan Khachatryan et al. Measurements of jet multiplicity and differential production cross sections of Z+jets events in proton-proton collisions at sqrt(s)=7 TeV. 2014.

[6] CMS Collaboration. Measurement of the differential production cross section of Z bosons in association with jets in pp collisions at sqrt(s) = 8 TeV. 2014.

[7] Vardan Khachatryan et al. Differential cross section measurements for the production of a W boson in association with jets in proton-proton collisions at sqrt(s) = 7 TeV. 2014.

[8] Johan Alwall, Michel Herquet, Fabio Maltoni, Olivier Mattelaer, and Tim Stelzer. MadGraph 5 : Going Beyond. *JHEP*, 1106:128, 2011.

[9] Torbjorn Sjostrand, Stephen Mrenna, and Peter Z. Skands. PYTHIA 6.4 Physics and Manual. *JHEP*, 0605:026, 2006.

[10] Z. Bern, L.J. Dixon, F. Febres Cordero, S. Hche, H. Ita, et al. Ntuples for NLO Events at Hadron Colliders. *Comput.Phys.Commun.*, 185:1443–1460, 2014.

[11] Serguei Chatrchyan et al. Rapidity distributions in exclusive Z + jet and γ + jet events in pp collisions at $\sqrt{s}$=7 TeV. *Phys.Rev.*, D88:112009, 2013.

[12] CMS Collaboration. Measurement of the Z/gamma*+jets/photon+jets cross section ratio in pp collisions at sqrt(s)=8 TeV. 2014.

[13] Serguei Chatrchyan et al. Measurement of the production cross sections for a Z boson and one or more b jets in pp collisions at sqrt(s) = 7 TeV. *JHEP*, 1406:120, 2014.

[14] Rikkert Frederix, Stefano Frixione, Valentin Hirschi, Fabio Maltoni, Roberto Pittau, et al. W and $Z/\gamma*$ boson production in association with a bottom-antibottom pair. *JHEP*, 1109:061, 2011.

[15] Serguei Chatrchyan et al. Measurement of the cross section and angular correlations for associated production of a Z boson with b hadrons in pp collisions at $\sqrt{s}$ = 7 TeV. *JHEP*, 1312:039, 2013.

[16] Serguei Chatrchyan et al. Measurement of the production cross section for a W boson and two b jets in pp collisions at sqrt(s) = 7 TeV. *Phys.Lett.*, B735:204, 2014.

[17] Serguei Chatrchyan et al. Measurement of associated W + charm production in pp collisions at $\sqrt{s}$ = 7 TeV. *JHEP*, 1402:013, 2014.

[18] John M. Campbell and R.K. Ellis. MCFM for the Tevatron and the LHC. *Nucl.Phys.Proc.Suppl.*, 205-206:10–15, 2010.

Properties Measurement of New (Higgs) Boson

Shivali Malhotra on behalf of the CMS Collaboration

Department of Physics & Astrophysics, University of Delhi, Delhi - 07, India

DOI: http://dx.doi.org/10.3204/DESY-PROC-2014-04/186

The precise determination of the mass, couplings and other properties of the particle discovered in 2012 around 125 GeV is important to establish precisely if it is a Standard Model Higgs boson. CMS experiment has collected lot more data since the discovery of this particle in July 2012 and has performed many of its properties measurements. In this talk, I will present some of these measurements. These measurements are based on data samples corresponding to integrated luminosities of up to 5.1 fb^{-1} at 7 TeV and up to 19.7 fb^{-1} at 8 TeV in proton-proton collisions at the LHC. The combined result for the measured mass, the best-fit signal for all the channels and different fits for couplings, using all the studied Higgs boson decay modes, will be described.

1 Introduction

The Standard Model (SM) is the most successful theory which describes many of the experimental results and predicts all the properties of the interactions of the known elementary particles. The Higgs boson is one of the predicted corner stones in the SM theory and is responsible for giving mass to all the fundamental particles. The Higgs boson has been searched for few decades with different experiments like Large Electron Positron Collider, Tevatron, but success came with Large Hadron Collider (LHC). The spectacular observation of a scalar particle with a mass ∼125 GeV by both CMS [1] and ATLAS [2] Collaborations, opens a crucial chapter of properties measurement. The measurement of the properties of the 125 GeV boson is important not only to confirm whether this is the SM Higgs boson but also to look for hints of beyond SM physics. The combination of the different decay modes of this boson i.e. WW, ZZ, $\gamma\gamma$, $\tau\tau$ and $b\bar{b}$, as well as measurements of the $t\bar{t}H$ production mode [3, 4, 5], are exploited to measure its properties. To reconstruct the mass of the Higgs boson, high resolution channels i.e. H$\rightarrow ZZ \rightarrow 4l$ (with $l = e, \mu$) and H $\rightarrow \gamma\gamma$, are considered. The statistical methodology used for the combination of all the Higgs analysis was developed by the ATLAS and CMS Collaborations in the context of the LHC Higgs Combination Group [6]. Systematic uncertainties and their correlations are modelled by the introduction of nuisance parameters with their expected distributions.

2 Mass Measurement

The accurate measurement of the mass of the boson is done using the invariant mass distribution of two decay modes namely, H $\rightarrow \gamma\gamma$ and H $\rightarrow ZZ \rightarrow 4l$ that are the two high resolution channels. A fit to the data is performed separately profiling independent signal strengths in three final states i.e. H $\rightarrow ZZ \rightarrow 4l$, H $\rightarrow \gamma\gamma$ without Vector Boson Fusion (VBF) tag

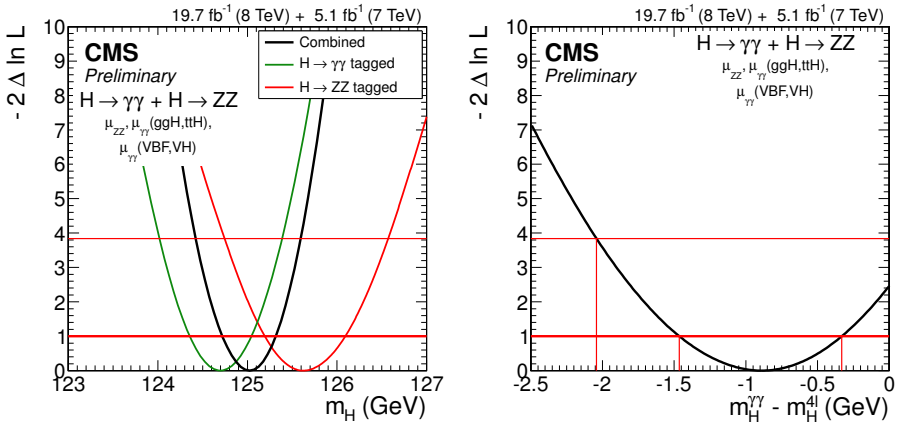

Figure 1: (Left) 1D test statistics $q(m_H)$ scan vs hypothesized Higgs boson mass m_H for the $\gamma\gamma$ (green) and $4l$ (red) final states separately and for their combination (black). (Right) Scan of the test statistic $q(m_H^{\gamma\gamma} - m_H^{4l})$ versus the difference between two individual mass measurements.

and H $\rightarrow$ $\gamma\gamma$ with VBF tag. The three signal strength are left free to reduce the model dependency of the mass determinations. Figure 1 (left) shows the likelihood scan as function of the mass of the H $\rightarrow$ ZZ and H $\rightarrow$ $\gamma\gamma$ channels and of their combination. The horizontal lines at 1.0 and 3.84 depicts the 68% and 95 % CL intervals. The mass is measured to be $m_H = 125.03^{+0.26}_{-0.27}(stat.)^{+0.13}_{-0.15}(syst.)$ GeV from the combination of the two high resolution channels.

Decay Channel	Expected (σ)	Observed(σ)
H $\rightarrow$ WW [7]	5.4	4.3
H $\rightarrow$ ZZ [8]	6.3	6.5
H $\rightarrow$ $\gamma\gamma$ [9]	5.3	5.6
H $\rightarrow$ $\tau\tau$ [10]	3.9	3.9
H $\rightarrow$ bb [11]	2.3	2.1

Table 1: Expected and observed significances of the excess for $m_H = 125.0$ GeV of the combinations of channels.

To quantify the compatibility of the two individual measurements, a scan of the test statistics $q(m_H^{\gamma\gamma} - m_H^{4l})$ versus the difference between two individual mass measurements from $\gamma\gamma$ and $4l$ final states is performed, Fig. 1 (right). The result comes out to be $m_H^{\gamma\gamma}$ - m_H^{4l} = $-0.87^{+0.54}_{-0.57}$ GeV and the two measurements agree at the 1.6σ level. Table 1, summarizes the expected and observed significance for individual channel for a SM Higgs boson mass of 125.0 GeV. We have used the combination of these five dominant decay channels for different compatibility tests of the Higgs boson.

3 Signal Strength

After the precise measurement of mass of the Higgs boson, the best fit value of the signal strength modifier, $\mu = \sigma/\sigma_{\rm SM}$ is calculated which quantifies the compatibility of an excess with the expectations from a SM Higgs boson. Evaluation of the signal strength by combining channels with respect to decay mode, Fig. 2 (left), or by combining with different production

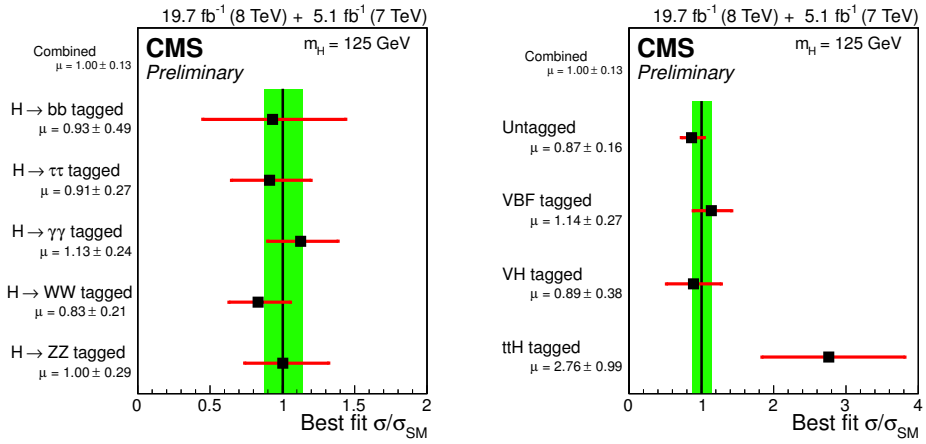

Figure 2: Values of the best-fit $\sigma/\sigma_{\rm SM}$ for sub-combinations by (left) predominant decay channels and (right) individual production modes. The vertical band shows the overall $\sigma/\sigma_{\rm SM}$ uncertainty while the horizontal bars indicate the ± 1 standard deviation uncertainties in the best-fit $\sigma/\sigma_{\rm SM}$ values for the individual modes; they include both statistical and systematic uncertainties.

tags, Fig. 2 (right), has been done. A slight excess in the $t\bar{t}$H-tagged sub-combination is due to the excesses in the $t\bar{t}$H-tagged H$\to\gamma\gamma$ and H$\to$leptons analyses. The combined best-fit signal strength for $m_H = 125$ GeV is found to be $1.00 \pm 0.09(stat.)\,^{+0.08}_{-0.07}\,(theo.) \pm 0.07(syst.)$.

4 Couplings to Fermions and Bosons

We map the vectorial and fermionic couplings into two scale factors, $\kappa_{\rm V}$ and $\kappa_{\rm f}$, respectively. Figure 3 (left) shows the likelihood scan as a function of $\kappa_{\rm V}$, $\kappa_{\rm f}$ with the cross indicating the best-fit values (1.01, 0.89) with respective uncertainties. The fit is compatible with the SM at the one sigma level with $\kappa_{\rm f}$ value being smaller than unity due to an excess in the VBF H $\to \gamma\gamma$ channel and deficit in the fermionic channels. The same $(\kappa_{\rm V}, \kappa_{\rm f})$ analysis is also performed separately for each Higgs boson decay mode to better visualize the contribution of individual channels, Fig. 3 (right).

5 Other Compatibility Tests

To test the custodial symmetry, we introduce two scaling factors $\kappa_{\rm W}$ and $\kappa_{\rm Z}$ that modify the SM Higgs boson couplings to the W and Z bosons and perform combination in two channels i.e. untagged pp$\to$H$\to$WW and pp$\to$H$\to$ZZ, to assess the consistency of the ratio $\lambda_{\rm WZ} = \kappa_{\rm W}/\kappa_{\rm Z}$ with unity. The result is $\lambda_{\rm WZ} = 0.94^{+0.22}_{-0.18}$ while assuming SM couplings to fermions, $\kappa_{\rm f} = 1$; which implies that the data are consistent with the SM expectation.

The asymmetry of couplings to fermions is checked by performing two combinations in which we allow for different ratios of the couplings to down/up fermions ($\lambda_{\rm du} = \kappa_{\rm d}/\kappa_{\rm u}$) or different

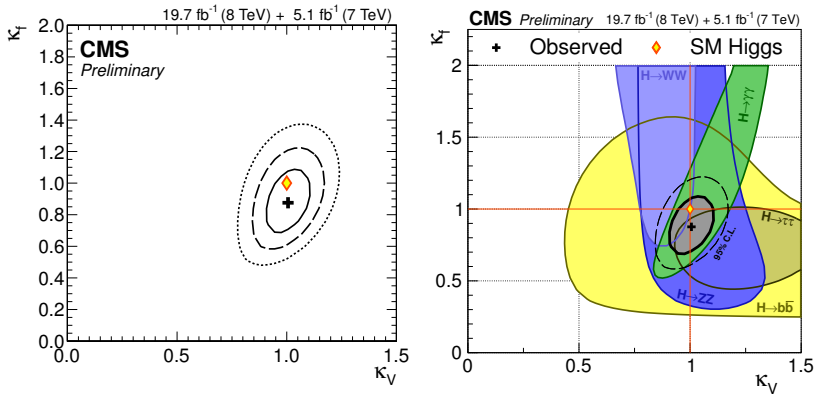

Figure 3: 2D test statistics $q(\kappa_{\rm V},\, \kappa_{\rm F})$ likelihood scan constrained to the (+,+) quadrant. The yellow diamond shows the SM point $(\kappa_{\rm V}, \kappa_{\rm f}) = (1,\, 1)$. (Left) The cross indicates the global best-fit values with the solid, dashed, and dotted contours showing the 68%, 95%, and 99.7% CL regions, respectively. (Right) The 68% CL contours for individual channels (colored swaths) and for the overall combination (thick curve) for the $(\kappa_{\rm V}, \kappa_{\rm f})$ parameters.

ratios of the couplings to leptons and quarks ($\lambda_{\rm lq} = \kappa_{\rm l}/\kappa_{\rm q}$) assuming $\Gamma_{BSM} = 0$. Both $\lambda_{\rm du}$ and $\lambda_{\rm lq}$ are found to be constrained within [0.66, 1.43] and [0.61, 1.49] respectively, at 95% CL.

We also explore a generic five-parameter model by making some assumptions with the scale factor for different couplings. The couplings to W and Z bosons are scaled by $\kappa_{\rm W}$ and $\kappa_{\rm Z}$, respectively; $\kappa_{\rm t}$ denotes the scale factor for couplings of up-type quarks; $\kappa_{\rm b}$ denotes the scale factor for couplings of down-type quarks; and κ_τ denotes the scale factor for all the charged leptons. The result of a model with five independent coupling scaling factors, assuming SM structure for loops is shown in Fig. 4.

Many other compatibility tests were also performed for checking beyond the SM physics scenarios [12].

6 Results

The excellent performance of the LHC machine and the CMS detector during Run I made the experiment able to collect data corresponding to an integrated luminosity of about 5 fb^{-1} at a collision energy of 7 TeV in 2011 and about 20 fb^{-1} at 8 TeV in 2012 and led to the discovery of a scalar particle. It was then required to understand its various properties and to check whether they are consistent with the Higgs boson predicted by SM. It was possible to measure the mass of the Higgs boson that resulted $m_H = 125.03^{+0.26}_{-0.27}(stat.)^{+0.13}_{-0.15}(syst.)$ GeV using the CMS detector, at this value the Higgs boson is allowed to decay in many different modes. For the mass measured at 125 GeV, the event yields obtained in the different analyses for specific decay modes and production mechanisms are consistent with those expected for the SM Higgs boson. The combined best-fit signal strength was also found compatible with the SM expectation. Searches for deviations of the couplings of the Higgs boson along with some other

compatibility tests were performed and no significant deviations were found. Run II of LHC may shed some more light with precision measurement of the above mentioned quantities while having more statistics in hand at higher energy and higher integrated luminosity.

References

[1] The CMS collaboration, arXiv:1207:7235 [hep-ex].

[2] The ATLAS collaboration, arXiv:1207:7214 [hep-ex].

[3] CMS Collaboration, "Search for the standard model Higgs boson produced in association with a top-quark pair in pp collisions at the LHC, JHEP **05** (2013) 145, doi:10.1007/JHEP05(2013)145, arXiv:1303.0763.

[4] CMS Collaboration, "Search for Higgs Boson Production in Association with a Top-Quark Pair and Decaying to Bottom Quarks or Tau Leptons, Technical Report CMS-PAS-HIG-13-019, CERN, Geneva, 2013.

[5] CMS Collaboration, "Search for the standard model Higgs boson produced in association with top quarks in multilepton final states, Technical Report CMS-PAS-HIG-13-020, CERN, Geneva, 2013.

[6] LHC Higgs Cross Section Working Group, "Handbook of LHC Higgs Cross Sections: 3. Higgs Properties", (2013). arXiv:1307.1347.

[7] CMS Collaboration, "Measurement of Higgs boson production and properties in the WW decay channel with leptonic final states", JHEP **01** (2014) 096, doi:10.1007/JHEP01(2014)096, arXiv:1312.1129.

[8] CMS Collaboration, "Measurement of the properties of a Higgs boson in the four-lepton final state", Phys. Rev. D **89** (2014) 092007, doi:10.1103/PhysRevD.89.092007, arXiv:1312.5353.

[9] CMS Collaboration, "Observation of the diphoton decay of the 125 GeV Higgs boson and measurement of its properties", CMS-HIG-13-001, CERN-PH-EP-2014-117, 2014. Submitted for publication in Eur. Phys. J. C.

[10] CMS Collaboration, "Evidence for the 125 GeV Higgs boson decaying to a pair of t leptons", JHEP **05** (2014) 104, doi:10.1007/JHEP05(2014)104, arXiv:1401.5041.

[11] CMS Collaboration, "Search for the standard model Higgs boson produced in association with a W or a Z boson and decaying to bottom quarks", Phys. Rev. D **89** (2014) 012003, doi:10.1103/PhysRevD.89.012003, arXiv:1310.3687.

[12] CMS Collaboration, "Precise determination of the mass of the Higgs boson and studies of the compatibility of its couplings with the standard model", CMS PAS HIG-14-009.

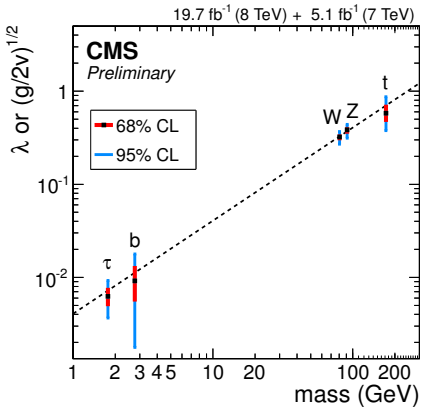

Figure 4: Summary of the fits for deviations in the coupling for the generic five-parameter model assuming SM structure for loops, expressed as function of the particle mass. The dashed line is taken from the fit to data with the model (M, ε)

Measurements of WV Boson Production and Limits on Charged aTGCs at CMS

Ilya Osipenkov on behalf of the CMS Collaboration

Department of Physics and Astronomy
Texas A&M University, College Station, TX, USA

DOI: http://dx.doi.org/10.3204/DESY-PROC-2014-04/184

We present a summary of the latest measurements of the WV production cross-sections, where V is either W or Z. The data sample(s) correspond to proton-proton collision events collected with the CMS detector at $\sqrt{s} = 7$ and 8 TeV. Subsequent searches for Anomalous Triple Gauge Couplings, which allow us to probe the non-Abelian structure in the Electroweak Sector, are described. We present exclusion limits on the corresponding couplings.

1 Introduction

Triple gauge boson couplings, which determine the self-interactions of W and Z bosons, are fixed by the gauge symmetry of the standard model (SM). Consequently, pair production of vector gauge bosons allows a direct test of the electroweak sector of the SM [1]. Observation of anomalous triple gauge boson couplings (aTGCs) would correspond to the presence of physics beyond the SM.

In this paper we summarize the measurements in the diboson final states $WZ \to \ell\nu\ell\ell$ [2], $WW \to \ell\nu\ell\nu$ [3] and $WV \to \ell\nu jj$ [4] in pp collisions in the Compact Muon Solenoid (CMS) detector at the Large Hadron Collider (LHC) [5]. Understanding of these processes is essential, as they serve as backgrounds for new physics searches and other measurements (*e.g.* Higgs production). Furthermore, for each channel we verify the Standard Model (SM) predictions by comparing the measured cross-section to the theory expectation. An additional enhancement of the spectrum in the high transverse momentum (p_T) region would correspond to nonzero aTGC values.

2 $WZ \to \ell\nu\ell\ell$

We present measurements of the $WZ \to \ell\nu\ell\ell$ production corresponding to the luminosities of 4.9 fb^{-1} collected at $\sqrt{s} = 7$ TeV and 19.6 fb^{-1} collected at $\sqrt{s} = 8$ TeV. In order to select the Z candidate the presence of two leptons of the same flavor (muons or electrons) and opposite charge with the transverse momentum $p_T > 20, 10$ GeV and mass near the Z resonance ($71 < m_{ll} < 111$ GeV) is required. In case of multiple pairs of candidates the one with the mass closest to the Z is selected. Likewise, in order to reconstruct the W, a lepton with $p_T > 20$ GeV, $MET > 30$ GeV are required. The remaining backgrounds can be separated into the non-peaking (*e.g.* $t\bar{t}$) and prompt lepton (real Z plus a lepton-like object) types, which are

taken from the Monte Carlo; as well as the real Z plus a jet faking a lepton, which is estimated from the sideband region in the data. Overall, we predict at total of 211 background out of the 1480 ($\sqrt{s} = 8$ TeV) events in the data after all of the cuts have been applied.

Upon subtracting the backgrounds a high purity signal is extracted. After accounting for the systematics, with the largest sources originating from the MET resolution as well as the data driven background estimates, cross section for each lepton combination is evaluated Fig. 1. The combined values are $20.8 \pm 1.3(stat.) \pm 1.1(syst.) \pm 0.5(lumi.)$, $24.6 \pm 0.8(stat.) \pm 1.1(syst.) \pm 1.1(lumi.)$ pb at $\sqrt{s} = 7$,8 TeV, while the $\sigma_{W^+Z}/\sigma_{W^-Z} = 1.94 \pm 0.25(stat.) \pm 0.04(syst.)$,$1.81 \pm 0.12(stat.) \pm 0.03(syst.)$. The measurements are consistent with the theory predictions of 17.8, 21.9 pb.

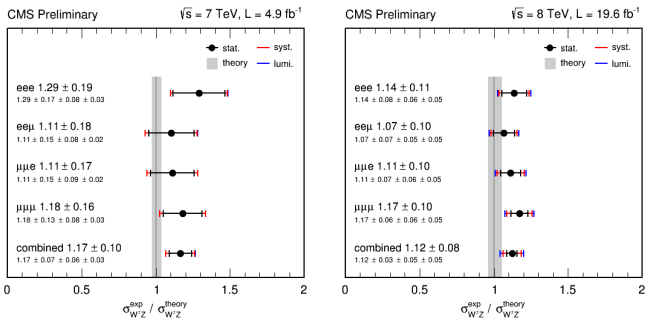

Figure 1: Ratio of measured inclusive cross-section to the theoretical prediction in the $WZ \to \ell\nu\ell\ell$ channel at $\sqrt{s} = 7$ TeV(left) and $\sqrt{s} = 8$ TeV(right).

3 $WW \to \ell\nu\ell\nu$

The $WW \to \ell\nu\ell\nu$ signal measurements correspond to the luminosities of 4.9 fb^{-1} collected at $\sqrt{s} = 7$ TeV and 4.92 fb^{-1} collected at $\sqrt{s} = 8$ TeV. We reconstruct W^+W^- signal by requiring two oppositely charged central leptons ($|\eta| < 2.4$,2.5 for muons, electrons) with $p_T > 20$ GeV. In order to further reduce background contamination the following cuts are implemented: remove events with jet $p_T > 30$ GeV and apply top-quark tagging techniques, require $MET > 45$ GeV (> 20 GeV in the μe channel), remove events with third lepton $p_T > 10$ GeV, reject photon-conversion electrons. The Top, Drell Yan and Diboson yields are determined from the data sideband region with the overall background contribution $\sim 30\%$ of the total event count.

We evaluate the cross section after subtracting the expected background contributions from the data. The main systematics are due to the jet veto uncertainty as well as the error in estimating the background yields. The measured cross sections are $52.4 \pm 2.0(stat.) \pm 4.5(syst.) \pm 1.2(lumi.)$, $69.9 \pm 2.8(stat.) \pm 5.6(syst.) \pm 3.1(lumi.)$ pb at $\sqrt{s} = 7$,8 TeV. Similarly to the WZ case, the results show a small ($\sim 1\sigma$) excess over the SM expectation, but overall are consistent with the theory predictions of 47.0, 57.3 pb.

In addition, we perform a search for the aTGCs based on the leading lepton p_T spectrum. The presence of anomalous signal would enhance the yield at high p_T values with an overall quartic dependence of the cross-section on the aTGCs. The systematic uncertainties are

incorporated into the likelihood function by introducing nuisance parameters with Gaussian constraints. We see no evidence for the anomalous signal and obtain 1-Dimensional limits of $-0.048 < \lambda < 0.048$, $-0.095 < \Delta g_1^Z < 0.095$, $-0.22 < \Delta\kappa_\gamma < 0.22$ at 95% C.L., with 2-D limits shown in Fig. 2.

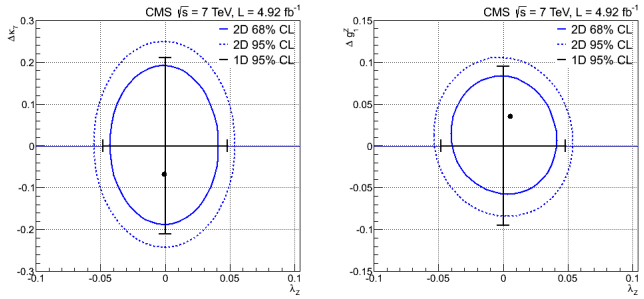

Figure 2: The 68% (solid line) and 95% C.L. (dashed line) aTGC limit contours, as well as the central value (point) for $\Delta g_1^Z = 0$ (left) and $\Delta\kappa_\gamma = 0$ (right). The corresponding 1-D 95% C.L. limits are shown along the axes.

4 $WV \to \ell\nu jj$

The first semileptonic channel measurement is performed for the 5.0 fb^{-1} CMS dataset collected at $\sqrt{s} = 7$ TeV. The analysis is particularly challenging due to the fact that vast majority of events in this final state originate from the $W + Jets$ irreducible background, but has a higher expected event count due to the larger branching fraction of W and Z bosons to quarks. We select events with on-shell W bosons by requiring lepton $p_T > 25$ GeV (35 GeV), $\eta < 2.1$ (2.4), W transverse mass > 30 GeV (50 GeV), $MET > 25$ GeV (30 GeV) and secondary lepton veto in the muon (electron) channel. Exactly two AK5 jets are reconstructed subject to PileUp corrections, isolation from leptons > 0.3, $p_T > 35$ GeV, $\eta < 2.6$ and jet b-tag veto on the secondary vertex. Additional requirements of dijet $p_{Tjj} > 20$ GeV, $|\Delta\eta_{jj}| < 1.5$ are placed in order to reduce the dominant $W + Jets$ background. A reasonable agreement between data and MC is observed.

In order to extract the cross section we perform an unbinned maximum likelihood for the dijet mass $40 < m_{jj} < 150$ GeV. The shape templates are taken from Monte Carlo (and multijet sideband), while the background yield contributions are free to float subject to Gaussian constraints. An empirical combination of default, alternate ME-PS and alternate QCD scale samples is used to describe the $W + Jets$ shape. The biases in the fit procedure and systematics are accounted for. A total of 2682 ± 482 $WW + WZ$ events is extracted out of 1.15×10^5 with a significance is 8.8σ using a simple likelihood ratio and 4.3σ using the profile likelihood ratio. The corresponding $WW + WZ$ cross section is $68.9 \pm 8.7(stat.) \pm 9.7(syst.) \pm 1.5(lumi.)$ pb, consistent with the SM prediction of 65.6 ± 2.2 pb.

Subsequently, limits on the aTGC parameters are set based on the hadronic $V \to jj$ p_T spectrum. We place an additional $75 < m_{jj} < 95$ GeV cut to enhance signal purity, normalize the backgrounds based on fit results and take $\Delta g_1^Z = 0$, since it is expected to be small. The

1-D limits of $-0.038 < \lambda < 0.030$, $-0.111 < \Delta\kappa_\gamma < 0.142$ at 95% C.L. are set, with 2-D limits shown in Fig. 3.

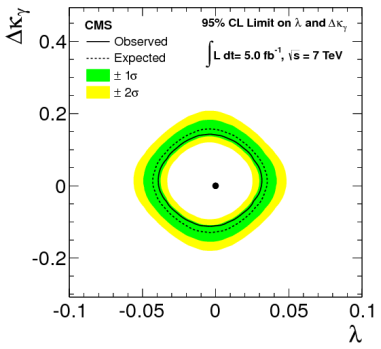

Figure 3: Observed (solid) and expected (dashed) exclusion limits at 95% CL for anomalous triple gauge couplings set based on the semileptonic WV final state $V \to jj$ p_T spectrum. The dark green(inner) and light yellow(outer) bands correspond to the one and two sigma intervals, respectively, in the expected limit distribution. The SM expectation is shown by the solid dot.

5 Summary

We implement the selections and measure the WV diboson productions for $WZ \to \ell\nu\ell\ell$, $WW \to \ell\nu\ell\nu$ and $WW + WZ \to \ell\nu jj$ final states at CMS. Excesses are observed for several channels, but no evidence for physics beyond SM is found. Furthermore, the presence of Anomalous Triple Gauge Couplings is expected to modify the spectrum at high values of p_T. We do not find evidence for such anomalous interactions between the charged vector bosons and set either competitive or the strongest limits to date.

References

[1] K. Hagiwara *et al.*, Low energy effects of new interactions in the electroweak boson sector. Phys. Rev. **D48** 2182 (1993).

[2] CMS Collaboration, Measurement of WZ production rate, CMS Physics Analysis Summary **CMS-PAS-SMP-12-006** (2012).

[3] S. Chatrchyan *et al.*, Measurement of the W^+W^- cross section in pp collisions at $\sqrt{s} = 7$ TeV and limits on anomalous $WW\gamma$ and WWZ couplings, Eur. Phys. J. **C73** 2610 (2013);
S. Chatrchyan *et al.*, Measurement of W^+W^- and ZZ production cross sections in pp collisions at $\sqrt{s} =$ 8 TeV, Phys. Lett. **B721** 190 (2013). (http://arxiv.org/abs/1301.4698).

[4] S. Chatrchyan *et al.*, Measurement of the sum of WW and WZ production with W+dijet events in pp collisions at $\sqrt{s} = 7$ TeV, Eur. Phys. J. **C73** 2283 (2013).

[5] The CMS Collaboration *et al.*, The CMS experiment at the CERN LHC. JINST **3** S08004 (2008).

Search for the Standard Model Higgs boson decaying to b quark with CMS experiment

Silvio Donato[1 2 3 4] on behalf of the CMS Collaboration

[1] Scuola Normale Superiore, Piazza dei Cavalieri, 7 - 56126, Pisa, Italy
[2] INFN Sezione di Pisa, Largo B. Pontecorvo, 3 - 56127 Pisa, Italy
[3] CERN, 1211 Geneve 23, Switzerland
[4] silvio.donato@cern.ch

DOI: http://dx.doi.org/10.3204/DESY-PROC-2014-04/188

A search for the standard model (SM) Higgs boson decaying to bottom quarks pairs is presented. Two production channels have been analyzed: vector-boson fusion and associated production with a vector boson decaying to leptons. The search is performed on data collected with the CMS detector at LHC during 2011 and 2012, at center-of-mass energies of 7 and 8 TeV, corresponding to integrated luminosities of about $5.\,\mathrm{fb}^{-1}$ and $19.0\,\mathrm{fb}^{-1}$, respectively. A 95% confidence level upper limit of 1.79 (0.89) times SM Higgs boson cross section has been observed (expected) at a Higgs boson mass of 125 GeV. An excess of events is observed above the expected background with a local significance of 2.2 standard deviations, which is consistent with the expectation from the production of the SM Higgs boson. The signal strength corresponding to this excess, relative to that of the SM Higgs boson, is 0.97 ± 0.48.

1 Introduction

In 2012, CMS [1] and ATLAS collaborations have observed a Higgs boson in the $\gamma\gamma$, ZZ, WW decay channels and its mass is about $m_H \approx 125\,\mathrm{GeV}$ [2, 3]. More recently, an evidence of the decay of the Higgs boson to a τ pair has been presented [4, 5]. This paper presents the search performed by CMS for the standard model (SM) Higgs boson decaying to bottom quarks, one of the most important decay channels not yet seen [6, 7].

Although the Higgs boson decay to b quark has a high branching ratio, the channel has a low sensitivity due to the large QCD background. Indeed the b-quark QCD production cross section is some 10^8 times larger than the Higgs boson cross section. In order to cope with such a large background, the topologies of two distinctive production modes have been exploited: the vector-boson associated production (VH) and the vector-boson fusion (VBF). These production modes have about one tenth of the cross-section of the gluon-gluon fusion dominant mode, but their topologies are useful to reduce the background.

2 Signal topologies

In the VH production, only the leptonic decays of the vector bosons are considered. Here, the topology is defined by the presence of two b jets from the Higgs boson decay, and at least one isolated charged lepton or large missing transverse energy (MET). These requirements make the QCD background negligible.

The VBF signal, is characterized by the presence of two b jets from the Higgs boson decay and two energetic quark-jets with a large η separation. No gluons participate in the interaction, so a low additional hadronic activity is expected. Nevertheless, in this channel the QCD background remains the main background.

3 Signal and background regions

The main processes that can simulate the VH signal topology are: W/Z + jets and $t\bar{t}$ production. Their shapes are taken from simulation whereas their normalizations are data-driven. The analysis is divided in six sub-channels, according to the vector-boson decay mode: $W \rightarrow e\nu\,, \mu\nu\,, \tau\,(1-\text{prong})\nu$ and $Z \rightarrow ee\,, \mu\mu\,, \nu\nu$. In addition, the channels are binned in two or three vector-boson p_T bins. In each bin a signal region is defined cutting on: jet kinematic variables, b-tagging discriminants, lepton momentum and/or MET, number of additional leptons and jets. Inverting some cuts, up to five control regions are defined for $t\bar{t}$ and W/Z + heavy/light quark jets backgrounds. They are used to evaluate up to seven scale factors to apply to $t\bar{t}$ and W/Z + 0/1/2b-jets background normalizations.

The main background in the VBF analysis is the multi-jet QCD production. This background is estimated directly from data. Minor backgrounds are W/Z + jets and $t\bar{t}$ productions and they are taken from simulation. The signal regions are defined using an Artificial Neural Network (ANN). It is trained to separate the signal from the backgrounds, using simulations. With the exception of the b-jets kinematic it exploits the most discriminants variables: $\Delta\eta$ between the most forward/backward jets, b-tagging discriminants and additional hadronic activity in the event. Five signal regions are defined using the ANN output, as shown in Figure 1. In each region the background and the signal yield are obtained with a fit to the $b\bar{b}$ jet mass distribution. The QCD background is extrapolated from the sidebands using a fifth-degree Bernstein polynomial, while the signal and the minor backgrounds shapes and are taken from simulations.

4 Multi BDT (VH)

In order to reduce the background in VH analysis, three specialized BDT are trained to reject the $t\bar{t}$, W/Z + jets and WW/WZ/ZZ backgrounds. The BDT variables are: Higgs boson candidate mass and p_T, b-tag discriminants, lepton momentum and MET, number of additional leptons and jets, other kinematic variables.

The final multi-BDT score distribution is realized as following. An event rejected by the $t\bar{t}$ BDT gets a score between -1 and -0.5. The other events that fail the W/Z + jets BDT have a score between -0.5 and 0. Again, the other events that fail the WW/WZ/ZZ BDT have a score between 0 and 0.5. A final BDT is applied to reject all backgrounds and it assigns a score between 0.5 and 1. In this way the combined multi-BDT is more powerful than the classic one-step BDT.

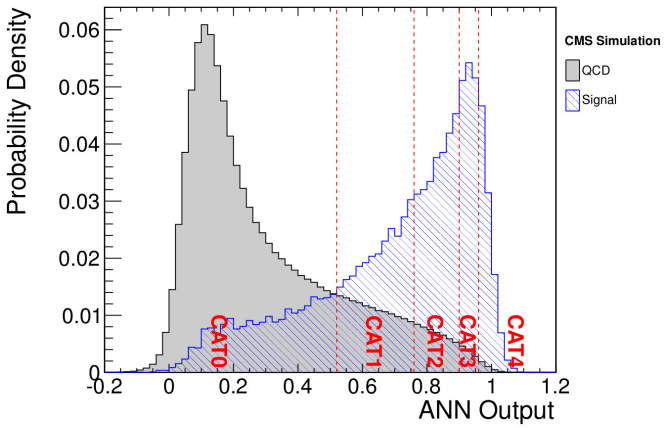

Figure 1: Probability distribution of the ANN output for signal and background, for VBF analysis. The vertical dashed lines define the signal regions used in the analysis.

The last step is the extraction of the signal. In the VH analysis this is obtained with a fit of the multi-BDT score distribution using the shapes from simulation and the data-driven scale factors.

5 Results

In the VH analysis an upper limits of 1.89 (0.95) times the SM Higgs boson cross section at 125 GeV with 95% C.L. has been observed (expected), as shown in Figure 2(a). Corresponding to an excess of events of 2.1 standard deviations and to a signal strength of $\mu = 1.0 \pm 0.5$. The Figure 2(b) shows the distribution of the bb dijet invariant mass for the VH analysis, combining all sub-channels.

In the VBF channel an upper limit of 3.6 (3.0) times the SM Higgs boson cross section at 125 GeV with 95% C.L. has been observed (expected), as shown in Figure 3(a). It corresponds to a signal strength of $\mu = 0.7 \pm 1.4$. The Figure 3(b) shows the bb dijet invariant mass distribution in the most sensitive signal region.

A combination of the two analysis gives a signal strength of $\mu = 0.97 \pm 0.48$. It corresponds to an excess of events of 2.2 standard deviations from the expected background.

6 Conclusions

A search for the SM Higgs boson decaying to bottom quarks has been presented. Two production channels have been studied: the associated production with vector boson decaying to leptons (VH) and the vector-boson fusion (VBF). An excess of events of 2.2 standard deviations at a mass of 125 GeV has been reported that corresponds to a signal strength of $\mu = 0.97 \pm 0.48$.

References

[1] S. Chatrchyan *et al.* [CMS Collaboration], JINST **3** (2008) S08004.

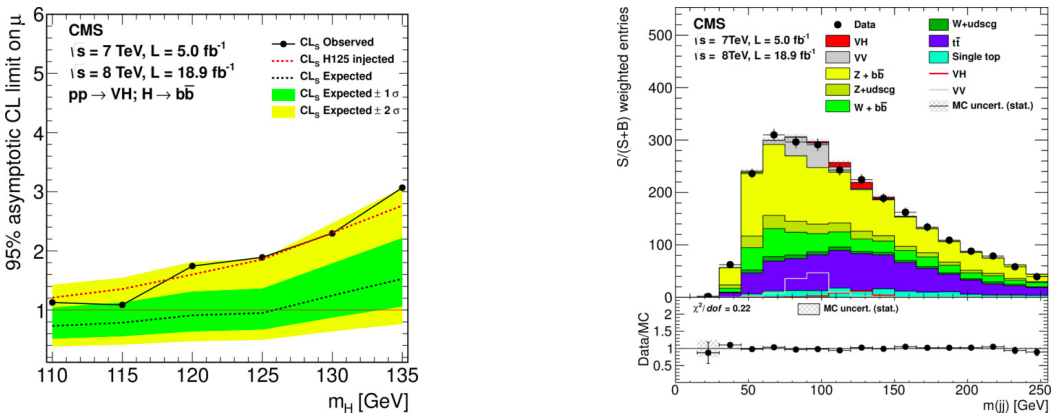

(a) (b)

Figure 2: On the left, the 95% CL upper limits on the signal strength for the SM Higgs boson hypothesis as a function of the Higgs boson mass, for the VH analysis. On the right, the b-jet pair invariant mass distribution in the VH analysis.

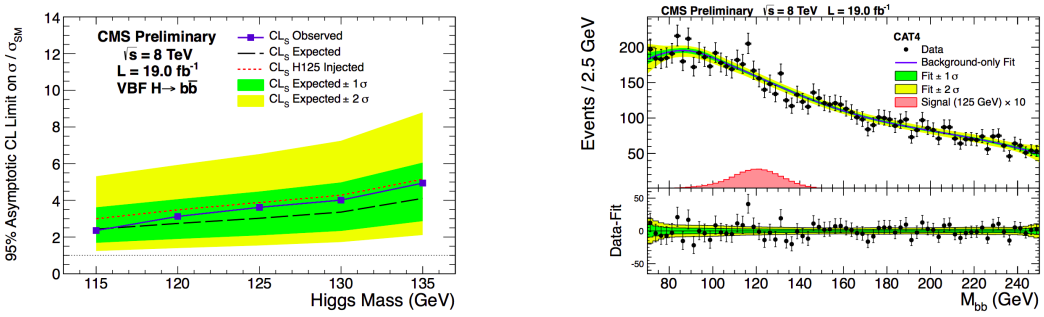

(a) (b)

Figure 3: On the right, the b-jet pair invariant mass distribution in the VBF analysis.

[2] S. Chatrchyan *et al.* [CMS Collaboration], Science **338** (2012) 1569.

[3] G. Aad *et al.* [ATLAS Collaboration], Science **338** (2012) 1576.

[4] S. Chatrchyan *et al.* [CMS Collaboration], CMS-HIG-13-004, CERN-PH-EP-2014-001.

[5] G. Aad *et al.* [ATLAS Collaboration], ATLAS-CONF-2013-108.

[6] S. Chatrchyan *et al.* [CMS Collaboration], Phys. Rev. D **89** (2014) 012003.

[7] S. Chatrchyan *et al.* [CMS Collaboration], CMS-PAS-HIG-13-011.

Recent theoretical and experimental results on top quark mass measurements

Roberto Franceschini

CERN, 1211 Geneve 23, Switzerland

DOI: http://dx.doi.org/10.3204/DESY-PROC-2014-04/317

In this contribution I will review recent experimental results on the measurement of the top quark mass. I will also review recent proposals about new methods proposed for the extraction of the top quark mass. Finally I will comment on recent detailed studies of the theoretical uncertainties in measurements based on templates fitting.

1 Introduction

The top quark mass is a key parameter of the Standard Model of particle physics. Indeed it is one of the free parameters of the theory that needs to be measured to fully define it. The top quark mass is also an input of many precision predictions of the Standard Model that are needed to assess its validity up to higher energy scales, possibly up to the Planck scale.

The great importance of the top quark mass for Standard Model and Beyond the Standard Model physics is motivation for the large efforts that the experimental community has put in its measurement. Remarkably, the LHC and TeVatron experiments have recently combined their results and obtained a combined measurement $173.34 \pm 0.27(stat) \pm 0.71(syst)$ GeV [1]. The uncertainty is dominated by systematic errors, in particular the measurement of hadornic jets, and is likely to not improve much when more data will be added to the analyses. The dominance of systematic errors in the current measurement is certainly a great motivation to think about new methods to mesure the top quark mass. At the end of Run-2 of the LHC it is foreseen to have few 1/ab of integrated luminosity, which would yield some *1 billion top pairs* produced at the LHC. The prospect to have such large sample of top quarks makes possible to consider measurement of the top quark mass that exploit very special final states (such as for instance J/ψ states or other exclusive decays) or exploit features of kinematic distributions that are not hugely populated (such as for instance end-point regions and tails). The hope is that among these alternative approaches to the top quark mass measurement one can find methods that are based on experimentally clean quantities and that exploit observables which are well under theoretical control. The balance of these two needs will be a key issue for the methods that will provide a reliable *precision* determination of the top quark mass.

The measurement of top quark mass through the measurement of the total inclusive $pp \to t\bar{t}$ cross-section is one instance of theoretically clean quantity, as it can be computed to high order in QCD, but, unfortunately, suffers of large uncertainties on the experimental side. The issue here has to do with the fact that the experiments measure the cross-section in the region of phase space accessible to their acceptance, not the total cross-section. The total cross-section

is obtained using MonteCarlo simulations to extrapolate from a fiducial region of phase-space to the total phase-space. Such extrapolation suffers of uncertainties that at the moment make impossible to measure the top quark mass better than a few GeV [2]. On the other hand the measurements that are more under control on the experimental side, and that has been possible to carry out with the current top quark sample, tend to be difficult to reliably interpret on a theory standpoint. One issue above all that can be mentioned is that the currently most precise measurement do require the construction of templates, whose matching with data, determines the top quark mass and its uncertainty. These templates can only be built from samples of exclusive events, that necessarily come from event generators. The accuracy of these events generators is often questioned when measurements at less than 1% are quoted; furthermore even the theoretical definition of the quantity that is measured with current template procedures might be not understood at this level of accuracy [3]. For these reasons it is useful to think about new quantities that can be used to measure the top quark mass having in mind from the very beginning the possibility to both compute and measure them *accurately*.

2 A portrait from different angles

One recent effort in the direction of measuring the top quark mass using a theoretically robust quantity is the measurement of the end-point of the invariant mass distribution of the lepton and the b-jet from the top decay [4]. The accuracy of this mass measurement is expected to reach a quite interesting sub-GeV level [5, 6]. Furthermore, by the end of the run of the LHC, with a luminosity of order 1/ab, other measurements are foreseen to become useful and to attain a similar level of accuracy [5, 6] thanks to the high statistics, reduced systematic errors and the improved theoretical calculations that will be available by then.

The fact that several new top quark mass measurement will be feasible with the large LHC top quark data set is extremely welcome. In fact to measure this mass with a precision well below the 1% level, one needs to carefully assess several delicate effects, most of which are particularly tough to control theoretically due to the nature of strong interactions and hadronic physics. The hope is that, by obtaining several independent measurements, each based on different experimental objects and possibly suffering of different theoretical uncertainties, we can obtain a *global* picture for the top quark mass measurement. In this picture it is likely that each single measurement will have a set of assumptions that can hardly be tested in the measurement itself or in other available data. For instance each measurement will have to deal in its own way with the many issues that exist in our *description* of hadronic physics: effect of higher order corrections, the estimation of theory uncertainties from scale variations and possible functional dependence of the scale on the kinematics, effect of finite width of unstable particles and radiation in the decay of resonances, effect of hadronization of partons and color neutralization. Each measurement will have different sensitivity to these effects and its interpretation will depend on our choice about how to address each of these issues. In the end the best knowledge of the top quark mass will emerge from the *combination* of truly independent, possibly uncorrelated, measurements. The variety of angles under which we will be able to observe the top quark will be the biggest strength of its mas measurement.

3 Issues with resonance reconstruction and templates

A very important issue with the top mass measurement has to do with the reconstruction of a resonance in the events that are used to measure the mass. Intuitively we expect that the most straightforward way to measure a resonance mass is to measure all its decay products and to compute the mass of the total four-vector. For instance for a Z boson one might want to look at $Z \to \mu^+\mu^-$ events and compute $\left(p_{\mu^+} + p_{\mu^-}\right)^2$. This procedure will definitively be good enough for most uses of the measured mass, however issues arise when one seeks *precision* and radiative corrections are added to this picture. In fact one has to remember that charged leptons come with an associated spectrum of emitted radiation that in reality makes the decay $Z \to \mu^+\mu^- +$ photons. The existence of these corrections to the naive (leading order) picture requires to move away from the simple picture outlined above and motivates complementary approaches to the mass measurement. In fact one can attempt to derive the Z boson mass from properties of just a subset of its decay products, even from just one of the leptons. This is a possibility actually very meaningful to entertain because it avoids to have to specify how the Z boson is reconstructed. This is even more true for the measurement of masses of particles where the final state is partly invisible, such as W bosons decaying leptonically and, as a consequence, top quarks. Furthermore, not having to reconstruct a resonance it is possible to measure the mass using more inclusive final states, which is a bonus for the accuracy of theory calculations. A recent attempt to obtain a mass measurement from inclusive single lepton distribution has been discussed in Ref. [7], which finds that the theory uncertainty on the top quark mass from such observable could be as low as 0.8 GeV.

Another interesting result from Ref. [7] has to do with the inherent uncertainties that should be evaluated when templates are used to extract the top quark mass. The fact is that templates are only as good as the approximation to real hadronic physics that has been put in the calculation or event generator used to obtain the templates. Therefore it is very important to scrutiny the effect on the measurement that arises from the several choices that one has to do in the making of the templates. For instance one needs to study the impact of the measurement of the presence of parton shower corrections, spin correlations treatment, and even the precise relation between the event kinematics and the choice of scales that are introduced in the calculation. Some of these effects my be not so relevant in other aspects of top quark physics, still, due to the differential nature of the information that is used in the top quark mass extraction, they might have a significant impact when one tries to extract the top quark mass better than 1% accuracy that is interesting nowadays. Ref. [7] discusses a few examples of leptonic observables that suffer from these *theory biases* and in particular highlights how in some cases even a higher order calculation seems to not help much to cure these largely unpredictable biases.

4 Phenomenological Lorentz invariants

The last issue discussed above motivates to consider observables that are as much as possible insensitive to the effects that are difficult to incorporate in the calculations used to produced the templates. In this respect observables that are invariant under Lorentz transformations are naturally interesting to look at. The reason is that many details about the events that produce the top quarks become irrelevant. In fact all the effects that amount to change the boost distribution of the top quark in the given production environment are not important.

One can simply compute these observables in the top quark rest frame and, by virtue of the invariance, carry the prediction to the laboratory frame. The example of the mass of the muon pair above perfectly displays the utility of Lorentz invariants. However, from the discussion above we also know that it is crucial to observe *all* the products of the decay, including the cloud of real photons (that can be energetic in some cases) that accompany the charged leptons.

A possible solution to this problem is to retrieve Lorentz invariant quantities from information encoded in the laboratory frame *distribution* of suitable Lorentz-variant quantities. The key idea is that distributions do retain the full information on the kinematics in the top quark rest frame and that, in suitable experimental conditions, one can reliably extract the top quark rest frame quantities from these distributions. Observables that have been considered so far are: a specially weighted median of the inclusive lepton energy distribution [8] and the position of the peak of the inclusive energy distribution of the b-jet [9]. The extraction of Lorentz invariants from the distribution of Lorentz-variants is potentially advantageous because can be carried out from the observation of a *single particle* among all the decay products of the top. This simplifies the issue of adding radiative corrections as one can base the top quark mass extraction on the study of a single distribution that is fully inclusive with respect to the presence of extra radiation. The further consequence of dealing with a single particle measurement is that there is no need to proceed to a resonance reconstruction. Furthermore a single particle observable avoids all the issues connected to the identification of the correct pair of particles to be combined to reconstruct a resonance from its invariant mass. The study of NLO corrections to the energy distribution of leptons and b-jets for the top mass measurement is currently underway.

5 Conclusions

The determination of the top quark mass with uncertainty below 1 GeV is a very challenging task both theoretically and experimentally. After the epoch of measurements based on a limited sample of top quarks, the LHC will make possible a variety of mass measurements that need large statistics. The combination of these measurement will provide a *global* assessment of the top mass, whose consistency will make us confident that the small error of these measurements is actually backed up by a solid *precision* understanding of QCD in top quark physics.

References

[1] ATLAS, CDF, CMS and D0 Collaborations. First combination of Tevatron and LHC measurements of the top quark mass. *ArXiv:1403.4427*.

[2] CMS Collaboration. Determination of the top quark pole mass and strong coupling constant from the $t\bar{t}$ production cross section in pp collisions at $\sqrt{s} = 7$ TeV. *Phys.Lett.*, B728:496–517(2013).

[3] A. H. Hoang and I. W. Stewart. Top Mass Measurements from Jets and the Tevatron Top-Quark Mass. *Nucl. Phys. B Proc. Supp.*, 185:220–226(2008).

[4] CMS Collaboration. Measurement of masses in the $t\bar{t}$ system by kinematic endpoints in pp collisions at $\sqrt{s}$ = 7 TeV. *Eur.Phys.J.*, C73:2494(2013).

[5] Juste et al. Determination of m_{top} circa 2013: methods, subtleties, perspectives. *ArXiv:1310.0799*.

[6] CMS Collaboration. Projected improvement of the accuracy of top quark mass measurements at the upgraded LHC. CMS-PAS-FTR-13-017

[7] S. Frixione and A. Mitov. Determination of the top quark mass from leptonic observables. *ArXiv:1407.2763*.

[8] Kawabataa et al. Weight function method for precise determination of m_{top} at the LHC. *ArXiv:1405.2395*.

[9] Agashe et al. A simple, yet subtle 'invariance' of two-body decay kinematics. *Phys. Rev. D*, 88(5):057701

Combined measurements of the properties of the Higgs boson using the ATLAS detector

Peter Kluit[1] on behalf of the ATLAS Collaboration

[1]Nikhef, Science Park 105 , 1098 XG Amsterdam , The Netherlands

DOI: http://dx.doi.org/10.3204/DESY-PROC-2014-04/227

The combination of the measurements of the Higgs boson properties by the ATLAS detector at the LHC will be presented. Firstly, the measurements of the spin and parity CP of the observed boson will be discussed. Secondly, the results for the production of the Higgs boson in different channels through the gluon-gluon and vector-boson fusion processes will be presented. Finally, coupling fits are performed to the data and the Standard Model symmetries and mass dependence are tested and discussed. It is concluded that the observed boson is compatible with one Standard Model CP-even Higgs boson.

1 Introduction

In this paper the combination of the measurements of the properties of Higgs boson by the ATLAS detector at the LHC [1] will be discussed. The Higgs boson is observed in several final states; initially it was discovered in the $\gamma\gamma$, ZZ and WW channels [2]. Here I will summarize what is currently known about the Higgs spin and CP properties and the Higgs couplings to bosons, quarks and leptons.

The Higgs spin and CP properties have been studied in the three di-boson channels. Subsequently, the analyses probing different CP and spin hypotheses have been combined [3]. The angular and momentum distributions of the bosons and their decay products are sensitive to the spin and CP of the produced boson. By fitting these distributions to the data for the hypothesis of a Standard Model (SM) Higgs boson (0^+) and an alternative spin CP hypothesis ($\mathrm{J^P} = 2^+, 1^+, 1^-$ or 0^-), exclusion limits are obtained. The results, shown in Fig. 1, are compatible with a CP-even scalar boson and the alternative hypotheses are excluded at 97.8% CL or higher.

In the following, I will discuss in more detail the combination of Higgs measurements in the $\gamma\gamma$, ZZ, WW [2], $\tau\tau$ [4] and $b\bar{b}$ [5] channels. The Higgs can be produced in gluon-gluon fusion (ggF), vector boson fusion (VBF) and W or Z associated production (VH). The channels were divided into categories that correspond to the production mode and final states. The di-boson channels included categories enriched in ggF and VBF; the $b\bar{b}$ channel was only analyzed in the VH final state. The paper will mainly focus on the results of the Higgs boson coupling measurements and their interpretation. A detailed description of the event selection, channels, categories and fit procedure can be found in Ref. [6].

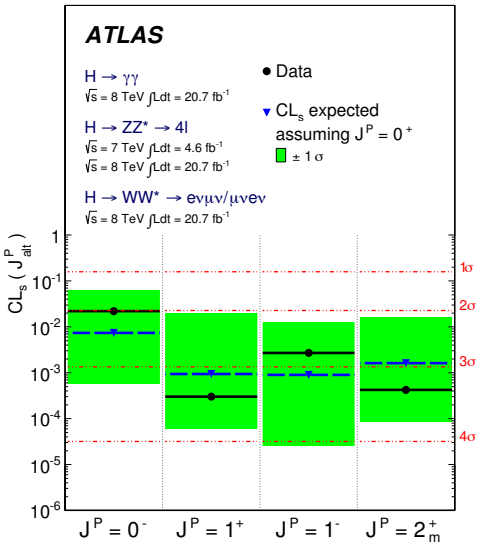

Figure 1: Expected (blue triangles/dashed lines) and observed (black circles/solid lines) confidence level CLs for alternative spin–parity hypotheses assuming a 0^+ signal. The green band represents the 68% CL expected exclusion range for a J^P signal. For the spin-2 hypothesis, the results for a specific 2^{+m} model, are shown.

2 Combination of the Higgs measurements

The inclusive signal strength μ normalised to the SM expectation, obtained by combining the five listed channels, is $\mu = 1.30^{+0.18}_{-0.17}$.

Because of the VBF enriched event categories, it is possible to measure the VBF fraction defined as: $\mu_{VBF}/\mu_{ggF+ttH} = 1.4^{+0.5}_{-0.4}(stat)^{+0.4}_{-0.3}$. This provides 4.1σ evidence for the production of Higgs bosons through VBF.

In the coupling fits $\kappa_i = g_i/g_i^{SM}$ is fitted, where g_i is the coupling of the Higgs boson to e.g. fermions (F) or bosons (V). The Higgs boson couplings are measured in simplified benchmark models. It is assumed that only one CP-even scalar Higgs boson with $m_H = 125.5\ GeV$ is produced. Its width is neglected, i.e. the narrow-width approximation is used.

In the first model the coupling ratios to fermions are put equal to κ_F and of all bosons to κ_V. This allows to test the SM difference of fermion and boson couplings under the assumption that there are no new physics contributions to the total width. The result is $\kappa_F = 1.15 \pm 0.08$ and $\kappa_V = 0.99^{+0.17}_{-0.15}$ as shown in Fig. 2. Note that the result is compatible with the SM, where one expects values of 1. It is possible to fit the ratio λ_{FV} defined as κ_F/κ_V. In that case no assumption on the total width is need. The result is $\lambda_{FV} = 0.86^{+0.17}_{-0.15}$ and shown in Fig. 2.

It is possible to test the custodial symmetry of the SM directly in the Higgs sector by fitting λ_{WZ} thus allowing different couplings to the W and Z bosons. The result is shown in Fig. 2: $\lambda_{WZ} = 0.94^{+0.14}_{-0.29}$, compatible with the SM expectation.

Many extensions of the SM predict different couplings to up- and down-type fermions. In that case λ_{ud} is constrained to the range 0.78 - 1.15 at 68% CL as shown in Fig. 2. It can be further shown that there is 3.6σ evidence for the coupling of the Higgs boson to down-type fermions.

Another test is the measurement of the lepton and quark couplings. Here λ_{lq} is constrained to the range 0.99 - 1.5 at 68% CL, shown in Fig. 2. A vanishing coupling of the Higgs boson to leptons is excluded at 4σ.

The loop contributions in SM processes are sensitive to possible new physics processes. To quantify this sensitivity, the couplings to gluons κ_g and photons κ_γ are measured to be: $\kappa_g = 1.08^{+0.15}_{-0.13}$ and $\kappa_\gamma = 1.19^{+0.15}_{-0.12}$. It is assumed that the $\kappa_{F,V}$ values are 1 and only SM particles contribute to the total width.

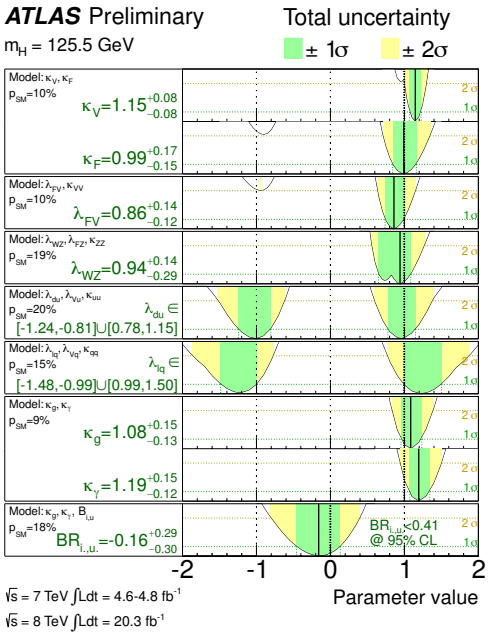

Figure 2: Summary of the coupling scale factor measurements for $m_H = 125.5\ GeV$. The best-fit values are represented by the solid black vertical lines. The measurements in the different benchmark models, separated by double lines in the figure, are strongly correlated, as they are obtained from fits to the same experimental data. For each model the compatibility of the SM hypothesis with the best-fit point is given by p_{SM}.

Finally, the mass scaling of the couplings is tested by parametrising deviations from the SM prediction in terms of two additional parameters ϵ and M in the formulae: $\kappa_{f,i} = v\frac{m^{\epsilon}_{f,i}}{M^{1+\epsilon}}$ and $\kappa_{V,j} = v\frac{m^{2\epsilon}_{V,j}}{M^{2+\epsilon}}$, where v is the vacuum expectation value of 246 GeV and $m_{f,V}$ denote to the fermion and boson masses. In the SM ϵ is zero and M equals v. The result of the fit is shown in Fig. 3. The deviation of the Higgs boson couplings to fermions (bosons) from a linear (quadratic) scaling with the particle masses is less than 10% [7].

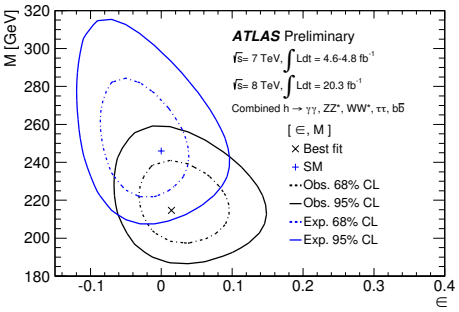

Figure 3: Two-dimensional likelihood scan of ϵ and M. The likelihood contours corresponding approximately to 68% CL (1σ) and 95% CL (2σ) respectively, are shown for both the data and the prediction for a SM Higgs boson. The best fit to the data and the SM expectation are indicated as $\times$ and $+$ respectively.

3 Conclusions

The spin and CP of the observed particle is consistent with a CP-even scalar boson. The boson is produced in ggF and VBF processes with cross sections and branching ratios that are consistent with a SM Higgs boson. The measured couplings are consistent with the SM predictions and the underlying symmetries and mass scalings have been measured. In the near future the final Run-1 Higgs analysis results will be published. We look forward to higher statistics Run-2 results for which the projections can be found in Ref. [8].

References

[1] ATLAS Collaboration, JINST **3** (2008) S08003, *The ATLAS Experiment at the CERN Large Hadron Collider.*

[2] ATLAS Collaboration, Phys. Lett. **B716** 1 (2012), *Observation of a new particle in the search for the Standard Model Higgs boson with the ATLAS detector.*

[3] ATLAS Collaboration, Phys. Lett. **B726** 120 (2013), *Evidence for the spin-0 nature of the Higgs boson using ATLAS data.*

[4] ATLAS Collaboration, ATLAS-CONF-2013-108, *Evidence for Higgs Boson Decays to the $\tau^+\tau^-$ Final State with the ATLAS Detector.*

[5] ATLAS Collaboration, ATLAS-CONF-2013-079, *Search for the bb decay of the Standard Model Higgs boson in associated (W/Z)H production with the ATLAS detector.*

[6] ATLAS Collaboration, ATLAS-CONF-2014-009, *Updated coupling measurements of the Higgs boson with the ATLAS detector using up to 25 fb^{-1}.*

[7] ATLAS Collaboration, ATLAS-CONF-2014-010, *Constraints on New Phenomena via Higgs Boson Coupling Measurements with the ATLAS Detector.*

[8] ATLAS Collaboration, ATL-PHYS-PUB-2013-014, *Projections for measurements of Higgs boson cross sections, branching ratios and coupling parameters with the ATLAS detector at a HL-LHC.*

Top-quark physics results from CMS

Jeremy Andrea for the CMS collaboration

Institut Pluridisciplinaire Hubert CURIEN, France

DOI: http://dx.doi.org/10.3204/DESY-PROC-2014-04/232

Recent results on top-quark physics from the CMS collaboration are presented. Among the many measurements performed by CMS, some of the most significant, related to the $t\bar{t}$ and single top production, top-quark mass and top properties measurements, are shown.

1 Introduction

The top quark is the heaviest particle observed. In many aspects, it is of a major interest in particle physics. It decays before it hadronizes, which allows for precise measurement of the top-quark properties. It also has the largest couplings to the Higgs boson, due to its large mass, and thus could play an special role in the electroweak symmetry breaking. While top-quark physic is crucial for our understanding of the Standard Model (SM), it is providing a very important window to potential new physics. Indeed, top-quark events have signatures comparable to many new physics prediction (BSM), and a good understanding of the top-quark background is mandatory for validating the detector performance and the simulation, but also for improving theoretical calculations and Monte-Carlo generation. Furthermore, precise measurements related to the top-quark can be used to indirectly probe new physics when searching for deviations with respect to the SM predictions.

While many major contributions to the top-quark physics were performed by the CMS collaboration [1], only some of the most significant results are presented in this proceeding. In the following, the top-quark pair and single-top-quark production cross section measurements will be first discussed. After discussing top-quark mass measurements, the top-quark properties, as well as the corresponding search for new physics, are discussed.

2 Top-quark production

The measurement of top-quark production cross sections are performed in both the $t\bar{t}$ and in single top channels, either inclusive [2], differential [3], or in association with additional particles [4, 5].

The most precise top-quark pair cross section measurement at 8 TeV is obtained in the dileptonic $e\mu$ channel, as it suffers from a very low background contamination, mainly the residual $Z/\gamma^* \to \tau\tau$ events with the τ decaying leptonically, and single-top-quark events in the tW channel. The event selection requires two isolated high p_T leptons with opposite signs, at least two high p_T jets with at least one b-tagged jet. The jet and b-tagged jet multiplicities after the event selection is presented in Fig.1.

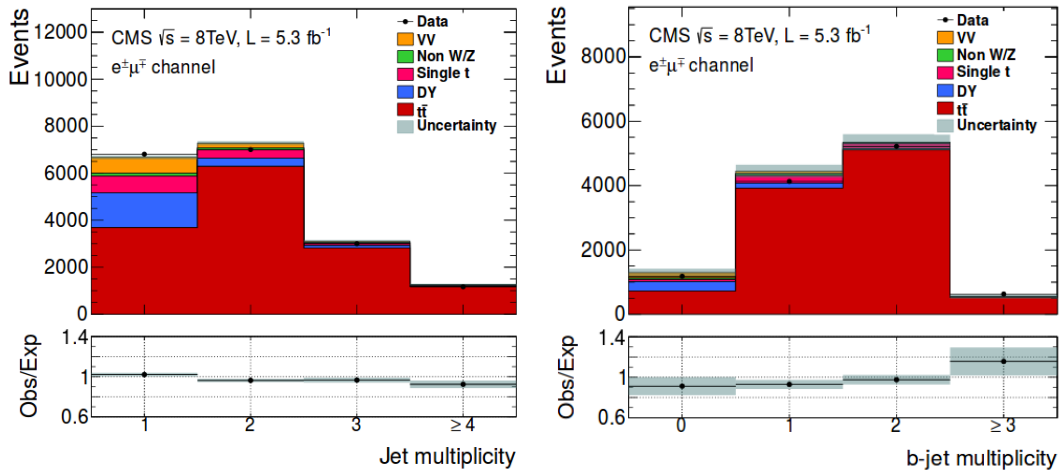

Figure 1: Jet and b-tagged jet multiplicities after the dilepton $e\mu$ event selection.

With the very large luminosity delivered by the LHC, the uncertainty is largely dominated by the systematics, with the largest contributions coming from the Jet Energy Scale (JES), the modelling of the $t\bar{t}$ signal and the luminosity. A simple counting experiment is already able to reach a very high level of precision, as demonstrated in [2]. The inclusive $t\bar{t}$ cross section is measured, with an overall precision of 5.8% , to be :

$$\sigma_{t\bar{t}} = 239.0 \pm 2.1(stat.) \pm 11.3(syst.) \pm 6.2(lumi.). \quad (1)$$

The top-quark production can also be studied through the single-top modes : the s-channel, the t-channel and the tW-channel, the two latest being observed at CMS [6]. The t-channel cross section is measured in the leptonic channel, after selecting events with one high p_T isolated lepton, at least one jet, a large missing transverse energy and a large transverse mass of the W candidates. The cross sections is extracted from the $|\eta|$ distribution of the recoiling jet in various signal and control regions, defined by different jet and b-tagged jet multiplicities, and by different reconstructed top-quark mass requirements. The measured cross section at 8 TeV is :

$$\sigma_{t-chan.} = 83.6 \pm 2.3(stat.) \pm 7.4(syst.). \quad (2)$$

The mains systematic uncertainties are related to the signal modelling, the jet selection and the b-tagging. Several other interesting measurements can also be performed using the same event selection and similar techniques, such as the top/anti-top cross sections ratio $\sigma_{t-chan.}(t)/\sigma_{t-chan.}(\bar{t})$ $(= 83.6 \pm 2.3(stat.) \pm 7.4(syst.).)$ which is sensitive to PDF, or the measurement of $|V_{tb}| > 0.92$, at 95% confidence level.

The first observation of the tW-channel was also performed for the first time by the CMS collaboration [7]. The measurement is performed in the dilepton channel, using an event selection similar to the $t\bar{t}$ inclusive cross section analysis. A boosted decision tree is used to discriminates signal against backgrounds, and fitted in various signal and background regions

(using categorization in jet and b-tagged jet multiplicities). The tW cross section is measured to be 23.4 ± 5.4, with a significance of 6.1σ.

3 Top-quark mass measurement

The top-quark mass is measured by the CMS collaboration through different channels and techniques. The most precise measurement is performed with the 8 TeV dataset with $t\bar{t}$ lepton+jets events [8] using the ideogram technique. The event selection ask for one isolated leptons with a high p_T (either a muon or an electron), at least 4 high p_T jets with two b-tagged jets. A high purity of events can be reached, and a kinematic fit is used to improve the rate of correct jet-to-parton assignments by cutting on the goodness of the kinematic fit.

The correction factor the the Jet Energy Scale (JSF) is fitted simultaneously with the top-quark mass using a likelihood fit technique. The measured mass and JSF are found to be :

$$m_t = 172.04 \pm 0.19(stat. + JSF) \pm 0.75(syst.) GeV, JES = \quad 1.007 \pm 0.002(stat.) \pm 0.012(syst.). \tag{3}$$

This result constitutes the most precise single measurement of the top-quark mass. The main systematic uncertainties are related to the JSF, the Jet Energy Resolution, the pile-up and the signal modelling. The different mass measurements performed within CMS are also combined[9] and improve slightly the overall precision.

4 Top-quark properties and search for new physics

As the top-quark decays before it hadronizes, the decay product of the top-quarks can be used to probe the top-quark properties. In particular, the $t\bar{t}$ spin correlation can be used to probe the $t\bar{t}g$ couplings and to search for new physics [10]. The signatures that carries most of the spin information is the $t\bar{t}$ in the dileptonic channel. Spin correlation, and the corresponding asymmetry, can be measured from the azimuthal angle $\Delta\phi(ll)$ between the two charged leptons in the $t\bar{t}$ rest frame. The differential $t\bar{t}$ cross section as a function of $\Delta\phi(ll)$, unfolded at parton level, can be seen in Fig.2 (left plot).

The differential cross section can also be used to probe new physics, by searching for chromomagnetic dipole-moment $\hat{\mu}_t$. By comparing the unfolded distribution to theoretical predictions, the real part of $\hat{\mu}_t$ was found to be within the range $-0.043 < Re(\hat{\mu}_t) < 0.0117$ at 95% confidence level.

New physics in top events can also be performed by searching for flavour changing neutral current (FCNC) interactions, which are highly suppressed by the GIM mechanism in the SM. Top-quark FCNC are searched for in top decays in $t\bar{t}$ events [11], when a top-quark decays into a c or an u quark and a Z boson. The search is performed in the three-lepton signature by asking for three isolated leptons (electrons or muons) with high p_T, and a pair of opposite-sign and same-flavour leptons compatible with the Z boson mass. At least two jets, with at least one b-tagged jet, is also required. No excess over the data is observed. Exclusion limits are calculated from the observed number of events with reconstructed top-quark masses compatible

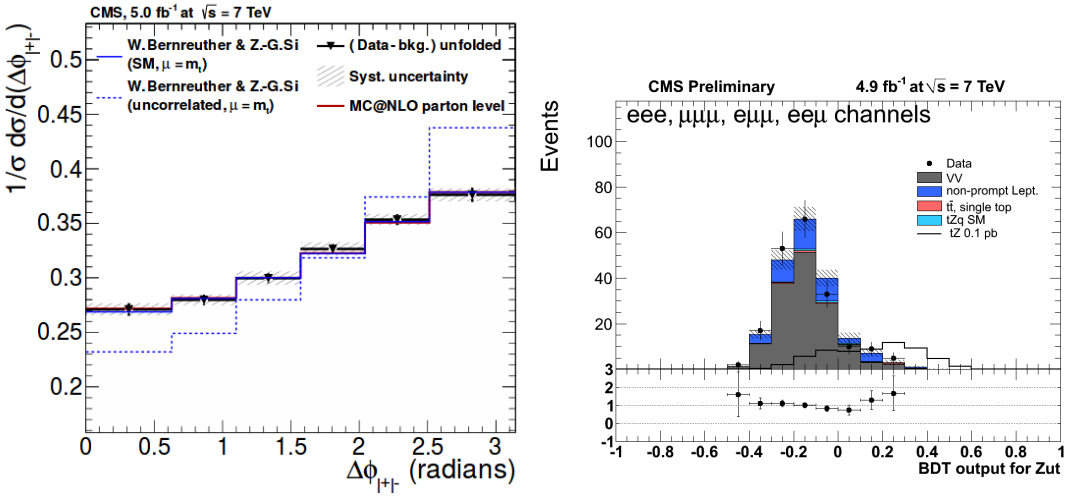

Figure 2: Left, $\Delta\phi(ll)$ differential cross section in $t\bar{t}$ events. Right : BDT distribution after the tZ selection.

with the known top-quark mass. Limit on the decay branching fraction of top quark into Zq is found to be $Br(t \to Zq) < 0.05\%$ at 95% confidence level.

Similar searches can be performed in the single top signature, as the search for a top-quark produced in association with a Z boson [12]. This channel has the advantage of being sensitive to the flavour of the quark q entering into the FCNC vertex tZq. The event selection is similar to [11], but with a looser jet selection. The analysis uses a BDT to extract the signal from the backgrounds, and to calculate exclusion limits. The BDT distribution in data and simulation can be found on Fig.2, right plot. Exclusion limits on the branching ratios are found to be $Br(t \to Zu) < 0.056$ and $Br(t \to Zc) < 7.12\%$. Similarly, on can probe $t\gamma q$ FCNC interactions by searching for a top quark produced in association with a real photon [13]. The corresponding limits on the top-quark branching fractions are $Br(t \to \gamma u) < 0.0279$ and $Br(t \to \gamma c) < 0.0161\%$.

5 Conclusion

The CMS collaboration covers a wide range of top-related topics and only a tiny fraction of the performed measurements is presented in this document. While these measurements correspond to a big step forward in our understanding of top-quark physics, there are still many open questions that need to be answered. Future runs of the LHC can provide the amount of data needed to perform those important investigations.

References

[1] The CMS collaboration, JINST 03 (2008) S08004

[2] The CMS collaboration, JHEP 02 (2014) 024

[3] The CMS collaboration, EPJ C73 (2013) 2339
[4] The CMS collaboration, Eur. Phys. J. C 74 (2014) 3014
[5] The CMS collaboration, Eur. Phys. J. C 74 (2014) 3060
[6] The CMS collaboration, JHEP 06 (2014) 090
[7] The CMS collaboration, PRL 112 (2014) 231802
[8] The CMS collaboration, CMS PAS TOP-14-001
[9] The CMS collaboration, CMS PAS TOP-14-015
[10] The CMS collaboration, CMS PAS TOP-14-004
[11] The CMS collaboration, PRL 112 (2014) 171802
[12] The CMS collaboration, CMS PAS TOP-12-021
[13] The CMS collaboration, CMS PAS TOP-14-003

Search for the Higgs boson decaying to two photons in CMS

Martina Malberti[1] on behalf of the CMS Collaboration

[1]University of California Riverside, USA

DOI: http://dx.doi.org/10.3204/DESY-PROC-2014-04/233

A search for Higgs bosons has been carried out in the Higgs to two photons decay channel with the CMS detector at the Large Hadron Collider. The analysis is based on proton-proton collision data collected in 2011-2012 at centre of mass energies of 7 and 8 TeV corresponding to integrated luminosities of 5.1 fb^{-1} and 19.7 fb^{-1}, respectively. The analysis strategy and measurements of the mass, couplings, and spin-parity are reported.

1 Introduction

In 2012, the ATLAS and CMS collaborations observed a new particle compatible with the Higgs boson postulated by the standard model (SM) [1, 2]. Here, the search through its decay to two photons is presented. Results based on the full CMS Run I dataset collected in 2011-2012 at centre of mass energies of 7 and 8 TeV are reported [3].

2 Analysis strategy

Despite the small branching ratio (0.23% for $m_{\text{H}} = 125$ GeV), the $H \to \gamma\gamma$ decay channel is characterized by a clean experimental signature, with two high transverse momentum isolated photons, which allow high precision for mass reconstruction. Photon candidates are reconstructed starting from energy deposits in the CMS electromagnetic calorimeter (ECAL). The ECAL single channel response is monitored and corrected for crystal transparency losses and is equalized between the different channels exploiting the $\phi-$simmetry of the energy flow, $\pi^0 \to \gamma\gamma$, $W \to e\nu$ and $Z \to ee$ decays [4]. Higher level corrections for shower containment, material and pileup effects are implemented through a multivariate regression, which provides also an estimate of the per photon energy resolution. Residual corrections, estimated from data to Monte Carlo (MC) comparisons in $Z \to ee$ events, are applied to correct the photon energy scale in data and to match the resolution of simulated events to the one observed in data.

A boosted decision tree (BDT), employing shower shapes and isolation variables, is used to discriminate prompt photons from jets misidentified as photons.

The di-photon vertex assignment is based on a multivariate approach with the transverse momenta of the tracks associated to the vertex, their correlation with the di-photon kinematics and the information from conversions as inputs. A further BDT is trained to estimate the

per event probability to assign the correct vertex (∼80% for an average pileup of about 20 interactions per bunch crossing).

To achieve the maximum sensitivity, events are splitted in categories exploiting their different mass resolution and signal-over-background ratio. The event information, including the kinematics, photon quality, mass resolution and probability to assign the correct vertex, is combined in a multivariate classifier (referred to as di-photon BDT), which is built in such a way to be mass independent and to have high values for events with good di-photon mass resolution and high probability of being signal rather than background. The output of the di-photon BDT is used to define untagged event classes. The boundary of the untagged categories are chosen to minimize the expected uncertainty on the signal strength measurement. In addition, categories tagged by the presence of additional objects in the final state are defined to target specific production modes: Higgs boson events produced via Vector Boson Fusion (VBF) have two jets with large rapidity gap; events from the associated VH (V = W, Z) production are tagged by the presence of one or more charged leptons, large missing transverse energy, or jets from the decay of the W or Z boson; and those from $t\bar{t}H$ production are characterized by the presence of b-jets and additional leptons or jets from the top decay. In total, 25 mutually exclusive event classes are defined: 14 in the 8 TeV dataset and 11 in the 7 TeV dataset.

For each event category, a signal and a background model are built. The signal model is obtained from a parametric fit of the simulated invariant mass of the two photons after having applied all the corrections derived from data to MC comparisons in $Z \to ee$ and $Z \to \mu\mu\gamma$ events. The background model is fitted from data. A smoothly falling background is expected, but the shape is *a priori* unknown. A discrete profiling method in which the choice of the function is included as discrete nuisance parameter in the likelihood to extract results is used. All reasonable families of functions are considered (exponentials, power laws, polynomials, Laurent series) and data are allowed to select the one which fits the best. The uncertainty resulting from the envelope around the negative log-likelihood curve of all the different functions takes therefore into account the model assumption.

3 Results

The inclusive di-photon invariant mass spectrum for all the selected events in the 7 and 8 TeV datasets is shown in Fig. 1-left. An excess of events is observed at a mass of 124.7 GeV with a significance of 5.7σ (Fig. 1-right). The corresponding measured signal strenght μ relative to the standard model expectation is $\mu = 1.14^{+0.26}_{-0.23} = 1.14 \pm 0.21(\text{stat.}) \, ^{+0.09}_{-0.05}(\text{syst.}) \, ^{+0.13}_{-0.09}(\text{theo.})$. The main sources of systematic uncertainties on the signal yield are the theoretical uncertainty on the production cross section and branching ratio, the shower shape modeling and the energy scale and resolution uncertainties.

The mass of the observed boson is determined via a 1-dimensional likelihood scan (Fig. 2-left) in which the relative signal strengths for couplings to fermions and bosons are floated to make the measurement less model dependent. The measured mass is $m_{\text{H}} = 124.70 \pm 0.31$ (stat.) $\pm$ 0.15 (syst.) GeV, where the main systematic uncertainties are due to the non-linearity in the extrapolation from the m_{Z} scale to the m_{H} scale and to imperfections in the modeling of the differences between electrons and photons in the MC simulation.

The measured signal strengths when considering different production modes separately are $\mu_{\text{ggH,t}\bar{\text{t}}\text{H}} = 1.13^{+0.37}_{-0.31}$ and $\mu_{\text{VBF,VH}} = 1.16^{+0.63}_{-0.58}$ (Fig. 2-right).

A test of the SM 0^+ hypothesis against a spin-2 graviton-like model with mininimal cou-

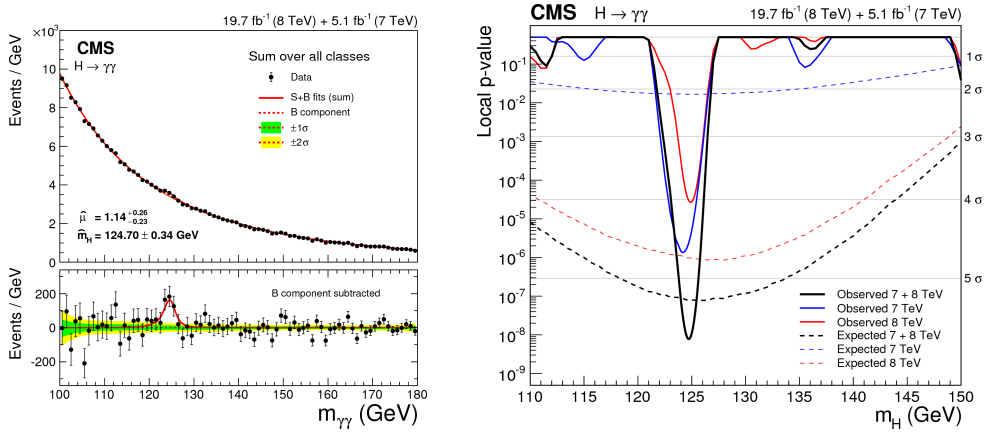

Figure 1: Left: invariant mass of the two photons for all the events selected in the 7 and 8 TeV datasets. Right: local p-values as a function of m_{H} for the 7 TeV, 8 TeV, and the combined dataset.

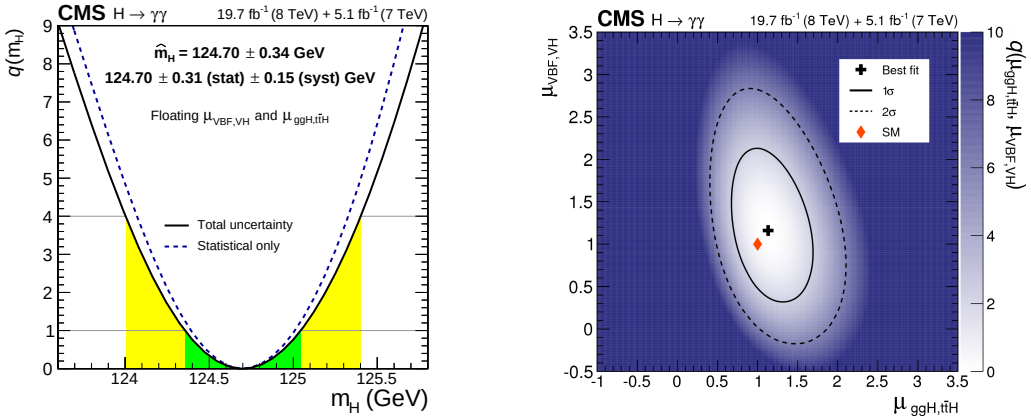

Figure 2: Left: likelihood scan as a function of the mass with $\mu_{\mathrm{ggH,t\bar{t}H}}$ and $\mu_{\mathrm{VBF,VH}}$ floated independently. Right: likelihood scan as a function of $\mu_{\mathrm{ggH,t\bar{t}H}}$ and $\mu_{\mathrm{VBF,VH}}$; the 1σ and 2σ uncertainty contours are shown, the cross indicates the best-fit values and the diamond represents the standard model expectation.

plings, 2^+_m [5], was performed. The variable used to discriminate between the two hypothesis is the cosine of the scattering angle in the Collins-Soper frame [6]. Figure 3 shows the test statistic $-2\ln(L_{2^+_m}/L_{0^+})$ as function of the fraction $f_{q\bar{q}}$ of $q\bar{q}$ production. The hypothesis 2^+_m is disfavoured at a 94% C.L. for pure gluon fusion production.

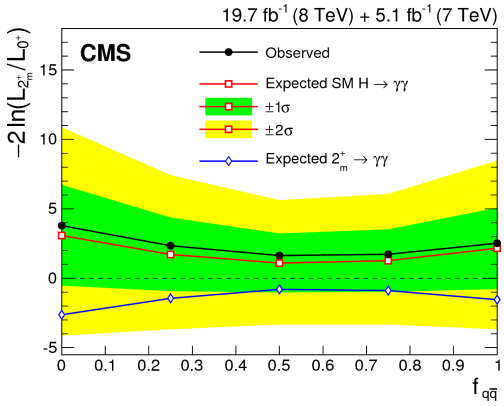

Figure 3: Test statistic for pseudo-experiments generated under the standard model 0^+ hypothesis (open squares) and the graviton-like 2^+_m hypothesis (open diamonds), as a function of the fraction $f_{q\bar{q}}$ of $q\bar{q}$ production. The full dots correspond to the observed distribution in the data.

4 Conclusions

The search for the Higgs boson through its decay to two photons in CMS was reported. The analysis is based on the full CMS Run I dataset collected at 7 and 8 TeV. A clear signal, with a local significance of 5.7σ, is observed at a mass of 124.7 GeV and the measured properties are consistent with the expectations from a standard model Higgs boson.

References

[1] ATLAS Collaboration, Phys. Lett. **B716** (2012) 1-29

[2] CMS Collaboration, Phys. Lett. **B716** (2012) 30

[3] CMS Collaboration, arXiv:hep-ex/1407.0558 (2014)

[4] CMS Collaboration, JINST **8** (2013) P09009

[5] Y. Gao et al. Phys. Rev. **D 81** (2010) 075022

[6] J. C. Collins and D. E. Soper, Phys. Rev. **D 16** (1977) 2219

Measurement of the angular production asymmetries in top quark pair lepton plus jets and dilepton final states

Kamil Augsten for the D0 Collaboration

Czech Technical University in Prague, Prague, Czech Republic

DOI: http://dx.doi.org/10.3204/DESY-PROC-2014-04/154

We present the measurement of the forward-backward asymmetry in the $t\bar{t}$ quark pair production in $p\bar{p}$ collisions in the lepton+jets and dilepton final states. Measurements use the full data set collected by the D0 detector in Run II corresponding to an integrated luminosity of 9.7 fb^{-1}. We present the most recent measurement of the lepton-based asymmetries both in lepton+jets and dilepton final states and their combination. We also present the top-quark based asymmetry as an inclusive measurement and differentially in $m_{t\bar{t}}$. These results are corrected for efficiency, acceptance and resolution effects to parton level. Measurements are compared to theory predictions.

1 Introduction

The top quark and its properties play an important role in the Standard Model (SM) and may probe for new physics. The forward-backward charge asymmetry was observed in fermion production in e^+e^- collisions in the 1980's, which was confirmation of the electroweak theory and observation of the mediation through Z-boson. Similar process might occur in strong sector as heavy mediators of strong interaction that have axial component, so called axigluons [1]. Top pair production in $p\bar{p}$ collisions mediated by axigluons would result in effect that as experimentally observable as a forward-backward asymmetry. Different models also suggest non-zero forward-backward asymmetry in top pair production.

In the SM, positive asymmetry appears at the α_s^3 level with numeric prediction of 9 % [2], which is next-to-leading order (NLO) QCD with the electroweak (EW) corrections. Recent preliminary NNLO calculation reported ~ 10 % asymmetry [3].

Asymmetry A_{FB} is defined as

$$A_{FB} = \frac{N_F - N_B}{N_F + N_B}, \tag{1}$$

where $N_F = N(x > 0)$ (forward events) and $N_B = N(x < 0)$ (backward events) for any angular variable x, for example η. The asymmetry $A_{FB}^{t\bar{t}}$ is defined with $x = \Delta y = y_t - y_{\bar{t}}$, a variable that is invariant under the boost along the beam axis. Similarly, the asymmetry A_{FB}^{l} in lepton direction is defined with the signed rapidity ($q_l y_l$) of the lepton from $t\bar{t}$ decay. Both asymmetries can be defined in the lepton+jets[1] (l+jets) and dilepton decay channels. Additionally for the

[1] By lepton are denoted here only electron and muon.

dilepton channel, the asymmetry A_{FB}^{ll} is defined based on the difference in rapidity between the positive and negative lepton.

This overview focuses on the latest measurements by the D0 experiment with the full Tevatron data set of 9.7 fb^{-1} in both l+jets and dilepton channels.

2 Asymmetry in Lepton Production from $t\bar{t}$ decay

2.1 Lepton + Jets Channel

The asymmetry A_{FB}^{l} in the l+jet channel [4] is measured in four sub-channels: l+3jets with 1 b-tag, l+4jets with 1 b-tag, l+3jets with 2 or more b-tags, and l+4jets with 2 or more b-tags. It includes l+3jets events, where one of the jets lost, to maximize the statistical sensitivity. It approximately doubles the statistics. However, this implies larger background, especially the production of W boson in association with jets. Leptons from the decay of the inclusively produced W bosons are produced asymmetrically in forward and backward direction. This effect is studied in Monte Carlo (MC) and analysis calibrates it using comparison of MC prediction and data in the orthogonal region, the W+jets background dominated 3 jets and 0 b-tag channel, which is not used for the measurement. The difference is accounted as systematic uncertainty. To maximize the analysis precision, the A_{FB}^{l} was measured separately in each sub-channel and combined afterwards. The result is corrected for the detector efficiency and resolution. The asymmetry is measured to be $4.2 \pm 2.3(\text{stat.})^{+1.7}_{-2.0}(\text{syst.})$ % and can be compared to MC@NLO prediction of 2.3 % or SM calculation of 3.8 ± 0.3 % [2]. The result is for leptons within rapidity range of 1.5. Fig. 1 (left) shows breakdown of the result to each sub-channel. The measurement of the A_{FB}^{l} in l+jets channel includes study of the asymmetry dependence on the transverse momentum of the lepton (p_T^l) from the $t\bar{t}$ decay. This provides an additional information that helps to distinguish between different models. The A_{FB}^{l} dependency measured in data after subtracting the contribution of the calibrated W+jets background as well as other background sources is shown in Fig. 1 (right) compared to the MC@NLO prediction.

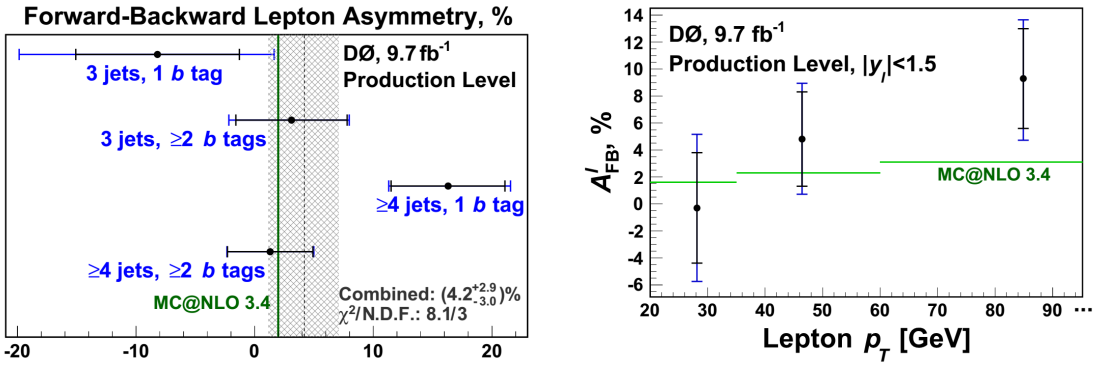

Figure 1: Left - Measured parton-level A_{FB}^{l} by sub-channel. The vertical line shows the MC@NLO prediction. Right - Predicted and observed parton-level asymmetries as a function of lepton transverse momentum. In both plots the statistical uncertainties are indicated by the inner, and the total uncertainties by the outer error bars.

2.2 Dilepton Channel

D0 performed measurements of asymmetry in lepton production in dilepton $t\bar{t}$ events [5], where two leptons (electrons or muons) are selected to have opposite charge and are accompanied by one jet in $e\mu$ channel and at least two jets in ee, $e\mu$, and $\mu\mu$ channels. Those four channels are treated separately to account for differences in purity and later combined together. Two asymmetry definitions are considered: A^l_{FB} with $x = q_l\eta_l$ and A^{ll}_{FB} with $x = \Delta\eta$. Additional acceptance cuts $|\eta| < 2.0$ and $|\Delta\eta| < 2.4$ are applied. The observed asymmetries are corrected for the detector efficiency and extrapolated to the full acceptance with scaling factor derived from MC@NLO. The corrected and extrapolated results are $A^l_{FB} = 4.4 \pm 3.7(\text{stat.}) \pm 1.1(\text{syst.})$ % and $A^{ll}_{FB} = 12.3 \pm 5.4(\text{stat.}) \pm 1.5(\text{syst.})$ % and can be compared to the SM NLO calculations [2] of $A^l_{FB} = 3.8 \pm 0.3$ % and $A^{ll}_{FB} = 4.8 \pm 0.4$ %.

2.3 Combination

To make a combination in A^l_{FB} for l+jets and dilepton channels we need first both results in the same lepton rapidity region. For the $|y_l| < 1.5$ region, the l+jets result has been already mentioned, $4.2 \pm 2.3(\text{stat.})^{+1.7}_{-2.0}$ (syst.) %, and dilepton channel gives $4.3 \pm 3.4(\text{stat.}) \pm 1.0$ (syst.) %. The combination is done using Best Linear Unbiased Estimator (BLUE) method [6] resulting in $A^l_{FB} = 4.2 \pm 2.4$ %. This value is extrapolated to cover the full phase space - $A^l_{FB} = 4.7 \pm 2.3(\text{stat.}) \pm 1.5(\text{syst.})\% = 4.7 \pm 2.7$ % and it is in agreement with the SM calculation $A^l_{FB} = 3.8 \pm 0.3$ % [2].

3 Inclusive $t\bar{t}$ Production Asymmetry in Lepton + Jets Channel

Similarly to the asymmetry in lepton production in l+jets channel the inclusive $t\bar{t}$ production asymmetry [7] is measured with addition of the l+3jets events. As this measurement requires the full reconstruction of the $t\bar{t}$ decay, partial reconstruction algorithm [8] with high probability of correct reconstruction of the sign is implemented. The reconstructed Δy distribution is unfolded accounting for the differences in the signal to background ratio in the measured subchannels. The measurement uses regularized unfolding (package TUnfold) and the asymmetry at the parton level is measured to be $A^{t\bar{t}}_{FB} = 10.6 \pm 2.7(\text{stat.}) \pm 1.3(\text{syst.})$ % which is consistent with the SM calculation $A^{t\bar{t}}_{FB} = 8.8 \pm 0.9$ % [2].

For the differential measurement a 2D unfolding algorithm was developed and the dependencies of the forward-backward asymmetry on the $|\Delta y|$ and on the invariant mass ($m_{t\bar{t}}$) of the $t\bar{t}$ system were studied and are shown on Fig. 2. The correlations between bins are taken into account in the fit of the measured asymmetry and slope is compared to the prediction from MC@NLO. The dependencies are in agreement with the SM predictions.

4 Conclusion

We present recent measurements of the angular production asymmetries in top quark pair lepton+jets and dilepton final states with the D0 detector in full 9.7 fb^{-1} data set. The asymmetry in lepton production from $t\bar{t}$ decay is combined for both channels and extrapolated

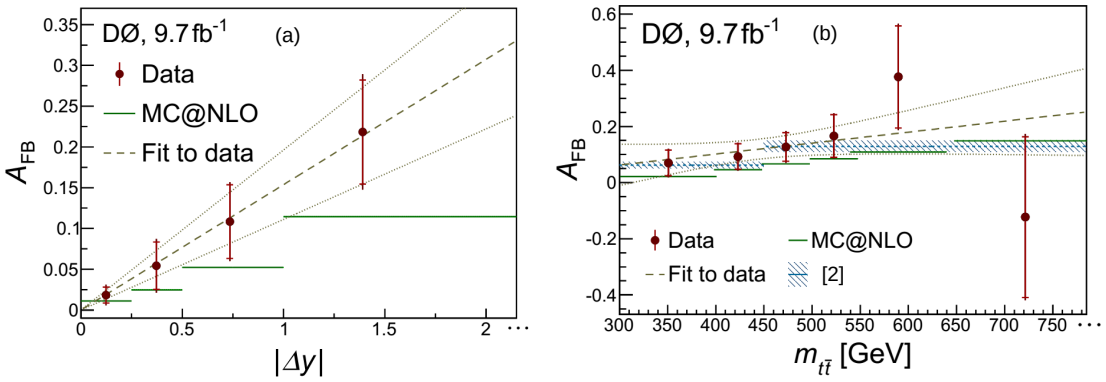

Figure 2: The dependencies of the forward-backward asymmetry on (a) the $|\Delta y|$ and on (b) the invariant mass of the $t\bar{t}$ system. The D0 data points are shown with total uncertainties and are compared to MC@NLO and [2] prediction. The dashed line shows the fit to the data with the dotted lines indicating the fit uncertainty. The last bin has no upper boundary.

to the full acceptance, $A^l_{FB} = 4.7 \pm 2.7$ %, while SM calculation predicts $A^l_{FB} = 3.8 \pm 0.3$ %. The inclusive $t\bar{t}$ production asymmetry in the l+jets channel corrected to the parton level as $A^{t\bar{t}}_{FB} = 10.6 \pm 3.0$ %. It agrees with SM prediction of $A^{t\bar{t}}_{FB} = 8.8 \pm 0.9$ % (NLO + QCD EW) and is in even better agreement with the recent NNLO + QCD EW prediction of ~ 10 %. The D0 results are consistent with SM-based calculations.

References

[1] P. H. Frampton, J. Shu and K. Wang, Phys. Lett. B **683**, 294 (2010).

[2] W. Bernreuther and Z.-G. Si, Phys. Rev. D **86**, 034026 (2012).

[3] M. Czakon, *Latest developments in generators and NNLO computations*, 7th International Workshop on Top Quark Physics, Cannes, France (2014).

[4] V. Abazov *et al.* (D0 Collaboration), Phys. Rev. D **90**, 072001 (2014).

[5] V. Abazov *et al.* (D0 Collaboration), Phys. Rev. D **88**, 112002 (2013).

[6] L. Lyons, D. Gibaut and P. Clifford, Nucl. Instrum. Meth. A **270**, 110 (1988); A. Valassi, Nucl. Instrum. Meth. A **500**, 391 (2003).

[7] V. Abazov *et al.* (D0 Collaboration), Phys. Rev. D **90**, 072011 (2014).

[8] R. Demina, A. Harel and D. Orbaker, arXiv:1310.3263 [hep-ex].

On a four dimensional formulation for dimensionally regulated amplitudes

A.R. Fazio

Departamento de Fisíca, Universidad Nacional de Colombia
Ciudad Universitaria, Bogotá, D.C. Colombia

DOI: http://dx.doi.org/10.3204/DESY-PROC-2014-04/149

We propose a pure four-dimensional formulation (FDF) of the d-dimensional regularization of one-loop scattering amplitudes. In our formulation particles propagating inside the loop are represented by massive internal states regulating the divergences. We present explicit representations of the polarization and helicity states of the four-dimensional particles propagating in the loop. They allow for a complete, four-dimensional, unitarity-based construction of d-dimensional amplitudes. Finally we show how the FDF allows for the recursive construction of d dimensional one-loop integrands, generalizing the four-dimensional open-loop approach.

1 Introduction

The recent development of novel methods for computing one-loop scattering amplitudes in gauge field theory has been highly stimulated by a deeper understanding of their kinematics enforced by on-shellness [1][2] and generalized unitarity [3][4]. Analyticity and unitarity of scattering amplitudes have then been strengthened by the complementary classification of the mathematical structures present in the residues of singular points.

The use of unitarity cuts and complex momenta for on-shell internal particles turned unitarity based methods into very efficient tools for computing scattering amplitudes. These methods exploit two general properties of scattering amplitudes such as unitarity and analyticity: the former granting that amplitudes can be reconstructed from the knowledge of their generalized singularity structures; the latter granting that the residues at singular points factorize in the product of simpler amplitudes [5][6][7].

However one-loop scattering amplitudes arising from a dimensionally regulated theory are the sum of one part containing polylogarithms, the so called "cut constructible" part, and the rational part, which is a rational function of the external spinors and polarizations. Contrarily to the cut-constructible, the rational part cannot be detected in four dimensions.

Based on the paper [8] this talk addresses the possibility of fully reconstructing a one loop amplitude in its cut-constructible and rational part in quantum chromodynamics (QCD) by just gluing tree level amplitudes. Such trees will be obtained by extending the definition of the helicity eigenstates entering the state sum in the propagators of quark and gluons, whithout leaving the four space-time dimensions.

This point of view combines the generalized unitarity cuts in $d = 4 - 2\epsilon$ dimensions with the Four Dimensional Helicity Scheme (*FDH*). The d-dimensional unitarity cuts detect also the

rational part by generalized on-shell conditions and generalized residues [9]. The former imply the vanishing of massive denominators, where the mass term depends both on the physical mass (vanishing or not) of the particle across the cut and on the effective mass parameter encoding the extra-dimensional dependence. Generalized residues computed on the cuts are generated by tree level amplitudes, which depend on the effective mass parameter, hence from the extra dimensions regulating the integrals, either from the generalized polarizations vectors associated to the cut particles, or from the extended algebra of the metric tensor and of the Dirac matrices in the definition of the Feynman rules.

In order to compute the constituting blocks of tree level amplitudes by using the helicity spinor formalism the *FDH* scheme will be used [10], in which the external particles are described by four dimensional Lorentz labels (momenta and helicities) and the internal particles (the so called "unobserved") have still the same numbers of helicity states like in four dimensions. In *FDH* scheme the momenta of the unobserved particles are kept in d dimensions as well as the metric tensor and the Dirac matrices, therefore in diagrammatic computations the algebraic manipulations are implemented by separating the four dimensional algebra from the extra-dimensional one.

In this talk we show that dimensionally regularized one-loop QCD amplitudes in *FDH* scheme can be simply calculated by generalizing the helicity eigenstates of the unobserved particles, by including an effective mass parameter in a pure four-dimensional formalism. The generalized four dimensional polarizations and propagators should be used for tree level and one loop computations avoiding any special decomposition of the particle running around the loop. We want to demonstrate that by an appropriate generalization of the cutted internal legs no supersymmetric decomposition [11] will be needed neither the introduction of new particles and new interactions [12] to afford separately the computation of the cut constructible and the rational part of a scattering amplitude.

2 Generalized internal legs

In this section we are going to provide the explicit expression of the cut legs of a one-loop amplitude involving fermion or vector particles in the loop. Those wave functions will be needed to compute the tree amplitudes to be merged in the reconstruction of the S-matrix elements by unitarity. Their dynamics is described by a pure four dimensional quantum field theory dual to the dimensionally regularised one. The following explicit construction of generalized spinors for fermions and polarization vectors for gluons is suitable for a numerical implementation of such an on-shell procedure of computation. In the following discussion we will decompose a d-dimensional momentum $\bar{\ell}$ as follows

$$\bar{\ell}^\alpha = \ell^\alpha + \mu^\alpha \qquad \bar{\ell}^2 = \ell^2 - \mu^2 = m^2, \tag{1}$$

while its four-dimensional component ℓ will be expressed in terms of the massless momenta $\ell^\flat$ and q_ℓ as

$$\ell = \ell^\flat + \hat{q}_\ell\,, \qquad \hat{q}_\ell \equiv \frac{m^2+\mu^2}{2\,\ell\cdot q_\ell} q_\ell\,. \tag{2}$$

Spinors – The legs of the cut fermion propagtors in the loop have to fulfill the following completness relation [8]

$$\sum_{\lambda=\pm} u_\lambda(\ell)\,\bar{u}_\lambda(\ell) = \ell + i\mu\gamma^5 + m \tag{3}$$

which is satisfied by the following four dimensional spinors

$$u_+(\ell) = \left|\ell^\flat\right\rangle - \frac{(m-i\mu)}{\left[\ell^\flat\, q_\ell\right]}\left|q_\ell\right], \quad u_-(\ell) = \left|\ell^\flat\right] - \frac{(m+i\mu)}{\left\langle\ell^\flat\, q_\ell\right\rangle}\left|q_\ell\right\rangle. \tag{4}$$

Polarization vectors – In the light-cone gauge the d-dimensional polarization vectors fulfill the following relation

$$\sum_{i=1}^{d-2} \varepsilon^\alpha_{i\,(d)}\left(\bar{\ell},\bar{\eta}\right)\varepsilon^{*\beta}_{i\,(d)}\left(\bar{\ell},\bar{\eta}\right) = -\bar{g}^{\alpha\beta} + \frac{\bar{\ell}^\alpha\ \bar{\eta}^\beta + \bar{\ell}^\alpha\,\bar{\eta}^\beta}{\bar{\ell}\cdot\bar{\eta}} - \frac{\bar{\eta}^2\bar{\ell}^\alpha\bar{\ell}^\beta}{(\bar{\eta}\cdot\bar{\ell})^2}, \tag{5}$$

where $\bar{\eta}$ is an arbitrary d-dimensional momentum such that $\bar{\ell}\cdot\bar{\eta}\neq 0$. Gauge invariance in d dimensions guarantees that the unitarity cuts are independent of $\bar{\eta}$. Assuming a four dimensional description we can take the vector μ fixed. The choice $\bar{\eta}^\alpha = \mu^\alpha$ allows for disentangling the four-dimensional contribution from the d-dimensional one:

$$\sum_{i=1}^{d-2} \varepsilon^\alpha_{i\,(d)}\left(\bar{\ell},\bar{\eta}\right)\varepsilon^{*\beta}_{i\,(d)}\left(\bar{\ell},\bar{\eta}\right) \quad = \quad \left(-g^{\alpha\beta} + \frac{\ell^\alpha\ell^\beta}{\mu^2}\right) - \left(\tilde{g}^{\mu\nu} + \frac{\mu^\alpha\mu^\beta}{\mu^2}\right). \tag{6}$$

The first term is related to the cut propagator of a massive gluon whose polarization vectors are

$$\varepsilon^\mu_+(\ell) = -\frac{\left[\ell^\flat\left|\gamma^\mu\right|\hat{q}_\ell\right\rangle}{\sqrt{2}\mu} \quad \varepsilon^\mu_-(\ell) = -\frac{\left\langle\ell^\flat\left|\gamma^\mu\right|\hat{q}_\ell\right]}{\sqrt{2}\mu} \quad \varepsilon^\mu_0(\ell) = \quad \frac{\ell^{\flat\mu} - \hat{q}^\mu_\ell}{\mu}. \tag{7}$$

3 Open loop

The FDF of d-dimensional one-loop amplitudes is compatible with methods generating recursively the integrands of one-loop amplitudes and leads to the complete reconstruction of the numerator of Feynman integrands as a polynomial in ℓ^ν and μ. Our scheme allows for a generalization of the current implementations of these techniques, reconstructing only the four-dimensional part of the numerator of the integrands, which is polynomial in ℓ. In the following we describe how the open-loop technique [13] has to be generalized within the FDF scheme. The subtrees $w^\beta(i)$ recursively merged by connecting their cut lines to vertices and propagators have the following form

$$w^\beta(i) = \frac{X^\beta_{\gamma\delta}(i,j,k)w^\gamma(j)w^\delta(k)}{p_i^2 - m_i^2 + i\epsilon}, \tag{8}$$

where $\frac{X^\beta_{\gamma\delta}}{p_i^2-m_i^2+i\epsilon}$ describes a vertex connecting i,j,k to a propagator attached to i. For one loop amplitudes the numerators of Feynman integrals can be computed by tree-level techniques. For the open loop with indices α and β where a single propagator has been cutted and the

denominator stripped out, the numerator of the amplitude's integrand satisfies the recursive relation

$$\mathcal{N}^{\beta}_{\ \alpha}\left(\mathcal{I}_n,\ell,\mu\right)=X^{\beta}_{\gamma\delta}\left(\mathcal{I}_n,i_n,\mathcal{I}_{n-1}\right)\mathcal{N}^{\gamma}_{\ \alpha}\left(\mathcal{I}_{n-1},\ell,\mu\right)w^{\delta}\left(i_n\right) \tag{9}$$

where w^{δ} is the expression related to the tree-level topology i_n. To achieve the Feynman diagrams expressions in FDH scheme by our FDF formulation the vertices $X^{\beta}_{\gamma\delta}$ are obtained by the Feynman rules in [8]

$$X^{\beta}_{\gamma\delta}=Y^{\beta}_{\gamma\delta}+\ell^{\nu}\,Z^{\beta}_{\nu;\,\gamma\delta}+\mu\,W^{\beta}_{\gamma\delta}\,. \tag{10}$$

Therefore the tensor coefficients of the covariant decomposition of the numerator in a given topology are obtained by the recursive relation

$$\mathcal{N}^{[a]\,\beta}_{\nu_1\cdots\nu_j;\,\alpha}\left(\mathcal{I}_n\right)=\left[Y^{\beta}_{\gamma\delta}\,\mathcal{N}^{[a]\,\gamma}_{\nu_1\cdots\nu_j;\,\alpha}\left(\mathcal{I}_{n-1}\right)+Z^{\beta}_{\nu_1;\,\gamma\delta}\,\mathcal{N}^{[a]\,\gamma}_{\nu_2\cdots\nu_j;\,\alpha}\left(\mathcal{I}_{n-1}\right)+W^{\beta}_{\gamma\delta}\,\mathcal{N}^{[a-1]\,\gamma}_{\nu_1\cdots\nu_j;\,\alpha}\left(\mathcal{I}_{n-1}\right)\right]w^{\delta}(i_n).$$

The recursive generation of integrands within the FDF can be suitably combined with public codes like Samurai and Ninja.

4 Conclusions and outlook

A four-dimensional formulation (FDF) of dimensional regularization of one-loop scattering amplitudes has been applied to generalized unitarity techniques. At one loop the cut-constructible part and the rational part of scattering amplitudes have been computed by the same on-shell methods. The inclusion of the fermion mass and the two loop case will be analysed elsewhere.

References

[1] F.Cachazo, P. Svrcek and E. Witten, JHEP 09 006 (2004).

[2] R. Britto, F. Cachazo, B. Feng, Nucl. Phys. B715 499 (2005).

[3] Z. Bern, L.J. Dixon, D.C. Dunbar, D.A. Kosower, Nucl. Phys. B425 217 (1994).

[4] R. Britto, F. Cachazo, B. Feng, Nucl. Phys. B725 275 (2005).

[5] C. F. Berger and D. Forde, Ann.Rev.Nucl.Part.Sci. 60,181 (2010).

[6] R. Britto, J.Phys. A44, 454006 (2011), 34 pages.

[7] R. Ellis, Z. Kunszt, K. Melnikov, and G. Zanderighi, Phys.Rept. 518 (2012) 141-250 (2011).

[8] A.R. Fazio, P. Mastrolia, E. Mirabella, W.J. Torres, arXiv:14044783 [hep-ph].

[9] Z. Bern and A. G. Morgan, Nucl. Phys., B467 479 (1996).

[10] A. Signer, D. Stockinger, Nucl.Phys. B808 88 (2009).

[11] A. Brandhuber, S. McNamara, B. J. Spence, G. Travaglini, JHEP 0510 11 (2005).

[12] R. Pittau, JHEP 1202 29 (2012).

[13] F. Cascioli, P. Maierhofer, S. Pozzorini, Phys. Rev. Lett. 108 111601 (2012).

Chapter 10

Beyond standard model

Search for electroweak supersymmetry production at CMS

Mario Masciovecchio[1] on behalf of the CMS Collaboration

[1] Institute for Particle Physics, ETH Zürich, 8093 Zürich, Switzerland

DOI: http://dx.doi.org/10.3204/DESY-PROC-2014-04/195

The latest results from the CMS experiment [1] at the LHC on searches for supersymmetry produced through electroweak production channels are presented using about 20 fb^{-1} of data from the 8 TeV LHC run. A variety of complementary final state signatures and methods are used, such as searches with Higgs, W, and Z bosons in the final state, to probe gaugino and slepton production.

1 Introduction

Many searches for supersymmetry (SUSY) at the LHC focused on models with strongly interacting new particles in final states with high levels of hadronic activity have constrained the squarks and gluinos to be heavier than several hundreds GeV. Other searches are focused on the direct electroweak production of charginos $\tilde{\chi}i^{\pm}$ and neutralinos $\tilde{\chi}^0$, i.e., mixtures of the SUSY partners of the gauge and Higgs bosons, and of sleptons $\tilde{l}$, i.e., the SUSY partners of leptons. Such production modes may dominate if the strongly interacting SUSY particles are heavy. A wide variety of signal topologies are targeted by electroweak SUSY searches at CMS. Here, searches are presented for electroweak pair production of neutralinos and charginos that decay to h^0h^0, h^0Z, and h^0W final states.

2 Gauge Mediated Supersymmetry Breaking models with Higgs bosons in the final state

A R-parity conserving gauge mediated SUSY breaking (GMSB) model is considered [2], in which the two lightest neutralinos $\tilde{\chi}_1^0$ and $\tilde{\chi}_2^0$, and the lightest chargino $\tilde{\chi}_1^{\pm}$ are higgsinos, approximately mass degenerate, with $\tilde{\chi}_1^0$ being the lightest of the three states. The lightest SUSY particle (LSP) is a gravitino $\tilde{G}$, i.e., the SUSY partner of the graviton. The $\tilde{\chi}_2^0$ and $\tilde{\chi}_1^{\pm}$ higgsinos decay to the lightest higgsino $\tilde{\chi}_1^0$, plus Standard Model (SM) particles with low transverse momentum. The $\tilde{\chi}_1^0$ is the next-to-lightest SUSY particle (NLSP) and it undergoes a two-body decay to a $h^0\tilde{G}$, or $Z\tilde{G}$, with $\tilde{G}$ being nearly massless and stable.

2.1 Search in the $\mathbf{h^0h^0 \to b\bar{b}b\bar{b}}$

With a branching fraction of about 0.56, Higgs decays to $b\bar{b}$ represent the most likely decay mode of the Higgs boson. Therefore, the $h^0(\to b\bar{b})h^0(\to b\bar{b})$ final state provides a sensitive

search channel for SUSY h^0h^0 production. Each Higgs boson is reconstructed in its decay to a $b\bar{b}$ pair. The data are consistent with the Standard Model predictions within uncertainties (Fig. 1).

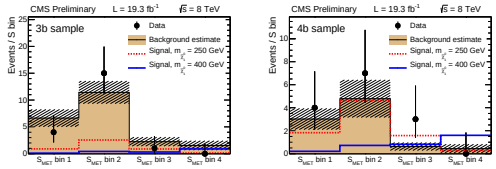

Figure 1: Results of search for $h^0(\to b\bar{b})h^0(\to b\bar{b}) + E_{\mathrm{T}}^{\mathrm{miss}}$ final states.

2.2 Search in the h^0h^0, h^0Z, h^0W channels with one $h^0 \to \gamma\gamma$

Searches for h^0h^0, h^0Z, h^0W states in channels with one Higgs boson that decays to photons are described. The other boson (h^0, Z, or W) decays to a final state with at least one lepton (electron or muon).

2.2.1 h^0Z, h^0W to $\gamma\gamma$ + jets

For the h^0Z and h^0W channels with $h^0 \to \gamma\gamma$ and either $W \to 2$ jets or $Z \to 2$ jets, the vector boson candidate is formed from two jets that yield a dijet mass m_{jj} consistent with the mass of a W or Z boson. The Higgs boson is reconstructed from a pair of photons. The data are consistent with the Standard Model predictions within uncertainties (Fig. 2).

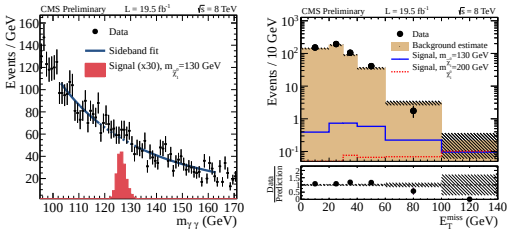

Figure 2: Results of search for h^0Z, h^0W to $\gamma\gamma$ + jets final states.

2.2.2 h^0h^0, h^0Z, h^0W to $\gamma\gamma$ + leptons

Searches for h^0h^0, h^0Z, h^0W states in channels with one Higgs boson that decays to photons are described. The other boson (h^0, Z, or W) decays to a final state with at least one lepton (electron or muon). A sample with at least one muon and an orthogonal sample with no muons but at least one electron are selected. For the muon channel, the data exhibit a small deficit with respect to the SM background estimate, while for the electron channel, there is an excess of 2.1 standard deviations (Fig. 3).

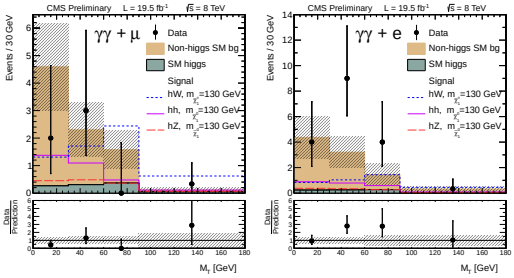

Figure 3: Results of search for h^0h^0 h^0Z, h^0W to $\gamma\gamma$ + leptons final states.

2.3 Search in the h^0Z channel with $h^0 \to b\bar{b}$ and $Z \to l^+l-$

A search in the h^0Z channel, with $h^0 \to b\bar{b}$ and $Z \to l^+l^-$ (with $l = e, \mu$) is presented. Events are required to contain exactly one same flavour opposite sign dilepton pair, with a dilepton invariant mass in the Z boson mass region. , and at least two tagged b jets, with the di-jet mass reconstructed from the two most b-like jets in the Higgs boson mass region. Data are in agreement with Standard Model prediction (Fig. 4).

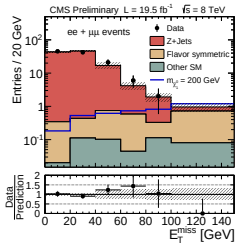

Figure 4: Results of search for h^0Z to $b\bar{b}$ + l^+l^- final states.

2.4 Interpretation

Figure 5 presents the 95% confidence level exclusion region for the GMSB higgsino NLSP scenario in the two-dimensional plane of the $\tilde{\chi}_1^0 \to h^0\tilde{G}$ branching fraction versus the higgsino mass $m_{\tilde{\chi}_1^0}$. The combination of the results discussed above exclude a significant fraction of the plane.

3 $h^0W + E_T^{miss}$

Searches for direct electroweak production of SUSY charginos and neutralinos in final states with a Higgs boson are presented [3]. A $\tilde{\chi}^{\pm}]\tilde{\chi}^0$ pair is produced, and decays to a W boson, a Higgs boson, and missing transverse energy from escaping lightest SUSY particles. Three channels are explored, depending on the particles detected in the final state: single lepton,

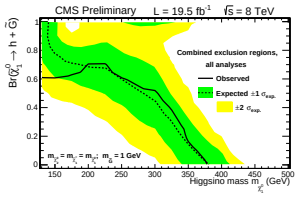

Figure 5: Observed and expected 95% confidence level exclusion regions for higgsino pair production.

same sign dilepton, and multilepton channels. The data are consistent with the Standard Model backgrounds (Fig. 6). Results are combined with the ones presented in Sec. 2.2.2 and

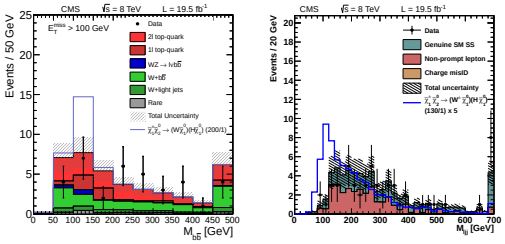

Figure 6: Results of searches for $h^0W + E_T^{miss}$ final states.

are used to set constraints on the mass of charginos and neutralinos up to 204 GeV (Fig. 7).

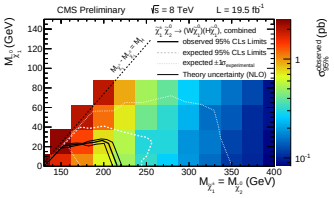

Figure 7: Interpretation of searches for $h^0W + E_T^{miss}$ final states.

References

[1] S. Chatrchyan et al. The CMS experiment at the CERN LHC. *JINST*, 3:S08004, 2008.

[2] Vardan Khachatryan et al. Searches for electroweak neutralino and chargino production in channels with Higgs, Z, and W bosons in pp collisions at 8 TeV. 2014.

[3] Vardan Khachatryan et al. Searches for electroweak production of charginos, neutralinos, and sleptons decaying to leptons and W, Z, and Higgs bosons in pp collisions at 8 TeV. *Eur.Phys.J.*, C74(9):3036, 2014.

Third Generation SUSY Searches at CMS

Florent Lacroix[1] on behalf of the CMS collaboration

[1]University of California Riverside, CA 92521, U.S.A.

DOI: http://dx.doi.org/10.3204/DESY-PROC-2014-04/191

In this talk, the latest results from CMS on searches for stop and sbottom squarks are presented. Searches for direct squark production and indirect production through gluino cascades in a variety of decay channels are reviewed. The results are based on 20/fb of data collected during the 8 TeV LHC run.

1 Introduction

Supersymmetry (SUSY) is a popular extension of the standard model (SM), offering an additional symmetry of nature between fermions and bosons. A new supersymmetric partener particle (sparticle) is proposed for each SM particle, providing an elegant mechanism to mitigate the hierarchiy problem. The symmetry is not exact, as no sparticles have been observed experimentally; however the stabilising features of SUSY can survive if sparticles are not too much heavier than their SM partners. The third generation in particular offers scope to search for SUSY because of the relatively large mass of the top quark. The mass difference between the stop quark and its SUSY partener the top squark must be small to provide a "natural" solution to the hierarchy problem, and similarly for the bottom quark and the sbottom squark. They may be accessible at the TeV scale, and pair produced at the LHC.

This paper presents the latest results of the searches performed with the CMS detector [1] looking for direct and indirect production of the third generation squarks in a variety of decay channels. The results are based on the data collected during the 2012 8 TeV LHC run.

2 Direct top squark production

Light (stop1) and heavy (stop2) stop squarks can be directly pair produced at the LHC via gluon fusion or quark annihilation and are investigated in CMS by a broad search program.

2.1 Light stop results

Several analyses have been performed in CMS to search for the direct production of a pair of light stop, assuming that the stop decays to a top quark and a neutralino: a fully hadronic search using a top tagger [2], an inclusive analysis based on the razor variables [3], a fully hadronic analysis using the MT2 variable [4] and an analysis looking to the single-lepton final state [5]. The razor and single-lepton results have been combined in a recent publication [6].

If the mass difference between the stop squark and the lighest supersymmetric particle (LSP) is very small, the stop decays to a charm quark and the LSP through loop. In this case the

charm jets are expected to be relatively soft and hidden by the low energy QCD background events or too soft for the CMS detector to identify. However these events can be detected if they are accompanied by initial state radiation (ISR). Provided final state particles are invisible, such events contain a high pt jet and missing transverse energy. A monojet analysis have been designed to search for these events [7].

No significant deviations from the standard model predictions have been observed in all these analyses. Results are interpreted as exclusion limits on Simplified Model Spectra and are presented in Figure 1.

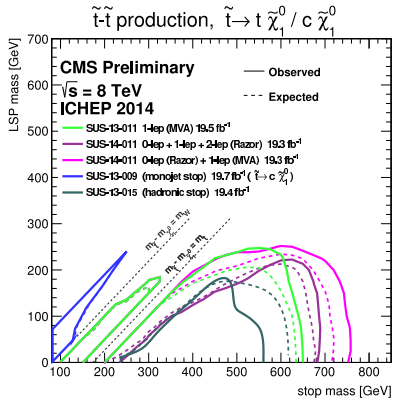

Figure 1: Expected and observed limit curves for stop pair production, assuming 100% branching fraction of the stop decay mode to a top quark and a neutralino or, in case of a highly compressed spectrum, the stop decay mode to a charm quark and a neutralino.

The stop squark can also decay into a chargino and a b-jet, with the chargino decaying into a W boson and a neutralino. This model has been studied in the reference [5] where the limits obtained are shown for different mass relations for the chargino, neutralino and stop squark. The sensitivity is dependent on assumptions made on the chargino polarization and the left/right handedness of the coupling. An other interpretation with chargino is presented in the reference [6], assuming a mass difference of 5 GeV between the chargino and the neutralino, resulting in a decay with a virtual W.

2.2 Heavy stop results

Several analyses are looking to heavy stop pair production. In this case the stop2 decays to stop1 and either a Higgs boson or a Z boson. The resuls of the single-lepton+2 opposite charge leptons analysis [8], the same-sign dileptons analysis [9] and the 3-leptons analysis [10] have been combined and are presented in the reference [11]. The limits obtained for Higgs only and Z only decays are presented in Figure 2, but mixed branching ratio scenario results are also avialable in the reference [11].

2.3 Other direct stop searches

Some R-parity violating models have also been investigated by CMS, with a search for anomalous production of events with three or more isolated leptons and at least one b-jet produced [12].

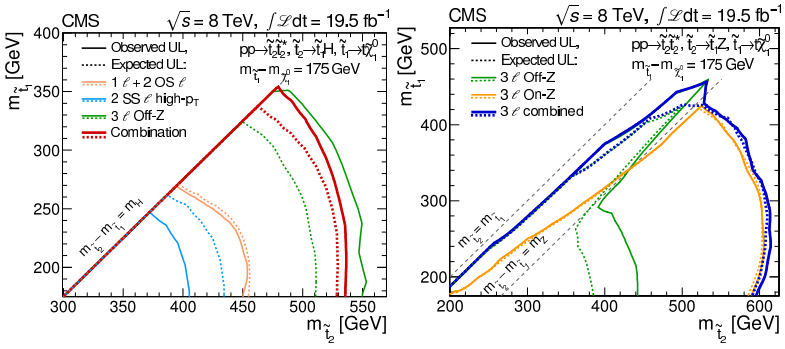

Figure 2: Observed (expected) exclusion contours, which are indicated by the solid (dashed) curves for the contributing channels. The excluded region in the m(stop1) and m(stop2) parameter space is obtained assuming that the stop2 decays to stop1 and a Higgs boson in the left plot and assuming a decay to stop1 and Z boson in the right plot.

There is also a program of gauge mediated susy breaking scenarios using diphoton Higgs decays [13] and three leptons events [10].

3 Direct sbottom production

Instead of a pair of stop squarks, a pair of sbottom squarks can be produced in LHC collisions. Three decays of the sbottom squarks have been investigated:

- b quark and a neutralino;
- top quark and a chargino, with the chargino decaying in a W boson and a neutralino;
- b quark and a neutralino 2, with the neutralino 2 decaying in a Z boson and a neutralino 1.

The first model has been investigated by a dedicated sbottom search [14] and with the inclusive MT2 analysis [4]. A multilepton search [15], the same-sign dilepton search [9] and the three leptons search [10] have been used to search for the second model with a chargino. The third model has been investigated by the three leptons search [10], assuming a mass difference between the neutralinos of 110 GeV. In this case the neutralino 2 is indeed decaying only to a Z boson and the LSP, the decay with a Higgs boson being forbidden.

4 Gluino mediated production

Stop and sbottom are also searched in gluino mediated processes, looking for deviation in specific final states that can be produced if an intermidiate third generation squark has been involved in the process. They have been investigated in models where the stop/sbottom squarks are produced off-shell, in which case the third generation squarks existence is probed indirectly.

The first simplified model considered (T1bbbb) is when the pair produced gluinos decay to two b jets and a neutralino. This leads to a purely hadronic final state and has been

investigated by the razor analysis [6], the met+ht analysis [16], the alphaT analysis [17] and the MT2 analysis [4].

The other simplified model considered (T1tttt) is when the gluinos decay to two top quark and a neutralino. All the lepton multiplicities in the final state are investigated by different analyses: 0-lepton analyses [4, 6, 16, 17], 1-lepton analyses [18], 2-leptons analyses [9, 19] and 3-leptons analyses [10, 15].

The results of these two models are presented in Figure 3.

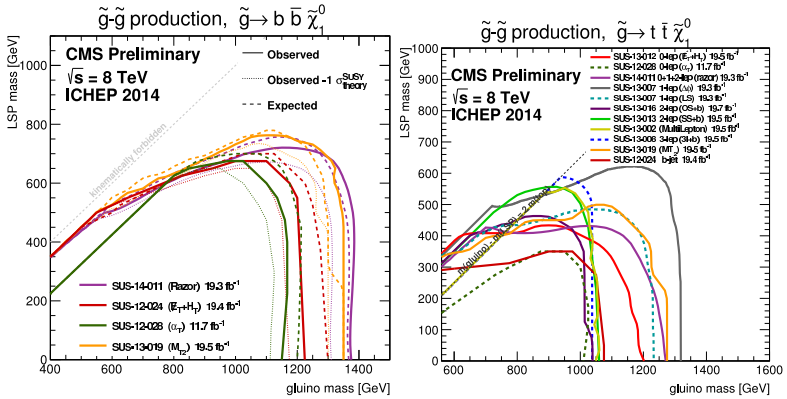

Figure 3: Expected and observed limit curves in the (LSP mass, gluino mass) plane for the T1bbbb (left) and T1tttt (right) simplified models.

The mixed branching ratios scenarios (T1tbbb, T1ttbb and T1tttb) have also been studied with the razor analysis [6]. The limits obtained for mixed branching ratios lie within the T1bbbb and the T1tttt contours. So the limit obtained with the razor analysis for the model where both gluinos decay to top quarks can be considered as a conservative branching ratio independent limit.

The gluino mediated stop and sbottom squarks production has also been investigated when the stop/sbottom are produced on-shell. On-shell stop squark in gluino decay are investigated by the single-lepton search [18], the same-sign dilepton search [20] and the three lepton search [10]. Two analyses interpret their results in term of on-shell sbottom squark: the same-sign dilepton search [20] and the three lepton search [10].

5 Conclusion

The CMS program to discover third generation SUSY is wide and rich, covering many topologies and final states. So far no significant hint of SUSY particle has been observed, putting the naturalness of the SM Higgs under severe pressure. However the missing corners need to be explored, in particular with the future data taken with a higher energy in the centre of mass.

References

[1] S. Chatrchyan *et al.* [CMS Collaboration], "The CMS experiment at the CERN LHC," JINST **3**, S08004 (2008).

[2] CMS Collaboration [CMS Collaboration], "Search for top squarks in multijet events with large missing momentum in proton-proton collisions at 8 TeV," CMS-PAS-SUS-13-015.

[3] CMS Collaboration [CMS Collaboration], "Search for supersymmetry using razor variables in events with b-jets in pp collisions at 8 TeV," CMS-PAS-SUS-13-004.

[4] CMS Collaboration [CMS Collaboration], "Search for supersymmetry in hadronic final states using MT2 with the CMS detector at sqrt(s) = 8 TeV," CMS-PAS-SUS-13-019.

[5] S. Chatrchyan *et al.* [CMS Collaboration], "Search for top-squark pair production in the single-lepton final state in pp collisions at $\sqrt{s}$ = 8 TeV," Eur. Phys. J. C **73**, 2677 (2013) [arXiv:1308.1586 [hep-ex]].

[6] CMS Collaboration [CMS Collaboration], "Exclusion limits on gluino and top-squark pair production in natural SUSY scenarios with inclusive razor and exclusive single-lepton searches at 8 TeV.," CMS-PAS-SUS-14-011.

[7] CMS Collaboration [CMS Collaboration], "Search for top squarks decaying to a charm quark and a neutralino in events with a jet and missing transverse momentum," CMS-PAS-SUS-13-009.

[8] CMS Collaboration [CMS Collaboration], "higgs from stop decay (h to bb)," CMS-PAS-SUS-13-021.

[9] CMS Collaboration [CMS Collaboration], "Search for new physics in events with same-sign dileptons and jets in pp collisions at 8 TeV," CMS-PAS-SUS-13-013.

[10] CMS Collaboration [CMS Collaboration], "Search for supersymmetry in pp collisions at sqrt(s) = 8 TeV in events with three leptons and at least one b-tagged jet," CMS-PAS-SUS-13-008.

[11] V. Khachatryan *et al.* [CMS Collaboration], "Search for top-squark pairs decaying into Higgs or Z bosons in pp collisions at $\sqrt{s}$=8 TeV," Phys. Lett. B **736**, 371 (2014) [arXiv:1405.3886 [hep-ex]].

[12] S. Chatrchyan *et al.* [CMS Collaboration], "Search for top squarks in *R*-parity-violating supersymmetry using three or more leptons and b-tagged jets," Phys. Rev. Lett. **111**, no. 22, 221801 (2013) [arXiv:1306.6643 [hep-ex]].

[13] S. Chatrchyan *et al.* [CMS Collaboration], "Search for top squark and higgsino production using diphoton Higgs boson decays," Phys. Rev. Lett. **112**, 161802 (2014) [arXiv:1312.3310 [hep-ex]].

[14] CMS Collaboration [CMS Collaboration], "Search for direct production of bottom squark pairs," CMS-PAS-SUS-13-018.

[15] S. Chatrchyan *et al.* [CMS Collaboration], "Search for anomalous production of events with three or more leptons in pp collisions at sqrt(s) = 8 TeV," Phys. Rev. D **90**, 032006 (2014) [arXiv:1404.5801 [hep-ex]].

[16] S. Chatrchyan *et al.* [CMS Collaboration], "Search for gluino mediated bottom- and top-squark production in multijet final states in pp collisions at 8 TeV," Phys. Lett. B **725**, 243 (2013) [arXiv:1305.2390 [hep-ex]].

[17] S. Chatrchyan *et al.* [CMS Collaboration], "Search for supersymmetry in hadronic final states with missing transverse energy using the variables α_T and b-quark multiplicity in pp collisions at $\sqrt{s}$ = 8 TeV," Eur. Phys. J. C **73**, 2568 (2013) [arXiv:1303.2985 [hep-ex]].

[18] S. Chatrchyan *et al.* [CMS Collaboration], "Search for supersymmetry in pp collisions at $\sqrt{s}$=8 TeV in events with a single lepton, large jet multiplicity, and multiple b jets," Phys. Lett. B **733**, 328 (2014) [arXiv:1311.4937 [hep-ex]].

[19] CMS Collaboration [CMS Collaboration], "Search for supersymmetry in pp collisions at sqrt(s) = 8 Tev in events with two opposite sign leptons, large number of jets, b-tagged jets, and large missing transverse energy.," CMS-PAS-SUS-13-016.

[20] S. Chatrchyan *et al.* [CMS Collaboration], "Search for new physics in events with same-sign dileptons and jets in pp collisions at $\sqrt{s}$ = 8 TeV," JHEP **1401**, 163 (2014) [arXiv:1311.6736, arXiv:1311.6736 [hep-ex]].

Search for Higgs Bosons Beyond the Standard Model with the CMS Detector

Matthias Schröder on behalf of the CMS Collaboration

DESY, Notketraße 85, 22607 Hamburg, Germany

DOI: http://dx.doi.org/10.3204/DESY-PROC-2014-04/190

After a Higgs boson with a mass near 125 GeV has been discovered, it is still unclear whether this is the Higgs boson predicted by the standard model (SM). Various models with extended Higgs sectors are being considered, such as the minimal supersymmetric extensions of the SM. Recent results of searches for non-SM Higgs bosons with the CMS detector are presented, which are based on pp collision data collected at centre-of-mass energies of 7 and 8 TeV corresponding to integrated luminosities of about 5 and 20 fb^{-1}.

While the recently discovered Higgs boson with a mass near 125 GeV [1] is consistent with the standard model (SM) expectations, non-SM couplings are only excluded up to branching ratios of $\approx 30\%$ with the current data [2]. Furthermore, numerous BSM models predict extended Higgs sectors. The minimal supersymmetric extension (MSSM) [3], for example, requires two complex Higgs doublets, one of which couples to the u-type and one to the d-type fermions. After electroweak symmetry breaking, five physical states remain: a light and a heavy CP-even boson h and H, an CP-odd boson A, all of which are neutral and collectively denoted Φ, and two charged bosons $\mathrm{H}^{\pm}$. At tree level, the MSSM Higgs sector is completely defined by two parameters, conventionally chosen as the mass $\mathrm{m_A}$ of the CP-odd boson and the ratio $\tan\beta$ of the vacuum expectation values of the two doublets.

In this article, recent results of direct searches both for additional Higgs bosons and for non-SM decays of the 125 GeV boson conducted by the CMS experiment [4] at the LHC are reviewed: a search for a heavy neutral Higgs boson $\Phi \to \tau\tau$, for a light charged Higgs boson $\mathrm{H}^+ \to \mathrm{c\bar{s}}$, and for lepton-flavour violating Higgs boson decays $\mathrm{H} \to \mu\tau$. The analyses are performed with 4.9 and 19.7 fb^{-1} of data collected at centre-of-mass energies $\sqrt{s}$ of 7 and 8 TeV, respectively. A particle-flow algorithm [5] is used to reconstruct the individual particles in the events, from which hadronically decaying taus τ_h, the missing transverse momentum $\not\!\!E_\mathrm{T}$, and jets are clustered. Jets initiated by b-quarks are identified (b-tagged) with a likelihood discriminant combining track-based lifetime and secondary-vertex information [6].

1 Searches for heavy neutral Higgs bosons

At the LHC, the neutral MSSM Higgs bosons Φ are expected to be predominantly produced either in gluon-gluon fusion or in b-quark associated production. For larger values of $\tan\beta$, the latter mode dominates, and at the same time, the branching fraction ($\mathcal{B}$) to τ leptons is also enhanced relative to the SM over the whole $\mathrm{m_A}$ range. CMS has performed a search for $\Phi \to \tau\tau$ using the full 25 fb^{-1} of the 7 and 8 TeV data and considering five $\tau\tau$ final-states, $\mathrm{e}\tau_\mathrm{h}$, $\mathrm{e}\mu$, $\mu\tau_\mathrm{h}$,

$\mu\mu$, and $\tau_h\tau_h$ [7]. Events are collected using a combination of e, μ, and τ_h triggers, whose criteria varied during the data-taking periods. Offline, events are further selected requiring two oppositely charged, well isolated leptons. Additional channel-dependent selection criteria are applied to suppress contributions from SM background processes; for example, in the $\mu\tau_h$ channel the transverse mass of the μ and the $\not\!\!E_T$ is required to be less than 30 GeV to reject W+jets events. Moreover, the selected events are split into two categories of either 0 or ≥ 1 b-tagged jets to enhance the sensitivity to the different production modes.

The invariant mass $m_{\tau\tau}$ of the di-τ system is reconstructed from the leptons and $\not\!\!E_T$ in the event using a maximum-likelihood technique based on a model of the τ-decay phase-space and the $\not\!\!E_T$ resolution, which results into a relative mass resolution of typically 20% at 90 GeV. The $m_{\tau\tau}$ distribution observed in the $\mu\tau_h$ 0-b-tag channel is shown in Fig. 1 (left). The dominant SM background contribution arises from $Z \to \tau\tau$ events and is determined from data with an embedding technique, where the muons in $Z \to \mu\mu$ events are replaced by simulated τ-decay products. Further important backgrounds are due to W+jets and QCD-multijet events with jets mis-identified as τ_h and μ and are estimated from signal-depleted control regions in data.

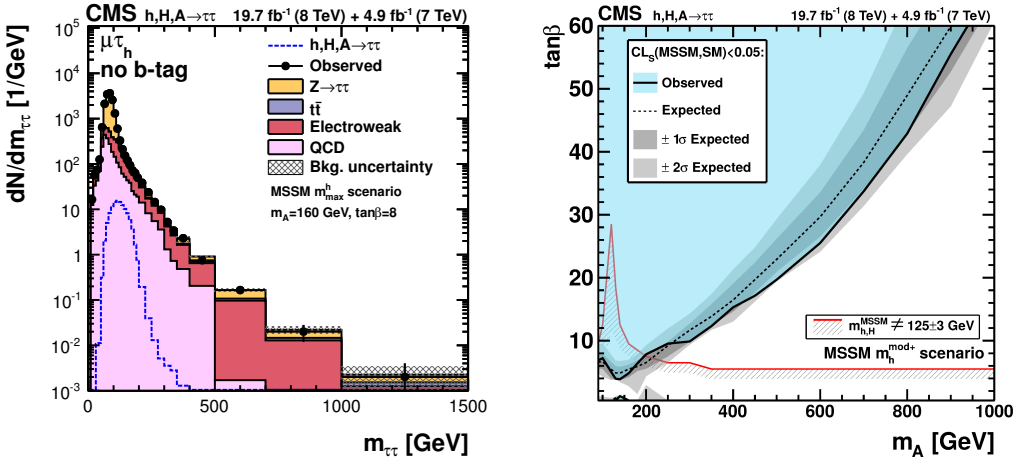

Figure 1: $m_{\tau\tau}$ distribution in the $\mu\tau_h$ 0-b-tag channel (*left*) and 95% C. L. exclusion limits on the MSSM parameters m_A and $\tan\beta$ (area above the black lines is excluded) in the $m_h^{\text{mod+}}$ scenario (*right*); the region above the red line is compatible with a 125 GeV Higgs boson.

In all channels, the observed data agree well with the SM-only expectation. Thus, model-independent upper limits are derived on the resonance production rate $\sigma \times \mathcal{B}(\Phi \to \tau\tau)$. The results are also interpreted as constraints on the MSSM parameters, expressed as limits at 95% confidence level (C. L.) in $(\tan\beta, m_A)$ space assuming the other MSSM parameters to be fixed at certain benchmark values. In all cases, the signal hypothesis is tested against a background plus SM-Higgs hypothesis, thus taking into account the Higgs boson at 125 GeV. Likewise, the MSSM interpretation is not only performed in the traditionally used m_h^{max} benchmark scenario but also in several other recently proposed scenarios [8] that are compatible with either h or H having a mass of 125 GeV in most parts of the parameter space. This is not the case in the m_h^{max} scenario, which is therefore disfavoured by data. The sensitivity in the $m_h^{\text{mod+}}$ scenario [8], for example, reaches up to $m_A = 1$ TeV and down to $\tan\beta = 5$ at low m_A, cf. Fig. 1 (right).

2 Search for light charged Higgs bosons

If the charged Higgs boson H^+ predicted by the MSSM is lighter than the mass difference of the t- and b-quarks, t quarks can decay as $t \to H^+b$, and if $\tan\beta < 1$, the H^+ decays predominantly to a $c\bar{s}$-quark pair (charge conjugation is implied). CMS has performed a search for light H^+ bosons in $t\bar{t} \to H^+(\to c\bar{s})bW^-(\to \mu\nu)b$ events in $19.7\,\text{fb}^{-1}$ of data at $\sqrt{s} = 8\,\text{TeV}$ [9].

Events are collected triggering on an isolated μ with $p_T > 24\,\text{GeV}$. Offline, exactly one μ is required to suppress contributions from Z+jets and $t\bar{t}$ events. Furthermore, four central jets with $p_T > 30\,\text{GeV}$, two of which are b-tagged, and $\not{E}_T > 20\,\text{GeV}$ are required. After this selection, the expected SM contributions arise almost exclusively from $t\bar{t}$ events in the semi-leptonic decay channel. Assuming that the $t\bar{t}$ production cross-section remains un-altered, a signal would manifest in the invariant dijet-mass distribution of the two non-b-tagged jets as a deficit of events at the W mass and an excess at the H^+ mass compared to the SM expectation due to the additional decay-channel. The mass resolution is significantly improved using a kinematic fit to reconstruct the $t\bar{t}$ event, where the t-quark mass is constraint to 172.5 GeV.

Since no significant deviation is observed, model-independent upper limits at 95% C. L. on $\mathcal{B}(t \to H^+b)$ are derived assuming $\mathcal{B}(H^+ \to c\bar{s}) = 100\%$, cf. Fig. 2 (left). The limits range from 2 to 7% for H^+ masses between 90 and 160 GeV.

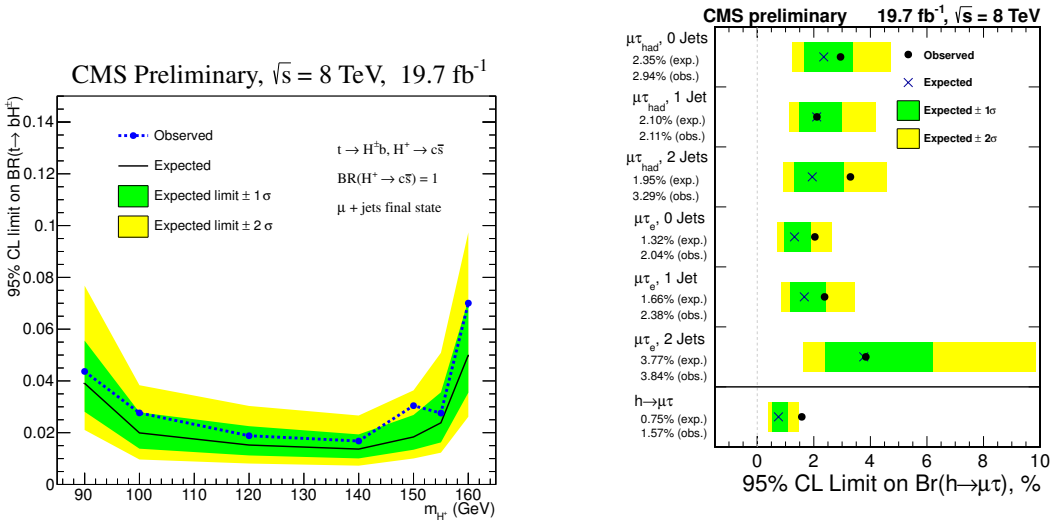

Figure 2: Upper limits at 95% C. L. on $\mathcal{B}(t \to H^+b)$ assuming $\mathcal{B}(H^+ \to c\bar{s}) = 100\%$ (*left*) and on $\mathcal{B}(H \to \mu\tau)$ in the different channels and their combination (*right*).

3 Search for lepton-flavour violating Higgs boson decays

While lepton-flavour violating (LFV) Higgs boson decays are not allowed in the SM, they can occur naturally in various BSM models such as composite-Higgs and Randall-Sundrum models. CMS has performed the first direct search for LFV decays $H \to \mu\tau$ of the 125 GeV Higgs boson in the $\mu\tau_e$ and $\mu\tau_h$ final states using $19.7\,\text{fb}^{-1}$ of 8 TeV data [10].

Events are collected triggering on an isolated μ and e with p_{T} above 17 and 8 GeV, respectively, in the $\mu\tau_{\mathrm{e}}$ channel and an isolated μ with $p_{\mathrm{T}} > 17$ GeV in the $\mu\tau_{\mathrm{h}}$ channel. Offline, the leptons are required to have opposite charge, and events are further divided into jet-multiplicity categories to enhance the sensitivity to different production modes. Further selection criteria to suppress SM contributions exploit that the μ in signal events stems promptly from the LFV decay and thus tends to have larger p_{T} than in SM $\mathrm{H} \to \tau_{\mu}\tau_{\mathrm{e/h}}$ events for example. An important residual background arises from $\mathrm{Z} \to \tau\tau$ and is estimated from data using the aforementioned embedding technique. Depending on the channel, further main backgrounds are due to W+jets, QCD-multijet, and $\mathrm{t\bar{t}}$ events, in which jets are mis-reconstructed as leptons or τ_{h} and which are determined from control regions in data using estimates of the mis-reconstruction rate. The invariant $\mu\tau$ mass is approximated from the μ, the visible τ decay products τ_{vis}, and the $\not{E}_{\mathrm{T}}$ component along τ_{vis}, which is assumed to be collinear to the ν due to the high boost of the τ.

No significant excess of events above the SM expectation is observed in the mass distributions. The combined upper limit at 95% C. L. on the LFV $\mathcal{B}(\mathrm{H} \to \mu\tau)$ is $(0.75 \pm 0.38)\%$ expected and 1.57% observed, cf. Fig. 2 (right). Interpreted as signal, it corresponds to $\mathcal{B}(\mathrm{H} \to \mu\tau) = (0.89^{+0.40}_{-0.37})\%$, i. e. a significance of 2.5 standard deviations. The limit is also translated into constraints on $\mu\tau$ Yukawa couplings, improving earlier results from indirect measurements by an order of magnitude.

4 Conclusions

CMS has performed a wide variety of searches both for non-SM properties of the 125 GeV Higgs boson and for additional Higgs bosons. In this article, searches for heavy neutral and for light charged Higgs bosons as well as for lepton-flavour violating decays have been discussed, which have been performed with up to $25\,\mathrm{fb}^{-1}$ of 7 and 8 TeV data. No significant deviation from the SM is observed, and the results are used to derive valuable constraints on the BSM-Higgs parameter space, which mostly exclude for example the low-$\mathrm{m_A}$ region of the MSSM.

References

[1] CMS Collaboration. Observation of a new boson with mass near 125 GeV in pp collisions at $\sqrt{s} = 7$ and 8 TeV. *JHEP*, 1306:081, 2013.

[2] CMS Collaboration. Precise determination of the Higgs boson mass and studies of the compatibility of its couplings with the standard model. CMS Physics Analysis Summary CMS-PAS-HIG-14-009, CERN, 2014.

[3] H.P. Nilles. Supersymmetry, supergravity and particle physics. *Physics Reports*, 110(1-2):1–162, 1984.

[4] CMS Collaboration. The CMS experiment at the CERN LHC. *JINST*, 3:S08004, 2008.

[5] CMS Collaboration. Particle-flow event reconstruction in CMS and performance for jets, taus, and MET. CMS Physics Analysis Summary CMS-PAS-PFT-09-001, CERN, 2009.

[6] CMS Collaboration. Performance of b tagging at $\sqrt{s} = 8$ TeV in multijet, $\mathrm{t\bar{t}}$ and boosted topology events. CMS Physics Analysis Summary CMS-PAS-BTV-13-001, CERN, 2013.

[7] CMS Collaboration. Search for neutral MSSM Higgs bosons decaying to a pair of tau leptons in pp collisions. CMS Physics Analysis Summary CMS-PAS-HIG-13-021, CERN, 2014.

[8] M. S. Carena et al. MSSM Higgs Boson Searches at the LHC: Benchmark Scenarios after the Discovery of a Higgs-like Particle. *Eur.Phys.J.*, C73:2552, 2013.

[9] CMS Collaboration. Search for a light charged Higgs boson in the $\mathrm{H}^{+} \to \mathrm{c\bar{s}}$ channel at CMS. CMS Physics Analysis Summary CMS-PAS-HIG-13-035, CERN, 2014.

[10] CMS Collaboration. Search for Lepton Flavour Violating Decays of the Higgs Boson. CMS Physics Analysis Summary CMS-PAS-HIG-14-005, CERN, 2014.

Search for Dark Matter at CMS

Kerstin Hoepfner on behalf of the CMS collaboration
RWTH Aachen University, Otto-Blumenthal-Str., 52074 Aachen, Germany

DOI: http://dx.doi.org/10.3204/DESY-PROC-2014-04/193

The latest results from CMS searches for dark matter are presented based on 20/fb of pp collision data collected at $\sqrt{s}$= 8 TeV at the LHC. Analyses are performed in several final states, including a single jet/photon/W-boson or a single top quark as well as production in association with $t\bar{t}$-pairs. No indication of dark matter was found so far and exclusion limits on the DM-nucleon scattering cross section are set using an effective field approach.

1 The dark matter model

Indications for the existence of dark matter (DM) are one of the strongest hints for physics beyond the SM. Many experiments seek their detection and understanding of their nature. Candidates particles for dark matter occur in many theoretical models. They may also be pair produced in pp collisions at the LHC and directly be searched for without specific theoretical assumptions. Up to now, such production has been described by an effective field theory (EFT) without modeling a specific messenger, assuming a contact interaction between Standard Model (SM) particles and DM. This approach allows to probe different models, while being specific enough to make predictions. The EFT description is valid as long as the messenger mass M is larger than the energy and momentum transfer in the partonic collision. Then two characterizing parameters fully determine the interaction, the scale of the effective interaction $\Lambda = M/\sqrt{(}g_{DM}g_{SM})$ and the mass of the dark matter candidate M_χ. Different assumptions for the coupling with DM are possible, such as vector, scalar and axial-vector coupling.

Weakly interaction DM particles would not yield a detectable signal in the detector and rather contribute to missing transverse energy (MET) which can also be created by neutrinos or other weakly interacting particles. Therefore, their detection has to be based on additional particles - the emission of a single photon or a single jet as initial-state or final-state radiation or through a recoiling particle, such as a W- or a Z-boson. The CMS experiment [1] has performed such searches using the full 2012 pp dataset at $\sqrt{s}$=8 TeV.

2 The mono-X search channels

The pioneering search for pair-produced DM at hadronic colliders exploits the single jet + MET final state [2]. It is challenged by the trigger and high QCD background. Single-jet trigger thresholds would be far too high, therefore the trigger either uses MET above 120 GeV or a jet+MET combination with jet transverse momentum p_T >80 GeV and MET>105 GeV. To suppress instrumental and beam-related backgrounds, events are rejected if less than 20% of

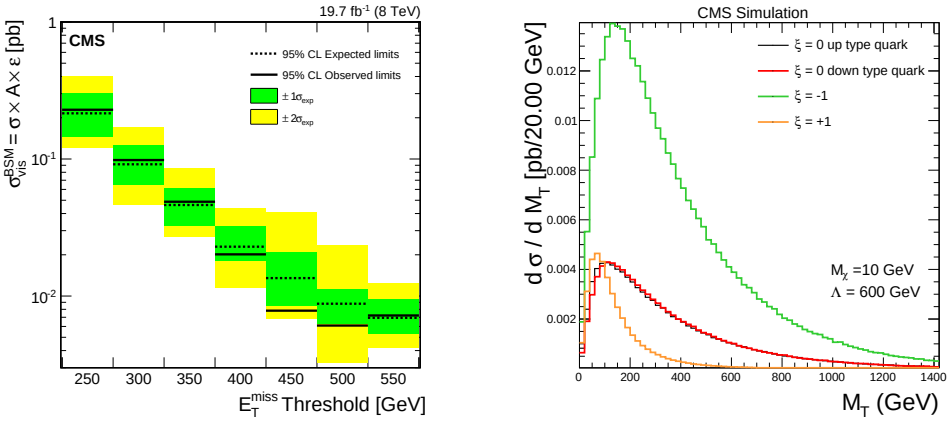

Figure 1: Left: The monojet analysis searches the MET distribution after all selections in seven bins. Shown are the model-independent observed and expected 95% C.L. upper limits on the visible cross section times acceptance times efficiency ($\sigma \times A \times \epsilon$) for non-SM production of events. Right: The mono-W channel could disentangle potentially different couplings to up- and down-type quarks, described by the parameter ξ. The resulting cross section and M_T shape would differ strongly.

the energy of the highest p_T jet is carried by charged hadrons or more than 70% of this energy is carried by either neutral hadrons or photons. The most energetic jet is required to have $p_T >$ 110 GeV within $|\eta| < 2.4$. A second jet is only allowed if nearby, in order to suppress QCD dijet events. The dominant backgrounds after all selection steps are due to Z($\nu\nu$) and W+jet events, estimated from data samples of Z($\mu\mu$) andW($\mu\nu$) events. The analysis is performed in seven regions of MET (see Fig. 1-left). Upper limits on the cross section × acceptance × efficiency ($\sigma \times A \times \epsilon$) are placed ranging from 2 pb for MET>250 GeV to 10^{-2}pb for MET>500 GeV.

The same $\sqrt{s}$=8 TeV dataset was used for searches with a single photon [3] instead. Events are triggered with either a single photon or a photon+MET cross trigger with offline thresholds of MET>140 GeV and p_T^γ >145 GeV. A tight photon ID rejects fakes. Events with either a single lepton or hadronic activity are being vetoed. The dominant irreducible backgrounds after selection are due to $Z(\to \nu\nu) + \gamma$ and $W(\to \ell\nu) + \gamma$ along with fake photon backgrounds. Searching in six bins of p_T^γ shows that data are compatible with the SM expectation and 90% C.L. limits are set on Λ using effective operators in the EFT approach. The resulting DM-nucleon cross section limits are depicted in Fig. 2-left.

The monolepton channel [4] – where DM recoils against a W-boson which subsequently decays to an electron(muon) and corresponding neutrino – is special as it allows to disentangle possibly different couplings to the up- or the down-type quark. Their relative coupling strength is parametrized by the factor ξ with the considered values of 0, +1, -1, following ref.[5]. The factor ξ could modify either the up or down-type quark couplings with the resulting M_T distributions shown in Fig. 1-right. The coupling changes the total cross section and the shape of the spectrum which in turn impacts the sensitivity. While the very high end of the transverse mass spectrum is nearly background free, at lower masses the small signal has to be separated from background.

In the monolepton search, candidate events with at least one high transverse momentum lepton are selected using single electron(muon) triggers with offline p_T >100(45) GeV. The lepton reconstruction is optimized for high momenta. The main observable is the transverse mass (M_T) of the lepton-MET spectrum. The main background $W \to \ell\nu$ is described with an M_T-binned k-factor for higher order QCD and electroweak corrections. Other backgrounds are Z/DY, ttbar, multi-jet QCD and di-boson processes, all are derived from simulation using NLO cross sections (except QCD). In order to suppress backgrounds, events exhibiting a back-to-back kinematics are selected. The three cases of ξ with related cross sections yield three limits on λ which subsequently are translated to limits of the DM-nucleon cross section (see Fig. 2-right).

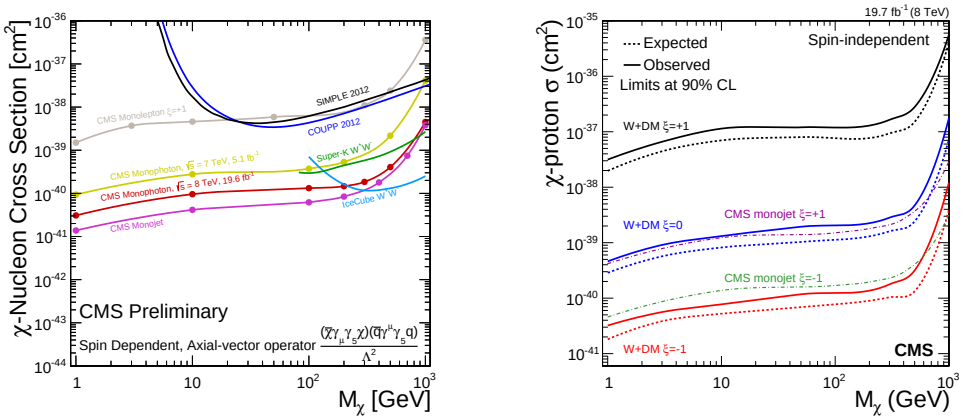

Figure 2: Dark matter nucleon exclusion limits with EFT assumption for different channels addressing the spin dependent (axial-vector) coupling (left) and spin independent (vector) coupling (right).

3 Using top quarks

Unlike the previously discussed vector and axial-vector couplings which are simply proportional to Λ^{-2}, scalar couplings do contain a mass term (m_q/Λ^3 for D1 and m_q/Λ^2 for C1). Such searches are therefore performed best with top quarks. A single DM particle could be produced along with a top-quark in the s- or t-channel [6] or DM pairs in association with top-quark pairs [7, 8]. All channels require large MET due to DM, with thresholds of 320 GeV and 350 GeV for the monotop and top-pair channel, respectively. Depending on the W decay originating from $t \to Wb$, the final state contains several jets or jets plus leptons.

The fully hadronic channel is used in the monotop search [6], thus yielding three final state jets of which one has to be b-tagged and the two leading ones exhibit p_T >60 GeV. No isolated electron or muon should be present. Along with the MET requirement this selection removes about 4/5 of the background. The main remaining backgrounds are $t\bar{t}$ (with the leptonic decay of the W and undetected lepton) and V+jets while QCD multi-jet and diboson events are largely suppressed by the b-tag. The invariant mass of the three leading jets in selected events with one b-tag is depicted in Fig. 3-left. Data are compared to the simulated backgrounds and a

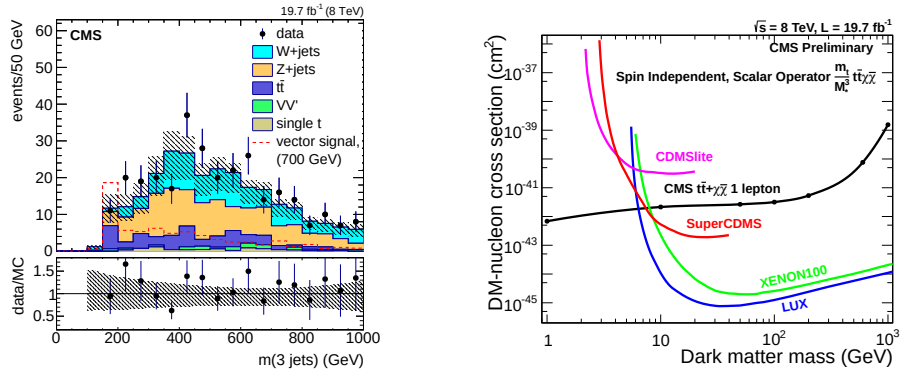

Figure 3: Left: The invariant mass of the three leading jets in selected events with one b-tag in the monotop DM search. Measured data points are compared to the simulated backgrounds (stacked histograms) and one of the signal models (solid line) scaled to 19.7/fb. The shaded area represents systematic uncertainties. Right: The 90% C.L. upper limits on the dark matter-nucleon spin-independent scattering cross sections for the scalar operator considered in the ttbar analysis, compared to results from selected direct detection experiments.

signal model. In the full 8 TeV data sample, no deviation from the SM expectation is observed and DM masses below 655(327) GeV are excluded at 95% C.L. for vector(scalar) couplings.

Assuming DM may be pair-produced in association with top-quarks, searches are performed in the dilepton $\ell\ell bb + MET$ [7] and the semi-leptonic $\ell jjjb + MET$ final state [8]. Events are selected with one lepton + $\geq$3 jets + $\geq$1 b-jet along with the MET requirement. Both W-bosons are reconstructed via M_T. According to its final state, the dilepton search rather selects events with 2 leptons + $\geq$2 jets and applies cuts on the scalar sum of leptons and jets, and lepton opening angle. The main background for both analyses is $t\bar{t}$. Signal efficiencies are about 1-2% but the background is also very low. Using the EFT description from above with the characteristic parameters Λ and M_χ, values of Λ <120(90) GeV are excluded in the semi-leptonic(dileptonic) channel for M_χ <100 GeV. Combining both results, the excluded DM-nucleon cross sections are shown in Fig. 3-right for a scalar operator where other channels rarely set limits due to their low sensitivity.

4 Summary

Several analyses based on the full 2012 data sample search for pair-produced DM in pp collisions at the LHC but found no significant indication of such signals. Based on an effective field approach for the SM-DM interaction, limits on the DM-nucleon scattering cross section are being set for different types of interaction (vector, axial-vector and scalar).

References

[1] CMS Collaboration, The CMS experiment at the CERN LHC, JINST 3, S08004 (2008).

[2] CMS Collaboration, Search for dark matter, extra dimensions, and unparticles in monojet events in proton-proton collisions at $\sqrt{s} = 8$ TeV, $[arXiv : 1408.3583[hep - ex]]$, CMS-PAS-EXO-12-048

[3] CMS Collaboration, Search for Dark Matter and Large Extra Dimensions in the photon + Missing Transverse Energy final state in pp Collisions at $\sqrt{s} = 8$ TeV in the CMS Experiment with 19.6 fb^{-1} of data, CMS-PAS-EXO-12-047

[4] CMS Collaboration, Search for physics beyond the standard model in final states with a lepton and missing transverse energy in proton-proton collisions at $\sqrt{s} = 8$ TeV, $[arXiv : 1408.2745[hep - ex]]$, CMS-PAS-EXO-12-060, CMS-PAS-EXO-13-004

[5] Yang Bai Tim M.P. Tait, Searches with Mono-Leptons, Phys.Lett. B723 (2013), $[arXiv : 1208.4361[hep - ph]]$, doi 10.1016/j.physletb.2013.05.057

[6] CMS Collaboration, Search for monotop signatures in proton-proton collisions at sqrt(s) = 8 TeV, $[arXiv : 1410.1149[hep - ex]]$, CMS-PAS-B2G-12-022

[7] CMS Collaboration, Search for the Production of Dark Matter in Association with Top Quark Pairs in the Di-lepton Final State in pp collisions at $\sqrt{s}$=8 TeV, CMS-PAS-B2G-13-004

[8] CMS Collaboration, Search for the Production of Dark Matter in Association with Top Quark Pairs in the Single-lepton Final State in pp collisions at $\sqrt{s} = 8$ TeV, CMS-PAS-B2G-14-004

Search for heavy Resonances in Two-Particle Final States with Leptons, Jets and Photons at CMS

Andreas Güth[1] on behalf of the CMS collaboration

[1]III. Physikalisches Institut A, RWTH Aachen University, Aachen, Germany

DOI: http://dx.doi.org/10.3204/DESY-PROC-2014-04/185

At the LHC, the production of heavy resonances decaying into a pair of particles can be probed at unprecedented centre-of-mass energies. Two-particle resonances are predicted in a variety of BSM models and can be searched for in a largely model-independent fashion. Results from searches for resonances in final states with leptons, jets and photons based on the full dataset of 20 fb^{-1} taken by the CMS detector in 2012 in proton-proton collisions at a centre-of-mass energy of 8 TeV are presented. They are interpreted in terms of various theories of BSM physics ranging from generic heavy resonances such as the Z' to excited quarks or Randall-Sundrum gravitons. In the absence of a significant deviation from the expected SM background, 95% CL limits are set on model parameters of the theories under study.

1 Introduction

Searches for heavy resonances constitute an important part of the effort devoted to the test of beyond the Standard Model (BSM) physics carried out by the CMS collaboration at the LHC [1]. This note can only present an excerpt of the full program and is therefore restricted to three exemplary analyses with singly produced resonances which decay into a pair of reconstructed objects. The common feature of these searches is the distinct signal shape of the resonance on top of smoothly falling backgrounds. This leads to shape-based searches which are robust against deviations in the background spectrum in the region of high invariant mass of the two-object system.

2 Dilepton resonances

The search for narrow dilepton resonances in the dimuon and dielectron final states [2] focuses on the mass range above $M_{\ell\ell} = 200$ GeV, well above the Z peak. The interpretation of the results is carried out in terms of different spin-1 Z' signal models. With an invariant mass resolution of about 1% in the dielectron channel above $M_{ee} = 500$ GeV and 4% ($M_{\mu\mu} = 1$ TeV) to 9% ($M_{\mu\mu} = 3$ TeV) in the dimuon channel, the CMS detector is well-suited for the task of finding TeV-scale dilepton resonances. The selection of dimuon events is based on a dataset satisfying a single-muon trigger requirement with a central muon within $|\eta| < 2.1$ and $p_T > 40$ GeV. Two isolated muons, which satisfy identification criteria optimized for the efficient selection of

muons at high p_T, with $p_T > 45$ GeV and $|\eta| < 2.4$ have to be present in the event. The two selected muons are required to carry opposite electric charge, originate from the same vertex and have an opening angle smaller than $\pi - 0.02$ radians, where the latter requirement rejects background from cosmic muons. The invariant mass distribution of selected muon pairs in data is compared to the expectation from SM backgrounds in Fig. 1. Over the entire mass range, the background is dominated by the irreducible $Z/\gamma^* \to \ell\ell$ process. In the search region above $M_{\mu\mu} = 200$ GeV, the Drell-Yan contribution amounts to 80% of the expected background with $t\bar{t}$ and diboson production dominating the remaining 20%.
Dielectron events are selected based on a double-electron trigger asking for two clusters in the electromagnetic calorimeter (ECAL) with $E_T > 33$ GeV. Events containing two isolated electrons with $E_T > 35$ GeV are split into two categories for further analysis: a dielectron sample with both electrons in the central part of the ECAL with $|\eta| < 1.44$ and one with a central electron and the second electron in the ECAL endcap with $1.56 < |\eta| < 2.5$. These subsets of the dielectron candidates differ in background composition and invariant mass resolution.

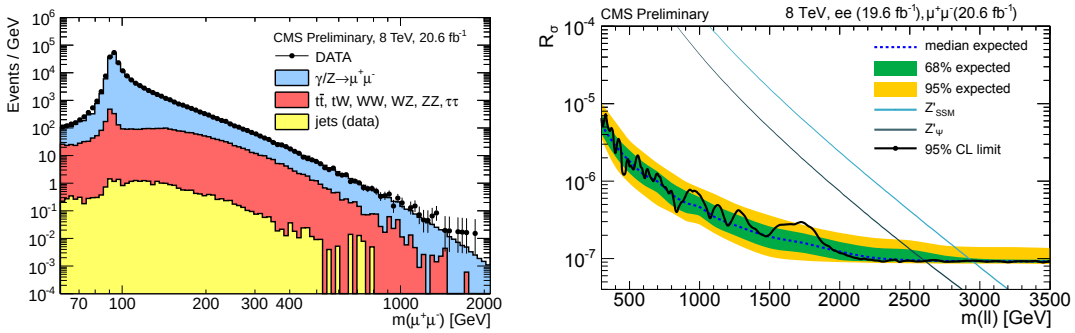

Figure 1: Left: Invariant mass distribution of selected muon pairs. Right: 95% confidence level limits on the cross section ratio R_σ as a function of signal mass.

No significant excess is observed in either dilepton channel and limits on two Z' models are set: a sequential SM Z'_{SSM} and a Z'_ψ expected in certain grand unified theories. In order to reduce the impact of systematic uncertainties on the results, limits are determined on the cross section ratio R_σ between the spin-1 Z' signal and the SM Drell-Yan cross section (including the branching ratios), rather than on the signal cross section. The cross sections in the ratio are evaluated in the mass range $0.6\ M_{Z'} - 1.4\ M_{Z'}$ and $60 - 120$ GeV for the signal and SM Drell-Yan processes, respectively. A Bayesian limit setting procedure using an unbinned likelihood with a uniform prior for the signal cross section is used to derive lower limits on the signal mass at 95% confidence level (CL). Combination of the dimuon channel and the two dielectron channels yields lower limits on the Z' mass of 2960 GeV and 2600 GeV for the Z'_{SSM} and Z'_ψ signals, respectively. The limits on R_σ are shown in Fig. 1.

3 Dijet resonances

At a hadron collider such as the LHC, searches for resonance production in the dijet final state [3] probe a variety of BSM models. At a signal mass of 1 TeV, the signal cross sections for the different resonance models considered (Table 1) cover a wide range from the pb regime in

case of weakly coupling models such as the Z'_{SSM} up to several nb for string resonances. The models further differ in the type of jets in the final state (qq, qg, gg or a combination).

This leads to different resonance shapes depending on the signal under study, with larger low-mass tails in final states containing gluon jets. The statistical interpretation is therefore carried out with different signal shapes, depending on the final state.

The jet reconstruction starts from the particle-flow (PF) CMS event reconstruction and builds jets using the anti-k$_T$ algorithm with jet parameter $R = 0.5$ (AK5 jets). Among the jets with $p_T > 30$ GeV and $|\eta| < 2.5$, the two leading jets are selected and two "wide jets" are formed around them by adding the Lorentz vectors of all other jets within $\Delta R = \sqrt{(\Delta\eta)^2 + (\Delta\phi)^2} = 1.1$. The two wide jets then form the dijet system used in the analysis with invariant mass M_{jj}. This approach reduces the sensitivity to gluon radiation off the two partons from the resonance decay. The event selection is performed on a dataset obtained from a combination of two triggers selecting events with the scalar sum of the jet transverse momenta above $H_T = 650$ GeV or with $M_{jj} > 750$ GeV, respectively. The selection of two wide jets is performed as described above and they both have to fall within $|\eta| < 2.5$. Requiring a small pseudorapidity gap of $|\Delta\eta_{jj}| < 1.3$ reduces the SM dijet background. Events with $M_{jj} < 890$ GeV are rejected. The resulting dijet mass spectrum is depicted in Fig. 2 and compared to the expectation.

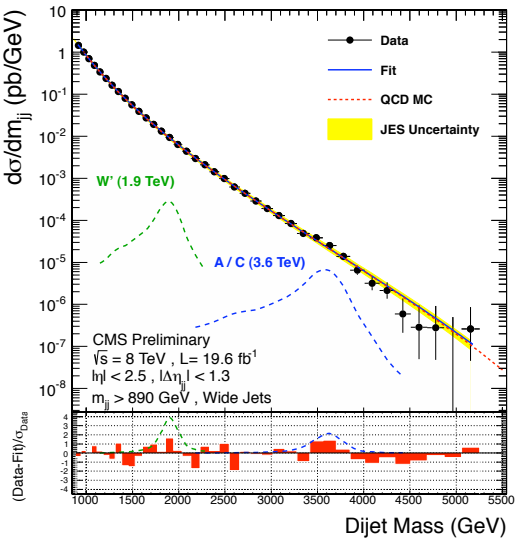

Figure 2: Invariant mass distribution of selected wide jet pairs. Signal distributions are shown for W' and axigluon/coloron signals.

In the absence of a significant excess, upper limits are set on the product of signal cross section, branching ratio, and acceptance for the various resonance models. The 95% CL upper limits are obtained from a Bayesian approach with uniform prior for the signal cross section and derived for the three different combination of jet types, qq, qg, and gg, all of which come with different resonance shapes. The observed limits on the cross section for signals with qq final state are stronger than for those with gg final state by a factor 2 to 3. The corresponding excluded ranges of the resonance mass for different signal models are given in Table 1 and reach up to 5 TeV in case of string resonances. Searches for dijet resonances have also been performed by the CMS collaboration with b-tagged jets [4] and W/Z-tagged jets [5].

Model	Final State	Obs. Mass Excl. [TeV]
String Resonance	qg	[1.20 , 5.08]
Excited Quark	qg	[1.20 , 3.50]
E_6 Diquark	qq	[1.20 , 4.75]
Axigluon/Coloron	$q\bar{q}$	[1.20 , 3.60]+ [3.90 , 4.08]
Color Octet Scalar	gg	[1.20 , 2.79]
W' Boson	$q\bar{q}$	[1.20 , 2.29]
Z' Boson	$q\bar{q}$	[1.20 , 1.68]
RS Graviton	$q\bar{q}$+gg	[1.20 , 1.58]

Table 1: Excluded resonance mass ranges at 95% CL for the different signal models.

4 Photon+jet resonances

The search for resonances in the photon+jet invariant mass spectrum [6] is motivated by theories of quark compositeness at an energy scale Λ involving excited quark states q^*. The production of the excited quark via quark-gluon fusion and the decay into the photon+quark final state involve strong and electromagnetic gauge couplings with a coupling modifier f as a free parameter. A combination of spin-1/2, mass degenerate excitations of the first generation quarks $q^* = (u^*, d^*)$ is used as the signal model.

Photon+jet pairs are selected from a dataset that has been collected with a single-photon trigger with $E_T > 150$ GeV. The presence of at least one isolated photon with $p_T > 170$ GeV in the central part of the ECAL with $|\eta| < 1.44$ is requested. Selected AK5 jet candidates have to be separated in $\eta - \phi$ space by $\Delta R > 0.5$ from the selected photon. The leading jet with $p_T > 170$ GeV and $|\eta| < 3$ is chosen. The dominant backgrounds in this search, QCD photon+jet production and dijet events with a jet misidentified as a photon, are produced predominantly via t-channel diagrams. These contributions are reduced by requiring $|\Delta\eta_{\gamma j}| < 2.0$ and a back-to-back topology $|\Delta\phi_{\gamma j}| > 1.5$. The invariant mass $M_{\gamma j}$ has to exceed 560 GeV. After selection, the expected background composition is dominated by SM photon+jet production, which contributes 80.5%, followed by dijet events with 18.5% and electroweak backgrounds with 1%. The invariant mass resolution ranges from 4.5% at $M_{\gamma j} = 1$ TeV to 3% at $M_{\gamma j} = 3$ TeV. The observed invariant mass distribution exhibits no significant deviation from the background expectation, and bounds in the two-parameter space of coupling modifier f and the excited quark mass M_{q^*} at 95% CL are obtained, as shown in Fig. 3. For the choice $f = 1$ and $\Lambda = M_{q^*}$, excited quarks are excluded at 95% CL in the mass range 0.7 TeV $< M_{q^*} <$ 3.5 TeV.

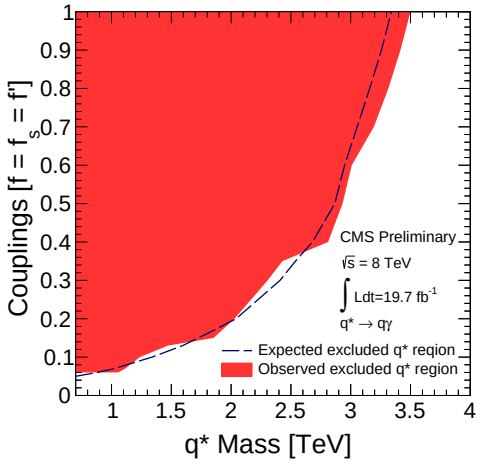

Figure 3: 95% CL bounds in the two-parameter space of coupling modifier f and M_{q^*}, assuming $\Lambda = M_{q^*}$.

References

[1] CMS collaboration, *The CMS experiment at the CERN LHC*, JINST **3** S08004 (2008).

[2] CMS collaboration, *Search for Narrow Resonances in Dilepton Mass Spectra in pp Collisions at* $\sqrt{s}$*= 8 TeV*, CMS Physics Analysis Summary **CMS-PAS-EXO-12-061** (2013).

[3] CMS collaboration, *Search for Narrow Resonances using the Dijet Mass Spectrum with 19.6* fb^{-1} *of pp Collisions at* $\sqrt{s}$*=8 TeV*, CMS Physics Analysis Summary **CMS-PAS-EXO-12-059** (2013).

[4] CMS collaboration, *Search for Heavy Resonances Decaying into* $b\bar{b}$ *and bg Final States in pp Collisions at* $\sqrt{s}$ *= 8 TeV*, CMS Physics Analysis Summary **CMS-PAS-EXO-12-023** (2013).

[5] CMS collaboration, *Search for massive resonances in dijet systems containing jets tagged as W or Z boson decays in pp collisions at* $\sqrt{s}$ *= 8 TeV*, JHEP **08** 173 (2014).

[6] CMS collaboration, *Search for excited quarks in the* γ*+jet final state in proton-proton collisions at* $\sqrt{s}$ *= 8 TeV*, arXiv:hep-ex/1406.5171 (2014).

Constraints on new phenomena through Higgs coupling measurements with the ATLAS detector

Camilla Maiani[1] on behalf of the ATLAS Collaboration

[1]DSM/IRFU (Institut de Recherches sur les Lois Fondamentales de l'Univers), CEA Saclay (Commissariat à l'Energie Atomique et aux Energies Alternatives), Gif-sur-Yvette, France

DOI: http://dx.doi.org/10.3204/DESY-PROC-2014-04/229

The ATLAS experiment at the Large Hadron Collider has measured the couplings of the newly found Higgs boson to other particles using about 25 fb^{-1} of proton-proton collision data at 7 and 8 TeV center-of-mass energy. These measurements have been used to contrain the parameters on new physics phenomena. In this document a short review of such studies is presented. No deviations from the Standard Model are observed. Perspectives at the High-Luminosity LHC are also discussed.

1 Introduction

The ATLAS [1] and CMS [2] Collaborations at the Large Hadron Collider (LHC) announced the discovery of a new particle in the summer of 2012 [3, 4]. The measurements of the new-found particle's mass [5, 6], coupling parameters [5, 6] and spin-parity [7, 8, 9] are compatible, within experimental uncertainties, with those of a Standard Model (SM) Higgs boson. The question remains open whether the Higgs sector is extended, and a whole family of Higgs-like bosons exists at higher mass, as predicted by many Beyond the SM (BSM) theories. At ATLAS, some BSM are tested by performing both direct searches for new particles, and indirectly by using the Higgs boson coupling measurements to put constraints. In this report, a short review of some of the indirect searches performed is described, a full discussion can be found in Ref. [10]. Perspectives at the High-Luminosity (HL) LHC [11], are also discussed.

2 Methodology and statistical treatment

The analyses presented use the full data sample collected by ATLAS during the first run of the LHC in 2011 and 2012, corresponding to about 25 fb^{-1} of proton-proton collision data at 7 and 8 TeV center-of-mass energy. The measurements of the Higgs boson couplings to bosons and fermions in all studied channels are considered: $h \to \gamma\gamma$, $h \to ZZ^\star \to 4\ell$, $h \to WW^\star \to \ell\nu\ell'\nu'$, $h \to \tau\tau$ and $h \to b\bar{b}$. The direct search for $Zh \to \ell\ell +$ invisible is also considered in the studies presented in Sec. 5. Relying on the Higgs coupling measurements confidence intervals are set on the BSM parameters based on a profile likelihood ratio test [12], following the method described in Ref. [13, 14]. The likelihood function used is defined as the product of the likelihood functions

in each channel, and depend on the parameters of interest, such as the signal strength, the Higgs boson mass m_h or the couplings. Experimental and theoretical systematic uncertainties are introduced in the likelihood by means of nuisance parameters. In each decay channel, the likelihood describes the optimal observable for signal to background separation; in the $h \to \gamma\gamma$ case, for example, the discriminant observable is the di-photon invariant mass. The signal shape is extracted from Monte Carlo (MC), whereas the background shape comes from either MC or data driven estimates.

3 Two-Higgs-doublet model

A simple extension of the SM is a class of models named Two-Higgs-Doublet Models (2HDMs) [15]. These models predict the existence of an additional Higgs doublet: one neutral CP-even boson H, one neutral CP-odd boson A, and two charged bosons $H^{\pm}$. Different couplings to vector bosons and fermions are tested [10]. Limits are set on the $(\cos(\beta-\alpha), \tan(\beta))$ plane and are found to be consistent with the SM expectations for all the coupling configurations tested. In Fig. 1, limits obtained in one case considered are shown.

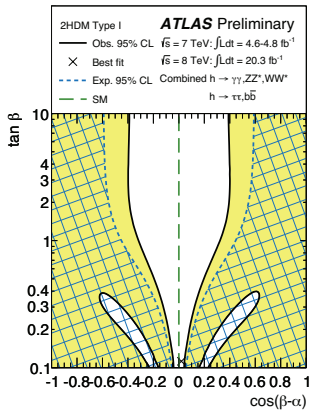

Figure 1: Regions of the $(\cos(\beta-\alpha), \tan(\beta))$ plane for a coupling configuration of 2HDMs excluded by fits to the measured rates of the Higgs boson production and decays. The cross marks the best fit value, the light shaded and hashed regions indicate the observed and expected 95% confidence level exclusions. [10]

4 Simplified minimal supersymmetric model

Supersymmetry [16] was introduced to solve the hierarchy problem, and provides Weakly Interacting Massive Particles (WIMPs) that are good candidates for dark matter. In this study, limits have been set, within the simplified Minimal SuperSymmetric Model (MSSM) formalism, in the (m_A, $\tan(\beta)$) plane. Results are shown in Fig. 2 (left). The observed (expected) lower limit at 95% Confidence Level (CL) on m_A is 400 GeV (280 GeV) for $2 \leq \tan(\beta) \leq 10$. Everything is consistent with the SM, although there is still a large unexplored region for $\tan(\beta) > 1$.

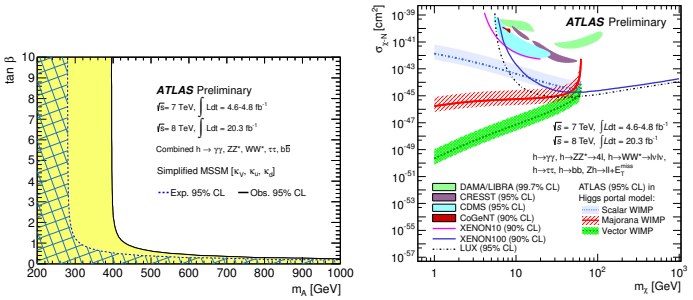

Figure 2: Left: regions of the $(m_A, \tan(\beta))$ plane excluded in a simplified MSSM model via fits to the Higgs boson production and decay rates. The light shaded and hashed regions indicate the observed and expected 95% CL exclusions respectively. [10] Right: ATLAS 95% CL upper limit on the WIMP-nucleon scattering cross section in a Higgs portal model as a function of the dark matter candidate's mass for different spin configurations. Excluded and allowed regions from direct detection experiments are also shown. [10]

5 Higgs portal to dark matter

In the "Higgs portal to dark matter" models [17, 18] a WIMP is introduced as a dark matter candidate, that interacts very weakly with all SM particles except the Higgs boson. From the Higgs boson coupling measurements, and from direct searches of $Zh \to \ell\ell +$ invisible, the upper limit at 95% CL on the Branching Ratio of the Higgs boson to invisible final states (BR_{inv}) is found to be $BR_{inv} < 0.37$, where the expectation is 0.39. The upper limit is then transformed into constraints on the coupling of the WIMP to the Higgs boson as a function of its mass [18] to allow for comparison with direct searches for dark matter [19]. The results are shown in Fig. 2 (right) for different spin configurations of the WIMP. The ATLAS experiment results dominate in a broad region at low mass.

6 Perspectives at HL LHC

The LHC is expected to be brought to the high luminosity phase in 2023. Five to ten times the nominal luminosity will be reached in the HL-LHC collisions, and about 3000 fb^{-1} of proton-proton data will be collected by 2030 at 14 TeV of center-of-mass energy. Experimental precisions of 1.5% and 3% are expected on the couplings of the Higgs boson to vector bosons and fermions respectively. In the Higgs portal to dark matter studies expected limits on BR_{inv} will be set at the level of 8 to 16% in direct $Zh \to \ell\ell +$ invisible searches, and of 12 to 15% in indirect searches from coupling measurements.

7 Summary

The data collected during the first phase of the operation at the LHC have been used to extract a first measurement of the Higgs boson couplings. Such measurements allow to perform indirect

searches for new physics at high energy. The results presented show an impressive consistency with the SM, and allow to set limits on the parameters of the BSM models studied.

Acknowledgements

This report was supported by the European Research Council, Grant Agreement N^o 279170 DIBOSON.

References

[1] ATLAS Collaboration, JINST **3** S08003 (2008).

[2] CMS Collaboration, CMS-TDR-008-1/2 (2006).

[3] ATLAS Collaboration, Phys. Lett. **B 716** 1 (2012), [arXiv:1207.7214].

[4] CMS Collaboration, Phys. Lett. **B 716** 30 (2012), [arXiv:1207.7235].

[5] ATLAS Collaboration, Phys. Lett. **B 726** 88 (2013), [arXiv:1307.1427].

[6] CMS Collaboration, CMS-PAS-HIG-13-005 (2013).

[7] ATLAS Collaboration, Phys. Lett. **B 726** 120 (2013), [arXiv:1307.1432].

[8] CMS Collaboration, Phys. Rev. Lett. **110** 081803 (2013), [arXiv:1212.6639].

[9] CMS Collaboration, [arXiv:1312.5353].

[10] ATLAS Collaboration, ATLAS-CONF-2014-010 (2014), http://cds.cern.ch/record/1670531/files/ATLAS-CONF-2014-010.pdf.

[11] ATLAS Collaboration, ATL-PHYS-PUB-2013-015 (2013), https://cds.cern.ch/record/1611189/files/ATL-PHYS-PUB-2013-015.pdf.

[12] G. Cowan *et al.*, Eur. Phys. J. **C 71** 1554 (2011).

[13] ATLAS Collaboration, Phys. Rev. **D 86** 032003 (2012).

[14] ATLAS and CMS Collaborations, ATL-PHYS-PUB-2011-011 CERN-CMS-NOTE-2011-005 (2011), https://cds.cern.ch/record/1375842/files/ATL-PHYS-PUB-2011-011.pdf.

[15] LHC Higgs Cross Section Working Group, [arXiv:1307.1347]; T. Lee, Phys. Rev. **D 8** 1226 (1973); J. F. Gunion and H. E. Haber, Phys. Rev. **D 67** 075019 (2003), [arXiv:hep-ph/0207010]; G. Branco *et al.*, Phys. Rept. **516** 1 (2012), [arXiv:1106.0034].

[16] H. Miyazawa, Prog. Theor. Phys. **36** no. 6 1266 (1966); P. Ramond, Phys. Rev. **D 3** 2415 (1971); Y. Golfand and E. Likhtman, JETP Lett. **13** 323 (1971); A. Neveu and J. Schwarz, Nucl. Phys. **B 31** 86 (1971); A. Neveu and J. Schwarz, Phys. Rev. **D 4** 1109 (1971); J.-L. Gervais and B. Sakita, Nucl. Phys. **B 34** 632 (1971); D. Volkov and V. Akulov, Phys. Lett. **B 46** 109 (1973); J. Wess and B. Zumino, Phys. Lett. **B 49** 52 (1974); J. Wess and B. Zumino, Nucl. Phys. **B 70** 39 (1974).

[17] ATLAS Collaboration, [arXiv:1402.3244]; B. Parr and F. Wilczek, [arXiv:hep-ph/0605188]; S. Kanemura *et al.*, Phys. Rev. **D 82** 055026 (2010), [arXiv:1005.5651]; P. J. Fox *et al.*, Phys. Rev. **D 85** 056011 (2012), [arXiv:1109.4398]; L. Lopez-Honorez *et al.*, Phys. Lett. **B 716** 179 (2012), [arXiv:1203.2064]; ATLAS Collaboration, Phys. Rev. Lett. **112** 041802 (2014), [arXiv:1309.4017].

[18] A. Djouadi *et al.*, Phys. Lett. **B 709** 65 (2012), [arXiv:1112.3299].

[19] XENON10 Collaboration, Phys. Rev. Lett. **107** 051301 (2011), [arXiv:1104.3088]; XENON100 Collaboration, Phys. Rev. Lett. **109** 181301 (2012), [arXiv:1207.5988]; P. Belli *et al.*, Phys. Rev. **D 84** 055014 (2011), [arXiv:1106.4667]; G. Angloher *et al.*, Eur. Phys. J. **C 72** 1971 (2012), [arXiv:1109.0702]; CDMS Collaboration, Phys. Rev. Lett. **111** (2013), [arXiv:1304.4279]; CoGeNT Collaboration, Phys. Rev. Lett. **107** 141301 (2011), [arXiv:1106.0650]; LUX Collaboration, [arXiv:1310.8214].

Searches for dark matter and extra dimensions with the ATLAS detector

Christophe Clément[1] on behalf of the ATLAS Collaboration

[1]Stockholm University, Fysikum, 106 91 Stockholm, Sweden

DOI: http://dx.doi.org/10.3204/DESY-PROC-2014-??/204

This paper presents the results of different approaches to finding evidence for dark matter with the ATLAS experiment at LHC. These include searches for events with large missing transverse momentum and a single jet, photon or W/Z boson. Searches for hidden sectors in events with long-lived particles resulting in displaced hadronic vertices or lepton-jet signatures are also reported. Finally, studies sensitive to the presence of extra spatial dimensions are described, as for example classical and quantum black holes and other non-resonant phenomena. Results from $\sqrt{s} = 8$ TeV ATLAS data taking are presented.

1 Dark Matter

The origin of dark matter is one of the outstanding questions in contemporary physics. Collider experiments such as ATLAS are sensitive to the pair production of so-called Weakly Interacting Massive Particles (WIMPs) in association with an initial state radiation jet, photon or W/Z, $p+p \to \chi\chi+X$, where χ denotes the WIMP and X is either a jet, photon or W/Z. The χ pair escapes the detector undetected, leading to a signature of missing transverse energy ($E_{\mathrm{T}}^{\mathrm{miss}}$). The remaining signal characteristics are determined by the nature of X.

In the case of hadronically decaying W/Z [1], the two daughter quarks are boosted and yield a large cone jet. The large jet is reconstructed using the Cambridge-Aachen algorithm [2] of size $\Delta R = 1.2$, with transverse momentum $p_{\mathrm{T}} > 250$ GeV and $|\eta| < 1.2$. It is required that two anti-k_T jets of size $\Delta R = 0.4$ are also found inside the fat jet and that the momentum is fairly distributed between them as expected from W/Z decays, this is ensured by $\sqrt{y} = \frac{\min(p_{\mathrm{T}1}, p_{\mathrm{T}2})\Delta R_{\mathrm{jj}}}{m_{\mathrm{jet}}} > 0.4$, where m_{jet} is the invariant mass of the two small jets, and p_{T1}, p_{T2} are their momenta and ΔR_{jj} is the inter-jet distance. Finally for consistency with a W/Z decay, it is required $50 < m_{\mathrm{jet}} < 120$ GeV. A veto is applied against leptons, photons and light jets. Two signal regions are defined with $E_{\mathrm{T}}^{\mathrm{miss}} > 350$ and 500 GeV.

In the case of leptonically decaying W [3], a single electron (muon) with $p_{\mathrm{T}} > 125$ GeV (45 GeV) is required. The same lepton-dependent selection cut value is applied on the $E_{\mathrm{T}}^{\mathrm{miss}}$. The final discriminating variable is the transverse mass $m_{\mathrm{T}} = \sqrt{2p_{\mathrm{T}}E_{\mathrm{T}}^{\mathrm{miss}}(1-\cos\phi_{\ell\nu})}$, where $\phi_{\ell\nu}$ is the distance in the azimuthal angle ϕ between the charged lepton and the direction of $E_{\mathrm{T}}^{\mathrm{miss}}$. Several signal regions are used with different thresholds on m_{T} but start to be sensitive to new physics at $m_{\mathrm{T}} > 252$ GeV.

If the associated boson is Z decaying into two charged leptons [4], the identification of the final state relies on the presence of two same flavour leptons denoted ℓ (electrons or muons),

with $p_{\mathrm{T}} > 20$ GeV and such that their invariant mass is within 10 GeV of the Z-boson mass, and $|\eta|$ of the dilepton system is required to be within 2.5. The dilepton system is required to balance $E_{\mathrm{T}}^{\mathrm{miss}}$ in both direction and magnitude, with $\Delta\phi(E_{\mathrm{T}}^{\mathrm{miss}}, p_{\mathrm{T},\ell\ell}) > 2.5$, where $p_{\mathrm{T},\ell\ell}$ is the transverse momentum of the dilepton system, and $|E_{\mathrm{T}}^{\mathrm{miss}} - p_{\mathrm{T},\ell\ell}| < 0.5$. Several signal regions are defined by a final selection on the $E_{\mathrm{T}}^{\mathrm{miss}}$ which ranges from 150 to 450 GeV.

The results from ATLAS dark matter searches are translated into upper limits on the WIMP-nucleon cross section as function of the WIMP mass (m_χ) in Fig. 1 using an effective field theory approach [5], in the case of spin-independent (left panel) and spin-dependent interactions (right panel).

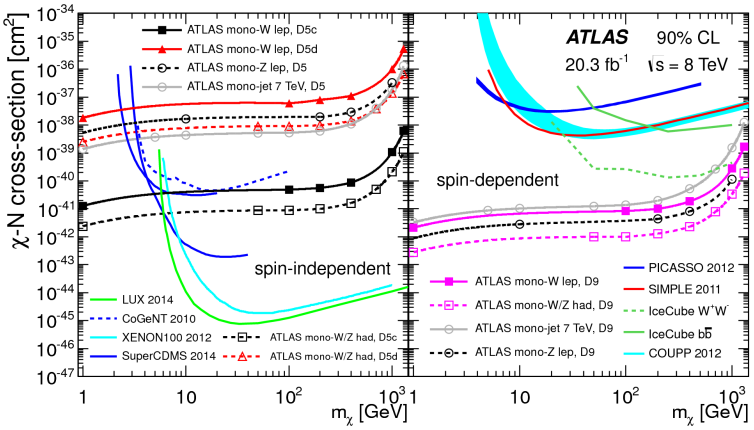

Figure 1: Summary of ATLAS upper limits on WIMP-nucleon cross section for spin-independent (spin-dependent) interactions on the left (right) panel.

2 Hidden Valley

A number of extensions of the Standard Model of particle physics (SM) involve a hidden sector that is weakly coupled to the SM, via a heavy communicator scalar particle, Φ_{HS} of mass m_Φ [6]. In the model considered here the Φ_{HS} couples to mass in the same manner as the Higgs. A confining gauge in the Hidden Sector leads to the existence of so-called valley-hadrons and include long-lived valley-pions denoted here π_v. Using a dedicated trigger that looks at the ratio of energy in the hadron calorimeter (E_{H}) to that in the electromagnetic calorimeter (E_{EM}), the ATLAS experiment looks for π_v decaying into SM hadrons deep in the electromagnetic calorimeter or inside the hadronic calorimeter [7]. The signal is searched for by selecting collisions which present two hadronic jets with $E_{\mathrm{H}}/E_{\mathrm{EM}} > 1.2$ and p_{T} of the leading jet greater than 60 GeV, and no tracks close to the jet. Standard model backgrounds are reduced by requiring $E_{\mathrm{T}}^{\mathrm{miss}}$ <50 GeV. Figure 2 shows the resulting exclusion limits on the proper decay length of the π_v as function of its mass $m_{\pi v}$ and m_Φ.

3 Black Holes

Black holes relevant to particle physics are predicted in models with n extra dimensions. While SM particles are confined to the usual 3+1 dimensions, gravity is permitted to propagate to the extra dimensions. In this class of models the fundamental gravity scale $M_{\rm D}$ is given by $M_{\rm D}^{2+n} = M_{\rm Planck}^2 R^{-n}/8\pi$, where $M_{\rm Planck}$ is the usual Planck mass and R is the size of the extra dimensions. The fundamental gravity scale $M_{\rm D}$ could potentially be as small as a few TeV and thus requires investigation at LHC. Two types of black holes are investigated, quantum black holes (QBH), semi-classical black holes (BH).

The QBH are relevant when the black holes are produced close to their production threshold $M_{\rm th}$. In this regime the QBH decays into two high $p_{\rm T}$ particles, including lepton+quark final states that violate baryon and lepton numbers. The signal region [8] is defined by the presence of a single electron or muon with $p_{\rm T} > 130$ GeV and a jet. The final discriminating variable is the invariant mass of the lepton-jet system $M(\ell, jet)$ required to be larger than $0.9M_{\rm th}$ in the electron channel and larger than $([0.95 - 0.05 \times M_{\rm th}]/1{\rm TeV}) \times M_{\rm th}$ in the muon channel.

The semi-classical approximation of thermal black holes where the BH loses mass and angular momentum via Hawking radiation is valid if $M_{\rm th} >> M_{\rm D}$, the BH decays to a high particle multiplicity, high $p_{\rm T}$ particle final state including both leptons and hadrons. The signal region [9] is defined by requiring at least one electron or muon with $p_{\rm T} > 100$ GeV and at least two more particles with $p_{\rm T} > 100$ GeV. The final discriminating variable is the scalar sum of the $p_{\rm T}$ of all particles with $p_{\rm T} > 60$ GeV, including both leptons and jets, and denoted $\sum p_{\rm T}$. The signal region is defined by $\sum p_{\rm T} > 2000$ GeV.

Figure 3 presents a selection of the ATLAS exclusion limits on QBH (left) and semi-classical black holes (right). In the case of QBH, production thresholds of up to 5.5 TeV are excluded. In the case the semi-classical black holes n =2 to 6 extra dimensions have been investigated, two models have been considered for black hole production and decay using CHARYBDIS [10] and BLACKMAX [11]. Both rotating and non-rotating black holes have been considered. In all cases production thresholds below 5−6 TeV are excluded for $M_{\rm D}$ between 1.5−4 TeV.

Acknowledgments

The author would like to acknowledge support from the Swedish Research Council and Stockholm University Natural Science Faculty.

MC sample m_Φ, $m_{\pi v}$ [GeV]	excluded range 30% BR $\Phi_{\rm HS} \to \pi_{\rm v}\pi_{\rm v}$ [m]	excluded range 10% BR $\Phi_{\rm HS} \to \pi_{\rm v}\pi_{\rm v}$ [m]
126, 10	0.10 - 4.38	0.13 - 2.30
126, 25	0.27 - 10.01	0.37 - 5.12
126, 40	0.54 - 12.11	0.86 - 5.62

Figure 2: ATLAS excluded range at 95% CL for the proper decay length of the π_v for different masses $m_{\pi v}$ and m_Φ and values of the branching ratio (BR) of $\Phi_{\rm HS} \to \pi_v\pi_v$.

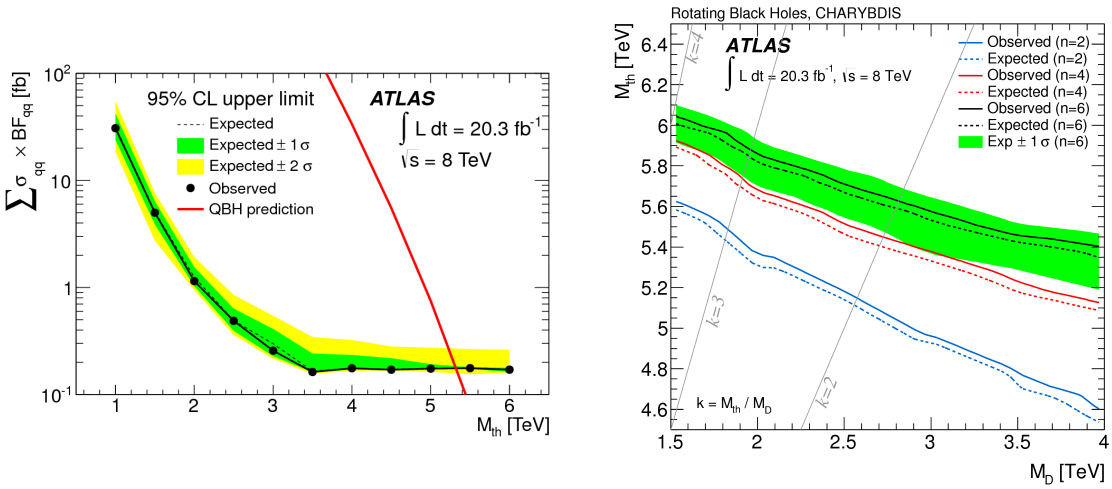

Figure 3: Left: ATLAS upper limit at 95% CL on the total quantum black hole production cross section given by the sum over all quark-quark production channels times the branching ratio of each channel into the quark+lepton final state, as function of the production threshold M_{th}. Right: ATLAS excluded region in the case of semi-classical black holes, in the plane $M_{\mathrm{D}}, M_{\mathrm{th}}$, reproduced here in the scenario of rotating black holes simulated with CHARYBDIS.

References

[1] ATLAS Collaboration, Phys. Rev. Lett. 112, 041802 (2014).

[2] Y. L. Dokshitzer et *al.*, J. High Energy Phys. 08 (1997).

[3] ATLAS Collaboration, J. High Energy Phys. 09, 037 (2014).

[4] ATLAS Collaboration, Phys. Rev. D 90, 012004 (2014).

[5] J. Goodman et *al.*, Phys.Rev. D 82, (2011).

[6] M. J. Strassler and K. M. Zurek, Phys. Lett. B 651, 374379 (2007).

[7] ATLAS Collaboration, Public Conference Result, ATLAS-CONF-2014-041 (2014).

[8] ATLAS Collaboration, J. High Energy Phys. 08, 103 (2014).

[9] ATLAS Collaboration, Phys. Rev. Lett. 112, 091804 (2014).

[10] J. A. Frost et al., J. High Energy Phys. 10, 014 (2009).

[11] D.-C. Dai et *al.*, Phys. Rev. D 77, 076007 (2008).

Search for New Physics with Top quarks in ATLAS at 8 TeV ($t\bar{b}$, $t\bar{t}$, vector-like quarks)

David Calvet on behalf of the ATLAS Collaboration

LPC Clermont-Ferrand, BP80026, 63171 Aubière cedex, France

DOI: http://dx.doi.org/10.3204/DESY-PROC-2014-04/206

This contribution presents results from searches for new resonances (W', Z', g_{KK}), decaying to a top-antibottom pair or a top-antitop pair, including the use of boosted top quark reconstruction techniques. Results from the search for vector-like quarks (focusing on the decay channels $T \to Zt$ and $B \to Zb$) are also presented. These searches use the data sample recorded in 2012 at $\sqrt{s} = 8$ TeV centre-of-mass energy by the ATLAS experiment at the LHC. Data are in good agreement with the Standard Model predictions, therefore limits are derived on the production of these new processes.

1 Introduction

The Standard Model (SM) of particle physics is a tremendous success, in particular with the recent discovery at LHC of a new scalar boson that is compatible with the one predicted by the Brout-Englert-Higgs mechanism. However, several aspects indicate that the SM cannot be the ultimate theory and many extensions[1] have been proposed in the past. Most of them predict the existence of new heavy particles, usually coupled preferentially to the top quark due to its very high mass. Among these new particles, this contribution will focus on W' decaying to $t\bar{b}$, new $t\bar{t}$ resonances (Z' and g_{KK}) and vector-like quarks (VLQ), with the ATLAS [1] detector.

2 $W' \to t\bar{b}$

In the SM, the W boson couples only to left-handed fermions. It is therefore natural to search for a partner of the W that would couple to right-handed fermions, the W'_R. Moreover, some theories beyond the SM (BSM), including extra-dimensions or technicolor, predict the existence of a heavier partner of the standard W, still coupling to left-handed fermions, the W'_L. In this contribution, the W' is supposed to decay mainly to $t\bar{b}$ (or $\bar{t}b$), with an unknown coupling constant g', and the analysis presented here [2] is designed for the reconstruction of the hadronic decay of the top quark. The main target of this analysis is a very heavy W' (from 1.5 to 3 TeV), thus ensuring the decay products are highly boosted.

The selected events must have been triggered by the presence of at least 700 GeV of transverse energy in the calorimeters. Events are not accepted if a high quality electron or muon is present. Each event must contain exactly one b- and one top-quark candidate. The b-quark candidate is a small-R (R=0.4) b-tagged jet with $p_T > 350$ GeV. Being highly boosted, the

[1] In this contribution, only non-SUSY extensions of the SM are considered.

top-quark candidate must be reconstructed as a single large-R (R=1.0) jet with $p_T > 350$ GeV. Both jets must be well separated[2] ($\Delta R > 2.0$). The events are then splitted in two categories: the *one b-tag* category and the *two b-tag* category. In the latter one, a small-R b-tagged jet must be present inside the top-quark candidate.

The background is composed of 99% multijet events in the one b-tag category and of 88% multijet events and 11% $t\bar{t}$ events in the two b-tag category. The multijet background is estimated from data using control regions while the $t\bar{t}$ background is estimated from Monte Carlo (MC) simulation. Figure 1 shows the distributions of the mass of the two jets (m_{tb}) observed in the data for the two categories. The result of background-only fits to these spectra are also shown and exhibits no excess with respect to the SM production. Therefore, 95% confidence level (C.L.) upper limits on the production cross-sections times BR($W' \to t\bar{b}$) are derived as a function of the W' mass, and range from 0.16 pb to 0.33 pb for the W'_L, and from 0.10 pb to 0.21 pb for the W'_R. Assuming $g' = g_{\rm SM}$, these limits can be translated to a lower limit of 1.68 TeV (1.63 TeV expected) for the mass of the W'_L and 1.76 TeV (1.85 TeV expected) for the mass of the W'_R. Removing this assumption, limits can be set in the $(g' - m_{W'})$ plane as can be seen in Fig. 2.

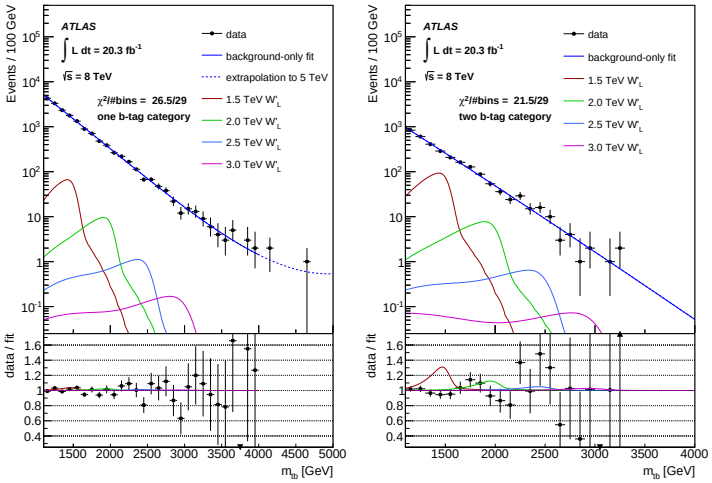

Figure 1: m_{tb} distributions in data in the one b-tag (left) and two b-tag (right) categories. Background-only fits are shown and the bottom plots show the ratio of the data and the fit. Potential W'_L signal shapes with $g'_L = g_{\rm SM}$ are also overlaid.

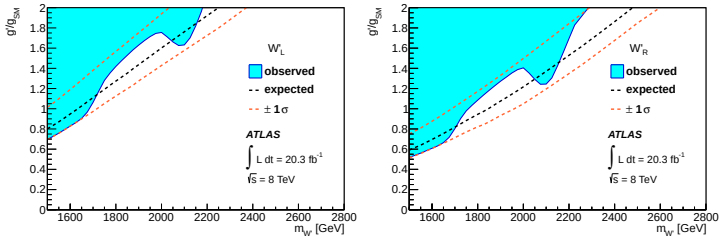

Figure 2: Observed and expected 95% C.L. limits on the ratio of coupling $g'_L/g_{\rm SM}$ ($g'_R/g_{\rm SM}$) of the W'_L (W'_R) model as a function of the W' mass.

3 $g_{KK}/Z' \to t\bar{t}$

New bosons that could decay to $t\bar{t}$ are predicted by several BSM models. In the analysis [3] described in this contribution, two benchmark models are tested: a narrow leptophobic Z' and a Kaluza-Klein (KK) excitation of the gluon in the Randall-Sundrum model.

[2] $\Delta R = \sqrt{\Delta\eta^2 + \Delta\phi^2}$

The selected events must have been triggered by the presence of one electron or muon and each event must contain at least one b-tagged jet. The events are then splitted in two categories: the *resolved* and the *boosted* ones. In the resolved category, the $t\bar{t}$ system is reconstructed using the lepton, the missing transverse momentum and three or four small-R jets. In the boosted category, the top quark that decays leptonically is reconstructed using the lepton, the missing transverse momentum and one small-R jet, while the hadronically decaying top is reconstructed as one high-mass large-R jet.

Figure 3 shows the distribution of the mass of the reconstructed $t\bar{t}$ system observed in data, compared to the SM prediction. No significant excess is observed, therefore 95% C.L. upper limits on the production cross section of new bosons are set. For the Z', these limits can be translated to a lower limit on its mass of 1.8 TeV, while for the KK gluon, the limit on the mass is 2.0 TeV. These results have been obtained with 70% of the statistics available, a refined analysis on the full dataset is being performed.

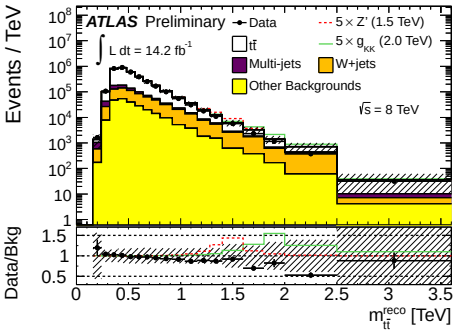

Figure 3: The $t\bar{t}$ invariant mass spectrum, summing the spectra from the resolved and boosted categories.

4 Vector-like quarks

The simple implementation of a fourth generation of quarks is now excluded by the LHC data. Vector-like quarks, predicted by various BSM models, including composite Higgs, are not ordinary quarks because their left- and right-handed components have the same weak isospin. Thanks to this property, such new quarks are still allowed by the current data. In the analysis [4] described in this contribution, the new T (with charge +2/3) and B quarks (with charge -1/3) are searched for, both in the pair and single production processes, concentrating on the $T \to Zt$ and $B \to Zb$ decays, but also including the decays $T \to Wb/Ht$ and $B \to Wt/Hb$.

The selected events must have been triggered by the presence of one electron or muon. Each event must contain at least two central jets ($|\eta| < 2.5$) and an opposite-sign same-flavour pair of electrons or muons that is compatible with the mass of the Z boson and with a p_T above 150 GeV. The events are then splitted in two categories: the *dilepton* category when no additional lepton (e or μ) is present, and the *trilepton* category when at least a third lepton is present. The number of b-tagged jets must be at least one in the trilepton category and at least two in the dilepton category. For the selection of the pair production signal, the scalar sum of the p_T of the jets must also be at least 600 GeV in the dilepton category. For the single production, the presence of at least one forward jet ($2.5 < |\eta| < 4.5$) is required in both categories. Background processes are dominated by Z+jets, WZ and $t\bar{t} + Z$ and are estimated from simulated samples. For the Z+jets samples, a reweighting is applied, determined from a fit of the Z p_T spectrum observed in data in the zero b-tag control region. After selection of the dilepton events, the spectra of the mass of the $Z - b$ system (m_{Zb}) observed in data are compared to the expected ones, both for the pair production selection and for the single production. Similarly, for the trilepton events, the spectra of the scalar sum of the p_T of the jets and the leptons (H_T) are examined. All observed spectra are compatible with the expectations, thus 95% C.L. upper limits on the T and B production cross sections are set.

For the pair production, these limits can be translated to lower limits on the mass of the

new quarks assuming some specific values of the decay branching ratios. In the case of $SU(2)$ singlets, these limits are 685 GeV for the B and 655 GeV for the T. If the new quarks are members of $SU(2)$ doublets, the limits are 755 GeV for the B and 735 GeV for the T. Without any assumption on the branching ratios, lower limits on the masses can be set for any configuration, as shown in Figure 4: the best sensitivity is achieved in the lower-left corner, where the branching ratio to Zb/t is 1.

For the single production, the upper limits on the production cross sections are shown in Figure 5 as a function of the new quark mass. As for the pair production, the limits on the T single production are obtained combining the dilepton and trilepton categories, while the limits on the B single production are obtained only with the dilepton events, the trilepton ones being insensitive to this signal.

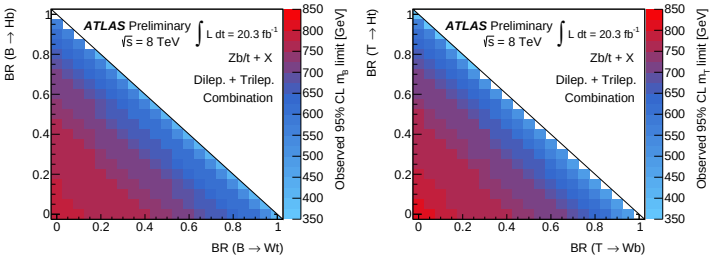

Figure 4: Observed 95% C.L. lower limits on the mass of the B (left) and the T (right) quark as a function of the branching ratios, assuming the pair production hypothesis.

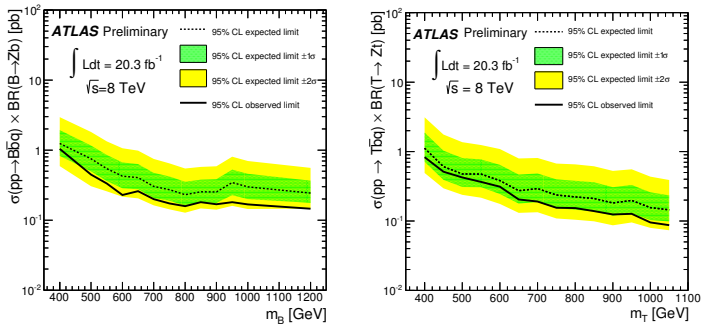

Figure 5: Expected and observed 95% C.L. upper limits on the single production cross section times the branching ratio as a function of the B (left) and the T (right) quark mass.

5 Conclusion

Many analyses are performed by the ATLAS Collaboration searching for non-SUSY new bosons or new fermions with top quarks. In this contribution, only the most recent results have been presented for the W' decaying to $t\bar{b}$, new $t\bar{t}$ resonances and vector-like quarks. The W' search presented here is focusing on high mass W' (above 1.5 TeV), leading to highly boosted top quarks, and the candidates are reconstructed in a fully hadronic mode. The $t\bar{t}$ resonances search combines the resolved and boosted topologies and constrains the Z' and g_{KK} productions. The VLQ search that was presented is designed for the decays $T \to Zt$ and $B \to Zb$ with the Z boson decaying to electrons or muons. None of these analyses exhibit any deviation from the SM prediction, therefore various limits have been derived.

References

[1] ATLAS Collab., JINST 3 S08003 (2008), doi:10.1088/1748-0221/3/08/S08003.

[2] ATLAS Collab., arXiv:1408.0886 [hep-ex].

[3] ATLAS Collab., ATLAS-CONF-2013-052, `https://cds.cern.ch/record/1547568`.

[4] ATLAS Collab., ATLAS-CONF-2014-036, `https://cds.cern.ch/record/1735195`.

Searches for direct pair production of third generation squarks with the ATLAS detector

Giulio Usai[1] on behalf of the ATLAS collaboration

[1]University of Texas at Arlington Arlington, USA

DOI: http://dx.doi.org/10.3204/DESY-PROC-2014-04/208

Naturalness arguments for weak-scale supersymmetry favour supersymmetric partners of the third generation quarks with masses not too far from those of their Standard Model counterparts. Top or bottom squarks with masses less than a few hundred GeV can also give rise to direct pair production rates at the LHC that can be observed in the data sample recorded by the ATLAS detector. This note presents recent ATLAS results from searches for direct stop and sbottom pair production.

1 Introduction

Supersymmetry (SUSY) [1, 9] is an extension of the Standard Model (SM) which can resolve the hierarchy problem by introducing supersymmetric partners to the known fermions and bosons. The dominant contributions for the radiative corrections to the Higgs mass are loop diagrams with top quarks. These can be canceled (naturally) if the supersymmetric partner of the top quark (stop) has a mass below the TeV range. A light bottom squark is also likely because the partners of the left-handed top and bottom squarks share the same mass term in the SUSY-breaking Lagrangian. In R-parity conserving supersymmetric models, the SUSY particles are produced in pairs and the lightest supersymmetric particle (LSP) is stable. In many models the LSP is the lightest neutralino, $\tilde{\chi}_1^0$, which is only weakly interacting and provides a candidate particle to address the dark matter problem.

In these proceedings, a summary of ATLAS searches for third generation squarks is presented. All the searches are based on the 2012 dataset of p p collisions at $\sqrt{s} = 8$ TeV representing about 20 fb^{-1} of integrated luminosity.

2 The ATLAS detector

The ATLAS detector [10] consists of an inner detector (ID) operating in a 2 T superconducting solenoid, a calorimeter system and a muon spectrometer with a toroidal magnetic field. The ID tracking system includes a silicon pixel detector, a silicon microstrip detector (SCT), and a transition radiation tracker (TRT). It provides tracking information for charged particles in a pseudo-rapidity range $|\eta| < 2.5$ and allows identification of jets originating from b-hadron decays. The ID is surrounded by high-granularity liquid-argon (LAr) sampling electromagnetic calorimeters. An iron/scintillator tile calorimeter provides hadronic energy measurements in

the central pseudo-rapidity range ($|\eta| < 1.7$). In the forward regions ($1.5 < |\eta| < 4.9$), it is complemented by two end-cap calorimeters using LAr as the active material and copper or tungsten as an absorber. The muon spectrometer (MS) surrounds the calorimeters and consists of three large superconducting eight-coil toroids, a system of tracking chambers, and detectors for triggering.

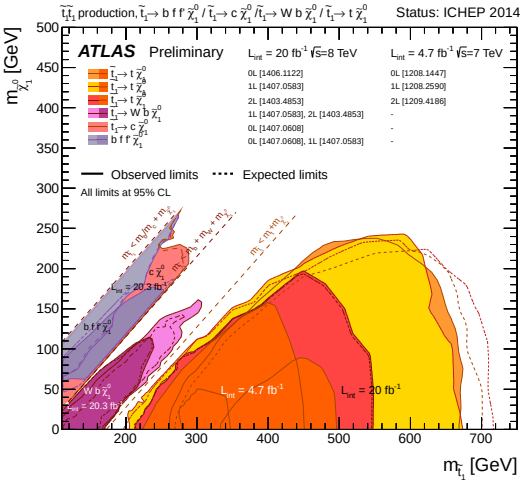

Figure 1: Summary of top squark pair production searches. Exclusion limits at 95% CL are shown in the stop-neutralino mass plane.

3 Top squark searches

The decay of the top squark depends on the mass splitting between the stop and its possible decay products, leading to very different topologies depending on the mass spectrum. For a heavy stop, the dominant decays would be $\tilde{t_1} \to t\tilde{\chi}_1^0$ (kinematically allowed if $m(\tilde{t_1}) > m(t) + m(\tilde{\chi}_1^0)$) and $\tilde{t_1} \to b\tilde{\chi}_1^\pm$ which is allowed if $m(\tilde{t_1}) > m(b) + m(\tilde{\chi}_1^\pm)$.

If the $\tilde{t_1} \to t\tilde{\chi}_1^0$ decay is kinematically forbidden, the stop could have a three-body decay $\tilde{t_1} \to bW\tilde{\chi}_1^0$ via an off-shell top and if the mass difference between the stop and the lightest neutralino is smaller than the sum of the W boson and b-quark masses, eventually the decay can proceed with an off-shell W or with a loop decay to a charm quark and the lightest neutralino $\tilde{t_1} \to c\tilde{\chi}_1^0$.

The searches for a heavy stop decay are designed based on the decay of the W boson in the top or chargino decay modes, leading to topologies with zero, one or two leptons.

Searches for stop decay in the fully hadronic channel [11] require up to six jets (two of which b-tagged) and show a very good sensitivity at high stop masses. This is reached using large radius ($\Delta R = 1.2$) re-clustering techniques that become very efficient in boosted topologies.

The semi-leptonic analyses [12] make use of shape fits in the E_T^{miss} and m_T variables to distinguish a potential stop signal from the $t\bar{t}$ background showing good sensitivity for high and medium stop masses. The shape-fit techniques push the sensitivity toward the kinematic limit for the stop decay though top. Here the kinematic properties of the signal closely resemble the

$t\bar{t}$ pairs production making this region very challenging. (Stop pairs production cross-section is typically a few percent of the top pairs production and LSPs are very soft).

The fully leptonic final state analyses [13] target both $\tilde{t_1} \to b\tilde{\chi}_1^{\pm}$ and $\tilde{t_1} \to t\tilde{\chi}_1^0$ decays, making use of a generalization of the transverse mass variable (m_{T2}) as a discriminator between signal and background.

Two other analyses target the very small Δm values, using charm-tagging jets techniques and the monojet selections [14]. These analyses show good sensitivity in this very challenging region up to the kinematic limit. Both these approaches use ISR or FSR to select boosted stops and explore the very compressed decay spectra.

4 Bottom squark searches

The direct production of bottom squarks is targeted by complementary analyses, which are sensitive to different decay modes. A fully hadronic final state search [15] selects events with two b-jets and large E_T^{miss}, and is sensitive to the $\tilde{b_1} \to b\tilde{\chi}_1^0$ decay mode. Selection with large values of invariant and cotransverse mass of the two b-jets is sensitive to large values of $\Delta m(\tilde{b_1}, \tilde{\chi}_1^0)$, while the sensitivity to small values of the mass difference is achieved by looking for events with a hard jet produced by initial or final state radiation. We require an untagged leading jet. The observed number of events is in agreement with the SM expectations for both selections. The resulting limits in the sbottom, neutralino mass plane are shown in Fig. 2.

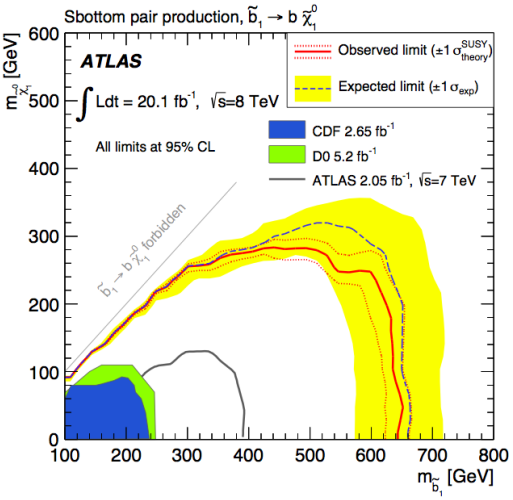

Figure 2: Expected and observed exclusion limits at 95% CL in the $\tilde{b_1}$ $\tilde{\chi}_1^0$ mass plane for the sbottom pair production scenario considered.

A search in events with two same-sign leptons [16] is sensitive to the $\tilde{b_1} \to t\tilde{\chi}_1^{\pm} \to tW\tilde{\chi}_1^0$ decay mode and places exclusion limits on the $\tilde{b_1}$ $\tilde{\chi}_1^{\pm}$ mass plane for fixed neutralino mass values. A search with three b-jets [17] in the final state places limits on models with $\tilde{b_1} \to b\tilde{\chi}_2^0 \to bh\tilde{\chi}_1^0$ where h is the CP-even Higgs boson.

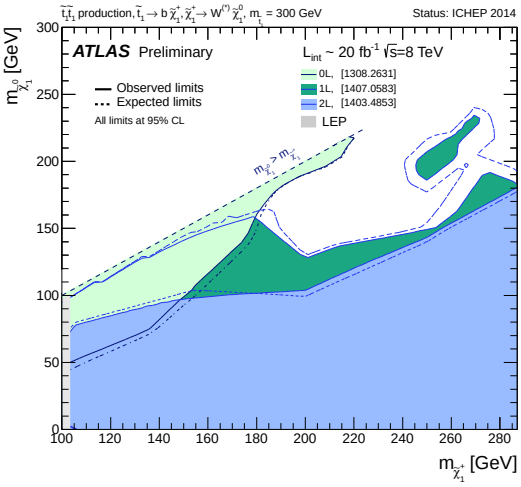

Figure 3: Summary of top squark pair production searches. Exclusion limits at 95% CL are shown in the chargino-neutralino mass plane for stop of 300 GeV.

5 Summary

ATLAS has a number of dedicated searches sensitive to direct production of third-generation squarks. These proceedings give a short reference to these searches, with emphasis on new results.

No significant excesses over the SM expectations are observed, and exclusion limits are set on squark masses. Figure 1 summarizes the exclusion limits obtained by ATLAS as a function of the stop and neutralino masses for simplified models with different stop decays. Under the many assumptions used on these models, stop masses up to about 700 GeV are excluded for a massless neutralino, while for massive neutralinos of 250-300 GeV, stop sensitivity falls to 450-500 GeV. Many important holes are still present close to the various kinematic limits, as illustrated in Figure 3 in the chargino-neutralino mass plane.

References

[1] H. Miyazawa, Prog. Theor. Phys. 36 (6), 1266 (1966)
[2] R. Ramond, Phys. Rev. D3, 2415 (1971)
[3] Y. Golfand, E. Likhtman, JETP Lett. 13, 323 (1971)
[4] A. Neveu, J. Schwarz, Nucl. Phys. B31, 86 (1971)
[5] A. Neveu, J. Schwarz, Phys. Rev. D4, 1109 (1971)
[6] J. Gervais, B. Sakita, Nucl. Phys. B34, 632 (1971)
[7] D. Volkov, V. Akulov, Phys. Lett. B46, 109 (1973)
[8] J. Wess, B. Zumino, Phys. Lett. B49, 52 (1974)
[9] J. Wess, B. Zumino, Nucl. Phys. B70, 39 (1974)
[10] ATLAS Collaboration, JINST 3, S08003 (2008)
[11] ATLAS Collaboration, JHEP 09, (2014) 015

[12] ATLAS Collaboration, submitted to JHEP (arXiv:1407.0583)
[13] ATLAS Collaboration, JHEP 06, (2014) 124
[14] ATLAS Collaboration, Phys. Rev. D. 90, 052008 (2014)
[15] ATLAS Collaboration, JHEP 10, (2013) 189
[16] ATLAS Collaboration, JHEP 06, (2014) 035
[17] ATLAS Collaboration, submitted to JHEP (arXiv:1407.0600)

Chapter 11

Flavour physics - CKM and beyond

New physics searches with b-hadrons at the ATLAS experiment

Lidia Smirnova on behalf of the ATLAS Collaboration

Lomonosov Moscow State University, Faculty of Physics,
119991, Moscow, GSP-1, Leninskie gory 1-2, Russia

DOI: http://dx.doi.org/10.3204/DESY-PROC-2014-04/216

Flavour changing neutral currents and precision measurements of CP violation are investigated by the ATLAS experiment as probes to new physics beyond the standard model. This talk presents the most recent results on the search for the rare decay $B_s^0 \to \mu^+\mu^-$, as well as the latest update on the study of the various angular amplitudes contributing to flavour tagged $B_s^0 \to J/\psi(\mu^+\mu^-)\phi(K^+K^-)$ decays. The latter analysis measures the CP-violating phase ϕ_s, as well as the average B_s meson lifetime Γ_s and the decay width difference $\Delta\Gamma_s$.

1 Introduction

The searches with b-hadrons can present indirect evidence for new physics and show the size of new effects. They are complementary to direct searches. The talk presents the most recent results on the search for the rare decay $B_s^0 \to \mu^+\mu^-$ [1] and the latest update on the study of the various angular amplitudes contributing to flavour tagged $B_s^0 \to J/\psi(\mu^+\mu^-)\phi(K^+K^-)$ decays [2]. Both results are based on the integrated luminosity of 4.9 fb^{-1}, collected in 2011 for pp data at $\sqrt{s} = 7$ TeV.

2 Search for $B_s^0 \to \mu^+\mu^-$ rare decay

The decay $B_s^0 \to \mu^+\mu^-$ is highly suppressed in the standard model (SM) and therefore is of particular interest in the search for new physics. The existence of new hypothetical particles may change the branching fraction for this decay and, thus, demonstrate the presence of new physics. The SM predicts the branching fraction for the $B_s^0 \to \mu^+\mu^-$ decay to be $(3.23 \pm 0.27) \cdot 10^{-9}$ [3]. The CMS and LHCb common results with all RUN-1 collected data show evidence for $\mathscr{B}(B_s^0 \to \mu^+\mu^-) = (2.9 \pm 0.7) \cdot 10^{-9}$ [4, 5, 6]. The ATLAS [7] experiment sets the upper limit $\mathscr{B}(B_s^0 \to \mu^+\mu^-) < 2.2 \cdot 10^{-8}$ at 95% C.L. with half of the integrated 2011 luminosity (2.4 fb^{-1}) [8].

A new analysis was performed with the data in the di-muon invariant mass region from 5066 to 5666 MeV removed from the analysis until the procedures for event selection, as well as for the signal and limit extractions were completely defined.

The $B_s^0 \to \mu^+\mu^-$ branching fraction is measured with respect to the prominent reference decay $B^\pm \to J/\psi K^\pm$. The branching fraction can be written as $\mathscr{B}(B_s^0 \to \mu^+\mu^-) = N_{\mu^+\mu^-} \times \mathrm{SES}$,

where single-event sensitivity SES $= \frac{\mathscr{B}(B^{\pm}\to J/\psi K^{\pm})}{N_{J/\psi K^{\pm}}} \cdot \frac{f_u}{f_s} \cdot R_{A_\epsilon}$, $N_{\mu^+\mu^-}$ and $N_{J/\psi K^{\pm}}$ are the event numbers of the corresponding decays, $\frac{f_u}{f_s}$ is relative b-quark hadronisation probability of $B^{\pm}$ and B_s^0, taken from previous measurements, and R_{A_ϵ} is the acceptance and efficiency ratio for the two decays. A limit on $\mathscr{B}(B_s^0 \to \mu^+\mu^-)$ is derived by assuming $\mathscr{B}(B^0 \to \mu^+\mu^-)$ to be negligible.

Monte Carlo simulated event samples were adjusted by an iterative re-weighting procedure with re-weighting based on simulation, followed by a data driven re-weighting. This procedure uses the comparison of MC events to the sample of $B^{\pm} \to J/\psi K^{\pm}$ events in collision data. Only candidates with odd event numbers are used in the re-weighting procedure, while the remaining sample is used for the yield measurement. The weights are cross-checked on the $B_s^0 \to J/\psi\phi$ control channel.

Only events containing candidates for $B_s^0 \to \mu^+\mu^-$ and $B^{\pm} \to J/\psi K^{\pm}$ are retained for this analysis. The sidebands for signal events are [4766, 5066] and [5666, 5966] MeV. For the reference channel, the signal region is [5180, 5380] MeV and sidebands are [4930, 5130] and [5430, 5630] MeV. After preselection, approximately $3.9 \cdot 10^5$ $B_s^0 \to \mu^+\mu^-$ and $2.5 \cdot 10^5$ $B^{\pm} \to J/\psi K^{\pm}$ candidates are obtained in the signal regions.

Two categories of background are considered: a continuum with smooth dependence on the di-muon invariant mass, and various sources of resonant contributions, most of which come from the $B_{(s)}^0 \to h^+h'^-$ decays (with h being a kaon or pion) when both daughters are misidentified as muons in the detector. The combinatorial background from $b\bar{b} \to \mu^+\mu^- X$ decays provides a reasonable description for event variables, used for background suppression, in sidebands. The contribution of the resonant background is estimated from MC.

The Boosted Decision Tree (BDT) algorithm was found to be the best performing discrimination between the signal and background events. It uses 13 variables. Distributions from $B^{\pm} \to J/\psi K^{\pm}$ events simulated with MC are compared to data after the side-band background subtraction for all discriminating variables and variables used in the preselection. The optimisation procedure aims at selecting the best performing BDTs and obtaining the final selection cuts in the BDT output variable q and in the invariant mass window Δm. The signal region is defined as $\pm\Delta m$ centred around a mass of 5366.33 MeV. The optimization is performed by maximizing the estimator $P = \frac{\epsilon}{1+\sqrt{B}}$, where ϵ is the signal efficiency and B is the number background events selected. The 2-dimensional optimization on the BDT output requirement and the signal region width is performed on the signal MC sample and the odd-numbered data events from sidebands. The optimization gives a maximum P value of 0.0145 with BDT output > 0.118 and $|\Delta m| < 121$ MeV.

The branching fraction for the reference channel is calculated as a product of $\mathscr{B}(B^{\pm} \to J/\psi K^{\pm}) = (1.016 \pm 0.033) \cdot 10^{-3}$ and $\mathscr{B}(J/\psi \to \mu^+\mu^-) = (5.93 \pm 0.06)\%$. The ratio $\frac{f_u}{f_s}$ is taken from $\frac{f_s}{f_d} = 0.256 \pm 0.020$ using $\frac{f_d}{f_u} = 1$. The ratio R_{A_ϵ} is evaluated using MC samples and found to be $0.267 \pm 1.8\% \pm 6.9\%$. The reference channel yield $N_{J/\psi K^{\pm}}$ is determined from a multi-dimensional unbinned extended maximum likelihood fit to the distribution of the invariant-mass of the $\mu^+\mu^- K^{\pm}$ system and its event-by-event uncertainty. The combined result for $N_{J/\psi K^{\pm}}$ gives 15214 even-numbered events with an uncertainty $\pm 1.1\%$ (stat.) and $\pm 2.4\%$ (syst.). The SES value is obtained as $(2.07 \pm 0.26) \cdot 10^{-9}$.

To extract the upper limit on the $\mathscr{B}(B_s^0 \to \mu^+\mu^-)$ the standard implementation of the CLs method in ATLAS is used. Before unblinding the signal region, the expected number of background events in this region is found to be 6.75. After unblinding, 6 events are counted in

the signal region and used in CLs analysis. The observed CLs as a function of $\mathscr{B}(B_s^0 \to \mu^+\mu^-)$ is shown in Fig. 1a. The observed limit is $\mathscr{B}(B_s^0 \to \mu^+\mu^-) < 1.5(1.2) \cdot 10^{-8}$ at 95% (90%) CL.

3 CP violation parameter ϕ_s and $\Delta\Gamma_s$ from angular amplitudes of $B_s^0 \to J/\psi\phi$ decay

New phenomena beyond SM may alter CP violation in B-decays. A channel $B_s^0 \to J/\psi\phi$ is expected to be sensitive to new physics contributions. CP violation in this channel occurs due to interference between direct decays and decays with B_s^0—$\bar{B}_s^0$ mixing, characterized by Δm_s of heavy (B_H) and light (B_L) mass eigenstates, and is measured by the weak phase ϕ_s. It is small in SM: the predicted value is $\phi_s = -0.0368 \pm 0.0018$ rad [9]. The width difference $\Delta\Gamma_s = \Gamma_H - \Gamma_L$ is not expected to be significantly affected by new physics and is useful for the SM prediction test. The average decay width is $\Gamma_s = (\Gamma_H + \Gamma_L)/2$.

Previous ATLAS measurement of ϕ_s, Γ_s and $\Delta\Gamma_s$ from fully reconstructed decays $B_s^0 \to J/\psi(\mu^+\mu^-)\phi(K^+K^-)$ with only statistical CP states separation with 4.9 fb^{-1} is published in [10]. The results are updated with the flavour tagged time-dependent angular analysis [2].

The determination of the initial flavor of neutral B-mesons can be inferred from the B-meson that is produced from another b-quark in the event. The calibration of the method is performed in events containing the decays $B^\pm \to J/\psi K^\pm$.

Several methods are available to infer the flavor of the opposite-side b-quark. First, the measured charge of a muon from semileptonic decay of the B-meson provides a strong separation power and it can be enhanced by considering a weighted sum of the charge q_i of the tracks in the cone ΔR around muon:

$$Q_\mu = \frac{\sum_i^{N_{\rm tr}} q_i \cdot (p_T^i)^k}{\sum_i^{N_{\rm tr}} (p_T^i)^k},$$

where $k = 1.1$, number of tracks $N_{\rm tr}$ includes tracks with $p_T > 0.5$ GeV and $|\eta| < 2.5$, $\Delta R = 0.5$. If no muon is present, a b-tagged jet is required in the event, which is seeded from calorimeter clusters with an energy threshold of 10 GeV and a minimum b-tag weight of -0.5. The jet is reconstructed using the anti-k_t algorithm with a cone size 0.6. The jet charge $Q_{\rm jet}$ is defined similar to Q_μ, where the sum is over the tracks associated with the jet. In both cases, the tracks associated with the signal decay products are excluded from the sum.

Candidates for $B_s^0 \to J/\psi\phi$ decays are selected by following requirements: no displaced vertex or time cuts applied in the trigger or offline; J/ψ mass window adapted separately for barrel and endcap regions; ϕ mass window of 22 MeV; kaons $p_T > 1$ GeV; B-vertex fit quality χ^2/d.o.f. < 3. In total, 131k B_s^0 candidates within $5.15 < m(B_s^0) < 5.65$ GeV are used in the fit.

An unbinned maximum likelihood fit is performed on the selected events to extract the parameters of the $B_s^0 \to J/\psi(\mu^+\mu^-)\phi(K^+K^-)$ decay. The fit uses reconstructed mass and proper time with the uncertainties, the tag probability and the transversity angles $\Omega(\theta_T, \psi_T, \phi_T)$, defined in the rest frames of $J/\psi(\theta_T, \phi_T)$ and $\phi(\psi_T)$. The likelihood function includes the combination of signal and background probability density functions. The full simultaneous maximum likelihood fit contains 25 free parameters. The number of signal B_s^0 mesons extracted from the fit is 22670 ± 150. The solution with $\Delta\Gamma_s > 0$ is considered.

The results for physics parameters are

$$\phi_s = 0.12 \pm 0.25\,(\text{stat.}) \pm 0.05\,(\text{syst.})\,\text{rad},$$

$$\Delta\Gamma_s = 0.053 \pm 0.021\,(\text{stat.}) \pm 0.010\,(\text{syst.})\,\text{ps}^{-1},$$
$$\Gamma_s = 0.667 \pm 0.007\,(\text{stat.}) \pm 0.004\,(\text{syst.})\,\text{ps}^{-1},$$
$$|A_{\parallel}(0)|^2 = 0.220 \pm 0.008\,(\text{stat.}) \pm 0.009\,(\text{syst.}),$$
$$|A_0(0)|^2 = 0.529 \pm 0.006\,(\text{stat.}) \pm 0.012\,(\text{syst.}),$$
$$\delta_{\perp} = 3.89 \pm 0.47\,(\text{stat.}) \pm 0.11\,(\text{syst.})\,\text{rad}.$$

The values are consistent with those obtained in the untagged analysis [10] and reduce the statistical uncertainty on ϕ_s by 40%. The fit demonstrates sensitivity to the strong phase $\delta_{\perp}$. Likelihood contours in the $\phi_s - \Delta\Gamma_s$ plane are presented in Fig. 1b. The results are consistent with the values predicted in the standard model.

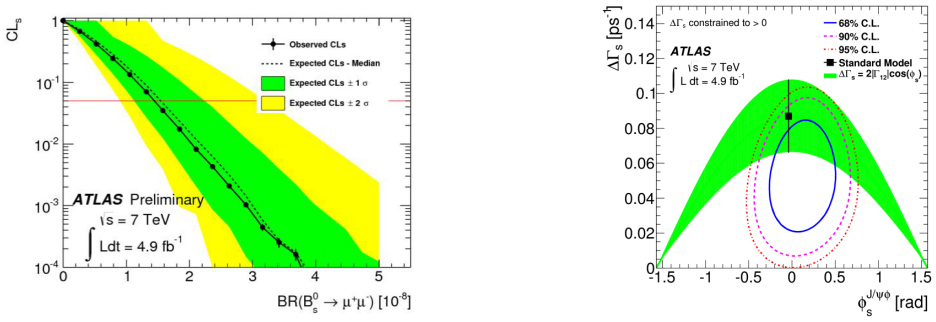

(a) (b)

Figure 1: (a) Observed CL_s as a function of $\mathscr{B}(B_s^0 \to \mu^+\mu^-)$. (b) Likelihood contours in the $\phi_s - \Delta\Gamma_s$ plane.

4 Conclusions

ATLAS results from the full 2011 data for pp collisions at 7 TeV ($4.9\,\text{fb}^{-1}$) are obtained for new physics searches in the rare decay $B_s^0 \to \mu^+\mu^-$ selection and $B_s^0 \to J/\psi\phi$ decay parameters measurement. The flavour tagged time dependent angular analysis is used for $B_s^0 \to J/\psi\phi$ improving on the previous ATLAS measurement without tagging. All results are consistent with the predictions of the standard model.

References

[1] ATLAS Collaboration, ATLAS-CONF-2013-076, https://cds.cern.ch/record/1562934
[2] ATLAS Collaboration, Phys. Rev. D 90 (2014) 052007
[3] Buras et al., Eur.Phys.J. **C72** (2012) 2172
[4] CMS Collaboration, Phys. Rev. Lett. 111 (2013) 101804
[5] LHCb Collaboration, Phys. Rev. Lett. 111 (2013) 101805
[6] CMS and LHCb Collaborations, CMS-PAS-BPH-13-007, https://cds.cern.ch/record/1564324
[7] ATLAS Collaboration, JINST **3**, S008003 (2008)
[8] ATLAS Collaboration, Phys. Lett. B 713 (2012) 387
[9] UTfit collab., M.Bona et al., Phys.Rev.Lett. 97 (2006) 151803
[10] ATLAS Collaboration, JHEP 12 (2012) 072

The New Muon $g-2$ Experiment at Fermilab

David Kawall[1] on behalf of the E989 Collaboration

[1]Department of Physics, University of Massachusetts Amherst, MA 01003, USA

DOI: http://dx.doi.org/10.3204/DESY-PROC-2014-04/132

Experiment E989 is under preparation at Fermilab, intending to measure the anomalous magnetic moment of the muon $g_\mu - 2$ to an accuracy of 140 ppb, a fourfold improvement over the Brookhaven E821 result. The latter differs by more than 3 standard deviations from Standard Model predictions, perhaps hinting at new physics and motivating a more sensitive comparison. The techniques of the new experiment to reduce experimental statistical uncertainties by a factor four and systematics by a factor three will be described.

1 Introduction and current status of the muon $g-2$ value

The magnetic moment of a fundamental particle is given by $\vec{\mu} = g(e\hbar/2m)\vec{S}/\hbar$, where $\vec{S}$ is the spin operator and $g = 2$ was predicted by Dirac for point-like spin 1/2 particles such as the electron or muon. This leading order prediction of the Standard Model (SM) is perturbed by radiative corrections. These couple the fields of virtual particles to the muon, leading to additional contributions so g_μ deviates from 2. The sum of all such corrections is characterized by the anomalous magnetic moment $a_\mu \equiv \frac{1}{2}(g_\mu - 2)$.

The largest contribution to a_μ comes from the Schwinger term, which involves the exchange of an additional virtual photon and contributes a_μ(QED, Leading-Order)$=\alpha_{\rm QED}/2\pi \approx 1.16 \times 10^{-3}$. The Schwinger term contribution to the electron a_e was confirmed experimentally by Kusch and Foley in 1947.

The modern SM prediction for a_μ includes QED contributions calculated to order $\alpha^5_{\rm QED}$ [1], weak interaction contributions calculated to 2 loops [2], and hadronic contributions. The latter are usually described in terms of a leading-order (LO) hadronic vacuum polarization (HadVP) and higher-order HadVP, where the LO HadVP is best determined from a dispersion relation and measurements of e^+e^- scattering into hadronic final states made by BABAR, KLOE, CMD2, and SND (see [3, 4] for details and references). The hadronic light-by-light contribution (Had-LBL) is determined from the "Glasgow Consensus" and is discussed in [5].

Abundant hadronic decay data of τ from LEP and CLEO can be used with isospin breaking corrections and the assumption of CVC to evaluate the LO HadVP contribution to a_μ. Since the τ data just has the isovector part of the contribution, the isoscalar part from e^+e^- scattering must be introduced by hand, so e^+e^- and τ evaluations of LO HadVP are not fully independent. Early τ-based evaluations were different from those based on e^+e^- scattering. Recently it has been shown that after properly accounting for $\gamma - \rho$ mixing the results are consistent [6].

The SM prediction is compared with the experimental result from Brookhaven E821 [7] in Table 1, where a 3.6 σ difference is observed. Using a different evaluation of the LO HadVP contribution, $(6949.1 \pm 42.7) \times 10^{-11}$, from [8], reduces the discrepancy to 3.3 σ.

There is great interest in this discrepancy since the Standard Model is incomplete, and many models of physics beyond the Standard Model, such as supersymmetry (SUSY), predict new particles which contribute to the muon anomaly and naturally cause such a discrepancy. For instance, given a mass scale Λ, the SUSY contribution in terms of $\tan\beta$ and the SUSY μ-parameter is [9] (see Fig. 1):

$$a_\mu(\text{SUSY}) \approx \text{sign}(\mu) \times 130 \times 10^{-11} \times \tan\beta \times \left(\frac{100\text{ GeV}}{\Lambda}\right)^2.$$

Thus a_μ measurements are potentially sensitive to SUSY interactions at the TeV scale. Technicolor models and models with extra spatial dimensions also predict contributions to a_μ. The muon anomaly is sensitive to new physics in a manner which is unique and complementary to other searches for new physics. It is more sensitive to new physics than the electron anomaly by a factor $(m_\mu/m_e)^2 \approx 43{,}000$. Anomaly contributions come from interactions which are CP- and flavor-conserving, chirality-flipping, and which appear in loops. This complements LHC searches for new physics since those observables are typically chirality-conserving. Further, the tanβ parameter and sign(μ) parameter which are important in many SUSY models are difficult to measure at the LHC, and determined better by a precision $g-2$ measurement [9]. Lower energy precision tests such as electric dipole moment (EDM) searches are sensitive to CP-violating interactions, and searches such as $\mu \to e$ conversion are flavor-violating. Muon $g-2$ is primarily sensitive to leptonic couplings so it complements precision s and B physics experiments that search for the hadronic couplings of new physics.

Whether the discrepancy between theory and experiment for a_μ is an indication of new physics can only be resolved by reducing the uncertainties. New precision measurements and analysis of e^+e^- scattering data from BESIII, Novosibirsk, and Frascati, and lattice QCD calculations of LO HadVP [10] should reduce the theoretical uncertainties. The discrepancy also motivates the new high rate, next generation $g_\mu - 2$ experiment E989 at Fermilab [11].

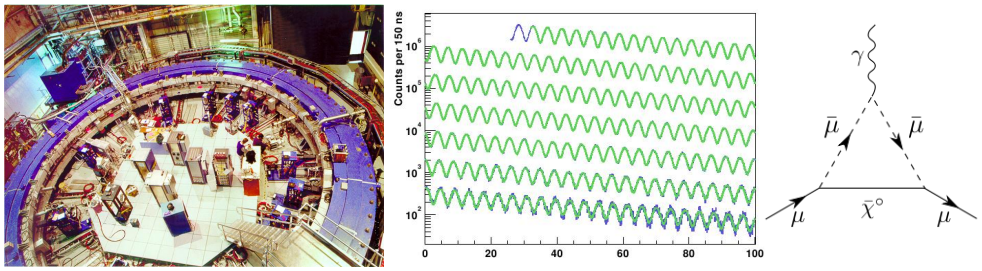

Figure 1: Left: The BNL E821 storage ring. Center: The BNL E821 "wiggle" plot showing the anomalous precession ω_a. Right: A one-loop SUSY contribution to a_μ from a smuon and chargino loop.

2 Overview of experimental technique

The experiment E989 will inject polarized muons through a superconducting inflector into a 7.1 m radius magnetic storage ring with electric quadrupoles for vertical focusing and scraping

Source		Contribution	Uncertainty
a_μ(QED)	=	116 584 718.951	$\pm$ 0.080 (α^5)
a_μ(HadVP; LO)	=	6 923	$\pm$ 42 (Exp)
a_μ(HadVP; HO)	=	-98.4	$\pm$ 0.6 (Exp) $\pm$ 0.4 (Rad)
a_μ(Had-LBL)	=	105	$\pm$ 26
a_μ(Weak; 1 loop)	=	194.8	
a_μ(Weak; 2 loop)	=	-41.2	$\pm$ 1 (Had) $\pm$ 2$\rightarrow$ 0 (Higgs)
a_μ(SM Theory)	=	116 591 802	$\pm$ 49 $\times 10^{-11}$ (0.42 ppm)
a_μ(E821 Expt.)	=	116 592 089	$\pm$ 63 $\times 10^{-11}$ (0.54 ppm)
Δ(Expt.-Theory)	=	287	$\pm$ 80 $\times 10^{-11}$ (3.6 σ)

Table 1: Standard model prediction from M. Davier *et al.* [4] for a_μ in units of 10^{-11}, and the experimental result from BNL E821 [7].

(essentially a Penning trap, see Fig. 1) [7, 11]. A magnetic kicker is pulsed on during the first turn, resulting in $\approx$ 10^4 muons on a stable orbit per fill. While stored, the muon spin vector precession frequency ω_S is faster than the momentum vector cyclotron frequency ω_C. The difference frequency ω_a is proportional to a_μ:

$$\vec{\omega}_a = \vec{\omega}_S - \vec{\omega}_C = -\frac{e}{m}\left[a_\mu \vec{B} - \left(a_\mu - \left(\frac{mc}{p}\right)^2\right)\frac{\vec{\beta}\times\vec{E}}{c}\right], \quad (1)$$

where $B = 1.45$T is the storage ring magnet field, and $\vec{E}$ is the electric field from the electrostatic quadrupoles. The electric field dependence cancels by using muons at the magic momentum $p_{\rm magic} = m_\mu c/\sqrt{a_\mu} \approx 3.094$ GeV/c, $\gamma \approx 29.3$.

To extract a_μ from Eq. 1, experiment FNAL E989 is required to measure two quantities precisely (*i*) the anomalous muon spin frequency precession frequency $\omega_a \approx 2\pi \times 229$ kHz and (*ii*) the magnetic field $\vec{B}$ averaged over the muon distribution in the ring. The magnetic field is measured using pulsed NMR [12, 13] and expressed in terms of the Larmor precession frequency a free proton would exhibit in the same field, $\omega_p \approx 2\pi \times 61.79$ MHz, using the relation $\hbar\omega_p = 2\mu_p B$.

The anomalous precession frequency ω_a is measured by detecting positrons from the decay of stored μ^+. Parity violation in this weak decay leads to a correlation between the positron emission direction and the muon spin direction. The lab frame positron energy is given approximately in terms of the rest frame energy E^* and rest frame angle between muon spin and positron direction θ^* by $E_{\rm lab} \approx \gamma E^*(1+\cos\theta^*)$. Detecting decay e^+ above 1.9 GeV corresponds to to a cut on θ^* and allows the reconstruction of the muon spin direction as a function of time. The resulting positron spectrum $N(t) \approx N_0 e^{-t/(\gamma\tau)}[1 + A\cos(\omega_a t + \phi)]$ from BNL E821 is seen in Fig. 1. Corrections are applied for muons not at the magic momentum, and for the pitching motion from vertical betatron oscillations.

The positron energies and arrival times will be determined by 24 calorimeters in the interior of the storage ring. The calorimeters have a 6×9 array of PbF_2 Čerenkov crystals with attached SiPMs read by 12 bit ADCs digitizing at 800 MSPS. Timing resolution is better than 100 ps, and spatial/temporal separation resolves e^+ arriving >5 ns apart. Gain stability over a fill of 0.1% requires a precision laser calibration system and mV SiPM bias stability. Information

about the muon spatial and momentum distribution in the ring will come from fiber beam monitors, a fast-rotation analysis [7], and from several sets of straw tracking chambers. The latter will also be used for an improved limit on the electric dipole of the muon. The systematics on the extraction of ω_a will be held to 70 ppb.

A significant, 20-fold improvement in detected positrons comes from several advantages of FNAL over BNL. First a more intense muon beam will be injected into the ring at a rate of about 12 Hz versus < 0.5 Hz at BNL. Unlike BNL, the muon beam will be free of pion contamination due the much longer decay line used - this yields much smaller backgrounds and allows the detectors to remain on during muon injection. Other improvements in the overall efficiency lead to an expected statistical precision of 100 ppb.

The magnetic field measurement will be improved by upgrades to the NMR measurement system, improved NMR probes and procedures, coupled with a more homogeneous and stable storage ring magnetic field, in part from an experimental hall with $\pm 1^{\circ}$C stability. The goal is a field measurement with an accuracy on the equivalent precession frequency of a free proton weighted by the muon distribution $\tilde{\omega}_p$ to 70 ppb.

3 Summary

The E989 experiment is under construction at Fermilab, intending to measure the anomalous magnetic moment of the muon a_μ to an accuracy of 140 ppb. Comparison of the experimental result with theoretical predictions yields a precise check of the Standard Model, with sensitivity to new physics. The first stored muons are expected around 2017.

Acknowledgments

This work was supported by the U.S Department of Energy Grant DE-FG02-88ER40115.

References

[1] T. Aoyama, M. Hayakawa, T. Kinoshita, and M. Nio, Phys. Rev. Lett. **109**, 111808 (2012).

[2] A. Czarnecki and W.J. Marciano, "Electromagnetic Dipole Moments and New Physics," in *Lepton Dipole Moments*, ed. by B.L. Roberts and W. Marciano, World Scientific, Singapore, pp.11-68, (2010).

[3] M. Davier, "Hadronic Vacuum Polarization and Lepton Anomalous Magnetic Moments," in *Lepton Dipole Moments*, ed. by B.L. Roberts and W.J. Marciano, World Scientific, Singapore, 2010, p. 273.

[4] M. Davier, A. Hoecker, B. Malaescu, and Z. Zhang, *Eur. Phys. J.* **C**71, 1515 (2011), erratum *Eur. Phys. J.* **C**72, 1874 (2012).

[5] J. Prades, E. de Rafael, and A. Vainshtein, "The Hadronic Light-by-Light Scattering Contribution to the Muon and Electron Anomalous Magnetic Dipole Moments," in *Lepton Dipole Moments*, ed. by B.L.Roberts and W.Marciano, World Scientific, Singapore, 2010, pp. 303–318; and arXiv:0901.0306v1 [hep-ph].

[6] F. Jegerlehner and R. Szafron, Eur. Phys. J. **C71**, 1632 (2011).

[7] G.W. Bennett et al. (BNL E821 Muon g-2 Collaboration), *Phys. Rev. D* **73**, 072003 (2006).

[8] K. Hagiwara et al., *J. Phys. G: Nucl. Part. Phys.* **38**, 085003 (2011).

[9] A. Czarnecki and W.J. Marciano, Phys. Rev. D**64**, 013014 (2001).

[10] C. Aubin and T. Blum, *Nucl. Phys. Proc. Suppl.* **181**, 251 (2006).

[11] The proposal to DOE can be found at http://gm2.fnal.gov

[12] R. Prigl *et al.*, Nucl. Instrum. Methods A **374**, 118 (1996).

[13] X. Fei, V.W. Hughes and R. Prigl, Nucl. Instrum. Methods A **394**, 349 (1997).

Measurements of CP Violation and Mixing in Charm Decays at LHCb

Michael Alexander on behalf of the LHCb collaboration

University of Glasgow, University Avenue, Glasgow, UK, G12 8QQ

DOI: http://dx.doi.org/10.3204/DESY-PROC-2014-04/244

During run I, the LHCb experiment at the LHC, CERN, collected 1.0 fb^{-1} of pp collisions at $\sqrt{s} = 7\,\text{TeV}$ and 2.0 fb^{-1} at $\sqrt{s} = 8\,\text{TeV}$, yielding the world's largest sample of decays of charmed hadrons. This sample is used to search for direct and indirect *CP* violation in charm and to measure D^0 mixing parameters. Recent measurements from several complementary decay modes are presented.

1 Introduction

The LHCb detector is a forward-arm spectrometer, with pseudo-rapidity coverage $2 < \eta < 5$, specifically designed for high precision measurements of decays of b and c hadrons [1]. During run I, the experiment collected 1.0 fb^{-1} of pp collisions at $\sqrt{s} = 7\,\text{TeV}$ and 2.0 fb^{-1} at $\sqrt{s} = 8\,\text{TeV}$, yielding the world's largest sample of decays of charmed hadrons. This allows *CP* violation and mixing in charm to be studied with unprecedented precision in many complementary decay modes. The Standard Model (SM) predicts *CP* asymmetries to be $\mathcal{O}(10^{-3})$ or less in charm interactions [2, 3]; observation of significantly larger *CP* violating effects could indicate new physics.

For a decay $\text{D} \to f$ and its *CP* conjugate $\bar{\text{D}} \to \bar{f}$, with amplitudes A_f and $\bar{A}_{\bar{f}}$ respectively, direct *CP* violation is quantified by $A_d = (|A_f|^2 - |\bar{A}_{\bar{f}}|^2)/(|A_f|^2 + |\bar{A}_{\bar{f}}|^2)$. For D^0 mesons, the mass eigenstates $|\text{D}_{1,2}\rangle$, with masses $m_{1,2}$ and widths $\Gamma_{1,2}$, are defined in terms of the flavour eigenstates, $|\text{D}^0\rangle$ and $|\bar{\text{D}}^0\rangle$, as $|\text{D}_{1,2}\rangle = p|\text{D}^0\rangle \pm q|\bar{\text{D}}^0\rangle$, with p and q complex, satisfying $|p|^2 + |q|^2 = 1$. The rate of mixing is quantified by $x \equiv 2(m_2 - m_1)/(\Gamma_1 + \Gamma_2)$ and $y \equiv (\Gamma_2 - \Gamma_1)/(\Gamma_1 + \Gamma_2)$. *CP* violation in mixing is quantified by $A_m \equiv (|q/p|^2 - |p/q|^2)/(|q/p|^2 + |p/q|^2)$ and the interference between mixing and decay (when $f = \bar{f}$) by $\lambda_f \equiv q\bar{A}_f/pA_f = \left|q\bar{A}_f/pA_f\right| e^{i\phi}$.

The flavour of the D^0 meson at production is determined using either $\text{D}^{*+} \to \text{D}^0\pi_s^+$ decays, where the charge of the "soft pion", π_s, track gives the D^0 flavour, or $\text{B} \to \text{D}^0\mu^- X$ decays, where the charge of the μ track gives the D^0 flavour.

2 Multi-body D decays

Multi-body D decays are sensitive to *CP* violation due to the interference of different resonances across the multi-body phase space. In $\text{D}^0 \to \text{K}^+\text{K}^-\pi^+\pi^-$ decays, triple products of final state particle momenta in the D^0 rest frame, defined as $C_T \equiv \vec{p}_{\text{K}^+} \cdot (\vec{p}_{\pi^+} \times \vec{p}_{\pi^-})$ and

$\bar{C}_T \equiv \vec{p}_{\mathrm{K}^-} \cdot (\vec{p}_{\pi^-} \times \vec{p}_{\pi^+})$ for D^0 and $\overline{\mathrm{D}}^0$ mesons respectively, are odd under T. The decay rate asymmetries

$$A_T \equiv (\Gamma(C_T > 0) - \Gamma(C_T < 0))/(\Gamma(C_T > 0) + \Gamma(C_T < 0)),$$
$$\bar{A}_T \equiv (\Gamma(-\bar{C}_T > 0) - \Gamma(-\bar{C}_T < 0))/(\Gamma(-\bar{C}_T > 0) + \Gamma(-\bar{C}_T < 0)),$$

are thus sensitive to *CP* violation. However, final state interactions introduce significant asymmetries, and so the difference $a_{CP}^{T\text{-odd}} \equiv \frac{1}{2}(A_T - \bar{A}_T)$ is used to access the asymmetry of the D^0 meson. The observable $a_{CP}^{T\text{-odd}}$ is by definition insensitive to production and detection asymmetries, so is very robust against systematic uncertainties.

Using 3 fb^{-1} of data, the phase space integrated measurements are found to be [4]

$$A_T = (-7.18 \pm 0.41(\mathrm{stat}) \pm 0.13(\mathrm{syst}))\%,$$
$$\bar{A}_T = (-7.55 \pm 0.41(\mathrm{stat}) \pm 0.12(\mathrm{syst}))\%,$$
$$a_{CP}^{T\text{-odd}} = (0.18 \pm 0.29(\mathrm{stat}) \pm 0.04(\mathrm{syst}))\%.$$

This shows no evidence of *CP* violation but achieves a significant improvement in precision over the previous world average of $a_{CP}^{T\text{-odd}} = (0.11 \pm 0.67)$[5].

The same measurements are also performed in 32 bins of Cabibbo-Maksimowicz phase space variables, defined as the invariant mass squared of the $\pi^+\pi^-$ ($\mathrm{K}^+\mathrm{K}^-$) pair, $m^2_{\pi^+\pi^-}$ ($m^2_{\mathrm{K}^+\mathrm{K}^-}$); the cosine of the angle of the π^+ (K^+) with respect to the direction opposite to the D^0 momentum in the $\pi^+\pi^-$ ($\mathrm{K}^+\mathrm{K}^-$) rest frame, $\cos(\theta_\pi)$ ($\cos(\theta_\mathrm{K})$); and the angle between the $\mathrm{K}^+\mathrm{K}^-$ and $\pi^+\pi^-$ planes in the D^0 rest frame, ϕ. The asymmetries are extracted in each bin of phase space and $a_{CP}^{T\text{-odd}}$ calculated. A χ^2 test for consistency across the phase space is performed, yielding a p-value of 74 %. Similarly, binning in the decay time of the D^0 candidates and performing the same test gives sensitivity to indirect *CP* violation. This yields a p-value of 72 %, so there is no evidence for direct or indirect *CP* violation.

A complementary method for studying *CP* violation in multi-body D meson decays is to examine *CP* asymmetries across the multi-body phase space directly. Signal yields are obtained in bins of the multi-body phase space, and the test statistic $S^i_{CP} \equiv (N_i(\mathrm{D}^0) - \alpha N_i(\overline{\mathrm{D}}^0))/\sqrt{\alpha(N_i(\mathrm{D}^0) + N_i(\overline{\mathrm{D}}^0))}$, calculated in each bin i, where $\alpha \equiv N(\mathrm{D}^0)/N(\overline{\mathrm{D}}^0)$ cancels any global production and detection asymmetries. A χ^2 test for consistency with zero *CP* violation is performed using $\chi^2 = \Sigma_i {S^i_{CP}}^2$ and $N_{bins} - 1$ degrees of freedom. This analysis has been performed on $\mathrm{D}^0 \to \mathrm{K}^+\mathrm{K}^-\pi^+\pi^-$ and $\mathrm{D}^0 \to \pi^+\pi^-\pi^+\pi^-$ candidates, using 1 fb^{-1} of data, for which the nominal binning scheme yields a p-value of 9.1 % (41 %) for $\mathrm{D}^0 \to \mathrm{K}^+\mathrm{K}^-\pi^+\pi^-$ ($\mathrm{D}^0 \to \pi^+\pi^-\pi^+\pi^-$) [6]. The decay $\mathrm{D}^+ \to \pi^-\pi^+\pi^+$ has also been studied in this way, using 1 fb^{-1} of data [7]. Various binning schema are used, as well as an unbinned method to measure *CP* asymmetries, all of which yield p-values of more than 20 %. Thus, no evidence for *CP* violation is found in these decay modes.

3 *CP* violation in $\mathrm{D}^\pm_{(s)} \to \mathrm{K}^0_\mathrm{S} h^\pm$

The singly-Cabibbo-suppressed (SCS) decays $\mathrm{D}^\pm \to \mathrm{K}^0_\mathrm{S}\mathrm{K}^\pm$ and $\mathrm{D}^\pm_s \to \mathrm{K}^0_\mathrm{S}\pi^\pm$ offer a means of measuring direct *CP* violation with high precision. The *CP* asymmetry is defined as

$\mathcal{A}_{CP}^{\mathrm{D}^\pm_{(s)}\to \mathrm{K}^0_\mathrm{S} h^\pm} \equiv (\Gamma(\mathrm{D}^+_{(s)}\to \mathrm{K}^0_\mathrm{S} h^+) - \Gamma(\mathrm{D}^-_{(s)}\to \mathrm{K}^0_\mathrm{S} h^-))/(\Gamma(\mathrm{D}^+_{(s)}\to \mathrm{K}^0_\mathrm{S} h^+) + \Gamma(\mathrm{D}^-_{(s)}\to \mathrm{K}^0_\mathrm{S} h^-))$, while the measured asymmetry is

$$\begin{aligned}\mathcal{A}_{\mathrm{meas}}^{\mathrm{D}^\pm_{(s)}\to \mathrm{K}^0_\mathrm{S} h^\pm} &\equiv (N_{\mathrm{sig}}^{\mathrm{D}^+_{(s)}\to \mathrm{K}^0_\mathrm{S} h^+} - N_{\mathrm{sig}}^{\mathrm{D}^-_{(s)}\to \mathrm{K}^0_\mathrm{S} h^-})/(N_{\mathrm{sig}}^{\mathrm{D}^+_{(s)}\to \mathrm{K}^0_\mathrm{S} h^+} + N_{\mathrm{sig}}^{\mathrm{D}^-_{(s)}\to \mathrm{K}^0_\mathrm{S} h^-})\\ &\simeq \mathcal{A}_{CP}^{\mathrm{D}^\pm_{(s)}\to \mathrm{K}^0_\mathrm{S} h^\pm} + \mathcal{A}_{\mathrm{prod}}^{\mathrm{D}^\pm_{(s)}} + \mathcal{A}_{\mathrm{det}}^{h^\pm} + \mathcal{A}_{\mathrm{K}^0_\mathrm{S}}.\end{aligned}$$

Here N_{sig} is the number of signal candidates of the given decay, $\mathcal{A}_{\mathrm{prod}}^{\mathrm{D}^\pm_{(s)}}$ is the production asymmetry of the $\mathrm{D}^\pm_{(s)}$ meson, $\mathcal{A}_{\mathrm{det}}^{h^\pm}$ is the detection asymmetry of the $h^\pm$ meson, and $\mathcal{A}_{\mathrm{K}^0_\mathrm{S}}$ is the combined detection and *CP* asymmetry of the K^0_S meson. Assuming negligible *CP* violation in the Cabibbo-favoured (CF) decays $\mathrm{D}^\pm_s\to \mathrm{K}^0_\mathrm{S}\mathrm{K}^\pm$, $\mathrm{D}^\pm\to \mathrm{K}^0_\mathrm{S}\pi^\pm$ and $\mathrm{D}^\pm_s\to \phi\pi^\pm$, the production and detection asymmetries cancel in the double difference

$$\begin{aligned}\mathcal{A}_{CP}^{DD} &\equiv \left[\mathcal{A}_{\mathrm{meas}}^{\mathrm{D}^\pm_s\to \mathrm{K}^0_\mathrm{S}\pi^\pm} - \mathcal{A}_{\mathrm{meas}}^{\mathrm{D}^\pm_s\to \mathrm{K}^0_\mathrm{S}\mathrm{K}^\pm}\right] - \left[\mathcal{A}_{\mathrm{meas}}^{\mathrm{D}^\pm\to \mathrm{K}^0_\mathrm{S}\pi^\pm} - \mathcal{A}_{\mathrm{meas}}^{\mathrm{D}^\pm\to \mathrm{K}^0_\mathrm{S}\mathrm{K}^\pm}\right] - 2\mathcal{A}_{\mathrm{K}^0_\mathrm{S}},\\ &= \mathcal{A}_{CP}^{\mathrm{D}^\pm\to \mathrm{K}^0_\mathrm{S}\mathrm{K}^\pm} + \mathcal{A}_{CP}^{\mathrm{D}^\pm_s\to \mathrm{K}^0_\mathrm{S}\pi^\pm},\end{aligned}$$

while the K^0_S asymmetry is calculable, so the sum of the *CP* asymmetries can be measured. Similarly the individual *CP* asymmetries can be accessed using

$$\begin{aligned}\mathcal{A}_{CP}^{\mathrm{D}^\pm\to \mathrm{K}^0_\mathrm{S}\mathrm{K}^\pm} &= \left[\mathcal{A}_{\mathrm{meas}}^{\mathrm{D}^\pm\to \mathrm{K}^0_\mathrm{S}\mathrm{K}^\pm} - \mathcal{A}_{\mathrm{meas}}^{\mathrm{D}^\pm_s\to \mathrm{K}^0_\mathrm{S}\mathrm{K}^\pm}\right] - \left[\mathcal{A}_{\mathrm{meas}}^{\mathrm{D}^\pm\to \mathrm{K}^0_\mathrm{S}\pi^\pm} - \mathcal{A}_{\mathrm{meas}}^{\mathrm{D}^\pm_s\to \phi\pi^\pm}\right] - \mathcal{A}_{\mathrm{K}^0_\mathrm{S}},\\ \mathcal{A}_{CP}^{\mathrm{D}^\pm_s\to \mathrm{K}^0_\mathrm{S}\pi^\pm} &= \mathcal{A}_{\mathrm{meas}}^{\mathrm{D}^\pm_s\to \mathrm{K}^0_\mathrm{S}\pi^\pm} - \mathcal{A}_{\mathrm{meas}}^{\mathrm{D}^\pm_s\to \phi\pi^\pm} - \mathcal{A}_{\mathrm{K}^0_\mathrm{S}}.\end{aligned}$$

Using 3 fb^{-1} of data the results thus obtained are [8]

$$\begin{aligned}\mathcal{A}_{CP}^{\mathrm{D}^\pm\to \mathrm{K}^0_\mathrm{S}\mathrm{K}^\pm} + \mathcal{A}_{CP}^{\mathrm{D}^\pm_s\to \mathrm{K}^0_\mathrm{S}\pi^\pm} &= (+0.41\pm 0.49(\mathrm{stat})\pm 0.26(\mathrm{syst}))\%,\\ \mathcal{A}_{CP}^{\mathrm{D}^\pm\to \mathrm{K}^0_\mathrm{S}\mathrm{K}^\pm} &= (+0.03\pm 0.17(\mathrm{stat})\pm 0.14(\mathrm{syst}))\%,\\ \mathcal{A}_{CP}^{\mathrm{D}^\pm_s\to \mathrm{K}^0_\mathrm{S}\pi^\pm} &= (+0.38\pm 0.46(\mathrm{stat})\pm 0.17(\mathrm{syst}))\%.\end{aligned}$$

These are the most precise measurements of their kind to date and show no evidence of *CP* violation.

4 Mixing and *CP* violation in $\mathrm{D}^0\to \mathrm{h}^+\mathrm{h}^{(\prime)-}$ decays

Decays of $\mathrm{D}^0\to \mathrm{h}^+\mathrm{h}^{(\prime)-}$ provide a means of measuring direct and indirect *CP* violation, as well as mixing, in the D^0 system. The measured *CP* asymmetry in $\mathrm{D}^0\to \mathrm{K}^+\mathrm{K}^-$ and $\mathrm{D}^0\to \pi^+\pi^-$ decays, flavour tagged using $\mathrm{B}\to \mathrm{D}^0\mu^- X$ decays, is $\mathcal{A}_{\mathrm{meas}}^{\mathrm{D}^0\to \mathrm{h}^+\mathrm{h}^-} = \mathcal{A}_{CP}^{\mathrm{D}^0\to \mathrm{h}^+\mathrm{h}^-} + \mathcal{A}_{\mathrm{det}}^{\mu^\pm} + \mathcal{A}_{\mathrm{prod}}^{\mathrm{B}}$. The $\pi^+\pi^-$ and $\mathrm{K}^+\mathrm{K}^-$ final states are *CP* eigenstates, so have no detection asymmetry. Defining $\Delta\mathcal{A}_{CP} \equiv \mathcal{A}_{\mathrm{meas}}^{\mathrm{D}^0\to \mathrm{K}^+\mathrm{K}^-} - \mathcal{A}_{\mathrm{meas}}^{\mathrm{D}^0\to \pi^+\pi^-} = \mathcal{A}_{CP}^{\mathrm{D}^0\to \mathrm{K}^+\mathrm{K}^-} - \mathcal{A}_{CP}^{\mathrm{D}^0\to \pi^+\pi^-}$, the nuisance asymmetries cancel. Similarly to the analysis described in Sec. 3, CF decays can be used to cancel nuisance asymmetries as $\mathcal{A}_{CP}^{\mathrm{D}^0\to \mathrm{K}^+\mathrm{K}^-} = \mathcal{A}_{\mathrm{meas}}^{\mathrm{D}^0\to \mathrm{K}^+\mathrm{K}^-} - \mathcal{A}_{\mathrm{meas}}^{\mathrm{D}^0\to \mathrm{K}^-\pi^+} + \mathcal{A}_{\mathrm{det}}^{\mathrm{K}^\mp\pi^\pm}$, and $\mathcal{A}_{\mathrm{det}}^{\mathrm{K}^\mp\pi^\pm}$ can be calculated using the asymmetries of $\mathrm{D}^+\to \mathrm{K}^-\pi^+\pi^+$ and $\mathrm{D}^+\to \mathrm{K}^0_\mathrm{S}\pi^+$ decays, and the known $\mathcal{A}_{\mathrm{K}^0_\mathrm{S}}$. The asymmetry $\mathcal{A}_{CP}^{\mathrm{D}^0\to \pi^+\pi^-}$ can then be determined using $\mathcal{A}_{CP}^{\mathrm{D}^0\to \pi^+\pi^-} = \mathcal{A}_{CP}^{\mathrm{D}^0\to \mathrm{K}^+\mathrm{K}^-} - \Delta\mathcal{A}_{CP}$.

Using 3 fb^{-1} of data yields [9]

$$\begin{aligned}\Delta\mathcal{A}_{CP} &= (+0.14 \pm 0.16(\text{stat}) \pm 0.08(\text{syst}))\%,\\ \mathcal{A}_{CP}^{\text{D}^0\to\text{K}^+\text{K}^-} &= (-0.06 \pm 0.15(\text{stat}) \pm 0.10(\text{syst}))\%,\\ \mathcal{A}_{CP}^{\text{D}^0\to\pi^+\pi^-} &= (-0.20 \pm 0.19(\text{stat}) \pm 0.10(\text{syst}))\%.\end{aligned}$$

Indirect *CP* violation in $\text{D}^0 \to \text{K}^+\text{K}^-$ and $\text{D}^0 \to \pi^+\pi^-$ decays can be measured using

$$A_\Gamma \equiv \frac{\hat{\Gamma}(\text{D}^0 \to f) - \hat{\Gamma}(\overline{\text{D}}^0 \to f)}{\hat{\Gamma}(\text{D}^0 \to f) + \hat{\Gamma}(\overline{\text{D}}^0 \to f)} \approx \eta_{CP}\left[\frac{1}{2}(A_m + A_d)y\cos\phi - x\sin\phi\right].$$

Here, $\hat{\Gamma}$ is the inverse of the effective lifetime of the decay and η_{CP} is the *CP* eigenvalue of f. The effective lifetimes are measured directly using a data-driven, per-candidate correction for the selection efficiency on 1 fb^{-1} of data, yielding [10]

$$\begin{aligned}A_\Gamma(\pi\pi) &= (+0.033 \pm 0.106(\text{stat}) \pm 0.014(\text{syst}))\%,\\ A_\Gamma(\text{KK}) &= (-0.035 \pm 0.062(\text{stat}) \pm 0.012(\text{syst}))\%.\end{aligned}$$

Thus, no evidence for direct or indirect *CP* violation in $\text{D}^0 \to \text{h}^+\text{h}^-$ decays is found.

Mixing in the D^0 system is measured using the ratio of the decay rates of "wrong sign" DCS $\text{D}^0 \to \text{K}^+\pi^-$ to "right sign" CF $\text{D}^0 \to \text{K}^-\pi^+$ as a function of D^0 decay time, as

$$R(t) = \frac{N_{WS}(t)}{N_{RS}(t)} = R_D + \sqrt{R_D}y't + \frac{x'^2 + y'^2}{4}t^2,$$

where $R_D = \left|\frac{A_{DCS}}{A_{CF}}\right|^2$, $x' = x\cos(\delta) + y\sin(\delta)$, $y' = -x\sin(\delta) + y\cos(\delta)$, and $\delta = \arg\left(\frac{A_{DCS}}{A_{CF}}\right)$. Using 3 fb^{-1} of data yields [11]

$$x'^2 = (5.5 \pm 4.9) \times 10^{-5}, y' = (4.8 \pm 1.0) \times 10^{-3}, R_D = (3.568 \pm 0.066) \times 10^{-3}.$$

Allowing for *CP* violation yields:

$$A_D \equiv (R_D(\text{D}^0) - R_D(\overline{\text{D}}^0))/(R_D(\text{D}^0) - R_D(\overline{\text{D}}^0)) = (-0.7 \pm 1.9)\%,$$

$$0.75 < |q/p| < 1.24, (68.3\ \%\ \text{CL}).$$

These are the most precise measurements of mixing in the D^0 system and of *CP* violation in $\text{D}^0 \to \text{K}^+\pi^-$ decays to date.

5 Conclusions

There is a rich programme of charm physics studies at the LHCb experiment, with many complementary measurements already performed using some or all the 3 fb^{-1} of data collected during run I. No evidence for *CP* violation has been found, though constraints of $\mathcal{O}(10^{-3})$ have been achieved in many decay modes. Mixing in the D^0 system has also been measured to unprecedented precision. With run II shortly to begin, and the LHCb upgrade in the near future, there are great prospects for future measurements with precisions of $\mathcal{O}(10^{-4})$, which will tightly constrain, or potentially discover, new physics.

References

[1] The LHCb collaboration. The LHCb Detector at the LHC. *JINST*, 3(S08005), 2008.

[2] Joachim Brod, Alexander L. Kagan, and Jure Zupan. Size of direct CP violation in singly Cabibbo-suppressed D decays. *Phys.Rev.*, D86:014023, 2012.

[3] M. Bobrowski, A. Lenz, J. Riedl, and J. Rohrwild. How Large Can the SM Contribution to CP Violation in $D^0 - \bar{D}^0$ Mixing Be? *JHEP*, 1003:009, 2010.

[4] The LHCb collaboration. Search for CP violation using T-odd correlations in $D^0 \to K^+K^-\pi^+\pi^-$ decays. *JHEP*, 1410:5, 2014.

[5] The Heavy Flavor Averaging Group. `http://www.slac.stanford.edu/xorg/hfag/`, August 2014.

[6] The LHCb collaboration. Model-independent search for CP violation in $D^0 \to K^-K^+\pi^-\pi^+$ and $D^0 \to \pi^-\pi^+\pi^+\pi^-$ decays. *Phys.Lett.*, B726:623–633, 2013.

[7] The LHCb collaboration. Search for CP violation in the decay $D^+ \to \pi^-\pi^+\pi^+$. *Phys.Lett.*, B728:585–595, 2014.

[8] The LHCb collaboration. Search for CP violation in $D^\pm \to K^0_S K^\pm$ and $D^\pm_s \to K^0_S\pi^\pm$ decays. *JHEP*, 1410:25, 2014.

[9] The LHCb collaboration. Measurement of CP asymmetry in $D^0 \to K^-K^+$ and $D^0 \to \pi^-\pi^+$ decays. *JHEP*, 1407:041, 2014.

[10] The LHCb collaboration. Measurements of indirect CP asymmetries in $D^0 \to K^-K^+$ and $D^0 \to \pi^-\pi^+$ decays. *Phys.Rev.Lett.*, 112(4):041801, 2014.

[11] The LHCb collaboration. Measurement of D^0-$\bar{D}^0$ mixing parameters and search for CP violation using $D^0 \to K^+\pi^-$ decays. *Phys.Rev.Lett.*, 111:251801, 2013.

Perspective Study of Charmonium and Exotics above $D\bar{D}$ Threshold

M. Yu. Barabanov, A. S. Vodopyanov

Joint Institute for Nuclear Research, Joliot-Curie 6, Dubna, Moscow region Russia 141980

DOI: http://dx.doi.org/10.3204/DESY-PROC-2014-04/11

The spectroscopy of exotic states with hidden charm is discussed. Together with charmonium it is a good testing tool for theories of strong interactions including QCD in both perturbative and non-perturbative regime, lattice QCD, potential models and phenomenological models. An elaborated analysis of exotics spectrum is given, and attempts to interpret recent experimental data in the above $D\bar{D}$ threshold region are considered. Experimental data from different collaborations (BES, BaBar, Belle, LHCb) are analyzed with special attention given to new states with hidden charm which were discovered recently. Some of these states can be interpreted as higher-lying charmonium states and tetraquarks with hidden charm. It has been shown that charge/neutral tetraquarks must have their neutral/charge partners with mass values differ by few MeV. This hypothesis coincides with that proposed by Maiani and Polosa. But much more data on different decay modes are needed before firmer conclusions can be made. These data can be derived directly from the experiments using the high quality antiproton beam with momentum up to 15 GeV/c and proton-proton collisions with momentum up to 26 GeV/c.

1 Introduction

The study of strong interactions and hadron matter in the process of antiproton-proton annihilation and proton-proton collisions seems to be a challenge nowadays. One of the main goals of contemporary physics is to search for new exotic forms of matter, which must manifest in the existence of charmed hybrids and multiquark states such as meson molecules and tetraquarks [1, 2]. The researches of spectrum of charmed hybrids $c\bar{c}g$ and tetraquarks with hidden charm ($cq\bar{c}\bar{q}'$, and q and $q' = u,\ d,\ s$) together with the charmonioum spectrum are promising to understand the dynamics of quark interactions at small distances. It is a good testing tool for the theories of strong interactions: QCD in both perturbative and non-perturbative regimes, QCD inspired potential models, phenomenological models, non-relativistic QCD and LQCD.

Charmed hybrids $c\bar{c}g$ represent themselves as the states with an excited gluonic degree of freedom. These states are described by different models and calculation schemes (LQCD, bag model, flux tube model) [1, 2]. All model predictions and calculations agree that the mass of the lowest-lying charmonium hybrids is between 3.9 and 4.6 GeV/c^2 and that the state with $J^{PC} = 1^{-+}$ has the lowest mass. Until now, discussions have been focused only around the lowest-lying charmonium hybrids. Four of these states $J^{PC} = 2^{-+},\ 1^{-+},\ 1^{--},\ 0^{-+}$ correspond to a $c\bar{c}$ pair with $J^{PC} = 0^{-+}$ or 1^{--}, coupled to a gluon in the lightest mode with $J^{PC} = 1^{+-}$. The other four states $J^{PC} = 2^{+-},\ 1^{+-},\ 1^{++},\ 0^{+-}$ with the gluon mode

$J^{PC} = 1^{-+}$ are, probably, a bit heavier. The expected mass splitting between the states 1^{-+} and 0^{+-} is about 150 - 250 MeV. Three of these eight charmonium hybrids have spin-exotic quantum numbers 1^{-+}, 0^{+-}, 2^{+-}, so mixing effects with nearby $c\bar{c}$ states are excluded for them thus making their experimental identification especially easy. The next possible hybrid states with quantum numbers 2^{++}, 2^{+-}, 1^{++}, 1^{+-}, 0^{+-}, 0^{++} correspond to $c\bar{c}$ pairs with quantum numbers $J^{PC} = 1^{+-}$ or $J^{PC} = (0,1,2)^{++}$ coupled to a gluon in the lightest mode with $J^{PC} = 1^{+-}$. The states with quantum numbers 2^{--}, 2^{-+}, 1^{--}, 1^{-+}, 0^{-+}, 0^{--} correspond to pair $c\bar{c}$ with quantum numbers $J^{PC} = 1^{+-}$ or $J^{PC} = (0,1,2)^{++}$ coupled to a gluon mode with $J^{PC} = 1^{-+}$. One can find a possibility of the existence of hybrid state with exotic quantum numbers $J^{PC} = 0^{--}$. The most interesting and promising decay channels of charmed hybrids are as follows: $\bar{p}p \to \tilde{\eta}_{c0,1,2}(0^{-+},\ 1^{-+},\ 2^{-+})\eta \to \chi_{c0,1,2}(\eta, \pi\pi; \ldots)$; $\bar{p}p \to \tilde{h}_{c0,1,2}(0^{+-},\ 1^{+-},\ 2^{+-})\eta \to \chi_{c0,1,2}(\eta, \pi\pi; \ldots)$; $\bar{p}p \to \tilde{\Psi}(1^{--},\ 2^{--}) \to J/\psi(\eta, \omega, \pi\pi; \ldots)$; $\bar{p}p \to \tilde{\eta}_{c0,1,2}, \tilde{h}_{c0,1,2}, \tilde{\chi}_{c1}(0^{-+},\ 1^{-+},\ 2^{-+},\ 0^{+-},\ 1^{+-},\ 2^{+-},\ 1^{++},\ 2^{++})\eta \to D\bar{D}^*_J\eta$.

Two generic types of multiquark states have been described in the literature [3, 4, 5]. The first one, the molecular state, is comprised of two charmed mesons bound together to form a molecule. These states are by nature loosely bound. Molecular states bound through two mechanisms: quark/colour exchange interactions at short distances and pion exchange at a large distance. Since the mesons inside the molecule are weakly bound, they tend to decay as if they are free. The second type is a tightly bound four-quark state, so called tetraquark that is predicted to have properties that are different from those of a molecular state. In the model of Maiani [4, 5], for example, the tetraquark is described as a diquark-diantiquark structure in which the quarks group into the colour-triplet scalar and vector clusters and the interactions are dominated by a simple spin-spin interaction. Here, strong decays are expected to proceed via rearrangement processes followed by dissociation that gives rise, for example, to such decays as: $p\bar{p} \to X \to J/\psi\ \rho \to J/\psi\ \pi\pi$; $p\bar{p} \to X \to J/\psi\ \omega \to J/\psi\ \pi\pi\pi$; $p\bar{p} \to X \to \chi_{cJ}\pi$; $p\bar{p} \to X \to D\bar{D}^* \to D\bar{D}\gamma$; $p\bar{p} \to X \to D\bar{D}^* \to D\bar{D}\eta$. A prediction that distinguishes tetraquarks containing a $c\bar{c}$ pair from conventional charmonia is possible existence of multiplets which include members with non-zero charge $cu\bar{c}\bar{d}$, strangeness $cd\bar{c}\bar{s}$, or both $cu\bar{c}\bar{s}$.

2 Calculation of exotics spectrum

For this purpose we have fulfilled the elaborated analysis of the spectrum of charmed hybrids and tetraquarks with the hidden charm in the mass region above $D\bar{D}$ threshold. The analysis of spectrum of charmonium [6, 7] was carried out earlier. Different decay modes of charmed hybrids and tetraquarks such as decays into charmonium and light mesons and decays into $D\bar{D}^*_J$ and $D\bar{D}^*$ pairs, were, in particular, analyzed. A special attention was given to the new states with the hidden charm discovered recently [2, 3, 4, 5]. The experimental data from different collaborations like Belle, BaBar, LHCb, BES were carefully analyzed. Using the combined approach based on the quarkonium potential model and confinement model [8, 9], more than twenty charmed hybrids are expected to exist in the discussed mass region (see Figs. 1, 2).

Charmed hybrids with exotic quantum numbers are marked with dark colour and charmed hybrids with nonexotic quantum numbers – with light colour. The results of calculations for hybrids are in good agreement with the well accepted picture that the quartet 1^{--}, $(0,1,2)^{-+}$ is lower in mass than 1^{++}, $(0,1,2)^{+-}$. The mass splitting between the states 1^{-+} and 0^{+-} is about 200 MeV/c^2. More than twenty tetraquarks with hidden charm (see Fig. 3) are expected to exist in the mass region above $D\bar{D}$ threshold.

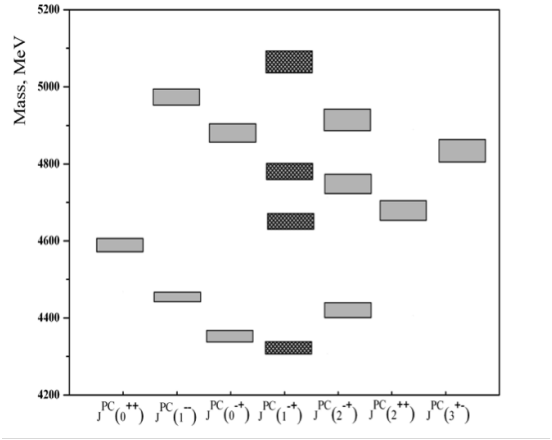

Figure 1: The spectrum of charmed hybrids with quantum numbers $J^{PC} = 3^{+-}$, 2^{++}, 2^{-+}, 1^{-+}, 1^{--}, 0^{-+}, 0^{++}.

The black-white boxes correspond to the recently revealed XYZ states with the hidden charm that may be interpreted as tetraquarks. White boxes correspond to the tetraquark states which have not been found yet. But a possibility of existence of these states is predicted in the framework of the combined approach. It has been shown that charge/neutral tetraquarks with hidden charm must have their neutral/charged partners with mass values which differ by few MeV. This assumption coincides with that proposed earlier by Maiani and Polosa [10] and can shed light on the nature of neutral $X(3872)$, $X(4350)$ and charged $Z_c(3885)^{\pm}$, $Z_c(3900)^{\pm}$, $Z_c(4020)^{\pm}$, $Z_c(4025)^{\pm}$, $Z_c(4200)^{\pm}$, $Z_c(4050)^{\pm}$, $Z_c(4250)^{\pm}$, $Z_c(4430)^{\pm}$ states. The quantum numbers J^{PC} of the $X(3872)$ meson have been recently determined by LHCb [11]. One can find that $X(3872)$ may be interpreted as tetraquark state with $J^{PC} = 1^{++}$, and $X(4350)$ as the tetraquark state with $J^{PC} = 2^{++}$. New state $Z_c(3900)^{\pm}$ observed by BES [12] together with $Z_c(4050)^{\pm}$, $Z_c(4250)^{\pm}$, $Z_c(4430)^{\pm}$ states may be interpreted as charge tetraquarks with $J^{PC} = 1^{+}$. New state $Z_c(4020)^{\pm}$ observed by BES [13] may be interpreted as charge tetraquark with $J^{PC} = 1^{+}$. The proposed approach doesn't distinguish the states $Z_c(3900)^{\pm}$ and $Z_c(3885)^{\pm}$ as well $Z_c(4025)^{\pm}$ and $Z_c(4020)^{\pm}$ states. The values of their masses and widths coincide in the framework of the combined approach. Two states (one charge and one neutral) with $J^{PC} = 1^{++}$ are expected to exist in the mass range of 4200 - 4300 MeV. The new charged state $Z_c(4250)^{\pm}$ observed by Belle may be a good candidate for the one of them.

To confirm that the predicted states actually exist and can be found experimentally, their widths and branching ratios were calculated [7, 9]. The feature of the considered states is their narrowness compared with light unflavored mesons, baryons and hybrids. The states we find in this model have small widths; their values are of the order of several tens of MeV. This fact facilitates experimental searches. The values of the calculated widths coincide (within the experimental error) with the experimentally determined values for the XYZ particles; the correspondence of the mass values has been discussed above. This fact strongly suggests that some of the XYZ particles may be interpreted as higher-lying charmonium states [6, 7] and tetraquarks as it can be verified by the experiments with antiproton beams with momentum up to 15 GeV/c and proton-proton collisions with momentum up to 26 GeV/c. The values of

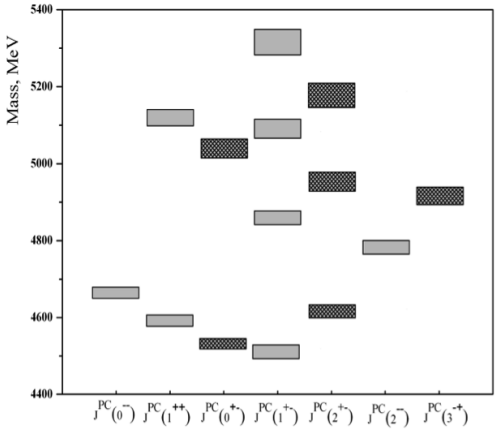

Figure 2: The spectrum of charmed hybrids with quantum numbers $J^{PC} = 3^{-+},\ 2^{--},\ 2^{+-},\ 1^{+-},\ 1^{++}, 0^{+-},\ 0^{--}$.

branching ratios in the considered decay channels of charmonium and exotics are of the order of $\beta \approx 10^{-1} - 10^{-2}$ dependent of their decay mode. From this one can conclude that the branching ratios are significant and searches for charmonium and exotics, and studies of the main characteristics of their spectrum seem to be promising.

3 Conclusion

The prospects for future exotics research are related with the results obtained below:

A combined approach has been employed to study charmonium and exotics on the basis of the quarkonium potential model and a confinement model that uses a three-dimensional sphere embedded into the four-dimensional Euclidian space of the decay products.

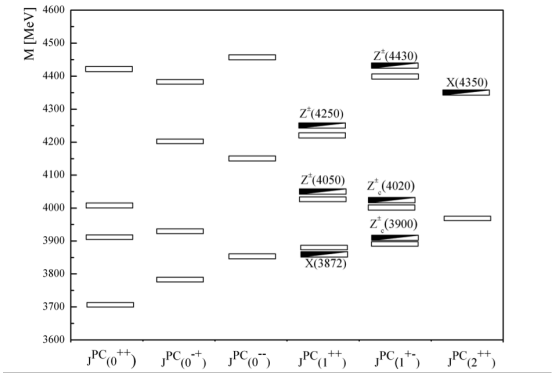

Figure 3: The spectrum of tetraquarks with hidden charm.

The most interesting and promising decay channels of charmed hybrids and tetraquarks with the hidden charm have been analyzed. Many new states above $D\bar{D}$ threshold are expected to exist in the framework of this model.

The recently discovered states with the hidden charm above the $D\bar{D}$ threshold (XYZ particles) have been analyzed. Ten of these states can be interpreted as higher-lying tetraquark states with hidden charm. The necessity of further studies of the XYZ particles and improved measurements of their main characteristics has been demonstrated.

References

[1] W. Erni *et al.*, arXiv:0903.3905v1 [hep-ex] (2009).

[2] N. Brambilla *et al.*, Eur. Phys. J. C 71: 1534, 1 (2011).

[3] J. Beringer *et al.*, Review of Particle Physics, Phys. Rev. 86 (2012).

[4] S. Godfrey and S. Olsen, Ann. Rev. Nucl. Part. Sci. 58, 51 (2008).

[5] S. Olsen, arXiv : 0909.2713v1 [hep-ex] (2009).

[6] M.Yu. Barabanov, A.S. Vodopyanov, Fizika Elementarnyh Chastits Atomnogo Yadra Pisma, 8, N.10, 63 (2011) / Phys. Part. Nucl. Lett. N.10, 1069 (2011).

[7] M.Yu. Barabanov, A.S. Vodopyanov, S. L. Olsen, Yadernaya Fizica, V.77, N.1, 1 (2014) / Phys. At. Nucl., V.77, N.1,1 26 (2014).

[8] M.Yu. Barabanov et al., Russ. Phys. J., 50, 1243 (2007).

[9] M.Yu. Barabanov et al., Hadronic J., 32, N.2, 159 (2009).

[10] N.V. Drenska, R. Fassini, A.D. Polosa, arXiv: 0902.2803 [hep-ph] (2009).

[11] R. Aaij et al., arXiv: 1302.6269v1 [hep-ex] (2013).

[12] M. Ablikim *et al.*, arXiv: 1303.5949v1 [hep-ex] (2013).

[13] M. Ablikim *et al.*, arXiv: 1308.2760v1 [hep-ex] (2013).

CP Violation in B Decays at LHCb

Shu-Faye Cheung on behalf of the LHCb collaboration

Department of Physics, University of Oxford, Oxford OX1 3RH, United Kingdom

DOI: http://dx.doi.org/10.3204/DESY-PROC-2014-04/243

A selection of recent results from studies of *CP* violation in the decays of B mesons are presented, which were performed using pp collision data at $\sqrt{s} = 7$ TeV and 8 TeV collected by the LHCb experiment during Run I, corresponding to an integrated luminosity of 3.0 fb^{-1}.

1 Model-independent measurement of γ with $B^\pm \to D(\to K^0_S\pi^+\pi^-, K^0_S K^+K^-)K^\pm$ decays

Indirect searches for New Physics (NP) can be performed at LHCb with precision measurements of the CKM Unitarity Triangle parameters. One of these, the angle $\gamma \equiv \arg[-(V_{ud}V^*_{ub})/(V_{cd}V^*_{cb})]$, can be measured in $B^\pm \to DK^\pm$ decays, where D is an admixture of D^0 and $\overline{D}^0$ mesons decaying to the same final state. The ratio of amplitudes $A(B^\pm \to \overline{D}^0 K^\pm)/A(B^\pm \to D^0 K^\pm)$ is $r_B e^{i(\delta_B \pm \gamma)}$, where r_B is the colour-suppression factor, δ_B is the strong-phase difference and γ is the weak-phase difference. LHCb has measured γ in $B^\pm \to DK^\pm$ decays with many D final states. These are summarised in [1] and have a combined measurement of $\gamma = (72.9^{+9.2}_{-9.9})^\circ$.

In the case $D \to K^0_S h^+h^-$, where $h = \pi$ or K, the strong-phase difference between the D^0 and $\overline{D}^0$ decay, δ_D, varies in the Dalitz plot. A model-independent method is used, in which averaged values of δ_D in bins of the Dalitz plot are provided externally. The relative signal yield in each Dalitz plot bin is given by the Cartesian parameters $x_\pm = r_B \cos(\delta_B \pm \gamma)$ and $y_\pm = r_B \sin(\delta_B \pm \gamma)$; the relative yield of flavour-tagged $D^0 \to K^0_S h^+h^-$ decays, which is measured using ${}^{(}\overline{B}{}^{)}0 \to ({}^{(}\overline{D}{}^{)}0\pi^\pm)\mu^\mp X$ decays (X are any other particles produced in the ${}^{(}\overline{B}{}^{)}0$ decay that are not reconstructed); and the amplitude-weighted values of $\cos\delta_D$ and $\sin\delta_D$ integrated over the bin, which are obtained with quantum-correlated $\psi(3770) \to D\overline{D}$ decays by the CLEO experiment [2]. A model-dependent measurement of γ with $D \to K^0_S\pi^+\pi^-$ decays, in which the values of δ_D are obtained with an amplitude model of the D^0 decay, has also been performed at LHCb using 1.0 fb^{-1} of data [3].

Approximately 2260 (320) $B^\pm \to DK^\pm$, $D \to K^0_S\pi^+\pi^-$ ($K^0_S K^+K^-$) decays are selected. The Cartesian parameters $x_\pm$ and $y_\pm$ are directly measured and found to be $x_+ = (-7.7 \pm 2.4 \pm 1.0 \pm 0.4) \times 10^{-2}$, $x_- = (2.5 \pm 2.5 \pm 1.0 \pm 0.5) \times 10^{-2}$, $y_+ = (-2.2 \pm 2.5 \pm 0.4 \pm 1.0) \times 10^{-2}$ and $y_- = (7.5 \pm 2.9 \pm 0.5 \pm 1.4) \times 10^{-2}$ [4], where the uncertainties are statistical, experimental systematic, and the systematic due to the CLEO measurements, respectively. These are the most accurate measurements of $x_\pm, y_\pm$ to date. Figure 1 shows the measured values of $x_\pm$ and $y_\pm$ with likelihood contours corresponding to statistical uncertainties only. The *CP* observables are extracted and found to be $\gamma = (62^{+15}_{-14})^\circ$, $\delta_B = (134^{+14}_{-15})^\circ$ and $r_B = (8.0^{+1.9}_{-2.1}) \times 10^{-2}$ [4].

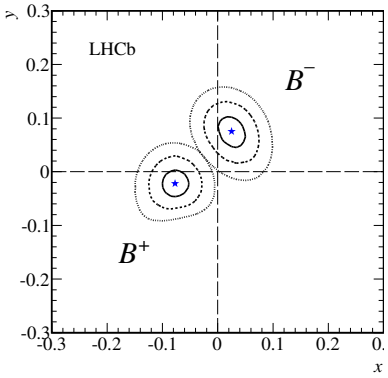

Figure 1: Central values (stars) of $x_\pm$ and $y_\pm$ and the 1-, 2- and 3-standard deviation regions for statistical uncertainties only [4].

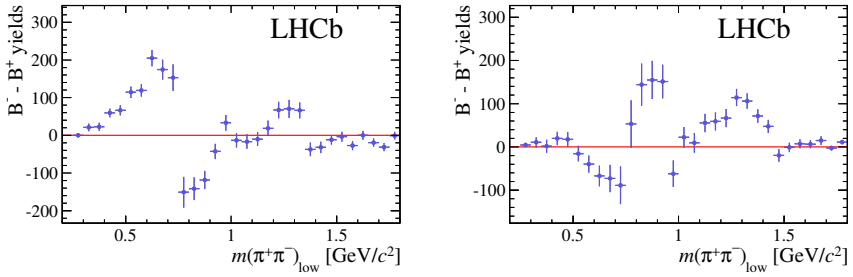

Figure 2: Difference between the number of $B^- \to \pi^-\pi^+\pi^-$ and $B^+ \to \pi^+\pi^+\pi^-$ events as a function of $m(\pi^+\pi^-$ low) in the region (left) $\cos\theta < 0$ and (right) $\cos\theta > 0$, where $\cos\theta$ is the helicity angle between like-sign pions in the $m(\pi^+\pi^-$ low) rest frame. [5]

2 Inclusive and local *CP* asymmetries in $B \to$ three-body charmless decays

Direct *CP* violation can occur through the presence of both weak- and strong-phase differences between tree- and loop-level diagrams of a given decay. In decays of charged B mesons to three charged charmless mesons, the CKM matrix elements involved give rise to the weak-phase difference while the strong-phase difference could be due to several sources, the relative strength of which may vary over the phase space. These sources can be classified into two categories, interference and rescattering, which can be studied by measuring local *CP* asymmetries.

Four channels are studied: $B^\pm \to \pi^\pm\pi^+\pi^-$, $K^\pm\pi^+\pi^-$, $\pi^\pm K^+K^-$ and $K^\pm K^+K^-$. The level of direct *CP* violation is quantified by A_{CP}, the asymmetry between the observed number of B^- and B^+ mesons, corrected for detection, production and kaon matter-interaction asymmetries. The inclusive A_{CP} measurements are $\mathcal{O}(1\%)$ and incompatible with zero, and are positive for $B^\pm \to \{\pi^\pm, K^\pm\}\pi^+\pi^-$ but negative for $B^\pm \to \{\pi^\pm, K^\pm\}K^+K^-$. Large asymmetries are observed in localised regions of the Dalitz plot: $A_{CP} = \mathcal{O}(10$–$30\%)$ in the region

$1.0 < m(\pi^+\pi^-), m(K^+K^-) < 1.5$ GeV/c^2. The oppositely-signed asymmetries for the different modes is a characteristic signature of CPT conservation in $\pi\pi \leftrightarrow KK$ rescattering. The dominance of long- over short-distance interference effects can be studied by measuring A_{CP} for $B^\pm \to \pi^\pm\pi^+\pi^-$ as a function of $m(\pi^+\pi^-$ low) for positive and negative $\cos\theta$, where $\cos\theta$ is the angle between the like-sign pions in the $m(\pi^+\pi^-$ low) rest frame. As can be seen in Figure 2, A_{CP} changes sign near the $\rho(770)$ resonance, and in different directions for the two $\cos\theta$ ranges. In this region of phase space, A_{CP} can be as large as 50–60% [5].

These findings reveal that direct *CP* violation is dominated by different physical processes inducing strong-phase differences across the phase space. The study of amplitude analyses is essential to understanding the contributions of these processes.

3 ϕ_s and T-odd triple product asymmetries in $B_s^0 \to \phi\phi$ decays

The $B_s^0 \to \phi\phi$ decay proceeds via loop diagrams only, allowing searches for new heavy particles participating in the quantum loops. This can be probed using the *CP*-violating phase ϕ_s, the phase difference between decays with and without mixing, which is small ($< 10^{-2}$) in the Standard Model (SM) and can be significantly enhanced in NP models [6].

The phase ϕ_s is measured by tagging the initial flavour of the B_s^0 meson at production, using flavour-tagging algorithms that have a combined tagging efficiency of 26% with a 33% mistag rate. The $\phi\phi$ final state is a linear combination of *CP*-even and *CP*-odd final states with different decay-time and angular distributions, hence an angular analysis in the helicity angle basis is performed to distinguish the various states, as seen in Figure 3. The data are corrected for their angular acceptance using simulated data and for their decay-time acceptance using $B_s \to D_s\pi$ decays. The B_s^0 mixing parameters are constrained to LHCb measurements. It is found that $\phi_s = -0.17 \pm 0.15\,(\text{stat.}) \pm 0.03\,(\text{syst.})$, which is in agreement with SM theory predictions. The level of direct *CP* violation $|\lambda|$, defined as the absolute ratio between the decay amplitudes of $B_s^0 \to \phi\phi$ and $\overline{B}_s^0 \to \phi\phi$, is found to be $|\lambda| = 1.04 \pm 0.07\,(\text{stat.}) \pm 0.03\,(\text{syst.})$. This is consistent with the hypothesis of no direct *CP* violation.

The $B_s^0 \to \phi\phi$ decay offers a second complementary probe of *CP* violation that is independent of decay time or initial B_s^0 flavour, and instead relies on a simple counting experiment. Two T-odd triple-product quantities can be constructed from the kinematics of the decay, $U \equiv \sin\Phi\cos\Phi$ and $V \equiv \pm\sin\Phi$, where Φ is the angle between the two $\phi \to K^+K^-$ decay planes. The sign of V depends on the value of $\cos\theta_1\cos\theta_2$, where $\theta_{1,2}$ is the angle between the K^+ track momentum in the $\phi_{1,2}$ meson rest frame and the $\phi_{1,2}$ momentum in the B_s^0 rest frame. The asymmetries in the signs of U and V, A_U and A_V, are *CP*-violating quantities with SM expectations close to zero. A non-zero asymmetry would indicate either the presence of *CP* violation or final state interactions. The results are consistent with the hypothesis of *CP* conservation, $A_U = -0.003 \pm 0.017 \pm 0.006$ and $A_V = -0.017 \pm 0.017 \pm 0.006$ [6], where the first uncertainty is statistical and the second uncertainty is systematic.

4 Conclusions

There is a broad and exciting programme of studies of *CP* violation in B decays at LHCb. Using data collected from Run I, many of these results have been comparable to those obtained

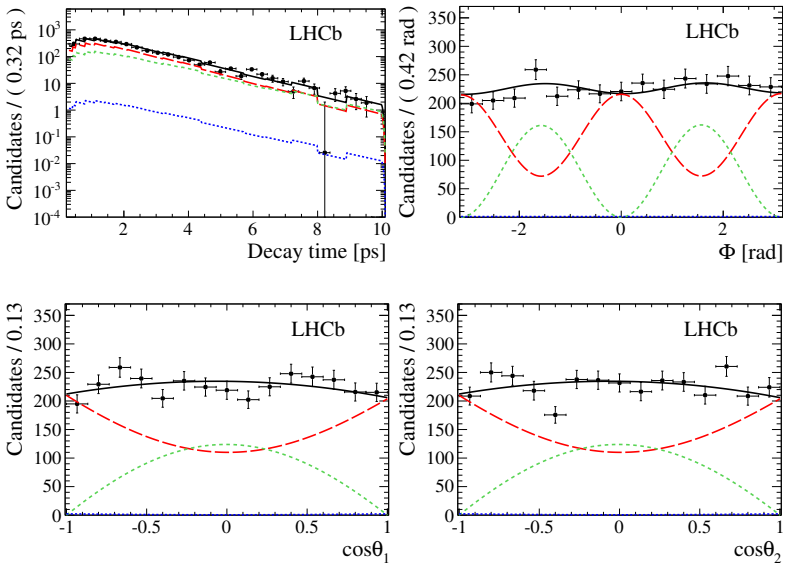

Figure 3: Decay time and helicity angle distributions of $B_s^0 \to \phi\phi$, where Φ is the angle between the two $\phi \to K^+K^-$ decay planes and $\theta_{1,2}$ is the angle between the K^+ track momentum in the $\phi_{1,2}$ meson rest frame and the $\phi_{1,2}$ momentum in the B_s^0 rest frame. The (black points) background-subtracted data are shown with the (solid black) result of the fit, and the (long-dashed red) *CP*-even *P*-wave, (short-dashed green) *CP*-odd *P*-wave and (dotted blue) *S*-wave contributions [6].

by the *B*-factories. Many of these results are statistically-limited and will be improved with the data collected during Run II in 2015–2018, which is expected to collect data corresponding to an integrated luminosity of 5 fb^{-1}.

Acknowledgments

Funding for this work, and attendance at this conference was provided by the Croucher Foundation (Hong Kong), St Cross College and the Department of Physics, University of Oxford.

References

[1] LHCb Collaboration, LHCb-CONF-2014-004 (2014).

[2] CLEO Collaboration, Phys. Rev. **D82** 112006 (2010).

[3] LHCb Collaboration, Nucl. Phys. **B888** 169-193 (2014).

[4] LHCb Collaboration, Submitted to JHEP, arXiv:1408.2748.

[5] LHCb Collaboration, Submitted to Phys. Rev. D, arXiv:1408.5373.

[6] LHCb Collaboration, Phys. Rev. **D90** 052011 (2014).

Recent results on the charmed hadron systems at Belle

Changwoo Joo[1] on behalf of the Belle Collaboration

[1]Seoul National Univ, 1 Gwanak-ro, Gwanak-gu, Seoul, 151-747, Korea

DOI: http://dx.doi.org/10.3204/DESY-PROC-2014-04/252

CP violation and mixing in the charm meson system are expected to be very small in the standard model (SM), hence it can be a good probe to search for new physics beyond the SM. The Belle experiment, with high statistics e^+e^- collision data taken at the KEKB energy-asymmetric collider using the Belle detector, is a very good place to study charmed hadron systems. In this presentation we report recent results from Belle on CP violation and mixing in the neutral D meson system. We also present recent results from Belle in the charmed baryon spectroscopy, including new measurements of mass, width, and absolute branching fractions of various charmed baryons.

The Belle experiment is excellent place to study charmed hadron systems since it has large relative cross-section for charmed hadron production and clean event environment combined with high luminosity. In this proceeding, we report recent results from Belle on CP violation and mixing in the neutral D meson system. We also present result from Belle in the charmed baryon spectroscopy.

1 Neutral D meson system

The mixing rate and the size of CP violation (CPV) in charm sector is expected to be very small in standard model (SM) [1, 2]. Thus, the measurement of $D^0 - \bar{D}^0$ mixing and CPV could provide probe to search for beyeond SM [3, 4]. $D^0 - \bar{D}^0$ mixing occures becauase the mass eigenstate ($|D_{H,L}>$) is different from flavor eigen sate ($|D^0>, |\bar{D}^0>$). The mass eigenstate can be represented by flavor eigenstate, namely $|D_{H,L}>= p|D^0> \pm q|\bar{D}^0>$. The phenomenology of meson mixing is decribled by two parameters, $x = \Delta M/\Gamma$ and $y = \Delta\Gamma/2\Gamma$, whrere ΔM and $\Delta\Gamma$ are mass and width differnce between two mass eigen state, Γ is average decay width of mass eigenstates. The direct CPV can be measured by decay rate comparison between paricle and anti-paricle system. The indirect CPV parameters are |q/p| and arg(q/p), the former is CPV in mixing and the later is CPV in interference of decay with and without mixing.

1.1 Mixing in $D^0 \to K^+\pi^-$ decay [5]

The mixing parameters of the K^0, B^0 and B^0_S mesons are well esteblished [6]. Rcently the D^0 mixing have been observed in hadron collider experiment [7, 8]. ; This is first observation of $D^0 - \bar{D}^0$ minxing from e^+e^- collider by measuring time dependent ratio of the $D^0 \to K^+\pi^-$ and $D^0 \to K^-\pi^+$ decay. We named the $D^0 \to K^+\pi^-$ decay as wrong sign (WS) decay

and $D^0 \to K^-\pi^+$ decay as right sign (RS) decay. The RS decay amplitude is sum of the amplitude from Cabibbo-favored (CF) decay $D^0 \to K^-\pi^+$ and $D^0 - \bar{D}^0$ mixing followed by the doubly Cabibbo-suppressed (DCS) decay $\bar{D}^0 \to K^-\pi^+$, where the later is much smaller than former one so it is neglected. The WS decay amplitude is sum of two comparable amplitudes from DCS decay $D^0 \to K^+\pi^-$ and $D^0 - \bar{D}^0$ mixing followed by the CF decay $\bar{D}^0 \to K^+\pi^-$. Then time-dependent WS to RS decay rates are $\Gamma_{RS}(\tilde{t}/\tau) \approx |A_{CF}|^2 e^{-\tilde{t}/\tau}$ and $\Gamma_{WS}(\tilde{t}/\tau) \approx |A_{CF}|^2 e^{-\tilde{t}/\tau}(R_D + \sqrt{R_D}y'\frac{\tilde{t}}{\tau} + \frac{x'^2+y'^2}{4}(\frac{\tilde{t}}{\tau})^2)$, respectively, the $\tilde{t}$ proper true decay time, τ is D^0 lifetime, $|A_{CF}|$ is the CF decay amplitude, R_D is the ratio of DCS to CF decay rates, $x' = xcos\delta + ysin\delta$ and $y' = ycos\delta - xsin\delta$ where δ is the strong phase difference between the DCS and CF decay. The time resolution in B factory is comparable with D^0 decay time, so we extract the time resolution function $R(t/\tau - \tilde{t}/\tau)$ from D^0 mean decay time. Then the WS, RS decay rate ratio becomes $\mathbf{R}(t/\tau) = \frac{\int_{-\infty}^{+\infty} \Gamma_{WS} R(t/\tau - \tilde{t}/\tau) d(\tilde{t}/\tau)}{\int_{-\infty}^{+\infty} \Gamma_{RS} R(t/\tau - \tilde{t}/\tau) d(\tilde{t}/\tau)}$.

The χ^2/ndf for mixing hypothesis is 4.2/7 and no mixing hypothesis is 33.5/9, the mixing hypothesis excludes non-mixing hypothesis with 5.1σ.

1.2 Mixing and indirect CPV in $D^0 \to K^0_s\pi^+\pi^-$ decay [9]

So far there is no evidence of indirect CP violation in D meson system. Experimental estimation of indirect CP violation is $1-|q/p| = 0.12 \pm 0.17$ [6]. This study is search for indirect CP violation using $D^0 \to K^0_s\pi^+\pi^-$ decay channel. The analysis is done with three dimensional decay amplitude analysis, two is dalizt plot variable $m(K^0_s\pi^+)$ and $m(K^0_s\pi^-)$, and the rest one is time. As a result, the indirect parameter is $|q/p| = 0.90^{+0.16+0.05+0.06}_{-0.15-0.04-0.05}$ and $arg(q/p)(^\circ) = -6 \pm 11 \pm 3^{+3}_{-4}$. It shows no evidence of indirect CP violation.

1.3 CPV in $D^0 \to \pi^0\pi^0$ decay [10]

CP violation in charm decay is very small to observe so experimantal observation could indicate new physics. So far only existing CP violation study of $D^0 \to \pi^0\pi^0$ decay is from CLEO [11], the direct CP asymmetry ΔA_{CP} is $(0.1 \pm 4.8)\%$. In this study, direct CPV is estimated using $D^0 \to \pi^0\pi^0$ decay. The asymmetry is $A_{rec} = \frac{N_{rec}^{D^{*+} \to D^0\pi^+_x} - N_{rec}^{D^{*-} \to D^0\pi^+_x}}{N_{rec}^{D^{*+} \to D^0\pi^+_x} + N_{rec}^{D^{*-} \to D^0\pi^+_x}} \approx A_{CP} + A_{FB}(cos\theta^*)$. The A_{CP} can be extracted removing A_{FB} using asymmetry on the $cos\theta^*$ where θ^* is polar angle of D^*. Using decay channel $D^0 \to \pi^0\pi^0$, the measured asymmetry is $A_{CP}(D^0 \to \pi^0\pi^0) = (-0.03 \pm 0.64(stat) \pm 0.10(sys))\%$ which is consistent with no CP violation.

2 New measurement of charmed baryon

2.1 Branching fraction of $\Lambda_c^+ \to pK^-\pi^+$ decay [12]

A number of charmed baryons decay into Λ_c^+. And $\Lambda_c^+ \to pK^-\pi^+$ is the reference mode for the measurement of branching fractions of the Λ_c^+ baryon, so it's important to measure the absolute branching fraction. The Particle Data Group combines several measurements from the ARGUS and CLEO Collaborations to determine $\mathcal{B}(\Lambda_c^+ \to pK^-\pi^+) = (5.0 \pm 1.3)\%$ [13, 14]. The dominant contribution to the uncertainty is from the model dependce of branching fraction extraction [15]. In the proceeding, we present the first model-independent absolute branching fraction measurement of the $\Lambda_c^+ \to pK^-\pi^+$ decay.

The absolute branching fraction is given by $\mathcal{B}(\Lambda_c^+ \to pK^-\pi^+) = \frac{N(\Lambda_c^+ \to pK^-\pi^+)}{N_{inc}^{\Lambda_c^+} f_{bias} \varepsilon(\Lambda_c^+ \to pK^-\pi^+)}$, where $N_{inc}^{\Lambda_c^+}$ is the number of inclusively reconstructed Λ_c^+, $N(\Lambda_c^+ \to pK^-\pi^+)$ is the number of reconstructed $\Lambda_c^+ \to pK^-\pi^+$ within inclusive Λ_c^+ sample, $\varepsilon(\Lambda_c^+ \to pK^-\pi^+)$ is reconstruction efficiency of $\Lambda_c^+ \to pK^-\pi^+$ decay within inclusive Λ_c^+ sample, f_{bias} is the factor that takes into account potential dependenace of the inclusiv Λ_c^+ reconstruction efficiency on the Λ_c^+ decay mode.

To get the inclusive Λ_c^+ baryons, we used missing mass method for $e^+e^- \to c\bar{c} \to D^{(*)-}\bar{p}\pi^+\Lambda_c^+$ decay. Then we search the decay product of $\Lambda_c^+ \to pK^-\pi^+$ decay in the sample of inclusive Λ_c^+ baryon. The efficiency of $\Lambda_c^+ \to pK^-\pi^+$ and f_{bias} are detemined by MC simluation. The MC simulation shows that Λ_c^+ inclusive reconstruction efficiency weakly depends on the Λ_c^+ decay mode, therefore we need correction for true inclusive Λ_c^+ sample. The factor $f_{bias} = \varepsilon^{inc}_{\Lambda_c^+ \to pK^-\pi^+} / \bar{\varepsilon}^{inc}_{\Lambda_c^+}$ is necessay for this correction.

As a result, the branching fraction is $\mathcal{B}(\Lambda_c^+ \to pK^-\pi^+) = (6.84 \pm 0.24(stat) \pm^{+0.21}_{-0.27} (sys))\%$, that is consistant with previous result and this result improves the previous measurement by factor 5.

2.2 Measurement of mass and width of the $\Sigma_c(2455)^{0/++}$ and $\Sigma_c(2520)^{0/++}$ baryons [16]

The properties of the $\Sigma_c^{0/++}$ baryons have been measured many experiments, but uncertainty remains large [15]. For example, decay width of the $\Sigma_c^{0/++}$ is 10% of its central value, and the mass spilitting $m(\Sigma_c(2455)^{++}) - m(\Sigma_c(2455)^0)$ is about 40%. Because of mass hierarchy between u and d quarks, mass of $\Sigma_c^0(udc)$ should be havier than $\Sigma_c^{++}(uuc)$. However the experimetal results shows opposite mass hiearchy with large error [17]. In this situation, precise mass and width measurement is necessay.

The $\Sigma_c^{0/++}$ baryons are reconstructed via $\Sigma_c^{0/++} \to \Lambda_c^+(\to pK^-\pi^+)\pi_s^{-/+}$ decay channel, where π_s is low momentum pion. The feed down from $\Lambda_c(2595, 2620)^+$ is removed with mass cut on $m(\Lambda_c^+\pi^+\pi^-)$,

The fitting functions for signal is Breit-Wiegner function convolved with detector resolution function. The random back ground function is threshold function. There is feed down around $\Delta M = 185$ MeV/c^2, we confirmed that the origin of the peak is from $\Xi_c^0 \to \Lambda_c^+\pi^-$. This peak is describled by Gaussian funcion. The χ^2/ndf for fit result is 350/347 for zero charge, 343/350 for double charge. The mass and width from fitting result is on table 1. This result shows better uncertainty than previous result.

	ΔM_0(MeV/c^2)	Γ(MeV/c^2)	M_0(MeV/c^2)
$\Sigma_c(2455)^0$	$167.29 \pm 0.01 \pm 0.02$	$1.76 \pm 0.04^{+0.09}_{-0.21}$	$2453.75 \pm 0.01 \pm 0.02 \pm 0.14$
$\Sigma_c(2455)^{++}$	$167.51 \pm 0.01 \pm 0.02$	$1.84 \pm 0.04^{+0.07}_{-0.20}$	$2453.97 \pm 0.01 \pm 0.02 \pm 0.14$
$\Sigma_c(2520)^0$	$231.98 \pm 0.11 \pm 0.04$	$15.41 \pm 0.41^{+0.20}_{-0.32}$	$2518.44 \pm 0.11 \pm 0.04 \pm 0.14$
$\Sigma_c(2520)^{++}$	$231.99 \pm 0.10 \pm 0.02$	$14.77 \pm 0.25^{+0.18}_{-0.30}$	$2518.45 \pm 0.10 \pm 0.02 \pm 0.14$

Table 1: The measurement of mass and with of the $\Sigma_c(2455)^{0/++}$ and $\Sigma_c(2520)^{0/++}$. The first error is stastical error and second error is systematical error. The third error on M_0 is from mass error of Λ_c^+

2.3 Search for doubly charmed baryon and charmed strange baryon at Belle [18]

In recent years, there has been significant progress in charmed baryon spectroscopy. So far, there are no experimentally established doubley charmed baryon. The SELEX collaboration reported evidence of Ξ_{cc}^{+} in the $\Lambda_c^+ K^- \pi^+$ and pD^+K^- final state [19]. However, the result is not supported by FOCUS, BABAR, Belle nor LHCb. In this study, we improve the search using more data and more channels.

The first decay channel is $\Xi_{cc}^{+(+)} \to \Lambda_c^+ K^- \pi^+ (\pi^+)$ and $\Lambda_c^+ \to pK^-\pi^+$. We searched the mass region of 3.2∼4.0 GeV/c^2, no significance signal is seen in the data. The local significance is lower than 3σ. The upper limit of production cross section and Branching fraction with 95% C.L. is around 10fb^{-1}.

The sesond decay channel is $\Xi_{cc}^{+(+)} \to \Xi_x^0 \pi^+ (\pi^+)$ and $\Xi_c^0 \to \Xi^0 \pi -, \Lambda K^- \pi^+, pK^- K^- \pi^+$. We searched same mass range with first decay cheannel, still there is no significant signal over mass range. The highst signal is around 3.553 GeV/c^2, but it is not significant with look elsewhere effect.

And we also searched the strange charmed baryon $\Xi_c^+(3055)$ and $\Xi_c^+(3123)$, using the decay channel $\Xi_c^+(3055, 3123) \to \Lambda_c^+ K^- \pi^-$ over the mass range 2.9∼3.2 GeV/c^2. We observed the significant signal of $\Xi_c^+(3055)$ with 6.8σ, while no peak of $\Xi_c^+(3123)$. The upper limit of $\Xi_c^+(3123)$ cross section and branching ratio is $1.6 \pm 0.6 \pm 0.2$fb^{-1}.

In summary, searching $\Xi_{cc}^{+(+)}$ using more data and more decay channels doesn't show the signal over the mass range of 3.2∼4.0 GeV/c^2. For the strange charmed baryon search, we obersed $\Xi_c^+(3055)$ with 6.8σ, but couldn't see the peak of $\Xi_c^+(3123)$.

References

[1] A. A. Petrov, Int. J. Mod. Phys. A 21, 5686 (2006).

[2] A. F. Falk, Y. Grossman, Z. Ligeti, and A.A. Petrov, Phys. Rev. D 65, 054034 (2002).

[3] E. Golowich, J. Hewett, S. Pakvasa, and A.A. Petrov, Phys. Rev. D 79, 114030 (2009).

[4] Y. Grossman, A. L. Kagan, and Y. Nirm Phys. Rev. D 75, 036008 (2007).

[5] B. R. Ko *et al.*. (Belle Collaboration) Phys. Rev. Lett. **112**, 111801 (2014).

[6] Y. Aubert *et al.*. (Heavy Flavor Averaging Group), arXiv:1207.1158v2.

[7] R. Aaij *et al.*. (LHCb Collaboration), Phys. Rev. Lett. **110**, 101802 (2013).

[8] T. Aaltonen *et al.*. (CDF Collaboration), Phys. Rev. Lett. **111**, 231802 (2013).

[9] T. Peng *et al.*. (Belle Collaboration) Phys. Rev. D. **89**, 091103 (2014).

[10] N. K. Nisar *et al.*. (Belle Collaboration) Phys. Rev. Lett. **112**, 211601 (2014).

[11] G. Bonvicini *et al.*. (CLEO Collaboration) Phys. Rev. D. **63**, 071101 (2014).

[12] A. Zupanc *et al.*. (Belle Collaboration) Phys. Rev. Lett. **113**, 042002 (2014).

[13] H. Albrecht *et al.*. (ARGUS Collaboration) Phys. Lett. B. **207**, 109 (1988).

[14] G. D. Crawford *et al.*. (CLEO Collaboration) Phys. Rev. D. **45**, 752 (1992).

[15] J. Beringer *et al.*. (Particle Data Group) Phys. Rev. D. **86**, 01001 (2012).

[16] S. H. Lee *et al.*. (Belle Collaboration) Phys. Rev. D. **89**, 091102 (2014).

[17] E. M. Aitala *et al.*. (E791 Collaboration) Phys. Lett. B. **379**, 292 (1996).

[18] Y. Kato *et al.*. (Belle Collaboration) Phys. Rev. D. **89**, 052003 (2014).

[19] M. Mattson *et al.*. (SELEX Collaboration) Phys. Rev. Lett. **89**, 112001 (2002).

Exploring the long-distance structure of the $X(3872)$

Feng-Kun Guo[1], *Carlos Hidalgo-Duque*[2], *Juan Nieves*[2], *Altug Ozpineci*[3], *Manuel Pavón Valderrama*[4]

[1]Helmholtz-Institut für Strahlen- und Kernphysik and Bethe Center for Theoretical Physics, Universität Bonn, D-53115 Bonn, Germany
[2]Instituto de Física Corpuscular (IFIC), Centro Mixto CSIC-Universidad de Valencia, Institutos de Investigación de Paterna, Aptd. 22085, E-46071 Valencia, Spain
[3] Middle East Technical University - Department of Physics TR-06531 Ankara, Turkey
[4] Institut de Physique Nucléaire, Université Paris-Sud, IN2P3/CNRS, F-91406 Orsay Cedex, France

DOI: http://dx.doi.org/10.3204/DESY-PROC-2014-04/2

In this work we use an effective field theory (EFT) approach to study the $X(3872)$ resonance, assuming a heavy meson-heavy antimeson molecule as its inner structure. From this EFT we extract some direct consequences for the hidden charm and bottom hadronic spectrum.

Within this EFT we also study the decay $X(3872) \to D^0\bar{D}^0\pi^0$. This decay is unique since it is more sensitive to the long-distance part of the $X(3872)$ wave function than the $X(3872) \to J/\psi\pi\pi$ and $X(3872) \to J/\psi\pi\pi\pi$ modes. We also show that the possible $D\bar{D}$ Final State Interactions (FSI) effects can lead to experimental constrains on the Low Energy Constants (LECs) that appear in the EFT and the possible existence of a loosely $D\bar{D}$ bound state.

1 Introduction

The current understanding of the hadronic spectrum is a milestone in particle physics. The success of the conventional quark model (where mesons and baryons are the only possible quark composites) in the classification of known particles and the prediction of different states is outstanding. However, beyond the quark model there are other exotic possibilities that QCD allows. These exotics (glueballs, tetraquarks, hadronic molecules...), though theoretically predicted, have not been experimentally confirmed yet.

The existence of hadronic molecules, first predicted in the mid-70s by Voloshin and Okun [1] was based on the similarities these systems shared with the deuteron. The best candidate to fit this hadronic molecule description is the $X(3872)$, discovered by Belle in 2003 [2] in the $J/\psi\pi\pi$ channel. Based on the closeness to the $D\bar{D}^*$ threshold this resonance is thought to be a $D\bar{D}^*$ with quantum numbers $J^{PC} = 1^{++}$. These quantum numbers were later confirmed in 2011 by the LHCb collaboration [3]. Taking into account this experimental information, it seems likely that the hadronic molecule component of the $X(3872)$ wave function plays an important role in the description of the resonance.

In this work we use an EFT to describe these heavy meson-heavy antimeson molecules. In Sec. 2 the main features of this EFT are briefly explained since they have been extensively

covered in previous works. In Sec. 3, the computation of the $X(3872) \to D^0\bar{D}^0\pi^0$ decay width is carried out. Finally some conclusions are established in Sec. 4.

2 The heavy meson-heavy antimeson EFT

In this section the EFT that is going to be used along this work is introduced. At leading order (LO), the description of heavy meson-heavy antimeson molecules can be done with a contact potential determined by Heavy Quark Spin Symmetry (HQSS) as proposed in [4]. This LO lagrangian, when considering the isospin degrees of freedom, depends exclusively on four undetermined LECs. Other subleading effects such as pion exchanges and coupled channel effects are less important than expected and can be taken into account by the errors of the order $\mathcal{O}\left(\frac{1}{m_Q}\right)$, that will be introduced to account for not considering the next order in the EFT expansion [5].

The lagrangian provides the kernel that is employed in a Lippmann-Schwinger Equation (LSE). Poles in the T-matrix give rise to the different molecular states. The LSE, however, has a ultraviolet divergent two-body loop function. This divergence can be treated employing several regularization methods. We are using a gaussian regulator Λ and we choose two different gaussian regulators $\Lambda = 0.5(1.0)$ GeV, see [6, 7] for details.

Now, assuming some experimental resonances are heavy meson-heavy antimeson molecules we can fix some linear combination of the four undetermined LECs in the lagrangian. For that purpose, we find that the $X(3872)$ and the $Z_b(10610)/Z_b'(10650)$ [10] are perfect candidates. As already said, the $X(3872)$ can be thought as a $D\bar{D}^*$ with quantum numbers $J^{PC} = 1^{++}$. In the Z_bs case, we are dealing with resonances whose quark content must be of, at least, four quarks since they have $I_{Z_b} = 1$. Even more, its closeness to the $B\bar{B}^*$ and $B^*\bar{B}^*$ threshold respectively, suggest that a molecular interpretation with quantum numbers $J^{PC} = 1^{+-}$ is very sensible.

Thanks to these two assumptions we can fix three different linear combinations on LECs. Two of them come from the $X(3872)$ assumption (where we have also taken into account the isospin violating decays in the fit, see [7] for further information) and the third one comes from the experimental masses of the Z_bs resonances. This means that there is still an undetermined LEC in our model, that we will call C_{0A} without loss of generality.

We have used this scheme in previous works, predictions for HQSS heavy meson-heavy antimeson molecules [6, 7, 8] and pentaquark-like states that will be partners of the $X(3872)$ and $Z_b(10610)/Z_b'(10650)$ resonances [9]. In these works we found that there was almost no dependence on the regulation method used and that the small differences that appear can be accounted in the expansion errors too.

3 $X(3872) \to D^0\bar{D}^0\pi^0$ decay

So far, the only experimental information about the $X(3872)$ we have used in the analysis is its mass and the ratio of its $X(3872) \to J/\psi\pi\pi$ and $X(3872) \to J/\psi\pi\pi\pi$ decay widths. In these decays, the $D(\bar{D})$ and $\bar{D}^*(D^*)$ components of the $X(3872)$ have to be close so its charm quark and antiquark can form a charmonium state. Therefore, we can extract little information about the long-distance structure of the $X(3872)$. This long-distance structure of the resonance could become a very important piece of information to differenciate between two exotic structures like tetraquarks and hadronic molecules.

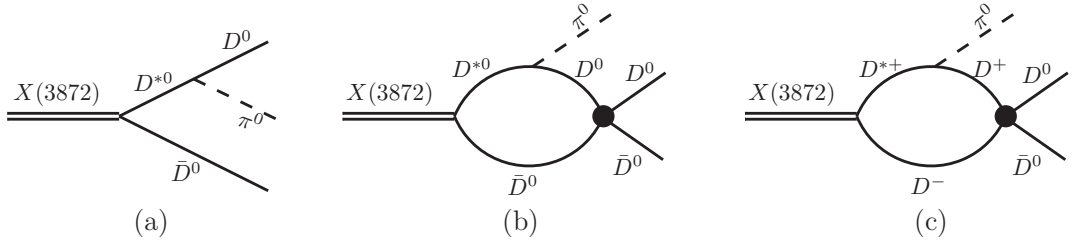

Figure 1: Feynman diagrams for the decay $X(3872) \to D^0\bar{D}^0\pi^0$. The charge conjugate channel is not shown but included in the calculations.

Hence, the detailed analysis of different decays where the $X(3872)$ inner components keep their individual properties is crucial for the full comprehension of the resonance. The $X(3872) \to D^0\bar{D}^0\pi^0$ (already observed in [11]) decay looks like a perfect probe of the long-distance structure of the $X(3872)$. As it can be seen in Fig.1, the $X(3872)$ can decay despite its $D^{*0}(\bar{D}^{*0})$ and $\bar{D}^0(D^0)$ inner components are substancially separated. It should already be noticed that this is the only $X(3872) \to D\bar{D}\pi$ decay channel since the charged decays are kinematically forbidden.

In this decay, there are two contributions. The tree level contribution is depicted in Fig.1a (and its corresponding charge conjugated diagram). From the $X(3872)$ pole residue we determine the $X(3872)D^0\bar{D}^0$ coupling and we obtain [12]:

$$\Gamma(X(3872) \to D^0\bar{D}^0\pi^0)_{\text{tree}} = 44.0^{+2.4}_{-7.2}\left(42.0^{+3.6}_{-7.3}\right)\ \text{keV}, \tag{1}$$

for $\Lambda = 0.5$ (1.0) GeV, respectively. Next, we include the possible FSI between the D-mesons and the $\bar{D}$-antimesons, as shown in the Feynman diagrams of Fig.1b and Fig.1c. In this case, we need for the computation of the decay width the four LECs of our model. Our results, therefore, will be a function of the undetermined LEC C_{0A}. The results obtained are displayed in Fig.2, being the grey band the results coming from the tree level calculation.

As can be observed, there is no appreciable dependence on the gaussian regulator in the results. However, the inclusion of FSI mechanism has created a *bump* in the decay width curve. This is caused by the interferences due to the possible existence of a $D\bar{D}$ bound state with quantum numbers $J^{PC} = 0^{++}$. For that reason, a precise experimental value of the $X(3872) \to D^0\bar{D}^0\pi^0$ decay width could be an important asset in the determination of the fourth, still undetermined, LEC and can also rule out or confirm the existence of this $D\bar{D}$ bound state, predicted in several theoretical models.

4 Conclusions

In this work, we have studied the decay of the $X(3872)$ resonance into $D^0\bar{D}^0\pi^0$ using an EFT based on a hadronic molecule assumption for the $X(3872)$ and HQSS. We show that $D\bar{D}$ FSI effects can be important specially if a near threshold pole exists. Besides, this decay may be used to measure the so far unknown parameter C_{0A} of the HQSS EFT employed in this work. Such information is valuable to better understand the interaction between heavy-light mesons and heavy-light antimesons.

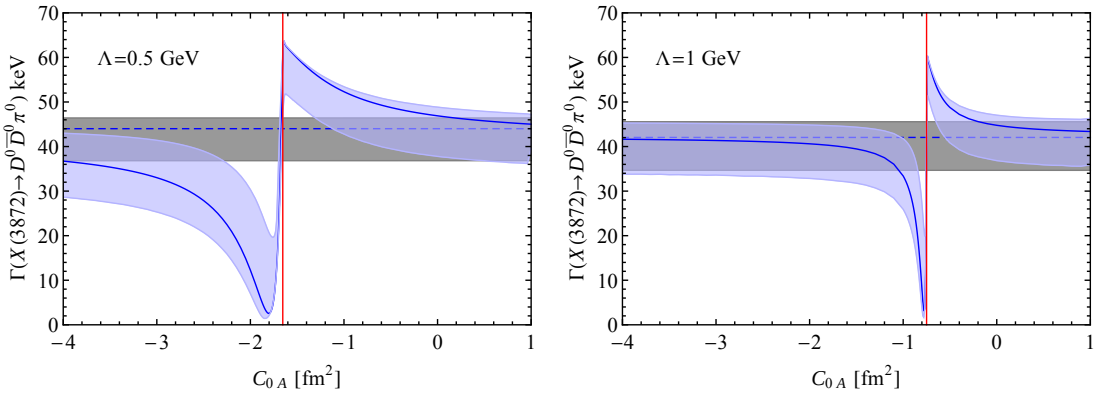

Figure 2: Dependence of the $X(3872) \to D^0\bar{D}^0\pi^0$ partial decay width on the C_{0A} LEC. The UV cutoff is set to $\Lambda = 0.5$ GeV (1 GeV) in the left (right) panel. The blue error bands contain $D\bar{D}$ FSI effects, while the grey bands stand for the tree level prediction. The vertical lines denote the values of C_{0A} for which a $D\bar{D}$ bound state is generated at the $D^0\bar{D}^0$ threshold.

Acknowledgments

C. H.-D. thanks the support of the JAE-CSIC Program. This work is supported in part by the DFG and the NSFC through funds provided to the Sino-German CRC 110 "Symmetries and the Emergence of Structure in QCD", by the NSFC (Grant No. 11165005), by the Spanish Ministerio de Economía y Competitividad and European FEDER funds under the contract FIS2011-28853-C02-02 and the Spanish Consolider-Ingenio 2010 Programme CPAN (CSD2007-00042), by Generalitat Valenciana under contract PROMETEO/2009/0090 and by the EU HadronPhysics3 project, grant agreement no. 283286.

References

[1] M. B. Voloshin and L. B. Okun, JETP Lett. **23** (1976) 333 [Pisma Zh. Eksp. Teor. Fiz. **23** (1976) 369].

[2] S. K. Choi *et al.* [Belle Collaboration], Phys. Rev. Lett. **91** (2003) 262001

[3] R. Aaij *et al.* [LHCb Collaboration], Phys. Rev. Lett. **110** (2013) 222001

[4] M. T. AlFiky, F. Gabbiani and A. A. Petrov, Phys. Lett. B **640** (2006) 238

[5] M. P. Valderrama, Phys. Rev. D **85** (2012) 114037

[6] J. Nieves and M. P. Valderrama, Phys. Rev. D **86** (2012) 056004

[7] C. Hidalgo-Duque, J. Nieves and M. P. Valderrama, Phys. Rev. D **87** (2013) 7, 076006

[8] F. K. Guo, C. Hidalgo-Duque, J. Nieves and M. P. Valderrama, Phys. Rev. D **88** (2013) 054007

[9] F. K. Guo, C. Hidalgo-Duque, J. Nieves and M. P. Valderrama, Phys. Rev. D **88** (2013) 5, 054014

[10] I. Adachi *et al.* [Belle Collaboration],

[11] G. Gokhroo *et al.* [Belle Collaboration], Phys. Rev. Lett. **97** (2006) 162002

[12] F. K. Guo, *et al.*, Eur. Phys. J. C **74** (2014) 2885

Chiral Perturbation Theory tests at NA48 and NA62-R_K experiments at CERN

Flavio Costantini[1] for the NA48/2 Collaboration : Cambridge, CERN, Dubna, Chicago, Edinburgh, Ferrara, Firenze, Mainz, Northwestern, Perugia, Pisa, Saclay, Siegen, Torino, Wien and the NA62-R_K Collaboration: Birmingham, CERN. Dubna, Fairfax, Ferrara, Firenze, Frascati, Mainz, Merced, Moscow, Napoli, Perugia, Pisa, Protvino, Roma I, Roma II, Saclay, San Luis Potosi, Stanford, Sofia, Torino, TRIUMF.

[1]Dipartimento di Fisica, Università di Pisa and INFN Pisa
Largo B. Pontecorvo 3, 56127 Pisa (Italy)

DOI: http://dx.doi.org/10.3204/DESY-PROC-2014-04/16

Final results from an analysis of about 400 $K^{\pm} \to \pi^{\pm}\gamma\gamma$ rare decay candidates collected by the NA48/2 and NA62-R_K experiments at CERN during low intensity runs with minimum bias trigger configurations are presented. The results include a model-independent decay rate measurement and fits to Chiral Perturbation Theory (ChPT) description. The data support the ChPT prediction for a cusp in the di-photon invariant mass spectrum at the two pion threshold.

1 Introduction

The NA48/2 experiment at the CERN SPS has collected a large sample of charged kaon decays in 2003–04 (corresponding to about 2×10^{11} $K^{\pm}$ decays in the vacuum decay volume). The experiment featured simultaneous K^+ and K^- beams and was optimized for the search for direct CP violating charge asymmetries in the $K^{\pm} \to 3\pi$ decays [1]. Its successor, the NA62-R_K experiment, collected a 10 times smaller $K^{\pm}$ decay sample with low intensity beams and minimum bias trigger conditions in 2007–08. NA62-R_K used the same detector as NA48/2, while the data taking conditions were optimized for a measurement of the ratio of the rates of the $K^{\pm} \to \ell^{\pm}\nu$ decays ($\ell = e, \mu$) [2]. In particular, the main trigger chain required the presence of an electron ($e^{\pm}$).

The large data samples accumulated by both experiments have allowed precision studies of a range of rare $K^{\pm}$ decay modes. Recent measurements of the rare decay $K^{\pm} \to \pi^{\pm}\gamma\gamma$ (denoted $K_{\pi\gamma\gamma}$ below) from the above data samples [3, 4] are reported here.

2 Beam and detector

The beam line has been designed to deliver simultaneous narrow momentum band K^+ and K^- beams derived from the primary 400 GeV/c protons extracted from the CERN SPS. Secondary beams with central momenta of 60 GeV/c (for NA48/2) or 74 GeV/c (for NA62-R_K) were used.

The beam kaons decayed in a fiducial decay volume contained in a 114 m long cylindrical vacuum tank. The momenta of charged decay products were measured in a magnetic spectrometer, housed in a tank filled with helium placed after the decay volume. The spectrometer comprised four drift chambers (DCHs), two upstream and two downstream of a dipole magnet which provided a horizontal transverse momentum kick of 120 MeV/c (for NA48/2) or 265 MeV/c (for NA62-R_K) to charged particles. Each DCH was composed of eight planes of sense wires. A plastic scintillator hodoscope (HOD) producing fast trigger signals and providing precise time measurements of charged particles was placed after the spectrometer. Further downstream was a liquid krypton electromagnetic calorimeter (LKr), an almost homogeneous ionization chamber with an active volume of 7 m^3 of liquid krypton, $27X_0$ deep, segmented transversally into 13248 projective $\sim 2\times 2$ cm^2 cells and with no longitudinal segmentation. The LKr information is used for photon measurements and charged particle identification. An iron/scintillator hadronic calorimeter and muon detectors, not used in the present analysis, were located further downstream. A detailed description of the detector can be found in Ref. [5].

3 The $K^\pm \to \pi^\pm\gamma\gamma$ decay in the ChPT

Measurements of radiative non-leptonic kaon decays provide crucial tests of Chiral Perturbation Theory (ChPT) describing weak low energy processes. The $K_{\pi\gamma\gamma}$ decay has attracted the attention of theorists over the last 40 years [6, 7, 8, 9], but remains among the least experimentally studied kaon decays.

In the ChPT framework, the $K_{\pi\gamma\gamma}$ decay receives two non-interfering contributions at lowest non-trivial order $\mathcal{O}(p^4)$: the pion and kaon loop amplitudes which depend on an a priori unknown $\mathcal{O}(1)$ parameter $\hat{c}$, and the pole amplitude. Higher order unitarity corrections from $K \to 3\pi$ decays modify the decay spectrum significantly; in particular, they lead to non-zero differential decay rate at zero di-photon invariant mass [8]. The total decay rate is predicted to be $\mathcal{B}(K_{\pi\gamma\gamma}) \sim 10^{-6}$, with the pole amplitude contributing 5% or less [8, 9]. The ChPT predictions for the differential rate $d\Gamma/dz$ with $z = (m_{\gamma\gamma}/m_K)^2$, where $m_{\gamma\gamma}$ is the di-photon invariant mass, for several values of $\hat{c}$, are presented in Fig. 1. These spectra exhibit a characteristic cusp structure at twice the pion mass due to the dominant pion loop amplitude.

Experimentally, the only published $K_{\pi\gamma\gamma}$ observation is that of 31 K^+ decay candidates in the kinematic region 100 MeV/$c < p^*_\pi <$ 180 MeV/c (p^*_π is the π^+ momentum in the K^+ frame) by the BNL E787 experiment [10].

4 Measurements of the $K^\pm \to \pi^\pm\gamma\gamma$ decay

New measurements of the $K_{\pi\gamma\gamma}$ decay have been performed using two minimum bias data sets: 1) two special $K^\pm$ decay samples collected by the NA48/2 experiment at $\sim 10\%$ of the nominal beam intensity during 12 hours in 2003 and 54 hours in 2004; 2) a subset of the NA62-R_K data sample collected over the whole duration of the data taking with downscaled trigger conditions with an effective downscaling factor of about 20. The employed trigger conditions required a time coincidence of signals in both HOD horizontal and vertical strip planes within the same quadrant and an energy deposit of at least 10 GeV in the LKr calorimeter. The resulting effective kaon fluxes used for the NA48/2 and NA62-R_K $K_{\pi\gamma\gamma}$ analyses are similar, but the background conditions and resolution on kinematic variables differ significantly. The $K_{\pi\gamma\gamma}$ decay rate was measured with respect to the normalization decay chain with a large and well

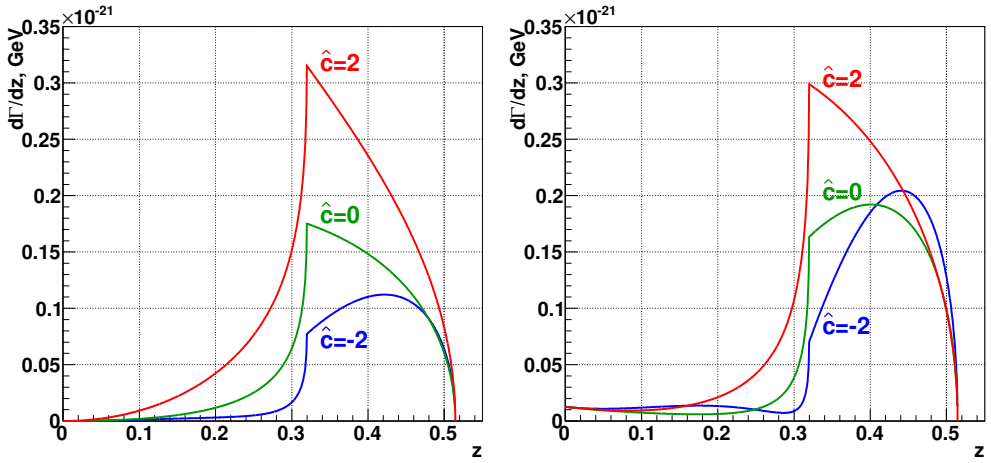

Figure 1: Differential rate ($d\Gamma/dz$) of the $K_{\pi\gamma\gamma}$ decays according to the $\mathcal{O}(p^4)$ (left) and $\mathcal{O}(p^6)$ (right) descriptions [7, 8] for several values of $\hat{c}$. The $\hat{c}$-independent pole contribution is also shown. For the $\mathcal{O}(p^6)$ parameterization, values of polynomial contributions [8] $\eta_i = 0$ and $K^\pm \to 3\pi^\pm$ amplitude parameters from a fit to experimental data [11] are used.

known branching fraction: the $K^\pm \to \pi^\pm\pi^0$ decay followed by the $\pi^0 \to \gamma\gamma$ decay. Signal and normalization samples have been collected with the same trigger logic.

Signal events are selected on the basis of spectrometer and LKr calorimeter information in the kinematic region $z = (m_{\gamma\gamma}/m_K)^2 > 0.2$ to reject the $K^\pm \to \pi^\pm\pi^0$ background, as well as other backgrounds from the π^0 decays, peaking at $z = (m_{\pi^0}/m_K)^2 = 0.075$. The residual background contamination is due to $K^\pm \to \pi^\pm\pi^0\gamma$ and $K^\pm \to \pi^\pm\pi^0\pi^0$ decays, with photons either missing the LKr acceptance of forming merged clusters in the LKr calorimeter. The event selection includes an upper limit for the transverse size of the LKr clusters, which reduces the background due to merged clusters. The $\pi^\pm\gamma\gamma$ invariant mass spectra of the selected $K_{\pi\gamma\gamma}$ candidates, with the expectations of the signal and background contributions from MC simulations, are displayed in Fig. 2: 149 (232) decay candidates with a background contamination of 10% (7%) are observed in the NA48/2 (NA62-R_K) data set.

A model-independent measurement of the z spectrum in the kinematic range $z > 0.2$ has been performed for the NA48/2 and NA62-R_K data sets. The partial branching fractions in bins of the z variable have been measured: they are model-independent because the considered z bin width is sufficiently small for the acceptances in z to have a negligible dependence on the assumed $K_{\pi\gamma\gamma}$ kinematical distribution. In addition, the y-dependence of the differential decay rate expected within the ChPT framework is weak [8, 9]. The final results of the measurements of the partial branching fractions in bins of the z variable are presented in Fig. 3 (left). The model-independent branching fraction in the kinematic region $z > 0.2$ is computed by summing over the z bins: $\mathcal{B}_{\rm MI}(z > 0.2) = (0.965 \pm 0.061_{\rm stat} \pm 0.014_{\rm syst}) \times 10^{-6}$.

Measurements of the ChPT parameter $\hat{c}$ have been made for both NA48/2 and NA62-R_K data samples by performing log-likelihood fits to the reconstructed z spectra. The data spectra of the z kinematic variable, together with signal and background expectations from simulations, are displayed in Fig. 3 (centre, right): they support the ChPT prediction of the cusp at $2m_\pi$ threshold. The values of the $\hat{c}$ parameter in the framework of the ChPT $\mathcal{O}(p^4)$

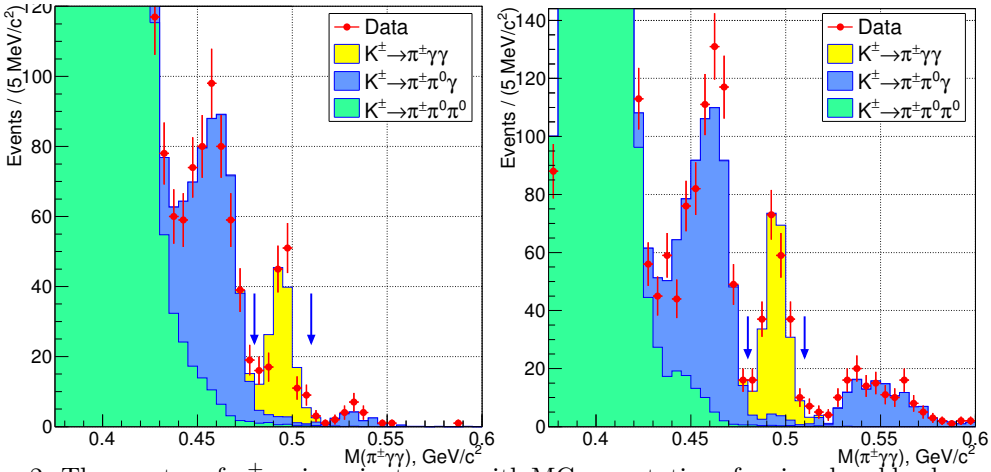

Figure 2: The spectra of $\pi^{\pm}\gamma\gamma$ invariant mass with MC expectations for signal and backgrounds: NA48/2 data (left) and NA62-R_K data (right). The signal region is between the 2 arrows.

$\mathcal{B}(K_{\pi\gamma\gamma}) \times 10^6$

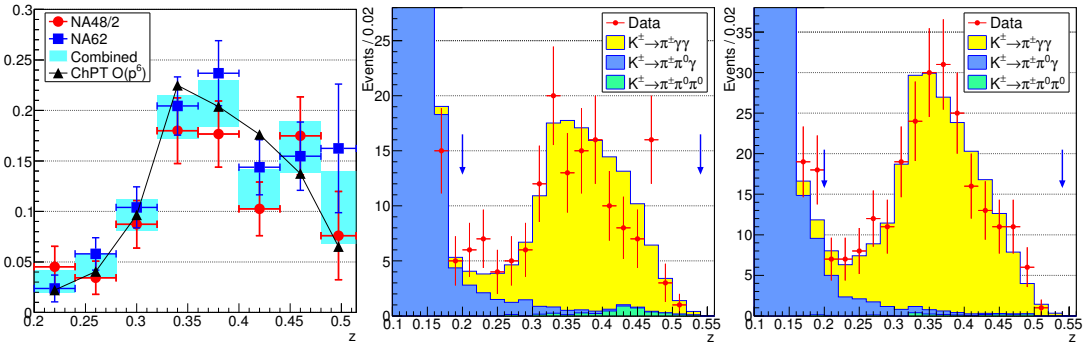

Figure 3: Left: measurements of partial model-independent branching fractions of the $K_{\pi\gamma\gamma}$ decay in bins of the z kinematic variable from the NA48/2 and NA62-R_K data samples. The spectra of $z = (m_{\gamma\gamma}/m_K)^2$ with MC expectations for signal (best fit) and backgrounds: NA48/2 data (centre) and NA62-R_K data (right). The signal region ($0.2 < z < 0.52$) is between the 2 arrows.

and $\mathcal{O}(p^6)$ parametrizations according to the formulation of [8] have been obtained. The $\mathcal{O}(p^6)$ parametrization involves a number of external inputs. In this analysis, they have been fixed as follows: the polynomial contribution terms are $\eta_1 = 2.06$, $\eta_2 = 0.24$ and $\eta_3 = -0.26$ as suggested in [8], while the $K^{\pm} \to 3\pi^{\pm}$ amplitude parameters come from a fit to the experimental data [11].

The results of the fits are presented in Table 1: they are in agreement with the earlier BNL E787 ones. A combination of results from the two experiments has been performed, taking into account the large positive correlation of the systematic uncertainties of the two measurements. The combined results are also presented in Table 1. The uncertainties are dominated by the statistical ones; the systematic errors on the combined results are dominated by those due to background subtraction. The branching ratio in the full kinematic range corresponding to the combined value of the $\hat{c}$ parameter within the $\mathcal{O}(p^6)$ formulation is $\mathcal{B}(K_{\pi\gamma\gamma}) = (1.003 \pm 0.056) \times 10^{-6}$.

Table 1: Results of fits to the ChPT parameters [8] of the $K^{\pm} \to \pi^{\pm}\gamma\gamma$ di-photon mass spectra.

	NA48/2 measurement	NA62-R_K measurement	Combined
$\hat{c}$, $\mathcal{O}(p^4)$ fit	$1.37 \pm 0.33_{\rm stat} \pm 0.14_{\rm syst}$	$1.93 \pm 0.26_{\rm stat} \pm 0.08_{\rm syst}$	$1.72 \pm 0.20_{\rm stat} \pm 0.06_{\rm syst}$
$\hat{c}$, $\mathcal{O}(p^6)$ fit	$1.41 \pm 0.38_{\rm stat} \pm 0.11_{\rm syst}$	$2.10 \pm 0.28_{\rm stat} \pm 0.18_{\rm syst}$	$1.86 \pm 0.23_{\rm stat} \pm 0.11_{\rm syst}$

References

[1] J.R. Batley *et al.*, Eur. Phys. J **C52** (2007) 875.

[2] C. Lazzeroni *et al.*, Phys. Lett. **B719** (2013) 326.

[3] J.R. Batley *et al.*, Phys. Lett. **B730** (2014) 141.

[4] C. Lazzeroni *et al.*, Phys. Lett. **B732** (2014) 65.

[5] V. Fanti *et al.*, Nucl. Instrum. Methods **A574** (2007) 433.

[6] L.M. Sehgal, Phys. Rev. **D6** (1972) 367.

[7] G. Ecker, A. Pich and E. de Rafael, Nucl. Phys. **B303** (1988) 665.

[8] G. D'Ambrosio and J. Portolés, Phys. Lett. **B386** (1996) 403.

[9] J.-M. Gérard, C. Smith and S. Trine, Nucl. Phys. **B730** (2005) 1.

[10] P. Kitching *et al.*, Phys. Rev. Lett. **79** (1997) 4079.

[11] J. Bijnens, P. Dhonte and F. Persson, Nucl. Phys. **B648** (2003) 317.

Detailed study of the K_{e4} decay mode properties from the NA48/2 experiment at CERN

Patrizia Cenci[1] on behalf of the NA48/2 Collaboration: Cambridge, CERN, Dubna, Chicago, Edinburgh, Ferrara, Firenze, Mainz, Northwestern, Perugia, Pisa, Saclay, Siegen, Torino, Wien

[1]INFN Perugia, Via A. Pascoli, 06123 Perugia, Italy

DOI: http://dx.doi.org/10.3204/DESY-PROC-2014-04/17

The NA48/2 Collaboration at CERN has accumulated an unprecedented statistics of rare semileptonic four-body K_{e4} decay modes $K^{\pm} \to \pi^+\pi^- e\nu$ and $K^{\pm} \to \pi^0\pi^0 e\nu$, with nearly 1% background contamination. Final results from the analyses of the full K_{e4} data samples are described. The most accurate measurements to date of form factors and branching ratios have been achieved by NA48/2, bringing new inputs to low energy QCD description and stringent tests of predictions from Chiral Perturbation Theory and Lattice QCD.

1 Introduction

The NA48/2 experiment at CERN has collected the largest world sample of charged kaon decays with the main goal of searching for direct CP violation [1]. The beam line was designed to deliver simultaneous K^+ and K^- beams at 60 GeV/c central momentum, produced by 400 GeV/c primary protons from the CERN SPS impinging on a beryllium target. Charged particle momenta were measured by a magnetic spectrometer consisting of four drift chambers (DCH) and a dipole magnet. The spectrometer was located in a tank filled with helium at atmospheric pressure and followed by a scintillator trigger hodoscope. A liquid Krypton electromagnetic calorimeter was exploited to measure the energy of electrons and photons. A hadron calorimeter and a muon veto system, essential to distinguish muons from pions, were located further downstream. Details of the experimental apparatus are available in [2].

2 K_{e4} decay mode properties

The study of semileptonic four-body K_{e4} decays is extremely interesting due to the well-known Standard Model (SM) electroweak amplitude responsible for the leptonic part and the small number of hadrons in the final state. In the non-perturbative QCD regime, at energies below 1 GeV, the developments of Chiral Perturbation Theory (ChPT) [3] and Lattice QCD [4] have reached precision levels competitive with the most accurate experimental results.

The NA48/2 experiment has collected high statistics samples of $K^{\pm} \to \pi^+\pi^- e^{\pm}\nu$ [K^{+-}_{e4}] and $K^{\pm} \to \pi^0\pi^0 e^{\pm}\nu$ [K^{00}_{e4}] candidates, several orders of magnitude larger than the world ones. The latest NA48/2 results from the study of K^{+-}_{e4} decays [5][6] and new results from K^{00}_{e4} data analysis [7] will be reviewed.

2.1 K_{e4} Form Factors and Branching Ratios

K_{e4} decay kinematics is conveniently described by five variables [8]: the squared dipion invariant mass $S_\pi = M^2_{\pi\pi}$, the squared dilepton invariant mass $S_e = M^2_{e\nu}$, the angle θ_π of the pion in the dipion rest frame with respect to the flight direction of the dipion in the kaon rest frame, the angle θ_e of the lepton in the dilepton rest frame with respect to the flight direction of the dilepton in the kaon rest frame, the angle ϕ between dipion and dilepton rest frames.

K_{e4} decay amplitude is given by the product of a leptonic weak current and a (V-A) hadronic current, expressed in terms of three axial-vector (F, G and R) and one vector (H) complex form factors. Due to the smallness of the electron mass, R does not contribute to K_{e4} decay rates. In the isospin symmetry limit, hadronic form factors can be developed in partial wave expansion and expressed in term of S- and P- wave components (the D-wave contribution can be neglected):

$$F = F_s e^{i\delta_s} + F_p e^{i\delta_p} cos\theta_\pi, \qquad G = G_p e^{i\delta_p}, \qquad H = H_p e^{i\delta_p}.$$

Considering a unique phase δ_p for all the P-wave form factors in absence of CP violating weak phases, the decay probability depends on the real form factor magnitudes F_s, F_p, G_p, H_p and a single phase shift $\delta = \delta_s - \delta_p$.

High precision measurements of K^{+-}_{e4} and K^{00}_{e4} hadronic form factors and branching ratios (BR) have been published by NA48/2 [5][6][7]. Decay rates are measured relative to the $K_{3\pi}$ normalization channels, $K^\pm \to \pi^+\pi^-\pi^\pm$ [$K^{+-}_{3\pi}$] for the K^{+-}_{e4} mode and $K^\pm \to \pi^0\pi^0\pi^\pm$ [$K^{00}_{3\pi}$] for the K^{00}_{e4} one. The main background sources are given, respectively, by $K^{+-}_{3\pi}$ and $K^{00}_{3\pi}$ events with a fake electron due to charged pion misidentification or with $\pi^\pm \to e^\pm\nu$ decays.

The measurements of BR(K^{+-}_{e4}) and BR(K^{00}_{e4}) are obtained from the number of reconstructed signal, background and normalization events, corrected for different acceptances and trigger efficiencies in the signal and normalization modes. The PDG [9] values are used for BR($K^{+-}_{3\pi}$) and BR($K^{00}_{3\pi}$). Since in both K_{e4} analyses the topologies of candidate and normalization events are similar in terms of the number of detected charged ($e^\pm$ or $\pi^\pm$) and neutral ($\pi^0\pi^0$ or $\pi^+\pi^-$) particles, signal and normalization samples are collected concurrently employing the same trigger logic and common selections as far as possible. This leads to the partial cancellation of systematic effects induced by imperfect beam description, local detector and trigger inefficiencies and makes the measurement independent on the absolute kaon flux measurements. A detailed Monte Carlo simulation has been developed to include full detector geometry, DCH alignment, local inefficiencies and beam properties.

K^{+-}_{e4} decays. Nearly 1.13×10^6 K^{+-}_{e4} candidates with about 0.6% background contamination have been reconstructed by NA48/2. The form factor analysis is performed in the five-dimensional space of the kinematic variables [8] to take into account the precise knowledge of experimental acceptance and resolution. The large data statistics allows to define grids of equal population five-dimensional boxes. Hadronic form factors and their dependence on energy are obtained by adjusting the expected number of simulated events to the observed data events. Positive and negative kaon charges are analysed separately to account for the different beam geometries. The results are consistent for both kaon charges and are combined according to their statistical error. Form factors are expressed as Taylor series expansion of $q^2 = S_\pi/(4m^2_{\pi^+}) - 1$ and $y^2 = S_e/(4m^2_{\pi^+})$ dimensionless invariants [10]. Only relative form factors can be measured, normalized to the overall scale factor $f_s{=}F_s(q^2 = 0, S_e = 0)$. The S- and P-wave form factors and their variation with energy have been measured [5][6]. F_s is described by one curvature and two slopes: $F_s = f_s[1 + (f'_s/f_s)q^2 + (f''_s/f_s)q^4 + (f'_e/f_s)y^2]$; G_p by one slope and an offset: $G_p = f_s[(g_p/f_s) + (g'_p/f_s)q^2]$; F_p and H_p by constants. The first evidence for a negative 5% contribution from F_p and for a S_e dependence of F_s have been established.

The BR value, evaluated from 16 statistically independent subsamples separately for K^+ and K^-, is $\mathrm{BR}(K^{+-}_{e4}) = (4.257 \pm 0.004_{stat} \pm 0.016_{syst} \pm 0.031_{ext}) \times 10^{-5}$, inclusive of $K_{e4\gamma}$ decays. The 0.8% total error is dominated by the external uncertainty from the PDG value of the normalization mode $\mathrm{BR}(K^{+-}_{3\pi})$.

The BR measurement allows assigning absolute values to the relative form factors. The overall form factor normalization is $f_s = 5.705 \pm 0.017_{exp} \pm 0.031_{ext}$, ($\sigma_{exp} = \sigma_{stat} \oplus \sigma_{syst}$). The main error is the external one, due to uncertainties on the PDG values of kaon lifetime, CKM matrix element $|V_{us}|$ and $\mathrm{BR}(K^{00}_{3\pi})$ [9]. The 0.6% total relative precision improves previous results of a factor of 2 to 4.

K^{00}_{e4} decays. An unprecedented statistics of 65210 K^{00}_{e4} candidates has been collected by NA48/2, with (1.00±0.02)% background [7]. The formalism for studying K^{00}_{e4} decays is simpler because of two identical particles, $\pi^0\pi^0$, in the final state. As G and H form factors are antisymmetric in the exchange of the two pions, they do not contribute to the decay probability. At leading order only the S-wave component of the partial wave expansion is present and the differential rate depends on a single complex hadronic form factor $F = F_s e^{i\delta_s}$ with magnitude F_s, whose variation with (S_π, S_e) has been studied. A data sample free of radiative effects is selected. F_s is estimated by fitting the data in the (S_π, S_e) plane (Dalitz plot) where the event density is proportional to F_s^2. A grid is defined with equal population bins. A sample of Monte Carlo simulated events, including acceptance and resolution effects, trigger efficiency, radiative corrections and a constant F_s value is distributed over the same grid as the data. A formalism based on the q^2 and y^2 variables has been used for a direct comparison with K^{+-}_{e4} results.

Fig. 1(a) shows the ratio of the q^2 distributions for data and simulated events in equal population bins. Above q^2=0 the distribution is similar to the K^{+-}_{e4} one, while it is depleted at negative values. The line corresponds to the empirical description using the best fit-parameters: a degree-2 polynomial for positive q^2 values and a cusp-like function below zero. Only statistical errors are represented. A possible interpretation of the observed deficit of events for negative q^2 values can be related to final state charge exchange scattering processes ($\pi^+\pi^- \to \pi^0\pi^0$) in the K^{+-}_{e4} mode, as observed in the $K^{00}_{3\pi}$ mode analysis [11]. A more elaborate description of the K^{00}_{e4} amplitude is needed to extract more information on physical quantities from the result reported here. Fig. 1(b) shows the comparison of form factor results for K^{+-}_{e4} and K^{00}_{e4} data in the (q^2, y^2) formulation, displayed in the (f'_s/f_s, f''_s/f_s) plane. All contours are 68% C.L., errors are statistical only. The smaller area in the charged mode is due to the larger statistics. The correlations between fitted parameters are very similar and the results for K^{+-}_{e4} and K^{00}_{e4} decays are consistent within statistical errors.

Exploiting a model independent form factor description, $\mathrm{BR}(K^{00}_{e4})$, inclusive of radiative decays, has been measured with respect to the $K^{00}_{3\pi}$ normalization mode. The global result is $\mathrm{BR}(K^{00}_{e4}) = (2.552 \pm 0.010_{stat} \pm 0.010_{syst} \pm 0.032_{ext}) \times 10^{-5}$, given by the combination of the values obtained for ten statistically independent sub-samples. The 1.4% relative precision is dominated by the external uncertainty from the normalization mode $\mathrm{BR}(K^{00}_{3\pi})$ [9]. This result improves the current world average BR by more than one order of magnitude.

Both total rate and form factor descriptions are used to obtain the absolute form factor value. A long distance electromagnetic correction δ_{EM} to the total rate, not yet available in the literature, should be taken into account. The absolute form factor value is $(1+\delta_{EM}) \times f_s = 6.079 \pm 0.012_{stat} \pm 0.027_{syst} \pm 0.046_{ext}$. The main external uncertainty is due to the errors on the PDG values of kaon lifetime, CKM matrix element $|V_{us}|$ and $\mathrm{BR}(K^{00}_{3\pi})$ [9]. A difference from the K^{+-}_{e4} result has been observed, statistically significant as experimental errors are mostly uncorrelated. A more precise theoretical description of the K^{00}_{e4} mode, including radiative,

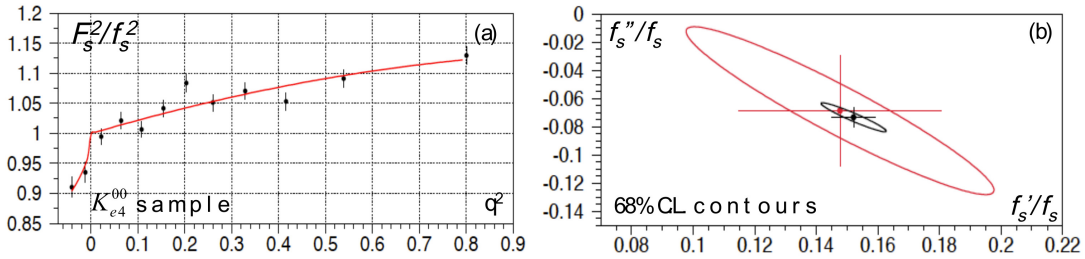

Figure 1: (a) Ratio of q^2 distributions for data and simulated K_{e4}^{00} events. The line corresponds to the empirical description using the best fit parameters. Errors are statistical only. (b) Form factor comparison in the (f_s'/f_s, f_s''/f_s) plane for K_{e4}^{+-} (black, smaller area) and K_{e4}^{00} (red) decays in the (q^2, y^2) series expansion formulation. Only statistical errors are plotted

isospin symmetry breaking and re-scattering effects, should be considered before drawing any solid conclusion.

Phase shift and scattering lenghts in the $\pi\pi$ system. The asymmetry of the dilepton with respect to the dipion system is strictly related to the phase difference between S- and P-waves in $\pi\pi$ scattering. Hadronic form factors in the S- and P-waves have been obtained from K_{e4}^{+-} data analysis, concurrently with the phase difference between the S- and P-wave states of the $\pi\pi$ system, leading to precise determinations of a_0^0 and a_0^2, the isospin I=0 and I=2 S-wave $\pi\pi$ scattering lengths, with accuracy competitive with the most elaborate theoretical predictions. Combining K_{e4}^{+-} results with the former NA48/2 measurements based on the study of $K_{3\pi}^{00}$ decays [12], an improved determination of a_0^0 and the first precise measurement of a_0^2 are obtained: $a_0^0 = 0.2210 \pm 0.0047_{stat} \pm 0.0040_{syst}$, $a_0^2 = -0.0429 \pm 0.0044_{stat} \pm 0.0028_{syst}$, $a_0^0 - a_0^2 = 0.2639 \pm 0.0020_{stat} \pm 0.0015_{syst}$ [5].

This result confirm the prediction of Lattice QCD and ChPT [13]. The latest world average experimental values are now dominated by the NA48/2 experimental precision.

References

[1] R. Batley *et al.*, Eur. Phys. J **C52** 875 (2007).
[2] V. Fanti *et al.*, Nucl. Instrum. Method **A574** 433 (2007).
[3] S. Weinberg, Physica A **96** 327 (1979).
[4] G. Colangelo *et al.*, Eur. Phys. J **C71** 1695 (2011).
[5] J. Batley *et al.*, Eur. Phys. J. **C70** 635 (2010).
[6] J. Batley *et al.*, Phys. Lett. **B715** 105 (2012).
[7] J. Batley *et al.*, J. High Energy Phys. **1408** 159 (2014).
[8] N. Cabibbo, A. Maksymowicz, Phys. Rev. **137** B433 (1965).
[9] J. Beringer *et al.*, Phys. Rev. **D86** 010001 (2012).
[10] G. Amoros, J. Bijnens, J. Phys. **G25** 1607 (1999).
[11] N. Cabibbo, Phys. Rev. Lett. **93** (2004) 121801.
[12] J. Batley *et al.*, Eur. Phys. J. **C64** 589 (2009).
[13] G. Colangelo, J. Gasser, H. Leutwyler, Phys. Lett. **B488** 261 (2000).

Recent flavor physics results at CMS

Paolo Ronchese[1]

[1]University and INFN Padova, via Marzolo 8, 35131 Padova, Italy

DOI: http://dx.doi.org/10.3204/DESY-PROC-2014-04/234

Thanks to the excellent tracking and muon identification performance, combined with a flexible trigger system, the CMS experiment at the Large Hadron Collider is conducting a rich and competitive program of measurements in the field of heavy flavor physics. In this talk we review our most recent results on heavy flavour physics, based on a data sample collected by the CMS detector.

1 Introduction

There are several motivations to study heavy flavour physics at LHC: advance beauty and charm spectroscopy, test QCD and effective theories, look for indirect evidence or constraints to new physics beyond the standard model, or simply try to have the best as possible description of the environment where direct new physics searches are conducted. In the following most recent results obtained by CMS will be shown.

All results are obtained with data collected at a center of mass energy $\sqrt{s} = 7$ TeV collected in 2011, with an integrated luminosity $\mathcal{L} \sim 5$ fb^{-1}, or $\sqrt{s} = 8$ TeV collected in 2012, with an integrated luminosity $\mathcal{L} \sim 20$ fb^{-1}. All measurements involve dimuons, most of the times originating from a resonance such as J/ψ or Υ. The presence of two muons in the final state allows maintaining a sustainable trigger rate at the high luminosities provided by LHC; the offline reconstruction of a vertex with the two muon candidates was also common for the involved analyses.

2 Mesons

The very rare exclusive decay $\mathcal{B}(B^0_{d,s} \to \mu^+\mu^-)$ was looked for since a very long time; the decay rate is highly suppressed and could be modified by new physics processes [1]. CMS measured its branching ratio by comparison with the decay $B^+ \to J/\psi K^+$, used for normalization:

$$\mathcal{B}(B^0_{d,s} \to \mu^+\mu^-) = \frac{N_{\rm sig}}{N_{\rm nrm}} \frac{\epsilon_{\rm nrm}}{\epsilon_{\rm sig}} \frac{f_u}{f_{d,s}} \mathcal{B}(B^\pm \to J/\psi K^\pm \to \mu^+\mu^- K^\pm) \qquad (1)$$

The B^0_s to B^+ production cross section ratio f_s/f_u has been assumed to be equal to LHCb measurement [2] $f_s/f_d = 0.256 \pm 0.020$, the corresponding ratio for B^0_d has been assumed to be 1. Signal and background have been discriminated by categorizing events by mean of a BDT variable

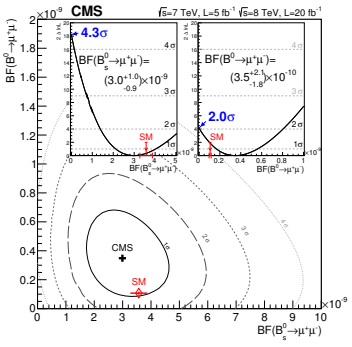

Figure 1: Comparison of CMS measurements with SM predictions in the $\mathcal{B}(B_s^0 \to \mu^+\mu^-), \mathcal{B}(B_d^0 \to \mu^+\mu^-)$ plane.

and fitting invariant mass distributions in each category to determine the signal yield and obtain the results [3]:

$$\mathcal{B}(B_s^0 \to \mu^+\mu^-) = (3.0^{+1.0}_{-0.9}) \times 10^{-9}, \qquad \mathcal{S} = 4.3\sigma,$$
$$\mathcal{B}(B_d^0 \to \mu^+\mu^-) = (3.5^{+2.1}_{-1.8}) \times 10^{-10}, \qquad \mathcal{S} = 2.0\sigma,$$
$$\mathcal{B}(B_d^0 \to \mu^+\mu^-) < 1.1 \times 10^{-9} \ (95\% \text{ C.L.})$$

A comparison with the SM predictions [4] is shown in Fig. 1.

A preliminary combination of these results with the corresponding from LHCb has been performed [5]; LHCb had updated its measurement of f_s/f_d in the meanwhile [6] so the result has been rescaled before the combination:

$$\mathcal{B}(B_s^0 \to \mu^+\mu^-) = (2.9 \pm 0.7) \times 10^{-9}, \ (f_s/f_u = 0.259 \pm 0.015),$$
$$\mathcal{B}(B_s^0 \to \mu^+\mu^-) = (3.6^{+1.6}_{-1.4}) \times 10^{-10}.$$

In the decay $B_s^0 \to J/\psi\phi$ the final state is unflavoured, so that it can be reached directly or after an oscillation $B_s^0 \to \bar{B}_s^0 \to J/\psi\phi$ leading to an interference between the two channels, and has no definite CP, so that an angular analysis is required to disentangle the odd and even components [7]. The differential decay rate

$$\frac{d^4\Gamma(B_s(t))}{d\Theta dt} = f(\Theta, t; \alpha) \propto \sum_{i=1}^{10} O_i(\alpha, ct) \cdot g_i(\Theta) \tag{2}$$

can be expressed as a function of decay time t and angles $\Theta = \vartheta, \varphi, \psi$, as shown in Fig. 2, with a set of parameters α, including the amplitude and phases of S-wave and P-wave processes, the B_s^0 lifetime τ_{B_s}, the width difference between the two CP states $\Delta\Gamma_s$ and the interference phase ϕ_s. When in the event we find a second b-hadron decaying semileptonically it can be used to determine the flavour, although with some dilution due to its own oscillation or cascade decays. The tagging information has been introduced in the differential decay rate and the events PDF has been fitted [8] by constraining the mass difference to the world average and assuming there's no direct CP violation:

$$\phi_s = (-0.03 \pm 0.11 \pm 0.03) \text{ rad},$$
$$\Delta\Gamma_s = (0.096 \pm 0.014 \pm 0.007) \text{ ps}^{-1}$$

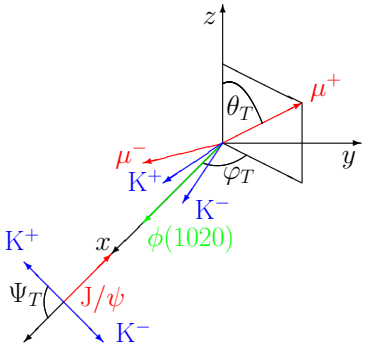

Figure 2: Angle definitions in $B_s^0 \to J/\psi\phi$ decays.

Another important heavy-flavoured hadron to study is the $B_c^\pm$, which carries two heavy flavours, beauty and charm, that can be produced only in higher order processes and decay in a competition between the c and b quarks. A measurement of its cross section production and decay branching ratio can help in understanding the involved processes and is of

course propaedeutic for more refined investigations. CMS has studied $B_c^{\pm}$ mesons in the decay channels to J/ψ and one or three pion(s); a fit to the invariant mass peaks for the two channels allows a determination of the ratios of cross section times branching fraction [9]:

$$\frac{\sigma(B_c^{\pm}) \times \mathcal{B}(B_c^{\pm} \to J/\psi\pi^{\pm})}{\sigma(B^{\pm}) \times \mathcal{B}(B^{\pm} \to J/\psi K^{\pm})} = \left(0.48 \pm 0.05 \pm 0.04^{+0.05}_{-0.03}(\tau_{B_c})\right) \times 10^{-2},$$

$$\frac{\mathcal{B}(B_c^{\pm} \to J/\psi\pi^{\pm}\pi^{+}\pi^{-})}{\mathcal{B}(B_c^{\pm} \to J/\psi\pi^{\pm})} = 2.43 \pm 0.76^{+0.05}_{-0.03}.$$

The invariant mass of the $J/\psi\pi^{\pm}$ is shown in Fig. 3; the $B_c^{\pm}$ reconstruction efficiency has been determined assuming a lifetime $\tau_{B_c} = (0.452 \pm 0.032)$ ps and the effect of the corresponding uncertainty has been quoted explicitly in the systematic error.

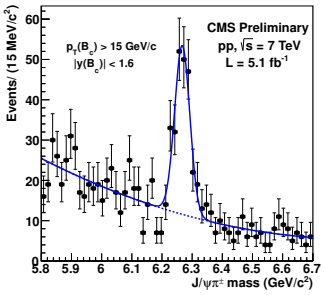

Figure 3: $J/\psi\pi^{\pm}$ invariant mass distribution.

3 Quarkonia

At CMS quarkonia are reconstructed by combining opposite charge muons and fitting a common vertex; this allowed the measurement of several properties of $\psi(n\mathrm{S})$ and $\Upsilon(n\mathrm{S})$, as production cross section and polarization. Recently the differential cross section for the production of prompt J/ψ and ψ' have been measured with 2011 data [10]; due to the integrated luminosity 100 times bigger than the one corresponding to 2010 data used for previous measurement the p_T acceptance was increased reaching 95 GeV in 4 rapidity bins. The event yield in the various p_T and rapidty bins was determined by mean of a simultaneous fit to invariant mass and flight distance to discriminate prompt and non prompt components while the acceptance was computed for several scenarios, corresponding to full longitudinal, transverse or null polarization. In Fig. 4 the differential cross section vs. p_T is shown, in the unpolarized production scenario.

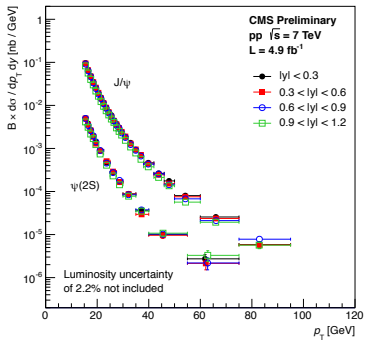

Figure 4: Differential cross section for prompt J/ψ and $\psi(2\mathrm{S})$ production.

The measurement of the simultaneous production of two J/ψ mesons in the proton-proton collisions provides general insight into how particles are produced in the collision; J/ψ pairs produced in single-parton scattering are strongly correlated, while large values of rapidity difference $|\Delta y|$ are possible for production due to double-parton scattering [11]. The differential cross section for the production of charmonium pairs has been measured [12] in bins of rapidity difference $|\Delta y|$; acceptance has been determined by assuming unpolarized J/ψ production. The results are shown in Fig. 5; the cross section increase at $|\Delta y| > 2.6$ can be a hint of double parton scattering.

In addition to S-wave quarkonia at LHC also P-wave states are produced; they contribute with their decay to J/ψ and Υ production while the relative production of themselves is sensitive to singlet or octet states in the production mechanism.

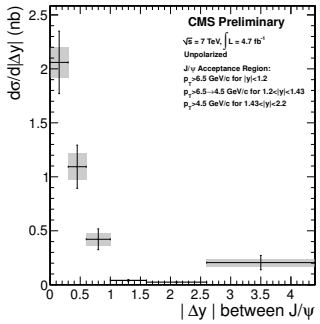

Figure 5: Double J/ψ production cross section vs. rapidity difference.

At CMS $\chi_b(1P)$ states can be reconstructed in the decay channel to $\Upsilon(1S)\gamma$, with the photon converting into an e^+e^- pair in the interaction with the detector material [13]; the conversion probability multiplied by the efficiency of reconstructing two low-p_T tracks is very small, but the mass resolution is high enough to distinguish the two states χ_{b1} and χ_{b2} having a very small mass difference $\Delta M = 19$ MeV. The ratio

$$R_b = \frac{\sigma(pp \to \chi_{b2}X)\mathcal{B}(\chi_{b2} \to \Upsilon(1S)\gamma)}{\sigma(pp \to \chi_{b1}X)\mathcal{B}(\chi_{b1} \to \Upsilon(1S)\gamma)} \qquad (3)$$

has been measured in Υ transverse momentum bins and plotted in Fig. 6. No significant dependence on p_T was observed.

4 Conclusions

CMS has produced several results in heavy-flavour physics: B_s^0 decay to $\mu^+\mu^-$ has been observed, angular analysis in B_s^0 decays has been performed to measure width difference and mixing interference phase, single and double charmonium, as well as P-wave bottomonium cross sections have been measured to investigate production mechanisms.

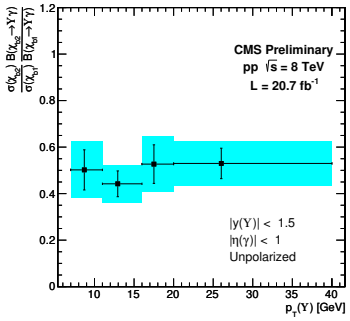

Figure 6: Cross section ratio $[\sigma(pp \to \chi_{b2}X)\mathcal{B}(\chi_{b2} \to \Upsilon(1S)\gamma)]/[\sigma(pp \to \chi_{b1}X)\mathcal{B}(\chi_{b1} \to \Upsilon(1S)\gamma)]$ vs. p_T^Υ, under the hypothesis of unpolarized production.

References

[1] K. De Bruyn *et al.*, Phys. Rev. Lett. **109** 041801 (2012).

[2] LHCb Collaboration, JHEP **04** 001 (2013).

[3] CMS Collaboration, Phys. Rev. Lett. **111** 101804 (2013).

[4] A. J. Buras *et al.*, Eur. Phys. J. **C72** 2172 (2012).

[5] CMS and LHCb Collaborations, CMS PAS BPH-13-007 (2014).

[6] LHCb Collaboration, LHCb-CONF-2013-011 (2013).

[7] I. Dunietz *et al.*, Phys. Rev. **D63** 114015 (2001).

[8] CMS Collaboration, CMS PAS BPH-13-012 (2014)

[9] CMS Collaboration, CMS PAS BPH-12-011 (2013).

[10] CMS Collaboration, CMS PAS BPH-14-011 (2014)

[11] C. Kom *et al.*, Phys. Rev. Lett. **107** 082002 (2011).

[12] CMS Collaboration, CMS PAS BPH-11-021 (2013).

[13] CMS Collaboration, CMS PAS BPH-13-005 (2013).

Search for exotics at $BABAR$

Elisabetta Prencipe[1] on behalf of the $BABAR$ Collaboration

[1]Forschungszentrum Jülich, Leo Brandt Strasse, 52428 Jülich, Germany
(previously addressed at JGU, University of Mainz, Germany)

DOI: http://dx.doi.org/10.3204/DESY-PROC-2014-04/201

One of the most intriguing puzzles in hadron spectroscopy are the numerous charmonium-like states observed in the last decade, including charged states that are manifestly exotic. The $BABAR$ experiment has extensively studied those in B meson decays, initial state radiation processes and two photon reactions. The study of the process $B \to J/\psi\phi K$, with a search for the resonant states X(4140) and X(4270) in their decays to $J/\psi\phi$, will be highlighted. The recent results of the Dalitz analysis of η_c to 3 pseudoscalar mesons, via 2-photon interactions, will be presented in this report [Contribution talk: ID 201].

1 Introduction

Several new Charmonium-like states have been observed at $BABAR$, revealing a spectrum too rich to be uniquely described by potential models[1]. Different hypotheses have been proposed from theorists to explain their nature, such as hybrid charmonium states, diquark-antidiquark states or $D^0\bar{D}^{0(*)}$ molecules[2]. The QCD spectrum is much richer than that of the naive quark model, as the gluons, which mediate the strong force between quarks, can also act as principal components of entirely new types of hadrons. These gluonic hadrons fall into two general categories: glueballs (excited states of pure glue) and hybrids (composed by a quark, an antiquark, and excited glue). The additional degrees of freedom carried by gluons allow glueballs and hybrids to have spin-exotic quantum numbers J^{PC} that are forbidden for normal mesons and other fermion-antifermion systems. Exotic quantum numbers (e.g. 0^{--}, 0^{+-}, 1^{-+}, 2^{+-}) are the easiest way to distinguish gluonic hadrons from $q\bar{q}$ states. Predictions for hybrids come mainly from calculations based on the bag model, flux tube model, and constituent gluon model and recently, with increasing precision, from Lattice QCD. New forms of matter, such as glueballs or molecular states, are predicted by QCD to populate the low mass region of the hadron mass spectrum[3]. This motivates the study of the J/ψ radiative and hadronic decays.

Two analyses will be shortly summarized in this report: the Dalitz analysis of $\eta_c \to K^+K^-\eta/\pi^0$ via 2-photon interactions and the study of the invariant mass systems of $J/\psi\phi$, $J/\psi K$ and KKK in B decays. The first is relevant to several issues in light meson spectroscopy, and it is recently published by $BABAR$[4]. No Dalitz plot analysis has been performed on η_C three-body decays until now. The second presents a new determination of the branching fraction (BF) of $B^{\pm,0} \to J/\psi K^+K^-K^{\pm,0}$ and $B^{\pm,0} \to J/\psi\phi K^{\pm,0}$, using eight times more data than that reported by the PDG[5], and search for exotic states.

2 Decay of $\eta_c \to K^+K^-\eta/\pi^0$ to via 2-photon interactions

Recently, a search for exotic resonances was performed by $BABAR$ through Dalitz plot analyses of χ_{c1} states[6]. Scalar mesons are still a puzzle in light-meson spectroscopy, as there are too many states and they are not consistent with the quark model. In particular, the $f_0(1500)$ resonance, discovered in $\bar{p}p$ annihilations, has been interpreted as a scalar glueball[7]. However, no evidence for the $f_0(1500)$ state has been found in charmonium decays. Another glueball candidate is the $f_0(1710)$ discovered in radiative J/ψ decays. Recently, $f_0(1500)$ and $f_0(1710)$ signals have been incorporated in a Dalitz plot analysis of $B \to 3K$ decays[8]. Charmless $B \to XK$ could enanche gluonium production[9]. Another puzzling state is the $K_0^*(1430)$, never observed as clear peak in $K\pi$ invariant mass. Its parameters were measured from the LASS experiment in $K^-p \to K^-\pi^+n$[10].

We describe a study of the decays $\eta_c \to K^+K^-\eta$ and $\eta_c \to K^+K^-\pi^0$, with $\eta \to \pi^+\pi^-\pi^0$, $\eta \to \gamma\gamma$ and $\pi^0 \to \gamma\gamma$, produced in two-photon interactions. The data sample used is 519 fb^{-1} at $BABAR$. Two-photon events in which at least one of the interacting photons is not quasireal are strongly suppressed by a dedicated selection. A clear peak of η_c is seen, and well reconstructed in the invariant mass systems of $K^+K^-\eta$ and $K^+K^-\pi^0$. The Dalitz analysis is then performed for $\eta_c \to K^+K^-\eta$ and $\eta_c \to K^+K^-\pi^0$: the projection of the invariant mass distributions and their unbinned maximum likelihood fit are shown in Fig. 1, and 2. A clear peak at the mass of $K_0^*(1430)$ is observed in both cases, together with other expected structures. Amplitude parameterization is performed in a standard way for a pseudoscalar meson decaying to 3 pseudscalar mesons. Full interference is allowed among the amplitudes of all resonances in the Dalitz. No evidence for interferences between signal and background is found, so a sum of inchoerent resonances is used for fitting the sidebands. The non-resonant contribution is included in the fit. From our fit, we learn that the model provides an adeguate description of data for $\eta_c \to K^+K^-\eta$, while the isobar model does not describe properly the data for $\eta_c \to K^+K^-\pi^0$. Scanning the likelihood as function of the $K_0^*(1430)$ mass and width, we obtain: m$(K_0^*(1430)) = 1438 \pm 8 \pm 4$ MeV/c^2 and $\Gamma(K_0^*(1430)) = 210 \pm 20 \pm 12$ MeV.

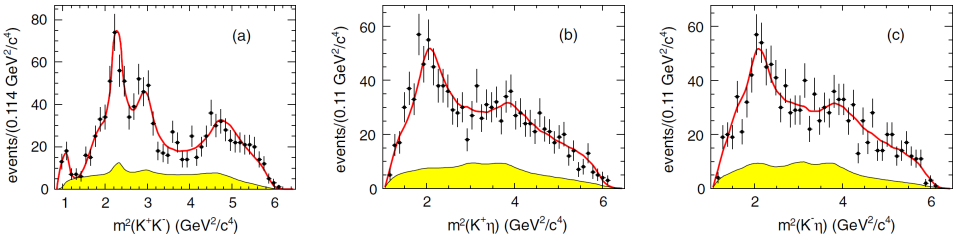

Figure 1: Projections from the Dalitz plot of $\eta_c \to K^+K^-\eta$. The shaded (yellow) histograms show the estimated background. The state $K_0^*(1430)$ is seen as clear peak in (b) and (c).

In this work also the pseudoscalar meson mixing angle is evaluated: $\theta_P = (3.1^{+3.1}_{-5.0})^\circ$, and it differs 2.9σ deviation from expectations. This issue involves in theoretical discussions where the siglet and octet mixing angle should be considered separately.

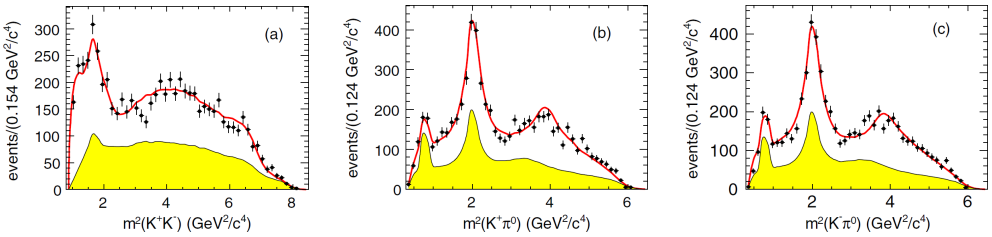

Figure 2: Projections from the Dalitz plot of $\eta_c \to K^+K^-\pi^0$. The shaded (yellow) histograms show the estimated background. The state $K_0^*(1430)$ is seen as clear peak in (b) and (c).

3 Analysis of the decay $B \to J/\psi KKK$

Several resonant structures, whose masses are above the $D\bar{D}^*$ threshold, are not predicted by potential models. For example, the X(3872) have been seen in $B \to XK, X \to J/\psi\ \pi^+\pi^-$, or Y(4260) was observed by investigating the process $e^+e^- \to \gamma_{ISR}X$, $X \to J/\psi\pi^+\pi^-$[11, 12, 13]; but no indication of new states has been observed in the $J/\psi\ K^+K^-$ invariant mass system, until the paper quoted in Ref. [14] highlighted the possibility of a couple of resonant states, decaying to $J/\psi\phi$, with $\phi \to K^+K^-$ and $J/\psi \to \mu^+\mu^-$. These observations are controversial. *Strangeness* in charmonium seems a sector still to be exploited. The rare decay $B \to J/\psi KKK$, in particular $B \to J/\psi\phi K$, is interesting because it is a promising place to search for new resonances, as it proceeds, at quark level, via the weak transition $b \to c\bar{c}s$. It could be a quasi 2-body decay, $B \to X_gK$, with $X_g \to J/\psi\phi$, where $X_g = |gc\bar{c}s\bar{s}>$, with gluonic contribution (g).

An unbinned maximum likelihood fit is performed to extract the yield and calculate the BFs. Detailed explanation on these calculations are presented in Ref. [15], together with the relevant discussion for the non-resonant K^+K^- contribution to the BF of $B \to J/\psi KKK$ and systematic uncertainty calculation. Here we report only the relevant information for the analysis of the three invariant mass distributions: $J/\psi\phi$, $J/\psi K$, KKK, for both B^+ and B^0 samples. In this analysis we calculate also: $R_\phi = \mathcal{B}(B^0 \to J/\psi\phi K_S^0)/\mathcal{B}(B^+ \to J/\psi\phi K^+) = 0.48 \pm 0.09 \pm 0.02$, and $R_{2K} = \mathcal{B}(B^0 \to J/\psi K^+K^-K_S^0)/\mathcal{B}(B^+ \to J/\psi K^+K^-K^+) = 0.52 \pm 0.09 \pm 0.03$; we find values in agreement with the expectation of the spectator quark model (e.g., ratio R$\sim$0.5). These are first measurements. For the first time the non-resonant K^+K^- contribution to the BF of $B \to J/\psi KKK$ is observed. No evidence of signal is found for $B^0 \to J/\psi\phi$, in agreement with theoretical predictions: we evaluate UL$<1.01 \cdot 10^{-6}$ at 90% confidence level (CL). We search for the resonant states reported by the CDF Collaboration in the $J/\psi\phi$ mass spectrum. The masses and the widths in our fit are fixed to values according to Ref. [14]. We observed significant efficiency decrease at low $J/\psi\phi$ mass, due to the inability to reconstruct slow kaons in the laboratory frame, as a result of energy loss in the beampipe and SVT material. We model the resonances with an inchoerent sum of two S-wave relativistic Breit-Wigner (BW) functions with parameters fixed to the CDF values [14]. A non-resonant contribution is described according to PHSP. The decay of a pseudoscalar meson to two vector states contains high spin contributions which could generate non-uniform angular distributions. However, due to the limited data sample (212 yield for B^+ and 50 for B^0, in the signal area, respectively) we do not include such angular terms, and assume that the resonances decay isotropically. The fit function is weighted by the inverse of the two-dimentional efficiency computed on the Dalitz plots (see the

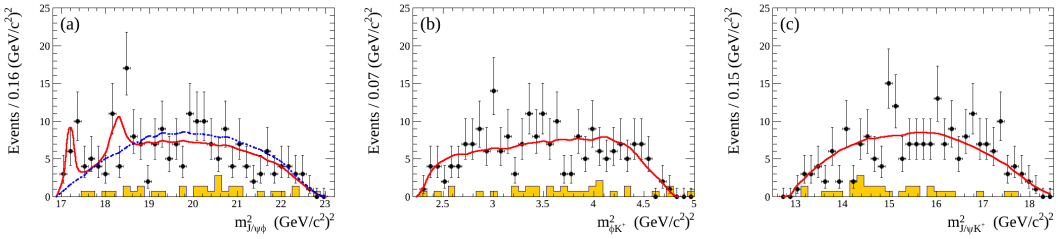

Figure 3: Dalitz plot projections for $B^+ \to J/\psi\phi K^+$ on (a) $m^2_{J/\psi\phi}$, (b) $m^2_{\phi K^+}$, and (c) $m^2_{J/\psi K^+}$. The continuous (red) curves are the results from fit model performed including the $X(4140)$ and $X(4270)$ resonances. The dashed (blue) curve in (a) indicates the projection for fit model with no resonances included in the fit. The shaded (yellow) histograms indicate the evaluated background. Within systematic effects, a significance $<2\sigma$ was found for both peaks in (a).

continuous red curve in Fig. 3. Using the Feldman-Cousins method[16], we obtain the ULs at 90% CL: $BF(B^+ \to X(4140)K^+) \times BF(X(4140) \to J/\psi\phi)/BF(B^+ \to J/\psi\phi K^+) < 0.135$, and $BF(B^+ \to X(4270)K^+) \times BF(X(4270) \to J/\psi\phi)/BF(B^+ \to J/\psi\phi K^+) < 0.184$. The $X(4140)$ limit may be compared with the CDF measurement of $0.149 \pm 0.039 \pm 0.024$ [14] and the LHCb limit of 0.07 [17]. The $X(4270)$ limit may be compared with the LHCb limit of 0.08. We find that the hypothesis that the events are distributed uniformly on the Dalitz plot gives a poorer description of the data.

References

[1] N. Brambilla *et all*, *CERN Yellow Report*, hep-ph/0412158 (2005); Eur. Phys. J. C **71**, 1534 (2011); arXiv:1404.3723 [hep-ph] (2014).

[2] Barnes and Godfrey, PRD **69**, 054008 (2004); Eichten, Lane and Quigg, PRD **69**, 094019 (2004); Swanson, PLB **588**, 189 (2004); Tornqvist, PLB **590**, 209 (2004); Suzuki, PRD **72**, 114013 (2005); Maiani, *et all*, PRD **71**, 014028 (2005).

[3] V. Mathieu, N. Kochelev and V. Vento, Int. J. Mod. E**18**, 1 (2009).

[4] J.P. Lees *et all* (*BABAR* Coll.), Phys. Rev. D **79**, 112004 (2014).

[5] B. Aubert *et all* (*BABAR* Coll.), Phys. Rev. Lett. **91**, 071801 (2003).

[6] G. S. Adams *et all* (CLEO Coll.) Phys. Rev. D **84**, 112009 (2011).

[7] C. Amsler and F. Close, Phys. Rev. D **53**, 295 (1996).

[8] J.P. Lees *et all* (BABAR Coll.) Phys. Rev. D **85**, 112010 (2012).

[9] X.-G. He and T.C. Yuan, hep-ph/0612108.

[10] D. Aston *et all* (LASS Coll.), Nucl Phys. **B296**, 493 (1988).

[11] B. Aubert *et all* (*BABAR* Coll.), Phys. Rev. D. **71**, 071103 (2005); Phys. Rev. D **77**, 111101 (2008); Phys. Rev. D. **73**, 011101 (2006).

[12] S.K. Choi *et all* (*Belle* Coll.), Phys. Rev. Lett. **91**, 262001 (2003);

[13] B. Aubert *et all* (*BABAR* Coll.), Phys. Rev. Lett. **95**, 142001 (2005);

[14] T. Aaltonen *et all* (CDF Coll.), Phys. Rev. Lett. **102**, 242002 (2009); hep-ex/1101.6058 (2011).

[15] J.P. Lees *et all* (BABAR Coll.), hep-ex/1407.7244 (2014).

[16] G. J. Feldman and R. D. Cousins, Phys. Rev. D. **57**, 3873 (1998).

[17] R. Aaij *et all* (LHCb Coll.), Phys. Rev. D **85**, 091103(R) (2012).

Chapter 12

String theory

Why does black hole describe the deconfinement phase?

Masanori Hanada

Stanford Institute for Theoretical Physics, Stanford University, Stanford CA 94305, USA
Yukawa Institute for Theoretical Physics, Kyoto University, Kitashirakawa Oiwakecho, Sakyo-ku, Kyoto 606-8502, Japan
The Hakubi Center for Advanced Research, Kyoto University, Yoshida-Ushinomiya-cho, Sakyo-ku, Kyoto 606-8501, Japan

DOI: http://dx.doi.org/10.3204/DESY-PROC-2014-04/160

In the gauge/gravity duality, the deconfinement transition in the gauge theory is identified with the formation of black hole in the dual gravity theory. By assuming this correspondence, many predictions on QGP have been made. In this talk, we justify this approach quantitatively, and also provide an intuitive understanding. Firstly we give quantitative evidence for this identification from the thermodynamic study of the supersymmetric theory. We show that string theory and gauge theory give the same answer, even at finite temperature, including the $1/N$ correction. Then we consider generic gauge theories and show that the deconfinement transition is the condensation of very long and self-intersecting QCD strings, which is analogous to the formation of a black hole in string theory.

1 Introduction

In the gauge/gravity duality conjecture [1], the deconfinement phase of the gauge theory is dual to a black hole geometry in the gravity side [2]. In the first part of this talk, we give quantitative evidence for this identification, by solving a concrete example in both gauge and gravity sides, at the level of the string theory (i.e. finite α' and finite g_s). In the second part, we give an intuitive way of understanding this correspondence, without referring to a sophisticated dictionary of the duality. Our argument does not assume the dual gravity description, and hence it is applicable to generic gauge theories including QCD.

2 Quantitative test of the gauge/gravity duality

Let us consider the $U(N)$ maximally supersymmetric Yang-Mills theory in flat $(p+1)$-dimensional spacetime ($p = 0, 1, 2$ and 3), whose action is given by

$$S = \frac{1}{g_{YM}^2} \int d^{p+1}x \; Tr \left\{ \frac{1}{4} F_{\mu\nu}^2 + \frac{1}{2} \left(D_\mu X_i \right)^2 - \frac{1}{4} [X_i, X_j]^2 \right\} + (fermions), \tag{1}$$

where μ, ν run from 1 to $p+1$ and X_i ($i = 1, 2, \cdots, 9-p$) are scalar fields. In [3], it has been conjectured that this theory is in the deconfining phase at any nonzero temperature, in the

sense that the Polyakov loop has nonzero expectation value, and that it describes full string dynamics around the black p-brane. Near the horizon, the metric of the black p-brane geometry is given by

$$\begin{aligned} ds^2 &= \alpha' \left\{ \frac{U^{(7-p)/2}}{g_{YM}\sqrt{d_p N}} \left[-\left(1 - \frac{U_0^{7-p}}{U^{7-p}}\right) dt^2 + dy_\parallel^2 \right] \right. \\ &\quad \left. + \frac{g_{YM}\sqrt{d_p N}}{U^{(7-p)/2}\left(1 - \frac{U_0^{7-p}}{U^{7-p}}\right)} dU^2 + g_{YM}\sqrt{d_p N} U^{(p-3)/2} d\Omega_{8-p}^2 \right\}, \end{aligned} \tag{2}$$

where the Yang-Mills coupling g_{YM} and the size of the gauge group N in the corresponding super Yang-Mills theory are used. A constant α' is the square of the string length, $(t, y_\parallel)$ represent the $(p+1)$-dimensional extension of the brane, U and Ω are the radial and angular coordinate of the transverse directions, and U_0 is the place of the horizon. The Hawking temperature is

$$T_H = \frac{(7-p) U_0^{(5-p)/2}}{4\pi \sqrt{d_p g_{YM}^2 N}}, \tag{3}$$

where $d_p = 2^{7-2p}\pi^{(9-3p)/2}\Gamma((7-p)/2)$. The string coupling constant is given by

$$g_s = (2\pi)^{2-p} g_{YM}^2 \left(\frac{d_p g_{YM}^2 N}{U^{7-p}} \right)^{\frac{3-p}{4}}. \tag{4}$$

When $\lambda = g_{YM}^2 N$ is fixed, it behaves as $g_s \propto 1/N$, in the same way as in 't Hooft's identification. The Hawking temperature and the mass of the black brane are identified with the temperature and the energy $E \equiv -\partial \log Z / \partial\beta$ of the gauge theory, where Z is the partition function.

In this work we study the case of $p = 0$. The gauge theory is quantum mechanics of $N \times N$ matrices, which was originally proposed as the matrix model of M-theory [4]. It can be studied extensively by using the Monte Carlo method. In the gravity side, the black hole mass can be calculated by adding stringy corrections to the black 0-brane geometry shown above. The result is [5]

$$\frac{1}{N^2} E_{gravity} = (7.41\, T^{2.8} + a\, T^{4.6} + \cdots) + (-5.77\, T^{0.4} + b\, T^{2.2} + \cdots)\tfrac{1}{N^2} + O\left(\tfrac{1}{N^4}\right), \tag{5}$$

where $T = \lambda^{-1/3} T_H$ is dimensionless effective temperature and a, b are unknown constants. The energy $E_{gravity}$ is also made dimensionless, by multiplying $\lambda^{-1/3}$. In the following, we simply set $\lambda = 1$ without loss of generality. Higher order terms in each power of $1/N$ represent to the α' corrections, which appear because strings are not point-like. If the gauge/gravity duality conjecture is correct, this expression must be reproduced from the matrix quantum mechanics.

The $O(N^0)$ terms of the dual gravity prediction (5) have been tested previously. In particular, the α' correction $a\, T^{4.6}$ has been confirmed with $a = -5.58(1)$, by looking at $T \gtrsim 0.5$ [7].

In order to study the $1/N$ correction, we must study rather small values of N. Here we study $N = 3, 4$ and 5. (That we have to take N small caused a technical problem which required a proper treatment; see [8].) We also have to study low temperature where the α' correction becomes small, because there are too many fitting parameters otherwise. At $0.08 \le T \le 0.11$, we estimated the coefficient of $1/N^2$ by using a fitting ansatz $E_{gauge} = 7.41 T^{2.8} + c_1(T)/N^2 + c_2(T)/N^4$ for each fixed value of T. We confirmed that $c_1(T)$ is consistent with $-5.77 T^{0.4}$. This is very strong evidence that the gauge/gravity duality holds at quantum gravity level.

3 Why the deconfinement phase describes the black hole

In this section, motivated by the numerical confirmation in Sec. 2, we give an intuitive explanation for the duality based on [6]. As a concrete example, let us consider pure $U(N)$ Yang-Mills theory. The Hilbert space is spanned by Wilson loops acting on the vacuum $|0\rangle$, as $W_C W_{C'} \cdots |0\rangle$. Here W_C represent the Wilson loop along a closed contour C. In the standard identification of the Feynman diagrams and the string world-sheet [9], the Wilson loop is naturally interpreted as the creation operator of the string.

In the large-N limit and at sufficiently strong coupling, the energy of the string is approximately proportional to its length. In the confinement phase, the energy is of order N^0 per unit volume, and hence a typical state is a finite-density gas of loops with finite length. In this gas, two loops can intersect with each other and combined to form a longer string. Alternatively, when a loop intersects with itself, it can be split into two shorter loops. However such joining and splitting are suppressed at large-N.

In the deconfinement phase, the energy density is of order N^2. In this phase the loops necessarily intersect $O(N^2)$ times. Although the interaction at each intersection is $1/N$-suppressed, small interactions at many intersections accumulate to a non-negligible amount. A standard entropic argument shows that typical state consists of finitely many very long and self-intersecting strings, whose lengths are of $O(N^2)$. In the string theory, it is natural to interpret such very long and self-intersecting strings as a black hole [10, 11]. In this sense, *the deconfinement transition can be understood as the formation of a 'black hole' through condensation of QCD strings.*

When we identify the long string with a black hole, fluctuations of the string near the horizon are regarded as open strings attached to black hole (Fig. 1). In terms of the gauge theory, these open strings are open Wilson lines which have N color degrees of freedom at their endpoints. Therefore, we can interpret that the black hole is made from N D-branes.

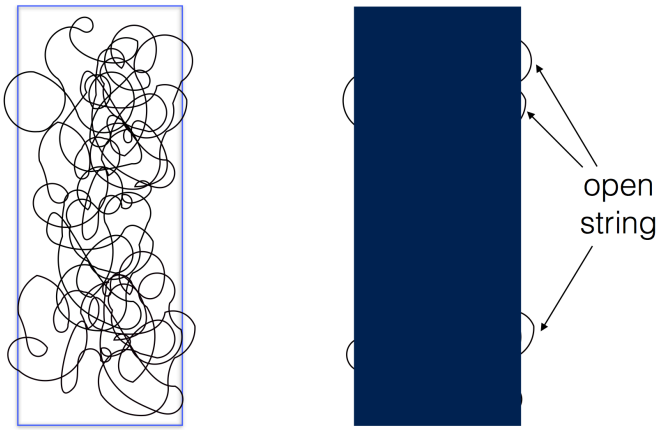

Figure 1: Closed string picture (left) and open string picture (right) [6].

In the Euclidean theory, the deconfinement is characterized by the condensation of the Polyakov loop, which can naturally be related to the black hole geometry in the gravity dual [2]. This can be explained from our picture as follows. First notice that the condensation of the

Polyakov loop is equivalent to the disappearance of the linear confinement potential between a pair of probe quark and anti-quark. In terms of strings, the linear potential in the confining phase appears because an open string connecting probes must be stretched as they are separated. In the deconfining phase, however, as soon as a short open string is introduced, it intersects with closed strings many times, and they immediately interact at one of the intersections to form a long open string (Fig. 2). Therefore, probes can be separated without stretching the open string, or equivalently, without costing energy. Note that the interaction is crucial for this argument; the deconfining phase cannot be described by free strings à la Hagedorn.

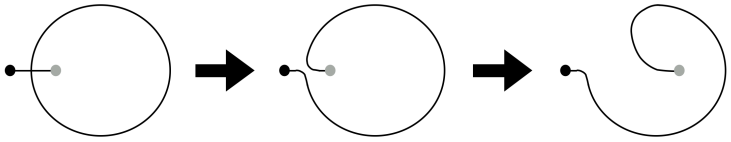

Figure 2: Deconfinement of a pair of probe quark and anti-quark [6].

In order to test this picture, we have estimated the deconfinment temperature of the lattice gauge theory with spatial lattice and continuum time [12]. We performed numerical simulation and confirmed the prediction.

Acknowledgments

I would like to thank Y. Hyakutake, G. Ishiki, J. Maltz, J. Nishimura and L. Susskind for collaborations. I was supported in part by the Grant-in-Aid of the Japanese Ministry of Education, Sciences and Technology, Sports and Culture (MEXT) for Scientific Research (No. 25287046), and the National Science Foundation under Grant No. PHYS-1066293 and the hospitality of the Aspen Center for Physics.

References

[1] J. M. Maldacena, Adv. Theor. Math. Phys. **2**, 231 (1998).
[2] E. Witten, Adv. Theor. Math. Phys. **2**, 505 (1998).
[3] N. Itzhaki, J. M. Maldacena, J. Sonnenschein and S. Yankielowicz, Phys. Rev. D **58**, 046004 (1998).
[4] T. Banks, W. Fischler, S. H. Shenker and L. Susskind, Phys. Rev. D **55**, 5112 (1997).
B. de Wit, J. Hoppe and H. Nicolai, Nucl. Phys. B **305**, 545 (1988).
[5] Y. Hyakutake, PTEP **2014**, no. 3, 033B04.
[6] M. Hanada, J. Maltz and L. Susskind, arXiv:1405.1732 [hep-th].
[7] M. Hanada, Y. Hyakutake, J. Nishimura and S. Takeuchi, Phys. Rev. Lett. **102**, 191602 (2009).
[8] M. Hanada, Y. Hyakutake, G. Ishiki and J. Nishimura, Science **344**, 882 (2014).
[9] G. 't Hooft, Nucl. Phys. B **72**, 461 (1974).
[10] L. Susskind, In *Teitelboim, C. (ed.): The black hole* 118-131.
[11] G. T. Horowitz and J. Polchinski, Phys. Rev. D **55**, 6189 (1997).
[12] J. B. Kogut and L. Susskind, Phys. Rev. D **11**, 395 (1975).

Chapter 13

New concepts and techniques for accelerators and particle detectors

Future Opportunities with Germanium Detectors at the China Jinping Underground Laboratories

Lucia Garbini[1], *Iris Abt*[1], *Sabine Irlbeck*[1], *Bela Majorovits*[1], *Matteo Palermo*[1], *Oliver Schulz*[1]
[1]Max-Planck-Institute for Physics, Föhringer Ring 6, 80805 München, Germany

DOI: http://dx.doi.org/10.3204/DESY-PROC-2014-04/8

The China Jinping underground Laboratory (CJPL) is the deepest underground laboratory in operation in the world. The extremely low muon flux makes CJPL a good candidate to host low background experiments looking for rare events like neutrino-less double-beta decays ($0\nu\beta\beta$ decay) or dark matter (DM) interactions. Feasibility and R&D studies are performed to combine these two searches in a common "One-Ton-Germanium facility" to be built in a low-background environment such as CJPL.

1 Rare event searches

The Standard Model (SM) is one of the most successful theories ever produced in physics. Nevertheless, there are experimental evidence, such as the presence of "Dark Matter" (DM) in the universe, neutrino oscillations and baryon asymmetry, which demands at least extensions of the SM framework. Neutrinos and DM are two sectors of particle physics which might give us hints about the expected new physics beyond the SM.

The isotope ^{76}Ge can decay via normal double beta ($\beta\beta$) decay. Thus, it is a candidate for neutrino less double beta ($0\nu\beta\beta$) decay and germanium detectors are used to search for it. The observation of ($0\nu\beta\beta$) decay would demonstrate Lepton Number Violation (LNV) and establish the neutrino as a Majorana particle. Germanium detectors are also used for direct DM searches. Weekly interacting massive particles (WIMPs) should interact in the germanium crystal depending on their mass and the cross section. So far neither DM nor ($0\nu\beta\beta$) decay has been observed and limits have been established on both these processes.

The requirements on the germanium detectors are quite different for the two searches. Nevertheless, detector development studies are being performed aiming to build a detector which fulfills the different technical requirements for both searches, and which can be used in a 1-ton germanium multipurpose facility. The huge exposure achievable with 1 ton of germanium will, however, not improve the sensitivity of the experiment unless the background is low enough. Therefore, such an experiment should be built as deep as possible underground.

2 The China Jinping Underground Laboratory

Several underground facilities are in operation all around the world. The deepest underground laboratory is the China JinPing Underground Laboratory (CJPL) [1] with a rock overburden of 2400 m and a measured muon flux [2] of around 60 muons per square meter per year. The

CJPL is located in the south western province of Sichuan in China. It was built in the central part of one of the support tunnels of the Jinping hydro-power project managed by the Yalong river company. It has a horizontal access suitable for heavy transports. Its total volume of 2000 m^3 is divided in three sections hosting three different experiments as shown in Fig. 1a.

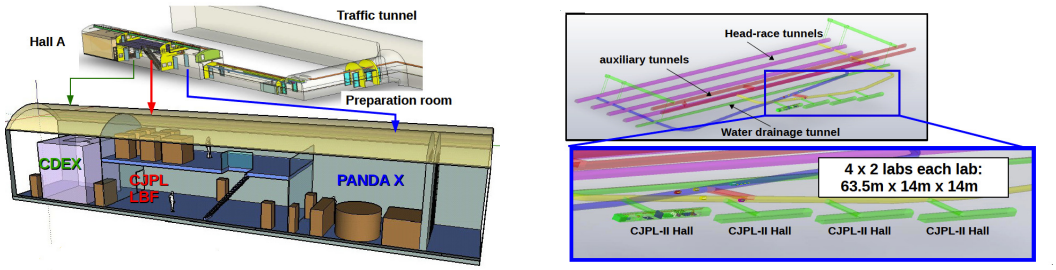

Figure 1: China Jinping Underground Laboratory: (a) shows the Experimental Hall A in CJPL-I; (b) shows the plan for CJPL-II with 4 new experimental double-halls.

The CJPL Low Background Facility [3] (CJPL-LBF) uses high purity germanium detectors as low background spectrometers to investigate environmental samples and select materials for low background experiments, especially for PANDA-X [4] and the China Dark Matter Experiment (CDEX) [5]. PANDA-X and CDEX are direct DM search experiments. The former uses liquid Xenon as target material, while the latter uses Germanium. PANDA-X has, in its first stage, a fiducial mass of 30 kg, easily scalable to 1 ton. Data taking is on going since March 2014, with first results already published in August 2014 [6]. CDEX, in its first stage CDEX-1, uses two high-purity germanium detectors. A 20 g low energy-threshold germanium detector is used to investigate how to lower the energy threshold and be sensitive to extremely low recoil energies corresponding to low-mass WIMP interactions. A 1 kg p-type point-contact germanium detector allows the CDEX collaboration to test software techniques to reject background events using pulse shape analysis. A first limit on WIMP interaction cross-sections was already published [7]. The CDEX collaboration plan to install further germanium detectors.

A plan to significantly enlarge CJPL to become CJPL-II [8] has already been accepted and tunneling will start in fall 2014. In Fig. 1b, the structure of CJPL-II is shown. Four new double halls, with a total volume of about 96000 m^3, will be built to host not only the physics experiments themselves, but also support technology.

CJPL is to become an international laboratory hosting experiments operated by international collaborations. In preparation of this, the Tsinghua university, operating the laboratory, has entered a Sino-German cooperation with the Max-Planck-Institute for physics (MPI) in Munich, the university of Tübingen and the Shanghai Jaotong university. Within this cooperation, germanium detector development and the realization of CJPL-II are discussed.

3 Detector development at the MPI in Munich

The feasibility of a 1-ton germanium multipurpose facility in a laboratory like CJPL is studied. Since the muon induced background would be extremely low in CJPL, other kinds of background will become more important. One of the most dangerous and often limiting sources of background, both for $0\nu\beta\beta$ decay and DM searches, is surface contamination, e.g. from lead,

resulting in α-background. Therefore, it is really crucial to characterize the detector response to α particles in order to be able to identify such events. This is one of the physics goals of the detector development studies performed at the MPI with the GALATEA test stand [9].

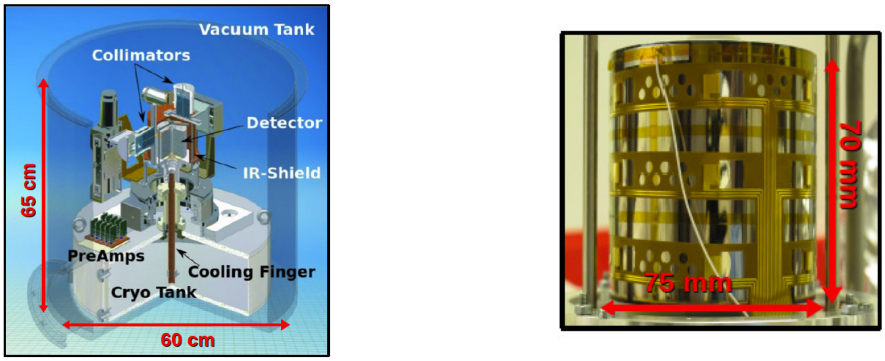

Figure 2: Detector development at the MPI: (a) a sketch of the GALATEA test stand [9]; (b) the detector prototype used to characterize alpha-induced events, Supersiegfried [10].

In Fig. 2a, a sketch of the GALATEA test stand is presented. The detector prototype SuperSiegfried (SuSie) [10] shown in Fig. 2b is an 18+1 fold segmented true-coaxial high-purity germanium detector. The 19th segment is a 5 mm thick disk at the top of the detector. Inside GALATEA, there is no material between source and detector and thus the detector can be probed also with minimally penetrating sources like alphas and betas. A system of three motors moves two collimators in order to facilitate 3d scans. A ^{241}Am source was placed inside the top collimator to irradiate the passivated top-surface of SuSie with alpha particles.

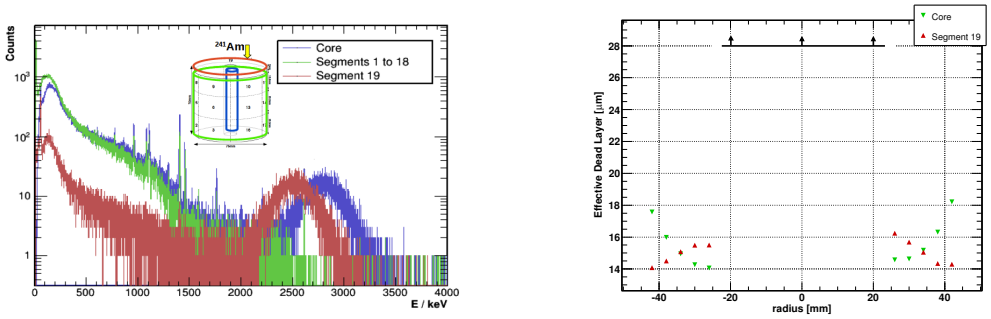

Figure 3: Top-surface scan with a ^{241}Am alpha source: (a) energy spectra as measured with (blue) the core, all 19 segments but the top segment (green) and the top segment (red); (b) the thickness of the effective dead layer at different radii for both electrons (green) and holes (red).

Figure 3a shows typical energy spectra obtained with SuSie when the top is irradiated with alphas at a given point. The blue histogram is the energy spectrum obtained from the core, the red histogram from the top segment and the green one from all the segments but the top segment. The bump around 2 MeV is due to the alpha radiation. It only occurs in the core and the top-segment spectra, because alphas of about 5 MeV only penetrate around 20 μm.

The detector has an effective dead layer on top which consists of the passivation layer and an area of low field underneath. Only energy deposited underneath that layer is recorded. The position of the bump in the spectrum, i.e. the average energy deposited in the detector, should indicate the loss in the effective dead layer. However, the position of the bump is different for core and top segment. This indicates that the picture of well defined layers is oversimplified. The energy recorded in the core (segment) is dominated by the drift of electrons (holes). The two different charge carriers are subject to different trapping effects. This is a typical feature of surface events [11]. If the source is placed at large radii, the electrons are trapped with a higher probability as the holes due to their long path and the effective dead layer is thicker for electrons than for holes. As the source is moved towards the core, i.e. the center of the detector, the situation reverses and holes are more likely trapped than electrons; the effective dead layer for electrons (holes) decreases (increases). Figure 3a shows the recorded spectra at a point where more holes than electrons are trapped and thus, the energy recorded in the core is higher than in the top segment. Figure 3b shows the thickness of the effective dead layers at different radii for electrons (green) and holes (red). At radii below 25 mm, the effective dead layers increase such that they cannot be probed with alphas; this is due to detector geometry.

4 Outlook and Acknowledgments

Germanium detectors are good candidates for future dark matter and $0\nu\beta\beta$ searches. The optimization of the detectors faces many challenges. The characterization of alpha events on the surface and their identification through spectra and pulse shape analysis is one of them. The groups involved plan to conduct further studies on the feasibility of a 1-ton detector at CJPL.

We would like to thank the Sino-German center in Beijing for funding the Sino-German cooperation on germanium detector development.

References

[1] H. S. Chen, Eur. Phys. J. Plus **127** (2012) 105.

[2] Y. C. Wu, X. Q. Hao, Q. Yue, Y. J. LI, J. P. Cheng, K. J. Kang, Y. H. Chen and J. Li *et al.*, Chin. Phys. C **37** (2013) 8, 086001 [arXiv:1305.0899 [physics.ins-det]].

[3] Y. Mi, H. Ma, Z. Zeng, J. Cheng, J. Su and Q. Yue, arXiv:1403.1724 [physics.ins-det].

[4] X. Cao, X. Chen, Y. Chen, X. Cui, D. Fang, C. Fu, K. L. Giboni and H. Gong *et al.*, Sci. China Phys. Mech. Astron. **57** (2014) 1476 [arXiv:1405.2882 [physics.ins-det]].

[5] K. J. Kang *et al.* [CDEX Collaboration], Front. Phys. China **8** (2013) 412 [arXiv:1303.0601 [physics.ins-det]].

[6] M. Xiao *et al.* [PandaX Collaboration], arXiv:1408.5114 [hep-ex].

[7] Q. Yue *et al.* [CDEX Collaboration], arXiv:1404.4946 [hep-ex].

[8] J. Li, X. Ji, W. Haxton and J. S. Y. Wang, arXiv:1404.2651 [physics.ins-det].

[9] I. Abt, A. Caldwell, B. Doenmez, L. Garbini, S. Irlbeck, B. Majorovits, M. Palermo and O. Schulz, arXiv:1409.0493 [physics.ins-det].

[10] D. Lenz PhD-thesis: Pulse Shapes and Surface Effects in Segmented Germanium Detectors

[11] S. Irlbeck PhD-thesis:The GALATEA Test Facility and a First Study of alpha-induced Surface Events in a Germanium Detector.

Upgrading the ATLAS Tile Calorimeter Electronics

Gabriel Popeneciu on behalf of the ATLAS Tile Calorimeter System collaboration

INCDTIM, Donat 67-103, 400293 Cluj-Napoca, Romania

DOI: http://dx.doi.org/10.3204/DESY-PROC-2014-04/63

The Tile Calorimeter is the central hadronic calorimeter of the ATLAS experiment at LHC. Around 2024, after the upgrade of the LHC the peak luminosity will increase by a factor of 5 compared to the design value, thus requiring an upgrade of the Tile Calorimeter readout electronics. Except the photomultipliers tubes (PMTs), most of the on- and off-detector electronics will be replaced, with the aim of digitizing all PMT pulses at the front-end level and sending them with 10 Gb/s optical links to the back-end electronics. One demonstrator prototype module is planned to be inserted in Tile Calorimeter in 2015 or 2016 that will include hybrid electronic components able to probe the new design.

1 Introduction

The first running of the Large Hadron Collider (LHC) with proton-proton collisions at centre of mass energies up to 8 TeV produced some significant results with the discovery of Higgs Boson and measurements of Standard model processes. For future running the LHC energy and luminosity will be increased in stages, ultimately resulting in the high luminosity HL-LHC. This stage is scheduled around 2024 and plans to increase the peak luminosity to a value of 5-7x10^{34}cm^{-2}s^{-1} with a pileup close to 200 collisions per beam crossing.

The HL-LHC presents some difficult challenges for the detectors because the new operational conditions imply a higher radiation level that can lead to single point failures of electronics or the integrated radiation dose can lead to a permanent component failure. Another challenge is in dealing with the events high rates which requires more efficient trigger algorithms.

The ATLAS Tile Calorimeter [1] (TileCal) is a cylindrical hadronic sampling detector with steel absorbers and scintillating plastic tiles, located in the most central region of the ATLAS experiment [2] at CERN. It consists of a central barrel (divided in half barrels) and two extended barrels along the beam axis. Each barrel is segmented azimuthally into 64 modules reading out up to 48 photomultiplier channels. The Photomultiplier Tubes (PMTs) and the front-end electronics are situated in the outermost part of the modules, in extractable so called super-drawers. TileCal contains a total of 256 super-drawers comprising 9852 PMT readout channels.

The light generated by charged particles crossing scintillating tiles are collected by wavelength shifting fibers and sent to the PMTs. The analog signals produced by PMTs are conditioned and digitized by the

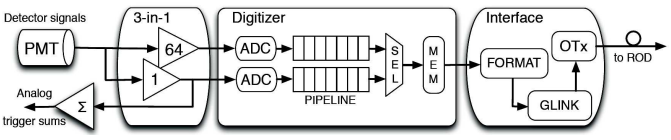

Figure 1: Current Tile Calorimeter readout architecture.

front-end electronics every 25 ns,
while analog tower sums are transmitted to the Level-1 trigger system. When an accept trigger signal is received, data for the selected events are sent to the back-end electronics in the ATLAS counting room where the Read Out Driver (ROD) receives the data at 100 kHz maximum rate. Figure 1 shows the dataflow of the current readout architecture.

To meet the challenges of HL-LHC, a multi-phase upgrade program of the ATLAS experiment has been developed: Phase-0, Phase-I and Phase-II [3]. While TileCal mechanics and optics will stay together with their PMTs, TileCal electronics will undergo major upgrades, because by the time of Phase-II, the current electronics will have reached their end of life and the maximum total integrated radiation dose.

2 Tile Calorimeter electronics for HL-LHC

A full redesign and replacement of the readout electronics of Tile Calorimeter is mandatory to implement redundancy in the signal processing and power distribution, use of radiation-tolerant components and using reliable protocols with error correction for data transmission.

The readout architecture for Phase-II points to a full digital readout where the front-end electronics will transmit digital data from all the channels to the back-end electronics in the counting room for every bunch crossing using high-speed fibre optic links. The data will be pre-processed and transmitted to the first level of trigger with improved precision and granularity. The signal chain for the new readout architecture is shown in Figure 2.

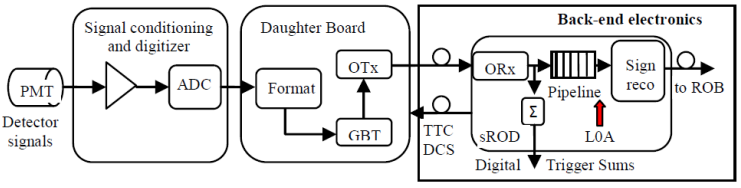

Figure 2: Tile Calorimeter readout architecture for the HL-LHC.

Since redundancy is of utmost importance to achieve maximum reliability, the new front-end electronics will be split into four independent units operating in parallel [4], as is shown in Figure 3. The new design, moving from dependent drawers to independent mini-drawers, reduces the complexity and internal connections, provides a complete redundant readout from cell to back-end electronics and a redundant power supply system.

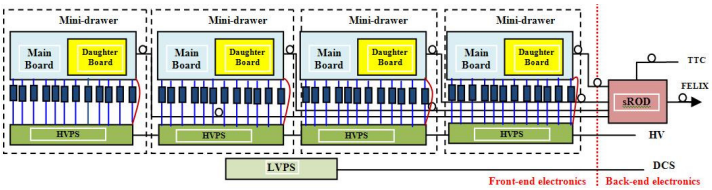

Figure 3: Block diagram of the upgraded super-drawer electronics.

3 Tile Calorimeter Demonstrator Project

To evaluate and qualify the new concept, a prototype called TileCal Demonstrator was developed. In order to gain field experience with the new design, the Demonstrator will replace one super-drawer of the current system for next LHC Run 2 and it must be compatible with present system insofar as it also provides analog trigger signals. Due to this functionality, the prototype is called hybrid Demonstrator. The existing system was redesigned with the respect

to mechanics, electronics, and power distribution.

Mechanics - The current front-end electronics are installed in super-drawers, each composed of two drawers. The modularity implemented by the new concept allows half size drawers called mini-drawers, so that one super-drawer is composed of four mini-drawers. Each mini-drawer is equipped with up to 12 PMTs with corresponding Front-end boards, one Main board, one Daughter board, one High Voltage regulation board and one Adder base board as is shown in Figure 4 (left). The mini-drawers offer a good alignment precision, required in insertion and extraction procedures, due to the improved mechanical links between mini-drawers and a more efficient internal water cooling system. Electrical services organized in two flexible carriers provide easy connection and disconnection of all electrical and optical cables.

The advantages of the Demonstrator super-drawer, shown in Figure 4 (right), consist in an easier access and reduced demand for wide detector opening for TileCal electronics servicing. Also, failing mini-drawers can be more easily replaced than in the present situation, with a minimal radiation exposure of the servicing personnel.

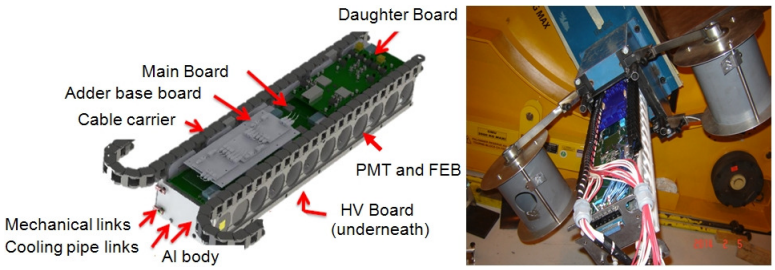

Figure 4: Mini-drawer design (left), Demonstrator and manipulation tooling (right).

Electronics - To improve the reliability and redundancy the new electronics are made as independent as possible and taking in consideration the predicted radiation levels, reliable radiation tolerant components are used.

Front-End Boards (FEB) - three different alternatives are being evaluated: modified 3-in-1 card (redesign of existing FEB), FE-ASIC alternative (including ADCs in an ASIC) and QIE alternative (a charge integrating ASIC). The Demonstrator prototype is equipped with the first version, still based on discrete components but with better linearity, lower noise than current version and acceptable radiation tolerance.

Main Board (MB) - provides the control, monitoring and readout of the FEBs and delivers digitized data to the Daughter Board [5]. MB prototype is divided into halves each hosting six FEBs. Each half has a separated low voltage power supply and is diode-ORed with the other half, ensuring the complete functionality if the power supply for one half stops working.

Daughter Board (DB) - provides high speed communication between the front-end and back-end electronics using redundant high speed links at data rates 10 Gb/s [6]. DB implements slow control functionalities as the distribution of Detector Control System (DCS) commands needed for the control and monitoring of the Main Board and the high voltage power supplies. DB prototype is divided into two separate halves, each equipped with one Kintex 7 field-programmable gate array (FPGA) and one Quad Small Form-factor Pluggable (QSFP) optical module and it can be remotely configured from back-end electronics via safe path using tolerant GBTx and will in turn be able to configure Main Board FPGAs.

Power - Instead of the current daisy-chain power distribution that has proved to be prone to voltage drops, each super-drawer will be outfitted with redundant power supplies.

Low Voltage power distribution - use a three stage power scheme with 200 V from the control room to local power supplies in the TileCal module. Boards receive down-regulated power at +10 V and Point Of Load (POL) regulators locally produce the required voltages. Diode coupling two independent 10 V supplies will provide increased redundancy.

High Voltage power distribution - two solutions are under evaluation to provide HV to the front-end electronics: voltage regulation in ATLAS counting room versus front-end (HV Opto board). For Demonstrator is implemented the second solution, introducing the possibility of switching on/off individual PMTs, based on the current design and for a better linearity the passive dividers have been replaced by active ones.

Back-End Electronics - The upgraded Read Out Driver (sROD) [7] performs the following functions: receiving and processing readout data, interfacing the DCS and the front-end electronics, as well as the reception and distribution of Timing Trigger and Control (TTC) information towards the detector. It was developed a prototype, able to readout a complete hybrid Demonstrator super-drawer. The connectivity between the two Xilinx FPGAs and the optical modules and peripherals is shown in Figure 5. The Virtex 7 FPGA is connected to 4 QSFP providing high speed communication with front-end electronics at a maximum data rate of 160 Gb/s. The Kintex 7 FPGA interfaces the hybrid Demonstrator with current system sending data to the present ROD and receiving TTC information and interfaces with trigger system.

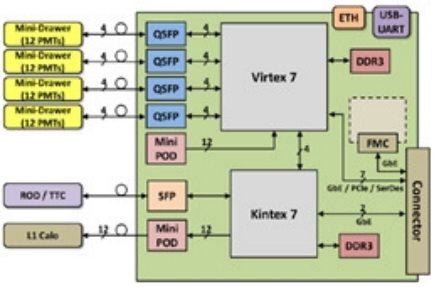

Figure 5: Block diagram of sROD Demonstrator.

4 Summary

The new operational conditions for HL-LHC, with higher radiation levels and data rates, require the implementation of a complete redesign of the Tile Calorimeter readout electronics.

The upgrade plan is to develop a system with full digitization of signals and data transmission at bunch-crossing rate, with a reduced number of possible single points of failure, higher radiation tolerance and higher redundancy on the readout and in power distribution.

To gain an experience and to evaluate the Tile Calorimeter new electronics before the full replacement around 2024, it was developed a hybrid Demonstrator which combines current features, like analog path with the requirements for Phase-II upgrade. It is planned to outfit one full Tile Calorimeter module with the hybrid Demonstrator electronics during first ATLAS opening in LHC Run 2.

References

[1] ATLAS Collaboration, Eur. Phys. J. 1193 (2010).

[2] ATLAS Collaboration, JINST **3** S08003 (2008).

[3] ATLAS Collaboration, CERN-LHCC 2012-022, https://cds.cern.ch/record/1502664/ (2013).

[4] F. Tang *et al.*, IEEE Trans. Nucl. Sci. **60** 1255-1259 (2013).

[5] F. Tang *et al.* on behalf of ATLAS Tile Clorimeter Group, IEEE NSS-MIC Conf. Proc. 6829443 (2013).

[6] S. Muschter *et al.* on behalf of ATLAS Tile Clorimeter Group, JINST **8** C03025 (2013).

[7] F. Carrio *et al.* on behalf of ATLAS Tile Clorimeter Group, JINST **9** C02019 (2014).

Perspectives for the Phase II Upgrade of CMS

David Petyt[1] for the CMS collaboration

[1]STFC Rutherford Appleton Laboratory, Didcot OX11 0QX, United Kingdom

DOI: http://dx.doi.org/10.3204/DESY-PROC-2014-04/194

The LHC Phase II upgrade (HL-LHC) will provide considerable increases in instantaneous and integrated luminosities, leading to a total of 3000 fb^{-1} by around 2035. This data will allow precision measurements of Higgs properties and vector boson scattering processes, and will provide substantially higher sensitivity to searches for new physics. Various subdetectors of CMS will need to be upgraded in order to operate efficiently in such a high rate and high radiation environment. CMS will receive new tracking detectors and new forward instrumentation for calorimetry and muon tagging along with an increase in the capability of the online trigger and data acquisition system. The CMS Phase II upgrade program and the expected performance of the replacement detectors will be reviewed.

1 Introduction

The CMS detector [1] has been designed to provide high performance in the harsh radiation environment of the LHC. During LHC Run I, the detector has recorded data with instantaneous luminosities close to the design goal of 1×10^{34} $\text{cm}^{-2}\text{s}^{-1}$, with an average number of simultaneous interactions per bunch crossing (pileup) of about 25. The excellent performance of the CMS detector and reconstruction algorithms in this environment has led to the discovery of a Higgs-like boson in 2012 [2].

The HL-LHC upgrade, planned for 2025, will significantly increase the instantaneous luminosity that can be provided to CMS, with a total integrated luminosity of 3000 fb^{-1} expected to be delivered by 2035. It has been shown [3] that the significantly larger dataset provided by HL-LHC can considerably expand the sensitivity and reach of CMS to various key physics signatures, including the precise measurement of Higgs boson couplings (including VBF processes), searches for supersymmetry and heavy vector gauge bosons, and precise measurements of electroweak processes.

The large instantaneous and integrated luminosities provided by the HL-LHC upgrade place stringent constraints on the performance, radiation tolerance and longevity of the CMS subdetectors and readout systems. Figure 1 shows the predicted fluence of neutrons in CMS after an accumulated dose of 3000 fb^{-1}. The fluence reaches 1×10^{16} n/cm^2 in the pixel detector and forward calorimeters. In addition, the level of pileup will increase significantly, with an average of about 140 interactions per bunch crossing expected at an instantaneous luminosity of 5×10^{34} $\text{cm}^{-2}\text{s}^{-1}$. The modifications to CMS that will be required to maintain the current level of performance in this challenging enviromnent are summarised below.

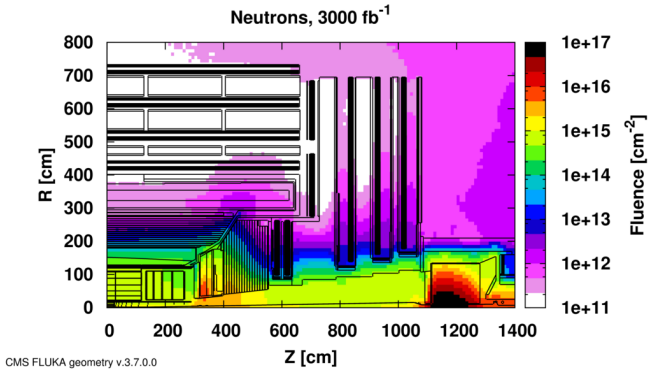

Figure 1: Neutron fluence in the CMS cavern after an integrated luminosity of 3000 fb^{-1}.

2 Upgrade Plans

2.1 Tracker and Pixel detectors

The CMS Tracker will suffer significant radiation aging and must be completely replaced for Phase II. The granualarity of both the outer tracker and pixel detectors will be increased by about a factor of 4 in order to maintain adequate track reconstruction performance at the much higher pileup levels expected at HL-LHC luminosities. For the outer tracker, this will be achieved by shortening the lengths of silicon sensor strips relative to those in the current detector. The upgraded pixel detector will implement smaller pixels and thinner sensors to achieve improved impact parameter resolution and better two-track separation. The pixel coverage will also be extended close to $|\eta| = 4$ to provide increased tracking acceptance and improved suppression of pileup contributions in forward jets. Significant R&D activity is ongoing to identify suitable radiation tolerant silicon sensor technologies and to develop protoype readout modules and support structures.

The predicted performance of the Phase II detector at 140 PU is shown in Figure 2, and is compared to the performance of the Phase I tracker at 50 PU. A number of design improvements will lead to a much lighter outer Tracker providing significantly improved p_T resolution and a lower rate of photon conversions, compared to the present detector. In addition, the module design will be capable of providing fitted tracks with p_T >2 GeV to the Level-1 trigger at 40 MHz. This will ensure powerful background rejection at the earliest stage of the online event selection.

2.2 Calorimeters

The electromagnetic and hadronic endcap calorimeters will also suffer significant radiation damage, and must be replaced for Phase II. Two concepts are currently under consideration, with the potential for higher radiation tolerance and finer granularity to mitigate pileup effects. These include an Electromagnetic Endcap calorimeter, with a Shashlik design (LYSO or CeF_3 crystals interleaved with tungsten plates) followed by a Hadronic Endcap (HE) which would be a rebuild of the present brass/scintillator detector with more radiation tolerant components. The second concept is a High Granularity Calorimeter (HGC) with planes of silicon sensors and

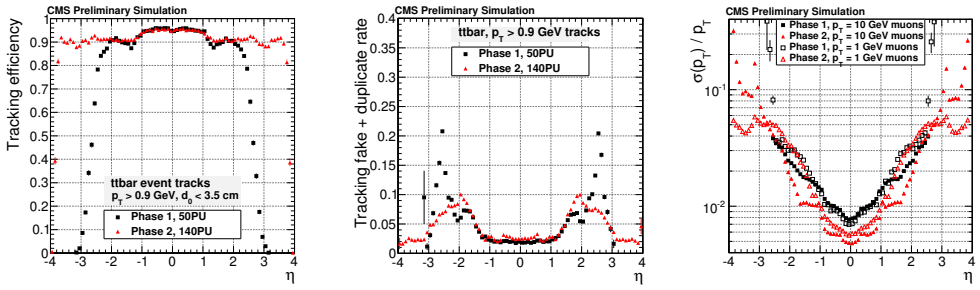

Figure 2: Projected performance of the Phase II tracker for events with an average pileup of 140. The performance of the Phase I tracker for 50 PU is shown for comparison. Left: tracking efficiency; Centre: rate of fake/duplicate tracks; Right: track momentum resolution. The plots assume no detector ageing.

tungsten or brass absorber, organised in electromagnetic and hadronic sections, followed by a rebuilt brass-scintillator HE to provide a total depth of $10\lambda_I$. A more detailed description of these designs can be found in [4].

The front-end electronics of the barrel electromagnetic calorimeter will also be replaced. The data will be transferred off-detector at 40 MHz, simultaneously overcoming present limitations in trigger latency (6.4 μs) and acceptance rate. A new front-end chip will be designed with a shorter shaping time to mitigate the anticipated aging-induced noise increase in the avalanche photodiodes (APD), and for better out-of-time pileup rejection.

2.3 Muon detectors

To maintain good Level-1 muon trigger acceptance in the endcap regions ($1.5 < |\eta| < 2.4$) it is proposed to enhance the existing muon stations with additional chambers that make use of new detector technologies with higher rate capability. The front two stations are in a region where the magnetic field is still reasonably high and will use Gas Electron Multiplier (GEM) chambers for good position resolution. The two rear stations will use low-resistivity Resistive Plate Chambers (RPC) with lower granularity but good timing resolution to mitigate backgrounds. In addition, the implementation of a GEM station behind the new endcap calorimeters is being proposed in order to increase the coverage for muon detection to $|\eta| \simeq 3$.

2.4 Trigger

The Level-1 (L1) trigger accept rate will be increased to provide maximum acceptance for interesting physics events during Phase II running. The trigger latency will also be increased to 12.5 μs to provide sufficient time for the hardware track reconstruction and the matching of tracks to muons and calorimeter energy deposits. This change will require upgrades of the readout electronics in several of the existing subdetectors that will be retained for Phase II. With these modifications, CMS is expected to be able to operate up to 200 PU without significant data loss.

Based on the expected performance of the trigger with track information, we propose to operate with a L1-trigger acceptance rate of 500 kHz for beam conditions corresponding to 140

PU. This will allow us to maintain similar thresholds to those anticipated for use in Phase I.

2.5 Online and offline computing

The Data Acquisition (DAQ) system will be upgraded to provide the increase of bandwidth and computing power needed to accommodate the larger event size and L1 trigger rate. The bandwidth and computing power requirements will increase relative to Phase I by factors of about 10 and 15 respectively for operation at 140 PU. This is within the projected network and computing technology capabilities that are expected to exist at the time of Phase II. The rate of recorded data will increase at 140 PU to about 5 kHz from the corresponding LHC Run 1 levels of between 0.5 and 1.0 kHz. To minimize the computing needs, both for online and offline reconstruction, a significant R&D effort has started to improve the algorithms used for data reconstruction and to adapt the CMS software and computing model to new technologies and resources.

2.6 Infrastructure

Planning for the installation of the new subdetectors for Phase II is still at an early stage, but an initial evaluation of the work sequence and time estimates indicates that the full scope of work can be accomplished in a shutdown of approximately 30 months duration. This is anticipated to take place during LHC Long Shutdown 3 (2023-2025).

3 Summary

The HL-LHC upgrade will provide a large additional dataset that will allow the full exploitation of the physics potential of the LHC. CMS has conducted a detailed study to determine the necessary requirements to operate efficiently in such a high rate and high radiation environment. New tracking devices and forward calorimeters with enhanced radiation tolerance and granularity will be required. Significant upgrades to the capability of the online trigger and data acquisition systems are also needed to maintain and enhance the acceptance to interesting physics signals. Dedicated R&D programmes and prototyping steps are ongoing to identify suitable technologies and to finalise detector designs. These will be documented in a Technical Proposal, to be released in 2015, and in Technical Design Reports, to be completed in 2016-17.

References

[1] CMS Collaboration, *The CMS Experiment at the CERN LHC*, JINST **3** (2008) S08004.

[2] CMS Collaboration, *Observation of a new boson at a mass of 125 GeV with the CMS experiment at the LHC*, Phys. Lett. **B716** 1 (2012).

[3] CMS Collaboration, *Projected Performance of an Upgraded CMS Detector at the LHC and HL-LHC: Contribution to the Snowmass Process*, `arXiv:1307.7135`

[4] M. Peruzzi, *Evolution studies of the CMS ECAL endcap response and upgrade design options for High-Luminosity LHC*, these proceedings.

Evolution Studies of the CMS ECAL Endcap Response and Upgrade Design Options for High-Luminosity LHC

Marco Peruzzi on behalf of the CMS Collaboration

Institute for Particle Physics, ETH Zurich
Otto-Stern-Weg 5, CH-8093 Zurich, Switzerland

DOI: http://dx.doi.org/10.3204/DESY-PROC-2014-04/196

The operation of the CMS electromagnetic calorimeter (ECAL) during the High-Luminosity running of the LHC will be characterized by radiation levels and hadron fluences significantly beyond the design values. Moreover, a large increase in the number of proton-proton interactions per bunch crossing is expected with respect to the current conditions. Studies of the ECAL performance evolution based on LHC collision data, as well as irradiation and beam tests, indicate that its endcaps will need to be upgraded. An overview of the different replacement options under consideration is presented.

Introduction

The CMS electromagnetic calorimeter (ECAL) is a homogeneous crystal calorimeter. It consists of 75,848 lead tungstate ($PbWO_4$) scintillating crystals. ECAL is separated into a barrel region, covering the pseudorapidity range up to $|\eta| = 1.479$, and two endcap regions that extend the coverage up to $|\eta| = 3$. The crystals are arranged in a hermetic and quasi-projective geometry. $PbWO_4$ features a small radiation length (0.89 cm), a small Molière radius (2.19 cm), and a fast scintillation response. These properties have made it possible to build a compact and granular homogeneous calorimeter providing excellent energy resolution, response linearity and particle identification capability at the LHC [1].

Very different operating conditions are expected for the High-Luminosity (HL) running of the LHC, that is scheduled to take place between about 2025 and 2035, up to a final delivered integrated luminosity of about 3000 fb^{-1}. The instantaneous luminosity is expected to reach a value of $5 \cdot 10^{34}$ cm^{-2} s^{-1}, with about 140 proton-proton interactions taking place on average in the same bunch crossing (pileup). The radiation levels in the endcap region are strongly position-dependent. At high values of the pseudorapidity ($|\eta| \sim 2.6$), the photon dose rate will be about 30 Gy/h and the fluence of energetic hadrons will be of the order of $1.8 \cdot 10^{14}$ cm^{-2}. These values exceed by a factor of at least four those the ECAL was designed to withstand.

The ECAL has played a crucial role in many analyses performed with LHC collision data, including the discovery of the Higgs boson in CMS [2]. This will still be the case for a large class of physics analyses that will be performed with HL-LHC data. Therefore, the long-term physics reach of the CMS experiment will strongly depend on an enduring ECAL performance. It is crucial to understand in detail how the properties of $PbWO_4$ crystals evolve under irradiation

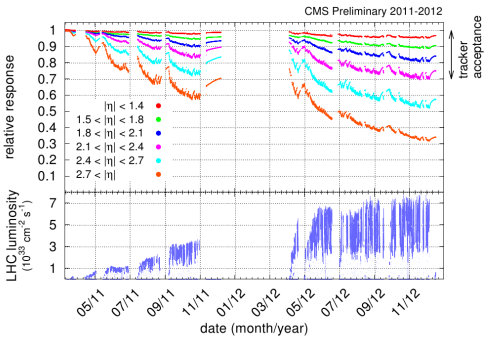

Figure 1: Relative response to laser light measured by the ECAL laser monitoring system, averaged over all crystals in bins of pseudorapidity, for the 2011 and 2012 data taking periods. [3]

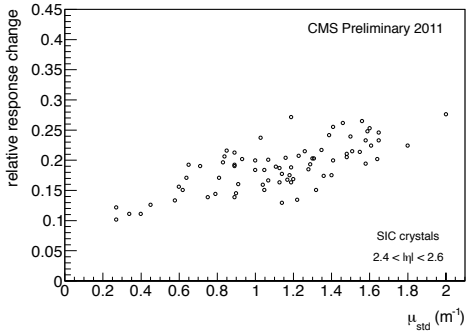

Figure 2: Correlation between relative change of response from ECAL monitoring data and the absorption coefficient, μ_{std}, induced by a standard γ irradiation in crystals produced by the Shanghai Institute of Ceramics. [4]

and to study the performance of the calorimeter in high pileup conditions.

Performance evolution

A loss of transparency of the $PbWO_4$ crystals under irradiation has been established with the LHC collision data collected so far [3]. A laser light injection system has been used to continuously monitor this effect during the data-taking. The loss of transparency has been observed to be strongly correlated with the LHC instantaneous luminosity and with the crystal position in the detector, being the largest at high values of $|\eta|$ (Fig. 1). These monitoring data have been used to correct the crystal response as a function of time and stabilize the energy scale of objects whose energy measurement is based on ECAL.

The main mechanism leading to the transparency loss observed in the detector so far is the formation of colour centres due to ionizing radiation. This type of damage is not cumulative and recovers with time when the irradiation stops (as can be seen in Fig. 1). The loss of transparency measured in the detector with collision data correlates with the results obtained from photon irradiation during the crystal quality control tests before installation (Fig. 2). However, another component of transparency loss is observed to arise after hadron irradiation [4]. It consists of an induced absorption length due to interactions of energetic hadrons with the crystal lattice. It does not recover at room temperature when irradiation stops and therefore builds up during the data-taking. At the large values of integrated luminosity expected at the HL-LHC, this ageing component will become the dominant one. The transparency loss extends throughout the $PbWO_4$ transmission band and causes the lower band edge to shift towards higher wavelengths. The residual light output is expected to be about 10% of the nominal one at $|\eta| \sim 2$ after 3000 fb^{-1}, leading to a contribution to the Higgs diphoton invariant mass peak resolution of the order of several percent (Fig. 3) [5]. On the other hand, the transparency loss will remain acceptable in the barrel region, because of the much lower radiation levels there.

Another effect due to crystal transparency loss is the amplification of the effective noise in the ECAL readout electronics. The electric signal pulse from the ECAL photosensors is sampled by an ADC at 40 MHz. A conversion factor from ADC counts to energy is then applied. While the electronic noise stays constant in units of ADC counts, the loss of transparency will lead to larger conversion factors, effectively amplifying the energy equivalent of the noise. This effect will strongly degrade the trigger performance in the endcap region, increasing the energy thresholds required on electron and photon triggers. The ECAL resolution will also be worsened by non-uniformity of light collection and non-linearity. In conclusion, all terms (stochastic, noise, constant) of the endcap ECAL resolution are worsened by the crystal hadron radiation damage [6]. Moreover, the large number of pileup interactions expected at the HL-LHC will significantly increase the detector occupancy. In these conditions, energy deposits from adjacent bunch crossings will bias the crystal energy readout. The main handle available to fight this effect is increasing the detector granularity.

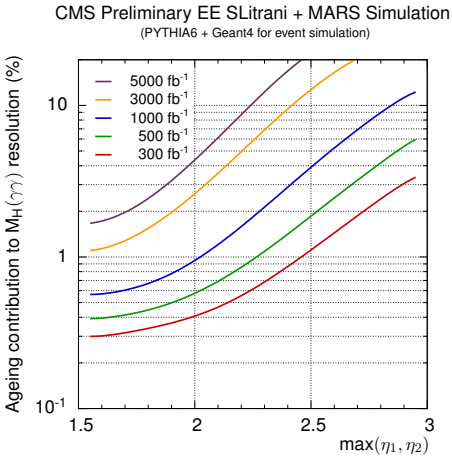

Figure 3: Contribution to the Higgs mass resolution due to the ECAL ageing, for the two photon decay of the Higgs boson in the endcap regions. [5]

Upgrade options

The loss of performance justifies an upgrade of the ECAL endcaps for operation in HL-LHC conditions. Several options have been studied for replacing the CMS electromagnetic and hadronic (HCAL) calorimeters in that region with sampling calorimeters based on new technologies, with finer granularity than the existing devices. The two main design schemes under consideration are described in the following sections.

Sampling design using inorganic scintillating crystals

A sampling calorimeter based on radiation-hard inorganic scintillating crystals interleaved with heavy absorber material plates has been proposed to replace the ECAL endcaps. The light produced in the crystals is wavelength-shifted and extracted towards the photosensors by capillaries or fibres running in the longitudinal direction of the channel (Fig. 4). Two scintillating materials under consideration are LYSO and CeF_3. Both have been studied in irradiation tests and have been shown to be able to withstand larger hadron fluences than $PbWO_4$ (Fig. 5) [7]. CeF_3 even shows a spontaneous recovery of the hadron damage when irradiation stops. The proposed absorber material is tungsten. This design aims at a stochastic term in the calorimeter resolution of about 10%. The low radiation length and Molière radius of this configuration lead to a very compact and granular design. Two prototypes have been realized and successfully tested in beams. One uses LYSO crystals with fibres running through the channel; the other uses CeF_3 crystals with fibres running along chamfers located at the channel corners [8].

High-granularity design

A replacement of both ECAL and HCAL endcaps with a highly segmented (longitudinally and transversally) system, based principally on silicon sensors, has also been proposed. The aim of this design is to obtain an excellent three-dimensional shower profile reconstruction and particle identification. The current proposal consists of a total of about 600 m^2 of silicon sensors of different thickness, segmented into about 9 million channels and interleaved with varying amounts of heavy absorber material. Current R&D studies aim at a highly integrated design of sensors, absorber material and cooling infrastructure.

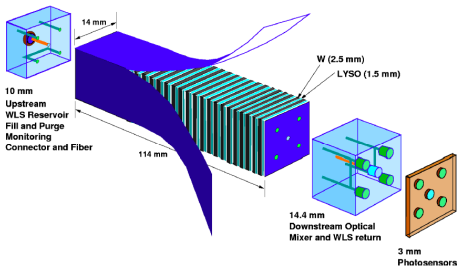

Figure 4: Sketch of a Shashlik configuration based upon interleaved W and LYSO scintillating crystal layers.

Conclusions

The High-Luminosity running of the LHC poses a significant challenge in terms of radiation levels and number of pileup interactions. The mechanisms of radiation damage to the ECAL $PbWO_4$ crystals have been studied with LHC data and irradiation tests and have been found to lead to a strong loss of physics performance in the endcap regions in HL-LHC conditions, while the barrel region will continue to perform well. It is therefore necessary to replace the ECAL endcaps with a more radiation-hard and granular detector. Two options are currently being considered: one is based on a sampling design using heavy inorganic scintillators, while the other consists of a high-granularity silicon-based detector.

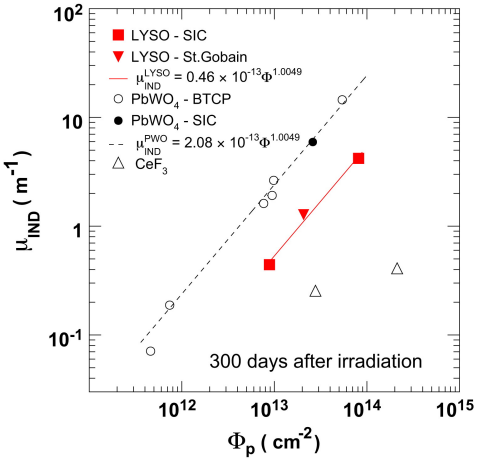

Figure 5: Induced absorption at the peak-of-emission wavelength for $PbWO_4$, LYSO and CeF_3, measured longitudinally through the crystals, as a function of integrated proton fluence, for various producers - SIC, BTCP, St. Gobain. [7]

References

[1] CMS Collaboration, JINST **8** (2013) P09009 [arXiv:1306.2016 [hep-ex]].

[2] CMS Collaboration, Phys. Lett. B **716**, 30 (2012) [arXiv:1207.7235 [hep-ex]].

[3] CMS Collaboration, CMS-DP-2013-007.

[4] CMS Collaboration, CMS-DP-2012-027.

[5] CMS Collaboration, CMS-DP-2013-026.

[6] CMS Collaboration, CMS-DP-2013-022.

[7] G. Dissertori *et al.*, Nucl. Instrum. Meth. A **745** (2014) 1 [arXiv:1309.3872 [physics.ins-det]].

[8] R. Becker *et al.*, [arXiv:1405.6202 [physics.ins-det]].

The STAR Heavy Flavor Tracker (HFT)

Joachim Schambach[1], *Eric Anderssen*[2], *Giacomo Contin*[2], *Leo Greiner*[2], *Joe Silber*[2], *Thorsten Stezelberger*[2], *Xiangming Sun*[3], *Michal Szelezniak*[4], *Flemming Videbæk*[5], *Chinh Vu*[2], *Howard Wieman*[2], *Sam Woodmansee*[2]

[1]University of Texas, 1 University Station, Austin, TX 78712, USA
[2]Lawrence Berkeley National Laboratory, Berkeley, CA 94720
[3]Central China Normal University (CCNU), Wuhan, China
[4]Institut Pluridisciplinaire Hubert Curien (IPHC), Strasbourg, France
[5]Brookhaven National Laboratory, Upton, NY 11973, USA

DOI: http://dx.doi.org/10.3204/DESY-PROC-2014-04/83

The heavy quark hadrons are suggested as a clean probe for studying the early dynamic evolution of the dense and hot medium created in high-energy nuclear collisions. The Heavy Flavor Tracker (HFT) of the STAR experiment, designed to improve the vertex resolution and extend the measurement capabilities in the heavy flavor domain, was installed for the 2014 heavy ion run of RHIC. It is composed of three different silicon detectors arranged in four concentric cylinders close to the STAR interaction point. The two innermost layers are based on CMOS monolithic active pixels (MAPS), featured for the first time in a collider experiment, and the two outer layers are based on pads and strips. The two innermost HFT layers are placed at a radius of 2.8 and 8 cm from the beam line and accommodate 400 ultra-thin (50 μm) high resolution MAPS sensors arranged in 10-sensor ladders to cover a total silicon area of 0.16 m^2. Each sensor includes a pixel array of 928 rows and 960 columns with a 20.7 μm pixel pitch, providing a sensitive area of ~ 3.8 cm^2. The sensor features 185.6 μs readout time and 170 mW/cm^2 power dissipation, allowing it to be air cooled, which results in a global material budget of only 0.5% radiation length per layer in the run 14 detector. A novel mechanical approach to detector insertion enables effective installation and integration of the pixel layers within a 12 hour shift during the on-going STAR Run. After a detailed description of the design specifications and the technology implementation, the detector status and operations during the 200 GeV Au+Au RHIC run of 2014 will be presented in this paper. A preliminary estimation of the detector performance meeting the design requirements will be reported.

1 Introduction

Results from experiments over the last decade at the Relativistic Heavy Ion Collider (RHIC) suggest that a hot and dense matter with strong collectivity has been formed in central Au+Au collisions with energies up to $\sqrt{s} = 200$ GeV [1]. The high temperatures and densities of nuclear matter generated in these collisions create conditions in which a phase of deconfined quarks and gluons, the so-called Quark-Gluon Plasma (QGP), should exist. Due to their mass, heavy quarks such as charm and bottom quarks, are only produced by hard processes early in the collision and not by thermal processes after the equilibration of the plasma, which makes mesons containing

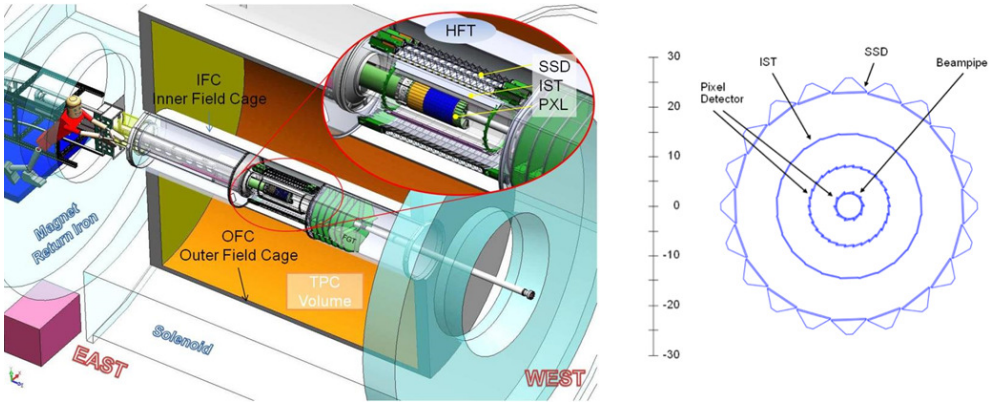

Figure 1: Schematic view of the HFT inside the TPC inner field cage.

heavy quarks an ideal probe for studying the initial conditions of the produced QGP. Most of these heavy quarks produced in the collision end up in open heavy flavor particles that in the past were hard to detect in the STAR experiment due to their low abundance and the large combinatorial background. For that reason STAR installed a new micro-vertex detector for the 2014 heavy ion run at RHIC, called the "Heavy Flavor Tracker" [2], which allows the direct topological reconstruction of the decay vertices from open heavy flavor meson decays which happen close the primary collision vertex due to the small decay length of open heavy flavor particles.

2 HFT and PXL Design

The STAR experiment uses a Time Projection Chamber (TPC) inside a 0.5 T magnetic field as its main tracking detector. Using tracks found in the TPC, the primary interaction vertex can be resolved with a Distance of Closest Approach (DCA) pointing resolution of about 1 mm. Open flavor mesons that are produced at the collsion vertex have a decay length that is very small; for example the $c\tau$ of the D^0 meson is 120 μm. Thus, to be able to reconstruct these decay vertices, the primary physics requirements on the new "HFT" detector system is to provide vertex pointing resolution to resolve vertices displaced from the primary vertex by less than about 150 μm. The basic idea in the design of the HFT is to use tracks found in the TPC and add additional space points on these tracks towards the primary vertex with increasing resolution. The HFT therefore consists of 3 different silicon detector subsystems arranged in 4 concentric layers around the primary vertex as seen in Figure 1: the "Silicon Strip Detector" (SSD), the "Intermediate Silicon Tracker" (IST), and the "PIXEL" (PXL) detector.

The outermost Si detector system, the SSD is an existing detector consisting of double sided silicon strip modules with a 95 μm pitch at a distance of of 22 cm from the beam. The electronics for this detector was upgraded to achieve faster trigger rates compatible with other STAR detectors. The IST at 14 cm radius consists of single-sided double-metal silicon pad sensors with a 600 μm x 6 mm pitch. The SSD and IST detector layers redundantly guide tracks from the TPC to the two innermost layers of the HFT, the PXL detector.

The PXL detector, shown in Figure 2, consists of two layers at radii 2.8 cm and 8 cm using

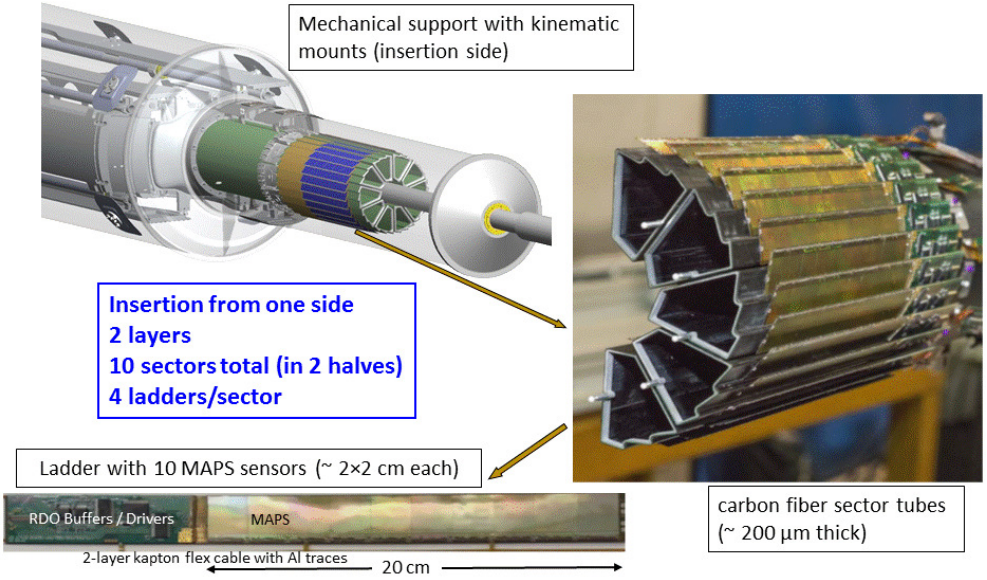

Figure 2: Schematic view of the PXL sub-detector system of the HFT.

state-of-the-art ultra thin CMOS Monolithic Active Pixel Sensors (MAPS) [3, 4, 5, 6]. Mechanically, the PXL detector is subdivided into 10 sectors, each consisting of a thin trapezoidal carbon fiber sector tube with four 10-sensor ladders mounted on each tube, one at the inner diameter, and 3 at the outer diameter. The sensors are thinned to 50 μm thickness, and are mounted on an aluminum conductor flex cable that provides the signal path to the electronics at the end of the flex cable containing the buffers and drivers for the sensor signals. This construction results in a total radiation length X/X_0 of as little as 0.4% per layer in the low-mass region.

The sectors are assembled into two halves on unique mechanical supports that allow for the insertion and retraction of the whole PXL detector from one side side of STAR in only about 12 hours, by pushing the detector halves along rails inside a support cylinder and locking them into a reproducible position with kinematic mounts. The sensor chip used for the PXL detector is the "Ultimate" sensor developed by IPHC in Strasbourg, France. These sensors use pixels with a pitch of 20.7 μm pitch arranged in a 928 (rows) by 960 (columns) array (a total of $\sim 890k$ pixels per sensor) on a 20.22 mm x 22.71 mm chip with a high-resistivity epitaxial layer for increased radiation hardness and increased signal-to-noise performance. Each pixel includes readout and correlated double sampling (CDS) circuitry for signal extraction and noise subtraction. The readout is done by reading each pixel row in parallel through programmable threshold discriminators at the end of each column. The resulting digital data are then passed through a zero-suppresion logic block located below the pixel array on the same chip, which delivers run-length encoded hit addresses for up to 9 hit clusters per row to on-chip memory for intermediate buffering. The memory is arranged in two banks of up to 1500 words each which allows simultaneous read and write operations. The data are read out bit-serially from one of these memory banks over two "Low-Voltage Differential Signaling" (LVDS) outputs per sensor, each running at 160MHz. The signal integration time of the whole sensor is

185.6 μs. Configuration by the JTAG protocol allows the control of many internal parameters and programming of internal test features. A power dissipation of only $\sim 170\ mW/cm^2$ allows these sensors to be operated at room temperature with just air cooling. The readout electronics for the PXL detector follows the mechanical segmentation of the detector and is divided into 10 parallel identical systems. After leaving the ladders, the sensor signals are transmited over $\sim 2m$ of thin twisted pair cables to "Mass Termination Boards" (MTB) at the end of the mechanical structure of the PXL system, which contain buffers and drivers for the signals, as well as latchup protected power supplies for the sensors. Each MTB services the 4 ladders of one sector, i.e. there are 10 MTBs in the PXL detector. Each MTB is connected to an FPGA-based Readout (RDO) board in the low radiation area of the STAR experimental hall with $\sim 11\ m$ of twisted-pair cable. The 10 RDO boards are mounted in a 9U-size crate; each RDO provides trigger based hit selection, buffers and formats the resulting data into event structures, and then sends it over 100 m optical fiber to one of two PCs in the STAR DAQ room, where the data are combined with the rest of the STAR data for event building and final storage. Control, configuration and monitoring of the PXL sensors is done from a control PC, which is connected via USB to the RDO boards. The control PC interfaces to the STAR Slow Controls system to provide monitoring and control of the PXL system to the STAR shift crew.

3 PXL Status and Performance

Two complete PXL detectors and 40 spare ladders have been fabricated by the fall of 2014, and the first PXL detector was installed before the 2014 heavy ion run of RHIC. Because of production issues only 2 of the inner ladders were produced with Aluminum-conductor flex cables, while the rest of the ladders were constructed using alternative Copper-conductor flex cables. This resulted in an increase of the radiation length from the design value of 0.4% to 0.5%. The SSD and IST detectors were installed into STAR during the fall of 2013, while the PXL detector was installed in January of 2014, shortly before the beginning of the 2014 heavy ion run of RHIC. The PXL detector was inserted and cabled into the STAR TPC inner flied cage and operational within a 2 day installation. At the time of the first PXL detector installation all 400 sensors of the PXL system were tested to be working properly with less than 2000 bad pixels out of more than 365 million total. The discriminator thresholds were adjusted to give a fake hit rate of $\sim 1.5 * 10^{-6}$ for all sensors based on an automatic scan of noise rates versus discriminator threshold.

Before the beginning of the heavy ion run the PXL and IST detectors were included in a STAR cosmics run. This run was used for commisioning and integration of the PXL readout electronics with the existing STAR DAQ, Trigger, and Slow Controls systems. Data from this cosmics run were used for alignment and efficiency studies of the PXL detector. The efficiency of the PXL detector was obtained from these data by finding (straight) cosmics ray tracks in the TPC with hits on 3 PXL sensors, and looking for hits on a fourth sensor at the position of a straight-line fit through these three hits extrapolated to the fourth sensor. The analysis of these data were done before normal beam operation and before detector operation optimization was complete. Nevertheless, the average efficiency over all sensors was determined to be 97.2%.

During construction all pixel positions on the sectors as well as the position of the sectors within a detector half were measured in a coordinate measurement machine (CMM). The different parts of the PXL system were then aligned using these same cosmic ray data by looking at the residuals resulting from comparing hit positions to the track projections and adjusting

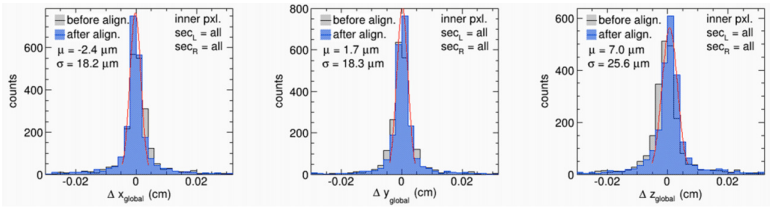

Figure 3: PXL hit residual to cosmic track before and after PXL sector-to-sector alignment.

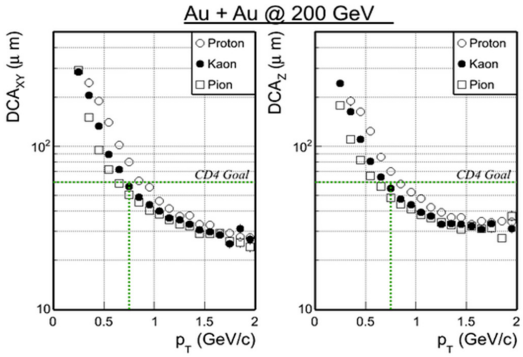

Figure 4: DCA resolution in x-y (left panel) and z (right panel) for TPC tracks with 1 IST hit and hits in both layers of PXL vs. transverse momentum.

the positions of the sensors in order to minimize these residuals. Gaussian fits to these residuals after the alignment was done result in a $\sigma \leq 25\ \mu m$ (see Figure 3), which exceeds the PXL design goals.

The cosmic ray run was followed by a run period of Au+Au collisions at 14.5 GeV from mid February until mid March 2014, which was used to optimize the sensor performance and minimal data taking during stable beam operation. The next 14 weeks were devoted to 200 GeV Au+Au collisions during which a total of $1.2B$ mimimum bias events with PXL included were recorded. Daily PXL noise runs with beam collisions were taken to reassess the sensor status, find hot or not-working pixels, and to verify the noise levels. Periodic threshold-vs-noise scans were performed to readjust the discriminator thresholds. During the final ^{3}He+Au run of RHIC, PXL was only occasionally turned on for further performance and sensor damage studies.

After the survey and preliminary alignment corrections described above were completed, the 200 GeV data were used to estimate the pointing resolution of the PXL detector to the interaction vertex. The DCA resolution for tracks found in the TPC which include 1 IST hit and 1 hit in both layers of PXL as a function of transverse momentum p_T for protons, pions and kaons are shown in Figure 4. For kaons with $p_T = 750 MeV/c$ this DCA resolution exceeds the design goal of 60 μm, in fact, for p_T larger than 1.5 GeV/c, the DCA resolution is better than 30 μm. A more detailed deterimination of the alignment corrections is still ongoing which will further improve these results.

During the 14.5 GeV Au+Au run and into the first two weeks of the 200 GeV Au+Au run first indications of sensor damage manifested itself that seemed to be related to the STAR

radiation environment. The sensor damage took on many different forms: increased digital current, damaged or total loss of pixel columns, damaged configuration registers, loss of full or partial sub arrays, etc. Most of the damage occured in the sensors of the innermost layer of PXL, but even some sensors in the outer layer displayed these kind of damages. After several changes to the operational parameters of the running detector when this damage was detected, further damage to the installed detector for the rest of the run was greatly reduced or stopped. These methods included: turning on the PXL sensors when the collision rate started to fall below a certain threshold, power-cycling the sensors and reloading the sensor configutration periodically, and, most importantly, reducing the threshold at which the power supplies would over-current closer to the normal operational current of the sensors. A total of 15 of the 400 sensors in the PXL detector were damaged, which still allowed us to complete the physics run successfully. We plan on implementing these operational methods from the beginning of the 2015 RHIC run, thus hopefully limiting damage to the PXL sensors in the future. Further investigations of the cause of the observed damage is ongoing.

4 Conclusions

The new HFT micro-vertex detector at STAR enables or enhances open heavy flavor measurements at STAR, thus allowing us to study the early dynamic evolution of the dense and hot medium created in high-energy heavy ion collisions at RHIC. As part of this detector, state-of-the-art MAPS technology was used successfully for the first time in a collider experiment in the PXL subdetector. All three sub-detector systems of the HFT were installed and commisioned during the 2014 RHIC heavy ion run, and more than 1.2 billion Au+Au 200 GeV minimum bias events were recorded with the IST and PXL detectors included. Preliminary studies of the DCA pointing resolution performance show that the detector meets or exceeds the design goals. A second PXL detector was constructed during the summer of 2014 and will be installed in STAR before the 2015 RHIC run. The PXL ladders with damaged sensors were replaced after the 2014 run, and this detector was shipped to STAR to serve as a hot spare. Sensor damage related to the radiation environment in STAR was observed, but seems to be very limited by implementing operational methods.

Acknowledgments

We gratefully acknowledge the PICSEL group of IPHC Strasbourg (M. Winter *et al.*) for the development of the PXL detector sensors.

References

[1] J. Adams *et al.*, Nucl. Phys. A, vol. 757, 102 (2005).

[2] D. Beavis *et al.*, *The STAR Heavy Flavor Tracker Technical Design Report*, available at: https://drupal.star.bnl.gov/STAR/starnotes/public/sn0600 (2011).

[3] C. Hu-Guo, *et al.*, Nucl. Instr. And Meth. **A623** 480 (2010).

[4] A. Dorokhov *et al.*, Nucl. Instr. And Meth. **A624** 432 (2010).

[5] A. Dorokhov *et al.*, Nucl. Instr. And Meth. **A650** 174 (2011).

[6] L. Greiner *et al.*, Nucl. Instr. And Meth. **A650** 68 (2011).

Evaluation of the MPD/NICA detector capabilities for studies of hyperon production in HIC

Veronika Vasendina, Alexander Zinchenko for the MPD Collaboration

JINR, 141980 Dubna, Moscow region, Russia

DOI: http://dx.doi.org/10.3204/DESY-PROC-2014-04/178

One of the main tasks of NICA/MPD physics program is a study of the strangeness production in nuclear collisions. In this paper the MPD detector performance for measurements of Λ, $\bar{\Lambda}$, Ξ^-, $\bar{\Xi}^+$, Ω^- and $\bar{\Omega}^+$ hyperons in central Au+Au collisions at NICA energies is presented.

1 Introduction

The main goal of studying heavy-ion collisions is to explore the properties of nuclear matter under extreme density and temperature conditions. Production of strange particles is of particular interest because enhanced production of rare strange hadrons (Ξ^-, $\bar{\Xi}^+$, Ω^-, $\bar{\Omega}^+$), in A+A collisions (relative to the yields from elementary pp reactions) was predicted as a signal for the QGP formation [1].

At present, a complete theoretical description of the (multi)strangeness production mechanism at collision energies ($\sqrt{s}$) of several GeV has not yet been achieved. In order to better understand the dynamics of hot and dense hadronic matter the MPD experiment at NICA [2] will provide new precise experimental data on the total yields, rapidity, transverse momentum, and azimuthal angle distributions of hyperons. The production of baryons and antibaryons with different strangeness content in central heavy ion collisions will be compared with that in proton induced reactions where no QGP formation is expected.

The goal of this study is to evaluate the performance of the MPD detector for reconstruction of hyperons in Au+Au collisions.

2 MPD detector: geometry, event reconstruction and particle identification

The detailed description of the MPD geometry can be found in Refs. [2, 3, 4]. The present analysis is based on the detectors covering the mid-rapidity region ($|\eta|$ <1.3): the main tracker Time Projection Chamber (TPC) and barrel Time-Of-Flight system (TOF), comprising a so-called start version. The overall detector material budget is dominated by the contribution from the TPC inner and outer cages which are multilayer structures made of composite materials like kevlar and tedlar with high strength and long radiation length. As a result, the total amount of the material does not exceed 10% of the radiation length in the region of interest.

The track reconstruction method is based on the Kalman filtering technique (see, e.g. [5]) and the number of TPC points per track was required to be greater than 10 to ensure a good precision of momentum and dE/dx measurements. In addition, we have restricted our study to the mid-rapidity region with $|\eta|$ <1.3. The track finding efficiency in TPC for primary and secondary tracks is shown in Fig. 1 as a function of the track transverse momentum. The transverse momentum resolution as a function of p_T can be seen on the right panel of Fig. 1. The result has been obtained with the assumption on the TPC coordinate resolution of 0.5 and 1.0 mm in transverse and longitudinal directions, respectively.

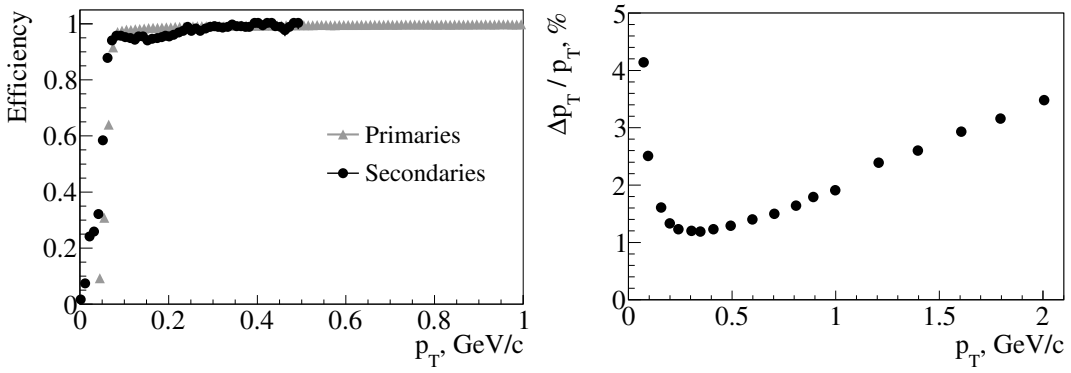

Figure 1: Track reconstruction efficiency as a function of track p_T for primary and secondary particles (left); relative transverse momentum resolution for primary tracks with $|\eta|$ <1.3 reconstructed in TPC (right).

The reconstructed tracks served as an input to the primary and secondary vertex reconstruction procedures based on the Kalman filtering formalism [6].

For all the reconstructed in the TPC tracks the specific energy loss dE/dx is calculated as a truncated mean of the charges of TPC hits assigned to the tracks. The truncation level of 70% was chosen, i.e. 30% of hits with the highest charges were excluded from the mean value.

Next, the TPC reconstructed tracks are extrapolated to the TOF detector and matched to the TOF hits. For the matched candidates the mass square (M^2) is derived through the relation:

$$M^2 = (p/q)^2 \left(\frac{c^2 t^2}{l^2} - 1 \right)$$

where p is the track momentum, q is its charge, t is the time-of-flight from TOF, l is the path length from the collision vertex to the TOF hit, and c is the speed of light.

Particle identification (PID) in the MPD experiment will be achieved by combining specific energy loss (dE/dx) and time-of-flight measurements. The basic detector parameters, namely, dE/dx and TOF resolutions of $\sigma_{dE/dx} \approx 6\%$ and $\sigma_{TOF} \approx 100$ ps will provide a high degree of selectivity for hadrons at momenta below 2 GeV/c.

An identified hadron candidate is assumed to lie within the boundaries of the PID ellipse (3σ around the nominal position for a given particle specie) in the $dE/dx - M^2$ space . In addition, the probability for a given particle to belong to each of the species can be calculated knowing the widths of the corresponding distributions (along the dE/dx and M^2 axes) and

the difference from the predicted position for the specie. It was found that by requiring this probability to be greater than 0.75 one can obtain high PID efficiency and low contamination.

3 Simulations: event generator, data sets and results

The software framework for the MPD experiment (MpdRoot [7]) is based on FairRoot and provides a powerful tool for detector performance studies, development of algorithms for reconstruction and physics analysis of the data [2]. The event samples used for the present study were produced with the UrQMD [8] generator at $\sqrt{s} = 9$A GeV.

Produced by the event generators particles have been transported through the detector using the GEANT3 transport package (describing particle decays, secondary interactions, etc.).

Multistrange hyperons were reconstructed using their decay modes into a charged particle and a Λ hyperon followed by Λ decay into a proton and a pion. The event topology (decay of a relatively long-lived particle into two particles) defines the selection criteria: relatively large distance of the closest approach (DCA) to the primary vertex of decay products, small track-to-track separation in the decay vertex, relatively large decay length of the mother particle. Moreover, both the DCA and two-track separation cuts should be more efficient if applied in χ^2 - space, i.e if normalized to their respective errors.

For $\Xi^{\pm}$ ($\Omega^{\pm}$) Λ-candidates in the invariant mass interval $\pm 3\sigma$ around the peak position were combined with negative pions (kaons) to form $\Xi^{\pm}$ ($\Omega^{\pm}$)-candidates. In the selection procedure, additional acceptance cuts were introduced to find the significance maximum for this cascade decay topology.

The results for hyperon simulations (Figs. 2-4) have been obtained for 10^4 to $5 \cdot 10^5$ central events, corresponding to about 30 seconds - 28 minutes of running time at the NICA collision rate of 6 kHz [9].

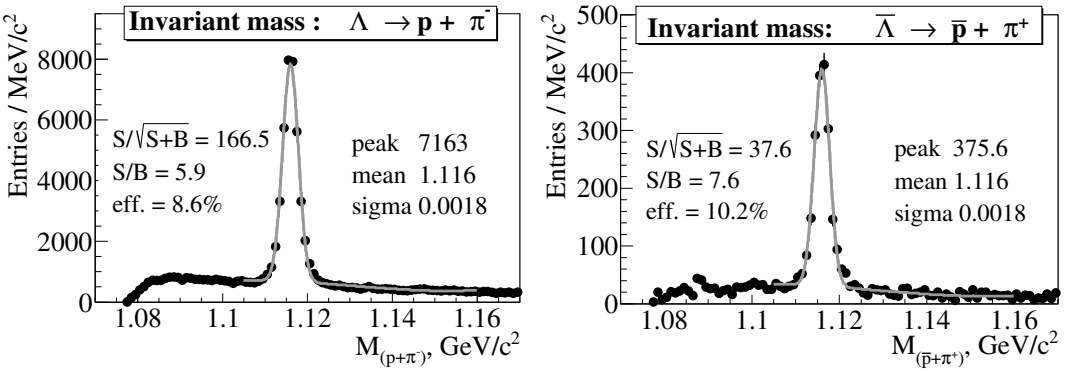

Figure 2: Reconstructed invariant mass of proton (antiproton) and π^- (π^+).

During the selection procedure we observed a large drop in the overall reconstruction efficiency when the low-p_T cut-off of decay products was increased from 0.1 to 0.2 GeV/c. Therefore, keeping the MPD detector ability of reconstructing very low momentum particles (at least, down to $p_T = 0.1$ GeV/c - see left panel of Fig. 1) is of crucial importance for measurements of multistrange hyperons.

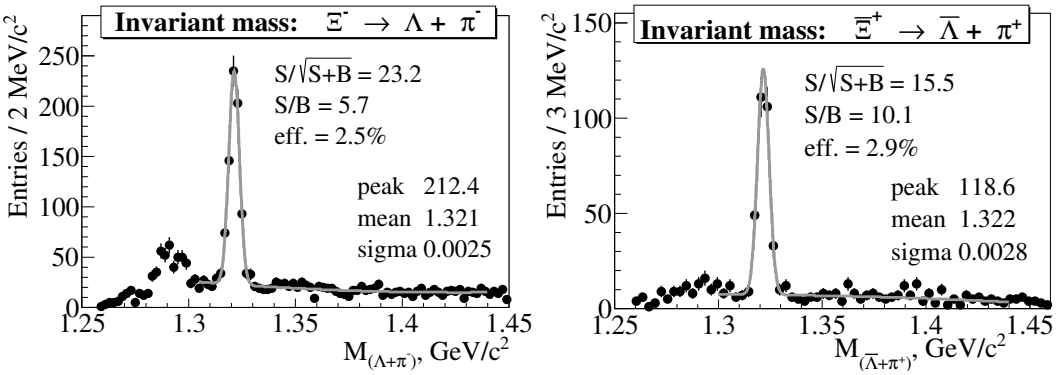

Figure 3: Reconstructed invariant mass of Λ ($\bar{\Lambda}$) candidate and π^- (π^+).

In conclusion we can mention that the current design of the MPD/NICA detector will make it possible to reconstruct (multi)strange hyperons in central Au+Au collisions with the invariant mass resolution of $\lesssim$3.5 MeV/c^2, efficiency above 1% and signal-to-background ratio $S/B \gtrsim 6$.

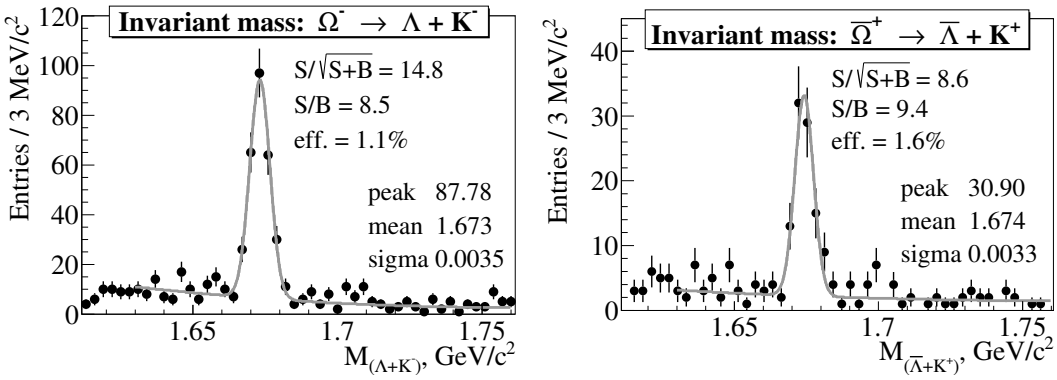

Figure 4: Reconstructed invariant mass of Λ ($\bar{\Lambda}$) candidate and K^- (K^+).

References

[1] J. Rafelski and B. Mulle, Phys. Rev. Lett. **48** 1066 (1982).

[2] K. U. Abraamyan et al., Nucl. Instrum. Meth. **A628** 99 (2011).

[3] http://nica.jinr.ru/files/CDR_MPD/MPD_CDR_en.pdf.

[4] A. Zinchenko, these Proceedings.

[5] R. Fruehwirth, Nucl. Instr. and Meth. **A262** 444 (1987).

[6] R. Luchsinger and Ch. Grab, Comp. Phys. Comm., **76** 263 (1993).

[7] http://mpd.jinr.ru/.

[8] http://urqmd.org/.

[9] http://nica.jinr.ru.

Study of Tin-Silver Solder Ball Bump Bonded Hybrid Silicon Pixel Detector

S. Arab[1], *S. Choudhury*[1], *G. Dolinska*[1], *E. Garutti*[2], *K. Hansen*[1], *M. Hoffmann*[2], *I. Korol*[1], *H. Perrey*[1], *D. Pitzl*[1], *J. Pöhlsen*[2], *V. Sola*[2], *S. Spannagel*[1], *G. Steinbrück*[2]

[1]Deutsches Elektronen-Synchrotron DESY - Hamburg, Germany
[2]University of Hamburg, Germany

DOI: http://dx.doi.org/10.3204/DESY-PROC-2014-04/45

For the connection of front-end readout chips to a silicon sensor of a hybrid pixel detector an in-house flip-chip bump bonding process using precision tin-silver solder balls has been implemented at DESY. The electrical testing of the bump connections follows immediately using an automated probe station by sensing a capacitively induced charge. The bump bonding quality and results from thermal stress testing has been reported. The pixel detector modules have been evaluated in the DESY electron test beam in terms of tracking efficiency and position resolution which has been summarized.

1 Introduction

The process of bump bonding of the silicon sensor to the front-end readout electronics is defining step in the fabrication of a hybrid pixel detector and the procedure of pixel detector module production at DESY with bump bonding of the front-end readout chip to the silicon sensor and quality tests of the bump bond by electrical method and radioactive source have been outlined. The module has also been tested in the electron beam at DESY in terms of charge collection, noise, tracking efficiency and position resolution. The PSI designed and IBM fabricated front-end readout chip [1] measuring 150 x 100 μm^2 has been used to establish the process of high precision tin-silver solder ball bump bonding at DESY to the silicon sensor [2] fabricated from 285 μm thick silicon. The pixels are arranged in an array of 52 columns and 80 rows in a single read-out chip with a double column readout structure for data and time stamp buffers. The new readout chip is an evolution of the one used for the present detector with lower charge thresholds and increased readout link speeds with higher time stamp and data buffer sizes and Fast Input Fast Output (FIFO) buffer. The sensor technology remains the same with n^+ in n substrate as the collection of electrons is advantageous because of their higher mobility compared to holes, which causes a larger Lorentz drift of the signal charges. This drift leads to charge sharing between neighbouring pixels and thus improves the spatial resolution. Furthermore, the higher mobility of electrons makes them less prone to trapping, which leads to a higher signal charge after high fluences of charged particles. After irradiation induced space charge sign inversion, the highest electric field in the sensor is located close to the n^+ electrodes used to collect the charge, which is also an advantage. The choice of n-substrate requires a double sided sensor process, meaning that both sides of the sensor need photo-lithographic processing. The double sided sensors have a guard ring scheme where all sensor edges are at a ground potential, which

greatly simplifies the design of detector modules which ensures a high signal charge at moderate bias voltages ($\leq$ 600 V) after high hadron fluences. The n-side isolation is implemented through a moderated p-spray technique with a punch through biasing grid. The sensor wafer sample in this study has been obtained from PSI which were processed on approximately 285 μm thick n-doped diffusion oxygenated float zone silicon.

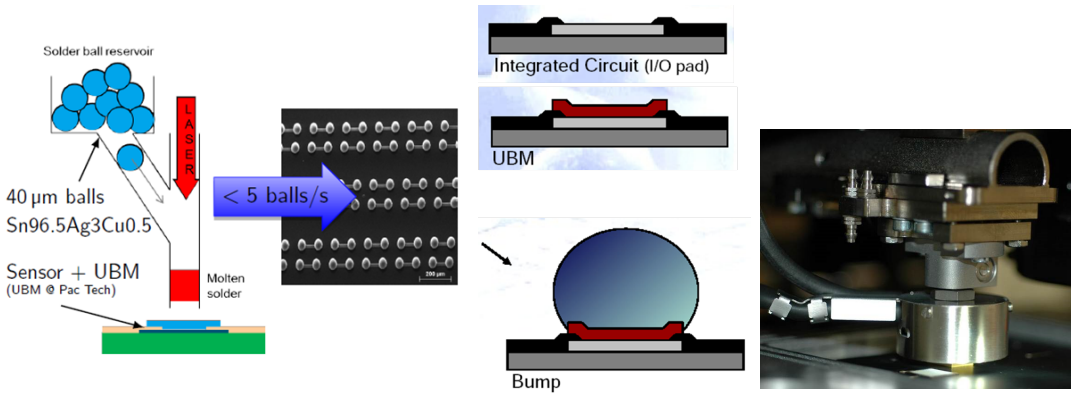

Figure 1: The bump bonding process with the solder ball deposition from SB^2 laser jetting system and the Femto flip-chip bonder for the connection of the sensor and readout chip.

2 Sn-Ag Solder Ball Bump Bonding at DESY

The bump bonding process remains a crucial and the most expensive step towards production of a silicon pixel detecor module and this process has been assembled at DESY with a SB^2 laser jetting system [3] and flip chip bonder [4] to make high precision tin-silver solder ball connections of the readout chip to the silicon sensor.

2.1 Bump Bonding Technique

The bump bonding process can be divided into 3 steps: under-bump metal (UBM) composed of Ni-Pd-Au deposition, solder sphere deposition, and flip chip bonding with re-flow soldering followed by the bare module electrical tests. This is done using an SB^2 step motor controlled bump deposition machine from PacTech. Solder balls of 40 μm diameter with a composition of 96.5% Sn, 3% Ag and 0.5% Cu are dropped though a capillary, molten by a laser and then placed onto the bump pad of the sensors where they solidify. The step-motor places the solder balls with a rate just below 5 Hz, which results in approximately 5 h bump deposition time per sensor with a 16-chip assembly. The next step is the bonding of the sensor onto the read-out chip using a Finetech Femto flip-chip bonder, to form the mechanical and electrical connection. The electronics wafers are thinned by back grinding and the sensor and electronics wafer are cut to get the sensor tiles and the front-end chips. The readout chip is aligned on the sensor tile in such a way that the front-end bumps face the relative sensor bump pads. The tuning of the process parameters has been performed using glass substrates in order to better

investigate the effects on bumps by simple inspection under microscope. The chosen mating pressure is 160 N/chip, applied on the wafers heated around the melting point of tin at 240°C in a formic acid atmosphere. The resulting bump height after the flip-chip bonding process is 26 μm (reduced from 40 μm diameter solder ball).

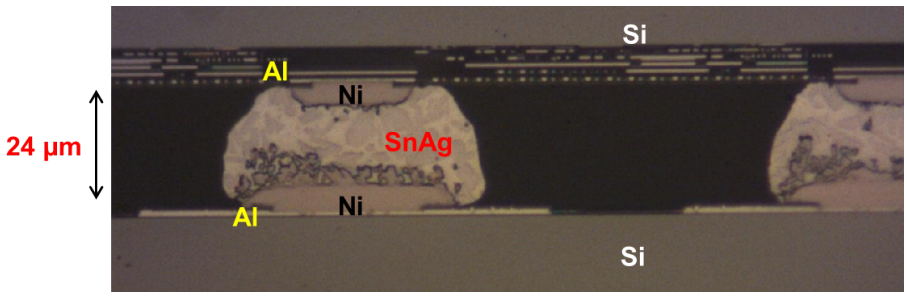

Figure 2: The side view of the bump bonds with the nodule cut across vertically and polished to examine under microscope.

2.2 Test of Bump Bonding Quality

To test that the front-end readout chip is performing as expected, scans of the analog response is carried out. The sensor is kept at a bias voltage of -100 V. A charge is injected into each pixel 10 times and the response recorded. The result should equal 10 and should have a uniform output for a perfect chip, and the result is as expected for 4160 pixels in the single chip module. This is termed as the "pixel alive test" which is to demonstrate the fully functional pixels in the module. The next step is electrical testing of the quality of the bumps and this is done by charge pulses and inducing the charge capacitively directly through the air capacitance between the readout chip and the sensor and then reading out the analog pulse height through the sensor and subsequently bump bonds. In case of missing bumps, the pulse height distribution would be at zero and if the pulse is read through good bumps, then this would be seen at positive values. The pulse height map is shown in Figure 3 with 2 missing bumps at the top left corner (row 0 col 78, row 0 col 79) and 4158 perfect bonds well separated and at positive values. This test is reconfirmed with a radioactive β-ray source. A ^{90}Sr source has been used for inducing signals in the sensor. The β-spectrum of the daughter decay of ^{90}Y has an endpoint energy of about 2.3 MeV and therefore contains particles which approximate a minimum ionising particle. From the hit map, 2 missing bonds can be seen at the top left edge of the module thereby confirming the validity of the electrical testing.
The module is then subjected to several thermal stress cycles from temperature -17°C to +25°C back and forth over a span of one week. The bump bonding test is performed before the start of the the thermal stress cycle and then at the end of each high and low temperature cycle and finally at the end of the cycle, and all tests show the same result as had been obtained previously in Figure 3 showing that the connections are intact and no dislocation of the bumps have taken place due to the thermal stress. The thermal stress cycle establishes the strenghth of the solder ball bump connections and its ability to withstand temperature fluctuations.

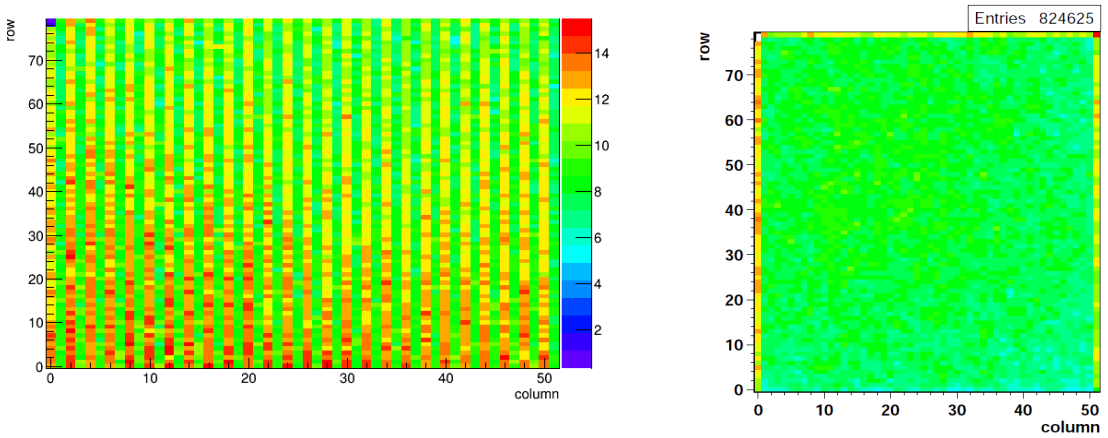

Figure 3: The pulse height map for bump bonding test from capacitively induced charge across the sensor through the air gap capacitor between readout chip and sensor (on left) and the hit map from a β-ray ^{90}Sr source for confirmation of the bump bonding electrical test (on right).

3 Beam Test Studies in DESY Electron Beam

New detectors are required to be tested in an environment similar to that in which they will be exposed in order to determine the performance. A beam test, where the device is read out within a beam of particles, is preferable to using a radioactive source in a laboratory since the statistics will be much higher. The particle type and energy is usually well known within a beam test, however the exact position of a particle at any given time is difficult to determine. Therefore, a set of well understood detectors known as a telescope is used in beam test experiments to track the charged particles. These tracks can be reconstructed offline to evaluate the efficiency and charge sharing performance of the devices under test for various parameters such as the tilt angle, threshold or bias voltage.

3.1 Test Beam Experimental Setup at DESY

The data studied in this analysis was taken at the DESY electron beam with the EUDET pixel telescope having 6 planes of Mimosa 26 sensor developed for ILC [5] with the pixel device under test midway and a reference pixel for timing reference mounted at the end of the beam line. The DESY synchrotron accelerates electrons and then a carbon fibre placed in the beam line produces photons through bremsstrahlung radiation. These photons impact a metal plate which converts them to pairs of electron and positron. A dipole magnet spreads the beam out as a function of the sign and energy. The desired beam energy within the range of 1-6 GeV is chosen with a collimator. The beam line has been configured to provide 5.2 to 5.6 GeV electrons. The beam size is approximately 3 cm (FWHM) and the beam intensity has been tuned to 1 kHz/cm^2. The EUDET telescope [6, 7] consists of two arms each equipped with three sensors. The positions of the sensors along the beam axis can be adapted to the respective requirements. Between the two arms optional mechanical x-y support stage that allows to position the Pixel Device Under Test (DUT) and Reference Pixel (REF) with a few micron precision is installed. Since the telescope is read out at a rate of 112 μs in a rolling shutter mode and the DUTs are read out every 400 ns, the reference sensor is primarily there to

determine if a hit on the DUT is registered thus serving as a timing reference. The sensors are read out by dedicated data-reduction boards that transfer their data to a computer where the data acquisition software is running. A trigger system including four scintillators connected to photomultiplier tubes allows to trigger on particles passing the telescope. For this, two pairs of scintillators (1x2 cm^2), each pair perpendicular to each other, are located in coincidence either side of the telescope to trigger on the incident particles.
The Mimosa sensors typically provide a signal-to-noise ratio for minimum ionising particles (MIPs) of 20-40 and a detection efficiency for MIPs of $> 99\%$ depending on the thresholds. The Mimosa 26 sensor is a combination of the Mimosa 22 sensor [8] and the SuZe01 chip [9] that performs online data sparsification. The sensor is subdivided into 1152 columns of 576 pixels with a pitch of 18.4 μm providing a high granularity. The sensitive area of the sensors is approximately 21 x 10.6 mm^2. On each pixel an amplification and CDS circuit is implemented. The sensor is read out in a column-parallel mode with a pixel-readout frequency of 80 MHz which results in a integration time of about 112 μs. Each column is equipped with a discriminator that performs an offset compensation and a second column double sampling.

3.2 Readout Chip Characterization and Data Acquisition

A threshold setting is required for the front-end card to limit the noise recorded from the module. The output from a threshold scan for the pixel device is tuned to 3100 electrons which is important for charge sharing and influences position resolution and efficiency after irradiation. The measured noise is 160 electrons obtained from the width of the threshold curve. There is a higher level of noise for a lower threshold tuning. The noise for the SnAg bump bonded pixel modules at DESY is similar to Indium bump bonded pixel modules at PSI with the same readout chip.
The data acquisition system is the one for EUDET pixel telescope with a flexible data acquisition software (EUDAQ) [10, 11, 12] for testing the pixel module with the MIMOSA sensors of the telescope system for track interpolation and extrapolation to the DUT. The hardware of the telescope and of the connected DUTs is read out by separate producer tasks that are connected to the "run control" and the "data collector". The latter receives the data streams, builds the events and stores the data on the storage device. The "log collector" provides an interface for the producers for the collection of logging messages. One part of the EUDAQ software is the online-monitoring system (RootMonitor) that makes use of the object-oriented data analysis framework ROOT [13] implemented in C++. The RootMonitor can be used together with the EUDAQ system during data taking as well as a stand-alone application reading and analysing raw data files. The RootMonitor is able to handle different sensor types for the various telescope planes. It provides a simple fixed-frame cluster reconstruction algorithm. Seed pixel candidates are identified and starting from the pixel with the highest signal-to-noise ratio clusters are constructed by joining neighbouring pixel to the cluster if certain thresholds are fulfilled. Thus it starts from one hit candidate and then assigns all 8 neighbouring hit pixels to the cluster. This procedure is repeated until all hit pixel are joined into clusters. The cluster position is reconstructed in the RootMonitor by determining the centre-of-gravity for each cluster which is a signal-weighted average of the pixel positions belonging to the cluster.

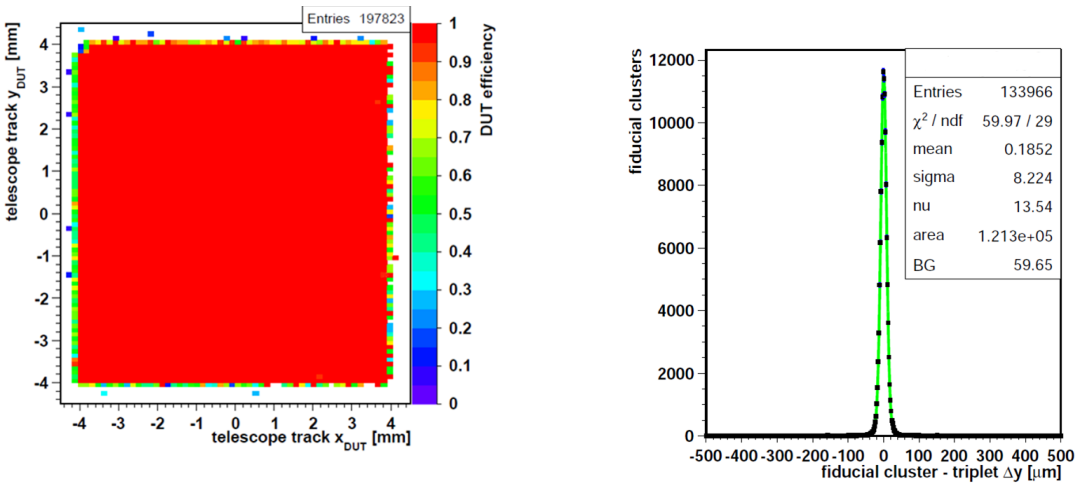

Figure 4: The map of tracking efficiency in a single-chip module (on left) and the position resolution with a fit to Gaussian (on right).

3.3 Test Beam Measurements and Data Analysis

The offline analysis software (EUTelescope) [14, 15] for the telescope data is based on Marlin [16, 17, 18] and Linear Collider In / Out (LCIO) [19, 20]. The EUTelescope software makes use of the Marlin analysis framework which divides the analysis in several individual small tasks. The behaviour of these processors can be controlled with steering files. The data is stored in the LCIO format which was developed to provide a persistent data model and interface. The pedestal and noise information are determined and hit pixels are grouped into clusters by applying a loose selection and quality criteria. The cluster coordinates are transformed from the local reference frame to the global telescope reference frame using the geometry description provided by the GEAR [21] package. After determining the alignment constants of the individual planes, the fitter reconstructs tracks using this collection of corrected hits. These tracks can be used for an extrapolation to the DUT surface in order to determine the predicted positions of hits in the DUT plane. For all hit pixels the number of neighbouring hit pixels is determined, whereas diagonal neighbours are ignored. The list of hit pixels obtained in the previous step is sorted with decreasing neighbours in order to determine the seed candidates. For pairs of pixel with equal number of neighbours, the pixel with the larger number of diagonal neighbours is preferred. The resulting list is processed starting from the seed candidate with the highest number of neighbours. All hit pixels in a fixed x-y frame around the seed pixel are merged into the cluster and removed from the pixel collection and from the list of seed candidates.
In order to be able to reconstruct tracks with the telescope and to extrapolate these tracks to the DUT plane, the geometrical positions of the sensor planes have to be known with high precision. Beam particles passing the telescope planes create clusters in the sensors which are spatially correlated between the individual planes. The EUTelescope software packages provides a processor (EuTelMille) that uses MILLEPEDE [22, 23] for the determination of the alignment constants in order to reduce the bias and the uncertainty of the fitted track parameters and to minimize the χ^2 of the tracks. Each parametrisation of a track depends on local parameters that vary between the tracks and on global parameters - the alignment constants. The processor

EuTelMille takes as an input a collection of hits and then for all combination of hits straight lines are fitted to these groups of hits independently in x and y direction. In order to suppress fake tracks resulting from combinatoric background, cuts on the residual distributions for all sensor planes can be specified in the corresponding steering file. The derivatives of the tracks with respect to all local and global parameters are stored in a binary file that can be read by Millepede. The Millepede software determines in a simultaneous linear least-squares fit of all local and global track parameters the alignment constants for the sensor planes.
Charge sharing improves track position resolution, but charge that is shared between two (or more) neighbouring pixels reduces the charge each pixels receives. This increases the likelihood that the charge per pixel is below threshold, but this is done away with a low charge threshold. Charge sharing will increase when the sensor is tilted, since particle tracks will pass through multiple pixels. The coordinate measured by a pixel detector is obtained by the position of the centre of the cluster of hit pixels associated with a track, plus a correction (conventionally called the η function) which is a function of the charge sharing, the cluster width and the track angle. The position resolution is calculated by comparing the track position interpolated by the telescope planes and the pixel hit position calculated using charge sharing between rows. The difference of this distribution which is termed as the residual is fitted to a Gaussian. The residuals are calculated separately for x and y and are the difference between the position of the reconstructed track and the position of the cluster centre. The Gaussian shape is due to charge sharing at the edge of the pixels and is wider with increase in multiple scattering. The best position resolution of 7.0 μm for the lower threshold of 1.8 ke is reached at the angle where optimal charge sharing between neighboring pixels occurs, that is where the particles most likely traverse two pixel cells. This optimal angle is determined by the pixel geometry from inverse tangent of the ratio of pixel width in row direction to sensor thickness and is 19.3° along the row direction in which the pixels have a width of 100 μm and the sensor thickness being 285 μm. The position resolution of 7.0 μm is obtained from the residual width 8.2 μm in Figure 4, correcting for the telescope resolution of 4.3 μm.
The tracking efficiency for a pixel sensor is defined as the ratio of the number of measured hits close to a track, against the total hits predicted. These expected hits are determined using reconstructed tracks from the beam test. The tracks are extrapolated from the telescope hits to the DUT plane. To reduce fake tracks, a matching hit in the reference sensor is required. The tracking efficiency is thus defined as the ratio of the DUT hit linked to isolated telescope track with link to REF hit to all the isolated telescope tracks with link to REF hit. The isolation in the telescope track is required due to pileup in the telescope (3-5 tracks/event) which leads to confusion and random overlays at the REF plane. With the module tilted at 19.3°, the efficiency is 99.96% in the fiducial region as observed in Figure 4 and is also observed to remain constant with time. Finally, the test beam profile at vertical tracking incidence in Figure 5 reaffirms the electrical bump bonding test in the laboratory with the observed 2 missing bump connections.

4 Conclusion

The procedure for Femto flip-chip bump bonding with a SB^2-Jet (Laser Solder Jetting System) using high pecision Sn-Ag solder balls to connect the read-out chip to the silicon sensor has been successfully implemented at DESY for production of a hybrid silicon pixel detector. The SB^2 solder ball jetter places the Sn-Ag bumps at a rate of 4.5 Hz and then a flip chip bonder makes

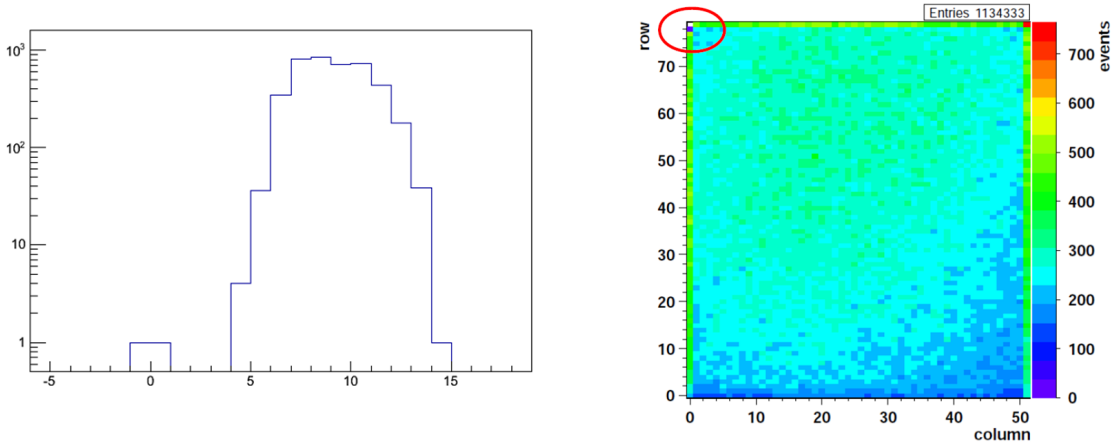

Figure 5: The pulse height distribution from capacitively induced charge across the sensor through the air gap capacitor between readout chip and sensor showing bump bonding test (on left) and the test beam profile shown at vertical incidence to reaffirm the bump bonding electrical test (on right).

the connection at 240°C with 160 N tacking force with re-flow in a formic acid atmosphere. The quality for the bump bonding has been tested electrically and with radioactive source in the laboratory and using the electron test beam at DESY and subsequently through several thermal stress cycles and the module quality is found to be excellent. The position resolution of the module is 7.0 μm with a tracking efficiency of up to 99.96% in the fiducial region for the optimum charge sharing tilt angle between pixels. In a similar way other high quality modules have been produced and tested at DESY successfully preparing the laboratory for the production of a silicon pixel detector.

Acknowledgments

The authors would like to thank the pixel detector group of Roland Horisberger at PSI for the front-end readout chip and sensor used for this study and the DESY accelerator personnel for the smooth and steady delivery of the test beam during the data taking periods.

References

[1] H. Chr. Kaestli et. al., "Design and performance of the CMS pixel detector readout chip", Nucl. Instr. Meth. A 565, 188 (2006).

[2] T. Rohe et. al., "Planar sensors for the upgrade of the CMS pixel detector", Nucl. Instr. Meth. A 650, 136 (2011).

[3] PacTech - Solder Jetting & Solder Deballing and Reballing,
URL $http://www.pactech.com/index.php?option=com\_content\&view=article\&id=16\&Itemid=6$.

[4] FineTech - Femto Flip-Chip Bonder,
URL $http://eu.finetech.de/products/micro-assembly/fineplacerr-femto.html$.

[5] J. Brau, Y. Okada and N. Walker (Ed.) et. al., "ILC Reference Design Report Volume 1 - Executive Summary", arXiv:0712.1950 [physics.acc-ph].

[6] D. Haas, "The EUDET High Resolution Pixel Telescope - Towards the Final Telescope", EUDET-Report-2008-02, 2008.

[7] L. Reuen and J. Furletova, "JRA1 - The DEPFET sensor as the first fully integrated DUT in the EUDET pixel telescope: The SPS test beam 2008", EUDET-Memo-2008-34, 2008.

[8] G. Claus et. al., "JRA1 Milestone IDC Prototype ready", EUDET-Memo-2008-03, 2008.

[9] A. Himmi et. al., "A Zero Suppression Micro-Circuit for Binary Readout CMOS Monolithic Sensors", Proceedings of TWEPP-09: Topical Workshop on Electronics for Particle Physics, Paris (France), pg. 426-430, 2009.

[10] M. Pohl, D. Haas and E. Corrin, "JRA1 - Data acquisition system", EUDET-Memo-2006-07, 2006.

[11] D. Haas, "The DAQ for the EUDET pixel telescope", Proceedings of 2007 International Linear Collider Workshop (LCWS07 and ILC07), Hamburg (Germany).

[12] E. Corrin, "EUDAQ Software User Manual", EUDET-Memo-2010-01, 2010.

[13] R. Brun and F. Rademakers, "ROOT: An object oriented data analysis framework", Nucl. Instr. Meth. A 389, 81 (1997).

[14] A. Bulgheroni et. al., "Eutelescope: tracking software", EUDET-Memo-2007-20, 2007.

[15] A. Bulgheroni et. al., "EuTelescope - the JRA1 tracking and reconstruction software: a status report (Milestone)", EUDET-Memo-2008-48, 2008.

[16] F. Gaede, "Marlin and LCCD: Software tools for the ILC", Nucl. Instrum. Meth. A 559, 177 (2006).

[17] "Marlin". URL *http* : *//ilcsoft.desy.de/portal/software_packages/*.

[18] J. Engels and F. Gaende, "Marlin - A Software Framework for ILC detector R&D", EUDET-Report-2007-11, 2007.

[19] F. Gaede et. al., "LCIO: A persistency framework for linear collider simulation studies", arXiv: physics/0306114.

[20] "LCIO", URL *http* : *//lcio.desy.de/*.

[21] "GEAR - A geometry description toolkit for ILC reconstruction software".
URL *http* : *//ilcsoft.desy.de/portal/software_packages/gear*.

[22] V. Blobel and C. Kleinwort, "A New Method for the High-Precision Alignment of Track Detectors", DESY-02-077 pg. 10, 2002.

[23] V. Blobel, "Millepede", URL *http* : *//www.desy.de/ blobel*.

Chapter 14

Poster contributions

Measurement of Drell-Yan and associated jet cross section at low and high invariant masses

Samantha Dooling[1]

[1]DESY, Notketraße 85, 22607 Hamburg, Germany
on behalf of the CMS Collaboration

DOI: http://dx.doi.org/10.3204/DESY-PROC-2014-04/281

The first measurement of the Drell-Yan and associated jet cross section as a function of the Drell-Yan mass is presented using an integrated luminosity of 4.9 fb^{-1} in the di-muon channel of proton-proton collisions recorded with the CMS detector. Cross Sections as a function of the Drell-Yan transverse momentum are measured differentially in the Drell-Yan mass. The p_{T} spectrum of the Drell-Yan allows to study multiple-gluon emissions and resummation effects.

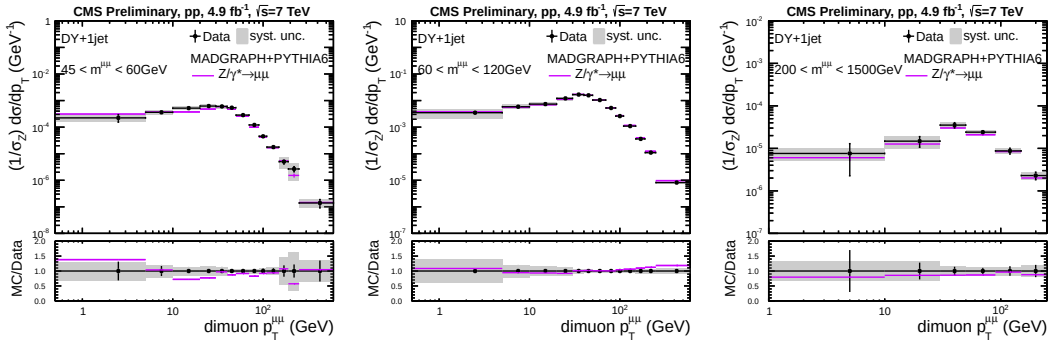

Figure 1: Di-muon p_{T} distribution at low and high invariant masses for DY+1 jet production. Corrected data is compared to MC predictions.

The production of Drell-Yan (DY) lepton pairs in hadron-hadron collisions is a suitable process to study the effect of the soft-gluon resummation in perturbative quantum chromodynamics (pQCD). While DY lepton pair production at large transverse momenta can be described by fixed order calculations in pQCD, at small p_{T} resummation of soft gluons to all orders in perturbation theory is required [1].

The detailed measurements of inclusive DY lepton pair production as well as DY lepton pair production in association with jets, especially in the mass range above the Z mass (and in the range of $m^{\mu\mu} \sim 125$ GeV), is important for a later comparison with Higgs production, which can be used to determine the differences of soft gluon and multi-jet resummation in a quark or gluon induced process [2].

The p_{T} spectrum of the DY lepton pair is of special interest to test contributions from perturbative multi-gluon resummation. In the case of the inclusive DY production the maximum of the DY p_{T} distribution is around 5 GeV. When requiring DY in association with additional jets the maximum shifts to higher p_{T} and the phase space for multi-gluon emissions is enlarged. In Fig. 1 the comparison of DY production and at least one jet above a p_{T} of 30 GeV is shown. The first measurement of the differential DY and associated jets cross section as a function of the DY di-muon mass is presented in [3]. The di-muon p_{T} distribution for DY+1 jet production in the invariant mass regions of 45-60, 60-120, and 200-1500 GeV is presented. The corrected data points are compared to matrix element plus parton shower predictions. The MC generator MADGRAPH+PYTHIA6 is used. MADGRAPH produces the DY boson with maximum four hard partons in the matrix element calculation at leading-order. The underlying event and parton shower is generated by PYTHIA6 using the tune Z2*. The comparison to data presents a good agreement over the whole phase space.

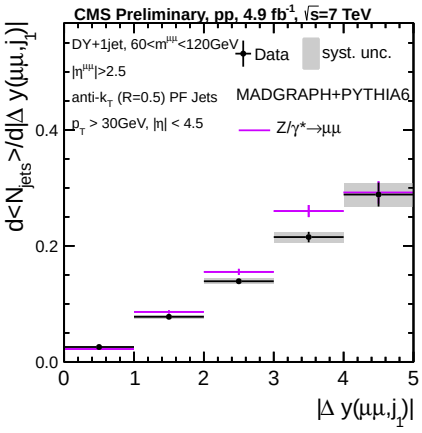

Figure 2: Average jet multiplicity as a function of the rapidity separation between the leading jet and the forward DY production.

Multi-jet emissions in a rapidity interval between the DY pair and the leading jet is a sensitive probe for multi-gluon emissions. The average jet multiplicity of jets with $p_{\mathrm{T}} > 30$ GeV between the leading jet and the forward DY production ($|\eta^{\mu\mu}| > 2.5$) as a function of the rapidity separation $|\Delta y(\mu\mu, \mathrm{j})|$ is presented in Fig. 2. The average jet multiplicity increases with increasing separation between the DY lepton pair and the leading jet from 0 to 0.3 at large rapidity separation. The general behaviour is reproduced by MADGRAPH simulation.

Acknowledgements

I am grateful to the PANIC organizers and staff for the invitation to an exciting conference. I want to thank all PANIC participants for a nice atmosphere and interesting discussions.

References

[1] Dokshitzer, Y. L. and Diakonov, D. and Troian, S. I., Phys. Lett. B**79** (1978) 269, Collins, J. C. and Soper, D. E. and Sterman, G. F., Nucl. Phys. B**250** (1985) 199.

[2] Cipriano, P. and Dooling, S. and Grebenyuk, A. and Gunnellini, P. and Hautmann, F. and Jung, H. and Katsas, P., Phys. Rev. D**88** (2013) 097501.

[3] CMS Collaboration, CMS-PAS-FSQ-13-003, "Measurement of the double differential Drell-Yan and associated jet cross sections at low and high invariant masses in proton-proton collisions at $\sqrt{s} = 7$ TeV", http://cds.cern.ch/record/1670353 (2014).

Hadroproduction of electroweak gauge boson plus jets and TMD parton density functions

Samantha Dooling[1]

[1]DESY, Notketraße 85, 22607 Hamburg, Germany

DOI: http://dx.doi.org/10.3204/DESY-PROC-2014-04/282

If the production of electroweak gauge bosons final states is sensitive to effects of the initial state's transverse momentum distribution, appropriate generalizations of QCD shower evolution are required. We propose a method to treat these effects based on QCD transverse momentum dependent (TMD) factorization at high energy. We illustrate the approach presenting results for production of W-boson + n jets at the LHC.

The approach of collinear factorization, which separates the long-distance terms and the short-distance contributions in the cross section calculation in the collinear approximation, is very successful for sufficiently inclusive observables. However, for more exclusive observables, like e.g. the boson transverse momentum $p_\perp$, the cross section also depends on the scale $p_\perp$. It is necessary to include consistently $p_\perp$ effects already at the beginning of the calculation, which were neglected in the traditional approaches.

We propose an approach to electroweak boson plus jets production, which takes into account dynamical and kinematical issues via transverse momentum dependent (TMD) QCD evolution equations, with corresponding parton density functions and perturbative matrix elements. Traditional approaches have focused on the boson spectrum in the low-$p_\perp$ Sudakov region, and on the treatment of large logarithms for transverse momenta small compared to the boson invariant mass. Our work treats physical effects which persist at high $p_\perp$ and can affect final states with high jet multiplicities.

We use the transverse momentum dependent QCD factorization [1], which is valid up to arbitrarily large $p_\perp$. We couple this with CCFM [2] evolution equations for TMD gluon and valence quark densities using the results recently obtained in [3]. Using the parton branching Monte Carlo implementation of TMD evolution developed in [3] we make predictions, including uncertainties, for final-state observables associated with W-boson production. We study jet transverse momentum spectra and azimuthal correlations. We use the TMD distribution set JH-2013-set2 [3]. We compare the results to the measurements of ATLAS ($|\eta^{\rm jet}| < 4.4$) and CMS ($|\eta^{\rm jet}| < 2.4$). The uncertainties on the predictions are determined according to the method [3].

Figure 1 (top) shows the total transverse energy distribution $H_{\rm T}$ for production of W-boson $+ \geq 1$ jets, with $p_{\rm T}^{\rm jet} > 30$ GeV. In Fig. 1 (middle) we present the $p_\perp$ spectrum of the third jet associated with W production. It is observed that the detailed shapes of the subleading jets can be described by the TMD formalism. In Fig. 1 (bottom) the angular correlation in azimuthal separation between the third jet and the W-boson. Predictions of the structure of angular correlations are a distinctive feature of the TMD exclusive formulation. The shape of the experimental measurements is well described, within the theoretical uncertainties, both at

large $\Delta\phi$ and down to the decorrelated, small-$\Delta\phi$ region.

In conclusion, this work shows how TMD evolution equations at high energies can be used to take into account QCD contributions to the production of electroweak bosons plus multi-jets due to finite-angle soft gluon radiation, and estimate the associated theoretical uncertainties. This will be relevant both to precision studies of Standard Model physics and to new physics searches for which vector boson plus jets are an important background.

Acknowledgements

We are grateful to the PANIC organizers and staff for the invitation to an exciting conference. We want to thank all PANIC participants for a nice atmosphere and interesting discussions.

References

[1] S. Catani, M. Ciafaloni and F. Hautmann, Phys. Lett. B242 (1990) 97; Nucl. Phys. B366 (1991) 135; Phys. Lett. B307 (1993) 147; S. Catani and F. Hautmann, Phys. Lett. B315 (1993) 157; Nucl. Phys. B427 (1994) 475

[2] M. Ciafaloni, Nucl. Phys. B296 (1988) 49, S. Catani, F. Fiorani and G. Marchesini, Nucl. Phys. B336 (1990) 18, G. Marchesini, Nucl. Phys. B445 (1995) 49.

[3] F. Hautmann and H. Jung, Nucl. Phys. B883 (2014) 1

[4] S. Dooling, F. Hautmann and H. Jung, Physics Letters B736 (2014) 293

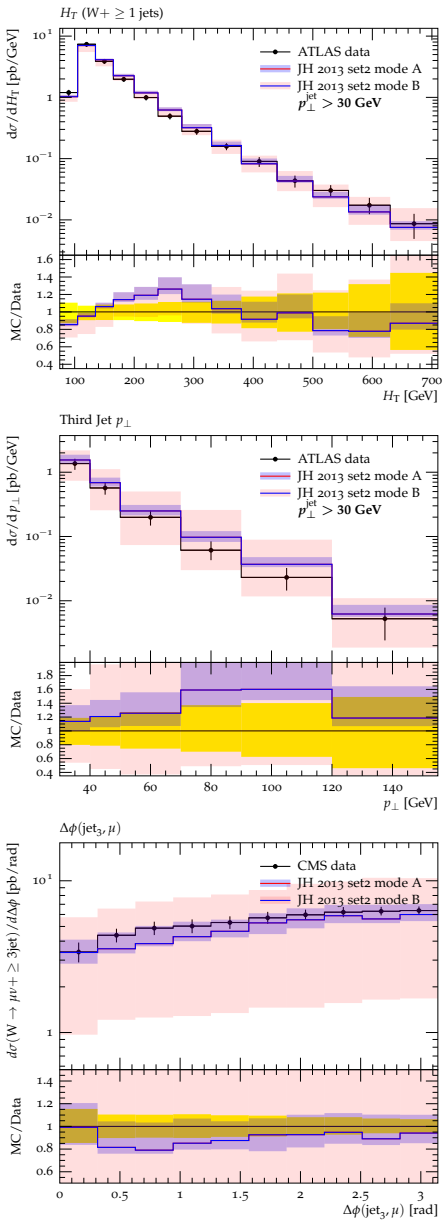

Figure 1: Total transverse energy H_T, third jet $p_\perp$, and angular correlation in final states with W-boson + jets at the LHC.

The Z' Boson of the Minimal $B - L$ Model as a Higgs Boson Factory

A. Gutiérrez-Rodríguez

Facultad de Física, Universidad Autónoma de Zacatecas
Apartado Postal C-580, 98060 Zacatecas, México.

DOI: http://dx.doi.org/10.3204/DESY-PROC-2014-04/20

We study the Higgs boson production in the minimal $B - L$ model at the future linear colliders ILC and CLIC, with the reactions $e^+e^- \to (Z, Z') \to Zh$. We evaluate the total cross section of Zh considering the complete set of Feynman diagrams at tree level.

1 Introduction

The existence of a heavy neutral (Z') vector boson is a feature of many extensions of the Standard Model (SM). In particular, one (or more) additional $U(1)'$ gauge group provides one of the simplest extensions of the SM. Additional Z' gauge bosons appear in Grand Unified Theories (GUTs) [1], Superstring Theories [2], Left-Right Symmetric Models (LRSM) [3] and in other models such as models of composite gauge bosons [4]. In particular, it is possible to study some phenomenological features associated with this extra neutral gauge boson by considering a minimal $B - L$ (baryon number minus lepton number) model.

The $B - L$ symmetry plays an important role in various physics scenarios beyond the SM: Firstly, the gauge $U(1)_{(B-L)}$ symmetry group is contained in a GUT described by a $SO(10)$ group [5]. Secondly, the scale of the $B-L$ symmetry breaking is related to the mass scale of the heavy right-handed Majorana neutrino mass terms providing the well-known see-saw mechanism [6] to explain light left-handed neutrino masses. Thirdly, the $B - L$ symmetry and the scale of its breaking are tightly conneted to the baryogenesis mechanism through leptogenesis [7] via sphaleron interactions preserving $B - L$.

The minimal $B - L$ model [8] is attractive due to its relatively simple theory structure, and the crucial test of the model is the detection of the new heavy neutral (Z') gauge boson. Analyses of precision electroweak measurements indicate that the new Z' gauge boson should be heavier than about 1.2 TeV [9]. On the other hand, recent bounds from the LHC indicate that the Z' gauge boson should be heavier than about 2 TeV [10], while future LHC runs at 13 TeV could increase the Z' mass bounds to higher values, or we may be lucky and find evidence for its presence. Further studies of the Z' properties will require a new linear collider [11], which will also allow us to perform precision studies of the Higgs sector. Detailed discussions on the minimal $B - L$ model can be found in the literature [8, 12].

It is possible to search for the Higgs boson from this model using the process of Higgstralung, a mechanism similar to the one used to search for the SM Higgs boson. However, the existence

of a new heavy gauge bosons could also provide new Higgs production mechanisms, which could probe its non-standard origin. In this work, we are analyzing how the Z' gauge boson of the minimal $U_{(B-L)}$ model could be used as a factory of Higgs bosons.

Our aim in the present work is to analyze the Higgs production cross section from processes like $e^+e^- \to (Z, Z') \to Zh$ in the framework of the minimal $B - L$ model.

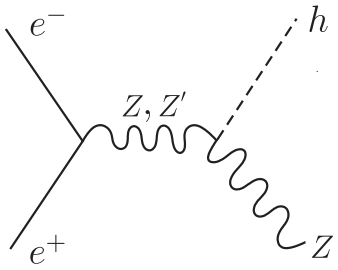

Figure 1: Feynman diagram for the process $e^+e^- \to Zh$ in the minimal $U(1)_{(B-L)}$ model.

2 The Total Cross section of the Process $e^+ + e^- \to Zh$

In this section, we calculated the Higgs production cross section via the process $e^+e^- \to Zh$ in the context of the minimal $U_{(B-L)}$ model at a future high-energy and high-luminosity linear electron-positron colliders, such as the ILC or CLIC.

The contributing Feynman diagram is shown in figure 1. The expression for the respective cross section in the context of the minimal $U(1)_{(B-L)}$ model is given by

$$\begin{aligned}
\sigma(e^+e^- \to Zh) &= \frac{\pi\alpha^2[(g_V^e)^2 + (g_A^e)^2]}{48sx_W^2(1-x_W)(1-m_Z^2/s)^2}\sqrt{\lambda}[\lambda + 12m_Z^2/s] \\
&+ \frac{[f(\theta')\cos\beta - g(\theta')\sin\beta]^2[(g_V^{'e})^2 + (g_A^{'e})^2]}{384\pi s(1-x_W)(1-m_{Z'}^2/s)^2}\sqrt{\lambda'}[\lambda' + 12m_{Z'}^2/s] \\
&+ \frac{\alpha[f(\theta')\cos\beta - g(\theta')\sin\beta][g_V^e g_V^{'e} + g_A^e g_A^{'e}]}{24sx_W(1-x_W)(1-m_Z^2/s)(1-m_{Z'}^2/s)}\sqrt{\lambda}[\lambda + 12m_Z^2/s], \qquad (1)
\end{aligned}$$

where

$$\begin{aligned}
\lambda &= (1 - x_Z - x_h)^2 - 4x_Z x_h, & \lambda' &= (1 - x_{Z'} - x_h)^2 - 4x_{Z'}x_h, \\
f(\theta') &= \sin 2\theta'(\frac{4m_Z^2}{v^2} - g_1^2) + \frac{4g_1 m_Z}{v}\cos 2\theta', & g(\theta') &= \frac{4v'}{v}g_1^2 \sin 2\theta', \\
g_V^e &= \frac{1}{2}\cos\theta' + 2x_W\cos\theta' + \frac{2g_1'}{g}\cos\theta_W\sin\theta', & g_A^e &= \frac{1}{2}\cos\theta', \\
g_V^{'e} &= -\frac{1}{2}\sin\theta' + 2x_W\sin\theta' + \frac{2g_1'}{g}\cos\theta_W\cos\theta', & g_A^{'e} &= -\frac{1}{2}\sin\theta',
\end{aligned}$$

with $x_Z = m_Z^2/s$, $x_{Z'} = m_{Z'}^2/s$, $x_h = m_h^2/s$, $x_W = \sin^2\theta_W$, $\beta = \frac{\pi}{9}$, $v = 246$ GeV, $v' = 2000$ GeV.

The first term of equation 1 corresponds to the cross section from the process with the exchange of a Z boson, while the second and third term comes from the contribution of the minimal $U(1)_{(B-L)}$ model and of the interference respectively. The SM expression for the cross section of the reaction $e^+e^- \to Zh$ can be obtained when the mixing angle and the coupling constant are decoupled in the limited $\theta' = 0$ and $g'_1 = 0$. In this case the terms that depend on θ' and g'_1 in equation 1 are zero and the total expression is reduced to the one given in ref. [13] for the SM.

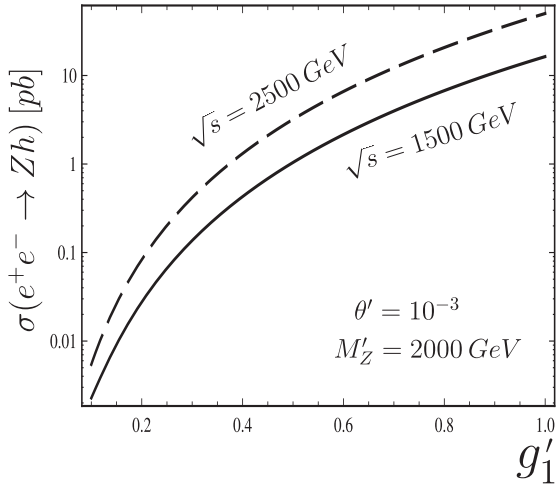

Figure 2: The total cross section for the process $e^+e^- \to Zh$ as a function of the coupling constant g'_1.

3 Results and Conclusions

Using the numerical values $\alpha = 1/128$, $x_W = \sin^2\theta_W = 0.2314$, $m_Z = 91.18$ GeV, $M_h = 125$ GeV, and $\Gamma_Z = 2.49$ GeV, we obtain the cross section $\sigma = \sigma(\sqrt{s}, m_{Z'}, \theta', g'_1)$.

We plot the total cross section of the reaction $e^+e^- \to Zh$ in figure 2 as a function of the coupling constant g'_1 for $m_{Z'} = 2000$ GeV and $\sqrt{s} = 1500, 2500$ GeV. We observed that the total cross section increases as g'_1 increases.

In conclusion, we have analyzed the total cross section of the reaction $e^+e^- \to Zh$ in the context of the minimal $U(1)_{(B-L)}$ model with an additional heavy gauge boson at the high energies expected at the ILC and CLIC colliders. We observed an increase in the total cross section when g'_1, the free parameter of the $U(1)_{(B-L)}$, increases.

Acknowledgments

We acknowledge the support received from the organizing committee of the 20th Particles & Nuclei International Conference (PANIC 14) Hamburg, Germany 2014. We also appreciate the support of PIFI (México).

References

[1] R. W. Robinett, *Phys. Rev.* **D26**, 2388 (1982).

[2] M. Green and J. Schwarz, *Phys. Lett.* **B149**, 117 (1984).

[3] R. N. Mohapatra and G. Senjanovic, *Phys. Rev. Lett.* **44**, 912 (1980).

[4] U. Baur, *et al.*, *Phys. Rev.* **D35**, 297 (1987).

[5] W. Buchmuller, C. Greub and P. Minkowski, *Phys. Lett.* **B267**, 395 (1991).

[6] R. N. Mohapatra and G. Senjanovic, *Phys. Rev. Lett.* **44**, 912 (1980).

[7] M. Fukugita and T. Yanagida, *Physics of Neutrinos and Applications to Astrophysics*, (Springer, Berlin, 2003).

[8] L. Basso, A. Belyaev, S. Moretti and C. H. Shepherd-Themistocleous, *Phys. Rev.* **D80**, 055030 (2009).

[9] P. Langacker, *Rev. Mod. Phys.* **81**, 1199178 (2009).

[10] S. Chatrchyan, *et al.*, *Phys. Rev.* **D87**, 114015 (2013).

[11] B. C. Allanach, *et al.,* arXiv: hep-ph/0403133.

[12] J. L. Díaz-Cruz, *et al.*, *J. Phys. G: Nucl. Part. Phys.* **40**, 125002 (2013).

[13] V.D. Barger, K.m. Cheung, A. Djouadi, B.A. Kniehl and P.M. Zerwas, *Phys. Rev.* **D49**, 79 (1994).

$1/N_c$ corrections to the baryon axial vector current in large-N_c chiral perturbation theory

María A. Hernández-Ruiz

Unidad de Ciencias Químicas, Universidad Autónoma de Zacatecas,
Apartado Postal 585, 98160, Zacatecas, México.

DOI: http://dx.doi.org/10.3204/DESY-PROC-2014-04/23

We study the effects of the decuplet-octet mass difference for the baryon axial vector current at one-loop order in large-N_c baryon chiral perturbation theory, where N_c is the number of color. The baryon axial vector current is considered within the combined framework of large-N_c baryon chiral perturbation theory and the baryon axial vector couplings are extracted. We extend the g_A analysis by including all effects that are suppressed by $1/N_c^2$ relative to the tree level value, which includes taking into account the nonvanshing decuplet-octet mass difference.

1 Introduction

The generalization of quantum chromodynamics (QCD) from $N_c = 3$ to $N_c \gg 3$ color charges, called large-N_c QCD, has opened a path to substantial progress in understanding strong interactions at both the formal and phenomenological levels. Formal successes spring from the fact that large-N_c QCD exhibits a well-defined limit, meaning that the renormalization group equations remain finite and nontrivial as $N_c \to \infty$. Phenomenological successes build on these formal $1/N_c$ power-counting results, but add one extra ingredient: Observables calculated to appear at relative orders $\mathcal{O}(1/N_c)$, $\mathcal{O}(1/N_c^2)$, and so on, which is precisely the origin of the $1/N_c$ expansion [1].

In the large-N_c limit a spin-flavor symmetry emerges for baryons and this symmetry can be used to classify large-N_c baryon states and matrix elements [1, 2], which has led to remarkable insights into the understanding of the nonperturbative QCD dynamics of hadrons. Applications of this formalism to the computation of static properties of baryons range from masses, couplings to magnetic moments [3, 4], to name but a few. In particular, in this work we will describe the baryon axial-vector couplings, and as a result we obtain corrections at relative orders $\mathcal{O}(1/N_c)$ and $\mathcal{O}(1/N_c^2)$. This work is organized as follows. In Section 2, the renormalization of the baryon axial vector current is presented, and contains a detailed numerical analysis, our conclusions are presented in Section 3.

2 Renormalization of the baryon axial vector current

The baryon axial vector current A^{kc} is renormalized by the one-loop diagrams displayed in Fig. 1. These loop graphs have a calculable dependence on the ratio m_Π/Δ, where m_Π is the

meson mass and $\Delta \equiv M_T - M_B$ is the decuplet-octet mass difference. The contribution from Fig. 1(a,b,c) contains the full dependence on the ratio Δ/m_Π and can be written as [5]

$$\begin{aligned}\delta A^{kc} &= \frac{1}{2}\left[A^{ja},\left[A^{jb},A^{kc}\right]\right]\Pi^{ab}_{(1)} - \frac{1}{2}\left\{A^{ja},\left[A^{kc},\left[\mathcal{M},A^{jb}\right]\right]\right\}\Pi^{ab}_{(2)} \\ &+ \frac{1}{6}\left(\left[A^{ja},\left[\left[\mathcal{M},\left[\mathcal{M},A^{jb}\right]\right],A^{kc}\right]\right] - \frac{1}{2}\left[\left[\mathcal{M},A^{ja}\right],\left[\left[\mathcal{M},A^{jb}\right],A^{kc}\right]\right]\right)\Pi^{ab}_{(3)} + \dots .\end{aligned} \tag{1}$$

The baryon axial vector current A^{kc} is a spin-1 object, an octet under $SU(3)$, and odd under time reversal. Its $1/N_c$ expansion reads

$$A^{kc} = a_1 G^{kc} + \sum_{n=2,3}^{N_c} b_n \frac{1}{N_c^{n-1}}\mathcal{D}^{kc}_n + \sum_{n=3,5}^{N_c} c_n \frac{1}{N_c^{n-1}}\mathcal{O}^{kc}_n, \tag{2}$$

where the unknown coefficients a_1, b_n, and c_n have expansions in powers of $1/N_c$ and are order unity at leading order in the $1/N_c$ expansion. At $N_c = 3$ the series (2) can be truncated as

$$A^{kc} = a_1 G^{kc} + b_2 \frac{1}{N_c}\mathcal{D}^{kc}_2 + b_3 \frac{1}{N_c^2}\mathcal{D}^{kc}_3 + c_3 \frac{1}{N_c^2}\mathcal{O}^{kc}_3. \tag{3}$$

The matrix elements of the space components of A^{kc} between SU(6) symmetric states yield the values of the axial vector couplings. For the octet baryons, the axial vector couplings are g_A, as defined in experiments in baryon semileptonic decays, normalized in such a way that $g_A \approx 1.27$ for neutron β decay. The other terms are spin-dependent and represent $\mathcal{M}_{hyperfine}$ introduced in the $1/N_c$ baryon chiral Lagrangian [5]

$$\mathcal{M}_{hyperfine} = \frac{m_2}{N_c} J^2. \tag{4}$$

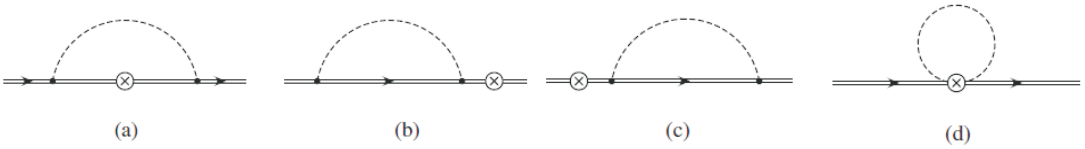

Figure 1: One loop corrections to the baryon axial vector current.

In Eq. (5), $\Pi^{ab}_{(n)}$ represents a symmetric tensor which contains meson loop integrals with the exchange of a single meson: A meson of flavor a is emitted and a meson of flavor b is reabsorbed. This tensor decomposes into flavor singlet **1**, flavor octet **8**, and flavor **27** representations as [5]

$$\Pi^{ab}_{(n)} = F^{(n)}_{\mathbf{1}}\delta^{ab} + F^{(n)}_{\mathbf{8}} d^{ab8} + F^{(n)}_{\mathbf{27}}\left[\delta^{a8}\delta^{b8} - \frac{1}{8}\delta^{ab} - \frac{3}{5}d^{ab8}d^{888}\right], \tag{5}$$

The función $F^{(n)}(m_\Pi, \Delta, \mu)$ along with its derivatives are given explicitly in [3]

$$F^{(n)}(m_\Pi, \Delta, \mu) \equiv \frac{\partial^n F(m_\Pi, \Delta, \mu)}{\partial \Delta^n}. \tag{6}$$

Operator products axial vector current and hyperfine mass	Orders $(1/N_c)$	Operator products SU(6) spin-flavor
AAA	$\mathcal{O}(1/N_c)$	$GGG, GG\mathcal{D}_2, G\mathcal{D}_2\mathcal{D}_2, GG\mathcal{D}_3$ and $GG\mathcal{O}_3$
	$\mathcal{O}(1/N_c^2)$	$\mathcal{D}_2\mathcal{D}_2\mathcal{D}_2, G\mathcal{D}_2\mathcal{D}_3$ and $G\mathcal{D}_2\mathcal{O}_3$
$AAA\mathcal{M}$	$\mathcal{O}(1/N_c)$	$GGGJ^2$ and $GG\mathcal{D}_2J^2$
	$\mathcal{O}(1/N_c^2)$	$GD_2D_2J^2$, $GG\mathcal{D}_3J^2$ and $GG\mathcal{O}_3J^2$
$AAA\mathcal{M}\mathcal{M}$	$\mathcal{O}(1/N_c)$	$GGGJ^2J^2$
	$\mathcal{O}(1/N_c^2)$	$GG\mathcal{D}_2J^2J^2$

Table 1: Relative orders $(1/N_c)$ to the operator products.

3 Results and Conclusions

In summary, we conclude that in the large-N_c limit, decuplet and octet baryon states become degenarate, the difference Δ between the SU(3) invariant masses of the decuplet and octet baryons given by $\Delta \equiv M_T - M_B \propto 1/N_c$.

The analysis was performed at one-loop order, where the corrections to the baryon axial vector coupling arise at relative orders $1/N_c$, $1/N_c^2$, and so on, which is precisely the origin of the $1/N_c$ expansion. The predicted values for g_A are listed in Table 1. Our final results referring to the degeneracy limit $\mathcal{O}(\Delta^0)$, and in the case of a nonvanishing decuplet-octet mass difference for both $\mathcal{O}(\Delta^1)$ and $\mathcal{O}(\Delta^2)$ have been analyzed in Ref. [3, 6]. In Table 1 shows the numerical values of the g_A axial vector couplings for various semileptonic processes in the $1/N_c$ expansion, individually for the flavor singlet **1**, octet **8**, and **27** contributions, the degeneracy limit (AAA), the leading ($AAA\mathcal{M}$), and the next-to-leading ($AAA\mathcal{M}\mathcal{M}$). The singlet corrections are $1/N_c$ suppressed with respect to the tree-level value. Subsequent suppressions of the octet and **27** contributions are also noticeable. The results are perfectly consistent both with the expectations from the $1/N_c$ expansion and the experimental data.

Acknowledgments

The author would like to express their gratitude to Local Organizing Committee of PANIC2014 also acknowledge support.

References

[1] E. E. Jenkins, Ann. Rev. Nucl. Part. Sci. **48**, 81 (1998) [hep-ph/9803349].

[2] R. F. Dashen, E. E. Jenkins and A. V. Manohar, Phys. Rev. D **51**, 3697 (1995) [hep-ph/9411234].

[3] R. Flores-Mendieta, M. A. Hernandez-Ruiz and C. P. Hofmann, Phys. Rev. D **86**, 094041 (2012). [arXiv:1210.8445 [hep-ph]].

[4] G. Ahuatzin, R. Flores-Mendieta and M. A. Hernandez-Ruiz, Phys. Rev. D **89** (2014) 3, 034012 [arXiv:1011.5268 [hep-ph]].

[5] R. Flores-Mendieta, C. P. Hofmann, E. Jenkins and A. V. Manohar, Phys. Rev. D **62**, 034001 (2000). [arXiv:hep-ph/0001218].

[6] R. Flores-Mendieta and C. P. Hofmann, Phys. Rev. D **74**, 094001 (2006). [arXiv:hep-ph/0609120].

Process	Total	Tree	**1**		**8**		**27**	
			Figures 1(a)-1(c), $\mathcal{O}(\Delta^0)$					
			$\mathcal{O}(\frac{1}{N_c})$	$\mathcal{O}(\frac{1}{N_c^2})$	$\mathcal{O}(\frac{1}{N_c})$	$\mathcal{O}(\frac{1}{N_c^2})$	$\mathcal{O}(\frac{1}{N_c})$	$\mathcal{O}(\frac{1}{N_c^2})$
$n \to pe^-\bar{\nu}_e$	1.275	1.121	−0.212	−0.338	0.079	0.292	0.004	−0.001
$\Sigma^\pm \to \Lambda e^\pm \nu_e$	0.629	0.745	−0.042	−0.321	−0.005	0.147	−0.002	0.000
$\Lambda \to pe^-\bar{\nu}_e$	−0.879	−0.628	0.175	0.133	−0.058	−0.063	0.000	0.003
$\Sigma^- \to ne^-\bar{\nu}_e$	0.340	0.704	0.442	−0.783	−0.037	0.022	−0.001	0.008
$\Xi^- \to \Lambda e^-\bar{\nu}_e$	0.361	−0.117	0.077	−0.023	−0.047	0.206	0.005	−0.019
$\Xi^- \to \Sigma^0 e^-\bar{\nu}_e$	0.820	0.793	−0.150	−0.239	−0.028	−0.104	0.004	0.008
$\Xi^0 \to \Sigma^+ e^-\bar{\nu}_e$	1.160	1.121	−0.212	−0.338	−0.041	−0.145	0.005	0.012

TABLE 2: Relative orders $1/N_c$ and $\mathcal{O}(\Delta^0)$ to the coupling constants g_A.

1		**8**		**27**	
Figures 1(a)-1(c), $\mathcal{O}(\Delta^1)$					
$\mathcal{O}(\frac{1}{N_c})$	$\mathcal{O}(\frac{1}{N_c^2})$	$\mathcal{O}(\frac{1}{N_c})$	$\mathcal{O}(\frac{1}{N_c^2})$	$\mathcal{O}(\frac{1}{N_c})$	$\mathcal{O}(\frac{1}{N_c^2})$
−0.103	0.464	0.048	−0.218	0.000	−0.002
−0.026	0.065	0.012	−0.052	0.000	0.001
0.084	−0.490	−0.018	0.138	0.000	0.002
−0.029	−0.239	−0.003	0.047	0.000	−0.001
−0.032	0.398	0.009	−0.050	0.000	0.003
−0.073	0.328	−0.017	0.077	0.000	−0.002
−0.105	0.466	−0.024	0.109	0.000	−0.003

Continuing, TABLE 2: Relative orders $1/N_c$ and $\mathcal{O}(\Delta^1)$ to the coupling constants g_A.

1		**8**		**27**		**1**	**8**	**27**
Figures 1(a)-1(c), $\mathcal{O}(\Delta^2)$						Figure 1(d)		
$\mathcal{O}(\frac{1}{N_c})$	$\mathcal{O}(\frac{1}{N_c^2})$	$\mathcal{O}(\frac{1}{N_c})$	$\mathcal{O}(\frac{1}{N_c^2})$	$\mathcal{O}(\frac{1}{N_c})$	$\mathcal{O}(\frac{1}{N_c^2})$	$\mathcal{O}(\frac{1}{N_c})$	$\mathcal{O}(\frac{1}{N_c})$	$\mathcal{O}(\frac{1}{N_c})$
0.002	−0.043	0.001	−0.023	0.000	0.000	0.303	−0.101	0.002
0.002	−0.023	−0.001	0.006	0.000	0.000	0.201	−0.067	0.001
0.000	0.030	0.000	0.008	0.000	0.000	−0.170	−0.028	0.004
−0.004	−0.006	0.000	0.002	0.000	0.000	0.190	0.032	−0.004
−0.001	−0.008	0.000	−0.005	0.000	0.001	−0.032	−0.005	0.001
0.001	−0.030	0.000	−0.008	0.000	−0.001	0.214	0.036	−0.005
0.002	−0.043	0.000	0.011	0.000	−0.001	0.303	0.050	−0.007

Continuing, TABLE 2: Relative orders $1/N_c$ and $\mathcal{O}(\Delta^2)$ to the coupling constants g_A.

Forward-backward multiplicity correlations in pp collisions at high energy in Monte Carlo model with string fusion

Vladimir Kovalenko, Vladimir Vechernin

Saint Petersburg State University, Russia

DOI: http://dx.doi.org/10.3204/DESY-PROC-2014-04/82

The correlations between multiplicities in two separated rapidity windows, is studied in the framework of the Monte Carlo model based on the picture of string formation in elementary collisions of colour dipoles. The hardness of the elementary collisions is defined by a transverse size of the interacting dipoles. The dependencies of the forward-backward correlation strength on the width and position of the pseudorapidity windows, as well as on transverse momentum range of observed particles were studied. It is demonstrated that taking into account of the string fusion effects improves the agreement with the available experimental data.

1 Introduction

Long-range correlation studies between observables in two separated rapidity windows are considered [1] as a tool for investigation of the initial stages of the hadronic and nuclear collisions, preceding the creation of a hot and dense medium. Because of the non-perturbative nature of multiparticle production in a soft region, one has to apply the various semiphenomenological approaches, such as the model of quark-gluon string formation. At high energies, due to multiparton interactions, the formation of several pairs of strings becomes possible. The interaction between the strings could be observed as a collective phenomena in pp collisions.

Experimentally, the multiplicity correlation coefficient, defined as $b_{\rm corr} = \frac{\langle n_B n_F\rangle - \langle n_B\rangle\langle n_F\rangle}{\langle n_F^2\rangle - \langle n_F\rangle_2}$, has been measured in a wide energy range [2–4] as a function of pseudorapidity windows width, their position and transverse momentum region. In the present paper, we study $b_{\rm corr}$ using the Monte Carlo model, that incorporates string collectivity effects in the form of string fusion [5], and compare the results with the data at $\sqrt{s}$ from 200 to 7000 GeV.

2 Monte Carlo model

The Monte Carlo model [6] is based on the partonic picture of nucleon interaction. It preserves the energy and angular momentum conservation in the nucleon initial state and uses the dipole approach [7] for description of elementary partonic collisions. Multiplicity and transverse momentum are obtained in the approach of colour strings, stretched between projectile and target

partons. The interaction of strings is realized in accordance with the string fusion model prescriptions [5]. Namely the mean multiplicity μ and the mean transverse momentum p_T of the particles produced from a cluster of k overlapping strings are related to those $(\mu_1, p_{T\,1})$ from a single string: $\mu = \sqrt{k}\mu_1, p_T = \sqrt[4]{k}p_{T\,1}$. For realization of the string fusion prescription, we have used the discrete approach, in which a lattice with the cell area equal to the string transverse area $\pi r_{\rm str}^2$ is introduced. The strings are thought to be fused if their transverse position centres belong to the same cell. For the multiplicity from one string (or a cluster of fused strings) we used Poisson distribution, with Gaussian transverse momentum spectra of produced particles.

However, in order to provide to provide the possibility of a direct comparison with experimental data, the correct description of the transverse momentum spectra is required. For this purpose the MC model [6] has been extended by taking into account the hardness of elementary collision. For this the mechanism similar to the one in DIPSY event generator [7], has been incorporated in our model with the string fusion. It was assumed that the hardness an elementary collision is inversely proportional to the transverse size of the interacting dipoles: $d_i = |\vec{r}_1 - \vec{r}_2|, d_i' = |\vec{r_1}' - \vec{r_2}'|$. The mean transverse momentum of particles produced by a single string has the contributions from both edges of the string plus the additional constant term p_0, corresponding to the intrinsic string transverse momentum: ${p_{T\,1}}^2 = \frac{1}{d_i^2} + \frac{1}{{d_i'}^2} + p_0^2$. Accordingly, in the version with string fusion, the transverse momentum of a cluster of strings: $p_T^4 = \sum_{i=1}^{k} {p_{T\,1_i}}^4$, where ${p_{T\,1_i}}^2 = \frac{1}{d_i^2} + \frac{1}{{d_i'}^2} + p_0^2$.

Parameters of the model are constrained from the data on total inelastic cross-section and multiplicity [6]. In the present study, for the case with string fusion we have used $r_{\rm str}$= 0.2fm (in the case with string fusion). For the intrinsic string transverse momentum we have used $p_0 = 0.2{\rm GeV}/c$, which provides a reasonable description of the transverse momentum distribution in pp collisions at the LHC energies.

3 Results

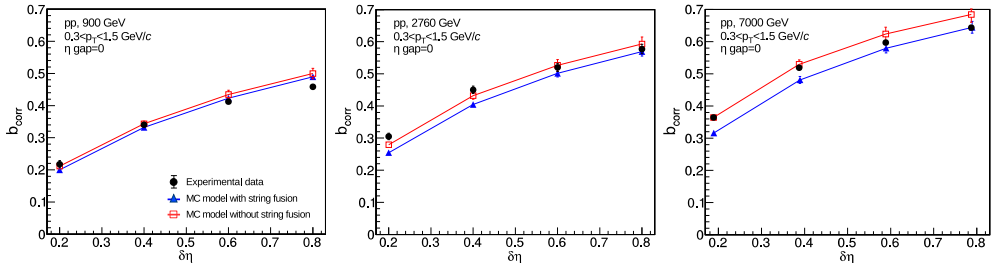

Figure 1: Correlation coefficient as a function of the pseudorapidity windows width ($\delta\eta$) at midrapidities (η gap = 0). Lines – the results of calculation in the model with and without string fusion, points – the experimental data [2].

Figure 1 shows the dependence of the correlation coefficient on the width of the pseudorapidity windows at three energies. The cuts on the transverse momentum ($0.3 < p_T < 1.5{\rm GeV}/c$) applied in MC model calculations, enable direct comparison with the ALICE experimental data [2]. It was found that the general trends, like the growth of $b_{\rm corr}$ with collision energy and width of pseudorapidity windows) are well described by the model. The role of string fusion raises with $\sqrt{s}$, but using only midrapidity experimental data on multiplicity correlation

coefficient at present energies it is hard to distinguish between cases with and without string fusion. Also, it should be noted that at the small gap between rapidity windows there is a contribution of short-range correlation effects in the data (such as the decays of resonances), which are currently not accounted by the model.

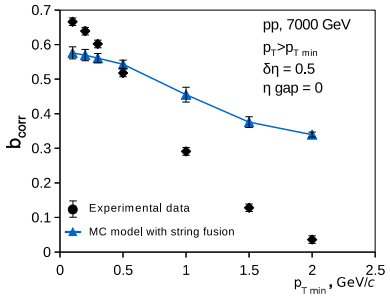

Figure 2: Correlation coefficient as a function of the lower transverse momentum bound. Line – the result of calculation in Monte Carlo model with string fusion, points – the experimental data [3].

In Fig. 2 the dependence of $b_{\rm corr}$ on the transverse momentum region of accounted particles is shown. The correlation coefficient is studied as the function of the lower bound of the p_T interval, and compared to the ATLAS experimental data [3]. The qualitative agreement of $b_{\rm corr}$ with experimental data is found. The increase of $p_{T\,\rm min}$ is accompanied by the decrease of the multiplicity in the given transverse momentum region, which restricts the phase space for particle production and the number of "active" strings, which leads to the decrease of correlation coefficient. Numerically, the model calculations overestimate the value of the correlation coefficient in the hard transverse momentum area. It could be an indication that the direct approach with the soft strings is applicable at the p_T region below $\sim$ 1GeV/c, and different processes (such as jet fragmentation) begin playing a role at higher p_T. On the other hand, this dependence is very sensitive to the shape of the transverse momentum spectra. Whereas, the description of the p_T spectra in our approach has an effective character and does not account the jet production and other hard phenomena accurately.

Figure 3 shows the dependence of $b_{\rm corr}$ on the η gap at four energies, calculated in the Monte Carlo model, with a comparison to the experimental data [3,4]. The model calculations do not discriminate pp and p$\bar{\rm p}$ scattering. The model reproduces the growth of the correlation coefficient with collision energy and qualitatively describes the decrease of the correlation coefficient with with increase of the gap between pseudorapidity windows. Note that the short-range effects, such as the resonances decays and jets, which could contribute to the correlation coefficient at small η gap are not accounted by the model. The results indicate that taking into account of the string fusion effects improves the agreement with the data.

4 Summary and conclusions

The forward-backward multiplicity correlation strength in pp collisions at high energy is studied in the Monte Carlo model with string formation and fusion. The Monte Carlo model reasonably describes the main features of the behaviour of the correlation coefficient in a wide energy range, such as general growth of the correlation coefficient with collision energy and with increase of

pseudorapidity window size. The decrease of $b_{\rm corr}$ with the increase of the gap between windows and with increase of the lower $p_{\rm T}$ bound is also qualitatively described. It is found that the version of the model with inclusion of string fusion effects is better supported by the data compared to the case without string fusion.

Acknowledgments

The authors acknowledge Saint-Petersburg State University for the research grant 11.38.197.2014. V. Kovalenko acknowledges Saint-Petersburg State University for the Special Rector's Scholarship. He is also grateful to the Dynasty Foundation.

References

[1] B. Alessandro *et al.* (ALICE Collaboration), J. Phys. G **32**, 1295 (Section 6.5.15, p. 1749) (2006).

[2] G.A. Feofilov *et al.* (for ALICE collaboration), PoS (Baldin ISHEPP XXI) 075 (2012).

[3] G. Aad *et al.* (ATLAS Collaboration), JHEP 07, 019 (2012).

[4] R.E. Ansorge *et al.* (UA5 Collaboration), Z. Phys C **37** 191 (1988).

[5] N.S. Amelin, N. Armesto, M.A. Braun, E.G. Ferreiro, C. Pajares, Phys. Rev. Lett. **73** 2813 (1994);
M.A. Braun, R.S. Kolevatov, C. Pajares, V.V. Vechernin, Eur. Phys. J. C **32** 535 (2004);
M.A. Braun, C. Pajares, and V.V. Vechernin, Phys. Let. B **493** 54 (2000).

[6] V.N. Kovalenko, Phys. Atom. Nucl. **76** 1189 (2013), arXiv:1211.6209 [hep-ph];
V. Kovalenko, V. Vechernin, PoS (Baldin ISHEPP XXI) 077 (2012), arXiv:1212.2590 [nucl-th];
V. Kovalenko, PoS (QFTHEP 2013) 052 (2013).

[7] C. Flensburg, G. Gustafson, L. Lönnblad, Eur. Phys. J. C **60** 233 (2009);
G. Gustafson, Acta Phys. Polon. B **40** 1981 (2009);
C. Flensburg, G. Gustafson, L. Lönnblad, JHEP 8, 103 (2011).

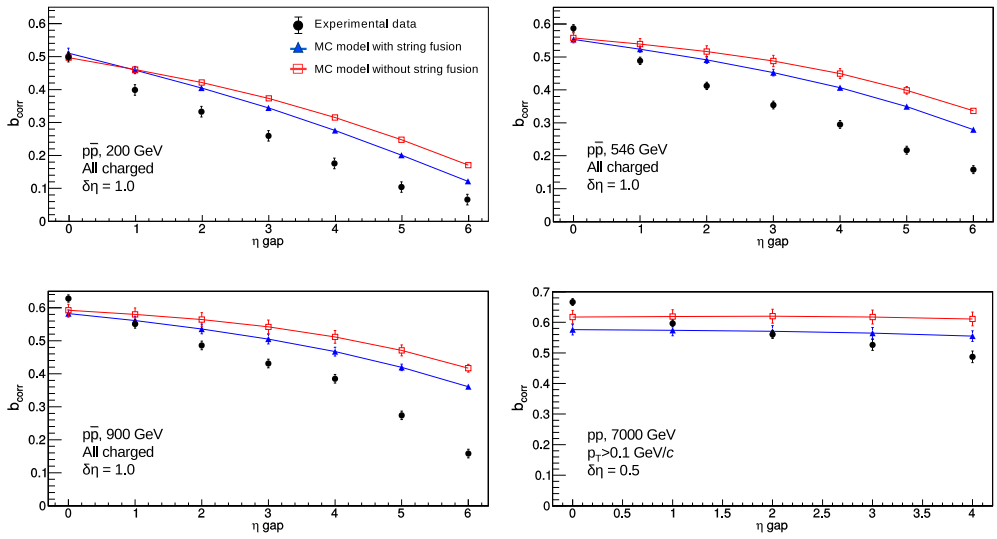

Figure 3: Correlation coefficient as a function of the pseudorapidity gap. Lines – calculation in Monte Carlo model with and without string fusion, points – experimental data [3, 4].

On the Binding Energies of Λ-Hyperons in Hyperhydrogen

Patrick Achenbach, Josef Pochodzalla, Florian Schulz

Institut für Kernphysik, Johannes Gutenberg-Universität, 55099 Mainz, Germany

DOI: http://dx.doi.org/10.3204/DESY-PROC-2014-04/12

The study of the binding energies of the Λ-hyperon in the lightest hypernuclei can reveal details of the strong nucleon-hyperon interaction. The binding energy of the Λ-hyperon, B_Λ, is defined as the Λ-hyperon separation energy from the non-strange core: $B_\Lambda = (M_{core} + M_\Lambda - M_Y)c^2$ where M_Y, M_{core} and M_Λ are the masses of the hypernucleus, its core and the Λ-hyperon respectively.

For many decades visual detectors like nuclear emulsions, with spatial resolutions better than one micrometer to track production and decay, and helium bubble chambers were employed. The masses of hypernuclei $A < 14$ were determined by analyzing the kinetic energies of decay products from the weak pionic decays. No bound states of Λp or Λn were found. The lightest systems are the s-shell ($A \leq 5$) hyperhydrogen and hyperhelium isotopes. The statistical error for the binding energies in light hypernuclei with the emulsion method ranges from 0.02 MeV for ${}^{5}_{\Lambda}$He to more than 0.7 MeV for ${}^{8}_{\Lambda}$He [1–3]. In one of these compilations a possible systematic error of 0.15 MeV [3] is quoted. In a later work by D.H. Davis systematic errors of the order of 0.04 MeV are given [4].

This era was followed by spectroscopic measurements at secondary, mesonic beams achieving energy resolutions of the order of $\Delta B_\Lambda \sim 1.5$ MeV (FWHM) [5]. Only recently energy resolutions of ~ 0.5 MeV (FWHM) have been achieved in the $(e, e'K^+)$ reaction using a dedicated kaon spectrometer at Jefferson Lab. The best reaction spectroscopy data in terms of resolution was reported for ${}^{12}_{\Lambda}$B [6] and ${}^{7}_{\Lambda}$He [7]. During the last three years the new method of decay-pion spectroscopy was pioneered at the Mainz Microtron MAMI, that has the potential to achieve mass measurements of several light hypernuclei with a precision comparable or better than with the emulsion technique.

${}^{3}_{\Lambda}$H decay mode	N	B_Λ (MeV)	Ref.
${}^{3}_{\Lambda}\mathrm{H} \to \pi^- + {}^{1}\mathrm{H} + {}^{2}\mathrm{H}$	24	$+0.23 \pm 0.11$	[1]
${}^{3}_{\Lambda}\mathrm{H} \to \pi^- + {}^{3}\mathrm{He}$	58	$+0.06 \pm 0.11$	[1]
both modes	82	$+0.15 \pm 0.08$	[1]
${}^{3}_{\Lambda}\mathrm{H} \to \pi^- + {}^{1}\mathrm{H} + {}^{2}\mathrm{H}$	16	-0.11 ± 0.13	[2]
${}^{3}_{\Lambda}\mathrm{H} \to \pi^- + {}^{3}\mathrm{He}$	86	$+0.05 \pm 0.08$	[2]
both modes	102	$+0.01 \pm 0.07$	[2]
${}^{3}_{\Lambda}\mathrm{H} \to \pi^- + {}^{1}\mathrm{H} + {}^{2}\mathrm{H}$	6	$+0.33 \pm 0.21$	[3]
${}^{3}_{\Lambda}\mathrm{H} \to \pi^- + {}^{3}\mathrm{He}$	26	$+0.13 \pm 0.15$	[3]
both modes	32	$+0.20 \pm 0.12$	[3]
mean (both modes)	204	$+0.13 \pm 0.05$	[1]

Table 1: Binding energies of ${}^{3}_{\Lambda}$H from emulsion experiments as compiled by Refs. [1–3]. The number of uniquely identified events, N, for determining B_Λ is given for two decay modes. The mean value was evaluated in Ref. [1] using both modes.

The lightest strange nuclear system is the hypertriton ${}^{3}_{\Lambda}\mathrm{H}$, found to be just bound. Available data on ${}^{3}_{\Lambda}\mathrm{H}$ is summarized in Table 1. From the Table it is seen that the number of uniquely identified events for determining B_Λ was in total of the order ~ 200 from different decay modes, analyzed and compiled in three different works. The mean value was evaluated in Ref. [1] using both decay modes to be $(0.13 \pm 0.05)\,\mathrm{MeV}$. The distribution of binding energies of ${}^{3}_{\Lambda}\mathrm{H}$ determined from pionic two-body and three-body decays is shown in Fig. 1. The FWHM of the distribution of binding energies is 2.1 MeV corresponding to a width $\sigma = 0.89\,\mathrm{MeV}$ if the distribution were Gaussian, which would allow for a determination of its mean value with a statistical uncertainty of $\Delta B_\Lambda = 0.89\,\mathrm{MeV}/\sqrt{204} = 0.06\,\mathrm{MeV}$. The published B_Λ values are shown in Fig. 2. From the data one can deduce that the mean B_Λ value of the 176 events of the two-body mode is 0.07 MeV and of the 46 events of the three-body mode is 0.13 MeV. The B_Λ values evaluated by Ref. [2] and by Ref. [1] differ by $(0.14 \pm 0.11)\,\mathrm{MeV}$.

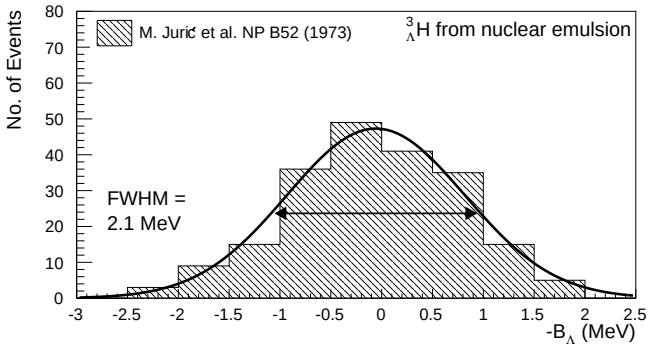

Figure 1: Distribution of binding energies of ${}^{3}_{\Lambda}\mathrm{H}$ determined from pionic two-body and three-body decays observed in emulsion experiments as compiled in Ref. [1]. A Gaussian function was fitted to the distribution for the illustration of the dispersion of the values with a FWHM of 2.1 MeV. The total number of events was 204 and the mean value was evaluated in Ref. [1] to be $B_\Lambda = 0.13 \pm 0.05\,\mathrm{MeV}$.

When going from a mass $A = 3$ to a $A = 4$ system the binding energy of the Λ-hyperon increases by about 1 MeV. Table 2 summarizes the B_Λ values for ${}^{4}_{\Lambda}\mathrm{H}$. The mean value was evaluated in Ref. [1] using only three-body decay modes to be $(2.04 \pm 0.04)\,\mathrm{MeV}$. In the same publication the B_Λ values for the $\pi^- + {}^1\mathrm{H} + {}^3\mathrm{H}$ decay mode, $2.14 \pm 0.07\,\mathrm{MeV}$, and for $\pi^- + {}^2\mathrm{H} + {}^2\mathrm{H}$ mode, $1.92 \pm 0.12\,\mathrm{MeV}$, are reported separately. They differ by $(0.22 \pm 0.14)\,\mathrm{MeV}$. The mean B_Λ value of the 760 events of the two-body mode reported by Refs. [2, 3] is 2.28 MeV which would indicate a $\sim 0.2\,\mathrm{MeV}$ stronger binding. This decay mode is not included because of the larger systematic error in the pion range-energy relation for pion ranges greater than 3 cm [1].

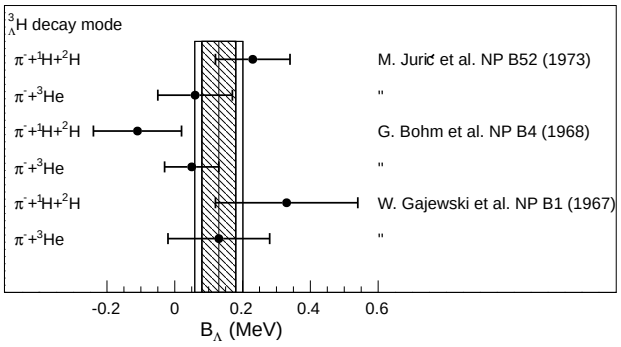

Figure 2: Measurements of the binding energy of ${}^{3}_{\Lambda}\mathrm{H}$ determined from two-body and three-body pionic decays observed in emulsion experiments [1–3] (with statistical errors only). The mean value was evaluated in Ref. [1] (shaded bands with statistical and total uncertainties).

The mirror pair of hypernuclei ${}^{4}_{\Lambda}$H and ${}^{4}_{\Lambda}$He is especially important because it is used as the main source of information about the charge symmetry breaking (CSB) in the ΛN interaction. Charge symmetric interactions do not distinguish between the nucleon isospin channels Λp and Λn. CSB effects in the strong interaction occurs because of the difference between the masses of the quarks in hadronic and nuclear systems. In mirror hypernuclei the binding energies of the Λ-hyperon could reveal CSB contributions in the strong interaction. The distribution of binding energies of $A = 4$ hypernuclei is shown in Fig. 3. The binding energies for the (0^+) ground states, $B_\Lambda({}^{4}_{\Lambda}\mathrm{H}) = 2.04 \pm 0.04$ MeV and $B_\Lambda({}^{4}_{\Lambda}\mathrm{He}) = 2.39 \pm 0.03$ MeV systematically differ, the difference being $\Delta B_\Lambda = 0.35 \pm 0.06$ MeV. However, the FWHM of the distributions of binding energies is larger than 1 MeV. The Coulomb correction due to core compression induced by the presence of the Λ-hyperon in the nucleus was calculated to be less than 0.05 MeV [8]. If the mirror pair difference is as large as 0.35 MeV the CSB effect in the ΛN interaction would be much larger than in the NN interaction.

${}^{4}_{\Lambda}$H decay mode	N	B_Λ (MeV)	Ref.
${}^{4}_{\Lambda}\mathrm{H} \to \pi^- + {}^{1}\mathrm{H} + {}^{3}\mathrm{H}$	56	$+2.14 \pm 0.07$	[1]
${}^{4}_{\Lambda}\mathrm{H} \to \pi^- + {}^{2}\mathrm{H} + {}^{2}\mathrm{H}$	11	$+1.92 \pm 0.12$	[1]
both three-body modes	67	$+2.08 \pm 0.06$	[1]
${}^{4}_{\Lambda}\mathrm{H} \to \pi^- + {}^{1}\mathrm{H} + {}^{3}\mathrm{H}$	63		[2]
${}^{4}_{\Lambda}\mathrm{H} \to \pi^- + {}^{2}\mathrm{H} + {}^{2}\mathrm{H}$	7		[2]
both three-body modes	70	$+2.08 \pm 0.06$	[2]
${}^{4}_{\Lambda}\mathrm{H} \to \pi^- + {}^{4}\mathrm{He}$	552	$+2.29 \pm 0.04$	[2]
${}^{4}_{\Lambda}\mathrm{H} \to \pi^- + {}^{1}\mathrm{H} + {}^{3}\mathrm{H}$	21		[3]
${}^{4}_{\Lambda}\mathrm{H} \to \pi^- + {}^{2}\mathrm{H} + {}^{2}\mathrm{H}$	2		[3]
both three-body modes	23	$+1.86 \pm 0.10$	[3]
${}^{4}_{\Lambda}\mathrm{H} \to \pi^- + {}^{4}\mathrm{He}$	208	$+2.26 \pm 0.07$	[3]
mean (three-body)	155	$+2.04 \pm 0.04$	[1]

Table 2: Binding energies of ${}^{4}_{\Lambda}$H from emulsion experiments as compiled by Refs. [1–3]. The number of uniquely identified events for determining B_Λ is given for three decay modes. The mean value was evaluated in Ref. [1] using only the three-body modes.

At the Mainz Microtron MAMI the first high-resolution spectroscopy of pions from decays of hypernuclei was performed. The associated strangeness production with the incident electron beam on a thin ^{9}Be target was tagged by the detection of kaons with the spectrometer KAOS. Pions were detected in coincidence with two high-resolution spectrometers. Details on the setup, the experimental conditions, and the identification of pionic weak decays can be found in Refs. [9, 10]. The binding energy of stopped ${}^{4}_{\Lambda}$H was deduced from the two-body decay mode ${}^{4}_{\Lambda}\mathrm{H} \to \pi^- + {}^{4}\mathrm{He}$ with a 10^{-3} relative momentum resolution [11]. Details on the statistical and systematic error are found in the reference.

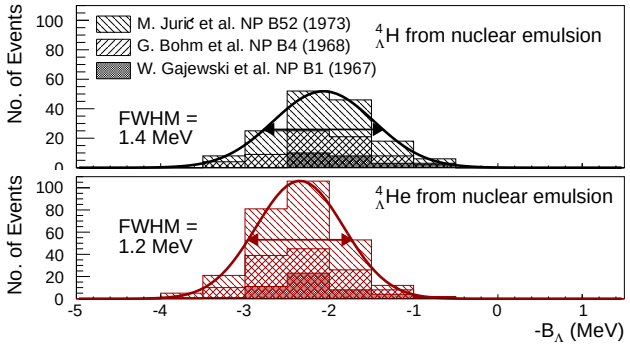

Figure 3: Distribution of binding energies of ${}^{4}_{\Lambda}$H and ${}^{4}_{\Lambda}$He determined from pionic three-body decays observed in emulsion experiments as compiled in Refs. [1–3]. A Gaussian function was fitted to the distribution for the illustration of the dispersion of the values with a FWHM of 1.2–1.4 MeV. The total number of events was 155 resp. 279 and the mean value was evaluated in Ref. [1] to be $B_\Lambda = 2.04 \pm 0.04$ MeV resp. 2.39 ± 0.03 MeV.

In Fig. 4 the preliminary MAMI result on the binding energy of ${}^{4}_{\Lambda}\mathrm{H}$ is compared to the emulsion experiments [1–3]. Full circles present evaluations from three-body decays, open circles from two-body decays, error bars on the emulsion values are statistical only. The mean values were evaluated in Ref. [1] excluding data from the two-body decay mode, where the shaded bands show statistical and total uncertainties. The error bars on the MAMI value are statistical (inner) and total (outer). The figure also shows the data from the pioneering decay-pion spectroscopy with a stopped K^--beam at KEK [12].

A major effort in hypernuclear physics is to understand the interaction between hyperons and nucleons. Parameters of many employed phenomenological models are fitted to reproduce the binding energies of light hypernuclei. Many theoretical descriptions include ΛNN three-body forces and charge symmetry breaking terms to yield an agreement with available experimental data over a wide range of hypernuclear masses. In the literature the binding energies of the light hyperhydrogen isotopes are often quoted with errors of $0.04 - 0.05\,\mathrm{MeV}$. One should be aware of systematic errors. A cross-check of the experimental values with an independent method with high resolution seems timely and necessary.

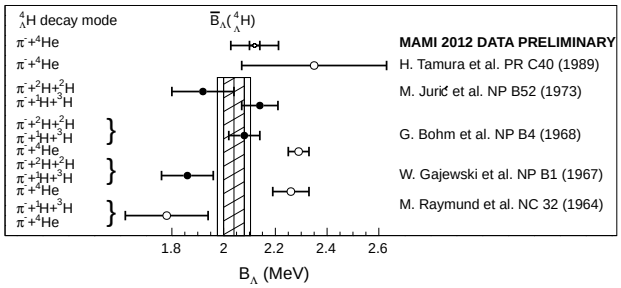

Figure 4: Measurements of the binding energy of ${}^{4}_{\Lambda}\mathrm{H}$ determined from different pionic decays. Details are discussed in the text.

This work was supported in part by Deutsche Forschungsgemeinschaft (SFB 1044), by Carl Zeiss Foundation, by European Community Research Infrastructure Integrating Activity HadronPhysics2 (SPHERE).

References

[1] Jurić, M. et al., Nucl. Phys. **B52** 1 (1973).

[2] Bohm, G. et al., Nucl. Phys. **B4** 511 (1968).

[3] Gajewski, W. et al., Nucl. Phys. **B1** 105 (1967).

[4] Davis, D. H., Nucl. Phys. **A547** 369 (1992).

[5] Hashimoto, O. and Tamura, H., Prog. Part. Nucl. Phys. **57** 564 (2006).

[6] Tang, L. et al. (HKS Collaboration), Phys. Rev. **C90** 034320 (2014).

[7] Nakamura, S. N. et al. (HKS Collaboration), Phys. Rev. Lett. **110** 012502 (2013).

[8] Bodmer, A. and Usmani, Q., Phys. Rev. **C31** 1400 (1985).

[9] Achenbach, P. et al. (A1 Collaboration), Few-Body Syst. **55** 887 (2014).

[10] Esser, A. et al. (A1 Collaboration), Nucl. Phys. **A914** 519 (2013).

[11] Esser, A., Nagao S., Schulz, F., Achenbach, P. et al. (A1 Collaboration), *Observation of ${}^{4}_{\Lambda}H$ hyperhydrogen by decay-pion spectroscopy in electron scattering*, arXiv:1501.06823 (2015).

[12] Tamura, H. et al., Phys. Rev. **C40** 479 (1989).

Two Component Model with collective Flow for Hadroproduction in heavy-ion Collisions.

Nadezda Chernyavskaya[1,2], *Alexander Bylinkin*[1,2], *Andrey Rostovtsev*[3]

[1]ITEP, Bolshaya Cheremushkinskaya 25, 117218, Moscow, Russia
[2]MIPT, Institutskiy per. 9, 141700 Dolgoprudny, Moscow Region, Russia
[3]IITP RAS, Bolshoy Karetny per. 19, 127994 Moscow, Russia

DOI: http://dx.doi.org/10.3204/DESY-PROC-2014-04/47

Hadroproduction in high-energy collisions can be described by two distinct mechanisms [1, 2]. In this approach [1] the charged particle spectra are aproximated as a function of the particles' transverse momentum p_T by a sum of an exponential (Boltzmann-like) and a power-law distributions:

$$\frac{d\sigma}{p_T dp_T} = A_e \exp\left(-E_{Tkin}/T_e\right) + \frac{A}{(1+\frac{p_T^2}{T^2 \cdot N})^N}, \tag{1}$$

where $E_{Tkin} = \sqrt{p_T^2 + M^2} - M$ with M equal to the produced hadron mass. A_e, A, T_e, T, N are the free parameters obtained from the fit to the experimental data. The exponential term stands for the release of 'thermalized' particles by the preexisting valence quarks and a quark-gluon cloud coupled to them inside the colliding baryon. The power-law term accounts for the fragmentation of mini-jets formed by the secondary partons produced at the first stage of the collision.

The goal of this work is to compare the shapes of charged hadron spectra produced in $\gamma\gamma$ and pp interactions (already studied in [2, 3]) with a more complex case of heavy-ion collisions.

ALICE Collaboration [4] provides data on lead-lead collisions in the range of transverse momentum p_T up to 50 GeV. Figure 1 shows experimental data on $\gamma\gamma$ [5], pp [6] and lead-lead [4] collisions fitted with the parameterization introduced (1). From the shape of the lead-lead collision's spectrum one can notice that an additional power-law term is needed to describe the data in terms of the introduced approach :

$$\frac{d\sigma}{p_T dp_T} = A_e \exp\left(-E_{Tkin}/T_e\right) + \frac{A}{(1+\frac{p_T^2}{T^2 \cdot N})^N} + \frac{A_1}{(1+\frac{p_T^2}{T_1^2 \cdot N_1})^{N_1}} \tag{2}$$

For heavy-ion collisions nuclear modification factor R_{AA} is an important variable. Figure 2(a) shows R_{AA} for lead-lead collisions measured at ALICE [4] together with contributions from the three terms of eq. (2) independently, each of them divided over the spectrum in pp-collisions measured at the same c.m.s. energy [6]. Studying of the R_{AA} for lead-lead collisions at ALICE [4] can help us to understand the following picture of hadroproduction [7]:

1. The bulk of low-p_T particles originates from the 'quark-gluon soup' formed in the heavy-ion collision and has an exponential p_T distribution, as shown by the red dashed line in Figs. 1 and 2.

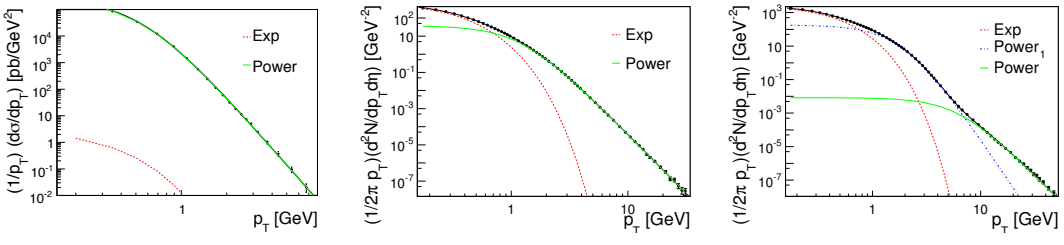

(a) (b) (c)

Figure 1: Charged particle spectra in $\gamma\gamma$ [5] a), pp [6] b) and in central lead-lead collisions [4] c) fitted to the function (2): the red (dashed) line shows the exponential term and the green (solid) and blue (dash-dot) lines - two power-law terms.

2. The high-p_T tail (green solid line in Figs. 1 and 2) accounts for the mini-jets that pass through the nuclei. When these jets hadronize into final state particles *outside* the nuclei, we get the same power-law term parameter N as in pp-collisions (Figs. 1 b) and c)), resulting in a constant suppression (R_{AA}) of high-p_T (> 20 GeV) particles (Fig. 2). While passing through the nuclei these jets should loose about $\frac{dE}{dz} \cdot R_A \sim 7$ GeV [8], where R_A is the radius of the nuclei. Therefore, hadrons with $p_T < 7$ GeV produced from these jets will be largely suppressed, as it seen in the Fig. 2.

3. However if the mini-jet fragmentation occurs before the produced particles leave the nuclei volume, they are affected by multiple rescatterings from the media, loose energy and their distribution (blue dash-dot line in Fig. 1 and 2) becomes closer to the exponent.

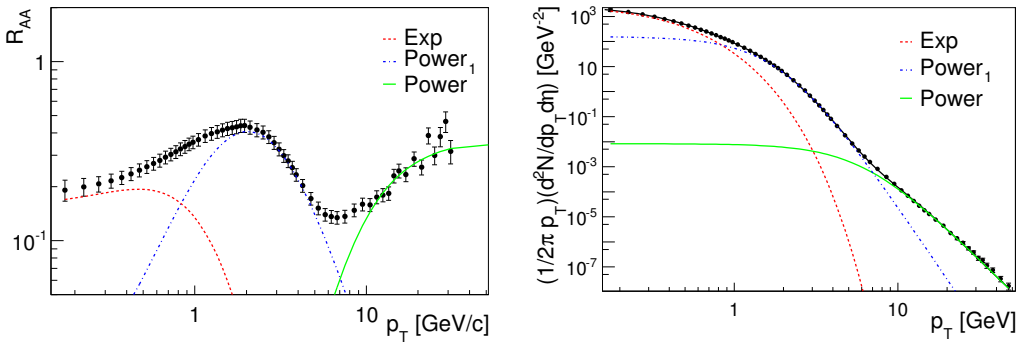

(a) (b)

Figure 2: (a): R_{AA} measured for central Pb-Pb collisions [4] shown with the terms of (2) independently divided over the fit (1) of the pp-data at the same c.m.s energy: the red (dashed) line shows the exponential term and the green (solid) and blue (dash-dot) lines - two power-law terms. (b): Central lead-lead collisions [4] fitted with (4): the red (dashed) line shows the hydrodynamic term and the green (solid) and blue (dash-dot) lines - two power-law terms.

One can see, hadroproduction dynamics can be characterized by complexity (number of involved partons) of the colliding system: $\gamma\gamma$ collisions, pp-collisions, heavy-ion collisions.

In heavy-ion collisions when a large colliding system is formed, one should also take effects of the 'collective motion' into account [9] and the multiparticle production is usually considered in terms of relativistic hydrodynamics. Therefore, it is suggested to modify the introduced approach (1) using recent theoretical calculations [9]. The idea of hydrodynamic approach is that the thermalized system expands collectively in longitudinal direction generating the transverse flow by the high pressure in the colliding system. The distidution function is still the Boltzmann distribution, but it is boosted to the expanding system. According to this approach the radiation of thermalized particles can be parameterized by the following formula:

$$\frac{\mathrm{d}n}{p_T \mathrm{d}p_T} \propto \int_0^R r\ \mathrm{d}r\ m_T\ I_0\left(\frac{p_T \sinh\rho}{T_e}\right) K_1\left(\frac{m_T \cosh\rho}{T_e}\right), \tag{3}$$

where $\rho = tanh^{-1}\beta_r$ and $\beta_r(r) = \beta_s(\frac{r}{R})$, with β_s standing for the surface velocity. In this analysis we take $\beta_s = 0.5c$ which is consistent with previous observations [9]. We substitute the exponential term in (1) by (3) and use this hydrodynamic approach to fit the recent experimental data on lead-lead collisions measured by the Alice Collaboration [4] at $\sqrt{s} = 2.76$ TeV. These data are shown in Fig. 2(b) together with the fit:

$$\frac{\mathrm{d}n}{p_T \mathrm{d}p_T} = A_e \cdot \int_0^R r\ \mathrm{d}r\ m_T\ I_0\left(\frac{p_T \sinh\rho}{T_e}\right) K_1\left(\frac{m_T \cosh\rho}{T_e}\right) + \frac{A}{(1+\frac{p_T^2}{T^2 \cdot N})^N} + \frac{A_1}{(1+\frac{p_T^2}{T_1^2 \cdot N_1})^{N_1}}. \tag{4}$$

Hydrodynamic extension slightly modifies the description of data and an additional power-law term is still needed. But the temperatures T_e obtained from the fits with and without transverse flow taken into account differ significantly [12] (Fig. 3)

The thermalized production of charged hadrons (described by function (3)) can be extracted from the whole statistical ensemble and in this paper it is proposed to study the variations of the temperature-like parameter T_e in (3) with the centrality and the c.m.s. energy in heavy-ion collisions. It is interesting to consider the experimental data measured at RHIC and LHC together and combine it in terms of energy density. In this paper we consider the experimental data measured in AuAu collisions at $\sqrt{s} = 200$ GeV/N and $\sqrt{s} = 130$ GeV/N by PHENIX [13, 14] and PbPb collisions at $\sqrt{s} = 2.76$ TeV/N by ALICE [4].

Having calculated the energy density ε based on theoretical caculations [15], one can plot the temperature T_e extracted from (4) as a function of it, as shown in Fig. 3. A smooth transition in the T_e values between ALICE and RHIC measurements is observed.

One can notice interesting behavior of the temperature T_e as a function of energy density ($\varepsilon \propto T_e^4 + B$), which is in a good agreement with the Bag model [16], with $B = 0.25$ GeV/fm^3, as determined from the fit in Fig. 3. Next, one can see that the temperature T_e of the final state particles reaches a certain limit for high energy densities. This might be explained from QGP theory that considers the phase transition temperature T_c from QGP to final state hadrons. For high values of ε one can notice, that the observed freeze-out temperature is $T_{fo} \approx 145$ MeV, and (as one can expect) is slightly below the critical temperature $T_c \sim 155 - 160$ MeV for QGP obtained in different calculations [17, 18]. That gives us another confirmation of applicability of such an approach (4) to decribe hadroproduction in heavy-ion collisions.

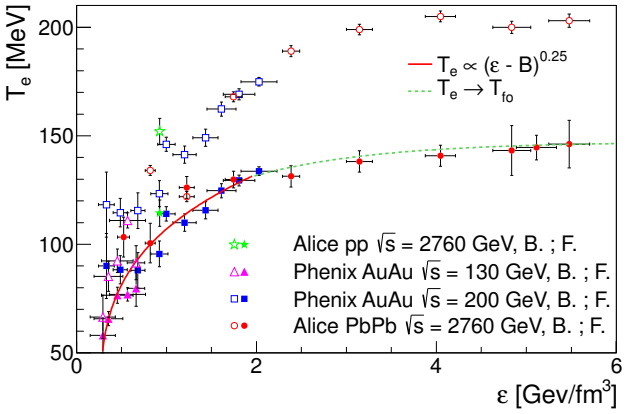

Figure 3: Temperature of the final state hadrons coming from the 'thermalized' part of the spectra in heavy-ion collisions as a function of energy density. Full points show the results extracted from the fit by taking into account the collective flow 4 (F. in the legend); open points show the results when using a fit with the Boltzmann exponent 2 (B. in the legend). Solid line stands for the $T_e \propto (\varepsilon - B)^{0.25}$ fit and dashed line shows $T_e \to const$ behavior.

References

[1] A. A. Bylinkin and A. A. Rostovtsev, Phys. Atom. Nucl. **75** (2012) 999 Yad. Fiz. **75** (2012) 1060; A. A. Bylinkin and A. A. Rostovtsev, arXiv:1008.0332 [hep-ph].

[2] A. A. Bylinkin and A. A. Rostovtsev, arXiv:1404.7302 [hep-ph].

[3] A. A. Bylinkin and A. A. Rostovtsev, Eur. Phys. J. C **72**, 1961 (2012) arXiv:1112.5734 [hep-ph].

[4] B. Abelev *et al.* [ALICE Collaboration], Phys. Lett. B **720** (2013) 52 [arXiv:1208.2711 [hep-ex]].

[5] G. Abbiendi *et al.* [OPAL collaboration], Phys.Lett.B**651**:92-101,2007

[6] B. B. Abelev *et al.* [ALICE Collaboration], Eur. Phys. J. C **73** (2013) 2662 [arXiv:1307.1093 [nucl-ex]].

[7] A. A. Bylinkin, N. S. Chernyavskaya and A. A. Rostovtsev, Phys. Rev. C **90** (2014) 018201 [arXiv:1405.3055 [hep-ph]].

[8] X. -N. Wang, Phys. Rept. **280** (1997) 287 [hep-ph/9605214].

[9] E. Schnedermann, J. Sollfrank and U. W. Heinz, Phys. Rev. C **48** (1993) 2462 [nucl-th/9307020].

[10] C.Tsallis, J.Stat.Phys., **52**, 479, 1988.

[11] R. Hagedorn, Riv. Nuovo Cim. **6N10** (1984) 1.

[12] A. A. Bylinkin, A. A. Rostovtsev and N. S. Chernyavskaya, arXiv:1305.0387 [hep-ph].

[13] S. S. Adler *et al.* [PHENIX Collaboration], Phys. Rev. C **69** (2004) 034909 [nucl-ex/0307022].

[14] K. Adcox *et al.* [PHENIX Collaboration], Phys. Rev. C **69** (2004) 024904 [nucl-ex/0307010].

[15] I. N. Mishustin and J. I. Kapusta, Phys. Rev. Lett. **88** (2002) 112501 [hep-ph/0110321].

[16] A. Chodos, R. L. Jaffe, K. Johnson, C. B. Thorn and V. F. Weisskopf, Phys. Rev. D **9** (1974) 3471.

[17] F. Karsch, K. Redlich and A. Tawfik, Eur. Phys. J. C **29** (2003) 549 [hep-ph/0303108].

[18] A. Majumder and B. Muller, Phys. Rev. Lett. **105** (2010) 252002 [arXiv:1008.1747 [hep-ph]].

Identification of hadronic tau decays in CMS.

Raman Khurana[1] on behalf of the CMS collaboration

[1] Saha Institute of Nuclear Physics, Kolkata-700 064, India

DOI: http://dx.doi.org/10.3204/DESY-PROC-2014-04/181

The algorithm used for reconstruction and identification of hadronic tau decays by the CMS experiment at the LHC is presented. The tau reconstruction in CMS takes advantage of the particle-flow algorithm which allows to reconstruct individual hadronic decay modes. The performance of the algorithm in terms of tau identification efficiency and rates for jets to be misidentified as hadronic tau decays is measured in *pp* collision data recorded in 2012 at a center-of-mass energy ($\sqrt{s}$) of 8 TeV, corresponding to an integrated luminosity of 19.7 fb^{-1}.

1 Tau leptons and their decay

Tau is the heaviest known lepton ($m_\tau = 1.78$ GeV/c^2) which decays into lighter leptons (BR $\sim 35\%$) or hadrons τ_h (BR $\sim 65\%$) in the presence of upto two neutrinos. CMS has developed Hadron Plus Strips (HPS) [1, 2] algorithm for reconstruction of hadronic tau decay modes. It uses decay mode identification techniques which allows to reconstruct hadronic tau decays, denoted by τ_h, with high efficiency and suppress the potentially large backgrounds from quarks and gluons that occasionally hadronize into low particle multiplicity jets.

2 Particle Flow and Hadron Plus Strips algorithm

CMS utilises the fine granularity of the calorimeters, precision tracking and muon system to identify and reconstruct final state particles in an event. This is achieved by the use of particle flow (PF) [3] algorithm to make the best use of information available from all the sub-detectors and reconstruct all the stable partiles (namely, charged hadrons, photons, neutral hadrons, muons and electrons) in the detector. The resulting list of particles is used to reconstruct hadronic decays of taus by the HPS algorithm.

The HPS algorithm is designed to reconstruct individual decay modes of the tau. This requires reconstruction of the neutral pions that are produced in the majority of hadronic tau decays. The high probability for photons originating from $\pi^0 \to \gamma\gamma$ decays to convert within the volume of the tracking detector is accounted for by clustering the photon constituents of the jet that seeds the tau reconstruction into $\eta - \phi$ *strips*. The size of the strips, 0.20×0.05, is enlarged in η direction, taking into consideration the bending of e^+e^- pairs produced by photon conversions in the 3.8 Tesla magnetic field. Strips containing one or more photons and passing a cut $p_T > 2.5$ GeV on the sum of photon transverse momenta are kept as π^0 candidates for further processing. The τ_h candidates are built by combining the the neutral objects with charged hadrons reconstructed by the PF algorithm. Figure 1 (left) shows the

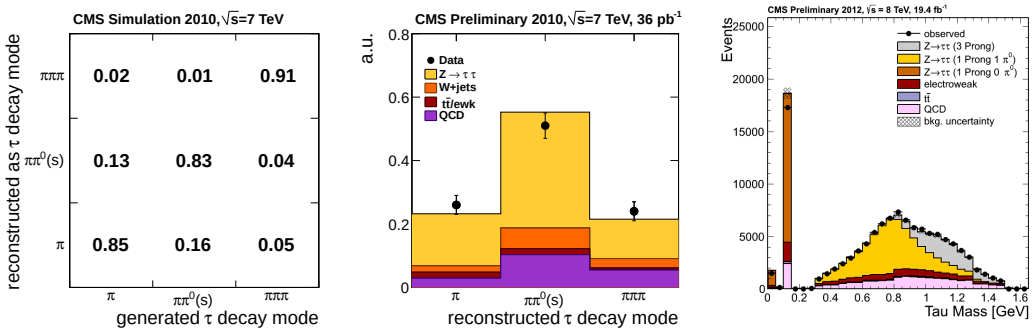

Figure 1: Performance of the decay mode reconstruction.

fraction of generated taus of a given type reconstructed in a certain decay mode for a sample of simulated $Z \to \tau\tau$ events. A data-to-Monte Carlo (MC) comparison in $Z \to \tau\tau \to \mu\tau_h$ events of the number of taus reconstructed in different tau decay modes and of the τ_h candidate mass is shown in Figure 1.

Requiring reconstructed hadronic tau candidates to pass strict isolation requirements constitutes the main handle to reduce the large jet background. Being colorless and produced in decays of colorless bosons, tau leptons are typically isolated with respect to other particles in the event, and so are their decay products, in contrast to quark and gluon jets. The isolation sum is computed using two different approaches :

- Cut based isolation : The isolation of the τ_h candidates is computed by summing the transverse momenta of charged particles of $p_T > 1$ GeV plus photons of $E_T > 1.5$ GeV within a cone of size of $\triangle R = 0.5$ centered on the τ_h direction. The contribution of pile-up to the τ_h isolation is subtracted by means of $\triangle\beta$ corrections.

$$I_\tau = \Sigma p_T^{charged}\,(d_Z < 0.2 \text{ cm}) + \max\left(p_T^\gamma - \triangle\beta, 0\right) \tag{1}$$

  The $\triangle\beta$ corrections are computed by summing the p_T of charged particles that have a longitudinal impact parameter $d_Z > 0.2$ cm with respect to the τ_h production vertex and are within a cone of size $\triangle R = 0.8$ around the τ_h direction. The sum is scaled by a factor 0.4576, chosen to make the τ_h identification efficiency insensitive to pile-up.

$$\triangle\beta = 0.4576 \cdot \Sigma p_T^{charged}\,(d_Z > 0.2 \text{ cm}) \tag{2}$$

- Multivariate (MVA) approach : The MVA-based tau identification discriminator utilizes the transverse impact parameter of *leading* (highest p_T) track of the τ_h candidate. In case of τ_h candidates reconstructed in the three charged hadron decay mode the distance between the tau production and decay vertex, reconstructed by fitting the three tracks to a common vertex, is used as additional handle to remove the jet $\to \tau_h$ background. A boosted decision tree discriminator (BDT) has been trained to discriminate hadronic tau decays (*signal*) from quark and gluon jets (*background*).

Several working points are provided, corresponding to looser or tighter cuts on the isolation p_T-sum I_τ and on the MVA output respectively, and yielding different tau identification efficiency and jet $\to \tau_h$ misidentification rates.

3 Efficiency and misidentification rate

The efficiency to identify hadronic tau decays is measured in Z$\rightarrow \tau\tau \rightarrow \tau_\mu\tau_h$ events selected in the 2012 data using the *tag*-and-*probe* method. The hadronic tau identification efficiency ϵ_τ is defined as the ratio of the number of genuine hadronic taus passing the tau identification discriminator under study over the total number of genuine hadronic taus:

$$\epsilon_{tau} = \frac{N^{\tau}_{pass}}{N^{\tau}_{pass} + N^{\tau}_{fail}} \tag{3}$$

The number of hadronic taus passing and failing the tau identification discriminator under study, N^{τ}_{pass} and N^{τ}_{fail}, is obtained via a simultaneous template fit. The multiplicity of tracks within a cone size $\triangle R = 0.5$ around the τ_h candidate, N_{tracks}, is used as observable to perform the fit. The efficiency measured in data and simulation is shown in Fig. 2 along with the data-to-simulation scale factors for both cut based and MVA-based tau identification discriminators. The probability for quark and gluon jets to be misidentified as hadronic tau decays is measured in QCD multijet events. The results are shown in Fig 3.

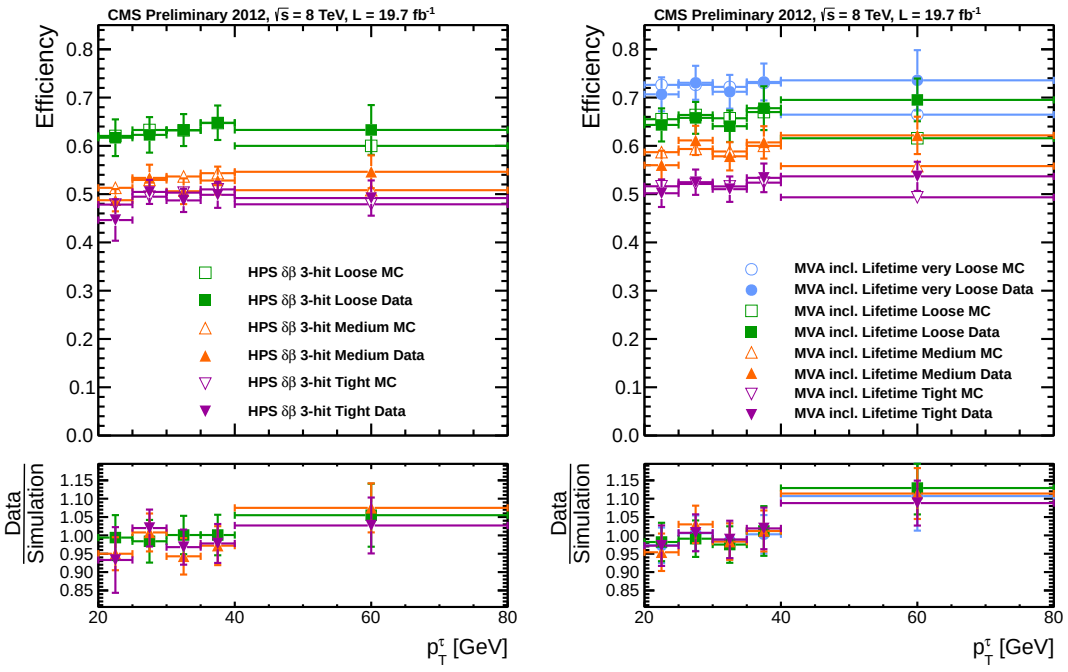

Figure 2: Tau identification efficiency measured as function of p_T in $Z \rightarrow \tau\tau \rightarrow \tau_\mu\tau_h$ events compared to Monte Carlo predictions, for the cut based HPS combined isolation (left) and for the MVA-based tau identification discriminator that includes tau lifetime information (right).

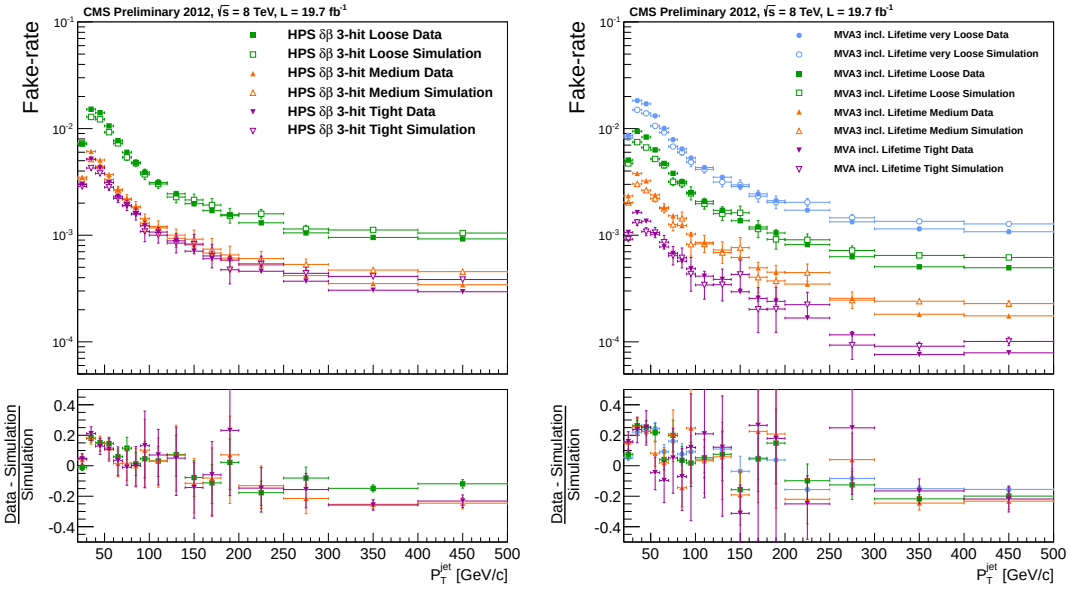

Figure 3: Jet $\rightarrow \tau_h$ misidentification rate in QCD multijet events, for cut based (left) and MVA-based (right) tau identification discriminators.

4 Conclusions

CMS has developed an advanced and robust τ_h reconstruction algorithm, which has been successfully commissioned with the data collected in LHC run 1. The decay mode of the tau is reconstructed correctly with a probability higher than 80%. The tau identification efficiency amounts to 50–60% and is almost independent as function of p_T, while the jet $\rightarrow \tau_h$ misidentification rate varies strongly with p_T, ranging from about 1% for low p_T jets and loose tau identification criteria to $\mathcal{O}(10^{-4})$ for high p_T jets and tight tau identification criteria.

References

[1] CMS Collaboration, *Performance of tau-lepton reconstruction and identification in CMS*, *JINST* **7** (2012) P01001, [ins-det/1109.6034].

[2] CMS Collaboration, Tau ID Performance, CMS-DP-2014-015, https://cds.cern.ch/record/1704439

[3] CMS Collaboration, Particle-Flow Event Reconstruction in CMS and Performance for Jets, Taus, and E_T^{miss}, CMS-PAS PFT-09-001 (2009).

Search for Supersymmetry in Events with one Photon, Jets and missing transverse Energy at $\sqrt{s} = 8$ TeV

Maximilian Knut Kiesel on behalf of the CMS collaboration

1. Physikalisches Institut B, RWTH Aachen University, Aachen, Germany

DOI: http://dx.doi.org/10.3204/DESY-PROC-2014-04/278

Gauge mediated supersymmetry breaking (GMSB) [1] is a scenario for physics beyond the standard model (SM) which can stabilize the mass of the SM Higgs boson, allow the grand unification of forces, and avoid the flavor problems endemic in other SUSY breaking scenarios.

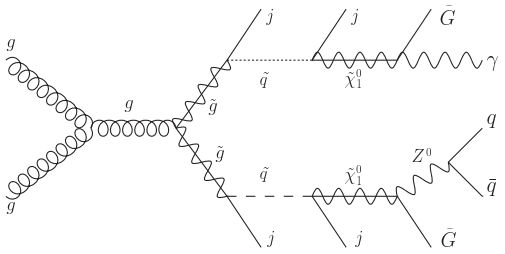

Figure 1: Event diagram for a typical photon final state expected within the GGM framework for a wino-like neutralino. A gluino pair is produced, which decays via squarks to neutralinos. The neutralinos decay to a photon or Z boson and a gravitino.

This search [2] is interpreted in the context of General Gauge Mediation (GGM) [3], in which the lightest SUSY particle is the gravitino ($\tilde{G}$) and the next-to-lightest SUSY particle the lightest neutralino ($\tilde{\chi}_1^0$), which can decay to a photon and a $\tilde{G}$ if the $\tilde{\chi}_1^0$ is bino- or wino-like. A typical process is shown in Fig. 1. R-parity is assumed to be conserved.

The data was recorded with the CMS detector [4] at the LHC during the 2012 run period with a center-of-mass energy of $\sqrt{s} = 8\,\text{TeV}$. It corresponds to an integrated luminosity of $19.7\,\text{fb}^{-1}$. On trigger level, one photon candidate with large transverse momentum and hadronic activity is required.

For the signal region, events with at least one photon reconstructed in the central part of the detector and with a transvere momentum $p_{\text{T}^*} \geq 110\,\text{GeV}$, hadronic activity $H_{\text{T}} \geq 500\,\text{GeV}$, two jets, missing transverse energy $\not{E}_{\text{T}} \geq 100\,\text{GeV}$, but no electrons nor muons are selected. The $\not{E}_{\text{T}}$ and the particles which are clustered to jets are reconstructed using the particle-flow (PF) algorithm. The H_{T} is the scalar sum of the transverse momentum of all jets and all photon-like objects. The transverse momentum of the photon (p_{T^*}) is not estimaded by the energy deposit in the electromagnetic calorimeter only, but is estimated by the $p_{\text{T}}$of the matched jet to the photon. This measurement of the transverse momentum is compatible for real photons and jets with a large neutral electromagnetic component. This is important for the major background estimation method, which relies on a similar kinematic for both types of objects. In addition, the photon identification requires that the energy deposits in the calorimeters must be photon-like. To discriminate between electrons and photons, the activity in in the

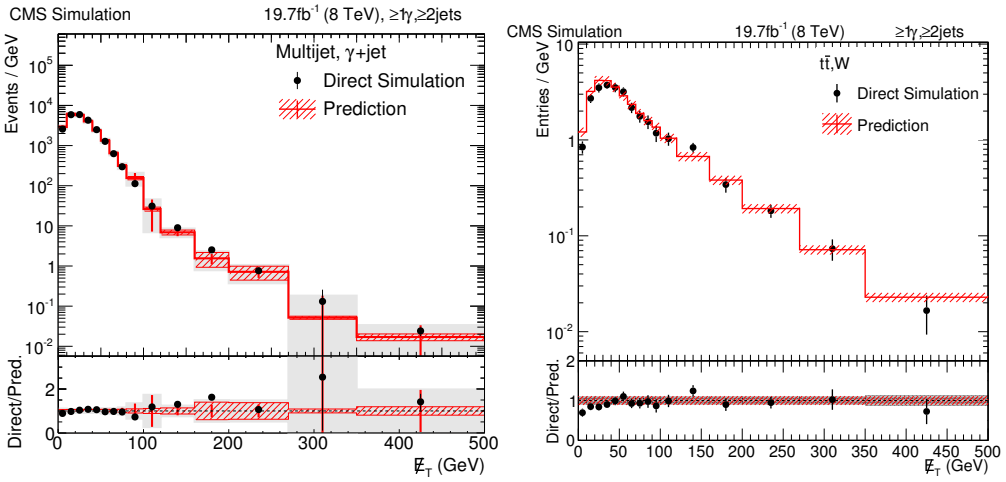

Figure 2: $\not\!\!E_{\mathrm{T}}$ distribution for simulated multijet and photon plus jet events (left) and simulated $\mathrm{t\bar{t}}$ and W boson events (right). The hatched area shows the systematical uncertainty of the data-driven background estimation method, and the gray area the total uncertainty.

tracker between vertex and the energy deposit in the calorimeter is restricted. Photons are also required to be isolated from other particles. Therefore, the sums of p_T of all charged hadrons, neutral hadrons and photons (except for the photon candidate itself), reconstructed with the PF algorithm within $\Delta R < 0.3$ to the photon candidate are calculated. These isolation deposits from charged hadrons ($\mathrm{I}_{\pm}$), neutral hadrons (I_0), and photons (I_γ) are required to be smaller than a threshold depending on the photon's transverse momentum.

The dominant background from SM processes origins from photon plus jet, or multijet events where one jet is misidentified as a photon. Mismeasurement of jets can lead to large $\not\!\!E_{\mathrm{T}}$ in these events. The contribution of these events to the signal region is estimated simultaneously from events with photon-like jets and low missing transverse energy using data. The photon-like jets are similar to the photon with respect to the shower shape, the tracker activity and the hadronic component, but have larger isolation deposits $\mathrm{I}_{\pm}$, I_0, and I_γ. The ratio of the number of events in the signal region to the number of events in this control region is calculated for $\not\!\!E_{\mathrm{T}} < 100\,\mathrm{GeV}$ in bins of $p_{\mathrm{T}*}$ and the hadronic recoil. Hadronic recoil is the vectorial sum of the p_T of all jets, excluding the photon(-like) object. Events of the control sample with $\not\!\!E_{\mathrm{T}} \geq 100\,\mathrm{GeV}$ are scaled by this weight to estimate the contribution of multijet and photon plus jet production in the signal region. This method is tested on simulation: Figure 2 (left) shows the $\not\!\!E_{\mathrm{T}}$ distribution for simulated multijet and photon plus jet events compared to the prediction by the method described above. The direct simulation is in agreement with the prediction from simulation.

The contribution from electrons being misidentified as photons is estimated also from data. The probability of an electron faking a photon ($f_{e\to\gamma}$) is measured using the tag-and-probe method with $Z \to ee$ events. The rate is evaluated in bins of p_{T}, number of tracks emerging from the Z-boson vertex, and the number of vertices. A multidimensional fit is used to parametrize the misidentification probability. To estimate the background, a control region with electrons is defined by selecting photon candidates with hits in the tracker, which can be extrapolated to the energy deposit in the calorimeter. This sample is scaled event-by-event by $f_{e\to\gamma}$. Figure 2 (right)

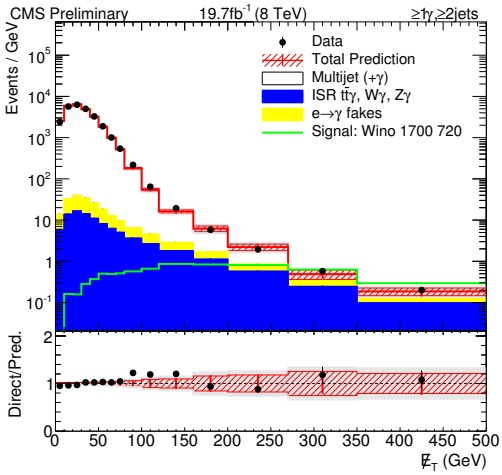

Figure 3: Total standard model background prediction as a function of $\not{E}_{\mathrm{T}}$ compared to data. In addition GGM signal benchmark point with a wino-like neutralino with a neutralino mass of 375 GeV, a squark mass of 1700 GeV, and a gluino mass of 720 GeV is shown. The bottom ratio plot shows the event yields relative to the total background prediction. The hatched area represents the systematic uncertainty, the error bars the statistic uncertainty and the gray band the total uncertainty.

shows the $\not{E}_{\mathrm{T}}$ distribution for simulated $\mathrm{t\bar{t}}$ and W boson events compared to the prediction by the method described above. The direct simulation is in agreement with the prediction from simulation. Especially for high $\not{E}_{\mathrm{T}}$, initial and final state radiation (ISR/FSR) contribute to the signal region. MADGRAPH [5] is used to simulate $\mathrm{t\bar{t}}\gamma$, $\mathrm{W}\gamma$, and $\mathrm{Z}\gamma \to \nu\nu\gamma$ processes, which are scaled by a common scale factor. This scale factor is estimated by comparing MCFN [6] calculations, cross-section measurements and verification in a control region with $\mathrm{Z}\gamma \to \mu\mu\gamma$ events. Events with electrons or muons are rejected in order to reduce the contribution from events with initial and final state radiation.

Figure 3 shows the total SM background prediction and the signal selection as function of $\not{E}_{\mathrm{T}}$. A signal benchmark point with a $\tilde{\chi}_1^0$ mass of 375 GeV, a squark mass of 1700 GeV, and a gluino mass of 720 GeV is drawn in addition. The data is in agreement with the SM background prediction. The event yields, the background composition and the yields for the same signal benchmark point is shown in Table 1 for the bins used in the statistical interpretation. The result is interpreted in the GGM framework for bino- or wino-like neutralino scenarios as function of squark and gluino masses. The $\tilde{\chi}_1^0$ mass (and in the wino-like neutralino scenario the lightest chargino mass) is set to 375 GeV. Multi-channel counting experiments in the six distinct $\not{E}_{\mathrm{T}}$-bins shown in Table 1 are combined into a single limit. The $\mathrm{CL_s}$ method is used to determine exclusions at 95% confidence level. Possible contamination of signal in the control sample used for background estimation is found to be of the order of 5–40%, and is considered in the limit calculation. Figure 4 shows the observed cross section limit (left) and the corresponding exclusion contours (right) for a wino-like neutralino scenario. For the bino-like neutralino scenario, gluino (squark) masses of 1100 (1350) GeV are excluded.

$\not{E}_T$ Range [GeV]	[100, 120)	[120, 160)	[160, 200)	[200, 270)	[270, 350)	[350, ∞)
Multijet(+photon)	991±164	529±114	180±69	95.6±45	11.7±12	9.1±9
Electron	37.3±4	42.5±5	23.0±3	19.2±2	7.7±1.0	4.1±0.6
ISR/FSR	53.6±27	72.5±36	44.9±23	40.1±20	19.7±10	14.7±7
Background	1082±166	644±119	248±73	155±50	39.0±16	27.8±12
Data	1286	774	232	136	46	30
Signal	18.8±3	53.1±5	50.5±5	82.3±7	77.7±7	67.3±6
Backg. from signal	2.1	5.0	5.6	9.9	26.7	13.5
Acceptance [%]	0.3	0.9	0.8	1.3	1.2	1.1
Exp. limit [pb]	5.23	1.21	0.57	0.24	0.14	0.11
Obs. limit [pb]	6.03	1.89	0.55	0.21	0.18	0.11

Table 1: Resulting event yields, estimated background, and yields for a GGM signal scenario for a wino-like neutralino scenario with a neutralino mass of 375 GeV, a squark mass of 1700 GeV, a gluino mass of 720 GeV, and a cross section of 316 fb. The combined observed (expected) CLs cross-section limit for this point is 99 fb (91 fb) at 95% CL.

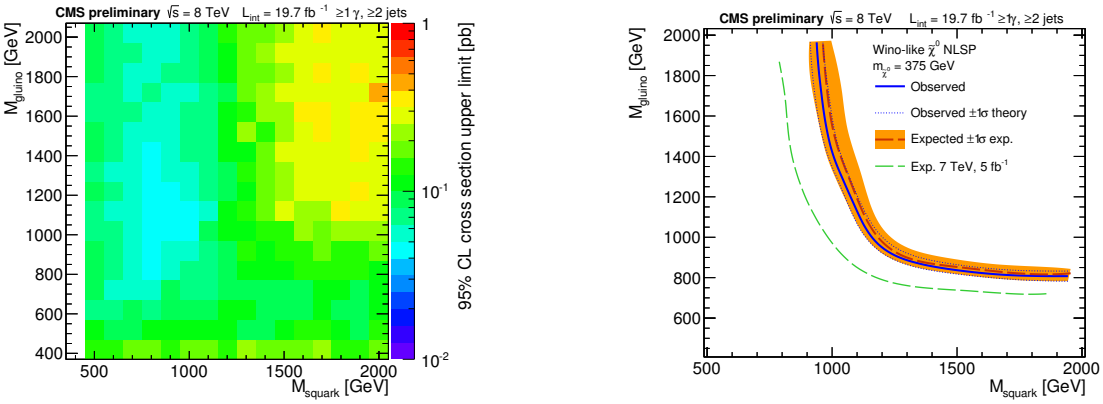

Figure 4: Observed upper limits (left) and exclusion contours (right) at 95% C.L. on the signal cross section in the gluino-squark mass space for the wino-like neutralino scenario. The exclusion contour of the previous analysis [7] is drawn in addition.

References

[1] Pierre Fayet. Mixing Between Gravitational and Weak Interactions Through the Massive Gravitino. *Phys.Lett.*, B70:461, 1977.

[2] CMS Collaboration. Search for supersymmetry in events with one photon, jets and missing transverse energy at $\sqrt{s} = 8$ TeV. CMS-PAS-SUS-14-004. 2014.

[3] Patrick Meade, Nathan Seiberg, and David Shih. General Gauge Mediation. *Prog.Theor.Phys.Suppl.*, 177:143–158, 2009.

[4] S. Chatrchyan et al. The CMS experiment at the CERN LHC. *JINST*, 3:S08004, 2008.

[5] Johan Alwall, Michel Herquet, Fabio Maltoni, Olivier Mattelaer, and Tim Stelzer. MadGraph 5 : Going Beyond. *JHEP*, 1106:128, 2011.

[6] John M. Campbell, Heribertus B. Hartanto, and Ciaran Williams. Next-to-leading order predictions for $Z\gamma$+jet and Z $\gamma\gamma$ final states at the LHC. *JHEP*, 1211:162, 2012.

[7] Serguei Chatrchyan et al. Search for new physics in events with photons, jets, and missing transverse energy in pp collisions at $\sqrt{s} = 7$ TeV. *JHEP*, 1303:111, 2013.

Statistical criteria for possible indications of new physics in tritium β-decay spectrum

Aleksei Lokhov[1], *Fyodor Tkachov*[2]

[1]Dept. of Experimental Physics, Institute for Nuclear Research RAS, 142190 Troitsk, Russia
[2]Dept. of Theoretical Physics, Institute for Nuclear Research RAS, 117312 Moscow, Russia

DOI: http://dx.doi.org/10.3204/DESY-PROC-2014-04/167

The method of quasi-optimal weights is applied to constructing (quasi-)optimal criteria for various anomalous contributions in experimental spectra. Anomalies in the spectra could indicate physics beyond the Standard Model (additional interactions and neutrino flavours, Lorenz violation etc.). In particular the cumulative tritium β-decay spectrum (for instance, in Troitsk-ν-mass, Mainz Neutrino Mass and KATRIN experiments) is analysed using the derived special criteria. Using the power functions we show that the derived quasi-optimal criteria are efficient statistical instruments for detecting the anomalous contributions in the spectra.

1 Introduction

Studying anomalies in experimental spectra extends our understanding of experimental setups. Besides anomalous contributions could also indicate new physics beyond the Standard Model. For instance, in tritium β-decay spectra possible additional interactions can lead to a step-like anomaly near the end-point while the excistance of the forth neutrino (with the mass of a few keV) induces a kink structure in the region of several keV from the end-point. Here we consider these two possible anomalous contributions.

The search for an anomaly should be based on a statistically reliable inference about presence or absence of the anomaly. Such inference is provided by special statistical criteria. One can construct the criteria according to each particular situation and accounting for some additional information about the theoretical model or experimental setup. The various approaches here are as follows:

1. Direct fit with additional parameters (the mass of neutrino and the mixing parameter, the amplitude and the position of the step) [1], [2], [3].
2. Searching for the kink with various filters [3].
3. Wavelet analysis [4].
4. Seaching for special functional dependencies.
5. Constructing special statistical criteria for the heavy neutrino or the step accounting for the uncertainties of other parameters (based on the method of quasi-optimal weights [5]). In the paper we present two examples of construction of the special statistical tests.

2 Step-like anomaly in Troitsk-ν-mass spectrum

Any deviations at the very end of the spectrum have crucial influence on the estimations of the neutrino mass squared. The spectrum of the Troitsk-ν-mass experiment is cumulative. The numbers of electrons are measured for a set of energies (these numbers have Poisson distributions). After that the measured data points are fitted with the theoretical curve. There are four fitted parameters in the Troitsk-ν-mass spectrum. One of them is the neutrino mass squared.

The first data analysis [1], performed with the standard Minuit routines, yielded rather controversial result: the estimate of the neutrino mass squared lies far beyond physically relevant range, it appears to be large and negative. This was interpreted as due to an excess of electrons near the end-point energy of the tritium β-decay spectrum; in cumulative spectra, such an excess takes the form of a step. Such a step is described by two parameters, the height and the position. Including these into the fit, a satisfactory value for the neutrino mass squared was obtained.

The recently finished new analysis [2] (exploiting the method of the quasi-optimal weights [5] and improved theoretical model of the experimental setup as well), yielded physically relevant values (within errors) of the neutrino mass squared while the step-structure has not been accounted for. The goodness-of-fit test included into the fitting procedure is not tuned to feel the anomalous contributions of this step-like form. It will be nice to have convenient, robust statistical criteria, particularly targeted to the described anomaly. We also should take into account that the position of the step is unknown and even may vary in time. We have constructed three special criteria and with them one can perform the standard procedure of the test of hypotheses [6], [7]. The null-hypothesis is that the height of the step is zero, the alternative - the height is positive. We use the fit from the new analysis [2].

The first criterion is constructed via routines of the method of quasi- optimal moments. And it is by construction the Locally Most Powerful (LMP) one. Locally here means near the null-hypothesis. The distributions for the experimental counts are $f_i(N) = \frac{\mu_i'^N e^{-\mu_i'}}{N!}$, where $\mu_i' \to \begin{cases} \mu_i + \Delta_-, i > m \\ \mu_i + \Delta_+, i \le m \end{cases}$, i stands for the number of an experimental point. Here m is defined by the inequality $E_m \le E_{st} \le E_{m+1}$. Constructing the weights

$$\omega_i^+(N) = \frac{\partial \ln f_i}{\partial \Delta_+} = \begin{cases} 0, & i > m \\ \frac{N}{(\mu_i + \Delta_+)} - 1, & i \le m \end{cases}, \omega_i^-(N) = \frac{\partial \ln f_i}{\partial \Delta_-} = \begin{cases} 0, & i \le m \\ \frac{N}{(\mu_i + \Delta_-)} - 1, & i > m \end{cases}$$

and solving the corresponding equations $h^{exp} = \sum\limits_i \omega_i = 0$ one obtains the statistics of the LMP criterion $\overline{\Delta} = \Delta_+ - \Delta_-$ – the estimate for the height of the step. $\overline{\Delta}$ can be also presented as a weighted sum of experimental counts $\overline{\Delta} = \sum_{i=1}^{M} w_i \cdot N_i$

Recalling the uncertainty of the step position it is useful to decrease the sensitivity of our criteria to the position of the step, even loosing some sensitivity to the step itself. For this we slightly change the weights in the sum of the LMP test (see Fig. 1), to suppress the values near the position of the step, saving the properties of the LMP test in the rest areas. The corresponding statistics is $S_{q-opt} = \sum\limits_i^k w_i \cdot \xi_i$, where $\xi_i = \frac{N_i - \mu_i}{\sqrt{\mu_i}}$ and $w_i = \begin{cases} \frac{(m-i)}{m}, & i \le m, \\ \frac{(m-i)}{M-m}, & i > m. \end{cases}$

One more criterion, $S_{pair} = \sum\limits_i \xi_i \cdot \xi_{i+1}$, constructed somehow speculatively, exploits the following idea: if the anomaly is a deviation of several neighbour points to one side of the

fitting curve (Fig. 3) than it will increase the value of the statistics S. Thus the pairwise neighbours' correlations test can be used as a criterion for rather general class of anomalies.

We can compare all these criteria using the standard tool of Power Functions. The power function is simply the probability of a criterion to reject the null hypothesis while it is in fact false. As on can see on Fig. 4 the LMP (1) is the best here, the quasi-optimal (2) is slightly less powerful, the pairwise neighbours correlations test (3) comes third and the conventional tests (4,5) are the least sensitive. The situation changes if the assumed position of the step is not correct. The left graph in Fig. 5 shows that the LMP test (1) is loosing its sensitivity rather rapidly while two other special tests remain rather powerful.

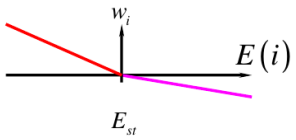

Figure 1: The quasioptimal weights for the step-like anomaly searches

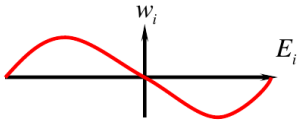

Figure 2: The quasioptimal weights for the heavy neutrino searches

Figure 3: The idea of the pairwise neighbours correlations criterion

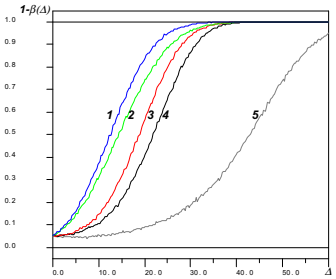

Figure 4: The power functions for the special and conventional criteria

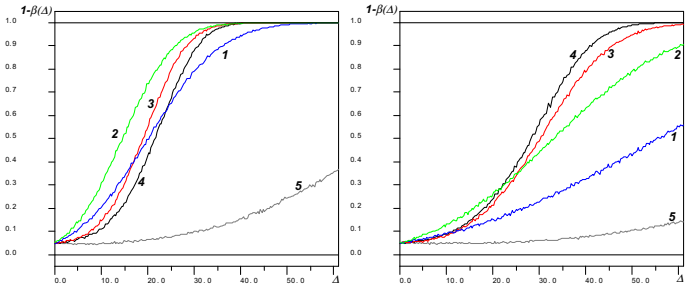

Figure 5: The power functions of the five criteria for the cases when the actual step position is shifted from the assumed position E_m by 12 eV (left) and 25 eV (right)

3 Heavy neutrino searches

Similarly to the case of step-like anomaly one can derive special criteria for the search of a heavy neutrino in β-decay spectrum

$$\frac{d\Gamma}{dE} = \sin^2\theta\left(\frac{d\Gamma}{dE}\right)_{m_{keV}} + \cos^2\theta\left(\frac{d\Gamma}{dE}\right)_{m_{light}}.$$

The spectrum $\frac{d\Gamma}{dE}(E_i, m) = S_{i,m}$ is again measured in a number of points with various retarding potentials. The spectrum is defined by the mixing parameter $U^2 = \sin^2\theta$ and the mass of the

heavy neutrino m_{keV}. The mass of the light neutrino is considered to be $m_{light} = 0$. Thus the theoretical means are $\mu_i' = U^2 S_{i,m_H} + (1-U^2) S_{i.m=0}$. The first test (the LMP) is obtained via the method of quasi-optimal weights and it is by construction the most sensitive one in case when the mass of the heavy neutrino is well-known. The corresponding weights are as follows:

$$\omega_i = \frac{\partial \ln f_i}{\partial U^2} = \left(\frac{N}{U^2 S_{i,m_H} + (1-U^2) S_{i,m=0}} - 1 \right) \cdot (S_{i,m_H} + S_{i,0}).$$

Using these weights one constructs an equation $\frac{1}{M} \sum_{i=1}^{M} \omega_i = 0$ for the mixing parameter estimate $\widehat{U^2}$ – the statistics of the LMP criterion.

To reduce the sensitivity of our test to the mass we modify the weights (for instance, as shown in Fig. 2) to obtain the quasi-optimal criterion $S_{q-opt} = \sum_{i}^{k} w_i \cdot \xi_i$. It is more robust and require no information about the exact mass of the additional neutrino. The universal pairwise neighbours correlatiosn test can be exploited in the case of kink searches as well.

4 Conclusions

We illustrated the new approach to the search for anomalies in experimental spectra with account for the parameters with uncertainties (the position of the step-like anomaly and the mass of the additional neutrino in our examples). We showed that the Locally Most Powerful criterion for each anomalous contribution can be constructed via the method of quasi-optimal moments. Than the LMP test can be tuned to reduce the influence of the unknown parameters of the spectra. With the help of the power functions the constructed criteria are proved to be more efficient in searches for the specific anomalous contributions. The next step is to compare the sensitivity of the constructed tests with the wavelet analysis [4], direct fitting and search for the kink with filters [3]. The approach appears to be useful for the future searches of the heavy neutrino in Troitsk [8], [9] and Karlsruhe [3].

One of the authors (A.L.) would like to thank Christian Sander and Alexander Schmidt for the invitation to participate in PANIC14, Matthias Kasemann, Kristina Price and all the organising committee for their fantastic job in organising this conference.

The work has been supported by RFBR grant 14-02-31055.

References

[1] V.M. Lobashev, Nucl. Phys. A. **719** 153 (2003).

[2] V.N. Aseev *et al.*, Phys. Rev. D. **84** 112003 (2011).

[3] S. Mertens *et al.*, arXiv:1409.0920 (2014).

[4] S. Mertens *et al.*, arXiv:1410.7684 (2014).

[5] F.V. Tkachov, arXiv:physics/0704127 (2006).

[6] A.V. Lokhov, F.V. Tkachov, P.S. Trukhanov, Nucl. Instrum. Meth. A**686** 162 (2012).

[7] A.V. Lokhov, F.V. Tkachov, P.S. Trukhanov, Nucl. Phys. A **897** 218 (2013).

[8] D. Abdurashitov *et al.*, arXiv:1403.2935 (2014).

[9] A.I. Belesev *et al.*, J. Phys. G: Nucl. Part. Phys **41** 015001 (2014).

Monitoring of Cabling Activities during the LHC LS1

Stefano Meroli, Simao Costa Machado, Fabio Formenti, Marten Frans, Jean-Claude Guillaume, Serge Oliger, Daniel Ricci

CERN, European Organization for Nuclear Research, 1211 Geneve 23, Switzerland

DOI: http://dx.doi.org/10.3204/DESY-PROC-2014-04/176

The development of a reliable monitoring system was a key element in the successful consolidation and upgrade of the cabling infrastructure of the CERN accelerator complex during the LHC first shutdown period. This paper presents the implementation and use of this monitoring system during the two year-long shutdown, focusing on improvements delivered in project management and providing practical examples of applications.

1 Introduction

The Large Hadron Collider (LHC) at CERN entered into its first long shutdown period (LS1) in February 2013 [1]. In this framework, the consolidation and upgrade of the cabling infrastructure of the CERN accelerator complex represented one of the most challenging projects in terms of complexity and workload [2]. The undertaking has required substantial project management effort and a significant deployment of resources, consisting of CERN staff and industrial support contractors [3]. A monitoring system has been then developed to support the project management dealing with project preparation and execution.

2 The goals

The consolidation and upgrade of the cabling infrastructure consisted of a large number of activities distributed over 350 worksites. They were carried out to a tight schedule and often in radioactive environments or as part of a coordinated activity with other CERN groups. Table 1 provides a numerical summary of the project.

	Project cost	Cable length installed	Connectors installed
Copper Cabling	14.3 MCHF	1000 km	21000
Optical Fibre Cabling	7.3 MCHF	260 km	95000
Total	21.6 MCHF	1260 km	116000

Table 1: Consolidation and upgrade of the cabling infrastructure, the main numbers.

Performing the cabling activities in these conditions turned out to be very demanding in terms of work organization and execution, requiring anticipation of strategic actions and a fast turn-around control of project status.

For this reason CERN has developed a ***comprehensive*** monitoring system, supporting the project management, to deal with all critical aspects of the project such as duration, cost, resource availability, safety (namely: radiation dose absorbed by the personeel) and installation quality. During the LS1 the monitoring system has served the dual purposes of recording project performance as well as of predicting its future evolution, warning on possible coming issues and easing the identifications of delays and the implementation of changes to the project.

3 The monitoring system structure

The monitoring system consisted of a set of software, tools and procedures working together with the aim of summarizing the large number of data sources in simple graphs and tables.

Weekly meeting with industrial support contractors, inspections on the worksites as well as reports from activity supervisors have assured ***quick*** feedback on the six most challenging aspects of the project. Based on this input, a dedicated software system processed the information allowing comparisons of actual outcomes with the original baseline and forecasts. The scheme in Figure 1 shows the structure implemented with the six aspects monitored.

The ***activity duration*** was followed through an in-house software system called GESMAR, in which industrial support staff introduced on a daily basis the information for each pulled cable, connector assembly and test. They also updated the progress of the mechanical installation, the cable removal, the reworking and activity verification. Stock availability and timely delivery of the ***material*** on the worksite were verified in parallel. The number of CERN and industrial support contractor ***staff*** deployed on the worksite (roughly 150 people in total) was constantly monitored by using the accelerator access control systems installed on the site or through feedback from the activity supervisors. Monitoring of the ***project cost*** was required to make sure that the project remained within the budget margin. Reports on payments to industrial contractors were provided together with forecasts of budget engagements. The CERN safety rules demand a precise estimation and follow up of the ***radiation dose*** absorbed by workers. Daily reports alerted project manager in case the absorbed dose exceeded the estimated limit. Finally the ***quality*** of the installation delivered to the users was verified by continuous field inspections. Warning notes were issued in case of the quality requirements were at risk of not being satisfied.

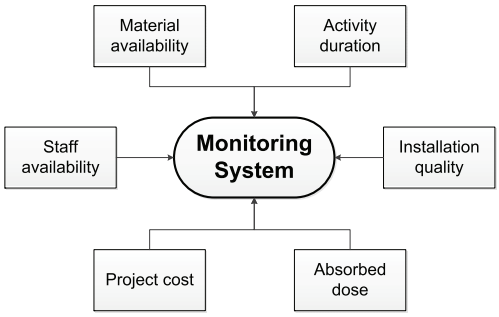

Figure 1: Monitoring system structure.

4 Data analysis and reporting

Automatic reports on overall project performance were extracted daily and used as indicators. Offline analysis and the cross checking of the collected data allowed detection of potential

activity issues like planning delays, resources constraints or failures to comply with the approved working procedures.

The example of the PS Booster cabling activity has showed the effectiveness of the tool (see Figure 2). During the cabling installation, the tool predicted that the radiation dose absorbed by the workers would exceed the safety limit, alerting management and allowing a pre-emptive adjustment to the method used.

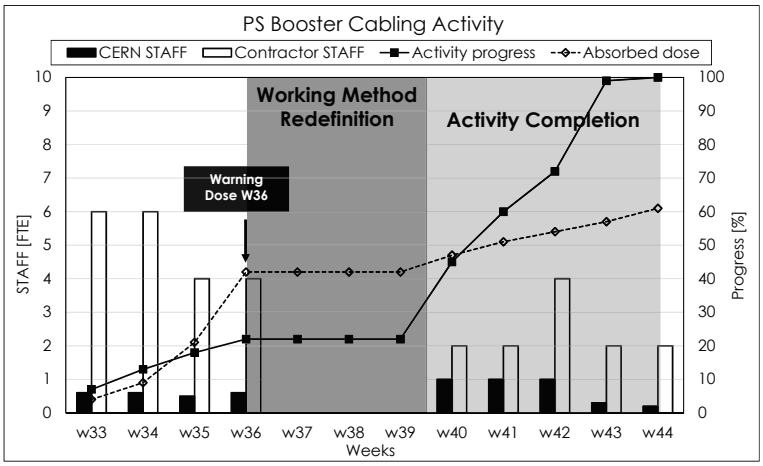

Figure 2: PS Booster activity report.

Figure 3 shows a set of graphs used to review the overall project performance.

The number of activities completed was monitored weekly in order to define the overall project completion percentage. More or less resources were assigned to the worksites in case of delay or required acceleration of the schedule, guaranteeing the respect of the deadlines and preventing a domino effect on the whole project planning. As it can be seen in Figure 3(a) the actual progress followed the original baseline all along the LS1. Only a minor delay occurred due to the addition of unforeseen activities to the planning, slowing down the overall project execution.

Figure 3(b) shows the non-conformities detected on the worksites grouped by four categories: organization (i.e. problem related to the industrial support contract internal organisational), planning (i.e. non respect of the mutually deadlines agreed), quality (i.e. problems associated to the quality of the works performed) and security (i.e. non respect of safety rules and regulations). The analysis allowed the identification, classification and definition of corrective actions for the installations, delivering improvement to the working method and bringing about significant improvements to the global quality of the installations.

Figures 3(c) and (d) show respectively the industrial support contract and CERN staff load curve over the entire LS1 period. Forecast load curves, based on estimates of future workload, have allowed resource requirements to be set up in advance. During 2014, additional resources had been put in place to cope with unforeseen cabling activities, leading management to engage an additional industrial support contract. The load curves also addressed changes to the planning to mitigate manpower constraints. Activities were anticipated or postponed to smooth as much as possible the load curve and prevent wherever possible the presence of troublesome peaks and holes (planning "agility").

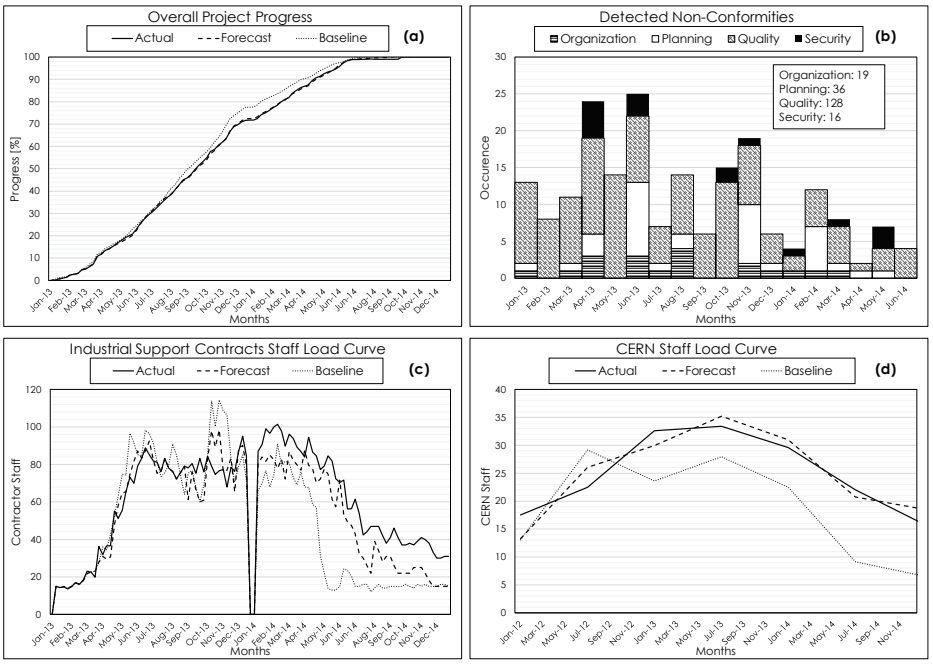

Figure 3: (a) overall project progress; (b) distribution of non-conformities detected during the work execution; (c) industrial support contract staff load curve; (d) CERN staff load curve

5 Conclusion

The implementation of a monitoring system played a fundamental role in the successful execution of the cabling activities during the LS1. About 1300 kilometers of cables, distributed in different machine areas and representing an investment of about 21.6 MCHF, have been installed respecting the schedule. The system proved its effectiveness throughout the LS1 by assisting the project management in the definition of anticipated strategic actions and to implement changes to the project. Furthermore the tool supported the improvement of the general working method allowing the Long Shutdown 2 to be planned on a much more informed basis.

Acknowledgments

Authors wish to thank James Dilwyn Devine for supporting in the review of this document.

References

[1] K. Foraz *et al.*, *LHC Long Shutdown: a parenthesis for a challenge*, 4th International Particle Accelerator Conference IPAC13, Shanghai, Cina (2013).

[2] F. Duval, *LS1: electrical engineering upgrades and consolidation*, Chamonix Workshop on LHC Performance, Chamonix, France (2012).

[3] S. Meroli *et al.*, *The management of large cabling campaigns during the Long Shutdown 1 of LHC*, JINST **C03042** 9 (2014).

Search for supersymmetry in opposite-sign same-flavour lepton pairs with the CMS detector

Jan-Frederik Schulte[1] on behalf of the CMS Collaboration

[1]I. Physikalisches Institut B, RWTH Aachen University, Germany

DOI: http://dx.doi.org/10.3204/DESY-PROC-2014-04/283

A search for Supersymmetry in events with opposite-sign same-flavour lepton pairs is presented. This final state, in addition to requirements on the number of jets and missing transverse energy, allows for a large reduction as well as a precise estimation of standard model backgrounds. In the cascade decays of new heavy particles, correlated production of leptons can lead to distinctive 'edges' in the dilepton invariant mass spectrum, caused by the mass differences between the new particles. Presented is the search for such a mass edge in a dataset of pp collisions at $\sqrt{s} = 8\,\text{TeV}$, corresponding to $19.4\,\text{fb}^{-1}$, collected with the CMS detector [1] at the CERN LHC.

This analysis [2] focuses on the correlated production of same-flavor (SF) opposite-sign (OS) leptons in cascade decays of new heavy particles. Examples for this are decays of the second neutralino into the first neutralino and a SF OS lepton pair, either via an intermediate slepton or on- or off-shell Z bosons, as illustrated in Fig. 1. The mass difference between the two neutralinos sets an upper limit on the invariant mass of the lepton pair, leading to a characteristic edge. The experimental signatures of these decays are the SF OS lepton pair, missing transverse energy (E_T^{miss}) from the undetected LSPs, and several jets from other parts of the cascade and the decay of the second initially produced sparticle.

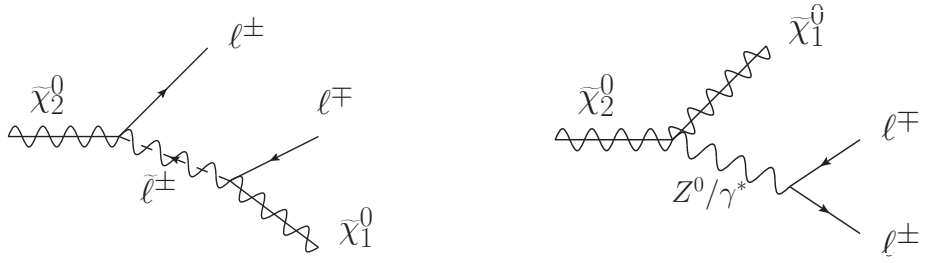

Figure 1: Diagrams of the possible decay modes of the second neutralino resulting in an edge in the dilepton invariant mass sepctrum.

The considered event samples are collected with dilepton triggers, requiring two light leptons (e,μ) with $p_T > 17\,\text{GeV}$ for the first and $p_T > 8\,\text{GeV}$ for the second lepton. Events are then required to contain two SF OS light leptons with $p_T > 20\,\text{GeV}$ and a pseudorapidity of $|\eta| < 2.4$. The dilepton invariant mass $m_{\ell\ell}$ is required to be greater than 20 GeV. The event sample is split

into the 'central' (both leptons $|\eta| < 1.4$) and 'forward' (at least on lepton $|\eta| > 1.6$) regions. Three regions are defined in E_T^{miss} and the number of jets N_{jets}. A control region enriched in events produced by the Drell-Yan process requires $N_{jets} \geq 2$ and $E_T^{miss} < 50\,GeV$. Events with exactly two jets and E_T^{miss} between 100 GeV and 150 GeV fall into a control region dominated by top-pair production. Finally, the signal region is defined by requiring either $E_T^{miss} > 150\,GeV$ and $N_{jets} \geq 2$, or $E_T^{miss} > 100\,GeV$ and $N_{jets} \geq 3$. A kinematic fit considers the mass range from 20 GeV to 300 GeV, while for a counting experiment the range is restricted to 20 GeV to 70 GeV.

Two types of standard model (SM) backgrounds contribute to the signal selection. The main source of backgrounds are flavor-symmetric processes, which produce SF lepton pairs as often as opposite flavor (OF) pairs. They are in turn dominated by dileptonic decays of top pairs, but also the Drell-Yan process where the boson decays to two tau leptons, W boson pair production or misidentified leptons contribute. The second type of backgrounds are processes producing a Z boson decaying into two light leptons.

Flavor-symmetric backgrounds are predicted from the OF sample, which in principle has the same event yield and kinematic properties as the SF sample. As this symmetry might be broken by the different efficiencies for trigger, reconstruction and identification of the different lepton flavors, a correction factor is derived from two independent methods, utilizing orthogonal event samples. The first method is the direct measurement of the ratio $R_{SF/OF}$ in the top-pair dominated control region. This method is limited by the statistical uncertainties of this measurement. The second method measures the efficiencies of the dilepton triggers (ϵ_{ee}^{trig},$\epsilon_{\mu\mu}^{trig}$,ϵ_{OF}^{trig}) as well as the ratio of the selection efficiencies for muons and electrons $r_{\mu e}$. The correction factor is then calculated as $R_{SF/OF} = \frac{1}{2}(r_{\mu e} + \frac{1}{r_{\mu e}}) \frac{\sqrt{\epsilon_{ee}^{trig} \epsilon_{\mu\mu}^{trig}}}{\epsilon_{OF}^{trig}}$. The precision of this method is limited by the systematic uncertainties introduced by the extrapolation of the efficiency measurements into the signal region. The results from both methods are consistent and are combined according to their respective uncertainties. The resulting values are $R_{SF/OF} = 1.00 \pm 0.04$ for central leptons and $R_{SF/OF} = 1.11 \pm 0.07$ for forward leptons.

For the counting experiment at low $m_{\ell\ell}$, the background from SM processes containing a Z boson is estimated by first deriving an estimate for the contribution of these processes on the Z peak for $m_{\ell\ell}$ between 81 GeV and 101 GeV with two independent methods. The first one uses the balance of the Z against the jets in the event to predict the contribution of these backgrounds in regions with high E_T^{miss}. The second predicts the contribution from Z bosons using events with single photons. The results of both methods are consistent and are averaged according to their uncertainties. The prediction for the Z peak region is extrapolated to low masses using a scale factor, determined in the Drell-Yan enriched control region.

The results of the counting experiment at low invariant masses are shown in Tab. 1. For the dominant flavor-symmetric backgrounds a precision of the estimate of 5% for the central region and 10% for the forward region has been achieved. In the forward region there is good agreement between background expectation and observation, while in the central region there is a small excess with a local significance of 2.6σ. This can also be seen in Fig. 2, which shows the invariant mass distribution in the signal region separately for central and forward leptons.

The search for a kinematic edge in the dilepton mass spectrum is performed using an unbinned maximum likelihood fit, simultaneous to the ee, $\mu\mu$ and OF event samples in both the central and forward lepton selection. The only parameter shared between the models for the forward and central selection is the position of the edge $m_{\ell\ell}^{edge}$. The fit model consists of four components. The signal model is a triangular shape, smeared with the expected detector

	Central	Forward
Observed [SF]	860	163
Flav. Sym. [OF]	$722 \pm 27 \pm 29$	$155 \pm 13 \pm 10$
Drell–Yan	8.2 ± 2.6	1.7 ± 1.4
Total estimates	730 ± 40	157 ± 16
Observed – Estimated	130^{+48}_{-49}	6^{+20}_{-21}
Significance [σ]	2.6	0.3

Table 1: Results of the counting experiment for event yields in the signal regions. Statistical and systematic uncertainties are added in quadrature, except for the flavor symmetric backgrounds.

resolution:

$$\mathcal{P}_S(m_{\ell\ell}) = \frac{1}{\sqrt{2\pi}\sigma} \int_0^{m_{\ell\ell}^{edge}} dy \cdot y \cdot e^{\frac{-(m_{\ell\ell}-y)^2}{2\sigma^2}}. \quad (1)$$

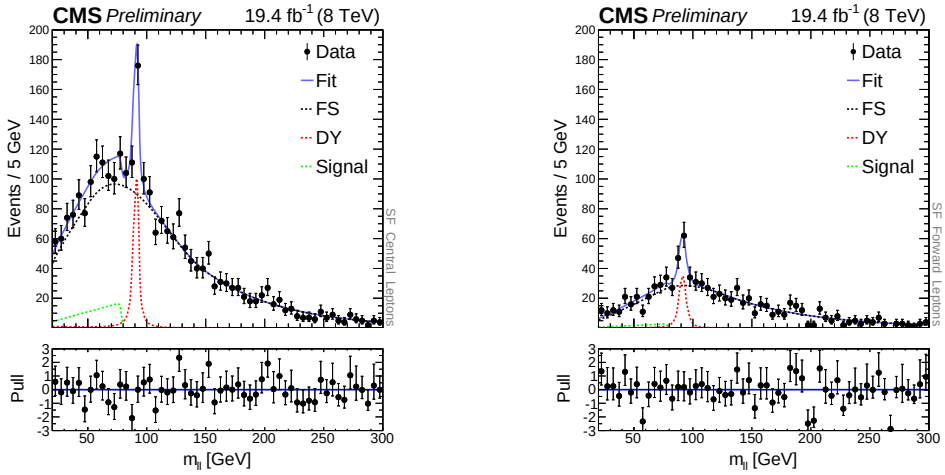

Figure 2: Invariant mass distriubtions in the signal region. The data is shown as black points, while the background prediction is shown as a red line. The total uncertanty on the background is indicated in blue. The Drell-Yan background component is shown in green (colored version can be found online).

Backgrounds containing a Z boson are described by a Breit-Wigner distribution convolved with a double-sided Crystal Ball function for the peak component and a falling exponential for the continuum component. The model is in a first step fitted in the Drell-Yan enriched control region. Afterwards, all parameters are fixed and only the normalization is a free parameter in the fit in the signal region. Flavor-symmetric backgrounds are described by a model consisting of three parts; a kinematic turnon at low $m_{\ell\ell}$, an exponential fall at high $m_{\ell\ell}$, and a polynomial

to describe the transition between the two:

$$\mathcal{P}_{FSE}(m_{\ell\ell}) = \begin{cases} \mathcal{P}_{FSE,1}(m_{\ell\ell}) = c_1 \cdot m_{\ell\ell}^{\alpha} & \text{if } 20GeV < m_{\ell\ell} < m_{\ell\ell}^{(1)} \\ \mathcal{P}_{FSE,2}(m_{\ell\ell}) = \sum_{i=0}^{3} c_{2,i} \cdot m_{\ell\ell}^{i} & \text{if } m_{\ell\ell}^{(1)} < m_{\ell\ell} < m_{\ell\ell}^{(2)} \\ \mathcal{P}_{FSE,3}(m_{\ell\ell}) = c_3 \cdot e^{-\beta m_{\ell\ell}} & \text{if } m_{\ell\ell}^{(2)} < m_{\ell\ell} < 300GeV \end{cases}$$

The background yields for the flavor-symmetric backgrounds in the SF and OF categories are connected via the correction factor $R_{SF/OF}$, which is a nuisance parameter in the fit. The fit results are shown in Tab. 2. The best fitted value for the edge position is 78.7±1.4 GeV and the fitted signal yield is 126±41 events in the central and 22±20 events in the forward region. The local significance of the result is 2.4σ. The invariant mass distributions together with the fit result are shown in Fig. 3.

	Central	Forward
Drell–Yan	158 ± 23	71 ± 15
Flav. Sym. [OF]	2270 ± 44	745 ± 25
$R_{SF/OF}$	1.03	1.02
Signal events	126 ± 41	22 ± 20
$m_{\ell\ell}^{\text{edge}}$ [GeV]	78.7 ± 1.4	
Local Significance [σ]	2.4	

Table 2: Results of the unbinned maximum likelihood fit for event yields in the signal regions.

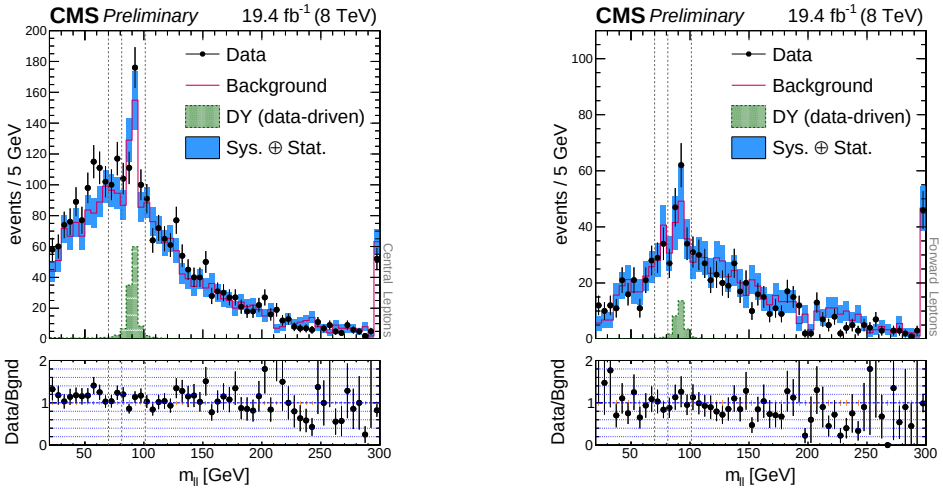

Figure 3: Invariant mass distriubtions in the signal region. The data is shown as black points, while the fit result is shown in blue. The different fit components are shown in green for the signal model, black for the model for flavor-symmetric backgrounds and in red for the Drell-Yan background (colored version can be found online).

A search for Supersymmetry in same-flavor opposite-sign dilepton events with jets and E_T^{miss} has been presented. SM backgrounds are predicted from data with high precision. A fit is performed in search for a edge in the dilepton invariant mass spectrum. Although a small excess has been observed at low invariant masses, no evidence for a statistically significant signal has been observed. This result highlights the opportunities of high precision searches at the LHC and preparations are ongoing to repeat this analysis in 2015.

References

[1] S. Chatrchyan et al. The CMS experiment at the CERN LHC. *JINST*, 3:S08004, 2008.

[2] Search for physics beyond the standard model in events with two opposite-sign same-flavor leptons, jets, and missing transverse energy in pp collisions at sqrt[s] = 8 TeV. Technical Report CMS-PAS-SUS-12-019, CERN, Geneva, 2014.

Chiral two- and three-nucleon interactions used in ring diagram method for binding energy of ^{4}He

Yiharn Tzeng[1], *Shwu-Yun Tsay Tzeng*[2], *T. T. S. Kuo*[3]

[1]Institute of Physics, Academia Sinica, Taipei 11529, Taiwan, ROC
[2]Dept. of Electro-Optical Engineering, National Taipei University of Technology, Taipei 10608, Taiwan, ROC
[3]Department of Physics, State University New York at Stony Brook, New York 11794, USA

DOI: http://dx.doi.org/10.3204/DESY-PROC-2014-04/50

In this work, we carry out ring-diagram calculationsfor ^{4}He using the chiral N^{3}LO two-nucleon potential $V_{2N}$with and without the inclusion of an in-medium three-nucleon (NNN) force $\bar{V}_{3N}$, derived from the leading-order chiral NNN force V_{3N}.

The ring-diagram method [1] is based on the the linked-diagram expansion [2] where the ground-state energy shift ΔE_0 is given by $\Delta E_0 = E_0 - E_0^{\rm free} = \lim_{t'\to-\infty}[\frac{\langle\Phi_0|VU(0,t')|\Phi_0\rangle}{\langle\Phi_0|U(0,t')|\Phi_0\rangle}]_{\rm linked}$ with $U(0,t')$ the time-evolution operator, and E_0 and $E_0^{\rm free}$ respectively the true and non-interacting ground-state energies of the nuclear system with the nuclear hamiltonian $H = T + V$, Φ_0 the system's unperturbed shell-model ground-state wave function. Here we take $V = V_{2N} + \bar{V}_{3N}$.

In calculating ΔE_0, we include only all-order sum of the *pphh* ring diagrams as illustrated in Fig. 1. As shown, diagrams (b), (c) and (d) are respectively the 1st-, 4th- and 8th-order *pphh* diagrams. It may be noted that our ring-diagram calculation reduces to the usual Hartree-Fock (HF) one if only the first order ring diagram (b) is included. A main purpose of our present work is to study the effect of the particle-hole excitations, which are not included in the HF case, to the binding energies of finite nuclei. Indicated by (a) of the Figure is the mean field single particle (s.p.) propagators where the HF one-bubble insertions are included to all orders.

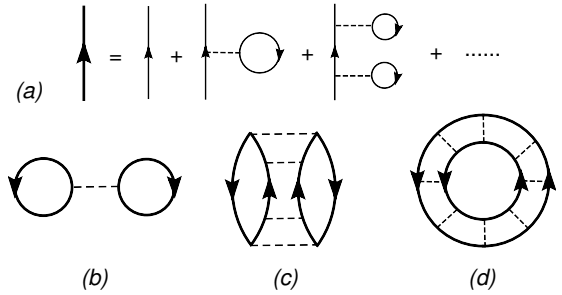

Figure 1: The *pphh* ring-diagrams for the ground state energy shift of closed-shell nuclei; (a) self-energy insertions on the single-particle propagator, and (b) to (d) all-order ring diagrams.

Summing up these ring diagrams to all orders, one has the ground-state energy shift from V as [1]

$$\Delta E_0 = \int_0^1 d\lambda \sum_m \sum_{ijkl\in P} Y_m(ij,\lambda) Y_m^*(kl,\lambda) \times \langle ij|V|kl\rangle, \tag{1}$$

where (i,j,k,l) are each a shell-model s. p. wave function, and P denotes a chosen shell-model space composed of a set of hole (h) and particle (p) orbits.

The amplitudes Y above are calculated from an RPA-type equation, namely

$$\sum_{ef}[(\epsilon_i+\epsilon_j)\delta_{ij,ef} + \lambda(1-n_i-n_j)\langle ij|V|ef\rangle] \times Y_m(ef,\lambda) = \omega_m(\lambda) Y_m(ij,\lambda); \quad (i,j,e,f)\in P, \tag{2}$$

where λ is a strength parameter, to be integrated from 0 to 1 as in Eq. 2. The occupation factors are $n_a = 1$ for $a = h$, and $= 0$ otherwise. Thus the amplitudes $Y_m(ij)$ has only either hh ($i = h$, $j = h'$) or pp ($i = p$, $j = p'$) components. The transition amplitudes Y can be classified into two types, one dominated by hh and the other by pp components. We include only the former, denoted by Y_m, for the calculation of the all-order sum of the $pphh$ ring diagrams.

We use HF s.p. spectrum ϵ_j in the above RPA equation, as indicated earlier in Fig. 1, namely $\epsilon_j = \langle j|K_{sp}|j\rangle + \sum_h \langle jh|V|jh\rangle$ where K_{sp} denotes the s. p. kinetic energy operator. Note that j and h are each oscillator s. p. wave function.

To carry on, we need first describe the V_{3N} to be employed. The leading contribution to V_{3N} occurs at N^{2}LO in the chiral power counting and is composed of a long-range two-pion exchange $V_{3N}^{2\pi}$, a medium-range one-pion exchange $V_{3N}^{1\pi}$, and a pure contact interaction V_{3N}^{ct}:

$$V_{3N}^{(2\pi)} = \sum_{i\neq j\neq k} \frac{g_A^2}{8f_\pi^4} \frac{\vec{\sigma}_i\cdot\vec{q}_i\,\vec{\sigma}_j\cdot\vec{q}_j}{(\vec{q}_i^{\,2}+m_\pi^2)(\vec{q}_j^{\,2}+m_\pi^2)} F_{ijk}^{\alpha\beta}\tau_i^\alpha\tau_j^\beta, \tag{3}$$

$$V_{3N}^{(1\pi)} = -\sum_{i\neq j\neq k} \frac{g_A c_D}{8f_\pi^4\Lambda_\chi} \frac{\vec{\sigma}_j\cdot\vec{q}_j}{\vec{q}_j^{\,2}+m_\pi^2} \vec{\sigma}_i\cdot\vec{q}_j\,\vec{\tau}_i\cdot\vec{\tau}_j, \qquad V_{3N}^{(\mathrm{ct})} = \sum_{i\neq j\neq k} \frac{c_E}{2f_\pi^4\Lambda_\chi}\vec{\tau}_i\cdot\vec{\tau}_j, \tag{4}$$

with $g_A = 1.29$, $f_\pi = 92.4$ MeV, $\Lambda_\chi = 700$ MeV, and $m_\pi = 138.04$ MeV/c^2 the average pion mass, $\vec{q}_i = \vec{p}_i{}' - \vec{p}_i$ is the difference between the final and initial momentum of nucleon i and $F_{ijk}^{\alpha\beta} = \delta^{\alpha\beta}\left(-4c_1m_\pi^2 + 2c_3\vec{q}_i\cdot\vec{q}_j\right) + c_4\epsilon^{\alpha\beta\gamma}\tau_k^\gamma\vec{\sigma}_k\cdot(\vec{q}_i\times\vec{q}_j)$. The low-energy constants $c_1 = -0.76\,\mathrm{GeV}^{-1}$, $c_3 = -4.78\,\mathrm{GeV}^{-1}$, and $c_4 = 3.96\,\mathrm{GeV}^{-1}$ appear already in the N^{2}LO two-nucleon potential and are thus constrained by low-energy NN phase shifts [3]. The constants c_D and c_E are typically fit to reproduce the properties of light nuclei [4, 5].

As mentioned earlier, the interaction $V = (V_{2N} + \bar{V}_{3N})$ will be employed in our calculations. V_{2N} is the NN interaction obtained from a N^{3}LO chiral two-body potential [6] and $\bar{V}_{3N}$ is a density-dependent two-body interaction obtained from the chiral three nucleon force by closing one pair of external lines and summing over the filled Fermi sea (k_F) of nucleons [7]. $\bar{V}_{3N}$ and V_{3N} are related by $\langle ab|\bar{V}_{3N}|cd\rangle = \sum_{h\le k_F}\langle abh|V_{3N}|cdh\rangle$, where the matrix elements are anti-symmetrized. Possible over-counts are carefully treated. $\bar{V}_{3N}$ is dependent of k_F or its corresponding density n.

We then calculate effective low momentum V_{low-k} matrix elements [8] from V_{2N} and V_{3N} for the use in the ring diagram calculations. Starting from the half-on-shell T-matrix in the

Lippmann-Schwinger equation, one defines the effective low-momentum T-matrix as

$$T_{\mathrm{low}-k}(p',p,p^2) = V_{\mathrm{low}-k}(p',p) + \int_0^\Lambda q^2 dq V_{low-k}(p',q)\frac{T_{low-k}(q,p,p^2)}{p^2-q^2+i0^+} \tag{5}$$

where Λ denotes a momentum space cut-off and $(p',p) \leq \Lambda$. The T-matrix in Eq.(5) is required to satisfy the condition $T(p',p,p^2) = T_{low-k}(p',p,p^2);\ (p',p) \leq \Lambda$. Earlier studies shew nuclear properties obtained from V_{low-k} being rather insensitive on Λ in the vicinity of 2.1 fm^{-1} [8]. Hence we set the cut-off in Eq. (5) $\Lambda \approx 2.1$ fm^{-1}.

To calculate the V_{low-k} matrix with V_{3N} included, we have used the Bertsch formula $\hbar\omega = 45.0A^{-1/3} - 25.0A^{-2/3}$. we adopt the magnitudes of parameters $c_D,\ c_E$ in Eqs. (4) from the c_E vs. c_D curve in [5] where the authors determined values of these two parameters from fitting binding energies of $A = 3$ nuclei. The nucleon density arising from the contact term [7] of Eq. (4) for the nucleus is chosen from the experimental charge density profile $\rho(r)$ vs. r from [9] as that approximately at the nucleus' RMS radius. The RMS radius for ^{4}He is 1.6757 fm [10] In this way, we set the density around the RMS radius to be $0.3\rho_0$ for ^{4}He, with $\rho_0 = 0.17$/fm^3.

The empirical Coulomb energy $E_{coul}/A = 0.717 \times Z^2/A^{4/3}$ is added to the nuclear system's ground state energy. Note that the non-interaction ground state energy E_0^{free} already takes care of the center of mass motion part. Hence our ring diagram expansion of ΔE_0 involves no CM excitation problems.

Shown in Fig. 2 is the dependence of ground state energy per nucleon (or -BE/A) for ^{4}He on the 3N force constant c_D appearing in Eq. (4). In the figure, results from the first order ring diagram ("HF"), up to the second order one("Up to 2nd"), and all order ring diagrams ("Ring(all)") are all calculated with V_{3N} included. Experimental data [11] are displayed for comparison. Although the contribution from diagrams up to the second order one improves quite significantly comparing to that from the first order one alone, contribution from higher order diagrams is needed to fill the discrepancy so that the experimental binding energy can be obtained.

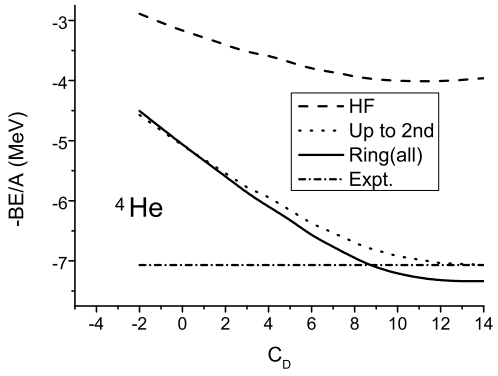

Figure 2: Dependence of $-BE/A$ of ^{4}He on the parameter c_D of V_{3N}.

As shown in Table I, our results from $V_{2N} + \bar{V}_{3N}$ with parameter c_D= 8.5 and its corresponding c_E from [5] at density ρ/ρ_0= 0.3 for ^{4}He fits the experimental data [11] quite well. In

the Table we also examine the importance of V_{3N} to the nuclear binding energy. As expected, the binding energy obtained from V_{2N} alone is too weak. The deviation between results with and without V_{3N} gets wider when all ring diagrams are included.

Table 1: Ground-state energy E_0/A (or -BE/A)(in MeV) of ^{4}He calculated with 1st-, (1st+2nd)- and all-order ring diagrams. The parameter $c_D = 8.5$ of $\bar{V}_{3N}$ is employed.

		ρ/ρ_0	1st	1st+2nd	all rings	Expt
^{4}He	V_{2N}	–	-3.46	-5.36	-5.39	
	V_{2N}+$\bar{V}_{3N}$	0.3	-3.96	-6.77	-7.05	-7.073

In conclusion, our calculated ground state energy per nucleon fits the experimental data quite well when V_{3N} is added in and all orders of ring diagrams are included. Contributions from ring diagrams with orders higher than 2 can not be ignored. As expected, binding energy obtained with V_{2N} alone is too weak. This study shows that the three-nucleon force is important in nuclear systems. We have found that the above results are also true for several other closed-shell nuclei. This will appear in other separate publications.

References

[1] H. Q. Song, S. D. Yang and T.T.S. Kuo, Nucl. Phys. **A462**, 491 (1987); Yiharn Tzeng, T. T. S. Kuo,Nucl. Phys. A485, 85 (1988).

[2] T. T. S. Kuo and E. Osnes, *Lecture Notes in Physics* (Springer-Verlag, New York), Vol. 364 (1990) p.1.

[3] M. C. M. Rentmeester, R. G. E. Timmermans, and J. J. de Swart, Phys. Rev. C **67** (2003) 044001.

[4] A. Nogga, H. Kamada and W. Glockle, Phys. Rev. Lett. **94**, 944 (2000); S.C. Peiper, K. Varga and R. B. Waringa, Phys. Rev. **C66**, 044310 (2002).

[5] P. Navratil, V.G. Gueorguiev, J.P. Vary, W.E. Ormand and A. Nogga, Phys. Rev. Lett. **99**, 042501 (2007).

[6] D. R. Entem, R. Machleidt, and H. Witala, Phys. Rev. C **65**, 064005 (2002).

[7] J. W. Holt, N. Kaiser and W. Weise, Phys. Rev. **C79**, 054331 (2009); J. W. Holt, N. Kaiser and W. Weise, Phys. Rev. **C81**, 024002 (2010).

[8] S. K. Bogner, T. T. S. Kuo and L. Coraggio, Nucl. Phys. **A684**, (2001) 432; S. K. Bogner, T. T. S. Kuo, L. Coraggio, A. Covello, and N. Itaco, Phys. Rev. C **65**, 051301(R) (2002); S. K. Bogner, T. T. S. Kuo, and A. Schwenk, Phys. Rep. **386**, 1 (2003).

[9] J.S.Mccarthy, I. Sick, and R.R. Whitney, Phys. Rev. C **15**, 1396 (1977); H. de Vries, C.W. de Jager, and C. de Vries, At. Data Nucl. data Tables, **36**, 495 (1987)

[10] I. Angeli, K.P. Marinova, Atomic and Nucl. Data Tables **99** 69 (2013).

[11] B.Pfeiffer,K.Venkataramaniaih,U.Czok,C.Scheidenberger, Atomic and Nucl. Data Tables **100** 403-535 (2014); Nuclear data from Brookhaven National Laboratory, http://www.nndc.bnl.gov/chart/

Higgs boson as a gluon trigger: the study of QCD in high pile-up environments

H. Van Haevermaet[1,2], *P. Cipriano*[1], *S. Dooling*[1], *A. Grebenyuk*[3], *P. Gunnellini*[1,2], *F. Hautmann*[4,5,6], *H. Jung*[1,2], *P. Katsas*[1]

[1]Deutsches Elektronen Synchrotron, D 22603 Hamburg
[2]Universiteit Antwerpen, Elementaire Deeltjes Fysica, B 2020 Antwerpen
[3]Université Libre De Bruxelles, I.I.H.E., B 1050 Bruxelles
[4]University of Sussex, Physics & Astronomy, Brighton BN1 9QH
[5]University of Oxford, Physics Department, Oxford OX1 3NP
[6]Rutherford Appleton Laboratory, Chilton OX11 0QX

DOI: http://dx.doi.org/10.3204/DESY-PROC-2014-04/280

1 Introduction

To study QCD one typically measures processes in single proton-proton collisions. A particular interesting one is the Drell-Yan $q\bar{q} \xrightarrow{\gamma^*/Z^0} l^+l^-$ process, which is produced through an electroweak current that couples to quarks. A big advantage is its clean final state, which only involves the decay leptons. This allows us to use the process to precisely measure quark structure functions, quark induced parton showers, and underlying event properties. The properties and structure functions of gluons however, have to be determined indirectly. But with the recent discovery [1] of the Higgs boson, this picture changes. In the heavy top limit, the Higgs boson directly couples to gluons and can be produced with the gluon fusion $gg \to H$ process through a colour singlet current [2]. The access to this new production process opens up a whole new interesting area of possible QCD measurements, where we can directly study gluon induced effects. In addition, if we only look at decay channels of the Higgs boson like $H \to ZZ \to 4l$, we have access to the same clean final state as in the Drell-Yan process. In order to produce enough statistics for detailed measurements, current accelerators like the LHC at CERN have to operate at very high beam intensities. This high luminosity allows one to measure differential distributions, e.g. the transverse momentum [3] of the Higgs, but it also creates a condition in which on average much more than one proton-proton collision happens per bunch crossing. This so called pile-up (PU) can easily reach, given the LHC run conditions, scenarios where PU = 40 (i.e. 40 additional proton-proton collisions occur on top of the one signal event). This implies that the phase space will be completely filled with extra hadronic activity coming from the pile-up events, which makes a study of QCD in the Higgs or Drell-Yan channels extremely difficult. To assess whether one can still perform QCD measurements in such harsh environments we initiated a new program using the Higgs boson as a gluon trigger [4]. The main idea is to compare Higgs and Drell-Yan production in the same invariant mass range, and then look at different observables, such as the transverse momentum of the bosons, to measure the difference in soft multi-gluon emissions. Here we present pile-up studies to show

whether the Higgs to Drell-Yan comparison stays valid in high pile-up environments.

The Monte Carlo event generator samples used in this study are all produced with Pythia 8.185 [5]. All samples contain proton-proton collisions at $\sqrt{s} = 7$ TeV, with the 4C tune [6] to describe the underlying event properties. The Higgs sample is generated by activating the gluon fusion process $gg \to H$, while the Drell-Yan sample is generated using the single Z^* production process $f\bar{f} \to Z^{0*}$. The bosons are produced within the same invariant mass range of $115 < \mathrm{M} < 135$ GeV and in addition, to avoid complications with the leptonic final states, they are set stable. The Higgs mass is set to 125 GeV. To study the effect of additional pile-up events, samples with a fixed amount of PU = 5 and PU = 20 are produced. This is done by adding a specified number of small-p_T QCD process events to the signal event. All jets are constructed with the anti-k_T algorithm [7] with a distance parameter R = 0.5.

2 Transverse momentum spectra

Initial studies presented in [4] show the implicit difference in the inclusive p_T spectra of Higgs and Drell-Yan production, due to different soft gluon emissions. Here we analyse what happens when one includes additional PU events. By definition, as we put the bosons stable, the p_T spectra should be independent. This is confirmed in figure 1a, where both the PU = 0 and PU = 20 scenarios are compared for Higgs and Drell-Yan production. Thus, if the experimental reconstruction of the leptonic decay products is stable in high PU environments, the p_T spectrum should be stable. One can then take the ratio (Higgs/DY) of both spectra and use this observable to directly quantify the gluon versus quark radiation effects.

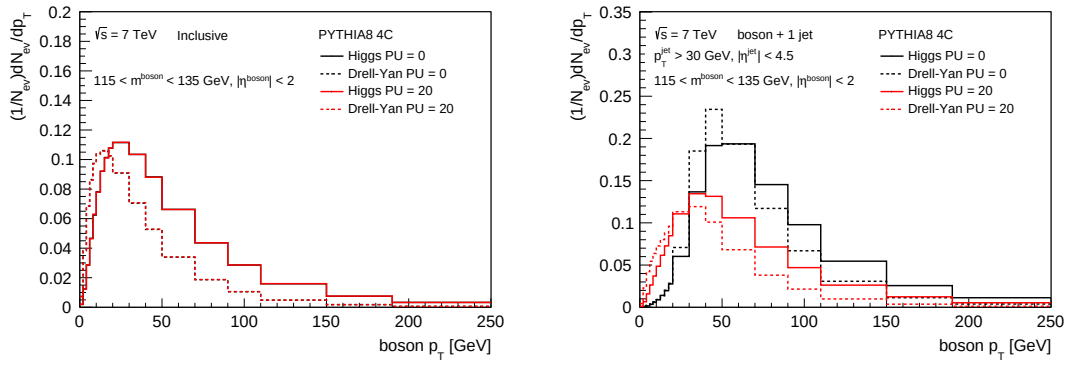

(a) (b)

Figure 1: The inclusive (a) and boson + 1 jet (b) Higgs and Drell-Yan transverse momentum p_T spectra for PU = 0 and PU = 20 scenarios.

In addition, one can look at the boson + 1 jet production process. This topology is expected to be more sensitive to gluon versus quark emission effects, as hard radiation accompanies the boson production. However, requiring an additional hard jet ($p_\mathrm{T} > 30$ GeV/c, $|\eta| < 4.5$) shifts the spectrum towards higher transverse momenta as a result of the induced p_T balance between the boson and the hard jet. As such, the contribution of gluon versus quark induced effects will actually become less pronounced in the p_T spectrum. These effects are illustrated in figure

1b. Furthermore, figure 1b also shows the results of adding additional PU events. In this case, both spectra shift to lower values. This is the consequence of jet mismatching that occurs due to the extra PU activity. That is, in the presence of PU, there is a higher probability that a high p_{T} jet comes from an independent PU interaction and is identified as the jet coming from the signal event, which can result in a matching of a high p_{T} jet with a low p_{T} boson.

3 Underlying event observables

A very interesting observable to study QCD in proton-proton collisions is the underlying event activity [8]. Common measurements [8, 9] look at the charged particle multiplicity and scalar p_{T} sum in the so called *transverse* region, which is defined as $60^{\mathrm{o}} < |\Delta\phi| < 120^{\mathrm{o}}$, with $\Delta\phi$ the difference in azimuthal angle between the charged particle and the leading (high p_{T}) object, in our case the Higgs or Z boson, that defines the hard scale of the event. With the produced boson in the *towards* region ($|\Delta\phi| < 60^{\mathrm{o}}$), and the recoil jet in the *away* region ($|\Delta\phi| > 120^{\mathrm{o}}$), the transverse region is only sensitive to the underlying event. Furthermore, when only the leptonic decay channel of the bosons is considered, one has access to a clean final state, with no contributions from final state radiation (FSR), resulting in a sensitivity to only initial state radiation (ISR) and multiple parton interactions (MPI). Obviously, when including additional proton-proton collisions to the event, the number of charged particles (and the scalar p_{T} sum) will increase drastically and directly scale to the number of PU events. However, we can show that when we subtract the underlying event activity in the Drell-Yan process, from the underlying event in the Higgs process, i.e.:

$$\frac{dn}{dp_{\mathrm{T}}}\,(\mathrm{H}-\mathrm{DY}) = \frac{dn}{dp_{\mathrm{T}}^{\mathrm{H}}} + \frac{dn}{dp_{\mathrm{T}}^{\mathrm{PU}}} - \left(\frac{dn}{dp_{\mathrm{T}}^{\mathrm{DY}}} + \frac{dn}{dp_{\mathrm{T}}^{\mathrm{PU}}}\right), \tag{1}$$

the PU contribution completely cancels out. This is confirmed in figures 2a and 2b that show the result of the subtraction. For both additional PU activity of 5 and 20 the subtracted underlying event stays stable. This implies that even in high PU environments one is able to measure small-p_{T} QCD physics. It is possible to subtract the PU contribution and study the difference in underlying event activity between Higgs and Drell-Yan production, which is directly sensitive to gluon versus quark induced ISR.

4 Summary

The Higgs $gg \to H$ production process provides new perspectives for interesting QCD measurements that allow us to directly probe gluon physics. This is possible due to the electroweak current, which, in the heavy top limit, directly couples to gluons. In addition, the colour singlet state and leptonic decay channels allow us to study events in which no complications from final state effects occur. We presented a novel method that compares Higgs and Drell-Yan production in the same invariant mass and rapidity range to perform a direct measurement of gluon versus quark induced processes. First we investigated the inclusive and boson + 1 jet p_{T} spectra. The inclusive spectrum is found to be sensitive to soft multi-gluon emissions, and is stable in high PU environments. The boson + jet event topologies however suffer from PU effects, that originate from the jet mismatching between signal and PU events. In addition we also studied the underlying event activity by looking at the charged particle multiplicity and scalar Σp_{T} in

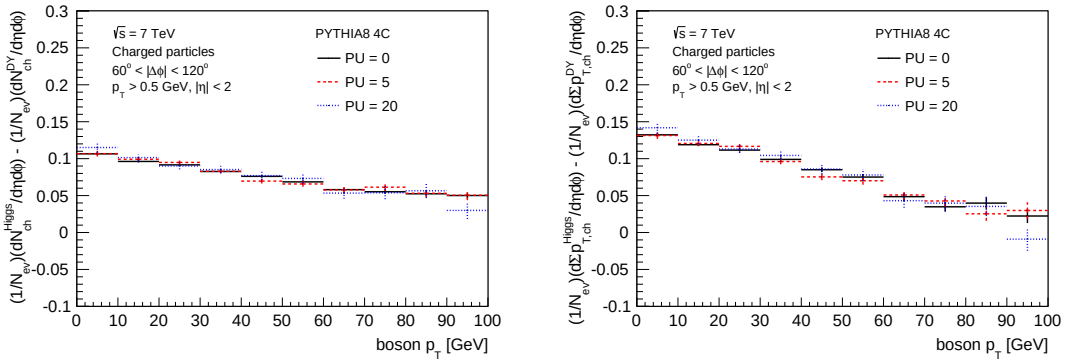

(a) (b)

Figure 2: The subtracted average charged particle multiplicity (a), and average scalar sum of transverse momenta (Σp_{T}) (b) in the transverse region of the azimuthal plane versus transverse momentum p_{T} of the produced boson. For PU = 0, PU = 5 and PU = 20 scenarios.

the transverse region. We constructed the subtracted underlying event observable (see eq. 1) and found that it is stable in high PU environments. Thus, by comparing Higgs to Drell-Yan production we can subtract the PU contributions, and directly measure the difference in gluon versus quark induced initial state radiation effects. Such that one can still access (small-p_{T}) QCD physics in high pile-up environments.

Acknowledgements

We are grateful to the organisers, convenors and participants of the PANIC conference for this opportunity to present and discuss our results in the poster session. The primary author is funded by the Research Foundation of Flanders (FWO).

References

[1] ATLAS Coll. (G. Aad et al.), Phys. Lett. **B716** (2012) 1; CMS Coll. (S. Chatrchyan et al.), Phys. Lett. **B716** (2012) 30.

[2] H. M. Georgi, S. L. Glashow, M. E. Machacek, and D. V. Nanopoulos, Phys. Rev. Lett. **40**, 692 (1978); J. Ellis, M.K. Gaillard and D. Nanopoulos, Nucl. Phys. **B106** (1976) 292; M.A. Shifman, A.I. Vainshtein, M.B. Voloshin and V.I. Zakharov, Sov. J. Nucl. Phys. **30** (1979) 711.

[3] ATLAS Coll., ATLAS note ATLAS-CONF-2013-072.

[4] P. Cipriano et al., Phys. Rev. D **88**, 097501 (2013).

[5] T. Sjöstrand, S. Mrenna, P. Skands, Comput.Phys.Commun.178:852-867 (2008).

[6] R. Corke and T. Sjöstrand, JHEP **1103** (2011) 032, [arXiv:1011.1759].

[7] M. Cacciari, G. P. Salam, G. Soyez, JHEP **0804** (2008) 063.

[8] R.D. Field, arXiv:1010.3558 [hep-ph].

[9] CMS Coll. (S. Chatrchyan et al.), JHEP **1109** (2011) 109.

List of Authors